Investigating the Effects of Fluorine Substituents on Organic Dyes in Dye-Sensitized Solar Cells

Saifaldeen Muwafag Abdalhadi[1]* iD , Nabeel Mohammed[2] iD , Khalida Ali Thejeel[3] iD ,

Hazim Al-Zubaidi[4] iD

[1]Department of Remote Sensing, College of Remote Sensing and Geophysics, Al-Karkh University of Science, Baghdad, Iraq.
[2]Department of Biology, College of Education Al-Hawija, University of Kirkuk, Kirkuk, Iraq.
[3]Department of Geophysics, College of Remote Sensing and Geophysics, Al-Karkh University of Science, Baghdad, Iraq.
[4]Governmental programs department, Ministry of Higher Education and Scientific Research.

Abstract: We synthesized and evaluated five organic dyes that featured both mono- and di-substituted fluorine atoms for application in dye-sensitized solar cells (DSSCs). The dye structure was designed with *N, N*-dimethylaniline as a donor, fluorophenyl as an π-conjugated bridge, and cyanoacetic acid as an anchoring and acceptor group. The fluorine substituents are strong electron-withdrawing groups, introducing different numbers and positions of fluorine atoms (*ortho* and *meta*) that were expected to the ability of the acceptor parts of the dye. The results showed that adding the fluorine mono-substitution in the *ortho* position can enhance the efficiency of the solar cells in comparison with the meta-substitution and unsubstituted one. However, the di-substitution by fluorine atoms in two *ortho* positions and *ortho*, *meta* positions reduced the performance of the solar cells. The reason was related to the effect of π-conjugation between the fluorine substituent and the carbonyl group of the carboxylic acid. The DSSCs based on dye **14** achieved the best results with power conversion efficiency (PCE) = 3.33%, (J_{sc} = 5.43 mA cm^{-2}, V_{oc} = 0.81V and FF = 75.85%) under standard conditions with I_3^-/I^- as the electrolyte.

1. INTRODUCTION

Photovoltaic technologies have significantly developed over the last two decades, starting by investigating new types of solar cells such as quantum dot cells and thin film crystal cells, followed by improving the efficiency of other photovoltaic cells such as perovskite solar cells, from 14.0% to 22.1%, and three junction solar cells, from 32%.6 to 44.4% (1-5). In the present day, silicon solar cells are restricted to the photovoltaic market, despite their environmental effects and expensive production, the new generation of solar cells, such as dye-synthesized solar cells (DSSCs) has become one of the most important of the third generation solar cells due to their several advantages such as easy to fabrication, colorful, work in dark condition, vast design organic dye as an active layer and

environmentally friendly (6-8). In addition, natural dyes could be used in DSSCs as an active layer, and carbonaceous material was used instead of expensive metals as an auxiliary electrode to reduce the cost of the fabrication process (9). The first report on DSSC was done by O'Regan and Grätzel in 1991 with an efficiency of 7.1% (10) and after several years, the efficiency of DSSC was improved to 14.7% (11).

The DSSCs were made from four main components: the first part is a photo-anode which is made from mesoporous nano-oxide layers such as TiO_2 or ZnO, the second part is a monolayer of organic or organometallic dye and was used as an active layer to harvest the light and generate the electrical power, the third part is the electrolyte solution and usually used iodine couple redox (I^-/I_3^-) in an aprotic

solvent to transfer the electron from auxiliary electrode to the dye. The last part is a counter electrode which is made from conductive glass coated by a platinum or graphene layer (12, 13).

The dyes of the DSSC play an important role in the efficiency of the solar cells and all the dyes should have photophysical and electrochemical properties such as luminescent, covering the ultraviolet-visible spectra to the near-infrared region, and hydrophobic properties to enhance the stability of the solar cells (14). Two types of dyes can be used as an active layer in DSSC; the first type is an organometallic dye, such as Ru-family complexes (N3, N719, and C101), (15-17) These have many advantages such as stability in the oxide state, gave instance charge transfer from metal to the ligand in the visible region and effective charge injection to the nano-semiconductor layer. The limitation of the organometallic dye is related to the cost of novel metal, low extinction coefficients, and decomposition or isomerization during purification (18, 19). The second type of dye is a metal-free organic dye and usually used dyes based on the chromophore such as coumarins (20), indolines (21), and triphenylamines (22) which absorb the light around 650 nm. These types of dyes usually have many advantages if compared with organometallic dyes such as high extinction coefficients (>2.50 × 10^4 M^{-1} cm^{-1}, in the visible region), flexibility in dye design, ease of purification and more economical than organometallic dye (23). In general, many efficient organic dyes have been reported with typical configuration for dye structure design, which is often considered as a donor π-bridge, and acceptor parts.

In this work, we designed and synthesized five simple organic free metal dyes with different fluorine positions and used these dyes as a dye in DSSCs (Scheme 1). The design of these dyes was represented by *N, N*-dimethylaniline as a donor part, benzene with different fluorine substitution as a π-conjugated bridge, and cyanoacetic acid as an acceptor part. All these dyes were characterized by ^1H NMR, ^{13}C NMR spectroscopies, and mass spectrometry, as well as all the results, were supported by the computational study. Several studies in the past were rented the fluorine atoms substitution in the π-bridge or acceptor parts in the organic dye for DSSCs and all of these introduced single position substitution within the molecular structure of the dye, (24, 25) thus improving the knowledge, we increased the substitution of the fluorine by mono-fluoro and di-fluoro at different positions. The idea for using fluorination to their spacer units was to create more efficient dyes for DSSCs by decreasing the lowest unoccupied molecular orbital (LUMO) energy level of the dye when increasing the number of fluorine atoms due to their highly electron-weighing ability as well as the fluorine atoms were substituted in π-bridge unit (benzene ring) for additional acceptor unit to improve the transfer of an electron from donor to anchoring group by electron-withdrawing effect and reduced the energy gap of the dye (26).

2. EXPERIMENTAL

2.1. General Information
All starting materials were supplied by Sigma-Aldrich® and Alfa Aesar®. The solvents were used without any purification. All reactions were performed under a nitrogen atmosphere and monitored using TLC plates. ^1H NMR spectra and ^{13}C NMR were recorded at 400 MHz and 100 MHz respectively on Bruker Avance III 400 spectrometers. UV-Vis absorption spectra were performed on a Shimadzu (UV-3600 UV-Vis-NIR spectrophotometer). The optical energy gap (E_{opt}) was calculated by using the absorption edge of the λ_{max} absorption peak by equation E_{opt} (eV) = 1240/λ (nm). Mass spectra were obtained on a JEOL SX-102A by using the fast atom bombardment (FAB) or electron impact (EI) technique. Elemental analysis was obtained on a Heraeus CHN-O Rapid Elementary Analyzer. The spectra are obtained in the Supplementary Information Section at the end of the article.
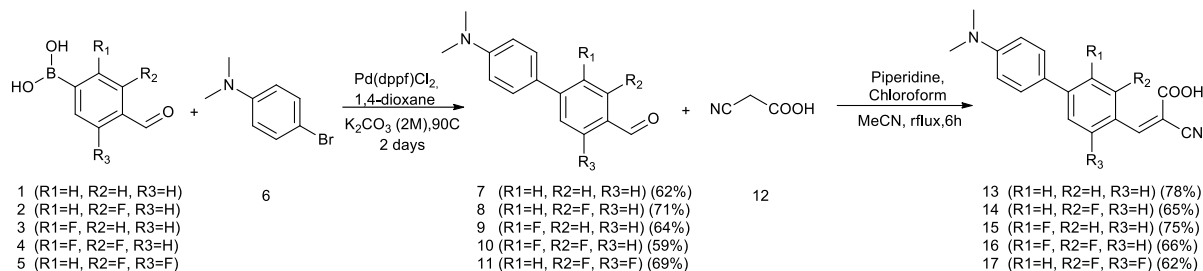
2.2. Synthesis
2.2.1. General procedure for the synthesis of compounds 7-11
Boronic acid derivative 1-5 (2.0 mmol) and 4-Bromo-*N, N*-dimethylaniline (0.40 g, 2.0 mmol) were introduced to the 2-neck round bottom flask under a nitrogen atmosphere. 1,4-dioxane (15 mL) was added and the reaction mixture was stirred for 10 min at 50 ℃. An aqueous solution of 2 M K_2CO_3 (0.20 mL, 0.40 mmol) and Pd(dppf)Cl$_2$ (6.3 mg) was added and the mixture was stirred at 100 ℃ (monitored by TLC). After 2 days, the mixture was cooled to room temperature, poured into cold water (40 mL), and extracted with dichloromethane (3 × 40 mL) in a separating funnel. The organic layer was dried over MgSO$_4$ and the solution was concentrated under reduced pressure. The crude compound was purified by column chromatography.

2.2.2. General procedure for the synthesis of compounds 13-17
Aldehyde derivative 7-11 (0.5 mmol), cyanoacetic acid (60 mg, 0.7 mmol), and MgSO$_4$ (60 mg, 0.26 mmol) were added in a mixture of acetonitrile and chloroform 1: 1 (10 mL + 10 mL), and the mixture was stirred for 15 minutes under nitrogen atmosphere. Piperidine (0.10 mL, 0.13 mmol) was added and the mixture was stirred at reflux for 6 hours. Afterward, the reaction was allowed to cool to room temperature, and cold water (50 mL) was added to the mixture in a separating funnel. The aqueous layer was extracted with ethyl acetate (3 × 40 mL) and then, the organic extracts were dried over MgSO$_4$. The crude solution was dried under vacuum and purified by column chromatography.

Scheme 1: Synthesis of organic dyes **13**-**17** for DSSCs.

2.3. Spectral Data for the Products

4'-(dimethylamino)-[1,1'-biphenyl]-4-carbaldehyde (**7**) $C_{15}H_{15}NO$, m.p.:147-150 ℃; (^1H NMR, 400 MHz, DMSO, TMS) δ_H: 9.95 (s, 1H, CHO), 7.91 (d, 2H, J_{HH} = 7.8 Hz, CH-Ar), 7.73 (d, 2H, J_{HH}= 7.8 Hz. CH-Ar), 7.37 (d, 2H, J_{HH} = 6.8 Hz. CH-Ar), 6.88 (d, 2H, J_{HH} = 6.8 Hz. CH-Ar), 2.91 (s, 6H, NCH$_3$). (^{13}C NMR, 100 MHz, DMSO, TMS) δ_C: 191.90, 147.92, 143.52, 138.04, 131.23, 130.43, 128.14, 127.80, 114.58, 39.99. Anal. calcd.; C = 79.97; H = 6.71; N = 6.22. Found C,= 79.91; H = 6.75; N = 6.18. EI-MS: *m/z* 225.

4'-(dimethylamino)-3-fluoro-[1,1'-biphenyl]-4-carbaldehyde (**8**) $C_{15}H_{14}FNO$, m.p.:149-152 ℃; (^1H NMR, 400 MHz, DMSO, TMS) δ_H: 10.12 (s, 1H, CHO), 7.95 (d, 1H, J_{HH} = 10.5 Hz, CH-Ar), 7.60 (d, 2H, J_{HH} = 10.5 Hz,), 7.40 (d, 2H, J_{HH} = 8.1 Hz, CH-Ar), 6.87 (d, 2H, J_{HH} = 8.1 Hz, CH-Ar), 2.95 (s, 6H, NCH$_3$). (^{13}C NMR, 100 MHz, DMSO, TMS) δ_C: 185.79, 162.12, 148.44, 145.23, 138.82, 130.28, 128.62, 128.35, 124.29, 114.21, 113.68, 42.90. Anal. calcd.; C = 74.06; H = 5.80; N = 5.76; Found C = 73.98; H = 5.77; N = 5.69; EI-MS: *m/z* 243.

4'-(dimethylamino)-2-fluoro-[1,1'-biphenyl]-4-carbaldehyde (**9**) $C_{15}H_{14}FNO$, m.p.: 154-157 ℃; (^1H NMR, 400 MHz, DMSO, TMS) δ_H: 9.94 (s, 1H, CHO), 7.80 (m, 3H, CH-Ar), 7.75 (d, J_{HH}= 8.2 Hz, 2H, CH-Ar), 7.52 (d, J_{HH} = 8.2 Hz, 2H, CH-Ar), 2.98 (s, 6H, NCH$_3$). (^{13}C NMR, 100 MHz, DMSO, TMS) δ_C: 190.67, 158.67, 150.45, 139.09, 130.88, 128.77, 128.26, 127.90, 127.38, 115.79, 115.11, 44.61. Anal.calcd; C = 74.06; H = 5.80; N = 5.76; Found C = 74.71; H = 5.79; N = 5.77; EI-MS: *m/z* 243.

4'-(dimethylamino)-2,3-difluoro-[1,1'-biphenyl]-4-carbaldehyde(**10**) $C_{15}H_{13}F_2NO$, m.p. 166-169 ℃; (^1H NMR, 400 MHz, DMSO, TMS) δ_H: 10.14 (s, 1H, CHO), 7.71 (s, 1H, CH-Ar), 7.64 (s, 1H, CH-Ar), 7.58 (d, J_{HH} = 10.1 Hz, 2H, CH-Ar), 7.42 (d, J_{HH} = 10.1 Hz, 2H, CH-Ar), 2.99 (s, 6H, NCH$_3$). (^{13}C NMR, 100 MHz, DMSO, TMS) δ_C: 187.18, 149.59, 149.52, 145.20, 135.81, 128.83, 127.44, 126.35, 126.03, 123.45, 115.08, 43.22. Anal.calcd; C = 68.96; H = 5.02; N = 5.36; Found C = 69.05; H = 5.12; N = 5.33; EI-MS: *m/z* 261.

4'-(dimethylamino)-3,5-difluoro-[1,1'-biphenyl]-4-carbaldehyde(**11**) $C_{15}H_{13}F_2NO$, m.p. 164-167 ℃; (^1H NMR, 400 MHz, DMSO, TMS) δ_H: 10.15 (s, 1H, CHO), 7.55 (s, CH-Ar), 7.40 (d, J_{HH} = 9.3 Hz, 2H, CH-Ar), 6.97 (d, J_{HH} = 9.3 Hz, 2H, CH-Ar), 2.94 (s, 6H, NCH$_3$). (^{13}C NMR, 100 MHz, DMSO, TMS) δ_C: 180.68, 160.83, 148.63, 145.90, 130.16, 128.45, 114.16, 111.71, 110.04, 42.01. Anal.calcd; C = 68.96; H = 5.02; N = 5.36 Found C = 69.02; H = 5.02; N = 5.38; EI-MS: *m/z* 261.

(*E*)-2-cyano-3-(4'-(dimethylamino)-[1,1'-biphenyl]-4-yl)acrylic acid (**13**) $C_{18}H_{16}N_2O_2$, m.p. > 250 ℃; (^1H NMR, 400 MHz, DMSO, TMS) δ_H: 8.48 (s, 1H, C=CH), 7.51(d, J_{HH} = 7.1, 2H, CH-Ar), 7.49 – 7.41 (m, 4H, CH-Ar), 6.74 (d, J_{HH} = 7.8, 2H, CH-Ar), 2.88 (s, 6H, CH$_3$). (^{13}C NMR, 100 MHz, DMSO, TMS) δ_C: 162.67, 147.92, 140.14, 138.99, 133.97, 130.44, 128.82, 127.80, 114.57, 111.24, 102.51, 41.90. Anal.calcd; C = 73.95; H = 5.52; N = 9.58; Found C = 73.88; H = 5.49; N = 9.59; (FAB)$^+$ [M]$^+$: *m/z* 292.

(*E*)-2-cyano-3-(4'-(dimethylamino)-3-fluoro-[1,1'-biphenyl]-4-yl)acrylic acid (**14**) $C_{18}H_{15}FN_2O_2$, m.p. > 250 ℃; (^1H NMR, 400 MHz, DMSO, TMS) δ_H: 8.45 (s, 1H, C=CH), 7.54 – 7.40 (m, 5H, CH-Ar), 6.76 (d, J_{HH} = 7.1 Hz, 2H, CH-Ar), , 2.92 (s, 6H, CH-Ar). (^{13}C NMR, 100 MHz, DMSO, TMS) δ_C: 162.07, 159.15, 156.53, 148.44, 143.74, 141.18, 130.36, 129.81, 128.35, 126.34, 119.28, 114.89, 111.24, 105.75, 42.98. Anal.calcd; C = 69.67; H = 4.87; N = 9.03; Found C = 69.63; H = 4.91; N = 8.96; (FAB)$^+$ [M]$^+$: *m/z* 310.

(*E*)-2-cyano-3-(4'-(dimethylamino)-2-fluoro-[1,1'-biphenyl]-4-yl)acrylic acid (**15**) $C_{18}H_{15}FN_2O_2$, m.p. > 250 ℃; (^1H NMR, 400 MHz, DMSO,TMS) δ_H; 8.44 (s, 1H, C=CH), 7.60 (d, J_{HH} = 7.8 Hz, 1H, CH-Ar), 7.42 (d, J_{HH} = 10.2 Hz, 2H, CH-Ar), 7.29 (d, J_{HH} = 7.8 Hz, 2H, CH-Ar) 6.76 (d, J_{HH} = 10.2 Hz, 2H, CH-Ar), 2.81 (s, 6H, CH$_3$). (^{13}C NMR, 100 MHz, DMSO, TMS) δ_C; 161.97, 159.35, 150.45, 139.10, 133.58, 128.79, 126.76, 126.49, 124.48, 115.11, 113.17, 111.24, 102.58, 42.01. Anal.calcd; C = 69.67; H = 4.87; N = 9.03; Found C = 69.60; H = 4.77; N = 9.12; (FAB)$^+$ [M]$^+$: *m/z* 310.

(*E*)-2-cyano-3-(4'-(dimethylamino)-2,3-difluoro-[1,1'-biphenyl]-4-yl)acrylic acid (**16**) $C_{18}H_{14}F_2N_2O_2$, m.p. > 250 ℃; (^1H NMR, 400 MHz, DMSO, TMS) δ_H: 8.49 (s, 1H, C=CH), 7.44 (d, 2H, J_{HH} = 6.4 Hz, CH-Ar),7.34 (s, 1H, CH-Ar), 7.22 (s, 1H, CH-Ar), 6.75 (d, J_{HH} = 6.4 Hz, 2H, CH-Ar), 2.80 (s, 6H, CH$_3$). (^{13}C NMR, 100 MHz, DMSO,TMS) δ_C: 162.87, 149.59, 146.99, 145.09, 142.46, 129.71, 128.83, 127.43, 126.35, 122.66, 121.90, 115.08, 109.25, 104.69, 43.09. Anal.calcd; C = 65.85; H = 4.30; N = 8.53; Found C = 65.71; H = 4.31; N = 8.59; (FAB)$^+$ [M]$^+$: *m/z* 328.

(***E***)-2-cyano-3-(4'-(dimethylamino)-3,5-difluoro-[1,1'-biphenyl]-4-yl)acrylic acid (**17**) $C_{18}H_{14}F_2N_2O_2$, m.p. > 250 ℃; (^{1}H NMR, 400 MHz, DMSO, TMS) δ_H: 8.51 (s, 1H, C=CH), 7.49 (d, 2H, J_{HH} = 9.0 Hz, CH-Ar), 7.27 (s, 2H, CH-Ar), 6.84 (d, J_{HH} = 9.0 Hz, 2H, CH-Ar), 2.81 (s, 6H, CH$_3$). (^{13}C NMR, 100 MHz, DMSO, TMS) δ_C; 163.01, 160.59, 157.96, 148.63, 145.84, 142.32, 130.16, 128.54, 114.16, 112.21, 111.24, 111.19, 108.77, 43.17. Anal.calcd; C, 65.85; H, 4.30; N, 8.53; Found C, 65.82; H, 4.33; N, 8.48; (FAB)$^+$ [M]$^+$: *m/z* 328.

3. FABRICATION OF DSSCs

Indium tin oxide (ITO) glass sheets (2 cm × 2 cm, 15 Ω/sq) were cleaned in distilled water by using an ultrasonic bath (5 minutes) and then rinsed with absolute ethanol. The TiO$_2$ paste was prepared by adding absolute ethanol (5 mL) to the TiO$_2$ nano-powder (3 g, ~ 25 nm) with grinding for 15 minutes, then added acetic acid (0.1 mL) and Triton X-100 (0.05 mL) to paste with grinding for 30 minutes to prevent the aggregation of the TiO$_2$ particles .

The doctor blade technique was used to prepare the TiO$_2$ film on ITO glass by applying two parallel strips of scotch tape on the conductive side of the ITO glass to deposit the TiO$_2$ past on the conductive glass between the two pieces of the scotch tape and coating by the doctor blade method. After one hour the scotch tape was removed carefully and the coated glass was dried for 15 minutes at 75 °C and then sintered for 45 minutes at 400 °C, Finally, the coated glass was cooled down to room temperature, and then placing the coated glass to the solution of the dye for 2 hours under dark condition. The electrolyte solution I_3^-/I^- was formed by adding 1.0 M KI and 0.10 M I$_2$ to the acetonitrile solvent and stored in a dark container. H$_3$PtCl$_6$ solution in isopropanol (3 mg/mL) was used to prepare the counter electrode of the cells by depositing the solution onto ITO glass by spin coating technique. Finally, coated glass and counter electrode were combined with added few drops of electrolyte solution on an active layer for the photovoltaic measurement device.

4. RESULT AND DISCUSSION

4.1. Synthesis

Five dyes with different fluoro substitutions (**13**-**17**) were prepared according to Scheme 1. These dyes were synthesized by using two simple steps involving the Suzuki cross-coupling reaction the and Knoevenagel condensation reaction. The first step was represented by a Suzuki cross-coupling reaction between 4-Bromo-*N*, *N*- dimethylaniline, and boronic acid derivatives (**1**-**5**) by using Pd(dppf)Cl$_2$ as a catalyst and this reaction gave a good yield (~ 60%-70%). The next step was obtained with a Knoevenagel condensation reaction to prepare the final compound (**13**-**17**). The reaction was performed between aldehyde derivatives (**7**-**11**) and cyanoacetic acid with a small amount of piperidine as a catalyst and the yields of final products were rounded between ~ 62%-78%. There is a big difference between the yields of the final compounds and that is because of the steric hindrance between fluorine atoms and the cyanoacetic acid group which led to a decrease in the quantity of the yield.

4.2. Optical properties

The UV-Vis spectra of five compounds are shown in Figure 1 and the related photochemical properties are reported in Table 1. All organic compounds show two significant absorption peaks at 280-320 nm and 440-500 nm. The first absorption peaks are attributed to the electron transition of π - π*, and the second absorption bands are attributed to the transition of intramolecular charge transfer (ICT) from a donor (dimethylaniline) to an acceptor (cyanoacetic acid). It is not much different in the absorption maxima between these dyes. However, the absorption maxima band of compounds **15** and **16** exhibited a slight red shift from the original compound **13**, while the compounds **14** and **17** showed a blue shift and that could be from the steric effect between fluorine atoms in ortho position and cyanoacetic acid part as well as deportation of a carboxylic acid with the solvent (27, 28). The range of molar extinction coefficients of these compounds is between 2.22-2.30 × 10^4 M^{-1} cm^{-1} and that is higher than from standard dye N719 (1.41 × 10^4 M^{-1} cm^{-1}) which is given a good light harvesting nature for the dyes.

Table 1: Shows the optical and theoretical parameters of the dyes (**13**-**17**).

Compound	λ_{abs}^{a}(nm)	λ_{max}^{b} (ε × 10^{-4}, dm^3 mol^{-1} cm^{-1})	E_{opt}^{c} (eV)	E$_{HOMO}$^{d} (eV)	E$_{LUMO}$^{d} (eV)	E$_{gap}$^{d} (eV)
13	474	2.26	2.07	-5.71	-3.09	2.48
14	458	2.28	2.23	-5.58	-3.17	2.41
15	502	2.22	1.96	-5.65	-3.28	2.42
16	489	2.25	2.10	-5.62	-3.28	2.34
17	467	2.27	2.09	-5.51	-3.29	2.22

^{a} Maximum of absorption in THF (1 × 10^{-4} M), ^{b} extinction coefficient, ^{c} optical energy gap, and ^{d} theoretical calculation.
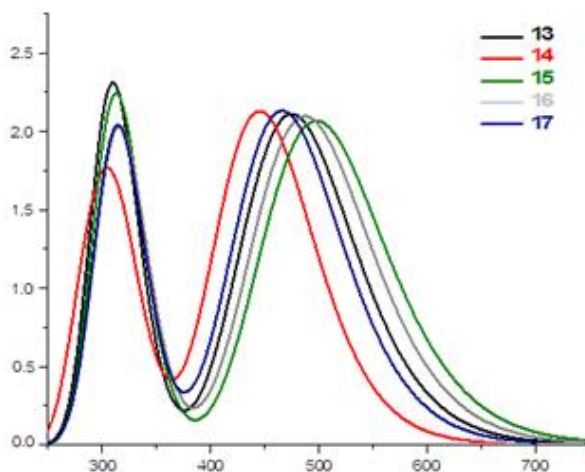
Figure 1: Absorption spectra of dyes **13-17** in THF (1×10^{-4}). Y axis is absorbance, and X axis is wavelength in nanometers.

4.3. Theoretical Calculations

Density functional theory (DFT) and time-dependent-density functional theory (TD-DFT) were calculated using Gaussian 09. The geometry optimization of all dyes and the vibrational harmonic frequencies were computed using Becke's three-parameter hybrid, and Lee Yang Parr's gradient corrected correlation (B3LYP) functional with standard split valence 6-311G (d,p) as a basis set under vacuum (29). All the calculations have been done by using the polarization function for heavy atoms (d) and hydrogen atoms (p). All results show the absence of imaginary frequency which indicates that the optimizations of all structures were rare energy minima (30). The optimization geometry (Figure 2) of the dyes was observed as the dihedral angle between two benzene rings of about 30°, for compounds **13**, **14,** and **17**, while this angle was evaluated to 35° for compounds **15** and **16** due to the steric effect between fluorine atom and the other benzene ring. These angles gave good solubility for all the dyes because they prevent aggregation due to π-stacks between the surfaces of molecules (31).

The highest occupied molecular orbital (HOMO) and lowest unoccupied molecular orbital (LUMO) were reported in Figure 2 and Table 1. For all dyes, the electron distribution of HOMO was delocalized in the donor part (dimethylaniline) and the electron distribution of LUMO was spread over the acceptor's arm (Fluoro- benzene and cyanoacetic acid) which is indicative that gave a good charge separation during the excitation process. The HOMOs level of the dyes **13**,**14**,**15**,**16**, and **17** are -5.7, -5.58, -5.65, -5.62, and 5.51 eV, respectively and all of these levels are lower than the energy level of the electrolyte solution I_3^-/I^- (-4.8) which indicate that the excited electron was relaxed easily form energy level of redox solution to the HOMOs level of the dyes. Also, the LUMOs level of the dyes **13**,**14**,**15**,**16**, and **17** are -3.09, -3.17, -3.28, -3.28, and -3.29 respectively and all of these levels are higher than the conduction band (CB) of the TiO_2 (-4.0 eV) which indicate that the excited electron was easily transfer from HOMOs level of the dyes to the CB of the TiO_2 (32).

The lowest energy gap was represented with compound **17,** (2.22 eV) due to the effect of two fluorine atoms with high electronegativity, which decreased the LUMO level of the dye, while the highest energy gap was illustrated with compound **13**, (2.48 eV) which indicate that the π-bridge with the fluorine atom played the important role in the excitation of electrons. The energy gap of the dyes is arranged in order **13** (2.48 eV), **15** (2.42 eV), **14** (2.41 eV), **16** (2.34 eV), **17** (2.22 eV).

Dyes	Optimization Geometry	HOMO	LUMO
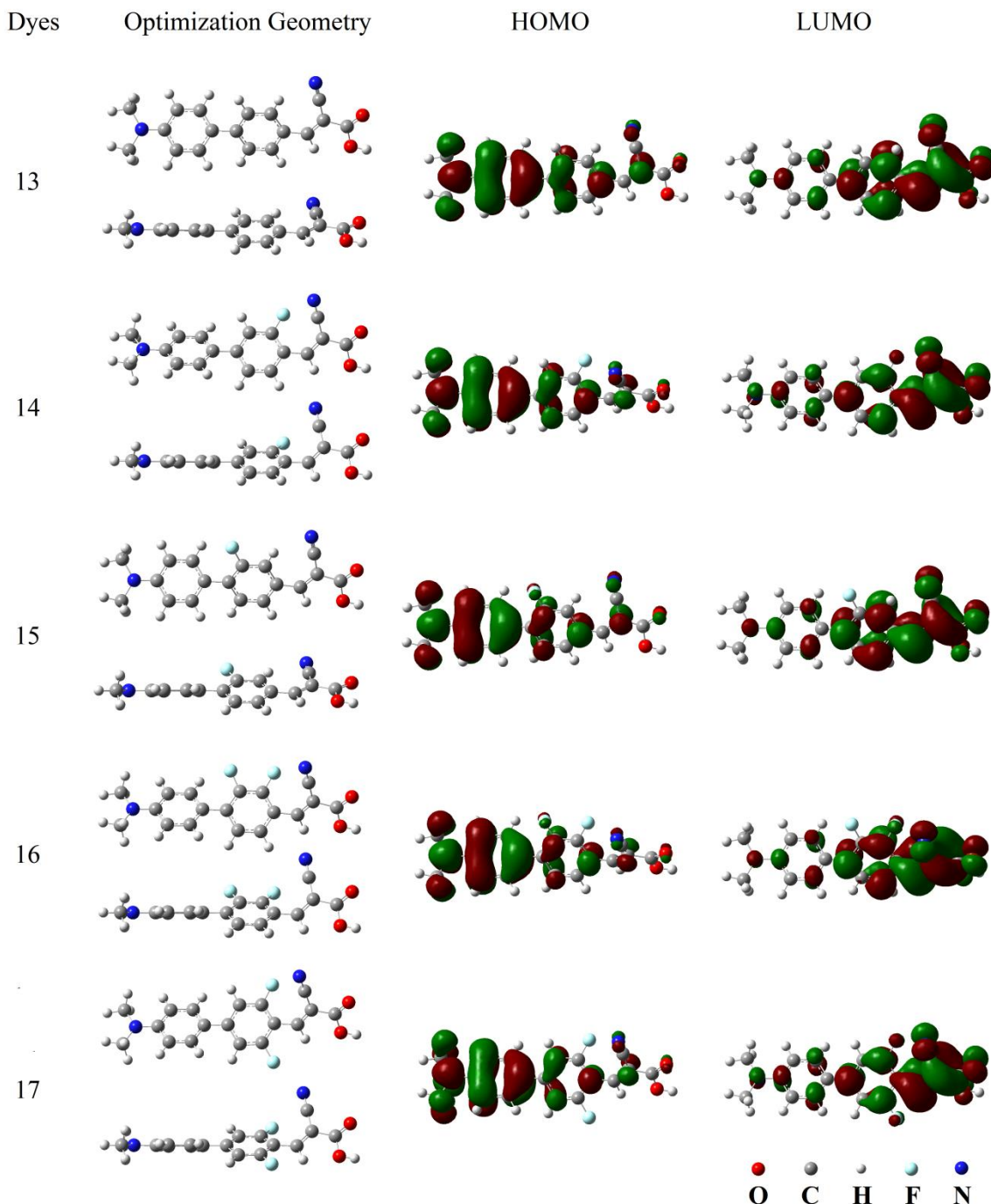
Figure 2: The optimization geometries, HOMOs, and LUMOs for prepared dyes.

4.5 Device Testing and Photovoltaic Performance

The photovoltaic properties were investigated for all dyes in DSSCs, the current density and voltaic performance (*J-V*) were measured in Table 2 and shown in Figure 3. The measurements of the solar cells were done under the standard condition at AM 1.5G and solar irradiation (100 mW cm^{-2}). The control dye N719 was included as a comparison. In general, the performances of dyes **13**, **14**, and **15** were slightly better than difluoro substitution and that could be due to the deviation conformation (steric effect) between the bulk cyanoacrylate group and difluorophenyl moieties, which decreased the effect of π-conjugation. The dye **14** exhibited a higher power conversion efficiency (PCE) of 3.33% with a J_{sc} of 5.43 mA cm^{-2}, V_{oc} of 0.81 V, and *FF* of 75.85%. While compound **16** showed a lower PCE of 2.14% under the same condition (J_{sc} = 3.94 mA cm^{-2}, V_{oc} of 0.80 V, and *FF* of 71.10%). The DSSCs devices based on compound **14** exhibited a higher J_{sc} and molar extinction coefficient, which compensated for the negative impact of the UV-Vis absorption spectra. Furthermore, compared with dye **13** (non-fluorine substitution), dye **14** and **15** (mono-fluorine substitution) gives slightly higher current density 5.43 and 5.08 mA cm^{-2} respectively, while compound **16** and **17** (di-fluoro substitution) shows slightly lower current density 3.94 and 4.14 mA cm^{-2} respectively, which indicate that the compound **14** and **15** had a strong electronic coupling with the surface (TiO$_2$) and hence increase of the dye uptake. On the other hand, the efficiency of the dyes was affected directly by the fluorine atom position, the *ortho*-fluorine substituted **14** gives a higher PCE than *meta*-fluorine substituted **15** and that could be by

the resonance conjugation between the *ortho*-fluorine substituted and carbonyl group of carboxylic acid which increased the basicity of dye and improvement the TiO$_2$ affinity.

Table 2: Photovoltaic performance of the DSSCs under global conditions (AM 1.5, 100 mW cm^{-2}).

Dye	J_{sc} (mA cm^{-2})	V_{oc} (V)	*FF* (%)	PCE (%)
13	4.52	0.87	76.68	3.01
14	5.43	0.81	75.85	3.33
15	5.08	0.80	76.63	3.11
16	3.94	0.80	71.10	2.41
17	4.14	0.82	74.90	2.54
N719	10.30	0.92	79.96	7.57
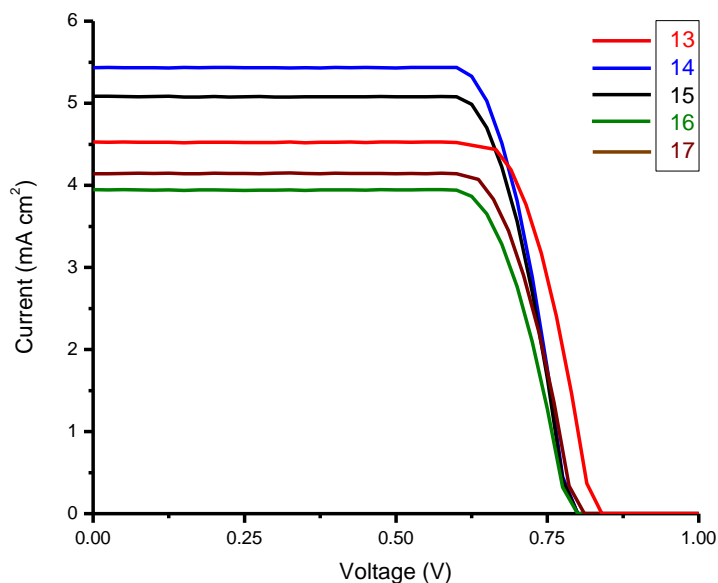
Figure 3: Current density vs. voltage (*J–V*) curves for dyes **13**,**14**,**15**,**16**, and **17**.

5. CONCLUSION

In summary, a series of non-metal dyes containing different fluoro-positions on a π-bridge were analyzed. The mono-fluoro substituted compounds exhibited similar PCE values to the non-substituted ones. In contrast, the di-fluoro substituted showed a lower PCE due to increasing the dihedral angle between the benzene ring and the cyanoacetic acid group and that reduced the ability of the conjugation system, therefore the value of J_{sc} was low. The device based on dyes **14** and **15** had higher J_{sc} values (5.48 and 5.08 mA cm^{-2} respectively) than dyes **13**, **16**, and **17** (4.52, 3.94, and 4.14 mA cm^{-2} respectively) which was in agreement with PCE values of the dyes. These results showed that the addition of electron-withdrawing on the ortho position could increase the PCE of the DSSCs.

6. CONFLICT OF INTEREST

There are no conflicts of interest.

7. ACKNOWLEDGMENT

8. REFERENCES

1. Sharma S, Jain KK, Sharma A. Solar Cells: In Research and Applications—A Review. Mater Sci Appl [Internet]. 2015 Dec 1;06(12):1145–55. Available from: <URL>.

2. Abdulrazzaq OA, Saini V, Bourdo S, Dervishi E, Biris AS. Organic Solar Cells: A Review of Materials, Limitations, and Possibilities for Improvement. Part Sci Technol [Internet]. 2013 Sep 3;31(5):427–42. Available from: <URL>.

3. Ajayan J, Nirmal D, Mohankumar P, Saravanan M, Jagadesh M, Arivazhagan L. A review of photovoltaic performance of organic/inorganic solar cells for future renewable and sustainable energy technologies. Superlattices Microstruct [Internet]. 2020 Jul 1;143:106549. Available from: <URL>.

4. Day J, Senthilarasu S, Mallick TK. Improving spectral modification for applications in solar cells: A review. Renew Energy [Internet]. 2019 Mar 1 [cited 2023 Oct 24];132:186–205. Available from: <URL>.

5. Abdulhussein SF, Abdalhadi SM, Hanoon HD. Synthesis of new imidazole derivatives dyes and application in dye sensitized solar cells supported by

DFT. Egypt J Chem [Internet]. 2022 Feb 5;65(9):211–7. Available from: <URL>.

6. Abdalhadi SM, Al-Baitai AY, Al-Zubaidi HA. Synthesis and Characterization of 2,3-Diaminomaleonitrile Derivatives by One-Pot Schiff Base Reaction and Their Application in Dye Synthesized Solar Cells. Indones J Chem [Internet]. 2020 Dec 22;21(2):443. Available from: <URL>.

7. Cariello M, Abdalhadi SM, Yadav P, Decoppet J-D, Zakeeruddin SM, Grätzel M, et al. An investigation of the roles furan *versus* thiophene π-bridges play in donor–π-acceptor porphyrin based DSSCs. Dalt Trans [Internet]. 2018;47(18):6549–56. Available from: <URL>.

8. Abdalhadi SM, Connell A, Zhang X, Wiles AA, Davies ML, Holliman PJ, et al. Convenient synthesis of EDOT-based dyes by CH-activation and their application as dyes in dye-sensitized solar cells. J Mater Chem A [Internet]. 2016;4(40):15655–61. Available from: <URL>.

9. Gong J, Sumathy K, Qiao Q, Zhou Z. Review on dye-sensitized solar cells (DSSCs): Advanced techniques and research trends. Renew Sustain Energy Rev [Internet]. 2017 Feb;68:234–46. Available from: <URL>.

10. O'Regan B, Grätzel M. A low-cost, high-efficiency solar cell based on dye-sensitized colloidal TiO_2 films. Nature [Internet]. 1991 Oct;353(6346):737–40. Available from: <URL>.

11. Kakiage K, Aoyama Y, Yano T, Oya K, Fujisawa J, Hanaya M. Highly-efficient dye-sensitized solar cells with collaborative sensitization by silyl-anchor and carboxy-anchor dyes. Chem Commun [Internet]. 2015;51(88):15894–7. Available from: <URL>.

12. Devadiga D, Selvakumar M, Shetty P, Santosh MS. Dye-Sensitized Solar Cell for Indoor Applications: A Mini-Review. J Electron Mater [Internet]. 2021 Jun 1;50(6):3187–206. Available from: <URL>.

13. Mohammed N, Shakkor SJ, Abdalhadi SM, Al-Bayati YK. Two multifunctional benzoquinone derivatives as small molecule organic semiconductors for bulk heterojunction and perovskite solar cells. Main Gr Chem [Internet]. 2022 Dec 20;21(4):943–52. Available from: <URL>.

14. Sharma K, Sharma V, Sharma SS. Dye-Sensitized Solar Cells: Fundamentals and Current Status. Nanoscale Res Lett [Internet]. 2018 Dec 28;13(1):381. Available from: <URL>.

15. Talodthaisong C, Wongkhan K, Sudyoadsuk T, Saengsuwan S, Jitchati R. Comparison of the DSSC Efficiency on Synthetic N3 Dyes. Adv Mater Res [Internet]. 2015 Dec;1131:165–8. Available from: <URL>.

16. Portillo-Cortez K, Martínez A, Dutt A, Santana G. N719 Derivatives for Application in a Dye-Sensitized Solar Cell (DSSC): A Theoretical Study. J Phys Chem A [Internet]. 2019 Dec 26;123(51):10930–9.

Available from: <URL>.

17. Liu S, Liu J, Wang T, Wang C, Ge Z, Liu J, et al. Preparation and photovoltaic properties of dye-sensitized solar cells based on zinc titanium mixed metal oxides. Colloids Surfaces A Physicochem Eng Asp [Internet]. 2019 May;568:59–65. Available from: <URL>.

18. Numata Y, Islam A, Chen H, Han L. Aggregation-free branch-type organic dye with a twisted molecular architecture for dye-sensitized solar cells. Energy Environ Sci [Internet]. 2012;5(9):8548–52. Available from: <URL>.

19. Ahmad S, Guillén E, Kavan L, Grätzel M, Nazeeruddin MK. Metal free sensitizer and catalyst for dye sensitized solar cells. Energy Environ Sci [Internet]. 2013;6(12):3439–66. Available from: <URL>.

20. Sarrato J, Pinto AL, Malta G, Röck EG, Pina J, Lima JC, et al. New 3-Ethynylaryl Coumarin-Based Dyes for DSSC Applications: Synthesis, Spectroscopic Properties, and Theoretical Calculations. Molecules [Internet]. 2021 May 14;26(10):2934. Available from: <URL>.

21. Al-horaibi SA, Asiri AM, El-Shishtawy RM, Gaikwad ST, Rajbhoj AS. Indoline and benzothiazole-based squaraine dye-sensitized solar cells containing bis-pendent sulfonate groups: Synthesis, characterization and solar cell performance. J Mol Struct [Internet]. 2019 Nov;1195:591–7. Available from: <URL>.

22. Pati PB, Yang W, Zade SS. New dyes for DSSC containing triphenylamine based extended donor: Synthesis, photophysical properties and device performance. Spectrochim Acta Part A Mol Biomol Spectrosc [Internet]. 2017 May;178:106–13. Available from: <URL>.

23. Lee C-P, Lin RY-Y, Lin L-Y, Li C-T, Chu T-C, Sun S-S, et al. Recent progress in organic sensitizers for dye-sensitized solar cells. RSC Adv [Internet]. 2015;5(30):23810–25. Available from: <URL>.

24. Chang YJ, Chow TJ. Highly efficient triarylene conjugated dyes for sensitized solar cells. J Mater Chem [Internet]. 2011;21(26):9523–31. Available from: <URL>.

25. Chen D-Y, Hsu Y-Y, Hsu H-C, Chen B-S, Lee Y-T, Fu H, et al. Organic dyes with remarkably high absorptivity; all solid-state dye sensitized solar cell and role of fluorine substitution. Chem Commun [Internet]. 2010;46(29):5256–8. Available from: <URL>.

26. Chen B-S, Chen D-Y, Chen C-L, Hsu C-W, Hsu H-C, Wu K-L, et al. Donor–acceptor dyes with fluorine substituted phenylene spacer for dye-sensitized solar cells. J Mater Chem [Internet]. 2011;21(6):1937–45. Available from: <URL>.

27. Wang Z-S, Cui Y, Dan-oh Y, Kasada C, Shinpo A, Hara K. Thiophene-Functionalized Coumarin Dye for Efficient Dye-Sensitized Solar Cells: Electron

Lifetime Improved by Coadsorption of Deoxycholic Acid. J Phys Chem C [Internet]. 2007 May 1;111(19):7224–30. Available from: <URL>.

28. Yang H-Y, Yen Y-S, Hsu Y-C, Chou H-H, Lin JT. Organic Dyes Incorporating the Dithieno[3,2-*b*:2',3'- *d*]thiophene Moiety for Efficient Dye-Sensitized Solar Cells. Org Lett [Internet]. 2010 Jan 1;12(1):16–9. Available from: <URL>.

29. Frisch MJ, Trucks GW, Schlegel HB, Scuseria GE, Robb MA, Cheeseman JR, et al. Gaussian 16 Rev. C. 01, Wallingford, CT. Wallingford, CT. 2016;

30. Chen X, Jia C, Wan Z, Yao X. Organic dyes with imidazole derivatives as auxiliary donors for dye-sensitized solar cells: Experimental and theoretical investigation. Dye Pigment [Internet]. 2014 May;104:48–56. Available from: <URL>.

31. Aulakh RK, Sandhu S, Tanvi, Kumar S, Mahajan A, Bedi RK, et al. Designing and synthesis of imidazole based hole transporting material for solid state dye sensitized solar cells. Synth Met [Internet]. 2015 Jul;205:92–7. Available from: <URL>.

32. Duvva N, Eom YK, Reddy G, Schanze KS, Giribabu L. Bulky Phenanthroimidazole–Phenothiazine D−π−A Based Organic Sensitizers for Application in Efficient Dye-Sensitized Solar Cells. ACS Appl Energy Mater [Internet]. 2020 Jul 27;3(7):6758–67. Available from: <URL>.

Synthesis and Biological Evaluation of 1*H*-(Indole-5-yl)-3-Substituted-1,2,4-Oxadiazoles as Novel 5-Lox Inhibitors

**Berihu Tekluu[1]* , Siddaiah Vidavalur[1] , Sunanda Kumari Kadiri[2]**

[1]Aksum University, College of Natural and Computational Sciences, Department of Chemistry, Axum, Ethiopia.
[1]Andhra University, College of Science and Technology, Department of Organic Chemistry and FDW, Visakhapatnam, Andhra Pradesh, India
[2]Gitam University, Department of Microbiology & FST Visakhapatnam, Andhra Pradesh, India

Abstract: A series of indolyloxadiazoles were synthesized from amidoxime and indole 3-carboxaldehyde using CAN as a catalyst and PEG as a solvent. In *vitro,* a 5-LOX inhibitory assay has been performed for all the synthesized compounds. Among the tested compounds, **4bf** showed the highest potency (IC_{50} 18.78 μg/ml). The synthesized compound carried out docking on the 5-LOX enzyme protein crystal structure. Compound (**4bf**) docked snugly into the receptor site with a score of -9.1 Kcal/mol, and it showed strong hydrogen bond interactions with two key amino acids, **His368** and **Asn555**.

*Corresponding author. E-mail: tekluberihu@gmail.com

1.   INTRODUCTION

Over the past decades, the synthesis of heterocyclic compounds has become the cornerstone of synthetic organic chemistry due to the wide variety of their applications in medicinal and pharmaceutical chemistry (1). The key field of medicinal chemistry is the investigation of heterocycles as favored structures in drug discovery (2). Among them, oxadiazole and indole ring systems are ubiquitous structural units and important pharmacophores in several alkaloids and many biologically active compounds (3). Some of the recent studies have shown that 1,2,4-oxadiazole and its derivatives were reported to possess peptide inhibitory activity (4), anti-hyperglycemic (5), antiparasitic (6), anti-inflammatory (7), muscarinic (8), anticancer (9), antifungal (10), antibacterial (11), antitumor (12), histemic-H_3 (13), and signal transduction (14) activities.

Indole derivatives have a wide range of biological and pharmacological actions (15). Specifically, 3-substituted indole derivatives exhibit a variety of pharmacological effects, including antibacterial (16), anti-inflammatory (17), antitumor (18), anticancer (19), antihypertensive (20), antidepressant (21), antiviral (22) and anti-HIV (23) activities. Oxadiazole and indole-containing substances exhibit a diversity of biological roles. Therefore, the linked molecules of 3-substituted indole and oxadiazole frame structures, indole-based oxadiazoles, are useful physiologically active agents. Indole-substituted 1,2,4-oxadiazoles exhibit a broad spectrum of biological activities, including anticancer activity (24). Indole-substituted 1,2,4-oxadiazoles also act as 5-HT3 antagonists (25). Recently, oxadiazole ring containing indole alkaloids such as phidianidines A and B **(Fig. 1)** have been isolated by Marianna, C. et al., 2011 from the marine opisthobranch *mollusk phidianamilitaris* (26).
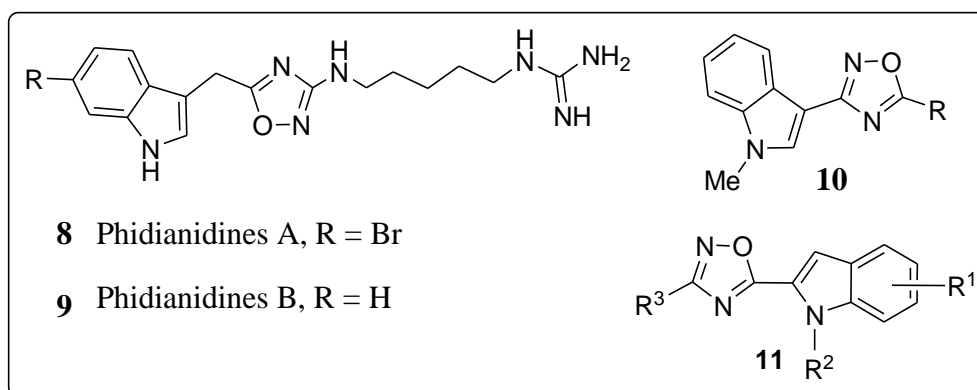
Figure 1: Bioactive indole substituted 1,2,4-oxadizoles

Lipoxygenases (LOXs), which are widely distributed in both the plant and animal kingdoms, belong to a class of non-heme iron-containing enzymes that catalyze the hydroperoxidation reaction of fatty acids to peroxides (27). In recent years, multi-functional inhibitors of 5-LOX and other enzymes in the arachidonic acid metabolic network have been paid much attention. Leukotrienes (LTs) have been identified as mediators of a variety of inflammatory and allergic reactions, including asthma, rheumatoid arthritis, inflammatory bowel disease, psoriasis, allergic rhinitis (28), stroke (29) and anticancer drugs (30). 5-LOX inhibitors structural and functional diversity of naturally occurring indole has made it a privileged pharmacophore in drug development where indole-based natural and synthetic compounds (31) find myriad properties as antibacterial anti-inflammatory (32), antitumor (33), anticancer (34), activities.

This is prompted by the wide range of activities of indole-substituted oxadiazoles and due to insufficient effective synthetic methods for synthesizing indole-substituted oxadiazoles and primarily focused on synthesizing a series of 1H-(indole-5-yl)-3-substituted 1,2,4-oxadiazoles and examining their 5-lipoxygenase inhibitory effects.

2.   EXPERIMENTAL

All the chemicals used were of synthetic grade procured from Sigma Aldrich. Progress of the reactions was monitored by analytical thin layer chromatography (TLC) using E-Merck 0.25 mm silica gel plates using ethyl acetate/hexane as a solvent system. Visualization was accomplished with UV light (256 nm) and an iodine chamber. Synthesized compounds were purified by column chromatography (silica gel 100-200 mesh) using a hexane and ethyl acetate mixture. Melting points were measured in open capillary tubes and were uncorrected; all the ^{1}H NMR and ^{13}C NMR spectra were recorded in CDCl$_3$/DMSO-d_6 solvent (400 MHz for ^{1}H and 100 MHz for ^{13}C) relative to TMS internal standard.

2.1. General procedure for the synthesis of 1H-(indole-5-yl)-3-substituted 1,2,4-oxadiazoles (4aa-4ah; 4ba-4bf)

In a 50-mL round-bottom flask equipped with a magnetic bar, benzonitriles (**1**) (1.0 mmol), hydroxylamine hydrochloride (0.5 mmol, 34.7 mg), triethylamine (0.9 mmol) and EtOH (1.5 mL) were added. The reaction mixture was heated to 80 °C under vigorous stirring. The reaction progress was monitored by TLC. After completion, the mixture (**2a**) cooled to room temperature and concentrated by using a rotary evaporator to remove ethanol solvent and then 1H-indole-3-carbaldehyde (**3a**) (1.2 mmol), CAN (0.5 mmol) and PEG (1.5 mL) were added to the round-bottom flask, and the mixture was stirred at 80 °C. The reaction progress was monitored by TLC; after completion, the reaction mixture was cooled to room temperature, and then the solution was extracted with ethyl acetate. The obtained organic layer was dried over anhydrous Na$_2$SO$_4$ and concentrated by using a rotary evaporator to get crude compound **4aa**, which was further purified by column chromatography on silica gel using petroleum ether/ethyl acetate as the eluent to give the desired target product (**4aa-4ah; 4ba-4bf**)

2.1.1. 3-(3-Phenyl-1,2,4-oxadiazol-5-yl)-1H-indole (4aa) (35)
White Solid; Yield: 83%; Mp: 170-172 °C; ^{1}H NMR (400 MHz, DMSO-d_6): δ 12.29 (d, 1H), 8.45 (d, 1H), 8.25 (d, 2H, J = 8 Hz), 8.15 (d, 1H, J = 2.8 Hz), 7.61 (t, 4H), 7.32 (d, 2H); ^{13}C NMR (100 MHz, DMSO-d_6): δ 173.7, 168.0, 137.0, 131.7, 131.3, 129.6, 127.5, 127.2, 124.8, 123.5, 122.2, 120.6, 113.1, 100.3; LC-MS: *m/z* = 262.1 [M+H]$^+$; Anal. Calcd. For C$_{16}$H$_{11}$N$_3$O: C, 73.57; H, 4.23; N, 16.07; Found: C, 73.54; H, 4.25; N, 16.01.

2.1.2. 3-(3-p-Tolyl-1,2,4-oxadiazol-5-yl)-1H-indole (4ab)
Yellow Solid; Yield: 81%; Mp: 137-139 °C; ^{1}H NMR (400 MHz, CDCl$_3$): δ 8.95 (d, 1H), 8.45 (d, 1H), 8.43 (d, 2H, J = 8 Hz), 7.82 (d, 1H), 7.52-7.50 (d, 1H, J = 8 Hz), 7.39-7.36 (m, 4H, J = 12 Hz), 2.46 (s, 3H); ^{13}C NMR (100 MHz, CDCl$_3$): δ 173.1, 168.4, 141.2, 136.1, 134.8, 129.5, 128.4, 127.4, 124.5, 123.8, 122.4, 121.3, 111.7, 102.8, 21.6; LC-MS: *m/z* = 276.8 [M+H]$^+$; Anal. Calcd. For C$_{17}$H$_{13}$N$_3$O: C, 74.17; H, 4.73; N, 5.79; Found: C, 74.09; H, 4.77; N, 5.75.

2.1.3.   3-(3-m-Tolyl-1,2,4-oxadiazol-5-yl)-1H-indole (4ac)
Yellow Solid; Yield: 84%; Mp: 204-206 °C; ^{1}H NMR (400 MHz, DMSO-d_6): δ 8.95 (d, 1H), 8.45 (d, 1H), 8.14 (d, 2H), 7.82 (d, 1H), 7.74 (d, 1H), 7.36 (m, 4H), 2.46 (s, 3H); ^{13}C NMR (100 MHz, DMSO-d_6): δ 173.1, 168.4, 141.2, 136.4, 134.8, 130.5, 128.6, 127.5, 124.8, 123.6, 122.4, 121.3, 119.7, 115.8, 111.7, 102.8, 21.9; LC-MS: m/z = 276.7 [M+H]$^+$; Anal. Calcd. For $C_{17}H_{13}N_3O$: C, 74.17; H, 4.73; N, 5.79; Found: C, 74.09; H, 4.75; N, 5.77.

2.1.4.   3-(3-(4-Methoxyphenyl)-1,2,4-oxadiazol-5-yl)-1H-indole (4ad)
Blue Solid; Yield: 82%; Mp: 121-122 °C; ^{1}H NMR (400 MHz, DMSO-d_6): δ 12.2 (d, 1H), 8.23 (d, 1H, J = 2.4 Hz), 8.22 (d, 1H J = 3.2 Hz), 8.065-8.06 (d, 2H, J = 2 Hz), 7.572-7.553 (d, 3H, J = 8 Hz), 7.292-7.273 (d, 2H J = 7.6 Hz), 3.84 (s, 3H); ^{13}C NMR (100 MHz, DMSO-d_6): δ 173.4, 167.7, 162.0, 136.9, 134.8, 131.1, 129.2, 124.8, 123.8, 122.1, 120.6, 119.5, 113.1, 100.4, 55.8; LC-MS: m/z = 292.8 [M+H]$^+$; Anal. Calcd. For $C_{17}H_{13}N_3O_2$: C, 70.06; H, 4.47; N, 14.41; Found: C, 70.03; H, 4.49; N, 14.38.

2.1.5.   3-(3-(4-Chlorophenyl)-1,2,4-oxadiazol-5-yl)-1H-indole (4ae) (36)
White Solid; Yield: 78%; Mp: 158-160 °C; ^{1}H NMR (400 MHz, DMSO-d_6): δ 12.29 (d, 1H), 8.43(d, 1H), 8.21 (d, 2H, J = 6.8 Hz), 8.05 (d, 1H, J = 8.1 Hz), 7.65 (d, 3H), 7.27 (d, 2H, J = 7.5 Hz); ^{13}C NMR (100 MHz, DMSO-d_6): δ 174.0, 167.0, 136.9, 134.6, 134.3, 131.7, 129.0, 126.8, 125.1, 124.7, 123.8, 122.1, 120.5, 113.3; LC-MS: m/z = 296.08 [M+H]$^+$; Anal. Calcd. For $C_{16}H_{10}ClN_3O$: C, 64.96; H, 3.40; N, 14.20; Found: C, 64.95; H, 3.45; N, 14.17.

2.1.6.   3-(3-(3-Chlorophenyl)-1,2,4-oxadiazol-5-yl)-1H-indole (4af)
Colorless Solid; Yield: 83%; Mp: 110-112 °C; ^{1}H NMR (400 MHz, DMSO-d_6): δ 12.30 (d, 1H), 8.23 (d, 1H, J = 4 Hz), 8.22 (s, 1H, J = 4 Hz), 8.21 (d, 1H, J = 6.4 Hz), 7.65 (m, 4H, J = 4 Hz), 7.64 (m, 2H, J = 4 Hz); ^{13}C NMR (100 MHz, DMSO-d_6): δ 174.0, 167.0, 136.9, 134.9, 134.3, 131.6, 129.1, 127.1, 126.1, 124.7, 123.8, 122.1, 120.5, 118.8, 113.3, 100.1; LC-MS: m/z = 296.9 [M+H]$^+$; Anal. Calcd. For $C_{16}H_{10}ClN_3O$: C, 64.96; H, 3.40; N, 14.20; Found: C, 64.95; H, 3.44; N, 14.15.

2.1.7.   3-(3-(4-Bromophenyl)-1,2,4-oxadiazol-5-yl)-1H-indole (4ag)
Yellow Solid; Yield: 75%; Mp: 155-157 °C; ^{1}H NMR (400 MHz, DMSO-d_6): δ 12.28 (d, 1H), 8.43 (d, 1H), 8.14 (d, 1H, J = 4 Hz), 8.13 (d, 2H, J = 4 Hz), 7.78 (d, 2H J = 8 Hz), 7.59 (d, 1H), 7.31 (t, 2H, J = 2.4 Hz); ^{13}C NMR (100 MHz, DMSO-d_6): δ 173.9, 167.3, 136.9, 132.7, 132.6, 131.4, 129.6, 127.5, 126.4, 124.8, 122.5, 120.5, 113.2, 100.2; LC-MS: m/z = 341.2 [M+H]$^+$; Anal. Calcd. For $C_{16}H_{10}BrN_3O$: C, 56.46; H, 2.96; N, 12.38; Found: C, 56.41; H, 2.98; N, 12.35.

2.1.8.   3-(3-(3-Bromophenyl)-1,2,4-oxadiazol-5-yl)-1H-indole (4ah)
Colorless Solid; Yield: 68%; Mp: 174-176 °C; ^{1}H NMR (400 MHz, DMSO-d_6): δ 12.28 (d, 1H), 8.43 (s, 1H), 8.25 (d, 1H), 8.11 (d, 2H), 7.75 (d, 2H), 7.53 (t, 1H), 7.31 (t, 2H); ^{13}C NMR (100 MHz, DMSO-d_6): δ 173.9, 167.3, 136.9, 132.7, 131.4, 130.6, 128.5, 127.5, 124.8, 122.3, 120.5, 118.8, 113.1, 100.2; LC-MS: m/z = 341.2 [M+H]$^+$; Anal. Calcd. For $C_{16}H_{10}BrN_3O$: C, 56.46; H, 2.96; N, 12.34; Found: C, 56.44; H, 2.99; N, 12.32.

2.1.9. 5-Bromo-3-(3-phenyl-1,2,4-oxadiazol-5-yl)-1H-indole (4ba)
White Solid; Yield: 76%; Mp: 211-213 °C; ^{1}H NMR (400 MHz, DMSO-d_6): δ 12.44 (d, 1H), 8.46-8.44 (s, 1H, J = 8 Hz), 8.31 (d, 1H, J = 3.2 Hz), 8.11-8.10 (d, 2H, J = 4 Hz), 7.58 (d, 2H), 7.54-7.53 (m, 2H, J = 4 Hz), 7.43-7.42 (m, 1H, J = 4 Hz); ^{13}C NMR (100 MHz, DMSO-d_6): δ 173.0, 168.1, 135.7, 132.4, 131.8, 129.6, 127.5, 127.0, 126.5, 126.2, 122.6, 115.2, 114.9, 100.0; LC-MS: m/z = 341.2 [M+H]$^+$; Anal. Calcd. For $C_{16}H_{10}BrN_3O$: C, 56.47; H, 2.96; N, 12.34; Found: C, 56.42; H, 3.01; N, 12.30.

2.1.10.   5-Bromo-3-(3-p-tolyl-1,2,4-oxadiazol-5-yl)-1H-indole (4bb)
White Solid; Yield: 72%; Mp: 217-219 °C; ^{1}H NMR (400 MHz, DMSO-d_6): δ 12.40 (d, 1H), 8.44 (s, 1H), 8.30 (d, 1H), 8.11 (d, 2H), 7.54 (d, 2H), 7.40 (d, 2H), 2.40 (s, 3H); ^{13}C NMR (100 MHz, DMSO-d_6): δ 173.0, 168.1, 138.7, 135.7, 132.4, 129.5, 127.8, 126.9, 126.5, 125.7, 124.7, 121.6, 115.2, 114.6, 100.1, 21.5; LC-MS: m/z = 355.8 [M+H]$^+$; Anal. Calcd. For $C_{17}H_{12}BrN_3O$: C, 57.62; H, 3.41; N, 11.86; Found: C, 57.59; H, 3.45; N, 11.82.

2.1.11.   5-Bromo-3-(3-m-tolyl-1,2,4-oxadiazol-5-yl)-1H-indole (4bc)
White Solid; Yield: 70%; Mp: 216-218 °C; ^{1}H NMR (400 MHz, DMSO-d_6): δ 12.40 (d, 1H), 8.446-8.442 (s, 1H, J = 1.6 Hz), 8.436-8.433 (d, 1H, J = 2 Hz), 7.54-7.53 (s, 2H, J = 4 Hz), 7.45 (d, 1H, J = 3.6 Hz), 7.45-7.40 (t, 3H, J = 8 Hz), 2.50 (s, 3H); ^{13}C NMR (100 MHz, DMSO-d_6): δ 173.0, 168.1, 138.9, 135.7, 132.4, 129.5, 127.8, 126.9, 126.5, 126.2, 124.7, 122.6, 115.2, 114.9, 100.0, 21.3; LC-MS: m/z = 355.2 [M+H]$^+$; Anal. Calcd. For $C_{17}H_{12}BrN_3O$: C, 57.60; H, 3.39; N, 11.85; Found: C, 57.58; H, 3.42; N, 11.83.

2.1.12.   5-Bromo-3-(3-(4-methoxyphenyl)-1,2,4-oxadiazol-5-yl)-1H-indole (4bd)
Yellow Solid; Yield: 73%; Mp: 190-192 °C; ^{1}H NMR (400 MHz, DMSO-d_6): δ 8.33 (d, 1H, J = 1.6 Hz), 8.32 (d, 1H), 8.072-8.05 (d, 2H, J = 8.8 Hz), 7.57-7.55 (d, 3H, J = 8 Hz), 7.409-7.404 (d, 2H, J = 1.6 Hz), 3.85 (s, 3H); ^{13}C NMR (100 MHz, DMSO-d_6): δ 172.8, 167.8, 162.0, 136.3, 135.7, 132.4, 129.2, 126.6, 122.6, 121.1, 119.3, 115.5, 100.0, 55.8; LC-MS: m/z = 371.8 [M+H]$^+$; Anal. Calcd. For $C_{17}H_{12}BrN_3O_2$: C, 55.12; H, 3.25; N, 11.35; Found: C, 55.10; H, 3.30; N, 11.32.

2.1.13.   5-Bromo-3-(3-(3-chlorophenyl)-1,2,4-oxadiazol-5-yl)-1H-indole (4be)

White Solid; Yield: 72%; Mp: 215-217 °C; ^{1}H NMR (400 MHz, DMSO-d_6): δ 12.43 (d, 1H), 8.48-8.46 (s, 1H, J = 8Hz), 8.298-8.293 (s, 1H, J = 2Hz), 8.206-8.202 (s, 1H, J = 8Hz), 8.115-8.095 (d, 1H, J = 8Hz), 7.816-7.814 (d, 1H, J = 8Hz), 7.58-7.56 (d, 2H, J = 8Hz), 7.446-7.442 (m, 1H, J = 1.6Hz); ^{13}C NMR (100 MHz, DMSO-d_6): δ 173.3, 166.9, 135.7, 134.6, 132.7, 131.9, 129.8, 129.2, 126.5, 126.4, 126.3, 122.7, 122.6, 115.3, 115.0, 99.8; LC-MS: m/z = 375.7 [M+H]$^+$; Anal. Calcd. For $C_{16}H_9BrClN_3O$: C, 51.28; H, 2.42; N, 11.21; Found: C, 51.26; H, 2.44; N, 11.17.

2.1.14.   5-Bromo-3-(3-(3-bromophenyl)-1,2,4-oxadiazol-5-yl)-1H-indole (4bf)

Yellow Solid; Yield: 68%; Mp: 127-129 °C; ^{1}H NMR (400 MHz, DMSO-d_6): δ 12.48-12.47 (d, 1H, J = 4Hz), 8.496-8.488 (s, 1H, J = 3.2Hz), 8.306-8.301 (s, 1H, J = 2Hz), 8.078-8.068 (d, 2H, J = 4Hz), 7.652-7.641 (d, 3H, J = 4.4Hz), 7.57-7.55 (t, 1H, J = 8Hz); ^{13}C NMR (100 MHz, DMSO-d_6): δ 173.4, 167.1, 135.7, 134.3, 132.8, 131.7, 129.0, 127.0, 126.5, 126.3, 126.2, 122.7, 122.6, 115.3, 115.0, 99.8; LC-MS: m/z = 420.11 [M+H]$^+$; Anal. Calcd. For $C_{16}H_9Br_2N_3O$: C, 45.84; H, 2.16; N, 10.03; Found: C, 45.77; H, 2.20; N, 10.01.

3. RESULTS AND DİSCUSSİON

A series of amidoximes from corresponding benzo-nitriles (**1a**) was prepared by reacting with hy-droxylamine hydrochloride, TEA, in ethanol under refluxing conditions. These amidoximes were fur-ther treated with 1*H*-indole-3-carboxaldehyde to afford the 1*H*-(indole-5-yl)-3-substituted-1,2,4-oxadiazoles. In a model study, benzamidoxime **(2a)** was treated with 1*H*-indole-3-carboxaldehyde **(3a)** in the presence of cerium ammonium nitrate (CAN) and polyethylene glycol (PEG) solvent at 80 °C, and it is formed the desired product **4aa** (scheme 1), albeit in a low yield of 60% (**Table 1, entry 1**). After the formation of product **4aa**, the reaction conditions were optimized in order to in-crease the yields. Thus, different solvents were screened, and the results are summarized in **Table 1**. PEG solvent was found to be the most superior in terms of product yields (**Table 1, entry 1**). The product yields maxi-mazed from 60% to 85% when the amount of CAN increases from (2 mol% to 5 mol%) (**Table 1, entry 5**). Further, increas-ing the quantity of CAN to 10 mol % decreased yields to 80% (**Table 1, entry 6**). The effect of temperature on the reaction rate, as well as on the yields of the products, was also investigated. On increasing the temperature from 80 °C to 120 °C, the product yields decreased (**Table 1, entries 7, 8**). Therefore, the subsequent reactions of several substituted benzamidoximes with 1*H*-indole-3-carboxaldehydes were carried out in the presence of CAN (5 mol%) as catalyst, PEG solvent, and temperature at 80 °C. The progress of the reac-tions was monitored by TLC analysis (using EtOAc-hexane as the eluent).

Table 1: Optimization of reaction conditions 4**aa**[a]

S.No	Solvent	Catalyst (mol %)	T (°C)	Yield[b] (%)
1	PEG	CAN (2 %)	80	60
2	CH$_3$CN	CAN (2 %)	80	40
3	DMF	CAN (2 %)	80	35
4	THF	CAN (2 %)	80	25
5	**PEG**	**CAN (5 %)**	**80**	**85**
6	PEG	CAN (10%)	80	80
7	PEG	CAN (5 %)	100	80
8	PEG	CAN (5 %)	120	78

[a]Reaction conditions: **1a** (1.5 equiv.), **2a** (1.2 equiv.), **3a** (1.2 equiv.), CAN (x equiv.), TEA (2 equiv.), NH$_2$OH.HCl, (3 equiv.), solvent (1.5 mL), and temperature 80 °C, [b]Isolated yields.

With optimized conditions in hand, the scope of the reaction was investigated, and the results are summarized in **Table 2**. As expected, various ben-zamidoximes were reacted smoothly with 1*H*-indole-3-carboxaldehyde to give the corresponding products in good to excellent yields (**Table 2, en-tries 4ab**-**4ah**). 5-Bromo-1*H*-indole-3-carboxaldehyde also undergoes smooth transfor-mation with different substituted benzamidoximes and affords the desired products (**Table 2, entries 4ba**-**4bf**) in good yields.
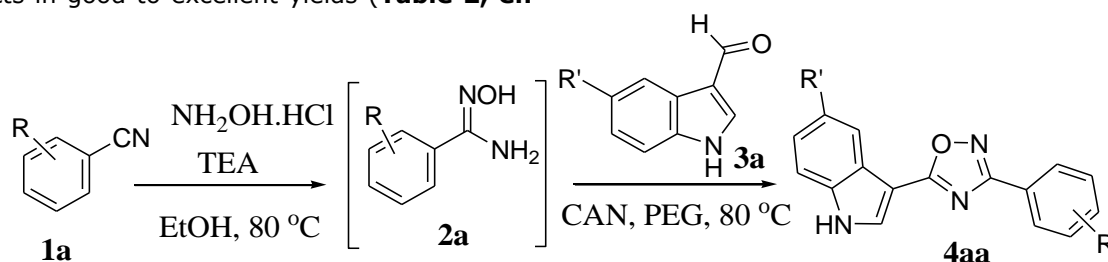
Scheme 1: Synthesis of oxadiazoles: Reagents and conditions: (i) NH$_2$OH.HCl, aqueous ethanol, reflux, 7 h; (ii) 1*H*-indole-3-carboxaldehyde, CAN, PEG, 80°C

Table 2: Structures and Yields of the Synthesized Compounds[a]

4aa, 85%

4ab, 81%

4ac, 84%

4ad, 82%

4ae, 78%

4af, 83%

4ag, 75%

4ah, 68%

4ba, 76%

4bb, 72%

4bc, 70%

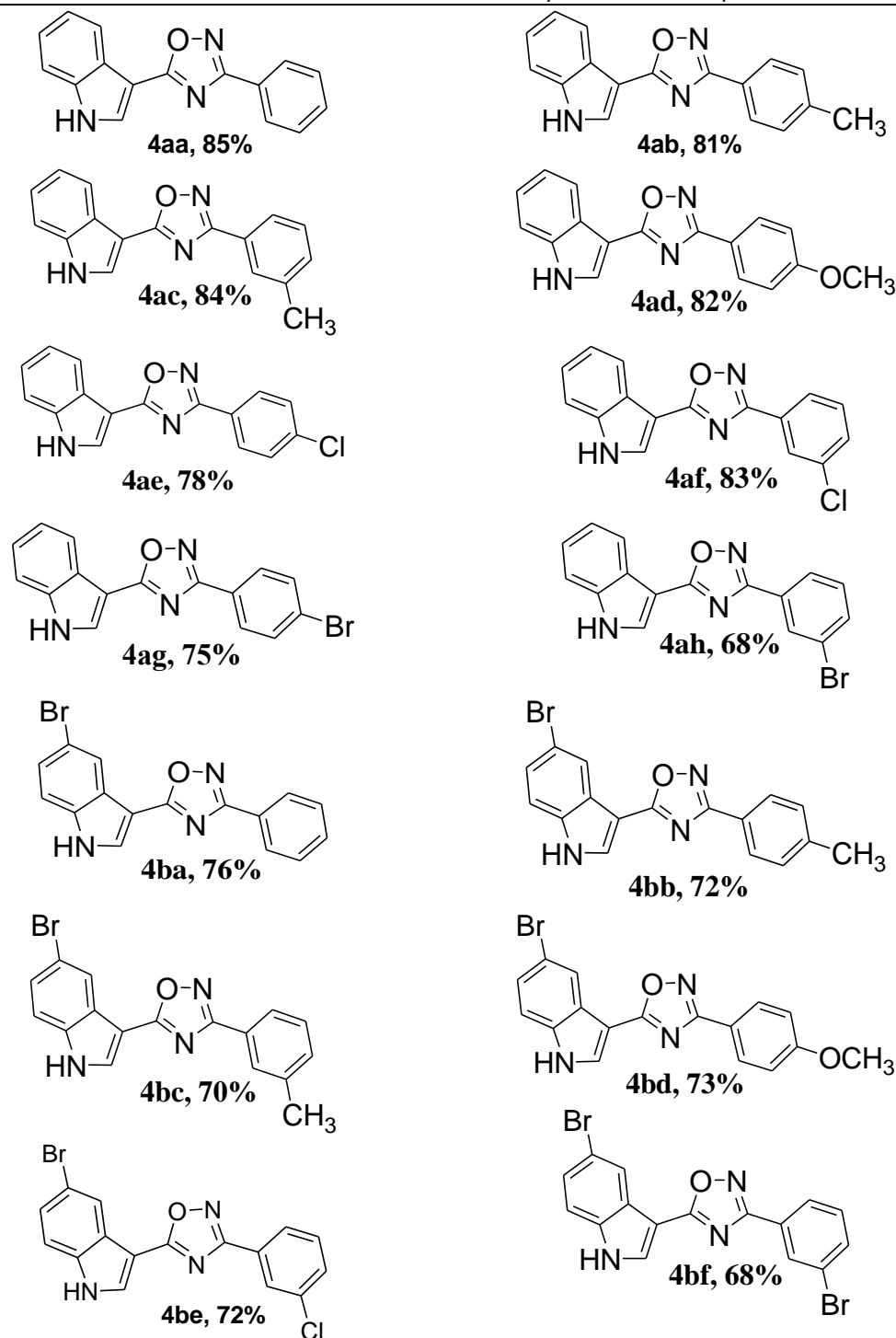4bd, 73%

4be, 72%

4bf, 68%

[a]Reaction conditions: **1a** (1.5 equiv.), **2a** (1.2 equiv.), **3a** (1.2 equiv.), CAN (x equiv.), TEA (2 equiv.), $NH_2OH.HCl$ (3 equiv.), solvent (1.5 mL), and temperature 80 °C.

3.1.   Biological Activity

3.1.1. 5-Lipoxygenase enzyme inhibitory activity
All the synthesized 1*H*-(indole-5-yl)-3-substituted 1,2,4-oxadiazoles were evaluated for 5-lipoxygenase (5-LOX) assay and found to have a significant 5-LOX enzyme inhibitory activity with IC_{50} range from 18.78 µg/ml to >100 µg/ml (**Table 3**). Compounds **4af** and **4bc** showed moderate

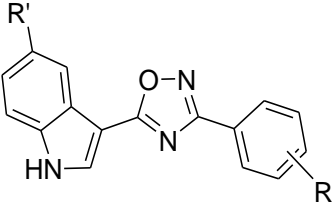enzyme inhibitory activity with IC_{50} of 25.78, 26.72, and 27.86 µg/ml, respectively. Bromo-substituted indolyl compounds **4ag, 4bb**, and **4bd** showed effective enzyme inhibitory activity with IC_{50} of 23.13, 20.86, 23.51, and 20.48 µg/ml, respectively. Amongst the synthesized compounds, **4bf** showed the highest potency with IC_{50} of 18.78 µg/ml in the in *vitro* 5-lipoxygenase inhibitory as-

say. Nordihydroguaiaretic acid (positive control) inhibited 5-LOX with IC_{50} of 36.49 µg/ml.

The docking studies with the protein crystal structure of the 5-LOX enzyme further evaluated the anti-inflammatory potential of the synthesized compounds. The docking score and dock pose were analyzed to gain clear insight into probable interactions of synthesized compounds with the enzyme. Docking simulations were performed on X-ray crystallographic structures available for 5-LOX (3V99.pdb). The protein structures were thoroughly verified for breaks or missing residues,

and necessary corrections were made in the pdb files. Docking simulations were performed by considering the entire protein as a receptor to obtain information regarding all possible interaction sites. The 5-LOX enzyme contains a relatively large and flexible receptor site. The catalytic iron is held in place with the help of three histidines (HIS551, 368, and 373), ASN555, and ILE674. The docking simulations were performed with the help of Auto Dock Vina. Partial flexibility allowed for the amino acids present close to the active site.

Table 3: Inhibitory activities of 1H-(indole -5-yl)-3-substituted 1,2,4-oxadiazoles

Entry	Compound	R'	R (3/4)	IC_{50} µg/ml
1	4aa	H	H	31.07
2	4ab	H	4-CH_3	30.13
3	4ac	H	3-CH_3	30.70
4	4ad	H	4-OCH_3	37.89
5	4ae	H	4-Cl	>100
6	4af	H	3-Cl	25.78
7	4ag	H	4-Br	23.13
8	4ah	H	3-Br	>100
9	4ba	Br	H	>100
10	4bb	Br	4-CH_3	20.86
11	4bc	Br	3-CH_3	26.72
12	4bd	Br	4-OCH_3	23.51
13	4be	Br	3-Cl	27.86
14	4bf	Br	3-Br	18.78
	Standard *			36.49

IC_{50} represents the concentration of a drug that is required for 50% inhibition expressed in µg/ml.
*Nordihydroguaiaretic acid as a positive control.

Amongst the synthesized compounds, **4bf** showed the highest potency (IC_{50} 18.78 µg/ml) in the in *vitro* 5-LOX inhibitory assay. The compound docked snugly into the receptor site with a score of

-9.1 Kcal/mol. It showed strong hydrogen bond interactions with two key amino acids His368 and Asn555. Additionally, it also showed non-covalent

interactions with several other lipophilic amino acids present in the receptor channel. The oxadiazole moiety was found to be critical for the bioactivity as it has formed very strong salt bridge interactions with Asn555. This series showed A similar trend for other bioactive compounds, which showed potent enzyme inhibition (MIC<30 μg/ml). The introduction of a halogen on *C*-3 of benzene significantly potentiated the bioactivity.
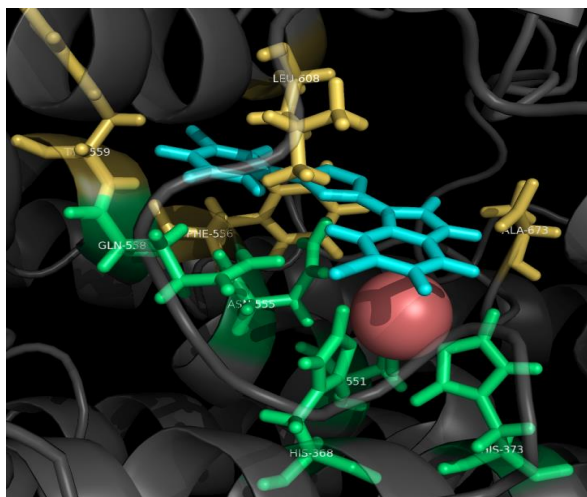
Figure 2: Docking poses of the compound 4bf. Ligand (aqua blue), Fe (salmon red), and active site residues making polar contacts (light yellow)

4bf showed the highest potency (IC$_{50}$ 18.78 μg/ml) in the in *vitro* 5-LOX inhibitory assay. Amino acid interactions of compound **4bf** is Gly175, Val176, Phe178, **His368**, Ile407, **Asn555**, Phe556, Gln558, Tyr559, Val605, Leu608, Phe611, Ala673. Dock Score of -9.1 Kcal/mol.

4.   CONCLUSION

In conclusion, a series of indolyloxadiazoles from amidoxime and indole 3-carboxaldehyde using CAN as a catalyst and PEG as a solvent were synthesized, and an In *vitro* 5-LOX inhibitory assay was performed. Among the tested compounds, **4bf** showed the highest potency (IC$_{50}$ 18.78 μg/ml). The synthesized compound carried out docking on the 5-LOX enzyme protein crystal structure. The compound (**4bf**) docked snugly into the receptor site with a score of -9.1 Kcal/mol, and it showed strong hydrogen bond interactions with two key amino acids, **His368** and **Asn555**. The obtained dock scores and the bioactivity findings correlated well.

5.   CONFLICT OF INTEREST

The authors agree there are no conflicts to declare.

6.   ACKNOWLEDGMENT

7.   REFERENCES

1.   Knölker HJ, Reddy KR. Isolation and synthesis of biologically active carbazole alkaloids. Chemical reviews. 2002 Nov 13;102(11):4303-428. Available from: <URL>

2.   Tale RH, Rodge AH, Keche AP, Hatnapure GD, Padole PR, Gaikwad GS, Turkar SS. Synthesis and antibacterial, antifungal activity of novel 1, 2, 4-oxadiazole. Journal of Chemical and Pharmaceutical Research. 2011;3(2):496-505. Available from: <URL>

3.   Pace A, Pierro P. The new era of 1, 2, 4-oxadiazoles. Organic & biomolecular chemistry. 2009;7(21):4337-48. Available from: <URL>

4.   Borg S, Luthman K, Nyberg F, Terenius L, Hacksell U. 1, 2, 4-Oxadiazole derivatives of phenylalanine: potential inhibitors of substance P endopeptidase. European Journal of Medicinal Chemistry. 1993 Jan 1;28(10):801-10. Available from: <URL>

5.   Behalo MS, Aly AA, Wasfy AF, Rizk MM. Synthesis of some novel 1, 2, 4-triazole derivatives as potential antimicrobial agents. European Journal of Chemistry. 2013 Jun 30;4(2):92-7. Available from: <URL>

6.   Haugwitz RD, Martinez AJ, Venslavsky J, Angel RG, Maurer BV, Jacobs GA, Narayanan VL, Cruthers LR, Szanto J. Antiparasitic agents. 6. Synthesis and anthelmintic activities of novel isothiocyanatophenyl-1, 2, 4-oxadiazoles. Journal of Medicinal Chemistry. 1985 Sep;28(9):1234-41. Available from: <URL>

7.   Dahlgren SE, Dalhamn T. The Anti-Inflammatory Action of Phenyl-Methyl-Oxadiazole (PMO): An Experimental Study on the Guinea-Pig Trachea. Acta Pharmacologica et Toxicologica. 1972 Jul;31(3):193-202. Available from: <URL>

8.   Manfredini S, Lampronti I, Vertuani S, Solaroli N, Recanatini M, Bryan D, McKinney M. Design, synthesis and binding at cloned muscarinic receptors of N-[5-(1'-substituted-acetoxymethyl)-3-oxadiazolyl] and N-[4-(1'-substituted-acetoxymethyl)-2-dioxolanyl] dialkyl amines. Bioorganic & medicinal chemistry. 2000 Jul 1;8(7):1559-66. Available from: <URL>

9.   Kumar D, Patel G, Chavers AK, Chang KH, Shah K. Synthesis of novel 1, 2, 4-oxadiazoles and analogues as potential anticancer agents. European Journal of Medicinal chemistry. 2011 Jul 1;46(7):3085-92. Available from: <URL>

10.   Kode NR, Vanden Eynde JJ, Mayence A, Wang G, Huang TL. Design and synthesis of N 1, N 5-bis [4-(5-alkyl-1, 2, 4-oxadiazol-3-yl) phenyl] glutaramides as potential antifungal prodrugs. Molecules. 2013 Sep 12;18(9):11250-63. Available from: <URL>

11.   Fortuna CG, Berardozzi R, Bonaccorso C, Caltabiano G, Di Bari L, Goracci L, Guarcello A, Pace A, Piccionello AP, Pescitelli G, Pierro P. New potent antibacterials against Gram-positive multiresistant pathogens: Effects of side chain modification and chirality in Linezolid-like 1, 2, 4-oxadiazoles. Bioorganic & Medicinal Chemistry. 2014 Dec 15;22(24):6814-25. Available from: <URL>

12.   Maftei CV, Fodor E, Jones PG, Daniliuc CG, Franz MH, Kelter G, Fiebig HH, Tamm M, Neda I. Novel 1, 2, 4-oxadiazoles and trifluoromethylpyridines related to natural products: Synthesis, structural analysis and investigation of their antitumor activity. Tetrahedron. 2016 Mar 3;72(9):1185-99. Available from: <URL>

13. Clitherow JW, Beswick P, Irving WJ, Scopes DI, Barnes JC, Clapham J, Brown JD, Evans DJ, Hayes AG. Novel 1, 2, 4-oxadiazoles as potent and selective histamine H3 receptor antagonists. Bioorganic & Medicinal Chemistry Letters. 1996 Apr 9;6(7):833-8. Available from: <URL>

14. Vu CB, Corpuz EG, Merry TJ, Pradeepan SG, Bartlett C, Bohacek RS, Botfield MC, Eyermann CJ, Lynch BA, MacNeil IA, Ram MK. Discovery of potent and selective SH2 inhibitors of the tyrosine kinase ZAP-70. Journal of Medicinal Chemistry. 1999 Oct 7;42(20):4088-98. Available from: <URL>

15. Wright AE, Pomponi SA, Cross SS, McCarthy P. A new bis-(indole) alkaloid from a deep-water marine sponge of the genus Spongosorites. The Journal of Organic Chemistry. 1992 Aug;57(17):4772-5. Available from: <URL>

16. Bhambi D, Salvi VK, Jat JL, Ojha S, Talesara GL. Synthesis and antimicrobial activity of some new indole containing isoxazolines and phthalimidoxy derivatives of thiazolidinone and thiohydantoin. Journal of Sulfur Chemistry. 2007 Apr 1;28(2):155-63. Available from: <URL>

17. Mumuni M, Attama AA, Kunle OO. Formulation in vitro and in vivo evaluation of SRMS-based heterolipid-templated homolipid delivery system for diclofenac sodium. Drug Delivery. 2016 Mar 23;23(3):907-15. Available from: <URL>

18. Tohid SF, Ziedan NI, Stefanelli F, Fogli S, Westwell AD. Synthesis and evaluation of indole-containing 3, 5-diarylisoxazoles as potential pro-apoptotic antitumour agents. European Journal of Medicinal Chemistry. 2012 Oct 1; 56:263-70. Available from: <URL>

19. Nguyen CH, Lhoste JM, Lavelle F, Bissery MC, Bisagni E. Synthesis and antitumor activity of 1-[[(dialkylamino) alkyl] amino]-4-methyl-5H-pyrido [4, 3-b] benzo [e]-and-benzo [g]) indoles. A new class of antineoplastic agents. Journal of Medicinal Chemistry. 1990 May;33(5):1519-28. Available from: <URL>

20. Safdy ME, Kurchacova E, Schut RN, Vidrio H, Hong E. Tryptophan analogs. 1. Synthesis and antihypertensive activity of positional isomers. Journal of Medicinal Chemistry. 1982 Jun;25(6):723-30. Available from: <URL>

21. Williams JD, Chen JJ, Drach JC, Townsend LB. Synthesis and antiviral activity of 3-formyl-and 3-cyano-2, 5, 6-trichloroindole nucleoside derivatives. Journal of Medicinal Chemistry. 2004 Nov 4;47(23):5766-72. Available from: <URL>

22. Saundane AR, Halu A, Kirankumar NM. Synthesis and biological evaluation of some novel indole analogues containing triazolopyrimidine moiety. Monatshefte für Chemie-Chemical Monthly. 2017 Aug; 148:1497-511. Available from: <URL>

23. Wakchaure ND, Shejwal SS, Deshmukh VK, Chaudhari SR. Review on Common Methods to Synthesize Substituted1H-Indole-2, 3-Dione (Isatin) Derivatives and Their Medicinal Significance. American J. PharmTech Res. 2012;2(4):288-310.

24. Wang P, Liu J, Xing H, Liu Y, Xie W, Zhao G. Synthesis and anticancer activity of novel 5-(indole-2-yl)-3-substituted 1, 2, 4-oxadiazoles. Drug Discoveries & Therapeutics. 2012 Jun 30;6(3):133-9. Available from: <URL>

25. Swain CJ, Baker R, Kneen C, Moseley J, Saunders J, Seward EM, Stevenson G, Beer M, Stanton J, Watling K. Novel 5-HT3 antagonists. Indole oxadiazoles. Journal of Medicinal Chemistry. 1991 Jan;34(1):140-51. Available from: <URL>

26. Carbone M, Li Y, Irace C, Mollo E, Castelluccio F, Di Pascale A, Cimino G, Santamaria R, Guo YW, Gavagnin M. Structure and cytotoxicity of phidianidines A and B: first finding of 1, 2, 4-oxadiazole system in a marine natural product. Organic Letters. 2011 May 20;13(10):2516-9. Available from: <URL>

27. Peters-Golden M, Henderson Jr WR. Leukotrienes. New England Journal of Medicine. 2007 Nov 1;357(18):1841-54.

28. Young RN. Inhibitors of 5-lipoxygenase: a therapeutic potential yet to be fully realized. European Journal of Medicinal Chemistry. 1999 Sep 1;34(9):671-85. Available from: <URL>

29. Helgadottir A, Manolescu A, Thorleifsson G, Gretarsdottir S, Jonsdottir H, Thorsteinsdottir U, Samani NJ, Gudmundsson G, Grant SF, Thorgeirsson G, Sveinbjornsdottir S. The gene encoding 5-lipoxygenase activating protein confers risk of myocardial infarction and stroke. Nature Genetics. 2004 Mar 1;36(3):233-9. Available from: <URL>

30. Rådmark O, Samuelsson B. Microsomal prostaglandin E synthase-1 and 5-lipoxygenase: potential drug targets in cancer. Journal of Internal Medicine. 2010 Jul;268(1):5-14. Available from: <URL>

31. Xiong WN, Yang CG, Jiang B. Synthesis of novel analogues of marine indole alkaloids: Mono (indolyl)-4-trifluoromethylpyridines and bis (indolyl)-4-trifluoromethylpyridines as potential anticancer agents. Bioorganic & Medicinal Chemistry. 2001 Jul 1;9(7):1773-80. Available from: <URL>

32. Chandra T, Garg N, Kumar A. Synthesis and anti-inflammatory activity of indole derivatives. International Journal of ChemTech Research. 2010 Apr;2(2):762-3. Available from: <URL>

33. Tohid SF, Ziedan NI, Stefanelli F, Fogli S, Westwell AD. Synthesis and evaluation of indole-containing 3, 5-diarylisoxazoles as potential pro-apoptotic antitumour agents. European Journal of Medicinal Chemistry. 2012 Oct 1; 56:263-70. Available from: <URL>

34. Nguyen CH, Lhoste JM, Lavelle F, Bissery MC, Bisagni E. Synthesis and antitumor activity of 1-[[(dialkylamino) alkyl] amino]-4-methyl-5H-pyrido [4, 3-b] benzo [e]-and-benzo [g]) indoles. A new class of antineoplastic agents. Journal of Medicinal Chemistry. 1990 May;33(5):1519-28. Available from: <URL>

35. Gupta PK, Hussain MK, Asad M, Kant R, Mahar R, Shukla SK, Hajela K. A metal-free tandem approach to prepare structurally diverse N-heterocycles: synthesis of 1, 2, 4-oxadiazoles and pyrimidinones. New Journal of Chemistry. 2014;38(7):3062-70. Available from: <URL>

36. Ziedan NI, Stefanelli F, Fogli S, Westwell AD. Design, synthesis and pro-apoptotic antitumour properties of indole-based 3, 5-disubstituted oxadiazoles. European Journal of Medicinal Chemistry. 2010 Oct 1;45(10):4523-30. Available from: <URL>

RESEARCH ARTICLE

Determination of Micro Amounts of Promethazine Hydrochloride in Pure and Pharmaceutical Samples Using UV-visible Spectrophotometry

Israa Talib Humeidy[1*]

[1]University of Tikrit, College of Engineering, Department of Chemical Engineering, Tikrit, Iraq

Abstract: This study presents the development of a novel, facile, and overly sensitive spectrophotometric approach for quantifying promethazine hydrochloride (PRO) within its pharmaceutical formulations. The method capitalizes on an oxidative coupling reaction, achieved through the oxidation of the compound in an acidic milieu utilizing ammonium cerium (IV) sulfate dehydrate (Ce^{+4}) solution. This process leads to the creation of a green-colored solution, which, upon conjugation with 5-aminosalicylic acid, exhibits maximum absorption at a wavelength of 598 nm. The methodology investigated several parameters, encompassing oxidation duration, temperature, quantities of oxidizing agent and coupling reagent, and determining the stoichiometric ratio between promethazine hydrochloride and 5-aminosalicylic acid. The established ratio was confirmed to be 1:1. Numerous organic solvents were evaluated, with water emerging as the optimal choice due to its pronounced absorption characteristics at the 598 nm wavelength. The applicability of Beer's law was verified over a concentration range of 2 - 28 µg/mL of promethazine hydrochloride, with a calculated molar absorption coefficient of 1.9606×10^4 L/mol·cm. The Sandell sensitivity index was determined as 0.0164 µg/cm^2, while the relative standard deviation (RSD) ranged from 0.8553- 1.2671%. Notably, recovery percentages were also within the 99.88 – 100.34% range. The efficacy of this technique was effectively demonstrated through its successful application in the analysis of pharmaceutical formulations containing promethazine hydrochloride, employing the standard method as a benchmark.

1. INTRODUCTION

As a neuroprotective antidepressant, promethazine hydrochloride belongs to the first generation of antihistamines in the phenothiazines pharmacological class (1). It is frequently utilized because of its sedative, antihistamine, antipsychotic, anticholinergic, and analgesic effects. On the other hand, Promethazine hydrochloride can affect humans by altering their reproductive, endocrine, and cardiac systems. Therefore, it is crucial to check for it in commercial and pharmaceutical formulations (2).

This medication treats respiratory allergies (such as allergic rhinitis), skin allergies, motion nausea, and as an analgesic before and after surgery. However, it is only a weak antipsychotic (i.e., schizophrenia). Because it has anti-emetic qualities, it is also used as an analgesic to treat post-operative vomiting. It

also treats eczema and itching in adults and children (3, 4). Promethazine hydrochloride has negative effects on the cardiovascular system, the central nervous system, the gastrointestinal tract, and the central nervous system, which include dry mouth, sleepiness, blurred vision, and dizziness (5). Take the medication 30 minutes before your trip to prevent dizziness.

To avoid additional symptoms, take the tablets or drink them with food. You can also use the medication as a suppository (6).

Promethazine hydrochloride is easily dissolved in water, and Scheme 1 depicts its structural formula (7).
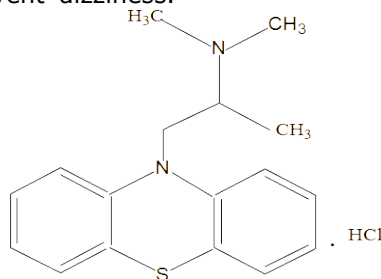
Scheme 1: The chemical structure of promethazine hydrochloride.

Promethazine hydrochloride has been measured using various analytical techniques due to the medication's therapeutic value, such as the ion-selective electrode, which relies on the drug and tetraphenyl boron (III) forming an ion pair (8).

The synthesis of ionic selective electrodes for promethazine hydrochloride with molybdophosphoric acid also involved the utilization of various plasticizers: dibutyl phthalate (DBPH), dibutyl phosphate (DBP), dioctyl phthalate (DOP), and tributyl phosphate (TBP) (9). Furthermore, the synthesis of a highly sensitive and selective electrode for promethazine incorporated the use of ammonium phosphomolybdate (10). Promethazine hydrochloride has been quantified utilizing a few flow injection techniques, such as continuous flow injection through the oxidation of the drug with sodium persulfate in an aqueous solution and the detection of colored cationic radicals produced using a home-made 3SX3-3D sun photometer (11). Promethazine hydrochloride was also measured using a 3SX3-3D solar cell microphotometer, and persulfate was trapped in water crystals using the flow/stop injection method (12). Additionally, promethazine was detected utilizing the flow injection approach with chemiluminescence, which was based on the Luminol-H_2O_2-Fe (III) system's merging region principle (13).

A mixture of water, methanol, and acetic acid (79:20:1 v/v/v) was employed as the eluting phase on a Kromasil Silica column with a detector of prominent diode array at 249 nm and a flow rate of 1 mL/min to estimate Promethazine hydrochloride using the RP-HPLC method (14). Promethazine hydrochloride was separated and quantified using a different HPLC technique on a column of Vancomycin Chirobiotic V (250 mm, 4.6 mm) utilizing

methanol, acetic acid, and triethylamine as the mobile phase at a flow rate of 1 mL/min with a UV-detector at 254 nm (15).

Finally, several spectrophotometric techniques have been described for measuring Promethazine hydrochloride. Some of these techniques involve oxidizing Promethazine hydrochloride with iron (III), and the resulting iron (II) reacts with 1,10-phenanthroline at pH 3.01 to form a stable complex, giving a maximum absorption at 504 nm (16) or sodium hypochlorite in a medium of sulfuric acid to develop a pinkish-red product with maximum absorption (17). Additionally, when chromium trioxide was used as an oxidizing agent in an acidic solution to oxidize promethazine hydrochloride, the resultant product had the maximum absorption at 515 nm (18).

Promethazine hydrochloride was determined in pharmaceuticals by using p-amino benzoic acid as a coupling reagent in the presence of N-bromosuccinimide, and the reaction resulted in the production of a bluish-green product with maximum absorption at 603 nm (19). Promethazine hydrochloride was also determined in pharmaceuticals by using p-chloroaniline as a coupling reagent in the presence of ammonium cerium (IV) sulfate dehydrates as an oxidizing agent (20).

Another spectrophotometric method for measuring promethazine hydrochloride was used, and it was based on the formation of a colored ion-pair complex between promethazine hydrochloride and methyl blue dye in an acidic medium, which gave a maximum absorption of 480 nm (21); the resulting spectrophotometric method was also used for the measurement of Promethazine hydrochloride and paracetamol by using the zero-pass method, and (22). Additionally, metoclopramide hydrochloride

(23), hypochlorite in environmental samples (24), chloramphenicol (25), and procaine (26) have all been determined using methazine as a coupling reagent in addition to several pharmaceutical drugs in their pure form (27).

The study aims to present a straightforward spectrophotometric method for determining promethazine hydrochloride in its

2. EXPERIMENTAL

2.1 Apparatus used

The experiments were conducted using the following equipment: Shimadzu UV- Visible Spectrophotometer 1800, double beam, with quartz cells (1cm), water bath (Clifton), pH meters 3310 (Janeway), delicate balance type (Sartorius BL 210).

2.2. Chemical reagents and materials used

The Pharmaceutical and Medical Supplies Company-SDI, Samarra, Iraq, provided the promethazine hydrochloride (pure standard powder), and Fluka and Sigma-Aldrich provided all other analytical chemical reagents (5-aminosalicylic acid, ammonium cerium (IV) sulfate dehydrate, sulfuric, nitric, hydrochloric, acetic, and phosphoric acids, phenergan injection, histazine syrup, and organic solvents) that were of the highest possible quality. Each solution was made from scratch with distilled water.

2.2.1 The parent solution, 250µg/mL

Promethazine hydrochloride was dissolved in 1.0 g of distilled water, and a 100 mL volumetric flask was used to add more distilled water to create a parent solution of the medication (1000 µg/mL). Transferring 25 mL of the parent solution into a volumetric flask (100 mL), adding distilled water to the mark, and shielding it from light by placing it in a darkened bottle were the steps needed to create the working solution (250 µg/mL), which is the concentration utilized in the suggested approach.

2.2.2. 5-aminosalicylic acid solution (1×10^{-2} M)

To get the appropriate concentration, 0.1531 g of 5-aminosalicylic acid powder was dissolved in 10 mL of ethanol, and the volume was then increased to 100 mL in a volumetric flask with distilled water.

2.2.3 Ammonium cerium (IV) sulfate dehydrate solution(2×10^{-2} M)

Ammonium cerium (IV) sulfate dehydrate powder $(Ce(NH_4)_4(SO_4)_4.2H_2O)$ weighing 1.2651 g is dissolved in a suitable volume of distilled water, and the volume is then filled with 100 mL distilled water.

pharmaceutical and pure forms due to its significance in the medical field and its use in treating numerous diseases. This method involves oxidizing the drug with ammonium cerium (IV) sulfate dehydrate as an oxidant, then pairing it with 5-aminosalicylic acid as a coupling reagent. The process was successfully applied to identify Promethazine hydrochloride in pharmaceutical formulations.

2.2.4 Sulfuric acid solution (1.5 M (

In a 100 mL volumetric flask, a precise 8.20 mL of concentrated sulfuric acid (18.29 M) was added to a certain amount of distilled water. The volume was then brought to the target using the same solvent.

2.2.5 Pharmaceutical solutions

2.2.5.1 Phenergan injection solution 250 µg/mL

Phenergan is available as a 2 mL injection with a promethazine HCl dosage of 2.5 percent.

This solution was created by adding one injection of 2 mL to a volumetric flask (100 mL) and filling the remaining space with distilled water to the top to create a preparation solution with a concentration of 500 µg/mL. then 50 mL of the above solution was diluted with distilled water to 100 mL to make one with a concentration of 250 µg/mL.

2.2.5.2 Histazine syrup solution 250 µg/mL

Each 5 mL of the histazine preparation, which is made by the United Company for Pharmaceutical Industries and Medical Supplies in Amman, Jordan, contains 5 mg Promethazine hydrochloride, and the solution was made by adding 50 mL of this composition to a volumetric flask (100 mL) and filling the volume to the mark with distilled water to get a solution with a 500 µg/mL concentration, then 50 mL of the above solution was diluted to 100 mL with distilled water to obtain a concentration of 250 µg/mL.

Photograph 1: Left, Phenergan injection solution 250 µg/mL; right, Histazine syrup solution 250 µg/mL.

3. PRELIMINARY STUDY

Promethazine hydrochloride is first oxidized in an acidic medium with the help of an oxidizing agent (ammonium cerium (IV) sulfate dehydrate). Then, the product is combined with the 5-aminosalicylic acid reagent, producing a green solution with maximum absorption at 598 nm compared to the blank solution.
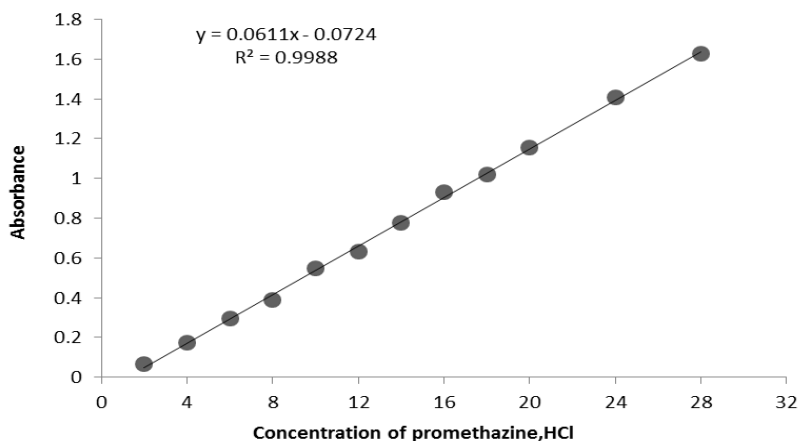
3.1 Calibration curve with its statistical data

Using the ideal conditions described in the general approach above, the following were used to construct a titration curve for Promethazine hydrochloride: - For a set of volumetric flasks (25 mL), different volumes (0.2-2.8 mL) of promethazine hydrochloride (250 μg/mL) were taken as represented (2.0 - 28.0 μg/mL). To complete the oxidation reaction and stabilize the generated product, 2.0 mL of reagent (1 x 10^{-2} M), 1.2 mL of an oxidizing agent (2 x 10^{-2} M), and 1.8 mL of sulfuric acid solution (1.5 M) were added and left for 15 minutes.

$$y = 0.0611x - 0.0724$$
$$R^2 = 0.9988$$

Figure 1: Promethazine calibration curve.

The components in each standard flask were diluted to the mark with distilled water, and the absorbance of each solution was measured against a reagent blank produced in the same manner but without promethazine hydrochloride. By plotting absorption versus concentration, it was discovered that Beer's law obeys a concentration range of 2-28 μg/mL with a correlation coefficient of 0.998 and that the molar absorbance value of the green color product was 1.9606 x 10^4 L/mol.cm and the

Sandell's sensitivity index was 0.0164 g/cm^2, Figure 1.

3.1.1 The proposed method's precision and accuracy

The proposed method's efficiency was statistically assessed (accuracy and precision measurement) by measuring the absorbance of two distinct concentrations of promethazine HCl placed within the Beer-Lambert limits at 598 nm. The results shown in Table 1 demonstrate that the procedure is effective and satisfactory.

Table 1: The accuracy and precision results

RE%	Average recovery%	Recovery*%	RSD%	Conc. of PRO μg/mL
-0.12	100.11	99.88	1.2671	4
0.34		100.34	0.8553	6

* Average of five determinations

3.1.2 Study of LOD& LOQ
The drug's limit of detection (LOD) was calculated by determining the lowest detectable concentration of the analyte (LOD = 3.3 B / S). The drug's quantification limit (LOQ) was calculated by determining the lowest detectable concentration (LOQ = 10B / S), where S represents the slope of the standard curve, and

B represents the standard deviation of the blank reagent (28).
Table 2 summarizes the LOD and LOQ results for the current approach, which include critical features in the analysis such as Beer's law concentration range, molar absorption coefficient, Sandell's sensitivity, LOQ, LOD, slope, R, RSD, and RE.

Table 2: A summary of analytical quantitative properties and statistical data of the coupling reaction of promethazine hydrochloride with 5-amino salicylic acid reagent.

Statistical values	Analytical quantitative parameters
1.9606×10^4	Molar Extinction Coefficient (liter/mol.cm)
2 - 28	Beer's law range (µg/mL)
0.0164	Sandell's sensitivity (µg/cm^2)
0.0611	Slope
0.0724	Intercept
0.876489	LOD (µg/mL)
2.92163	LOQ (µg/mL)
-0.12 – 0.34	Range of relative error*(%)
0.8553- 1.2671	RSD* (%)
100.11	Average recovery*(%)
70	stability of formed product (min.)

* Average of five determinations

3.2. 10 study the stoichiometry of the analytical reaction

Two approaches were used to determine the chemical stoichiometric ratio of the coupling product under optimal working conditions (continuous variation and molar ratio). Equal concentrations of drug and reagent (7.79×10^{-4}M) were created using these two procedures. In the first method (continuous variation), increasing amounts of drug solution (1.0 -9.0 mL) and decreasing amounts of reagent solution (9.0 - 1.0 mL) were placed in a series of volumetric flasks (25 mL), then the optimum amounts of the remaining additives were added and diluted with distilled water to the mark. At 598 nm, the solutions' absorbance was measured compared to their blank solutions. The results confirmed that the chemical stoichiometric ratio of the coupling product was created in a 1:1 ratio when promethazine HCl was combined with a 5-aminosalicylic acid reagent, as shown in Figure 2 (29).

The second method (molar ratio) was used to ensure that the chemical ratio of the reaction between the promethazine HCl and the 5-aminosalicylic acid reagent is 1:1. The technique was implemented by adding increasing volumes of the reagent (0.25- 4.50 mL) to a few volumetric flasks (25 mL) holding a fixed volume (2 mL) of the drug, then the remaining additives are supplemented according to optimal conditions. The solutions were diluted to the proper volume with distilled water, and the absorbance at 598 nm was measured in comparison to the respective blank solutions. The second method (molar ratio) was used to ensure that the chemical ratio of the reaction between the promethazine HCl and the

5-aminosalicylic acid reagent is 1:1. The method was implemented by adding increasing volumes of the reagent (0.25- 4.50 mL) to a few volumetric flasks (25 mL) holding a fixed volume (2 mL) of the drug, then the remaining additives are supplemented according to optimal conditions. The solutions were diluted to the proper volume with distilled water, and the absorbance at 598 nm was measured compared to the respective blank solutions. It was discovered that the method complies with the continuous variation method, and Figure 3 demonstrates that the ratio is 1:1 in the two methods (29).

The proposed form of the oxidative coupling reaction created by promethazine hydrochloride (PRO) with the 5-aminosalicylic acid reagent in the presence of ammonium cerium (IV) sulfate dehydrate as the oxidizing agent is illustrated below based on the results reported in Figures (2,3).

4. RESULTS AND DISCUSSION

4.1 The final UV- Visible spectra

After achieving optimal conditions, UV-Vis spectrophotometry of the compound formed by the reaction of 5-aminosalicylic acid reagent with promethazine hydrochloride in the presence of ammonium cerium (IV) sulfate dehydrate as an oxidizing agent in a dilute acidic medium of sulfuric acid was performed to obtain a maximum absorption at 598 nm against the blank reagent, which does not absorb in this region. The final absorption spectra of the generated, green-colored complex against the blank reagent are depicted in Figure 4.
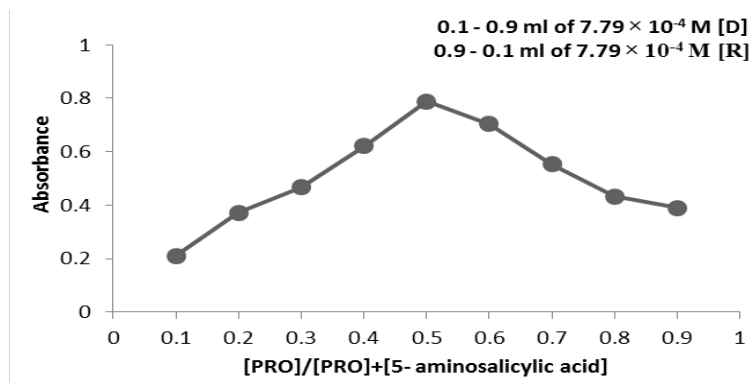
Figure 2: Continuous variation diagram of coupling product: promethazine hydrochloride - 5-aminosalicylic acid.
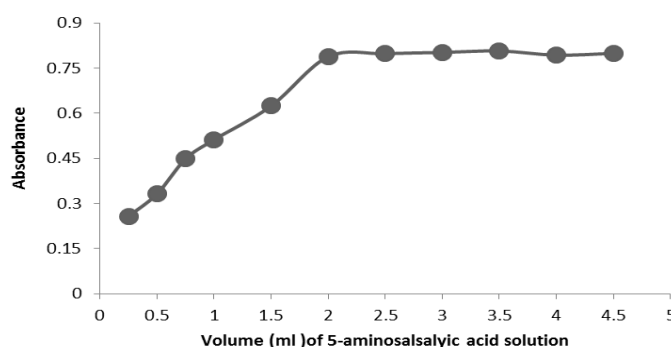

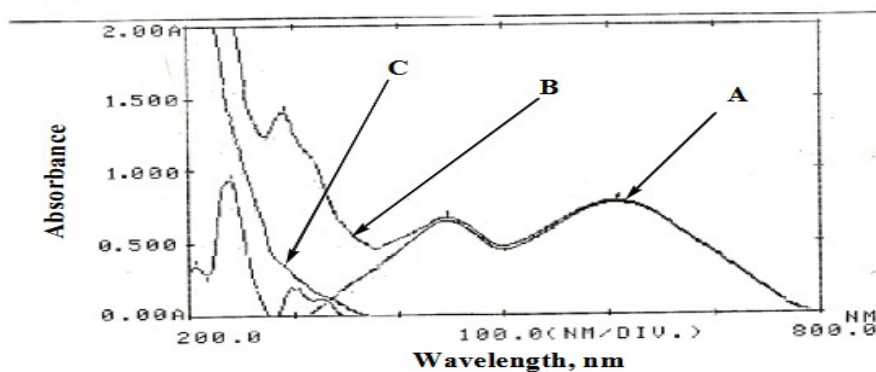**Figure 3:** Molar ratio diagram of coupling product: promethazine hydrochloride - 5-aminosalicylic acid

Figure 4. The ultimate absorption spectrum A = resulting complex versus the blank solution B= resulting complex versus the distilled water C= the blank solution versus distilled water

4.2 Optimal Experimental Variants

The green color changes depending on the parameters of the coupling reaction. As a result, it is critical to optimize the reaction conditions by investigating the various elements that influence the absorption of the green-colored product by adjusting one factor while keeping the other constant at 598 nm versus the blank reagent solution.

4.2.1 Choice of the most appropriate acid

In this study, different concentrations (0.25 - 1.5 M) of strong and weak acids (1.0 mL) were used, including sulfuric, nitric, hydrochloric, acetic, and phosphoric acids to determine the effect of acid type and concentration on the absorption of the green product, with sulfuric acid (1.5 M) chosen as the best acid because it gave the maximum absorption of the product at 598 nm, as shown in Table 3.

Table 3: Acid type effect.

Type of acid (1.0 mL)		Absorbance		
1.5 M	1.0 M	0.5 M	0.25 M	
0.645	**0.603**	**0.458**	**0.352**	**H_2SO_4**
0.287	0.265	0.248	0.225	HNO_3
0.585	0.521	0.436	0.358	HCl
0.147	0.126	0.119	0.103	CH_3COOH
0.079	0.063	0.057	0.029	H_3PO_4

4.2.2 Study the influence of the acid function
After selecting the optimal acid and maintaining its concentration, the pH influence was investigated using several amounts of sulfuric acid ranging from (0.3 - 3.0 mL) (1.5 M).

According to Table 4, 1.8 mL of this acid was enough to complete the reaction, and it was thus recommended for future research.

Table 4: Influence of the acid function

pH	Absorbance	Volume of H_2SO_4 (1.5M)
3.3	0.415	0.3
3.1	0.537	0.5
2.9	0.608	0.8
2.7	0.645	1.0
2.4	0.721	1.3
2.1	0.738	1.5
1.7	**0.755**	**1.8**
1.4	0.725	2.0
1.2	0.611	2.5
1.1	0.569	3.0

4.2.3 Effect of the amount of Ammonium cerium (IV) sulfate dehydration
During the testing to determine the most appropriate oxidizing agent, ammonium cerium (IV) sulfate dehydrate was discovered as an acceptable oxidizing agent. It was used in the coupling reaction of promethazine hydrochloride with 5-aminosalicylic acid, and the influence of different quantities (0.2 - 2.6 mL) of 0.02 M ammonium cerium (IV) sulfate dehydrate solution was tested. Figure 5 showed that 1.2 mL of ammonium cerium (IV) sulfate dehydrate solution was the ideal amount for obtaining the maximum absorption at 598 nm; hence, it was recommended for use in the following research.
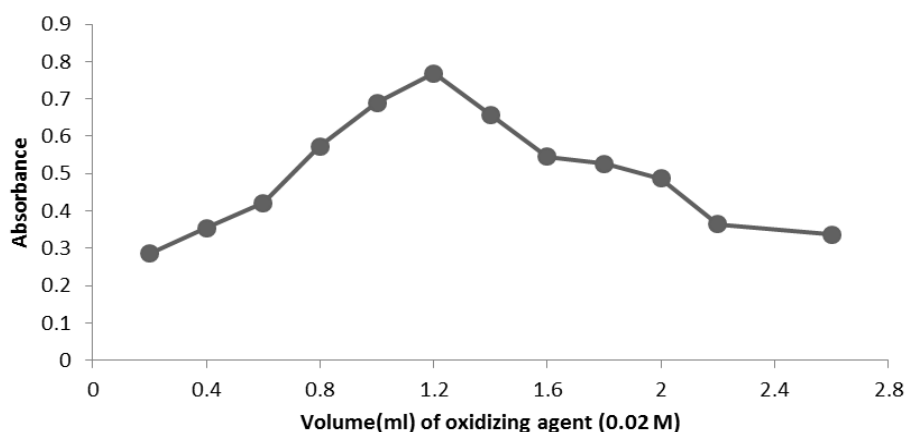

Figure 5: Effect of oxidizing agent volume

4.2.4 Effect of the amount of 5-aminosalicylic acid reagent

Following multiple testing of several conjugation reagents, including 4-chloroaniline, pyrocatechol, 5-aminosalicylic acid, and meta-

25

aminophenol, the best reagent was determined to be 5-aminosalicylic acid. The best volume of the 5-aminosalicylic acid reagent was then determined by experimenting with various amounts (0.250-4.000 mL) of (0.01 M) 5-aminosalicylic acid reagent. Due to the

maximum absorption at 598 nm, a volume of 2.00 mL of reagent was adequate for developing the green hue of the produced product. As a result, it was used in the following investigations, as shown in Figure 6.
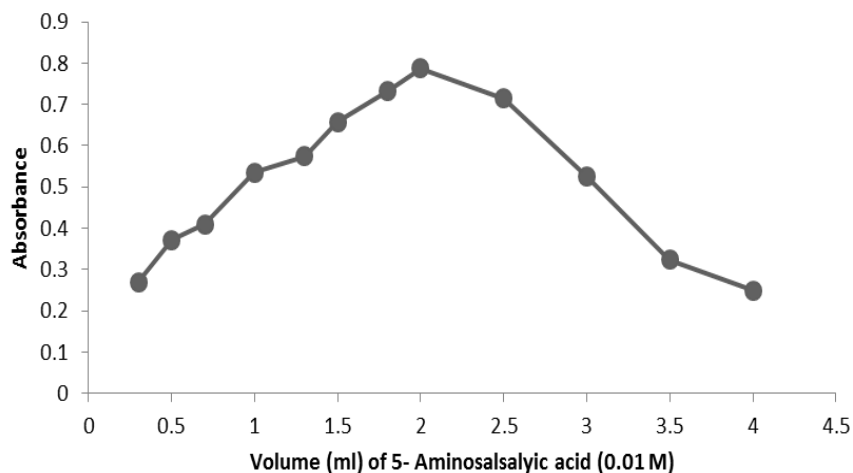

Figure 6: Effect of 5-aminosalicylic acid volume.

4.2.5 Effect of oxidation time and stability on the coupling reaction

The influence of oxidation duration on the period of color development and the stability of the created product was investigated, and the

analytical data presented in Figure 7 revealed that the formed product requires 15 minutes to achieve maximum absorption and remains stable for around 60 minutes.
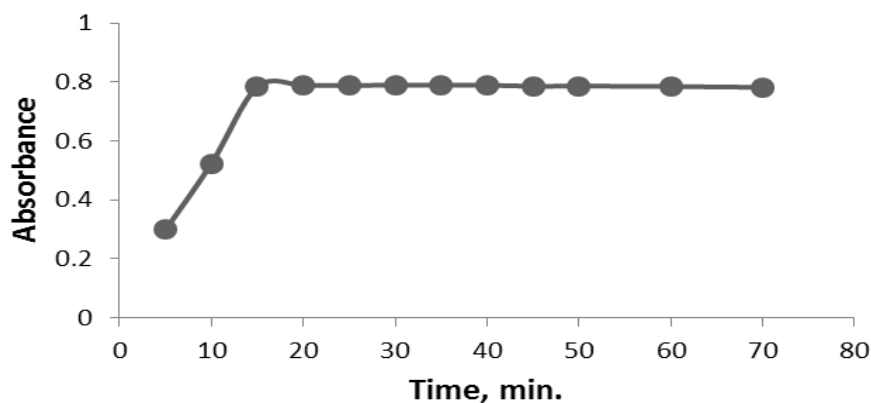

Figure 7: Effect of oxidation time.

4.2.6 Effect of temperature on the oxidative coupling reaction

The effect of temperature on coupling product absorption was investigated. In actuality, the color is created at room temperature (25°C);

hence, it is recommended that the reaction be performed at room temperature because the absorbance value decreases at higher temperatures, indicating product dissociation, Figure 8.
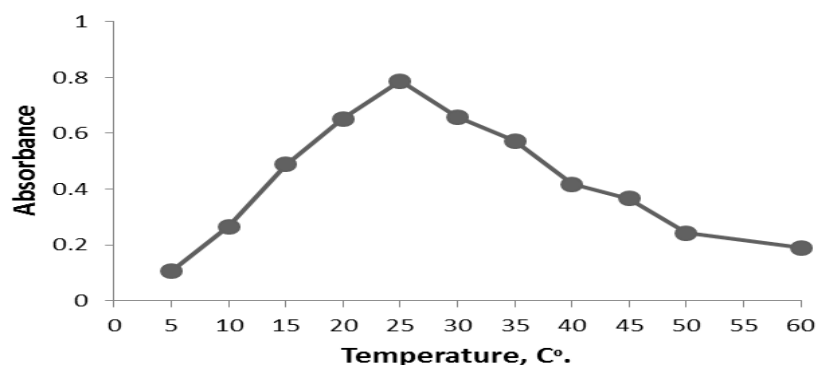
Figure 8: Effect of temperature.

4.2.7 Effect of the order of adding materials

Table 5: *Effect of the order of additions*

Absorbance	Order of addition	Order number
0.316	PRO + R + Ox + A	i
0.571	PRO + Ox + A + R	ii
0.788	**PRO + Ox + R + A**	**iii**
0.165	PRO + R + A+ Ox	iv
0.209	PRO +A + Ox + R	v
0.075	PRO + A+ R+ Ox	vi

A series of experiments were undertaken with a series of different additives according to the optimal circumstances and quantities discussed above to clarify the effect of the components sequencing addition on the absorption of the green product. The solutions' absorption was then measured compared to the blank solution.

Table 5 demonstrates that configuration (iii) is the correct layout for the coupling reaction, as used in future research.

Where:(PRO) promethazine hydrochloride solution, (R) 5-aminosalicylic acid solution, (Ox) ammonium cerium (IV) sulfate dehydrate solution, and (A) hydrochloric acid solution.

4.2.8 Effect of solvent types
Since dilution was done using these solvents rather than water, the influence of different organic solvents on coupling product absorption was investigated. The results in Table 6 clearly reveal that water is the best solvent because it showed the maximum absorption of the resultant solution at the wavelength of 598 nm when compared to the solvents employed; hence, it was chosen as a solvent in the following tests.

Table 6: The effect of different solvents.

Organic solvent	Acetone	CH$_3$OH	C$_2$H$_5$OH	CHCl$_3$	DMSO	Water
Abs	0.379	0.324	0.571	0.455	0.453	**0.788**
λ$_{max}$, nm	558	567	598	598	556	**598**

Based on the results presented in Figures (2,3) and in the sequence of additions, the proposed form of the oxidative coupling reaction formed by promethazine hydrochloride with 5- aminosalicylic acid reagent in the presence of ammonium cerium (IV) sulfate dehydrate as the oxidizing agent is shown below:
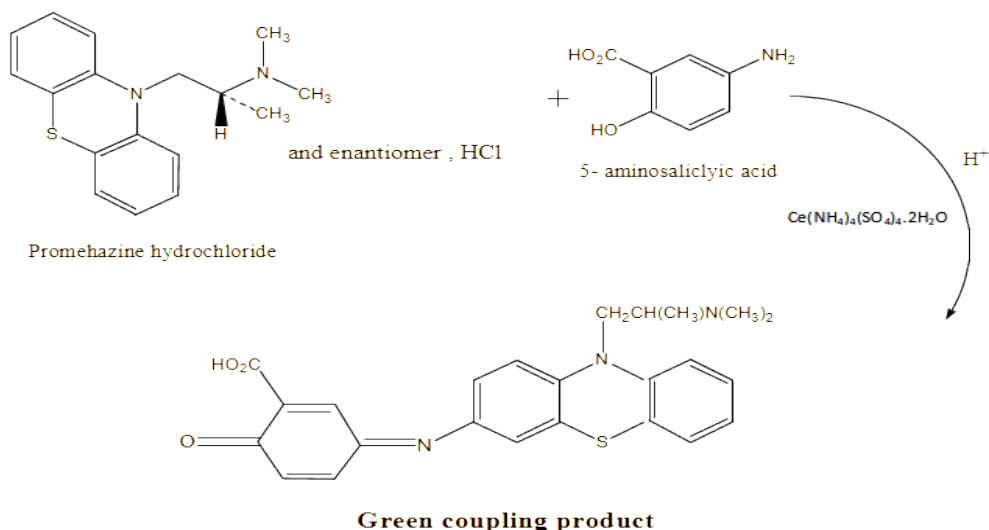
**Scheme 2:** Proposed chemical reaction between 5-aminosalicylic acid reagent and promethazine hydrochloride.

4.2.9 Proposed method applications to pharmaceutical preparations
Through the application of the standard addition method, the applicability of the proposed method has been successfully studied to examine several commercially available pharmaceutical preparations containing promethazine hydrochloride, as well as to know their efficacy, accuracy, and freedom from additives interference, Figures (9,10), Table 7.
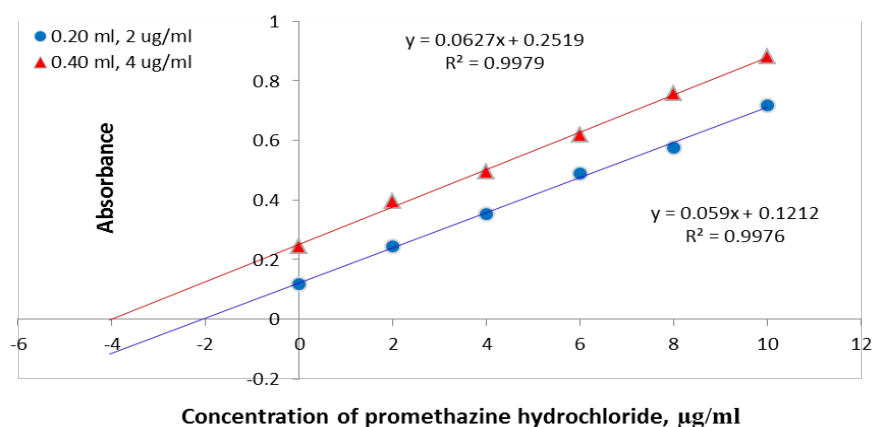
Figure 9: Standard addition procedure for promethazine hydrochloride in Phenergan injection
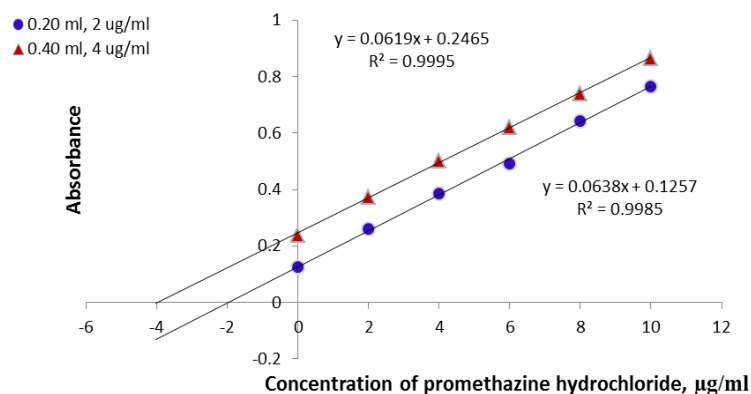
Figure 10: Standard addition procedure for promethazine hydrochloride in histazine syrup.

28

Table 7: Analytical results for determining promethazine hydrochloride in pharmaceutical formulations

Average content of the drug	Recovery*,%	PRO measured µg/mL	PRO present µg/mL	Pharmaceuticals used
101.58	102.7	2.054	2.000	**Phenergan injection**
	100.45	4.018	4.00	
99.025	98.50	1.970	2.00	**Histazine syrup**
	99.55	3.982	4.00	

* Average of five determinations.

The analytical results of the current method were compared with the official method using the F-test and the T-test, and the analytical results obtained showed no statistically significant differences, indicating that the current method can be used as an alternative method for determining promethazine hydrochloride in pure form and doses.

The current method was statistically evaluated by comparing it to the official method. It was discovered that the computed t value (0.258) is less than the tabulated t value (2.571) at a 95 percent confidence level for five degrees of freedom for PRO. The calculated F value (1.211) is less than the tabulated value (5.05) at a 95 percent confidence level for five degrees of freedom for promethazine hydrochloride. Statistical evaluation, T-test, and F-test results show that the present approach is reliable, and there is no discernible difference between the two ways because the present method is virtually additive-free.

5. CONCLUSIONS

The low value of comparative standard deviation and high value of recovery indicate that the colorimetric method used to assess the amount of promethazine hydrochloride is accurate and precise. The analytical results demonstrated that the innovative approach is simple, accurate, and appropriate for measuring the quantity of promethazine hydrochloride in pharmaceutical formulations, and it has also been used successfully to evaluate promethazine hydrochloride in pure and medicinal dosages (Phenergan injection and histazine syrup). Practically, it has been discovered that the main advantage of this method is that it is inexpensive and can save a significant amount of time and money when compared to HPLC and other modern technologies. Furthermore, this approach makes use of simple and commonly available chemicals to determine the promethazine hydrochloride formulation in pure and medical items without the need for special working conditions such as the use of expensive organic solvents, elevated temperatures, or extraction. The current procedure proved that additives (glucose, lactose, talc, sucrose, and starch) have no effect on the findings of the determination achieved under optimal conditions.

6. ACKNOWLEDGEMENT

7. REFERENCES

1.	Cantisani C, Ricci S, Grieco T, Paolino G, Faina V, Silvestri E, et al. Topical promethazine side effects: our experience and review of the literature. BioMed research international. 2013;1-9. Available from: <URL>

2.	Harvey RA, Clark M, Finkel R, Rey J, Whalen K. Lippincott's illustrated reviews: Pharmacology: Philadelphia; 2012.

3.	Ballington DA, Laughlin MM. Pharmacology. 3rd Ed.; Printed at Swastic Packaging; Delhi-92 (India); 2008. Available from: <URL>

4.	Katzung BG. Basic & clinical pharmacology.14th edition; 2018; 1105 – 1106.

5.	Seth D, VimLesh S. Textbook of Pharmacology, 3rd Ed; Printed in India; 2009.

6.	Bennett PN, Brown MJ. Clinical Pharmacology. 10th Ed. the library of congress, Spain 2008.

7.	Pharmacopoeia B, Commission BP. The stationery office. London, UK. 2009;1(123,128).

8.	Badawy SS, El Said SAES. Promethazine-Tetraphenyl Boron (III) Modified Carbon Paste Electrode for the Determination of Promethazine Hydrochloride. 2013. Available from: <URL>

9.	Al-Saidi KH, Ahmed ZW. Construction of Promethazine Hydrochloride Selective Electrodes in A PVC Matrix Membrane. Journal of Al-Nahrain University. 2011;14(4):11-7. Available from: <URL>

10.	Sarma B, Seema R. An electrochemical characteristics of promethazine HCl using ion selective electrodes. Int J Curr Res. 2017;9(11):60523-5.

11.	Shakir IM, Turkey NS. Flow injection analysis for the photometric determination of promethazine-HCl in pure and pharmaceutical preparation via

oxidation by persulphate using Ayah 3SX3-3D solar micro photometer. Baghdad Science Journal. 2013;10(4):1190-202. Available from: <URL>

12.   Shakir IM. Promethazine-HCl determination using entrapped persulphate in water crystals by flow injection/stopped-flow technique and Ayah 3SX3-3D solar cell micro photometer. Iraqi journal of science. 2015;56(1A):25-37. Available from: <URL>

13.   Jabbar HS, Faizullah AT. Flow injection analysis with chemiluminescence detection for determination of two phenothiazines. Int J Pharm Sci Res. 2015;6:474-81.

14.   Chaudhary J, Jain A, Saini V. Novel RP-HPLC method for estimation of paracetamol and promethazine simultaneously in syrup formulation. Journal of Research in Pharmacy. 2019;23(3):476-83. Available from: <URL>

15.   Saleh OA, El-Azzouny AA, Aboul-Enein HY, Badawy AM. A validated HPLC method for separation and determination of promethazine enantiomers in pharmaceutical formulations. Drug development and industrial pharmacy. 2009;35(1):19-25. Available from: <URL>

16.   Mahmood SS, Hashem OA, Khither MM. Determination of Promethazine Hydrochloride in pharmaceutical forms by Spectrophotometric Method. journal of kerbala university. 2018;14(3):28-38.

17.   Ahmed NR, Ahmed AI, Saadallah NC. Spectrophotometric estimation of promethazine hydrochloride in pharmaceutical preparations. European J Biomed Pharm Sci. 2020;7:79-84.

18.   Qader HA, Fakhre NA. Spectrophotometric determination of promethazine hydrochloride in pure and pharmaceutical dosage forms. ZJPAS. 2017;29:s107-s14.

19.   Abdulrahman LK, Al-Abachi AM, Al-Qaissy MH. Spectrophotmetric Micro determination of promrthazine hydrochloride in pharmaceutical. Baghdad Science Journal. 2005;2(3):471-6.

20.   Tagi RM, Al-Timimi RJ, Hassan MM, Hamzah MJ. Spectrophotometric determination of promethazine HCl in pure and dosage forms. Journal of Biotechnology Research Center. 2019;13(1):52-7. Available from: <URL>

21.   Al-Rufaie MMM. A sensitive spectrophotometric method for trace amounts determination of promethazine in drug formulations via ion pair complex formation. Malaysian Journal of Science. 2021:80-92. Available from: <URL>

22.   Al-Saidi KH, Hammza RA. Spectrophotometric determination of promethazine hydrochloride and paracetamol in pharmaceutical tablets. Al-Nahrain Journal of Science. 2014;17(1):14-23. Available from: <URL>

23.   M Al-Shaker Y. Spectrophotometric assay of metoclopramide hydrochloride in some pharmaceutical preparations via oxidation coupling reaction. Iraqi Journal of Pharmacy. 2013;13(1):41-50.

24.   Ahmed NR, Abdullah MS. Promethazine an environmental friendly reagent for novel estimation of hypochlorite in environmental samples. World Journal of pharmacy and Pharmaceutical Sciences. 2019;8(9):72-9.

25.   Al-Ward HS. Kinetic spectrophotometric methods for the determination of chloramphenicol in pharmaceutical preparations. Al-Nahrain Journal of Science. 2012;15(4):22-30. Available from: <URL>

26.   A AL-Da M, Al Q. A new colorimetric method for determination of procaine in pharmaceutical preparations via oxidative coupling organic reaction. journal of kerbala university. 2008;4(3):236-42.

27.   Mhemeed A. Spectrophotometric method for the determination of benzocaine by cerium ammonium sulphate with promethazine hydrochloride in pure and pharmaceuticals preparation. International Journal of Research in Pharmaceutical Sciences. 2019;10(2):1420-3. Available from: <URL>

28.   Humeidy IT. Spectrophotometric determination of cefotaxime sodium in pharmaceutical formulations. Materials Today: Proceedings. 2021;47:6043-9.

29.   Humeidy IT, Salman SA, Hashim KK. Spectrophotometric Determination of Methyldopa With 2, 6-Diaminopyridine Reagent Using Oxidative Coupling Reaction. Journal of Engineering Science and Technology. 2020;15(3):1824-39.

Preparation of the Nano-Sulfur from the Wastes (Foam) in the Al-Mishraq Sulfur Mine (Mosul/Iraq)

Saad Salih Ahmed[1]* iD **, Mote`a O. Abdulla[2]** iD **, Ammar Ahmed Hamdoon[3]** iD

[1]Nineveh Education Directorate Ministry of Education, Mosul, 41001, Iraq
[2]Mishraq Sulfur State Company, Ministry of Industry and Minerals-Iraq, 41001, Mosul, Iraq.
[3]Department of Chemistry, College of Education for Pure Sciences, University of Mosul, 41001, Mosul, Iraq.

Abstract: The research included estimating the elemental sulfur percentage in sulfuric foam waste, which was found to be 88.15%. Potassium polysulfide was prepared from this waste and used to prepare nano-sized sulfur particles through reduction processes. Stable suspensions were obtained for more than 30 days. The crystalline structure of the prepared samples was studied using X-ray diffraction (XRD). It showed a crystalline growth of nano-sized sulfur particles from the non-crystalline structure at a concentration of 0.5 mL. The crystalline bundles began to appear at a concentration of 1 mL, and their intensity increased, and good bundles appeared at a concentration of 1.5 mL. Scanning electron microscopy (SEM) and energy-dispersive X-ray spectroscopy (EDX) were used to study the same prepared samples, and the particle size range was (19.59-43.47 nm), (31.33-44.23 nm), and (31.52-62.64 nm). The method was characterized by its ease, low cost, and absence of harmful environmental gas emissions.

1. INTRODUCTION

Nanotechnology is considered one of the most important modern sciences due to its many contributions to various fields of knowledge. Nanomaterials, including sulfur, are important in fighting cancerous diseases and agricultural pests and using nano-sulfur in lithium batteries (1). In literature, many studies have focused on preparing and using nano-sulfur in several areas. For example, Guo and his colleagues successfully used ultra-small monodisperse sulfur molecules through a chemical reaction between sodium polysulfide and hydrochloric acid in a fine emulsion system (2). Deshpande and his colleagues prepared nano-sulfur from hydrogen sulfide gas (3). Xie X.Y and his colleagues added cysteine to the sulfur solution and studied the results using ultrasound waves to obtain nano-sulfur particles with different shapes and sizes (4). Chaudhuri, R. G., and Paria were able to prepare nano-sulfur using decomposition in an acidic medium of a sodium thiosulfate solution and using surface tension reducers to obtain nano-sulfur

with a size of 30 nm (5) IA, M and his team studied the antifungal activity using nano-sulfur deposited from a solution of sodium sulfide The study revealed that the average particle size of the nano-sulfur used in the antifungal activity was 25 nanometers (6). Teng and his team also studied the possibility of using nano-sulfur in various fields, including environmental treatments, water and soil purification, and the manufacturing of nanodevices through nanotechnology. The study concluded that nano-sulfur's unique properties and functions could lead to many applications (7). Shevchenko and his team used a new method to prepare biocompatible and biodegradable nano-sulfur particles, which were non-toxic and had a size of 10-20 nanometers. The results showed that nano-sulfur could be used as a promising anti-cancer agent by isolating copper (8). Xu, P.F. and his team prepared nano-sulfur as a disinfectant, antifungal, and antibacterial agent (9). Meselhy and his team studied the effect of nano-sulfur on rice plants and found that it improved their growth and reduced the toxicity and accumulation of arsenic in rice (10).

2. EXPERIMENTAL SECTION

2.1. Obtaining the raw material (foam)
The raw material used in the study (foam) was obtained from the General Company for Sulphur Al-Mashraq, which is in the form of ground gray granules.

2.2. Chemical Analysis
Many chemical analyses were carried out to identify the components of sulfur foam, as well as to estimate the elemental sulfur content in sulfur residues. The percentage of sulfide ions in a solution of potassium polysulfide was also evaluated. Additionally, the free sulfur percentage in the suspended solution of nano-sulfur was calculated according to standard methods (11,12).

2.3. Preparation of Potassium Polysulfide
Due to the high sulfur content in sulfur waste (Foam), according to the analyses conducted, it is possible to prepare multiple potassium sulfides from it per standard methods (13).

2.4. Preparation of Nanoscale Sulfur from Potassium Polysulfide
0.1, 0.2, 0.3, 0.4, 0.5, 1, 1.25, 1.5, 1.75, and 2.0 mL samples of potassium polysulfide solutions were added to a liter of distilled water. After several minutes, nanoscale sulfur was observed as suspended in the solution. The solution was studied using scanning electron microscopy (SEM), X-ray diffraction (XRD), and energy-dispersive X-ray spectroscopy (EDX).

3. RESULTS AND DISCUSSION

Nanotechnology is one of the most important fields of scientific research due to its wide range of applications and the unique properties of nanomaterials that differ from larger particles. Therefore, the study and application of nanomaterials have attracted the attention of many researchers. Based on this, we prepared nano-sulfur from the waste of sulfur foam, which is a byproduct of the chemical oxidation process used to purify in Mishraq sulfur.

3.1 The Chemical Analysis of Foam
The chemical oxidation is one of the methods used to purify sulfur in the Mishraq field, which results in sulfuric residues known as foam (14). Table 1 shows the components of these residues according to the analyses conducted.

Table 1: Components of the foam.

Parameters	wt(%)
Free Sulfur	88.15
Carbon	1.86
Ash	2.23
Acidity	1.53
Moisture	3.65
Bonded sulfur	2.58

The elemental sulfur content in the known sulfur wastes, called "foam", reached 88.15%, which is a good percentage that can be used to introduce elemental sulfur into similar reactions to those found in pure sulfur, especially since the other materials found in the foam are inert under normal conditions.

The Energy Dispersive X-ray Spectroscopy (EDX) of sulfur wastes (foam) can be used to obtain the composition or chemical analysis of the material, as the (EDX) technique provides the nature of the elements contained in the material as well as their percentage (15). In our study, we used the EDX spectral analysis to identify the basic elements that make up the foam material, as shown in Figure 1 and Table 2.
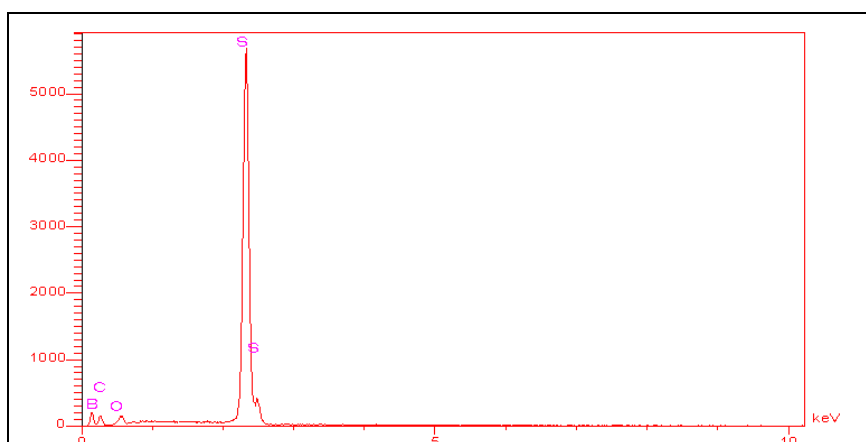
**Figure 1:** X-ray scattering energy spectrum of sulfur waste (foam).

Table 2: Percentages of basic elements of foam.

Element	wt (%)
S	80.90
C	16.30
O	2.80

It is clear from the table that the basic composition of foam material is sulfur, carbon, and oxygen.

3.2. X-ray Diffraction Measurements (XRD) for Foam
X-ray diffraction (XRD) technique was used to study the crystal structure of different materials (16). Table 3 and Figure 2 illustrate the results of these measurements.
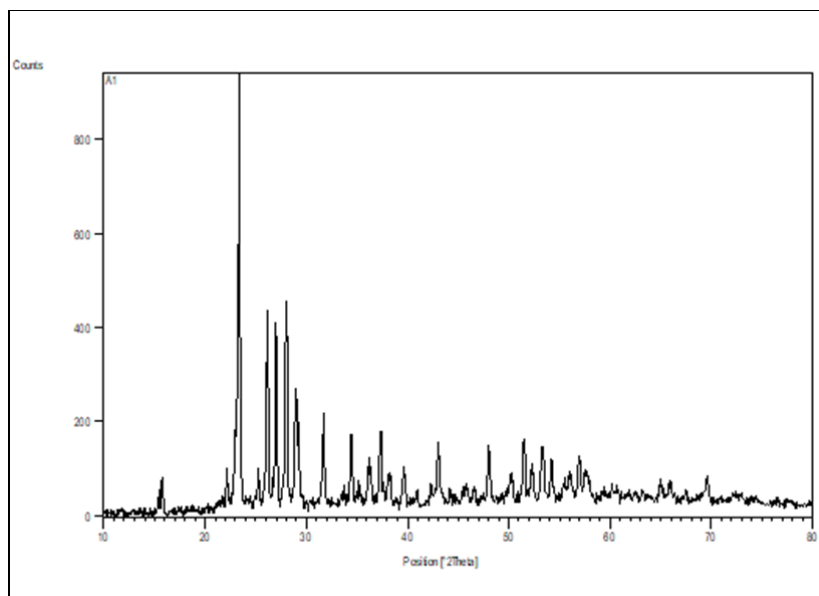
Figure 2: X-ray diffraction of foam.

Table 3: Values of diffraction angles 2θ, atomic distance d, and intensity I for foam sulfur residues.

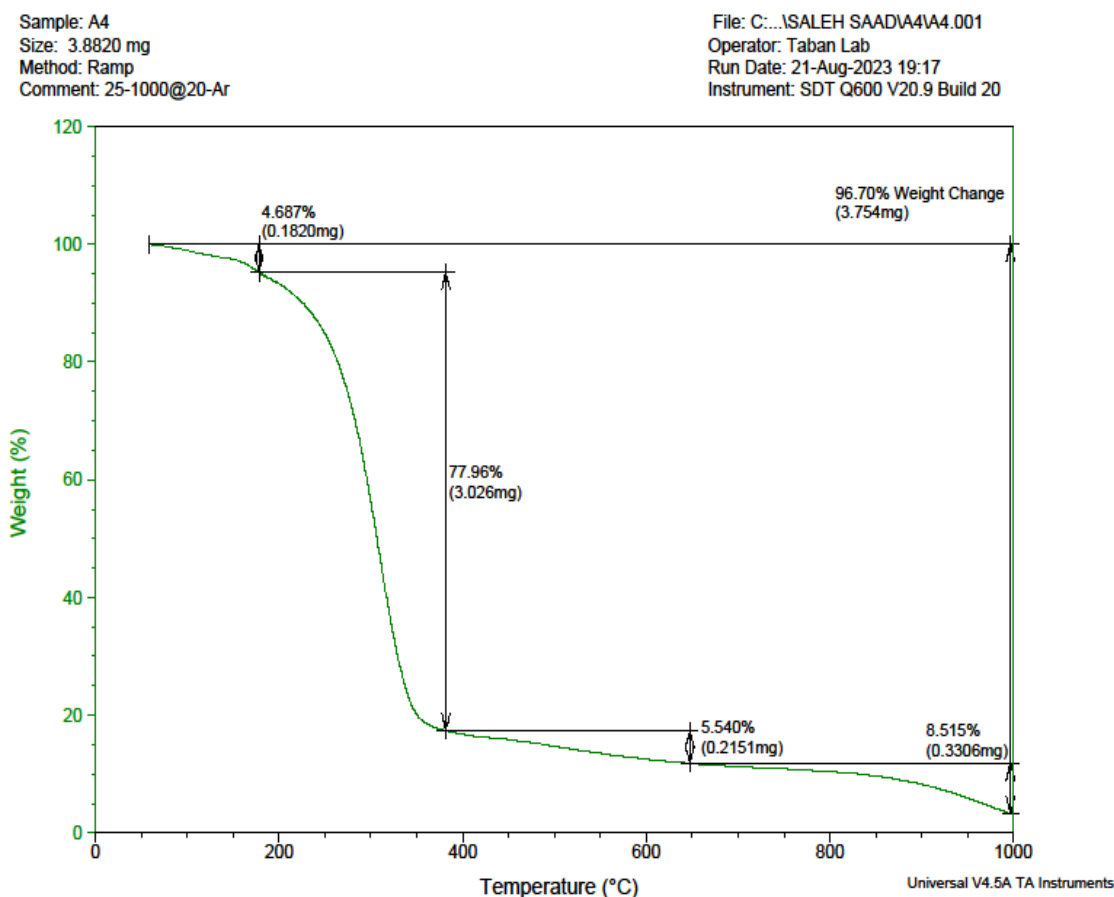| Peak number	2θ	d-spacing	I%
1-	11.6782	7.57785	0.83
2-	15.7284	5.63446	7.59
3-	22.2128	4.00213	6.49
4-	23.3760	3.80556	100.00
5-	26.1610	3.40640	44.59
6-	28.9413	3.08518	28.06
7-	36.1583	2.48424	11.29
8-	43.0481	2.10127	13.46
9-	46.5667	1.95036	2.59
10-	48.0697	1.89283	10.67

It is evident from Figure 2 that there are 30 peaks, the most important of which are mentioned in the above table. It was also observed that there are major bundles belonging to assigned sulfur through the values of diffraction angles 2θ and atomic distance d, most notably the bundle that appeared at 2θ = 23.3760, which matches the X-ray diffraction pattern of orthorhombic sulfur. These results were compared using the X-pert High Score Plus program linked to the X-ray diffractometer.

3.3. Thermogravimetric Analysis (TGA)
TGA is a method of thermal analysis that involves monitoring changes in chemical and physical properties that occur during an increase in temperature, thereby determining the nature of the material being analyzed. This is done by assessing the stability of the materials, identifying the absorbed moisture level, and determining the amount of non-organic components that usually remain until the end of the measurement due to their high resistance to temperature. In our study, TGA measurement was used to analyze the foam material, and Figure 3 shows the results of this analysis.

Figure 3: Thermogravimetric analysis of foam.

The measurement of the thermogravimetric analysis and through the figure showed changes in weight in four areas; at a temperature of 180 °C, the loss of moisture occurred completely, as the moisture water is immersed inside the sulfur smelter and needs more energy for getting rid of it, as the percentage of change in weight reached 4.687%. At a temperature of 375 °C, the loss of elemental sulfur occurs, as we note that the percentage of change in weight reached 77.86% at 650 °C, as there is a loss of sulfur consonant with carbon; in other words, the disintegration of carbo-sulfur compounds occurs, but at a temperature of 1000 °C, there is a loss of carbon and sulfur residues adsorbed within the fine pores, as the percentage of total weight loss reached 96.7%, while the remaining percentage, which is 3.3, represents metal oxides such as silica SiO_2, resulting from the use of slite clays in one of the stages of sulfur purification.

3.4. Preparation of Polysulfide Potassium
Since the sulfur residues foam contains a high percentage of elemental sulfur, which can react without intrinsic effects from the carbo-sulfur substances known as (carsul), which are separated by filtration, it was used in a polysulfide potassium preparation according to the following equation:

$$2KOH + carsul - xS \longrightarrow K_2S_x + carsul$$
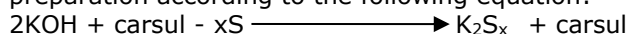
Carsul is separated from the solution by filtration, and then the percentage of sulfide in a polysulfide solution of potassium was estimated according to approved weighing methods (11), as the percentage of sulfide in the solution was 21.1 %.

3.5. Preparation of Sulfur Nanoparticles
Very few volumes of potassium polysulfide solution were used and diluted at a certain volume of water, as after a short period (less than two minutes), turbidity of the solution (i.e., a suspended solution is formed), the solution becomes more turbid over time.

It was found through the measurements that were made that the cause of turbidity is obtaining sulfur nanoparticles by diluting potassium polysulfide using different sizes of 0.1-2 mL/L. The cessation of hydrolysis has been noted to occur when the concentration of potassium polysulfide reaches 2%. After adding this ratio to the water, the solution is vigorously agitated to achieve a uniform mixture. Subsequently, potassium polysulfide material is introduced, resulting in the formation of a suspended solution. The sulfur nano concentration was found by iodometric analysis (14), and Table 4 shows the concentration of nano sulfur.

**Table 4:** Sulfur Nanoconcentrations in Dilute Solutions of K_2S_x.

Sample Number	Volume (mL) K_2S_x	NPs(ppm)
1	0.1	1120
2	0.2	2094
3	0.3	2969
4	0.4	3787
5	0.5	4580
6	0.75	6150
7	1	7145
8	1.25	6430
9	1.5	3125
10	1.75	1437
11	2	0

From the table, we can see a decrease in elemental sulfur concentration, which is due to a decrease in the percentage of polysodium sulfide degradation, which stops at a 2% volume of potassium polysulfide.

All models prepared by XRD X-ray diffractometer, SEM scanning electron microscope, and EDS scattering spectrometer were studied as follows:

3.6. Scanning Electron Microscope and Dispersed Energy Spectrum of Sulfur Nanoscales
The samples prepared from sulfur nanometers were studied by SEM. The magnified images show that it has a spherical shape and that the granular size range of the sulfur nanoparticles prepared for volumes 0.5, 1.0, and 1.5 mL was, respectively: 19.59-43.47 nm and 31.33-44.23 nm and 31.52-62.64 nm as shown in Figure 4.
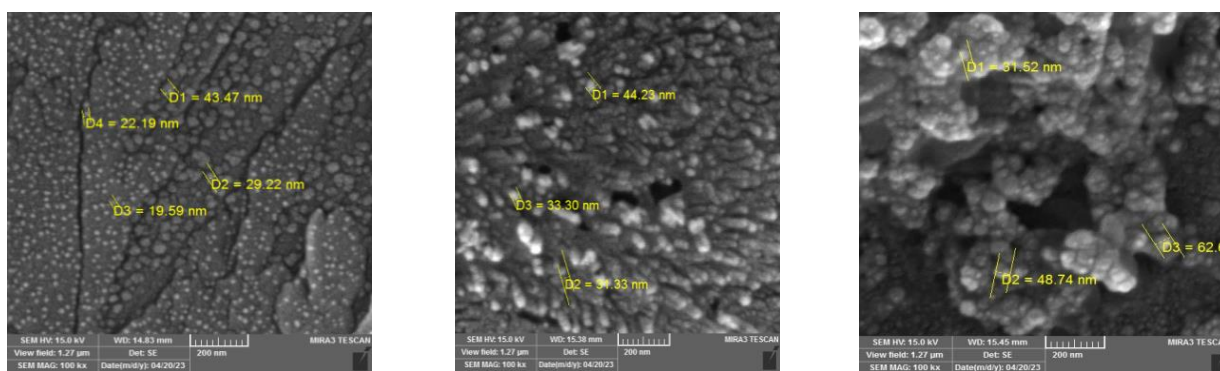
Figure 4: Scanning electron microscopy (SEM) images of diluted K_2S_x models (0.5, 1, and 1.5 mL).

The measurement of the sparse energy spectrometry of X-rays (EDX) also showed the presence of sulfur clearly in the dilute solutions, and Figure (5) and Table (5) illustrate this:
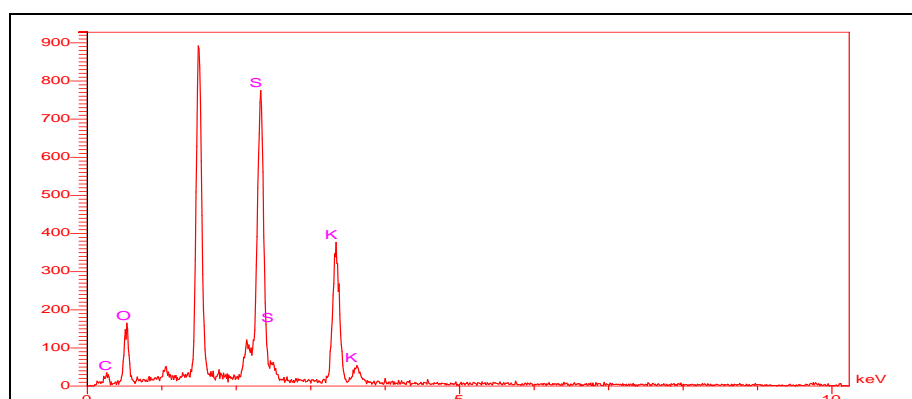

Figure 5: X-ray energy spectrum of the prepared nanoporous sulfur solution.

Table 5: The proportions of the basic elements of the prepared nano-sulfur solution.

| Element	Wt(%)
S	30.56
C	13.63
O	32.31
K	23.50

We notice from the figure the presence of sulfur clearly in the suspended solution, as well as the presence of potassium and oxygen, as the preparation of nano-sulfur was through the addition of potassium polysulfide as described in the experimental section, as well as the presence of carbon mainly in sulfur residues, and this indicates that the shape accurately matches the preparation process.

3.7. X-ray Diffraction Measurement of Prepared Nano-Sulfur

The X-ray diffraction pattern of the prepared models was measured using dilution at 0.5-1-1.5 mL (6-8). The measurement result shows the following:
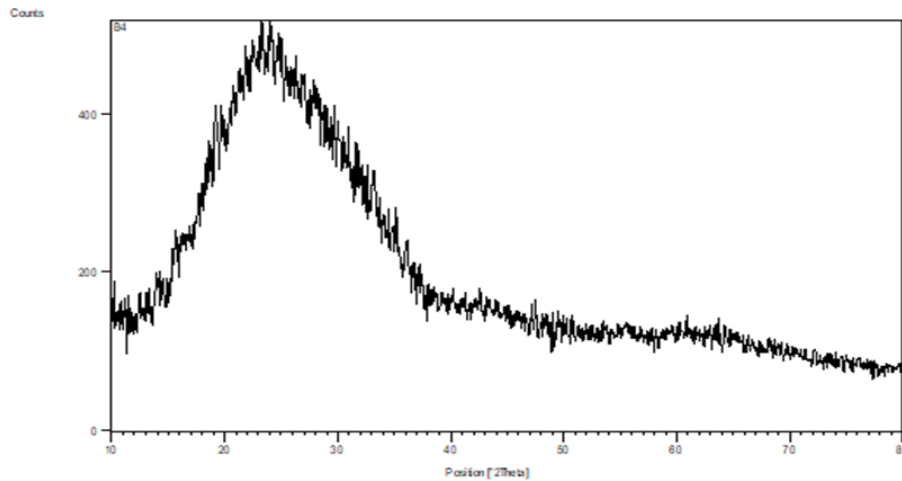
Figure 6: X-ray diffraction of nano-sulfur prepared from dilution 0.5 ml of K_2Sx solution.
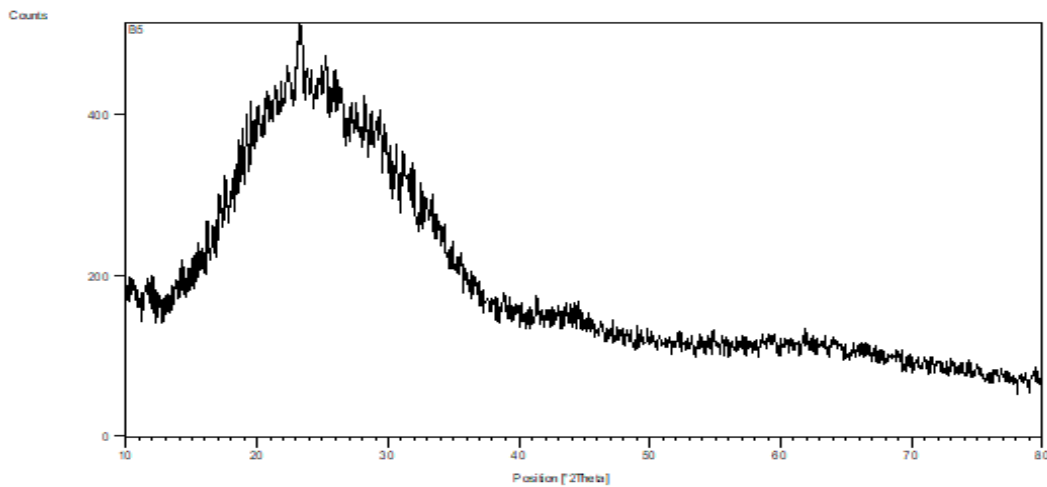
Figure 7: X-ray diffraction of sulfur nanoscale prepared from dilution of 1mL of K_2S_x solution.
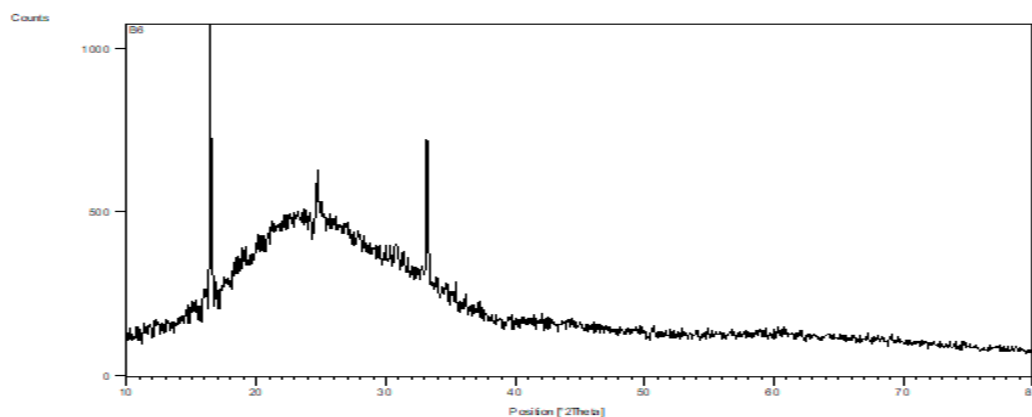
Figure 8: X-ray diffraction of nano-sulfur prepared from dilution of 1.5 mL of K2Sx solution.

We note from the three figures that by increasing the concentration from 0.5 mL / L to 1.5 mL / L there is a development in the crystal structure of the nano-sulfur resulting from dilution by moving from the amorphous structure to the crystal structure by increasing the concentration, in the concentration of 0.5 mL/L it is noted that the composition of the nano-sulfur is amorphous through the broadband $2\theta = 20\text{-}30$ as in Figure 6. At a concentration of 1 mL/L, despite the predominance of the amorphous phase, a crystal beam began to appear at $\theta = 24.73(2)$ as in Figure 7. While the concentration of 1.5 mL/L through Figure (8) showed that nano-sulfur is a mixture of crystalline sulfur through the three beams indicated in Table (6) and amorphous sulfur.

Table 6: Values of diffraction angles 2θ, atomic distance d, and intensity I For nanosulfur prepared from dilution 1.5 mL of K2Sx solution.

Peak number	2θ	d-spacing	(%) I
1-	16.4514	5.38842	100.00
2-	24.7394	3.59884	17.75
3-	33.1973	2.69873	55.95

4. CONCLUSIONS

1.   Solid sulfur residues resulting from the chemical method of purification of mining sulfur in Al-Mishraq contain a high percentage of elemental sulfur, which is suitable as a source of elemental sulfur instead of pure sulfur.
2.   The possibility of preparing a potassium polysulfide solution from sulfur residues as a raw material.
3.   Preparation of nano-sulfur without the use of contaminated chemicals.
4.   Obtaining non-crystalline sulfur as one of the forms of elemental sulfur.
5.   The possibility of immediate preparation of nano-sulfur in situ when used to combat agricultural pests.

5. CONFLICT OF INTEREST

There are no conflicts of interest.

6. ACKNOWLEDGMENTS

7. REFERENCES

1.   Sun GW, Zhang CY, Dai Z, Jin MJ, Liu QY, Pan JL, Wang YC, Gao XP, Lan W, Sun GZ, Gong CS. Construction of all-carbon micro/nanoscale interconnected sulfur host for high-rate and ultra-stable lithium-sulfur batteries: Role of oxygen-containing functional groups. Journal of Colloid and Interface Science. 2022 Feb 15;608:459-69. Available from: <DOI>.

2.   Guo Y, Zhao J, Yang S, Yu K, Wang Z, Zhang H. Preparation and characterization of monoclinic sulfur nanoparticles by water-in-oil microemulsions technique. Powder technology. 2006 Mar 1;162(2):83-6. Available from: <DOI>.

3.   Deshpande AS, Khomane RB, Vaidya BK, Joshi RM, Harle AS, Kulkarni BD. Sulfur nanoparticles synthesis and characterization from H 2 S gas, using novel biodegradable iron chelates in W/O microemulsion. Nanoscale Research Letters. 2008 Jun;3:221-9. Available from: <DOI>.

4.   Xie XY, Zheng WJ, Bai Y, Liu J. Cystine modified nano-sulfur and its spectral properties. Materials letters. 2009 Jun 30;63(16):1374-6. Available from: <DOI>.

5.   Chaudhuri RG, Paria S. A novel method for the templated synthesis of Ag2S hollow nanospheres in aqueous surfactant media. Journal of colloid and interface science. 2012 Mar 1;369(1):117-22. Available from: <DOI>.

6.   IA M, RM Z, AR S, AG M. The efficancy of micron and nanoscale sulfur the schutte fungi. International Journal of Sciences. 2013 Mar 1. Available from: <DOI>.

7.   Teng Y, Zhou Q, Gao P. Applications and challenges of elemental sulfur, nanosulfur, polymeric sulfur, sulfur composites, and plasmonic nanostructures. Critical Reviews in Environmental Science and Technology. 2019 Dec 17;49(24):2314-58. Available from: <DOI>.

8.   Shevchenko N, Steinhart M, Tomšík E. Single-step preparation of mono-dispersed sulfur nanoparticles for detention of copper. Journal of Nanoparticle Research. 2019 Nov;21:1-2. Available from: <DOI>.

9.   Xu PF, Liu ZH, Duan YH, Sun Q, Wang D, Zeng XF, Wang JX. Microfluidic controllable synthesis of monodispersed sulfur nanoparticles with enhanced antibacterial activities. Chemical Engineering Journal. 2020 Oct 15;398:125293. Available from: <DOI>.

10.   G Meselhy A, Sharma S, Guo Z, Singh G, Yuan H, Tripathi RD, Xing B, Musante C, White JC, Dhankher OP. Nanoscale sulfur improves plant growth and reduces arsenic toxicity and accumulation in rice (Oryza sativa L.). Environmental Science & Technology. 2021 Sep 27;55(20):13490-503. Available from: <DOI>.

11.   Willliams WJ, Handbook of Anion Determination, Butterworth &Co(publisher) Ltd. 1979, Pp:516. Available from: <DOI>.

12.   Abdullah Al-Sarraf and Muti` Obaid Abdullah, (2004). "Quality Manual of the General Company for Mishraq Sulfur" The General Company for Mishraq Sulfur - Second Revised Edition. Available from: <DOI>.

13.   Riegel ER, and Kent JA. "Riegel's Handbook of Industrial Chemistry" Springer Science and Business Media (2003), p. 143. Available from: <DOI>.

14.   Al-jubori MO. Study of the purification of sulfur raw materials and its refining products and their use in the chemical industries (Doctoral dissertation, Ph. D. thesis, University of Mosul-College of Education). Available from: <DOI>.

15.   Scimeca M, Bischetti S, Lamsira HK, Bonfiglio R, Bonanno E. Energy Dispersive X-ray (EDX) microanalysis: A powerful tool in biomedical research and diagnosis. European journal of histochemistry: EJH. 2018 Jan 1;62(1). Available from: <DOI>.

16.   Al-Saadi AKh, "Diagnosis and Characterization of Nanomaterials," Al-Amir House for Printing and Publishing, Technological University, (2021), pp. 169, 149, 128. Available from: <DOI>.

Removal of Methyl Orange from Aqueous Solution Using Orange Peel as a Low-Cost Adsorbent

Ahmed Lawal Mashi[*1] iD **, Abdulhafeez Abdulsalam**[2] iD

[1]Ibrahim Shehu Shema Centre for Renewable Energy Research, Umaru Musa Yar'adua University, Katsina, Nigeria
[2]Department of Pure and Industrial Chemistry, Umaru Musa Yar'adua University, Katsina, Nigeria

Abstract: The objective of this research was to evaluate the feasibility of using orange peels as a low-cost adsorbent to remove methyl orange (MO) from water solutions. The orange peel adsorbent underwent characterization through Scanning Electron Microscopy (SEM) and Fourier Transform Infrared (FTIR) Spectroscopy to determine its properties before and after adsorption. A series of batch adsorption experiments were carried out to investigate the effects of various parameters such as contact time, adsorbent dosage, particle size, and initial dye concentration on the adsorption process. In each case, varying the value of the parameter of interest while keeping all other parameters constant. Results revealed that the highest removal of the dye from the adsorbent was achieved at a contact time of 90 min, the adsorbent dosage of 0.5 g, a particle size of less than 63 μm, and an initial concentration of 300 mg/L. Furthermore, the adsorption rate increased with increasing contact time, adsorbent dosage, and initial concentration, while it decreased with increasing particle size of the adsorbent. Concentrations of methyl orange were analyzed using a UV-Vis spectrophotometer. The experimental equilibrium data was analyzed using Langmuir and Freundlich isotherm models. The Langmuir isotherm provided the best fit for the experimental data with a correlation coefficient value of 0.9964 and a maximum adsorption capacity of 17.69 mg/g.

1. INTRODUCTION

For a considerable period, water pollution has remained a critical issue. Pollutants like dyes, pesticides, and heavy metals have contributed to this problem (1). Water pollution presents significant hazards to both human beings and aquatic life (2). The textile sector is a significant contributor to water pollution. The wastewater generated from textile production facilities includes harmful dyes, which are carcinogenic and mutagenic (3).

Acid dyes are water-soluble anionic dyes that are typically applied to fibers. The majority of food dyes fall under the category of acid dyes. The azo group is the most prevalent chromophore found in acid dyes. Methyl orange, a commonly used water-soluble azo dye, serves as a pH indicator and is widely used in various industries, like the paper, textile, as well as food industries (4). Exposure to

Methyl orange can result in symptoms such as vomiting and diarrhea, and high concentrations can lead to death.

There are several methods available for removing dyes from aqueous solutions, including coagulation-flocculation, biological treatment, chemical precipitation, electrochemical treatment, and adsorption (1,5). Adsorption is a highly desirable process, primarily due to its low operational cost, ease of operation, and lack of regeneration issues (6). In recent times, adsorption has become a widely used method in both industrial and environmental protection appli-cations. Undoubtedly, activated carbon is the most commonly utilized adsorbent for removing organic dyes due to its high adsorption activity and large surface area. However, in some countries, its usage is regulated because of its high cost and regeneration issues (5).

Low-cost adsorbents used in water treatment should exhibit qualities such as low economic cost, availability, and disposability without regeneration. Studies have examined the effectiveness of various low-cost materials, such as rice straw, orange peel, grain husk, banana peel, and biochar, in treating textile wastewater. These agricultural wastes are effective as low-cost adsorbents (7).

Materials such as orange peel, banana peel, coconut shell and other agricultural wastes have been reported as adsorbents in the removal of methyl orange from previous studies (2,7,10). Orange peel contains cellulose, hemicellulose, lignin, pectin, and chlorophyll pigments, which possess functional groups like hydroxyl and carboxyl groups. These components make orange peel a suitable adsorbent (8). OP is a viable adsorbent due to its cost-effectiveness, abundance, biodegradability, non-toxicity, and non-regeneration (9).

The objective of this study was to evaluate the efficacy of using orange peels, a natural waste material with no economic value, as an adsorbent for the removal of methyl orange from water. The study utilized unmodified orange peels as the adsorbent and conducted isotherm studies to determine their adsorption capacity. Orange peels are readily available in Nigeria and the study aimed to explore the potential of this abundant and underutilized waste material for water treatment purposes.

2. EXPERIMENTAL SECTION

2.1. Preparation of Adsorbent
Orange peels (*Citrus sinensis*) were obtained from local market vendors and cleaned to eliminate any physical impurities. After cleaning, the orange peels were dried for two days in the shade, and then finely ground using a mortar and pestle. The resulting powder was stored in sealed containers and labeled as "Orange Peel Adsorbent". Particle size of a portion of the ground OP was determined by using sieves of varying mesh sizes (<63 μm, 63-106 μm and 106-150 μm) to investigate the effect of particle size on adsorption of methyl orange.

2.2. Characterization of the Adsorbent
The morphological properties of the OP adsorbent were examined using a Scanning Electron Microscope (Phenom SEM PW-100-012) at 500× magnification, both before and after adsorption. The differences observed were discussed. In addition, Fourier Transmission Infrared (Cary 630 Agilent Technologies FT-IR) analysis was conducted on the OP adsorbent at a resolution of 8 cm^{-1} to identify the presence of certain functional groups.

2.3. Preparation of Adsorbate
The adsorption capacity of unmodified OP adsorbent was tested using analytical grade MO, which has a minimum absorption wavelength of 464 nm. To prepare the MO solution, 1 g of the dye was dissolved in 1 L of distilled water to create a stock solution with a concentration of 1000 mg/L. Working solutions with lower concentrations were made by diluting the stock solution using Equation 1.

$$C_1V_1 = C_2V_2 \qquad \text{(Eq. 1)}$$

Figure 1: Structure of MO dye.

2.4. Batch Adsorption Experiment
Several experiments were conducted in a 100 cm^3 conical flask that contained 50 mL of methyl orange solution. Different parameters were taken into account, such as the contact time (30-90 min), the adsorbent dosage (0.1 – 0.5 g), the particle size of OP (<63 μm), and the initial concentration of the dye solution (300-1000 mg/L), while keeping other parameters constant. These parameters were selected in comparison with previous literatures (2,10), in order to explore the experimental reaction space which is expected to achieve the economic objective of this study. The experiments were performed at room temperature, and the mixture of methyl orange dye solution and unmodified OP adsorbent in a conical flask was sealed and agitated using a flask shaker (ST15 0SA – Barloworld) at 300 rpm. Samples were collected at specific contact times, filtered with Whatman filter paper (PW 184), and measured for the remaining dye amount using a UV/Vis Spectrophotometer at the maximum absorption wavelength of MO (464 nm). The removal efficiency of methyl orange was calculated using Equation 2.

$$\% \text{ removal} (\%R) = \frac{(C_0 - C_t)}{C_0} \times 100\% \quad \text{(Eq. 2)}$$

Where C_0 is the initial concentration of the dye solution and C_t is the concentration at a particular time interval.

The amount of dye adsorbed per weight of OP adsorbent (adsorption capacity) can be calculated using Equation 3.

$$\text{Adsorption capacity} (q_e) = \frac{V(C_0 - C_t)}{M} \quad \text{(Eq. 3)}$$

where C_0 is the initial concentration of the dye solution, C_t is the concentration at particular time intervals, V is the volume of adsorbate used and M is the mass of adsorbent used.

2.4.1. Adsorption Isotherms
The interaction between dye molecules and the surface of an adsorbent is described using isotherms (10). They show the relationship between the amount of dye adsorbed per unit weight of the adsorbent and the concentration of the dye in bulk at equilibrium (11). The two most commonly used isotherms are Langmuir and Freundlich isotherms. The Langmuir isotherm model assumes that adsorption occurs on a homogeneous surface composed of a single layer of adsorbent molecules (10). Equation 4 describes the Langmuir isotherm model.

$$C_e/q_e = \frac{1}{q_m K_L} + \frac{C_e}{q_m} \qquad \text{(Eq. 4)}$$

where C_e is the concentration of methyl orange in solution at equilibrium (mg/L), q_e is the adsorption capacity of OP (mg/g), q_m is the maximum adsorption capacity of OP (mg/L) and K_L is a constant relating to adsorption heat (L/mg) (12).

A linear plot of C_e / q_e against C_e can be used to determine the values of K_L and q_m (10). The R_L value is a parameter used to evaluate the favorability of the Langmuir model and is calculated using Equation 5. If $R_L>1$, the adsorption process is unfavorable, if $R_L=1$, it is considered to be a linear process, if $0<R_L<1$, it is favorable, and if $R_L=0$, the process is considered to be irreversible.

$$R_L = \frac{1}{(1+ K_L C_o)} \qquad \text{(Eq. 5)}$$

where K_L is the constant relating to adsorption heat and C_o is the initial concentration.

While the linear form of the Freundlich isotherm is given by Equation 6.

$$\ln q_e = \ln K_f + \frac{1}{n} \ln C_e \qquad \text{(Eq. 6)}$$

where C_e is the concentration of methyl orange in solution at equilibrium (mg/L), q_e is the adsorption capacity of OP (mg/g), K_f is a constant relating to adsorption capacity and n is a constant relating to adsorption intensity (12). A linear plot of $\ln q_e$ against $\ln C_e$ can be used to determine the values of K_f and n (10).

## 3. RESULTS AND DISCUSSION

3.1. Characterization
The adsorbent's surface morphology is depicted in Figure 2 representing the condition after adsorption. The observation revealed that the adsorbent

possesses clustered pores of various particle sizes after the adsorption experiment (13,14). The presence of pores increase the number of adsorption sites. Figure 2a shows that OP exhibits a uniform dispersion of vacant sites before adsorption while Figure 2b indicates shrinkage of the adsorption sites. It was further observed that the pore size reduced and became more uniform. This change was attributed to the filling up of the pores by methyl orange molecules, leading to particle aggregation, potential liquid bridge, and compaction within the pores of the orange peel adsorbent. This further confirms the presence of occurring adsorption on the adsorbent.

Figures 3 and 4 present the FT-IR spectrum of the adsorbent before and after adsorption respectively. The peak observed at 3324 cm^{-1} indicated the presence of the OH functional group, while the peak at 2921 cm^{-1} indicated the presence of C-H stretching vibrations. The peak observed at 1607 cm^{-1} indicated the presence of conjugated C=C bonds. The peak at 1737 cm^{-1} indicated the presence of carbonyl groups, such as esters, aldehyde, ketones, or carboxylic acid groups. The presence of carbonyl groups, such as esters, aldehyde, ketones, or carboxylic acid groups, is indicated by the peak at 1737 cm^{-1}. The peaks detected at 1369 cm^{-1} represented –CH$_2$– and –CH$_3$ bending vibrations. The results indicated the presence of cellulose, hemicellulose, and lignin. More peaks were detected in the fingerprint region after adsorption, as shown in Figure 5. This could be attributed to the presence of adsorbed methyl orange molecules. A slight shift in the wave number of the OH peak was observed, from 3324 cm^{-1} to 3387 cm^{-1}. This demonstrated the active involvement of the OH group in the adsorption process.
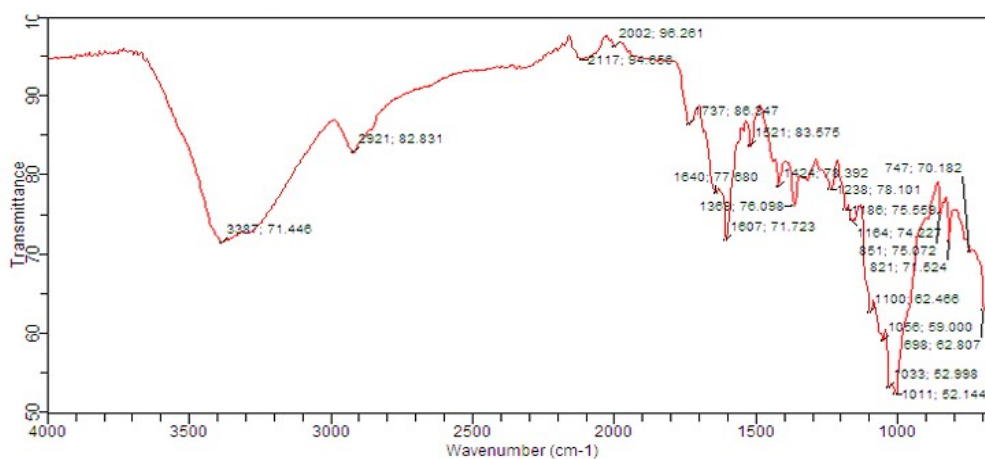
3.2. Effect of Contact Time
Batch adsorption experiments were conducted at room temperature, utilizing an adsorbent dosage of 0.5 g / 50 mL, an initial dye concentration of 0.5 g/L, and varying contact times of 30 min, 60 min, and 90 min, as shown in Figure 5. The results indicated that as the contact time increased, the percentage removal and adsorption capacity also increased. At a contact time of 30 min, the percentage removal of the dye was 24% and the adsorption capacity was 12 mg/g. This increased to 36% percentage removal and 16 mg/g adsorption capacity at a contact time of 60 mins. At a contact time of 90 minutes, the percentage removal further increased to 44% and the adsorption capacity increased to 22 mg/g. The increased time from 30 to 60 min suggests a 50% increment in OP removal whereas a 22% increment was noted between 60 min to 90 min. The steep increase from 60 min to 90 min is evidence of saturation of the pore sites by the OP which resulted in potential liquid bridging as noted by the SEM findings. In addition, the findings are consistent with the increased adsorption capacity as shown in Figure 5. Previous findings align with the results reported herein (15,16).
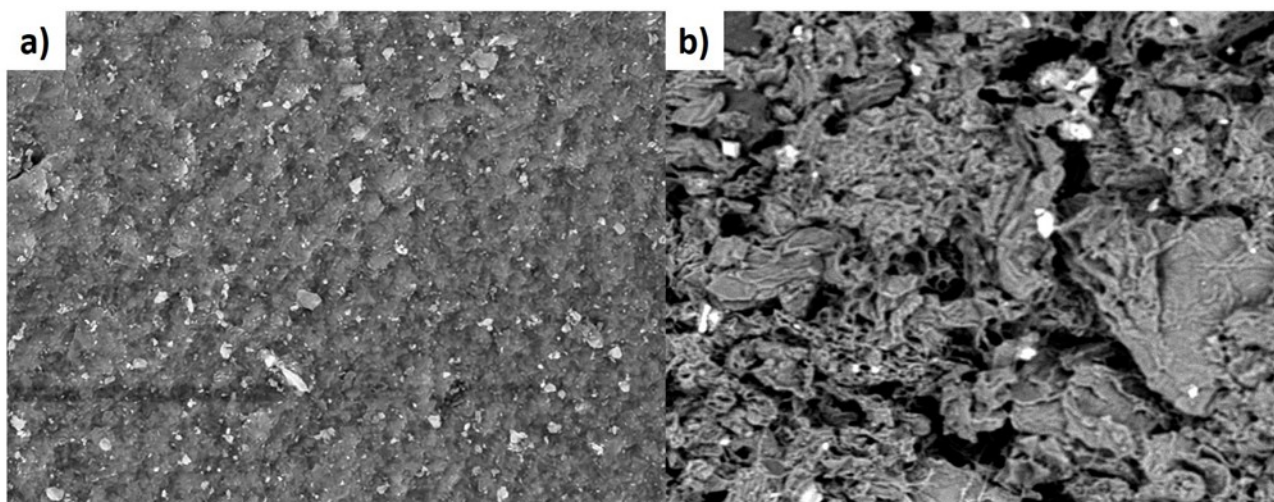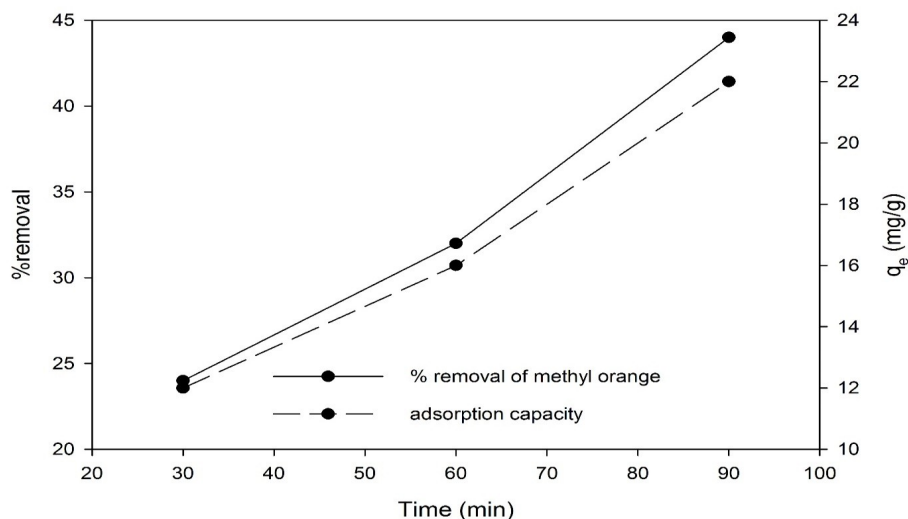
Figure 2: SEM Image of OP a) before b) after adsorption.
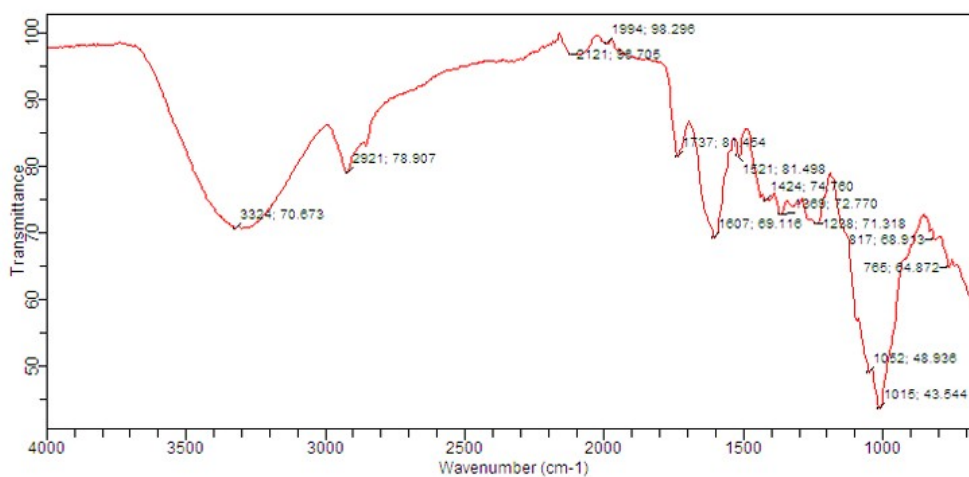
Figure 3: FT-IR spectrum of OP before adsorption.

**Figure 4:** FT-IR spectrum of OP after adsorption.

Figure 5: Effect of contact time on % removal.

3.3. Effect of Adsorbent Dose

The effect of the adsorbent dose was investigated by varying the amount of adsorbent (0.1 g, 0.3 g, and 0.5 g) as shown in Figure 6 and keeping all other parameters constant: initial concentration of dye solution (500 mg/L), contact time (30 min) and room temperature (17). It was discovered that there is an increase in percentage removal with an increase in adsorbent dose. It was also observed that as the adsorbent dose increased from 0.1 – 0.3 g the percentage removal increased from 4-16% and the adsorption capacity increased from 2 mg/g to 8 mg/g. Upon increase of the adsorbent dose from 0.3 – 0.5 g the percentage removal increased from 16% to 24% and the adsorption capacity increased from 8 mg/g to 12 mg/g. This observation is attributed to increased adsorption sites and surface area of the adsorbent which in turn provides additional vacancy for adsorbate take up (18).
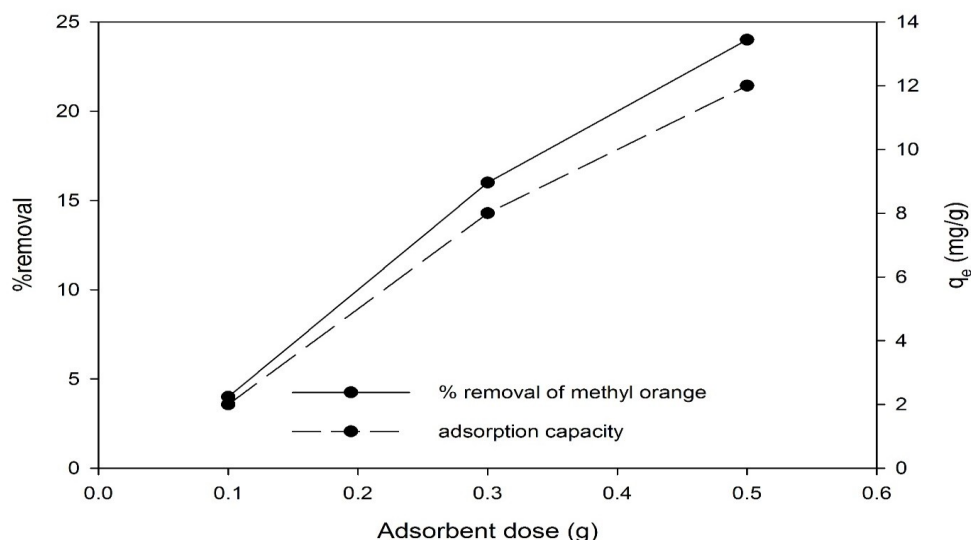
Figure 6: Effect of adsorbent dose on % removal.

3.4. Effect of Initial Concentration

Three different concentrations (300 mg/L, 600 mg/L, and 1000 mg/L) of methyl orange were used to investigate the effect of initial concentration on the percentage removal at constant values of adsorbent dosage (0.5 g / 50 mL), contact time (30 min), and at room temperature. As observed in Figure 7 as the concentration increases, the adsorption capacity also increases due to higher competition of methyl orange molecules on the OP at higher concentrations. On the other hand, the % removal decreases as the initial concentration is increased. During the experiment, all other parameters were kept constant. This observation agrees with the results from the work on the adsorption of methyl orange using a lala clamshell (10). At the initial concentration of 300 mg/L, the percentage removal was 40% and the amount of methyl orange adsorbed was 12 mg/g, at the initial concentration of 600 mg/L, the percentage removal

43

decreased to 23.3% and the amount of methyl orange adsorbed increased to 14 mg/g and at the initial concentration of 1000 mg/L, the percentage removal further decreased to 16% but the amount of dye adsorbed increased to 16 mg/g. The observed decreasing trend of % removal can be attributed to the saturation of adsorption sites on the OP at higher concentrations. The availability of unoccupied sites becomes limited for the adsorption of the methyl orange molecules to occur effectively (19).
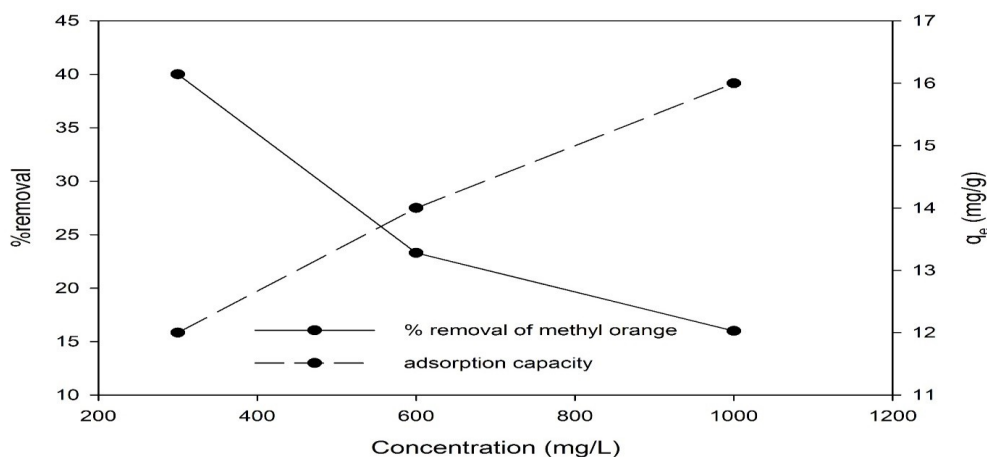
Figure 7: Effect of initial concentration on % removal.

3.5. Effect of Particle Size
The effect of the size of the adsorbent was investigated using three different sizes of OP adsorbent (<63 μm, 63-106 μm, and 106-150 μm) while other parameters were kept constant: 0.5 g / 50mL adsorbent dose, 30 min contact time and at room temperature. It was observed that % removal and adsorption capacity increases as the size of the adsorbent decreases. A significant inc-rease in the % removal and adsorption capacity was recorded between 63-106 μm and <63 μm as shown in Figure 8. Between particle sizes of 106-150 μm and 63-106 μm, % removal increased from 20% to 24% while adsorption capacity increased from 10mg/g to 12 mg/g and between particle sizes of 63-106 μm and <63 μm, % removal increased from 24% to 36% while adsorption capacity increased from 12 mg/g to 18 mg/g. The higher removal of methyl orange observed on the smallest particle size (<63 μm) can be linked to the rapid diffusion rate of methyl orange in and out of the OP adsorbent. In addition, the path length is shortened which exposes the pores to the methyl orange and is expected to eliminate the influence of intraparticle diffusion resistance. The result obtained agrees with similar research (7).

Figure 8: Effect of particle size on % removal.

3.6. Adsorption Isotherms
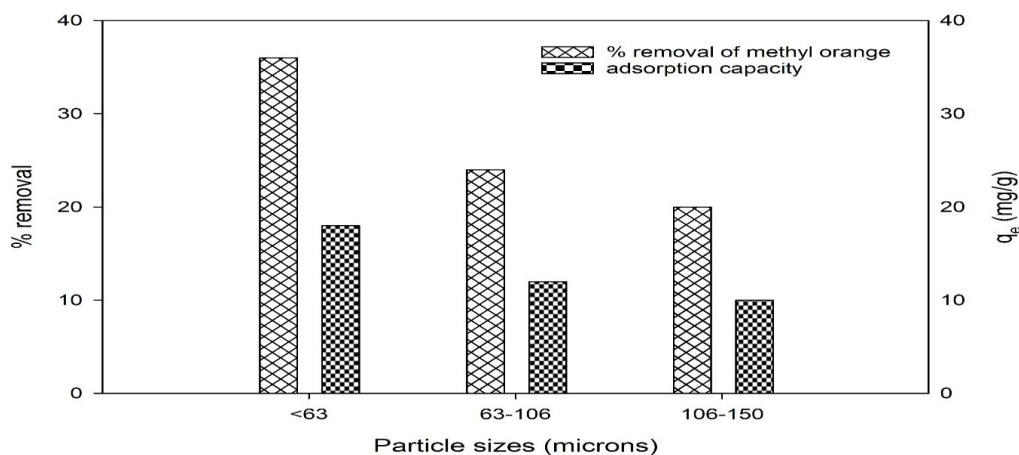The results from the experiments were studied using isotherm models. It was studied at different initial concentrations (300 mg/L, 600 mg/L, and 1000 mg/L) of the methyl orange solution, contact time of 30 min, 0.5 g / 50 mL adsorbent dose, and room temperature. The distribution and interaction of dyes on the surface of the adsorbent are illustrated using adsorption isotherm models (20). The two most used isotherm models are Langmuir and Freundlich isotherm models as shown in Tables 1 and 2. The experiment best fitted the Langmuir

isotherm model producing a straight line graph and a higher R^2 value of 0.9964 as illustrated in Figure 9. The calculated q_m was 17.69 mg/g which is not far from the value obtained by the experiment which is 16 mg/g. Therefore, Langmuir isotherm is favorable for the adsorption of methyl orange onto orange peel. R_L value shows the nature of the

adsorption process to be unfavorable if $R_L>1$, linear if $R_L = 1$, favorable if $0<R_L<1$, or irreversible if $R_L = 0$. The R_L value 0.0893 was obtained which falls in the range $0 < R_L < 1$. This further ascertains that the experiment was better fitted by Langmuir isotherm.

Table 1: Langmuir isotherm constants for adsorption of methyl orange onto orange peel.

q_m (mg/g)	K_L(L/mg)	R^2	R_L
17.69	0.0102	0.9964	0.0893

Table 2: Freundlich isotherm constants for adsorption of methyl orange onto orange peel.

K_f(mg/g)	N	R^2
4.4916	5.3333	0.9955
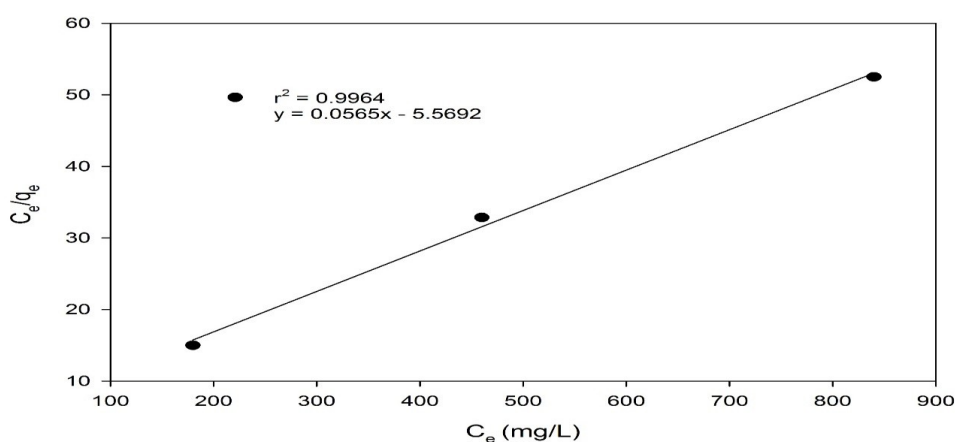
Figure 9: Langmuir isotherm curve.

4. CONCLUSION

The Experimental results showed that orange peel can be used as a low-cost adsorbent for the removal of methyl orange. It was observed that an increase in the reaction parameters showed an increasing trend for the removal of dye except for increased concentration which is due to saturation of adsorption sites. Scanning electron microscope analysis showed the aggregation of particles after adsorption. FT-IR analysis showed the presence of OH, C=O, and C=C conjugated bonds and showed that OH participated actively in the adsorption process. The adsorption experiment in this study was favored by the Langmuir isotherm model with an r^2 of 0.9964. It is concluded that orange peel is a favorable low-cost adsorbent due to its availability.

5. CONFLICT OF INTEREST

The authors declare no conflict of interest.

6. ACKNOWLEDGMENTS

7. REFERENCES

1. Rashid R, Shafiq I, Akhter P, Iqbal MJ, Hussain M. A state-of-the-art review on wastewater treatment techniques: the effectiveness of adsorption method. Environmental Science and Pollution Research 2021 Feb 1;28(8):9050–66. Available from: <URL>

2. Dakhil IH. Recycling of agriculture wastes for efficient removal of methyl orange dye using batch adsorption unit. IOP Conference Series: Materials Science and Engineering. 2020 Jul;881(1):012186. Available from: <URL>

3. Fallah S, Mamaghani HR, Yegani R, Hajinajaf N, Pourabbas B. Use of graphene substrates for wastewater treatment of textile industries. Advanced Composites and Hybrid Materials. 2020 Jun 1;3(2):187–93. Available from: <URL>

4. Ali AF, Atwa SM, El-Giar EM. 6 - Development of magnetic nanoparticles for fluoride and organic matter removal from drinking water. In: Grumezescu AM, editor. Water Purification [Internet]. Academic Press; 2017 [cited 2023 Apr 5]. p. 209–62. Available from: <URL>

5. Tang Y, Yang R, Ma D, Zhou B, Zhu L, Yang J. Removal of methyl orange from aqueous solution by adsorption onto a hydrogel composite. Polymers and Polymer Composites. 2018 Feb 1;26(2):161–8. Available from: <URL>

6. Lakshmana Naik R, Rupas Kumar M, Bala Narsaiah T. Removal of heavy metals (Cu & Ni) from wastewater using rice husk and orange peel as adsorbents. Materials Today: Proceedings. 2023 Jan 1;72:92–8. Available from: <URL>

7. Krika F, Benlahbib O el F. Removal of methyl orange from aqueous solution via adsorption on cork as a natural and low-coast adsorbent: equilibrium, kinetic and thermodynamic study of removal process. Desalination and Water Treatment. 2015 Mar 27;53(13):3711–23. Available from: <URL>

8. Deshmukh P, Khadse G, Shinde V, Labhasetwar P. Cadmium removal from aqueous solutions using dried banana peels as an adsorbent: kinetics and equilibrium modeling. Journal of Bioremediation and Biodegradation. 2017 Apr 24;08. Available from: <URL>

9. Bhattacharya AK, Naiya TK, Mandal SN, Das SK. Adsorption, kinetics and equilibrium studies on removal of Cr(VI) from aqueous solutions using different low-cost adsorbents. Chemical Engineering Journal. 2008 Apr 15;137(3):529–41. Available from: <URL>

10. Eljiedi AAA, Kamari A. Removal of methyl orange and methylene blue dyes from aqueous solution using lala clam (Orbicularia orbiculata) shell. AIP Conference Proceedings. 2017 May 19;1847(1):040003. Available from: <URL>

11. Subbaiah MV, Kim DS. Adsorption of methyl orange from aqueous solution by aminated pumpkin seed powder: Kinetics, isotherms, and thermodynamic studies. Ecotoxicology and Environmental Safety. 2016 Jun 1;128:109–17. Available from: <URL>

12. Mallakpour S, Hatami M. An effective, low-cost and recyclable bio-adsorbent having amino acid intercalated LDH@Fe3O4/PVA magnetic nanocomposites for removal of methyl orange from aqueous solution. Applied Clay Science. 2019 Jun 15;174:127–37. Available from: <URL>

13. Arami M, Limaee NY, Mahmoodi NM, Tabrizi NS. Removal of dyes from colored textile wastewater by orange peel adsorbent: Equilibrium and kinetic studies. Journal of Colloid and Interface Science. 2005 Aug 15;288(2):371–6. Available from: <URL>

14. Mafra MR, Igarashi-Mafra L, Zuim DR, Vasques ÉC, Ferreira MA. Adsorption of remazol brilliant blue on an orange peel adsorbent. Brazilian Journal of Chemical Engineering. 2013 Sep;30:657–65. Available from: <URL>

15. Kratochvil D, Volesky B. Advances in the biosorption of heavy metals. Trends in Biotechnology. 1998 Jul 1;16(7):291–300. Available from: <URL>

16. Liu T. Treatment of model wastewater including eriochrome black t based on eggshell membrane. Advanced Materials Research. 2011;183–185:2120–3. Available from: <URL>

17. Omar S, Yusoff NSM, Muhamad MS, Hamidon N, Hamid NHA, Harun H, et al. The characterization of banana blossom peel and floret as an adsorbent for the removal of manganese from groundwater. Mater Sci Forum. 2020 Mar;981:362—8. <URL>.

18. Rattanapan S, Srikram J, Kongsune P. Adsorption of methyl orange on coffee grounds activated carbon. Energy Procedia. 2017 Oct 1;138:949–54. Available from: <URL>

19. Li WH, Yue QY, Gao BY, Ma ZH, Li YJ, Zhao HX. Preparation and utilization of sludge-based activated carbon for the adsorption of dyes from aqueous solutions. Chemical Engineering Journal. 2011 Jun 15;171(1):320–7. Available from: <URL>

20. Mozaffari Majd M, Kordzadeh-Kermani V, Ghalandari V, Askari A, Sillanpää M. Adsorption isotherm models: A comprehensive and systematic review (2010−2020). Science of The Total Environment. 2022 Mar 15;812:151334. Available from: <URL>.

RESEARCH ARTICLE

Indirect Determination of Diclofenac Sodium through Its Interaction with the Aniline Oxidation Peak

Rana H. Al-Hyali[1*] (iD), Amer Th. Al-Taee[1] (iD)

[1] Department of Chemistry /College of Science/University of Mosul, Iraq

Abstract: The voltammetric measurement of diclofenac sodium was investigated using an electrochemical sensor consisting of a glassy carbon electrode (GCE) modified with aniline conducting polymer and a differential pulse voltammetric (DPV) method.

Diclofenac sodium behavior was investigated through its interaction with poly aniline oxidation peak; due to diclofenac sodium adsorption on the surface of the bare glassy carbon electrode, it gives an unstable oxidation peak at 0.4V versus Ag/AgCl.saturated.KCl. We attempted to solve this issue by plating the electrode with aniline and monitoring the interaction peak between diclofenac sodium and aniline oxidation peak.

The impact of pH was investigated, optimum conditions were tested, and calibration curves were constructed. Glassy carbon/poly aniline electrode (GC/PAn) results in two straight lines with R^2 values of 0.9812 and 0.9772 when current is plotted against concentrations at low concentration and high concentration, respectively. The limit of detection (LOD) and limit of quantification (LOQ) were 0.1282×10^{-7} M and 0.4275×10^{-7} M, respectively. Compared with other sensors, it was observed that the proposed electrochemical sensor has a wider linear range and lower detection limit.

The suggested method was applied successfully for quantitating diclofenac sodium in tablet formulation supplied by Samaraa Drugs Industry (SDI) with accepted results of recovery of diclofenac sodium.

*Corresponding author. E-mail: ranahasan@uomosul.edu.iq

1. INTRODUCTION

Non-steroidal anti-inflammatory medication diclofenac sodium (figure 1), sodium [o-(2,6-dichloroanilino) phenyl] acetate, has potent analgesic and anti-fever characteristics. (1,2). Commonly used to treat inflammatory conditions such as musculoskeletal injuries, non-articular rheumatism, rheumatoid arthritis, ankylosing spondylitis, and osteoarthritis (3-5). In veterinary medicine, it can also be used to treat animals that produce food (6).

Voltaren, cataflam, dyloject, cambia, zipsor, and zorvolex are the brand names for diclofenac. It has been effective in treatment as it causes less

damage to the liver, stomach, kidneys, and heart (7).
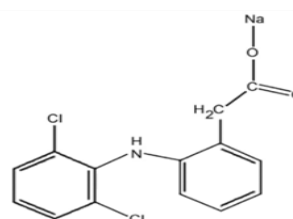
Figure 1. Structure of diclofenac sodium

Regarding quality assurance, diclofenac is effective with minimal side effects (8). Several analytical methods have been reported to determine diclofenac in pharmaceuticals, for example,

chromatography (9,10), capillary electrophoresis (11), differential scanning calorimetry (12), gravimetry (13), spectrometry (14,15) and fluorometric (16). The Brazilian Pharmacopoeia's standard method for determining diclofenac uses high-performance liquid chromatography technology (17).

Electrochemical methods have many advantages compared to other methods; they are characterized by high sensitivity, simplicity, low costs, selectivity, and low consumption as well. Therefore, it has been widely used to determine many medicinal compounds (18, 19). The bare electrodes have low selectivity and sensitivity upon electrically active compounds; the problems arise from the adsorption of the drug on the electrode surface, which causes poisoning or passivating of the electrode surface and loss of the electrode activity. To overcome these problems, the composites are designed by joining catalytic materials with exceptional conductive materials to modify the electrode surface (20-22). The applications of modified electrodes, especially carbon electrodes, have greatly progressed in the electrochemical study of biological compounds (23–25).

Many modified carbon paste electrodes (CPEs) have been described for measuring diclofenac in physiological samples and formulations of pharmaceuticals (26, 27).

Tyrosine was used to create a carbon paste electrode while investigating the oxidative behavior of diclofenac sodium (28). Cormusch et al. developed different electrodes sensitive to diclofenac by fusing the ion-pair complex formed between diclofenac, butyl rhodamine, and diclofenac with the dye safranine in a matrix of graphite (29–33). Diclofenac was electro-oxidized at a platinum electrode in 0.1M TBAClO$_4$/acetonitrile solution using a potentiometric sensor based on doped polypyrrole films (34).

Chitosan's capacity for adsorption and film formation and the significant catalytic characteristics of multi-walled carbon nanotubes (MWCNTs) were used to create an effective and straightforward sensor for detecting diclofenac sodium(35). A produced polymer with a diclofenac imprint was used to create a carbon paste electrode to develop a selective electrochemical sensor for diclofenac (MIP) (36).

A new electrochemical sensor was also developed to determine diclofenac sodium using titanium dioxide saturated with ruthenium (37). A modified gold electrode for determination of diclofenac using gold nanoparticles (AuNPs) and multi-walled

functional carbon nanotubes (f-MWCNTs) / graphene oxide (GO) composite film reported by Farzaneh Nasiri and co-workers (38).

In this study, the electrochemical behavior of diclofenac was examined using a glassy carbon bare electrode, and it was modified by the electrochemical polymerization of aniline. The sensor's response signal has significantly improved, which improves the electrochemical detection of diclofenac by interacting with the peak of polyaniline oxidation.

2. EXPERIMENTAL

2.1 Materials and Techniques

2.2. Instruments
The Swiss company Metrohm provided a computrace 797VA analyzer, which was used in conjunction with a three electrodes cell made up of an auxiliary electrode, 2mm diameter Pt-wire, reference electrode, Ag/AgCl/saturated KCl, and the working electrode, 2mm diameter GCE, as to perform the voltammetric measurements. The HANNA Company, Portugal, provided a (pH211) pH meter for the pH measurements.

2.3. Reagents and Chemicals
Samaraa Drugs Industry (SDI) supplied diclofenac sodium. To make a solution of phosphate buffer pH7, 1.5 ml (0.2M) of KH$_2$PO$_4$ and 30.5 ml of (0.2 M) K$_2$HPO$_4$ were combined, and the volume was then increased to 100 ml in a volumetric vial.

2.4. Procedure
The voltammetric cell was occupied with 10 ml of pH7, dissolved oxygen was removed by Nitrogen gas passed through it for five minutes before the measurements, the voltammograms were then recorded for a series of additions of a stock diclofenac sodium, and curves of calibration were created.

2.5. Pretreatment of Glassy Carbon Electrode
GCE was cleaned and ultrasonically sonicated in water for five minutes after being polished by aluminum oxide powder (0.05 μm) (39,40).

2.6. Electrochemical Polymerization of Aniline on GCE
The electrochemical polymerization of 0.1 M pure aniline in 10 ml of 0.5 M H$_2$SO$_4$ using cyclic voltammetric technique (CV) was used to create the poly aniline film under the best optimum conditions (Fig. 2) (41). The potential was scanned between (-0.1 – 0.9) for 5 cycles using scan rate = 0.02 V/s. Three reversible oxidation peaks are shown on the voltammogram: one at potential Ep1=0.204, second at Ep2=0.478, and third at Ep3=0.787.
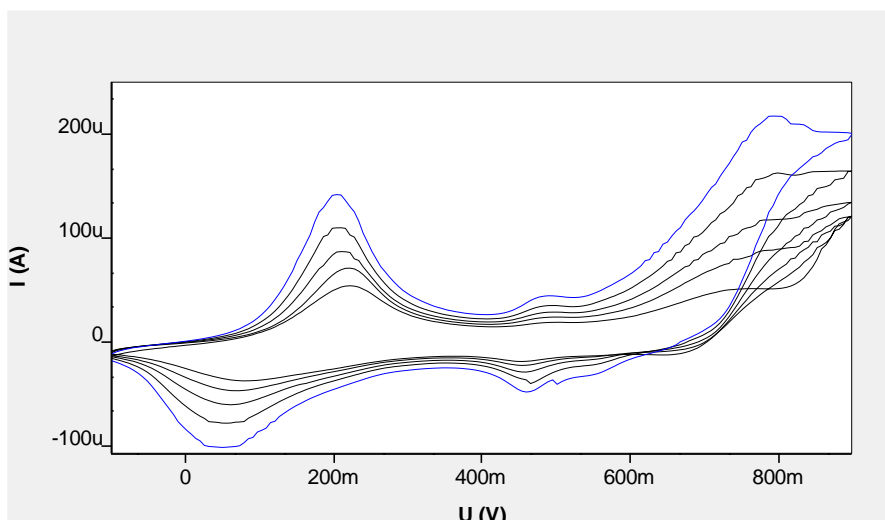
Figure 2. Electrochemical polymerization of aniline

2.7. Determination of Diclofenac Sodium in Pharmaceutical Dose Form:

Five tablets contents of the drug are crushed, and then a fine weight fraction equal to one tablet is dissolved in (10 ml) ethanol.

3. RESULTS AND DISCUSSION

3.1. Effect of Varying pH Levels:

Using 14.492×10^{-6} M of diclofenac sodium on GCE/PAn, various pHs were used to study the impact of pH on the diclofenac sodium oxidation peak potential (Ep) and peak current (Ip) (5-7). According to the results (Table 1), the larger diffusion current was found at pH 5, although a distortion of peak form was found at pH =4. The Plot of Ep versus pH, Figure 3, shows a straight line with a -0.064 value of intercept, which is close to the theoretical value determined by Hillson, which means the oxidation process involved one electron reduction (42).

Table 1. pH effect on the aniline oxidation peak

PH	Ep(V)	Ip(µA)
5	0.43	148
5.5	0.4	145
6	0.382	94.4
6.5	0.34	12.2
7	0.3	11

At pH=4 peak distortion was observed.
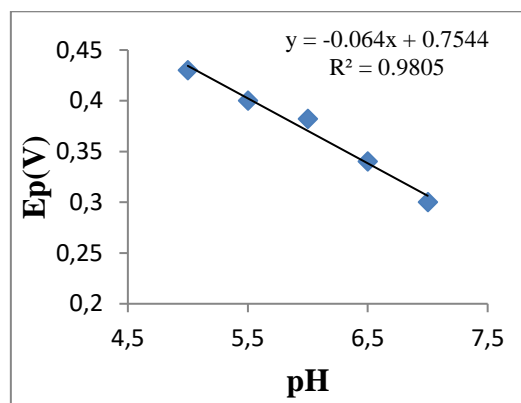
Figure 3. Effect of different pHs on the aniline oxidation peak

3.2. Optimum Conditions

Using 9.708×10^{-6} M aniline in phosphate buffer (pH 5) with GCE/PAn, optimum circumstances were studied to maximize the sensitivity of the sensor. The results are provided in table 2 provided the results, Figure 4 shows before and after optimum conditions voltammograms.

Table 2: Aniline optimum conditions in pH5 for aniline oxidation peak

Parameters	Condition Values
Deposition Potential (V)	6×10^{-1}
Deposition Time (s)	0.3×10^2
Equilibration Time(s)	0.1×10^2
Pulse Amplitude(V)	7×10^{-2}
Pulse Time(s)	3×10^{-2}
Voltage Step(V)	5×10^{-3}
Voltage Step Time(s)	4×10^{-1}
Sweep Rate(V/s)	125×10^{-4}
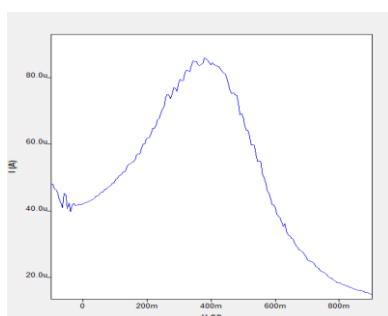
(a)
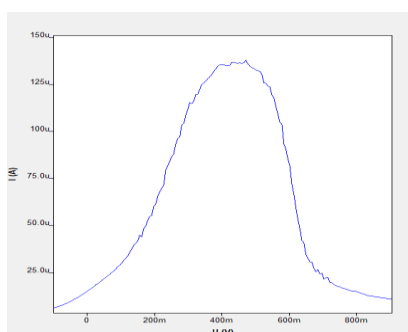
(b)

Figure 4: Differential pulse voltammograms of aniline in pH5 at GCE/Polyaniline
a-Before optimum conditions   b-After optimum conditions

3.3. Aniline oxidation Peak stability at GCE/PAn

Aniline oxidation peak stability was tested. Under the aforementioned optimum circumstances, differential pulse voltammograms were acquired at various intervals. Table 3 data makes it clear that the current of the oxidation peak has remained constant throughout the measurement period.

Table 3: Aniline oxidation peak stability at GCE

Time (minute)	Ip (μ A)
5	106
10	106
15	108
20	111
25	109
30	109
35	105
40	106
45	106
50	105
S. D	±2.02484567

3.4. Calibration Curve

The indirect determination of diclofenac sodium was done through the decrease in poly aniline oxidation peak at 0.4V with the addition of diclofenac. In order to produce the calibration curve, a series addition of 10^{-3} molar standard diclofenac sodium solution were added, and the voltammograms for each addition were recorded under the previously optimum conditions. Peak current is plotted against concentrations, and the findings show two straight lines, one at low concentrations $(0.489 - 5.836) \times 10^{-6}$ molar with R^2 values of 0.9812 and second at higher concentrations $(7.774-17.647) \times 10^{-6}$ molar with R^2 values of 0.9772. The limit of determination was 0.1282×10^{-7} M (LOD=$3\sigma_{\Delta Ip} \times$low Conc./ $x_{\Delta ip}$) and the limit of quantitation was 0.4275×10^{-7} M (LOQ=$10\sigma\Delta Ip \times$low Conc./ $x_{\Delta ip}$)

Table 4: Sequence additions of diclofenac sodium in low concentration range $(0.489-5.836) \times 10^{-6}$ M using GC/PAn modified electrode

Concentration of poly aniline $\times 10^{-6}$ (M)	Ip(μA)
1.794	139
Concentration of diclofenac sodium $\times 10^{-6}$ (M)	Ip(μA)
0.489	132
0.978	129
1.955	127
2.929	125
3.902	123
4.873	121
5.836	119
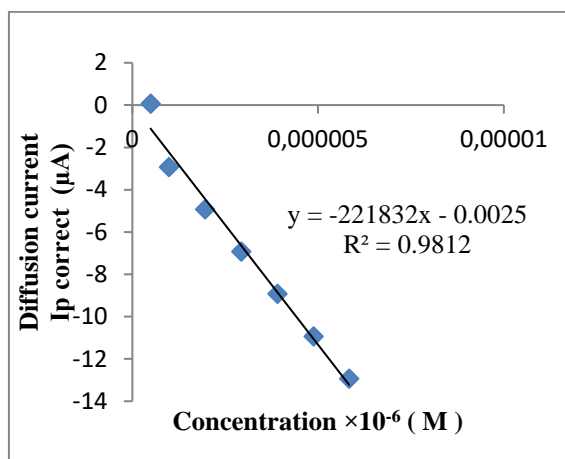
Figure 5. Calibration curve of diclofenac sodium at low concentration
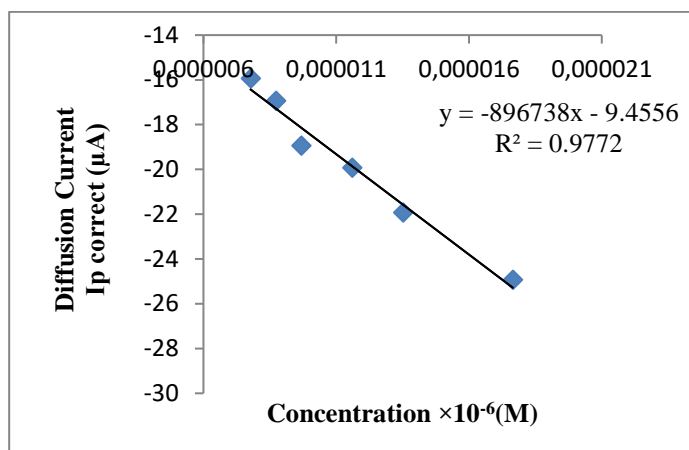
Figure 6: Calibration curve of diclofenac sodium at high concentration

Table 5: Sequence additions of diclofenac sodium in high concentration range (7.774 -17.647) $\times 10^{-6}$ M using GC/PAn modified electrode

Cocentration$\times 10^{-6}$ M	Ip (µA)
7.774	116
8.737	115
9.689	113
11.605	112
13.514	110
17.647	107

Table 6: Determination of diclofenac sodium in pharmaceutical formulation tablets

Taken Conc.$\times 10^{-6}$ (M)	Found Conc. $\times 10^6$(M)	Ip (Tablet) (µA)	Ip (Pure) (µA)	% Recovery	% Error
0.9794	0.9946	131	129	101.5	-1.55
1.9569	1.9877	129	127	101.5	-1.57
7.7821	8.0504	120	116	103.4	-3.44
8.7463	8.8984	117	115	101.7	-1.73
13.5397	13.7858	112	110	101.8	-1.81
17.341	17.8272	110	107	102.8	-2.80

The results show a good agreement between the taken (concentration of diclofenac sodium in tablets) and found (concentration of diclofenac sodium measured) concentrations with a good recovery obtained.

4. CONCLUSION

The glassy carbon electrode suffers from losing activity due to the adsorption of diclofenac sodium on its surface; the electrochemical plating of aniline on the bare glassy carbon electrode caused an enhancement and stabilization of electrode response, The indirect determination of diclofenac sodium through its interaction with aniline oxidation peak increased the sensitivity and stability of developed detector.

The developed electrode was applied to estimate diclofenac sodium in pharmaceutical formulations with acceptable percentage recoveries.

Table 7: Comparison of the proposed method with the methods mentioned in the literature:

Electrode	Linear Range (µM)	Detecton Limit (M)	References
Polyaniline/Reduced Graphene Oxide Nano-composite	16.9–270	3.71×10^{-6}	[36]
IL - modified CNT paste electrode	0.5-300	0.2×10^{-6}	[43]
F - MWCNTs / Au - PtNPs / Au	0.5−100	0.3×10^{-6}	[44]
f-MWCNTs /GCE	2−15	0.1×10^{-6}	[45]
PANI / rGO molecular imprinter	17−270	3.7×10^{-6}	[47]
Zinc / Fe-PANI / CPE	1−30	0.235×10^{-6}	[48]
GC / PAn	0.489-17.647	0.1282×10^{-7}	present work

The comparison of the suggested method with the methods reported in the literature shows that the present work has a better limit of detection with good linearity.

5. ACKNOWLEDGMENTS

6. REFERENCES

1. Ulubay M, Yurt KK, Kaplan AA, Atilla MK. The use of diclofenac sodium in urological practice: a structural and neurochemical based review. Journal of Chemical Neuroanatomy. 2018 Jan 1;87:32-6. Available from: <URL>

2. Li X, He Q, Li H, Gao X, Hu M, Li S, Zhai Q, Jiang Y, Wang X. Bioconversion of non-steroidal anti-inflammatory drugs diclofenac and naproxen by chloroperoxidase. Biochemical Engineering Journal. 2017 Apr 15;120:7-16. Available from: <URL>

3. Cunha S, Pena A, Fernandes J, Mussels as bioindicators of diclofenac contamination in coastal environments. Environ. Pollut. 2017; 225: 354- 360. Available from: <URL>

4. Shewaiter MA, Hammady TM, El-Gindy A, Hammadi SH, Gad S. Formulation and characterization of leflunomide/diclofenac sodium microemulsion base-gel for the transdermal treatment of inflammatory joint diseases. Journal of Drug Delivery Science and Technology. 2021 Feb 1;61:102110. Available from: <URL>

5. Sarhangzadeh K, Khatami AA, Jabbari M, Bahari S. Simultaneous determination of diclofenac and indomethacin using a sensitive electrochemical sensor based on multiwalled carbon nanotube and ionic liquid nanocomposite. Journal of Applied Electrochemistry. 2013 Dec;43(12):1217-24. Available from: <URL>

6. Davarani SSH, Pourahadi A, Nojavan S, Banitaba MH, Nasiri-Aghdam M. Electro membrane extraction of sodium diclofenac as an acidic compound from wastewater, urine, bovine milk, and plasma samples and quantification by high-performance liquid chromatography. Analytica chimica acta. 2012 Apr 13;722:55-62. Available from: <URL>

7. de Paiva Carvalho RL, Leonardo PS, Mendes GD, Lima FP, Lima MO, Marcos RL, Lopes-Martins RA. Pharmacokinetic and Pharmacodynamics of Sodium diclofenac (Topical and IM) associated with laser photobiomodulation on skeletal muscle strain in rats.

International Journal of Photoenergy. 2019 Mar 3;2019. Available from: <URL>

8. Kołodziejska J, Kołodziejczyk M. Diclofenac in the treatment of pain in patients with rheumatic diseases. Reumatologia/Rheumatology. 2018 Jun 30;56(3):174-83. Available from: <URL>

9. Roškar R, Kmetec V. Liquid chromatographic determination of diclofenac in human synovial fluid. Journal of Chromatography B. 2003 May 5;788(1):57-64. Available from: <URL>

10. Arcelloni C, Lanzi R, Pedercini S, Molteni G, Fermo I, Pontiroli A, Paroni R. High-performance liquid chromatographic determination of diclofenac in human plasma after solid-phase extraction. Journal of Chromatography B: Biomedical Sciences and Applications. 2001 Nov 5;763(1-2):195-200. Available from: <URL>

11. Jin W, Zhang J. Determination of diclofenac sodium by capillary zone electrophoresis with electrochemical detection. Journal of Chromatography A. 2000 Jan 28;868(1):101-7. Available from: <URL>

12. Bucci R, Magrì A, Magrì A. DSC in the chemical analysis of drugs. Determination of diclofenac in pharmaceutical formulations. Journal of thermal analysis and calorimetry. 2000 Aug 1;61(2):369-76. Available from: <URL>

13. Tubino M, Souza RL. Gravimetric method for the determination of diclofenac in pharmaceutical preparations. Journal of AOAC International. 2005 Sep 1;88(6):1684-7. Available from: <URL>

14. Souza RL, Tubino M. Spectrophotometric determination of diclofenac in pharmaceutical preparations. Journal of the Brazilian Chemical Society. 2005;16:1068-73. Available from: <URL>

15. Patel N P & Hinge M. Development and validation of UV spectroscopic method for simultaneous estimation of methocarbamol and diclofenac sodium in injection dosage form. *Wjpps*. 2016;*5*(4), 1625-1636. Available from: <URL>

16. Adhikari B, Majumdar S. Polymers in sensor applications. Progress in polymer science. 2004 Jul 1;29(7):699-766. Available from: <URL>

17. Yilmaz B. GC–MS determination of diclofenac in human plasma. Chromatographia. 2010 Mar;71:549-51. Available from: <URL>

18. Brahman PK, Pandey N, Kumar JS, Somarouthu P, Tiwari S, Pitre KS. Highly sensitive stripping voltammetric determination of a biomolecule, pyruvic acid in solubilized system and biological fluids. Arabian Journal of

Chemistry. 2016 Nov 1;9:S1897-904. Available from: <URL>

20. Reddy KR, Brahman PK, Suresh L. Fabrication of high performance disposable screen printed electrochemical sensor for ciprofloxacin sensing in biological samples. Measurement.2018;127:175-186. Available from: <URL>

21. Brahman PK, Suresh L, Lokesh V, Nizamuddin S. Fabrication of highly sensitive and selective nanocomposite film based on CuNPs/fullerene-C60/MWCNTs: An electrochemical nanosensor for trace recognition of paracetamol. Analytica Chimica Acta. 2016 Apr 21;917:107-16. Available from: <URL>

22. Brahman PK, Suresh L, Reddy KR, Bondili JS. An electrochemical sensing platform for trace recognition and detection of an anti-prostate cancer drug flutamide in biological samples. RSC advances. 2017;7(60):37898-907. Available from: <URL>

23. Brahman PK, Pandey N, Topkaya SN, Singhai R. Fullerene-C60-MWCNT composite film based ultrasensitive electrochemical sensing platform for the trace analysis of pyruvic acid in biological fluids. Talanta. 2015;134:554-559. Available from: <URL>

24. Sun D, Zhang Z, Ma W, Wang L. Preparation of a poly (L-tyrosine) modified electrode and voltammetric determination of dopamine. Chinese Journal of Analysis Laboratory. 2005;24(7):28.

25. Ly SY. Detection of dopamine in the pharmacy with a carbon nanotube paste electrode using voltammetry. Bioelectrochemistry. 2006 May 1;68(2):227-31. Available from: <URL>

26. Wang CY, Hu XY, Di Jin G, Leng ZZ. Differential pulse adsorption voltammetry for determination of procaine hydrochloride at a pumice modified carbon paste electrode in pharmaceutical preparations and urine. Journal of pharmaceutical and biomedical analysis. 2002 Aug 22;30(1):131-9. Available from: <URL>

27. Manea F, Ihos M, Remes A, Burtica G, Schoonman J. Electrochemical determination of diclofenac sodium in aqueous solution on Cu-doped zeolite-expanded graphite-epoxy electrode. Electroanalysis. 2010 Sep;22(17-18):2058-63. Available from: <URL>

28. Chethana BK, Basavanna S, Arthoba Naik Y. Voltammetric determination of diclofenac sodium using tyrosine-modified carbon paste electrode. Industrial & Engineering Chemistry Research. 2012 Aug 8;51(31):10287-95. Available from: <URL>

29. Kormosh Z, Hunka I, Bazel Y. An electrode immobilized in a graphite matrix with ion pair complex for the determination of diclofenac in pharmaceuticals. Journal of the Iranian Chemical Research. 2008; 25-32.

30. Kormosh Z, Hunka I, Bazel Y. Potentiometric determination of diclofenac in pharmaceutical formulation by membrane electrode based on ion associate with base dye. Chinese Chemical Letters. 2007 Sep 1;18(9):1103-6. Available from: <URL>

31. Kormosh Z, Hunka I, Bazel Y. Preparation and characterization of a diclofenac sensitive electrode based on a PVC matrix membrane. Acta Chimica Slovenica. 2008 Jun 1;55(2).

32. Shamsipur M, Jalali F, Ershad S. Preparation of a diclofenac potentiometric sensor and its application to pharmaceutical analysis and to drug recovery from biological fluids. Journal of pharmaceutical and biomedical analysis. 2005 Apr 29;37(5):943-7. Available from: <URL>

33. Maleki R, Matin AA, Hosseinzadeh R, Jouyban A. PVC membrane sensor for diclofenac: applications in pharmaceutical analysis and drug binding studies. Die Pharmazie-An International Journal of Pharmaceutical Sciences. 2007 Sep 1;62(9):672-7. Available from: <URL>

34. Oliveira MC, Bindewald EH, Marcolino Jr LH, Bergamini MF. Potentiometric determination of Diclofenac using an ion-selective electrode prepared from polypyrrole films. Journal of Electroanalytical Chemistry. 2014 Oct 15;732:11-6. Available from: <URL>

35. Shalauddin M, Akhter S, Bagheri S, Abd Karim MS, Kadri NA, Basirun WJ. Immobilized copper ions on MWCNTS-Chitosan thin film: Enhanced amperometric sensor for electrochemical determination of diclofenac sodium in aqueous solution. International Journal of Hydrogen Energy. 2017 Aug 3;42(31):19951-60. Available from: <URL>

36. Mostafavi M, Yaftian MR, Piri F, Shayani-Jam H. A new diclofenac molecularly imprinted electrochemical sensor based upon a polyaniline/reduced graphene oxide nano-composite. Biosensors and Bioelectronics. 2018 Dec 30;122:160-7. Available from: <URL>

37. Killedar L, Ilager D, Shetti NP, Aminabhavi TM, Reddy KR. Synthesis of ruthenium doped titanium dioxide nanoparticles for the electrochemical detection of diclofenac sodium. Journal of Molecular Liquids. 2021 Oct 15;340:116891. Available from: <URL>

38. Nasiri F, Rounaghi GH, Ashraf N, Deiminiat B. A new electrochemical sensing platform for quantitative determination of diclofenac based on gold nanoparticles decorated multiwalled carbon nanotubes/graphene oxide nanocomposite film. International Journal of Environmental Analytical Chemistry. 2021 Jan 26;101(2):153-66. Available from: <URL>

39. Al-Hyali RH, Al-Taee AT. A New GE/MWCNTs/PFA modified electrode for simultaneous determination of catechol and hydroquinone. Research Journal of Pharmacy and Technology. 2021;14(2):828-32. Available from: <URL>

40. Morrin A, Killard AJ, Smyth MR. Electrochemical characterization of commercial and home-made screen-printed carbon electrodes. Analytical letters. 2003 Jan 8;36(9):2021-39. Available from: <URL>

41. Xu H, Zhang J, Chen Y, Lu H, Zhuang J. Electrochemical polymerization of polyaniline doped with Cu 2+ as the electrode material for electrochemical supercapacitors. RSC Advances. 2014;4(11):5547-52. Available from: <URL>

42. Al-Taee AT, Al-Hyali RH. Electrochemical Behavior of Oxytocin Hormone Through Its Cysteine Reduction Peak Using Glassy Carbon Electrode Modified with Poly Furfurylamine and Multi-Walled Carbon Nanotubes. Egyptian Journal of Chemistry. 2021 Oct 1;64(10):5831-7. Available from: <URL>

43. Ensafi AA, Izadi M, Karimi-Maleh H. Sensitive voltammetric determination of diclofenac using room-temperature ionic liquid-modified carbon nanotubes paste electrode. Ionics. 2013 Jan;19:137-44. Available from: <URL>

44. Eteya MM, Rounaghi GH, Deiminiat B. Fabrication of a new electrochemical sensor based on AuPt bimetallic nanoparticles decorated multi-walled carbon nanotubes for determination of diclofenac. Microchemical Journal. 2019 Jan 1;144:254-60. Available from: <URL>

45. Slim C, Tlili N, Richard C, Griveau S, Bedioui F. Amperometric detection of diclofenac at a nano-structured multi-wall carbon nanotubes sensing films. Inorganic Chemistry Communications. 2019 Sep 1;107:107454. Available from: <URL>

46. Ahmed Anwar AA, Mahmoud R, El-Fatah GA, Farghali AA, Hassouna ME. Electrochemical determination of diclofenac sodium using modified carbon paste electrode-based Zn/Fe-PANI and its efficient removal using three different layered double hydroxides. International Journal of Environmental Analytical Chemistry. 2023 Jul 17:1-20. Available from: <URL>

Voltammetric performance of nanofiber structured over-oxidized poly(3,4-ethylenedioxythiophene) modified pencil graphite electrodes for dobutamine sensing

Ayşegül Özbek[1] (iD) **, Levent Özcan*[1]** (iD)

[1]Department of Biomedical Engineering, Faculty of Engineering, Afyon Kocatepe University, Ahmet Necdet Sezer Kampüsü, 03200 Afyonkarahisar, Türkiye

Abstract: A modified electrode was developed for the electrochemical sensing of dobutamine (DBT), one of the catecholamines. For this modification process, pencil graphite electrodes (PGE) were modified with over-oxidized nanofiber structured poly (3,4-ethylenedioxythiophene) (PGE/OPEDOTNF) by electropolymerization. The electrochemical performance of PGE/OPEDOTNF was evaluated by cyclic and differential pulse voltammetry. In addition, the performances of non-nanofiber PEDOT-modified PGE electrodes were also examined for comparison. The characterization of the modified electrodes was carried out by scanning electron microscopy and electrochemical methods. The signal of the modified electrodes was observed in a linear range of 0.1-2.0 µM against DBT using the differential pulse voltammetry method. The limit of detection and quantification are calculated as 0.026 µM and 0.086 µM, respectively. The effect of the interfering species was examined. It has been shown that DBT can be detected sensitively and selectively using pencil graphite electrodes modified with nanofiber-structured poly(3,4-ethylenedioxythiophene). The repeatability of PGE/OPEDOTNF electrodes was found to be 5.2%. PGE/OPEDOTNF electrodes remained stable for 15 days without losing their electrochemical activity.

1. INTRODUCTION

Organic compounds that regulate physiology as both disease markers and pharmaceuticals are called catecholamines (1). Catecholamines are essential because they are involved in many physiological and biochemical processes in humans. Dobutamine (DBT), one of the synthetic catecholamines, is widely used in clinical practice (2). DBT plays an essential role in the functioning of the central nervous, renal, hormonal, and cardiovascular systems. It transmits messages to parts of the brain for proper coordination of body movements. Abnormalities in the DBT level in the brain are associated with various neurological diseases such as Parkinson's, schizophrenia and psychiatric disorders such as epilepsy (3). DBT

increases contraction, increases heart rhythm, improves blood flow, relieves signs (symptoms) of coronary heart disease, and stimulates the heart's ß1-adrenoceptors. There is no significant increase in heart rate or systemic blood pressure following injection of DBT due to vasodilation caused by ß2-receptors. Therefore, DBT is widely used in medical treatment as an anticarcinogen, cardiostimulator, antioxidant, and antimutagen (4). DBT is an electroactive compound with catechol, secondary amine, and phenol functional groups (5). Since catecholamines such as DBT play an essential role in many physiological and biochemical processes, it is crucial to determine such compounds in body fluids or in environments where they dissolve in terms of clinical applications.

Various electrodes are used in the electrochemical determination of biologically important substances. In some cases where high voltages must be applied, the current values may not be at the desired levels. Similar problems can be overcome by using modified electrodes. Surface modification of the electrodes leads to some improvements in sensitive determinations and reproducibility, and in some cases, the selectivity increases by immobilization of functional groups on the relevant surface (5).

Conductive polymers with superior chemical, electronic, and mechanical properties are used to prepare electrochemical sensors for analytical purposes (6-10). Poly(3,4-ethylenedioxythiophene) (PEDOT), one of the conductive polymers, has many properties that make it a superior electrode material in sensor and biosensor production (11-13). These features include its high electronic and ionic conductivity, transparency, mechanical flexibility, and the presence of functional groups for chemical modification (14). In addition, the high electrocatalytic activity and environmental stability of PEDOT are why it is widely used to improve the performance of electrochemical sensors (15-16). PEDOT-modified electrodes have been used in the electrochemical determination of biologically important compounds such as ascorbic acid (AA), dopamine (DA), uric acid, serotonin, and glutathione (10, 12, 17, 18). There are a limited number of studies in the literature on the electrochemical determination of DBT (2, 4, 5, 19-26). Pencil graphite electrode (PGE) modified with nanofiber-structured PEDOT has not been studied for DBT determination.

Pencil graphite is widely used in electrochemical determinations due to its low cost (27-31). There are usually two types: larger-diameter wood tips or finer-diameter mechanical tips. The graphite tip used in wooden body ones is obtained by heating a mixture of graphite and clay in different proportions to achieve the desired hardness. Then, the product is impregnated with oil and wax for smooth and noiseless writing (32). PGE has high electrochemical activity, mechanical strength, low cost, and is easy to modify, miniaturize and regenerate. In addition, thanks to its graphite structure, PGE increases the electrochemical signal and reduces the overvoltage. Also, there are no time-consuming electrode surface cleaning and polishing steps. A highly effective trace analysis method occurs when used in sensitive and high-accuracy electrochemical techniques such as differential pulse, square wave, and stripping voltammetry. The reproducible signals of PGEs with well-defined voltammetric peaks have shown that the electrodes provide good sensitivity and reproducibility as a viable, renewable, and economical tool (33-35). Tavares and Barbeira determined that most pencil tips have an electrical resistance of fewer than 5 ohms, regardless of the manufacturer and hardness, and therefore are suitable for use as electrode material (36). Due to

the mentioned advantages, PGE was preferred and modified with nanofiber-structured PEDOT in our study.

2. EXPERIMENTAL SECTION

2.1. Chemicals and electrodes
3,4-ethylenedioxythiophene, lithium perchlorate, sodium carbonate, potassium chloride, sodium chloride, epinephrine, phenylalanine, glucose, and paracetamol were purchased from Sigma-Aldrich. DBT, uric acid, and dopamine were purchased from Alfa Aesar. Ascorbic acid was purchased from Roth. Ultra-pure water used for the preparation of stock and buffer solutions was obtained from the TKA Smart 2 Pure ultra-pure water device.

Pencil graphite electrode (PGE, 0.7 mm diameter, 2B, Faber Castell) and modified PGE were used as the working electrode, Pt foil (1x1 cm, Aldrich 99.9%) was used as the counter electrode and Ag/AgCl (3.0 M KCl) as the reference electrode. To attach the PGE used in electrochemical measurements, the system prepared from mechanical pencils with a metal tip was used. Experimental studies were conducted using a three-electrode system in a five-necked electrochemical cell.

2.2. Apparatus
Voltammetric measurements were performed by the IVIUM (CompactStat model) potentiostat-galvanostat system. The analysis and evaluation of the data were carried out with Ivium Soft software. pH measurements were carried out using a Thermo Scientific (Orion 3 Star model) pH meter. Scanning electron microscope (SEM) images were obtained using a NanoSEM 650 model (FEI Microscope) device.

2.3. Preparation of poly(3,4-ethylenedioxythiophene) modified electrodes
First, more electrodes were provided by dividing the PGEs into two in the middle. Then, these PGEs were ultrasonically washed with ultrapure water and ethanol for five minutes and then dried in the oven at 50° C for 1 hour. Thus, the PGEs are both cleaned of surface contamination and made ready for modification. The PGEs prepared were kept closed in a 10 mL beaker (Figure S1).

Electropolymerization was carried out in an aqueous solution containing 10 mM 3,4-ethylenedioxythiophene (EDOT), 0.10 M LiClO$_4$, 0.10 M Na$_2$CO$_3$ and 5% acetonitrile by volume (17). A certain number of voltage sweeps between −0.30 V and +1.25 V were applied to PGE, 1.0 cm of which was immersed in this solution, and a nanofiber-structured PEDOT (PEDOTNF) was obtained on the PGE surface (17). Then, the over-oxidation process of PEDOT was performed by applying 2.0 V voltage for 120 seconds in phosphate buffer (PB) solution at pH 7.0. Over-oxidation is a process that has also been applied in previous studies (7, 12, 37) so that the

electrochemical signals of conductive polymers do not interfere with the electroactivity of analytes. Later, the over-oxidized PEDOT (OPEDOTNF) was conditioned by performing a differential pulse voltammetric process between 0.0 V and +0.90 V in PB solution at pH 7.0. It has been determined that the conditioning process with DPV contributes to the reproducibility of the signals obtained with the modified electrode and is a process that helps a more effective over-oxidation. This process has also been applied in previous sensor work based on conductive polymers (38). The parameters of DPV are 20 mV/s scan rate, 50 ms pulse time, and 50 mV pulse amplitude. This process improves the base signal of differential pulse voltammetric measurements in the medium containing the analyte. After each process, the electrodes were cleaned by washing with ultrapure water. The process steps performed on the PGE surface are shown schematically in Figure S2.

The voltammograms in Figure 1a belong to obtaining the nanofiber-structured PEDOT on the PGE surface by voltage sweeps with three cycles. Figure 1b shows the voltammograms obtained during the cyclic voltammetric polymerization of non-nanofiber PEDOT in three cycles. Electroactivity wasn't observed until the voltage changed from -0.30 V to 0.80 V in the first cycle, and there was no increase in the current value. As the voltage increases towards higher voltage values than 0.80 V, EDOT starts to be oxidized,

and a sudden increase is observed in the current values. The peak of EDOT oxidation at 1.05 V is clearly seen. This oxidization provides the electropolymerization of EDOT molecules and PEDOT coating on the PGE surface in the form of a thin film. In each cycle, the electrochemical behavior of the PGE surface where electropolymerization takes place also changes. Therefore, in the second cycle, the current values arising from the PEDOT's own electroactivity were observed between -0.20 and 0.70 V. It is also seen that the EDOT monomer present in the medium starts to be oxidized at a lower voltage value (0.70 V) to electropolymerize. It is seen that as the voltage value increases, the oxidation current values of the EDOT are higher than in the first cycle. In the back cycle, the reduction current values of the polymer structure itself are more pronounced. Similar electroactivity was also observed for the third cycle. In addition, it is noteworthy that the oxidation peak currents of EDOT on both the PGE surface and the PEDOT-coated PGE surface in the voltammograms obtained in the solution without Na_2CO_3 (Figure 1b) are lower than those obtained in the solution containing Na_2CO_3 (Figure 1a). Apart from this, it is seen that the current values between -0.30 V and 0.70 V, in which PEDOT's own electroactivity is observed, are higher in the presence of Na_2CO_3 (Figure 1a) than in the absence of Na_2CO_3 (Figure 1b).
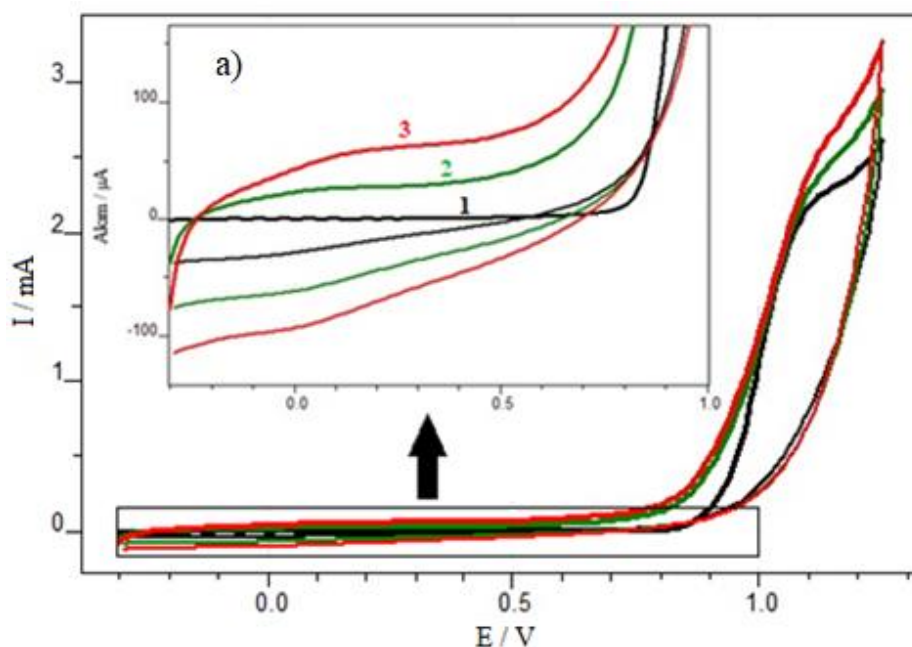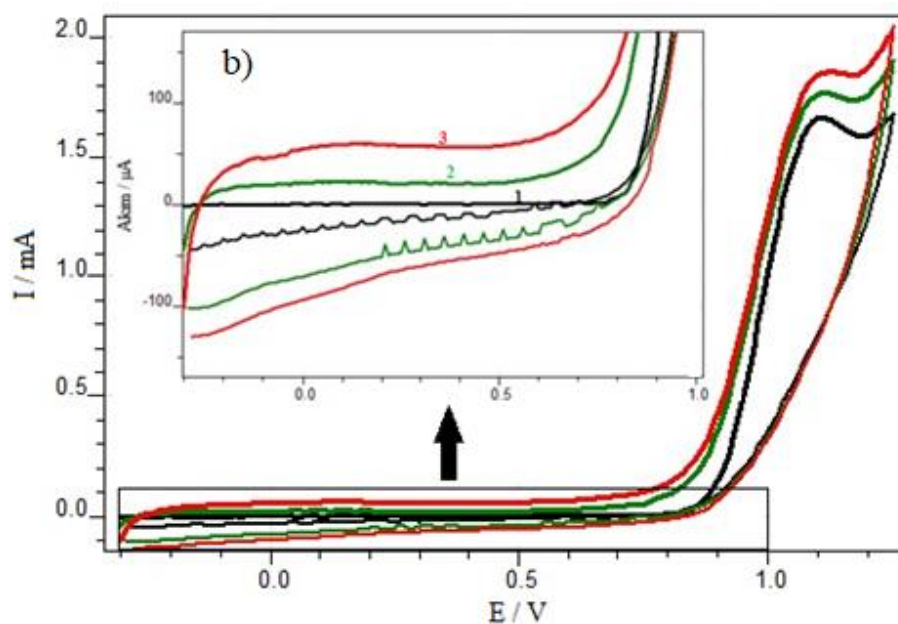
Figure 1: Voltammograms obtained on the PGE surface in a solution containing a) 10 mM EDOT + 0.10 M LiClO$_4$+ 0.10 M Na$_2$CO$_3$ b) 10 mM EDOT + 0.10 M LiClO$_4$.

3. RESULTS AND DISCUSSION

3.1. Surface morphology of PGE/OPEDOTNF electrodes

The surface morphology of PEDOT films was examined by scanning electron microscopy (SEM). The morphology of PEDOT films obtained by electrochemical methods depends on the counter ion, solvent, polymerization environment, etc., parameters used. In Figure 2, SEM images of modified electrodes obtained under optimum conditions are given. When LiClO$_4$ is used as the counter ion in the aqueous solution, the PEDOT (PEDOT) obtained on the electrode surface resembles the "cauliflower" structure (Figure 2a). On the other hand, the morphology of PEDOT (OPEDOTNF) obtained when Na$_2$CO$_3$ is present with LiClO$_4$ in an aqueous solution is in a nanofiber structure. While nanofibers vary in length between 350 and 650 nm, shorter ones are also found in places. The diameters of nanofibers are between 50 and 80 nm (Figure 2b). It is also seen that the tips of some nanofiber structures are in contact with each other. SEM images show that the surface area of nanofiber structure formation is increased compared to PGE. This increase in the surface area also significantly increased the sensitivity to the DBT molecule.

The effect of overoxidation on the morphology of PEDOT and PEDOTNF can be observed in Fig 2. When the images of the overoxidized structures in Figures 2a and b are compared with the images of the unoxidized structures in Figures 2c and d, it is seen that there is no significant difference in morphology. Nevertheless, especially in the cauliflower structured PEDOT (Figure 2c) and OPEDOT (Figure 2a) images, it is seen that the over-oxidized structure has relatively less roughness. Therefore, the over-oxidation conditions used in this study didn't cause a big difference in terms of physical appearance and durability. However, it has been determined from the studies that the over-oxidation process is effective in determining the DBT by using the voltammetric method. In Figures 2e and f, SEM images of both regions with and without electropolymerization on the PGE surface are given. The parts on the left side of the SEM images show the areas where the surface has been modified by electropolymerization. It is understood from these images that the nanofiber structure increases the electrode surface area.
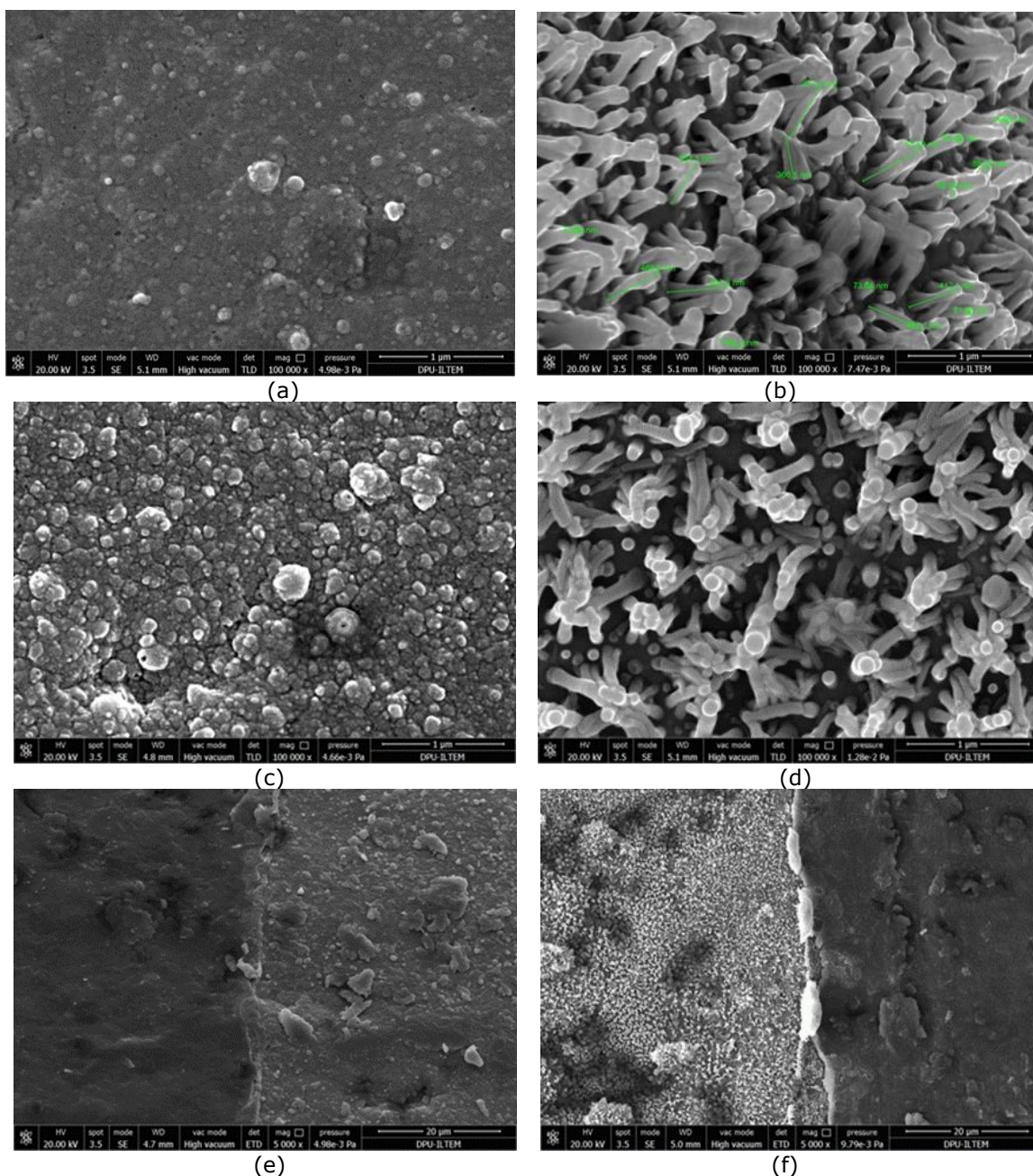
Figure 2: SEM images of (a) PGE/OPEDOT, (b) PGE/OPEDOTNF, (c) PGE/PEDOT, (d) PGE/PEDOTNF, (e) PEDOT coated (on the left) and uncoated (on the right) parts on the PGE surface and (f) PEDOTNF coated (on the left) and uncoated (on the right) on the PGE surface (Electrode preparation conditions: Number of cycles 2, over-oxidation voltage 2.0 V and time 120 s, DPV conditioning number: 1 time)

3.2. Effect of pH and nanofiber structure on DBT oxidation

To investigate the effect of modification of PGEs with nanofiber PEDOT and the effect of medium pH on electrode performance, PGEs were modified with nanofiber and non-nanofiber PEDOT. In the literature, Özcan and İlkbaş (17) used nanofiber PEDOT, which they obtained in 3 cycles, for the electrochemical determination of uric acid. Inspired by this data in the literature, 3-cycle electropolymerization was preferred at the beginning of this study. In this part of the study, overoxidation time and voltage values for PEDOT overoxidation were chosen the same as those in Özcan and İlkbaş's study (17). Then, optimization studies have also been made for these parameters.

All current values in this study are the average values obtained from 5-repetitive measurements.

One of the most important parameters that will affect the electrochemical response of DBT is the pH of the medium. Britton-Robinson Buffer (BRB) solution, which allows working in a wide pH range and is widely used in electrochemical studies, was selected as the electrolyte, and voltammetric measurements were carried out in BRB at different pH values containing 400 µM DBT. The oxidation peak currents-pH graph obtained by the cyclic voltammetry (CV) technique for DBT is shown in Figure 3. As seen in Figure 3, it reached at pH 2.0 the highest current value for DBT oxidation.
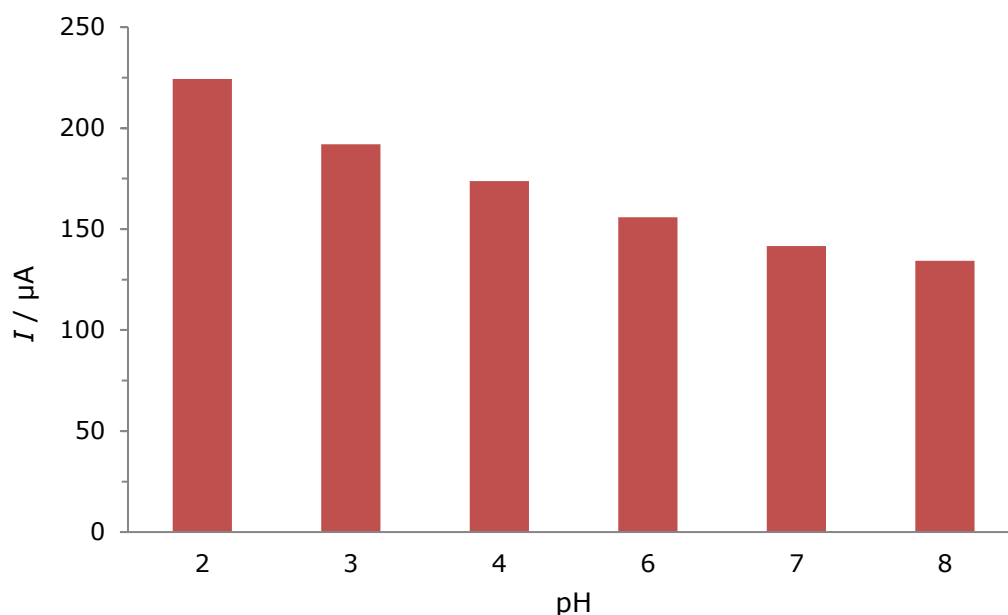
Figure 3: The peak currents obtained using CV for 400 µM DBT on PGE/OPEDOTNF-3cyc electrodes in BRB solutions at different pH values (Electrode overoxidation conditions: voltage: 2.0 V and time: 60 s, DPV applied between 0.0 and +0.90 V for conditioning 2 times).

Figure 4 shows the cyclic voltammograms obtained with PGE/OPEDOT-3cyc and PGE/OPEDOTNF-3cyc in BRB solution at pH 2.0 containing 400 µM DBT. When the cyclic voltammograms in Figure 4 are examined, it is seen that the oxidation peak current obtained for the DBT with PGE/OPEDOTNF-3cyc is approximately two times higher than that of PGE/OPEDOT-3cyc. The adsorption of more analytes may cause this significant increase in oxidation current obtained on the electrode surface as the nanofiber structure increases the surface area. It has been determined that the nanofiber structure provides significant improvement in the determination of the DBT by voltammetric technique due to the increase of the oxidation current of DBT.
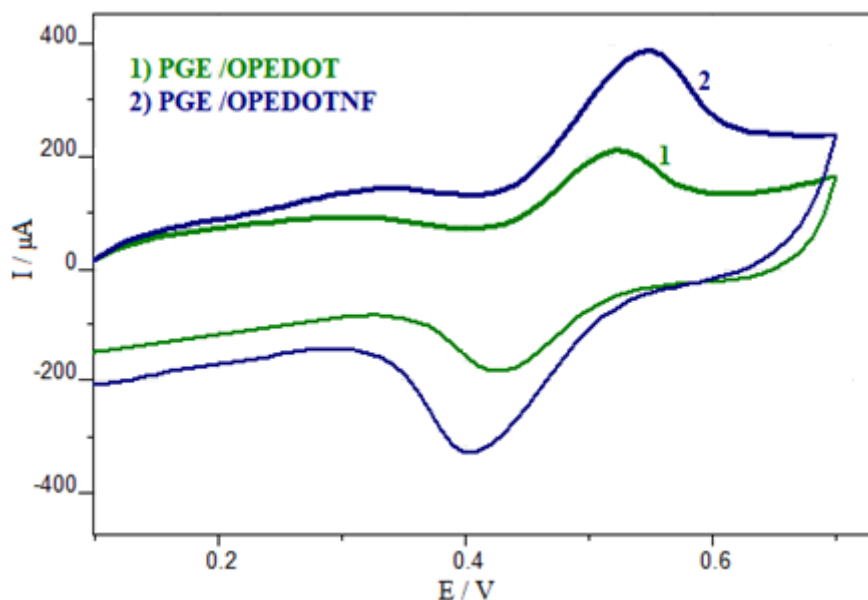
Figure 4: Cyclic voltammograms obtained with (1) non-nanofiber and (2) nanofiber structured PEDOT in BRB solution at pH 2.0 containing 400 µM DBT (Electrode over-oxidation conditions: voltage: 2.0 V and time: 60 s, DPV applied between 0.0 and +0.90 V for conditioning 2 times).

3.3. Determination of optimum conditions for electrode modification
In order to determine the optimum conditions, various parameters related to PGE/OPEDOTNF preparation were studied. It should be remembered once again that modified electrodes are prepared in two stages (see Figure S2). In the first step, PEDOT is electropolymerized on the PGE surface, and in the second step, PEDOT is over-oxidized. The over-oxidation process of the nanofiber-structured PEDOT was carried out to reduce the oxidation peak of PEDOT as much as possible. The observed peak due to the electroactivity of the PEDOT on the modified

electrode surface is prevented from hindering the oxidation peaks of DBT.

3.3.1. Effect of the number of cycles used for electropolymerization

The number of cycles appears as the first parameter that will affect the performance in obtaining PEDOT by CV. Properties such as film thickness and length of nanofiber structures on the PGE surface are parameters that change with the number of cycles and affect the electrochemical signal obtained for DBT. For this reason, it was determined how the electrode performance varies with the number of cycles. The graph of the peak current values obtained by CV for BRB solution at pH 2.0 containing 400 µM DBT using PGE/OPEDOTNF electrodes produced in cycles between 1 and 10 is given in Figure S3. The current value given for the number of zero cycles is the peak current of the unmodified PGE. When the data in Figure S3 are examined, it is seen that the current value of the modified electrode obtained in one cycle is high compared to the one obtained with PGE. The modified electrode obtained with two cycles reached the highest peak current. Therefore, in the later stages of the study, the electropolymerization of OPEDOTNF on the surface of PGEs was carried out by taking two cycles. The abbreviation of the modified electrode produced in two cycles is PGE/OPEDOTNF-2cyc.

Other parameters that may affect the peak current value are the parameters of PEDOT over-oxidation after electropolymerization. The electrochemical characteristics of the over-oxidized structure depend on the voltage applied for the over-oxidation and how long this voltage is applied. Therefore, optimization studies have been carried out for these parameters in the following stages.

3.3.2. Determination of over-oxidation parameters.

After the optimum number of cycles was determined as 2, the change of DBT peak current with the variation of applied voltages for the over-oxidation of the PGE/OPEDOTNF-2cyc was investigated. The peak current values obtained using the CV technique of 400 µM DBT in BRB solution at pH 2.0 with OPEDOTNF-2cyc by applying the voltage values between 1.4-2.2 V for 60 seconds are given in Figure S4. Since the highest peak current (257 µA) is reached at a voltage of 2.0 V, it was chosen as the optimum voltage value for the over-oxidation of the PGE/PEDOTNF. The abbreviation of the modified electrode prepared under these conditions is PGE/OPEDOTNF-2cyc-2V.

Then, PGE/OPEDOTNF-2cyc-2V was over-oxidized by applying 2.0 V for different times (40-220 seconds) in PB solution at pH 7.0. The peak current values obtained using the CV technique for 400 µM DBT are shown in Figure S5. The highest peak current was obtained with the over-oxidized electrode at 2.0 V for 120 seconds (PGE/OPEDOTNF-2cyc-2V-120s). For this reason, it

was concluded that the over-oxidation process for the electrode modification should be applied for 120 seconds at 2.0 V.

In addition, the effect of the number of DPV applied for conditioning was investigated by keeping the optimum voltage and time value constant (2.0 V and 120 seconds) for the over-oxidation of PGE/OPEDOTNF-2cyc-2V-120s electrodes. Until this stage, the DPV process was applied two times in the voltage range of 0.0 to +0.90 V for conditioning. In addition, to see whether there is a significant improvement as a result of the change in the number of repetitions performed for this process, the effect of the conditioning with DPV between 1 to 7 times on the cyclic voltammetric response of 400 µM DBT in BRB solution at pH 2.0 was investigated. The results are given in Figure S6. The result obtained without DPV conditioning is indicated with zero in the graph. When the figure is examined, the peak current, which increases until the number of applications of DPV is four, was then observed to decrease. To avoid spending too much time in the conditioning process, we preferred two times DPV conditioning. The abbreviation of the modified electrode obtained at these conditions is PGE/OPEDOTNF-2cyc-2V-120s-2DP.

3.3.3. Determination of DBT accumulation conditions on the modified electrode

In determining the trace amount of electroactive analytes, a pre-concentration can be made by applying a constant voltage to the electrode. This pre-concentration will further increase the sensitivity of voltammetric measurements. A lower DBT concentration (100 µM) was preferred to test the effect of pre-concentration in DBT determination.

PGE/OPEDOTNF-2cyc-2V-120s-2DP were immersed in BRB solution at pH 2.0 containing 100 µM DBT. Different voltage values were applied for an accumulation time of 250 seconds to ensure DBT accumulation on the modified electrode. The oxidation current values obtained for different deposition voltages are shown in Figure 5a. The highest current value for DBT with PGE/OPEDOTNF-2cyc-2V-120s-2DP was obtained as 410 µA at 0.20 V accumulation voltage. If the accumulation process is not performed, the current value was found as 105 µA with PGE/OPEDOTNF-2cyc-2V-120s-2DP and 10.8 µA with unmodified PGE. The results show that the accumulation process is important in amplifying the DBT signal, especially at low concentrations.

The cyclic voltammograms from which these data were obtained are given in Figure 5b. The base signal values obtained when the accumulation process is applied at different voltages change. To determine the current value originating from DBT only, the "Analysis/PeakfindAdvanced/Baseline Subtract/Automatic/Subtract Baseline" command was applied on the page where cyclic voltammograms were opened in IviumSoft software. The current values in the graph in Figure

5a are obtained by applying this process. This baseline correction was also applied to subsequent voltammetric measurements using the accumulative process.
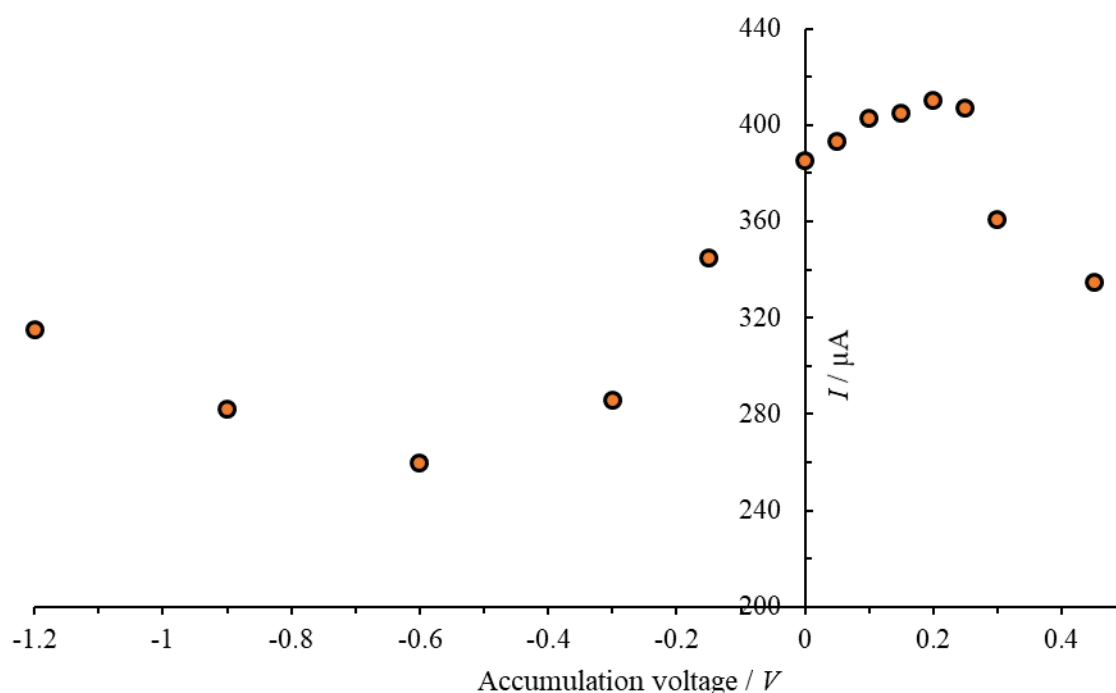
(a)
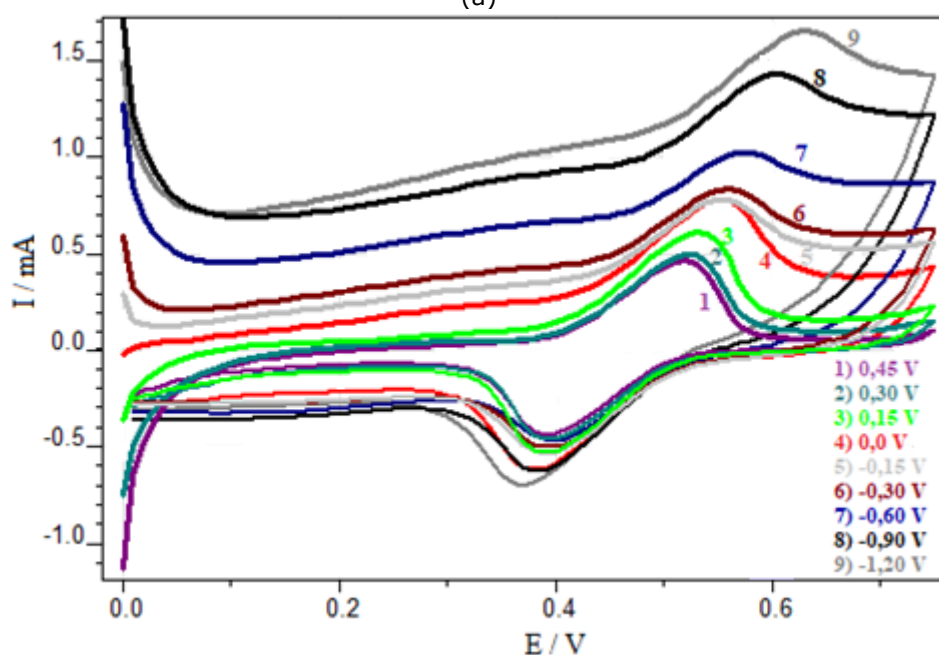
(b)

Figure 5: a) The effect of the accumulation voltage on the DBT oxidation current obtained by CV using PGE/OPEDOTNF-2cyc-2V-120s-2DP b) The corresponding cyclic voltammograms (in the presence of 100 μM DBT in BRB solution at pH 2.0, applied for 250 s accumulation time).

Cyclic voltammograms showing that accumulation increases the sensitivity of the PGE/OPEDOTNF-2cyc-2V-120s-2DP electrode is shown in Figure S7. The voltammogram obtained without accumulation with PGE is also included in the figure for comparison purposes. In order to investigate, the effect of the accumulation time, different accumulation times (seconds) were applied at 0.20 V to PGE/OPEDOTNF-2cyc-2V-120s-2DP in BRB solution at pH 2.0 containing 100 μM DBT. The relationship between peak current obtained for DBT oxidation versus accumulation time is shown in Figure S8. The results show that the longer the accumulation time, the higher the peak current. However, a deposition time of 350 seconds (5.8 minutes) was preferred, considering that long deposition times would prolong the determination time more than necessary. In this preference, the time required for repeated measurements, which must be made analytically, is also considered. The

calibration curve obtained for DBT by CV using PGE/OPEDOTNF-2cyc-2V-120s-2DP is given in

Figure 6. The results show that the CV technique can be used for sensitive determination of DBT.
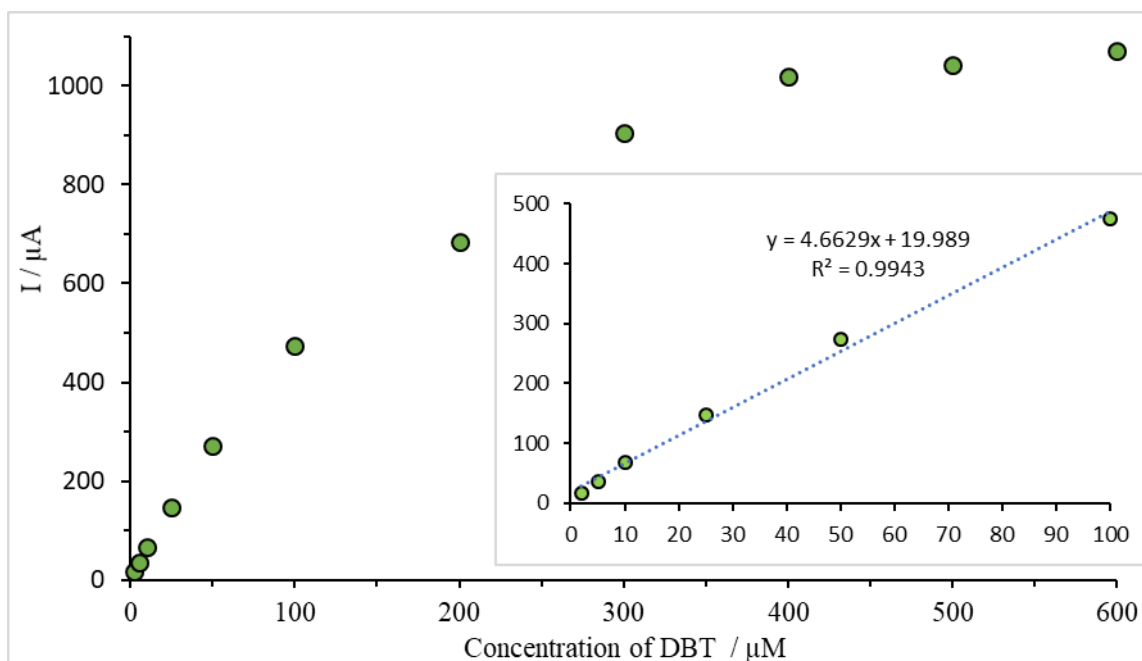
Figure 6: Calibration graph of PGE/OPEDOTNF-2cyc-2V-120s-2DP electrode obtained by CV at different DBT concentrations in BRB solution at pH 2.0 (Accumulation voltage: 2.0 V; accumulation time: 350 seconds, unstirred solution, data with baseline processing).

While preparing PGE/OPEDOTNF-2cyc-2V-120s-2DP, the over-oxidation process, which has been carried out so far and whose optimum conditions were determined as 120 seconds at 2.0 V, was carried out in phosphate buffer at pH 7.0. In order to determine the effect of the pH of the over-oxidation solution on DBT determinations, it was performed in PB solution at different pH values (6, 7, and 10). The current values obtained by CV technique in BRB solution at pH 2.0 containing 100 µM DBT using over-oxidized electrodes at different pH values are given in Figure S9. The values obtained in pH 7.0 PB solution were higher; this value was chosen as optimum. In addition, data obtained when deposition was performed by mixing is also given in Figure S9. In DBT determinations, a significant increase was observed in the oxidation peak current, as the mixing of the solution during deposition made it easier for the analyte to reach the electrode surface.

However, it is an effective strategy to use other electroanalytical methods, such as differential pulse voltammetry (DPV) or square wave voltammetry, to improve the sensitivity in determining electroactive compounds. Since DPV is widely used in detecting analyte signals with lower concentrations, it aims to increase the measurement sensitivity and lower the detection limit too much lower values. The DPV method was preferred to determine the analyte in the following parts. The necessary optimizations for DPV measurements were also worked.

3.4. Determination of dobutamine using the DPV technique
In the previous section, the parameters that will affect the DBT determinations were investigated by using the data obtained using the CV technique. Based on these data, the determined values for the number of cycles, over-oxidation voltage and time were used to prepare modified electrodes. In the measurements made using the DPV method at lower concentration values, the optimization of the parameters that will affect the accumulation of DBT on the electrode surface has been studied. Section 3.4 is related to these studies. Scan rate: 20 mV/s, pulse time:5 0 ms, and pulse amplitude: 50 mV were used in DPV measurements.

3.4.1. Effect of accumulation time and number of DPV processes used in conditioning
To determine the effect of accumulation time, 0.20 V for different times was applied to the PGE/OPEDOTNF-2cyc-2V-120s-2DP electrode immersed in BRB solution at pH 2.0 containing 20.0 µM DBT, and then DPV measurements were performed. To compare the current values obtained from the differential pulse voltammograms accurately, the peak current values obtained after baseline correction on the voltammograms were used. Baseline corrected, and uncorrected DP voltammograms obtained both with and without accumulation are presented in Figure S10. The results of the experiments carried out to determine the relationship between the current values and the accumulation time are

shown in the graph in Figure S11. While there is a remarkable increase until the 100th second, the increase in the current values after the 100th second is at lower levels. Therefore, it was decided that 100 seconds was a reasonable value for the accumulation time in this stage.

The potential of the number of DPV processes applied for conditioning the PGE/OPEDOTNF-2cyc-2V-120s electrode to affect the measurements in the new situation was also investigated. It was observed that the highest current value was reached with the modified electrode (PGE/OPEDOTNF-2cyc-2V-120s-1DP) obtained by conditioning once with the DP process (See Figure S12). Following these results, studies on the accumulation time were performed again using PGE/OPEDOTNF-2cyc-2V-120s-1DP. Since the sensitive DPV method and accumulation are used together, the DBT concentration was lowered ten times and selected as 2.0 mM. The graph of DBT oxidation current-accumulation time is shown in Figure S13. The data of Figure S13 were evaluated in terms of both high current values and a reasonable time. It was decided to apply the accumulation time of 250 seconds with a voltage value of 0.20 V on the surface of the PGE/OPEDOTNF-2cyc-2V-120s-1DP electrode. This accumulation time was used in interference, stability, and reproducibility studies.

3.4.2. Variation of oxidation current of DBT with concentration

Using PGE/OPEDOTNF-2cyc-2V-120s-1DP electrodes, the variation of DBT concentration and oxidation peak current values of DBT was measured using the DPV method. The graph obtained for three different deposition times (100, 250, and 400 s) is given in Figure 7. The linear range is between 0.1-4.0 μM for 100 seconds accumulation time, while the linear range is between 0.1-2.0 μM for 250 seconds accumulation time. As the accumulation time increases, the slope value of the linear concentration range increases, in which case more sensitive measurements can be made. For the 400-second accumulation time, the linear range narrowed while the slope value increased in accordance with the behavior mentioned above. The small graph at the bottom right of Figure 7 shows the linear range obtained with a correlation coefficient of 0.997 for a 250-seconds accumulation time. As a result of the calculations, the limit of detection (LOD) was found to be 0.026 μM, and the limit of quantification (LOQ) was 0.086 μM for the accumulation time of 250 seconds. LOD and LOQ values were calculated with the help of the following equations: LOD = 3 s / m and LOQ = 10 s / m (m is the slope of the linear equation obtained from the calibration graph in Figure 7., and s is the standard deviation of the current values obtained in BRT solution at pH 2 absence of DBT). Figure 8 shows the DP voltammograms obtained with PGE/OPEDOTNF-2cyc-2V-120s-1DP electrode for concentration values in the range of 0.1-8.0 μM in 250 seconds accumulation time.
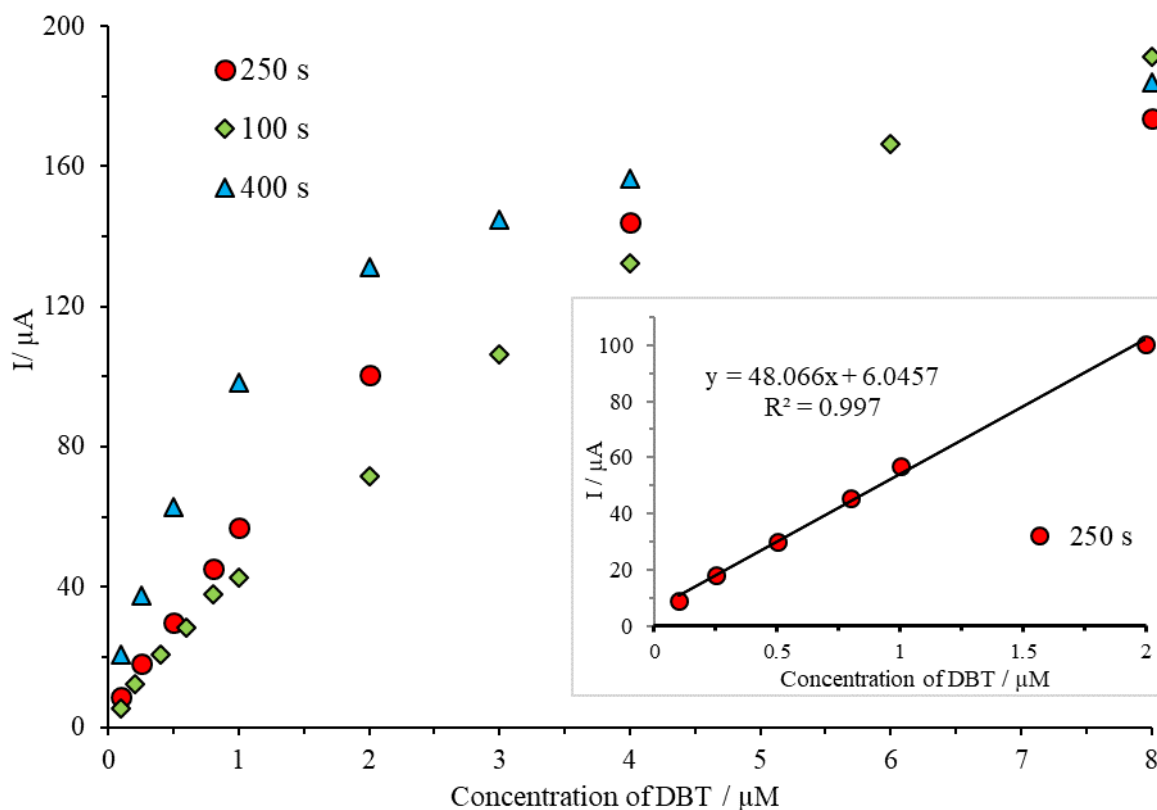
Figure 7: The effect of accumulation time (100 s, 250 s, and 400 s) on the calibration graph of PGE/OPEDOTNF-2cyc-2V-120s-1DP electrode obtained by DPV technique in BRB solution at pH 2.0. (Accumulation voltage: 0.20 V, solution stirring rate: 250 rpm).
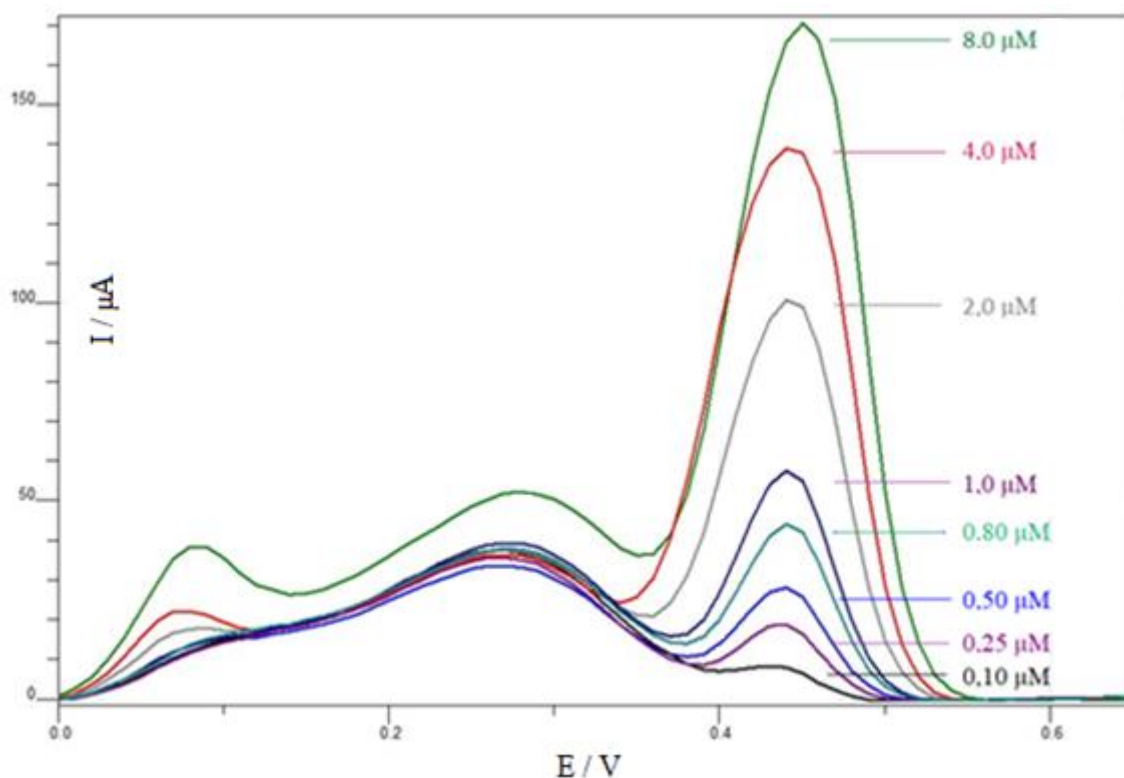
Figure 8: DP voltammograms obtained for DBT in BRB solution at pH 2.0 using the PGE/OPEDOTNF-2cyc-2V-120s-1DP electrode (Accumulation voltage: 0.20 V, accumulation time: 250 seconds, solution stirring rate: 250 rpm).

Linear range and LOD data are presented in Table 1 in comparison with the literature. LOD values are at lower concentrations than in some studies in the literature (3, 20, 22, 40).

Table 1: Comparison of the linear range and LOD of PGE/OPEDOTNF-2cyc-2V-120s-1DP in DBT determinations with the literature.

Modified Electrode	Linear Range (µM)	Limit of Detection, LOD (µM)	Reference
GQDs/NiMnO$_3$/CPE[a]	0.08–40	0.02	[5]
BNPs–MWCNTs/GCE[b]	0.005–1	0.009	[39]
PAO/GCE[c]	0.05–100	0.002	[2]
IL/GPE[d]	0.17–100	0.053	[20]
MgO-N/GCE[e]	1–30	0.092	[22]
AuCoPcCPE[f]	6.0–200	0.084	[3]
GC/CNT/ILC/RGO/CW[g]	0.02–40	0.000497	[25]
CPE/MWCNTPE[h]	18-1100	3.1	[40]
PGE/OPEDOTNF[i]	0.1-2.0	0.026	This study

[a] Graphene Quantum Dot-NiMnO$_3$ nanoparticle-Carbon paste electrode.
[b] Boehmite nanoparticle-Multi walled carbon nanotube-Glassy carbon electrode.
[c] Poly (Acridine Orange) film-Glassy carbon electrode.
[d] Ionic Liquid-Graphite paste electrode.
[e] MgO microflowers / Nafion-Glassy carbon electrode.
[f] Gold nanoparticle-Cobalt phthalocyanine modified carbon paste electrode.
[g] Glassy carbon electrode-Multi walled carbon nanotube-Ionic liquid crystal-Graphene-18-Crown-6.
[h] Carbon paste electrode-Multi walled carbon nanotube.
[i] Pencil graphite electrode-Over oxidized poly (3,4-ethylenedioxythiophene) nanofiber.

3.5. Effect of scanning rate on the current

Using the PGE/OPEDOTNF-2cyc-2V-120s-1DP electrode, cyclic voltammograms were recorded for 25 μM DBT (in BRB solution at pH 2.0) at scan rates in the range of 10-500 mV/s. The graph of the current values and cyclic voltammograms obtained for the oxidation of DBT against the scan rates can be seen in Figure S14. Figure 15a shows a plot of peak current values versus the square root of scan rates. Figure S15b shows the graph of the logarithms of the peak current values versus the logarithms of the scan rates, and the slope of the graph is 1.057. The linearity of the graphs in Figures S14 and S15b shows that the electrochemical oxidation of DBT is adsorption controlled. In addition, the fact that the slope of the graph in Figure S15b is close to 1.0 and the graph in Figure S15a is not linear supports that the oxidation current is adsorption controlled.

3.6. Interference study

Many different types of biological molecules coexist in body fluids. Knowing whether interfering species affect the analyte signal is important when working with real samples. Therefore, PGE/OPEDOTNF-2cyc-2V-120s-1DP electrodes were tested in the presence of 1.0 μM DBT and different concentrations of interference molecules. Electrolyte species found in physiological fluids such as KCl and NaCl and electroactive species such as uric acid, ascorbic acid, paracetamol, and phenylalanine found in body fluids were tested in the interference study. Neurotransmitter substances such as epinephrine and dopamine were also tested. The results obtained are given in Table 2 in comparison.

When the Table 2 is examined, the electrochemical signal is not seriously affected when the concentration of species such as glucose, NaCl, and KCl is 100 times higher than DBT. Epinephrine and dopamine, both electroactive and neurotransmitters like DBT, have interfering effects. One of the most important reasons for this may be that the modified electrode's improvement effect on the signal works for these interferent molecules. In addition, it is thought that the interfering species also accumulate on the electrode surface depending on their chemical structure and interaction degree during the accumulation process, and the interference effect reaches even higher levels than expected. Decreasing the DBT signal when non-electroactive species are at a concentration of 250, 500, or 1000 times higher than the DBT concentration may be related to the decrease in the amount of DBT accumulated on the electrode surface. Therefore, an additional modification to increase selectivity will be needed for the determination of DBT in the presence of interferent species. The molecular imprinting method could be an important alternative here. It is reported in the literature that conductive polymeric structures produced electrochemically by molecular imprinting method increase selectivity (41-43).

3.7. Stability and reproducibility of PGE/OPEDOTNF

The stability studies were carried out using PGE/OPEDOTNF-2cyc-2V-120s electrodes. Many electrodes prepared under the same conditions were kept in a closed plastic box, including desiccant material at room temperature. Stability studies were carried out using CV and DPV tecniques with disposable modified electrodes. CV measurements were performed using PGE/OPEDOTNF-2cyc-2V-120s-2DP electrode in BRB solution at pH 2.0 buffer containing 100 μM DBT. DPV measurements were performed using PGE/OPEDOTNF-2cyc-2V-120s-1DP electrode in BRB solution at pH 2.0 buffer containing 1 μM DBT. The measurement results for electrode stability is shown in Figure 9. When the PGE/OPEDOTNF-2dng-2V-120s-1DP electrode was used (Figure 9a), it was determined that the current value did not change significantly for 15 days and decreased by 4% on the 15th day. Then, the response of the electrode reduced day by day; for example, this decrease reached 36% for the 213th day. Similar behavior was observed for the PGE/OPEDOTNF-2dng-2V-120s-2DP electrode (Figure 9b).

To determine the reproducibility for PGE/OPEDOTNF-2cyc-2V-120s-1DP electrodes, the currents of the electrodes produced under the same conditions were measured by DPV in BRT solution at pH 2.0 containing 1.0 μM DBT. The standard deviation of the electrochemical response was calculated as 5.2% in 5 separate measurements performed with the modified electrodes.

Table 2: Effect of interfering species on the current response obtained by DPV technique using PGE/OPEDOTNF-2cyc-2V-120s-1DP for 1.0 µM DBT (Accumulation time: 250 s, Accumulation voltage: 0.20 V).

Interfering species	The concentration of the interfering species / (µM)	Change in Current[a] for 1.0 µM DBT with PGE/OPEDOTNF / (µA)	Deviation in current / (%)
Ascorbic acid	5 20	-0.16 -3.05	0.27 5.21
Dopamine	0.5 1 3	+10.07 +23.15 +57.07	17.21 39.57 97.56
Epinephrine	1 2 3	+16.34 +33.50 +40.64	27.94 57.28 69.48
Phenylalanine	100	-1.21	2.06
Glucose	25 100 250 1000	-1.23 -4.13 -5.06 -7.65	2.11 7.06 8.65 13.07
KCl	50 100 250 500	-1.09 -4.25 -7.94 -17.67	1.86 7.27 13.58 30.20
NaCl	25 50 100 250 500	-1.29 -1.95 -5.86 -8.65 -17.54	2.21 3.33 10.01 14.78 29.98
Paracetamol	10 15	-11.96 -19.82	20.45 33.89
Uric acid	2 4 8	-9.81 -15.59 -19.20	16.77 26.65 32.82

[a] The current without interfering species = 58.5 µA.
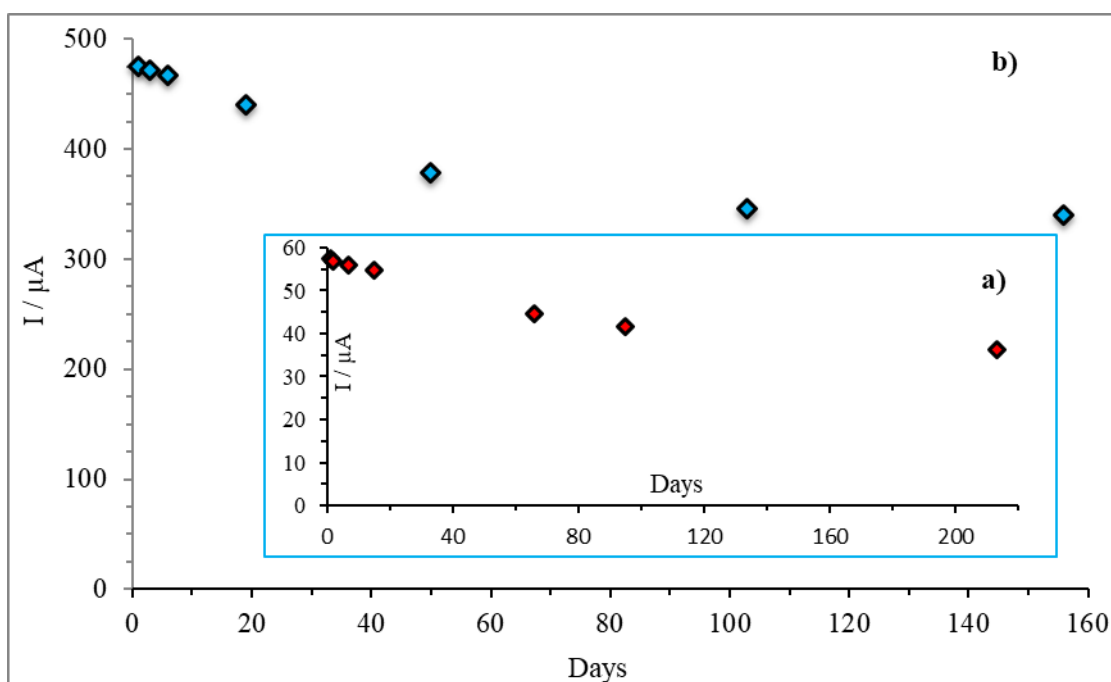
Figure 9: Life-time measurements for (a) 1 µM DBT with PGE/OPEDOTNF-2cyc-2V-120s-1DP using DPV and (b) 100 µM DBT with PGE/OPEDOTNF-2cyc-2V-120s-2DP using CV. (Accumulation voltage: 0.20 V).

4. CONCLUSION

A study was carried out on modifying the pencil graphite electrode with over-oxidized nanofiber structure PEDOT so that the DBT can be sensitively determined by voltammetric methods. It was determined that the oxidation current of DBT obtained with PGE modified with nanofiber-structured PEDOT was 2 times higher than that of non-nanofiber. Parameters that may affect the current response of modified electrodes against DBT were examined, and optimum conditions were determined. As a result of DPV measurements performed with PGE/OPEDOTNF-2cyc-2V-120s-1DP electrodes in the presence of DBT, it was observed that the response of the electrodes against DBT in the concentration range of 0.1 µM to 2.0 µM was linear. The limit of detection (LOD) was calculated as 0.026 µM, and the limit of quantification (LOQ) as 0.086 µM. In addition, interference studies have been made for DBT concentration. PGE/OPEDOTNF-2cyc-2V-120s-1DP electrodes have a reproducibility of 5.2% and can remain stable for 15 days without losing effectiveness. In addition, the modified PGE in this study provides a significant advantage in terms of cost since it is an electrode material that can be obtained very cheaply.

The data of this study, with some additional changes, will lead to future research and studies. Developing the electrochemical determination of biologically important compounds that are simple, inexpensive, and compatible with miniaturized systems has become very important. From this point of view, the study significantly contributed to determining DBT, which is one of the very important catecholamines.

5. CONFLICT OF INTEREST

There are no conflicts that need to be reported.

6. ACKNOWLEDGMENTS

7. REFERENCES

1. Venton BJ, Wightman RM. Psychoanalytical electrochemistry: Dopamine and behavior. Analytical Chemistry. 2003;75:414A-421A. Available from: <URL>

2. Zhang Y. Voltammetric behavior of dobutamine at poly (Acridine orange) film modified electrode and its determination by adsorptive stripping voltammetry. Analytical Letters. 2004;37:2031-2042. Available from: <URL>

3. Atta NF, Galal A, Abdel-Gawad FM, Mohamed EF. Electrochemistry and detection of dobutamine at gold nanoparticles cobalt-phthalocyanine modified carbon paste electrode. Journal of The Electrochemical Society. 2015;162:B304-B311. Available from: <URL>

4. Ekram H, Atta NF, Galal A, El-Gohary AR. Nano-Perovskite decorated carbon nanotubes composite for ultrasensitive determination of a cardio-stimulator drug. Journal of The Electrochemical Society. 2018;16:149-159. Available from: <URL>

5. Hasanpour F, Nekoeinia M, Semnani A, Shojaei S. NiMnO$_3$ nanoparticles anchored on graphene quantum dot: Application in sensitive electroanalysis of dobutamine. Microchemical Journal. 2018;142:17-23. Available from: <URL>

6. Reddy S, Xiao Q, Liu H, Li C, Chen S et al. Bionanotube/Poly (3, 4-ethylenedioxythiophene) nanohybrid as an electrode for the neural interface and dopamine sensor. ACS Applied Materials & Interfaces. 2019;11:18254-18267. Available from: <URL>

7. Ozkorucuklu SP, Ozcan L, Sahin Y. Alsancak G. Electroanalytical determination of some sulfonamides on overoxidized polypyrrole electrodes. Australian Journal of Chemistry. 2011;64(7):965-972. Available from: <URL>

8. Şahin M, Özcan L, Usta B, Şahin Y. Determination of ascorbic acid by polypyrrole potentiometric detector in ion chromatography. Biosensors and Bioelectronics. 2009;24(12):3492-3497. Available from: <URL>

9. Hosseinian M, Najafpour G, Rahimpour A. Amperometric urea biosensor based on immobilized urease on polypyrrole and macroporous polypyrrole modified Pt electrode. Turkish Journal of Chemistry. 2019;43(4):1063-1074. Available from: <URL>

10. Gorduk O. Differential pulse voltammetric determination of serotonin using an acid-activated multiwalled carbon nanotube-over-oxidized Poly(3,4-ethylenedioxythiophene) modified pencil graphite electrode. Analytical Letters. 2020;53:1034-1052. Available from: <URL>

11. Chen L, Liu X, Wang C, Lv S, Chen C. Amperometric nitrite sensor based on a glassy carbon electrode modified with electrodeposited poly(3,4-ethylenedioxythiophene) doped with a polyacenic semiconductor. Microchimica Acta, 2017;184:2073-2079. Available from: <URL>

12. Dinesh B, Vilian AE, Kwak CH, Huh YS, Saraswathi R et al. The Facile and simple synthesis of poly(3,4-ethylenedioxythiophene) anchored reduced graphene oxide nanocomposite for biochemical analysis. Analytica Chimica Acta. 2019;1077:150-159. Available from: <URL>

13. Liu S, Jiang X, Waterhouse GIN, Zhang ZM, Yu LMA. Cu_2O/PEDOT/graphene-modified electrode for the enzyme-free detection and quantification of glucose. Journal of Electroanalytical Chemistry. 2021;897:115558. Available from: <URL>

14. Butina K, Löffler S, Rhen M, Richter-Dahlfors A. Electrochemical sensing of bacteria via secreted redox active compounds using conducting polymers. Sensors and Actuators B: Chemical. 2019;297:126703. Available from: <URL>

15. Mariani F, Gualandi I, Tessarolo M, Fraboni B, Scavetta E. PEDOT: Dye-Based, flexible organic electrochemical transistor for highly sensitive pH monitoring. ACS Applied Materials & Interfaces. 2018;10:22474-22484. Available from: <URL>

16. Qian Y, Ma C, Zhang S, Gao J, Liu M et al. High performance electrochemical electrode based on polymeric composite film for sensing of dopamine and catechol. Sensors and Actuators B: Chemical. 2018;255:1655-1662. Available from: <URL>

17. Özcan A, İlkbaş S. Preparation of poly (3, 4-ethylenedioxythiophene) nanofibers modified pencil graphite electrode and investigation of over-oxidation conditions for the selective and sensitive determination of uric acid in body fluids. Analytica Chimica Acta. 2015;891:312-320. Available from: <URL>

18. Rajaram R, Kanagavalli P, Senthilkumar S, Mathiyarasu L. Au nanoparticle-decorated nanoporous PEDOT modified glassy carbon electrode: A new electrochemical sensing platform for the detection of glutathione. Biotechnology and Bioprocess Engineering. 2020;25(5):715-723. Available from: <URL>

19. Shvedene NV, Nazarova IA, Formanovsky AA, Otkidach DS, Pletnev IV. 3-(4-tolylazo) phenylboronic acid as the active component of polyhydroxy compounds-selective electrodes. Electrochemistry Communications. 2002;4:978-984. Available from: <URL>

20. Chernyshov DV, Shvedene NV, Antipova ER, Pletnev IV. Ionic Liquid-Based miniature electrochemical sensors for the voltammetric determination of catecholamines. Analytica Chimica Acta. 2008;621:178-184. Available from: <URL>

21. Rastogi PK, Ganesan V, Krishnamoorthi S. Ion exchange voltammetry at permselective copolymer modified electrode and its application for the determination of catecholamines. Journal of Electroanalytical Chemistry. 2012;676:13-19. Available from: <URL>

22. Ling YY, Huang QA,. Feng DX, Lii XZ, Wei Y. Electrochemical oxidation of dobutamine on a magnesium oxide microflowers–nafion composite film modified glassy carbon electrode. Analytical Methods. 2013;5:4580-4584. Available from: <URL>

23. Asadian E, Shahrokhian S, Jokar E. In-Situ electro-polymerization of graphene nanoribbon/polyaniline composite film: Application to sensitive electrochemical detection of dobutamine. Sensors and Actuators B: Chemical. 2014;196:582-588. Available from: <URL>

24. Negahban S, Fouladgar M, Amiri G. Improve the performance of carbon paste electrodes for determination of dobutamine using $MnZnFe_2O_4$ nanoparticles and ionic liquid. Journal of the Taiwan Institute of Chemical Engineers. 2017;78:51-55. Available from: <URL>

25. Atta NF, Galal A, Ahmed YM, Ekram H. Design strategy and preparation of a conductive layered electrochemical sensor for simultaneous determination of ascorbic acid, dobutamine, acetaminophen and amlodipine. Sensors and Actuators B: Chemical. 2019;297:126648. Available from: <URL>

26. Ibrahim H, Temerk Y. Synergistic electrocatalytic activity of In_2O_3@ FMWCNTs nanocomposite for electrochemical quantification of dobutamine in clinical patient blood and in injection dosage form. Talanta 2020;208:120362. Available from: <URL>

27. Karakaya S, Kartal B, Dilgin Y. Development and application of a sensitive, disposable and low-cost electrochemical sensing platform for an antimalarial drug: amodiaquine based on poly(calcein)-modified pencil graphite electrode. International Journal of Environmental Analytical Chemistry. 2020;1-14. Available from: <URL>

28. Gorduk O. Poly(glutamic acid) Modified pencil graphite electrode for the voltammetric determination of bisphenol A. Journal of the Turkish Chemical Society Section A: Chemistry. 2021;8(1):173-186. Available from: <URL>

29. Özcan A, İlkbaş S, Özcan AA. Development of a disposable and low-cost electrochemical sensor for

dopamine detection based on poly(pyrrole-3-carboxylic acid)-modified electrochemically over-oxidized pencil graphite electrode. Talanta 2017;165:489-495. Available from: <URL>

30. Özcan L. Electrochemical dopamine determination by Cu(II), Ni(II), Co(II) and Fe(II) metallophthalocyaninetetrasulfonate modified pencil graphite electrodes. Afyon Kocatepe Üniversitesi Fen ve Mühendislik Bilimleri Dergisi 2019;19(2):291-300. Available from: <URL>

31. Šafranko S, Stanković A, Asserghine A, Jakovljević M, Hajra S et al. Electroactivated disposable pencil graphite electrode-new, cost-effective, and sensitive electrochemical detection of bioflavonoid hesperidin. Electroanalysis. 2021;33(4):1063-1071. Available from: <URL>

32. Navratil R, Kotzianova A, Halouzka V, Opletal T, Triskova I et al. Polymer lead pencil graphite as electrode material: Voltammetric, XPS and raman study. Journal of Electroanalytical Chemistry. 2016;783:152-160. Available from: <URL>

33. Gao W, Song J, Wu N. Voltammetric behavior and square-wave voltammetric determination of trepibutone at a pencil graphite electrode. Journal of Electroanalytical Chemistry. 2005;576:1-7. Available from: <URL>

34. David IG, Popa DE, Buleandra M. Pencil graphite electrodes: A versatile tool in electroanalysis. Journal of Analytical Methods in Chemistry. 2017;1905968. Available from: <URL>

35. Kolahi-Ahari S, Deiminiat B, Rounaghi GH. Modification of a pencil graphite electrode with multiwalled carbon nanotubes capped gold nanoparticles for electrochemical determination of tramadol. Journal of Electroanalytical Chemistry. 2020;862:113996. Available from: <URL>

36. Tavares PHCP, Barbeira PJS. Influence of pencil lead hardness on voltammetric response of graphite reinforcement carbon electrodes. Journal of Applied Electrochemistry. 2008;38:827-832. Available from: <URL>

37. Özcan L, Şahin Y and Türk H. Non-enzymatic glucose biosensor based on overoxidized polypyrrole nanofiber electrode modified with cobalt(II) phthalocyanine tetrasulfonate. Biosensors and Bioelectronics. 2008;24(4):512-517. Available from: <URL>

38. Özcan L. Electrochemical epinephrine determination by nanofiber structured overoxidized polypyrrole modified pencil graphite electrodes. Avrupa Bilim ve Teknoloji Dergisi 2019;16:355-362. Available from: <URL>

39. Ghalkhani M, Salehi M. Electrochemical sensor based on multi-walled carbon nanotubes-boehmite nanoparticle composite modified electrode. Journal of Materials Science. 2017;52:12390-12400. Available from: <URL>

40. Fouladgar M. Direct voltammetric determination of dobutamine in pharmaceutical samples using multiwall carbon nanotubes paste electrode. ECS Solid State Letters. 2015;4:M15

41. Özcan L and Şahin Y. Determination of paracetamol based on electropolymerized-molecularly imprinted polypyrrole modified pencil graphite electrode. Sensors and Actuators B: Chemical. 2007; 127: 362–369. Available from: <URL>

42. Menon S, Jesny S, Kumar KG. A Voltammetric sensor for acetaminophen based on electropolymerized-molecularly imprinted poly(o-aminophenol) modified gold Electrode. Talanta 2018;179:668-675. Available from: <URL>

43. Crapnell RD, Hudson A, Foster CW, Eersels K, van Grinsven B et al. Recent advances in electrosynthesized molecularly imprinted polymer sensing platforms for bioanalyte detection. Sensors 2019;19:1204. Available from: <URL>

RESEARCH ARTICLE

A Novel Method to Assay Aspirin in Pharmaceutical Formulations by Smartphone Camera-Based Image Scanning Densitometry

Rimsha Khan[1,2]* iD , Jamil Anwar[1,2] iD

[1]Department of Chemistry, School of Science, University of Management and Technology, 54770, Lahore, Pakistan.
[2]School of Chemistry, University of the Punjab, 54000, Lahore, Pakistan.

Abstract: Aspirin, a widely-used anti-inflammatory drug, can lead to serious consequences when overdosed. Therefore, there's a need for simple, cost-effective methods to determine its concentration and mitigate potential risks. This study aimed to develop a method for assessing aspirin in pharmaceutical preparations without the need for expensive equipment and with minimal sensitivity to ambient light. In this work, aspirin was subjected to a reaction with Fe(III), leading to the formation of violet-colored spots on filter paper and a 96-microwell plate. These colored spots were then captured using a smartphone in normal lighting conditions and analyzed on a computer. The integrated density of each spot was measured using a novel grayscale technique, and a calibration curve was created to relate integrated density to aspirin concentration. Analytical parameters and reagent concentrations were optimized for accuracy. To validate the method, three commercial aspirin samples were assayed and compared to ultraviolet-visible spectrophotometry, a reference method. The developed technique demonstrated excellent precision (coefficient of variation <0.68%) and relative errors below 5.2%. When compared to traditional color models like red-green-blue (RGB) and hue-saturation-luminosity (HSL), the grayscale model showed superior correlation ($R^2 > 0.996$), while the RGB model yielded less precise results ($R^2 = 0.792$). This study showcased the effectiveness of a cost-effective methodology for accurate aspirin quantification using a smartphone camera, even in the presence of ambient light.

1. INTRODUCTION

Aspirin or acetylsalicylic acid is one of the most commonly used drugs in the world and its wider usage can be estimated by the fact that over 40,000 tons of the drug are consumed each year globally (1) with more than 17 million prescriptions in the United States alone (2). Aspirin was first introduced in the market by the Bayer Company in Germany in 1899. It is generally believed that Felix Hoffmann was the first to prepare acetyl ester of the acid and developed aspirin to help his rheumatic father (3). Aspirin belongs to a group of non-steroidal anti-inflammatory drugs that are characterized by their anti-inflammatory, analgesic, and antipyretic functions. Aspirin is routinely used in a wide range of painful conditions, including head, body, and muscle aches, arthritis, and many other common ailments (4). Today, aspirin is also taken by millions of people who benefit from its antithrombotic effect (5). The medical community has increasingly recommended routine therapy with low-dose aspirin, which significantly reduces the risk of death from a cardiovascular event (6).

The pharmaceutical activity of a drug depends upon the chemical characteristics of its molecules, thus any small variation in chemical properties and quantitative composition may lead to considerable variation in therapeutic effects. Aspirin overdose has potentially serious consequences leading to many side effects including nausea and vomiting, abdominal pain, lethargy, ringing in the ears, and dizziness (7). The most common cause of death

following an aspirin overdose is cardiopulmonary arrest usually due to pulmonary edema (8). Therefore, a proper assay and quantification technique to ascertain aspirin content in a multi-component pharmaceutical dosage and its stability is indeed necessary, vital, and appreciated to avoid overdose.

Numerous classical and instrumental methods have been used for the determination of aspirin in pharmaceutical formulations including titrimetric (9), potentiometric (10), ultraviolet-visible spectrophotometry (11), ion-selective electrode (12), high-performance liquid chromatography (13), and gas chromatography-mass spectrometry (14). Titrimetric, spectroscopic, and hyphenated chromatographic methods for the analysis of aspirin from various analgesic formulations have been recently compared by Anthony et al. (15). Aspirin has been successfully determined by oxidation-reduction reaction with $KMnO_4$ (16). The most commonly used methods for the quantitative analysis of aspirin are spectrophotometric in which Fe(III) salts are used as coloring reagents to form a violet complex, the absorbance of which is used as a measure of aspirin quantitatively (17). In 2006, Kohl et al. showed that similar absorbance work could easily be performed by using colored solutions and digital images obtained with charge-coupled devices (18). Since then, there have been several reports in which smartphones, scanners, and digital cameras were used as photometers (19-21). Our group has also quantified several species, including Fe, Ni, Hg, As, formaldehyde, and sulfide at the micro level by using spot tests and a flatbed scanner (22-25).

In the present age of information technology, the number of smartphone users has increased to almost 2.87 billion. Smartphones are replacing digital cameras and scanners due to more features including high-resolution cameras, better image acquisition technology, powerful processing units, fast and easy analysis, multiple image formats, and portability, making smartphone-based colorimetric analysis ideal for research in biomedical and pharmaceutical fields (26). Recently, Soares and Rocha employed spot tests and a smartphone for the analysis of uric acid in saliva (27). Franco et al. determined Cu^{+2} in distilled beverages by fabricating a smartphone case to minimize the effect of ambient light (28). Analysis of $KMnO_4$, $CoSO_4$, $NiSO_4$, $CuSO_4$, etc. has also been carried out using smartphone camera-based techniques (29). Additionally, smartphones coupled with paper-based analytical devices (PADs) have been gaining popularity for the analysis of biomolecules and ions (30, 31). Quantitative analysis of many antibiotics like vancomycin, gentamicin, neomycin sulfate resazurin, etc. has also been carried out using smartphone-based colorimetric techniques (32-34). However, it is reported that the images captured from a smartphone suffer from the effects of ambient light and may lead to poor accuracy (35).

In literature, the most commonly used method for making colorimetric measurements is reported to be the red-green-blue (RGB), which is a subtractive color model consisting of 8-bit pixels from 0 to 255 with 0 being black, 255 pure white, and the rest of the colors fall in between the range (22). The Hue-saturation-luminosity (HSL) color space is represented in three dimensions where hue corresponds to different color values from 0° to 360° on the color wheel, while saturation is the trueness of the color. Luminosity gives lightness or darkness to a color shade regardless of its saturation (36). Recently, da Silva and Borges used a 96-microwell plate and a flatbed scanner for the quantitative analysis of aspirin in pharmaceutical tablets using the RGB model (37). They employed a complexation reaction of aspirin with Fe(III) to get violet-colored solutions in a 96-microwell plate, the RGB intensity of which was measured by using the green component in ImageJ. However, it was reported that employing the same model using a smartphone camera led to poor results (R^2 <0.77) due to the effects of ambient light. Moreover, the figure for percent errors climbed to 14.1% even using a flatbed scanner.

In the present work, we addressed this gap by employing a novel grayscale quantification technique using smartphone camera-based analysis of aspirin spot tests and 96-microwell plate solutions. The main objective of this work is to develop a technique that can be applied to the quantitative analysis of aspirin regardless of the effects of ambient light. However, the effects of ambient light on RGB or grayscale measurements are not discussed in this paper and require further research. Our proposed grayscale method is robust, simple, accurate, adequately sensitive, and can be applied to black precipitation reactions and turbid solutions as well.

2. EXPERIMENTAL SECTION

2.1. Apparatus and Reagents

Micropipette (Pipettman 20-100 µL and Pipettman 0.2-2 µL), Whatman filter paper No. 42, and disposable 96-microwell plate (CITOTEST®) were used for carrying out spot tests and developing colored solutions in microwells. Single beam visible range spectrophotometer-Jenway 6300 with wavelength range 320-950 was used for reference measurements. Sigma-Aldrich Iron(III) chloride hexahydrate ($FeCl_3.6H_2O$) was used as a complexing agent. Sodium hydroxide (NaOH) and hydrochloric acid (HCl) were purchased from Merck and deionized water was used to prepare the solutions. Pure aspirin was obtained from a local pharmaceutical firm: LAHORE CHEMICAL & PHARMACEUTICAL WORKS (PVT) LTD. Three pharmaceutically formulated drug samples of aspirin from different manufacturers (Table 1) were obtained for method verification.

Table 1: Pharmaceutical samples of aspirin used in the study.

Trade name	Contents	Manufacturer
Disprin	Aspirin 300 mg	Reckitt Benckiser Pakistan Ltd.
Loprin	Aspirin 150 mg	Highnoon Laboratories Ltd.
Ascard	Aspirin 150 mg	Acto Laboratories Ltd.

2.2. Equipment and Software

Apple iPhone X with a 12-megapixel camera was used for image acquisition of the spots with a built-in camera app and default lighting mode. Adobe Photoshop 2020 (version 21.2.2) (Adobe Inc.) was used for the quantification of spots in a desktop computer (DELL OptiPlex 3020 core i7) running on Windows 10 with additional AMD Radeon graphics (R7 200 series). Microsoft Excel (Microsoft Inc.) and OriginPro 2018 (64-bit) SR1 (OriginLab) were used for data analysis and graph plots.

2.3. Preparation of Reagents and Standards

5000 µg/mL stock solution of aspirin was prepared by dissolving 0.5 g of pure aspirin in 5 mL of 1 M NaOH. The solution was hydrolyzed by heating and stirring for 30 minutes. After heating, the solution was transferred to a 100 mL volumetric flask and made up to mark with deionized water. Using a micropipette, 20, 40, 60, 80, 100, 120, and 140 µL of aspirin stock were added in test tubes followed by the addition of 0.5% acidified $FeCl_3.6H_2O$, to prepare standard solutions of concentration: 500, 1000, 1500, 2000, 2500, 3000 and 3500 µg/mL. For the 96-microwell plate method, 1000 µg/mL aspirin stock solution was prepared by dissolving 0.1 g of pure aspirin in 5 mL of 1 M NaOH. The solution was hydrolyzed by heating and stirring for 30 minutes and afterward, transferred to a 100 mL volumetric flask and made up to mark with deionized water. 0.5% acidified $FeCl_3.6H_2O$ was prepared by adding 2.50 g of the compound in a 500 mL volumetric flask. The solution was then made up to the mark with 0.2 M HCl. NaOH and HCl were prepared in

concentrations from 0.2 M to 1 M to observe the effects on color development.

2.4. Preparation of Samples

Each aspirin commercial tablet was weighed corresponding to 0.3 g and ground to a fine powder. The samples were hydrolyzed in 5 mL of 1 M NaOH with constant stirring and heating for 30 minutes on a hot plate and transferred to 50 mL volumetric flasks followed by the addition of deionized water. Working standards were prepared by necessary dilutions of the stock and made up to the mark with 0.5% acidified $FeCl_3.6H_2O$ to get violet colored solution of aspirin for both filter paper spot tests and 96-microwell plate method.

2.5. Development of Colored Spots and Image Acquisition

Three strips of Whatman filter paper were cut to approximately 14.5×1.5 cm in length. Using a micropipette, 1 µL drops of aspirin standards and samples were transferred from test tubes to filter paper. Violet-colored spots appeared on filter paper that remained stable for 5 minutes. For the 96-microwell method, aliquots of 10, 20, 30, 40, 50, 60, and 70 µL of aspirin stock were added in the first row of the 96-microwell plate followed by the addition of $FeCl_3.6H_2O$ to get violet-colored solutions with concentrations of 50, 100, 150, 200, 250 and 300 µg/mL. The solutions in each well were mixed well with the help of a micropipette tip. A similar method was used for samples followed by serial dilutions. The image of filter paper spots and 96-microwell plate was captured using iPhone X in standard lighting conditions and autofocus to avoid blurring.
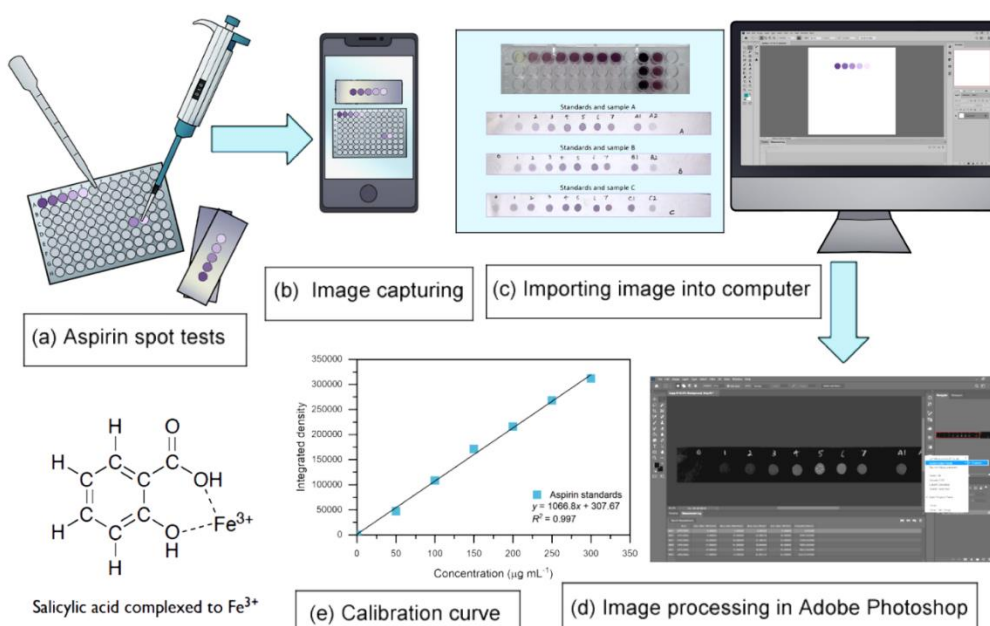

Figure 1: Graphical abstract of the proposed grayscale method for the smartphone camera-based quantitative analysis of aspirin.

2.6. Data Analysis

Images of filter paper spots and a 96-microwell plate were transferred to a computer using a USB cable in JPEG (Joint Photographic Experts Group) format. For the quantification procedure, images were imported into Adobe Photoshop in RGB mode with 8 bits per channel and converted from RGB to grayscale mode by going into the menu: Image/Mode/Grayscale. To make sure the boundaries of spots are well seen and sharp, the image was inverted in colors by going into the top menu: Image/Adjustments/Invert. The color balance of black and white was adjusted using the level correction feature as illustrated in Figure 2. The levels were corrected in such a way that the background of the image turns into pure black to give a value of 0, which minimizes the integrated density of the background and blank from the readings of standards and samples.
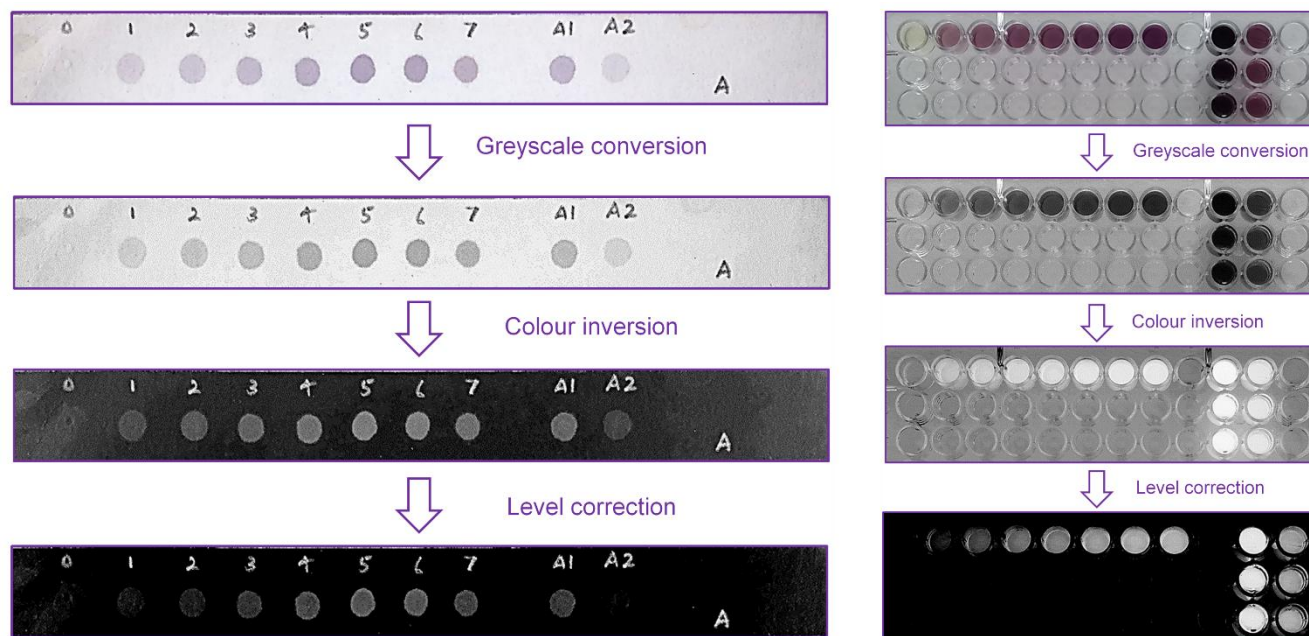
Figure 2: Image manipulation and editing of aspirin filter paper spots and 96-microwell plate in Adobe Photoshop.

After image editing, the procedure for measuring grayscale intensity was carried out using the measurement log feature in Adobe Photoshop (Figure 3). Custom data points were selected from options to get the desired values of gray maximum, minimum, mean, median, area, and integrated density. To get the values for integrated density, a selection of 50×50 pixels was made on the first spot using the elliptical marquee tool. The selection was saved by going into the top menu: select/save selection menu. The same selection was moved to the next spot by pressing CTRL+Shift and moving the cursor to the rest of the spots and selections were saved one by one. The measurements for each selection were recorded by clicking on the selection and selecting record measurements in the measurement log window. This gave values of gray maximum, minimum, mean, median, area, and integrated density at the same time. A similar method can also be performed in ImageJ using the measurement log feature. The measurements were performed in triplicates (n=3) and values were exported to Excel and OriginPro 9.5 to prepare calibration plots.
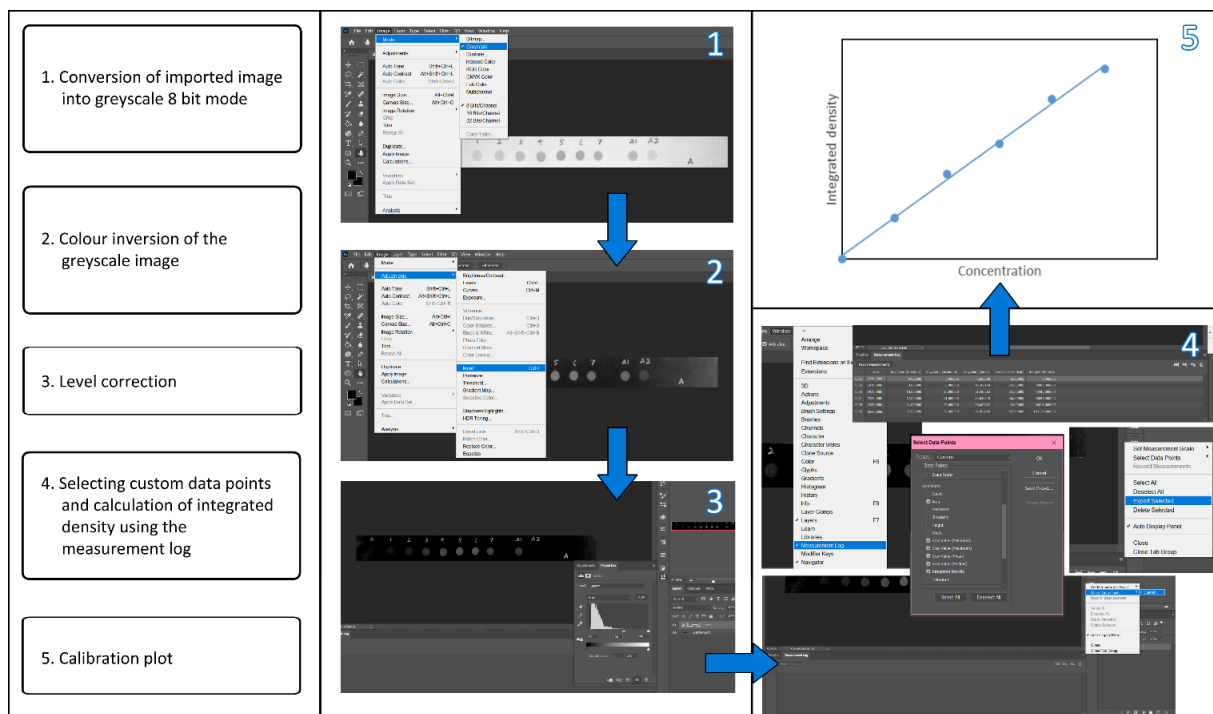
Figure 3: Schematic illustration of quantification of aspirin by the proposed grayscale method in Adobe Photoshop.

2.7. Reference Method

For UV/Visible spectrophotometry, 1000 µg/mL aspirin stock solution was prepared by dissolving 0.1 g of pure aspirin in 5 mL of 1 M NaOH and the solution was hydrolyzed by heating and stirring for 30 minutes. The hydrolyzed solution was transferred to a 100 mL volumetric flask and made up to mark with deionized water. Subsequent standards were prepared in the concentration range of 50-300 µg/mL. The absorbance of violet-colored aspirin solutions was measured at 530 nm and factors like linearity, standard deviation, and percent error were compared with both filter paper spot tests and the 96-microwell plate method.

3. RESULTS AND DISCUSSION

3.1. Preliminary Studies

A chemical reaction involving the formation of an aspirin-iron complex in this method is based on the complexation reaction of Fe(III) to give colored complexes where Fe(III) salts combine with salicylic acid to form a dark violet-colored complex and are used as an identification test for the presence of free salicylic acid present in aspirin. Acetylsalicylic acid hydrolyzes more rapidly in a basic medium than in acidic or aqueous media but optimizing the concentration of sodium hydroxide is important to avoid the formation of $Fe(OH)_3$ precipitates. This was overcome by using an acidified solution of $FeCl_3.6H_2O$ to neutralize excess sodium hydroxide. The absorbance spectra of violet colored aspirin complex showed maximum absorbance at 530 nm as shown in Figure 4, which follows previous studies (17).
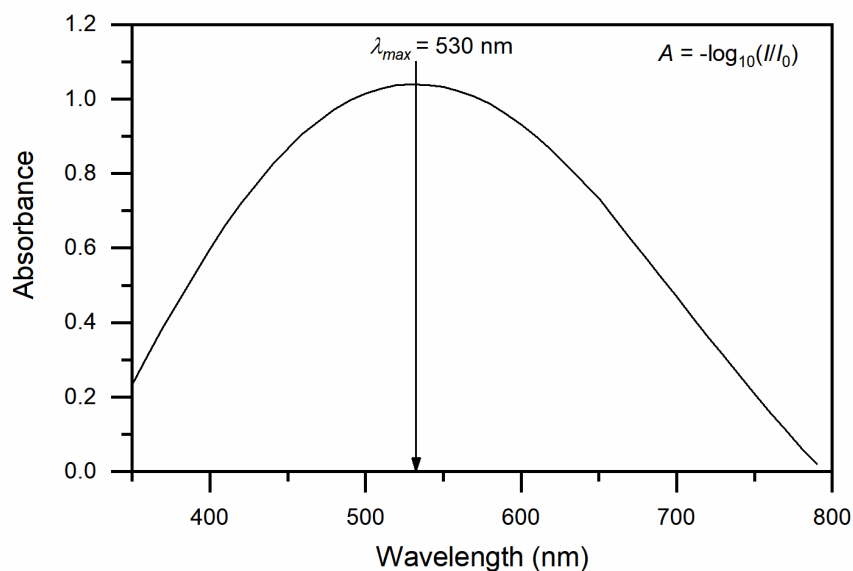
Figure 4: Absorbance spectra of violet colored aspirin-iron complex.

3.2. Effect of Reagent Concentration

The effect of reagent concentration was investigated by keeping the quantity of aspirin the same but varying the concentration of the reagents. Increasing HCl concentration resulted in a decrease in absorbance of the colored complex (Figure 5a) and the physical effect was also evident by observing the discoloration of the aspirin-iron complex. However, varying sodium hydroxide concentration had no considerable effect on absorbance as shown in Figure 5b. An increase in absorbance of the violet-colored complex was observed when changing $FeCl_3.6H_2O$ concentration from 0.1% to 0.5% (Figure 5c). Hence, 0.5% $FeCl_3.6H_2O$ prepared in 0.2 M HCl was selected as the optimum concentration in the present study.
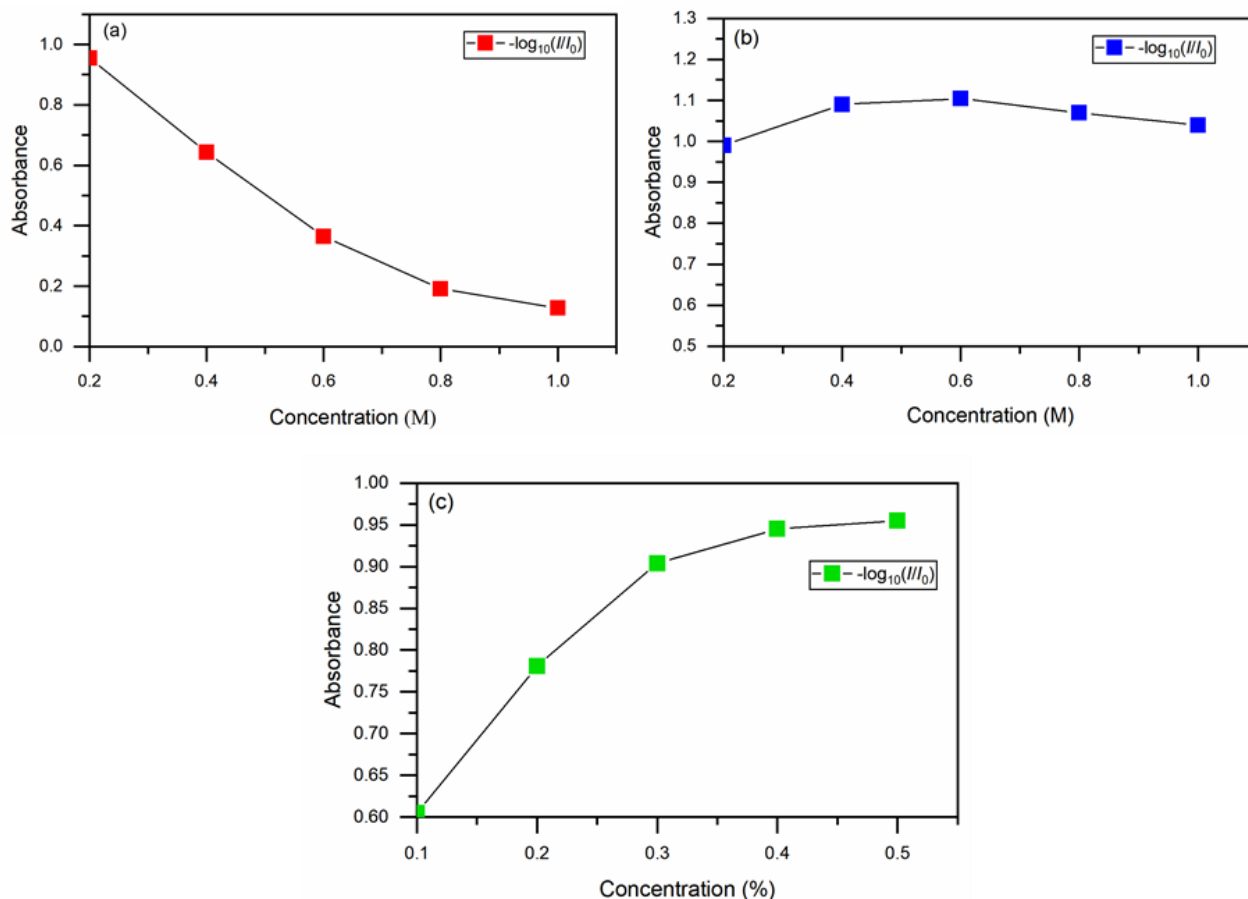
Figure 5: Effect of concentration of (a) HCl, (b) NaOH and (c) $FeCl_3.6H_2O$ on absorbance of colored complex of aspirin.

3.3. Analytical Performance

Quantitative measurements for filter paper aspirin spots were performed in the range of 500-2500 µg/mL. A calibration graph was plotted between the concentration and the integrated density of aspirin spots. To check time variation, aspirin spots were applied on three filter paper strips A, B, and C, and the image was captured after 1 minute, 3 minutes, and 5 minutes respectively and their linearity was compared. Relative standard deviation was found to be less than 2.02% for three sets of spots with R^2 greater than 0.996. Table 2 and Figure 6 compare calibration parameters of images of filter paper aspirin spots that were captured at different time intervals.

Table 2: Effect of time variation on calibration of filter paper aspirin spots.

Calibration parameters	Spots A	Spots B	Spots C	Mean	RSD (%)
Slope	49.305	49.987	55.674	51.655	5.53
Intercept	859.56	2103.0	2130.5	1697.69	34.9
R	0.998	0.999	0.999	0.998	0.05
R^2	0.996	0.998	0.997	0.997	0.08
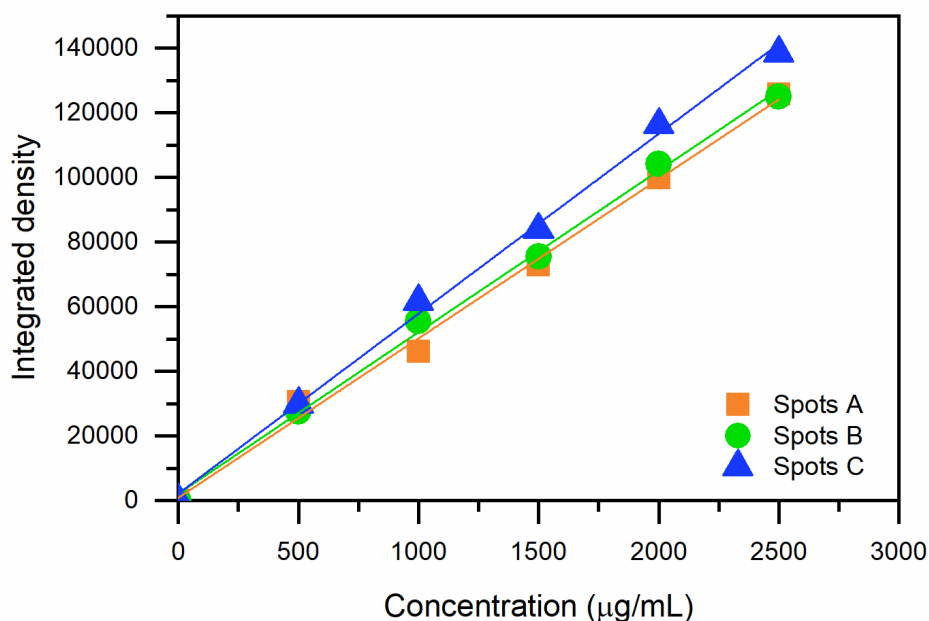
Figure 6: Effect of time variation on filter paper aspirin spots captured by smartphone.

Calibration analysis of 96-microwell plate aspirin also resulted in a good correlation with R^2 of 0.997 and relative standard deviation (RSD, n=3) less than 1.46%. The linear range was found to be the same as that of the reference method (50-300 μg/mL). UV-visible spectrophotometry of aspirin was performed in the range of 50-300 μg/mL and calibration was plotted between concentration versus absorbance of the aspirin solutions. The correlation coefficient (R^2) was found to be 0.996, which was comparable to filter paper spot tests and the 96-microwell plate method. Table 3 and Figure 7 compares the calibration parameters of aspirin filter paper spots tests and 96-microwell plate method with that of the reference. Both filter paper spot tests and the 96-microwell plate method provided precise results using smartphone-camera-based analysis with a correlation coefficient greater than 0.996 and no negative effects of ambient light on the results which were reported by da Silva and Borges (37).
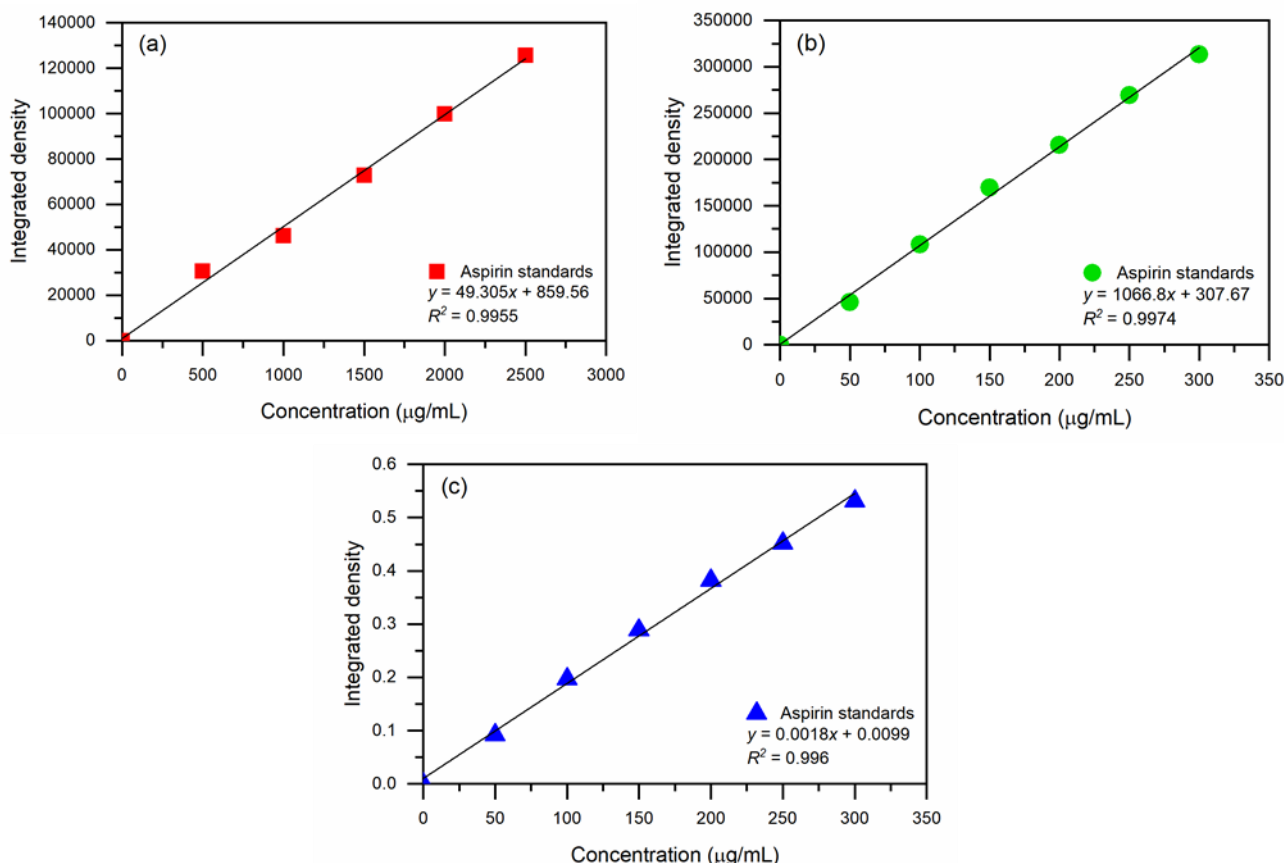
Figure 7: Aspirin calibration by (a) Filter paper spot tests, (b) 96-Microwell plate method and (c) Reference method.

Table 3: Comparison of filter paper spot tests and 96-microwell plate method with the reference method.

Calibration parameters	Filter paper spot tests	96-Microwell plate method	Reference method
Working range (µg/mL)	500-2500	50-300	50-300
Slope	49.305	1066.8	0.0018
Intercept	859.56	307.67	0.0099
R	0.998	0.998	0.998
R^2	0.996	0.997	0.996
Average RSD (%)	0.68	0.61	0.67

3.4. Method Verification

The proposed method was verified by application to aspirin samples in pharmaceutical drugs. Measurements for the mass of aspirin in three samples from different pharmaceutical brands were performed using the proposed grayscale technique for both filter paper and 96-microwell plate method and results were compared with that of spectrophotometry and that of drug label as presented in Table 4. Relative error was found to be less than 3.6% for filter paper spot tests which was better in comparison to the reference method (RE <4.7%). The results also did not differ much from the reference method in the case of 96-microwell plate spot tests (RE <5.2%), which proved that both of the methods could be accurate for smartphone-camera-based analysis by employing the proposed grayscale quantification technique.

Table 4: Determination of aspirin in pharmaceutical formulations.

Sample	Drug label	Reference method		Filter paper spot tests		96-Microwell plate method	
	(mg)	(mg)	RE (%)	(mg)	RE (%)	(mg)	RE (%)
Sample 1	300	298.81	0.4	297.61	0.8	286.02	4.7
Sample 2	300	289.22	3.6	290.65	3.1	284.43	5.2
Sample 3	300	285.77	4.7	289.16	3.6	290.41	3.2

3.5. Comparison of the Grayscale Method with Other Models

The proposed grayscale model was compared with RGB and HSL models using smartphone camera-based analysis for aspirin. RGB model for the analysis of aspirin is based on the absorbance of green color that reflects violet-blue color in the visible spectrum. Therefore, the green component was used for the regression analysis of aspirin spots. It was found that filter paper spot tests posed an advantage over a 96-microwell plate and the linearity was found to be good in the case of all three color models. The correlation coefficient was found to be 0.954 in the case of the RGB model which was better than the reported value (R^2 <0.7) in literature when using smartphones (37). All measurements were performed in Adobe Photoshop using the eyedropper tool. R^2 of 0.958 was observed for the HSL model using the saturation component, while the proposed grayscale model gave the most precise results with a correlation coefficient of 0.996. Figure 8 shows the calibration of aspirin spot tests using RGB, HSL, and grayscale models.
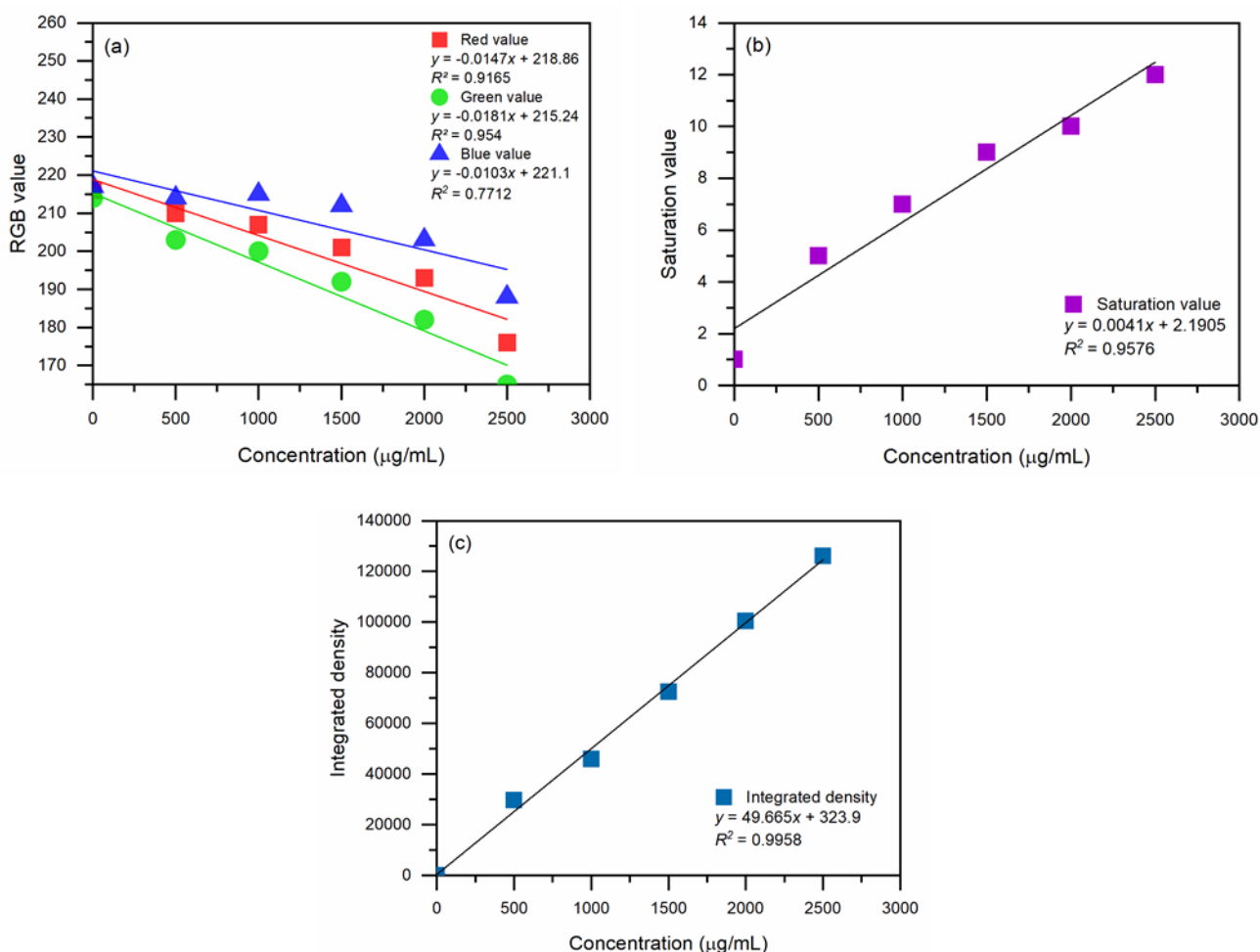
Figure 8: Aspirin calibration by filter paper spot tests using (a) RGB model, (b) HSL model and (c) proposed grayscale model.

The RGB, HSL, and grayscale models were also applied to the 96-microwell plate method using smartphone capture. RGB model gave results similar to that reported in the literature (R^2 =0.792) while better results were observed in the case of the HSL model (R^2 =0.97). The grayscale model gave the best results with R^2 of 0.997. The calibration of the 96-microwell plate method using three color models is shown in Figure 9. Table 5 compares the correlation coefficient values of RGB, HSL, and the proposed grayscale model for both filter paper and 96-microwell plate method.

Table 5: Comparison of RGB, HSL and grayscale models using aspirin spot tests and 96-microwell plate method.

Colour model	Correlation coefficient (R^2)	
	Filter paper spot tests	96-Microwell plate method
RGB	0.954	0.792
HSL	0.958	0.97
Grayscale	0.996	0.997
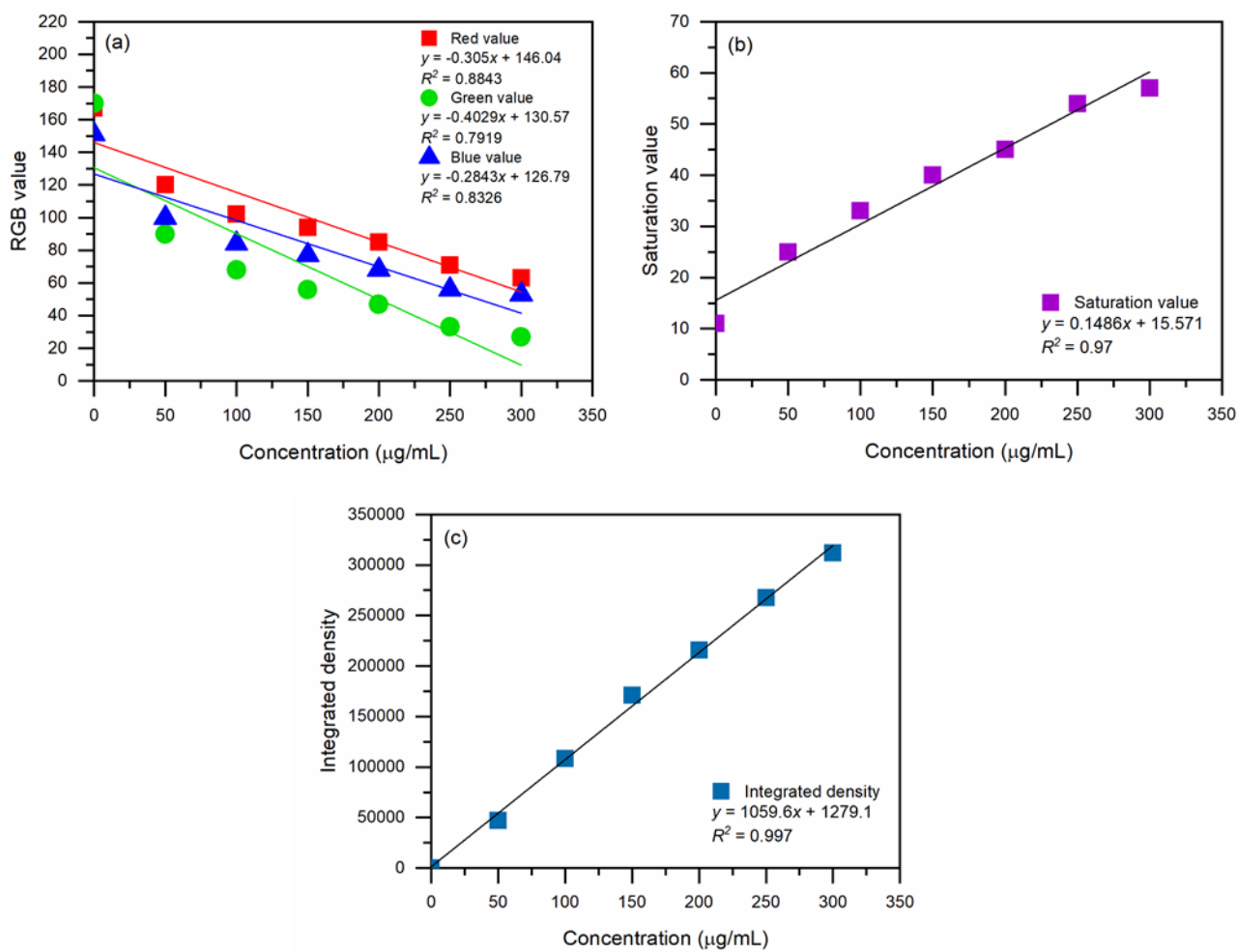
Figure 9: Aspirin calibration by 96-microwell plate method using (a) RGB model, (b) HSL model and (c) proposed grayscale model.

4. CONCLUSION

Smartphone camera-based image scanning densitometry was successfully employed for the quantification of aspirin using filter paper spot tests and the 96-microwell plate method. Both filter paper spot tests and the 96-microwell plate method have their advantages being low cost, simple, portable, and accurate. The present work provided an improved methodology for the analysis of aspirin based on grayscale quantification in Adobe Photoshop. The precision of the proposed technique was determined by comparison of spot tests and 96-microwell plate method with UV-visible spectrophotometry, resulting in a correlation coefficient (R^2) greater than 0.996. Three commercial samples of aspirin were assayed and compared with that of the drug label with relative errors lower than 5.2% for the 96-microwell plate method and less than 3.6% for a spot test method. Regression analysis of the proposed grayscale method was also compared with that of RGB and HSL models used in the literature. The grayscale method accounted for better results for both filter paper aspirin spot tests and the 96-microwell plate method and can be recommended for future research in pharmaceutical, medical, and other analytical fields.

5. CONFLICT OF INTEREST

The authors declare that there are no conflicts of interest to disclose.

6. ACKNOWLEDGMENTS

7. REFERENCES

1. Warner TD, Mitchell JA. Cyclooxygenase-3 (COX-3): Filling in the gaps toward a COX continuum? Proc Natl Acad Sci [Internet]. 2002 Oct 15;99(21):13371–3. Available from: <URL>.

2. The Top 300 of 2020 [Internet]. [cited 2023 Mar 12]. Available from: <URL>.

3. Desborough MJR, Keeling DM. The aspirin story – from willow to wonder drug. Br J Haematol [Internet]. 2017 Jun 20;177(5):674–83. Available from: <URL>.

4. Ugurlucan M, M. Caglar I, N. Turhan Caglar F, Ziyade S, Karatepe O, Yildiz Y, et al. Aspirin: from a Historical Perspective. Recent Pat Cardiovasc Drug Discov [Internet]. 2012 Apr 1;7(1):71–6. Available from: <URL>.

5. Yeomans ND. Aspirin: Old drug, new uses and challenges*. J Gastroenterol Hepatol [Internet]. 2011 Mar 17;26(3):426–31. Available from: <URL>.

6. Himmel A. Aspirin toxicity [Internet]. [cited 2023 Mar 12]. Available from: <URL>.

7. Morgan G. The Established and Emerging Uses of Aspirin. Basic Clin Pharmacol Toxicol [Internet]. 2006 Oct 13;99(4):283–6. Available from: <URL>.

8. Thisted B, Krantz T, Ström J, Sørensen MB. Acute salicylate self-poisoning in 177 consecutive patients treated in ICU. Acta Anaesthesiol Scand [Internet]. 1987 May 30;31(4):312–6. Available from: <URL>.

9. Braun RD. The titrimetric determination of acetylsalicylic acid in analgesic tablets. J Chem Educ [Internet]. 1985 Sep 1;62(9):811. Available from: <URL>.

10. Paseková H, Sales MG, Montenegro MC, Araújo AN, Polášek M. Potentiometric determination of acetylsalicylic acid by sequential injection analysis (SIA) using a tubular salicylate-selective electrode. J Pharm Biomed Anal [Internet]. 2001 Mar 1;24(5–6):1027–36. Available from: <URL>.

11. Bisht P, Kumar M, Saxena P, Kumar Gangwar A. To develop validated method of salicylic acid by UV-visible spectroscopy as impurity in pharmaceutical dosage form. World J Pharm Res [Internet]. 2020;9(7):1981–9. Available from: <URL>.

12. Fernandes JCB, Garcia CAB, Grandin LA, Oliveira Neto G de, Godinho OES. Determination of acetylsalicylic acid in tablets with salicylate ion selective electrode in a Batch Injection Analysis system. J Braz Chem Soc [Internet]. 1998 May;9(3):249–51. Available from: <URL>.

13. Saeed AM, Hamzah MJ, Ahmed NQ. Quantitative assay of aspirin and (salicylic acid and heavy metals as impuraties) in iraqi's market aspirin tablets using different analytical methods. Int J Appl Pharm [Internet]. 2018 Sep 8;10(5):167–72. Available from: <URL>.

14. Krokos A, Tsakelidou E, Michopoulou E, Raikos N, Theodoridis G, Gika H. NSAIDs Determination in Human Serum by GC-MS. Separations [Internet]. 2018 Jul 16;5(3):37. Available from: <URL>.

15. Anthony O, Moh'd HS, Mataka MA, Juma A, Odalo OJ, Peter OC. A Comparative Analysis of Aspirin from Various Analgesic Formulations Using Titrimetry, Spectroscopic and Hyphenated Chromatographic Techniques. J Pharm Anal Insights [Internet]. 2018;2(1):1–5. Available from: <URL>.

16. İbrahim B. Spectrophotometric determination of aspirin in different tablet samples using oxidation-reduction reaction with potassium permanganate. J Univ Raparin. 2016;3(6):123–8.

17. Abdulkadir MQ, Al-Mudhafar MMJ, Mohammed AA, Alzahawie SK. Colorimetric assay of aspirin using modified method. J Al-Nahrain Univ Sci [Internet]. 2009 Sep 1;12(3):1–7. Available from: <URL>.

18. Kohl SK, Landmark JD, Stickle DF. Demonstration of Absorbance Using Digital Color Image Analysis and Colored Solutions. J Chem Educ [Internet]. 2006 Apr 1;83(4):644. Available from: <URL>.

19. Volmer DA, Curbani L, Parker TA, Garcia J, Schultz LD, Borges EM. Determination of Titratable Acidity in Wine Using Potentiometric, Conductometric, and Photometric Methods. J Chem Educ [Internet]. 2017 Sep 12;94(9):1296–302. Available from: <URL>.

20. Soldat DJ, Barak P, Lepore BJ. Microscale Colorimetric Analysis Using a Desktop Scanner and Automated Digital Image Analysis. J Chem Educ [Internet]. 2009 May 1;86(5):617. Available from: <URL>.

21. Chang B-Y. Smartphone-based Chemistry Instrumentation: Digitization of Colorimetric Measurements. Bull Korean Chem Soc [Internet]. 2012 Feb 20;33(2):549–52. Available from: <URL>.

22. Anwar J, Waheed-uz-Zaman, Shafique MU, Salman M. Computational Quantification of Spot Tests by Image Scanning-A New Analytical Technique for Micro Samples. Anal Lett [Internet]. 2010 Jan 12;43(2):367–71. Available from: <URL>.

23. Salman M, Athar M, Waheed-uz-Zaman, Shafique U, Anwar J, Rehman R, et al. Micro-determination of arsenic in aqueous samples by image scanning and computational quantification. Anal Methods [Internet]. 2012 Jan 5;4(1):242–6. Available from: <URL>.

24. Shafique U, Anwar J, Salman M, Waheed-uz-Zaman, Dar A, Rehman R, et al. Novel methods to determine sulfide in aqueous samples by quantification of lead sulfide spots. J Sulfur Chem [Internet]. 2011 Apr;32(2):151–7. Available from: <URL>.

25. Dar A, Shafique U, Anwar J, Waheed-uz-Zaman, Naseer A. A simple spot test quantification method to determine formaldehyde in aqueous samples. J Saudi Chem Soc [Internet]. 2016 Sep 1;20:S352–6. Available from: <URL>.

26. Celikbas E, Ceylan AE, Timur S. Paper-based colorimetric spot test utilizing smartphone sensing for detection of biomarkers. Talanta [Internet]. 2020 Feb 1;208:120446. Available from: <URL>.

27. Soares S, Rocha FRP. Spot test for determination of uric acid in saliva by smartphone-based digital images: A new proposal for detecting kidney dysfunctions. Microchem J [Internet]. 2021 Mar 1;162:105862. Available from: <URL>.

28. de Oliveira Krambeck Franco M, Dias Castro GA,

Vilanculo C, Fernandes SA, Suarez WT. A color reaction for the determination of Cu2+ in distilled beverages employing digital imaging. Anal Chim Acta [Internet]. 2021 Sep 8;1177:338844. Available from: <URL>.

29. Šafranko S, Živković P, Stanković A, Medvidović-Kosanović M, Széchenyi A, Jokić S. Designing ColorX, Image Processing Software for Colorimetric Determination of Concentration, To Facilitate Students' Investigation of Analytical Chemistry Concepts Using Digital Imaging Technology. J Chem Educ [Internet]. 2019 Sep 10;96(9):1928–37. Available from: <URL>.

30. Li F, Wang X, Liu J, Hu Y, He J. Double-layered microfluidic paper-based device with multiple colorimetric indicators for multiplexed detection of biomolecules. Sensors Actuators B Chem [Internet]. 2019 Jun 1;288:266–73. Available from: <URL>.

31. Firdaus ML, Aprian A, Meileza N, Hitsmi M, Elvia R, Rahmidar L, et al. Smartphone Coupled with a Paper-Based Colorimetric Device for Sensitive and Portable Mercury Ion Sensing. Chemosens 2019, Vol 7, Page 25 [Internet]. 2019 May 17 [cited 2023 Nov 2];7(2):25. Available from: <URL>.

32. Mermer K, Paluch J, Kozak J. Smartphone-based digital image colorimetry for the determination of vancomycin in drugs. Monatshefte für Chemie - Chem Mon [Internet]. 2022 Sep 10;153(9):801–9.

Available from: <URL>.

33. de Santana PC, Lourenço FR. A smartphone-based bioassay for determining relative potency estimated from sigmoidal-response curves and respective measurement uncertainty. Microchem J [Internet]. 2020 May 1;154:104626. Available from: <URL>.

34. Saviano AM, Lourenço FR. Using image analysis to determine gentamicin potency by agar diffusion microbiological assay and its measurement uncertainty. Measurement [Internet]. 2019 Nov 1;146:315–21. Available from: <URL>.

35. Colzani H, T. Scolaro AM, L. Neves Gelinski JM, Marcel Borges E. Manganese Determination in Battery Using a Flatbed Scanner. Rev Virtual Química [Internet]. 2017;9(4):1672–85. Available from: <URL>.

36. Semary NA, Hadhoud MM, Abbas AM. An Effective Compression Technique for HSL Color Model. In: The 2011 World Congress on Computer Science and Information Technology, WCSIT'11 [Internet]. Cairo, Egypt; 2011. Available from: <URL>.

37. da Silva RS, Borges EM. Quantitative Analysis Using a Flatbed Scanner: Aspirin Quantification in Pharmaceutical Tablets. J Chem Educ [Internet]. 2019 Jul 9;96(7):1519–26. Available from: <URL>.

Enhanced Heavy Metal Removal from Wastewater Produced by Chemical Analysis Laboratory Using Calcium Oxide Precipitation: pH Improvement and Characterization of Precipitated Phases

Intissar Loughlaimi[1*] 🆔 , Zineelabidine Bakher[1] 🆔 , Abdeljalil Zouhri[1] 🆔

[1]HASSAN 1st University, Faculty of Sciences and Techniques, Department of Applied Chemistry and Environment, Settat, Casablanca road, km 3.5, P.C 539, Morocco.

Abstract: This article presents research results on the precipitation of heavy metals: Aluminum (Al), arsenic (As), cadmium (Cd), zinc (Zn), iron (Fe), chromium (Cr), copper (Cu), nickel (Ni), vanadium (V), and molybdenum (Mo) from wastewater generated in mining chemical analysis laboratory. Calcium oxide was used as the precipitating agent. The efficiency of heavy metal removal was achieved by increasing the dosage of precipitating reagent (8-28 g/L). Efficiencies greater than 90% are achieved. The efficiency of chemical precipitation depends on the pH of the process. Over a wide pH range from 6-11, the removal efficiency of zinc, iron, cadmium, and arsenic were approximately 99.9%. The optimum pH range for the removal of most elements was found to be between 8 and 11, where the removal efficiency of heavy metal ions reached up to 99%. Furthermore, X-ray diffraction results indicated that the metals in the wastewater precipitated in various forms as mentioned in Table 7, and not just as hydroxides, due to the presence of different ions in the solution.

1. INTRODUCTION

A reliable supply of high-quality water is essential for human well-being, social and economic progress, and the sustainability of the global ecosystem (1). As water resources become scarcer, the need to provide water to various parts of the world, including Morocco, is a pressing issue and may become even more of a concern in the future (2).

Due to the fundamental importance of water for the sustenance of all living beings, the phenomenon of rapid urbanization and development has resulted in a substantial increase in the demand for this vital resource. Moreover, water plays a crucial role in a diverse range of residential and industrial processes, including but not limited to petroleum refineries, agricultural practices, medicinal and pharmaceutical procedures. These activities introduce many toxic pollutants and waste substances into water (1). These contaminants fall into three main groups:

organic, inorganic, and biological particles. Industrial and urban activities that produce toxic heavy metals such as cadmium, copper, zinc, nickel, arsenic, chromium, and mercury are classified as hazardous and non-biodegradable (3-4). In this study we focus on inorganic groups containing heavy metal ions. Additionally, heavy metals are a common health issue. As they are teratogenic, carcinogenic and causes detrimental health problems (5). Even trace levels of heavy metals contamination can lead to bioaccumulation through the food chain. High levels of heavy metals are produced in the body when a person drinks water or eats food contaminated with heavy metals. For example, lead affects central nervous system disorders by altering the characteristics of early human physiological symptoms such as allergies, renal disorders, hepatic disorders, infertility, dermatitis, abdominal pain, gingivitis, migraines, and insomnia (6-7).

A number of special processes have been developed to remove metals from wastewater (8). The various treatment techniques include: chemical precipitation (9-10), coagulation/flocculation (11), adsorption (12), ion exchange (13), solvent extraction (14), electrochemical operation (15), biological operations (16-17), ultrafiltration (18) and membrane processes (19). Each technique has its own related advantages and drawbacks.

Among the various methods available, one viable option is to employ simple precipitation of metals in the form of insoluble hydroxides or carbonates. Chemical precipitation, extensively utilized in industrial applications, is particularly favored due to its inherent process control simplicity (3) and lower concentrations of all metals. The success of this method depends on the solubility of the precipitated metal compounds. If a metal has the ability to form an insoluble compound, it is possible to remove that compound through a clarification and filtration process. Although the number of precipitation methods available is limited, hydroxide and sulfide are predominantly used, with hydroxide precipitation being the most commonly used. The process involves a simple step: raising the pH of the effluent by adding lime (CaO) as a precipitant. This converts heavy metals to their corresponding hydroxides and immobilizes them (1).

Metal precipitation is the process of converting metal ions dissolved in water into solid metal compounds. This precipitation is influenced by two important factors: Concentration of metals and pH of water. Heavy metals in wastewater are typically present in relatively low concentrations ranging from 1 to 100 mg/L. These concentrations are considered diluted. Also, the pH of water containing these heavy metals is usually neutral or slightly acidic (pH<7.0). When metals are introduced into the treatment procedure, they exist in a dissolved state within the water, maintaining stability and being unable to solidify. The objective of employing hydroxide precipitation for metals' treatment is to manipulate the water's pH in such a way that the metals can undergo a transformation, forming precipitates that are insoluble. The concentration of hydroxide ions in the water is directly proportional to the pH level, therefore, a higher pH signifies elevated hydroxide concentrations. However, when lime is added to water containing dissolved metals, the metals react with hydroxide ions to form metal hydroxide solids. Once the metals have precipitated and formed solids, they can be easily removed, and the water, now depleted of metals, can be drained or reused (20).

In this article, calcium oxide was used to precipitate heavy metals present in wastewater: aluminum (Al), arsenic (As), cadmium (Cd), zinc (Zn), iron (Fe), chromium (Cr), copper (Cu), nickel (Ni), vanadium (V) and molybdenum (Mo). The objective of this study was to attend the maximum removal efficiency of all heavy metal ions from solution. In addition, the agglomeration of the precipitates during the treatment was investigated and characterized by inductively coupled plasma ICP to identify the different phases of precipitate.

2. EXPERIMENTAL STUDIES

2.1. Materials and Reagents
The wastewater of mining chemical analysis laboratory, which contains heavy metals, was used to be treated with chemical precipitation. The precipitating agent used in this treatment is calcium oxide (CaO) with different masses (8 g/L up to 28 g/L).

Table 1: Descriptive of products utilized.

Product	Descriptive	Provider
CaO	Purity: 99.9%	Sigma Aldrich[a]
Distilled water	Conductivity: 21.4 µS/cm pH: 7.610	

[a]: Analyzed by XRD

2.2. Measuring Instrumentations and Equipment
In the context of wastewater treatment, determining the optimal dosage of a precipitating agent can be a challenging task that necessitates the use of various analytical techniques. In this study, the GFL 3040 jar test from Gesells chaft Fuer Labortec Overhead Shakers was utilized to assess the effectiveness of different doses of a precipitating agent in treating wastewater.

To evaluate the changes in the pH of the solution during the treatment process, a Mettler Toledo pH meter was employed. This tool helped in understanding the impact of the dosage on the pH levels, as the addition of a precipitator can alter the pH of the solution.

The concentration of metal ions in the wastewater was analyzed using Inductively coupled plasma (ICP), a technique that uses plasma to ionize samples for analysis. This method provides highly accurate and precise measurements of trace elements, such as metals, in complex samples like wastewater.

In addition to Inductively coupled plasma ICP analysis, X-ray diffraction (XRD) examination was utilized to identify the important chemical compounds present in the sludge samples. This technique utilizes the diffraction pattern of X-ray to identify the crystal structure and composition of the sample, providing valuable information on the chemical compounds present in the wastewater. X-ray diffraction analysis was performed on all solids to characterize the solid phases present in various saturated solutions. This analysis was performed on

the BRUKER D2 phase shifter instrument with a LYNXEYE detector using a Cu-Ka wavelength of 1.541874 Å. Each stable solid was analyzed over a temperature range of 10 to 80 °C for 20 minutes.

In order to study the effects of precipitant dosages and initial pH on the removal of heavy metals, a series of polyethylene graduated flasks (500 mL) containing wastewater solution were prepared. Different masses of calcium oxide (CaO) (8 to 28 g/L) were added into each flask at a temperature of 24 °C. The flasks were then subjected to stirring at a

speed of 200 rpm for 15 minutes to allow for decantation, after which the mixture was filtered through a 0.45 µm membrane to obtain two phases; liquid and solid.

Subsequently, the final pH of the liquid was measured, and the remaining metal in the liquid phase was measured using ICP. In addition, the solid phase was analyzed using XRD. Through this process, a comprehensive understanding of the impact of precipitant dosages and initial pH on heavy metal removal can be gained (see Figure 1).
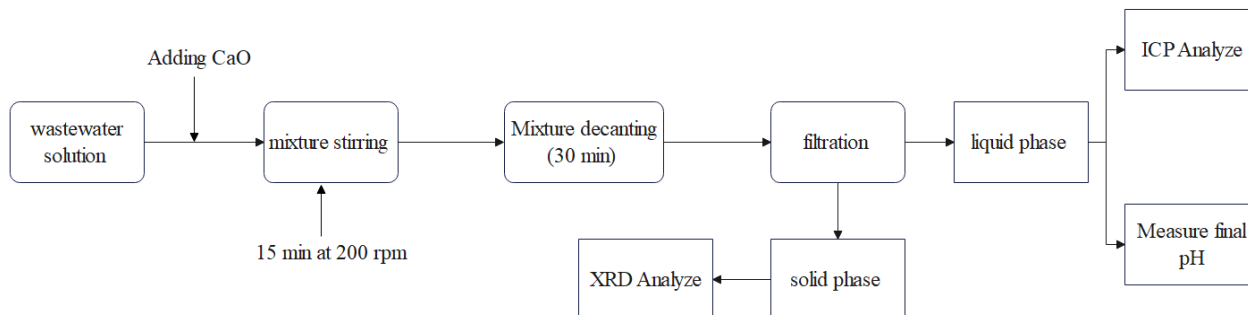
Figure 1: Representative schema of the process.

To calculate metal removal efficiency, we used the following equation:

$$R(\%) = \frac{C_i - C_f}{C_i} \times 100$$

R: Metal removal efficiency
C_i: Initial concentration of the metal
C_f: Final concentration of the metal

Table 2: Characterization of wastewater used in this study.

Parameters	Unites	Values for wastewater
pH	-	0.313
Conductivity	mS/cm	164.8
Al	%	0.992
Cu	ppm	50.59
Cd	ppm	23.76
Cr	ppm	229.8
As	ppm	10.96
Fe	%	0.484
Mo	ppm	8.666
Ni	ppm	50.96
V	ppm	203.2
Zn	ppm	426.4

Table 3: Operating conditions for ICP.

ICP	
Rf power (w)	1300.0
Plasma Ar flow (L/min)	12.0
Auxiliary Ar flow (L/min)	0.2
Nebuliser Ar flow (L/min)	0.7
Delay time (s)	40.0
Measurement mode:	
Axial	All
Radial	Iron, Aluminum, CaO

3. RESULTS AND DISCUSSION

The pH is considered an important operational factor that governs the interactions of a surface-active substance and metal ions in flotation processes because the pH affects the stability and precipitation behavior of heavy-metal ions in the solution.

Tables 4 and 5 present the outcomes of using various dosages (8, 12, 16, 20, 24, and 28 g/L) of calcium oxide to assess the most effective dosage for wastewater purification. The parameters analyzed include the final pH, residual metal concentration, and metal removal efficiency. Increased amounts of calcium oxide ranging from 8 to 28 g/L were examined in order to determine the optimal dosage for achieving effective wastewater purification.

As shown in Tables 3 and 4, the removal efficiency of zinc, iron, cadmium, and arsenic was approximately 100% over a wide pH range from 6-11, and for a dose lower than 12 g/L of lime. These results are similar to those stated in the references (15-21).

Each metal precipitates over a narrow pH range, above which the metal redissolves, as is the case for molybdenum. For pH 9.394 a concentration of 6.049 can achieved. For aluminum Al the concentration decreased to 0.023% at a pH of 6.93 which is close to the reported value obtained by Wei X Viadero R Buzby K (21), and for chromium the removal was 100% at a pH between 6.93 and 9.394. These results are in line with Dr C, Ramakrishnaiah P (22). It can also be seen that the removal of copper Co is 94.57% for pH= 6.93. The remaining for nickel Ni and vanadium V decreased from 50.96 ppm and 203.2 ppm to 8.647 ppm (pH= 8.614) and 2.979 ppm (pH= 11.345) respectively.

Table 4: Remaining concentrations of metals after treatment by chemical precipitation.

Dose of lime (g/L)		0.000	8.000	12.00	16.00	20.00	24.00	28.00
Final pH		0.637	6.930	7.974	8.614	9.394	11.34	11.75
Remaining concentration	Al (%)	0.992	0.023	0.024	0.024	0.023	0.021	0.023
	As	10.96	0.084	0.000	0.000	0.000	0.000	0.000
	Cd	23.767	0.316	0.000	0.000	0.011	0.000	0.000
	Cr	229.8	0.000	0.000	2.387	0.000	7.284	4.516
	Cu	50.59	2.749	4.269	6.426	8.562	4.877	3.251
	Fe	0.484	0.000	0.000	0.000	0.000	0.000	0.000
	Mo	8.666	29.85	22.32	28.01	6.049	9.041	172.3
	Ni	50.96	67.96	24.2	8.647	9.400	10.70	11.32
	V	203.2	63.20	59.45	14.4	5.745	2.979	6.148
	Zn	426.4	0.000	0.000	0.000	0.000	0.000	0.000

Table 5: Removal efficiency of metals.

| Element	Dose of lime	Final pH	Removal (%)
Al	8.000	6.930	97.68
	12.00	7.974	97.58
	16.00	8.614	97.58
	20.00	9.394	97.68
	24.00	11.34	97.88
	28.00	11.75	97.58
As	8.000	6.930	99.23
	12.00	7.974	100.0
	16.00	8.614	100.0
	20.00	9.394	100.0
	24.00	11.34	100.0
	28.00	11.75	100.0
Cd	8.000	6.93	98.67
	12.00	7.974	100.0
	16.00	8.614	100.0
	20.00	9.394	99.95
	24.00	11.34	100.0
	28.00	11.75	100.0
Cu	8.000	6.930	94.57
	12.00	7.974	91.56
	16.00	8.614	87.30
	20.00	9.394	83.07
	24.00	11.34	90.30
	28.00	11.75	93.57
Fe	8.000	6.930	100.0
	12.00	7.974	100.0
	16.00	8.614	100.0
	20.00	9.394	100.0
	24.00	11.34	100.0
	28.00	11.75	100.0
Mo	8.000	6.930	NC
	12.00	7.974	NC
	16.00	8.614	NC
	20.00	9.394	30.20
	24.00	11.34	NC
	28.00	11.75	NC
Ni	8.000	6.930	NC
	12.00	7.974	52.51
	16.00	8.614	83.03
	20.00	9.394	81.55
	24.00	11.34	79.00
	28.00	11.75	77.79
V	8.000	6.930	68.90
	12.00	7.974	70.74
	16.00	8.614	92.91
	20.00	9.394	97.17
	24.00	11.34	98.53
	28.00	11.75	96.97
Zn	8.000	6.930	100.0
	12.00	7.974	100.0
	16.00	8.614	100.0
	20.00	9.394	100.0
	24.00	11.34	100.0
	28.00	11.75	100.0

(NC: Not calculated)

3.1. Effect of pH

As shown in Figures 2 and 3 the effect of pH value on the removal of heavy metals, when the pH is increased from 2 to 11, the remaining concentration of metal ions decreases and the removal efficiency increases. The pH of the solution is an important factor that has an effect on precipitation. When the pH is low, the hydroxide metals will not form due to the large amount of H^+, which decreases the capacity of precipitation. As the pH increases, the $[OH^-]$ concentration increases to form an insoluble ion, which reduces the remaining concentration of heavy metals in solution.
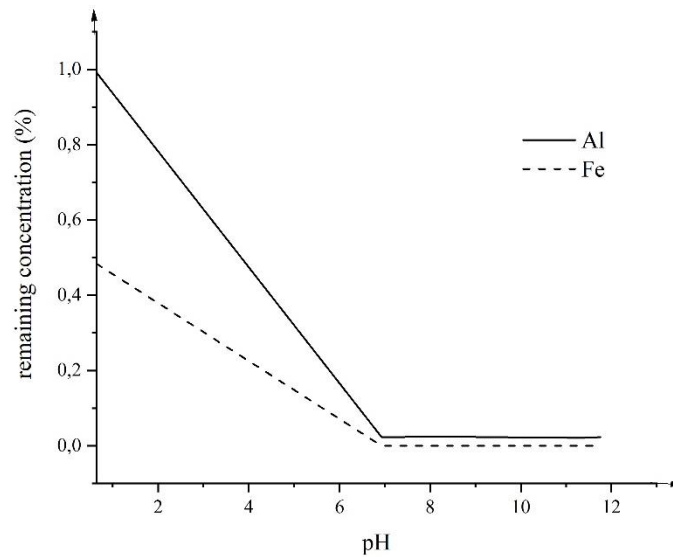
**Figure 2:** Effect of pH on removal of Al and Fe.
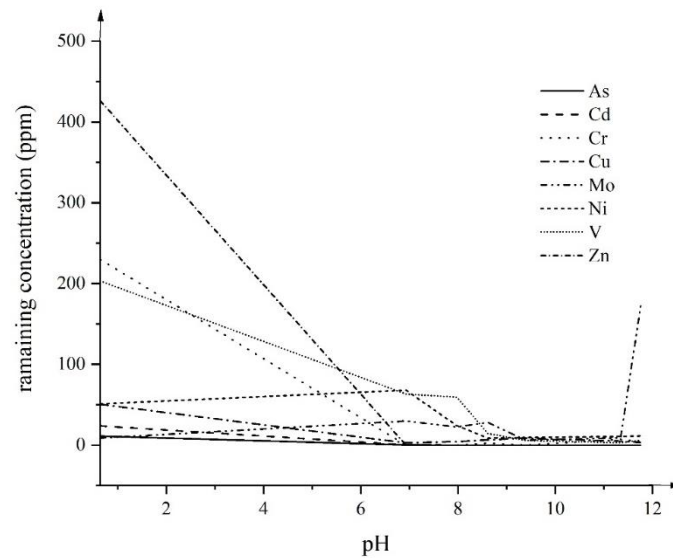
Figure 3: Effect of pH on removal of other metals.

3.2. Effect of Lime Dosage on pH

As shown in Figure 4, the pH value of solution can be increased by adding more calcium oxide to it. This increase in pH value results from the release of hydroxide ions (OH^-) in solution, which combines with the metal ions present in the solution to form insoluble hydroxides. The formation of these insoluble hydroxides precipitates metal ions, making them easier to remove from the solution.

It is important to note that the addition of CaO to the solution must be carefully controlled to avoid excessively increasing the pH value. An excessively high pH value can lead to the formation of unwanted precipitates, making it more difficult to remove the targeted metal ions from the solution.

In conclusion, the addition of CaO to the solution can increase the pH value, which is an important factor in the chemical precipitation method for removing heavy metal ions.
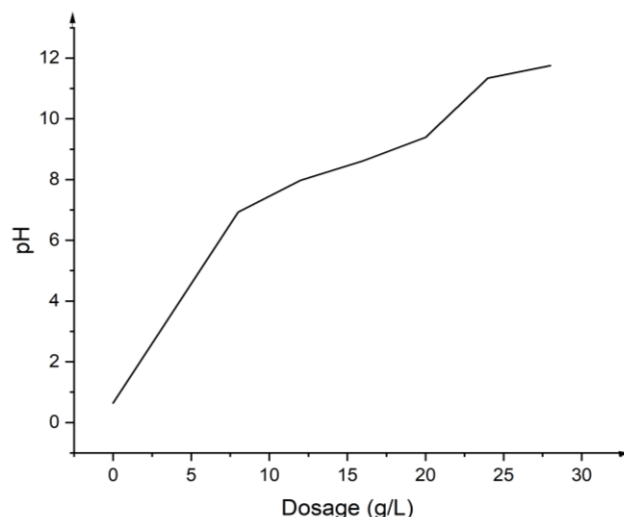
Figure 4: Effect of dosage calcium oxide on pH solution.

3.3. Process Description

Precipitation, as a chemical unit process, is used to remove unwanted soluble metal ions and specific anions from water or wastewater by converting them into insoluble forms. It is a widely used processing technology to remove heavy metals, phosphorus, and hardness. This processing method involves altering the ion balance to form precipitates that are insoluble and can be easily separated. The chemical precipitation process is typically followed by a solid's removal step, which may include coagulation and filtration to remove the formed precipitates. In certain cases, a chemical reduction step may precede the precipitation process to modify the properties of the metal ions, enabling their precipitation [23].

The main chemical reactions during the precipitation process and the conversion of the compound in the precipitate are as follows [24]:

- The process begins with the hydrolysis of lime, followed by its partial dissolution, resulting in a pH increment due to the formation of hydroxyl ions (reactions 1 and 2).
- Then, the hydroxyl ions follow a series of interactions with divalent and trivalent cations present (reactions 3 and 4).
- If any free sulfate exists, may involve simultaneous precipitation of gypsum (reaction 5), as shown in Table 6.

Table 6: Reactions of process.

Number of reaction	Reaction	Free Energy	Reference
1	$Ca0_{(s)} + H_2O \rightarrow Ca(OH)_{2\,(s)}$	$\Delta G°_{25°C} = -13.815\,Kcal$	-
2	$Ca(OH)_{2(s)} \rightarrow Ca^{2+}_{(aq)} + 2\,OH^-_{(aq)}$	$\Delta G° = -6.438\,Kcal$	[24]
3	$Me^{2+}_{(aq)} + 2OH^-_{(aq)} \rightarrow Me(OH)_{2(s)}$		
4	$Me^{3+}_{(aq)} + 3OH^-_{(aq)} \rightarrow Me(OH)_{3(s)}$		
5	$Ca^{2+}_{(aq)} + SO^{'2-}_{4(aq)} \rightarrow CaSO_{4(s)}$	$Ksp_{25°C} = 7.97 \times 10^4$	[24]
		$\Delta G°_{25°C} = -10.463\,Kcal$	-

(-) calculated in this study

3.4. Sludge Analyzing

The results presented in Figure 5 highlight the presence of additional phases in the system. This observation suggests that the precipitation mechanism of hydroxide metal has not been fully identified. The lack of identification of the hydroxide metal precipitation mechanism may be attributed to the presence of different metals in the solution. These metals may have an influence on the precipitation mechanism by altering the chemical and physical properties of the system. Moreover, the presence of other phases in the system may also suggest that there are complex chemical reactions

occurring in the solution. The mechanisms of these reactions may be influenced by several factors, including the concentration of metal ions and the pH of the solution.

In summary, the results presented in Figure 5 suggest that the precipitation mechanism of heavy metal ions in the industrial wastewater may be influenced by the presence of multiple metals. This finding underscores the importance of considering the presence of multiple metals when investigating the precipitation of heavy metal ions in industrial wastewater. The presence of multiple metals can

have a significant impact on the precipitation mechanism and can potentially result in the formation of additional phases.

Table 7: Elemental analysis references, content of patterns from X-pert highscore.

Visible	Ref. Code	Score	Compound Name	Scale Factor	Chemical Formula
*	00-019-0636	55	Iron Titanium	0.713	$FeTi$
*	01-085-0849	47	Calcium Carbonate	0.195	$CaCO_3$
*	01-073-0257	20	Aluminum Lithium Silicate	0.029	$LiAlSiO_4$
*	01-081-0119	33	Strontium Vanadium Oxide	0.057	$SrVO_{2.93}$
*	01-072-1214	58	Calcium Carbonate	0.484	$CaCO_3$
*	01-085-1989	18	Lithium Chromium Manganese Oxide	0.089	$Li(CrMnO_4)$
*	00-046-1217	61	Copper Nickel Zinc Oxide	0.544	$Cu_{1.02}ZnNi_{3.27}O_{5.29}$
*	01-075-0272	53	Nickel Zinc Oxide	0.471	Ni_7Zn_3O
*	00-043-1159	25	Aluminum Titanium Vanadium	0.103	$Al_3V_{0.33}Ti_{0.666}$
*	00-036-0811	21	Beryllium Arsenide	0.073	$BeAs_2$
*	00-029-0913	13	Molybdenum Boron Carbide	0.149	Mo_2BC
*	00-033-1442	13	Vanadium Oxide Phosphate	0.088	$V(PO_3)_3$
*	01-075-0272	58	Nickel Zinc Oxide	0.651	Ni_7Zn_3O
*	00-031-0871	25	Molybdenum Carbide	0.105	Mo_2C
*	00-036-0811	19	Beryllium Arsenide	0.123	$BeAs_2$
*	00-029-1380	10	Vanadium Oxide Hydroxide	0.185	$V_2O_2(OH)_3$
*	01-072-0132	27	Cadmium Thorium	0.065	Cd_2Th
*	01-077-2308	31	Lithium Zinc Chromium Oxide	0.578	$LiZn_2CrO_4$
*	00-034-1269	20	Potassium Arsenate	0.364	$K_4As_2O_7$
*	00-030-0203	8	Cadmium Arsenide	0.179	$Cd As$
*	00-036-0811	20	Beryllium Arsenide	0.064	$Be As_2$
*	01-075-0272	59	Nickel Zinc Oxide	0.474	Ni_7Zn_3O
*	00-048-1710	0	Aluminum Arsenide	0.218	$AlAs$
*	00-041-0406	13	Cadmium Bismuth Germanium Oxide	0.254	$CdBi_2GeO_6$

4. CONCLUSION

The treatment of industrial wastewater to remove heavy metal ions is a complex process that involves several factors. One of the most critical factors that influence the efficiency of this process is the pH value. Chemical precipitation method is widely used to remove heavy metal ions from industrial wastewater. In this method, a chemical reagent is added to the wastewater to form a precipitate that can be separated from the liquid phase.

In this study, the effect of pH value on the removal of heavy metal ions from industrial wastewater was investigated. The results of this study showed that the removal efficiency of heavy metal ions increases with an increase in pH value. Moreover, the optimum pH range for the removal of most elements was found to be between 8 and 11, where the removal efficiency of heavy metal ions reached up to 99% to 100%.

The pH value can be controlled by adjusting the dosage of the chemical reagent added to the wastewater. Calcium oxide (CaO) is a commonly used chemical reagent that can increase the pH value of wastewater. The results of this study showed that the optimal mass of calcium oxide required for the removal of heavy metal ions was approximately 16 to 24 g/L, which corresponds to a pH value range of 8.614 to 11.345.

It is important to note that the presence of other elements in the wastewater can also affect the pH value of the precipitation for each metal. X-ray diffraction (XRD) was used in this study to determine the form of the precipitate. The results of XRD analysis showed that the presence of other elements in the wastewater can influence the form of the precipitate, which can affect the efficiency of the removal process.

In conclusion, the pH value is an important factor that should be carefully controlled in the chemical precipitation method for the removal of heavy metal ions from industrial wastewater. The optimal pH range for the removal of most elements is between 8 and 11, and the dosage of calcium oxide should be carefully controlled to achieve the optimal pH value. The presence of other elements in the wastewater should also be considered when designing the treatment process.
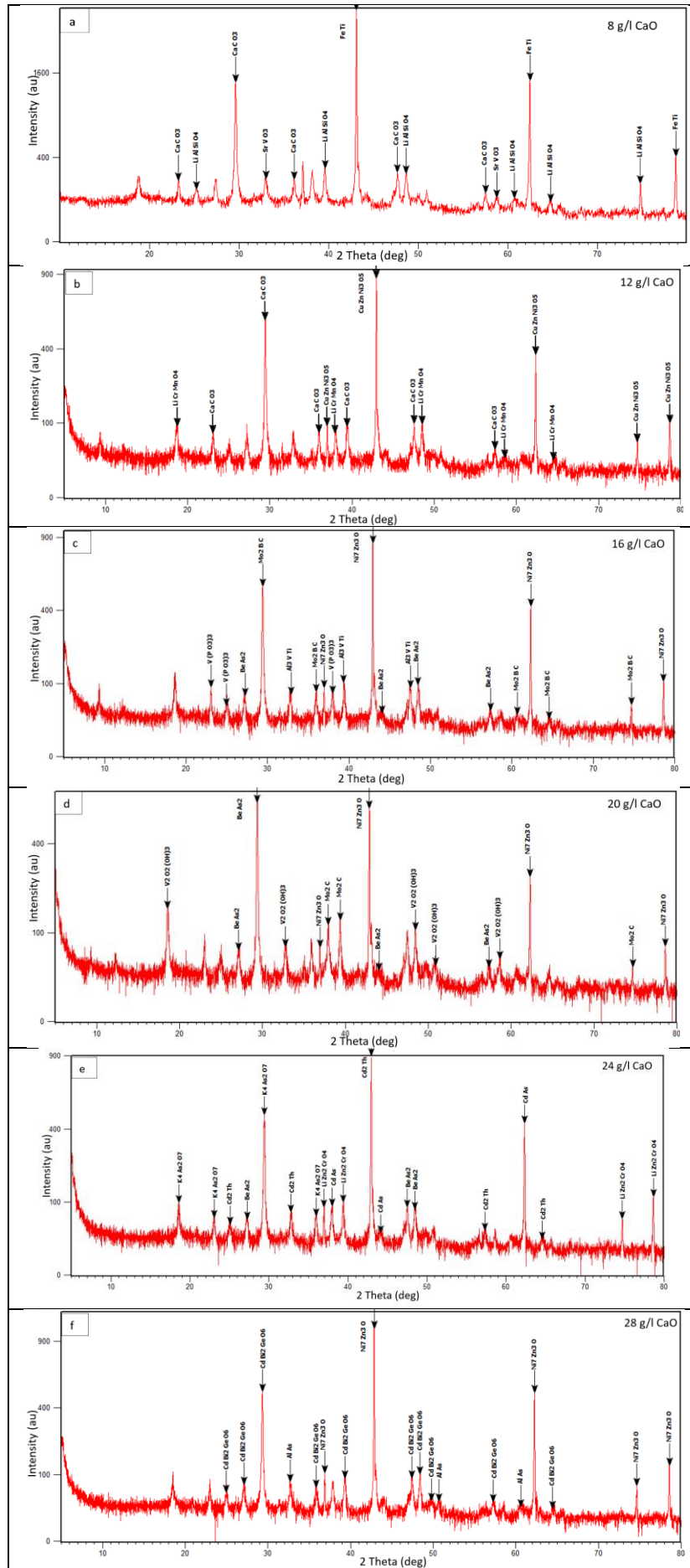
Figure 5: Diffractograms for sludges produced using different dosages of CaO by XRD: a) 8 g/L CaO, b) 12 g/L CaO, c) 16 g/L CaO, d) 20 g/L CaO, e) 24 g/L CaO, f) 28 g/L CaO.

5. REFERENCES

1. Brbooti MM, Abid BA, Al-Shuwaiki NM. Removal of heavy metals using chemicals precipitation. Engineering and Technology Journal [Internet]. 2011;29(3):595–612. Available from: <URL>.

2. Maftouh A, Fatni O El, Hajjaji S El, Jawish MW, Sillanpää M. Comparative review of different adsorption techniques used in heavy metals removal in water. Biointerface Research in Applied Chemistry [Internet]. 2022 Nov 1;13(4):397. Available from: <URL>.

3. Benalia MC, Youcef L, Bouaziz MG, Achour S, Menasra H. Removal of heavy metals from industrial wastewater by chemical precipitation: Mechanisms and sludge characterization. Arabian Journal for Science and Engineering [Internet]. 2022 May 25;47(5):5587–99. Available from: <URL>.

4. Azimi A, Azari A, Rezakazemi M, Ansarpour M. Removal of heavy metals from industrial wastewaters: A review. ChemBioEng Reviews [Internet]. 2017 Feb 1;4(1):37–59. Available from: <URL>.

5. Saleh TA, Mustaqeem M, Khaled M. Water treatment technologies in removing heavy metal ions from wastewater: A review. Environmental Nanotechnology, Monitoring & Management [Internet]. 2022 May 1;17:100617. Available from: <URL>.

6. Paulino AT, Minasse FAS, Guilherme MR, Reis A V., Muniz EC, Nozaki J. Novel adsorbent based on silkworm chrysalides for removal of heavy metals from wastewaters. Journal of Colloid and Interface Science [Internet]. 2006 Sep 15;301(2):479–87. Available from: <URL>.

7. Chen B, Qu R, Shi J, Li D, Wei Z, Yang X, et al. Heavy metal and phosphorus removal from waters by optimizing use of calcium hydroxide and risk assessment. Environ and Pollution [Internet]. 2011 Dec 30;1(1):38–54. Available from: <URL>.

8. Peters RW, Ku Y, Bhattacharyya D. Evaluation of recent treatment techniques for removal of heavy metals from industrial wastewater. AICHE Symposium Series [Internet]. 1985;243(81):165–203. Available from: <URL>.

9. Lin J-Y, Garcia EA, Ballesteros FC, Garcia-Segura S, Lu M-C. A review on chemical precipitation in carbon capture, utilization and storage. Sustainable Environment Research [Internet]. 2022 Oct 22;32(1):45. Available from: <URL>.

10. Pohl A. Removal of heavy metal ions from water and wastewaters by sulfur-containing precipitation agents. Water, Air, & Soil Pollution [Internet]. 2020 Oct 28;231(10):503. Available from: <URL>.

11. Feihrmann ANC, Baptista ATA, Lazari JP, Silva MO, Vieira MF, Vieira AMS. Evaluation of coagulation/ flocculation process for water treatment using defatted cake from moringa oleifera. Chemical Engineering Transactions [Internet]. 2017 Mar 20;57:1543–8. Available from: <URL>.

12. Jiuhui Q. Research progress of novel adsorption processes in water purification: A review. Journal of Environmental Sciences [Internet]. 2008 Jan 1;20(1):1–13. Available from: <URL>.

13. Cho G, Park Y, Hong Y-K, Ha D-H. Ion exchange: An advanced synthetic method for complex nanoparticles. Nano Convergence [Internet]. 2019 Dec 3;6(1):17. Available from: <URL>.

14. Xu L, Yan K, Mao Y, Wu D. Enhancing the dioxygen activation for arsenic removal by Cu^0 nano-shell-decorated nZVI: Synergistic effects and mechanisms. Chemical Engineering Journal [Internet]. 2020 Mar 15;384:123295. Available from: <URL>.

15. Razzak SA, Faruque MO, Alsheikh Z, Alsheikhmohamad L, Alkuroud D, Alfayez A, et al. A comprehensive review on conventional and biological-driven heavy metals removal from industrial wastewater. Environmental Advances [Internet]. 2022 Apr 1;7:100168. Available from: <URL>.

16. Musa MA, Idrus S. Physical and biological treatment technologies of slaughterhouse wastewater: a review. Sustainability [Internet]. 2021 Apr 22;13(9):4656. Available from: <URL>.

17. Oller I, Malato S, Sánchez-Pérez JA. Combination of Advanced Oxidation Processes and biological treatments for wastewater decontamination—A review. Science of the Total Environment [Internet]. 2011 Sep 15;409(20):4141–66. Available from: <URL>.

18. Landaburu-Aguirre J, García V, Pongrácz E, Keiski RL. The removal of zinc from synthetic wastewaters by micellar-enhanced ultrafiltration: statistical design of experiments. Desalination [Internet]. 2009 May 15;240(1–3):262–9. Available from: <URL>.

19. Foong CY, Wirzal MDH, Bustam MA. A review on nanofibers membrane with amino-based ionic liquid for heavy metal removal. Journal of Molecular Liquids [Internet]. 2020 Jan 1;297:111793. Available from: <URL>.

20. Ayres DM, Davis AP, Gietka PM. Removing heavy metals from wastewater (report) [Internet]. 1994. Available from: <URL>.

21. Wei X, Viadero RC, Buzby KM. Recovery of iron and aluminum from acid mine drainage by selective precipitation. Environmental Engineering Sciences [Internet]. 2005 Nov 20;22(6):745–55. Available from: <URL>.

22. Ramakrishnaiah CR, Prathima B. Hexavalent Chromium Removal from Industrial Wastewater by Chemical Precipitation Method. Int J Eng Res Appl [Internet]. 2012;2(2):599–603.

23. Wang LK, Vaccari DA, Li Y, Shammas NK. Chemical precipitation. In: Wang, L.K., Hung, YT., Shammas, N.K. (eds) Physicochemical Treatment Processes [Internet]. Totowa, NJ: Humana Press; 2005. p. 141–97. Available from: <URL>.

24. Balladares E, Jerez O, Parada F, Baltierra L, Hernández C, Araneda E, et al. Neutralization and co-precipitation of heavy metals by lime addition to effluent from acid plant in a copper smelter. Minerals Engineering [Internet]. 2018 Jun 15;122:122–9. Available from: <URL>.

RESEARCH ARTICLE

Degradation of Glycerol to Ethanol Using x/Y Zeolite Catalyst (x=H, Ni, Mo, NiMo) by the Sonication Method

Sumari Sumari[1]* iD **, Siti Khoirun Nisak[1]** iD **, Aman Santoso[1]** iD **, Nazriati Nazriati[1]** iD **,**

Muhammad Roy Asrori[1] iD

[1]Universitas Negeri Malang, Department of Chemistry, Malang, 65145, Indonesia.

Abstract: The performance of the Y Zeolite (YZ) catalyst can be improved by metal impregnation. The purposes of this study were to determine the characteristics and effectenes of the H/YZ, Ni/YZ, Mo/YZ, and NiMo/YZ catalyst, and the effect of the time of sonication on the glycerol degradation reaction to ethanol using the sonication method. The study began with the preparation and activation of YZ using NH_4Cl 1M solution. The activated YZ was then impregnated with nickel metal, molybdenum metal, and their mixtures. Catalyst characterization using XRD, XRF, acidity test, and surface area test. As a result, (a) nickel and molybdenum metals successfully impregnated into YZ, (b) H/YZ, Ni/YZ, Mo/YZ (Predictable), and NiMo/YZ (Predictable) catalysts had a crystalline phase, (c) the highest catalyst acidity value was NiMo/YZ of 1.0810 mmol/gram, (d) the largest catalyst surface area was H/YZ of 110.321 m^2/g. The NiMo/YZ catalyst is more effective than the H/YZ, Ni/YZ, and NiMo/YZ, because it produced the highest %yield ethanol both at 4 hours (4.49%) and 6 hours (27.33%). The time of sonication greatly influenced the percentage of ethanol yield in the glycerol degradation reaction. The longer the time of sonication, the higher % the yield of ethanol produced.

1. INTRODUCTION

The demand for fossil fuels increased economic growth and population in the world. In recent years, fossil fuels not balanced with petroleum reserves. Therefore, the government is currently promoting the use of biodiesel as an alternative fuel to replace fossil fuels (1). Increasing biodiesel production will be a big problem because biodiesel synthesis produces by-products (glycerol) by 10% of the weight of biodiesel (2). As biodiesel production increases, the amount of by-product (glycerol) also increases.

So far, glycerol waste from the biodiesel industry has become a useless material because of simpurities and its complex purification process, so the amount is abundant. On the other hand, The l utilization also resulted in a decrease in the selling price of glycerol from $ 0.33 to $ 0.04 per kilogram (3). The availability of glycerol could be a support fore the

development and transformation of glycerol into a product. Previous study, the degradation of glycerol was carried out under supercritical water conditions at 450 °C, 300 bar, and 30 minutes to produce methanol (4). The degradation of glycerol by hydrothermal proess was carried out at 150 °C, 50 bar, and a 2 hours assisted by microwaves to produce ethanol 7.4% (5). In addition, the degradation of glycerol assisted by ultrasonic waves using a ZAA catalyst wasproduce ethanol of 3.7% (6). Several studies showed that ethanol can be obtained through glycerol degradation, but it still requires high temperature and pressure that is less safe. Therefore, one potential method to the degradation of glycerol is sonication method (7).

The sonication method is a method using ultrasonic waves. The use of ultrasonic waves can accelerate reaction times and increase product yield (8). Furthermore, an increasing sonication time can increase degradation yields (9). Besides using the

sonication method, the degradation reaction also need a heterogeneous catalyst, because it is easily separated from the reaction mixture, has a large surface area, is easily regenerated, and has a high acidity level (10). One type of heterogeneous catalyst is the metal-impregnated catalyst. Y Zeolite is one type of synthetic zeolite that is widely developed in improving catalyst performance (11).

Y zeolite is a hydrated aluminsilicate mineral containing alkali or alkaline earth cations that can be exchanged with other cations, and can be modified to increase its activity and selectivity (12). The Y zeolite has several advantages including regular crystal structure, uniform pore size, large surface area, and thermal stability reaching 793 °C (13) i. The catalyst activity of the Y Zeolite can be increased by purging the metal into the zeolite pores. The catalyst is synthesized by by by impregnation metal into the zeolite producing the zeolite as a bifunctional catalyst (11). Metals that can be impregnated in zeolites are usually included in transition metals such as Pt, Pd, Ni, Mo, and others (14).

In this study, Ni and Mo metals are potentially used because they have unpaired electrons in d orbitals which can provide Lewis acid sites capable of adsorbing reactants on the catalyst surface. Ni and Mo metals have good catalytic properties (15), so they can be used as active catalysts. Cahyono has synthesized Ni/ZAA as a catalyst in the esof degradation of glycerol to ethanol (16). Furthermore, synthesized Mo/ZAA was used as a catalyst in the ess of glycerol to ethanol (17). ZAA was known as a natural zeolite that has impurities. So, industrial zeolite like Y zeolite is a potential alternative to replace ZAA as the support material. There is no reported study of Y Zeolite-supported Ni and Mo metals. Other studies report the success of NiMo supported on titania (18), NiMo/Al$_2$O$_3$-HY, and NiMo/Beta (19).

On the basis the above research, it can be seen that the Ni and Mo metals have been successfully impregnated into the natural zeolite type as catalyst in the degradation of glycerol to ethanol, but they have never been impregnated into the Y zeolite. Therefore, the effectiveness of the degradation of the glycerol using a synthesized catalyst under sonication method is very interesting to study. he purposes of this study are (1) to determine the characteristics of Y Zeolite which vehave been modified with Ni, Mo and their mixtures, (2) to determine the eeffectiveness of catalyst of H/YZ, Ni/YZ, Mo/YZ, and NiMo/YZ in the degradation ofglycerol to ethanol by sonication method, (3) to analyze the effect of sonication time on the eeffectiveness of the H/YZ, Ni/YZ, Mo/YZ and NiMo/YZ catalyst on the degradation of glycerol to ethanol.

2. EXPERIMENTAL SECTION

The instruments used include: Mortar and pestle, 60 Mesh softene, glass and ceramic tools, analytical balance (Durascale), spatula, shaker, oven, hot plate stirrer, water bath shaker, desiccator, furnace (Thermolyne), Spectronic-20 (Ganesys 20), Ultrasonic devices (Branson 1510), X-Ray Diffraction (XRD) (PANalytical X'Pert PRO), X-Ray Fluorescence (XRF) (PANanalytical Minipal 4) and Gas Chromatography (GC) (HP 5890). The materials used in this study include Y Zeolite, NH$_4$Cl 1 M solution, 100 ppm blue methylene solution, ammonia p.a, Ni(NO$_3$)$_2$·6H$_2$O salt, (NH$_4$)$_6$Mo$_7$O$_{24}$.4H$_2$O salt, technical glycerol, distilled water, and aqua-demineralization.

2.1. Preparation and Activation of Y Zeolite with NH$_4$Cl Solution 1 M
Y Zeolite was mashed and sieved with 60 Mesh sieve sieve sieve. The Y Zeolite was dried at 100 °C for 2 hours. The Y Zeolite was activated by mixing 10 grams of the Y Zeolite with 100 mL NH$_4$Cl 1 M. The precipitate was filtered and washed with distilled water to a neutral pH. The precipitate was then dried at a of 120 °C for 6 hours and calcined at 500 °C for 2 hours.

2.2. Impregnation of Active Y Zeolite with Ni, Mo, Ni-Mo Metals
Ni/YZ: 4.75 grams of the Y Zeolite mixed with nickel nitrate solution (1.2380 grams of nickel nitrate salt in 100 mL of water). The mixture was stirred using a water bath shaker for 24 hours at 65 °C with 130 rpm. The precipitate was filtered and washed with distilled water to a neutral pH. The precipitate was then dried at 120 °C for 6 hours and calcined at 500 °C for 2 hours. Mo/YZ: the same procedure as Ni/YZ, with a specific solution of ammonium heptamolibdat (0.46 grams of ammonium heptamolibdate salt in 100 mL of water). NiMo/YZ was synthesized by co-impregnation, i.e.: a) the same procedure of Mo/YZ synthesis with ½ grams of ammonium heptamolibdate salt, and it continued with b) the same procedure of Ni/YZ synthesis with ½ grams of nickel nitrate salt.

2.3. Characterization of The Catalysts
The synthesized catalysts were characterized by XRD and XRF. Also, the physical characterization is as follows:

2.3.1. The analysis of acidity level
0.300 g of the catalyst of was put into a desiccator which was saturated with ammonia vapor. The catalyst was left in contact with ammonia vapor for 24 hours. The catalyst was carefully weighed to a constant weight.

2.3.2. The analysis of the catalyst surface area
The analysis of the Surface Area Analysis was carried out using the Langmuir Isotherm Method: (1) maximum wavelength (λ max), 10 ppm methylene blue was absorbed at a wavelength of 600-700 nm using Spectronic-20, and (2) adsorption of standard solutions, standard solutions were prepared by dilution of standard 100 ppm methylene blue with variations in concentration of 1, 2, 3 and 4 ppm. Each solution was measured absorbance at the maximum wavelength (λ max) (3) surface area of catalysts: 0.01 gram of the catalyst was mixed with 20 mL of 18 ppm methylene blue. The mixture was then stirred using a shaker at 150 rpm for 30 minutes. The

catalyst precipitate was filtered. The filtrate was then analyzed at the maximum wavelength.

2.5. Glycerol Degradation

5 mL of Glycerol was mixed with 20 mL of distilled water in Erlenmeyer. The catalyst about 5% of the mass of glycerol was put into the Erlenmeyer. The mixture was sonicated with variations in time of 2, 4, and 6 hours with 60 °C at 42 kHz. The filtrate was then analyzed using GC.

3. RESULTS AND DISCUSSION

3.1. Preparation and Activation of Y Zeolite

The Y Zeolite sample used in this study has a white solid with a coarse grain texture. Therefore, the Y Zeolite needs to be prepared to obtain a smoother texture with a larger surface area. Generally, the Y Zeolite is composed of two components, namely the main metal component and the impurity metal component. The presence of these impurity metal components can cover the active sites of the Y Zeolite. The Y Zeolite needs to be activated to eliminate impurities and evaporate the water trapped in the pores of zeolite (20).

The Y Zeolite can be in two ways, i.e: physical and chemical activation. Physical activation is referred to grinding the Y Zeolite to get a smaller particle size. The refined Y Zeolite is then sieved using a 60 Mesh sieve and dried at 100 °C for 2 hours intending to to increase the surface area of the Y Zeolite Y and eliminate increase the surface area of the Y Zeolite Y and eliminate increase surface area of the Y Zeolite Y and eliminate the water content trapped in the Y Zeolite framework. Chemical activation is carried out by mixing the Y Zeolite with NH_4Cl solution 1 M. Chemical activation occurs through cation exchange reactions. The NH_4^+ cation is a cation that is easily absorbed by zeolite minerals because it has a high absorption selectivity for zeolites in the order $NH_4>$ Pb> Ag> Ba> Na> Sr (21). This cation exchange is based on equilibrium reactions and depends on the magnitude of the concentration of the solution, where the the concentration of NH_4Cl solution, the more Na^+ cations can be replaced with NH_4^+ cations (22). Based on the activation process, an H/YZ

catalyst was obtained in the form of a white solid with a fine powder texture. This H/YZ is an active Y Zeolite and can be used as a catalyst in the degradation of glycerol to ethanol.

3.2. Impregnation of Y Zeolite with Ni, Mo Metals and its Mixtures

In this study, metals impregnated into the pores of the Y Zeolite are Ni, Mo, and mixture. This impregnation aims to distribute Ni and Mo metals evenly into the pores or surfaces of the Y Zeolite, where they can act as active catalyst sites. Ni/YZ and Mo/YZ catalysts were prepared by wet impregnation. The metal impregnation process, a cation exchange reaction between H^+ ions with Ni^{2+} ions and Mo^{6+} ions. Chemically, cation exchange in the impregnation method is caused by the weak interaction of dipole ions between the Y Zeolite and H^+, so that it is easily replaced by Ni^{2+} and Mo^{6+} cations. Generally, cation exchange can be affected by the amount of ion charge. The greater the charge of ions, the easier it is to replace the position of other ions in a molecule. Ni^{2+} and Mo^{6+} ions have a higher charge than H^+ ions, consequently, Ni^{2+} and Mo^{6+} ions can easily replace H^+ positions of the Y Zeolite through cation exchange.

The coimpregnation method was then carried out. First, H/YZ is mixed with $(NH_4)_6Mo_7O_{24}$ solution to impregnate Mo metal in the Y Zeolite. After forming Mo/YZ, the $Ni(NO_3)_2$ solution is mixed with Ni solution for Ni metal impregnation. Zeolites that have been impregnated with Ni and Mo metals have different colors. Ni/YZ and NiMo/YZ catalysts were greenish-white powders while Mo/YZ catalysts were white powders. Physically, greenish-white Ni/YZ and NiMo/YZ indicated that the nickel metal impregnated into the Y Zeolite. The impregnated Y Zeolite was used as a catalyst in the degradation of glycerol. The catalysts formed up to this process are H/YZ, Ni/YZ, Mo/YZ, and NiMo/YZ shown in Figure 1.

3.3. Characterization of Catalysts

The results of the XRF on the initial Zeolites Y, H/YZ, Ni/YZ, Mo/YZ, and NiMo/YZ are shown in Table 1.
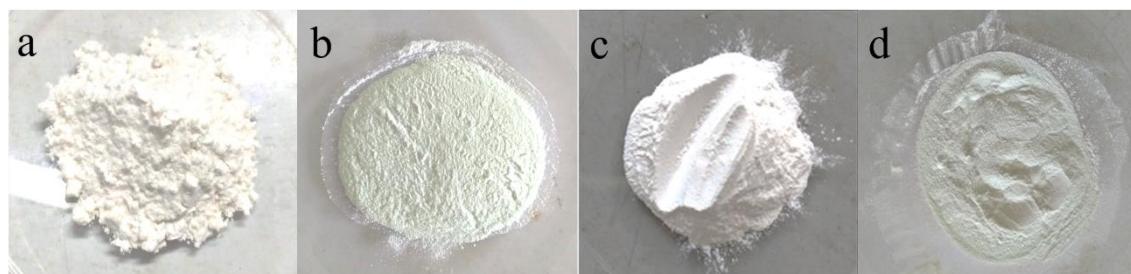
Figure 1: (a) H/Zeolit Y, (b) Ni/Zeolit Y, (c) Mo/Zeolit, (d) NiMo/YZ

Table 1: The results of the XRF of YZ, H/YZ, Ni/YZ, Mo/YZ dan NiMo/YZ.

Element	Content (%)				
	Y Zeolite	**H/YZ**	**Ni/YZ**	**Mo/YZ**	**NiMo/YZ**
Al	30.1	30.9	27.3	31.0	26
Si	64.3	64.7	44.6	64.9	41.9
P	1.7	1.6	0.96	1.4	0.91
K	0.4	-	-	-	-
Ca	2.0	1.5	0.75	1.4	0.83
Cr	0.15	0.12	0.078	0.12	0.092
Sc	-	-	0.01	-	-
Sr	-	0.01	-	-	-
Fe	0.82	1.03	0.48	0.78	0.49
Cu	0.16	0.16	-	0.14	-
Yb	0.2	-	-	0.2	-
Ni	0.16	-	25.8	-	28.2
Mo	-	-	-	Not detected	Not detected

Table 1 shows that the Y Zeolite containm Si of 64.3% and Al of 30.1%, so it can be calculated the mole ratio of Si/Al on the Y Zeolite of 2.2. This was consistent with a literature by that the mole ratio owned by the Y Zeolite ranges from 1.5 – 3 (23), so it can be said that the sample of zeolite used in this study was the Y Zeolite. Besides the Si and Al content, the XRF analysis results indicate the presence of other components which are impurities. The presence of these impurities will reduce the activity of the Y Zeolite as both an adsorbent and catalyst. Therefore activation is needed using NH_4Cl solution to remove these metal impurities.

Table 1 shows that the levels of impurities have decreased significantly and that even some impurities have disappeared after activation. Some impurities still stick to the Y Zeolite, but the levels are much lower than before the activation process. After activation, the Y Zeolite is impregnated with Ni, Mo metal and their mixture to increase the active site as a catalyst. The success of the impregnation of Ni and Mo metals can be seen in Table 1. On the basis the XRF test, it can be seen that Ni metal was successfully impregnated into the Y Zeolite because it was successfully detected by XRF instruments, while Mo metal was not detected by XRF. This is because the level of Mo impregnated into the Y Zeolite was too small at 5% in Mo/YZ and 2.5% in NiMo/YZ. Due to the undetectability of Mo metal, further analysis is needed to determine the presence of molybdenum in the Y Zeolite using XRD analysis.

XRD analysis was carried out on the Y Zeolite samples before and after being activated and impregnated with Ni, Mo metals, and their mixtures. The Y Zeolite sample can be analyzed by matching the 2θ data and d-spacing between the synthesized Y Zeolite and the standard Y Zeolite in JCPDS No. 38-0240. Based on the comparison of 2θ and d-spacing between the Y Zeolite and the standard Y Zeolite, it can be seen that there was a peak of 2θ are 14,01°, 19,86°, 22,20°, 24,38°, 28,25°, 31,65°, 34,77°, 37,67°,42,97°, 45,45°, 47,74° which similar to the peak 2θ the Y Zeolite standard in JCPDS No. 38-0240 (24). Based on the similarity of the 11 data, it can be interpreted that the zeolite sample used in this study was correctly the Y Zeolite. After it was proven that the sample used was the Y Zeolite, then the Y Zeolite was activated and impregnated with Ni, Mo metals and their mixture to enhance its active side as a catalyst. The XRD analysis results of the H/YZ, Ni/YZ, Mo/YZ, and NiMo/YZ catalysts are shown in Figure 2.
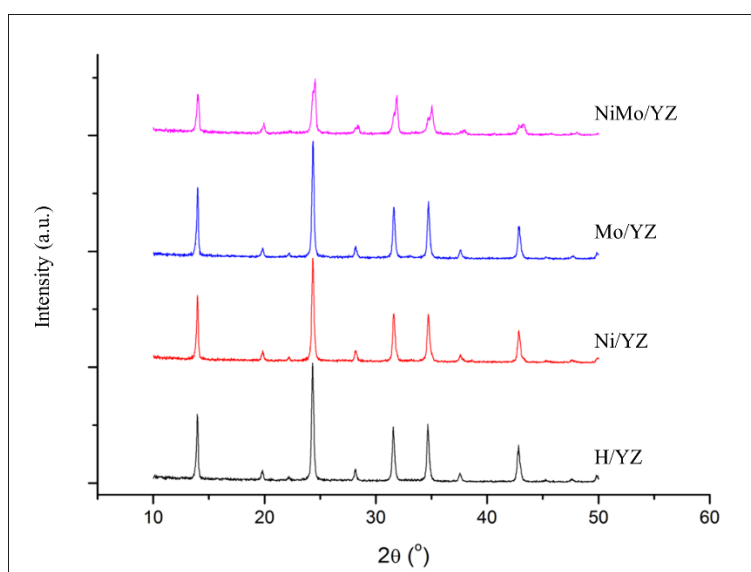

Figure 2: Diffractogram of H/YZ, Ni/YZ, Mo/YZ and NiMo/YZ.

Figure 2 showed that the catalyst formed has a crystalline phase which was indicated by the appearance of sharp peaks. However, the NiMo/YZ chromatogram slightly experienced a broad (decreased intensity). The decrease in catalyst intensity can occur due to the impregnation of two metals in zeolites (25). Based on Figure 2, the four catalysts have the same diffractogram pattern (not significantly different) so it can be said that the

presence of activation and impregnation does not damage the structure of the Y Zeolite. The successful impregnation of Ni and Mo metals can be seen based on the match of 2θ data from the analysis with 2θ data of NiO standard on JCPDS No. 73-1519 and 2θ data of MoO_3 standard in JCPDS No. 05-0508. The comparison of 2θ data between Ni/YZ and Mo/YZ with 2θ NiO and MoO_3 is shown in Table 2.

Table 2: 2θ Ni/YZ, Mo/YZ, and NiMo/YZ toward NiO and MoO_3 standards.

Ni/YZ	Mo/YZ	NiMo/YZ	NiO Standard	MoO_3 Standard
2θ	2θ	2θ	2θ	2θ
13.98	13.98	14.11	-	-
19.83	19.82	19.93	-	-
22.20	22.18	24.32	-	-
24.39	24.35	24.53	-	-
28.19	28.18	28.40	-	-
31.60	31.61	31.67	-	-
34.70	34.71	35.02	-	34.30
37.58	37.59	37.93	37.34	-
42.85	42.86	42.84	43.38	42.00
45.40	45.38	43.25	-	-
47.62	47.71	48.02	-	-
49.98	49.90	-	-	-

Based on Table 2, showed that the Ni and Mo metals have been successfully impregnated into the Y Zeolite was evidenced by the appearance of peaks of 37.58° and 42.85° on Ni/YZ which indicated the presence of NiO. The appearance of peaks of 34.71° and 42.84° on Mo/YZ did not surely indicate the presence of MoO_3. In co-impregnation, the mixture of Ni and Mo metals was not surely impregnated into the Y Zeolite. This was evidenced by the appearance of peaks of 37.93° and 42.84° which indicated the presence of NiO while the peaks of 35.02° and 42.84° indicated the presence of MoO_3 in the Y Zeolites. In this study, the term Mo/YZ and NiMo/YZ is considered predictable material, because no specific peaks of Molybdenum species appeared.

3.5. Acidity Level and Surface Area of The Catalyst on Glycerol Degradation
The determination of the acidity of the catalyst is based on the adsorption of ammonia gas by the gravimetric method. The acidity of the catalyst is the amount of base mmol adsorbed per gram of catalyst. The amount of base mmol adsorbed is equivalent to the amount of acid mmol in the Y Zeolite.

Table 3 shows that the acidity level of the Y Zeolite after being impregnated with Ni and Mo metals has increased. The presence of metal impregnation can increase the total acidity of the catalyst (25) because these metals can form Lewis acidic sites. The acidity level of the catalyst is related to the Brønsted and Lewis acid sites. The number of Brønsted and Lewis acid groups present on the surface is the total amount of acid contained in the catalyst. Based on the catalyst, the acidity level from highest to lowest respectively is NiMo/YZ> Ni/YZ> Mo/YZ> H/YZ. NiMo/YZ catalyst has the highest level of acidity because two metals form the Lewis acid site, so more

free-electron pairs from the ammonia base can be adsorbed by the catalyst.

The surface area of the catalyst can be determined by adsorbing methylene blue. This adsorption is a type of Langmuir isotherm, where only a monolayer layer will be formed at the time of maximum adsorption on the surface of the catalyst (26). Based on Table 3, the surface area of the catalyst before and after impregnation with Ni and Mo metals has decreased. The order of the catalyst surface area from largest to smallest is H/YZ> Ni/YZ> Mo/YZ> NiMo/YZ. The surface area of a catalyst will decrease with the presence of metal because these metals can cover a single layer of the Y Zeolite (27).

3.6. Degradation of Glycerol to Ethanol
In this study, the degradation of glycerol was carried out assisted by ultrasonic waves at a time variation of 2, 4, and 6 hours at 60 °C with the desired ethanol product. Glycerol degradation was carried out with glycerol:water ratio of 1:4.

The process of degradation will break the OH bond in glycerol to form a 2-propene-2,3 diol compound. Furthermore, the compound 2-propene-2,3 diol undergoes tautomerization to form acetol where, under the influence of ultrasonic waves, acetol will break apart to form methanol and ethanone radicals. Ethanone radicals can react again with H radicals obtained from the breakdown of water molecules to form acetaldehyde, ethanol, and 2,3-butanediol compounds. The advantage of using ultrasonic waves is that the degradation process will be faster and more products will be produced with a high %yield (7). After the filtrate was obtained, it was then tested using GC to determine the ethanol content. The results of the degradation product analysis are shown in Table 3.

Table 3: Physical characterization of catalyst acidity.

Catalyst	Acidity (mmol/gram)	Surface Area (m²/g)	Ethanol Yield by GC (%)		
			2 hours	4 hours	6 hours
H/YZ	0.5120	110.321	0	1.99	26.74
Ni/YZ	0.7755	105.701	0	2.25	25.87
Mo/YZ	0.5361	105.235	0	1.66	20.08
NiMo/YZ	1.0810	104.874	0	4.49	27.33

Table 3 showed that the % yield of ethanol increased with the time duration of sonication. Based on GC results, it can be seen that the biggest %yield was formed within 6 hours. The longer the reaction time, the longer the contact between ultrasonic waves and glycerol (28), so the degradation yield also increases. GC results showed that the highest catalytic activity in the glycerol degradation was the NiMo/YZ catalyst. The catalytic activity correlated with the highest acidity and the lowest surface area. This proves that the impregnation of two metals can increase zeolite activity as a catalyst, so the %yield produced is also greater. Without sonication and catalyst in the degradation of glycerol, the %yield of ethanol will be lower (7). Therefore, the order of ethanol product at 6 hours reaction was: NiMo/YZ > H/YZ > Ni/YZ > Mo/YZ. Also, the order of ethanol product at 4 hours reaction was: NiMo/YZ > Ni/YZ > H/YZ > Mo/YZ.

4. CONCLUSION

The catalysts formed in this study were H/YZ, Ni/YZ, Mo/YZ, and NiMo/YZ. The results of the analysis of catalyst characteristics include: (a) Ni and Mo metals were successfully impregnated into the Y Zeolite as indicated by the XRF and XRD results, (b) catalysts H/YZ, Ni/YZ, Mo/YZ, and NiMo/YZ have crystalline phase, (c) the acidity levels of catalyst H/YZ, Ni/YZ, Mo/YZ, and NiMo/YZ were 0.5120, 0.7754, 0.5362 and 1.0810 mmol/gram, (d) the surface area of catalyst H/YZ, Ni/YZ, Mo/YZ, and NiMo/YZ were 110.321, 105.701, 105.235 and 104.874 m²/gram, respectively. Based on the research, it can be seen that the NiMo/YZ catalyst had the highest catalytic activity because it produced the highest %yield of ethanol both at 4 hours (4.49%) and 6 hours (27.33%). Through the degradation process with time variations, it can be seen that the longer the time sonication, the higher % the yield of ethanol produced. The further study will evaluate the metal leaching during the catalytic reaction, and the decomposition product (by-product) of glycerol after the catalytic reaction.

5. CONFLICT OF INTEREST

The authors declare no conflict of interest.

6. ACKNOWLEDGEMENTS

7. REFERENCES

1. Sumari S, Santoso A, Asrori MR. A Review: Synthesis of Biodiesel from Low/Off Grade Crude Palm Oil on Pretreatment, Transesterification, and Characteristics. Orbital Electron J Chem [Internet]. 2021 Oct 5;13(4):385–91. Available from: <URL>.

2. Arcanjo MRA, Silva IJ, Rodríguez-Castellón E, Infantes-Molina A, Vieira RS. Conversion of glycerol into lactic acid using Pd or Pt supported on carbon as catalyst. Catal Today [Internet]. 2017 Jan 1;279:317–26. Available from: <URL>.

3. Anitha M, Kamarudin SK, Kofli NT. The potential of glycerol as a value-added commodity. Chem Eng J [Internet]. 2016 Jul 1;295:119–30. Available from: <URL>.

4. Carr AG, Shi X, Domene C, Leung AK, Green WH. Methanol formation from the treatment of glycerol in supercritical water and with ethylsulfide. J Supercrit Fluids [Internet]. 2016 Nov 1;117:80–8. Available from: <URL>.

5. Remón J, Zhu G, Budarin VL, Clark JH. Analysis and optimisation of a microwave-assisted hydrothermal process for the production of value-added chemicals from glycerol. Green Chem [Internet]. 2018 Jun 4;20(11):2624–36. Available from: <URL>.

6. Wardani RK. Degradasi Gliserol Menjadi Etanol Menggunakan Katals Zeolit Alam Aktif/Cu Dengan Bantuan Ultrasonik. Universitas Negeri Malang; 2016.

7. Kalla R, Sumarno S, Mahfud M. Non-Catalytic and γ-Al₂O₃ Catalyst-based Degradation of Glycerol by Sonication Method. Bull Chem React Eng Catal [Internet]. 2015 Dec 30;10(3):304–12. Available from: <URL>.

8. Maisarah QH, Hidayati N. Transesterifikasi Minyak Jelantah Menjadi Biodiesel Menggunakan Gelombang Ultrasonik dan Katalis Na₂O/Fly Ash. In: Prosiding Seminar Nasional Teknik Kimia "Kejuangan" [Internet]. Yogyakarta; 2019. p. 1–5. Available from: <URL>.

9. Kalla R, Sumarno S, Mahfud M. Degradasi Gliserol Katalitik Menggunakan Tanduk Getar. Pros SENIATI [Internet]. 2016 Mar 1;2(1):B.52-B.57. Available from: <URL>.

10. Praputri E, Sundari E, Firdaus F, Sofyan S. Penggunaan katalis homogen dan heterogen pada proses hidrolisis pati umbi singkong karet menjadi glukosa. J Litbang Ind [Internet]. 2018 Dec 28;8(2):105–10. Available from: <URL>.

11. Sriatun S, Taslimah T, Cahyo EN, Saputro FD. Sintesis dan Karakterisasi Zeolit Y. J Kim Sains dan Apl [Internet]. 2017 Apr 1;20(1):19–24. Available from: <URL>.

12. Weckhuysen BM, Yu J. Recent advances in zeolite chemistry and catalysis. Chem Soc Rev [Internet]. 2015 Oct 5;44(20):7022–4. Available from: <URL>.

13. Belaabed R, Elknidri H, Elkhalfaouy R, Addaou A, Laajab A, Lahsini A. Zeolite Y synthesis without organic template: The effect of synthesis parameters. J Mater Environ Sci [Internet]. 2017;8(10):3550–5. Available from: <URL>.

14. Trisunaryanti W. Sintesis dan Karakterisasi Katalis. In: Konversi Fraksi Aspal Buton Menjadi Fraksi Bahan Bakar [Internet]. Yogyakarta: Gadjah Mada University Press; 2018 [cited 2023 Nov 5]. Available from: <URL>.

15. Kordouli E, Pawelec B, Kordulis C, Lycourghiotis A, Fierro JLG. Hydrodeoxygenation of phenol on bifunctional Ni-based catalysts: Effects of Mo promotion and support. Appl Catal B Environ [Internet]. 2018 Dec 15;238:147–60. Available from: <URL>.

16. Cahyono R. Efektivitas Katalis ZAA dan Ni/ZAA untuk Degradasi Glisererol menjadi Etanol dengan bantuan Ultrasonik. Universitas Negeri Malang; 2018.

17. Skoplyak O, Barteau MA, Chen JG. Enhancing H_2 and CO Production from Glycerol Using Bimetallic Surfaces. ChemSusChem [Internet]. 2008 Jun 23;1(6):524–6. Available from: <URL>.

18. Petropoulos G, Zafeiropoulos J, Kordouli E, Sygellou L, Kordulis C, Lycourghiotis A, et al. Transformation of vegetable oils into green diesel over Ni-Mo catalysts supported on titania. Catal Today [Internet]. 2023 Nov 1;423:114268. Available from: <URL>.

19. Qi L, Peng C, Cheng Z, Zhou Z. Selective hydrocracking of poly-aromatics to mono-aromatics in a catalyst grading system of NiMo/Al2O3-HY and NiMo/Beta. Fuel [Internet]. 2023 Nov 1;351:128941. Available from: <URL>.

20. Ismettulloh M, Gumelar F, Nuryoto N, Kurniawan T. Modifikasi Zeolit Alam Bayah Menggunakan Asam Dan Pengaplikasiannya Dalam Pengurangan Amonium Pada Kolam Ikan Bandeng. J Integr Proses [Internet]. 2019 Jun 28;8(1):7–13. Available from: <URL>.

21. Las T, Zamroni H. Penggunaan Zeolit Dalam Bidang Industri dan Lingkungan. J Indones Zeolites [Internet]. 2002;1(1):27–34. Available from: <URL>.

22. Hernawan, Wahono SK, Maryana R, Pratiwi D. Modification of Gunungkidul Natural Zeolite as Bioethanol Dehydrating Agents. Energy Procedia [Internet]. 2015 Jan 1;65:116–20. Available from: <URL>.

23. Li J, Gao M, Yan W, Yu J. Regulation of the Si/Al ratios and Al distributions of zeolites and their impact on properties. Chem Sci [Internet]. 2023 Feb 22;14(8):1935–59. Available from: <URL>.

24. Rosman N, Harun Z, Jamalludin MR. The Characteristic of Synthesized Zeolite Rice Husk Particles via Different Routes. J Teknol [Internet]. 2014;69(9):127–30. Available from: <URL>.

25. Anggoro DD, Buchori L, Silaen GC, Utami RN. Preparation, Characterization, and Activation of Co-Mo/Y Zeolite Catalyst for Coal Tar Conversion to Liquid Fuel. Bull Chem React Eng Catal [Internet]. 2017 Aug 1;12(2):219–26. Available from: <URL>.

26. Farida Hanum, Rikardo Jgst Gultom, Maradona Simanjuntak. Adsorpsi Zat Warna Metı-len Biru Dengan Karbon Aktif Dari Kulit Durian Menggunakan Koh Dan NaOH Sebagai Aktıvator. J Tek Kim USU [Internet]. 2017 May 19;6(1):49–55. Available from: <URL>.

27. Haider MH, Dummer NF, Knight DW, Jenkins RL, Howard M, Moulijn J, et al. Efficient green methanol synthesis from glycerol. Nat Chem [Internet]. 2015 Dec 14;7(12):1028–32. Available from: <URL>.

28. Qadariyah L, Mahfud, Sumarno, Machmudah S, Wahyudiono, Sasaki M, et al. Degradation of glycerol using hydrothermal process. Bioresour Technol [Internet]. 2011 Oct 1;102(19):9267–71. Available from: <URL>.

Synthesis of Manganese(II), Iron(III), and Vanadium(IV) Complexes with New Schiff Bases and their Spectroscopic and Thermal Studies and Evaluation of their Antimicrobial Activity

Sinan Al-Bayati[1] iD **, Sarab Alazawi[1]*** iD **, Sadeem Al-Barody[1]** iD **, Anaam Rasheed[1]** iD **,**

Rehab Alhassani[1] iD

[1]Almustansiriyah University, Department of Chemistry, Faculty of Science, Baghdad, Iraq.

Abstract: Heterocyclic 3-acetyl coumarin with hydrazide derivatives and their metal complexes are a substantial family of pharmaceutical drugs used to treat infection, anti-inflammatory issues, diabetes, and neurological disorders in the field of medicinal chemistry. Cyclization of 5- floro-2-furaldehyde, ethyl acetoacetate, and urea or thiourea by $LaCl_3.7H_2O$, addition of hydrazine to form amine derivatives were performed, and respective Schiff base derivatives (L1, L2) were produced by adding acetyl coumarin in an ethanolic solution at ambient temperature. New ligands and its complexes of the V (IV), Fe (III) and Mn (II) ions were characterized using (FT-IR, UV, MS) and nuclear magnetic resonance (1H-NMR) as well as elemental analysis (CHN). The synthesized complexes chelate with ligands L1, L2 via (N, O₂) atoms. The structural geometry of the complexes was illustrated in the solid phase using FT-IR and UV-VIS spectroscopy, elemental analysis (CHNS), and flame atomic absorption, in addition to magnetic susceptibility and conductivity measurement. The antibacterial activity of the newly prepared ligands and their metal complexes was evaluated against *Pseudonomous aerugionosa* as a gram negative and *Bacillus subtilis* as a gram positive microorganism. Moreover, the antifungal activity against two fungi *Aspergillus flavus*, and *Saccharomyces cerevisiae* was studied for all compounds. The coordinated ligands significantly increased their bactericidal and fungicidal action compared to the free ligands, which did not exhibit any activity against the selected fungal and bacterial strains. The results focused on the synergetic relationship between the metal ion and the ligand, in addition to the structural variation.

1. INTRODUCTION

Flavonoids with open chain are compounds that contain an aliphatic three-carbon chain bridge with two aromatic rings that form during aldol condensation reaction (1). Chalcone is one of an important class of flavonoids; it is known as a versatile structure or an α-β-unsaturated keton that consists of active keto-ethylenic group (-CO-CH=CH) (2). Coumarins are considered a wide type of compounds in natural extracts, they are referred to as the second stage of metabolites in a number of higher-level plant species, particularly in leaves, seeds, and roots (3). Cou-marin plays a vital role in controlling plant development as metabolites and have a broad range of biological activities like anti-inflammatory (4), anti-cancer, and anti-oxidant (5). Biological activity of coumarin derivatives has become an attractive target for researchers owing to its broad effects on diseases and ability to reduce harm to common cells (6).

According to previous studies, which revealed that coumarin, chalcone fibrates can down-regulate the total cholesterol (TC), phospholipids (PL) and triglycerides (TG) and regulate the levels of VLDL, LDL, and HDL, on the other side, pyrimidine serves an essential function in human proliferation as ribonucleotide

bases in RNA and as deoxyribonucleotide bases in DNA, and it has been found to contribute to multiply biological activates (7). They are considered powerful tools for treatments and possess broad, interesting biological activities such as anti-tumor and anti-fungal and they are used for thyoid drugs and leukemia (8).

Schiff bases are reported to be important ligands to coordinate with metal ion to form complexes because they are easy to prepare, have a range of structural designs, and wide range of applications. These ligands have shown remarkable performance in terms of steric properties and electronic soft tuning of their metal complexes and have been widely employed as polychelate ligands. Schiff bases are created by

chemists as polydentate ligands and their complexes, and these have benefited several fields of chemistry (9).

In this work, we suggested the synthesis of new Schiff's base derivative ligands (L_1, L_2) via the reaction between hydrazide derivatives and 3-acetylcoumarin. The new ligands provide three potential donor sites for complexes with some transition metal ions. The complexes of the ligands (L1, L2) and their detailed characterization and outline of their structures are shown in (Figure 1). The prepared ligands and its complexes are candidates for potent toxic activity as antibacterial and antifungal.
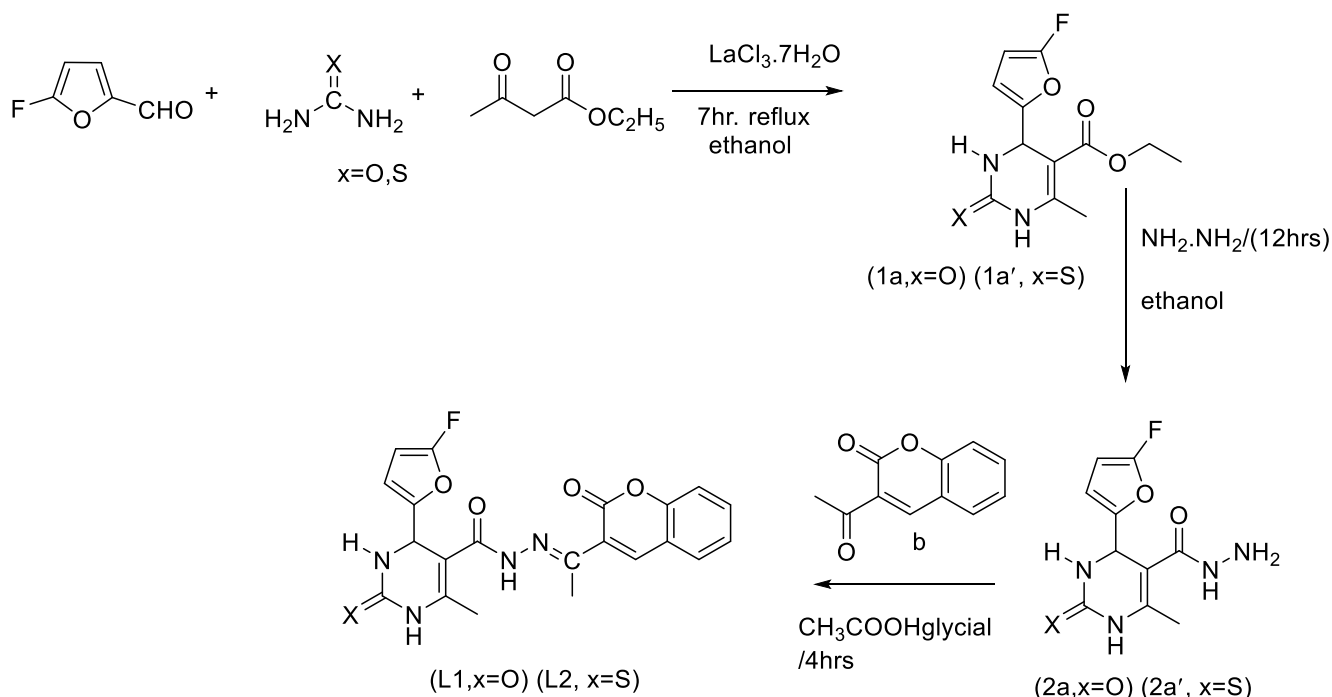
Figure 1: The route of synthesis L1, L2.

2. EXPERIMENTAL SECTION

2.1. Material and Methods
All solvents and chemicals were obtained from Sigma-Aldrich companies and used as received; there was no need for any further purification.

2.2. Instrumentation
Melting points for all synthesized compounds were recorded by a Stuart melting point (digital) SMP30 apparatus. A Shimadzu (FT-IR) model 4800s Spectrometer was used to measure the FT-IR spectrum between (4000-400) cm^{-1} using KBr discs. UV-Vis 16 ultraviolet spectrophotometer model Shimadzu is used to measure the UV -visible spectra at R.T. °C using 1-cm quartz cell and examined between 200-1100 nm at 10^{-3} M in DMSO. Atomic absorption (AA) technique has been recorded using a Shimadzu AA680G atomic absorption spectrophotometer at the laboratories of Ibn-Sinaa Company. Elemental analysis is used to determine C, H, N for the complexes of synthesized ligand [L1, L2] by Linear Regression Euro EA elemental analysis. Mass spectra was performed for ligand on GC-MS

(DIRECT PROBE) via ES technique. ^1H, ^{13}CNMR spectrum for the ligands were recorded at a Bruker DMX- 5000 spectrometer (400 MHz), using DMSO-d_6 solvent. Measurement of conductivity were carried out at RT as °C in DMSO solvent for solutions of samples using an Inolab multi 740, wtw 82362-Germany. Magnetic susceptibility of novel synthesized complexes were recorded at RT °C by auto magnetic susceptibility balance in Al-Mustansiriyah University, College of science, Chemistry Department. TG and DSC (differential scanning calorimetry) thermos grams in different ranges were carried out at R.T heating rate is 10 °C/min at university Abn Al-Hathim College.

2.3. Preparation of Ligand
2.3.1. Preparation of pyrimidine derivative (1a,1á)
Ethyl-4-(5-fluorofuran-2-yl)-6-methyl-2-oxo-1,2,3,4 tetrahydropyrimidine-5-carboxylate (1a), Ethyl-4-(5-fluorofuran-2-yl)-6-methyl-2-thioxo-1,2,3,4-tetrahydropyrimidine-5-carboxylate (1á)

Ethanolic solution of urea (0.6 g, 0.01 mole) or thiourea (0.76 g, 0.01 mole) was mixed with 5-

fluoro-2-furaldehyde (1.14 g, 0.01 mole) and ethylacetoacetate (1.3 g, 0.01 mole) and lanthanum chloride heptahydrate (3.7 g, 0.01 mole) was added to this solution. The resulting mixture was poured to crushed ice (25 g) with the stirring for 10 min, the precipitate product (1a) or (1á) was filtered, and then recrystallized from ethanol after washed with cold water.

2.3.2. Preparation of hydrazide (2a, 2á)
Ethyl-4-(5-fluorofuran-2-yl)-6-methyl-2-oxo-1,2,3,4-tetrahydropyrimidine-5-carbohydrazide (2a), 4-(5-fluorofuran-2-yl)-6-methyl -2-thioxo-1,2,3,4-tetrahydropyrimidine-5-carbohydrazide (2á).

A mixture of compound (1a) (2.68 g, 0.01 mole) or compound (1á) (2.84 g, 0.01 mole) and hydrazine hydrate (2.5 g, 0.05 mole) were dissolved in 25 mL of ethanol and refluxed for 12 hours. The solid product (2a) or (2á) was collected and crystallized from ethanol.

2.3.3. Preparation of coumarin derivative (b)
The compound (b) was prepared by reacting the sailcyldehyde (1.06 g, 0.01 mole) and ethyl aceto-acetate (1.3 g, 0.01 mole) with a drop of tripropyl amine in 25 mL absolute ethanol. The product was filtered and recrystallized from ethanol (10).

2.3.4. Preparation of hydrazine Schiff base ligands (L1, L2)
Ethyl-4-(5-fluorofuran-2-yl)-6-methyl -2-oxo-N-[1-(2-oxo-2H-chromen-3-yl) ethylidene]-1,2,3,4-tetrahydropyrimidine -5-carbohydrazide (L1).

Ethyl-4-(5-fluoro furan-2-yl)-6-methyl-N-[1-(2-oxo-2H-chromen-3-ethylidene]-2-thioxo-1,2,3,4-tetrahydro pyrimidine-5-carbohydrazide (L2).

The ligand (L1) or (L2) ware prepared by reaction compound (2a) (2.54 g, 0.01 mole) or compound (2á) (2.70 g, 0.01 mole) respectively with acetylcoumarin (b) (1.88 g, 0.01 mole) in (30 mL) absolute ethanol and drops of glacial acetic acid was added. The reaction mixture was refluxed for 4 hours, and then the product was obtained and crystallized from methanol. The physical data of synthesized ligands (L1 or L2) are described in Table 1.

2.3.5. Preparation of metal complexes
Ethanolic solution of metal ion salts, (0.228 g, 1 mmole) of $VOSO_4.5H_2O$ was added to ligand (L1) (0.424 g, 1 mmole) or (0.440 g, 1 mmole) of ligand (L2). While ethanolic solution (0.162 g, 1 mmole) of $FeCl_3.6H_2O$ or (0.198 g, 1 mmole) of $MnCl_2.4H_2O$ was added to an ethanolic solution of (2mmole of L1 or L2), respectively, and then stirred, the mixture was heated under reflux for two hours. A precipitate was formed, and the products were isolated by filtration and then recrystallized from cold ethanol. The physical properties of the prepared complexes are shown in Table 1.

Table 1: Physical properties of synthesized ligands and its complexes.

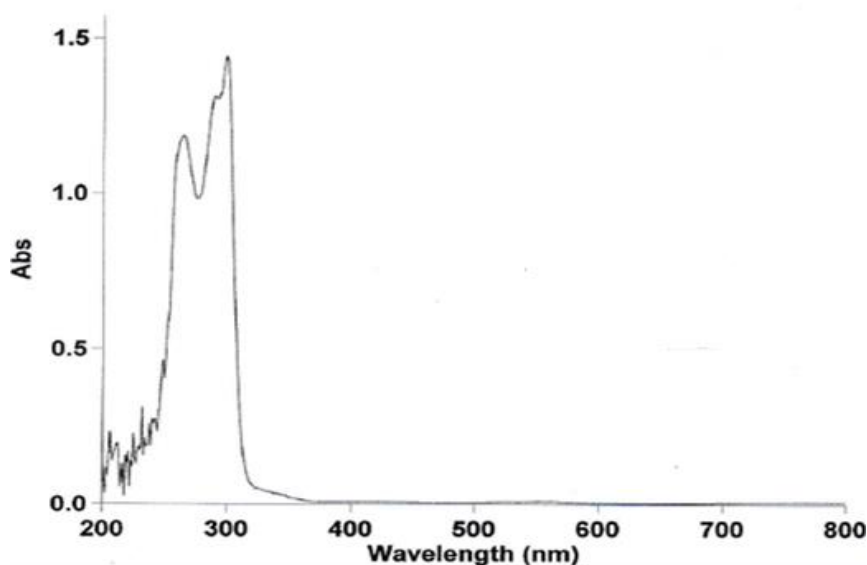| Comp.	Color	M.P. ℃	M.wt. g/mol	C%	H%	N%	S%	M%	M:L	Suggested formula
1a	Pale white	145-147	268.2	53.6	4.8	10.4	----	----	----	$C_{12}H_{13}FN_2O_4$
1á	Pale yellow	190-192	284.3	50.6	4.5	9.8	11.3	----	----	$C_{12}H_{13}FN_2O_3S$
2a	Brown	150-152	254.2	47.2	4.3	22.02	-----	----	----	$C_{10}H_{11}FN_4O_3$
2á	Gray	210-212	270.3	44.4	4.1	20.7	11.8	----	----	$C_{10}H_{11}FN_4O_2S$
b	Light yellow	120-122	188.2	70.1	4.3	----	----	----	----	$C_{11}H_8O_3$
L1	Yellow	115-117	424.4	93.0	6.2	20.7	----	----	----	$C_{21}H_{17}FN_4O_5$
L2	Green	218-220	440.5	57.2	3.8	12.7	7.3	----	----	$C_{21}H_{17}FN_4O_4S$
VO-L1	Dark green	123-125	580.3	43.4	3.3	9.6	---	8.7	1:1	$[VO(L1)H_2O]SO_4$
VO-L2		230-232	606.4	41.5	3.1	9.2	5.2	8.4	1:1	$[VO(L2)H_2O]SO_4$
Fe-L1	Brown	>300	1011.1	49.8	3.3	11.1	---	5.5	1:2	$[Fe(L1)_2]Cl_3$
Fe-L2		>300	1043.2	48.3	3.2	10.7	3.1	5.4	1:2	$[Fe(L2)_2]Cl_3$
Mn-L1	Dark yellow	130-132	974.7	51.7	3.5	11.49	---	5.6	1:2	$[Mn(L1)_2]Cl_2$
Mn-L2		266-268	1006.8	50.0	3.3	11.1	6.3	5.4	1:2	$[Mn(L2)_2]Cl_2$

3. RESULTS AND DISCUSSION

3.1. Electronic Absorption Spectra, Magnetic Susceptibility, and Conductivity Measurements
The UV spectra of free ligand (L1) mostly showed two intense maxima of 38460 п→п* and 28493 n →п* consequently Figure 2, whereas the UV spectrum of ligand (L2) exhibited intense bands at 35080 п→п* and 29150 n→п*, respectively, Table 2.

Table 2: Electronic spectra, magnetic moment (BM) and conductance in DMF for L1, L2 and their complexes.

| Compound	Maximum absorption v_{max}(cm^{-1})	Band Assignment	Suggested geometry	μeff. B.M	Molar Cond. S.cm².mol^{-1}
VO-L1	14084 15384 24390	$^2B_2g \rightarrow ^2Eg_2$ $^2B_2g \rightarrow ^2B_1g$ $^2B_2g \rightarrow ^2A_1g$	Square pyramidal	2.01	86.45
VO-L2	14085 15383 24395	$^2B_2g \rightarrow ^2Eg_2$ $^2B_2g \rightarrow ^2B_1g$ $^2B_2g \rightarrow ^2A_1g$	Square pyramidal	1.98	85.40
Fe-L1	15213 16993 33220	$^6A_2g \rightarrow ^4T_2g$ $^6A_2g \rightarrow ^4T_1g$ $^6A_2g \rightarrow ^4T_1g(p)$	Octahedral	5.26	----
Fe-L2	15195 17022 33311	$^6A_2g \rightarrow ^4T_2g$ $^6A_2g \rightarrow ^4T_1g$ $^6A_2g \rightarrow ^4T_1g(p)$	Octahedral	5.31	----
Mn-L1	15234 17128 34120	$^6A_2g \rightarrow ^4T_2g$ $^6A_2g \rightarrow ^4T_1g$ $^6A_2g \rightarrow ^4T_1g(p)$	Octahedral	5.21	18.50
Mn-L2	15255 17328 33396	$^6A_2g \rightarrow ^4T_2g$ $^6A_2g \rightarrow ^4T_1g$ $^6A_2g \rightarrow ^4T_1g(p)$	Octahedral	5.20	15.40

Figure 2: UV-visible spectrum of ligand L1.

3.1.1. Complexes of [V (IV)]
The product of oxovanadium VO (L1, L2) complex showed all three expected bands at [(14084, 15384, and 24390) cm^{-1} for L1 and (14084, 15384, and 24390) cm^{-1} for L2, which are assigned to $^2B_{2g} \rightarrow ^2Eg$, $^2B_{2g} \rightarrow ^2B1g$, and $^2B_{2g} \rightarrow ^2A_{1g}$ transitions, respectively. These bands are characteristic to square pyramidal geometry (9, 11). The magnetic moment [(2.01 BM) for L1, (1.98 BM) for L2] is higher than the spin value of the vanadium metal only, due to a higher orbital contribution, while the conductivity measurement in DMF revealed that the complex is to be ionic (Table 2 and Figure 3).
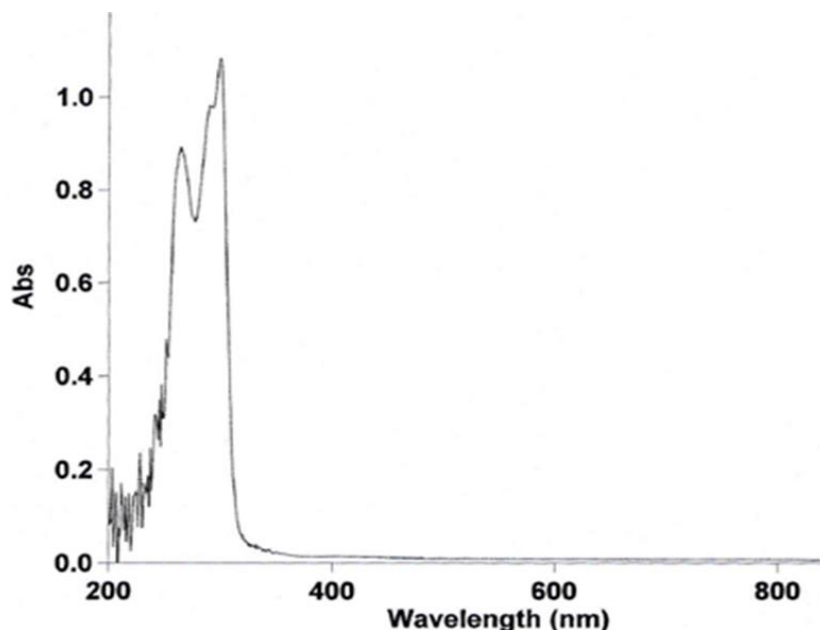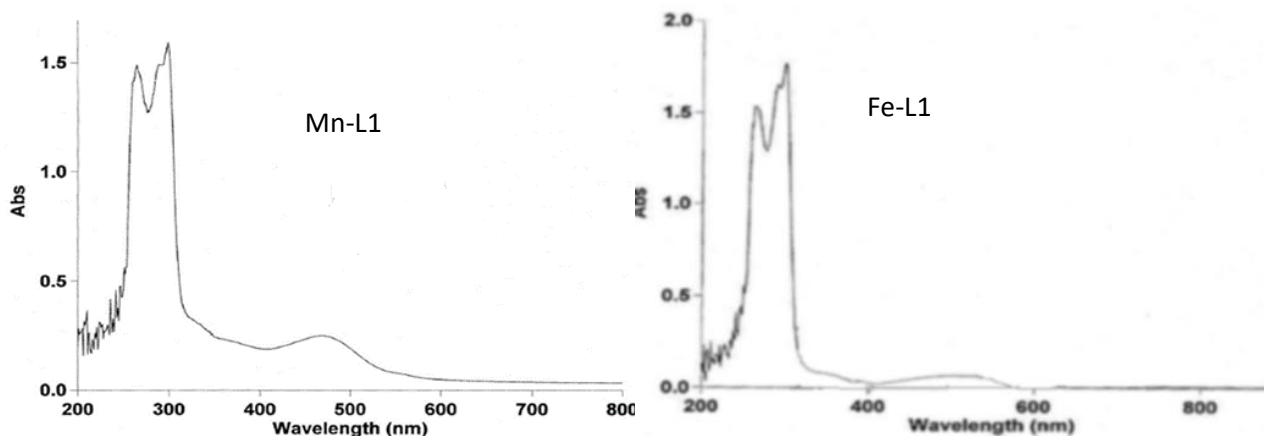
Figure 3: UV-visible spectrum of ligand VO-L1.

3.1.2. Complexes of [Fe (III)]

The prepared dark brown Fe (III) complex showed three bands at (15213, 16993, and 33220) cm^{-1} for L1 (15195, 17022, and 33311) cm^{-1} for L2 which are assigned to the transitions: $^6A_{1g} \rightarrow ^4T_{1g}$, $^6A_{1g} \rightarrow ^4T_{2g}$, $^6A_{1g} \rightarrow ^4T_{1g(p)}$, and (L1, L2)$\rightarrow$Fe (C.T), respectively, (12-14). The magnetic moment (5.26 BM), (5.31 BM) for L1, L2 respectively, with five unpaired electrons confirming an octahedral configuration (15, 16). The conductivity measurement in DMF showed that the complex was a higher conductor (Table 2); therefore, the three (Cl) atoms were not considered to be coordinated with metal ions and were located outside the coordination zone.

3.1.3. Complexes of [Mn(II)]

The UV/VIS spectrum of the Mn(II) complex displayed weak absorption bands at 15234, 17128, and 34120 cm^{-1} for L1, 15255, 17328, and 33396 cm^{-1} for L2, which were characteristic of the octahedral geometry of this complex. These bands may be assigned to $^6A_{1g} \rightarrow ^4T_{1g}$, $^6A_{1g} \rightarrow ^4T_{2g}$, and $^6A_{1g} \rightarrow ^4T_{1g(p)}$ transitions, respectively (17-20). The magnetic moment (5.21 BM for L1, 5.18 BM for L2) (21), with five unpaired electrons, is in the expected range of octahedral geometry around the central metal ion (11) and showed that the complex has a high spin, conductivity measurement in DMF showed that the complex was nonionic (Table 2 and Figure 4).

Figure 4: UV-visible spectrum of Mn-L1 and Fe-L1 Complexes.

3.2. Nuclear Magnetic Resonance Data

In the HNMR spectra of the newly synthesized ligand L1, L2, protons of NH (iminol) were observed as singlets at 9.3 ppm and 8.9 ppm as singlets were attributed to NH-pyrimidine ring, as expected. While the aromatic protons appeared at 6.4-7.92 ppm. The protons of furanyl ring were observed at 4.3-5.4 ppm and the protons of methyl were also observed as expected at 3.6 ppm (22) (Figure 5).
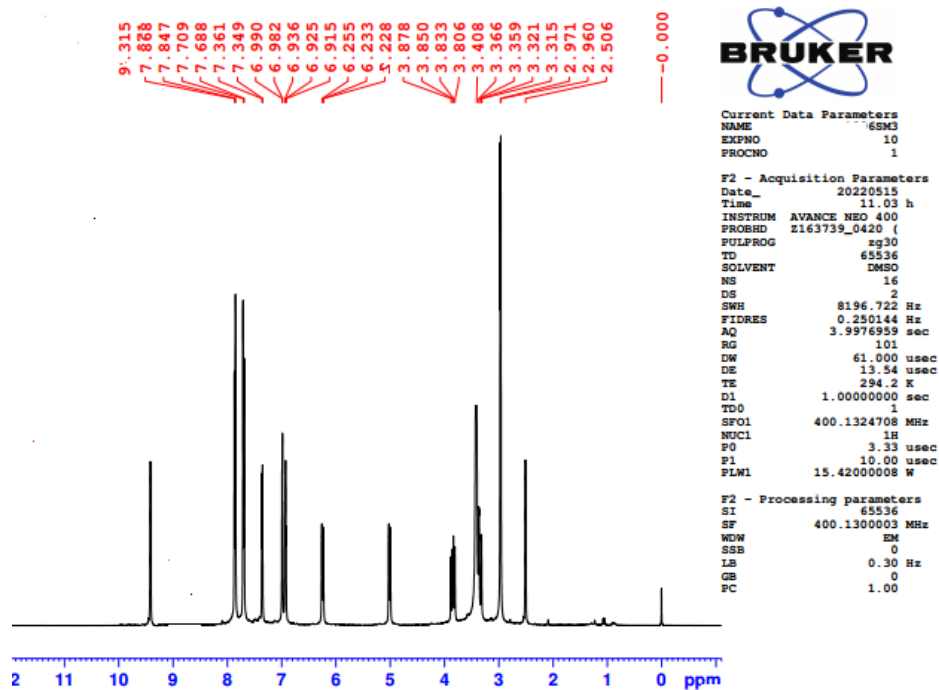
Figure 5: 1HNMR spectrum of ligands L1.

While the 1HNMR spectra for both ligand complexes showed a shift to the down field of protons of NH (iminol), which indicated a coordination with metal. Also, the carbonyl group shifted to the downfield, which confirmed coordination with the metal ion (12). The 13C-NMR spectrum of ligand (L1) is shown in Figure 6. The peaks of carbon at 118-147, 156, and 176 ppm were referred to as the aromatic carbon atoms (HC=N-) and (C=O), respectively (23) (Figure 6).
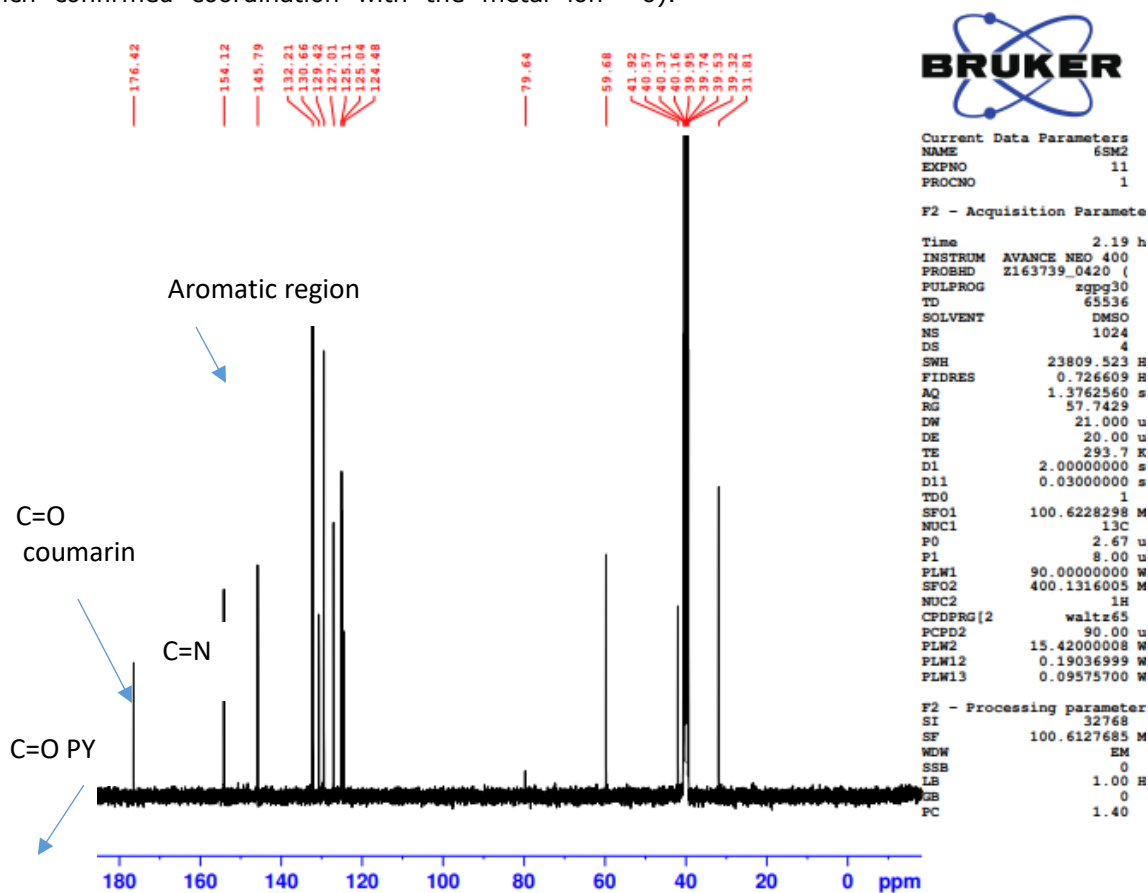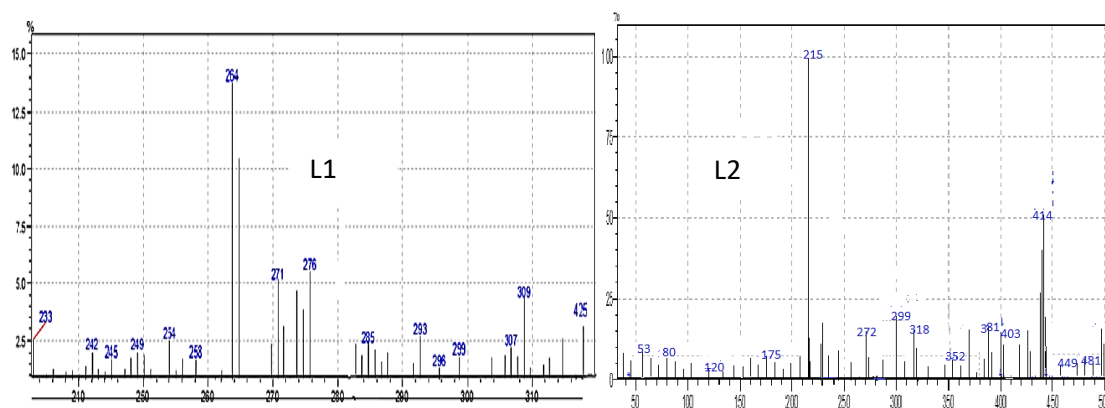

Figure 6: 13C NMR spectrum of ligands L1.

3.3. Mass Spectrum for Ligands
The positive ion mass spectral analysis of L1 is observed at m/z 425.0, which corresponds to (M+H)

Figure 7. While L2 shows main peak at m/z 441, which refers to M⁺.

Figure 7: Mass spectra of ligands L1&L2.

### 3.4. FT-Infrared Spectra of Synthesized Ligands
In FTIR spectrum of ligands 1a and 1á, the amino group band (3325 cm⁻¹) and carbonyl group band (1734 cm⁻¹) of ligand **b** disappeared; instead, the newly noticeable band at 1610 cm⁻¹ indicated an azomethine linkage (HC=N) (11) which proved the formation of Schiff base ligand (24). In FTIR spectra of metal complexes revealed that bands of ligand coordinated from three sites HC=N linkage, v(C=O) of coumarin ring and amide were shifted to lower frequencies (25). New weak bands were appeared in spectrum of complexes at 570-530 cm⁻¹ and 460-435 cm⁻¹ which assigned to v(M-N) and v(M-O) also supported the coordination (17). An intensive band at 970-960 cm⁻¹ referred to V=O and confirmed the coordination of vanadium towards the ligands L1.L2 (11) (Table 3, Figure 8).

Table 3: FT-IR spectra data (cm⁻¹) for ligands and its metal complexes.

Compound formula	v(C=O) amide	v(C=N)	v(C=O) coumarin ring	M-N	M-O	M-Cl	V=O
L1	1645	1610	1715	----	----	----	----
VO-L1	960	1585	1705	570	460	390	970
Fe-L1	1630	1580	1695	565	460	380	----
Mn-L1	1640	1590	1685	560	455	390	----
L2	1650	1600	1710	----	----	----	----
VO-L2	1640	1590	1695	565	450	370	960
Fe-L2	1645	1585	1700	550	455	385	----
Mn-L2	1642	1585	1680	530	435	395	----
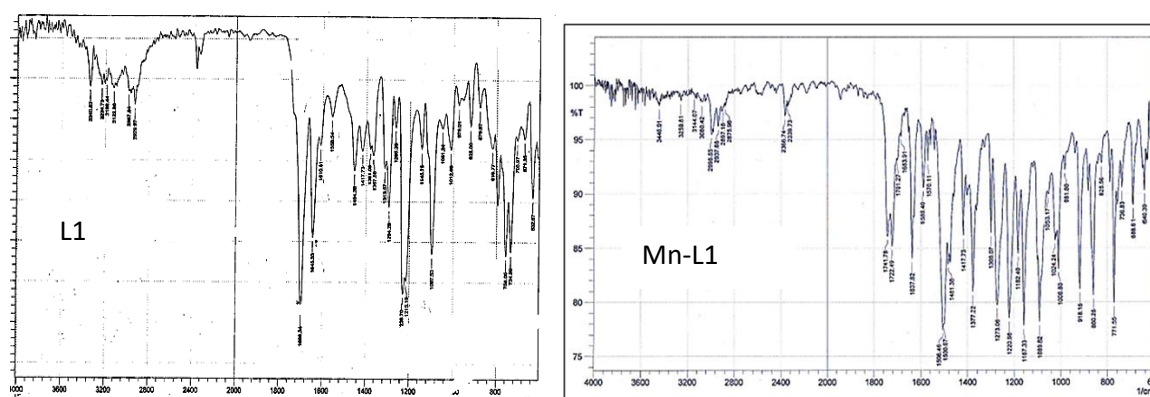
Figure 8: FT-IR spectra of ligand L1 and Mn-L1 complex.

The structure must be confirmed by FT-IR in the (4000-250) cm⁻¹ region in order to show M-N.M-Cl and M-O bonds. The answer to this part (ir FT-IR) device between 4000 and 250 nm not available.

All the findings of elemental and spectral analysis, as well as magnetic moment and conductivity measurements, confirmed the suggested structure of the new compounds, as shown in the following Figure 9.
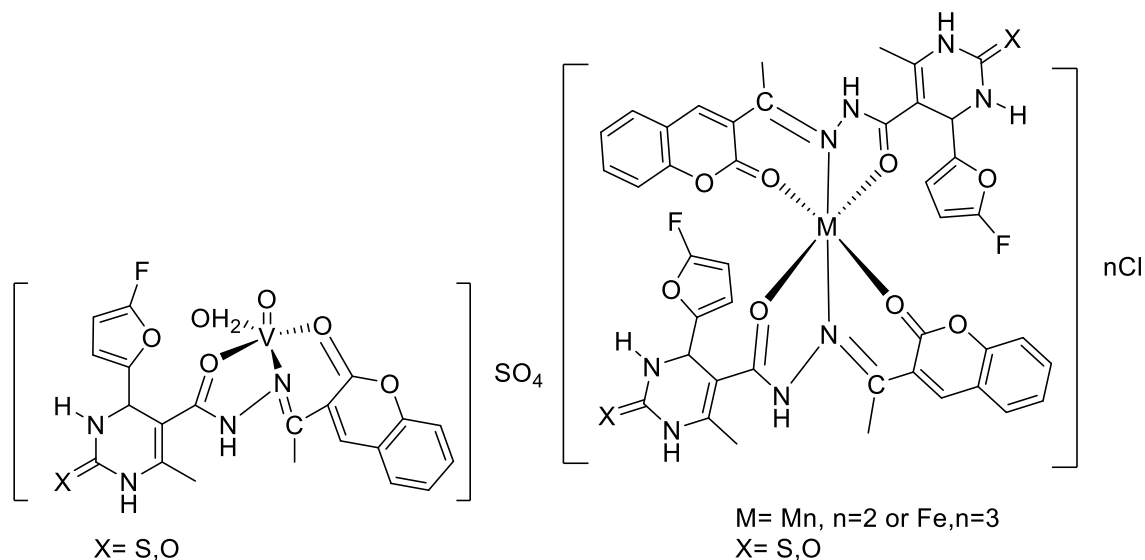
Figure 9: Proposal structure of complexes.

3.5. Thermal degradation of ligands and their complexes

Thermograms have been carried out in the range of 25 – 600 °C at a heating rate of 10 °C / min in an argon atmosphere. The results of TG suggested a mechanism for degradation $[Mn(L1)_2]Cl_2$ and $[Fe(L1)_2]Cl_3$ complexes to 351 °C. While the [L1] and $[VO\ (L1)\ H_2O]Cl_2$ complex was heated to 600 °C (Figure 14). The thermal degradation of [L1] is shown in Figure 10. The thermogram curve shows three decomposition steps. The TGA peak observed at 259.59 °C was assigned to the loss of (C-O) of furyl group fragment, (detd. 1.43 mg, 63%; calcd.=1.40 mg). The second step is carried out at 437.5 °C, which revealed to loss of (COO) of coumarin ring (obsd. 2.31 mg, 11.20%; calcd. =2.34 mg). A peak at 592.9 °C was observed in third step of decomposition related to the loss of CH=CHO attached to the furan ring (obsd. 2.46mg, 11.74%; calcd.= 2.30 mg). The differences in the weight may be related to a sublimation process which occurred at high temperature. The DSC curve recorded two peaks at 84.3 and 269.6 which refer to an exothermic decomposition process (18) (Figure 10). The thermal analysis clearly indicated that the complexes of $[Fe(L1)]Cl_3$ are decomposed, as shown in Figure 13. It also confirmed that the complex is stable up to 134 °C. The TGA peak is observed at 134 °C and is attributed to the loss of Cl coordination in the outer sphere (counter ions), (detd = 0.51 mg, 5.56%; calcd.= 0.5749 mg, see Figures 10, 11. TG thermogram of an argon atmosphere of $[Mn(L1)_2]Cl_2$, $[Fe(L1)_2]Cl_2$, respectively (17, 25) (Figure 13).
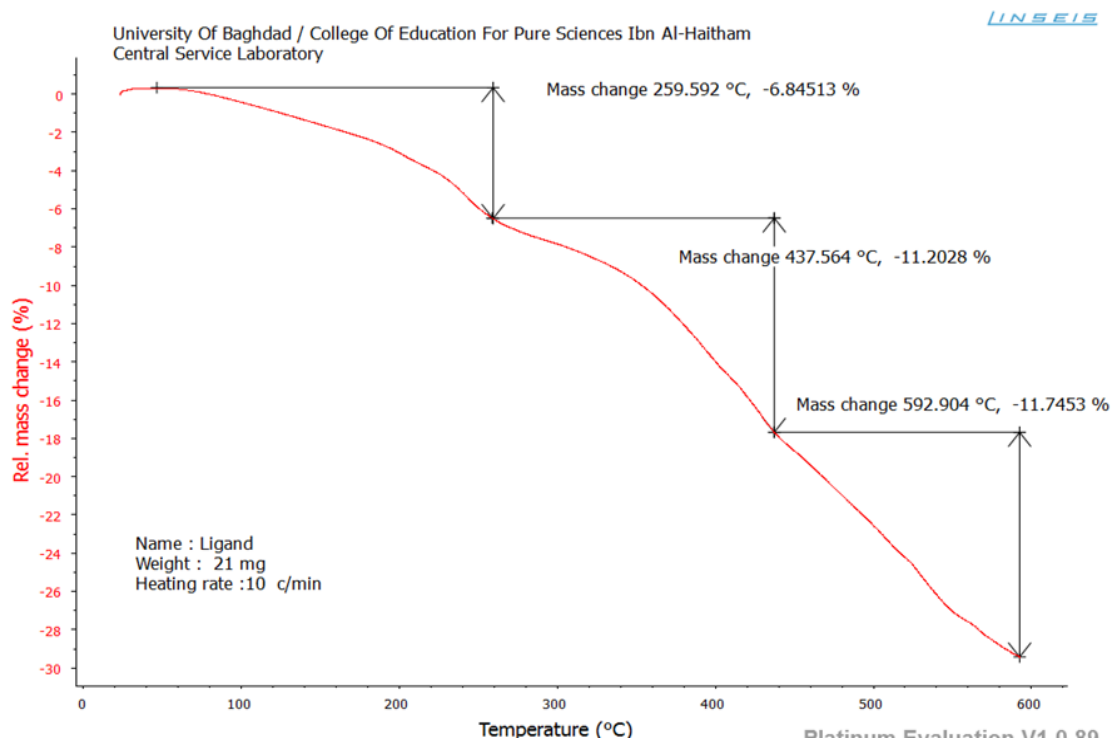
Figure 10: TG thermogram of an argon atmosphere [L1].
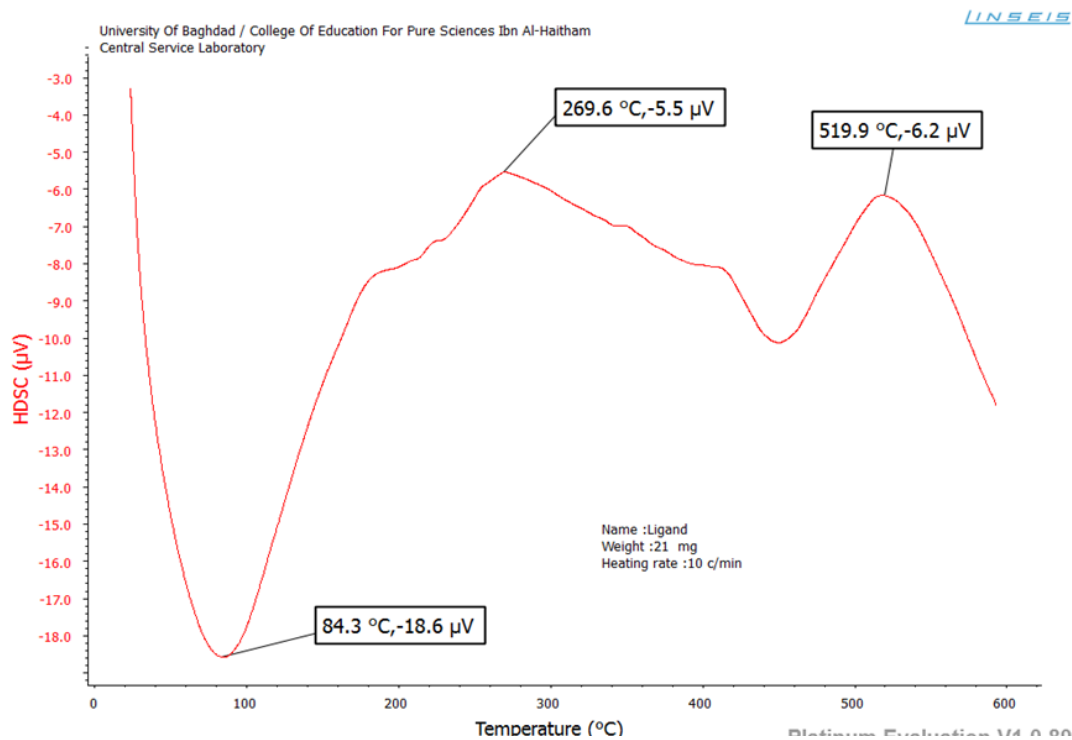
Figure 11: DSC thermogram of an argon atmosphere [L1].
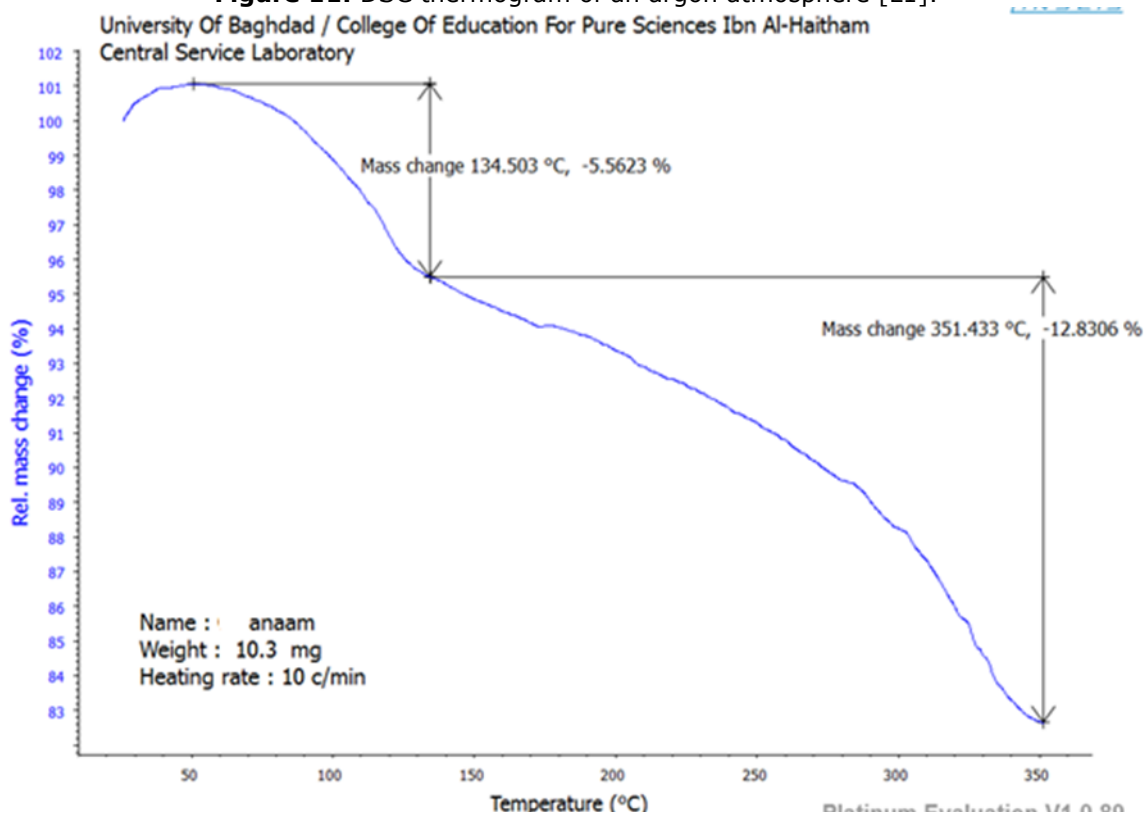
Figure 12: TG thermogram of an argon atmosphere [Mn (L1)]Cl$_2$.
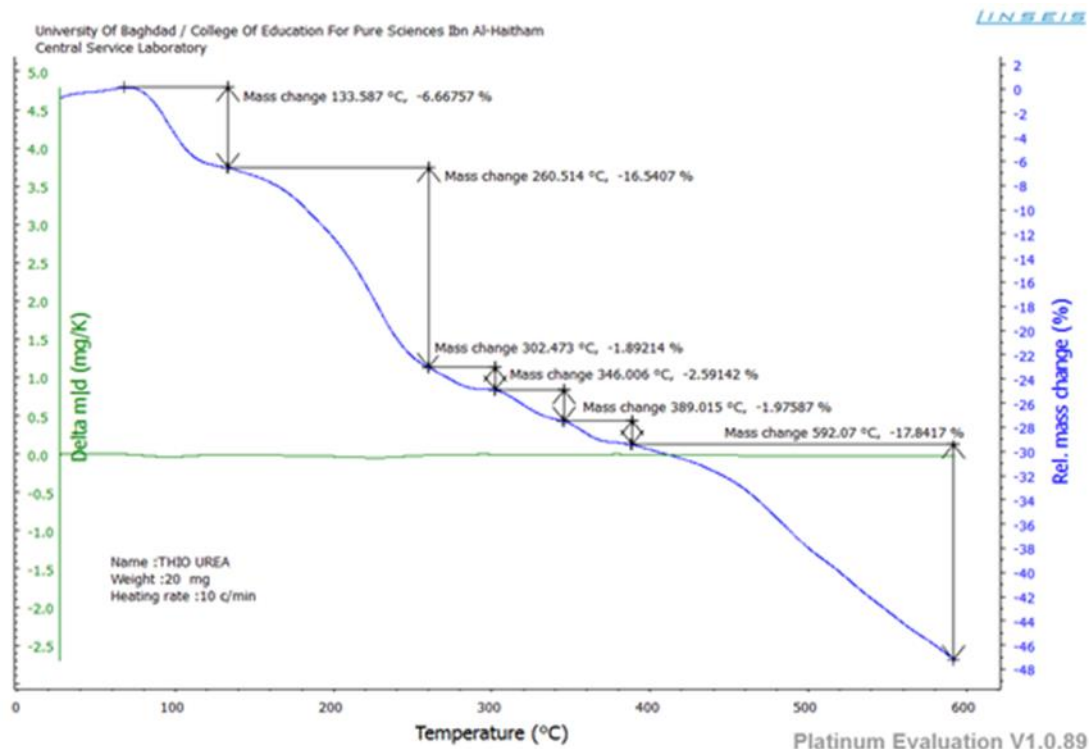
Figure 13: TG thermogram of an argon atmosphere $[Fe(L1)_2]Cl_3$.
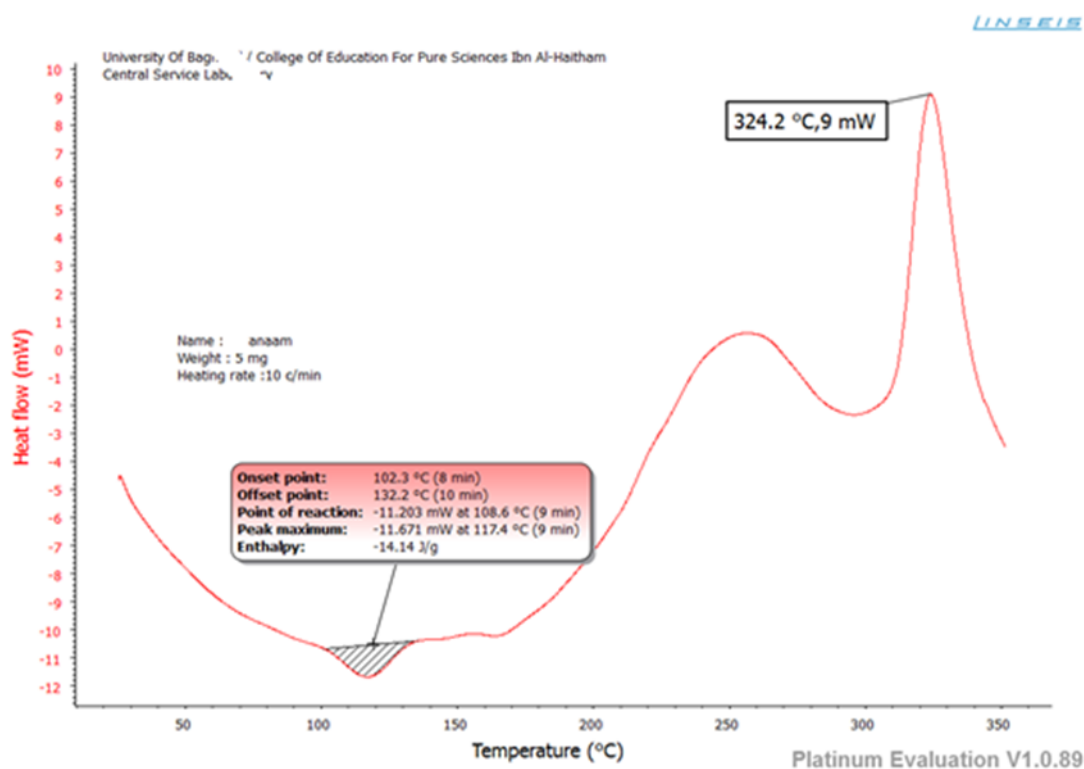
Figure 14: DSC thermogram of $[VO (L1) H_2O]Cl_2$ in argon atmosphere.

3.6. Study of Biological Activities for Ligands (L1, L2) and its Metal Antimicrobial Study

The ligands L1 and L2 and their complexes were tested *in vitro* for its capability to inhibit the growth of typical microorganisms *Pseudonomonas aerugionosa* and *Bacillus subtilis* (26). Also, it was tested against *Aspergillus flavus* and *Saccharomyces cerevisiae* fungi in DMSO as a blank solvent, (see Table 4). According to the data obtained, it can be summarized as the following:

1) L1 has high activity against both kinds of bacteria compared with activity of L2.
2) All corresponding complexes of L1 and L2 exhibited higher activity against both kinds of bacteria than the free ligands' activity (see Table 4).
3) The activity of the antifungal findings for all complexes revealed that the complexes of L1 were more toxic than complexes bearing L2, as

well as that the metal ion chelates of L1 and L2 ligands were highly toxic compared to their free ligands L1 and L2 against the same

microorganisms and under the same investigational conditions (18, 27).

Table 4: Antimicrobial activities of new ligands L1 and L2 and its metal complexes.

Compound	Pseudonomous aerugionosa	Bacillus subtilis	Saccharomyces cerevisiae	Aspergillus flavus
Control DMSO	-	-	-	-
(L1)	4	4	30	38
(L2)	-	-	43	40
VOL1	6	12	25	31
VOL2	4	6	32	39
FeL1	8	10	28	33
FeL2	4	8	38	42
MnL1	8	6	29	33
MnL2	6	4	32	40

Where:
6-8 (+)
8-10 (++)
>10 (+++)

Where:
30-40 (+++)
20-30 (++++)
10-20 (++++)

4. CONCLUSION

In conclusion, new complexes were synthesized and characterized by spectroscopic and analytical methods. The results showed that both new synthesized ligands coordinated with ion metals via three chelating atoms (NOO). Also, it was demonstrated that V(IV) complexes have a square pyramidal structure with a ratio of (1:1, M:L), while other complexes showed a octahedral configuration around Fe(III) and Mn(II) with a ratio of (1:2, M:L). Biological results confirmed that all ligands and their corresponding complexes were tested against some bacteria and fungi and exhibited low toxic activity by ligands L1 and L2, while their corresponding complexes with L1 exhibited highly toxic activity compared to their complexes with L2, so these complexes can be candidates to be antiviral or antibacterial agents.

5. CONFLICT OF INTEREST

The authors declare no conflicts of interest.

6. ACKNOWLEDGMENTS

7. REFERENCES

1. Ahmad F, Idris MHS, Adib AM. Synthesis and characterization some flavonoids derivatives [Internet]. Research Vote: 75148. Malaysia; 2006 [cited 2023 Nov 6]. Available from: <URL>.

2. Alajrawy OI. Synthesis and characterization of vanadium (IV) and (V) complexes with 2, 2`-bipyridine ligand. 2019;

3. Patil SA, Kandathil V, Sobha A, Somappa SB, Feldman MR, Bugarin A, et al. Comprehensive Review on Medicinal Applications of Coumarin-Derived Imine–Metal Complexes. Molecules [Internet]. 2022 Aug 16;27(16):5220. Available from: <URL>.

4. Hamid SJ, Salih T. Design, Synthesis, and Anti-Inflammatory Activity of Some Coumarin Schiff Base Derivatives: In silico and in vitro Study. Drug Des Devel Ther [Internet]. 2022 Jul;16:2275–88. Available from: <URL>.

5. Melagraki G, Afantitis A, Igglessi-Markopoulou O, Detsi A, Koufaki M, Kontogiorgis C, et al. Synthesis and evaluation of the antioxidant and anti-inflammatory activity of novel coumarin-3-aminoamides and their alpha-lipoic acid adducts. Eur J Med Chem [Internet]. 2009 Jul 1;44(7):3020–6. Available from: <URL>.

6. Sahoo S, Himanshu D, Sahoo B, Sahoo SS, Shukla S, Nandy S, et al. Synthesis of novel coumarin derivatives and its biological evaluations. Eur J Exp Biol [Internet]. 2012;2(4):899–908. Available from: <URL>.

7. Bader AT, Al-qasii NAR, Shntaif AH, El Marouani M, AL Majidi MIH, Trif L, et al. Synthesis, Structural Analysis and Thermal Behavior of New 1,2,4-Triazole Derivative and Its Transition Metal Complexes. Indones J Chem [Internet]. 2022 Dec 28;22(1):223–32. Available from: <URL>.

8. Shaban S, baghi hamza, Shafek S, zein nabila, Aiad I, Omran M. Synthesis and characterization of new 1,2,4-triazole anticancer scaffold derivatives: In Vitro study. Egypt J Chem [Internet]. 2021 Mar 31;64(8):4005–15. Available from: <URL>.

9. Ndahi NP, Garba H, Waziri I, Osunlaja AA, Putaya HAN. Complexes of Mn(II) and Fe (III) with Schiff bases Derived from Trimethoprim with Salicyldehyde and Benzaldehyde as Potential Antimicrobial Agents. Niger J Pharm Biomed Res [Internet]. 2018;3(1):53–9. Available from: <URL>.

10. Al-Warhi T, Sabt A, Elkaeed EB, Eldehna WM. Recent advancements of coumarin-based anticancer agents: An up-to-date review. Bioorg Chem [Internet]. 2020 Oct 1;103:104163. Available from: <URL>.

11. Sumrra SH, Ramzan S, Mustafa G, Ibrahim M, Mughal EU, Nadeem MA, et al. Complexes of Imino-1,2,4-triazole Derivative with Transition Metals: Synthesis and Antibacterial Study. Russ J Gen Chem [Internet]. 2018 Aug 16;88(8):1707–11. Available from: <URL>.

12. Bagihalli GB, Avaji PG, Patil SA, Badami PS. Synthesis, spectral characterization, in vitro antibacterial, antifungal and cytotoxic activities of Co(II), Ni(II) and Cu(II)

complexes with 1,2,4-triazole Schiff bases. Eur J Med Chem [Internet]. 2008 Dec 1;43(12):2639–49. Available from: <URL>.

13. Singh MS, Chowdhury S, Koley S. Advances of azide-alkyne cycloaddition-click chemistry over the recent decade. Tetrahedron. 2016 Sep;72(35):5257–83.

14. Ismail AH, Al-Bairmani HK, Abbas ZS, Rheima AM. Synthesis, Characterization, Spectroscopic and Biological Studies of Zn(II), Mn(II) and Fe(II) Theophylline Complexes in Nanoscale. Nano Biomed Eng [Internet]. 2020 Sep 18;12(3):253–61. Available from: <URL>.

15. Knittl ET, Abou-Hussein AA, Linert W. Syntheses, characterization, and biological activity of novel mono- and binuclear transition metal complexes with a hydrazone Schiff base derived from a coumarin derivative and oxalyldihydrazine. Monatshefte für Chemie - Chem Mon [Internet]. 2018 Feb 27;149(2):431–43. Available from: <URL>.

16. Shukla SN, Gaur P, Raidas ML, Chaurasia B, Bagri SS. Novel NNO pincer type Schiff base ligand and its complexes of Fe(IIl), Co(II) and Ni(II): Synthesis, spectroscopic characterization, DFT, antibacterial and anticorrosion study. J Mol Struct [Internet]. 2021 Sep 15;1240:130582. Available from: <URL>.

17. Patil SA, Prabhakara CT, Halasangi BM, Toragalmath SS, Badami PS. DNA cleavage, antibacterial, antifungal and anthelmintic studies of Co(II), Ni(II) and Cu(II) complexes of coumarin Schiff bases: Synthesis and spectral approach. Spectrochim Acta Part A Mol Biomol Spectrosc [Internet]. 2015 Feb 25;137:641–51. Available from: <URL>.

18. Al-Zaidi BH, Hasson MM, Ismail AH. New complexes of chelating Schiff base: Synthesis, spectral investigation, antimicrobial, and thermal behavior studies. J Appl Pharm Sci [Internet]. 2019 Apr;9(4):45–57. Available from: <URL>.

19. Priya B, Kumar A, Sharma N. Synthesis, Characterisation, and Biological Properties of Oxidovanadium(IV) 3,5-Dinitrosalicylhydroxamate Complexes. Aust J Chem [Internet]. 2020;73(1):61–72. Available from: <URL>.

20. Al-Hasani RAM, Rasheed AM, AL-bayati SM. Synthesis, Characterization and Bioactivities of V(III), Cr(III), Fe(III), Rh(III) and Al(III) Complexes with Bis(Salicylaldehyde)MalonylDihydrazone and 8-HydroxyQuinoline as Mixed Ligands. Iraqi Natl J Chem [Internet]. 2016;16(3):127–42. Available from: <URL>.

21. Akkasali R, Patil N, Angadi SD. Synthesis, Characterization and Microbial Activities of Metal Complexes with Coumarine Derivatives. Rasayan J Chem [Internet]. 2009;2(1):81–6. Available from: <URL>.

22. Yaul SR, Yaul AR, Pethe GB, Aswar AS. Synthesis and characterization of transition metal complexes with N, O-chelating hydrazone Schiff base ligand. Am J Sci Res [Internet]. 2009;4(4):229–34. Available from: <URL>.

23. Martínez RF, Ávalos M, Babiano R, Cintas P, Light ME, Jiménez JL, et al. Hydrazones from hydroxy naphthaldehydes and N-aminoheterocycles: structure and stereodynamics. Tetrahedron [Internet]. 2011 Mar 18;67(11):2025–34. Available from: <URL>.

24. Golcu A, Tumer M, Demirelli H, Wheatley RA. Cd(II) and Cu(II) complexes of polydentate Schiff base ligands: synthesis, characterization, properties and biological activity. Inorganica Chim Acta [Internet]. 2005 Mar 30;358(6):1785–97. Available from: <URL>.

25. Puckett CA, Ernst RJ, Barton JK. Exploring the cellular accumulation of metal complexes. Dalt Trans [Internet]. 2010 Jan 19;39(5):1159–70. Available from: <URL>.

26. Alazawi SM, Rasheed AM, Al-Bay SM, Abed AH. Synthesis, Spectral and Biological Studies of New 2-amino-3-cyanopyridine Derivatives and Their Transition Metals Complexes. Egypt J Chem [Internet]. 2021 Mar 15;64(6):2937–44. Available from: <URL>.

27. Al-Bayati S, Rasheed A, Zuhair E, Abid K, Khamis W. Synthesis and Spectroscopic Studies of New Alkoxy Schiff Base Complexes Based on Coumarin Moiety. Am J Chem [Internet]. 2018;8(1):1–7. Available from: <URL>.

Sorption Behaviors of Amorphous Titanium Phosphate Towards Neodymium and Dysprosium

Süleyman İnan[1]*

[1]Ege University, Institute of Nuclear Sciences, Bornova-İzmir, 35100, Türkiye

Abstract: Due to the limited supply of critical metals, their recovery from alternative sources has become a very important issue. In particular, end-of-life magnets contain significant amounts of neodymium (Nd) and dysprosium (Dy) ions and are considered secondary sources. The present study focused on the sorption and separation performance of titanium phosphate for Nd and Dy ions in an aqueous solution. In this regard, amorphous titanium phosphate (am-TiP) was prepared via one-step precipitation. XRD, SEM-EDS, FTIR, and BET analysis were utilized to enlighten the morphological, structural, and surface properties of am-TiP. The uptake of Nd^{3+} and Dy^{3+} ions was examined individually and in multiple element solutions depending on solution pH, contact time, metal concentration, and the presence of Co^{2+} ions. The maximum uptake capacity was 40.16 mg/g at pH 6 for Nd^{3+} and 26.95 mg/g at pH 4 for Dy^{3+}. Am-TiP has been observed to exhibit selectivity towards Nd^{3+} and Dy^{3+} ions in solutions containing Co^{2+} ions. The highest desorption yields obtained for Nd^{3+} and Dy^{3+} using 1.0 mol/L HCl were 95.2% and 97.4%, respectively.

1. INTRODUCTION

The group of metals known as Rare Earth (RE) metals, also called the rare-earth elements (REE), is composed of 15 elements that are located between lanthanum and lutetium on the periodic table. RE metals are used in hybrid vehicles, electric vehicles, wind turbines, solar panels, MR machines, and green energy technologies. Many high-end products such as LCD-LED TVs, magnets, rechargeable batteries, digital cameras, and mobile phones include RE metals (1,2).

Neodymium (Nd) has found various applications in different industries. It has been utilized as a coloring agent in glass production and as a component in laser crystals and welding goggles. However, its most widespread usage is in the production of permanent magnets, which are commonly used in wind turbines, electric motors, and computer hard drive spindles. Dysprosium (Dy), another critical rare-earth metal, is currently used for various applications. It is added to neodymium, iron, and

boron (NdFeB) containing magnets as an additive to enhance their high-temperature performance and increase their intrinsic coercivity. Dy is a valuable material in the nuclear sector, where it is commonly used as a radiation shielding component. Additionally, phosphors that contain Dy are employed as radiation detectors in the monitoring of ionizing radiation for clinical and environmental purposes (3).

Nd is a crucial component in the production of neodymium magnets, In addition to Nd and praseodymium (Pr), terbium (Tb) and Dy are essential constituents of Nd magnets, as they enhance their intrinsic coercivity. Nd magnets can contain up to 9% Dy by weight of the total magnet. Both the U.S. DOE and the European Commission have classified Dy and Nd as "critical materials" due to their crucial role in technology and the challenges in their supply (4).

The demand for RE metals is growing with the development industry. In this context, in addition

to primary sources, end-of-life magnets are considered as an alternative source for Nd and Dy supply. NdFeB magnets are a prominent type of magnet known for their high content of RE elements. These magnets typically contain around 31-32% of RE elements, which includes 21-31% of Nd and Pr, as well as 0-10% of Dy, along with minor amounts of Tb and Gd. Additionally, they can also contain up to 5% of cobalt (Co). After their service life has ended, these magnets can be a valuable source of RE elements (5,6). Recycling RE elements can offer a promising and efficient approach to solving the supply problem and environmental concerns related to primary resources such as mining.

Due to its simplicity and effectiveness, sorption is widely utilized for metal recovery and separation. Various materials have been tested for the sorption of Nd^{3+} and Dy^{3+} such as magnetic iron oxide (7), chitosan-manganese-ferrite beads (8), magnetic nano-hydroxyapatite (9), phosphorous functionalized nanoporous carbon (10), biochar (11), NaOH treated bark powder (12), and functionalized mesoporous silica (13).

The separation and recovery of RE metals have recently attracted attention with the use of tetravalent metal phosphate compounds. Avdibegovic et al. reported the ability of crystalline α-zirconium phosphate to effectively separate scandium (Sc) ions from acidic solutions containing iron (Fe) ions. They were successful in achieving high separation factors for Sc(III) over Fe(III) in hydrochloric acid solutions. This finding highlighted the potential of the material for Sc(III) separation (14). Promising results were obtained by Xu et al. for the recovery of metals individually from the Co, Nd, and Dy-bearing mixed solutions using zirconium phosphates (15,16). Recently, Sentürk and İnan have reported that amorphous tin(IV) phosphate has a selectivity for Nd^{3+} and Dy^{3+} in Co^{2+}-bearing solutions (17).

Although there is a growing demand for alternative materials that can efficiently and selectively separate and recover Nd and Dy from acidic leaching solutions, the reported use of metal(IV) phosphate compounds in this field is scarce. With this study, the potential application of am-TiP in the separation and recovery of Nd^{3+} and Dy^{3+} was investigated for the first time, as displayed in Figure 1.
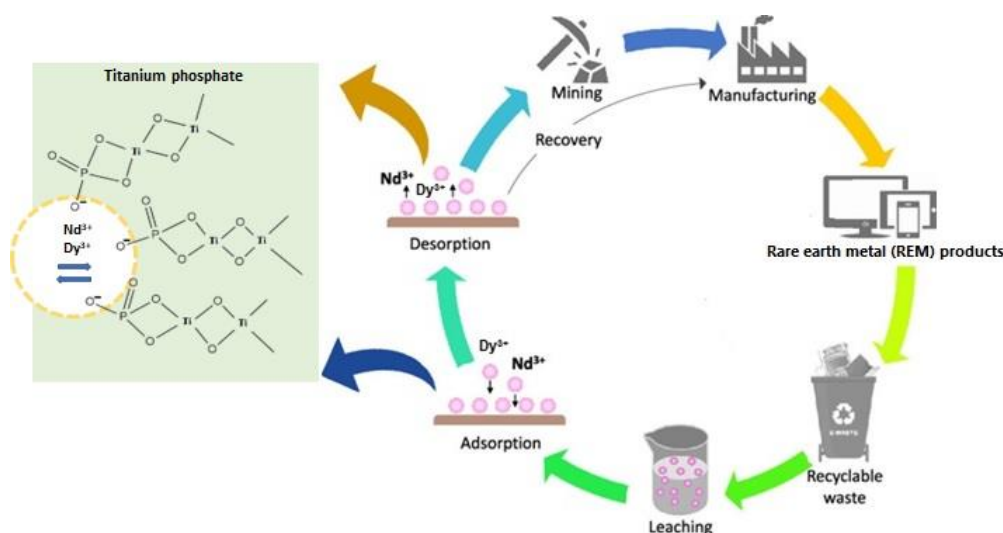
Figure 1: The use of am-TiP for the selective recovery of Nd^{3+} and Dy^{3+} via the sorption-desorption process.

To achieve this goal, am-TiP was prepared and characterized. The impact of process variables on Nd^{3+} and Dy^{3+} uptake was explored. Moreover, the capacity and selectivity of am-TiP were determined in mixed solutions of Nd^{3+}, Dy^{3+}, and Co^{2+} ions. Desorption and reusability studies were carried out to recover Nd^{3+} and Dy^{3+} from loaded am-TiP samples and to evaluate the process from an economic point of view.

2. EXPERIMENTAL SECTION

2.1. Chemicals
Titanium(IV) chloride ($TiCl_4$), sodium hydrogen phosphate (Na_2HPO_4), neodymium(III) nitrate-hexahydrate ($Nd(NO_3)_3 \cdot 6H_2O$), dysprosium(III) nitrate hydrate ($Dy(NO_3)_3 \cdot H_2O$), cobalt(II) nitrate

hexahydrate ($Co(NO_3)_2 \cdot 6H_2O$), nitric acid (HNO_3), sulfuric acid (H_2SO_4), hydrochloric acid (HCl) and ammonia (NH_3) were of analytical grade and supplied from Sigma Aldrich.

2.2. Instrumentation
To determine the crystalline structure, X-ray diffraction (XRD) pattern was recorded in the range of 5°-80° (Thermo Scientific). Chemical bonds and functional groups were identified by Fourier-Transform-Infrared-Spectroscopy (FTIR) in the range of 400-4000 cm^{-1} with an Attenuated Total Reflectance (ATR) apparatus (Perkin Elmer). Surface properties of am-TiP were determined by nitrogen gas adsorption in liquid nitrogen temperature using surface area and porosity analyzer (Micromeritics). The morphology of the surface and

data on the elemental composition was obtained by Scanning Electron Microscope (SEM) equipped with an Energy Dispersive Spectroscopy (EDS) detector (Thermo Scientific Apreo S). The amounts of Nd^{3+}, Dy^{3+}, and Co^{2+} in the solution were analyzed using Inductively Coupled Plasma-Optical Emission Spectroscopy (ICP-OES) (Perkin Elmer).

2.3. Synthesis of Am-TiP

The synthetic method used involved a one-step precipitation process conducted under acidic conditions. Specifically, 0.25 mol/L $TiCl_4$ was added dropwise to 0.25 mol/L Na_2HPO_4 solution under constant stirring at ambient conditions. The resulting mixture was allowed to age overnight, leading to the formation of the white gel-like precipitate.

Following the precipitation step, solid-liquid separation was accomplished through centrifugation at 4000 rpm (Nüve NF 800). The resulting filtrate was then subjected to multiple washings using deionized water and followed by drying at 55 °C for 72 h. The resulting material was ground using a mortar and then sifted using a 120-mesh (0.125 mm) sieve to achieve a grain size suitable for use in sorption tests.

2.4. Design of Experiments

The sorption capacity of am-TiP was evaluated by conducting experimental runs using the batch method at ambient temperature. To perform the experiments, an Erlenmeyer flask was charged with 0.1 g of am-TiP, and then 30 mL of an aqueous phase was introduced. The impact of various factors on the sorption process was investigated through the alteration of selected variables. Solution pH was adjusted to either 0.01-1 mol/L HNO_3 or NH_3. The sorption process was performed by contacting am-TiP with the aqueous phase in a thermostated shaker at 130 rpm. Once the sorption was complete, the suspension was filtered, and 10 mL of filtrate was collected from each sample. The concentration of Nd^{3+} and Dy^{3+} was analyzed using ICP-OES.

The impact of individual factors on the sorption of Nd^{3+} and Dy^{3+} was analyzed in single-element solutions. Initial pH was studied between pH 2 and 6. The contact time varied between 30 to 480 min. Isotherm studies were conducted using solutions containing 10 to 400 mg/L Nd^{3+} and Dy^{3+}.

In multi-element solutions, the influence of metal concentration and pH on the uptake of Nd^{3+}, Dy^{3+}, and Co^{2+} was evaluated by distribution coefficient (K_d) and selectivity coefficient (β). The effect of concentration was examined in equimolar Nd^{3+}, Dy^{3+}, and Co^{2+}-containing solutions over a concentration range of 0.075-1.2 mmol/L at pH 6.

Then, the impact of initial pH was studied in solutions containing Nd^{3+}, Dy^{3+}, and Co^{2+} at an equimolarity of 0.3 mmol/L over a pH range of 2-6.

Sorption characteristics were calculated using the following equations:
Distribution coefficient (K_d)

$$K_d = \frac{(C_i - C_e)}{C_e} \times \frac{V}{m} \, (mL/g)$$

Sorption capacity (q)

$$q = (C_i - C_e) \times \frac{V}{m} \, (mg/g) \qquad \text{(Eq. 2)}$$

Selectivity coefficient (β)

$$\beta_{1/2} = \frac{K_{d1}}{K_{d2}} \qquad \text{(Eq. 3)}$$

In Eqs. (1-3), K_d is the distribution coefficient (mL/g), β is the selectivity coefficient, K_{d1} and K_{d2} are the distribution coefficients of metal ion 1 and metal ion 2, respectively. C_i and C_e refer to concentration at initial and equilibrium conditions (mg/L), V refers to volume (mL), and m refers to the mass of am-TiP (g).

3. RESULTS AND DISCUSSION

3.1. Characterization of Am-TiP

No significant changes were observed in the FTIR spectra of am-TiP and metal-loaded am-TiP. Therefore, the only spectrum for am-TiP is given in Figure 2a. The presence of the sharp peak at 1035 cm^{-1} indicates the formation of the phosphate structure, as it corresponds to the asymmetric stretching vibration of Ti-O-P. Additionally, the asymmetrical stretching and bending vibrations of O-H are responsible for the peaks observed at 3400 and 1630 cm^{-1} (18).

The surface area and pore structure of am-TiP were evaluated using the BET and Barrett-Joyner-Halenda (BJH) techniques, respectively. BET surface area of am-TiP was measured as 170 m^2/g. BJH analysis showed that the mean pore diameter was 8.2 nm, indicating that the surface of am-TiP is primarily composed of mesopores. The XRD pattern presented in Figure 2b demonstrates that TiP has an amorphous structure. SEM images displayed in Figure 2(c-d) exhibit an irregular morphology and porous structure on the surface. EDS analysis of the surface pattern indicates that it contains 53.62% oxygen, 19.80% phosphorus, and 26.58% titanium by weight, as illustrated in Figure 2e.
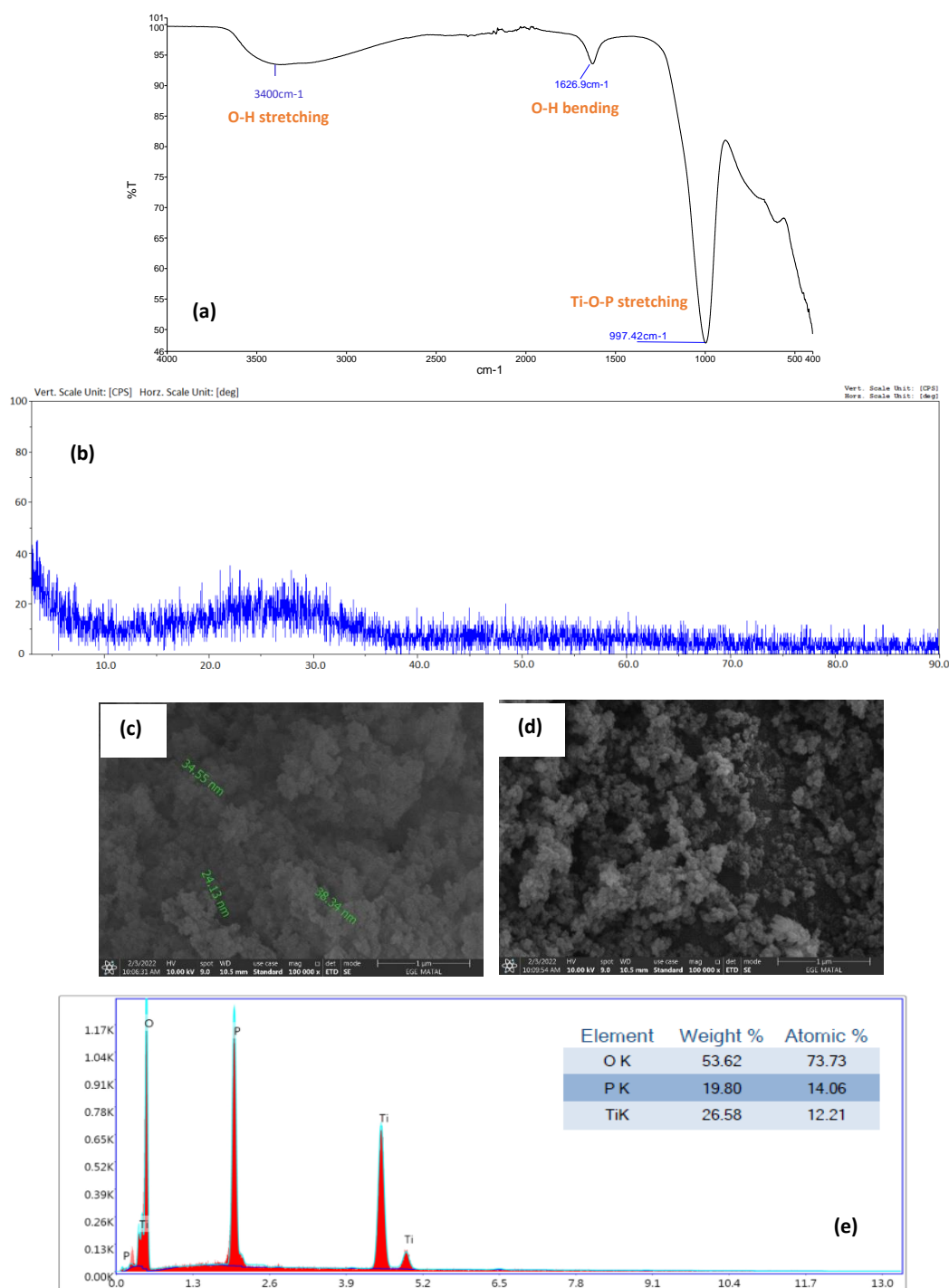
Figure 2: Characterization of am-TiP (a) FTIR spectra, (b) XRD curve, (c-d) SEM images, (e) EDS data.

3.2. Uptake Studies of Nd^{3+} and Dy^{3+} in Single-Element Solutions

3.2.1. The impact of initial pH

The effectiveness of an adsorbent can be affected by the pH level as it can alter the surface charge, ionization degree, and the speciation of the adsorbate. At a pH below the zero-charge point, the surface is likely to carry a positive charge which can lead to a significant decrease in metal adsorption due to the repulsion of metal cations. Additionally, competition occurs between metal ions and H^+ at low pH levels.
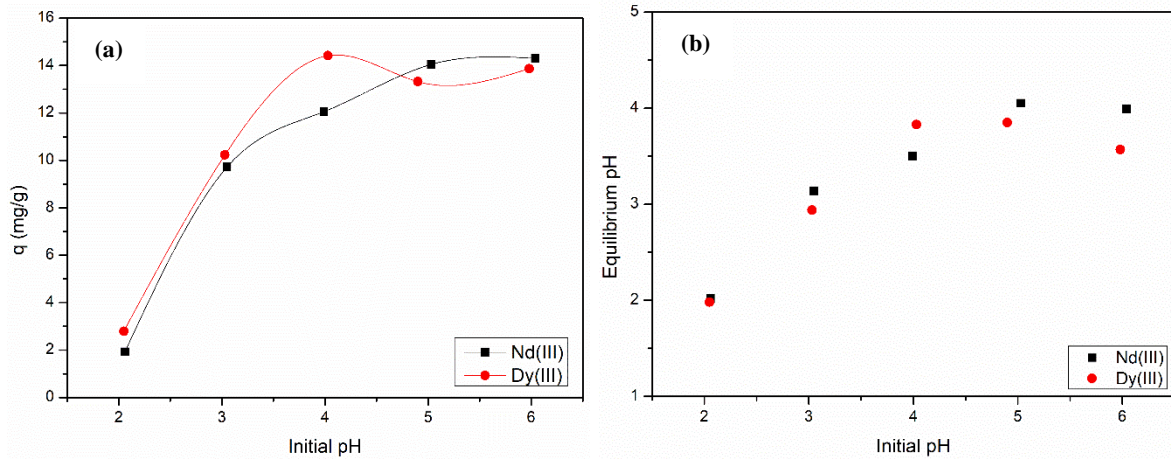
Figure 3: (a) The change in uptake capacity (q) as a function of initial pH, (b) the relationship between equilibrium pH and initial pH.
(Experimental conditions; C_i: 50 mg/L, t: 3 h, T: 25 °C, m_{am-TiP}: 0.1 g, V: 30 mL)

The impact of the initial pH on the sorption was examined in an acidic to neutral medium since leach solutions originating from the hydrometallurgical process have an acidic character. As shown in Figure 3a, increasing the pH from 2 to 5 resulted in a rise in Nd^{3+} adsorption from 1.93 to 14.05 mg/g. However, the rate of increase in adsorption capacity decreased significantly after reaching a maximum and became almost constant. On the other hand, Dy^{3+} uptake sharply increased between pH 2-4 and peaked at 14.42 mg/g at pH 4, followed by a slight decrease in capacity and a tendency to remain constant after pH 4 (Figure 3a). These trends for both RE metals are further confirmed by the plot in Figure 3b.
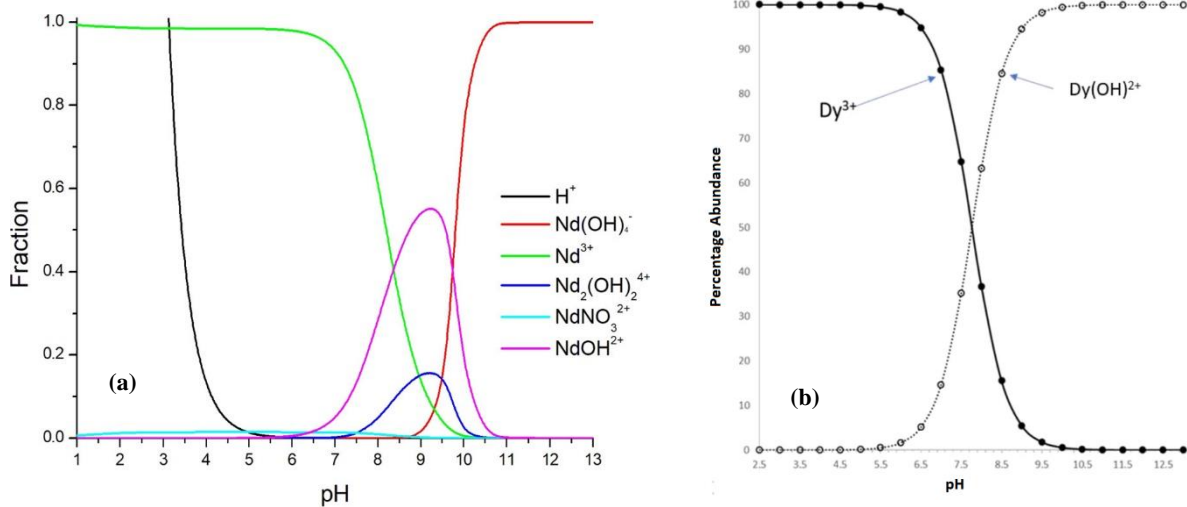
Figure 4: The fraction of (a) neodymium (19) and, (b) dysprosium (20) species as a function of pH.

The highest Nd^{3+} and Dy^{3+} uptake occurred with the range of pH 4.0-6.0 (Figure 3a) due to the reduced effect of hydrogen ions competition, which is confirmed by the speciation of neodymium and dysprosium ions (Figures 4a and 4b). According to Figures 4a and 4b, the trivalent form of Nd (Nd^{3+}) and Dy (Dy^{3+}) was predominant in the studied pH range.

3.2.2. The impact of contact time

The uptake of Nd^{3+} and Dy^{3+} was examined for 15-360 min while fixing the other factors constant. Figure 5 displays the impact of contact time on the sorption capacity of am-TiP for Nd^{3+} and Dy^{3+}. In both cases, there was a slight increase in uptake capacity with the increasing contact time, which then plateaued. For both ions, 60 min was determined to reach the equilibrium conditions, and further investigation was carried out for 60 min.
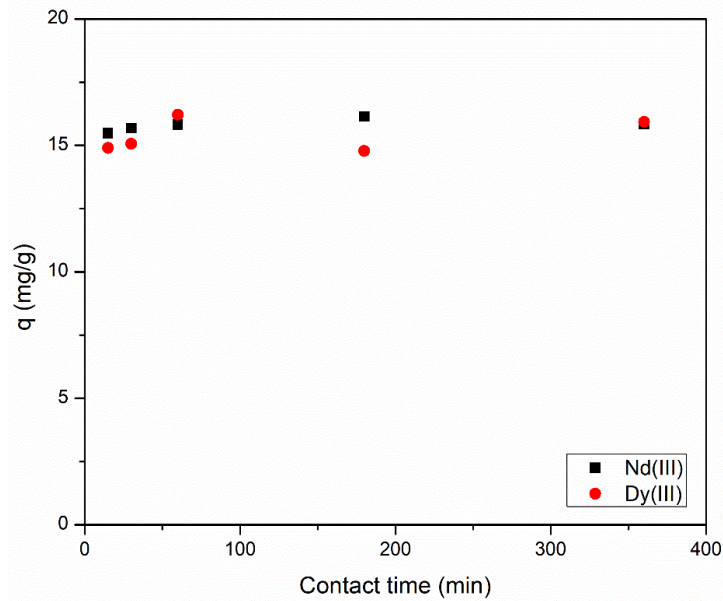
Figure 5: The change in uptake capacity (q) as a function of contact time.
(Experimental conditions: Nd^{3+}, pH: 6; Dy^{3+} pH: 4; C$_i$: 50 mg/L; T: 25 °C; m$_{am-TiP}$: 0.1 g; V: 30 mL)

3.2.3. The impact of metal concentration and isotherm studies
The impact of the initial metal concentration was explored by analyzing solutions with concentrations ranging from 10 to 400 mg/L. Figure 6 shows that the uptake of Nd^{3+} and Dy^{3+} increases as the concentration increases, and the maximum saturation capacity for the material has not been reached in the examined range.
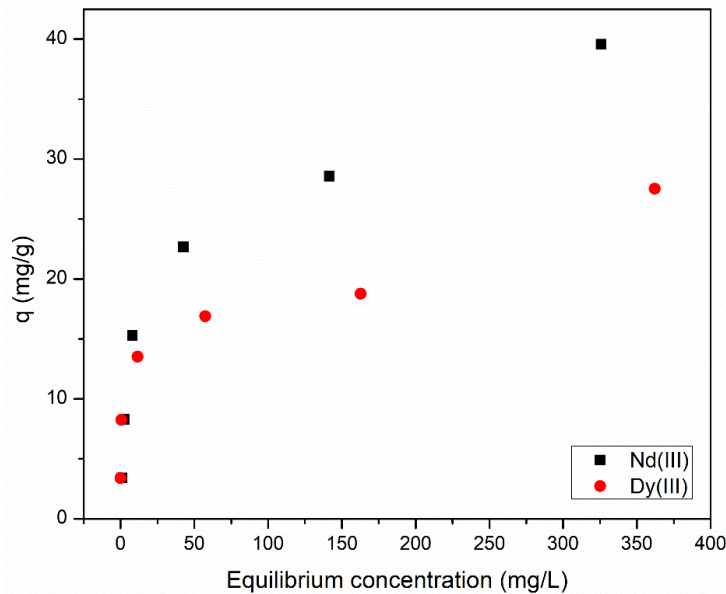
Figure 6: The change in uptake capacity (q) as a function of Nd^{3+} and Dy^{3+} concentrations.
(Experimental conditions; Nd^{3+}, pH: 6; Dy^{3+}, pH: 4; t: 60 min; T: 25 °C; m$_{am-TiP}$: 0.1 g; V: 30 mL)

The adsorption process is characterized by sorption isotherms. The data obtained from the sorption isotherms were analyzed employing Freundlich and Langmuir models. The Langmuir model assumes that the sorbate molecules form a monolayer on the surface of the sorbent, occupying specific homogeneous sites. The Langmuir equation is commonly linearized as follows (21):

$$\frac{C_e}{q_e} = \frac{C_e}{q_m} + \frac{1}{q_m b} \qquad \text{(Eq.4)}$$

where q$_e$ refers to the amount of metal ion sorbed at equilibrium (mg/g), C$_e$ refers to the concentration of a metal ion at equilibrium (mg/L), q$_m$ refers to monolayer sorption capacity (mg/g) and b refers to constant related to the free energy of sorption (L/g). Based on the data presented in Figure 7a and Table 1, it can be concluded that the Langmuir model fits the experimental data quite well for the sorption of both ions. It suggests that sorption on the surface occurs as a monolayer coverage.

118
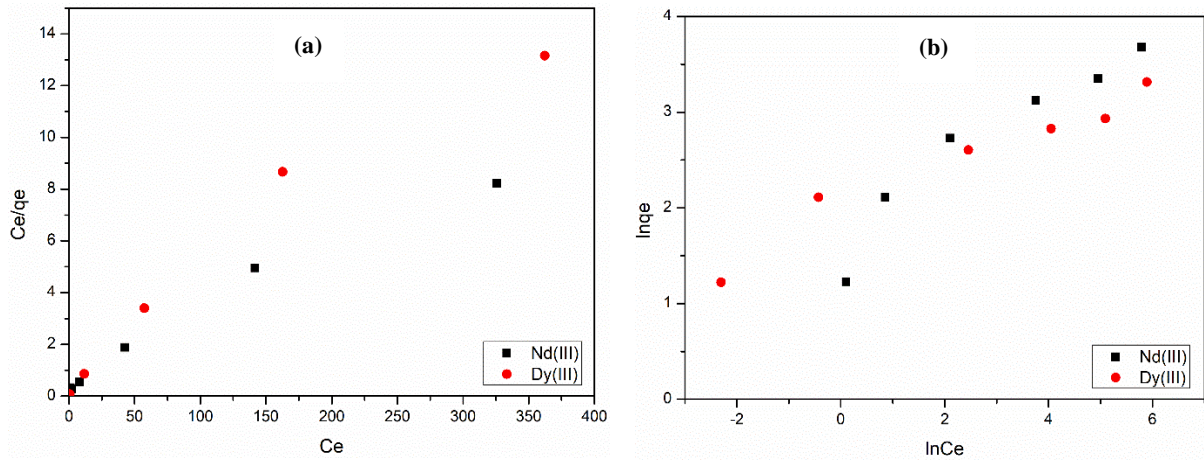
Figure 7: Sorption isotherm curves for Nd^{3+} and Dy^{3+} sorption on am-TiP (a) Langmuir isotherm, (b) Freundlich isotherm.

Table 1: Langmuir and Freundlich isotherm data.

Model	Parameters	Nd^{3+}	Dy^{3+}
Langmuir	q_m (mg/g)	40.16	26.95
	b (L/mg)	0.05	0.05
	R^2	0.976	0.959
Freundlich	1/n	0.38	0.22
	K_f (mol/g)	4.92	7.04
	R^2	0.913	0.946

Table 2: Nd and Dy adsorption performance of various adsorbents.

Sorbent	Rare earth metal	pH	Maximum capacity (mg/g)	Ref
Magnetic iron oxide	Nd^{3+}	8.2	24.88	(7)
Chitosan-manganese-ferrite beads	Nd^{3+}	6	37.87	(8)
Phosphorous functionalized nanoporous carbon	Dy^{3+}	6.6	344.6	(10)
HMVP supported mesoporous silica	Dy^{3+}	5	52.63	(13)
Amorphous tin phosphate (am-SnP)	Nd^{3+} Dy^{3+}	4 3	68.03 58.14	(17)
Expanded vermiculite	Nd^{3+}	3.3	29.57	(19)
Phosphorus functionalized adsorbent	Nd^{3+}	6	160	(23)
Ion-imprinted mesoporous silica	Dy^{3+}	2	22.33	(24)
Oxidized MWCN	Dy^{3+}	4-6	78	(25)
Amorphous titanium phosphate (am-TiP)	Nd^{3+} Dy^{3+}	6 4	40.16 26.95	Present study

The Freundlich model (22) describes multilayer sorption on heterogeneous surfaces, and the equation can be linearized as follows:

$$lnq_e = lnK_f + \frac{1}{n}lnC_e \qquad \text{(Eq. 5)}$$

In Eq. (5), K_f refers to a constant related to the sorption capacity (mol/g) and $1/n$ refers to a parameter dependent on the sorption intensity. The sorption data of Nd^{3+} and Dy^{3+} were found to fit the Freundlich model well, as indicated by the data presented in Table 1 and Figure 7b. K_f and $1/n$ values are calculated to be 4.92 and 0.38 for Nd^{3+} and 7.04 and 0.22 for Dy^{3+}, respectively. The obtained values of $1/n$ between 0 and 1 indicate that the sorption of Nd^{3+} and Dy^{3+} onto am-TiP is favorable under the tested conditions.

Table 2 presents a compilation of prior research on Nd^{3+} and Dy^{3+} sorption. The sorption capacity of am-TiP is competitive with other adsorbents in the slightly acidic-neutral region. Furthermore, its simple synthesis procedure is noteworthy. However, the sorption capacity in more acidic environments can be further improved by modification and functionalization.

3.3.   Uptake Studies of Nd^{3+} and Dy^{3+} in Ternary Solutions

Efficient recycling of Nd^{3+} and Dy^{3+} ions require selective separation from leachate solutions in the presence of Co^{2+} ions. Experiments were performed to determine the K_d values by utilizing ternary solutions consisting of Nd^{3+}, Dy^{3+}, and Co^{2+} at equimolar concentrations between 0.075-1.2 mmol/L.

Figure 8a illustrates the relationship between the K_d values and the initial metal concentration. K_d values decrease as the initial metal concentration increases from 0.075 to 1.2 mmol/L. In particular, the maximum K_d values observed were 2716.01 mL/g for Nd^{3+}, 8600.8 mL/g for Dy^{3+}, and 159.92 mL/g for Co^{2+}. The variation of $\beta_{Nd^{3+}/Co^{2+}}$, $\beta_{Dy^{3+}/Co^{2+}}$, and $\beta_{Nd^{3+}/Dy^{3+}}$ as a function of initial concentration is shown in Figure 8b. It was inferred that am-TiP can selectively separate Nd^{3+} and Dy^{3+} from Co^{2+} across all concentrations examined. The maximum $\beta_{Nd^{3+}/Co^{2+}}$ value obtained was 20.04 at 0.15 mmol/L initial concentration, whereas the maximum $\beta_{Dy^{3+}/Co^{2+}}$ value was found to be 53.78 at 0.075 mmol/L. Due to the structural similarities between Nd^{3+} and Dy^{3+}, the selectivity coefficient values of Nd^{3+} over Dy^{3+} were below 2, indicating that individual separation conditions for Nd^{3+} and Dy^{3+} should be improved.
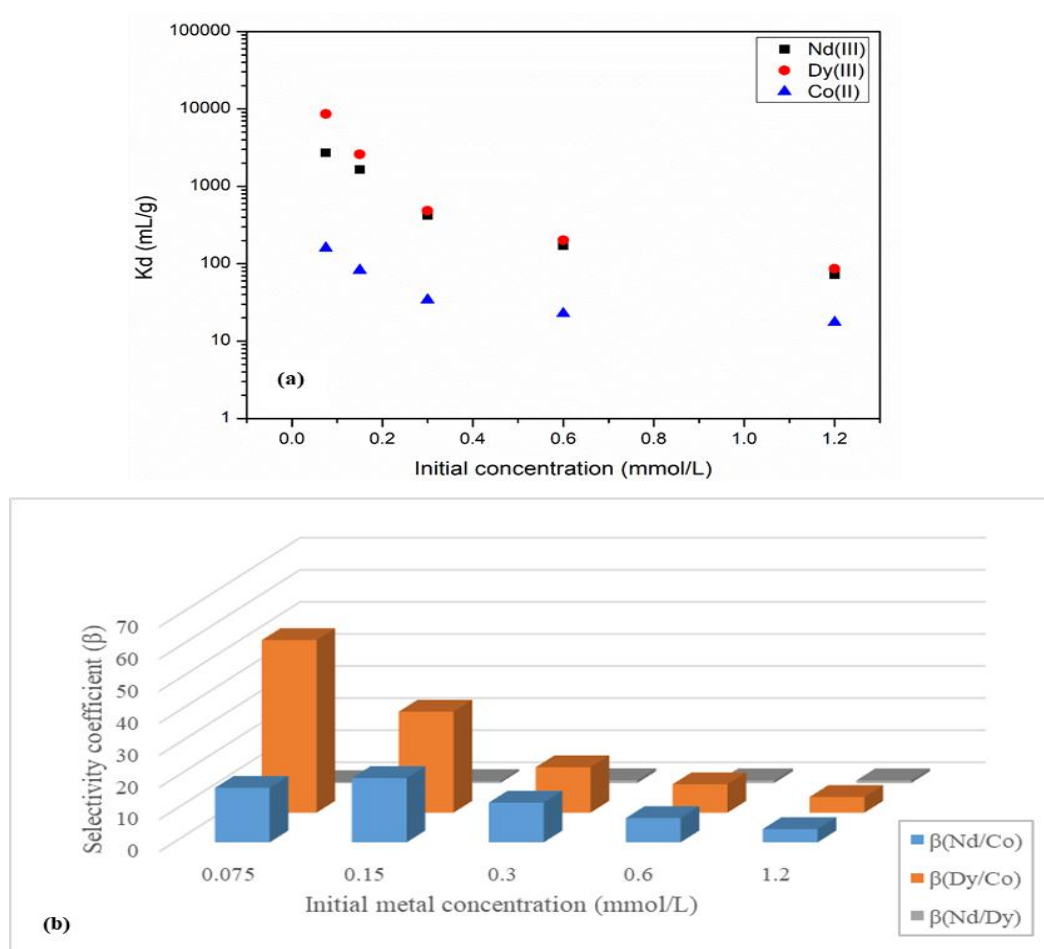
Figure 8: (a) K_d values and, (b) β values as a function of Nd and Dy concentration. (Experimental conditions: pH: 6; t: 60 min; T: 25 °C; m$_{am-TiP}$: 0.1 g; V: 30 mL)

Experimental runs were carried out to estimate the impact of initial pH on the sorption characteristics of am-TiP in mixed solutions. The tests were conducted using ternary solutions consisting of 0.3 mmol/L Nd^{3+}, Dy^{3+}, and Co^{2+} at pH values ranging from 2 to 6.

The impact of initial pH on the K_d values for Nd^{3+}, Dy^{3+}, and Co^{2+} is illustrated in Figure 9a. The metal uptake increased rapidly between pH 2 and 4, and the rate of increase decreased significantly after pH 4. At pH 6, the highest K_d values obtained were 400.60, 479.55, and 43.42 mL/g for Nd^{3+}, Dy^{3+}, and Co^{2+} respectively.

Figure 9b exhibits the changes in $\beta_{Nd^{3+}/Co^{2+}}$, $\beta_{Dy^{3+}/Co^{2+}}$, and $\beta_{Nd^{3+}/Dy^{3+}}$ concerning the initial pH. The data indicate that am-TiP can selectively extract Nd^{3+} and Dy^{3+} from Co^{2+} across all pH values tested. The values of $\beta_{Nd^{3+}/Co^{2+}}$ and $\beta_{Dy^{3+}/Co^{2+}}$ exhibited an upward trend until pH 4, followed by a minor decrease beyond pH 4. At pH 3, the maximum $\beta_{Nd^{3+}/Co^{2+}}$ was recorded as 9.48, while at pH 4, the maximum $\beta_{Dy^{3+}/Co^{2+}}$ was found to be 12.59.
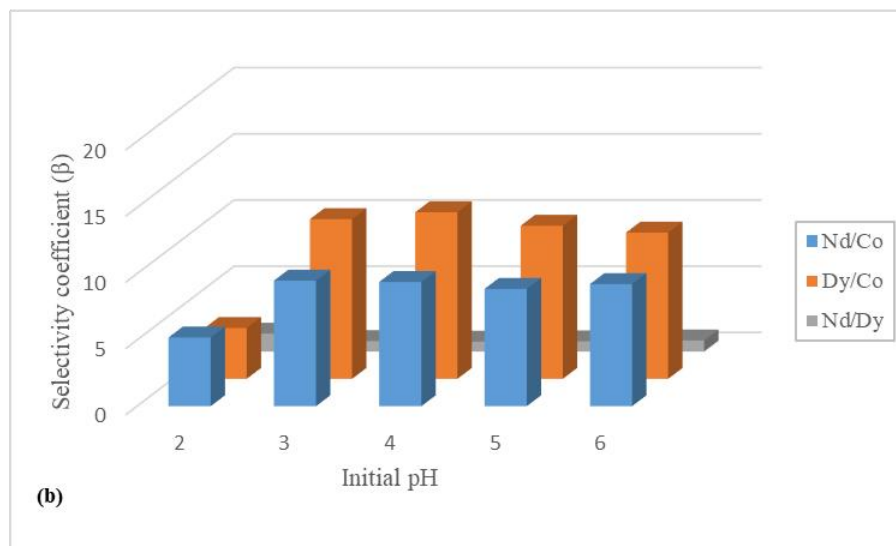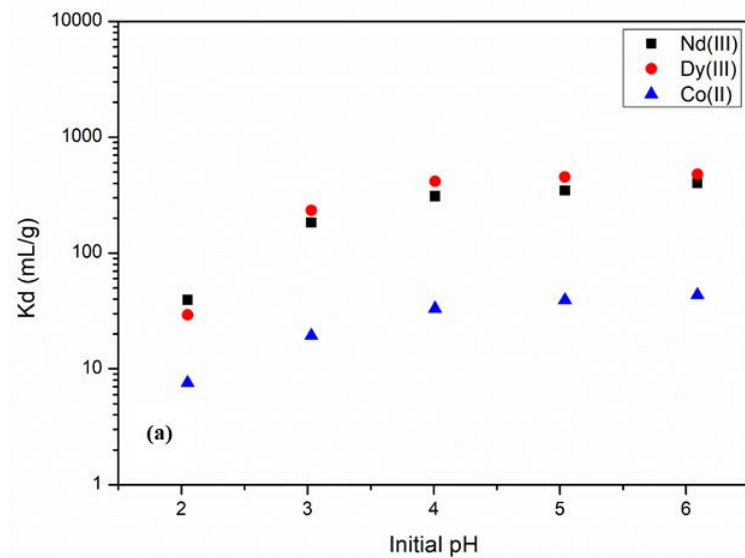
Figure 9: (a) K_d and (b) β values as a function of initial pH.
(Experimental conditions: C_i: 0.3 mmol/L; t: 60 min; T: 25 °C; $m_{am\text{-}TiP}$: 0.1 g; V: 30 mL)

3.4. Desorption Study and Reusability Tests

Effective control of metal-loaded sorbents after the sorption process is crucial for obtaining valuable data to design an efficient industrial operation. Hence, it is essential to perform desorption and re-use of the sorbents to recover the metals from wastewater streams in metal recovery processes (26). Based on the findings of the uptake experiments, loading tests were conducted in the following conditions:

- Initial pH: 6
- Metal concentration: Equimolar (0.3 mmol/L) Nd^{3+}, Dy^{3+}, and Co^{2+}
- Contact time: 60 min
- Temperature: 25 °C
- Amount of am-TiP: 0.1 g

- Solution volume: 30 mL

After filtration, the metal-loaded am-TiP samples were washed with deionized water and allowed to dry at 50 °C for 24 h. In the next step, the metal-loaded sorbents were subjected to treatment with HNO_3, H_2SO_4, and HCl solutions of 0.1 and 1 mol/L concentrations for 60 min. Table 3 presents the data obtained from the desorption experiments carried out for Nd^{3+} and Dy^{3+}.

Table 3: Desorption percentage of Nd^{3+} and Dy^{3+} in different elution solutions.

Metal	0.1 mol/L HNO_3	1 mol/L HNO_3	0.1 mol/L H_2SO_4	1 mol/L H_2SO_4	0.1 mol/L HCl	1 mol/L HCl
Nd^{3+}	79.7	84.7	74.5	78.2	86.3	95.2
Dy^{3+}	81.4	85.1	76.8	80.6	88.8	97.4

The elution test showed that HCl was the most efficient acid. In a one-step batch process, a concentration of 1 mol/L hydrochloric acid was able to elute 57.6% of Nd^{3+} and 61.2% of Dy^{3+}. At the same concentration, the maximum desorption percentages obtained were 95.2% for Nd^{3+} and 97.4% for Dy^{3+}. The desorption, at both 0.1 and 1 mol/L concentrations, decreased in the following order: HCl > HNO_3 > H_2SO_4. Once the most efficient elution solution was determined (HCl-1 mol/L), the reusability of am-TiP was evaluated. A significant reduction in the sorption of Nd^{3+} and Dy^{3+} on am-TiP was observed after the third cycle, indicating a decrease in the reusability of the sorbent. The decline in the metal uptake could be attributed to the deformation of active sites on the surface due to repeated sorption-elution cycles or hydrolysis reactions taking place between the eluent and functional groups present on the sorbent surface.

4. CONCLUSION

In the study, am-TiP, a tetravalent metal phosphate compound, was synthesized and characterized for the selective separation of Nd^{3+} and Dy^{3+} ions from the leaching solutions of end-of-life Nd-Fe-B magnets. The structure was confirmed to contain phosphate groups through FTIR and EDS analyses.

Solution pH and metal concentration parameters have remarkable impacts on metal uptake from single-element solutions. Am-TiP was found to be efficient for Nd^{3+} and Dy^{3+} in the acidic region. The monolayer capacity of am-TiP was determined to be 40.16 mg/g for Nd^{3+} and 26.95 mg/g for Dy^{3+}.

If Co^{2+} ions are present in a solution, recovering Nd^{3+} and Dy^{3+} ions may be problematic. Thus, material selectivity is a crucial concern when choosing appropriate materials. Am-TiP was observed to be selective for Nd^{3+} and Dy^{3+} ions in a wide range of pH and concentration, in ternary solutions containing Nd^{3+}, Dy^{3+}, and Co^{2+} ions. For the separation of Nd^{3+}/Co^{2+} and Dy^{3+}/Co^{2+}, am-TiP has relatively high β values of 20.04 and 53.78, respectively. As anticipated, the comparable structure of Nd and Dy makes it challenging to separate them from each other. Using 1 mol/L HCl, the recovery of 95.2% Nd^{3+} and 97.4% Dy^{3+} from the loaded am-TiP was achieved. Am-TiP was found to be reusable for up to three regeneration cycles while maintaining its effectiveness.

The findings of the current study suggest that am-TiP exhibits comparatively good uptake capacities for Nd^{3+} and Dy^{3+}, as compared to previously reported data in the literature. Moreover, the material displays selectivity towards the separation of Nd^{3+} and Dy^{3+} ions from Co^{2+} ions in ternary solutions.

5. CONFLICT OF INTEREST

The author declares that there is no conflict of interest.

6. ACKNOWLEDGMENTS

7. REFERENCES

1. Gupta CK, Krishnamurthy N (Nagaiyar). Extractive metallurgy of rare earths. CRC Press; 2005. 484 p.

2. Maden Tetkik ve Arama Genel Müdürlüğü MTA Doğal Kaynaklar ve Ekonomi Bülteni Yıl: 2012 Sayı: 13 Ocak-Haziran.

3. Riaño S, Binnemans K. Extraction and separation of neodymium and dysprosium from used NdFeB magnets: An application of ionic liquids in solvent extraction towards the recycling of magnets. Green Chemistry. 2015 May 1;17(5):2931–42. Available from: <DOI>

4. Bogart JA, Lippincott CA, Carroll PJ, Schelter EJ. An Operationally Simple Method for Separating the Rare-Earth Elements Neodymium and Dysprosium. Angewandte Chemie. 2015 Jul 6;127(28):8340–3. Available from: <DOI>

5. Binnemans K, Jones PT, Blanpain B, Van Gerven T, Yang Y, Walton A, et al. Recycling of rare earths: A critical review. Journal of Cleaner Production. 2013;51:1-22. Available from: <DOI>

6. Yang Y, Walton A, Sheridan R, Guth K, Gauß R, Gutfleisch O, Buchert M, Steenari BM, Gerven TV, Jones PT, Binnemans K. REE recovery from end-of-life NdFeB permanent magnet scrap: A critical review. Journal of Sustainable Metallurgy. 2017;3:122-149. Available from: <DOI>

7. Tu YJ, Lo SC, You CF. Selective and fast recovery of neodymium from seawater by magnetic iron oxide Fe3O4. Chemical Engineering Journal. 2015 Feb 5;262:966–72. Available from: <DOI>

8. Durán SV, Lapo B, Meneses M, Sastre AM. Recovery of neodymium (III) from aqueous phase by chitosan-manganese-ferrite magnetic beads. Nanomaterials. 2020 Jun 1;10(6):1–12. Available from: <DOI>

9. Gok C. Neodymium and samarium recovery by magnetic nano-hydroxyapatite. Journal of Radioanalytical and Nuclear Chemistry. 2014;301(3):641–51. Available from: <DOI>

10. Saha D, Akkoyunlu SD, Thorpe R, Hensley DK, Chen J. Adsorptive recovery of neodymium and dysprosium in phosphorous functionalized nanoporous carbon. Journal of Environmental Chemical Engineering. 2017 Oct 1;5(5):4684–92. Available from: <DOI>

11. Komnitsas K, Zaharaki D, Bartzas G, Alevizos G. Adsorption of scandium and neodymium on biochar derived after low-temperature pyrolysis of sawdust. Minerals. 2017 Oct 26;7(10). Available from: <DOI>

12. Devi AP, Mishra PM. Biosorption of dysprosium (III) using raw and surface-modified bark powder of Mangifera indica: isotherm, kinetic and thermodynamic studies. Environmental Science and Pollution Research. 2019 Mar 8;26(7):6545–56. Available from: <DOI>

13. Aghayan H, Mahjoub AR, Khanchi AR. Samarium and dysprosium removal using 11-molybdo-vanadophosphoric acid supported on Zr modified mesoporous silica SBA-15. Chemical Engineering Journal. 2013 Jun 1;225:509–19. Available from: <DOI>

14. Avdibegović D, Zhang W, Xu J, Regadío M, Koivula R, Binnemans K. Selective ion-exchange separation of scandium(III) over iron(III) by crystalline A-zirconium phosphate platelets under acidic conditions. Separation and Purification Technology. 2019 May 15;215:81–90. Available from: <DOI>

15. Xu J, Wiikinkoski E, Koivula R, Zhang W, Ebin B, Harjula R. HF-Free Synthesis of α-Zirconium Phosphate and Its Use as Ion Exchanger for Separation of Nd(III) and Dy(III) from a Ternary Co–Nd–Dy System. Journal of Sustainable Metallurgy. 2017 Sep 1;3(3):646–58. Available from: <DOI>

16. Xu J, Koivula R, Zhang W, Wiikinkoski E, Hietala S, Harjula R. Separation of cobalt, neodymium and dysprosium using amorphous zirconium phosphate. Hydrometallurgy. 2018 Jan 1;175:170–8. Available from: <DOI>

17. Şentürk M, İnan S. Sorption and separation studies of Nd(III) and Dy(III) using amorphous tin(IV) phosphate. Chemical Papers. 2023 Jul 1;77(7):3835–45. Available from: <DOI>

18. Dutta A, Gupta D, Patra AK, Saha B, Bhaumik A. Synthesis of 5-hydroxymethylfurural from carbohydrates using large-pore mesoporous tin phosphate. ChemSusChem. 2014 Mar;7(3):925–33. Available from: <DOI>

19. de Vargas Briaõ G, da Silva MGC, Vieira MGA. Efficient and selective adsorption of neodymium on expanded vermiculite. Industrial & Engineering Chemistry Research. 2021;60(13):4962–74. Available from: <DOI>

20. Lewis A, Guéguen C. Using chemometric models to predict the biosorption of low levels of dysprosium by Euglena gracilis. Environmental Science and Pollution Research. 2022 Aug 1;29(39):58936–49. Available from: <DOI>

21. Langmuir I. The adsorption of gases on plane surfaces of glass, mica and platinum. Journal of the American Chemical Society. 1918;40(9):1361-1403. Available from: <DOI>

22. Freundlich H. Über die Adsorption in Lösungen. Zeitschrift für Physikalische Chemie. 1907;57U(1):385-470. Available from: <DOI>

23. Park HJ, Tavlarides LL. Adsorption of neodymium(III) from aqueous solutions using a phosphorus functionalized adsorbent. Industrial & Engineering Chemistry Research. 2010 Dec 15;49(24):12567–75. Available from: <DOI>

24. Zheng X, Liu E, Zhang F, Yan Y, Pan J. Efficient adsorption and separation of dysprosium from NdFeB magnets in an acidic system by ion imprinted mesoporous silica sealed in a dialysis bag. Green Chemistry. 2016;18(18):5031–40. Available from: <DOI>

25. Koochaki-Mohammadpour SMA, Torab-Mostaedi M, Talebizadeh-Rafsanjani A, Naderi-Behdani F. Adsorption Isotherm, Kinetic, Thermodynamic, and Desorption Studies of Lanthanum and Dysprosium on Oxidized Multiwalled Carbon Nanotubes. Journal of Dispersion Science and Technology. 2014 Feb;35(2):244–54. Available from: <DOI>

26. Kwon TN, Jeon C. Desorption and regeneration characteristics for previously adsorbed indium ions to phosphorylated sawdust. Environmental Engineering Research. 2012;17(2):65–7. Available from: <DOI>

RESEARCH ARTICLE

Synthesis and Characterization of Two New Hofmann-Type-Like Compounds From Some Alkali Metal Atoms and Glycine Anhydride

Zeki Kartal[1] (iD), **Zarife Sibel Şahin[2]*** (iD)

[1]Retired Professor, Kütahya, 43000, Türkiye
[2] Sinop University, Department of Energy Systems Engineering, Sinop, 57000, Türkiye

Abstract: In this study, two new compounds with their closed formula, $C_8H_{10}K_2N_6NiO_4$, and $C_8H_{10}Na_2N_6NiO_4$, were synthesized, the first in crystal form and the second in powder form. Various properties of these compounds were characterized by SC-XRD and FT-IR methods. Theoretical information about the compounds was obtained with the help of the Gaussian 03 program. The molecular formula that best reflects the structural properties of this first 3D compound, which is in crystalline form and has polymeric properties, can be given as $\{K_2(GA)(H_2O)_2[Ni(CN)_4]\}_n$. With a similar thought, it can be suggested that the molecular formula that best reflects the structural properties of the second 3D compound in powder form and with polymeric properties will be $\{Na_2(GA)(H_2O)_2[Ni(CN)_4]\}_n$. The asymmetric unit of the $\{K_2(GA)(H_2O)_2[Ni(\mu_4\text{-}CN)_4]\}_n$ compound is composed of a half Ni(II) ion, one K(I) cation, two cyanide ligands, a half GA ligand molecule, and one bounded water ligand molecule. The structure of the compound, which consists of 3D polymeric chains, is formed by various bonds between the GA molecule, K(I) cations, water ligand molecules, and $Ni(CN)_4$ ions.

1. INTRODUCTION

The entry of Hofmann-type compounds and clathrates into scientific research began with synthesizing a new compound for the first time in 1897 (1). If a chemical complex has at least two components, this compound may be called "clathrate" in the chemical literature (2–4).

The clathrates, which have very different usage areas according to their structural properties, have recently been obtained by many researchers with very different properties and are still being obtained. More detailed information on clathrates can be found in previous studies (5,6).

The general formula of Hofmann-type compounds synthesized in scientific studies by researchers has formula as $M(II)LM'(II)(CN)_4.nG$ and $M(II)LM'(II)(CN)_4$, respectively. The meaning of each term in this formula has been explained broadly in various studies (2,4,7). Our published studies on the Hofmann-type compounds can be seen in the literature (8,9). One published article is about Hofmann-type-like clathrates formed by 4AP and water molecules (H_2O) (10).

A compound desired to be synthesized as the Hofmann type may occur in a form that does not fully comply with the "Hofmann type compounds" formula. Such compounds are called "Hofmann-type-like compounds". Hofmann-type-like compounds are usually formed by adding more ligand

molecules instead of two ligand molecules, attaching the solvent molecule to the transition metal atom, using another ligand alongside the first ligand, or replacing the transition metal atom with another metal atom.

A formula such as MLL'M'(II)(CN)$_4$ can be suggested for the structural formula of Hofmann-type-like compounds formed by chance or planning because of a chemical reaction. In this formula, M denotes any metal atom and L' additional ligand molecule in the reaction medium. Hofmann-type-like compounds can form polymeric layers ranging from 1D to 3D, depending on the type of chemical bonds formed between [M'(CN)$_4$]$^{2-}$ anions and [MLL']$^{2+}$ cations.

The results of replacing the transition metal atom in the Hofmann-type compound with another metal atom or adding a new ligand molecule to the structure of the Hofmann-type compound obtained from the same transition metal atom and the same ligand molecule can be seen by comparing their spectroscopic and crystalline data. If the change in the structure of the compound leads to a positive increase in the stability, volume, gas storage, and some other properties of the obtained crystal structure, further studies can be conducted on this subject. For this reason, we wanted to obtain new Hofmann-type-like compounds in crystal form by using some alkali metal atoms and a different ligand molecule (Glycine anhydride; GA) from the previous ones.

The structure with the closed formula (C$_4$H$_6$N$_2$O$_2$) and in which two oxo groups are bonded instead of two hydrogen atoms in the 2 and 5 position in a piperazine molecule is called "glycine anhydride" (GA). In the GA molecule, both N-H and C=O groups are in a Trans state concerning each other. Various studies and information about this GA molecule can be found in different literature, which is structurally small but interesting and important in terms of various properties (11,12).

This study aims to obtain crystal forms of Hofmann-type-like compounds using a different ligand molecule and two alkali metal atoms. In addition to the chemicals and GA ligand molecules routinely used to achieve the goal, the water molecule, which is abundant in the reaction medium, was also used as a second ligand or guest molecule. Also, the alkaline potassium (K) and sodium (Na) atoms were used instead of the transition metal atom. In this study, two new Hofmann-type-like compounds were obtained, one in crystal form and the other in powder form.

2. EXPERIMENTAL SECTION

2.1. Materials
Starting materials used to obtain the desired compounds: Glycine anhydride (GA, C$_4$H$_6$N$_2$O$_2$, Sigma Aldrich, 99%), potassium tetracyanonickelate(II) monohydrate {K$_2$[Ni(CN)$_4$]·H$_2$O, Fluka, 96%} and sodium tetracyanonickelate(II) trihydrate {Na$_2$[Ni(CN)$_4$]·3H$_2$O, Chempro Tech Co, 96%}. The starting materials used in the synthesis of the obtained compounds were used as they were obtained commercially.

2.2. Syntheses of Hofmann-Type-Like Compounds [M$_2$(GA)Ni(CN)$_4$]·(H$_2$O)n or [M$_2$(GA)(H$_2$O)$_n$Ni(CN)$_4$] [M(I) = K and Na)]
Procedures followed to obtain the first compound: 1 mmol of potassium tetracyanonickelate(II) monohydrate (0.259 g) was dissolved at 65 °C (50 mL), and 1 mmol of GA (0.114 g) was added to this solution. This mixture was stirred for 2 hours at 65 °C, then filtered and crystallized under normal atmospheric conditions. About two months after this study, a transparent, colorless, crystalline compound with a yield of approximately 61%, was obtained.

Procedures followed to obtain the second compound: 1 mmol of Na$_2$[Ni(CN)$_4$]·3H$_2$O (about 0.209 g) was dissolved at 65 °C (50 mL), and 1 mmol of GA (0.114 g) was added to this solution. As a result of all these chemical reactions, the Hofmann-type-like clathrate or Hofmann-type-like compound was suspended in aqueous media. Then, this mixture was stirred with a magnetic stirrer at 65 °C for one week. Afterward, the whole mixture was filtered, washed three times with distilled water and twice with pure ethyl alcohol, and dried. Despite all efforts, the crystal form of the second compound could not be obtained. Therefore, its powder form was obtained and used in all spectroscopic studies.

Through the utilization of experimental techniques and spectroscopic analyses, researchers were able to ascertain that the crystalline structure of the initial chemical can be represented by the formula K$_2$(GA)(H$_2$O)$_n$Ni(CN)$_4$. For brevity, this compound will be subsequently denoted as "1". Likewise, it was postulated that the chemical composition of the second compound, in its powdered state, may be represented by the formula Na$_2$(GA)(H$_2$O)$_n$Ni(CN)$_4$. The subsequent compound will be henceforth denoted as "2".

2.3. Instrumentation
The experimental values were obtained from Vertex 70 FT-IR Spectrometer for FT-IR, Perkin-Elmer optima 4300 DV ICP-OES for metal amounts, and CHNS-932 (LECO) for other atom

amounts. The amounts of metal and other components in the compounds are given in Table 1.

Crystal data of compound **1** were collected at normal room conditions (296 K) with the aid of a BRUKER D8-QUEST diffractometer. The crystal structure of the compound was resolved by direct methods; SHELXS-2013 (13) was refined by full-matrix least squares methods; SHELXL-2013 (14); data was collected by APEX2 (15); for molecular graphics: Mercury software (16) was used, and analyses were performed with WinGX (17) software. The information obtained on this subject and their details are shown in Table 2 (CCDC number: 2104239).

Table 1: Elemental analysis results of the compounds.

The compound and molecular weight M_r (g)	Found (%) / (Calculated) (%)					
	C	H	N	K	Na	Ni
$K_2(C_4H_6N_2O_2)(H_2O)_2Ni(CN)_4$ $M_r = 391.10$	25.19 (24.57)	2.49 (2.58)	21.88 (21.49)	19.76 (19.99)	- (-)	14.83 (15.01)
$Na_2(C_4H_6N_2O_2)(H_2O)_2Ni(CN)_4$ $M_r = 358.88$	26.31 (26.77)	2.59 (2.81)	23.67 (23.42)	- (-)	12.59 (12.81)	15.93 (16.35)

Table 2: The refinement parameters in compound **1**.

Empirical formula	$C_8H_{10}K_2N_6NiO_4$
Formula weight	391.13
Crystal system	Monoclinic
Space group	$P2_1/c$
a (Å)	9.6592 (18)
b (Å)	6.9310 (12)
c (Å)	12.3958 (19)
$\checkmark$ (°)	116.588 (11)
V (Å^3)	742.1 (2)
Z	2
D_c (g cm^{-3})	1.750
θ range (°)	3.4-28.3
Measured refls.	15887
Independent refls.	1852
R_{int}	0.058
S	1.07
R1/wR2	0.038/0.111
$\Delta X_{max}/\Delta\rho_{min}$ (eÅ^{-3})	0.53/-0.89

3. RESULTS AND DISCUSSION

3.1. Crystallographic Analysis of 1
The crystal structure studies for compound **1** show that it is a 3D polymeric coordination compound.

The asymmetric unit of compound **1** contains half Ni(II) ion, one K(I) cation, two cyanide ligands, half GA ligand, and one H_2O ligand (see Figure 1).
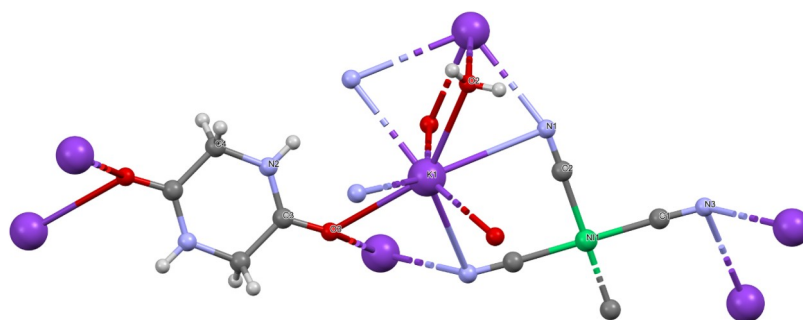
Figure 1: The molecular structure of compound **1** showing the atom numbering scheme.

In the 3D polymeric structure of compound **1**, the Ni(II) ion is surrounded by four carbon atoms of the four cyanide ligands [Ni1-C1 = 1.867(2) Å and Ni1-C2 = 1.863(3) Å] in a square planar form. The same bond length was 1.865(4) Å in a crystal structure we obtained earlier (9). The K(I) cation is coordinated by four cyanide nitrogen atoms [bond distances ranged between 2.919(3) - 3.238(3) Å], two oxygen atoms [K1-O3 = 2.992(2) Å and K1-O3^{vi} = 2.881(2) Å] from GA molecule and two oxygen atoms [K1-O2 = 2.842(2) Å and K1-O2^{iii} = 2.851(2) Å] from H_2O molecule [(iii) 1-x, 1-y, 2-z; (vi) 1-x, 1/2-y, 3/2-z]. In the studies of other researchers, K-N bond lengths were found to be between 2.704(2) and 2.937(3) Å (18). K-O bond lengths were also found to be between 2.69(1) and 3.17(1) Å in studies with different ligand molecules by other researchers and us (19,20). The Ni(II) ions and K(I) cations are bound to each other with cyanide ligands. In these bonds, the Ni···K intervals are between 5.487 Å and 5.852 Å, while the K···K intervals are 3.914 Å, 4.404 Å, 8.997 Å and 9.855 Å. In addition, as mentioned before, K(I) cations also formed bonds with the oxygen atoms of GA and H_2O ligands. Combining these ions and ligands with the indicated bonds produces a 3D coordination polymer (see Figure 2). The bond distances, bond angles and hydrogen bond parameters of compound **1** are given in Table 3, respectively. The molecules of compound **1** are also connected by strong hydrogen bonds (Table 4). These strong hydrogen bonds play a major role in creating a supramolecular network.

3.2. Spectral Examination of Compounds
The experimental spectra of compounds **1** and **2** are given in Figure 3 (a - d), as well as their theoretical spectra for comparison. When the FT-IR spectra of the compounds are examined, it is seen that there are a large number of similarities and a small amount of differences in them. The reason for these similarities is that the GA molecule, $Ni(CN)_4$ ion group, and the H_2O molecule are common in the structure of the compounds. The

reason for the differences in the spectra of compounds **1** and **2** is the presence of different alkaline metal (K and Na) atoms in the structure of each compound.

The spectral data of compound **1** were analyzed separately for the vibrations of GA, H_2O molecules, and $[Ni(CN)_4]^{2-}$ anions in its structure. Similar results apply to compound **2**. All spectral data of compounds are given in Tables S1 and S2.

3.2.1. Vibrations of the GA molecule
Peptides are short chains of amino acids, which are very important chemically and biologically, linked by peptide bonds. Peptides can be found structurally in the chain and cyclic forms. As the number of amino acids in a peptide's structure increases, both the structure and chemical function of that peptide increase. If the number of amino acids in the structure of a peptide is more than about fifty, that peptide is known as a "polypeptide", that is, a "protein" (21). Proteins are chemical compounds that are very valuable in terms of the vital behavior of living things. GA is an organic compound and is the smallest cyclic dipeptide consisting of a six-membered ring containing two amide bonds (22).

The GA molecule is among the components that make up several molecules with significant biological activity. In the cyclic ring of the GA molecule, all other atoms are located almost in the same plane, except for the hydrogen atoms bonded to the alpha-carbon atoms. The molecular structure of GA is shown in Figure S1 a. Since there are parts that can easily donate electrons, such as N-H, C=O, and ring structure in the structure of the GA molecule, it can make a very different number of bonds in the chemical reactions it participates in (23). The number of bonds to be made by the GA molecule in a chemical reaction depends on the degree of activity of its parts, such as N-H, C=O, and the ring structure.

Table 3: Selected bond distances and angles (Å, º).

Ni1-C1	1.867(2)	Ni1-C2	1.863(3)
K1-N1^{iii}	3.047(3)	K1-N1	3.238(3)
K1-N3^{vii}	2.919(3)	K1-N3^{i}	3.182(3)
K1-O3^{vi}	2.881(2)	K1-O3	2.992(2)
K1-O2	2.842(2)	K1-O2^{iii}	2.851(2)
C2-Ni1-C1^{i}	89.03(10)	C2-Ni1-C1	90.97(10)
K1-O2-K1^{iii}	86.89(6)	O2-K1-N1	60.20(6)
N1-K1-N1^{iii}	103.03(6)	N3^{i}-K1-N1	80.91(7)
N3^{vii}-K1-N1	140.30(8)	O3-K1-N1	139.96(7)
O2^{iii}-K1-N1	66.45(7)	O2-K1-O3	147.21(6)
Symmetry codes: (i) −x+2, −y+1, −z+2; (iii) −x+1, −y+1, −z+2; (vi) −x+1, y−1/2, −z+3/2; (vii) x−1, −y+1/2, z−1/2.			

Table 4: Hydrogen-bond parameters (Å, °).

D-H· · ·A	D-H	H···A	D···A	D-H···A
N2—H2···N1[iii]	0.86	2.16	2.962 (3)	154
O2—H2A···O3[viii]	0.83 (2)	2.05 (2)	2.860 (3)	167
O2—H2B···N3[ix]	0.81 (2)	2.36 (3)	3.080 (3)	149
Symmetry codes:	(iii) −x+1, −y+1, −z+2; (viii) x, −y+1/2, z+1/2; (ix) −x+2, y−1/2, −z+5/2.			
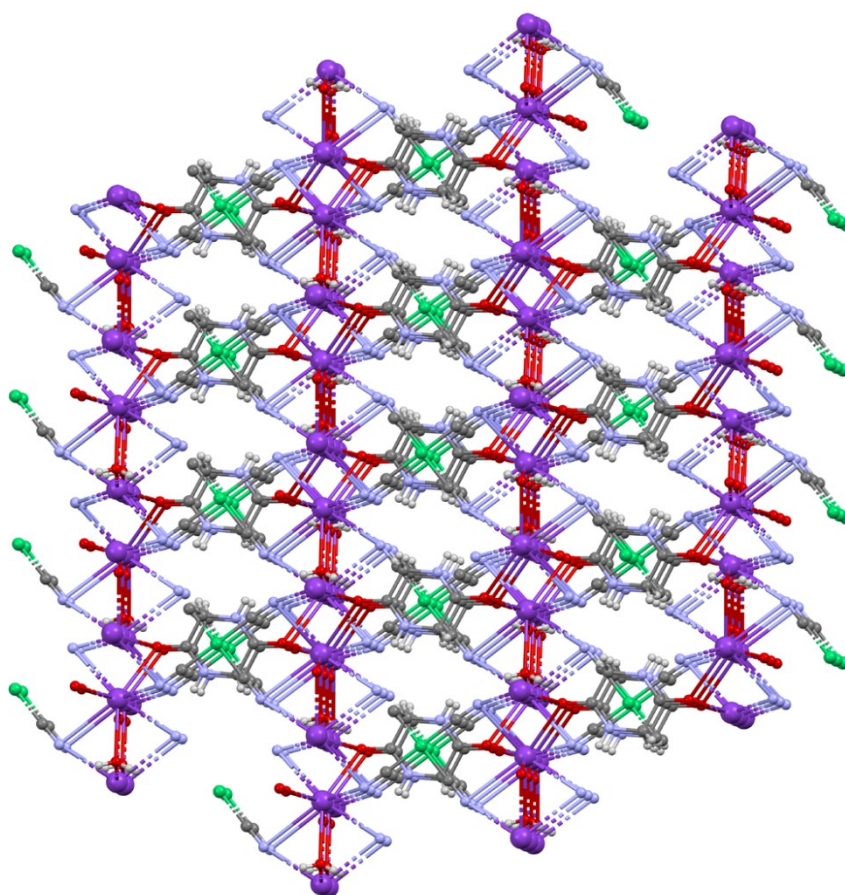
Figure 2: 3D supramolecular network in compound **1**.

The GA molecule has a flexible structure because its six-membered ring structure can change from the boat form to the planar form or vice versa with an energy difference of only a few kcal/mol. The GA molecule, which has a planar ring structure in its solid state, has C_{2h} symmetry. Since there are 14 atoms in the GA molecule's structure, it has a total of 36 vibration modes. Of these vibration modes, 12 of the 23 in-plane vibrations have Raman-active and A_g symmetry, while the other 11 have IR active and B_u symmetry. While 6 of the remaining 13 out-of-plane vibrations have Raman active and B_g symmetry, the other 7 have IR active and A_u symmetry (21,24).

When Figure S1 (a) is examined, it is understood that when the GA molecule forms a compound under normal conditions, it will only form bonds from its own oxygen atoms. Because the oxygen atoms in the structure of the GA molecule have the largest (-) charge values compared to other atoms. The SC-XRD examination of compound 1 shows that the GA molecule only makes bonds from oxygen atoms to other atoms in compound **1** (see Figure 1).

In the literature review on the GA molecule, it is seen that it makes zero bonds (guests) (25), two bonds (24), and four and more bonds (23) in some of its compounds. The number of bonds that any ligand molecule makes in a compound will cause changes in some vibration modes according to its free state because the bonds formed in a

compound will change the bond constant and bond length of the functional group forming that bond.

When Table S3 is examined, it is seen that the ν(NH) vibration of the GA molecule in compounds **1** and **2** shifts towards the low wavenumber region by 8 and 12 cm^{-1} values, respectively. The reason for this shift is the very weak interactions of the NH group's hydrogens with the cyanide group's carbon atoms.

Similarly, it is seen that the peak originating from Fermi resonance in the GA molecule in compounds **1** and **2** shifts towards the wavenumber region as high as 34 and 36 cm^{-1}, respectively. The reason for this shift is that the groups participating in forming the Fermi resonance are affected by the formation of the compound.

The amount of shift to high wavenumber in the combination bands occurring in the wavenumber range of approximately 3000 and 3100 cm^{-1} in the compounds is considerably higher than the other modes. It can be thought that this is due to the sum of the changes in the modes participating in the combination event.

Particularly, there appears to be a large shift in the modes of ν(CH) vibration of the GA molecule in compounds **1** and **2** to the higher wavenumber. The reason for this shift is that the CH groups' hydrogen interacts with the cyanide group's carbon atoms. These interactions make the stretching movements of the CH group difficult.

It is seen that the largest value of shifts in the vibration modes of the GA molecule in compounds occurs in the stretching vibrations of the carbonyl group (C=O). This shift is because the oxygen of the C=O group interacts with the alkali metal atoms and the hydrogen atoms of the other ligand molecules, such as water. These interactions make the stretching and bending movements of the C=O group more difficult. The reality of this situation is clearly seen in the values in the last row of Table S1.

It can be said that some minor shifts in the vibration frequencies of the GA ligand-constituting compounds are due to some changes in the environmental conditions of GA due to the formation of compounds. The vibration wavenumbers of the GA, which are most affected by environmental conditions or compound formation, and their shifts are marked in bold in Table S1 (with Δ sign).

In general, in vibration spectroscopy, the new vibration value that emerges as a result of the interaction of the stretching vibration of any functional group of a molecule and the overtone of

the bending vibration of that group is called "Fermi resonance vibration". Fermi resonance can also occur due to hydrogen bonds formed by any group with other atoms around it. From the examination of Table S3, the vibrational mode at 3331 cm^{-1} in the solid state IR spectrum of the GA molecule belongs to its free ν(NH) mode. The vibration peak at 3195 cm^{-1} is the Fermi resonance vibration, which arises from the interaction of the ν(NH) mode and the overtone of the δ(NH) bending mode (26)

In the IR spectra of the compounds, there is a peak at 535 and 547 cm^{-1}. While this peak is actually an IR inactive peak of the free GA molecule or $[Ni(CN)_4]^{2-}$ ion, it can be thought that it belongs to a peak that becomes IR active as a result of its contribution to the formation of compounds. Perhaps this vibration mode may have been composed of the sum of the vibration modes of some peaks with lower wavenumbers, or it may have been composed of the overtones of the vibration modes of those peaks with lower wavenumbers.

3.2.2. Vibrations of the H_2O in compounds
The presence of overlapping ν_{as}(OH) and ν_s(OH) modes in certain water compounds leads to the formation of a significantly broad vibration band in their vibration spectra, spanning a wavenumber range of around 3500 to 3200 cm^{-1}. A distinct and intense stretching vibration peak is observed at around 3600 cm^{-1} wavenumber when free water molecules are present within a chemical product. Nevertheless, it is worth noting that certain water compounds, including bound water molecules, exhibit distinct vibration modes that manifest at frequencies lower than the stretching vibration frequency observed in free water molecules. We have experimentally obtained these vibration modes at wavenumbers ν_{as}(OH) 3470 cm^{-1}, ν_s(OH) 3257 cm^{-1}, and δ(OH) 1641 cm^{-1}.

The presence of the NH group, C=O group, and even water molecules as ligands or guests in a chemical compound makes it very difficult to explain 1700-1550 cm^{-1}—all these vibration peaks specified overlap with each other in the same region. As a result of this overlap, each vibration peak does not appear on its own but as a single highly enlarged peak (27,28).

As seen in the experimental FT-IR spectra of compounds **1** and **2** in Figure 3 (a) and 3 (c), ν_{as}(OH) and ν_s(OH) stretching vibrations of the bonded water molecules have appeared at wavenumbers as individual peaks, 3565; 3456 cm^{-1} and 3576; 3472 cm^{-1}, respectively. According to these values obtained, the vibration modes ν_{as}(OH) and ν_s(OH) in compound **1** shifted to higher wavenumbers of 95 and 199 cm^{-1} compared to

their values in the free water molecule. In compound **2**, the shift values of $v_{as}(OH)$ and $v_s(OH)$ vibration modes to this high wavenumber were realized as 106 and 215 cm^{-1}.

When the broad peak located in the wavenumber range of approximately 1760 to 1550 cm^{-1} in the FT-IR spectrum of compound **1** is examined more closely, it is seen that it has another peak at 1646 cm^{-1} wavenumber in addition to the peak at 1669

cm^{-1} wavenumber. This new peak can be attributed to the bending vibration of the water molecule [$\delta(OH)$]. The same peak appeared in the FT-IR spectrum of compound **2** at 1653 cm^{-1}. According to these data, due to the participation of the water molecule in the formation of the compound, the $\delta(OH)$ vibration mode shifted to the wavenumber region as high as (5 and 12) cm^{-1} in compounds **1** and **2**, respectively.
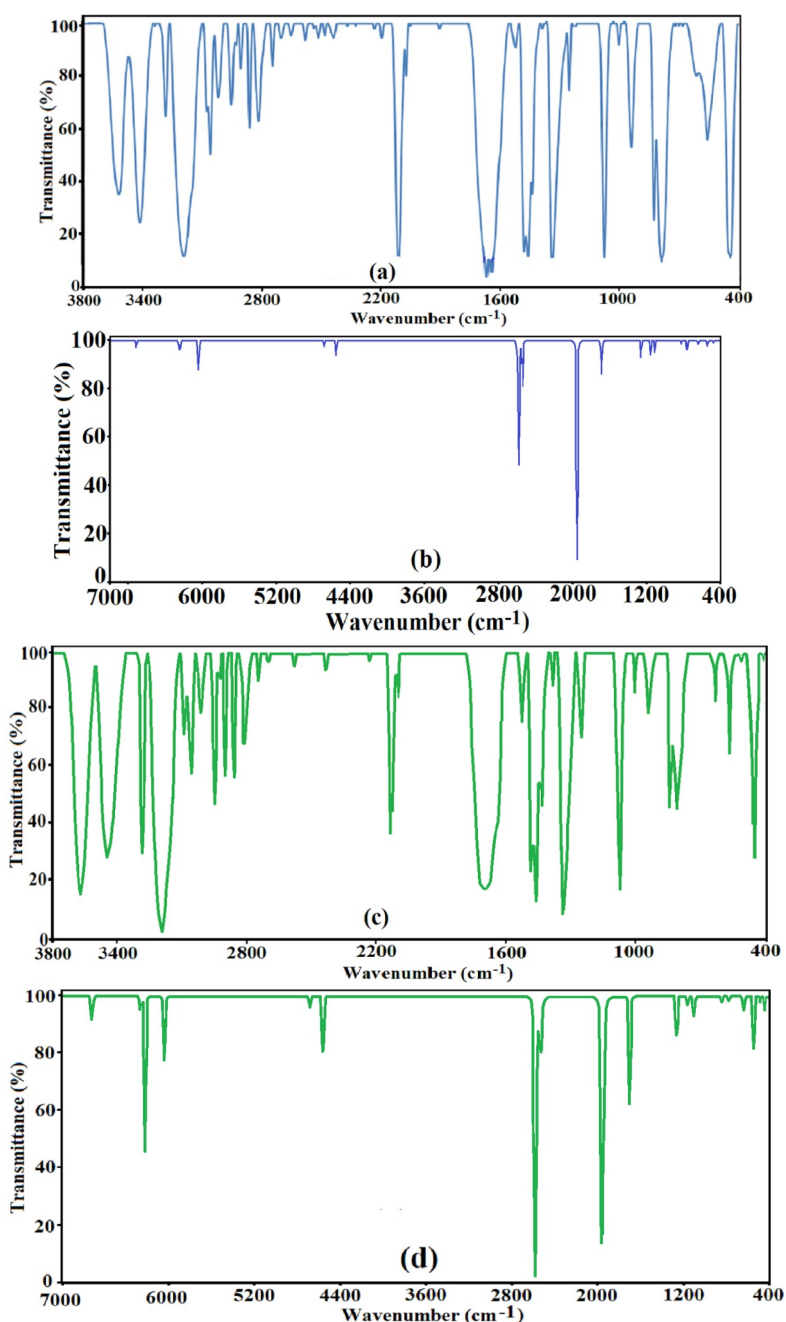
Figure 3: FT-IR spectra of compound **1** are experimental (a), theoretical (b), and FT-IR spectra of compound **2** are experimental (c), theoretical (d).

Some theoretical calculations with the Gaussian program and source searches have been made about the bonds between the oxygen atoms of the GA and H_2O ligand molecules of the K and Na metal atoms in compounds **1** and **2**. According to these studies, it has been observed that some of the wavenumbers of the Na-O stretching mode occur at values greater than 400 cm^{-1}, while all of the wavenumbers of the K-O stretching mode occur at wavenumbers less than 400 cm^{-1} (29). Since the working range of the FT-IR spectrometer used is in the range of 4000-400 cm^{-1} wavenumber, information about the K-O bonds in compound **1** could not be obtained.

An examination of Figure 3 (c) shows that the wavenumber of the stretching vibration [v(Na-O=C)] of the bond of the sodium atom in compound **2** with an oxygen atom of the GA molecule is 472 cm^{-1}. Similarly, it is seen that the wavenumber of the stretching vibration [v(Na-OH$_2$)] of the bond between the sodium atom in compound **2** and the oxygen atom of the water molecule is 412 cm^{-1} (29).

3.2.3. Vibrations of the [Ni(CN)$_4$]$^{2-}$ group in compounds
If there is a cyanide group in the structure of a chemical compound, there is usually a very sharp v(CN) band in the vibration spectrum of that chemical compound in the range of 2200-2000 cm^{-1} (30).

The determination of the [Ni(CN)$_4$]$^{2-}$ ion in the compounds **1** and **2** was based on the work of McCullough et al. for the Na$_2$[Ni(CN)$_4$]·3H$_2$O compound (31). Comparisons of [Ni(CN)$_4$]$^{2-}$ ions in both compound **1** and compound **2** with the vibration modes of [Ni(CN)$_4$]$^{2-}$ ions in K$_2$[Ni(CN)$_4$]·H$_2$O and Na$_2$[Ni(CN)$_4$]·3H$_2$O compounds are given in Table S2, respectively.

In the FT-IR spectrum of the K$_2$[Ni(CN)$_4$]·H$_2$O, the E$_u$ mode is at 2122 cm^{-1}. This vibration was observed at 2127 cm^{-1} in **1**. Similarly, the v(C≡N), E$_u$ stretching vibration mode of Na$_2$[Ni(CN)$_4$]·3H$_2$O is observed at 2130 cm^{-1}. This vibration was observed at 2139 cm^{-1} in **2**.

In general, it consists of ^{13}C atoms, about 1.11% of all carbon atoms of a substance. Therefore, the contribution of ^{13}C atoms in a substance to any event is very low. In the FT-IR spectra of compounds **1** and **2**, due to the replacement of the normal carbon atom of the cyanide group with a ^{13}C isotope carbon atom, a very weak intensity v(^{13}C≡N) vibration band appeared at 2086 and 2092 cm^{-1} wavenumbers, respectively.

In the FT-IR spectrum of K$_2$[Ni(CN)$_4$]·H$_2$O, the v$_9$(Ni–CN), E$_u$ mode, is observed at 544 cm^{-1}. This

vibration was observed at 591 cm^{-1} in **1**. Similarly, in the FT-IR spectrum of Na$_2$[Ni(CN)$_4$]·3H$_2$O, the v$_9$(Ni–CN), E$_u$ mode, is observed at 550 cm^{-1}. This vibration was observed at 596 cm^{-1} in **2**.

When the experimental and theoretical FT-IR spectra of the compounds are examined together, it can be thought that they are very different from each other. However, they support each other scientifically. The reasons why the experimental and theoretical FT-IR spectra appear different can be explained as follows. In the theoretical calculation, a compound is considered as gaseous and only as much as its empirical formula. As a result, the theoretical FT-IR spectrum of the compound has a plain appearance. Experimentally, the compound is in a crystalline form, solid state, and an almost infinite number of them interact.

For this reason, many atomic and intermolecular interactions are also active in the experimental FT-IR spectra. As a result, the experimental FT-IR spectrum of the compound has a more complex appearance. Another factor is the emergence of combination and overtone bands at high wavenumbers of vibration modes occurring at small wavenumbers while taking the experimental spectrum.

2.3. Computational Studies
Considering the similarity of the experimental data of compound **2**, which was obtained in powder form, to compound **1**, which was in crystal form, it was desired to obtain its 3D structure. For this purpose, Na atoms were taken instead of K atoms in the crystal structure of **1** in the Gaussian 03 program (32), and their bond lengths were optimized. In order to compare the experimental and theoretical results of both compounds studied, theoretical calculations were made by taking only the parts of them, indicating their empirical formula. The operation numbers assigned by the Gaussian 03 program to the atoms of GA and atoms of compounds **1** and **2** are given in Figure 4.

To compare with the experimental spectra of compounds **1** and **2**, their theoretical spectra were calculated with the Gaussian 03 program using the LanL2MB basis set by the DFT method. They are scaled with a recommended coefficient of 0.958 for the calculation method used. The theoretical spectra obtained for the compounds are given in Figure 3 (b) and (d), respectively.

3.3.1. Mulliken atomic charge values of the compounds
The Mulliken electronic charge values of each atom in the GA molecule and compounds **1-2** were calculated and displayed with the GaussView program (33). The results obtained are shown as 3D graphs in Figure S1.

The differences between the charge values of the two oxygen atoms of the free GA molecule and the charge values of the same two oxygen atoms of the GA molecule bonded in compounds **1** and **2** were calculated as 0.287e and 0.293e for compound **1**. Similarly, these differences were calculated as 0.200e and 0.249e for compound **2**.
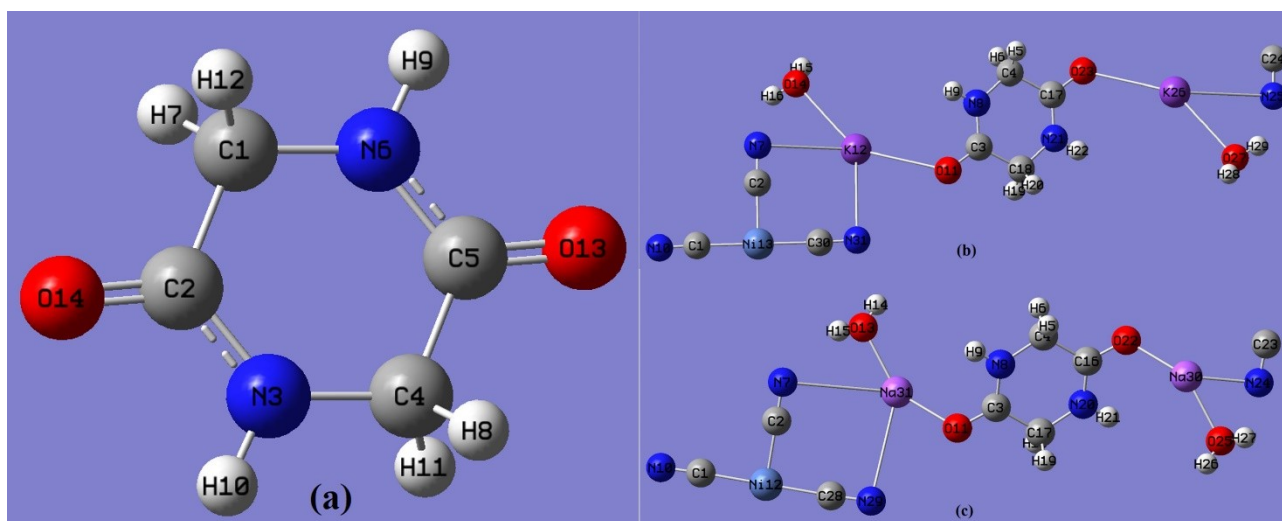
Figure 4: The numbering scheme is given by the Gaussian 03 program for the GA molecule (a), compounds **1** (b) and **2** (c).

It can be seen from the examination of Figure S1 that there are some charge changes in the other non-bonded atoms of the free GA molecule if it forms a compound. For example, the differences between the charge values of the two nitrogen atoms of the free GA molecule and the charge values of the same two nitrogen atoms of the GA molecule non-bonded in compounds **1** and **2** were calculated as 0.069e and 0.067e for compound **1**. As can be seen in Figure S1, these differences were calculated as 0.066e and 0.063e for compound **2**.

The two examples clearly show that the electrical charge values of bonding and non-bonding atoms in a molecule can change as a compound is formed. However, the change in the electric charge of the bonding atoms is always greater than the change in the electric charge of the non-bonding atoms.

3.3.2. Energy levels of compounds 1 and 2
As seen in Figure 5, the localization regions of the HOMO and LUMO states in both compounds overlap with almost the same parts of the compounds. Theoretical calculations with the Gaussian 03 program showed that a total of 129 molecular orbitals were found for compound **1**, of which 84 are occupied orbitals, and the remaining 45 are vacant orbitals. The HOMO and LUMO energy values are -0.13616 au (-3.705 eV) and -0.07847 au (-2.135 eV) in atomic units and electron volt units, respectively.

Similarly, 121 molecular orbitals were found for compound **2**, 76 of which are occupied and the remaining 45 are vacant. The HOMO and LUMO energy values are -0.16430 au (-4.471 eV) and -0.07365 au (-2.004 eV) in atomic units and electronvolt units, respectively.

In the HOMO and LUMO calculations for both compounds, the fact that compound **1** has more molecular orbitals than compound **2** is due to the fact that the K atom has more electrons in electronic arrangement than the Na atom.

The formulas for the electrochemical properties of a compound are given below.

$$\Delta E = A - I \text{ (Energy gap value) (Eq. 1)}$$
$$\chi = (I + A) / 2 = -\mu \text{ (Electronegativity, Negative chemical potential (Eq. 2)}$$
$$\eta = (I - A) / 2 \text{ (Chemical hardness) (Eq. 3)}$$
$$S = 1 / 2\eta \text{ (Chemical softness) (Eq. 4)}$$
$$\omega = \mu^2 / 2\eta \text{ (Electrophilicity index) (Eq. 5)}$$

Considering the theoretical values of the compounds in Table 5; **1** has a lower kinetic stability and a higher chemical activity than **2** since $\Delta E_1 < \Delta E_2$.

Some thermochemical properties of the compounds calculated using the HOMO and LUMO values are given in Table 6. These thermochemical properties give important information about compounds and their interactions with other compounds.
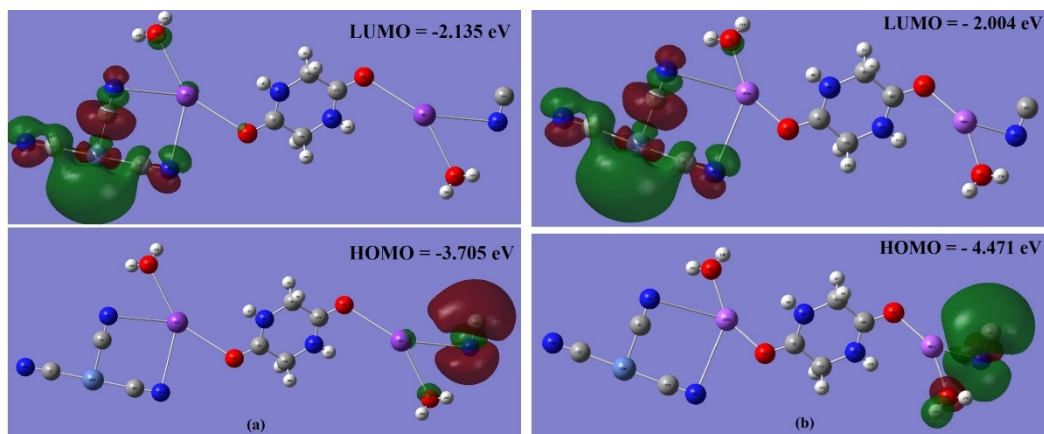
Figure 5: The HOMO and LUMO states in compounds **1** (a) and **2** (b).

Table 5: The chemical efficiency values of compounds in (au) and (eV) units.

Chemical efficiency values	Compounds			
	1		**2**	
HOMO (-I)	-0.13616	-3.705	-0.16430	-4.471
LUMO (-A)	-0.07847	-2.135	-0.07365	-2.004
ΔE	0.05770	1.57	0.09066	2.467
χ	0.10731	2.920	0.11899	3.238
μ	-0.10731	-2.920	-0.11899	-3.238
η	0.02885	0.785	0.04535	1.234
S $(au)^{-1}$; $(eV)^{-1}$	0.02352	0.640	0.01488	0.405
ω	0.20054	5.457	0.15603	4.246

Table 6: Thermochemical data of compounds 1 and 2.

Data		Values			
		1		**2**	
E_{Total} (Kcal/Mol)	Electronic	0.000		0.000	
	Translational	0.889	148.802	0.889	148.803
	Rotational	0.889		0.889	
	Vibrational	147.147		147.025	
Heat Capacity at constant volume C_v (Cal/Mol-Kelvin)	Electronic	0.000		0.000	
	Translational	2.981	63.077	2.981	56.284
	Rotational	2.981		2.981	
	Vibrational	57.115		50.322	
Total entropy S (Cal/Mol-Kelvin)	Electronic	0.000		0.000	
	Translational	43.774	170.561	43.520	146.503
	Rotational	37.224		36.244	
	Vibrational	89.562		66.739	
Zero point Vibrational Energy E_{v0} (Joules/Mol); (Kcal/Mol)		567268.7 135.58048		577074.1 137.92401	
Rotational constants (GHz)	A	0.57634		0.81293	
	B	0.03859		0.05316	
	C	0.03651		0.05036	

3.3.3. Analyses of natural bond orbitals of compounds 1 and 2

The compounds' natural bond orbitals (NBOs) were calculated in the NBO 3.1 program using the LanL2MB basis set by the DFT method. As a result of this study, it was found that there are 129 molecular orbitals for compound **1** and 121 molecular orbitals for compound **2**. It has been observed that there are 387 charge transitions between 129 molecular orbitals in compound **1** and 467 charge transitions between 121 molecular orbitals in compound **2**. Some of these charge transitions in both compounds were taken from the highest value to the lowest value according to their

second-order perturbation energies and are listed in Tables S3 and S4 for illustrative purposes.

The three strongest bonds in compound **1**, according to their [$E^{(2)}$] values, LP (1) C30 → σ* (C1 - Ni13), LP (1) C30 → π* (C30 - N31) and σ* (C2 -Ni13) → σ * (C1 - Ni13) it is seen that it consists of charge transitions between molecular orbitals. Similarly, the three strongest bonds in compound **2**, according to their [$E^{(2)}$] values, σ* (C16 - O22) → π* (C16 - O22), LP (1) C28 → σ* (C1 -Ni12) and π* (C3 - O11) → σ* (C3 - O11) it is seen that it consists of charge transitions between molecular orbitals. However, considering their [$E^{(2)}$] values, it can be said that the first three bonds in compound **2** are stronger than the first three bonds in compound **1**.

4. CONCLUSION

In this study, the first obtained structures in single crystal form and the second obtained in powder form were investigated. In addition, theoretical calculations were made with the Gaussian 03 program to determine some other properties of the compounds. The results obtained from the IR spectral, crystallographic, and theoretical calculation data of these compounds indicate that they are structurally consistent with each other.

The K(I) ions in compound **1** are coordinated by the four nitrogen atoms of the cyanide groups, the oxygen atoms of the GA and H_2O molecules, and other potassium atoms. Similarly, it can be assumed that the sodium atom in compound **2** is coordinated by the oxygen atoms of the GA and H_2O molecules, the nitrogen atoms of the cyanide groups, and other sodium atoms. Again, the Ni(II) ions in compounds **1** and **2** are coordinated by the four carbon atoms of the cyanide groups.

According to the experimental and theoretical results of the compounds, these compounds appear to be new examples of "Hofmann-type-like compounds". In future studies, the ability of newly obtained Hofmann-type-like compounds to store various types of molecules can be investigated, and these abilities can be compared with the similar abilities of Hofmann-type compounds.

5. CONFLICT OF INTEREST

The authors declare that there is no conflict of interest.

6. ACKNOWLEDGMENTS

7. REFERENCES

1. Hofmann KA, Küspert F. Verbindungen von Kohlenwasserstoffen mit Metallsalzen. Z Anorg Chem. 1897 Jan;15(1):204–7. Available from: <URL>.

2. Wells AF. Structural inorganic chemistry. 4th ed. Oxford: Clarendon Press; 1975. 1095 p. ISBN: 978-0-19-855354-0.

3. Iwamoto T. The Hofmann-Type and Related Inclusion Compounds. In: Atwood JL, Davies JED, McNicol DD, editors. Inclusion Compounds. London: Academic Publishers; 1985. p. 29–57.

4. Lewis RJ, editor. Hawley's Condensed Chemical Dictionary [Internet]. 1st ed. Wiley; 2007 [cited 2023 Nov 17]. Available from: <URL>.

5. Castellani B, Morini E, Filipponi M, Nicolini A, Palombo M, Cotana F, et al. Clathrate Hydrates for Thermal Energy Storage in Buildings: Overview of Proper Hydrate-Forming Compounds. Sustainability. 2014 Sep 30;6(10):6815–29. Available from: <URL>.

6. Nohako KL, Baker PGL, Iwuoha EI. Organic Clathrate Compounds as Suitable Transducers in Electrochemical Sensing. Int J Electrochem Sci. 2015;10:6959–74. Available from: <URL>.

7. Kartal Z, Şahin O, Yavuz A. Synthesis, crystal structure, and characterization of two heterometallic transitionmetal citrate complexes [M=Co(II) and Cd(II)]. Turk J Chem. 2019 Apr 3;43(2):555–67. Available from: <URL>.

8. Kartal Z. Synthesis, spectroscopic, thermal and structural properties of [M(3-aminopyridine)2Ni(μ-CN)2(CN)2]n (M(II)=Co and Cu) heteropolynuclear cyano-bridged complexes. Spectrochimica Acta Part A: Molecular and Biomolecular Spectroscopy. 2016 Jan;152:577–83. Available from: <URL>.

9. Kartal Z, Şahin O, Yavuz A. The synthesis of two new Hofmann-type M(3-aminopyridine) 2 Ni(CN) 4 [M = Zn(II) and Cd(II)] complexes and the characterization of their crystal structure by various spectroscopic methods. Journal of Molecular Structure. 2018 Nov;1171:578–86. Available from: <URL>.

10. Kartal Z, Şahin O. Synthesis, spectroscopic, thermal, crystal structure properties and characterization of new Hofmann-type-like clathrates with 4-aminopyridine and water. Turk J Chem. 2021 Jun 30;45(3):616–33. Available from: <URL>.

11. Bojarska J, Wolf WM. Ultra-Short Cyclo-Peptides as Bio-Inspired Therapeutics: Proline-Based 2,5-Diketopiperazines (DKP). In: The 1st International Electronic Conference on Biomolecules: Natural and Bio-Inspired Therapeutics for Human Diseases [Internet]. MDPI; 2020 [cited 2023 Nov 17]. p. 10. Available from: <URL>.

12. Sarangarajan TR, Panchanatheswaran K, Low JN, Glidewell C. Piperazine-2,5-dione–oxalic acid–water (1/1/2) and a redetermination of piperazine-2,5-dione,

both at 120 K: hydrogen-bonded sheets containing multiple ring types. Acta Crystallogr C Cryst Struct Commun. 2005 Feb 15;61(2):o118–21. Available from: <URL>.

13. Sheldrick GM. A short history of *SHELX*. Acta Crystallogr A Found Crystallogr. 2008 Jan 1;64(1):112–22. Available from: <URL>.

14. Sheldrick GM. Crystal structure refinement with *SHELXL*. Acta Crystallogr C Struct Chem. 2015 Jan 1;71(1):3–8. Available from: <URL>.

15. Bruker. APEX2. Bruker AXS Inc.; 2004.

16. Macrae CF, Sovago I, Cottrell SJ, Galek PTA, McCabe P, Pidcock E, et al. *Mercury 4.0* : from visualization to analysis, design and prediction. J Appl Crystallogr. 2020 Feb 1;53(1):226–35. Available from: <URL>.

17. Farrugia LJ. *WinGX* and *ORTEP for Windows* : an update. J Appl Crystallogr. 2012 Aug 1;45(4):849–54. Available from: <URL>.

18. Kartal Z, Şahin O, Yavuz A. The synthesis of two new Hofmann-type M(3-aminopyridine) 2 Ni(CN) 4 [M = Zn(II) and Cd(II)] complexes and the characterization of their crystal structure by various spectroscopic methods. Journal of Molecular Structure. 2018 Nov;1171:578–86. Available from: <URL>.

19. Kobrsi I, Zheng W, Knox JE, Heeg MJ, Schlegel HB, Winter CH. Experimental and Theoretical Study of the Coordination of 1,2,4-Triazolato, Tetrazolato, and Pentazolato Ligands to the [K(18-crown-6)] + Fragment. Inorg Chem. 2006 Oct 1;45(21):8700–10. Available from: <URL>.

20. Saritemur G, Nomen Miralles L, Husson D, Pitak MB, Coles SJ, Wallis JD. Two modes of *peri* -interaction between an aldehyde group and a carboxylate anion in naphthalaldehydate salts. CrystEngComm. 2016;18(6):948–61. Available from: <URL>.

21. Kartal Z, ŞahiN O, Yavuz A. Synthesis of Hofmann-type Zn(H2O)2Ni(CN)4.nG (G = water and 1,4-dioxane)clathrates and the determination of their structural properties by variousspectroscopic methods. Turk J Chem. 2019 Dec 9;43(6):1608–21. Available from: <URL>.

22. Mendham AP, Dines TJ, Snowden MJ, Withnall R, Chowdhry BZ. IR/Raman spectroscopy and DFT calculations of cyclic di-amino acid peptides. Part III: comparison of solid state and solution structures of cyclo(L -Ser- L -Ser). J Raman Spectroscopy. 2009 Nov;40(11):1508–20. Available from: <URL>.

23. Kartha G, Varughese KI, Lu CT. Structure of the 1:2 complex of 2,5-piperazinedione and formic acid. Acta Crystallogr B Struct Sci. 1981 Sep 1;37(9):1798–800. Available from: <URL>.

24. Wang L, Zhao L, Liu W, Chen R, Gu Y, Yang Y. Co-crystallization of glycine anhydride with the hydroxybenzoic acids: Controlled formation of dimers via synthons cooperation and structural characterization. Sci China Chem. 2012 Nov;55(11):2381–7. Available from: <URL>.

25. Nataraj A, Balachandran V, Karthick T. Molecular orbital studies (hardness, chemical potential, electrophilicity, and first electron excitation), vibrational investigation and theoretical NBO analysis of 2-hydroxy-5-bromobenzaldehyde by density functional method. Journal of Molecular Structure. 2013 Jan;1031:221–33. Available from: <URL>.

26. Tkatchenko A, Alfè D, Kim KS. First-Principles Modeling of Non-Covalent Interactions in Supramolecular Systems: The Role of Many-Body Effects. J Chem Theory Comput. 2012 Nov 13;8(11):4317–22. Available from: <URL>.

27. Nakamoto K. Infrared and Raman spectra of inorganic and coordination compounds. B: Applications in coordination, organometallic, and bioinorganic chemistry. 6. ed. Hoboken, NJ: Wiley; 2009. 408 p. ISBN: 978-0-471-74493-1.

28. Carmona P, Molina M, Escobar R. Studies on aminopyridines in aqueous solution by laser Raman spectroscopy. Spectrochimica Acta Part A: Molecular Spectroscopy. 1993 Jan;49(1):1–9. Available from: <URL>.

29. Khoma RE, Gelmboldt VO, Baumer VN, Shishkin OV, Koroeva LV. Synthesis and structure of aminoguanidinium sulfite monohydrate. Russ J Inorg Chem. 2013 Jul;58(7):843–7. Available from: <URL>.

30. Ma S, Wang M, Liu Y, Yang C, Chi L, Li Q. Ab initio study of spectroscopic properties and anharmonic force fields of MNH2 (M = Li, Na, K). Spectrochimica Acta Part A: Molecular and Biomolecular Spectroscopy. 2021 May;253:119591. Available from: <URL>.

31. Sharpe AG. The chemistry of cyano complexes of the transition metals. London: Acad. Pr; 1976. 11 p. (Organometallic chemistry). ISBN: 978-0-12-638450-5.

32. McCullough RL, Jones LH, Crosby GA. An analysis of the vibrational spectrum of the tetracyanonickelate(II) ion in a crystal lattice. Spectrochimica Acta. 1960 Jan;16(8):929–44. Available from: <URL>.

33. Frisch MJ, Trucks GW, Schlegel HB, Scuseria GE, Robb MA, Cheeseman JR, et al. Gaussian 03, Revision D. 01. Gaussian, Inc.; 2004.

34. Dennington R, Keith T, Millam J. Gauss View, Version 4.1.2. Semichem Inc; 2007.

RESEARCH ARTICLE

Supervised Machine Learning-Graph Theory Approach for Analyzing the Electronic Properties of Alkane

Zubainun Mohamed Zabidi[1] (iD) **, Nurul Aimi Zakaria[1]** (iD) **, Ahmad Nazib Alias[1*]** (iD)

[1]Faculty of Applied Sciences, Universiti Teknologi MARA Perak Branch Tapah Campus, 35400 Tapah Road, Malaysia

Abstract: The combination of advanced scientific computing and quantum chemistry improves the existing approach in all chemistry and material science fields. Machine learning has revolutionized numerous disciplines within chemistry and material science. In this study, we present a supervised learning model for predicting the HOMO and LUMO energies of alkanes, which is trained on a database of molecular topological indices. We introduce a new moment topology approach has been introduced as molecular descriptors. Supervised learning utilizes artificial neural networks and support vector machines, taking advantage of the correlation between the molecular descriptors. The result demonstrate that this supervised learning model outperforms other models in predicting the HOMO and LUMO energies of alkanes. Additionally, we emphasize the importance of selecting appropriate descriptors and learning systems, as they play crucial role in accurately modeling molecules with topological orbitals.

1. INTRODUCTION

Chemical graph theory is a multidisciplinary field combining graph theory and knowledge of chemistry. In chemistry, graph theory is used to analyze various chemical phenomena such as chemical compound composition and classification (1). Chemical graph theory uses the set of points connected by lines to determine structure-property relationships. The molecular structure represented a graph **G**, a set of mathematical structures consisting of several vertices and edges. In chemical graph theory, the molecular structure is typically a suppressed hydrogen with the carbon atom skeleton representing the covalent bond between carbon-carbon atoms (2). The molecular structure is associated with the topological index in chemical graph theory. Topological index is a numerical number invariant for each molecule based on the criteria set using graph theory. Topological indices have gained much attention in various areas of biology and chemistry (3). These are due to the topology indices' most important use in quantitative structure-property relationships (QSPR) and quantitative structure-activity relationships (QSAR) (4). Wiener invented the first topology index, known as the Wiener distance index. The Wiener index has been improved by Randic, known as the hyper-Wiener index (5). The improvement of the Wiener index is still ongoing to tailor the application requirement (6). There are various classes of topological indices, such as distance-based, vertex-degree-based, and spectrum-based topological indices (7).

Supervised learning has become a prominent approach in machine learning. It involves learning the input-output relationship of a system estab-lished from an input-output training sample. The input-output training sample is known as labeled training data or supervised data. This system is also called learning with a 'teacher' (8). The main

purpose of supervised learning is to develop an artificial system that can learn from examples such as the input-output training sample and make predictions of the output based on the input not given in the training set (test set) (9). Various techniques or algorithms exist for conducting supervised learning, including the Decision Tree algorithm, Random Forest (RF), Naïve Bayes algorithm (NB), Support Vector Machine (SVM) and artificial neural network (ANN) (10).

Modelling molecular structure-properties relationships using ANN and SVM as supervised learning starts with a selection topology index to represent the structure. This work aims to look into the applicability of the topology index to the highest occupied molecular orbital (HOMO) and the lowest unoccupied molecular orbital (LUMO). Here, we implement a modification of the moment index. The moment topological index was initially introduced by Dalfo et al. (11). However, the definition of ρ for its further applications is not clearly stated. Chang et al. have applied this index to biphenyl and polycyclic hydrocarbons and extremal polyphenyl chains (12). In this paper, we define the new value of ρ-moment based on the degree of vertices. Using the neural network-Graph theory and Support Vector Machine-Graph theory approaches, the relationship between the moment topology and electronic properties has been a new understanding of electronic properties in alkanes.

2. TOPOLOGY INDEXES AS MOLECULAR DESCRIPTORS

2.1 Molecular Descriptor using Degree Indexes

The Quantitative Structure Properties Relationship (QSPR) model is an important tool for chemical and biological disciplines. It assists in analyzing the physical and chemical properties of molecular structure. Quantitative structure-property relationship analysis (QSPR) is a method that relates the chemical, biological, and physical activities of a molecular compound. The topological index is an example of a molecular descriptor that uses graph theory. Vertex points represent the atoms in the chemical structure. At the same time, the chemical bonding is described by the edge (13). The degree based on the vertex is the most widely employed as a chemical descriptor (14, 15). If $G(V, E)$ is represented as the molecular graph with vertex and edge set, the connectivity index is given by Equation 1.

$$\chi(G) = \sum_{v,u \in V(G)} \frac{1}{\sqrt{d_v d_u}} \qquad \text{(Eq. 1)}$$

where d_v and d_u are the degrees of vertex u and v, respectively. Zhou and Trinajstić modified the connectivity index by replacing the multiplication product with the summation product (16). This

index is also known as the sum connectivity index. The sum connectivity index is given by Equation 2.

$$\chi^{+}(G) = \sum_{v,u \in V(G)} \frac{1}{\sqrt{d_v + d_u}} \qquad \text{(Eq. 2)}$$

Additionally, Estrada has changed the connectivity index by taking into account the degree of the vertex and edge. The equation that describes this index, which is also known as the atom–bond connectivity (ABC), is as follows: (Equation 3) (17).

$$\chi^{ABC}(G) = \sum_{v,u \in V(G)} \sqrt{\frac{d_v + d_u - 2}{d_v d_u}} \qquad \text{(Eq. 3)}$$

The geometry-arithmetic index, or the GA index, is another vertex degree-based topological index. Its definition may be found as Equation 4 (18).

$$GA(G) = \sum_{v,u \in V(G)} \frac{\sqrt{d_v d_u}}{(d_v + d_u)/2} \qquad \text{(Eq. 4)}$$

where $\sqrt{d_v d_u}$ represents the geometry means, and the denominator $(d_v + d_u)/2$ represents the arithmetic mean of end-vertex degrees of the edge.

2.2 Molecular Descriptor using Distance Indexes

A distance-based molecular topology index is another method for analyzing topological molecular structures. The Wiener index is the earliest distance index that has been introduced. The Wiener index of graph G is defined as the sum of all distances between pairs of the graph's vertices given by Equation 5.

$$W(G) = \frac{1}{2} \sum_{v \in V(G)} d(u,v) \qquad \text{(Eq. 5)}$$

where d (u,v) is the shortest distance in G. The Wiener index has been improved, known as the hyper-Wiener index, and its definition is as follows: (Equation 6)(19)

$$WW(G) = \frac{1}{2} \sum_{v \in V(G)} \left(d(u,v) + [d(u,v)]^2 \right) \qquad \text{(Eq. 6)}$$

The reciprocal of the distance between vertex u and v also has been introduced and defined in an Equation 7.

$$H(G) = \sum_{v \in V(G)} \frac{1}{d(u,v)} \qquad \text{(Eq. 7)}$$

The index in Equation 7 is also known as the Harary index (20). In endeavoring to relate graphic

structures with the chemical structure, Parikh word representable graphs (PWRGs) were developed (21). These graphs were based on the Wiener or Harary index calculations.

2. Three Combinations between Degree and Distance indexes

The degree and distance indexes can be combined into new topological indexes. The adjacency (*A*), degree (*v*), and distance matrices have been employed in the establishment of the Molecular Topological index (MTI index), which is based on matrix algebraic operations. The index is simplified using the following mathematical equation (22):

$$MTI = \sum v(D+A) \qquad \text{(Eq. 8)}$$

The Balaban index promises to be an extremely helpful molecular descriptor with appealing properties (23). Balaban index, *J* = *J* [*G* (*V, E*)], is calculated using the average-distance sum connectivity and defined as Equation 9:

$$J = q \sum_{ij} \frac{1}{\left(D_i \, D_j\right)^{1/2}} \qquad \text{(Eq. 9)}$$

where q is the number q of vertex adjacencies, and D_i is the distance sum of *G* (*V, E*) (23). While Ren has combined the distance and degree of the molecular graph to create a new index known as the Xu index (24). Xu index is defined as Equation 10.

$$Xu = n \log \left(\sum_{n}^{i} v_i s_i^2 \Big/ \sum_{n}^{i} v_i s_i \right) \qquad \text{(Eq. 10)}$$

where s_i is the distance sum of *G* (*V, E*) and v_i is the sum vertex-degree matrix of *G* (*V, E*).

3. METHOD OF CALCULATION

3.1 Topology Indices As The Input Data

3.1.1.Topology I: Moment Wiener Index
Dalfo et al. (11) have defined a moment topology index. In this paper, the value of *ρ* (moment constant) determines the weights between the vertices. We define a new moment topological index based on the degree of vertices. The moment Wiener indices is defined as follows:

$$DD1(G) = \frac{1}{2} \sum_{ij \in G} (u_i + u_j)(d_{ij}) \qquad \text{(Eq. 11a)}$$

$$DD2(G) = \frac{1}{2} \sum_{ij \in G} (u_i \cdot u_j)(d_{ij}) \qquad \text{(Eq. 11b)}$$

$$DD3(G) = \frac{1}{2} \sum_{ij \in G} |u_i - u_j|(d_{ij}) \qquad \text{(Eq. 11c)}$$

$$DD4(G) = \frac{1}{2} \sum_{ij \in G} \sqrt{u_i^2 + u_j^2}(d_{ij}) \qquad \text{(Eq. 11d)}$$

where d_{ij} is the shortest distance between vertices *i* and *j*. The numerical value of u_i and u_j is the degree of vertex *i* and *j*.

3.1.2 Topology II: Moment Harary indices
The Harary index of a graph *G (V, E)* is based on reciprocal distance and can be attained as the half-sum of all reciprocal distance elements (25). A new moment Harary indices is given by equation (12).

$$HH1(G) = \frac{1}{2} \sum_{ij \in G} (u_i + u_j)(d_{ij}^{-1}) \qquad \text{(Eq. 12a)}$$

$$HH2(G) = \sum_{ij \in G} (u_i \cdot u_j)(d_{ij}^{-1}) \qquad \text{(Eq. 12b)}$$

$$HH3(G) = \frac{1}{2} \sum_{ij \in G} |u_i - u_j|(d_{ij}^{-1}) \qquad \text{(Eq. 12c)}$$

$$HH4(G) = \frac{1}{2} \sum_{ij \in G} \sqrt{u_i^2 + u_j^2}(d_{ij}^{-1}) \qquad \text{(Eq. 12d)}$$

3.1.3 Topology III: Moment Balaban indices.
The Balaban index is also called the average-distance sum connectivity (23). The moment Balaban indices is defined as the moment of average-distance sum connectivity, that is:

$$JJ1(G) = q \sum_{ij \in G} \frac{1}{\sqrt{D1_i D1_j}} \qquad \text{(Eq. 13a)}$$

$$JJ2(G) = q \sum_{ij \in G} \frac{1}{\sqrt{D2_i D2_j}} \qquad \text{(Eq. 13b)}$$

$$JJ3(G) = q \sum_{ij \in G} \frac{1}{\sqrt{D3_i D3_j}} \qquad \text{(Eq. 13c)}$$

$$JJ4(G) = q \sum_{ij \in G} \frac{1}{\sqrt{D4_i D4_i}} \qquad \text{(Eq. 13d)}$$

where *q* is the number *q* of vertex adjacencies. The value of *D*1, *D*2, *D*3 and *D*4 correspond to the average row for the moment distance $(u_i + u_j)d_{ij}, (u_i \cdot u_j)d_{ij}, |u_i - u_j|d_{ij},$ and $\left(\sqrt{u_i^2 + u_j^2}\right)d_{ij}$,respectively. The computational algorithm for calculating Moment-Wiener, Harary and Balaban index is given in the appendix.

3.2 Machine learning modeling

In the supervised machine learning-Graph theory approach, the molecular descriptors were normalized according to the equation (14).

$$I_i = \frac{I_x - I_{min}}{I_{max} - I_{min}} \qquad \text{(Eq. 14)}$$

where I_x unnormalized input data, I_{max} is the maximum value of the sample, and I_{min} is the minimum value of value of the sample. After that, the main dataset is split into training and test set. The main dataset is then subjected to a machine learning model: artificial neural network and support vector machine. The machine learning model performance was measured using RMSE, which reflects the model's absolute fit and how near the predicted values are to the actual data points. It provides an objective depiction of the model's predicted accuracy. RMSE was determined by applying the Equation 15.

$$RMSE = \sqrt{\frac{1}{n}\sum_{i=1}^{n}(y'-y)^2} \qquad \text{(Eq. 15)}$$

Where n is the number of data, y is the experimental value, and y' is the prediction (calculated) value. The average relative error is calculated as the average of the prediction's absolute divergence from the actual value divided by the actual value.

$$RE = \frac{|y'-y|}{y} \qquad \text{(Eq. 16)}$$

The correlation coefficient r was computed using Equation 17:

$$r = \frac{n\sum(y \cdot y') - (\sum y)(\sum y')}{\sqrt{n\sum(y^2) - (\sum y)^2 - (\sum y')^2}} \qquad \text{(Eq. 17)}$$

where y and y' is the experimental and predicted value, respectively.

3.2.1 Artificial neural network (ANN)

Artificial neural networks (ANN) are a machine-learning approach that the models of biological neural networks inspire. In an artificial neural network, the information processing element consists of several artificial neurons. In the present work, the feedforward forward neural network has been used. ANN utilizes supervised learning methods during the learning or training process. The learning process occurs when each target point is used in the training set. The architecture of this work is given in Figure 1. The architecture of ANN consists of an input layer, a hidden layer, a bias unit, and an output layer. The input layer is the input numerical data from the topological index. The hidden layer is the intermediate layer between the input and layer. The hidden layer analogy in an artificial neural network can be compared to a collection of neurons. The activation function used to train the ANN is applied to the hidden layer. In this study, we use the sigmoidal function $1 / (1 + e^{-x})$ for this calculation. The bias units were attached to a hidden layer. The final layer of the ANN architecture is referred to as the output layer or output nodes. The conditional mean of output requires the knowledge of the joint probability density function of the random variables output and input layers. The learning rate in this calculation is 0.01.

3.2.2 Support Vector Machine (SVM)

The SVM method is a learning algorithm tool used for classification and regression. A non-linear function will transform the input data into high-dimensional feature space. Then, the samples will be separated by drawing a decision boundary (hyperplane) as a linear classifier (26). The linear classifier can be used to distinguish between "positive" and "negative" attributes from the independent variable. The training and test data are split using the split data operator. The training data set is exploited as a targeted point in the learning process. The type of kernel function parameter in this work uses the inner dot product. The machine learning calculation was calculated using Rapidminer Studio.

3.3 Molecular electronic properties (Learning Input)

The learning data or input is needed for the 'learning process' The learning and testing data consist of the Highest Occupied Molecular Orbital (HOMO) and Lowest Unoccupied Molecular Orbital (LUMO). The electronic properties of alkanes HOMO and LUMO were calculated using the semi-empirical self-consistent molecular MOPAC 2016. The detailed method for this calculation can be found in the literature (27).
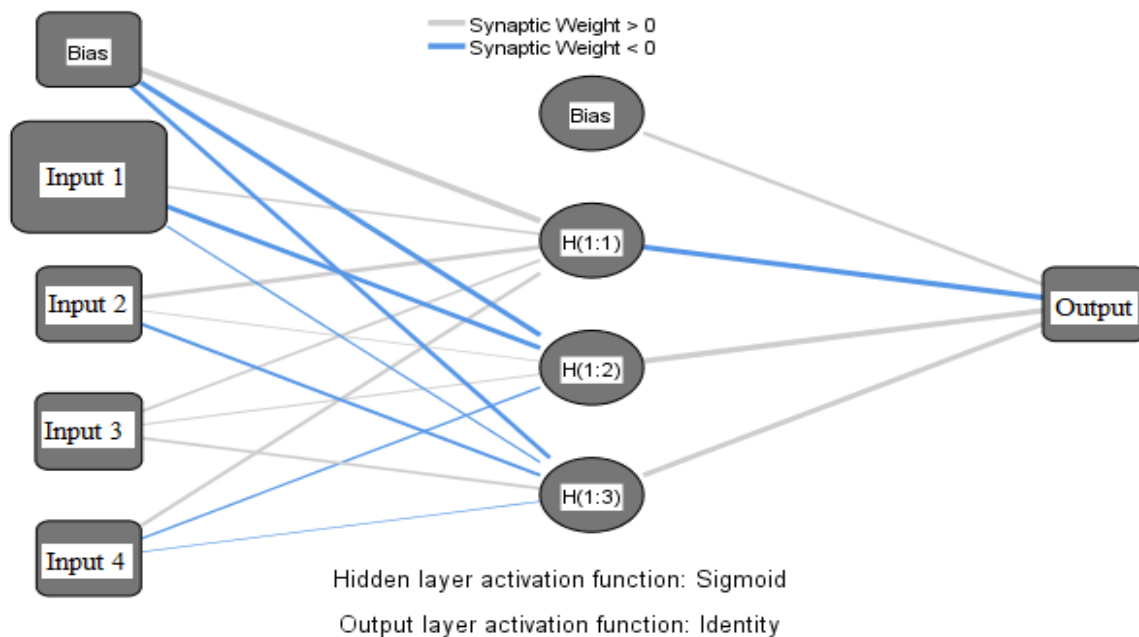
Figure 1. The architecture of ANN.

4. RESULTS

4.1 The artificial neural network-Graph theory approach

The neural network-Graph theory approach extracts complex patterns of molecular structure and relationships from large data sets to predict the electronic properties of alkanes. The moment topology index for 139 alkanes structure is given in Appendix B. The moment topology indices in 2D structural descriptors were more effective than in 3D descriptors (28). In 'normal' electronic calculation, the usual procedure is to find an orbital wave function suitable to the Schrödinger equation. In the supervised learning approach, the relation of molecular descriptors created a statistically optimized relationship with HOMO and LUMO. The relations of the moment topology index with the HOMO and LUMO energies as given in the supplementary table. The correlation plots for the calculated (predicted multilayer perceptron (MLP)) and observed combination topology index are given

in Figure 2. The function of ANN is to extract classical quantum chemistry calculations to perform molecular orbital calculations efficiently, incorporating molecular position with the relation of the topology index.

To evaluate whether the accuracy of our models is sufficient for the electronic application, the data was split into training and test sets. Table 1 presents the accuracy results of ANN training and test sets for HOMO and LUMO. The highest root mean square error (RMSE) and relative error for HOMO are the moment Wiener topology indices. These were followed by the moment Harary and Balaban indices. The result also shows the same pattern for LUMO. This indicates that moment Balaban indices are the most stable descriptor for alkanes' electronic properties. This is plausible due to the moment Balaban indices as descriptors can explain the molecular orbital basis of the saturated hydrocarbon (29). Furthermore, adding molecules or atoms distorts the topology from the linear curve.
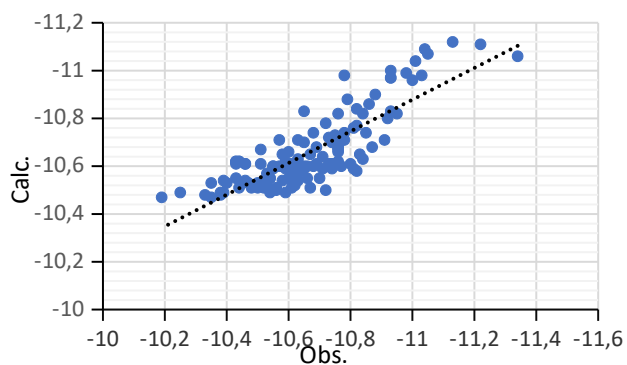
(a)
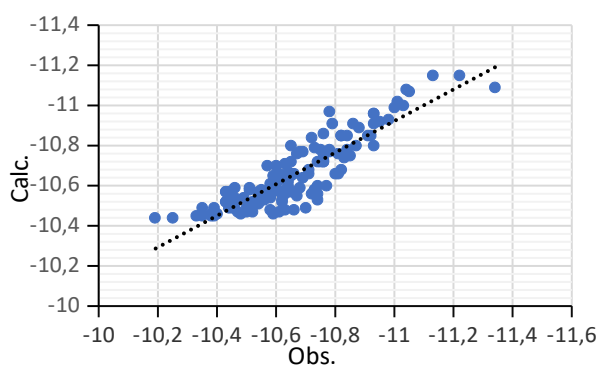
(b)
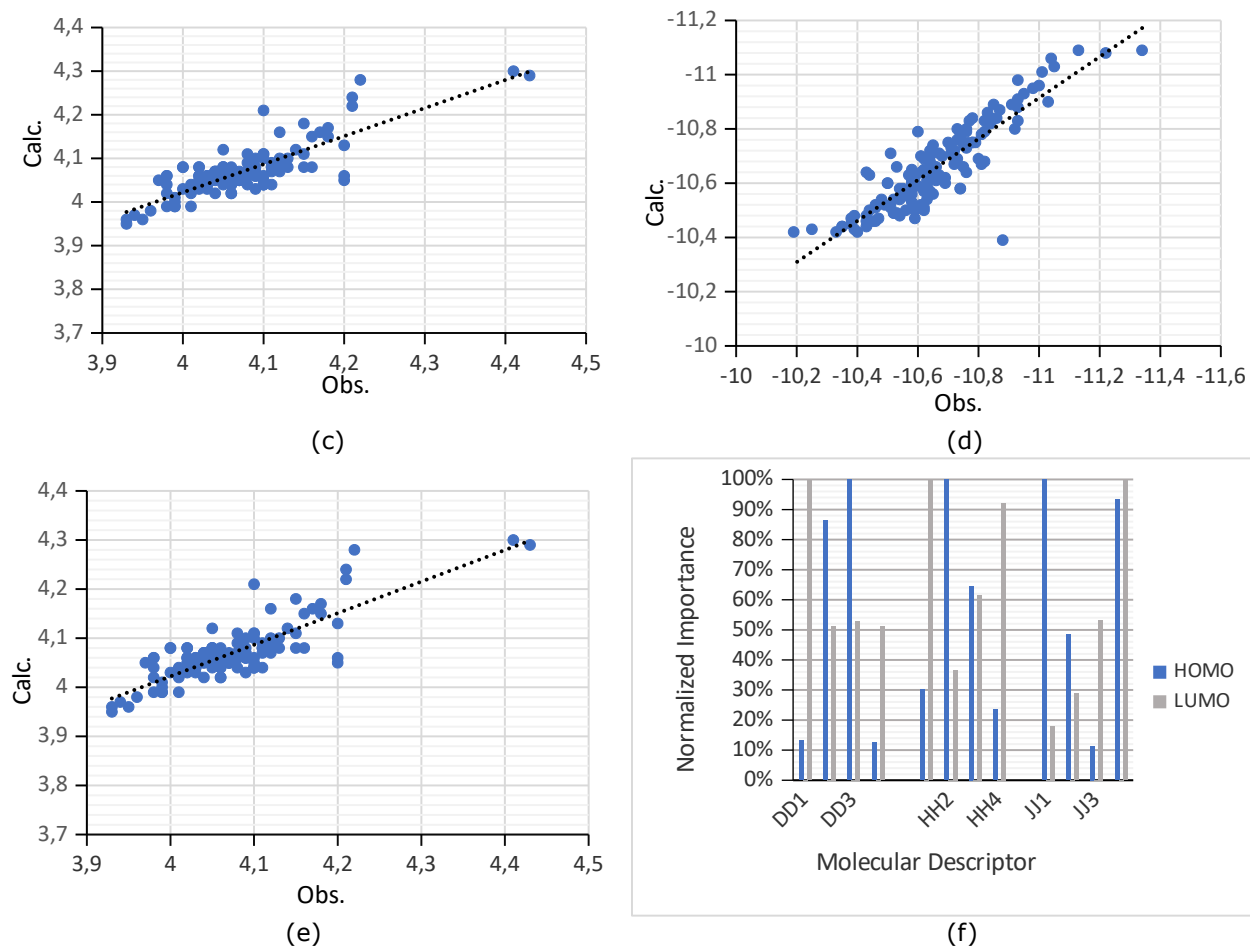
Figure 2: Correlation plots for observed versus calculated for (a) HOMO, (b) LUMO Moment Wiener Indices ; (c) HOMO, (d) LUMO Moment Harary Indices and (e) HOMO, (f) LUMO, Moment Balaban Indices respectively using ANN.

Table 1: Results of neural network modeling using moment Wiener, Harary, and Balaban indices.

| | HOMO[a] | | | | | | LUMO | | | | | |
| | Training set | | | Test set | | | Training set | | | Test set | | |
	r	RMSE	RE	r	RMSE	RE	r	RMSE	re	r	RMSE	RE
Moment Wiener	0.785	0.122	0.920	0.778	0.117	0.910	0.749	0.054	0.96	0.663	0.057	1.17
Moment Harary	0.889	0.091	0.640	0.834	0.097	0.770	0.841	0.048	0.91	0.711	0.057	1.14
Moment Balaban	0.947	0.067	0.470	0.900	0.077	0.54	0.883	0.041	0.75	0.729	0.049	0.89

[a]RMSE, Root mean square error and RE, relative error.
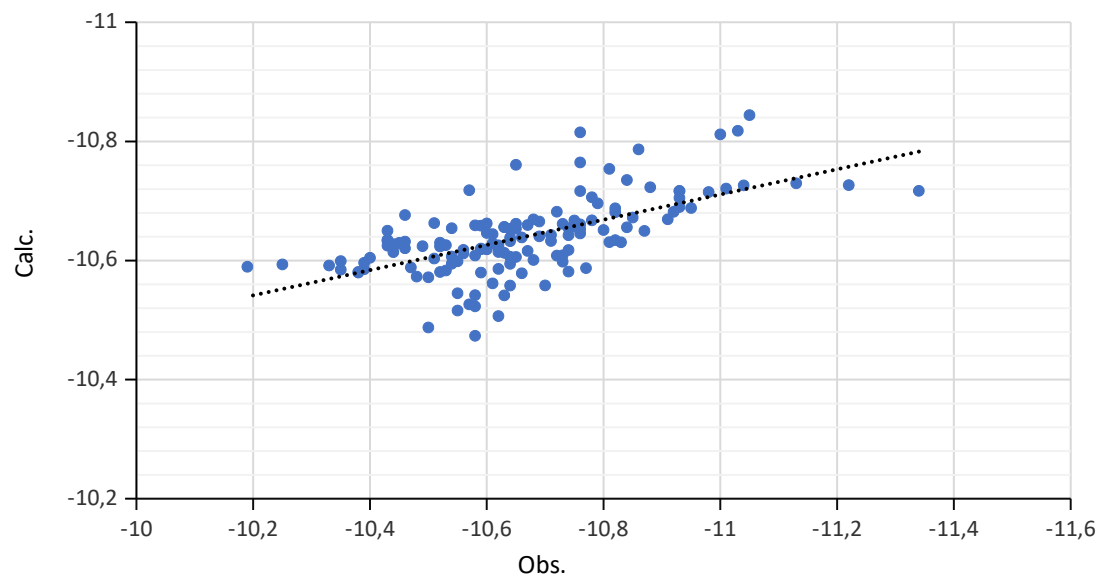
Figure 3: Graph of molecular descriptor versus independent variable importance.

Figure 3 shows each molecular descriptor's contribution to HOMO and LUMO energies. DD3 shows the highest value of HOMO, followed by DD2. However, DD1 and DD4 show a contribution of less than 15%. The contribution for DD1 and DD4 is 13.2% and 12.5%, respectively. This contradicts with LUMO energy, where DD1 contribute 100%. While DD2, DD3 and DD4 contribute more than 50%. In moment Harary indices, HH2 shows the highest contribution for HOMO, followed by HH2, HH3 and HH4. HH1 and HH4 significantly contribute more than 90% of LUMO energy. While HH3 contribute 61.6%. HH2 contributes less than 40%, which is 36.6%. Meanwhile, for the moment, Balaban indices JJ1 and JJ2 show a contribution of more than 90%. While JJ2 contributes 48.5% and JJ contributes 11.5%. JJ4 contributes 100% for LUMO energy, followed by JJ3 (53.3%), JJ2 (28.9%) and JJ1 (18%).

4.2 The Support Vector Machine-Graph Theory Approach

The Support Vector Machine-Graph theory approach is to model complex non-linear relationships of molecular structure from suitable kernel function. The model produced by the support vector depends on the subset of training data to predict the electronic properties of the alkanes molecule. Our model consists of a support vector machine task trained on electronic properties. The optimized

relation of the molecular descriptor with HOMO and LUMO energy was created statistically via the applied test model. The relations of the moment topology index with the HOMO and LUMO energies as given in the supplementary table. The correlation plots for the calculated and observed HOMO and LUMO energy for the combination of topology indices is given in Figure 3. The correlation plots assess the performance of the molecular graph represented from the perspective of projection to a very high-dimensional space via the linear kernel classification. This modelling is capable of appertaining the molecular structure with electronic properties.

SVM training and applying the model resulted in models showing slightly higher prediction accuracy than the ANN (Table 2). The lowest root means square error (RMSE) and relative error (RE) for HOMO and LUMO is the moment Balaban topology indices. These are followed by the moment Harary and Wiener indices. This indicates that moment Balaban index shows the highest stability. The difference between the RMSE and RE values for each of these indices is due to the classification of the dataset via SVM from the molecular indices. The smallest value for all molecule descriptors indices indicates that the SVM can correlate with HOMO and LUMO energy.
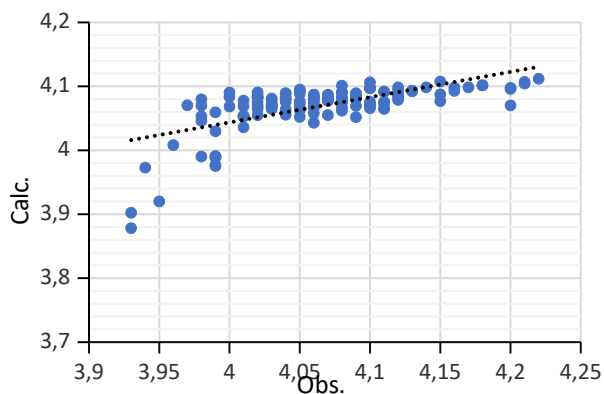
(a)

$$GA(G) = \sum_{v,u \in V(G)} \frac{\sqrt{d_v d_u}}{(d_v + d_u)/2}$$

(b)

(c)

(d)

(e)

(f)
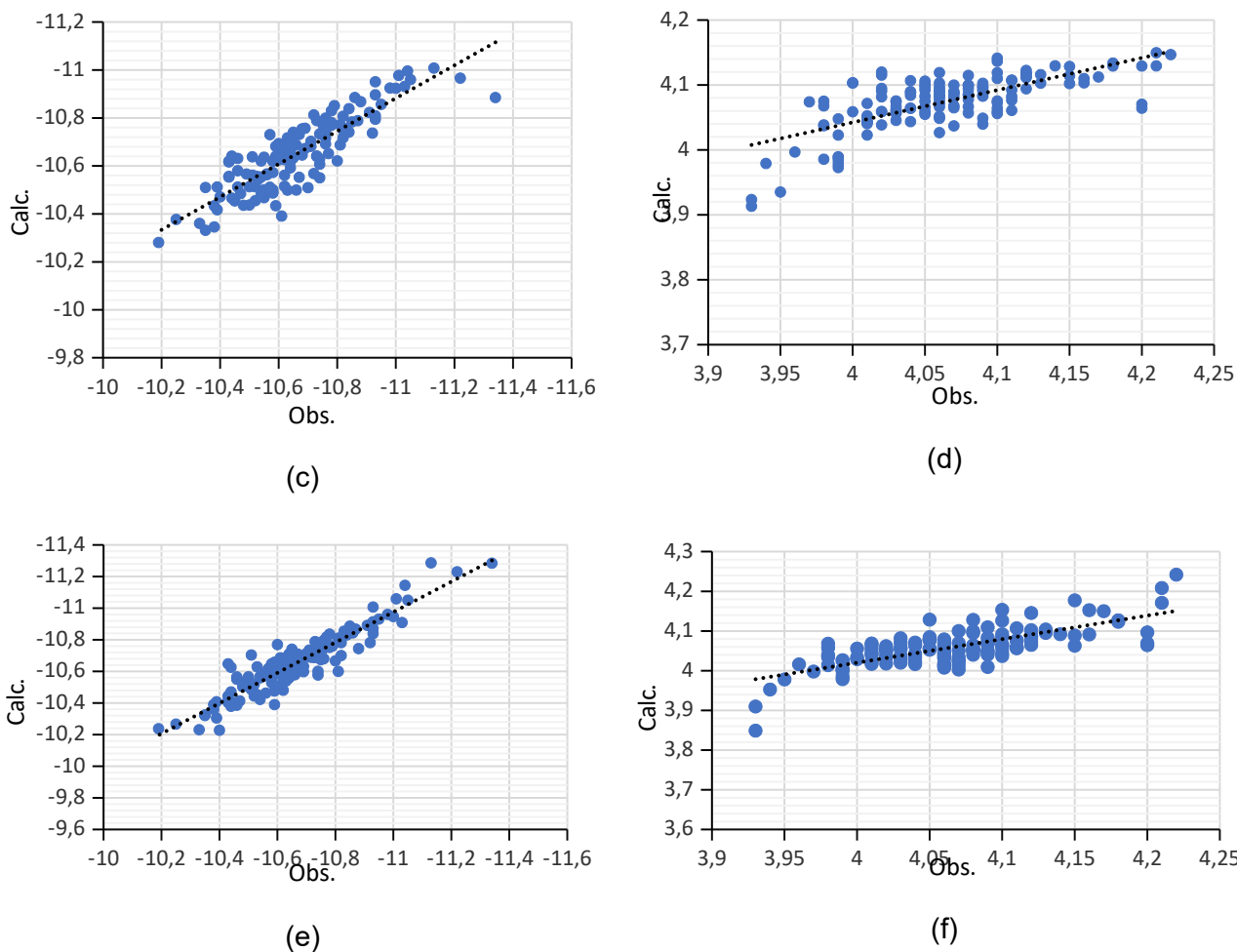
Figure 3: Correlation plots for observed versus calculated for (a) HOMO, (b) LUMO Moment Wiener Indices ; (c) HOMO, (d) LUMO Moment Harary Indices, and (e) HOMO, (f) LUMO Moment Balaban Indices respectively using SVM.

Table 2: Results of Support Vector Machine Using Moment Wiener, Harary, and Balaban Indices.

| | HOMO[a] | | | | | | LUMO | | | | | |
| | Training set | | | Test set | | | Training set | | | Test set | | |
	r	RMSE	RE	r	RMSE	RE	r	RMSE	RE	r	RMSE	RE
Moment Wiener	0.69	0.14	1.03	0.641	0.139	0.019	0.640	0.061	0.95	0.703	0.046	0.92
Moment Harary	0.89	0.089	0.60	0.821	0.100	0.80	0.768	0.051	0.8	0.75	0.043	0.91
Moment Balaban	0.947	0.062	0.42	0.904	0.081	0.58	0.830	0.044	0.79	0.728	0.044	0.87

145
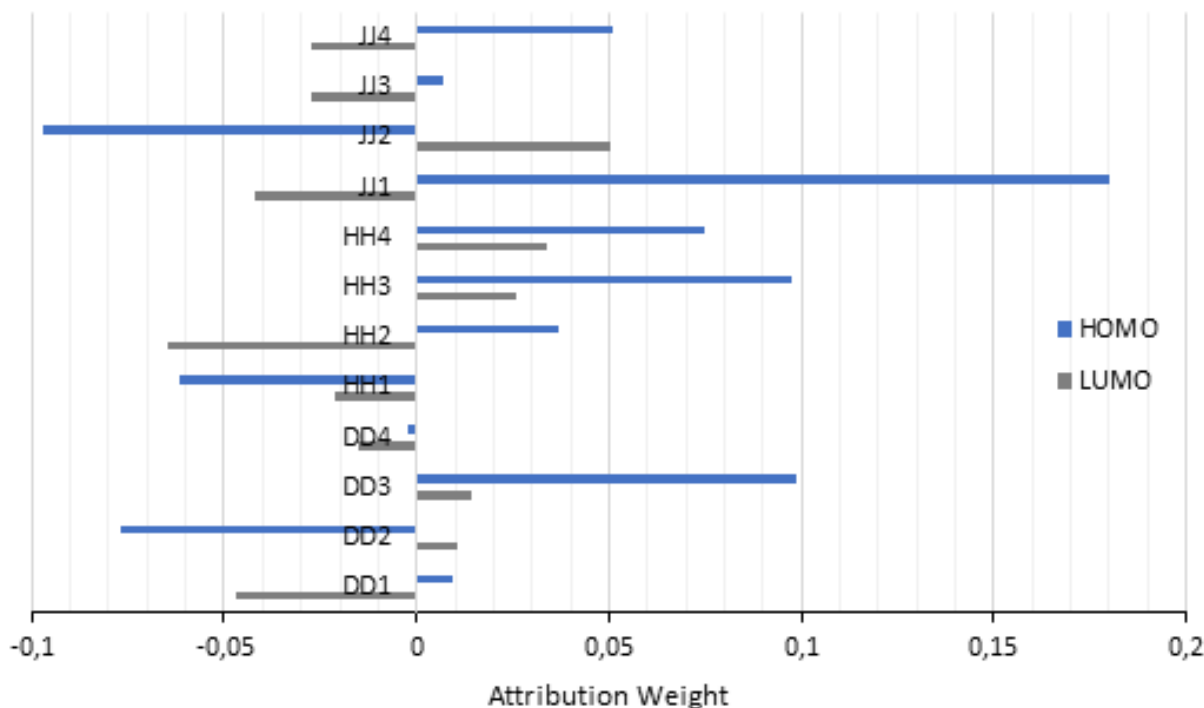
Figure 4: Molecular descriptor Independent variable attribution weight.

The graph of molecular descriptor independent variable attribution weight to HOMO and LUMO energy is shown in Figure 4. DD3 shows the positive and the highest value for the HOMO energy of moment Wiener. This is followed by DD1. DD2, and DD4 showing negative attribution weight. The positive attribution weight for LUMO energy is DD2 and DD3. At the same time, DD1 and DD4 have negative attribution weights. In moment Harary indices, HH2, HH3 and HH4 positively contribute to HOMO. Contrary to HH1, which shows negative attribution weight. HHH1 and HH2 show a negative contribution. Finally, Balaban indices JJ1, JJ2 and JJ3 show the positive attribution for HOMO energy and vice versa for JJ2. At the same time, only JJ2 shows positive attribution for LUMO energy. The variation of attribution weight indicators to classification (30). The effects of attribution weight are obtained from the similarity of the data features of the molecular topology indices.

5. DISCUSSION

The HOMO and LUMO energies reflect the electronic properties of saturated hydrocarbon of alkanes. Alkane is composed of that sigma (σ)-bonds which explain the behavior of electrons in the molecular structure. This bonding is responsible for C – H bond and basic framework C – C bonds. The electronic properties of the molecular structure suggest an interpretation in terms of the localization of electrons. Each molecule has its appropriate energy based on the position of atoms to form the molecules. In the topological approach, the indices

are calculated from suppress-hydrogen, which can be related to the sharing of the electron-induced by the σ-bonds. The topology indices lead to the fundamental concept, which is well-known in chemistry, that is, the octet rule. The octet rule refers to the tendency of atoms to combine so that each atom has eight electrons in the valence shell. However, we need to consider the correlation of electrons in electronic calculation. Therefore, the 'moment' topological approach has been introduced with the value ρ weight between the vertices gives all considerations from the molecular calculation. In the moment topology approach, both properties of graph molecule, that is, degree and distance, have been considered. The distance and derivative of the distance matrix represented the molecule. While ρ weight of $u_i + u_j$, $u_i \cdot u_j$ and $|u_i - u_j|$ are analogies to σ-conjugation, orbital overlapping or Coulomb descriptor(31-33). In comparison, $\sqrt{(u_u^2 + u_v^2)}$ is an analogy with elementary geometry (using Euclidean metrics) (7). The supervised learning can correlate between localized electrons through the whole molecule using topological indices as a molecular descriptor. In this work, the inductive supervise learning approach requires the functional relationship of topology indices that to be modeled. The supervised learning approach provides an improvement in molecular orbital calculation via the data splitting or partition in systematical modeling (learning experience by the machine) (34, 35). The sampling training data was applied to test the data set developing high accuracy in HOMO and LUMO energies (see Tables 1 and 2). SVM training resulted

in models showing slightly higher prediction accuracy than the ANN. The ANN system, in some cases, fails in non-linear classification. Therefore, in this finding, the chosen descriptors and learning system are vital; it is the set of how molecular has been assigned to be modeled with the topological orbital. The electronic properties of alkanes based on Zagreb and Sombor descriptors show low accuracy compares with current works (36). We also find that the Zagreb and Sombor indices are inadequate to assign as descriptors to the electronic structures of alkanes.

6. CONCLUSION

We have introduced a supervised learning model for predicting HOMO and LUMO energies of alkanes based on training artificial neural networks and support vector machines. A new moment topology approach has been introduced as molecular descriptors by taking consideration from the molecular structure perspective. The sampling training data and applied to test the data set, developing high accuracy in electronic properties. The low sum of square error and relative error shows the outperformance supervise learning modelling to the HOMO and LUMO energies of alkanes. SVM training resulted in models showing slightly higher prediction accuracy than the ANN systems. We also find that the chosen descriptors and learning system are of the vital importance, it is the set of how molecular has been assigned to be model with the topological orbital.

7. CONFLICT OF INTEREST

The authors declare no conflict of interest in this paper.

8. ACKNOWLEDGMENTS

The authors would like to thank Dr. James J. P. Stewart from MOPAC Inc. for his permission to use the MOPAC software.

9. APPENDIX

Algorithm for calculating Molecular topology index.

Step 1: Start
Step 2: Define distance Matrix D
Step 3: Calculate the adjacent Matrix A
    3.1 $a_{ij} = 1$ if $d_{i,j} = 1$
    3.2 $a_{ij} = 0$ if else
Step 4: Calculate the degree matrix $V \leftarrow \Sigma A^{<i>}$
Step 5: Calculate elements of k_i matrix
    5.1 $k_1 \leftarrow v_i + v_j$
    5.2 $k_2 \leftarrow v_i \cdot v_j$
    5.3 $k_3 \leftarrow |v_i - v_j|$
    5.4 $k_4 \leftarrow [v_i^2 + v_j^2]^{1/2}$
Step 6: Get Moment Wiener and Balaban Index
    6.1 Multiply elements k_{ij} with elements D_{ij}
    6.2 Sum all elements divided by 2
    6.3 Output DD1, DD2, DD3 and DD4 index
    6.4 Calculate the average-distance sum connectivity from DD1, DD2, DD3 and DD4 matrix
    6.5 Output JJ1, JJ2, JJ3 and JJ4 index
Step 7: Define inverse matrix H
    7.1 $h_{ij} = 1/d_{ij}$
    7.2 $h_{ii} = d_{ii}$
Step 8: Get Moment Harary Index
    8.1 Multiply elements k_{ij} with elements H_{ij}
    8.2 Sum all elements divided by 2
    8.3 Output HH1, HH2, HH3 and HH4 index
Step 9: Stop

10. REFERENCES

1. Takata M, Lin BL, Xue M, Zushi Y, Terada A, Hosomi M. Predicting the acute ecotoxicity of chemical substances by machine learning using graph theory. Chemosphere. 2020 Jan;238:124604. Available from: <URL>.

2. Tamilarasi C, others. QSPR analysis of novel indices with priority polycyclic aromatic hydrocarbons (PAHs). Turkish Journal of Computer and Mathematics Education (TURCOMAT). 2021;12(10):3992–9.

3. Kirmani SAK, Ali P, Azam F. Topological indices and QSPR / QSAR analysis of some antiviral drugs being investigated for the treatment of COVID -19 patients. Int J of Quantum Chemistry. 2021 May 5;121(9):e26594. Available from: <URL>.

4. Sporns O. Graph theory methods: applications in brain networks. Dialogues in Clinical Neuroscience. 2018 Jun 30;20(2):111–21. Available from: <URL>.

5. Randić M. Novel molecular descriptor for structure—property studies. Chemical Physics Letters. 1993 Aug;211(4–5):478–83. Available from: <URL>.

6. Boguñá M, Bonamassa I, De Domenico M, Havlin S, Krioukov D, Serrano MÁ. Network geometry. Nature Reviews Physics. 2021 Jan 29;3(2):114–35. Available from: <URL>.

7. Rada J, Rodríguez JM, Sigarreta JM. General properties on Sombor indices. Discrete Applied Mathematics. 2021 Aug;299:87–97. Available from: <URL>.

8. Van Engelen JE, Hoos HH. A survey on semi-supervised learning. Machine Learning. 2020 Feb;109(2):373–440. Available from: <URL>.

9. Prezhdo OV. Advancing Physical Chemistry with Machine Learning. Journal of Physical Chemistry Letters. 2020 Nov 19;11(22):9656–8. Available from: <URL>.

10. Pavithra M, Kumar PP, Divya P, Manjubala P, Jayalakshmi S. The significance of learning in data analytics: Supervised learning techniques. Global Journal of Internet Interventions and IT Fusion. 2021;4(1–2021).

11. Dalfó C, Fiol MA, Garriga E. Moments in graphs. Discrete Applied Mathematics. 2013 Apr;161(6):768–77. Available from: <URL>.

12. Chang C, Ren H, Deng Z, Deng B. The ρ --moments of vertex-weighted graphs. Applied Mathematics and Computation. 2021 Jul;400:126070. Available from: <URL>.

13. Cao J, Ali U, Javaid M, Huang C. Zagreb connection indices of molecular graphs based on operations. Complexity. 2020 Mar 30;2020:1–15. Available from: <URL>.

14. Chu YM, Julietraja K, Venugopal P, Siddiqui MK, Prabhu S. Degree- and irregularity-based molecular descriptors for benzenoid systems. European Physical Journal Plus. 2021 Jan;136(1):78. Available from: <URL>.

15. Kumar KA, Basavarajappa N, Shanmukha M. QSPR analysis of alkanes with certain degree based topological indices. Malaya Journal of Mathematik. 2020;8(1):314–30.

16. Zhou B, Trinajstić N. On a novel connectivity index. Journal of Mathematical Chemistry. 2009 Nov;46(4):1252–70. Available from: <URL>.

17. Estrada E, Torres L, Rodriguez L, Gutman I. An atom-bond connectivity index: modelling the enthalpy of formation of alkanes. Indian Journal of Chemistry. 1998;37:849-55. Available from: <URL>.

18. Vukičević D, Furtula B. Topological index based on the ratios of geometrical and arithmetical means of end-vertex degrees of edges. Journal of Mathematical Chemistry. 2009 Nov;46(4):1369–76. Available from: <URL>.

19. Shahni Karamzadeh N, Darafsheh MR. Topological Indices of Certain Graphs. Iranian Journal of Mathematical Chemistry [Internet]. 2022 Sep [cited 2023 Nov 27];13(3): 167-74. Available from: <URL>.

20. Alqesmah A, Alloush KAA, Saleh A, Deepak G. Entire Harary index of graphs. Journal of Discrete Mathematical Sciences and Cryptography. 2022 Nov 17;25(8):2629–43. Available from: <URL>.

21. Thomas N, Mathew L, Sriram S, Nagar AK, Subramanian KG. Certain Distance-Based Topological Indices of Parikh Word Representable Graphs. Cangul IN, editor. Journal of Mathematics. 2021 May 25;2021:1–7. <URL>.

22. Gutman I. On degree-and-distance-based topological indices. 2021;66(2):119-23.

23. Das KC. On the Balaban index of chain graphs. Bulletin of the Malaysian Mathematical Sciences Society. 2021;44:2123–38.

24. Ren B. A New Topological Index for QSPR of Alkanes. Journal of Chemical Information and Computer Sciences. 1999 Jan 25;39(1):139–43. Available from: <URL>.

25. Zhou B, Cai X, Trinajstić N. On Harary index. Journal of Mathematical Chemistry. 2008 Aug;44(2):611–8. Available from: <URL>.

26. Zhou ZH. Support Vector Machine. In: Machine Learning [Internet]. Singapore: Springer Singapore; 2021 [cited 2023 Nov 27]. p. 129–53. Available from: <URL>.

27. Alias AN, Zabidi ZM, Zakaria NA, Mahmud ZS, Ali R. Biological Activity Relationship of Cyclic and Noncyclic Alkanes Using Quantum Molecular Descriptors. Open Journal of Applied Sciences. 2021;11(08):966–84. Available from: <URL>.

28. Brown RD, Martin YC. The Information Content of 2D and 3D Structural Descriptors Relevant to Ligand-Receptor Binding. Journal of Chemical Information and Computer Sciences. 1997 Jan 1;37(1):1–9. Available from: <URL>.

29. Herndon WC, Ellzey ML, Raghuveer KS. Topological orbitals, graph theory, and ionization potentials of saturated hydrocarbons. Journal of the American Chemical Society. 1978 Apr;100(9):2645–50. Available from: <URL>.

30. Liu Z, Shao J, Xu W, Meng Y. Prediction of rock burst classification using the technique of cloud models with attribution weight. Natural Hazards. 2013 Sep;68(2):549–68. Available from: <URL>.

31. Woon KL, Chong ZX, Ariffin A, Chan CS. Relating molecular descriptors to frontier orbital energy levels, singlet and triplet excited states of fused tricyclics using machine learning. Journal of Molecular Graphics and Modelling. 2021 Jun;105:107891. Available from: <URL>.

32. Chou SH, Voss J, Bargatin I, Vojvodic A, Howe RT, Abild-Pedersen F. An orbital-overlap model for minimal work functions of cesiated metal surfaces. Journal of Physics: Condensed Matter. 2012 Nov 7;24(44):445007. Available from: <URL>.

33. Dewar MJS. σ-Conjugation and σ-Aromaticity. Bulletin des Soc Chimique. 1979 Jan;88(12):957–67. Available from: <URL>.

34. Li Z, Omidvar N, Chin WS, Robb E, Morris A, Achenie L, et al. Machine-Learning Energy Gaps of Porphyrins with Molecular Graph Representations. Journal of Physical Chemistry A. 2018 May 10;122(18):4571–8. Available from: <URL>.

35. von Lilienfeld OA. Quantum Machine Learning in Chemical Compound Space. Angewandte Chemie International Edition. 2018 Apr 9;57(16):4164–9. Available from: <URL>.

36. Zabidi ZM, Alias AN, Nurul AZ, Zaidatul SM, Rosliza A, Muhamad KY. Machine Learning Predictor Models in the Electronic Properties of Alkanes Based on Degree Topology Indices. Unpublished work. 2021;N/A.

Hadi AA et al. JOTCSA. 2024; 11(1): 149-160.

RESEARCH ARTICLE

Screening of Phytochemical Constituents in Ethanolic Extract from *Astragalus spinosus* Roots and Assessment of Its Anticancer, Antioxidant, and Antibacterial Activities

Ahmed Abdulrazzaq Hadi[1] [ID] **, Ameena Naeem Seewan**[1] [ID] **,**

Zina Abdulhussein Jawad [1] [ID] **, Ali Yahya Naoom**[1] [ID] **, Rusul Ridha Abdulmahdi**[2] [ID]

[1]Al Muthanna University, College of Basic Education, Department of Science, Al Muthanna Province, Iraq.
[2]Al-Muthanna University, Department of Quality Assurance and University Performance Al Muthanna Province, Iraq.

Abstract: The study aims to analyze the chemical components of *Astragalus spinosus* roots extract after the ethanolic extraction process using techniques such as gas chromatography-mass spectrometry, infrared, and UV-Vis spectroscopy to indicate the phytochemical content of the extract. The extract contained various compounds, including alkaloids, terpenoids, flavonoids, phenols, and carboxylic acids. Flavonoid and phenolic content were measured by the colorimetric method and found to be 511.19±35.75 and 24.64±0.07 mg, respectively. Subsequently, antibacterial, antioxidant, and anticancer activities were evaluated for the ethanolic extract. Antibacterial effectiveness was concentration-dependent against *Staphylococcus aureus* and *Streptococcus mutans*, showing optimal inhibition at 100 mg/mL with inhibition areas of 2.81±0.88 and 2.68±2.93 mm, respectively. Antioxidant activity was measured using DPPH with a 200 µg/mL of extract concentration, displaying maximum scavenging activity (71.85±6.43%) and FRAP activity (55.93±1.4%) at 0.64 µg/mL. The alcoholic extract exhibited decreasing vitality of (MCF-7) breast cancer cells as concentration increased, with viability reaching a minimum of 35.378 ± 5.072 at 400 µg/mL.

1. INTRODUCTION

Lately, there has been a notable increase on a global scale in the utilization of medicinal plants or herbal remedies as complementary or adjunctive treatments alongside conventional medicine (1,2). Currently, medicinal plants and their active constituents are widely acknowledged as a promising alternative approach for addressing and treating a variety of human ailments (3-7). *Astragalus spinosus* is an annual herbaceous species of the genus *Astragalus*. The *Astragalus spinosus* plant abounds in the deserts of Iraq and neighboring countries. The genus *Astragalus* consists of around 3000 species. The *Astragalus spinosus* bush is a compact perennial that reaches a height of approximately 70 cm and forms a semi-circular shape (8). Its growth cycle begins afresh in the spring. Notably, it stands out with its white blossoms that appear in January (9-10). Moreover, the plant is characterized by robust, cylindrical, and lengthy

thorns measuring up to 10 cm in length. Traditionally, these plants have been employed in native remedies to address conditions like hypertension, stomach ulcers, bronchitis, diabetes, and gynecological disorders (11). Additionally, various research efforts have explored their potential for anti-inflammatory, antiviral, immunomodulatory, analgesic, antioxidant, anticancer, and cardiotonic properties through diverse screening models (12-17). Therefore, *Astragalus spinosus* presented itself as a suitable candidate for investigating these therapeutic activities (18). Currently, cancer remains a widespread issue, with global projections indicating around 2 million new cancer cases diagnosed annually, resulting in an approximate 80% mortality rate, including cases of breast cancer (19). Breast cancer has the potential to metastasize beyond the breast through blood vessels and lymphatic vessels. To address breast cancer effectively, chemotherapy is frequently employed alongside other treatments like surgery, radiotherapy, or

hormonal therapy. The use of chemotherapy to treat breast cancer carries the possibility of inducing side effects that vary from short-lived and mild to more severe or potentially lasting. To address the challenges posed by this debilitating condition, there is a pressing necessity to explore novel medicines derived from natural sources, which can enhance the quality of life for patients (20). Contemporary drug discovery endeavors are increasingly highlighting the significance of natural origins. As a result, herbal therapy emerges as a potential option. According to several research sources, herbal extracts with antioxidant and anticancer properties have been identified as essential in managing disorders associated with inflammation (21). Healthcare specialists worldwide recognize the need to research medicinal plants to avoid these negative effects while maintaining optimal performance. As a result, it is critical to explore innovative medications derived from plants with fewer adverse effects.

2. EXPERIMENTAL SECTION

2.1. Chemicals and Analytical Devices
2.1.1. Chemicals and Apparatus
Analytical grade pure solvents, including ethanol, DMSO, and methanol (with a purity level of 99.5%), were obtained from the Central Drug House, India. The MTT assay kit consisted of MTT Solution (3-(4,5-dimethylthiazol-2-yl)-2,5-diphenyltetrazolium bromide) and a solubilization solution, ferric reducing antioxidant power assay and chemicals such as sodium dihydrogen phosphate dihydrate, iron chloride, potassium ferricyanide, trichloroacetic acid, and vitamin E were purchased from Merck, Malaysia. In the DPPH radical scavenging activity test, 2,2-diphenyl-1-picrylhydrazyl and ascorbic acid were obtained from Himedia, India. To measure total flavonoids and phenols, sodium nitrate, sodium hydroxide, aluminum chloride, and sodium carbonate were procured from Sigma Aldrich, Malaysia. The instruments used to determine the phytochemical constituents were gas chroma-tography-mass spectrometry [GC-MS (Mass Spectrometer 5977, Gas Chromatography

7890, Agilent), USA], Fourier-transform infrared spectroscopy (FTIR), performed using a Shimadzu FTIR 8400S instrument from Japan, and UV-visible spectrophotometry (Shimadzu UV-1650PC, Japan).

2.2. Collecting Plants and Extraction Procedure
Astragalus spinosus samples (depicted in Figure 1A) were collected during the period spanning October to November 2023 from the Salman district in the southern region of Iraq (at coordinates 30°30'19″N, 44°32'18″E) (herbarium no. 4227). After the collection, the roots underwent meticulous cleansing with running tap water and were subsequently air-dried in a shaded environment (as shown in Figure 1B). After achieving dryness, the roots were processed into a powdered form (as illustrated in Figure 1C) utilizing an electric blender, and the resulting powder was stored securely in an airtight container. To initiate the extraction procedure, 30 grams of finely ground *Astragalus spinosus* roots were inserted into a thimble. The Soxhlet extraction technique was employed, using 250 mL of ethanol within a hot Soxhlet apparatus. The extraction process was carried out over a period of 4 hours, ensuring that the temperature remained below the boiling point of the solvent. Following completion, the obtained extract was filtered using Whatman No. 1 filter paper, followed by concentration under reduced pressure utilizing a rotary evaporator (ISOLAB, Germany) at 80 °C. The resulting extract's weight was measured to ascertain its yield (expressed as a weight percentage) and subse-quently stored at a temperature of 4 °C for potential future investigations. The extraction yield was calculated using Equation 1a and b (22) and expressed as a weight percentage, as referenced.

$$Extraction\ yield\ (\%) = \frac{Weight\ of\ extracted\ root}{Dry\ weight\ of\ the\ root} \times 100$$

<div align="right">(Eq. 1a).</div>

$$Extraction\ yield\ (\%) = \frac{2.2\,g}{30\,g} \times 100 = 7.33\,wt\%$$

<div align="right">(Eq. 1b)</div>
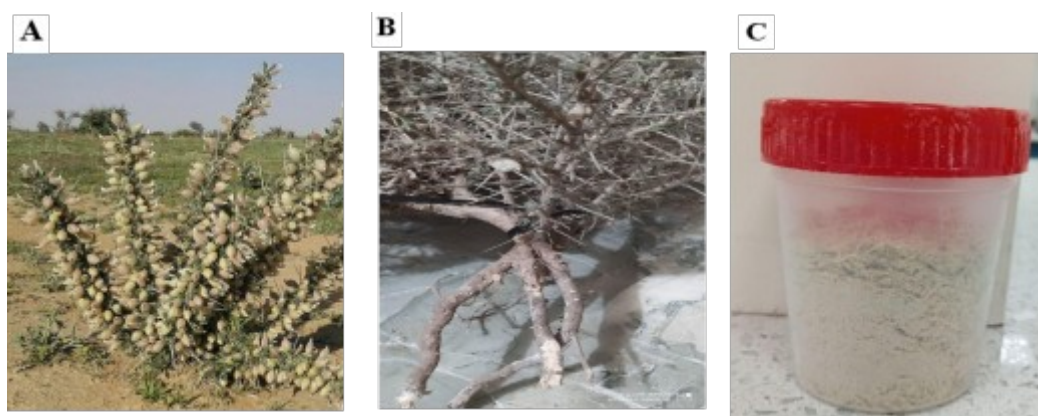
Figure 1: A: *Astragalus spinosus* plant, B: *Astragalus spinosus* roots, and C: Extracted *Astragalus spinosus* roots powder.

2.3. Identification and Quantification of Bioactive Compounds
2.3.1. Double Beam UV-Vis Spectrophotometry
The UV-Vis spectrum of *Astragalus* roots extract was measured using a UV-Vis (UV-1650 PC, Shimadzu, range 190 to 1100 nm) spectrophotometer using 100% ethanol as

a standard reference in the Central Laboratory, Department of Chemistry, College of Science, Al-Muthanna University.

2.3.2. Fourier Transform Infrared Spectroscopy (FTIR)
The infrared spectrum was recorded in the solid state of the EtOH extract of *Astragalus spinosus* roots by using the

84005-FTIR Shimadzu device using KBr disks within the range 400–4000 cm^{-1} of wavenumber at the Chemistry Laboratory within the Department of Chemistry, College of Science at Al-Muthanna University.

2.3.3 Gas Chromatography-Mass Spectrometry (GC-MS)
The GC-MS analysis took place within the laboratory of the Basra oil company, utilizing an Agilent Technologies 7890B GC system coupled with an Agilent Technologies 5977A MSD that included an electron ionization (EI) signal detector. The chromatography utilized HP-5ms with a 5% phenyl and 95% methyl siloxane composition, configured at dimensions of 30 m*250 mm*0.25m. The oven's starting temperature was set to 40 °C and sustained for a period of 5 minutes. Subsequently, the temperature was incrementally elevated at a rate of 8 °C per minute. Helium was employed as the carrier gas with a 1 mL/min flow rate, and a 3 mL/min purge flow was maintained. The total runtime for the GC procedure was 40 minutes. A pulsed split-less mode was engaged for the injection process, featuring an injection temperature of 290 °C, and the injected sample volume amounted to 0.5 microliters. The ion source temperature of the mass spectrometer was set at 230 °C, and scans were conducted at a speed of 1562 (N_2), encompassing a mass range of 44 to 750 m/z. In order to corroborate the identification of compounds, the data was cross-referenced with the NIST 2020 Library database.

2.4. In Vitro Cytotoxicity MTT Assay
The cells were cultivated at different densities, varying from 1×10^4 to 1×10^6 cells/mL. A total of 100 microliters of MCF-7 cells were introduced into 96 wells of the microplate, repeating the process for each concentration as well as the control. Afterward, the microplate was covered and placed in a 37 °C environment for a duration of 2 to 4 hours, all while maintaining a 5% CO_2 atmosphere. Following this, the RPMI-1640 culture medium was eliminated. Over a 48-hour period at 37 °C, 100 µL of *Astragalus spinosus* EtOH roots extract, at different levels of concentration (25, 50, 100, 200, and 400 µg/mL) was administered to each well containing treated cells in the microplate. For every concentration, three replicates were prepared. Following the administration of the extract, ten microliters of MTT solution were introduced, and a 4-hour incubation at 37 °C followed. Afterward, each well received 100 microliters of solubilization solution and was allowed to stand for 5 minutes. The absorbance readings were taken using an ELISA reader (ASYS/Austria) with a wavelength set at 575 nanometers. The percentage of growth inhibition (GI) for each concentration of the extract was computed using formula 2 (23):

$$Viability\,(\%) = \frac{Optical\ Density\ of\ Sample}{Optical\ Density\ of\ Control} \times 100$$
(Eq. 2)

Statistical significance was determined using ANOVA with Duncan's test at a confidence level of $p \leq 0.05$ (24). The outcomes were displayed as the average ± standard deviation. GraphPad Prism version 9 was utilized to conduct the statistical analyses. The evaluation of cytotoxicity using the human breast (MCF-7) cell line took place at the Department of Pharmacology, situated within the Center for Investigation of New Therapies at the University of Malaya in Malaysia.

2.5. In vitro Antioxidant Assay
To evaluate the antioxidant activity of the EtOH extract, the FRAP reductive ability test and the DPPH free radical scavenging test were performed.

2.5.1. Ferric Reducing Power (FRAP) Assay
To measure the reductive ability, the methodology used followed the procedure given in (25). A volume of 1 mL of EtOH roots extract (with concentrations ranging from 0.04 to 0.64 g/mL) was mixed with 1 mL of a phosphate buffer solution (pH of 6.6) at a concentration of 0.2 M, along with 1.5 mL of a potassium ferricyanide solution at a concentration of 1%. Subsequently, the mixture was introduced into an incubator at a temperature of 50 °C for a duration of 20 minutes. The process was stopped by introducing 1 mL of trichloroacetic acid (TCA) at a concentration of 10%. Following that, the resulting blend was subjected to centrifugation at a speed of 3000 revolutions per minute for a duration of 10 minutes. Then, a mixture was prepared by combining 2.5 mL of the suspension with 2 mL of distilled water and 0.5 mL of a liquid solution containing 1% ferric chloride. Following that, the absorbance was measured at a wavelength of 700 nm. The same steps were then replicated for vitamin E, and the complete procedure was repeated three times for each concentration.

2.5.2. DPPH Free Radical Scavenging Activity Assay
The antioxidant activity of EtOH extract of *Astragalus spinosus* roots with standard (vitamin C) was evaluated based on the DPPH-stabilized free radical scavenging effect, and the experiment was carried out according to the working method (26). For every test tube, 0.1 mL of the EtOH roots extract containing vitamin C, across different concentrations (0.0625, 0.125, 0.250, 0.500, and 1.000 µg/mL), was mixed with 3.9 mL of DPPH solution. Subsequently, these test tubes were positioned within an incubator adjusted to 37 °C for a duration of 30 minutes. Using a spectrophoto-meter and a 517 nm of wavelength, the absorbance of each solution was determined, and each concentration was replicated three times. Equation 3 (27) was employed to establish the relationship between a decrease in absorbance and an enhancement in the activity of scavenging free radicals:

$$Scavenging\ Activity\,(\%) = \frac{A_{control} - A_{sample}}{A_{control}} \times 100$$ (Eq. 3)

The measurements $A_{control}$ and A_{sample} represent the absorbance readings of the control and the sample, respectively.

2.6. Total Flavonoids and Total Phenols
Total flavonoid content was assessed using the colorimetric method (28). Firstly, take 3.2 mg of the EtOH extract and dissolve it in 5 mL of a 50% methanolic solution. Next, add 1 mL of a solution comprising 5% (w/v) sodium nitrate. Following a duration of 6 minutes, add 1 mL of a solution containing 10% (w/v) aluminum chloride to the mixture and leave it for 5 minutes. Following this, blend 10 mL of a 10% (w/v) sodium hydroxide solution into the mixture. The next step is to use distilled water to adjust the volume to 50 mL,

ensuring complete mixing. After 15 minutes, use a spectrophotometer to measure the absorbance at 450 nm to determine the total flavonoid concentration. This method was used across six different concentrations (2.5, 5, 10, 20, 40, and 80 g/mL), and the standard curve was created using curve-fitting techniques. The complete phenolic content was determined by applying the Folin-Ciocalteu method, as referenced in (29). To evaluate the content present in the extract, a solution containing 1 mL of the extract within the range of 100 to 500 μg/mL concentrations was blended with 2.5 mL of a Folin-Ciocalteu reagent (Sigma Aldrich, Malaysia) at a concentration of 10% (w/v). After an interval of 5 minutes, 2.0 mL of Na_2CO_3 (at a concentration of 75%) was added to the mixture, followed by incubation at 50 °C for 10 minutes with intermittent agitation. After the sample had cooled down, the absorbance of the samples was measured utilizing a UV spectro-photometer (Shimazu, UV-1900i) at a wavelength of 765 nm compared to a reference blank solution without extract. The data assembled were expressed as (mg/g) of gallic acid equivalents in (mg GAE/g) of the dry extract. The procedure was conducted within the Department of Pharmacology, located within the Center for Investigation of New Therapies at the University of Malaya in Malaysia.

3. RESULTS AND DISCUSSION

3.1. Analysis of Phytochemicals
A phytochemical investigation derived from *Astragalus spinosus* roots revealed various phytochemical compounds. The essential phytochemical constituents, including alkaloids, terpenoids, flavonoids, phenols, carboxylic acids, furans, and alkene derivatives, were detected in the ethanol extract, as illustrated in Table 1.

3.2. UV-Vis Spectrum
The UV-Vis spectrum of the extracted *Astragalus* plant roots dissolved in ethanol compared to pure ethanol as a reference solution exhibited three peaks at specific wavelengths (243.76 nm, 251.66 nm, and 272.63 nm), as shown in Figure 2. These peaks are of significant interest as they provide valuable insights into the molecular composition and electronic structure of the Astragalus root extract. The appearance of these peaks can be attributed to specific electronic transitions within the molecules present in the extract. The first two peaks, at 243.76 nm and 251.66 nm, correspond to electronic transitions as π → π* transitions. In this context, the π → π* transitions are associated with the (C=O) group and the (C=C) group (30). The third peak, observed at 272.63 nm, corresponds to a different type of electronic transition known as the n → π* transition (31). This transition also involves the (C=O) group, indicating the presence of carbonyl compounds in the *Astragalus* roots extract.

Table 1: Phytoconstituents of the ethanol fraction of *Astragalus spinosus* roots.

Test. no.	Phytochemical constituents	Test/ Reagents	Result
1	Flavonoids	NH_4 + Conc. H_2SO_4	++
2	Saponins	Foam test	-
3	Phenols	Ferric chloride test	+
4	Alkaloids	Dragendorff's test	+
5	Coumarins	Alcoholic NaOH	-
6	Terpenoids	Salkowski test	+
7	Glycosides	Acetic acid + $FeCl_3$	+

Key indicators: ++: abundant, +: moderate, -: absent.
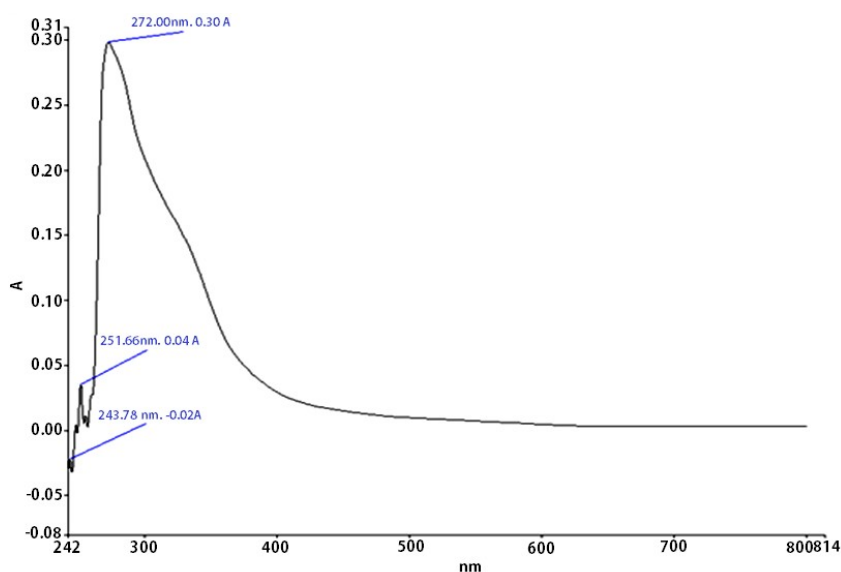
Figure 2: UV-Vis Spectrum of the EtOH roots extract.

3.3. FTIR Spectrum

Crude EtOH extract for *Astragalus spinosus* roots was assayed to determine the functional groups present, and the result is depicted in Figure 3. The spectrum showed broad bands at positions 3537.57 cm^{-1} and 3201.99 cm^{-1}, which are attributed to the stretching vibrations of υ(OH) groups in phenols and flavonoids, respectively. The peaks at 2931.94 and 2872.10 cm^{-1} correspond to asymmetric and symmetric stretching vibrations of υ(CH) in (CH$_2$) and (CH$_3$) groups, respectively (32). The spectral profile exhibits peaks at wave numbers 1728.28 cm^{-1} and 1737.92 cm^{-1}, corresponding to carbonyl groups' stretching vibrations (33). The bands within the 1631.83 and 1514.17 cm-1 range are ascribed to the stretching vibrations of υ(C=C) groups. The bending of the hydroxyl group was observed at wavenumber 1452.45 cm^{-1} (34).

3.4. GC-Mass Analysis

GC-MS analysis of the EtOH extract of *Astragalus spinosus* roots (Figure 4 and Table 2) has provided valuable insights into the chemical composition of this medicinal plant. The analysis revealed a total of 38 peaks, and through meticulous identification based on their retention time on the silica capillary column(35), the compounds present in the extract were characterized. The comprehensive chroma-togram can be observed in Figure 4, while the detailed information regarding the chemical constituents, including their retention time (RT), molecular formula, match score, and area (%), is presented in Table 2. Several prominent constituents have been identified among the diverse bioactive compounds detected in the GC-MS analysis of the ethanol fraction of Astragalus spinosus roots. Notably, 1,1-ethanediol diacetate is the main compound in this organ, constituting approximately 20.02% of the total identified compounds. Additionally, the following compounds were found in relatively significant amounts within the EtOH extract of *Astragalus spinosus* roots: pentadecanoic acid (17.39%), N-Methoxy-Formamide acid (13.10%), Benzyl Chloride (6.26%), 2-Methoxyphenol (4.55%), 1-Methyl-5-fluorouracil (3.98%), 5-Hydroxymethylfurfural (3.88%), 2-Methoxy-4-vinyl phenol (2.63%), 2,6-Dimethoxyphenol (2.40%), 3-Hydroxy-4-methoxy benzaldehyde (2.38%), Acetovanillone (2.08%), Butylated Hydroxytoluene (2.07%), 1-Hexadecene (1.77%), 2,4-Di-tert-butyl-6-nitrophenol (1.75%), 4-(1-Hydroxyallyl)-2-methoxy phenol (1.35%), 1-Hexadecanol (1.20%), Isophytol (1.17%), Pentadecanoic acid (1.16%) as the important compounds in the EtOH extract of *Astragalus spinosus*.
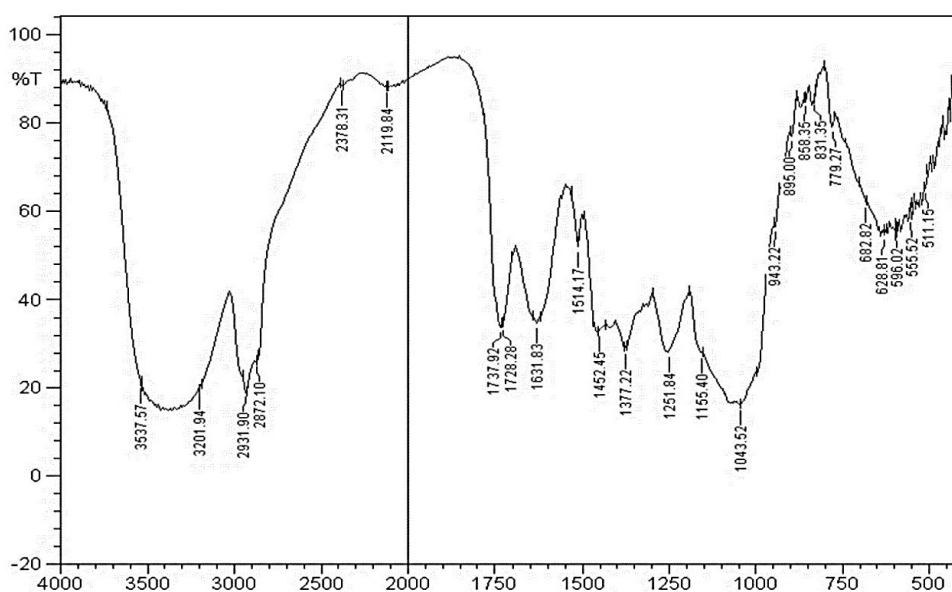
Figure 3: FTIR Spectrum of the EtOH roots extract.

It was found through the chromatogram and the table of GC-MS that the EtOH extract of the roots contains different chemical compounds belonging to different classes, which are alkaloids, terpenoids, flavonoids, phenols, esters, carboxylic acids, formamides, alkyl halides, furans, and alkene derivatives. Some alkaloids have shown promising potential in research as anticancer agents against human breast cancer (36). Research studies have investigated the specific anticancer properties of 1-methyl-5-fluorouracil (also known as 5-fluoro-1-methyluracil or 1-methyl-5-FU) (37). This compo-und serves as an analog of 5-fluorouracil (5-FU), a widely recognized chemotherapy medication emplo-yed in treating various cancer types, including breast cancer. 5-fluorouracil is classified as a pyrimidine analog that interferes with DNA synthesis and obstructs cell division in rapidly dividing cells, such as cancer cells. In clinical practice, 5-fluorouracil is frequently used in combination with other drugs to effectively treat breast cancer and other tumors. Terpenoids, commonly referred to as terpenes, function as antioxidants, defending cells against oxidative stress induced by free radicals (38). Various terpenoids showed inhibition by impeding the growth and multiplication of cancer cells. Overall, terpenoids have displayed a range of biological activities, including antimicrobial, anti-inflammatory, antioxidant, and anticancer attributes (39). Flavonoids are a diverse group of phenolic compounds that may be found in different parts of the plant. They have been extensively studied for their potential health benefits and medical applications. Some of the key medical applications of flavonoids 2-methoxyphenyl

(Guaiacol), 2-methoxy-4-vinyl phenol (4-Vinylguaiacol), and 4-(1-hydroxyallyl)-2-methoxyphenyl (Eugenol) are known for their antioxidant and antimicrobial pro-perties (40). It has been used in traditional medicine and has potential applications in treating respiratory disorders and as an antiseptic. As for phenolic and aromatic compounds such as 2,6-dimethoxy phenyl, butylated hydroxytoluene, and 2,4-di-tert-butyl-6-nitrophenol, they reported anti-oxidant and anti-inflammatory properties (41).
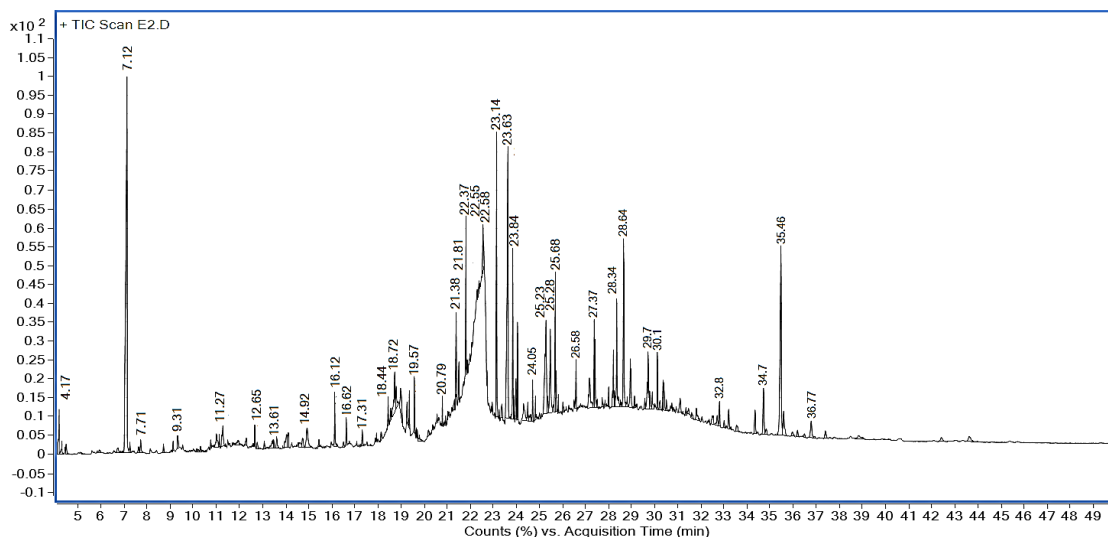
Figure 4: The comprehensive ion chromatogram for GC-MS examination of the *Astragalus spinosus* extracted roots.

Table 2: GC-MS peak identification for *Astragalus spinosus* roots.

Peak No.	RT	Name	CAS No.	Formula	Area %	Similarity Index
1	4.18	Methyl Formate	107-31-3	$C_2H_4O_2$	0.66	98.6
2	7.12	N-Methoxy-Formamide	34005-41-9	$C_2H_5NO_2$	13.107	79.5
3	7.72	Trimethyl Orthoformate	149-73-5	$C_4H_{10}O_3$	0.306	71.1
4	9.31	2-(Dimethylamino) ethylacetate	1421-89-2	$C_6H_{13}NO_2$	0.68	82.2
5	11.3	Benzyl chloride	100-44-7	C_7H_7Cl	0.65	97
6	12.7	2-Methoxyphenol	90-05-1	$C_7H_8O_2$	0.364	98.2
7	13.6	1-Methyl-5-fluorouracil	28564-83-2	$C_5H_5FN_2O_2$	0.298	93
8	14.9	5-Hydroxymethylfurfural	67-47-0	$C_6H_6O_3$	0.981	90.1
9	16.1	2-Methoxy-4-vinylphenol	7786-61-0	$C_9H_{10}O_2$	0.763	97.5
10	16.6	2,6-Dimethoxyphenol	91-10-1	$C_8H_{10}O_3$	0.448	96.9
11	17.3	3-Hydroxy-4-methoxybenzaldehyde	121-33-5	$C_8H_8O_3$	0.306	96.2
12	18.4	Acetovanillone	498-02-2	$C_9H_{10}O_3$	0.474	94.4
13	18.7	Butylated hydroxytoluene	128-37-0	$C_{15}H_{24}O$	3.884	70.1
14	19.6	1-Hexadecene	629-73-2	$C_{12}H_{26}O$	0.907	98.6
15	20.8	2,4-Di-tert-butyl-6-nitrophenol	20039-94-5	$C_{14}H_{21}NO_3$	0.341	85.1
16	21.4	4-(1-Hydroxyallyl)-2-methoxyphenol	32811-40-8	$C_{10}H_{12}O_3$	2.087	95.2
17	21.8	1-Hexadecanol	1000130-97-9	$C_{16}H_{34}O$	2.402	97.9
18	22.4	Isophytol	505-32-8	$C_{20}H_{40}O$	0.403	67.7
19	22.6	Pentadecanoic acid	1002-84-2	$C_{15}H_{30}O_2$	17.393	79
20	22.6	1,1-Ethanediol diacetate	542-10-9	$C_6H_{10}O_4$	20.02	75.6
21	23.1	Lidocaine	137-58-6	$C_{15}H_{22}N_2O_3$	3.985	98.3
22	23.6	3-Eicosene, (E)	57-10-3	$C_{20}H_{40}$	4.559	87.4

24	23.8	Ethyl palmitate	628-97-7	$C_{18}H_{36}O_2$	2.389	98.1
25	24.1	Methyl 3-(3,5-di tert-butyl-4-hydroxyphenyl) propionate	36294-24-3	$C_{19}H_{30}O_3$	1.173	93.2
26	25.2	7-Methyl-3,4-octadiene	37050-05-8	C_9H_{16}	1.2	71.5
27	25.3	9(E)-Octadecenoic acid	112-79-8	$C_{18}H_{34}O_2$	2.639	85.4
28	25.7	1-Hexadecanol	36653-82-4	$C_{16}H_{34}O$	2.074	95.6
29	26.6	Tetracosane	646-31-1	$C_{24}H_{50}$	0.646	94.5
30	27.4	2-Methyl-4-pentyltetrahydro-2H-thiopyran 1,1-dioxide	67715-80-4	$C_{11}H_{22}O_2S$	1.359	93
31	28.3	2-Palmitoylglycerol	23470-00-0	$C_{19}H_{38}O_4$	1.775	93.4
32	28.6	Denatonium benzoate	3734-33-6	$C_{15}H_{23}NO_2$	1.756	83.2
33	29.7	9,12,15-Octadecatrienal	26537-71-3	$C_{18}H_{30}O$	0.871	77.3
34	30.1	Heptacosane	593-49-7	$C_{24}H_{38}O_4$	0.776	96
35	32.8	4,6-cholestadienol	14214-69-8	$C_{27}H_{44}O$	0.462	67.6
36	34.7	Stigmasterol	83-48-7	$C_{29}H_{48}O$	1.164	87.5
37	35.5	Clionasterol	83-47-6	$C_{29}H_{50}O$	6.262	94.9
38	36.8	3,5-Stigmastadien-7-one	2034-72-2	$C_{29}H_{46}O$	0.436	74.5

3.5. Antibacterial Activity

The findings from Table 3 and Figure 5 present compelling evidence of the remarkable antibacterial potential exhibited by the EtOH extract of *Astragalus spinosus* roots. The results demonstrate a positive correlation between the extract's concentration and its antimicrobial activities against *S. aureus* and *S. mutans* bacteria. As the concentration of the EtOH roots extract increases, the inhibitory effects on bacterial growth become more effective, as indicated by the enlargement of the inhibition zone. A maximum zone of inhibition of 2.81 ± 0.88 mm and 2.68 ± 2.93 mm was recorded for *Astragalus spinosus* roots against *S. aureus* and *S. mutans*, respectively, at a 100 mg/mL concentration as compared to other tested concentrations. The outcomes detailed in Table 3 are presented in millimeters (mm), with three replicates so that statistical tests could be applied to evaluate the average ± standard deviation (S.D.).

Table 3: The ability of EtOH root extracts to inhibit the growth of the examined bacterial strains.

Concentration of the EtOH Extract (µg/mL)	Diameter of Inhibition Zone (mm)	
	Bacterial Strains	
	S. aureus	*S. mutans*
25	1.38 ± 0.67	1.54 ± 1.20
50	1.73 ± 0.33	2.09 ± 0.57
75	2.52 ± 0.58	2.56 ± 0.72
100	2.81 ± 0.88	2.68 ± 2.93

3.6. Cytotoxicity MTT assay

Cytotoxicity assessment was employed to evaluate the harmful impacts of the EtOH extract derived from the roots of *Astragalus spinosus* on the MCF-7 breast cancer cell line. The MTT assay was utilized to gauge cell viability and inhibition ratios for cancer cells, employing diverse concentrations of the alcoholic roots extract within the 12.5–400 µg/mL range. The influence of the EtOH roots extract on the MCF-7 breast cancer cell line demonstrated a reduction in cell viability that corresponded to the concentration, with cancer cell vitality diminishing as the extract concentration increased. Specifically, the viability of cancer cells revealed a minimum value of 35.378 ± 5.072 at 400 µg/mL while achieving a maximum value of 96.527 ± 0.722 at 25 µg/mL, and the assay is repeated three times as outlined in Table 4. The inhibition effectiveness of the root's alcoholic extract against the HdFn cell line yielded an IC50 of 62.39 µg/mL. In comparison, the inhibition efficiency against the MCF-7 breast cancer cell line resulted in an IC50 of 23.53 µg/mL (Figure 6).

Hadi AA et al. JOTCSA. 2024; 11(1): 149-160.

RESEARCH ARTICLE
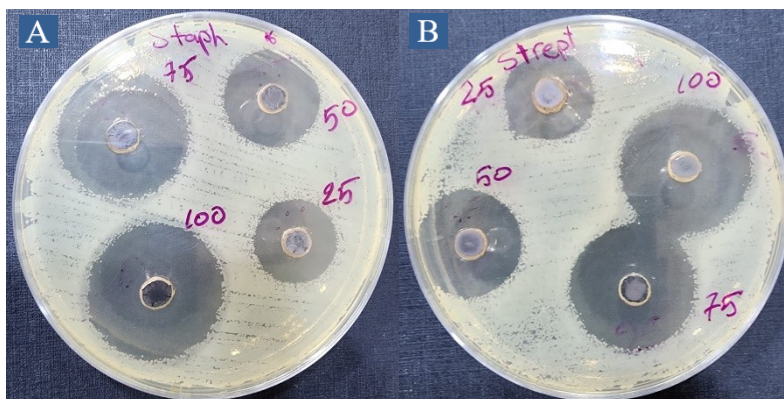
Figure 5: The inhibitory zone created by the EtOH extracts on the specified bacterial strains. (a) *S. aureus*. (b) *S. mutans*.

The EtOH extract demonstrates greater toxicity towards the MCF-7 cell line at elevated doses compared to lower doses. The outcomes indicate that the heightened dosage had a more pronounced toxic impact on cancer cells. This observation aligns with a referenced study that highlights how the suppression of cancer cells by plant extracts is contingent on the dosage (42). Research has substantiated that *Astragalus spinosus* exhibits anticancer properties through its possession of antioxidants, inducing a toxic effect on genes across all concentrations within MCF-7 cells (43). The toxicity of the EtOH extract towards cancer cells can be attributed to its elevated content of numerous anticancer components, including glycosides, flavonoids, phenols, and alkaloid compounds.

3.7. Antioxidant Study
The antioxidative characteristics of the EtOH extract were assessed using the DPPH radical scavenging assay. As illustrated in Figure 7A, the free radical scavenging capacities of the EtOH extract exhibited variability when compared to vitamin C. While ascorbic acid demonstrated higher potency at the initial concentration, the EtOH extract displayed greater scavenging abilities at other concentrations. Three tests were conducted in both DPPH and FRAP assays to assess differences, aiming to enhance precision by averaging the results obtained from these replicates. The extract's remarkable performance at a concentration of 1 µg/mL is particularly noteworthy, yielding a significantly high scavenging ability of (78.27±6.70), as detailed in Table 5 and Figure 7A. Furthermore, the EtOH extract outperformed vitamin E across all concentrations regarding free radical scavenging capabilities at the FRAP assay. At a concentration of 0.64 µg/mL, the extract showcased a higher scavenging ability of (0.55± 0.014), underscoring its robust antioxidative potential, with the lowest observed scavenging ability being (0.11±0.008) at a concentration of 0.04 µg/mL, as highlighted in Table 5 and Figure 7B. This substantiates the extract's capacity to neutralize free radicals effectively and suggests its promising role as a potent antioxidant agent.

Table 4: The impact of the EtOH extract from *Astragalus spinosus* roots on the (MCF-7) and (HdFn) cell lines.

Conc.(µg/mL)	Viable cell count of HdFn±SD	Viable cell count of MCF-7±SD
400	64.96±3.08[D]	35.37±5.07[F]
200	66.47±1.97[D]	42.20±2.72[E]
100	71.14±1.83[C]	54.01±3.23[D]
50	86.30±3.74[B]	64.69±4.71[C]
25	95.37±0.90[A]	75.03±4.98[B]
12.5	96.64±0.70[A]	96.52±0.72[A]

Distinct letters: significant variation (P ≤ 0.05).
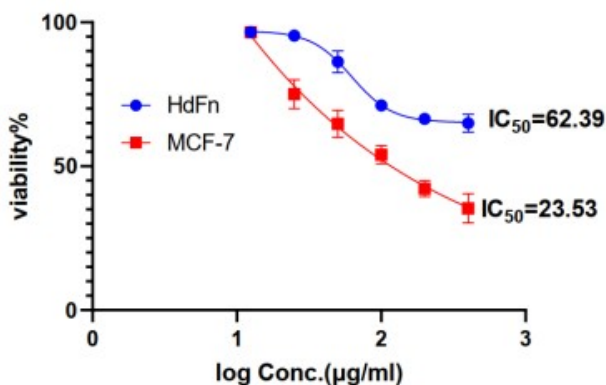
Figure 6: The effect of *Astragalus spinosus* roots EtOH extract in the MCF-7 and HdFn cell lines.

Table 5: Assessment of the antioxidant potential of the EtOH extract from *Astragalus spinosus* roots using the DPPH and FRAP assays.

Conc. (µg/mL)	DPPH assay Mean± S.D.		Conc. (µg/mL)	FRAP assay Mean± S.D.	
	Roots Extract	Vitamin C		Roots Extract	Vitamin E
0.062	29.57±4.47	39.66±2.25	**0.04**	0.11±0.008	0.101±0.001
0.125	53.36±4.33	41.33±10.01	**0.08**	0.31±0.010	0.108±0.001
0.250	65.69±1.23	48.33±8.50	**0.16**	0.41±0.005	0.114±0.004
0.500	71.85±6.43	53.00±10.53	**0.32**	0.45± 0.011	0.132±0.007
1.000	78.27±6.70	57.18±6.34	**0.64**	0.55± 0.014	0.211±0.015
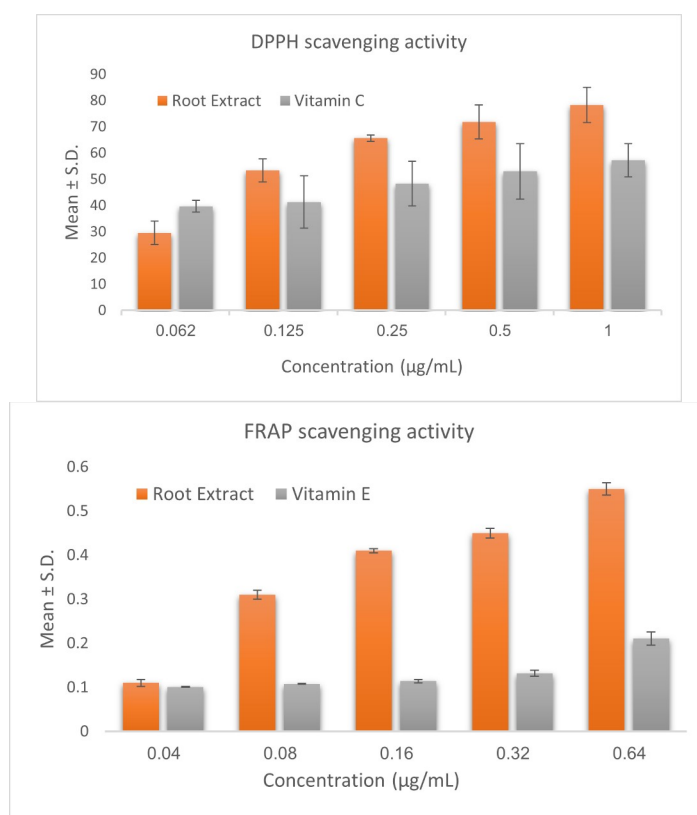
Figure 7: Evaluation of the antioxidant capacity of the extract derived from *Astragalus spinosus* roots, encompassing (A) the scavenging of DPPH radicals and (B) the FRAP scavenging activity.

157

4. CONCLUSION

This research yielded valuable insights into promising biological effects and phytochemical profiles, aiding in the identification and characterization of Iraqi *Astragalus* species. The present study employed GC-MS, FTIR, and UV-VIS analyses, as well as assessments of total flavonoids, total phenolics, antibacterial, antioxidant, and anticancer properties of the ethanol-extracted roots of *Astragalus spinosus*. The roots of *Astragalus spinosus* contain diverse phytochemical constituents that exhibit numerous pharmacological attributes. The GC-MS analysis identified 38 phytochemical components contributing to antimicrobial, antioxidant, anticancer, and related activities. Furthermore, this research provides compelling evidence of the roots extract's effectiveness against microbes (*S. aureus and S. mutans*), its antioxidant capabilities (measured through DPPH and FRAP assays), and its potential as an anticancer agent (evaluated against the MCF-7 cell line). Further research is required to identify and isolate specific bioactive chemicals, aiming to enhance our understanding of the intricate molecular processes of phytoconstituents' actions that contribute to biological activities, whether directly or indirectly.

5. CONFLICT OF INTEREST

There are no declarations of conflicts.

6. REFERENCES

1.   Shaito, A., Thuan, D. T. B., Phu, H. T., Nguyen, T. H. D., Hasan, H., Halabi, S. & Pintus, G. Herbal medicine for cardiovascular diseases: efficacy, mechanisms, and safety. Frontiers in pharmacology. 2020; 11: 422. Available from: <URL>.

2.   Weremczuk-Jeżyna I, Lebelt L, Piotrowska DG, Gonciarz W, Chmiela M, Grzegorczyk-Karolak I. The Optimization Growth of Dracocephalum Forrestii In Rita® Bioreactor, And Preliminary Screening Of The Biological Activity Of The Polyphenol Rich Extract. Acta Scientiarum Polonorum, Hortorum Cultus. 2023;22(2):45–59. Available from: <URL>.

3.   Abd Elkader, H. T. A. E., Essawy, A. E., & Al-Shami, A. S. Astragalus species: Phytochemistry, biological actions and molecular mechanisms underlying their potential neuroprotective effects on neurological diseases. Phytochemistry. 2022; 113293. Available from: <URL>.

4.   Uddin, G., Rauf, A., Siddiqui, B. S., & Shah, S. Q. Preliminary comparative phytochemical screening of Diospyros lotus Stewart. Middle-East Journal of Scientific Research. 2011; 10(1), 78-81. Available from:<URL>

5.   Essawy, A. E., Abd Elkader, H. T. A. E., Khamiss, O. A., Eweda, S. M., & Abdou, H. M. Therapeutic effects of astragaloside IV and Astragalus spinosus saponins against bisphenol A-induced neurotoxicity and DNA damage in rats. PeerJ. 2021; 9, e11930. Available from: <URL>

6.   Abd Elkader, H. T. A. E., Abdou, H. M., Khamiss, O. A., & Essawy, A. E. Anti-anxiety and antidepressant-like effects of astragaloside IV and saponins extracted from Astragalus spinosus against the bisphenol A-induced motor and cognitive impairments in a postnatal rat model of schizophrenia. Environmental Science and Pollution Research. 2021; 28, 35171-35187. Available from: <URL>

7.   Shawky, E., & Selim, D. A. Evaluation of the effect of extraction solvent and organ selection on the chemical profile of Astragalus spinosus using HPTLC-multivariate image analysis. Journal of Chromatography B. 2017; 1061, 134-138. Available from: <URL>

8.   Ahmed, M., & Al-Dousari, N. The environmental and economic importance of Astragalus Spinosus in land restoration. Journal of Taibah University for Science. 2020; 14(1), 1489-1495. Available from: <URL>

9.   Abd El-Ghani, M. M., El-Sayed, A. S., Moubarak, A., Rashad, R., Nosier, H., & Khattab, A. Biosystematic study on some Egyptian species of Astragalus. (Fabaceae). Agriculture. 2021; 11(2), 125. Available from: <URL>

10.   Almohammed, H. I., & Alanazi, A. D. In vitro/in vivo Assessment and Cellular Mechanisms of Astragalus spinosus Extract against Leishmania major. Pharmacognosy Magazine. 2022; 18(80), 830-835. Available from: <URL>

11.   Juwad, L. M., Mahmood, O. I., & khatlan Hameed, A. P. D. B. The Effect of Using Astragalus Spinosus Extracts as a Treatment for Leishmania Parasite in Terms of Histological Changes. Journal Healthcare Treatment Development (JHTD). 2023; 3(04), 32-42. Available from: <URL>

12.   Zeidan, M. M., & Raddam, Q. N. Physiological and histological protective role of Astragalus spinosus root alcoholic extract against oxidative stress induced by H2O2 in rabbits. In Journal of Physics: Conference Series. 2021; (Vol. 1879, No. 2, p. 022039). Available from: <URL>

13.   Ashour, M. A. Comparative chemical and biological investigations of three Saudi Astragalus species. Journal of Applied Biology and Biotechnology. 2019; 7(5), 56-61. Available from: <URL>

14.   Faraj, A. G., Osman, A. K. E., & Arbi, G. Contributions to the pollen morphology of genus Astragalus L. (Fabaceae) and its taxonomic implications. Asian Journal of Plant Sciences. 2013; 12(5), 176-189. Available from: <URL>

15.   Nayeem, N., Imran, M., Asdaq, S. M. B., Rabbani, S. I., Alanazi, F. A., Alamri, A. S., & Alhomrani, M. Total phenolic, flavonoid contents, and biological activities of stem extracts of Astragalus spinosus (Forssk.) Muschl. grown in Northern Border Province, Saudi Arabia. Saudi Journal of Biological Sciences. 2022; 29(3), 1277-1282. Available from: <URL>

16.   Ghabban, H., Alnomasy, S. F., Almohammed, H., Al Idriss, O. M., Rabea, S., & Eltahir, Y. Antibacterial, cytotoxic, and cellular mechanisms of green synthesized silver nanoparticles against some cariogenic bacteria (Streptococcus mutans and Actinomyces viscosus). Journal of Nanomaterials. 2022; 1-8. Available from: <URL>

17.   Al-Harbi, K. B., El-Ashmawy, I. M., & Al-Wabel, N. A. The antidiarrheal activity of the methanol extract of some plants native to Al-Qassim Region, Saudi Arabia. J. Food Agric. Environ. 2016; 14, 239. Available from: <URL>

18.   Ibrahim, R. S., El-Mezayen, N. S., & El-Banna, A. A. Alleviation of liver cirrhosis and associated portal-hypertension by Astragalus species in relation to their UPLC-MS/MS metabolic profiles: a mechanistic study. Scientific Reports. 2022;12(1):11884. Available from: <URL>.

19.   Łukasiewicz, S., Czeczelewski, M., Forma, A., Baj, J., Sitarz, R., & Stanisławek, A. Breast cancer—epidemiology, risk factors, classification, prognostic markers, and current treatment

Hadi AA et al. JOTCSA. 2024; 11(1): 149-160.

RESEARCH ARTICLE

strategies—an updated review. Cancers. 2021; 13(17), 4287. Available from: <URL>

20. Goldstein, A., & Rahman, S. Seeking impact: Global perspectives on outcome measure selection for translational and clinical research for primary mitochondrial disorders. Journal of Inherited Metabolic Disease. 2021; 44(2): 343-357. Available from: <URL>.

21. Jiang, D., Rasul, A., Batool, R., Sarfraz, I., Hussain, G., Mateen Tahir, M. & Li, X. Potential anticancer properties and mechanisms of action of formononetin. BioMed research international, Review Article. 2019. Available from: <URL>.

22. Dhanani, T., Shah, S., Gajbhiye, N. A., & Kumar, S. Effect of extraction methods on yield, phytochemical constituents and antioxidant activity of Withania somnifera. Arabian journal of chemistry. 2017; 10(1): S1193-S1199. Available from: <URL>.

23. Formagio, A. S. N., Vieira, M. C., Volobuff, C. R. F., Silva, M. S., Matos, A. I., Cardoso, C. A. L. & Carvalho, J. E. In vitro biological screening of the anticholinesterase and antiproliferative activities of medicinal plants belonging to Annonaceae. Brazilian Journal of Medical and Biological Research. 2015; 48: 308-315. Available from: <URL>.

24. Jobbágy, J., Dančanin, P., Krištof, K., Maga, J., & Slaný, V. Evaluation of the quality of irrigation machinery by monitoring changes in the coefficients of uniformity and non-uniformity of irrigation. Agronomy. 2021; 11(8): 1499. Available from: <URL>.

25. Fu, Wei, Chen, J., Cai, Y., Lei, Y., Chen, L., Pei, L. & Ruan, J. Antioxidant, free radical scavenging, anti-inflammatory and hepatoprotective potential of the extract from Parathelypteris nipponica (Franch. et Sav.) Ching. Journal of ethnopharmacology. 2010; 130(3): 521-528. Available from: <URL>.

26. Shah, P., & Modi, H. A. Comparative study of DPPH, ABTS and FRAP assays for determination of antioxidant activity. Int. J. Res. Appl. Sci. Eng. Technol. 2015; 3(6): 636-641. Available from: <URL>.

27. Bajpai, V. K., Baek, K. H., & Kang, S. C. Antioxidant and free radical scavenging activities of taxoquinone, a diterpenoid isolated from Metasequoia glyptostroboides. South African Journal of Botany, 2017;111: 93-98. Available from: <URL>.

28. Zahra, S. S., Ahmed, M., Qasim, M., Gul, B., Zia, M., Mirza, B., & Haq, I. U. Polarity based characterization of biologically active extracts of Ajuga bracteosa Wall. ex Benth. and RP-HPLC analysis. BMC Complementary and Alternative Medicine. 2017; 17(1): 1-16. Available from: <URL>.

29. Musci, M., & Yao, S. Optimization and validation of Folin–Ciocalteu method for the determination of total polyphenol content of Pu-erh tea. International journal of food sciences and nutrition. 2017; 68(8): 913-918. Available from: <URL>.

30. Vansco, M. F., Marchetti, B., & Lester, M. I. Electronic spectroscopy of methyl vinyl ketone oxide: A four-carbon unsaturated Criegee intermediate from isoprene ozonolysis. The Journal of Chemical Physics. 2018;149(24). Available from: <URL>.

31. McKenzie, T. G., Fu, Q., Wong, E. H., Dunstan, D. E., & Qiao, G. G. Visible light mediated controlled radical polymerization in the absence of exogenous radical sources or catalysts. Macromolecules. 2015; 48(12): 3864-3872. Available from: <URL>.

32. Al-Wabli, R. I., Resmi, K. S., Mary, Y. S., Panicker, C. Y., Attia, M. I., El-Emam, A. A., & Van Alsenoy, C. Vibrational spectroscopic studies, Fukui functions, HOMO-LUMO, NLO, NBO analysis and molecular docking study of (E)-1-(1, 3-benzodioxol-5-yl)-4, 4-dimethylpent-1-en-3-one, a potential precursor to bioactive agents. Journal of Molecular Structure. 2016; 1123:375-383. Available from: <URL>.

33. Farber, C., Li, J., Hager, E., Chemelewski, R., Mullet, J., Rogachev, A. Y., & Kurouski, D. Complementarity of raman and infrared spectroscopy for structural characterization of plant epicuticular waxes. ACS Omega 2019; 4(2): 3700-3707. Available from: <URL>.

34. Rbaa, M., Hichar, A., Dohare, P., Anouar, E. H., Lakhrissi, Y., Lakhrissi, B. & Zarrouk, A. Synthesis, characterization, biocomputational modeling and antibacterial study of novel pyran based on 8-hydroxyquinoline. Arabian Journal for Science and Engineering. 2021; 46(19): 5533-5542. Available from: <URL>.

35. Thomas JN, Roopkumar J, Patel T. Machine learning analysis of volatolomic profiles in breath can identify non-invasive biomarkers of liver disease: A pilot study. PLoS ONE. 2021; 16(11): e0260098. Available from: <URL>.

36. Manayi, A., Nabavi, S. M., Setzer, W. N., & Jafari, S. Piperine as a potential anticancer agent: a review on preclinical studies. Current medicinal chemistry. 2018; 25(37): 4918-4928. Available from: <URL>.

37. Arif, A. B., Susanto, S., Matra, D. D., & Widayanti, S. M. Identification of Bioactive Compounds and Their Benefits of Some Parts of Abiu (Pouteria caimito). Jurnal Hortikultura Indonesia. 2021; 12(1): 10-20. Available from: <URL>.

38. Ahmed, E., Arshad, M., Khan, M. Z., Amjad, M. S., Sadaf, H. M., Riaz, I. & Ahmad, N. Secondary metabolites and their multidimensional prospective in plant life. Journal of Pharmacognosy and Phytochemistry. 2017; 6(2):205-214. Available from: <URL>.

39. Murthy, H. N., Dalawai, D., Dewir, Y. H., & Ibrahim, A. Phytochemicals and biological activities of Garcinia morella (Gaertn.) Desr.: A review. Molecules. 2020; 25(23): 5690. Available from:> URL<.

40. Abdou, A., Idouaarame, S., Salah, M., Nor, N., Zahm, S., El Makssoudi, A. & Dakir, M. Phytochemical study: molecular docking of eugenol derivatives as antioxidant and antimicrobial agents. Letters in Organic Chemistry. 2022; 19(9): 774-783. Available from: <URL>.

41. Farmer, L. A., Haidasz, E. A., Griesser, M., & Pratt, D. A. Phenoxazine: a privileged scaffold for radical-trapping antioxidants. The Journal of organic chemistry. (2017); 82(19), 10523-10536. Available from: <URL>.

42. Jairaman, C., Alehaideb, Z. I., Yacoob, S. A. M., Alghamdi, S. S., Suliman, R. S., Venkataraman, A. & Rameshbabu, S. Rhizophora mucronata Lam. (Mangrove) Bark Extract Reduces Ethanol-Induced Liver Cell Death and Oxidative Stress in Swiss Albino Mice: In Vivo and In Silico Studies. Metabolites. 2022; 12: 1021. Available from: <URL>.

43. Tay, K. C., Tan, L. T. H., Chan, C. K., Hong, S. L., Chan, K. G., Yap, W. H. & Goh, B. H. Formononetin: a review of its anticancer potentials and mechanisms. Frontiers in pharmacology. 2019; 10: 820. Available from: <URL>.

RESEARCH ARTICLE

Iodine–β-Cyclodextrin: An Effective Corrosion Inhibitor for Carbon Steel in Sulfuric Acid Solution - Experimental Design and Investigating Thermodynamic Parameters

Tarik Attar[1,2]* (iD) **, Abbes Benchadli[2]** (iD) **, Amal Benkhaled[2]** (iD) **,**

Esma Choukchou-Braham[2] (iD)

[1]Ecole Supérieure en Sciences Appliquées de Tlemcen, ESSA-Tlemcen, BP 165 RP Bel Horizon, Tlemcen 13000, Algeria.
[2]Laboratoire de ToxicoMed, Université Abou Bekr Belkaïd, B.P. 119, Tlemcen 13000, Algeria.

Abstract: Widely used across industries, carbon steel is vulnerable to corrosion in aggressive environments, especially acidic ones. Thus, effective methods to mitigate metal corrosion from acids are crucial. Inhibitors are extensively used to prevent corrosion in industries, with the potential for improved protective performance. The design of experiments was employed to determine the optimal conditions for enhancing the inhibitor efficiency of Iodine–β-Cyclodextrin (Iodine/β-CD) in a sulfuric acid solution at temperatures ranging from 20°C to 50°C. The relationship between the factors and responses was established using response surface methodology (RSM), employing regression statistical analysis and probabilistic analysis. A single response was recorded: inhibitor efficiency was determined by measuring weight loss before and after immersion in the inhibitor solution. Thermodynamic parameters were also computed to determine adsorption and activation processes. The statistical analysis revealed that the quadratic models for inhibition efficiencies (IE) were highly significant with a coefficient of multiple regressions $R^2= 0.997$. Further validation of the model indicated a good fit (R^2 Adj= 0.994), and the experimentally observed values aligned well with predicted ones, demonstrating a highly significant model with $Q^2= 0.978$. The theoretical efficiency predicted by the RSM model was 88.41%, whereas the efficiency observed during the experimental test procedure with the best-evaluated variables was 82.45%. In conclusion, this paper aims to identify the optimal conditions for employing Iodine–β-Cyclodextrin as a new corrosion inhibitor for carbon steel, utilizing experimental design methods. The results indicate that iodine/β-CD exhibits remarkable corrosion inhibitory properties for carbon steel under specific conditions.

1. INTRODUCTION

Carbon steel is a widely used material in infrastructure, transportation, energy, and other industries due to its cost-effectiveness and mechanical strength. However, its susceptibility to corrosion poses risks such as leaks, pressure losses, and ruptures in piping systems. Consequently, implementing protective measures to counter acid-induced corrosion is vital, employing chemical and other means. Among these methods, corrosion inhibitors offer a cost-effective approach (1), effectively mitigating or preventing corrosion when added in low concentrations (2,3). Researchers have reported organic compounds with hetero-atoms like O, N, and S as efficient inhibitors for various metals (4-8). The inhibitive nature of a molecule and its adsorption onto a metal surface depends on factors such as size, chemical structure, surface charge distribution, specimen surface morphology, corrosive media type, and operating conditions (9-10). Investigating adsorption isotherms provides insights

into interactions between adsorbed molecules and the electrode surface, highlighting physical adsorption and chemical decomposition (11,12).

Cyclodextrins (CDs), important oligosaccharides produced through enzymatic amylose hydrolysis, have been extensively used in supramolecular chemistry due to their affordability and versatility. These molecules possess a central cavity whose size depends on the glucose units in the cycle (13). The central cavity, a functional site of CDs, is involved in molecular transportation and is widely applied in drug delivery (14). Various iodine/β-CD host-guest complexes have been synthesized and investigated for potential pharmacological activities. For instance, Wang et al. demonstrated the bacteriostatic and antifungal activities of iodine/β-CD (15). Additionally, a recent study revealed that sausages fortified with iodine/β-CD complex positively affected the iodine status of volunteers (16).

To efficiently study variables and responses while minimizing experiments, the Design of Experiments (DOE) offers an alternative to the traditional one-factor-at-a-time approach. DOE's utilization empowers researchers to effectively explore relationships among input variables, such as inhibitor concentration, temperature, and immersion time, as well as critical output variables like inhibition efficiency (17-19). This is achieved through statistical techniques, employing a systematic framework for data collection that surpasses traditional methods, thus enabling more efficient and effective analyses. In the domain of experimental design and optimization, the omnipresence of the Response Surface Methodology (RSM) software is evident. Guided by a multivariate methodology central to analytical optimization, the RSM approach enables the precise accommodation of experimental data through the application of a polynomial equation (20,21).

In this study, the primary investigation centers on the inhibitory effect of Iodine−β-Cyclodextrin on carbon steel corrosion in sulfuric acid using the weight loss method. Additionally, the study aims to evaluate thermodynamic parameters linked to the corrosion process and to examine the collaborative effects of inhibitor concentration, temperature, and immersion time using response surface methodology (RSM).

2. EXPERIMENTAL

2.1. Specimen Preparation
The carbon steel specimen utilized in the current study has the following chemical compositions (in wt%): 0.370% C, 0.230% Si, 0.680% Mn, 0.016%

S, 0.077% Cr, 0.011% Ti, 0.059% Ni, 0.009% Co, 0.160% Cu, with the remaining content being iron. The specimens underwent thorough mechanical polishing using SiC (300–1200) emery papers, followed by degreasing with acetone, washing with doubly distilled water, and final drying. All solvents and chemicals employed were of AR grade. Additionally, doubly distilled water was used to prepare the various concentrations of test solutions.

2.2. Weight Loss Method
The weight-loss method assesses the corrosion rate of a metal sample by quantifying the reduction in mass over a designated timeframe of exposure to a corrosive milieu. It yields outcomes that better reflect uniform corrosion compared to electrochemical methods, owing to its alignment with realistic experimental conditions (22). The weight loss measurements followed the procedures detailed in our prior work by Attar et al (23-25). Each measurement was conducted in triplicate, and the resulting weight loss means were both noted and documented.

The corrosion rate, designated as 'CR,' and the inhibitor's efficacy were computed using the subsequent equations:

$$CR = \Delta w/(S \times t) \qquad (1)$$

where Δw refers to the weight loss in milligrams (mg), S stands for the sample area in square centimeters (cm²), and t symbolizes the immersion time in hours (h).

The corrosion inhibition efficiency (IE %) and surface coverage (θ) were calculated from the values of CR:

$$IE(\%) = 100 \times (CR - CR_{Inh})/CR \qquad (2)$$

where CR represents the corrosion rate acquired in the absence of the inhibitor, while CR_{Inh} corresponds to the corrosion rate observed in the presence of the inhibitor.

2.3. Experimental Design
The investigation employed MODDE Software Version 9.1 for experimental design and statistical analysis. The primary aim was to develop a precise analytical model, discerning variable effects on response function and optimal conditions. The study employed RSM for experiment design, modeling, and corrosion inhibition process optimization. Parameters included temperature, inhibitor concentration, and exposure time at three levels. Seventeen experiments were conducted using RSM. Independent parameters and their levels are detailed in Table 1.

Table 1: Optimization of inhibition efficiency of an iodine−β-cyclodextrin on carbon steel in acid medium: weight loss and RSM approach.

Sl. no	Parameter	Code	Unit	Level		
				-1	0	$+1$
1	Inhibitor Concentration	Con	mol/L	1×10^{-5}	5.05×10^{-4}	1×10^{-3}
2	Temperature	Temp	°C	20	30	40
3	Immersion Time	Tim	hrs	1	2	3

2.4. Adsorption Considerations and Activation Energy Calculations

Adsorption and activation play crucial roles in the inhibition of corrosion for metals. Adsorption refers to the phenomenon where inhibitor molecules attach to the metal surface, creating a protective layer that effectively reduces the corrosion rate. To elucidate the adsorption mechanism of iodine/β-CD on the surface of the studied samples, a thorough analysis of various models of adsorption isotherms was conducted. The findings reveal that the Langmuir equation provides a more accurate description of this phenomenon for iodine/β-CD within a 0.5 M H_2SO_4 solution. The mathematical representation of the Langmuir adsorption isotherm takes the form:

$$C_{inh}/\theta = 1/K_{ads} + C_{inh} \tag{3}$$

Where C_{inh} represents the molar concentration of iodine/β-CD in units of mol/L, while θ signifies the surface coverage (expressed as a percentage of IE/100). The parameter K_{ads} corresponds to the adsorption constant, quantified in units of L/mol. By linear fitting of C_{inh}/θ versus C_{inh}, K_{ads} can be determined.

The determination of adsorption enthalpy (ΔH_{ads}) was accomplished employing the Van't Hoff equation:

$$\ln(K_{ads}) = (-\Delta H_{ads}/RT) + Const. \tag{4}$$

Through the execution of a regression analysis between the natural logarithm of K_{ads} and the reciprocal of temperature (1/T), a linear relationship manifested itself, revealing a slope equivalent to ($-\Delta H_{ads}/R$).

In this research paper, the Gibbs free energy of adsorption (ΔG_{ads}) was calculated at different temperature levels to explore the adsorption behavior of iodine/β-CD in a 0.5 M sulfuric acid solution. Gibbs free energy of adsorption, which is useful for determining inhibitor adsorption, can be calculated using the following equation:

$$\Delta G_{ads} = -RT\ln(55.5\ K_{ads}) \tag{5}$$

where ΔG_{ads} is Gibbs free energy of adsorption, J/mol; R is 8.314 J/(mol·K); T is the absolute temperature, K.

Additionally, the enthalpy of activation (ΔH_a) and entropy of activation (ΔS_a) were calculated using the alternative Arrhenius equation:

$$\ln(CR/T) = [\ln(R/Nh) + (\Delta S_a/R)] - \Delta H_a/RT \tag{6}$$

In this equation, h denotes Planck's constant, and N represents Avogadro's number. Plotting $\ln(CR/T)$ against 1/T resulted in a straight line with a slope of ($-\Delta H_a/R$) and an intercept of $[\ln(R/Nh) + (\Delta S_a/R)]$.

By applying the thermodynamic relation (Eq.7), one can calculate the variation in free energy of adsorption and activation for the corrosion process at different temperatures.

$$\Delta G = \Delta H - T\ \Delta S \tag{7}$$

3. RESULTS AND DISCUSSION

For the study, three independent variables, namely inhibitor concentration (Con), temperature (Temp), and immersion time (Tim) were selected across three distinct levels (equation 8). This equation delineates how the experimental variables interact to influence the Inhibition Efficiency (IE%).

$$\begin{aligned} IE(\%) = &73.606 + 2.636(Con) - 7.589(Temp) + \\ &2.345(Tim) + 1.795(Con)^2 + 2.141(Temp)^2 - \\ &9.769(Tim)^2 - 0.651(Con \times Temp) - 1.366(Con \times Tim) - \\ &2.583\ (Temp \times Tim) \end{aligned} \tag{8}$$

It was evident that the variables with the most substantial impact on IE were inhibitor concentration (Con) and immersion time (Tim), while the influence of temperature (Temp) was comparatively smaller. Coefficients in the model characterized by positive values denote a synergistic effect, whereas negative values indicate an antagonistic effect (26). Among the model factors, Con^2 and $Temp^2$ positively contribute to the formulation, whereas Tim^2, Con×Temp, Con×Tim, and Temp×Tim exert a negative influence on the developed model.

3.1. Statistical Test and Analysis of Models

The quadratic model generated was fitted to the data, and the response is depicted in the summary of the fit plot (Figure 1), which provides information about the model's strength and robustness, including Model Validity, Reproducibility, R^2, and Q^2. The values of these parameters are displayed in the following table.
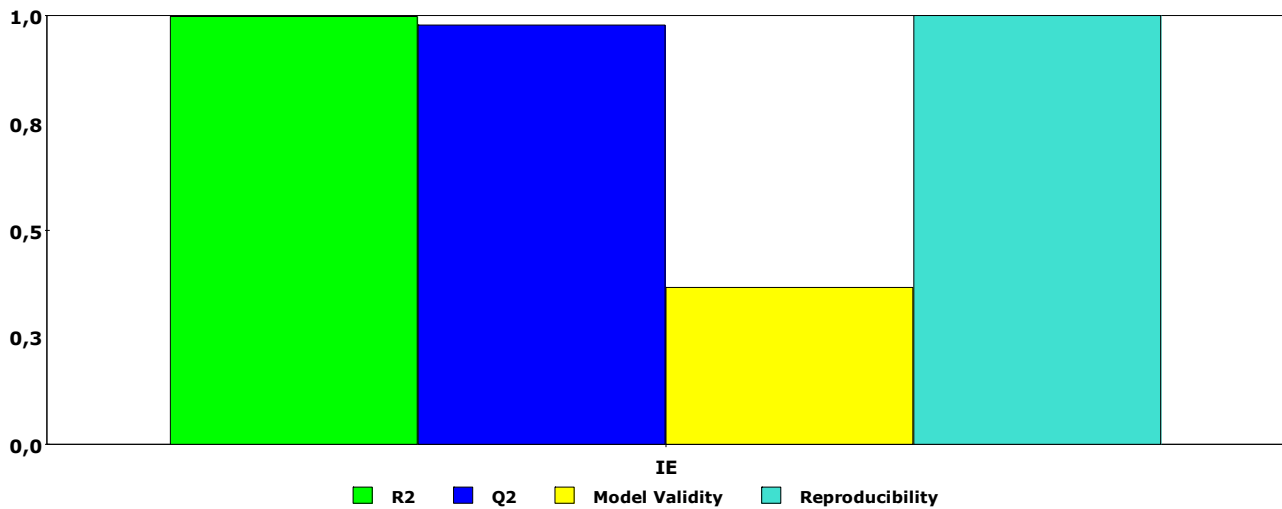
Figure 1: Summary of fit plot showing model fit (R²), predictability (Q²), model validity, and reproducibility.

Table 2 displays the statistical parameters acquired through ANOVA. The coefficient of determination (R^2) denotes the model's fit quality, with R^2 (0.997) suggesting that only 0.3% of the overall variations remain unaccounted for by the model.

Correspondingly, the value of Adj. R^2 (0.994) affirms the model's strong significance, signifying excellent concurrence between the predicted and experimental efficiencies of Iodine/β-CD (27).

Table 2: Displays the coefficients of factors, interactions, and probability values of approximate polynomials for the response variables in the experimental design.

R^2	R^2Adj.	Q^2	RSD	Conf. lev.	Model Validity	Reproducibility
0.997	0.994	0.978	0.623	0.95	0.366	0.999

The Q^2 value serves as an indicator of the model's predictive performance for future outcomes (28). As shown in Table 2, the obtained Q^2 value exceeds 0.9, indicating an excellent model for this study. A Q^2 value should surpass 0.1 for a significant model and exceed 0.5 for a good model. Furthermore, when Q^2 is above 0.9, the model is considered excellent (19, 29). Additionally, the difference between R^2 and Q^2 should be smaller than 0.3 for a good model. The model's residual standard deviation (RSD) was calculated to be 0.623. A small RSD value suggests

a strong model that closely aligns predicted values with actual responses (19).

The analysis maintains a 95 percent confidence level. When the Model Validity (0.366) bar exceeds 0.25, the model does not exhibit a Lack of Fit. Reproducibility refers to the variability among replicates about the overall variability. In this study, a value of 0.999 is nearly equivalent to unity. A reproducibility value of 1 signifies perfect reproducibility.
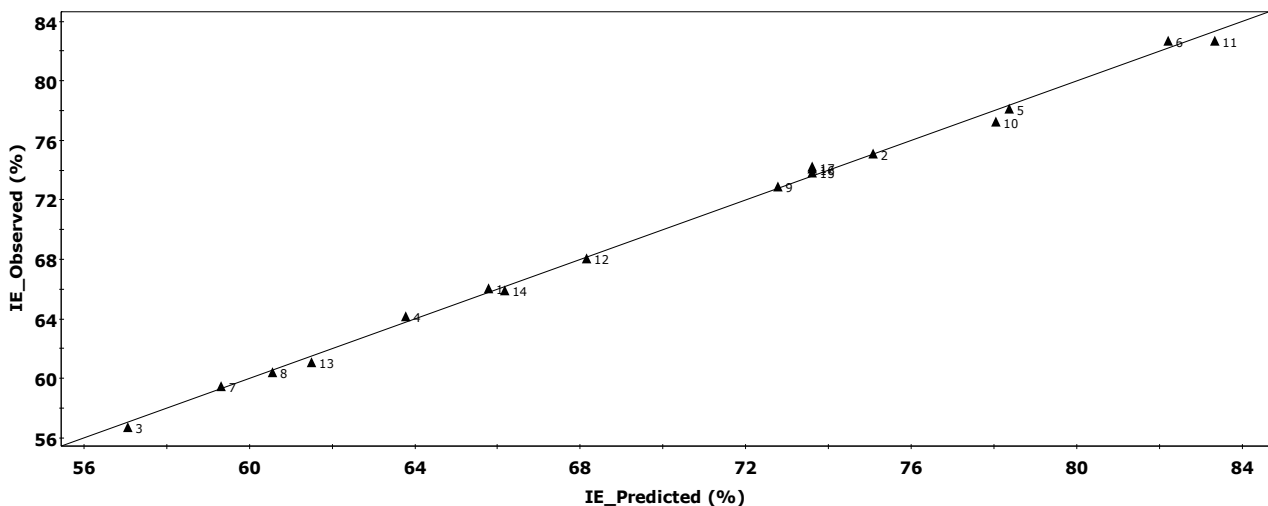
Figure 2: Illustrates the model fit graph, depicting the relationship between the experimental and predicted values.

As illustrated in Figure 2, a clear linear relationship emerged in the diagnostic plots comparing predicted inhibition efficiency to actual inhibition efficiency. These findings affirm the appropriateness of the design model for predicting the inhibition efficiency of the Iodine/β-CD. Furthermore, it demonstrates the model's suitability for predicting the response variables based on the experimental data (17, 27).

3.2. Main Effects
Figure 3 illustrates the impact of each examined parameter. Notably, the values attributed to each point correspond to the average corrosion IE achieved at that specific level, regardless of other parameter variations. The comprehensive mean is depicted across each panel. The observed correlation

between the escalation of corrosion IE and temperature elevation is evident within this study (Figure 3). As the concentration of iodine/β-CD increased, the inhibitor efficiency (IE%) also increased. The increase in surface coverage enhances accessibility and facilitates the adsorption of the active inhibitor components onto the surface of the corroding metal (30). The optimal efficiencies (IEs) are achieved when carbon steel is immersed in a solution with a concentration of 1×10^{-3} mol/L iodine/β-CD for a duration of 2 hours, at a temperature of 20°C. Conversely, the lowest IE was observed when carbon steel was subjected to a solution containing 1×10^{-5} mol/L of iodine/β-CD, immersed for 1 hour, and maintained at a temperature of 40°C.
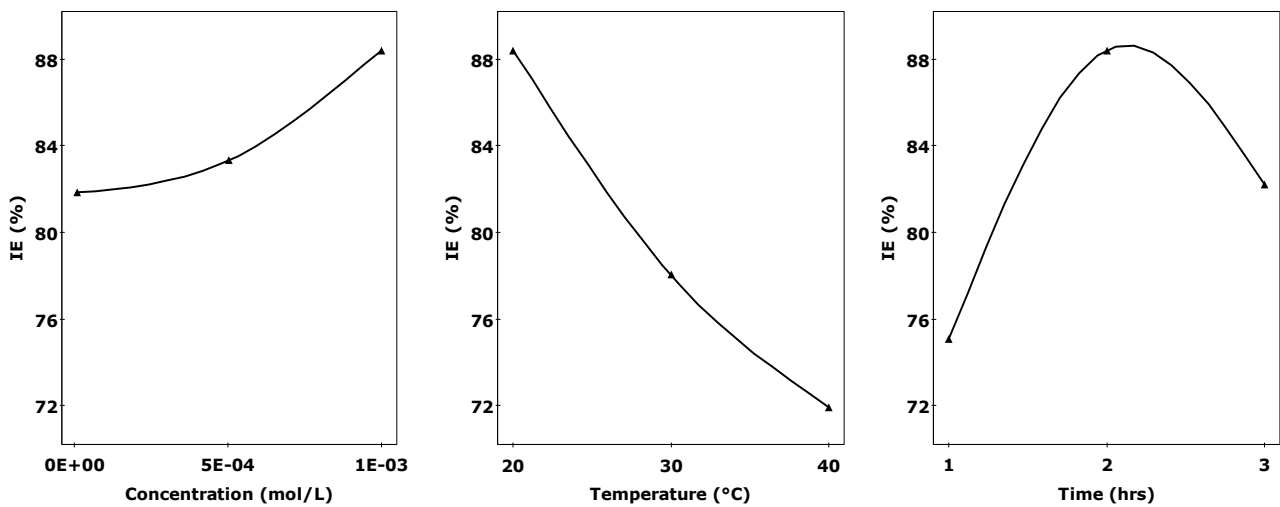
Figure 3: Optimizing the inhibition efficiency of Iodine/β-CD on carbon steel in sulfuric acid medium – medium-weight loss and RSM approach.

3.3. Contour Plots
Contour plots serve as graphical tools for illustrating the interplay among two or more variables using a three-dimensional space (31). Within corrosion

inhibition research, these plots find frequent application in displaying how various variables collaboratively influence the effectiveness of corrosion inhibitors.
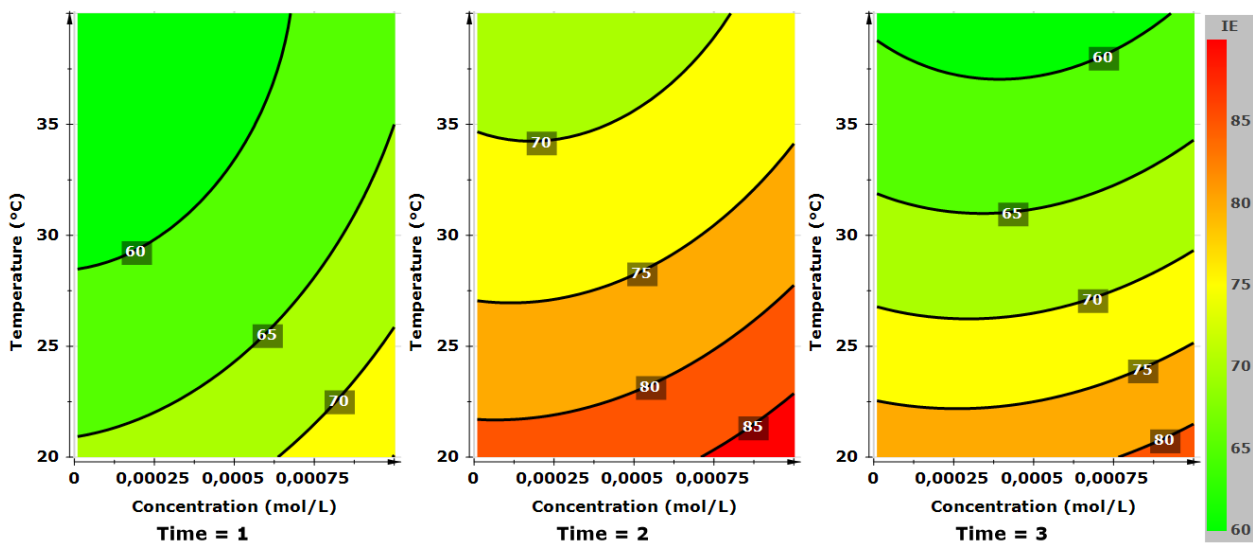
Figure 4: Contour plots illustrating the interactive effects of concentration, temperature, and immersion time on the corrosion inhibition efficiency of Iodine/β-CD on carbon steel in sulfuric acid, obtained through weight loss and RSM approach.

Figure 4 demonstrates the interaction effect through a contour plot involving temperature, inhibitor concentration, and exposure time on corrosion inhibition efficiency (IE). It confirms that corrosion IE moderately increases as the inhibitor concentration rises from the minimum to the maximum level. For any amount of Iodine–β-Cyclodextrin in the system, IE increases with an immersion time of up to 2 hours. The IE reaches its peak at the lowest temperature of 20°C and the highest concentration of Iodine/β-CD, as depicted in Figure 4. The results obtained align with those reported in the literature (32).

3.4. Adsorption Considerations and Activation Energy Calculations
3.4.1. Adsorption considerations
Table 3 provides a comprehensive summary of the equilibrium constants, free energy, enthalpy, and entropy associated with the adsorption process. The positive adsorption equilibrium constants demonstrate the feasibility of the inhibitor's adsorption onto the metal surface (33). This finding aligns with the trend observed, indicating that the inhibitor with better inhibition efficiency has a positive effect on the adsorption process.

Table 3: Thermodynamic parameters of Iodine/β-CD adsorption on carbon steel surface in sulfuric acid at various temperatures.

T (K)	R^2	K_{ads} (L/m^3)	ΔH_{ads} (kJ/mol)	ΔS_{ads} (J/mol K)	ΔG_{ads} (kJ/mol)
293	0.999	229.12		-14.47	-39.85
303	0.999	177.43	-35.61	-16.33	-40.56
313	0.998	92.49		-14.69	-40.21
323	0.998	62.72		-14.98	-40.45

The thermodynamic parameters for inhibitor adsorption provide valuable insights into the corrosion inhibition mechanism. An exothermic adsorption process ($\Delta H_{ads}<0$) may imply either chemisorption, physisorption, or a mixture of both processes. Conversely, an endothermic adsorption process ($\Delta H_{ads}>0$) is unequivocally assigned to chemisorption (34). A negative adsorption entropy value signifies a reduction in metal surface degradation, whereas a positive value indicates an enhancement in system disorder. The negative values of the free energy adsorption indicate the spontaneity of the process. Typically, if ΔG_{ads} values exceed -20 kJ/mol, the physisorption mechanism is favored, while values of -40 kJ/mol or lower suggest chemisorption. In this study, the obtained ΔG_{ads} values fall within the range of -39.85 to -40.45 kJ/mol, which lies between −20 and −40 kJ/mol (35,36). Based on the study's findings, the calculated enthalpy and free energy of adsorption values suggest a mechanism that extends beyond pure chemical or physical processes. Instead, they indicate a coexistence of physisorption and chemisorption between the inhibitor and the metal surface (37).

3.4.2. Activation energy calculations
The activation energy values for the corrosion reaction under different conditions are as follows: E_a = 35.96 kJ/mol for the blank, and E_a = 53.87 to 55.29 kJ/mol for iodine/β-CD, respectively (Table 4). When an inhibitor is present, the activation energy can either be lower or remain unchanged compared to the blank test, indicating a chemisorption mechanism. Conversely, higher values of E_a in the presence of the inhibitor suggest a physical adsorption mechanism (38).

The presence of positive ΔH_a values (Table 4), both in the absence and presence of the inhibitor, indicates the endothermic nature of the metal dissolution process, suggesting a gradual dissolution of carbon steel (39,40).

Table 4: Activation parameters for carbon steel corrosion in sulfuric acid with varying Iodine/β-CD concentrations.

C (mol/L)	R^2	E_a (kJ/mol)	ΔH_a (kJ/mol)	ΔS_a (J/mol K)	ΔG_a (kJ/mol)			
					293	303	313	323
-	0.971	35.96	33.41	-226.53	99.78	102.05	104.31	106.58
1×10^{-5}	0.994	53.87	51.32	-275.90	132.16	134.92	137.67	140.43
5×10^{-5}	0.993	54.46	51.91	-277.12	133.11	135.87	138.64	141.42
5×10^{-4}	0.988	55.29	52.73	-279.13	134.51	137.30	140.09	142.88
1×10^{-3}	0.991	54.92	52.36	-277.05	133.53	136.31	139.07	141.84

Upon comparing the ΔS_a values, it becomes evident that the entropy of activation reduces in the presence of the studied inhibitor compared to the free acid. The lower ΔS_a value further corroborates the decelerated metal dissolution in the presence of iodine/β-CD (41).

The ΔG_a values exhibited a positive trend, intensifying as the temperature elevated. This temperature rise corresponded to an increased spontaneity of the corrosion process, indicating enhanced solubility of the activated complex at higher temperatures (34). Moreover, the augmentation in concentration resulted in higher free energy of activation, attributed to the formation of

an unstable activated complex in the rate-determining transition state (42).

4. CONCLUSION

In this study, Iodine–β-Cyclodextrin was employed to investigate the efficiency of corrosion inhibition in a 0.5 mol/L sulfuric acid solution concerning carbon steel. The investigation considered various parameters, including inhibitor concentration, exposure time, and solution temperature. The results indicate that inhibition efficiency increases with higher inhibitor concentrations and decreases with rising temperatures. In the inhibited solution, the activation energy for the corrosion process exceeded that in the uninhibited solution. The enthalpy of activation signifies the endothermic character of metal dissolution, while the entropy of activation signifies a reduction in the rate of metal dissolution. Among the assortment of adsorption isotherm models, the Langmuir equation emerged as a more suitable descriptor for the phenomenon involving Iodine–β-Cyclodextrin within a sulfuric acid solution. Furthermore, the observed values of the Gibbs adsorption free energy, ranging from -39.85 to -40.45 kJ/mol, indicate the coexistence of both chemical and physical adsorption mechanisms for Iodine–β-CD.

The RSM optimization utilized in this study meticulously predicted process parameters to achieve the highest corrosion inhibition efficiency. This technique also offers crucial insights applicable across various scales, from laboratory experimentation to industrial processes. The statistical model developed for corrosion inhibition efficiency using RSM was found to be effective, as this equation successfully elucidated the experimental data with a confidence level of 95%. Numerical optimization of the corrosion inhibition process for Iodine–β-CD revealed that the optimal conditions for achieving maximum IE (88.41%) were a concentration of 1×10^{-3} mol/L, a temperature of 20 °C, and an exposure time of 2 hours. Employing response surface methodology (RSM) in conjunction with analysis of variance (ANOVA), substantial RSM-based models were constructed to predict IE. Additionally, R^2 statistics, adequate precision, and diagnostic plots were employed as primary metrics to validate the accuracy and sufficiency of the IE models.

5. ACKNOWLEDGMENTS

6. REFERENCES

1. Tamalmani K, Husin H. Review on Corrosion Inhibitors for Oil and Gas Corrosion Issues. Appl Sci [Internet]. 2020 May 14;10(10):3389. Available from: <URL>.

2. Benchadli A, Attar T, Choukchou-Braham E. Inhibition of Carbon Steel Corrosion in Perchloric Acid Solution by Povidone Iodine. Phys Chem Res [Internet]. 2019 Dec 1;7(4):837–48. Available from: <URL>.

3. Ortega Ramirez AT, Barrantes L, Casallas Martin BD, Cortés Salazar N. Application of green inhibitors for corrosion control in metals. review. DYNA [Internet]. 2021 May 20;88(217):160–8. Available from: <URL>.

4. Barrahi M, Elhartiti H, Saadouni M. Corrosion inhibition of mild steel by Fennel seeds (Foeniculum vulgare Mill) essential oil in 1 M hydrochloric acid solution. Int J Corros Scale Inhib [Internet]. 2019 Dec 26;8(4):937–53. Available from: <URL>.

5. Petrunin MA, Gladkikh NA, Maleeva MA, Maksaeva LB, Yurasova TA. The use of organosilanes to inhibit metal corrosion. A review. Int J Corros Scale Inhib [Internet]. 2019 Dec 26;8(4):882–907. Available from: <URL>.

6. Attar T, Nouali F, Kibou Z, Benchadli A, Messaoudi B, Choukchou-Braham E, et al. Corrosion inhibition, adsorption and thermodynamic properties of 2-aminopyridine derivatives on the corrosion of carbon steel in sulfuric acid solution. J Chem Sci [Internet]. 2021 Dec 19;133(4):109. Available from: <URL>.

7. Yamin JAA, Sheet EAE, Al-Amiery AA. ANN and DOE Analysis of Corrosion Resistance Inhibitor for Mild Steel Structures in Iraq. Mod Appl Sci [Internet]. 2019 Mar 31;13(4):80–8. Available from: <URL>.

8. Salman TA, Salman TA, Al-Amiery AA, Shaker LM, Kadhum AAH, Takriff MS. A study on the inhibition of mild steel corrosion in hydrochloric acid environment by 4-methyl-2-(pyridin-3-yl)thiazole-5-carbohydrazide. Int J Corros Scale Inhib [Internet]. 2019 Dec 26;8(4):1035–59. Available from: <URL>.

9. Benchadli A, Attar T, Messaoudi B, Choukchou-Braham E. Polyvinylpyrrolidone as a Corrosion Inhibitor for Carbon Steel in a Perchloric Acid Solution: Effect of Structural Size. Hungarian J Ind Chem [Internet]. 2021 Sep 21;49(1):59–69. Available from: <URL>.

10. Bouraoui MM, Chettouh S, Chouchane T, Khellaf N. Inhibition Efficiency of Cinnamon Oil as a Green Corrosion Inhibitor. J Bio- Tribo-Corrosion [Internet]. 2019 Mar 23;5(1):28. Available from: <URL>.

11. Attar T, Benkhaled A, Benchadli A, Choukchou-braham E. Etude de l'inhibition de la corrosion de l'acier au carbone en milieu sulfurique par polyéthylène glycol. Rev des matériaux énergies renouvelables [Internet]. 2022 Mar 28;6(1):1–7. Available from: <URL>.

12. Zarrok H, Zarrouk A, Salghi R, Ramli Y, Hammouti B, Al-Deyab SS, et al. Adsorption and Inhibition Effect of 3-Methyl-1-Propargylquinoxalin-2(1H)-One on Carbon Steel Corrosion in Hydrochloric Acid. Int J Electrochem Sci [Internet]. 2012 Sep 1;7(9):8958–73. Available from: <URL>.

13. Harada A. Cyclodextrin-Based Molecular Machines. Acc Chem Res [Internet]. 2001 Jun 1;34(6):456–64. Available from: <URL>.

14. Zhang J, Ma PX. Cyclodextrin-based supramolecular systems for drug delivery: Recent progress and future perspective. Adv Drug Deliv Rev [Internet]. 2013 Aug 1;65(9):1215–33. Available from: <URL>.

15. Wang T, Li B, Feng Y, Guo Q. Preparation, quantitive analysis and bacteriostasis of solid state iodine inclusion complex with β-cyclodextrin. J Incl Phenom Macrocycl Chem [Internet]. 2011 Feb 5;69(1–2):255–62. Available from: <URL>.

16. Polumbryk M, Kravchenko V, Pasichnyi V, Omelchenko C, Pachitskaya I. The effect of intake of sausages fortified with β-CD-I2 complex on iodine status and thyroid function: A preliminary study. J Trace Elem Med Biol [Internet]. 2019 Jan 1;51:159–63. Available from: <URL>.

17. Benchadli A, Mellal T, Attar T, Dali Youcef B, Choukchou-Braham E. Optimization of inhibition efficiencies process of polyvinylpyrrolidone using response surface methodology. Rev Mex Física [Internet]. 2022 Jun 23;68(4):041003. Available from: <URL>.

18. Omran MA, Fawzy M, Mahmoud AED, Abdullatef OA. Optimization of mild steel corrosion inhibition by water hyacinth and common reed extracts in acid media using factorial experimental design. Green Chem Lett Rev [Internet]. 2022 Jan 2;15(1):216–32. Available from: <URL>.

19. Attar T, Benchadli A, Mellal T, Youcef BD, Choukchou-Braham E. Use of Experimental Designs to Evaluate the Influence of Methyl Green Dye as a Corrosion Inhibitor for Carbon Steel in Perchloric Acid. Malaysian J Chem [Internet]. 2021;23(1):60–9. Available from: <URL>.

20. Kumari P, Lavanya M. Optimization of Inhibition Efficiency of a Schiff Base on Mild Steel in Acid Medium: Electrochemical and RSM Approach. J Bio- Tribo-Corrosion [Internet]. 2021 Sep 9;7(3):110. Available from: <URL>.

21. Haladu SA, Dalhat Mu'azu N, Ali SA, Elsharif AM, Odewunmi NA, Abd El-Lateef HM. Inhibition of mild steel corrosion in 1 M H2SO4 by a gemini surfactant 1,6-hexyldiyl-bis-(dimethyldodecylammonium bromide): ANN, RSM predictive modeling, quantum chemical and MD simulation studies. J Mol Liq [Internet]. 2022 Mar 15;350:118533. Available from: <URL>.

22. Attar T, Benchadli A, Messaoudi B, Choukchou-Braham E. Corrosion Inhibition Efficiency, Experimental and Quantum Chemical Studies of Neutral Red Dye for Carbon Steel in Perchloric Acidic Media. Chem Chem Technol [Internet]. 2022 Sep 30;16(3):440–7. Available from: <URL>.

23. Attar T, Benchadli A, Choukchou-Braham E. View of Corrosion inhibition of carbon steel in perchloric acid by potassium iodide. Int J Adv Chem [Internet]. 2019;7(1):35–41. Available from: <URL>.

24. Attar T, Benchadli A, Boulanouar M, Choukchou-Braham E. Corrosion Inhibition, Adsorption and Thermodynamic Properties of Poly (Sodium 4-Styrenesulfonate) on Carbon Steel in Phosphoric Acid Medium. French-Ukrainian J Chem [Internet]. 2022 Jul 14;10(1):70–83. Available from: <URL>.

25. Attar T, Benchadli A, Choukchou-Braham E. Inhibition of corrosion of copper by polyvinylpyrrolidone-iodine in sulfuric acid medium. Alger J Mater Chem [Internet]. 2022;5(1):1–8. Available from: <URL>.

26. Salam K, Agarry S, Arinkoola A, Shoremekun I. Optimization of operating conditions affecting microbiologically influenced corrosion of mild steel exposed to crude oil environments using response surface methodology. Br Biotechnol J. 2015;7(2):68–78.

27. Attar T, Choukchou-Braham E, Youcef BD, Benchadli A, Mellal T, Benabdelkader I. Application of polyvinylpyrrolidone-iodine complex as corrosion inhibitor for carbon steel using an experimental design method. Alger J Eng Technol [Internet]. 2022 Jun 28;6:14–8. Available from: <URL>.

28. Dennison TJ, Smith J, Hofmann MP, Bland CE, Badhan RK, Al-Khattawi A, et al. Design of Experiments to Study the Impact of Process Parameters on Droplet Size and Development of Non-Invasive Imaging Techniques in Tablet Coating. Sung S-Y, editor. PLoS One [Internet]. 2016 Aug 22;11(8):e0157267. Available from: <URL>.

29. Gao X, Dai K, Wang Z, Wang T, He J. Establishing quantitative structure tribo-ability relationship model using Bayesian regularization neural network. Friction [Internet]. 2016 Jun 28;4(2):105–15. Available from: <URL>.

30. Hamzat AK, Adediran IA, Alhems LM, Riaz M. Investigation of Corrosion Rate of Mild Steel in Fruit Juice Environment Using Factorial Experimental Design. Int J Corros [Internet]. 2020 Feb 27;2020:5060817. Available from: <URL>.

31. Sulaimon AA, Murungi PI, Tackie-Otoo BN, Nwankwo PC, Bustam MA. Quantitative and qualitative analyses of grafted okra for corrosion inhibition of mild steel in acidic medium. Front Chem [Internet]. 2023 Feb 24;11:1129673. Available from: <URL>.

32. Khormali A, Ahmadi S. Experimental and modeling analysis on the performance of 2-mercaptobenzimidazole corrosion inhibitor in hydrochloric acid solution during acidizing in the petroleum industry. J Pet Explor Prod Technol [Internet]. 2023 Nov 15;13(11):2217–35. Available from: <URL>.

33. Attar T, Benchadli A, Messaoudi B, Benhadria N, Choukchou-Braham E. Experimental and Theoretical Studies of Eosin Y Dye as Corrosion Inhibitors for Carbon Steel in Perchloric Acid Solution. Bull Chem React Eng Catal [Internet]. 2020 Aug 1;15(2):454–64. Available from: <URL>.

34. Attar T, Messaoudi B, Benchadli A, Seghiour I, Zenasni MA, Bousalem S, et al. Experimental and theoretical studies of polyvinylpyrrolidone-iodine on carbon steel corrosion in 1M hydrochloric solution. Rev Roum Chim [Internet]. 2021;66(8–9):761–70. Available from: <URL>.

35. Yang X, Fu S, Wang Q, Sun Q, Zhang J, Peng Y, et al. Protective behaviour of naphthylamine derivatives for steel reinforcement in the simulated concrete pore solutions: Detailed experimental and computational explorations. J Mol Struct [Internet]. 2022 Dec 15;1270:133898. Available from: <URL>.

36. Ahmed AH, Sherif E-SM, Abdo HS, Gad ES. Ethanedihydrazide as a Corrosion Inhibitor for Iron in 3.5% NaCl Solutions. ACS Omega [Internet]. 2021 Jun 8;6(22):14525–32. Available from: <URL>.

37. Danaee I, RameshKumar S, RashvandAvei M, Vijayan M. Electrochemical and Quantum Chemical Studies on Corrosion Inhibition Performance of 2,2'-(2-Hydroxyethylimino)bis[N-(alphaalpha-dimethylphenethyl)-N-methylacetamide] on Mild Steel Corrosion in 1M HCl Solution. Mater Res [Internet]. 2020 Jun 1;23(2):e20180610. Available from: <URL>.

38. Belarbi N, Dergal F, Abdelhamid El-Haci I, Attar T, Lerari D, Dahmani B, et al. Gravimetric, Electrochemical, and Surface Morphological Studies of Ammodaucus Lecotrichus Essential Oil as Corrosion Inhibitor for Copper Surface in Hydrochloric Acid Medium Analytical & Bioanalytical Electrochemistry. Anal Bioanal Electrochem [Internet]. 2021;13(3):340–57. Available from: <URL>.

39. Betti N, Al-Amiery AA, Al-Azzawi WK, Isahak WNRW. Corrosion inhibition properties of schiff base derivative against mild steel in HCl environment complemented with DFT investigations. Sci Rep [Internet]. 2023 Jun 2;13(1):8979. Available from: <URL>.

40. Benchadli A, Attar T, Choukchou-Braham E. Corrosion Inhibition of Carbon Steel (XC 38) in Hydrochloric Acid by Potassium Iodide. J Adv Res Sci Technol [Internet]. 2018;5(2):834–44. Available from: <URL>.

41. Ogunleye OO, Arinkoola AO, Eletta OA, Agbede OO, Osho YA, Morakinyo AF, et al. Green corrosion inhibition and adsorption characteristics of Luffa cylindrica leaf extract on mild steel in hydrochloric acid environment. Heliyon [Internet]. 2020 Jan 1;6(1):e03205. Available from: <URL>.

42. Abdul Rahiman AFS, Sethumanickam S. Corrosion inhibition, adsorption and thermodynamic properties of poly(vinyl alcohol-cysteine) in molar HCl. Arab J Chem [Internet]. 2017 May 1;10:S3358–66. Available from: <URL>.

RESEARCH ARTICLE

Microporous and Mesoporous Activated Carbons from Tea Stalk and Tea Stalk Pulps: Effect of Lignin Removal by One-Step and Two-Step Organosolv Treatment

Sibel Başakçılardan Kabakcı[1]* , **Basak Karakurt Cevik[1]** , **Gamze Sultan Bas Berkem[2]**

[1]Energy Systems Engineering Department, Faculty of Engineering, Yalova University, Türkiye.
[2]Polymer Materials Engineering Department, Faculty of Engineering, Yalova University, Türkiye.

Abstract: Delignification is a crucial pretreatment in the production of diverse value-added products from lignocellulosics. While modifying the surface functional groups, delignification also increases the specific surface area by providing a porous structure to the lignocellulosic biomass. Hydrothermal pretreatment can be used prior to delignification, to recover hemicellulose and boost delignification. By removing lignin and hemicellulose, cellulose-rich pulp becomes more accessible for activation. In the present study, three different activated carbons were prepared: activated carbon from tea stalk itself (ATS), activated carbon from tea stalk pulp obtained by using glycerol organosolv pretreatment (ATP), activated carbon from tea stalk hydrochar pulp obtained by using sequential hydrothermal pretreatment-organosolv delignification (AHTP). Each precursor was carbonized (at 800 °C) in the presence of KOH (KOH/precursor: 2/1). Activated carbons were characterized for their elemental content, surface functional groups, thermal stability, crystallinity, surface morphology, surface area and porous structure using elemental analysis (C-H-N-S), FTIR, TGA, XRD, SEM and, BET analysis, respectively. While hydrothermal pretreatment prior to organosolv pulping reduced the delignification yield, it also altered the pore structure of activated carbon. Among the activated carbons, only ATS had microporous structure with an average pore radius of 1 nm. ATP had the highest surface area (2056.72 m^2/g) and micropore volume (0.81 cm^3/g). Having mesopores (with an average pore radius of 5.74 nm) in its structure, AHTP had the least micropore volume (0.464 cm^3/g) and surface area (1179.71 m^2/g). The presence of micro and mesopores broadens the potential applications of activated carbon ranging from environmental applications to energy storage.

1. INTRODUCTION

Activated carbons are carbon-rich porous materials which are prepared from different resources such as coal, coke, peat and biomass. Having the highest share of lignocellulosic biomass, agricultural wastes and residues are sustainable raw materials to produce value-added products such as activated carbon (1-3). Several lignocellulosic feedstocks have been preferred as precursors such as pineapple leaf and coconut shell (4), kenaf and rapeseed (5), corn straw (6), oil palm

leaves (7), olive bagasse (8), cherry stones (9), almond shell wastes (10). Due to their high surface area, variable porosity and surface functional groups, activated carbons are used as adsorbents for the removal of water pollutants and air pollutants, as catalyst support for preparing catalyst, as electrodes in supercapacitors for storing ions, and as carbon nanotubes and carbon fiber.

The volume and diameter of pores, surface area, micropore volume and surface functional groups of

activated carbon are affected from the activating agent, activation type (physical or chemical), activation conditions, carbonization conditions, and the lignocellulosic precursor (11-13). The structural components of lignocellulose (namely cellulose, hemicellulose and lignin) have great impact on both yield and porous structure of activated carbon mainly due to their different chemical structure and thermal stability (14-17). In the study of Guo and Rockstraw (18), activated carbons of xylan, cellulose and lignin had different pore structures at same activation conditions. Lignin is the major component that contributes to the activated carbon yield, while cellulose, lignin and hemicellulose alter the porous structure (19, 20). Specific surface area and porosity of the activated carbon are higher as the precursor has high cellulose content (4). To take advantage of the high cellulose content, biomass can be partially delignified prior to activation/carbonization (6, 21-23). Chen et al. (6) fractionated cellulose, hemicellulose and lignin using NaOH and urea solution. Then, activated carbon samples were obtained by carbonizing those fractions under N_2 atmosphere at 800 ^oC in the presence of NaOH. Their study showed that activated carbon obtained from cellulosic fraction has better properties than activated carbon obtained from the lignocellulosic biomass itself. Mittal et al. (24) separated the cellulosic fraction by pretreating rice straw with an alkaline ionic liquid (choline hydroxide). The cellulosic fraction was carbonized at 600 °C for 3 hours under an argon atmosphere. In this study, adsorption capacity of mesoporous cellulose-based activated carbon was high. Han et al. (25) pre-treated poplar wood using CH_3COOH and $NaClO_2$ solution at 80 °C for 18 hours. The cellulose-rich fraction was carbonized at 1000 °C for 2 h (under argon atmosphere). It was observed that the pore size of the pretreated activated carbon was lower than the activated carbon obtained from poplar wood. Sun and Hong (26) used different cellulose-based polymers (α-cellulose, methyl cellulose, hydroxyethyl cellulose and cellulose acetate) as a precursor. First, the samples were carbonized under Ar atmosphere (at 400 or 500 °C), and then under CO_2 atmosphere for 2 h. Based on experimental results, the difference in functional groups in the cellulose samples not only affects the pore structure, but also improves the adsorption properties. As can be seen from the studies summarized above, activated carbons obtained from cellulose-rich precursors are better due to properties such as pore structure, pore size, surface area of activated carbon, and versatile surface functional groups.

One way to obtain cellulose-rich precursors is to delignify the biomass. There are various physico-chemical pretreatment methods for the delignification of lignocellulosic biomass such as acid pretreatment, NaOH pretreatment, ammonia pretreatment, organosolv pretreatment, ionic liquid pretreatment, deep eutectic solvent pretreatment (27). Among them, organosolv pretreatment has the advantage of lignin recovery while enriching cellulose in the pulp. In the organosolv treatment, lignocellulosic biomass is brought into contact with a solvent in the presence of a catalyst (28). This process can be carried out under pressure, or it can be carried out at atmospheric pressure at relatively higher temperatures. The type of solvent and biomass, particle size of the biomass, biomass/solvent ratio, pretreatment conditions (temperature, pressure, mixing speed, time) affect the extent of delignification (29). The cellulose-rich fraction is separated from the solution by filtration. Lignin is precipitated by diluting the organosolv solution with water. Solvent recovery is often attempted from the solution if the solvent has low boiling point temperature (30). Sometimes hydrothermal pretreatment is applied prior to organosolv pulping to recover the hemicellulose sugars, to increase the accessibility of enzymes to cellulose and to boost delignification (31-35). Hydrothermal pretreatment, which is a simple and low-cost method, uses water as a solvent and pretreatment is carried out at temperatures between 160-230 °C (36). In this method, where most of the hemicellulose is degraded, swelling and partial hydrolysis of cellulose and partial decomposition and repolymerization of lignin are observed depending on the conditions of the hydrothermal pretreatment (37). After hydrothermal pretreatment, the liquid fraction containing a high percentage of sugar can be converted into platform chemicals using different conversion methods (38). The solid fraction, which is named as hydrochar, can be used as an adsorbent for environmental applications, a solid fuel for the production of energy or energy carriers (such as syngas), a precursor for the preparation of activated carbon or can be further processed to produce high value-added products (39, 40).

There are many studies in the literature that focuses on using cellulose, microcrystalline cellulose, or cellulose-rich biomass as precursors for activated carbon preparation. Studies which use cellulose-rich pulp from organosolv treatment as a precursor are very rare. Unlike the others, in this study, delignification of lignocellulosic biomass was done by a single-stage glycerol-organosolv treatment and a sequential hydrothermal pretreatment-organosolv treatment separately. Cellulose-rich pulps obtained by both methods and the tea stalk itself were used as precursors to produce microporous-mesoporous activated carbon. Activated carbons are compared based on their properties and potential end-uses were discussed.

2. EXPERIMENTAL SECTION

2.1. Materials
Tea stalk samples were supplied from a tea processing factory. All tea stalk samples were dried (105 °C for 24 h) before analyses and pretreatments to prevent samples from rotting and to provide better conditions for

storage. After grinding, samples were sieved by using RESTCH AS 200 vibrating sieve to have a uniform particle size (250 µm). Dry tea stalk samples with uniform particle size are named as TS.

Chemicals including glycerol, NaOH and H_2SO_4 were of analytical grade and used without further purification.

2.2. Methods
2.2.1. Hydrothermal pretreatment
Hydrothermal pretreatment of TS was carried out in a 250 mL non-stirred, temperature-controlled, stainless-steel batch reactor. Hydrothermal pretreatment conditions were selected based on our previous study (pretreatment temperature: 220 °C, residence time: 90 min, tea stalk/water ratio: 1 g/4 mL) (41). After pretreatment, the reactor was cooled rapidly by using ice bath. Gases, which formed during the pretreatment were not collected. The mixture was filtered to separate hydrochar. The hydrochar of TS samples (named as HTS) were washed with deionized water and then dried in an oven at 105 °C for 24 h.

HTS samples were delignified by using alkaline glycerol organosolv treatment as explained below. The pulp obtained after sequential hydrothermal pretreatment and organosolv treatment was named as HTP.

### 2.2.2. Alkaline-glycerol organosolv treatment
Alkaline-glycerol organosolv method, which we previously used for delignification (42), was modified in this study to increase the lignin yield. 20 g tea stalk, 50 mL of 0.4 M NaOH solution and 150 mL glycerol were mixed in a three-necked glass reactor equipped with a reflux condenser and a thermocouple. First, the mixture was mixed for 30 min at 90 °C, then the temperature was raised to 115 °C. The mixture was continuously mixed for 90 min at this temperature. At the end of the treatment, pulp was separated from the liquor, and washed with hot water (water at 55 °C) and then dried in an oven at 100 °C for 24 h. The pulp obtained after organosolv pretreatment was named as TP.

To precipitate the lignin, filtrate was diluted with deionized water to 1L (at 55 °C) and the pH was decreased to 2-2.5 by using 0.1 M H_2SO_4. After precipitation, lignin was separated, washed with water and then dried. Characteristics of lignins are not given as they are beyond the scope of this article.

2.2.3. Preparation of activated carbon
Dry TS, TP and HTP samples were mixed with KOH at a ratio of 1:2 (wt:wt). After gently mixing KOH with the sample, the mixture in a ceramic boat was placed in a horizontal tubular furnace. The sample was heated at a heating rate of 10 °C/min up to 800 °C and kept at this temperature for 1h. During heating and cooling, tubular furnace was continuously flushed with nitrogen gas. After activation, samples were washed with 0.1 M HCl and deionized water. Then, the samples were dried at 105 °C for 24 h. Activated carbons obtained from TS, TP and HTP were named as ATS, ATP and AHTP respectively. Block diagrams regarding the preparation of ATS, ATP and AHTP are given in Figure 1.
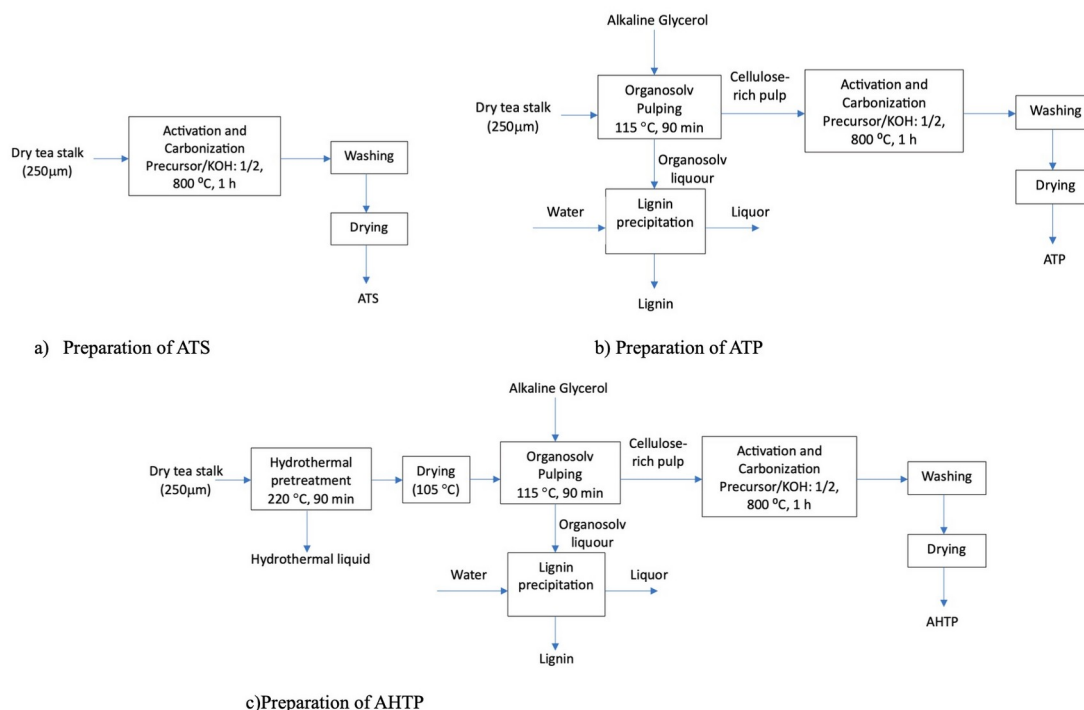
Figure 1: Preparation procedure and naming of the activated carbons.

2.3. Analyses

Proximate analyses of TS, HTS, TP and HTP were done using thermogravimetry method as described in Garcia,

Pizarro (43). The elemental analysis of TS, HTS, TP, HTP, ATS, ATP and AHTP were carried by an elemental analyzer (LECO, CHNS-932). Acid-insoluble lignin content of TS, TP and HTP was determined by using gravimetric method as described in NREL/TP-510-42618 (44). Holocellulose content of TS was determined as explained in Salim et al. (45).

Fourier Transform Infrared (FTIR) spectra of TS, HTS, TP, HTP, ATS, ATP and AHTP were obtained using a spectrometer (Perkin Elmer Spectrum 100) coupled with a universal attenuated total reflectance (ATR) sampling device with a diamond crystal. The spectra were recorded with a resolution of 4 1/cm, in the range from 400 to 4000 1/cm.

For thermal stability, thermogravimetric analyzer (Seiko, TG/DTA 6300) was used. Samples were heated from room temperature to 900 °C with a heating rate of 40 °C/min and maintained for 7 min.
Surface morphologies of HTS, ATS, ATP and AHTP were investigated by FEI Inc., Inspect S50 SEM. Samples were investigated under 20 kV in the high vacuum mode using secondary electrons with different magnifications.

The surface area and pore structure characteristics of ATS, ATP and AHTP were determined by using Quantachrome-Autosorb iQ BET analyzer at 77K in the relative pressure range of 0.001 and 0.99. Before analysis, samples were degassed at 180 °C for 24 h.

The XRD patterns of ATS, ATP and AHTP were collected using Rigaku Smartlab X-Ray diffractometer, operating at 40kVand 30 mA, with a scan range of 10 to 80 °, a step width of 0.02° and a scan speed of 1.0039 °/min.

3. RESULTS AND DISCUSSION

3.1. Characterization
The proximate analysis (volatile matter, fixed carbon and ash content) and ultimate analysis (C, H, N and S content) of TS, HTS, TP, HTP, ATS, ATP and AHTP are presented in Table 1. Tea stalk is a lignin-rich lignocellulosic biomass, which contains 33.9±1.1 % lignin and 49.2±1.3 holocellulose in its structure.

During hydrothermal pretreatment, biomass undergoes several reactions including hydrolysis, dehydration, decarboxylation, condensation, and polymerization (40). The extent of the reactions, which determines the hydrochar yield (mass ratio of hydrochar to biomass on dry weight basis), depend on the hydrothermal conditions and the type of biomass (especially lignin, cellulose and hemicellulose content). After hydrothermal pretreatment of TS, the hydrochar yield was calculated as 70.7±0.3 %. Due to the high lignin content of TS and moderate pretreatment temperature (220 °C), this hydrochar yield was expected as explained briefly in Gulec et al. (46).

After hydrothermal pretreatment, the volatile matter content of the tea stalk increased, the fixed carbon content decreased, and consequently the carbon content increased by 3%. Hydrothermal pretreatment also reduced the ash content of the TS by 5.3%.

Alkaline-glycerol organosolv pretreatment is an effective delignification method (28). When alkaline-glycerol organosolv treatment was applied directly to TS, 7.1±0.2 % lignin (acid-insoluble lignin) was detected in TP, showing that some of the lignin retained in the pulp. In the case of sequential hydrothermal pretreatment and organosolv treatment, the lignin content in HTP was 11.6±0.7 %. Based on acid-soluble lignin content, hydrothermal pretreatment prior to glycerol organosolv treatment reduced delignification.

The application of hydrothermal pretreatment before the organosolv treatment affected the pulp content. The carbon content of TP and HTP was close to each other (37.8% and 36.9%, respectively) and a small part of this carbon is fixed carbon. Cellulose-rich TP and HTP were found to have a lower carbon content than the average carbon content of a typical cellulose (44.06 %), and a higher fixed carbon content than a typical cellulose (4.35 %) (47). Since delignification was not 100% in both treatments, there was still lignin in both TP and HTP. The high fixed carbon content of TP and HTP can be explained by the high fixed carbon content of the residual lignin (23.09 %) (47).

Table 1: Proximate and ultimate analysis of TS, HTS, TP, HTP, ATS, ATP and AHTP.

	TS	HTS	TP	HTP	ATS	ATP	AHTP
Proximate analysis (wt.%, db.)							
VM	71.1	72.6	91.4	92.3	n.d.	n.d.	n.d.
FC	25.1	23.8	6.9	6	n.d.	n.d.	n.d.
Ash	3.8	3.6	1.7	1.7	n.d.	n.d.	n.d.
Ultimate analysis (wt.%, db.)							
C	46.6	48	37.8	36.9	61.3	56.3	52.3
H	5.5	5.4	8.3	8	0.5	0.2	0.2
N	2.6	2.3	0.5	0.6	1.1	0.5	0.4
S	0.1	0	0	0	0	0	0

VM: Volatile matter, FC: Fixed carbon, A: Ash, db: dried basis
* Proximate and ultimate analyses were done twice. Mean values were given in Table 1.

After activation-carbonization, the carbon content of TS, TP and HTP increased by 31.5%, 49% and 41.7%, respectively. Based on elemental analysis results, the oxygen content of ATP and AHTP was high. This was mainly due to high oxygen content of TP (51.7%) and HTP (52.8%). Not hydrothermal pretreatment but delignification definitely increased the oxygen content of the pulps. The oxygen-rich functional groups of TP, HTP, ATP and AHTP were also supported by the FTIR spectra.

3.2. Thermal Stability of TS, HTS, TP and HTP

Thermal stability is an important property of all bio-based materials. Figure 2 shows the TG and DTG curves of TS, HTS, TP and HTP. The thermogravimetric curve of TS showed a thermal degradation curve of a typical biomass. Moisture removal was observed in the first stage at temperatures between 25 °C and 110 °C. The thermal degradation of structural components (hemicellulose, cellulose and lignin) was seen at temperatures between 120 °C and 600 °C.

Like TS, the thermal degradation of HTS occurred in two stages at a wide temperature range. Hydrochar has a more stable structure compared to biomass since hemicellulose is partially degraded and light volatiles leave the structure during hydrothermal treatment. HTS was also more thermally stable than TS. Better thermal stability of the structure was also supported by the shifting of T_{max} (the temperature at which the mass loss

rate is maximum) from 337 °C to 344 °C after hydrothermal treatment.

While the thermal degradation of pure cellulose takes place in two stages (the first step is moisture removal), the thermal degradation of TP and HTP differs slightly from the typical thermogram of cellulose. This is because although it is rich in cellulose, there is some lignin in the pulp and chemical treatment of the cellulose disrupts the structure (48). Studies investigating the effects of chemical treatment on cellulose structure have shown that the thermal degradation of cellulose occurs in three stages, and the thermal degradation after moisture removal is between 110 °C – 285 °C and 288 °C – 600 °C (49, 50). In the present study, thermal degradation of both TP and HTP occurred in three steps. The mass loss in the first stage in both samples was due to the removal of moisture. The degradation of TP in the second stage was between 180 °C and 235 °C, with a T_{max} of 220 °C. The mass loss of TP in the third stage was between 280 °C and 344 °C, and the highest mass loss rate in this stage was seen at 322 °C.

The thermal degradation of HTP started with the removal of moisture. The second degradation was between 172 °C and 236 °C, with a T_{max} of 221 °C. The third stage of thermal degradation was observed at temperatures between 290 °C and 344 °C. At this stage, the temperature with the highest mass loss rate was determined as 327 °C. Application of hydrothermal pretreatment before the organosolv treatment slightly increased the thermal stability of the pulp.
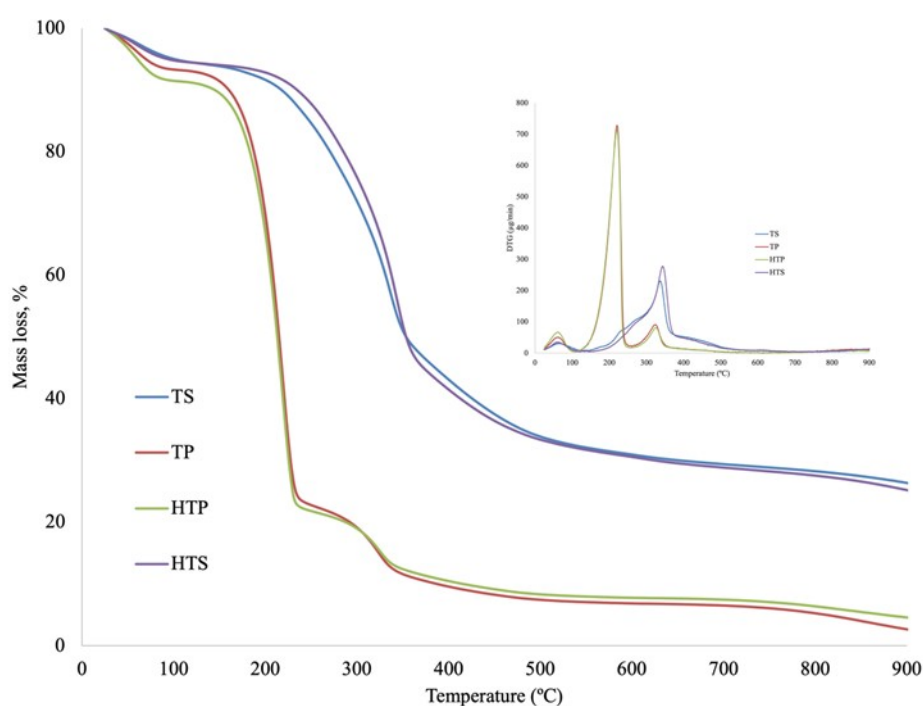

Figure 2: TG curves of TS, HTS, TP and HTP.

3.3. FTIR Analysis

The FTIR spectra of TS, HTS, TP and HTP are shown in Figure 3. Tea stalk has a broad peak at 3000-3800 1/cm (centered at 3338 1/cm) due to -OH stretching vibration in the hydroxyl functional groups (in compounds such as phenolics, aliphatic alcohols, carboxylic acids etc.) (51). The peaks at 2917 1/cm and 2849 1/cm correspond to stretching vibration of aliphatic C-H bond in -CH$_2$-structures (52). The peaks appearing between 2009-2160 1/cm originate from the stretching vibration of allene (C=C=C) and ketamine (C=C=N) groups in tea stalk (51, 53, 54). Stretching vibration of C=C bond in aromatic rings and C-H stretching appear at 1515 1/cm and 1362 1/cm. HTS has a similar FTIR spectra with that of TS. Only difference between them was the intensity of the bands of HTS at 1200-3600 1/cm region, which confirms that a degradation was observed but functional group was not changed. Compared to TS, the stretching vibration of -OH (at 3000-3600 1/cm), -CH (at 2800-3000 1/cm) and C=C=C (at 2000-2200 1/cm) in HTS structure were much lower. After hydrothermal pretreatment, the characteristic bands of lignin (1660-1638 1/cm) and (1400-1500 1/cm) were retained, with a slight decrease in intensities. Yu et al. (55) made a similar observation and concluded that the structure of lignin was slightly changed with temperature due to the cleavage of C-C, C=C and C-H bands. The characteristic stretching vibrations of cellulose at 1000-1400 1/cm region were slightly less due to partial degradation of cellulose under hydrothermal conditions.

The effect of delignification was observable from the FTIR spectra of TP and HTP. The wide peak appearing between 3000-3600 1/cm for all samples reflect the stretching vibration of -OH group. The bands at 2880 1/cm and 2920 1/cm were assigned to -CH stretching vibration of -CH^2 and -CH$_3$ groups. The peaks at 2160 1/cm, 2040 1/cm and 2000 1/cm were attributed to C=C=C and C=C=N stretchings. While FTIR spectra of TS reflects the conjugated carbonyl stretching (at 1660-1638 1/cm) and aromatic skeleton vibration in lignin (at 1600 1/cm, 1500 1/cm and 1440 1/cm) (56, 57); the intensity of the same peaks in the FTIR spectra of both TP and HTP were comparatively very low due to delignification. In all spectra, in-plane C-H deformation (at 1360 1/cm), in-plane O-H bending in cellulose structure (at 1320 1/cm) and C-C, C-O, C=O stretch (at 1240 1/cm) were observed.
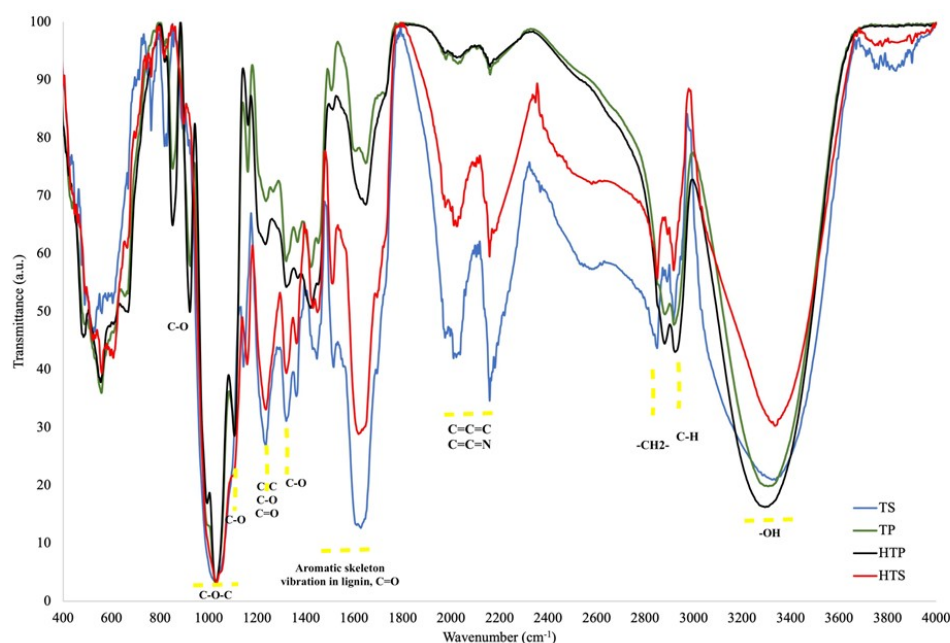

Figure 3: FTIR spectra of TS, HTS, TP and HTP.

Figure 4 shows the FTIR spectra of ATP, AHTP and ATS. The spectra of the activated carbons were similar, only the intensities of the vibrations altered. The stretching vibration of -OH in phenol and carboxyl groups centered at 3073 1/cm (58) was more intense in the spectra of ATS than that of ATP and AHTP. Similarly, C=O stretching vibration (in ketene groups) at 2420-2430 1/cm (59) was more intense in the spectra of ATS than that of ATP and AHTP. The spectra of all activated carbons showed the stretching vibration of C=C=C (in allene group) at 2160 1/cm (60, 61). C=O stretching vibration of carbonyl and carboxylate groups (such as ketones, aldehydes) was observed in the spectra of all activated carbons at 1600-1700 1/cm with same intensity (62). C=C stretching vibration of aromatic rings at 1560 1/cm (51) was also detected in all spectra. C-O stretching vibration (in ethers, alcohols, acids, esters) at 1017 1/cm (63) was much more intense in the spectra of ATP. AHTP and ATS showed stronger stretching at 1200 (C-C, C-O, C=O stretching vibration). Bending vibration of C-H in the aromatic rings at 820-840 1/cm (64) was observed in the spectra of AHTP and ATS.
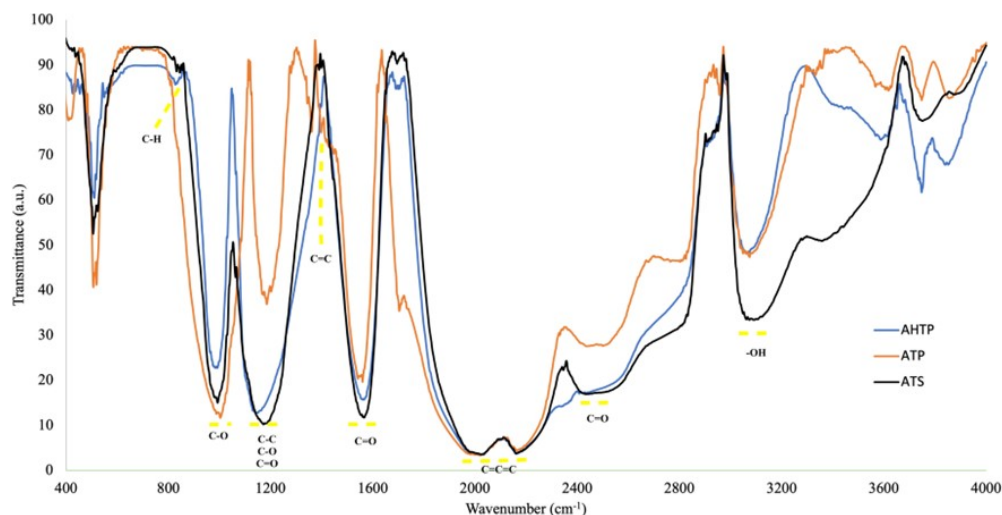
Figure 4: FTIR spectra of ATS, ATP and AHTP.

3.4. X-ray Diffraction Analysis

Depending on the type of biomass, cellulose is present in the structure as crystalline and amorphous form (65). Any pretreatment using chemicals such as acids, bases and solvents might affect the amorphous structure (66-70). In order to observe what extent the pretreatments changed the cellulose in the biomass structure, x-ray diffraction analysis was also performed on hydrochar and pulps.

XRD patterns of TP, HTP and HTS are presented in Figure 5. The XRD patterns of HTS exhibit diffraction peaks at 15° (101), 22° (002) and 34.5° (040), which indicates that both amorphous and crystalline cellulose structure was preserved during hydrothermal pretreatment (64). A similar result was observed by Fan et al. (71), who studied the hydrothermal carbonization of Chinese fan palm leaves at different temperatures. In the study of Fan et al. (72), a broad peak between 15° and 16°, which indicated amorphous structure, was observed in the XRD of hydrochars obtained at 180 and 220 °C, while this structure was not seen above 260 °C. In the x-ray diffractions of TP and HTP obtained by organosolv pretreatment and sequential hydrothermal-organosolv pretreatments, only broad peaks at 22° (002 plane) and 34.5° were observed. Alkaline-glycerol organosolv pretreatment completely removed the amorphous structure. Sun et al. (72), who applied glycerol organosolv treatment to wheat straw, showed that the amorphous structure (amorphous cellulose, lignin and hemicellulose) decreased (hence the crystal index increased) and the average crystal size of cellulose decreased.
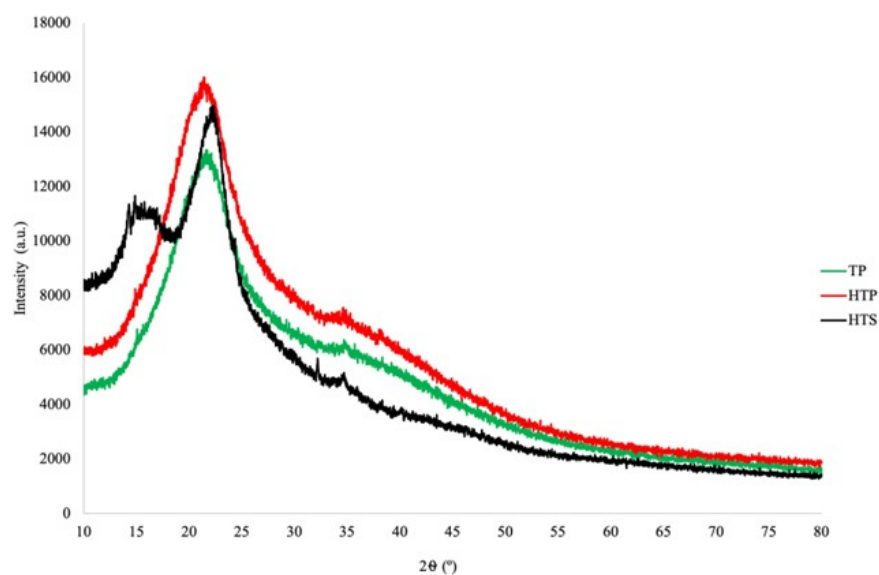
Figure 5: X-ray diffraction patterns of TP, HTP and HTS.

After carbonization and activation, a broad hump (indicating the amorphous graphitic carbon) between 17° and 35° was observed in the x-ray diffraction pattern of ATP, ATS and AHTP (73). A weaker and broader hump at 41-47° was also observable in all patterns, which is also a characteristic diffraction of amorphous graphite structure (74). Unlike ATP and ATS, AHTP shows sharp diffraction peaks of graphitic carbon

at 2θ=20°, 26°, 36°, 41°, 44°, 47.5°, 52°, 53.5°, 55.5°, 63° (55, 75). Obviously, AHTP has higher crystallinity compared to ATP and ATS.
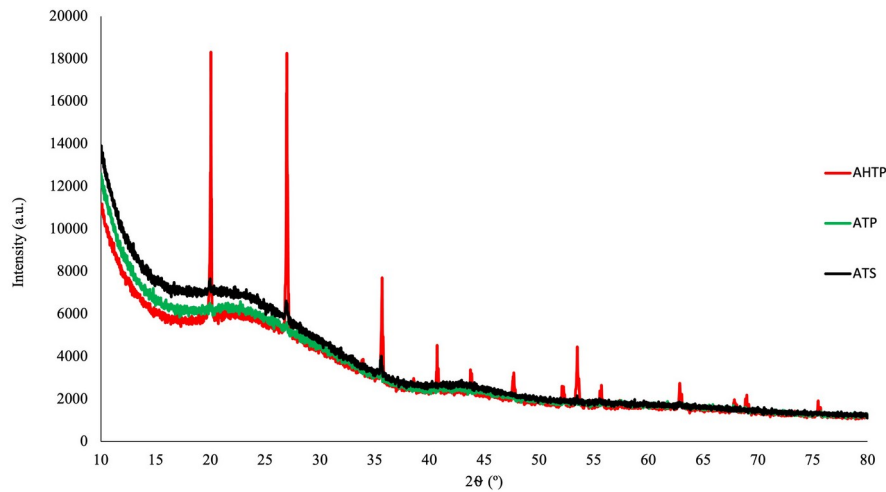
Figure 6: X-ray diffraction pattern of AHTP, ATP and ATS.

3.5. SEM Analysis

SEM provides micrographs that show surface morphology. The surface morphologies of HTS, ATS, ATP and AHTP can be seen in Figure 7. HTS shows an irregular and rough surface. The formation of microspheres or pores was not observed on the surface of HTS, showing that hydrothermal treatment temperature (220 °C) was not able to destruct lignocellulosic structure (76). The SEM image of ATS shows a dense porous structure with many three-dimensional channels. Activation of tea stalk with KOH resulted in well-developed micropores on the surface of the ATS. Although the SEM image of ATP was densely microporous like that of ATS, the presence of mesopores was noteworthy. Removal of lignin from the lignocellulosic structure leads pore formation. Therefore, mesopores in ATP were due to severe destruction of lignocellulosic structure by organosolv delignification, which was done prior to activation. AHTP images also show the porous structure with a wider range of pores compared to that of ATP. Both hydrothermal pretreatment and organosolv delignification corroded the lignocellulosic structure, which resulted in mesopore formation.
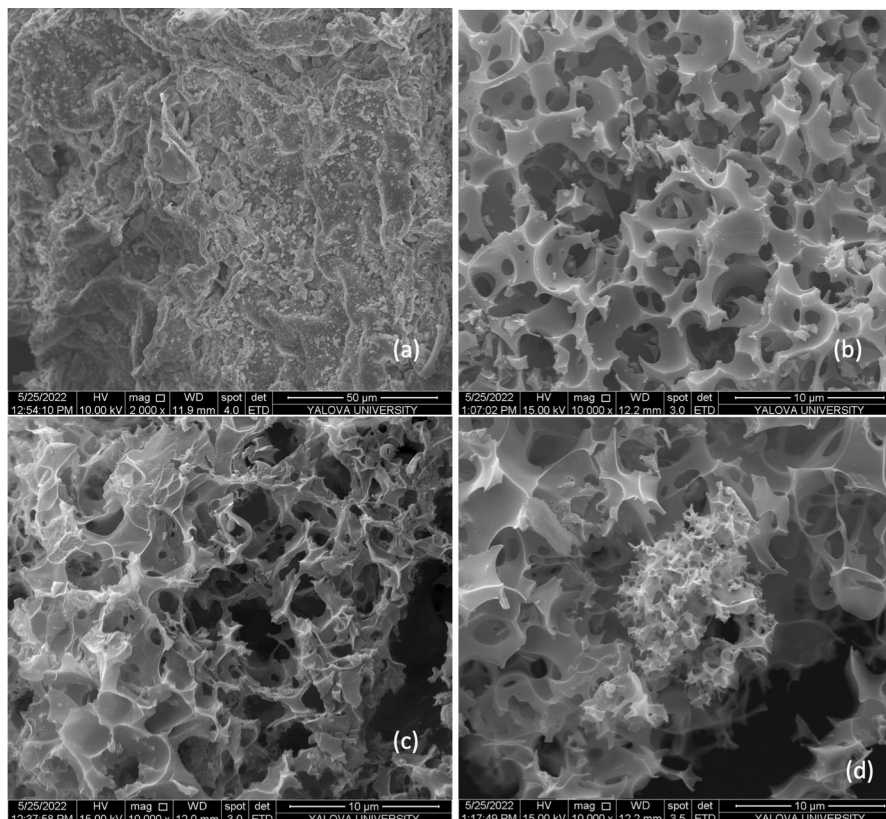
Figure 7: SEM images of (a) HTS (magnification of 2000x), (b) ATS, (c) ATP and (d) AHTP (magnification of 10000x).

3.6. BET Analysis

To have high adsorption capacity, activated carbons should possess morphological properties including amorphous structure, high surface area and high porosity (1). Obtaining N_2 adsorption-desorption isotherms is the most common method used to determine the surface area and pore characteristics of activated carbons. Pores can be classified as micropores (pore diameter <2 nm), mesopores (pore diameter between 2-50 nm), and macropores (pore diameter > 50 nm) (77).

Isothermal plots of ATP, AHTP and ATS are shown in Figure 8. N_2 adsorption-desorption isotherm of ATS is Type I isotherm (based on IUPAC classification), showing microporous characteristics. N_2 isotherm of ATS shows a steep N_2 uptake at very low relative pressures (P/P$_0$<0.1)

due to N_2-ATS interactions in narrow micropores by micropore filling (78).

Both ATP and AHTP show Type IV isotherm, with a steep uptake of N_2 at very low relative pressures and a sharp increase of N_2 adsorption at relative pressures higher than 0.9. ATP and AHTP are mesoporous activated carbons. Adsorption of N_2 in mesopores is due to physical interaction between N_2 molecules and activated carbon, and the interaction between N_2 molecules in the condensed state. Since AHTP has larger pores, N_2 adsorption due to condensation is higher. For both AHTP and ATP, hysteresis due to capillary condensation is not observed in the isotherm, showing that mesopores are either smaller in width or in conical/cylindrical form (78).
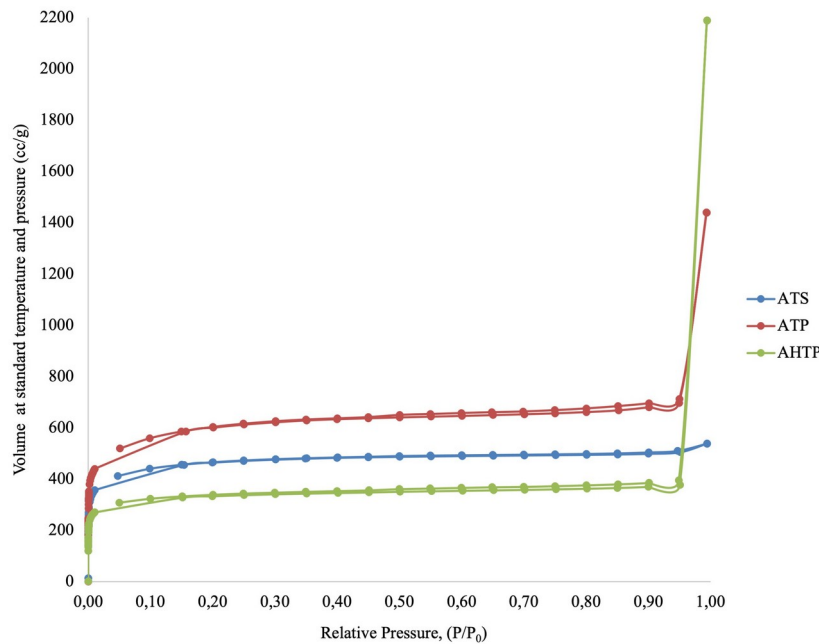
Figure 8: Nitrogen adsorption/desorption isotherms of ATS, ATP and AHTP.

The surface area and pore structure characteristics of ATS, ATP and AHTP are listed in Table 2. ATP has the highest surface area (2056.72 m²/g), where 86% of it comes from micropores. This is mainly due to the porosity enhancement by delignification (35, 79) and better accessibility of KOH to the active sites. Similar results were observed in studies that produced activated carbon from cellulose-rich precursors. Tsubota

et al. (21) first delignified bamboo powder with acetic acid-hydrogen peroxide solvent mixture and then carbonized the pulp in the presence of CO_2 at 800 °C. Regardless of the lignin content of the pulp, the surface areas of activated carbons varied between 1062.88 m²/g-1413 m²/g, and the average pore sizes varied between 1.7-2 nm.

Table 2: Comparison of surface area and pore characteristics.

Sample	S_{BET} (m²/g)	$S_{micropore}$ (m²/g)	$S_{micropore}/S_{BET}$	Average pore radius (nm)	V_{micro} (cm³/g)	V_{total} (cm³/g)
ATS	1643	1479.14	0.90	1.01	0.65	0.833
ATP	2056.72	1768.66	0.86	2.16	0.81	2.227
AHTP	1179.71	1055.53	0.89	5.74	0.46	3.386

S_{BET}: Surface area based on multi-point BET analysis

$S_{micropore}$: micropore area based on V-t method
V_{micro}: micropore volume

AHTP, with the largest average pore radius (5.74 nm), has the least micropore volume (0.464 cm^3/g) and surface area (1179.71 m^2/g). Sequential hydrothermal pretreatment and organosolv treatment destruct the lignocellulosic structure more resulting in a more porous precursor, which ended with mesoporous structure. ATS, having the lowest average pore radius, is microporous. Activated carbons of different lignocellulosic biomass (which are activated by KOH and carbonized at 800 °C) have similar pore diameter and surface area with ATS (80-84).

3.7. Possible Applications of the Microporous and Mesoporous Activated Carbons Prepared from Tea Stalk and Tea Stalk Pulp

This study showed that although the same activation and carbonization conditions are applied, pretreatments namely organosolv delignification and two-step hydrothermal-organosolv treatment affect the pore diameters, surface functional groups and specific surface areas of activated carbons. Nonetheless, those characteristics of activated carbons are important in determining the end use or application. Since the specific surface areas and pore structures of the prepared ATS, ATP and AHTP are different, the most appropriate end-use purpose of those activated carbons should differ. Possible uses are discussed below, considering the specific surface area and pore structure.

One of the processes in which activated carbon is used the most is adsorption. While micropores provide the main adsorption sites, mesopores provide diffusion channels for the absorbate (85). In liquid and gaseous adsorption processes, the pore size of the adsorbent and the molecular size of the adsorbate must be compatible (85). Due to the reason that gaseous adsorbate molecules are generally found in the range of 0.5–1.5 nm, the microporous activated carbons (average pore size <2 nm) are suitable for the adsorption of gases (86). Microporous activated carbons are mainly used for the adsorption of volatile organic compounds (VOCs), CH_4, N_2, and CO_2 (87). Since the presence of oxygen-containing functional groups lowers the adsorption capacity (88, 89), oxygen-rich microporous ATS might not be suitable to be used for the adsorption of VOCs. In the case of CH_4 and N_2 adsorption, it has been shown in studies that the pore size should be quite low (between 0.7 nm and 1.3 nm) for high adsorption capacity (86, 90, 91). Many experimental studies related to CO_2 adsorption show that both the preparation method and structural properties of the activated carbons are similar to ATS. The high specific surface area, micropore structure and presence of highly oxygenated functional groups of ATS make ATS a suitable candidate for CO_2 adsorption. Table 3 shows the structural properties of activated carbons and their CO_2 adsorption capacities that were obtained under similar conditions to our study.

Table 3: Structural properties of activated carbons and their CO_2 adsorption capacities reported in similar studies.

Precursor	Carbonization and activation conditions	Surface area (m^2/g)	Pore size (nm)	Micropore volume (cm^3/g)	CO_2 adsorption	Ref.
Pine nut shell	KOH/precursor: 2(wt ratio) T: 800 °C	1372	2.1532	0.6842	5.8 mmol/g (0 °C) 3.5 mmol/g (25 °C)	(92)
Walnut shell	KOH/precursor: 1(wt ratio) T: 800 °C	1868	< 4	0.55	9.56 mmol/g (0 °C) 5.17 mmol/g (25 °C) 4.34 mmol/g (40 °C)	(93)
Cucumber peels	KOH/precursor: 1(wt ratio) T: 800 °C	1769	2.334	0.692	6.095 mmol/g (0 °C) 4.37 mmol/g (10 °C) 3.52 mmol/g (25 °C)	(94)
Starch	KOH/precursor: 4 (wt ratio) T: 700 °C	2190	1.2	0.92	5.6 mmol/g (0 °C) 3.5 mmol/g (25 °C) 5.6 mmol/g (50 °C)	(95)
Cellulose	KOH/precursor: 4 (wt ratio) T: 700 °C	2370	1.2	0.96	5.8 mmol/g (0 °C) 3.5 mmol/g (25 °C) 1.8 mmol/g (50 °C)	
Sawdust	KOH/precursor: 4 (wt ratio) T: 700 °C	2250	1.2	0.91	5.5 mmol/g (0 °C) 2.9 mmol/g (25 °C) 1.8 mmol/g (50 °C)	
Sawdust	KOH/precursor: 2 (wt ratio) T: 800 °C	1940	0.9	0.82	5.8 mmol/g (0 °C) 3.9 mmol/g (25 °C) 3.1 mmol/g (50 °C)	
Olive mill waste hydrochar	KOH/precursor: 2 (wt ratio) T: 700 °C	888	< 1	0.294	1.350 mmol/g (0 °C, 1 bar) 2.984 mmol/g (0 °C, 101.3 kPa)	(96)

Camphor leaves	KOH/precursor: 2 (wt ratio) T: 800 °C	1736	< 1	0.357	4.8 mmol/g (0 °C) 2.42 mmol/g (25 °C) 1.45 mmol/g (50 °C)	(97)
Pristine wheat flour	KOH/precursor: 2 (wt ratio) T: 700 °C	1057	< 2	0.474	4.41 mmol/g (0 °C) 2.77 mmol/g (25 °C) 1.60 mmol/g (50 °C)	(98)
Peanut shell	KOH/precursor: 1 (wt ratio) T: 700 °C	956	<11	Not available	1.54 mmol/g (25 °C, 0.15 bar)	(99)
Sunflower seed shell	KOH/precursor: 1.25 (wt ratio) T: 700 °C	1790	< 1	Not available	1.46 mmol/g (25 °C, 0.15 bar)	
Pine nut shell	KOH/precursor: 2 (wt ratio) T: 700 °C	Not available	<1.1	Not available	7.7 mmol/g (0 °C, 1 bar) 5 mmol/g (25 °C, 1 bar) 3.3 mmol/g (0 °C, 0.15 bar) 2 mmol/g (25 °C, 0.15 bar)	(100)
Paulownia sawdust	KOH/precursor: 2 (wt ratio) T: 700 °C	831	<1	0.297	6.83 mmol/g (0 °C)	(101)
Paulownia sawdust	KOH/precursor: 4 (wt ratio) T: 800 °C	1555	<1	0.598	7.14 mmol/g (0 °C)	
Spent coffee grounds	KOH/precursor: 3 (wt ratio) T: 700 °C	1082	3	0.44	3.2 mmol/g (0 °C, 101 kPa) 2.7 mmol/g (25°C, 101 kPa)	(102)

Mesoporous activated carbons (2 nm < average pore size <50 nm) are more preferred in the adsorption of large molecules including dyes, pharmaceuticals, cyanobacterial toxins, pollutants and enzymes (103-105).

Table 4: Structural properties of mesoporous activated carbons and their reported adsorbates and adsorption capacities reported in similar studies.

Precursor	Carbonization and activation conditions	Surface area (m^2/g)	Pore size (nm)	Micropore volume (cm^3/g)	Adsorbate and adsorption capacity	Ref.
Dragon fruit peels	KOH/precursor: 2 (wt ratio) T: 700 °C	756.3	11.3	0.376	Adsorbate: methylene blue dye Maximum adsorption capacity: 195.2 mg/g	(106)
Yellow mombin fruit stones	KOH/precursor: 1 (wt ratio) T: 500 °C	167	4.82	0.027	Adsorbate: Dianix ® royal blue dye Maximum adsorption capacity: 82.28 mg/g	(107)
Rice straw	Precursor was soaked in 85 wt % KOH solution T: 400 °C for 1 h and then 700 °C for 1 h.	165.9	5.941	0.032	Adsorbate: Methylene blue dye Maximum adsorption capacity: 392.4 mg/g	(108)
					Adsorbate: Congo red dye Maximum adsorption capacity: 178.4 mg/g	
Rice straw	Precursor was first pre-carbonized at 400 °C for 1 h, then soaked in 85 wt% KOH solution, then carbonized at 700 °C for 1 h.	1973	2.292	0.769	Adsorbate: Methylene blue dye Maximum adsorption capacity: 527.6 mg/g	
					Adsorbate: Congo red dye Maximum adsorption capacity: 531.4 mg/g	
Sugarcane bagasse	KOH/precursor: 1 (wt ratio) T: 700 °C	1204	1.79	0.57	Adsorbate: Phenol Maximum adsorption capacity: 88 mg/g	(109)
Sawdust	KOH/precursor: 1 (wt ratio) T: 700 °C	1544	1.82	0.69	Adsorbate: Phenol Maximum adsorption capacity: 96.8 mg/g	
Potato peel	KOH/precursor: 4 (wt ratio) T: 600 °C	2394	<10 Average between: 2-4 nm	-	Adsorbate: Methylene Blue Maximum adsorption capacity: 2521 mg/g	(110)
Crab shell	KOH/precursor: 3 (wt ratio) T: 800 °C	1095.14	2.18	-	Adsorbate: Tetracycline Maximum adsorption capacity: 380.92 mg/g	(111)

Mesoporous activated carbons are also preferred as electrode materials in supercapacitors due to their high specific surface area, high pore volume, good thermal stability, and enhanced specific capacitance (112, 113). Apart from mesoporous structure, presence of oxygen-containing functional groups on the surface of the activated carbon also enhances electrochemical active sites (111). Table 5 shows the studies in which activated carbon was prepared under conditions similar to those we applied in the present study and used in supercapacitors. According to the studies in Table 5, having pores with a diameter of 2-5 nm enhances the transport of electrolytes. The large specific surface area, the presence of macropores alongside micropores, and the abundance of oxygenated functional groups make ATP and AHTP a suitable candidate for use in supercapacitors.

Table 5: Structural properties of activated carbons and their maximum specific capacitance reported in similar studies.

Precursor	Carbonization and activation conditions	Surface area (m²/g)	Pore size (nm)	Pore volume (cm³/g)	Maximum specific capacitance (F/g)	Ref.
Corncob	Carbonization at 400 °C for 4 h, then activation with KOH (KOH/precursor: 3 (wt ratio)) at 600 °C	800	Micropores in the range of 1.4-1.8 nm, mesopores in the range of 2.2-5 nm	0.337	390	(114)
Wastewater from vitamin C production, template: melamine foam	KOH/precursor: 5 (wt ratio) T: 700 °C	3837	2.32	2.22	217	(113)
Olive tree branches	Carbonization: 500 °C for 2 h Activation: KOH/precursor: 4 (wt ratio) 800 °C for 82 min	2980	0.8nm<pore size<5 nm	1.59	410	(115)
Biogas slurry	First drying, then carbonization at 650 °C for 1 h. Activation: KOH/precursor: 3 (wt ratio) 700 °C for 30 min	326.7	4.7	0.24	163	(116)
	First drying, then carbonization at 650 °C for 1 h. Activation: KOH/precursor: 3 (wt ratio) 700 °C for 60 min	514.7	4.7	0.38	182	
Coconut silk	Carbonization at 400 °C for 1 h. Activation: KOH/precursor: 4 (wt ratio) 900 °C for 1 h	2318	0.5- 5 (average 1.42)	0.87	631	(111)
Corn silk	Carbonization at 300 °C for 2 h. Activation: KOH/precursor: 3 (wt ratio) 850 °C for 4 h	2441	3.097 (average) (large pores (>30nm) were also seen in the structure)	1.890	174	(117)

4. CONCLUSION

In the present study, three different activated carbons were prepared: activated carbon from tea stalk itself, activated carbon from tea stalk pulp obtained by using glycerol organosolv pretreatment, and activated carbon from tea stalk hydrochar pulp obtained by using sequential hydrothermal pretreatment-organosolv delignification. The tea stalk itself and the cellulose-rich precursors were carbonized at 800 °C for 1 h in the presence of KOH.

The study showed that partial removal of lignin yielded activated carbons with more specific surface area and mesopores. Additionally, because delignification modified the functional groups of the biomass, the surface of activated carbon contained more oxygen-rich functional groups. While decreasing the lignin removal, hydrothermal pretreatment prior to delignification

ended up with mesoporous activated carbon with a larger pore diameter. Activated carbons (ATS, ATP and AHTP) obtained from tea stalk can be used in many applications from environmental applications to energy storage due to their different surface areas, micropore volumes and pore structures.

5. CONFLICT OF INTEREST

The authors declare that they have no known competing financial interests or personal relationships that could have appeared to influence the work reported in this paper.

6. ACKNOWLEDGMENTS

7. REFERENCES

1. Adeleye AT, Akande AA, Odoh CK, Philip M, Fidelis TT, Amos PI, et al. Efficient synthesis of bio-based activated carbon (AC) for catalytic systems: A green and sustainable approach. J Ind Eng Chem [Internet]. 2021 Apr 25;96:59–75. Available from: <URL>.

2. Darmawan S, Wistara NJ, Pari G, Maddu A, Syafii W. Characterization of Lignocellulosic Biomass as Raw Material for the Production of Porous Carbon-based Materials. BioResources [Internet]. 2016 Feb 29;11(2):3561–74. Available from: <URL>.

3. De Bhowmick G, Sarmah AK, Sen R. Lignocellulosic biorefinery as a model for sustainable development of biofuels and value added products. Bioresour Technol [Internet]. 2018 Jan 1;247:1144–54. Available from: <URL>.

4. Astuti W, Sulistyaningsih T, Prastiyanto D, Rusiyanto, Lanjar, Riayanti FI, et al. Influence of lignocellulosic composition in biomass waste on the microstructure and dye adsorption characteristics of microwave-assisted ZnCl2 activated carbon. Biomass Convers Biorefinery [Internet]. 2023 May 10;1:1–17. Available from: <URL>.

5. Nabais JMV, Gomes JA, Suhas, Carrott PJM, Laginhas C, Roman S. Phenol removal onto novel activated carbons made from lignocellulosic precursors: Influence of surface properties. J Hazard Mater [Internet]. 2009 Aug 15;167(1–3):904–10. Available from: <URL>.

6. Chen S, Xia Y, Zhang B, Chen H, Chen G, Tang S. Disassembly of lignocellulose into cellulose, hemicellulose, and lignin for preparation of porous carbon materials with enhanced performances. J Hazard Mater [Internet]. 2021 Apr 15;408:124956. Available from: <URL>.

7. Chanpee S, Kaewtrakulchai N, Khemasiri N, Eiad-ua A, Assawasaengrat P. Nanoporous Carbon from Oil Palm Leaves via Hydrothermal Carbonization-Combined KOH Activation for Paraquat Removal. Molecules [Internet]. 2022 Aug 19;27(16):5309. Available from: <URL>.

8. Demiral H, Demiral İ, Tümsek F, Karabacakoğlu B. Adsorption of chromium(VI) from aqueous solution by activated carbon derived from olive bagasse and applicability of different adsorption models. Chem Eng J [Internet]. 2008 Oct 15;144(2):188–96. Available from: <URL>.

9. Olivares-Marín M, Fernández JA, Lázaro MJ, Fernández-González C, Macías-García A, Gómez-Serrano V, et al. Cherry stones as precursor of activated carbons for supercapacitors. Mater Chem Phys [Internet]. 2009 Mar 15;114(1):323–7. Available from: <URL>.

10. Martínez de Yuso A, Izquierdo MT, Valenciano R, Rubio B. Toluene and n-hexane adsorption and recovery behavior on activated carbons derived from almond shell wastes. Fuel Process Technol [Internet]. 2013 Jun 1;110:1–7. Available from: <URL>.

11. Mohamad Nor N, Lau LC, Lee KT, Mohamed AR. Synthesis of activated carbon from lignocellulosic biomass and its applications in air pollution control—a review. J Environ Chem Eng [Internet]. 2013 Dec 1;1(4):658–66. Available from: <URL>.

12. González-García P. Activated carbon from lignocellulosics precursors: A review of the synthesis methods, characterization techniques and applications. Renew Sustain Energy Rev [Internet]. 2018 Feb 1;82:1393–414. Available from: <URL>.

13. Mohd Azmi NZ, Buthiyappan A, Abdul Raman AA, Abdul Patah MF, Sufian S. Recent advances in biomass based activated carbon for carbon dioxide capture – A review. J Ind Eng Chem [Internet]. 2022 Dec 25;116:1–20. Available from: <URL>.

14. Khezami L, Chetouani A, Taouk B, Capart R. Production and characterisation of activated carbon from wood components in powder: Cellulose, lignin, xylan. Powder Technol [Internet]. 2005 Sep 29;157(1–3):48–56. Available from: <URL>.

15. Suhas, Carrott PJM, Ribeiro Carrott MML. Lignin – from natural adsorbent to activated carbon: A review. Bioresour Technol [Internet]. 2007 Sep 1;98(12):2301–12. Available from: <URL>.

16. Xi Y, Yang D, Qiu X, Wang H, Huang J, Li Q. Renewable lignin-based carbon with a remarkable electrochemical performance from potassium compound activation. Ind Crops Prod [Internet]. 2018 Nov 15;124:747–54. Available from: <URL>.

17. Gayathiri M, Pulingam T, Lee KT, Sudesh K. Activated carbon from biomass waste precursors: Factors affecting production and adsorption mechanism. Chemosphere [Internet]. 2022 May 1;294:133764. Available from: <URL>.

18. Guo Y, Rockstraw DA. Physical and chemical properties of carbons synthesized from xylan, cellulose, and Kraft lignin by H3PO4 activation. Carbon N Y [Internet]. 2006 Jul 1;44(8):1464–75. Available from: <URL>.

19. Cagnon B, Py X, Guillot A, Stoeckli F, Chambat G. Contributions of hemicellulose, cellulose and lignin to the mass and the porous properties of chars and steam activated carbons from various lignocellulosic precursors. Bioresour Technol [Internet]. 2009 Jan

1;100(1):292–8. Available from: <URL>.

20. Rodriguez Correa C, Otto T, Kruse A. Influence of the biomass components on the pore formation of activated carbon. Biomass and Bioenergy [Internet]. 2017 Feb 1;97:53–64. Available from: <URL>.

21. Tsubota T, Nagata D, Kamimura S, Ohno T. Partial Delignification as Pretreatment for Nanoporous Carbon Material from Biomass. J Nanosci Nanotechnol [Internet]. 2017 Jan 1;17(1):815–20. Available from: <URL>.

22. Gao Y, Aliques Tomas M del C, Garemark J, Sheng X, Berglund L, Li Y. Olive Stone Delignification Toward Efficient Adsorption of Metal Ions. Front Mater [Internet]. 2021 Feb 12;8:605931. Available from: <URL>.

23. Keplinger T, Wittel FK, Rüggeberg M, Burgert I. Wood Derived Cellulose Scaffolds—Processing and Mechanics. Adv Mater [Internet]. 2021 Jul 14;33(28):2001375. Available from: <URL>.

24. Mittal N, Kaur M, Singh V. Adsorption studies on hydrophobic disperse dye using cellulose derived mesoporous activated carbon. In: 9th International Conference on Advancements and Futuristic Trends in Mechanical and Materials Engineering (AFTMME) [Internet]. Rupnagar; 2021. Available from: <URL>.

25. Han S, Wang J, Wang L. Preparation of hydrophobic, porous, and flame-resistant lignocellulosic carbon material by pyrolyzing delignified wood. Vacuum [Internet]. 2022 Mar 1;197:110867. Available from: <URL>.

26. Sun M, Hong L. Impacts of the pendant functional groups of cellulose precursor on the generation of pore structures of activated carbons. Carbon N Y [Internet]. 2011 Jun 1;49(7):2173–80. Available from: <URL>.

27. Banu Jamaldheen S, Kurade MB, Basak B, Yoo CG, Oh KK, Jeon B-H, et al. A review on physico-chemical delignification as a pretreatment of lignocellulosic biomass for enhanced bioconversion. Bioresour Technol [Internet]. 2022 Feb 1;346:126591. Available from: <URL>.

28. Sun C, Song G, Pan Z, Tu M, Kharaziha M, Zhang X, et al. Advances in organosolv modified components occurring during the organosolv pretreatment of lignocellulosic biomass. Bioresour Technol [Internet]. 2023 Jan 1;368:128356. Available from: <URL>.

29. Zhang Z, Harrison MD, Rackemann DW, Doherty WOS, O'Hara IM. Organosolv pretreatment of plant biomass for enhanced enzymatic saccharification. Green Chem [Internet]. 2016 Jan 18;18(2):360–81. Available from: <URL>.

30. Ferreira JA, Taherzadeh MJ. Improving the economy of lignocellulose-based biorefineries with organosolv pretreatment. Bioresour Technol [Internet]. 2020 Mar 1;299:122695. Available from: <URL>.

31. Vargas F, Domínguez E, Vila C, Rodríguez A, Garrote G. Biorefinery Scheme for Residual Biomass Using Autohydrolysis and Organosolv Stages for Oligomers and Bioethanol Production. Energy & Fuels [Internet]. 2016 Oct 20;30(10):8236–45. Available from: <URL>.

32. Espirito Santo M, Rezende CA, Bernardinelli OD, Pereira N, Curvelo AAS, deAzevedo ER, et al. Structural and compositional changes in sugarcane bagasse subjected to hydrothermal and organosolv pretreatments and their impacts on enzymatic hydrolysis. Ind Crops Prod [Internet]. 2018 Mar 1;113:64–74. Available from: <URL>.

33. Ibrahim Q, Kruse A. Prehydrolysis and organosolv delignification process for the recovery of hemicellulose and lignin from beech wood. Bioresour Technol Reports [Internet]. 2020 Sep 1;11:100506. Available from: <URL>.

34. Vedoya CI, Vallejos ME, Area MC, Felissia FE, Raffaeli N, da Silva Curvelo AA. Hydrothermal treatment and organosolv pulping of softwood assisted by carbon dioxide. Ind Crops Prod [Internet]. 2020 May 1;147:112244. Available from: <URL>.

35. Guo K-N, Zhang C, Xu L-H, Sun S-C, Wen J-L, Yuan T-Q. Efficient fractionation of bamboo residue by autohydrolysis and deep eutectic solvents pretreatment. Bioresour Technol [Internet]. 2022 Jun 1;354:127225. Available from: <URL>.

36. Sun Q, Chen W-J, Pang B, Sun Z, Lam SS, Sonne C, et al. Ultrastructural change in lignocellulosic biomass during hydrothermal pretreatment. Bioresour Technol [Internet]. 2021 Dec 1;341:125807. Available from: <URL>.

37. Sun D, Lv Z-W, Rao J, Tian R, Sun S-N, Peng F. Effects of hydrothermal pretreatment on the dissolution and structural evolution of hemicelluloses and lignin: A review. Carbohydr Polym [Internet]. 2022 Apr 1;281:119050. Available from: <URL>.

38. Scapini T, dos Santos MSN, Bonatto C, Wancura JHC, Mulinari J, Camargo AF, et al. Hydrothermal pretreatment of lignocellulosic biomass for hemicellulose recovery. Bioresour Technol [Internet]. 2021 Dec 1;342:126033. Available from: <URL>.

39. Cavali M, Libardi Junior N, de Sena JD, Woiciechowski AL, Soccol CR, Belli Filho P, et al. A review on hydrothermal carbonization of potential biomass wastes, characterization and environmental applications of hydrochar, and biorefinery perspectives of the process. Sci Total Environ [Internet]. 2023 Jan 20;857:159627. Available from: <URL>.

40. Lachos-Perez D, César Torres-Mayanga P, Abaide ER, Zabot GL, De Castilhos F. Hydrothermal carbonization and Liquefaction: differences, progress, challenges, and

opportunities. Bioresour Technol [Internet]. 2022 Jan 1;343:126084. Available from: <URL>.

41. Başakçılardan Kabakcı S, Baran SS. Hydrothermal carbonization of various lignocellulosics: Fuel characteristics of hydrochars and surface characteristics of activated hydrochars. Waste Manag [Internet]. 2019 Dec 1;100:259–68. Available from: <URL>.

42. Başakçılardan Kabakcı S, Tanış MH. Pretreatment of lignocellulosic biomass at atmospheric conditions by using different organosolv liquors: a comparison of lignins. Biomass Convers Biorefinery [Internet]. 2021 Dec 21;11(6):2869–80. Available from: <URL>.

43. García R, Pizarro C, Lavín AG, Bueno JL. Biomass proximate analysis using thermogravimetry. Bioresour Technol [Internet]. 2013 Jul 1;139:1–4. Available from: <URL>.

44. Sluiter A, Hames B, Ruiz R, Scarlata C, Sluiter J, Templeton D, et al. Determination of Structural Carbohydrates and Lignin in Biomass Laboratory Analytical Procedure (LAP) Issue Date: 7/17/2005. 2008; Available from: <URL>.

45. Md Salim R, Asik J, Sarjadi MS. Chemical functional groups of extractives, cellulose and lignin extracted from native Leucaena leucocephala bark. Wood Sci Technol [Internet]. 2021 Mar 23;55(2):295–313. Available from: <URL>.

46. Güleç F, Riesco LMG, Williams O, Kostas ET, Samson A, Lester E. Hydrothermal conversion of different lignocellulosic biomass feedstocks – Effect of the process conditions on hydrochar structures. Fuel [Internet]. 2021 Oct 15;302:121166. Available from: <URL>.

47. Fan Y, Cai Y, Li X, Jiao L, Xia J, Deng X. Effects of the cellulose, xylan and lignin constituents on biomass pyrolysis characteristics and bio-oil composition using the Simplex Lattice Mixture Design method. Energy Convers Manag [Internet]. 2017 Apr 15;138:106–18. Available from: <URL>.

48. de Morais Teixeira E, Corrêa AC, Manzoli A, de Lima Leite F, de Oliveira CR, Mattoso LHC. Cellulose nanofibers from white and naturally colored cotton fibers. Cellulose [Internet]. 2010 Jun 12;17(3):595–606. Available from: <URL>.

49. Kim DY, Nishiyama Y, Wada M, Kuga S. High-yield carbonization of cellulose by sulfuric acid impregnation. Cellulose [Internet]. 2001;8(1):29–33. Available from: <URL>.

50. Guo F, He Y, Hassanpour A, Gardy J, Zhong Z. Thermogravimetric analysis on the co-combustion of biomass pellets with lignite and bituminous coal. Energy [Internet]. 2020 Apr 15;197:117147. Available from: <URL>.

51. Kwasi Opoku B, Isaac A, Akrofi Micheal A, Kwesi Bentum J, Paul Muyoma W. Characterization of Chemically Activated Carbons Produced from Coconut and Palm Kernel Shells Using SEM and FTIR Analyses. Am J Appl Chem [Internet]. 2021;9(3):90–6. Available from: <URL>.

52. Zhang Z, Xu L, Liu Y, Feng R, Zou T, Zhang Y, et al. Efficient removal of methylene blue using the mesoporous activated carbon obtained from mangosteen peel wastes: Kinetic, equilibrium, and thermodynamic studies. Microporous Mesoporous Mater [Internet]. 2021 Feb 1;315:110904. Available from: <URL>.

53. Abbasi S, Hekmat F, Shahrokhian S. Dual redox electrolytes for improving the performance of asymmetric supercapacitors constructed from heteroatom-doped green carbon spheres. J Alloys Compd [Internet]. 2023 Sep 25;957:170452. Available from: <URL>.

54. Zhou H, Fu H, Wu X, Wu B, Dai C. Discrimination of tea varieties based on FTIR spectroscopy and an adaptive improved possibilistic c-means clustering. J Food Process Preserv [Internet]. 2020 Oct 1;44(10):e14795. Available from: <URL>.

55. Yu S, Xie M, Li Q, Zhang Y, Zhou H. Evolution of kraft lignin during hydrothermal treatment under different reaction conditions. J Energy Inst [Internet]. 2022 Aug 1;103:147–53. Available from: <URL>.

56. Wan C, Jiao Y, Wei S, Li X, Tian W, Wu Y, et al. Scalable Top-to-Bottom Design on Low Tortuosity of Anisotropic Carbon Aerogels for Fast and Reusable Passive Capillary Absorption and Separation of Organic Leakages. ACS Appl Mater Interfaces [Internet]. 2019 Dec 26;11(51):47846–57. Available from: <URL>.

57. Ferrer A, Alciaturi C, Faneite A, Ríos J. Analyses of Biomass Fibers by XRD, FT-IR, and NIR. In: Analytical Techniques and Methods for Biomass [Internet]. Cham: Springer International Publishing; 2016. p. 45–83. Available from: <URL>.

58. Pezoti O, Cazetta AL, Bedin KC, Souza LS, Martins AC, Silva TL, et al. NaOH-activated carbon of high surface area produced from guava seeds as a high-efficiency adsorbent for amoxicillin removal: Kinetic, isotherm and thermodynamic studies. Chem Eng J [Internet]. 2016 Mar 15;288:778–88. Available from: <URL>.

59. Ali R, Aslam Z, Shawabkeh RA, Asghar A, Hussein IA. BET, FTIR, and RAMAN characterizations of activated carbon from wasteoil fly ash. TURKISH J Chem [Internet]. 2020 Apr 1;44(2):279–95. Available from: <URL>.

60. Haghbin MR, Niknam Shahrak M. Process conditions optimization for the fabrication of highly porous activated carbon from date palm bark wastes for

removing pollutants from water. Powder Technol [Internet]. 2021 Jan 2;377:890–9. Available from: <URL>.

61. Njoku VO, Islam MA, Asif M, Hameed BH. Adsorption of 2,4-dichlorophenoxyacetic acid by mesoporous activated carbon prepared from H_3PO_4-activated langsat empty fruit bunch. J Environ Manage [Internet]. 2015 May 1;154:138–44. Available from: <URL>.

62. Islam MS, Ang BC, Gharehkhani S, Afifi ABM. Adsorption capability of activated carbon synthesized from coconut shell. Carbon Lett [Internet]. 2016 Oct 31;20:1–9. Available from: <URL>.

63. Zhang J, Yu L, Wang Z, Tian Y, Qu Y, Wang Y, et al. Spherical microporous/mesoporous activated carbon from pulping black liquor. J Chem Technol Biotechnol [Internet]. 2011 Sep 1;86(9):1177–83. Available from: <URL>.

64. Li J, Li K, Zhang T, Wang S, Jiang Y, Bao Y, et al. Development of Activated carbon from Windmill palm sheath fiber by KOH activation. Fibers Polym [Internet]. 2016 Jun 6;17(6):880–7. Available from: <URL>.

65. Chakraborty I, Rongpipi S, Govindaraju I, B R, Mal SS, Gomez EW, et al. An insight into microscopy and analytical techniques for morphological, structural, chemical, and thermal characterization of cellulose. Microsc Res Tech [Internet]. 2022 May 18;85(5):1990–2015. Available from: <URL>.

66. Barbash VA, Yaschenko O V., Shniruk OM. Preparation and Properties of Nanocellulose from Organosolv Straw Pulp. Nanoscale Res Lett [Internet]. 2017 Dec 31;12(1):241. Available from: <URL>.

67. Buendia-Kandia F, Brosse N, Petitjean D, Mauviel G, Rondags E, Guedon E, et al. Hydrothermal conversion of wood, organosolv, and chlorite pulps. Biomass Convers Biorefinery [Internet]. 2020 Mar 7;10(1):1–13. Available from: <URL>.

68. Tang S, Liu R, Sun FF, Dong C, Wang R, Gao Z, et al. Bioprocessing of tea oil fruit hull with acetic acid organosolv pretreatment in combination with alkaline H2O2. Biotechnol Biofuels [Internet]. 2017 Dec 8;10(1):86. Available from: <URL>.

69. Song X, Jiang Y, Rong X, Wei W, Wang S, Nie S. Surface characterization and chemical analysis of bamboo substrates pretreated by alkali hydrogen peroxide. Bioresour Technol [Internet]. 2016 Sep 1;216:1098–101. Available from: <URL>.

70. Zhang J, Wang Y, Zhang L, Zhang R, Liu G, Cheng G. Understanding changes in cellulose crystalline structure of lignocellulosic biomass during ionic liquid pretreatment by XRD. Bioresour Technol [Internet]. 2014 Jan 1;151:402–5. Available from: <URL>.

71. Fan J, Li F, Fang D, Chen Q, Chen Q, Wang H, et al. Effects of hydrophobic coating on properties of hydrochar produced at different temperatures: Specific surface area and oxygen-containing functional groups. Bioresour Technol [Internet]. 2022 Nov 1;363:127971. Available from: <URL>.

72. Sun FF, Wang L, Hong J, Ren J, Du F, Hu J, et al. The impact of glycerol organosolv pretreatment on the chemistry and enzymatic hydrolyzability of wheat straw. Bioresour Technol [Internet]. 2015 Jul 1;187:354–61. Available from: <URL>.

73. Dong H, Zhang L, Shao L, Wu Z, Zhan P, Zhou X, et al. Versatile Strategy for the Preparation of Woody Biochar with Oxygen-Rich Groups and Enhanced Porosity for Highly Efficient Cr(VI) Removal. ACS Omega [Internet]. 2022 Jan 11;7(1):863–74. Available from: <URL>.

74. Szewczyk I, Kosydar R, Natkański P, Duraczyńska D, Gurgul J, Kuśtrowski P, et al. Effect of the type of siliceous template and carbon precursor on physicochemical and catalytic properties of mesoporous nanostructured carbon-palladium systems. J Porous Mater [Internet]. 2020 Oct 24;27(5):1287–308. Available from: <URL>.

75. Cheng C, He Q, Ismail TM, Mosqueda A, Ding L, Yu J, et al. Hydrothermal carbonization of rape straw: Effect of reaction parameters on hydrochar and migration of AAEMs. Chemosphere [Internet]. 2022 Mar 1;291:132785. Available from: <URL>.

76. Wang S, Zhao S, Cheng X, Qian L, Barati B, Gong X, et al. Study on two-step hydrothermal liquefaction of macroalgae for improving bio-oil. Bioresour Technol [Internet]. 2021 Jan 1;319:124176. Available from: <URL>.

77. Chatterjee S, Saito T. Lignin-Derived Advanced Carbon Materials. ChemSusChem [Internet]. 2015 Dec 16;8(23):3941–58. Available from: <URL>.

78. Thommes M, Kaneko K, Neimark A V., Olivier JP, Rodriguez-Reinoso F, Rouquerol J, et al. Physisorption of gases, with special reference to the evaluation of surface area and pore size distribution (IUPAC Technical Report). Pure Appl Chem [Internet]. 2015 Oct 1;87(9–10):1051–69. Available from: <URL>.

79. Zheng K, Xiao L. Iron and nitrogen co-doped porous carbon derived from natural cellulose of wood activating peroxymonosulfate for degradation of tetracycline: Role of delignification and mechanisms. Int J Biol Macromol [Internet]. 2022 Dec 1;222:2041–53. Available from: <URL>.

80. Mistar EM, Alfatah T, Supardan MD. Synthesis and characterization of activated carbon from Bambusa vulgaris striata using two-step KOH activation. J Mater Res Technol [Internet]. 2020 May 1;9(3):6278–86. Available from: <URL>.

81. Guo Y, Wang Q. Fabrication and Characterization of Activated Carbon from Phyllostachys edulis Using Single-Step KOH Activation with Different Temperatures. Processes [Internet]. 2022 Aug 28;10(9):1712. Available from: <URL>.

82. Zhang H, Xing L, Liang H, Ren J, Ding W, Wang Q, et al. Efficient removal of Remazol Brilliant Blue R from water by a cellulose-based activated carbon. Int J Biol Macromol [Internet]. 2022 May 15;207:254–62. Available from: <URL>.

83. Thongpat W, Taweekun J, Maliwan K. Synthesis and characterization of microporous activated carbon from rubberwood by chemical activation with KOH. Carbon Lett [Internet]. 2021 Oct 22;31(5):1079–88. Available from: <URL>.

84. Abuelnoor N, AlHajaj A, Khaleel M, Vega LF, Abu-Zahra MRM. Activated carbons from biomass-based sources for CO2 capture applications. Chemosphere [Internet]. 2021 Nov 1;282:131111. Available from: <URL>.

85. Wang X, Cheng H, Ye G, Fan J, Yao F, Wang Y, et al. Key factors and primary modification methods of activated carbon and their application in adsorption of carbon-based gases: A review. Chemosphere [Internet]. 2022 Jan 1;287:131995. Available from: <URL>.

86. Blanco AAG, de Oliveira JCA, López R, Moreno-Piraján JC, Giraldo L, Zgrablich G, et al. A study of the pore size distribution for activated carbon monoliths and their relationship with the storage of methane and hydrogen. Colloids Surfaces A Physicochem Eng Asp [Internet]. 2010 Mar 20;357(1–3):74–83. Available from: <URL>.

87. Wang Q, Yu Y, Li Y, Min X, Zhang J, Sun T. Methane separation and capture from nitrogen rich gases by selective adsorption in microporous Materials: A review. Sep Purif Technol [Internet]. 2022 Jan 15;283:120206. Available from: <URL>.

88. Lillo-Ródenas MA, Cazorla-Amorós D, Linares-Solano A. Behaviour of activated carbons with different pore size distributions and surface oxygen groups for benzene and toluene adsorption at low concentrations. Carbon N Y [Internet]. 2005 Jul 1;43(8):1758–67. Available from: <URL>.

89. Zhu R, Yu Q, Li M, Zhao H, Jin S, Huang Y, et al. Analysis of factors influencing pore structure development of agricultural and forestry waste-derived activated carbon for adsorption application in gas and liquid phases: A review. J Environ Chem Eng [Internet]. 2021 Oct 1;9(5):105905. Available from: <URL>.

90. Liu C, Dang Y, Zhou Y, Liu J, Sun Y, Su W, et al. Effect of carbon pore structure on the CH4/N2 separation. Adsorption [Internet]. 2012 Nov 5;18(3–4):321–5. Available from: <URL>.

91. Djeridi W, Ouederni A, Wiersum AD, Llewellyn PL, El Mir L. High pressure methane adsorption on microporous carbon monoliths prepared by olives stones. Mater Lett [Internet]. 2013 May 15;99:184–7. Available from: <URL>.

92. Tang Z, Gao J, Zhang Y, Du Q, Feng D, Dong H, et al. Ultra-microporous biochar-based carbon adsorbents by a facile chemical activation strategy for high-performance CO_2 adsorption. Fuel Process Technol [Internet]. 2023 Mar 1;241:107613. Available from: <URL>.

93. Serafin J, Dziejarski B, Cruz Junior OF, Sreńscek-Nazzal J. Design of highly microporous activated carbons based on walnut shell biomass for H_2 and CO2 storage. Carbon N Y [Internet]. 2023 Jan 5;201:633–47. Available from: <URL>.

94. Kamran U, Rhee KY, Lee S-Y, Park S-J. Solvent-free conversion of cucumber peels to N-doped microporous carbons for efficient CO_2 capture performance. J Clean Prod [Internet]. 2022 Oct 1;369:133367. Available from: <URL>.

95. Sevilla M, Fuertes AB. Sustainable porous carbons with a superior performance for CO_2 capture. Energy Environ Sci [Internet]. 2011 Apr 28;4(5):1765–71. Available from: <URL>.

96. González B, Manyà JJ. Activated olive mill waste-based hydrochars as selective adsorbents for CO_2 capture under postcombustion conditions. Chem Eng Process - Process Intensif [Internet]. 2020 Mar 1;149:107830. Available from: <URL>.

97. Xu J, Shi J, Cui H, Yan N, Liu Y. Preparation of nitrogen doped carbon from tree leaves as efficient CO2 adsorbent. Chem Phys Lett [Internet]. 2018 Nov 1;711:107–12. Available from: <URL>.

98. Hong S-M, Jang E, Dysart AD, Pol VG, Lee KB. CO_2 Capture in the Sustainable Wheat-Derived Activated Microporous Carbon Compartments. Sci Rep [Internet]. 2016 Oct 4;6(1):34590. Available from: <URL>.

99. Deng S, Hu B, Chen T, Wang B, Huang J, Wang Y, et al. Activated carbons prepared from peanut shell and sunflower seed shell for high CO2 adsorption. Adsorption [Internet]. 2015 Feb 23;21(1–2):125–33. Available from: <URL>.

100. Deng S, Wei H, Chen T, Wang B, Huang J, Yu G. Superior CO_2 adsorption on pine nut shell-derived activated carbons and the effective micropores at different temperatures. Chem Eng J [Internet]. 2014 Oct 1;253:46–54. Available from: <URL>.

101. Zhu X-L, Wang P-Y, Peng C, Yang J, Yan X-B. Activated carbon produced from paulownia sawdust for high-performance CO_2 sorbents. Chinese Chem Lett [Internet]. 2014 Jun 1;25(6):929–32. Available from: <URL>.

102. Plaza MG, González AS, Pevida C, Pis JJ, Rubiera F. Valorisation of spent coffee grounds as CO_2 adsorbents for postcombustion capture applications. Appl Energy [Internet]. 2012 Nov 1;99:272–9. Available from: <URL>.

103. Delgado LF, Charles P, Glucina K, Morlay C. The removal of endocrine disrupting compounds, pharmaceutically activated compounds and cyanobacterial toxins during drinking water preparation using activated carbon—A review. Sci Total Environ [Internet]. 2012 Oct 1;435–436:509–25. Available from: <URL>.

104. Libbrecht W, Verberckmoes A, Thybaut JW, Van Der Voort P, De Clercq J. Soft templated mesoporous carbons: Tuning the porosity for the adsorption of large organic pollutants. Carbon N Y [Internet]. 2017 May 1;116:528–46. Available from: <URL>.

105. Danish M, Ahmad T. A review on utilization of wood biomass as a sustainable precursor for activated carbon production and application. Renew Sustain Energy Rev [Internet]. 2018 May 1;87:1–21. Available from: <URL>.

106. Jawad AH, Saud Abdulhameed A, Wilson LD, Syed-Hassan SSA, ALOthman ZA, Rizwan Khan M. High surface area and mesoporous activated carbon from KOH-activated dragon fruit peels for methylene blue dye adsorption: Optimization and mechanism study. Chinese J Chem Eng [Internet]. 2021 Apr 1;32:281–90. Available from: <URL>.

107. Brito MJP, Veloso CM, Santos LS, Bonomo RCF, Fontan R da CI. Adsorption of the textile dye Dianix® royal blue CC onto carbons obtained from yellow mombin fruit stones and activated with KOH and H3PO4: kinetics, adsorption equilibrium and thermodynamic studies. Powder Technol [Internet]. 2018 Nov 1;339:334–43. Available from: <URL>.

108. Sangon S, Hunt AJ, Attard TM, Mengchang P, Ngernyen Y, Supanchaiyamat N. Valorisation of waste rice straw for the production of highly effective carbon based adsorbents for dyes removal. J Clean Prod [Internet]. 2018 Jan 20;172:1128–39. Available from: <URL>.

109. El-Bery HM, Saleh M, El-Gendy RA, Saleh MR, Thabet SM. High adsorption capacity of phenol and methylene blue using activated carbon derived from lignocellulosic agriculture wastes. Sci Rep [Internet]. 2022 Mar 31;12(1):5499. Available from: <URL>.

110. Abbaci F, Nait-Merzoug A, Guellati O, Harat A, El Haskouri J, Delhalle J, et al. Bio/KOH ratio effect on activated biochar and their dye based wastewater depollution. J Anal Appl Pyrolysis [Internet]. 2022 Mar 1;162:105452. Available from: <URL>.

111. Sun J, Ji L, Han X, Wu Z, Cai L, Guo J, et al. Mesoporous Activated Biochar from Crab Shell with Enhanced Adsorption Performance for Tetracycline. Foods [Internet]. 2023 Mar 1;12(5):1042. Available from: <URL>.

112. Balathanigaimani MS, Shim W-G, Lee M-J, Kim C, Lee J-W, Moon H. Highly porous electrodes from novel corn grains-based activated carbons for electrical double layer capacitors. Electrochem commun [Internet]. 2008 Jun 1;10(6):868–71. Available from: <URL>.

113. Wu Y, Cao J-P, Zhuang Q-Q, Zhao X-Y, Zhou Z, Wei Y-L, et al. Biomass-derived three-dimensional hierarchical porous carbon network for symmetric supercapacitors with ultra-high energy density in ionic liquid electrolyte. Electrochim Acta [Internet]. 2021 Mar 1;371:137825. Available from: <URL>.

114. Karnan M, Subramani K, Srividhya PK, Sathish M. Electrochemical Studies on Corncob Derived Activated Porous Carbon for Supercapacitors Application in Aqueous and Non-aqueous Electrolytes. Electrochim Acta [Internet]. 2017 Feb 20;228:586–96. Available from: <URL>.

115. Ponce MF, Mamani A, Jerez F, Castilla J, Ramos PB, Acosta GG, et al. Activated carbon from olive tree pruning residue for symmetric solid-state supercapacitor. Energy [Internet]. 2022 Dec 1;260:125092. Available from: <URL>.

116. Enock TK, King'ondu CK, Pogrebnoi A, Jande YAC. Biogas-slurry derived mesoporous carbon for supercapacitor applications. Mater Today Energy [Internet]. 2017 Sep 1;5:126–37. Available from: <URL>.

117. Zou Z, Luo X, Wang L, Zhang Y, Xu Z, Jiang C. Highly mesoporous carbons derived from corn silks as high performance electrode materials of supercapacitors and zinc ion capacitors. J Energy Storage [Internet]. 2021 Dec 1;44:103385. Available from: <URL>.

Adsorptive Removal of Volatile Organic Compounds from Industrial Effluent Using Synthesized ZnO-CA Composite Base Adsorbent

Bamigboye Mercy Oluwaseyi [1]*, **Ayinla Ibrahim Kuranga** [1], **Orimolade Benjamin** [1], **Mustapha Ayuba Olanrewaju** [1], **Ojo Olayinka Abosede** [2], **Jamiu Wasiu** [1], **Abdulganiy Aishat A.** [1], **Oba Hameeda Sinmiloluwa** [1]

[1]Department of Industrial Chemistry, Faculty of Physical Sciences, University of Ilorin, Ilorin, Kwara state, Nigeria.
[2]Department of Animal Production, Fisheries and Aquaculture, Kwara State University, Malete, Kwara State, Nigeria.

Abstract: In this study, a composite adsorbent consisting of ZnO nanoparticles and cellulose acetate nanoparticles was prepared. The composite was extensively characterized through Scanning electron microscopy (SEM), Transmission Electron Microscopy (TEM), Energy Dispersive X-ray Spectroscopy (EDX), and Brunnaeur Emmet Teller analysis (BET). Batch adsorption experiments were carried out to study the effects of concentration of adsorbate (10- 80 mL), dose of adsorbent (0.1 – 1 g), pH(3-13), contact or exposure time (30-180 minutes) and temperature(30 - 70℃) on the removal of benzene and toluene using the synthesized adsorbent. The pseudo-second-order model well described the kinetics of adsorption studied, and Langmuir's isotherm best described the isotherm modeling of the adsorption data. Thermodynamic studies revealed that all the adsorption processes are feasible, endothermic, and spontaneous. The prepared adsorbent is suitable for removing benzene and toluene from wastewater.

Cite this: Oluwaseyi BM et al. Adsorptive Removal of Volatile Organic Compounds from Industrial Effluent Using Synthesized ZnO-CA Composite Base Adsorbent. JOTCSA. 2024; 11(1): 189-204.

1. INTRODUCTION

Nanoparticles exhibit considerably apparent physical, chemical, and biological characteristics when compared with their bulk counterparts. Nanoparticles have become a great subject of interest due to their diverse range and recent applications in numerous fields, including wastewater treatment (1). Several treatment methods have been demonstrated to effectively sequester volatile organic compounds from water. However, an effective and low-cost method based on nanotechnology can be used to decontaminate municipal and domestic wastewater effectively (1). Nano-sized particles have gained much more interest in recent years due to their desirable

properties and applications in different areas, such as catalysts (2), sensors (3, 4), photoelectron devices (5), and highly functional and effective devices (1). These nanomaterials have novel electronic, structural, and thermal properties of high scientific interest in basic and applied fields. One of the unique properties of some nanoparticles is the adsorption of pollutants. Several nanomaterials have adsorbent properties, which depend on the nanomaterial's size. Chemically modified nanomaterials, especially nanoporous materials, have also attracted much attention due to their large surface area (6).

Toluene and benzene are frequently used in industries as organic chemical solvents, for cleaning

machinery, and in other downstream processes. They can seep into groundwater through leakages in pipes and storage tanks and from improper disposal. The US Environmental Protection Agency (EPA) has recognized these substances as primary pollutants with deleterious effects on human health (6). They are also acknowledged as possessing evident carcinogenic characteristics (3). Therefore, removing these hazardous chemical substances from the ecosystem is important for the safety of humans, animals, and aquatic life.

Nanoparticles have become even more crucial as Metal Oxide materials have spread widely throughout human civilization. Due to their intriguing features and wide range of applications, ZnO nanoparticles stand out among them. ZnO nanoparticle production inspired by biological processes has been accomplished utilizing approved ecologically acceptable methods. Numerous studies have examined using natural resources to synthesize ZnO-CA nanoparticles (7), including DNA, silk, albumen, orange juice, pea starch, peptide architectures, and others (4).

Nanoscale metal oxides can increase the effectiveness of technologies and reduce the cost of water treatment due to their small size and high absorption efficiency (3). Therefore, in this study, the adsorption studies of toluene and benzene (8, 9, 10), two prominent volatile organic compounds, were performed using a composite of zinc oxide and cellulose acetate nanocomposites (11). The nanocomposites were fully characterized to ascertain their structural and morphological properties. Additionally, the adsorption process was optimized by studying factors such as adsorbent dose, initial concentration, solution pH affecting adsorption processes, etc (8).

This study aimed to synthesize a composite material using zinc oxide and cellulose acetate derived from agricultural waste and evaluate its adsorption properties/efficiency for the effective removal of benzene and toluene from wastewater. Benzene and toluene, amongst others, are volatile organic compounds commonly found in petroleum-based products, fuels, solvents, and various industrial processes and are considered pollutants and can be harmful to human health and the environment, even at low concentrations (8, 9).

2. MATERIALS AND METHODS

Benzene (anhydrous, 99.8%) and toluene (ACS, 99.7%) were purchased from Sigma Aldrich. ACS (American Chemical Society standards) reagent hydrochloric acid and sodium hydroxide solutions were used for pH adjustment. Zinc Nitrate Hexahydrate salt, Glacial Acetic Acid, Sulfuric acid, and Acetic Anhydride were also acquired from Sigma Aldrich.

2.1. Synthesis of Zinc Oxide Nanoparticles
A method reported by Muneer *et al.* (12) was used with slight modification. Zinc Nitrate Hexahydrate salt (29.785 g) was added to 100 mL 0.1% starch solution to obtain 1 M of zinc nitrate solution. NaOH solution(50 mL, 2M) was added drop-wise along the vessel's walls to the 1 M zinc nitrate solution in a 500 mL beaker while continuously stirring with a magnetic stirrer. The mixture was stirred for 2 hours and filtered through a 0.45 millipore filter paper using vacuum filtration. The paste of zinc hydroxide obtained was washed thrice with distilled water, dried in the oven at 80°C for 5 h, and later calcined in the muffle furnace at 500 °C for 2 h.

2.2. Synthesis of Cellulose Acetate
By procedures described by Okoli *et al. (13), about 25 g of synthesized cellulose* was dispersed in 100 mL of glacial acetic acid. The solution was kept in a water bath at 55 °C for 1 h with frequent stirring. An acetylation mixture of 0.8 mL of concentrated H_2SO_4 and 50 mL of acetic anhydride prepared in a round bottom flask was gradually added to the glacial acetic acid mixture. The resulting solution was kept in a water bath and heated for 2 h with occasional stirring at 55 °C. A clear colloidal solution was obtained, transferred into 1 L of distilled water, and filtered. The residue obtained was oven-dried at 60 °C. The product obtained was characterized using spectroscopic techniques.

2.3. Synthesis of ZnO-CA composites
The composite of ZnO-CA was prepared according to the method prescribed by Patnukao *et al.* (14). This was done at a ratio of 1:1, in which the mixture of each nanomaterial was dispersed in 0.5 M HCl to form a colloidal solution. The solution was stirred and evaporated to dryness in an oven. The composite formed was washed with deionized water, filtered, and further dried in an oven at 100 °C for 12 h and stored in a container.

2.4. Batch Adsorption Experiments
The amount of adsorption (equilibrium concentration) of the adsorbed benzene and toluene, Q_e, was calculated based on the difference between the initial (C_i mg/L) and final concentration (C_e mg/L) of the Benzene and Toluene in solution in every flask after a specified period of shaking, as follows:

$$Q_e = \frac{V(C_1 - C_e)}{M} \qquad \text{(Eq. 1)}$$

Where Qe = the amount of solute adsorbed out from the solution.
V = Adsorbate Volume,
C_1 = the concentration before adsorption,
C_e = the concentration after adsorption, and M = the weight in grams of the adsorbent (15).

2.4.1. Effect of Concentration of Adsorbate
Benzene and Toluene solutions (25 mL) with concentrations ranging from 10 — 80 mg/L were added to different conical flasks. Each adsorbent (0.1 g) was in contact with the solution. Other parameters were kept constant. Then, the mixtures were auto-shook in a flask-shaker at 150 rpm and 25 °C. After that, the flasks were withdrawn, the mixtures filtered, and the absorbance of the solutions measured (16).

2.4.2. Effect of Adsorbent Dose
Different adsorbent doses (0.1, 0.2, 0.3, 0.4, 0.5, and 1 g) were added to each flask, keeping other parameters constant. All the solution flasks were put inside the shaker at 1000 rpm and 25°C for 120 minutes. After 120 minutes, the flasks were retrieved from the shaker, and the benzene and toluene solutions were filtered from the adsorbents using millipore filter paper. The absorbance of each solution was then assessed (17).

2.4.3. Effect of pH
The working solutions (25 mL) were measured into different conical flasks. Using a pH meter, the pH of each of the solutions was adjusted to fall between the range 3 to 13 with 0.1 M HCl/0.1 M NaOH solution. The optimum dose of the adsorbent obtained from the study "EFFECT OF ADSORBENT DOSE" was contacted with each solution in the flask. Then, the flasks were placed inside the shaker for 120 minutes at 1000 rpm and 25°C. The mixtures were filtered, and the absorbance of the filtrate was assessed (18).

2.4.4. Effect of Adsorbent Contact Time
The equilibrium concentration of the benzene and toluene solutions, 25 mL each, was measured in conical flasks. The optimum pH and dose of adsorbent obtained above were set in this experiment. The flasks containing the solutions were loaded into the shaker at 1000 rpm and 25°C, lasting between 30 and 180 minutes, with the flasks removed at 30-minute intervals and other experiment parameters kept constant. Then, the solutions were filtered, and the absorbance of the solutions was measured. (12).

2.4.5. Effect of Temperature
Several conical flasks were filled with the benzene and toluene solutions at their equilibrium concentration (25 mL each). The optimal adsorbent dosages, contact times, and pH obtained were employed. The temperature ranged from 30 to 70 ^{0}C, and the resulting solutions were filtered and subjected to UV spectrophotometric analysis. (18).

3. RESULTS AND DISCUSSION

3.1. Characterisation of Adsorbent
3.1.1. SEM, Scanning Electron Microscopy Analysis
The synthesized cellulose acetate, zinc oxide, and their composites were analyzed by SEM (*ThermoFisher Scientific with model number Verios 5 XHR*), and the corresponding micrographs obtained at 20,000 and 5,000 magnifications are shown in Figure 1 below. The zinc oxide and cellulose acetate images show that the particles are in aggregated form and also developed many pores, which may have resulted from the absorbent's large surface area. In Figure 1 (e,f), the zinc oxide particles are encircled by cellulose acetate in the composite materials' SEM scans, showing that the cellulose acetate is firmly embedded with the zinc nanoparticles. The surface of the composite material appeared to be rough and coarse with many pores, which indicates the good performance of good adsorbents. This kind of morphology was also observed in the work reported by Imran *et al.* (20) in removing BTEX (Benzene, Toluene, Ethylbenzene, Xylene) using mango seed.
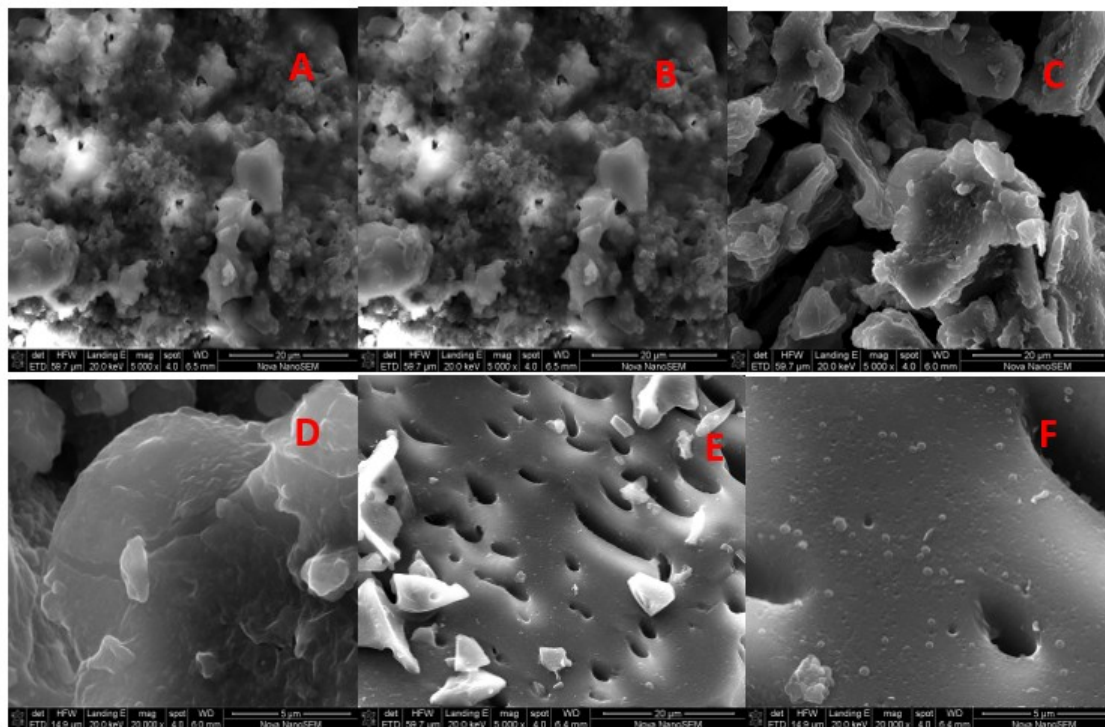
Figure 1: SEM micrograph of (a) ZnO at 20kx (b) ZnO at 5kx. (c) CA at 20kx   (d) CA at 5kx. (e) ZnO-CA at 20kx   (f) ZnO-CA at 5kx.

3.1.2. Transmission Electron Microscopy Result
The ZnO-CA composite's surface morphology was examined using a transmission electron microscope, Tecnai-12, FEI (Netherlands). As shown in Figure 2, the TEM imaging revealed that the adsorbent material is spherical clusters, which is the characteristic feature of well-defined adsorbents and has been reported to enhance the increase in adsorption properties. The surface covered with micropores showed that the adsorbents developed an elementary pore network, increasing the adsorbents' adsorption properties. In comparing the adsorbents, it can be revealed that the porosity of the surface of the composites observed indicated good adsorption characteristics. By employing CNT and nano iron as adsorbents for removing BTEX from aqueous solutions, Sud *et al*. (21) also noted this trend.

3.1.3. *Energy Dispersive X-ray Spectroscopy*
Energy Dispersive X-ray Spectroscopy (*Shimadzu with Model number: EDX-7200*) can be seen from the spectrum Figure 3 (a) that Zn and O show the highest peak, which is predominant, while Si and N are found to be minor elements present. The synthesized ZnO was shown by the spectrum's predominance of Zn and O. From Figure 3 (b), the

presence of Al, C S, N, and O as predominant elements indicates the presence of agricultural organic raw material used to synthesize cellulose acetate. The presence of Zn, O, and Si in the Figure 3 (c) spectrum shows that the ZnO is well embedded with cellulose acetate. It has been reported that the accuracy of the EDX spectrum can be affected by various factors, which might affect the nature or chemical composition of the adsorbent, and many elements may have overlapping peaks, which would also affect the nature of the sample (22).

3.1.4. Brunauer Emmett Teller (BET)
In this study, the BET of ZnO-CA was measured with a Quantachrome Nova 4200e instrument using the adsorption of N_2 at the liquid nitrogen temperature. The nanocomposite material was determined with a low-temperature adsorption/desorption method based on BET theory multilayer adsorption. The result showed the surface area to be 463.217 m^2/g, the micropore area to be 414.926 m2/, and the pore volume to be 0.310 cm^2/g. The BET surface of the material showed that the composite materials possess a high surface area, which is an important requirement for a good adsorbent.
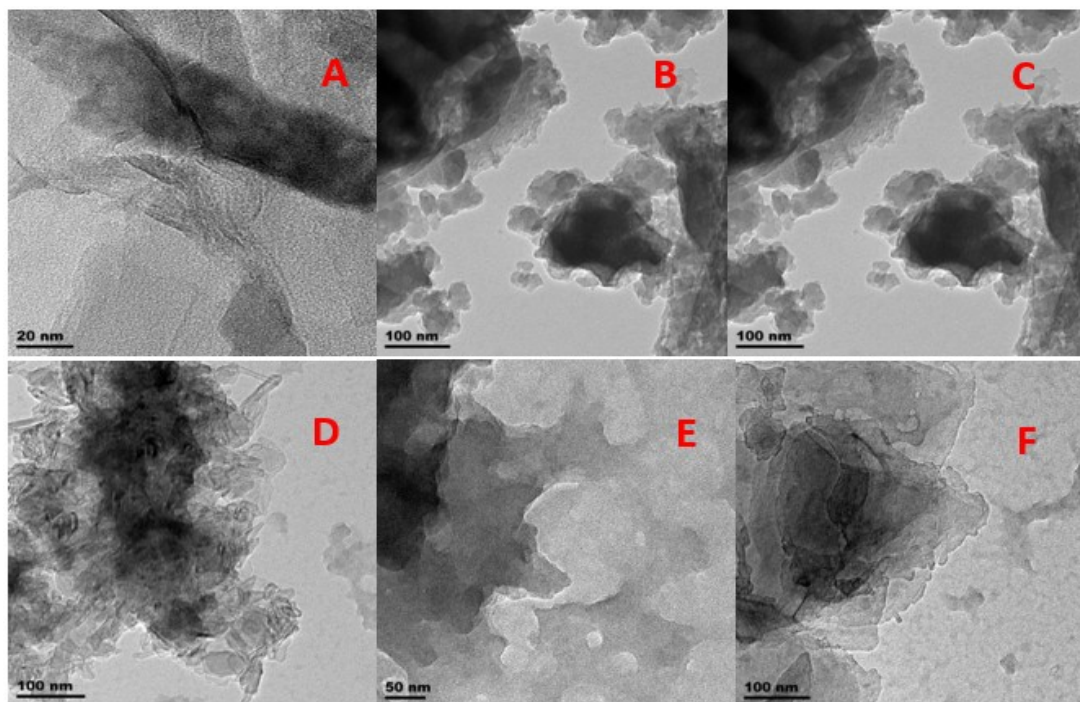
**Figure 2:** TEM micrographs of (a,b) ZnO nanoparticle (c,d) CA (e,f) ZnO-CA composite.
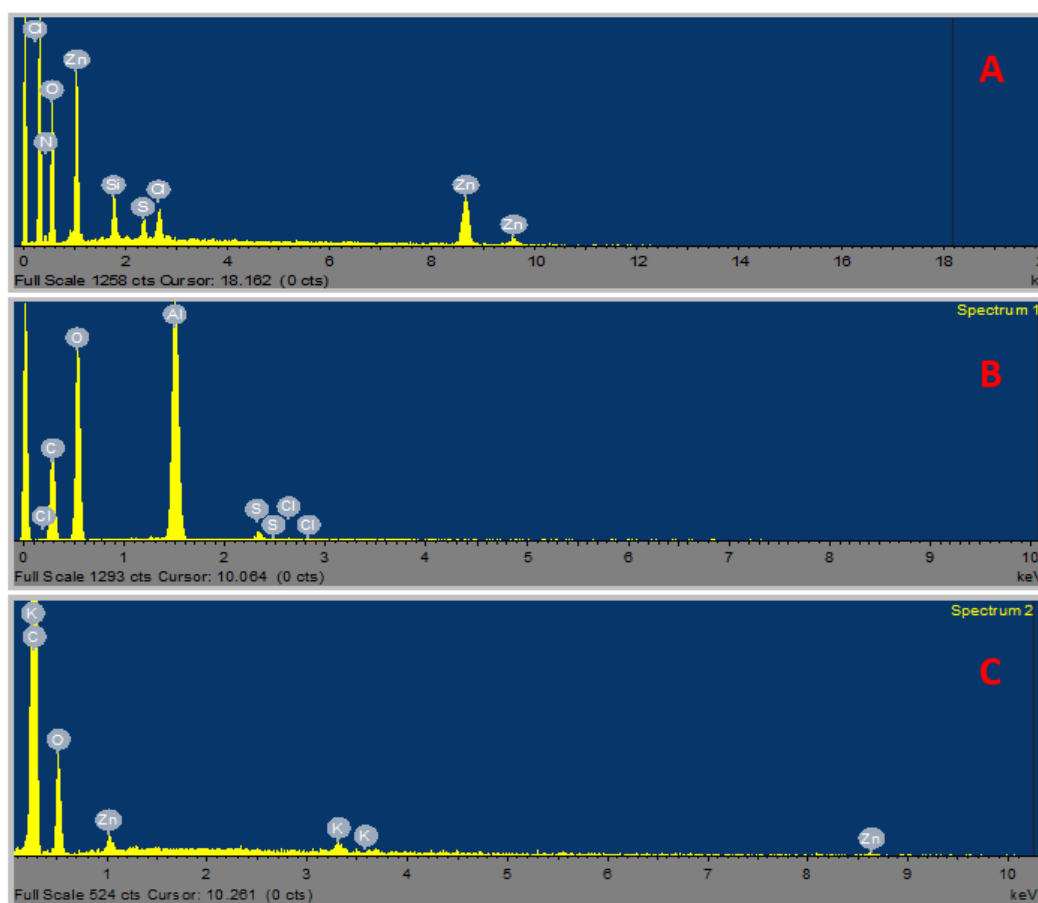
Figure 3: EDX spectra of (a) Zinc Oxide nanoparticle (b) CA (c) ZnO-CA nanocomposites.

193

3.2 Adsorption Studies Results

By serial dilution of the necessary amounts of the stock, standard working concentrations ranging from 10 to 60 mg/L of benzene and toluene were made from a 1000 mg/L stock solution. A Beckmann Coulter UV-visible spectrophotometer (Searchtech Spectrophotometer with *Model number:752N)* was used to scan the stock solution to determine the maximum wavelength at peak absorbance (λmax = 254 nm for benzene and 263 nm for toluene). Each dilution of the benzene and toluene was then measured at this maximum wavelength. The absorbances were read and plotted against concentrations to generate the calibration curve. Using extrapolation through the linearity range, the calibration curve was developed from the experimentation and produced the graph equations y=0.0031x for benzene and y=0.0404x for toluene.

3.2.1 Effect of initial concentrations of benzene and toluene

The inceptive concentration provides a noteworthy impetus to overcome all resistances of mass transfer of solutes between the solid and aqueous phases. In this investigation, initial concentrations of 10-80 mg/L were used to examine the effect of initial concentration on the adsorption of benzene and toluene by ZnO-CA composites, while other parameters like adsorbent dosage, pH, contact time, and temperature were held constant. The result of this effect is displayed below, where the adsorption capacity is plotted against the concentration. In general, this conclusion can be explained by the fact that the ratio of surface active sites to organic molecules is excessively high at low concentrations of benzene and toluene solutions. The species could, therefore, interact with the sorbent to sufficiently occupy the active sites on the adsorbent surface and can be eliminated from the solution (23).
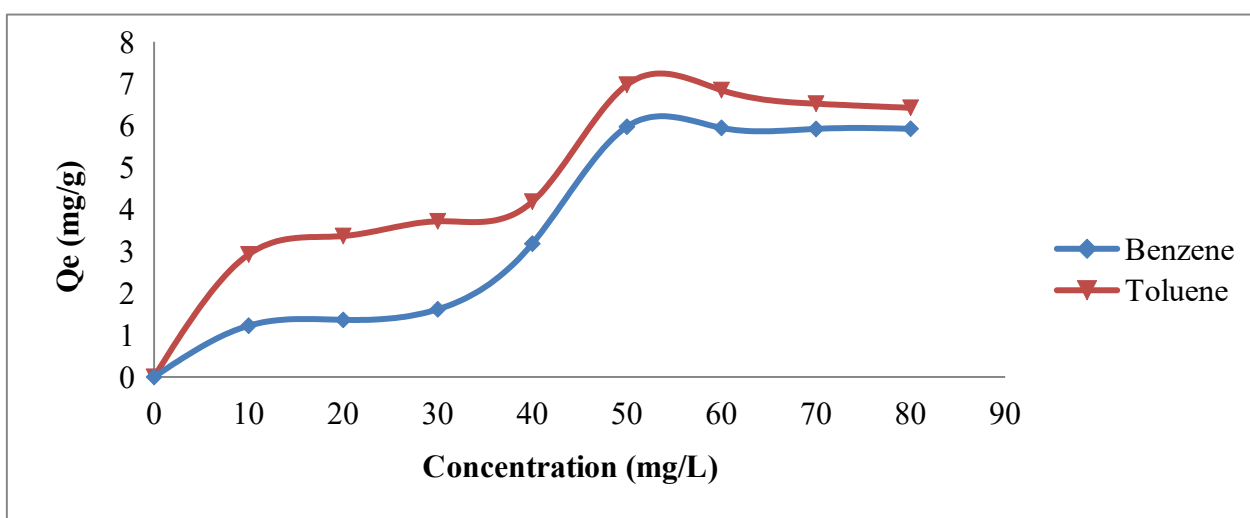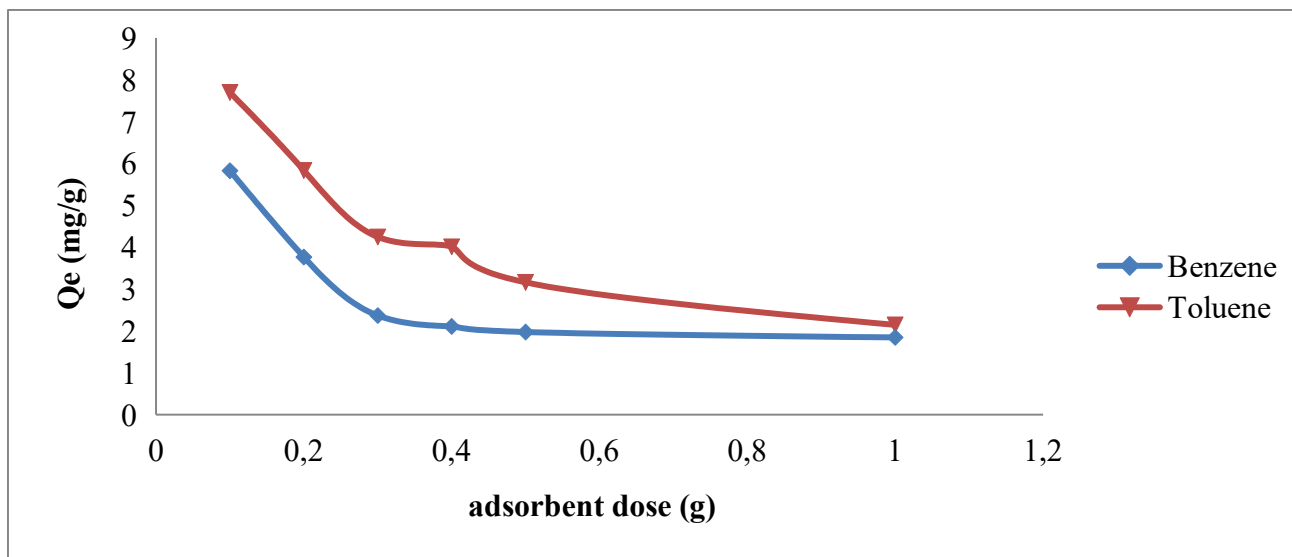

Figure 4: Conc. profile diagram for benzene and toluene adsorption onto ZnO-CA composite (Time: 180 mins, weight of adsorbent: 0.1 g, Temp: 303K, and Volume of adsorbates: 25 mL)

3.2.2. Effect of Adsorbent Dosage

Figure 5 depicts the plot showing the influence of adsorbent dose on the several adsorption systems under investigation. The dosages of the adsorbent ranged from 0.1 g to 1 g. The finding makes it abundantly evident that there was a drop in adsorption equilibrium capacity with an increase in adsorbent dose. This could have arisen from forming aggregates of the adsorbent, thereby limiting the number of sorption sites even after increasing the sorbent dose. A plausibility to this occurrence is that as the mass of the sorbent increases, more sorption sites are added, but the amount of adsorbate remains constant. This phenomenon is also expressed in equation (1), where the sorption amount is inversely proportional to the absorbent dose. The observed variation can be explored with pH fluctuations, structural packing (monolayer, cluster, multilayer), etc. In all adsorption systems, the highest adsorption capacity was recorded at 0.1 g, and the corresponding quantities adsorbed for benzene and toluene were 5.826 mg/g and 7.697 mg/g, respectively.
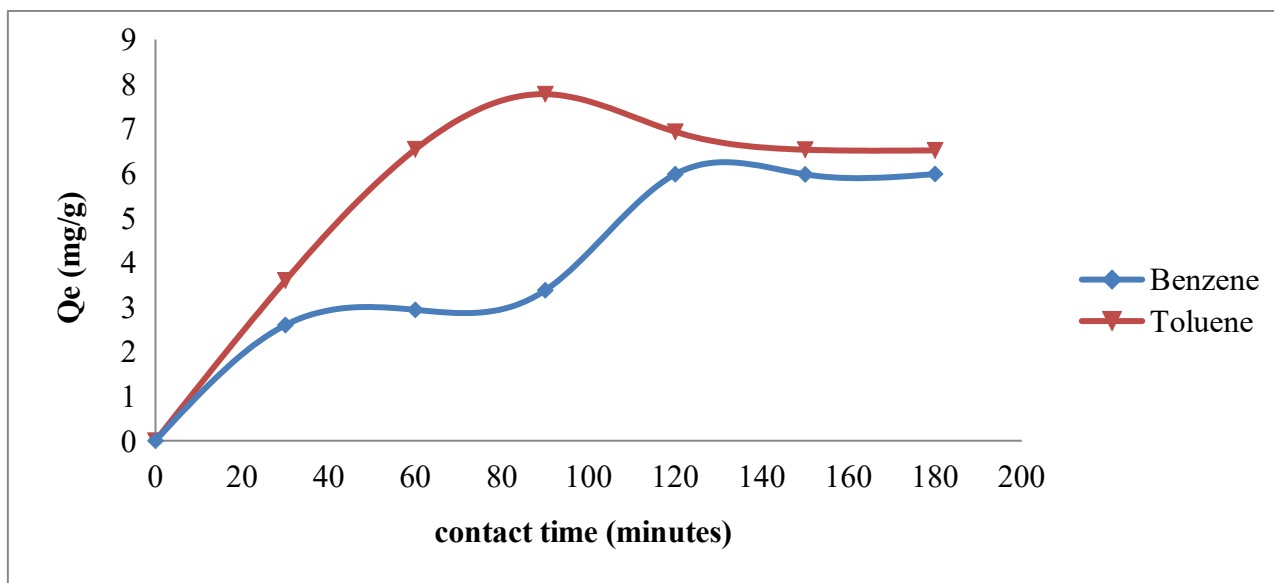
Figure 5: Conc. profile diagram for benzene and toluene adsorption onto ZnO-CA composite (Time: 180 mins, Conc: 50 mg/L, Temp: 303K, and Volume of adsorbates: 25 mL).

3.2.3. Effect of contact/exposure time

Regardless of the other experimental parameters impacting the adsorption kinetics, contact time is crucial in the adsorption system (23). Figure 6 below shows a time profile plot of the adsorption of Benzene and Toluene onto the ZnO-CA composite. The figures show that the amount adsorbed rises with increasing contact time, reaching equilibrium at 120 minutes for benzene and 90 minutes for toluene, respectively. The maximum amount adsorbed was found for Toluene and Benzene adsorption on the adsorbent, which was 7.773 mg/g and 5.978 mg/g, respectively. The order of adsorption capacity was toluene>benzene.
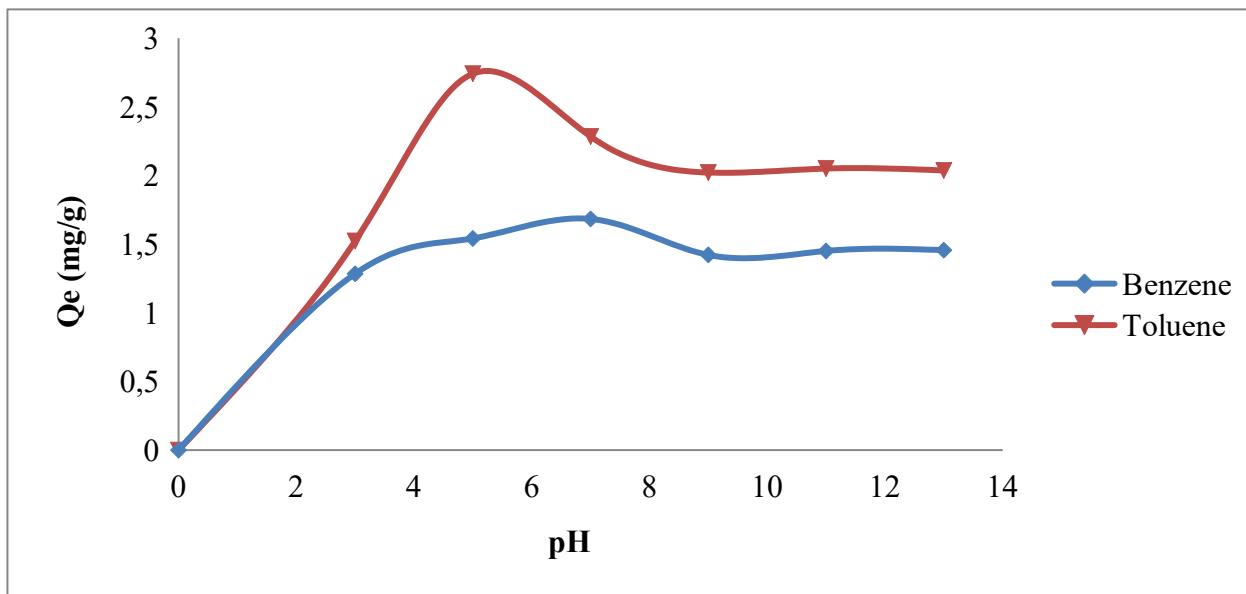

Figure 6: Time profile diagram for benzene and toluene adsorption onto ZnO-CA composite at (Time: 180 mins, Dose: 0.1 g, Conc: 50 mg/L, Temp: 303 K and Volume of adsorbate: 25 mL)

3.2.4. Effect of medium pH

As it affects the solubility of the organic compounds, the concentration of the counter ions on the functional groups of the adsorbent, and the degree of ionization, the initial pH of a solution(Hanna Instruments with Model number: HI2209 pH meter) is a highly significant factor to take into account in adsorption investigations. The plot of this study's experiment showing the influence of pH on the benzene and toluene adsorption capabilities onto ZnO-CA is presented in Fig. 7. The role of H$^+$ concentration was examined from ZnO-CA adsorbent at different pH. The result demonstrates that for both adsorbates, the highest adsorption was noted between pH 5 and 9, with the amount adsorbed increasing as pH increases. Similar

patterns have been documented in other literature (24).

Figure 7: pH profile diagram for benzene and toluene adsorption onto ZnO-CA adsorbent at (Time: 90 & 120 mins, Conc: 50 mg/L, Temp: 303K and Volume of adsorbate: 25 ml).

3.2.5 Effect of Temperature
The temperature is another crucial factor to consider during the adsorption process. The adsorption equilibrium constant and adsorbate solubility are both influenced by temperature (*Japson Thermometer with Model number JD14694*). Five different temperatures (30, 40, 50, 60, and 70 °C) were studied at derived optimized conditions. The adsorption efficiency for benzene and toluene diminishes as the temperature rises, as observed from the plot of benzene and toluene. This is because higher temperatures cause desorption, which is caused by the loss of volatile molecules and active sites for adsorption (25). The adsorption capacity typically decreases with temperature; the energy content and saturated vapor pressure can explain this behavior. The energy content increases with temperature; therefore, the adsorbent requires more energy to maintain a liquid form, which immediately impacts the adsorption balance.
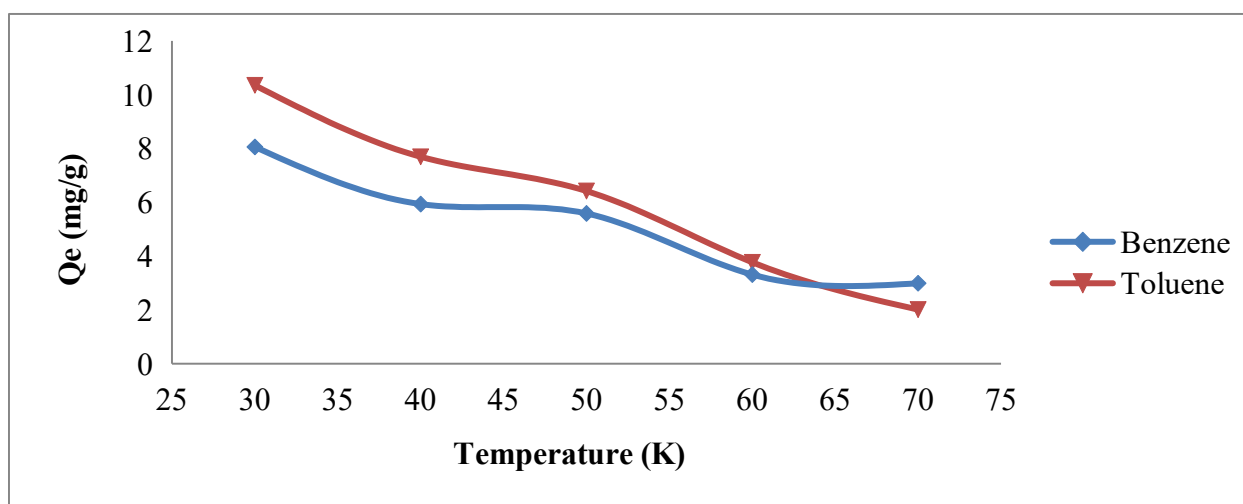
Figure 8: Temperature profile diagram for benzene and toluene adsorption onto ZnO-CA at (Time: 90 & 120 mins, Conc: 50 mg/L, pH: 5, 7 & 9 and Volume of adsorbates: 25 mL).

3.3. Adsorption Isotherm
An adsorption isotherm depicts the relationship between the quantity that has been adsorbed and the amount still in the solution at a certain temperature and equilibrium. As the adsorption process achieves an equilibrium condition, it describes how the distribution of the liquid phase onto the solid phase occurs (26). The equilibrium

sorption isotherm can be used to determine the adsorbents' performance and adsorption capacity (1). The current study examined the system's adsorption capacity using the Langmuir, Freundlich, and Temkin isotherms model, and plots were displayed.

3.3.1. Langmuir Adsorption Isotherm
For this model, the linearized form of Ce/qe vs Ce was plotted in Fig. 10, and Table 1 shows the

corresponding constant parameters. The value of R_L specifies whether the adsorption is irreversible if $R_L=0$, unfavorable if $R_L>1$, linear if $R_L=1$, and favorable if $0<R_L<1$. From the information gathered from the plot (Table 1), all of the systems' RL values are greater than 0 but less than 1, implying that the Langmuir isotherm is favorable for the three systems.
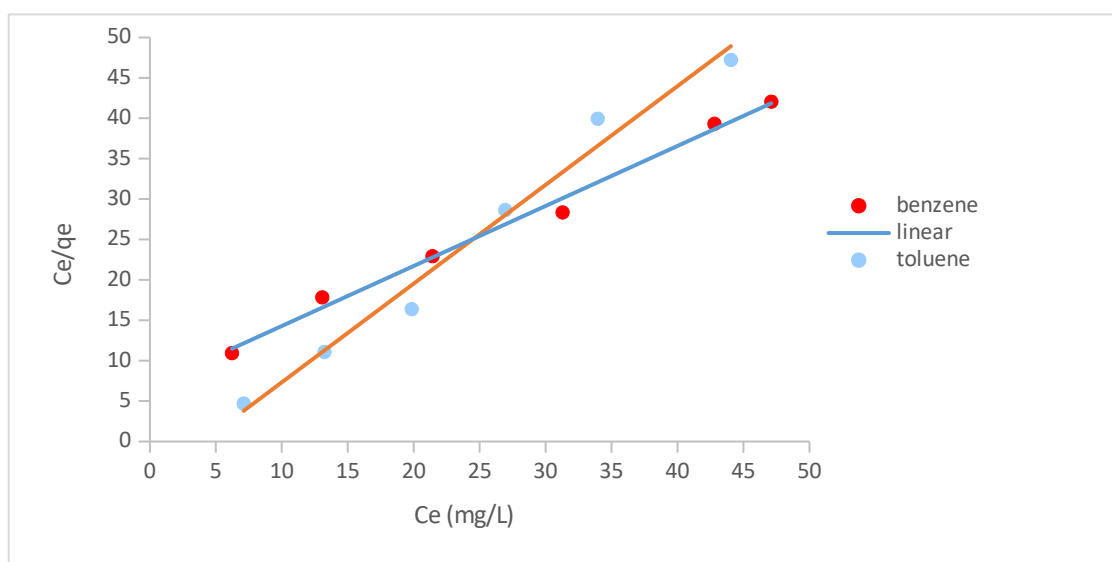
**Figure 9:** Langmuir isotherm plot of benzene and toluene on ZnO-CA composite.

3.3.2. Freundlich Adsorption Isotherm
For the sorption of benzene and toluene onto ZnO-CA composite, the model's plot of log Qe against log Ce demonstrated linearity, as shown in Fig. 10. From the plot, the regression coefficients and the Freundlich constants n and K_f were deduced. The n values for benzene and toluene are 3.245 and 6.989, respectively, and the regression coefficients R2 for benzene and toluene onto ZnO-CA composite were 0.932 and 0.401, respectively. These values fall between $1<n<10$, indicating that benzene and toluene adsorption onto the ZnO-CA composite is favorable. The values of K_f were calculated to be 0.303 and 0.105. Generally, it can be deduced that the adsorption of Benzene and Toluene was also well fitted to Freundlich adsorption isotherm due to the n value less than 10, except toluene adsorption on to adsorbent, which has a low R^2 value but the adsorption system still favorable.
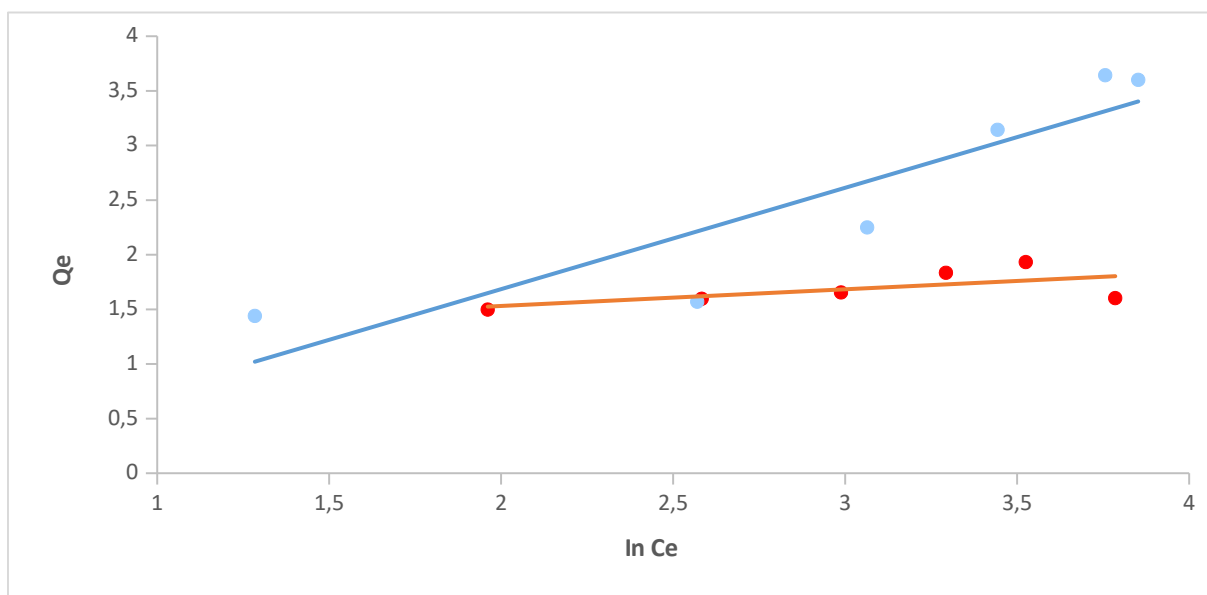
3.3.3. Temkin Adsorption Isotherm
The model's plot of Qe against ln Ce proved linear for the sorption of benzene and toluene onto ZnO-CA, as shown in Fig. 11. From the plot, the K_T, B, and the regression coefficient R^2 were deduced. The calculated K_T values are 2.364 and 2.109, while B values are 0.927 and 0.153; the regression coefficients (R^2) are 0.810 and 0.388 for benzene and toluene, respectively. The higher value of K_T and B indicates a high heat of adsorption and lower binding energy. These low values of binding energies and heat of adsorptions of the adsorption systems indicate physical adsorption (27).

From the isotherm plots and constant parameters, it can be deduced that the data were best fitted into the Langmuir isotherm, and the fitness order is Langmuir>Temkin>Freundlich.
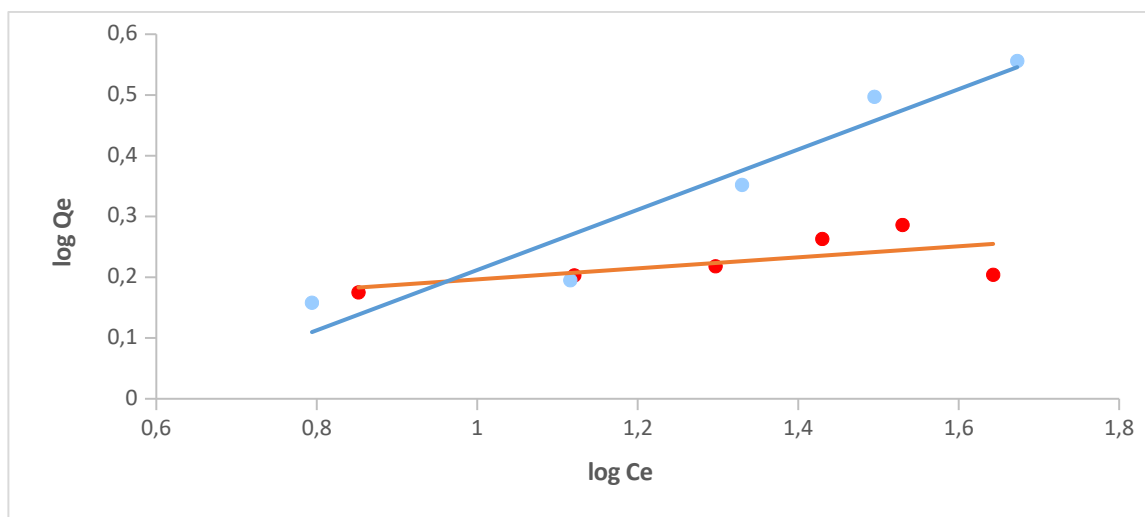
Figure 10: Freundlich isotherm plot for benzene (blue dots) and toluene (red dots) on ZnO-CA composite.

Figure 11: Temkin isotherm plot for benzene (blue dots) and toluene (red dots) on ZnO-CA composite.

Table 1: Isotherm Parameters for Benzene and Toluene Adsorption Systems.

Adsorption Models	Isotherm Parameters	Benzene	Toluene
Langmuir	q_m (mg/g)	5.731	5.358
	K_L (L/mg)	0.063	0.066
	R_L	0.051	0.066
	R^2	0.9926	0.9828
Freundlich	K_f	0.303	0.105
	n	3.245	6.989
	R^2	0.9320	0.4015
Temkin	K_T	2.164	2.219
	B	0.705	0.392
	R^2	0.8107	0.3882

### 3.4. Adsorption Kinetics

The adsorption rate uptake is very important when designing the adsorption system. The performance of a given adsorbent is of utmost importance to indicate the solute uptake rate. Chemical kinetics covers the factors impacting reaction rate as well as how rapidly chemical reactions happen. It has been noted that system variables, including concentration and temperature, as well as the adsorbent's physicochemical properties, determine the nature of the adsorption process (28).

3.4.1. Pseudo First Order Kinetic Model
The linearized plot of log (qe-qt) as a function of t was applied to understand the benzene and toluene uptake rate onto ZnO-CA adsorbent. The regression coefficients for the benzene and toluene onto the adsorbent were 0.882 and 0.848, respectively.
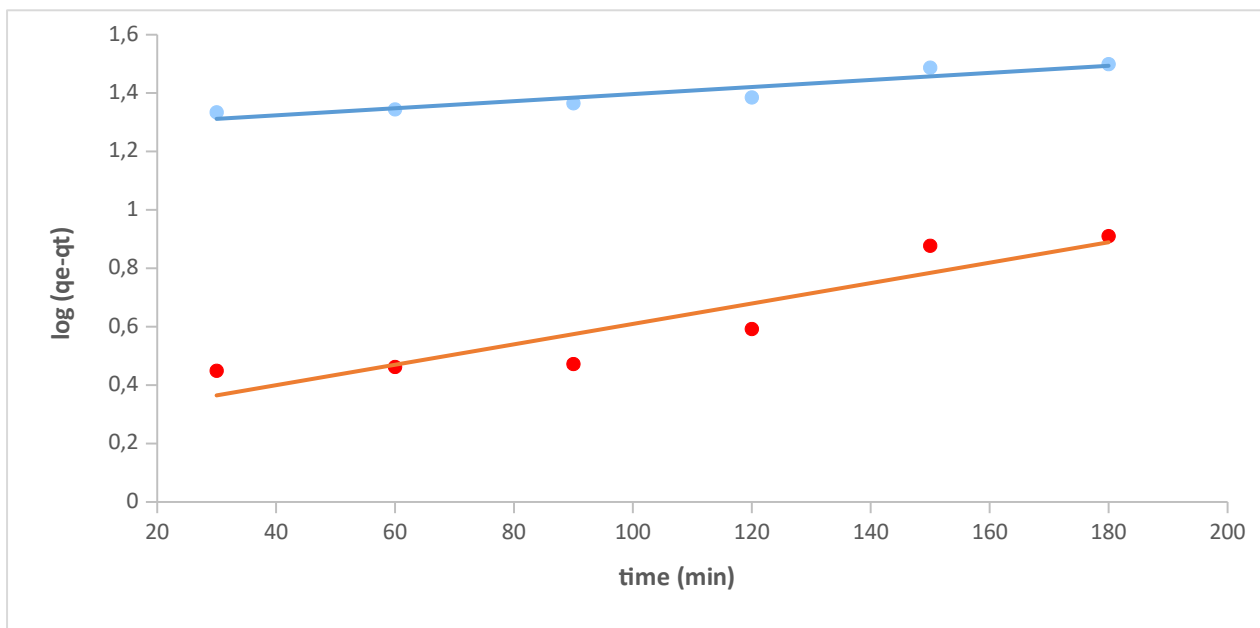
Figure 12: The linear plot of the Pseudo-first order model for benzene (blue dots) and toluene (red dots) onto Zn-CA

3.4.2. Pseudo Second order Kinetic model
Compared to the pseudo-first-order kinetic model, the charts generated for the pseudo-second-order model were more accurate. The pseudo-second-order kinetic plots, Fig. 13, exhibit superior linearity, with correlation coefficients for benzene and toluene, respectively, of 0.9978 and 0.9888.
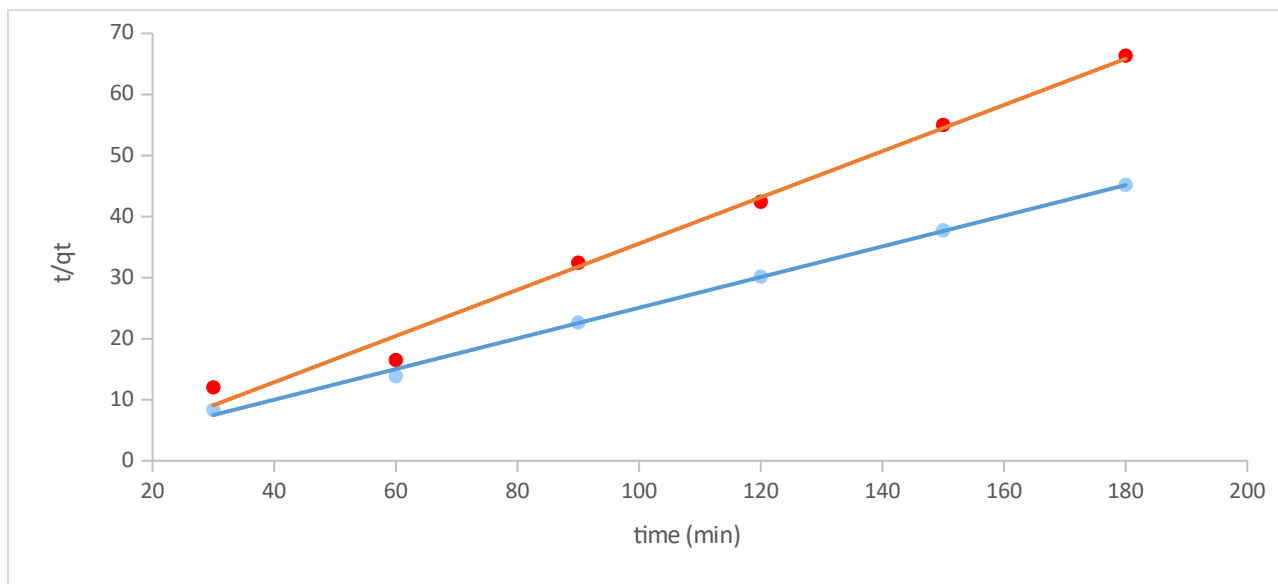
Figure 13: The linear plot of the Pseudo-second order model for benzene (blue dots) and toluene (red dots) onto ZnO-CA.
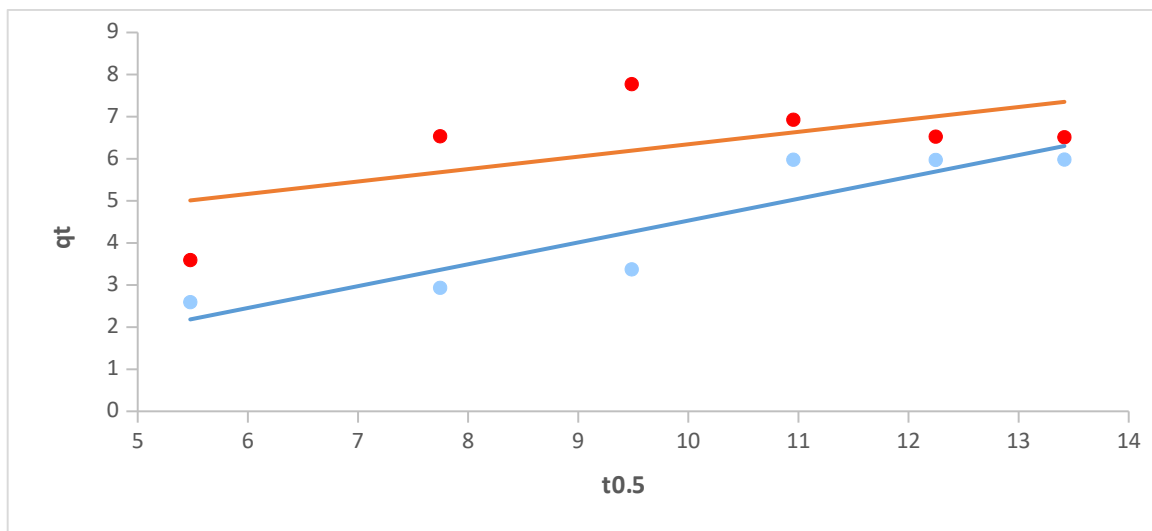
Table 2: Kinetics Parameters for Benzene and Toluene Adsorption Systems.

Kinetics models	Parameters	Benzene	Toluene
Pseudo-first order	q_e (mg/g)	8.793	1.819
	K_1 (min^{-1})	0.0023	0.0069
	R^2	0.8823	0.8486
Pseudo-second order	q_e (mg/g)	4.684	3.641
	K_2 (min^{-1})	2.423	0.063
	R^2	0.9978	0.9888

3.5. Adsorption Mechanism

The intraparticle diffusion model was used to identify the rate-controlling phases that make up the adsorption mechanism. The diffusion mechanism was depicted using the intraparticle diffusion model. It is widely accepted that the rate is constrained by mass transfer across the boundary layer, and the removal mechanism is difficult if the straight lines from the plots do not travel through the origin (29). At the rate-determining step, the value of constant C provides information about the thickness of the surface adsorption. According to certain reports, the more the pore contributes to adsorption, the larger the intercept (27). However, the fact that the line in the current investigation did not go through the origin showed that pore diffusion could not be the only process that controls how quickly benzene and toluene are removed, particularly in the early adsorption phases. Due to the great availability of adsorbing sites on the external surface, which becomes the main influence, the surface-adsorbate interaction is thought to control the step rate. The graph of q_t vs $t^{0.5}$ was plotted (Fig. 15), and the intraparticle diffusion constant k_{id} was evaluated from the slope, and the constant C was obtained from the intercept.

Figure 14: Intraparticle diffusion plot for benzene (blue dots) and toluene (red dots) adsorption on ZnO-CA.

Table 3: Intraparticle diffusion constant parameters for benzene and toluene adsorption.

Adsorbates	k_{id}(mg/g/min$^{0.5}$)	C	R^2
Benzene	0.518	0.657	0.839
Toluene	0.295	3.394	0.375
Xylene	1.010	2.855	0.836

3.6. Thermodynamic Studies

The orientation of the physicochemical adsorption reaction, the reaction's viability, and the adsorbed phase's stability can all be evaluated using thermodynamic parameters. The effects of the data from the temperature study were utilized to determine whether the benzene and toluene adsorption process on the ZnO-CA composite was feasible. Using the relevant equations, the thermodynamic characteristics of the adsorption process, such as the change in enthalpy (ΔH), entropy change (ΔS), and change in Gibbs free energy (ΔH), were calculated for the various systems.
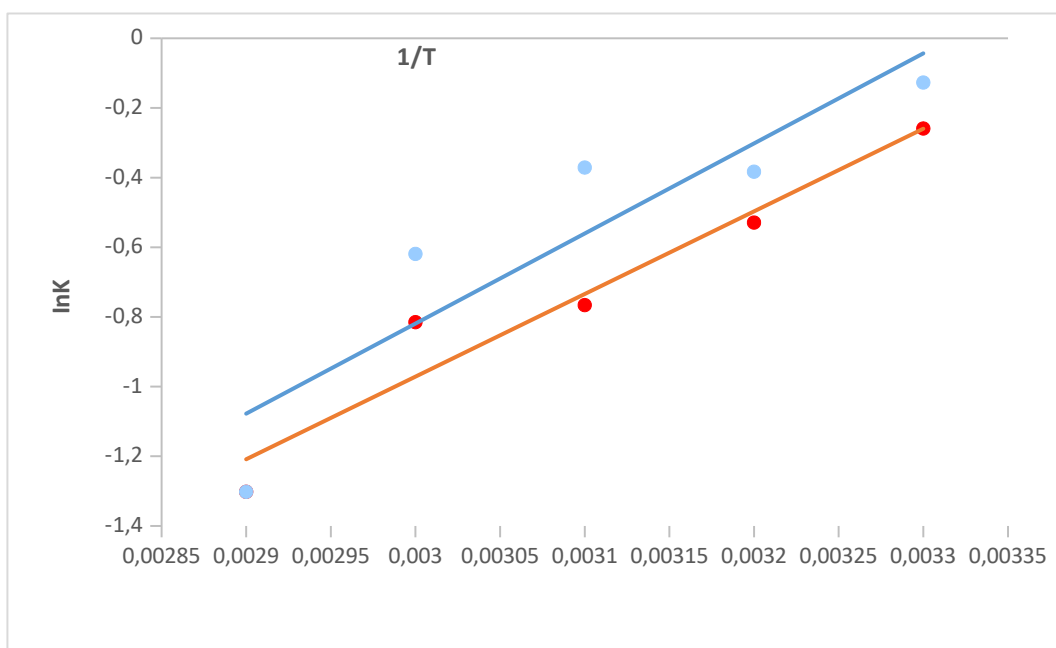
Figure 15: Thermodynamic plot for benzene (blue dots) and toluene (red dots) adsorption on ZnO-CA composite.

Oluwaseyi BM et al. JOTCSA. 2024; 11(1): 189-204.

RESEARCH ARTICLE

Table 4: Thermodynamic parameters for benzene and toluene onto the adsorbent.

Adsorbents	Temperature (K)	ΔG (KJ/mol)	ΔH (KJ/mol)	ΔS (J/mol/K)
BENZENE	303	-31.93		
	313	-99.67		
	323	-99.29	+4951.50	+164.225
	333	-171.73		
	343	-371.91		
TOLUENE	303	-65.45		
	313	-137.60		
	323	-205.03	+4541.02	+154.842
	333	-225.37		
	343	-371.91		

4. CONCLUSION

The synthesis of zinc oxide and cellulose acetate from agricultural waste through the precipitation route was successfully carried out. The composite was formed, and its components were successfully incorporated into each other, as seen in the SEM and TEM images, and were successfully incorporated into each other. The BET surface area, which was evaluated as 463.217 m^2/g, demonstrated the adsorbent has good adsorption properties. The batch adsorption experiment result shows that the quantity of benzene and toluene adsorbed depended on the amount of adsorbent dose, initial concentrations of the adsorbate, pH, contact time, and temperature. The Langmuir isotherm best reflected the adsorption data's isotherm modeling of the adsorption kinetics, which the pseudo-second-order model captured well. The value of n obtained from Freundlich adsorption parameters indicated favorable adsorption processes. The negative value of Gibb's free energy (ΔG) and positive values of entropy (ΔS) and enthalpy (ΔH) obtained from the thermodynamic studies revealed that all the adsorption processes are feasible, endothermic, and spontaneous. The outcome demonstrated that the adsorbent developed in this study could effectively remove benzene and toluene from wastewater.

The study demonstrates the feasibility and reproducibility of the synthetic process, composite formation, adsorption efficiency, and performance in the sequestration of benzene and toluene from wastewater.

5. CONFLICT OF INTEREST

The authors declare no conflict of interest.

6. ACKNOWLEDGMENTS

7. REFERENCES

1. Badmus MAO, Audu TOK, Anyata BU. Removal of Lead ion from Industrial Waste waters by Activated carbon from Periwinkle shells. Turkish J Env Sci. 2007; 31: 251-63.

2. Astruc D. Introduction: Nanoparticles in Catalysis. Chemical Reviews. 2020; 120. 461-463. Available from: <URL>.

3. Willner MR, Vikesland PJ. Nanomaterial enabled sensors for environmental contaminants. J Nanobiotechnol. 2018; 16: 95. Available from: <URL>.

4. Bueno CC, Garcia PS, Steffens C, Deda DK, de Lima Leite F. Nanosensors in Micro and Nano Technologies, Nanoscience and its Applications. 2017; 5:121-153, Available from: ISBN 9780323497800, <URL>.

5. . Wang B, Zhu X, Li S, Chen M, Liu N, Yang H, Ran M, Lu H, Yang Y. Enhancing the Photovoltaic Performance of Perovskite Solar Cells Using Plasmonic Au@Pt@Au Core-Shell Nanoparticles. Nanomaterials (Basel). 2019 ; 9(9):1263. Available from: <URL>. PMID: 31491914; PMCID: PMC6781053.

6. Jodeh S. The study of kinetics and thermodynamics of selected pharmaceuticals and personal care products on agriculture soil. Eur J Chemistry. 2012; 3: 468-74. Available from: <URL>.

7. Chaurasia V, Chand N, Bajpai SK. Water Sorption Properties and Antimicrobial Action of Zinc Oxide Nanoparticles-Loaded Cellulose Acetate Films. Journal of Macromolecular Science, Part A. 2010; 47(4): 309–317. <URL>.

8. Alshahrani F, Tawabini B, Saleh T. Removal of benzene, MTBE and toluene from contaminated waters using biochar-based liquid activated carbon. Sci Rep. 2022; 12: 19651. Available from: <URL>.

9. George Z K, Gordon M, Tariq J A, Sabereh S, Davoud B. Removal of Benzene and Toluene from Synthetic Wastewater by Adsorption onto Magnetic Zeolitic Imidazole Framework Nanocomposites. Nanomaterials 2022; 12(17): 3049. Available from: <URL>.

10. Hirra A, Khairiraihanna J, Nirmala G, Arunagiri A, Murugesan T. Investigation of green functionalization of multiwall carbon nanotubes and its application in adsorption of benzene, toluene & p-xylene from aqueous

solution. Journal of Cleaner Production. 2019. 221: 323-338. Available from: <URL>.

11. Potla D, Rajulapati S.B., Palliparambi A.A. Studies on removal of arsenic using cellulose acetate–zinc oxide nanoparticle mixed matrix membrane. Int Nano Lett. 2018; 8, 201–211. Available from: <URL>.

12. Muneer M, Bhatti IA, Adeel S. Removal of Zn, Pb and Cr in textile wastewater using rice husk as a biosorbent. Asian J Chem. 2010; 22: 7453 – 59.

13. Okoli J, Ezuma I. Adsorption Studies of Heavy Metals by Low-Cost Adsorbents management. J Appl Sci Environ Manage. 2014; 18(3): 443 - 48. Available from: <URL>.

14. Patnukao P, Kongsuwan A, Pavasant P. Batch studies of adsorption of copper and lead on activated carbon from Eucalyptus camaldulensisDehn. Bark J Environ Sci. 2008; 20: 1028 -34. Available from: <URL>.

15. Adegoke H, Adekola F. Removal of Phenol from Aqueous Solution by Activated Carbon Prepared from Some Agricultural Materials. Advances in Natural and Applied Sciences. 2010; 4(3): 293–98.

16. Radhika V, Subramanian S, Natarajan KA. Bioremediation of zinc using Desulfotom aculumnigrificans: Bioprecipitation and characterization studies. Water Res. 2006; 40(19): 3628 – 36. Available from: <URL>.

17. Ricordel S, Taha S, Ciss EI, Dorange G. Heavy metals removal by adsorption onto peanut husks carbon: Characterization, kinetic study and modeling Sep Purif. Technol. 2001; 24(3) : 389- 401. Available from: <URL>.

18. Sheng PX, Ting Y-P, Chen JP, Hong L. Sorption of lead, copper, cadmium, zinc and nickel by marine algal biomass: characterization of biosorptive capacity and investigation of mechanisms. J Colloid interface Sci. 2004; 275(1):131-41. Available from: <URL>.

19. Shukla A, Zhang YH, Dubey P, Shukla SS. The role of saw dust in the removal of unwanted materials from water. J Hazard material. 2002; 95(12): 137-52. Available from: <URL>.

20. Singh SR, Singh AP. Treatment of water containing chromium (vi) using Rice husk carbon as a new low cost adsorbent. Int J Environ Res. 2014; 6(4): 917-924. Available from: <URL>.

21. Sud D, Mahajan G, Kaur MP. Agricultural waste material as potential adsorbent for sequestering heavy metal ions from aqueous solutions- A review. Biores Techn. 2008; 99: 6017 – 6027. Available from: <URL>.

22. Joseph G. Scanning Electron Microscopy and X-ray microanalysis. 2003. ISBN 9780-306-47292-3. Retrieved 12 July, 2018

23. Walter GM, Hanna JA, Alen SJ. Treatment of Hazardous Shipyard Wastewater Using Dolomitic Adsorbent. Wat Res. 2005; 39(11): 2422 – 28. Available from: <URL>.

24. Wang SB, Boyjoo Y, Choueib A. Zeolitization of fly ash for sorption of dyes in aqueous solutions. Studies in surf Sci cataly. 2005; 158 : 161 – 168. Available from: <URL>.

25. Yun J, Choi D, Kim S. Equilibria and dynamics for mixed vapors of BTX in an activated carbon bed, *AIChE J.*, 1999; 45, 751- 60. Available from: <URL>.

26. Thomas JM, Thomas WJ. Introduction to the principles of heterogenous catalysis, 4th edition. Academy Press, New York. 1975; 33-49.

27. Dada AO, Inyibor AA, Oluyori AP. Comparative Adsorption of Dyes unto Activated Carbon Prepared From Maize Stems and Sugar Cane Stems. IOSR Journal of Applied Chemistry. 2012; 2(3): 38-43.

28. Adebayo G.B, Adegoke HI, Jamiu W, Balogun BB, Jimoh AA. Adsorption of Mn(II) and Co(II) ions from aqueous solution using Maize cob activated carbon: Kinetics and Thermodynamics Studies. J Appl Sci Environ Manage. 2015; 19(4): 737-48. Available from: <URL>.

29. Wiwid PP, Azlan K, Siti NMY, Che FI, Azmi M, Norhayati H, Illyas MI. Biosorption of Cu(II), Pb(II) and Zn(II) Ions from Aqueous Solutions Using Selected Waste Materials: Adsorption and Characterisation Studies. J Encap Adsor Sci. 2014; 4:25. Available from: <URL>.

Fe₃O₄@SA MNCs Synthesis, Characterization, and First-time Use in Hydrogen Production by NaBH₄ Hydrolysis

Adil Umaz[1]*

[1]Mardin Artuklu University, Department of Medical Laboratory, Mardin, 47100, Turkey

Abstract: Hydrogen is a clean energy carrier that will reduce dependence on fossil fuels and contribute to reducing the harmful effects on the environment resulting from using fossil fuels. Hydrogen is produced by the hydrolysis of sodium borohydride ($NaBH_4$), one of the chemical hydrides, using a catalyst. In this study, Fe_3O_4@Salicylic acid magnetic nano-catalyst (Fe_3O_4@SA MNCs) was synthesized using the co-precipitation technique. The structural, physical, and chemical properties of the produced Fe_3O_4@SA MNCs were characterized by FT-IR, XRD, VSM, SEM, and SEM-EDX methods. At room temperature, the effect on hydrogen production performance was examined in the amounts of Fe_3O_4@SA MNCs (10, 25, 50, 75, and 100 mg), NaOH (0, 10, 20, and 25 mg), and $NaBH_4$ (25, 50, 100, 150 and 200 mg). The highest hydrogen generation rates (HGR) were obtained using 10 mg Fe_3O_4@SA MNCs, 150 mg $NaBH_4$, and 0 mg NaOH at room temperature. The obtained HGR value was calculated as 400 mL g_{cat}^{-1}.min^{-1}. Fe_3O_4@SA MNCs were used for hydrogen production for the first time in this study. This study showed that Fe_3O_4@SA MNCs exhibit catalytic properties and are a promising, efficient catalyst in hydrogen production from $NaBH_4$.

***Corresponding author.** E-mail: adilumaz@gmail.com

1. INTRODUCTION

Population growth and rising living standards of individuals cause an increase in energy consumption. The decrease in fossil fuel reserves makes fossil fuel-based energy unsustainable. At the same time, due to fossil fuels, which are the dominant energy source, the world is facing serious climate change. Although fossil fuel-based energy meets a large part of the global energy demand, it has undesirable negative effects on humanity and the environment, such as greenhouse gas emissions, global warming, acid rain, and poor air quality. In order to prevent these vital negativities, researchers have started to focus on the search for innovative, carbon-free, sustainable alternative energy without environmental negative effects (1,2).

At this critical point, hydrogen energy is referred to as the best possible promising energy alternative that is environmentally friendly, renewable, and

sustainable. Considering the cost-effectiveness and reliability of hydrogen energy, it has the potential to solve many environmental problems. When hydrogen is used as a fuel, it is expressed as a zero pollution producer because it gives water as a by-product (no treatment required) along with its excellent efficiency in energy conversion. Hydrogen is the most common and most abundant element in the universe. Hydrogen is found in compounds with other elements, such as carbon and oxygen. With this, it is an excellent clean energy carrier after separation (3).

Hydrogen energy can be produced from a wide variety of primary energy sources using different substrates and technologies and then used as the main energy source. $NaBH_4$ is used in hydrogen production technologies for its advantages, such as non-flammability, stability, and non-toxicity. Also, the hydrolysis of $NaBH_4$ can be controlled by suitable catalysts. The hydrolysis of $NaBH_4$ is shown in Equation 1. The catalyst is used to

control the hydrolysis of NaBH4 and achieve higher reaction rates. The hydrolysis of $NaBH_4$ using inexpensive and environmentally friendly catalysts has recently received more attention (4,5).

$$NaBH_4 + 4H_2O \rightarrow NaBO_2 + 4H_2 \qquad (1)$$
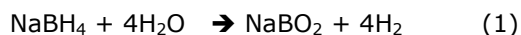
Nanotechnology offers effective materials with special structural design and a wide range of potential applications in environmental remediation solutions. The term "Nano" means a particle with at least one size less than 100 nm. Its nanoscale dimensions make its physical, optical, magnetic, chemical, mechanical, electrical, and magnetic properties significantly different from related materials. The application of nanomaterials in catalysis has attracted great interest. Nano-catalysts uniquely have selectivity, reactivity, enormous surface areas, and extended catalytic efficiencies. Homogeneous and heterogeneous catalysis applications are an evolving field. Excellent efficiency, highly selective, and fast catalytic systems are being developed through a green process. Research on environmentally friendly catalysis contributes to alleviating the pollution problem. Researchers continue to seek to obtain the ideal nano-catalyst with excellent stability, selectivity, and activity by green methods (6).

In nano-catalyst research, Fe_3O_4 with magnetic properties attracts great attention due to its attractive properties, such as low cost, easy preparation, easy modification, superparamagnetism, and non-toxicity (7). Fe_3O_4 consists of a magnetic core and has a good surface area/volume ratio. Fe_3O_4 has a high affinity, and a surfactant is often needed to both cause internal steric repulsion and modify its surface. Extensive studies have been carried out in various engineering applications with Fe_3O_4, whose surface is functionalized with appropriate functional groups (due to its optical, magnetic, electrical, catalytic, etc. properties) (8). Zero-valent metal nanoparticles supported on the bare surface of magnetite show reduced catalytic activity from incorporating iron into redox processes. Therefore, Fe_3O_4 needs to be coated with materials such as polymer, carbon, silica, etc. to support metal nanoparticles. Magnetically supported catalysts are considered promising materials with high activity and reusability due to their easy separation by an external magnetic field (9,10). Salicylic acid, which

has phenolic, benzoic, carboxylic, and hydroxyl characters as functional groups, adds a very high potential to catalytic activity due to its intramolecular H-H bond structures (11). Because salicylic acid is o-hydroxybenzoic acid, it has π electrons that belong to aromatic compounds and are produced by orbital overlap. Thus, salicylic acid is used in catalysis studies (12).

In this study, Fe_3O_4@SA MNCs were produced for hydrogen production from $NaBH_4$. Fe_3O_4@SA MNCs were used for hydrogen production for the first time in this study. The catalytic activity of the synthesized magnetic nano-catalyst regarding hydrogen production by NaBH4 hydrolysis was investigated. Hydrogen production from hydrolysis of $NaBH_4$ of Fe_3O_4@SA MNCs with different parameters in experimental sets was investigated. SEM-EDX, XRD, VSM, and FT-IR analyses were performed to determine the morphological and structural characterization of Fe_3O_4@SA MNCs.

2. EXPERIMENTAL

2.1. Chemicals and Solutions
All chemicals and solvents used in the reactions are of analytical purity. Iron (III) chloride hexahydrate ($FeCl_3.6H_2O$, 99.9%) and salicylic acid ($C_7H_6O_3$, 99%) were purchased from MERCK Chemical. Iron (II) chloride tetrahydrate ($FeCl_2$ $4H_2O$, 98%) was purchased from Alfa Aesar Chemical Company. In addition, Ammonia (NH_3, 28.0%) and ethanol (CH_3CH_2OH, 99.9%) were purchased from ISOLAB.

2.2. Fe_3O_4@SA MNCs Synthesis
$FeCl_3.6H_2O$ (12 mmol) and $FeCl_2.4H_2O$ (6 mmol) were mixed in 200 mL of pure water in a two-neck flask at room temperature for 30 minutes. The temperature of the system was increased to 70 °C. For co-precipitation, 50 mL of 8 M NH_3 was added to the solution (The solution was orange at first but turned black with the addition of NH_3). The resulting black magnetite (Fe_3O_4) nanoparticles were stirred for another 30 minutes. Salicylic acid (0.6 mmol) was then added to the reaction system, and the reaction was continued for 30 minutes at system temperature. After the mixture in the balloon was cooled, Fe_3O_4@SA MNCs were isolated from the environment with the help of a magnet. Fe_3O_4@SA MNCs were washed and dried (13,14). The MNCs synthesis scheme is shown in Figure 1.

FeCl$_3$.6H$_2$O + FeCl$_2$.4H$_2$O

Ar,
H$_2$O,
NH$_3$,
70 ^{o}C,
30 Min.

Salicylic acid
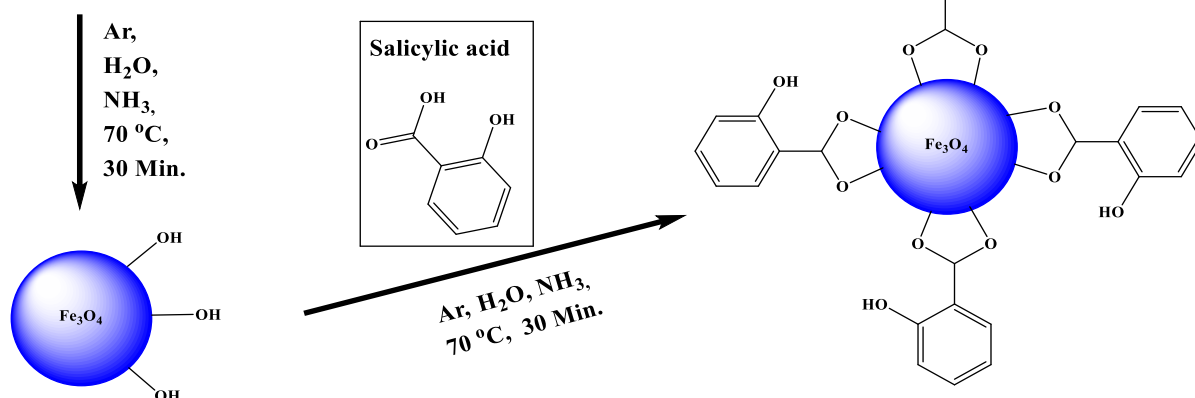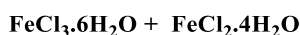
Figure 1. The synthesis scheme of Fe$_3$O$_4$@SA MNCs.

2.3. Characterization
It was done using Fourier transform infrared spectroscopy (FTIR) (Bruker Vertex 70, 4000-400 cm^{-1}) for identification of bonds in Fe$_3$O$_4$@SA MNCs structure, Vibrating Sample Magnetometer (VSM) for magnetization ability (Lake Shore 7407, -20000 – 20000 Oe), Scanning Electron Microscopy (SEM-EDX) (JEOL 6510) and X-ray Diffractometer (XRD) (Rigaku Smartlab).

2.4. Use of NaOH in Hydrogen Production
NaOH is generally used to inhibit the self-hydrolysis of NaBH$_4$. In this study, NaOH in amounts ranging from 0 to 25 mg was used to determine the effect of the amount of NaOH on hydrogen production.

2.5. Use of the Catalyst in Hydrogen Production
Fe$_3$O$_4$@SA MNCs in amounts ranging from 10 to 100 mg were used to determine the effect of catalyst amount on hydrogen production.

2.6. Hydrogen Production by NaBH$_4$ Hydrolysis
A round bottom reaction flask with a volume of 100 mL was utilized to introduce 150 mg of NaBH$_4$ and 10 mg of Fe$_3$O$_4$@SA MNCs. Following the addition of NaBH$_4$ and Fe$_3$O$_4$@SA MNCs, per the prescribed parameters, to the reaction flask at 25 °C, a volume of 20 mL of water was introduced. The solution was stirred at 500 rpm. The volume of

hydrogen released was measured depending on time using the water-gas displacement method through an inverted gas cylinder filled with water. In this study, the effects of NaBH$_4$ (25, 50,100, 150 and 200 mg), NaOH (0, 10, 20, and 25 mg), and Fe$_3$O$_4$@SA MNCs (10, 25, 50, 75, and 100 mg) on hydrogen production were investigated. The HGR value was determined using the following formula (15,16).

$$HGR = \frac{mL\ H_2}{gram\ of\ catalyst \times time} \qquad (2)$$

In this formula, mL H$_2$, the volume of hydrogen produced, the amount of catalyst used and the time (min) was the reaction time were listed.

3. RESULTS AND DISCUSSION

3.1. Fe$_3$O$_4$@SA MNCs Characterization
In the FTIR spectrum of Fe$_3$O$_4$@SA MNCs, the peak at 545 cm^{-1} is the characteristic peak of the stretching of the Fe-O bond. The peak at 1610 cm^{-1} belongs to the C-O stretching vibration. The peak around 3000 cm^{-1} belongs to =C-H stretching vibrations. The peak around 3500 cm^{-1} belongs to the stretching of the O-H bond (Figure 2). The obtained peaks indicate that the synthesis of Fe$_3$O$_4$@SA MNCs has occurred successfully. The results obtained are compatible with the literature (17).
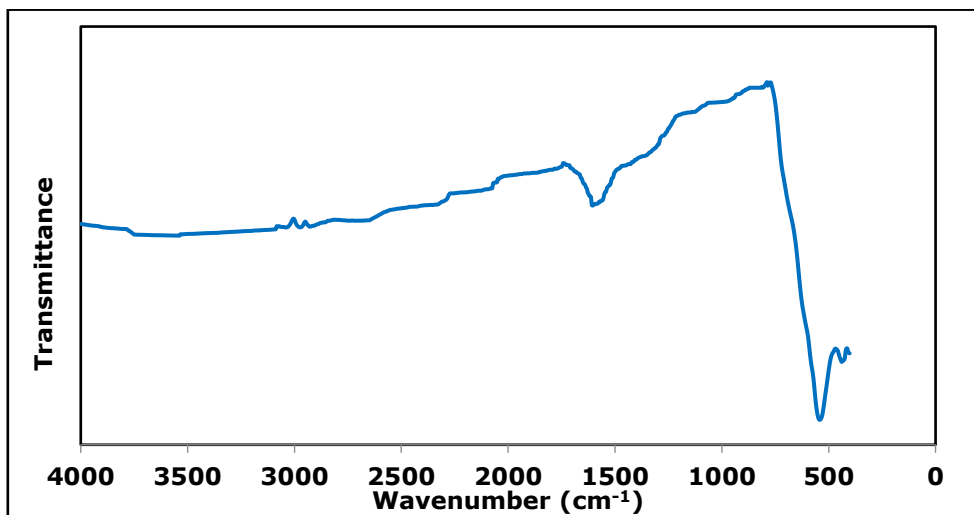
Figure 2. Fe_3O_4@SA MNCs FTIR spectrum.

Fe_3O_4@SA MNCs XRD patterns are given in Figure 3. Characteristic peaks at 2θ = 18.16°, 30.12°, 35.54°, 37.62°, 45.52°, 53.66°, 57.02°, 62.78° of Fe_3O_4@SA MNCs correspond to the crystal planes (1 1 1), (2 2 0), (3 1 1), (2 2 2), (4 0 0), (4 2 2), (5 1 1) and (4 4 0), respectively (Figure 3). The results show that Fe_3O_4@SA MNCs have a highly crystalline cubic spinel structure. The results obtained are compatible with the literature (18).
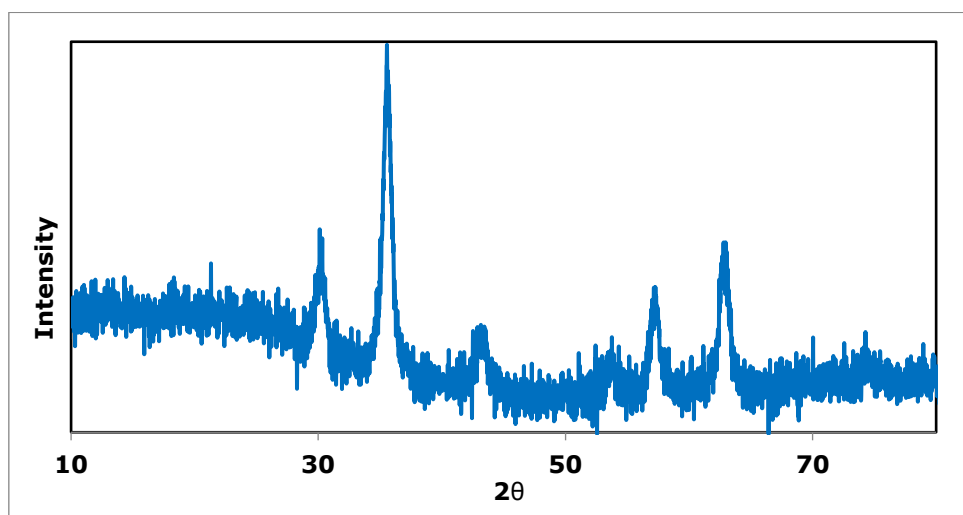
Figure 3: Fe_3O_4@SA MNCs XRD pattern.

The magnetic property of Fe_3O_4@SA MNCs is given in the VSM plot in Figure 4. Since hysteresis is not observed in the graph, it is understood that the sample is superparamagnetic. Saturation magnetic moment of Fe_3O_4@SA MNCs was found to be 52.8 emu/g (Figure 4). The high of this value indicates that Fe oxidation is either low or absent. The results obtained are compatible with the literature (19).
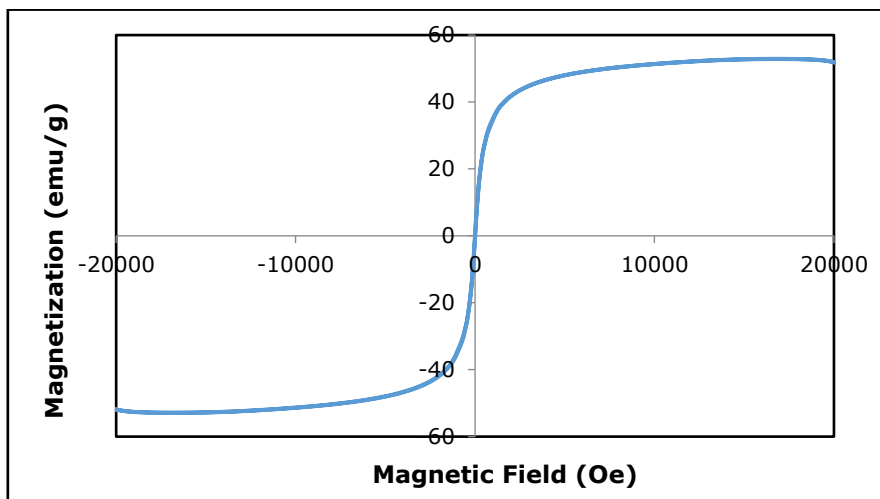
Figure 4: Fe₃O₄@SA MNCs VSM graphic.

Fe₃O₄@SA MNCs are given SEM images in Figure 5-A, SEM-EDS graph in Figure 5-B, and SEM-EDS-map graph in Figure 5-C. Figure 5-A shows that the morphology of Fe₃O₄@SA MNCs is spherical, spheres ranging in size from about 20 to 60 nm are adjacent to each other, and agglomeration is present. Its surface is rough. Figure 5-B shows that Fe₃O₄@SA MNCs, Fe (48.8%), O (33.1%), and C (18.1%) are formed. The obtained values show that the synthesis was successful. Figure 5-C demonstrates that the elemental distribution of Fe₃O₄@SA MNCs is very good. The results obtained are in accordance with the literature (18).
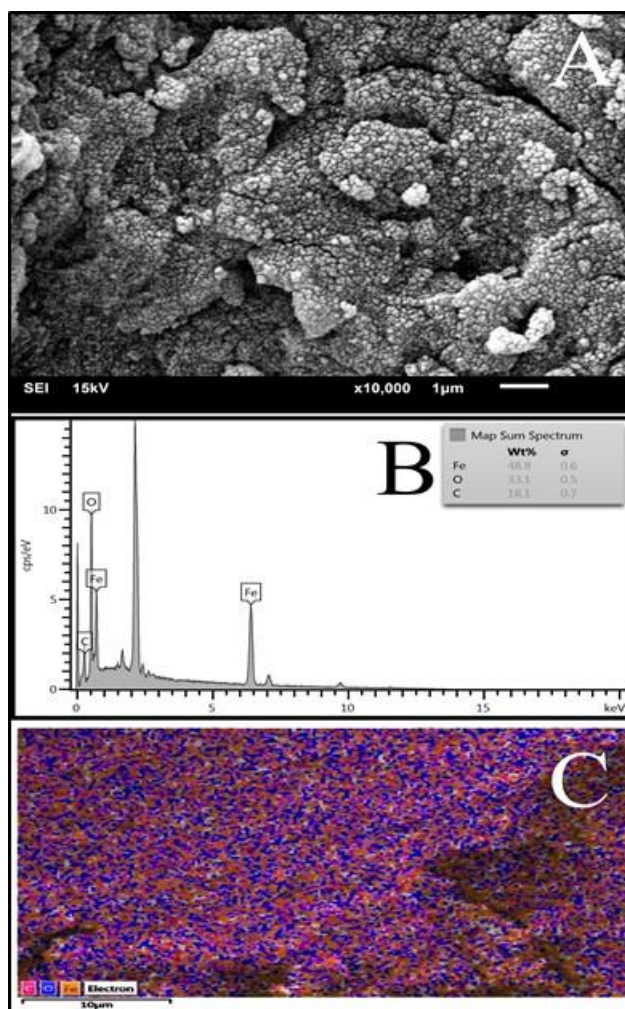
Figure 5: Fe₃O₄@SA MNCs A) SEM images, B) SEM-EDS graph, C) SEM-EDS-map graph.

3.2. NaBH₄ catalytic hydrolysis

3.2.1. Effect on hydrogen production of NaOH amount

To determine the appropriate amount of NaOH in the reaction solution, hydrogen productions were investigated using 50 mg Fe_3O_4@SA MNCs, 100 mg $NaBH_4$, and different amounts of NaOH (0, 10, 20, and 25 mg) at 25 °C. The resulting graph is shown in Figure 6. This graph illustrates a notable drop in the volume of hydrogen produced, from 84 mL to 12 mL, as the quantity of NaOH is augmented from 0 mg to 25 mg. The Fe_3O_4@SA MNCs exhibited optimal catalytic efficiency when NaOH was excluded from the solution. The best catalytic performance for the Fe_3O_4@SA MNCs used was achieved by not using NaOH in the solution, and the HGR value was 88 mL H_2 $gcat^{-1}$·min^{-1} was measured. It has been reported in the literature (20) that an increase in the amount of NaOH reduces the rate of hydrolysis. Using 10, 20, and 25 mg of NaOH, the HGR values were measured as 48, 16, and 12 mL H_2 $gcat^{-1}$·min^{-1}, respectively. The decrease in the HGR value is related to blocking the active sites on the Fe_3O_4@SA MNCs of the NaOH increase.

Figure 6: Effect on hydrogen volume in $NaBH_4$ hydrolysis of NaOH (Reaction conditions: 50 mg Fe_3O_4@SA MNCs, 100 mg $NaBH_4$, 0, 10, 20 and 25 mg NaOH and 25 °C).
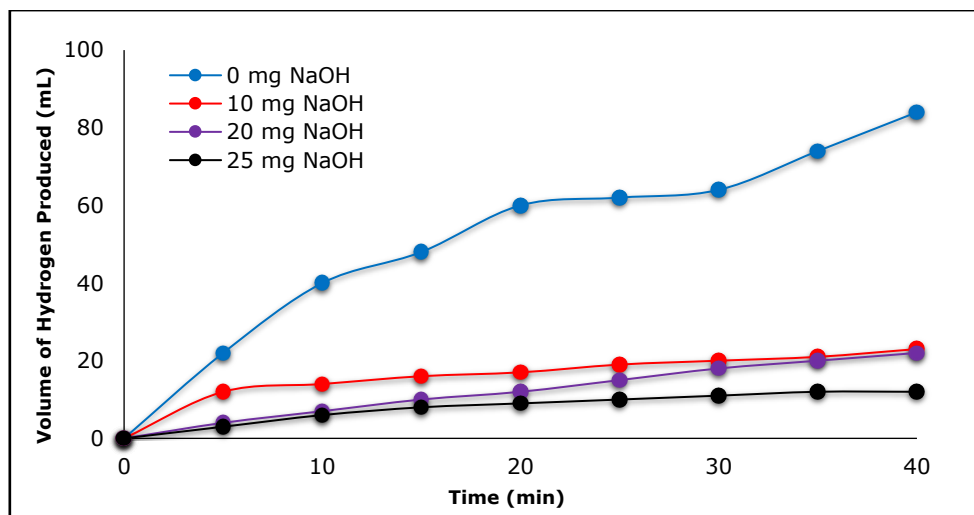
3.2.2. Effect on hydrogen production of NaBH₄ amount

The effect on the hydrogen production of $NaBH_4$ was investigated by using 25, 50, 100, 150, and 200 mg $NaBH_4$ at 25°C, keeping the amount of Fe_3O_4@SA MNCs (50 mg) constant. Figure 7 shows that when $NaBH_4$ is increased from 25 mg to 200 mg, the hydrogen produced increases significantly from 50 mL to 314 mL. The best catalytic performance for the Fe_3O_4@SA MNCs used was achieved by using 200 mg of $NaBH_4$, and the HGR value was 157 mL H_2 $gcat^{-1}$·min^{-1} was measured. As the amount of $NaBH_4$ used increases, the hydrogen volume and HGR value increase depending on time. It was determined that as the amount of $NaBH_4$ increased, the hydrogen volume increased depending on time. The results obtained are compatible with the literature (21-23).

3.2.3. Effect on hydrogen production of catalyst amount

The effect on hydrogen production of Fe_3O_4@SA MNCs amount (10, 25, 50, 75, and 100 mg) in 150 mg $NaBH_4$ hydrolysis at 25 °C was investigated. The obtained graph is shown in Figure 8. When the amount of Fe_3O_4@SA MNCs increased from 10 mg to 75 mg, the hydrogen produced increased significantly from 106 to 128 mL. When the amount of catalyst increased from 75 mg to 100 mg, a significant decrease was observed in the volume of hydrogen produced. The reason for this decrease is that the catalyst's active sites are filled in the reaction and cannot provide enough active sites for the substrate. The results obtained are compatible with the literature (24).
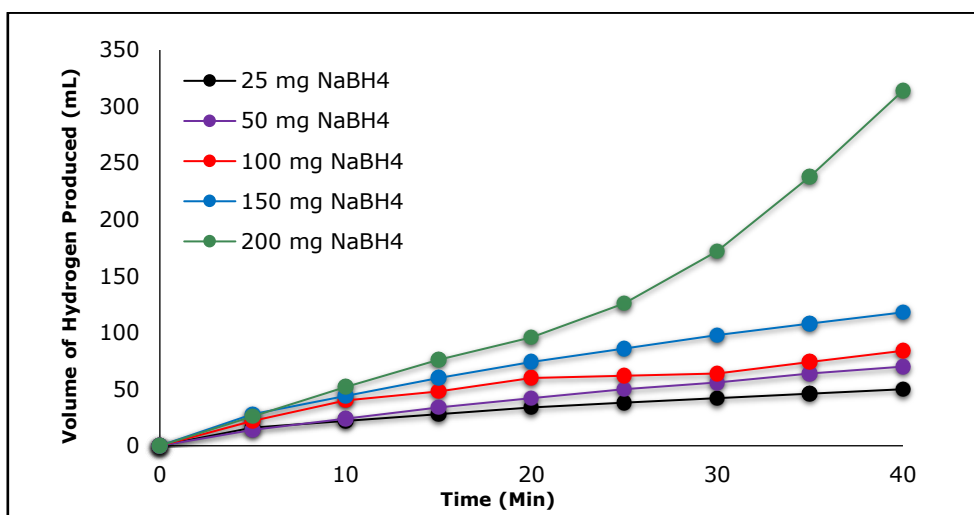
Figure 7: Effect on hydrogen volume of NaBH$_4$ using Fe$_3$O$_4$@SA MNCs (Reaction conditions: 50 mg nano-catalyst, 25, 50, 100, 150 and 200 mg NaBH$_4$ and 25 °C).
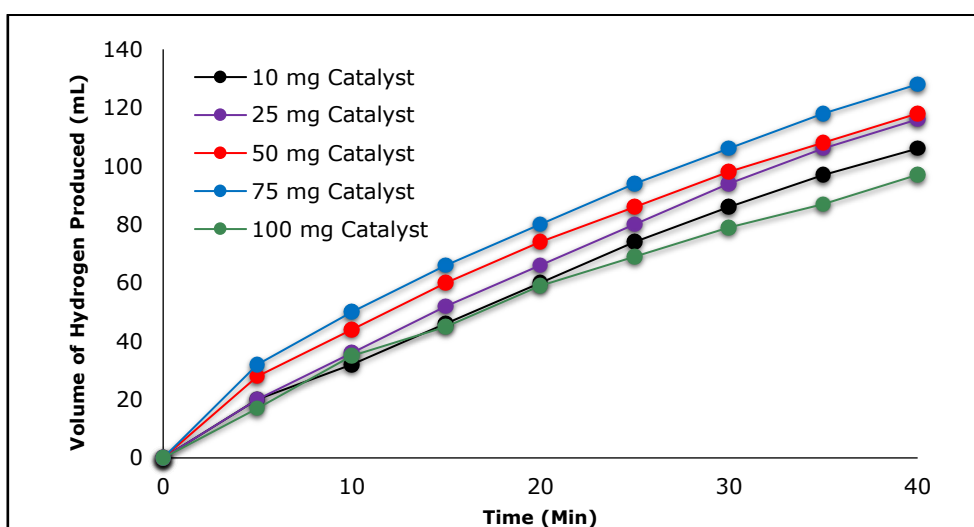
Figure 8: Effect on hydrogen volume by hydrolysis of NaBH4 of Fe$_3$O$_4$@SA MNCs (Reaction conditions: 10, 25, 50, 75, and 100 mg Fe$_3$O$_4$@SA MNCs, 150 mg NaBH$_4$ and 25 °C).

The best hydrogen production volume was achieved with 75 mg Fe$_3$O$_4$@SA MNCs, and the HGR value was measured as 85.33 mL H$_2$ gcat^{-1}·min^{-1}. The HGR values of 10, 25, 50, and 100 mg Fe$_3$O$_4$@SA MNCs were determined as 400, 160, 112, and 34 mL H$_2$ gcat^{-1}·min^{-1}, respectively. The highest HGR value was reached using a 10 mg catalyst. The HGR value increased until the optimum amount of Fe$_3$O$_4$@SA MNCs and then decreased. This is due to equation (2) used to calculate the HGR value.

Compared with Table 1, it was determined that the hydrolysis of NaBH$_4$ catalyzed by the Fe$_3$O$_4$@SA MNCs showed a lower HGR value than some catalysts, although it was comparable to other catalysts in the literature (Table 1). The reason for this can be said that the Fe$_3$O$_4$-supported structures in the literature have a more stable structure than the salicylic acid support material. Thus, higher HGR values can be obtained by

coating the Fe$_3$O$_4$ structure with a more stable material and binding different metals to this nano-catalyst.

3.2.4. Reusability of the Fe$_3$O$_4$@SA MNCs
The percentage yield results obtained from NaBH$_4$ catalyzed after five reusability cycles of Fe$_3$O$_4$@SA MNCs at 25 °C are shown in Figure 9. It shows the yield results (percentage comparison with cycle 1) obtained from NaBH$_4$ catalyzed by Fe$_3$O$_4$@SA MNCs after five reusability cycles (75 mg catalyst, 150 mg NaBH$_4$, and 20 mL pure water) at 25 °C. As shown in Fig. 9, the catalytic activity of Fe$_3$O$_4$@SA MNCs was found to decrease slightly. It can be said that this situation is due to the accumulation of sodium metaborate, which cannot be removed by washing the catalyst. The results obtained are compatible with the literature (28). Thus, Fe$_3$O$_4$@SA MNCs were found to be an effective catalyst for the hydrolysis of NaBH$_4$.

Table 1. Comparison of Fe_3O_4@SA MNCs with various catalysts used for hydrogen production by $NaBH_4$ hydrolysis.

Catalyst	Temperature (°C)	HGR (mL H_2 gcat^{-1}·min^{-1})	Ref.
Co/Fe_3O_4@C	25	1403	(9).
Oxidized Fe_2O_3	25	264	(25).
a-Fe_2O_3@N-C NSs	25	637	(25).
Fe_3O_4@SiO_2–Pt	25	800	(26).
Fe_3O_4@SiO_2–Pt/Ni	25	2500	(26).
Fe_3O_4@SiO_2–Pt@TiO_2	25	1500	(26).
Fe-B	25	618	(27).
Fe_3O_4@SA	25	400	This work
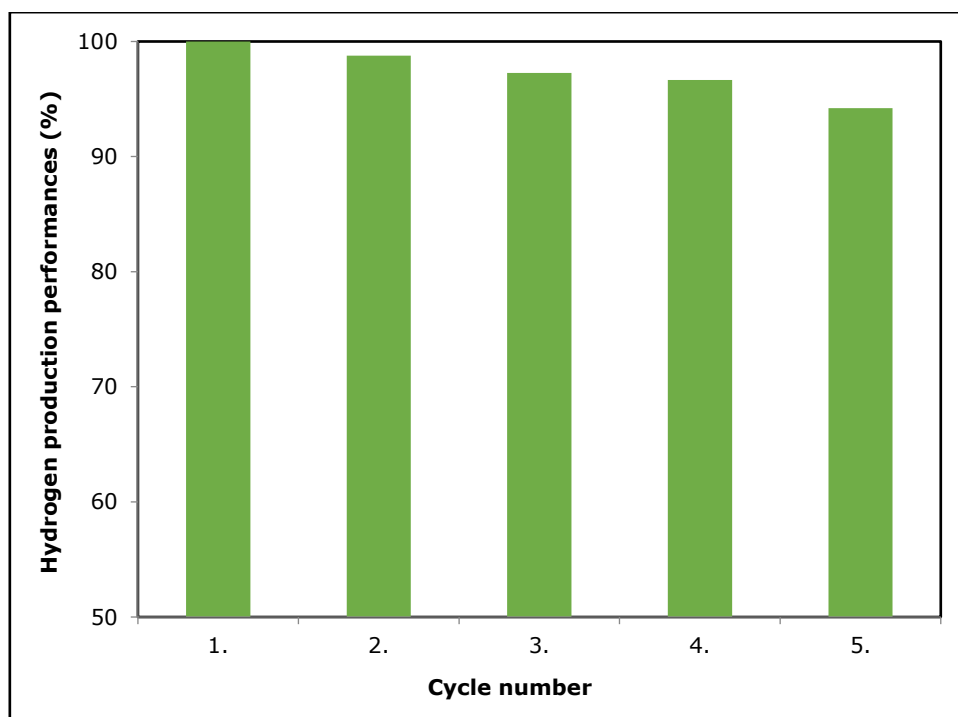
Figure 9: The reusability of Fe_3O_4@SA MNCs for hydrolysis of $NaBH_4$ at 25 °C.

3.3. Optimization of the Catalysis Process

In this study, optimum catalysis process conditions are given in Figure 9. The decrease in the amount of NaOH increased hydrogen production. The study with 0 mg NaOH produced 84 mL of hydrogen in 40 minutes, with other parameters remaining constant (Figure 9.A). Increasing the amount of $NaBH_4$ increased the hydrogen production. The study with 200 mg of $NaBH_4$ produced 314 mL of hydrogen in 40 minutes, with other parameters remaining constant (Figure 9.B). Increasing the amount of Fe_3O_4@SA MNCs increased hydrogen production. The study with 75 mg Fe_3O_4@SA produced 128 mL of hydrogen in 40 minutes, with other parameters remaining constant (Figure 9.C).
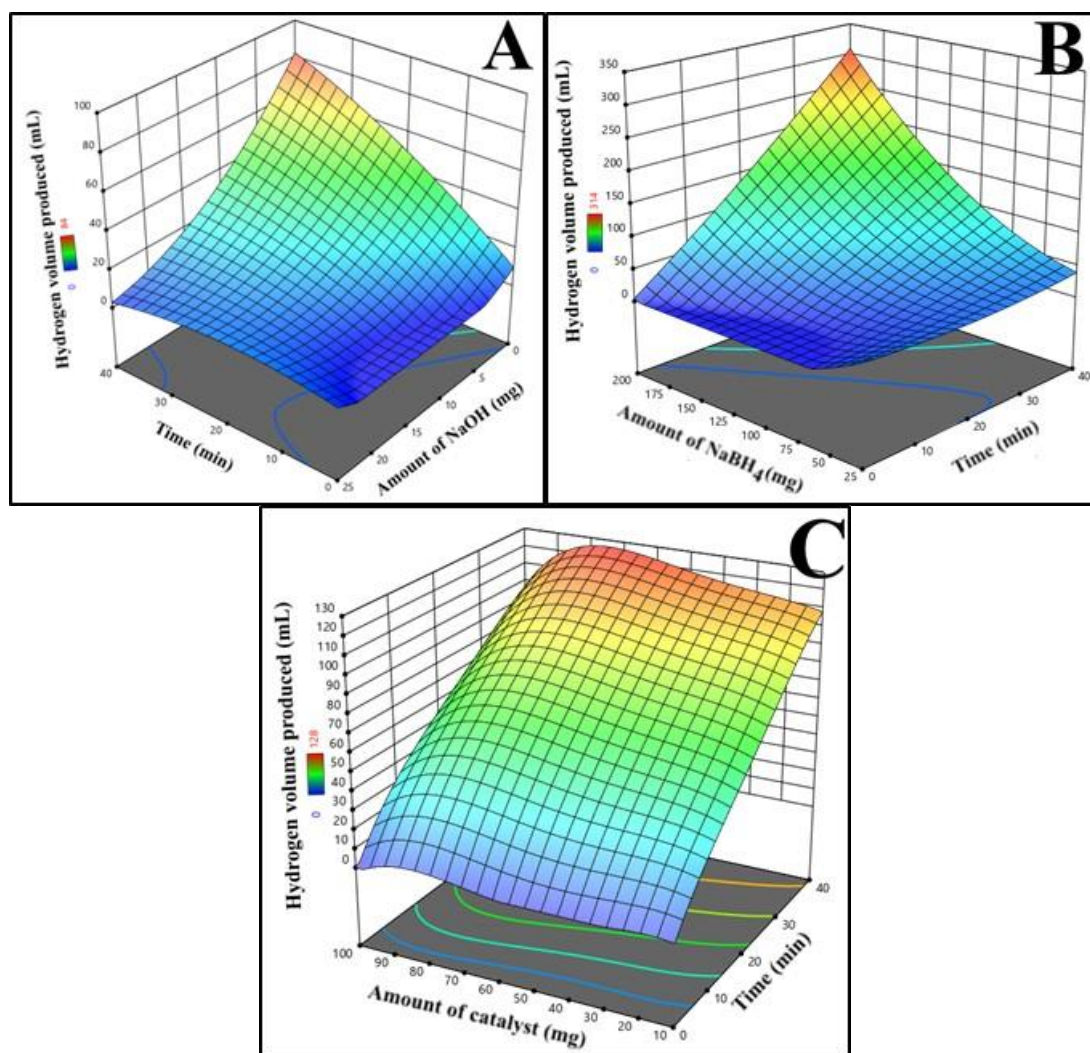
Figure 9: Optimization of the catalysis process A) NaOH amount-time graph, B) NaBH$_4$ amount-time graph, C) Fe$_3$O$_4$@SA MNCs amount-time graph.

3.4. A possible Mechanism of NaBH$_4$ Hydrolysis Catalyzed by Fe$_3$O$_4$@SA MNCs

The reaction mechanism of the catalyzed hydrolysis of NaBH$_4$ is assumed to occur by following the steps of the reaction mechanism, as shown in Figure 10. NaBH$_4$, catalyst, and water molecules are initially in the same environment. BH$_4^-$ ions and water molecules are chemically adsorbed on the catalyst. Second, the H$^-$ ion is transferred from the BH$_4^-$ ion to the catalyst. Third, hydrogen in hydric form (H$^-$) and BH$_3^-$ ions react with a water molecule to form H$_2$ and BH$_3$(OH)$^-$ ions. Hydrogen in each hydric form is transferred from the BH$_3$(OH)$^-$ ion to the catalyst. Finally, each cycle is repeated until 4 moles of H$_2$ are released, forming the B(OH)$_4^-$ form from the BH$_3$(OH)$^-$ ion. The proposed possible mechanism for NaBH$_4$ hydrolysis catalyzed by Fe$_3$O$_4$@SA MNCs is consistent with the literature (29,30). Since the reaction end product, B(OH)$_4^-$ is not supported by the catalyst, it reduces the rate of the hydrolysis reaction. It can be said that H$_2$ is produced more easily with the electrons coming from the BH$_4^-$ ions from the hydrogen ion excess in the environment. Thus, it reflects positively on hydrogen production volume and HGR value.
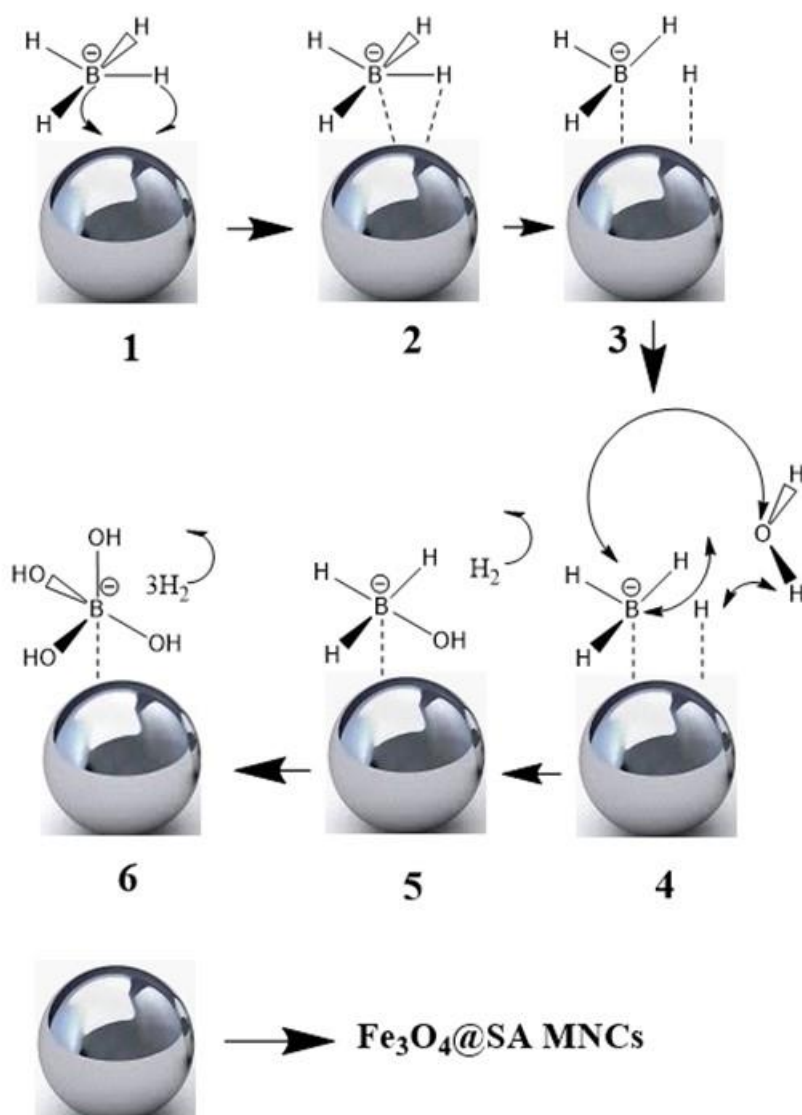
Figure 10: A possible mechanism of $NaBH_4$ hydrolysis catalyzed by Fe_3O_4@SA MNCs.

4. CONCLUSION

The use of Fe_3O_4@SA MNCs as a catalyst in hydrogen production was carried out for the first time in this study. Fe_3O_4@SA MNCs were produced by a simple, reliable, and inexpensive process. Characterizations with FT-IR, XRD, VSM, SEM, and SEM-EDX methods showed that Fe_3O_4@SA MNCs were successfully synthesized. To determine the effect of Fe_3O_4@SA MNCs on HGR, the amounts of $NaBH_4$, NaOH, and catalyst were examined. For Fe_3O_4@SA MNCs, the highest HGR value was obtained using 150 mg of $NaBH_4$, 10 mg of catalyst, 20 ml of distilled water, and no NaOH in the reaction. The obtained maximum HGR value is found as 400 mL H_2 $gcat^{-1} \cdot min^{-1}$. HGR values are comparable to values reported in the literature. The economic and large-scale production of Fe_3O_4-based magnetic nano-catalysts for hydrogen production by $NaBH_4$ hydrolysis offers a much simpler and more commercial process to make hydrogen the main fuel source.

5. CONFLICT OF INTEREST

The author declares that he has no conflicts of interest.

6. REFERENCES

1.   Arsad A, Hannan M, Al-Shetwi AQ, Hossain M, Begum R, Ker PJ, et al. Hydrogen electrolyser for sustainable energy production: A bibliometric analysis and future directions. International Journal of Hydrogen Energy. 2023;48(13):4960-83. Available from: <URL>

2.   Demirci S, Sunol AK, Sahiner N. Catalytic activity of amine functionalized titanium dioxide nanoparticles in methanolysis of sodium borohydride for hydrogen generation. Applied Catalysis B: Environmental. 2020;261:118242. Available from: <URL>

3.   Sadiq I, Ali SA, Ahmad T. Graphene-based derivatives heterostructured catalytic systems for sustainable hydrogen energy via overall water splitting. Catalysts. 2023;13(1):109. Available from: <URL>

4.	Bekirogullari M. Synthesis of waste eggshell-derived Au/Co/Zn/eggshell nanocomposites for efficient hydrogen production from NaBH4 methanolysis. International Journal of Hydrogen Energy. 2023. Available from: <URL>

5.	Sahiner N, Ozay O, Inger E, Aktas N. Superabsorbent hydrogels for cobalt nanoparticle synthesis and hydrogen production from hydrolysis of sodium boron hydride. Applied Catalysis B: Environmental. 2011;102(1-2):201-6. Available from: <URL>

6.	Agarwal N, Solanki VS, Pare B, Singh N, Jonnalagadda SB. Current trends in nanocatalysis for green chemistry and its applications-a mini-review. Current Opinion in Green and Sustainable Chemistry. 2023:100788. Available from: <URL>

7.	Kutluay S, Ece MŞ, Şahin Ö, Kahraman Z, Ferat Ö, Fesih A. Derik Halhalı Zeytin Çekirdeğinden Çevre Dostu Selülozik Manyetik Nano-Adsorbent Üretimi ve Benzen Gideriminde Kullanılması. Bitlis Eren Üniversitesi Fen Bilimleri Dergisi. 2021;10(4):1535-51. Available from: <URL>

8.	Ece MŞ. Fe3O4/AC@ SiO2@ EDTA Manyetik Nano-Adsorbentin Sentezlenmesi ve Toluenin Gaz Adsorpsiyonunda Kullanılması. Bitlis Eren Üniversitesi Fen Bilimleri Dergisi. 2020;9(2):561-72. Available from: <URL>

9.	Chen B, Chen S, Bandal HA, Appiah-Ntiamoah R, Jadhav AR, Kim H. Cobalt nanoparticles supported on magnetic core-shell structured carbon as a highly efficient catalyst for hydrogen generation from NaBH4 hydrolysis. International Journal of Hydrogen Energy. 2018;43(19):9296-306. Available from: <URL>

10.	Izgi MS, Ece MŞ, Kazici HÇk, Şahìn Ö, Onat E. Hydrogen production by using Ru nanoparticle decorated with Fe3O4@ SiO2-NH2 core-shell microspheres. International journal of hydrogen energy. 2020;45(55):30415-30. Available from: <URL>

11.	Yang M, Xu A, Du H, Sun C, Li C. Removal of salicylic acid on perovskite-type oxide LaFeO3 catalyst in catalytic wet air oxidation process. Journal of hazardous materials. 2007;139(1):86-92. Available from: <URL>

12.	Zhang P. Photocatalytic Reduction of Wo-3-Tio-2 Composite Catalyst in Cr (Ⅵ) Ion. International Journal of New Developments in Education. 2020;2(6). Available from: <DOI>

13.	Ece MŞ. Synthesis, characterization and investigation of some physical textures of magnetite-silica-L-Proline nanoparticles modified with some transition metals (Co, Mn, Cu, Ni). Materials Science and Engineering: B. 2023;292:116417. Available from: <URL>

14.	Kutluay S, Horoz S, Şahin Ö, Ekinci A, Ece MŞ. Highly improved solar cell efficiency of Mn-doped amine groups-functionalized magnetic Fe3O4@ SiO2 nanomaterial. International Journal of Energy Research. 2021;45(14):20176-85. Available from: <URL>

15.	Wei Y, Wang M, Fu W, Wei L, Zhao X, Zhou X, et al. Highly active and durable catalyst for hydrogen generation by the NaBH4 hydrolysis reaction: CoWB/NF nanodendrite with an acicular array structure. Journal of

alloys and compounds. 2020;836:155429. Available from: <URL>

16.	Balbay A, Saka C. Semi-methanolysis reaction of potassium borohydride with phosphoric acid for effective hydrogen production. International Journal of Hydrogen Energy. 2018;43(46):21299-306. Available from: <URL>

17.	Unal B, Durmus Z, Kavas H, Baykal A, Toprak M. Synthesis, conductivity and dielectric characterization of salicylic acid–Fe3O4 nanocomposite. Materials Chemistry and Physics. 2010;123(1):184-90. Available from: <URL>

18.	Abdolmohammad-Zadeh H, Salimi A. A magnetic adsorbent based on salicylic acid-immobilized magnetite nano-particles for pre-concentration of Cd (II) ions. Frontiers of Chemical Science and Engineering. 2021;15:450-9. Available from: <URL>

19.	Dheyab MA, Aziz AA, Jameel MS, Noqta OA, Khaniabadi PM, Mehrdel B. Simple rapid stabilization method through citric acid modification for magnetite nanoparticles. Scientific reports. 2020;10(1):10793. Available from: <URL>

20.	Huang Y, Wang K, Cui L, Zhu W, Asiri AM, Sun X. Effective hydrolysis of sodium borohydride driven by self-supported cobalt oxide nanorod array for on-demand hydrogen generation. Catalysis Communications. 2016;87:94-7. Available from: <URL>

21.	Yang L, Fan C, Zhang J, Zhang F, Li R, Yi S, et al. Poly (acrylic acid)-modified silica nanoparticles as a nonmetal catalyst for NaBH4 methanolysis. International Journal of Hydrogen Energy. 2021;46(45):23236-44. Available from: <URL>

22.	Al-Enizi AM, Nafady A, El-Halwany M, Brooks RM, Abutaleb A, Yousef A. Electrospun carbon nanofiber-encapsulated NiS nanoparticles as an efficient catalyst for hydrogen production from hydrolysis of sodium borohydride. International Journal of Hydrogen Energy. 2019;44(39):21716-25. Available from: <URL>

23.	Ghodke N, Rayaprol S, Bhoraskar S, Mathe V. Catalytic hydrolysis of sodium borohydride solution for hydrogen production using thermal plasma synthesized nickel nanoparticles. International Journal of Hydrogen Energy. 2020;45(33):16591-605. Available from: <URL>

24.	Deonikar VG, Rathod PV, Pornea AM, Puguan JMC, Park K, Kim H. Hydrogen generation from catalytic hydrolysis of sodium borohydride by a Cu and Mo promoted Co catalyst. Journal of Industrial and Engineering Chemistry. 2020;86:167-77. Available from: <URL>

25.	Nabid MR, Bide Y, Kamali B. Hydrogen release from sodium borohydride by Fe2O3@ nitrogen-doped carbon core-shell nanosheets as reasonable heterogeneous catalyst. International Journal of Hydrogen Energy. 2019;44(47):25662-70. Available from: <URL>

26.	Ro G, Hwang DK, Kim Y. Hydrogen generation using Pt/Ni bimetallic nanoparticles supported on Fe3O4@ SiO2@ TiO2 multi-shell microspheres. Journal of Industrial and Engineering Chemistry. 2019;79:364-9. Available from: <URL>

27.	Ocon JD, Tuan TN, Yi Y, de Leon RL, Lee JK, Lee J. Ultrafast and stable hydrogen generation from sodium borohydride in methanol and water over Fe–B

nanoparticles. Journal of power sources. 2013;243:444-50. Available from: <URL>

28.   Hayagreevan C, Siva B, Rahul R, Denisdon S, Jeevagan J, Adinaveen T, et al. Sulphonated silica and sulphonated silica/carbon particles as efficient catalysts for hydrogen generation from sodium borohydride hydrolysis. International Journal of Hydrogen Energy. 2021;46(68):33849-63. Available from: <URL>

29.   Zhang J, Li Y, Yang L, Zhang F, Li R, Dong H. Ruthenium nanosheets decorated cobalt foam for controllable hydrogen production from sodium borohydride hydrolysis. Catalysis Letters. 2022;152(5):1386-91. Available from: <URL>

30.   Demirci UB, Miele P. Reaction mechanisms of the hydrolysis of sodium borohydride: A discussion focusing on cobalt-based catalysts. Comptes Rendus Chimie. 2014;17(7-8):707-16. Available from: <URL>

Synthesis, Antimicrobial Evaluation, and Docking Study of Some New Isoxazoline Derivatives Derived from Chalcones

Inas Salim Mahdi[1]* , Ahmed Mutanabbi Abdula[2] ,

Abdulkadir Mohammed Noori Jassim[2]

[1]*Department of Agricultural Mechanization, College of Agricultural Engineering Science, University of Baghdad, Baghdad, Iraq*
[2]*Department of Chemistry, College of Science, Mustansiriyah University, Baghdad, Iraq*

Abstract: New 2-Isoxazoline derivatives containing furan moieties were synthesized from chalcones as starting materials, followed by antimicrobial activity. Chalcones were synthesized by reacting p-methoxy acetophenone or 3,4-(methylenedioxy)acetophenone with various aldehydes that were synthesized using Claisen-Schmidt condensation. Subsequently, the obtained products underwent cyclization with hydroxylamine hydrochloride to yield the corresponding 2-isoxazoline derivatives. The synthesized isoxazolines have been characterized via ^{1}H-NMR, FTIR, and GC-Mass spectroscopy. The new derivatives were screened for their activity against different bacterial species as well as Candida albicans and exhibited moderate to excellent activity as new antimicrobial agents. A docking study was conducted on most potent derivatives against glucoseamine-6-phosphate synthase (GlcN-6-P), the target enzyme for antimicrobial agents. The study aimed to understand how the discovered derivatives interact with the binding pocket residues of the enzyme.

1. INTRODUCTION

Heterocyclic compounds are extensively found in nature and are vital to life in different ways. Notably, these substances are significant due to the diverse range of physiological activities linked with this category of compounds, in addition to their great importance in the field of drug discovery (1). Heterocyclic rings exist in numerous important compounds and in the constituents of: vitamins B-complex, antibiotics, chlorophyll, heme, amino acids, enzymes, plant pigments, dye materials, genetic material DNA, etc..(2). Chalcones are naturally occurring substances that belong to the group of bicyclic compounds. They have been the focus of numerous scientists in recent times because of their vast biological capabilities and are considered important intermediates for the synthesis of isoxazolines (3). The word "chalcones" was first used by scientists Kostanecki & Tambor in 1899 (4). Chalcones (1,3 diphenyl-2-propen-1-ones) are derived from two aromatic rings with delocalized π-electron connected by an α,β-unsaturated carbonyl group. These compounds contain a (−C=O−CH=CH−) ketoethylenic group in their composition (5). Isoxazolines are heterocyclic compounds with

five-member rings called azoles with an oxygen atom adjacent to a nitrogen atom and a combined one paired-bond (6). The weak nitrogen-oxygen connections make isoxazolines promising candidates for ring cleavage, thus making it simple to change the substituents in their ring structures, which makes isoxazolines very useful intermediates in many synthetic processes of bioactive compounds (7). Isoxazolines are an important class of heterocyclic compounds that are broadly used in pharmaceuticals and treatments such as: anti-Alzheimer, anticancer (8), anticoagulant (9), anti-inflammatory (10), anti-tuberculosis (11), antidepressant (12), antioxidant (13), antimicrobial (14),(15), antitumor (16), anti-HIV & antiplatelet (17), and ulcer genic activity (18). In this article, we concentrate on the synthesis, characterization, and antimicrobial screening of new isoxazolines against two strains of bacteria; gram positive and gram negative as well as fungi, due to the recent and growing need to find and seek out new antimicrobial agents. The molecular target enzyme for antimicrobial treatment is (GlcN-6-P) synthase (19). A docking analysis was conducted to determine the binding posture of the new antimicrobial drugs and to highlight their mode of action. The docking outcomes improved the potential antimicrobial activity of the new compounds. The interactions between chalcone and isoxazoline derivatives and the active site of glucosamine-6-phosphate synthase were investigated using Autodock (4.2), a useful tool for investigating the binding coalition of tiny ligands to enzyme binding pockets (20).

2.   EXPERMENTAL SECTION

2.1. Materials
The chemicals and solvents utilized in this study were: furfural (Sigma-Aldrich, 99%), $NaNO_2$ (Merck, 99%), $CuCl_2.2H_2O$ (Sigma- Aldrich, 99.9%), 4-Chloroaniline (BDH, 99%), 4-Bromoaniline (CDH, 98%), 2,4-Dichloroaniline (Merck, 99%), 2-Chloro-4-nitroaniline (Flouro-chem, 97%), Ethanol (Sigma-Aldrich, ≥99.5%), NaOH (Sigma-Aldrich, 99%), 4-Methoxyacetphenone (Sigma-Aldrich, 99%), 3,4-(Methylenedioxy)acetophenone (Sigma-Aldrich, 99%), $NH_2OH.HCl$ (BDH, 99%).

2.2. Instrumentation
The melting points of the synthesized compounds were accomplished by using an electrothermal capillary apparatus a (digital Stuart scientific SMP30) and were uncorrected, at Al-Mustansiriyah University/ College of Science/ Department of Chemistry/ Iraq. The infrared spectra (FTIR) were recorded on (ALPHA II FTIR

Spectrometer-PLATINUM-ATR) (Bruker) in the range (400-4000cm^{-1}) at Al-Mustansiriyah University/ College of Science/ Department of Chemistry/ Iraq. The molecular weight of the prepared compounds was determined by using (Shimadzu model GCMS-QP2010 PLUS) at Samarra University/College of Education for Pure Science/ Iraq.^{1}H-NMR spectra of the prepared compounds were recorded by using TMS as an internal standard on (Bruker Avance Neo 400MHz) NMR spectrometer (Germany) in Al-Basrah University/ College of Education for Pure Science/ Department of Chemistry/ Iraq and (Brukerbiospin GmbH) at (400MHz) & (75MHz) at Gazi Osman Pasa (GOP) University/ Turkey.

2.3. Procedure
Note: All synthesized compounds have been investigated by TLC technique by using hexane:ethylacetate as eluent in different ratios.

2.3.1. Synthesis of 5-Arylfuran-2-carbaldehyde derivatives 1(a-d)
Aniline derivatives (0.136 mol) were dissolved in a mixture consisting of conc. HCl (33.07 mL) and distilled water (22.5 mL). The solution was cooled to 0-5°C, and then added a mixture consisting of sodium nitrite (9.5 gm, 0.138 mol) dissolved in distilled water (25 mL) was added progressively with continuous stirring for 10 min to produce diazonium salt. The solution was filtered and then furan-2-carboxyldehyde (15.4 gm, 0.16 mol) in distilled water (50 mL) was added along with a solution of $CuCl_2.2H_2O$ (5 gm, 0.04 mol) dissolved in distilled water (25 mL) and stirred at a temperature of 10-15°C. The temperature was gradually raised to 40°C and the mixture was stirred for 4h. The reaction progress was monitored by TLC using hexane:ethyl acetate (1:1). The precipitate formed was filtered and washed with sodium hydrogen carbonate solution (5%) and distilled water for several times, then dried and recrystallized with ethanol (21).
Note: In ^{1}H-NMR spectra, the signals at δ 2.5 and 7.26 ppm are for the solvents DMSO-d6 and CDCl$_3$, respectively.

5-(4-chlorophenyl)furan-2-carbaldehyde (1a)
Deep brown powder, yield (64%), m.p 114-116°C (21); FT-IR (cm^{-1}): 3110 (C-H furan), 3059 (C-H aromatic), 2834 (C-H aldehyde), 1673 (C=O), 1661 (C=C furan ring), 1589 (C=C aromatic ring), 1010 (C-Cl). ^{1}H-NMR (400MHz, CDCl$_3$) δ(ppm): 6.83(d,1H,CH furan, J=4.0Hz), 7.32(d,1H,CH furan, J=4.0Hz), 7.41(d,2H,Ar-H, J=8.0Hz), 7.75(d,2H,Ar-H, J=8.0Hz), 9.65(s,1H,CO-H aldehyde). Mass (EI) *m/z*: 206 M$^+$ for $C_{11}H_7ClO_2$.

5-(4-bromophenyl)furan-2-carbaldehyde (1b)
Brown powder, yield (65%), m.p 143-145°C (22); FT-IR (cm^{-1}): 3110 (C-H furan), 3056 (C-H aromatic), 2858 (C-H aldehyde), 1672 (C=O), 1660 (C=C furan ring), 1595 (C=C aromatic ring), 1039 (C-Br). ^{1}H-NMR (400MHz, CDCl$_3$) δ(ppm): 6.84(d,1H,CH furan, *J*=4.0Hz), 7.32(d,1H,CH furan, *J*= 4.0Hz), 7.57(d,2H,Ar-H, *J*=8.0Hz), 7.68(d,2H,Ar-H, *J*=8.0Hz), 9.65(s,1H,CO-H aldehyde). Mass (EI) *m/z*: 250 M$^+$ for C$_{11}$H$_7$BrO$_2$.

5-(2,4-dichlorophenyl)furan-2-carbaldehyde (1c)
Brown powder, yield (79%), m.p 148-150°C (21); FT-IR (cm^{-1}): 3158 (C-H furan), 3079 (C-H aromatic), 2842 (C-H aldehyde), 1677 (C=O), 1663 (C=C furan ring), 1585 (C=C aromatic ring), 1034 (C-Cl). ^{1}H-NMR (400 MHz, CDCl$_3$) δ(ppm): 7.32(d,1H,Ar-H, *J*=12.0 Hz), 7.37(d,1H,CH furan *J*=4.0 Hz), 7.50(d,1H,CH furan *J*=4.0 Hz), 7.96(d,1H,Ar-H, *J*=12.0 Hz), 7.35(s,1H,Ar-H), 9.70(s,1H, CO-H aldehyde). Mass (EI) *m/z* 240 M$^+$ for C$_{11}$H$_6$Cl$_2$O$_2$.

5-(2-chloro-4-nitrophenyl)furan-2-carbaldehyde (1d)
Orange powder, yield (75%), m.p 124-126°C; FT-IR (cm^{-1}): 3105 (C-H furan), 3034 (C-H aromatic), 2832 (C-H aldehyde), 1680 (C=O), 1664 (C=C furan ring), 1582 (C=C aromatic ring), 1341$_{sym.}$,1513$_{asym.}$(No$_2$), 1034 (C-Cl).^{1}H-NMR (400 MHz, CDCl$_3$) δ(ppm): 7.41(d,1H,CH furan, *J*=4.0Hz), 7.56(d,1H,CH furan, *J*=4.0Hz), 8.22(d,1H,Ar-H, *J*=8.0Hz), 8.25(d,1H,Ar-H, *J*=8.0Hz), 8.38(s,1H,Ar-H), 9.77 (s,1H,CO-H aldehyde). Mass (EI) *m/z*: 251 M$^+$ for C$_{11}$H$_6$ClNO$_4$.

2.3.2. Synthesis of Chalcone derivatives (General procedure) 2(a-h)
The preparation of chalcone derivatives was accomplished by using the procedure described in the published literature (23). To a solution of methyl ketone (0.001 mol) {4-Methoxy acetophenone or 3,4-(Methylenedioxy)acetophenone} in ethanol (10 mL), sodium hydroxide (40%,1 mL) was added, and the reaction mixture was stirred for 30 min. After that, 0.001 mol of aromatic aldehyde (previously prepared) 1(a-d) was added and stirred for 6-12 h. The completion of the reaction was checked by TLC using hexane:ethyl acetate as eluent (1:1). The precipitate was formed by adding crushed ice, then filtered, dried, and recrystallized with ethanol.

3-(5-(4-chlorophenyl)furan-2-yl)-1-(4-methoxyphenyl)prop-2-en-1-one (2a)
Yellow powder, yield (75%), m.p 169-171 °C; FT-IR (cm^{-1}): 3109 (C-H aromatic), 2839 (C-H aliphatic), 1646 (C=O chalcone), 1603 (CH=CH chalcone), 1587 (C=C aromatic), 1031 (C-Cl). ^{1}H-NMR (400MHz, DMSO-d$_6$) δ(ppm): 3.89(s,3H,O-CH$_3$), 7.11(d,2H,Ar-H, *J*=8.0Hz), 7.19(d,1H,CH furan, *J*=4.0Hz), 7.24(d,1H,CH furan, *J*=4.0Hz), 7.54-7.58(m,2H,Ar-H & 1H,CH chalcone), 7.73(d,1H,CH=C<u>H</u>-CO chalcone, *J*=16.0Hz), 7.96(d,2H,Ar-H, *J*=8.0Hz), 8.15(d,2H,Ar-H, *J*=8.0Hz). GC-Mass (EI) *m/z*: 338 M$^+$ for C$_{20}$H$_{15}$ClO$_3$.

3-(5-(4-bromophenyl)furan-2-yl)-1-(4-methoxyphenyl)prop-2-en-1-one (2b)
Yellow powder, yield (76%), m.p 185-187°C; FT-IR (cm^{-1}): 3109 (C-H aromatic), 2939 (C-H aliphatic), 1646 (C=O chalcone), 1599 (CH=CH chalcone), 1587 (C=C aromatic), 1029 (C-Br). ^{1}H-NMR (400MHz, DMSO-d$_6$) δ(ppm): 3.88(s,3H,-OCH$_3$), 7.11(d,2H,Ar-H, *J*=8.0Hz), 7.20(d,1H,CH furan, *J*=4.0Hz), 7.27(d,1H,CH furan, *J*=4.0Hz), 7.56(d,1H,C<u>H</u>=CH-CO chalcone, *J*=16.0Hz), 7.69(d,2H,Ar-H, *J*=8.0Hz), 7.75(d,1H,CH=C<u>H</u>-CO chalcone, *J*=16.0Hz), 7.91 (d,2H,Ar-H, *J*=8.0Hz), 8.16(d,2H,Ar-H, *J*=8.0Hz). GC-Mass (EI) *m/z*: 383 M$^+$ for C$_{20}$H$_{15}$BrO$_3$.

3-(5-(2,4-dichlorophenyl)furan-2-yl)-1-(4-methoxyphenyl)prop-2-en-1-one (2c)
Yellow powder, yield (84%), m.p 114-116°C; FT-IR (cm^{-1}): 3112 (C-H aromatic), 2836 (C-H aliphatic), 1648 (C=O chalcone), 1603 (CH=CH chalcone), 1583 (C=C aromatic), 1023 (C-Cl). ^{1}H-NMR (400 MHz, DMSO-d$_6$) δ(ppm): 3.88(s,3H,-OCH$_3$), 7.11(d,2H,Ar-H, *J*=8.0Hz), 7.25(d,1H,CH furan, *J*=4.0Hz) 7.39(d,1H,CH furan, *J*=4.0Hz), 7.56-7.80(m,1H,CH chalcone & 1H,Ar-H), 8.15(d,2H,Ar-H, *J*=8.0Hz), 8.20(d,1H,CH=C<u>H</u>-CO chalcone, *J*=8.0Hz). GC-Mass (EI) *m/z*: 373 M$^+$ for C$_{20}$H$_{14}$Cl$_2$O$_3$.

3-(5-(2-chloro-4-nitrophenyl)furan-2-yl)-1-(4-methoxyphenyl)prop-2-en-1-one (2d)
Orange powder, yield (80%), m.p 164-166°C; FT-IR (cm^{-1}): 3110 (C-H aromatic), 2838 (C-H aliphatic), 1648 (C=O chalcone), 1605 (CH=CH chalcone), 1583 (C=C aromatic), 1339$_{sym.}$, 1510$_{asym.}$(NO$_2$), 1019 (C-Cl). ^{1}H-NMR (400 MHz, DMSO-d$_6$) δ(ppm): 3.88(s,3H,-OCH$_3$), 7.11(d,2H,Ar-H, *J*=8.0Hz), 7.31(d,1H,CH furan, *J*=4.0Hz), 7.59(d,1H,C<u>H</u>=CH-CO chalcone, *J*=16.0Hz), 7.65(d,1H,CH furan, *J*=4.0Hz), 7.84(d,1H,CH=C<u>H</u>-CO chalcone, *J*=16.0Hz), 8.15(d,2H,Ar-H, *J*=8.0Hz), 8.25-8.46(m,3H,Ar-H). GC-Mass (EI) *m/z* 384 M$^+$ for C$_{20}$H$_{14}$ClO$_5$.

Mahdi IS et al. JOTCSA. 2024;11(1):217-232.

RESEARCH ARTICLE

1-(benzo[d][1,3]dioxol-5-yl)-3-(5-(4-chlorophenyl)furan-2-yl)prop-2-en-1-one (2e)
Yellow powder, yield (73%), m.p 165-167°C; FT-IR (cm^{-1}): 3108 (C-H aromatic), 2902 (C-H aliphatic), 1644 (C=O chalcone), 1603 (CH=CH chalcone), 1580 (C=C aromatic), 1042 (C-Cl). ^{1}H-NMR (400MHz, DMSO-d$_6$) δ(ppm): 6.18(s,2H,O-CH$_2$-O), 7.12(d,1H,Ar-H, *J*=8.0Hz), 7.20 (d,1H,CH furan, *J*=4.0Hz), 7.26(d,1H,CH furan, *J*=4.0Hz), 7.55 (d,2H,Ar-H, *J*=4.0Hz), 7.57(d,2H,Ar-H, *J*=4.0Hz), 7.65(d,1H,Ar-H, *J*=4.0Hz), 7.70(s,1H,Ar-H), 7.86 (d,1H,C<u>H</u>=CH-CO chalcone, *J*=8.0Hz), 7.98 (d,1H,CH=C<u>H</u>-CO chalcone, *J*=8.0Hz). GC-Mass (EI) *m/z*: 352 M$^+$ for C$_{20}$H$_{13}$ClO$_4$.

1-(benzo[d][1,3]dioxol-5-yl)-3-(5-(4-bromophenyl)furan-2-yl)prop-2-en-1-one (2f)
Yellow powder, yield (68%), m.p 180-182°C; FT-IR (cm^{-1}): 3106 (C-H aromatic), 2937 (C-H aliphatic), 1643 (C=O chalcone), 1602 (CH=CH chalcone), 1581 (C=C aromatic), 1022 (C-Br). ^{1}H-NMR (400MHz, DMSO-d$_6$) δ(ppm): 6.18(s,2H,O-CH$_2$-O), 7.11(d,1H,Ar-H, *J*=8.0Hz), 7.20(d,1H,CH furan, *J*=4.0Hz), 7.27(d,1H,CH furan, *J*=4.0Hz), 7.55(d,2H,Ar-H, *J*=16.0Hz), 7.67(d,1H,C<u>H</u>=CH-CO chalcone, *J*=12.0Hz), 7.70(s,1H,Ar-H), 7.72(d,2H,Ar-H, *J*=16.0Hz),7.86(d,1H,Ar-H,*J*=8.0Hz), 7.92(d,1H,CH=C<u>H</u>-CO chalcone, *J*=12.0Hz). GC-Mass (EI) *m/z*: 397 M$^+$ for C$_{20}$H$_{13}$BrO$_4$.

1-(benzo[d][1,3]dioxol-5-yl)-3-(5-(2,4-dichlorophenyl)furan-2-yl)prop-2-en-1-one (2g)
Yellow powder, yield (75%), m.p 158-160°C; FT-IR (cm^{-1}): 3111 (C-H aromatic), 2900 (C-H aliphatic), 1645 (C=O chalcone), 1606 (CH=CH chalcone), 1576 (C=C aromatic), 1024 (C-Cl). ^{1}H-NMR (400MHz, DMSO-d$_6$) δ(ppm): 6.18(s,2H,O-CH$_2$-O), 7.11(d,1H,Ar-H, *J*=8.0Hz), 7.26 (d,1H,CH furan, *J*=4.0Hz), 7.40(d,1H,CH furan, *J*=4.0Hz), 7.56(s,1H,Ar-H), 7.58-7.64(d,1H,C<u>H</u>=CH-CO chalcone & 1H,Ar-H), 7.76(d,1H,CH=C<u>H</u>-CO chalcone, *J*=16.0Hz), 7.80(d,1H,Ar-H, *J*=4.0Hz), 7.85(d,1H,Ar-H, *J*=8.0Hz), 8.23(d,1H,Ar-H, *J*=8.0Hz). GC-Mass (EI) *m/z*: 387 M$^+$ for C$_{20}$H$_{12}$Cl$_2$O$_4$.

1-(benzo[d][1,3]dioxol-5-yl)-3-(5-(2-chloro-4-nitrophenyl)furan-2-yl) prop-2-en-1-one (2h)
Yellow powder, yield (78%), m.p 211-213°C; FT-IR (cm^{-1}): 3105 (C-H aromatic), 2911 (C-H aliphatic), 1650 (C=O chalcone), 1607 (CH=CH chalcone), 1586 (C=C aromatic), 1352$_{sym.}$, 1477$_{asym.}$(NO$_2$), 1036 (C-Cl). ^{1}H-NMR (400MHz, DMSO-d$_6$) δ(ppm): 6.19(s,2H,O-CH$_2$-O), 7.13(d,1H,Ar-H, *J*=8.0Hz), 7.34(d,1H,CH furan, *J*=4.0Hz), 7.61(d,1H,C<u>H</u>=CH-CO chalcone, *J*=16.0Hz), 7.56(d,1H,Ar-H, *J*=4.0Hz), 7.69(d,

1H,CH furan, *J*=4.0Hz), 7.86 (d,1H,CH=C<u>H</u>-CO chalcone, *J*=16.0Hz)), 8.29-8.52(m,3H,Ar-H). GC-Mass (EI) *m/z*: 397 M$^+$ for C$_{20}$H$_{12}$ClNO$_6$.

2.3.3. Synthesis of 3,5-disubstituted aryl-isoxazoline derivatives (General procedure) 3(a-g)
These compounds were obtained according to the modified method reported in (24). Chalcone compounds (0.001 mol) were dissolved in ethanol absolute (10 mL), a solution of hydroxyl amine hydrochloride (0.0015 mol, 0.104 gm) dissolved in aqueous NaOH (40%, 2 mL) was added, and the resulting mixture was refluxed for 15h. The reaction was observed by TLC using hexane:ethyl acetate system (2:1). Crushed ice was added; the precipitate was filtered off, washed with distilled water, dried, and recrystallized with ethanol.

5-(5-(4-chlorophenyl)furan-2-yl)-3-(4-methoxyphenyl)-4,5-dihydroisoxazole (3a)
Light brown powder, yield (60%), m.p 130-133°C; FT-IR (cm^{-1}): 3167 (C-H aromatic), 2837 (C-H aliphatic), 1655 (C=N isoxazoline ring), 1595 (C=C aromatic), 1244 (C-O), 1023 (C-Cl). ^{1}H-NMR (400 MHz, DMSO-d$_6$) δ(ppm): 3.75(dd,1H,Ha-isoxazoline, *J*=4.0, 8.0 Hz), 3.82(s,3H,O-CH$_3$), 3.80-3.85 (m,1H,Hb-isoxazoline), 5.74-5.79(m appeared as triplet,1H,Hx- isoxazoline), 6.75(d,1H,CH furan, *J*=4.0), 7.02(d,1H,CH furan, *J*=4.0), 7.05(d,2H,Ar-H, *J*=12.0), 7.48(d,2H,Ar-H, *J*=8.0), 7.68-7.73(m,4H,Ar-H). GC-Mass (EI) *m/z*: 353 M$^+$ for C$_{20}$H$_{16}$ClNO$_3$.

5-(5-(4-bromophenyl)furan-2-yl)-3-(4-methoxyphenyl)-4,5-dihydroisoxazole (3b)
Orange powder, yield (49%), m.p 138-140°C; FT-IR (cm^{-1}): 3123 (C-H aromatic), 2836 (C-H aliphatic), 1650 (C=N isoxazoline ring), 1596 (C=C aromatic), 1251 (C-O), 1023 (C-Br). ^{1}H-NMR (400 MHz, DMSO-d$_6$) δ(ppm): 7.75(dd,1H,Ha-isoxazoline, *J*=8.0, 16.0 Hz), 3.83(s,3H,O-CH$_3$), 3.87(dd,1H,Hb-isoxazoline, *J*=4.0, 8.0 Hz), 5.73-5.78(m appeared as triplet,1H,Hx- isoxazoline), 6.75(d,1H,CH furan, *J*=4.0), 7.02(d,1H,CH furan, *J*=4.0), 7.05(d,2H,Ar-H, *J*=8.0), 7.61(d,2H,Ar-H, *J*=8.0), 7.65(d,2H,Ar-H, *J*=8.0), 7.70(d,2H,Ar-H, *J*=12.0). GC-Mass (EI) *m/z*: 398 M$^+$ for C$_{20}$H$_{16}$BrNO$_3$.

5-(5-(2,4-dichlorophenyl)furan-2-yl)-3-(4-methoxyphenyl)-4,5-dihydroisoxazole (3c)
Brown powder, yield (62%), m.p 86-88°C; FT-IR (cm^{-1}): 3070 (C-H aromatic), 2837 (C-H aliphatic), 1649 (C=N isoxazoline ring), 1597 (C=C aromatic), 1252 (C-O), 1023 (C-Cl). ^{1}H-

NMR (400 MHz, DMSO-d$_6$) δ(ppm): 3.76(dd,1H,Ha-isoxazoline, J=4.0, 8.0 Hz), 3.82(s,3H,O-CH$_3$), 3.80-3.85(m,1H,Hb-isoxazoline), 5.76-5.81(m appeared as triplet,1H,Hx-isoxazoline), 6.81 (d,2H,Ar-H, J=4.0), 7.04(d,2H,Ar-H, J=8.0), 7.12(d,1H,CH furan, J=4.0), 7.15(d,1H,CH furan, J=4.0), 7.29-7.42(m,3H,Ar-H). GC-Mass (EI) m/z: 388 M$^+$ for C$_{20}$H$_{15}$Cl$_2$NO$_3$.

5-(5-(2-chloro-4-nitrophenyl)furan-2-yl)-3-(4-methoxyphenyl)-4,5-dihydroisoxazole (3d)
Brown powder, yield (62%), m.p 86-88°C; FT-IR (cm^{-1}): 3072 (C-H aromatic), 2837 (C-H aliphatic), 1660 (C=N isoxazoline ring), 1598 (C=C aromatic), 1306 sym., 1510 asym. (NO$_2$), 1246 (C-O),1024 (C-Cl). ^{1}H-NMR (400MHz, DMSO-d$_6$) δ(ppm): 3.69(d,1H,Ha-isoxazoline, J=8.0 Hz), 3.73(s,3H,O-CH$_3$), 3.82(d,1H,Hb-isoxazoline, J=8Hz), 5.70-5.87(m,1H,Hx-isoxazoline), 6.67(d,1H,Ar-H, J=8.0), 6.98(d,1H,CH furan, J=4.0), 7.12(d,1H,Ar-H, J=8.0 Hz), 7.18(d,1H,CH furan, J=4.0), 7.34(d,1H,Ar-H, J=8.0), 7.64(d,1H,Ar-H, J=8.0 Hz), 7.87(d,1H,Ar-H, J=8.0 Hz). GC-Mass (EI) m/z: 398 M$^+$ for C$_{20}$H$_{15}$ClN$_2$O$_5$.

3-(benzo[d][1,3]dioxol-5-yl)-5-(5-(4-chlorophenyl)furan-2-yl)-4,5-dihydroisoxazole (3e)
Orange powder, yield (55%), m.p 88-90°C; FT-IR (cm^{-1}): 3121 (C-H aromatic), 2886 (C-H aliphatic), 1608 (C=N isoxazoline ring), 1585 (C=C aromatic), 1254 (C-O), 1040 (C-Cl). ^{1}H-NMR (400 MHz, DMSO-d$_6$) δ(ppm): 3.73(d,2H,CH$_2$ isoxazoline, J=8.0 Hz), 5.74-5.79(t,1H,CH isoxazoline, J=12.0 Hz), 6.11(s,2H,O-CH$_2$-O), 6.76(d,1H,CH furan, J=4.0 Hz), 7.02-7.05(m,1H,CH furan & 1H,Ar-H), 7.29(d,1H,CH furan, J=4.0 Hz), 7.32(d,1H,Ar-H, J=4.0 Hz), 7.49(d,2H,Ar-H, J=8.0 Hz), 7.72(d,2H,Ar-H, J=8.0 Hz). GC-Mass (EI) m/z: 367 M$^+$ for C$_{20}$H$_{14}$ClNO$_4$.

3-(benzo[d][1,3]dioxol-5-yl)-5-(5-(4-bromophenyl)furan-2-yl)-4,5-dihydroisoxazole (3f)
Light brown powder, yield (48%), m.p 96-98°C; FT-IR (cm^{-1}): 3120 (C-H aromatic), 2919 (C-H aliphatic), 1646 (C=N isoxazoline ring), 1607 (C=C aromatic), 1250 (C-O), 1038(C-Br). ^{1}H-NMR (400 MHz, DMSO-d$_6$) δ(ppm): 3.73(d,2H,CH$_2$ isoxazoline, J=12.0 Hz), 5.74-5.79(t,1H,CH isoxazoline, J=12.0 Hz), 6.11(s,2H,O-CH$_2$-O), 7.76(d,1H,CH furan, J=4.0 Hz), 7.03-7.05 (m,1H,CH furan & 1H,Ar-H), 7.24(d,1H,Ar-H, J=8.0 Hz), 7.31(s,1H,Ar-H), 7.61-7.67(m,4H,Ar-H). GC-Mass (EI) m/z: 412 M$^+$ for C$_{20}$H$_{14}$BrNO$_4$.

3-(benzo[d][1,3]dioxol-5-yl)-5-(5-(2,4-dichlorophenyl)furan-2-yl)-4,5-dihydroisoxazole (3g)
Brown powder, yield (65%), m.p 80-83°C; FT-IR (cm^{-1}): 3010 (C-H aromatic), 2891 (C-H aliphatic), 1654 (C=N isoxazoline ring), 1600 (C=C aromatic), 1250 (C-O), 1037 (C-Cl). ^{1}H-NMR (400 MHz, DMSO-d$_6$) δ(ppm): 3.75(d,2H,CH$_2$ isoxazoline, J=12.0 Hz), 5.77-5.82(t,1H,CH isoxazoline, J=12.0 Hz), 6.11(s,2H,O-CH$_2$-O), 6.82(d,1H,CH furan, J=4.0 Hz), 7.04(d,1H,Ar-H, J=12.0 Hz), 7.16(d,1H,CH furan, J=4.0 Hz), 7.83(d,1H,Ar-H, J=8.0 Hz), 7.31(s,1H,Ar-H), 7.52(d,1H,Ar-H, J=8.0 Hz), 7.74(s,1H,Ar-H), 7.83(d,1H,Ar-H, J=8.0 Hz). GC-Mass (EI) m/z: 402 M$^+$ for C$_{20}$H$_{13}$Cl$_2$NO$_4$.

2.4. Biological study

2.4.1. Evaluation of Antibacterial and Antifungal activity
Agar well-diffusion was utilized to study the antimicrobial activity of synthesized compounds against bacterial species: *Staphylococcus aureus* and *Staphylococcus epidermidis* (gram+ve) obtained from the dermatological infection, *Escherichia coli* and *klebsiella* (gram-ve) obtained from the gastrointestinal tract (GIT), as well as *Candida albicans* as fungi. DMSO was used as a solvent and amoxicillin & fluconazole as standard drugs, and the synthesized compounds will be in a solution at a concentration of 10000 μg/ml. This study was performed in the Department of Biology, College of Science, Mustansiriyah University. In brief, the sterilized agar [Muelles-Hitton agar] media were poured into petri dishes and allowed to solidify. The testing bacteria were distributed on the surface of the agar with sterile cotton swab, then holes were made and left it for 15 min. After that, 50μl of each compound solution were placed in the holes and the dishes were incubated at 37°C for 24h. The observed zones of inhibition around holes were measured in millimeters (25).

3. RESULTS AND DISCUSSION

Chalcone derivatives **(2a-2h)** were prepared via analogy method to Claisen-Schmidt condensation reaction as described in literature (26). In brief, acetophenone derivatives reacted with the corresponding 5-Arylfuran-2-carbaldehyde derivatives in ethanol in the presence of aqueous sodium hydroxide; later, the resulting chalcones were cyclized with hydroxylamine hydrochloride to produce isoxazoline derivatives **(3a-3g)** (27). In the following section, we will discuss more

details to characterize the chemical structure of   the newly synthesized compounds.

1a: R= 4-Cl
1b: R= 4-Br
1c: R= 2,4-diCl
1d: R= 2-Cl,4-NO$_2$
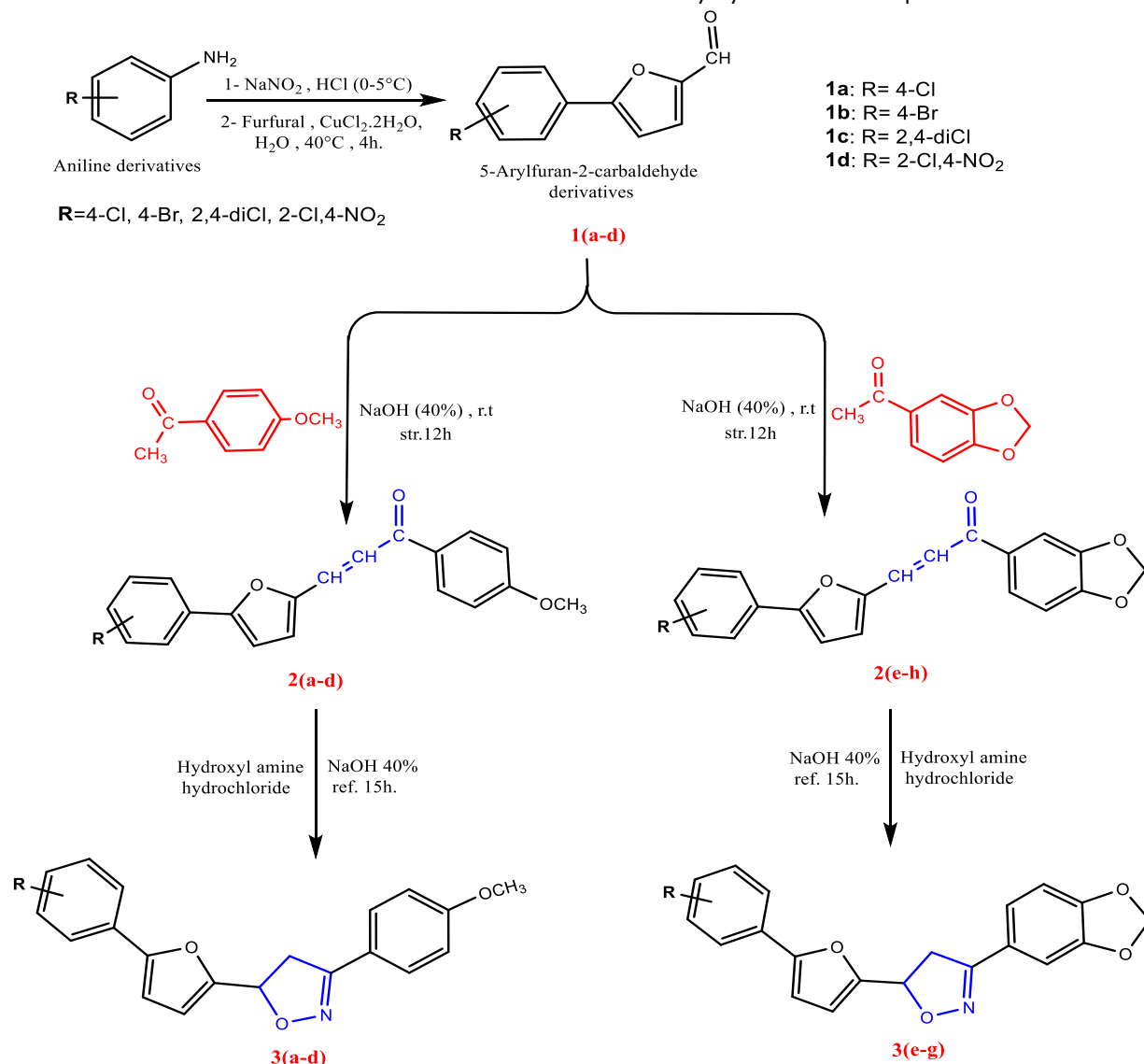
Scheme 1. Synthetic route of isoxazoline derivatives

The results of FTIR spectrum displayed that compound **1a** has weak sharp band at 2834 cm^{-1} attributed to C-H aldehyde, while a strong sharp band at 1673 cm^{-1} belongs to the stretching vibration of carbonyl group in the aldehyde compound. The C=C aromatic stretching vibration of furan ring appears as sharp strong band at 1661 cm^{-1} while the C=C aromatic stretching vibration of aromatic ring appears as medium strong band at 1589 cm^{-1}. The ^{1}H-NMR data of **1a** showed two doublet signals at 6.83 & 7.32 ppm which belong to (CH-CH) of furan ring, and protons of aromatic ring appear as two doublet signals at 7.41 & 7.75 ppm, as well as the presence of singlet signal at 9.65 ppm due to proton CO-H aldehyde. The mass spectrum of aldehyde compounds **1a** giving *m/z*: **206,** which represents the molecular ion **(M$^+$)** for **(C$_{11}$H$_7$ClO$_2$)**. FTIR spectrum of chalcone **2b** showed characteristic bands at 1646 cm^{-1} belong to C=O chalcone, 1599 cm^{-1} due to CH=CH chalcone and the CO-H aldehyde band disappeared. The ^{1}H-NMR data of **2b** summarized singlet signal at 3.88 ppm due to -OCH$_3$, doublet signal at 7.11 ppm belongs to aromatic ring proton. The two doublet signals appeared at 7.20 ppm & 7.27 ppm related to (CH-CH) furan while the doublet signal at 7.56 ppm belongs to C<u>H</u>=CH chalcone. The doublet signal at 7.69 ppm belongs to two aromatic ring protons while the doublet signal at 7.75 ppm related to other proton of CH=C<u>H</u> chalcone and finally the two doublet

signals at 7.91 ppm and 8.16 ppm belong to aromatic ring protons. The molecular ion in GC-mass spectrum showed m/z: **383(M$^+$)** and strongly confirmed the structure **(C$_{20}$H$_{15}$BrO$_3$)** of the prepared chalcone **2b**. The FTIR spectrum of isoxazoline compound **3b** exhibited characteristic bands at 2836 cm^{-1} due to C-H aliphatic of isoxazoline ring, 1650 cm^{-1} returned to C=N isoxazoline ring and the band that refers to carbonyl of chalcone disappeared. The ^{1}H-NMR spectrum of **3b** showed doublet of doublet signal at 3.75 ppm belonging to Ha-isoxazoline, singlet signal at 3.83 ppm belonging to O-CH$_3$, doublet of doublet signal at 3.87 ppm due to Hb-isoxazoline. The proton of Hx-isoxazoline appeared as multiplet signal at 5.73-5.78 ppm and disappeared the signals of CH=CH of chalcone. The two doublet signals appeared at

6.75 ppm and 7.02 ppm related to (CH-CH) furan, as well as four doublet signals appearing at: 7.05, 7.61, 7.65, and 7.70 ppm belonging to aromatic rings protons. The GC-Mass spectrum showed m/z: **398(M$^+$)** for **(C$_{20}$H$_{16}$BrNO$_3$),** which strongly confirmed the structure of isoxazoline **3b**.

Finally, this research included the in vitro assay of antimicrobial activity for the synthesized compounds against two strains of bacteria as well as fungi and exhibited good to moderate activity (according to previous studies, most of the chalcone and isoxazoline compounds have biological activity because they contain active groups in their composition), except chalcone **2g** did not exhibit any activity at a concentration of 10000 µg/ml, as illustrated in Table 1.

Table 1: Antimicrobial activity for the synthesized compounds

Comp.No.	Diameter of Inhibition zone (mm)				
	Gram positive bacteria		**Gram negative bacteria**		**Fungi**
	Staphylococcus aureus	*Staphylococcus epidermidis*	*Escherichia coli*	*Klebsiella sp.*	*Candida albicans*
2a	15	10	12	12	14
2b	13	11	12	10	14
2c	16	-	10	10	-
2d	-	12	12	12	15
2e	17	-	11	11	8
2f	16	11	11	11	10
2g	-	-	-	-	-
2h	17	12	12	12	10
3a	15	11	8	11	15
3b	15	13	8	10	15
3c	-	-	8	8	-
3d	12	11	8	9	13
3e	12	10	8	11	13
3f	15	11	8	13	13
3g	14	11	8	10	12
Amoxicilline	23	35	20	22	-
Floconazol	-	-	-	-	13

3.1. Docking study

One of the most significant computational methods for determining the ideal orientation of a small organic molecule to a particular receptor, enzyme, or binding pocket is the docking technique, which is such a flexible process that ligands and receptors must alter their shapes to fit together well (28). A three-dimensional array of structurally recognized receptors, proteins, or enzymes is used in the first phase of docking approaches to determine the best conformations and orientations for ligand binding (22). Scores that are optimally linked with free binding energy are used to rate the exploration of various positions inside the binding pocket (29). The docking study of the potent active derivatives 2h and 3b toward antimicrobial species inside the active site of glucosamine-6-phosphate synthase, antibacterial and antifungal agents' possible targets were investigated. The X-ray shows that the following residues are present in the enzyme's binding pocket, Cys 300, Gly 301, Thr 302, Ser 303, Ser 347, Gln 348, Ser 349, Thr 352, Val 399, Ser 401, Ala 602, and Lys 603 (30), as shown in Fig.1.
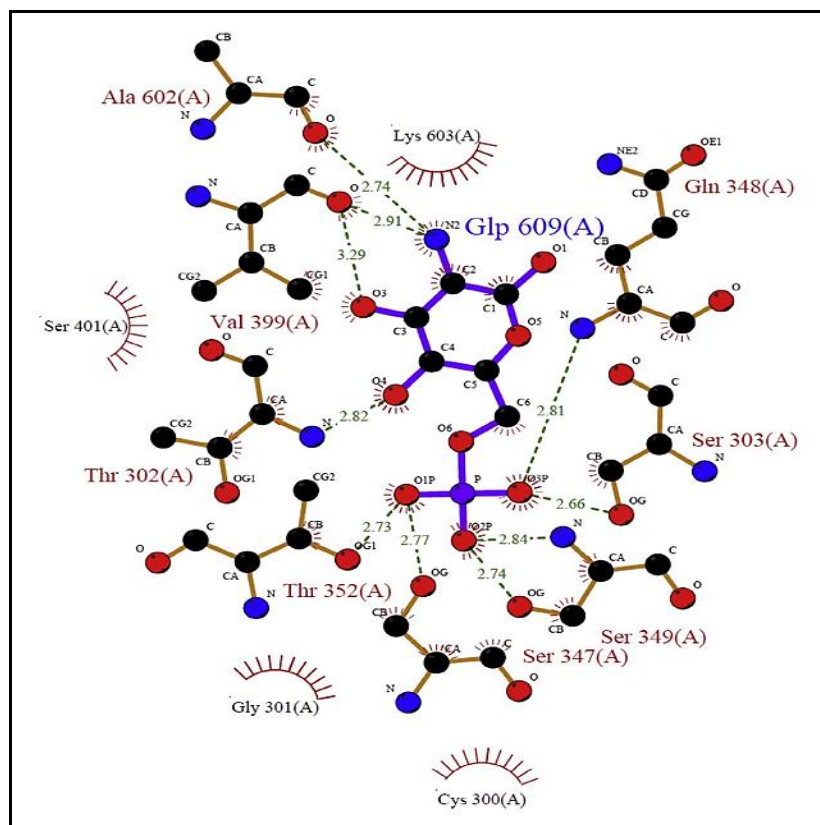
Figure 1. The binding of glucosamine-6-phosphate inside the active site of target enzyme.

The binding energy of active compounds **2h** and **3b** within the established 3D structure of the target enzyme was assessed using Autodock 4.2. The binding of the best-generated conformers to the target enzyme's binding pocket is illustrated in Figures 2 and 3, respectively.

Mahdi IS et al. JOTCSA. 2024;11(1):217-232.

RESEARCH ARTICLE

3D structure of glucoseamine-6-phosphate synthase (GlcN-6-P)

The first generated conformer inside the binding pocket of enzyme

The second generated conformer inside the binding pocket of enzyme

The third generated conformer inside the binding pocket of enzyme

The fourth generated conformer inside the binding pocket of enzyme

The fifth generated conformer inside the binding pocket of enzyme	The sixth generated conformer inside the binding pocket of enzyme
The seventh generated conformer inside the binding pocket of enzyme	**The eighth generated conformer inside the binding pocket of enzyme**
The ninth generated conformer inside the binding pocket of enzyme	**The tenth generated conformer inside the binding pocket of enzyme**

Figure 2. The docking of the best generated conformers of the potent discovered hit 2h inside the binding pocket of glucoseamine-6-phosphate synthase (GlcN-6-P).

3D structure of glucoseamine-6-phosphate synthase (GlcN-6-P)

The first generated conformer inside the binding pocket of enzyme

The second generated conformer inside the binding pocket of enzyme

The third generated conformer inside the binding pocket of enzyme

The fourth generated conformer inside the binding pocket of enzyme

The fifth generated conformer inside the binding pocket of enzyme

The sixth generated conformer inside the binding pocket of enzyme

The seventh generated conformer inside the binding pocket of enzyme	**The eighth generated conformer inside the binding pocket of enzyme**
The ninth generated conformer inside the binding pocket of enzyme	**The tenth generated conformer inside the binding pocket of enzyme**

Figure 3. The docking of the best generated conformers of the potent discovered hit 3b inside the binding pocket of glucoseamine-6-phosphate synthase (GlcN-6-P)

As indicated by molecular docking parameters (Table 2), the high ranking binding energy of compound **2h** was -8.35 kcal mol^{-1} for the best generated conformer. As indicated by Figure 2, the best conformer binds the active site with three H bonds. The intermolecular energy was -9.85 kcal mol^{-1}. Furthermore, the derivative **3b** fits the binding pocket with two hydrogen bonds, the first with HN residue of THR302 and the second with HG1 of THR352. The binding energy

of the best generated conformer was -8.13 kcal mol^{-1} with intermolecular energy equal to -9.32 kcal mol^{-1}. The docking results of all generated conformers of compounds **2h** and **3b** within the binding pocket are strongly proportional to the antibacterial activities, as shown in Table 1. The inhibition constant Ki, intermolecular energy, and hydrogen bonds were also determined and depicted in Table 2.

Table 2: Docking parameters of compound 2h and 3b

Compounds	Conformers	Binding Energy (Kcal mol^{-1})	Inhibition constant (µM)	Intermolecular energy (kcalmol^{-1})	H-bonds	Bonding
2h	1	-8.35	0.752×10^{-3}	- 9.85	4	SER401:HG:LIG:O ALA602:HN: LIG:O SER401:HN:LIG:O VAL607:HN: LIG:O
	2	-8.03	1.30	- 9.52	4	ASN600:HD22:LIG:O ALA602:HN:LIG:O SER401:HN:LIG:O SER401:HG:LIG:O
	3	-7.84	1.79	- 9.33	3	SER401:HG:LIG:O ALA602:HN:LIG:O SER401:HG:LIG:O
	4	-7.75	2.09	- 9.24	2	ALA602:HN:LIG:O SER401:HG:LIG:O
	5	-7.43	3.55	- 8.93	4	ASN600:HD22:LIG:O ALA602:HN:LIG:O SER401:HN:LIG:O SER401:HG:LIG:O
	6	-6.90	8.80	- 8.39	1	SER401:HG:LIG:O
	7	-6.89	8.90	- 8.38	2	GLN348:HN:LIG:O SER349:HN:LIG:O
	8	-6.87	9.23	- 8.36	3	GLN348:HN:LIG:O ASN305:HD22:LIG:O SER349:HN:LIG:O
	9	-6.81	10.21	- 8.30	2	GLN348:HN:LIG:O SER349:HN:LIG:O
	10	-6.76	11.12	- 8.25	2	ASN305:HD22:LIG:O SER401:HG:LIG:O
3b	1	-8.13	1.10	- 9.32	2	THR302:HN:LIG:N THR352:HG1:LIG:O
	2	-8.06	1.24	- 9.25	2	THR302:HN:LIG:N THR352:HG1:LIG:O
	3	-8.01	1.34	- 9.21	2	THR302:HN:LIG:N THR352:HG1:LIG:O
	4	-7.98	1.43	- 9.17	2	THR302:HN:LIG:N THR352:HG1:LIG:O
	5	-7.95	1.48	- 9.15	2	THR302:HN:LIG:N THR352:HG1:LIG:O
	6	-7.88	1.66	- 9.08	2	THR302:HN:LIG:N THR352:HG1:LIG:O
	7	-7.85	1.76	- 9.04	2	THR302:HN:LIG:N THR352:HG1:LIG:O
	8	-7.84	1.80	- 9.03	1	THR352:HG1:LIG:O
	9	-7.83	1.83	- 9.02	2	THR352:HG1:LIG:O THR302:HN:LIG:N
	10	**-7.79**	**1.69**	**- 8.98**	**1**	**THR352:HG1:LIG:O**

4. CONCLUSION

This project led to the synthesis of new chalcone compounds in order to create new active isoxazoline derivatives. The produced compounds were confirmed via spectroscopic techniques such as FTIR, ^{1}H-NMR, and GC-Mass spectroscopy. The antimicrobial activity was evaluated for new derivatives, and it was found that most of the synthesized compounds exhibited good to moderate antimicrobial activity. The effectiveness was confirmed by studying the docking study of the most potent compounds (**2h** and **3b**) and choosing the best conformation and orientation for these compounds to bind to the binding site of the enzyme glucosamine-6-phosphate synthase (GlcN-6-P synthase), the molecular target enzyme identified in microbial species, in order to clarify the activity of the new derivatives. The docking study promoted the idea that the newly discovered compounds could serve as novel antimicrobial agents.

5. SUPPORTING INFORMATION

Spectral data and antimicrobial figures for the newly synthesized compounds.

6. ACKNOWLEDGMENTS

7. REFERENCES

1. Avan I, Hall CD, Katritzky AR. Peptidomimetics via modifications of amino acids and peptide bonds. Chemical Society Reviews. 2014;43(10):3575–94. Available from: <URL>

2. Pozharskii AF, Katritzky AR, Soldatenkov AT. Heterocycles in life and society. Wiley Chichester; 2011. Available from: <DOI>

3. Michelini LJ, Castro MRC, Custodio JMF, Naves LFN, Vaz WF, Lobón GS, et al. A novel potential anticancer chalcone: Synthesis, crystal structure and cytotoxic assay. Journal of Molecular Structure. 2018;1168:309–15. Available from: <URL>

4. Sharma B, Agrawal SC, Gupta KC. Colour reactions of chalcones and their mechanism (a review). Oriental Journal of Chemistry. 2008;24(1):289. Available from: <URL>

5. Singh P, Anand A, Kumar V. Recent developments in biological activities of chalcones: A mini review. European Journal of Medicinal Chemistry. 2014;85:758–77. Available from: <URL>

6. Sagar P, Vilasrao K, Ramesh B, Sachin SM, Vijay P. Synthesis & Evaluation of isoxazole for their antimicrobial activity. International Journal of Comprehensive and Advanced Pharmacology. 2017;2:19–26.

7. Kaur K, Kumar V, Sharma AK, Gupta GK. Isoxazoline containing natural products as anticancer agents: A review. European Journal of Medicinal Chemistry. 2014;77:121–33. Available from: <URL>

8. Kudva NUN, Kotian SY, Basavanna V, Vicas CS, Byrappa SK, Shridevi D, et al. Synthesis, characterization, and evaluation of biological activities of imidazolyl-isoxazoline analogue. Biointerface Research in Applied Chemistry. 2020;10(6): 7187-7197. Available from: <URL>

9. Thalassitis A, Hadjipavlou-Litina DJ, Litinas KE, Miltiadou P. Synthesis of modified homo-N-nucleosides from the reactions of mesityl nitrile oxide with 9-allylpurines and their influence on lipid peroxidation and thrombin inhibition. Bioorganic & Medicinal Chemistry Letters. 2009;19(22):6433–6. Available from: <URL>

10. Filali I, Bouajila J, Znati M, Bousejra-El Garah F, Ben Jannet H. Synthesis of new isoxazoline derivatives from harmine and evaluation of their anti-Alzheimer, anti-cancer and anti-inflammatory activities. Journal of Enzyme Inhibition and Medicinal Chemistry. 2015;30(3):371–6. Available from: <URL>

11. Al Houari G, Kerbal A, Bennani B, Baba MF, Daoudi M, Hadda T Ben. Drug design of new antitubercular agents: 1, 3-dipolar cycloaddition reaction of para-substituted-benzadoximes and 3-para-methoxy-benzyliden-isochroman-4-ones. Arkivoc. 2008;12:42–50. Available from: <URL>

12. Bhardwaj S, Bendi A, Singh L. A Study on Synthesis of Chalcone Derived-5-Membered Isoxazoline and Isoxazole Scaffolds. Current Organic Synthesis. 2022;19(5):643–63. Available from: <URL>

13. Zeng Y, Zhang H, Wang B, Zhang L, Xue L, Zhao X. Synthesis and biological evaluation of various new bis-isoxazoline derivatives as potential antioxidant additives. Journal of Chemical Research. 2016;40(9):558–63. Available from: <URL>

14. Marri S, Kakkerla R, Murali Krishna MPS, Venkat Rajam M. Synthesis and antimicrobial evaluation of isoxazole-substituted 1, 3, 4-oxadiazoles. Heterocyclic Communications. 2018;24(5):285–92. Available from: <URL>

15. Motegaonkar MB. Synthesis and Analysis of Antimicrobial Properties of Isoxazoline. International Journal of Engineering Research & Technology. 2020;9:386–90. Available from: <DOI>

16. Alawad KM, Mahdi MF, Raauf AMR. Molecular Docking study, and In vitro Evaluation of Antitumor Activity of Some New Isoxazoline and Pyrazoline Derivatives of Nabumetone against breast cancer cell line (MCF-7). Al Mustansiriyah Journal of

Pharmaceutical Sciences. 2022;22(3):24–34. Available from: <URL>

17. Kumar KA, Jayaroopa P. Isoxazoles: molecules with potential medicinal properties. International Journal of Pharmaceutical and Chemical Sciences. 2013;3:294–304.

18. Kauthale S, Tekale S, Damale M, Sangshetti J, Pawar R. Synthesis, biological evaluation, molecular docking, and ADMET studies of some isoxazole-based amides. Medicinal Chemistry Research. 2018;27:429–41. Available from: <URL>

19. Lather A, Sharma S, Khatkar A. Virtual screening of novel glucosamine-6-phosphate synthase inhibitors. Combinatorial Chemistry & High Throughput Screening. 2018;21(3):182–93. Available from: <URL>

20. McConnell D. The problem of the carbonate apatites. Journal of the American Chemical Society. 1955;77(8):2344. Available from: <URL>

21. Puterová Z, Sterk H, Krutošíková A. Reaction of substituted furan-2-carboxaldehydes and furo [b] pyrrole type aldehydes with hippuric acid. Molecules. 2004;9(1):11–21. Available from: <URL>

22. Tomi IHR, Al-Daraji AHR, Abdula AM, Al-Marjani MF. Synthesis, antimicrobial and docking study of three novel 2, 4, 5-triarylimidazole derivatives. Journal of Saudi Chemical Society. 2016;20:S509–16. Available from: <URL>

23. Revanasiddappa BC, Kumar MV, Kumar H. Synthesis and Antioxidant Activity of Novel Pyrazoline Derivatives. Hygeia Journal for Drugs and Medicines. 2018;10(1):43-49. Available from: <URL>

24. Abdel-Rahman AA-H, Abdel-Megied AE-S, Hawata MAM, Kasem ER, Shabaan MT. Synthesis and antimicrobial evaluation of some chalcones and their derived pyrazoles, pyrazolines, isoxazolines, and 5, 6-Dihydropyrimidine-2-(1 H)-thiones. Monatshefte für Chemie - Chemical Monthly. 2007;138:889–97. Available from: <URL>

25. Mohamed MA, Nasr M, Elkhatib WF, Eltayeb WN. In vitro evaluation of antimicrobial activity and cytotoxicity of different nanobiotics targeting multidrug resistant and biofilm forming Staphylococci. BioMed Research International. 2018;2018. Available from: <URL>

26. Savin KA. Writing reaction mechanisms in organic chemistry. Academic Press; 2014.

27. Ismail AH, Abdula AM, Tomi IHR, Al-Daraji AHR, Baqi Y. Synthesis, antimicrobial evaluation and docking study of novel 3, 5-disubstituted-2-isoxazoline and 1, 3, 5-trisubstituted-2-pyrazoline derivatives. Medicinal Chemistry. 2021;17(5):462–73. Available from: <URL>

28. Fan J, Fu A, Zhang L. Progress in molecular docking. Quant Biol. 2019;7:83–9. Available from: <URL>

29. Ferreira LG, Dos Santos RN, Oliva G, Andricopulo AD. Molecular docking and structure-based drug design strategies. Molecules. 2015;20(7):13384–421. Available from: <URL>

30. Hussein SAA, Kubba A, Abdula AM. Docking study of some new 2, 5-Disubstituted-1, 3, 4-thiadiazole derivatives against glucosamine-6-phosphate synthase. Journal of Applied Chemistry. 2016;12(1):1–10. Available from: <DOI>

RESEARCH ARTICLE

GO@dopamine-Cu as a Green Nanocatalyst for the Efficient Synthesis of Fully Substituted Dihydrofuran-2(5*H*)-ones

Neda Niknam [1] iD , Nader Noroozi Pesyan* [1] iD

[1]Department of Organic Chemistry, Faculty of Chemistry, Urmia University, 57159, Urmia, Iran

Abstract: A new nanocatalyst graphene oxide@dopamine-Cu was synthesized, and its structure was characterized by fourier transform infrared (FT-IR), X-ray diffraction (XRD), scanning electron microscopy (SEM), transmission electron microscopy (TEM), Energy Dispersive X-ray Spectrometry (EDX), and thermogravimetric analysis – differential thermal analysis (TGA-DTA) techniques. The three-component one-pot reaction between an arylamine, aromatic aldehyde, and acetylenic carboxylate was achieved and formed methyl 5-oxo-2-aryl-4-(arylamino)-2,5-dihydrofuran-3-carboxylate derivatives (**4**) in the presence of the catalytic amount of graphene oxide@dopamine-Cu nanocatalyst in high yield. Molecular structures of products were characterized by FT-IR, ^{1}H, ^{13}C nuclear magnetic resonance (NMR), and Mass spectroscopy techniques. Representatively, the mass fragmentation of **4a** was discussed, and the structure was confirmed. Easy reaction, high performance, and easy catalyst recyclability are the main advantages of this work. This nanocatalyst is recycled up to five successive runs.

1. INTRODUCTION

Nowadays, green chemistry and its features have caused nanocatalysts to be significant in organic synthesis and the development of green chemistry. In addition, much attention has been focused on preparing novel catalysts, which are important objects (1–3). Preparing new composites using graphene oxide (GO) has recently attracted much attention worldwide. In this regard, the GO supports many catalysts designation and is highly applicable. Some of the advantages of GO include its active sites and pores' thermal stability, high selectivity, and high mechanical strength (4,5).

Furthermore, there are various functional groups such as carbonyl, hydroxyl, carboxylic acid, and epoxide on GO sheets, in which GO can easily make covalent bonds to various functional groups in other molecules. Also, the immobilization of some metallic nanoparticles (NPs) on GO made them used in many applications, such as catalysts, optoelectronics, and sensors for energy storage and generation (6–10). Using graphite oxidation for the synthesis of GO is one of the most known and useful protocols in the preparation of materials based on GO (11,12). Several oxygenic functional groups on GO sheet surface are caused to be hydrophilic (13), which can be reacted and functionalized by different reactants and organic ligands (14).

In recent years, multicomponent reactions (MCRs) have been one of the best tools in organic synthesis (15–19). The MCRs are one of the best ways to synthesize useful and accessible compounds used to synthesize pharmaceutical and drug compounds. The MCRs have a wide range of benefits such as high atom economy by reacting three or more

reactants in one step and the ability to synthesize assigned and desired compounds.

Many biologically active natural products and synthetic pharmaceutical drugs such as rubrolide A and benfurodil hemisuccinate have dihydrofuranone ring structure skeleton. The furanone five-membered heterocyclic compounds, including lactones, show a wide spectrum of biological and pharmacological behaviors such as anticancer, antibacterial, antifungal, and anti-oxidant (20–24). Full substituted furans are important in organic synthesis; they are important in many natural product compounds and are common structural textures in pharmaceuticals and flavors (25,26). Furan and dihydrofuran skeletons display several biological and pharmaceutical behaviors such as anticancer (27,28), anti-inflammatory (29,30), antimicrobial, (31–34) antifungal (35) and anti-viral HIV-1 (36) activities.

Several catalytic routes for the synthesis of 2(5*H*)-furanone were reported in the literature, e.g., acidic ionic liquid on silica-coated magnetic nanoparticles (19), graphene-oxide/Schiff base N_2O_4 ligand-palladium (14) and using BF@ Propyl /dopamine/ Palladium (37). Some synthetic routes have also been reported to access fully substituted furan derivatives, for example, the reaction of α-substituted ketones with β-dicarbonyl derivatives (38). Due to the eligibility and usability of these compounds, several various methods were achieved and used, such as $Pd(Ph_3P)_2Cl_2$ (34), $Al(HSO_4)_3$ (36), $FeCl_3$ (39), and lactic acid (40). These conditions suffer from the following problems, e.g., long reaction time, troublesome work-up, low yields, environmental pollution, and disagreeable reaction conditions. Herein, GO@dopamine-Cu as a recoverable nanocatalyst was used for the one-pot synthesis of full substituted dihydrofuran-2(5*H*)-one derivative (**4**) in high yield.

2. EXPERIMENTAL SECTION

2.1 Materials and Instruments
Chemicals were purchased from Fluka, Merck, and Aldrich Chemicals. All products were determined by comparing spectral data (^{1}H NMR and ^{13}C NMR) and physical data with valid samples. FT-IR spectra were measured by a Perkin Elmer Spectrum Version 10.02.00 spectrometer using KBr pellets. Mass spectra were measured by a Shimadzu GC MS-QP 1000 EX. The Buchi 510 apparatus was used to obtain melting points. The ultrasonic apparatus for sonication was used SONICA 50Hz 230/240 V. The TEM, SEM, and EDX analyses were taken by Zeiss-EM10C-100KV, EM3200, and FESEM-SIGM (Germany), respectively. TGA analysis was measured using the PYRIS DIAMOND model.

2.2. Synthesis of GO@dopamine-Cu

2.2.1. Preparation of graphene oxide
In a 500-mL round bottom flask equipped with a magnetic stirrer, 2.5 g of natural graphite were placed together with 50 mL of concentrated sulfuric acid (98%). The mixture was swirled for 30 min. Subsequently, 1.25 g of sodium nitrate were added to the flask and violently mixed. Next, the reaction mixture was transferred from the flask into an ice bath. Proceed by introducing 7 g of potassium permanganate ($KMnO_4$) and gradually adding 25 mL of hydrogen peroxide (30% concentration) while continuously stirring the solution for 45 min. The reaction mixture, which was black, underwent a washing process using 1 mL of hydrochloric acid (37%). Subsequently, the mixture was subjected to centrifugation and subsequent drying.

2.2.2. Immobilization of 2-(3,4-dihydroxy phenyl)ethyl amine (dopamine) on graphene oxide
In a 250 mL round-bottom flask containing a magnetically stirred setup, 0.5 g of graphene oxide (GO) and 25 mL of toluene were combined and dispersed. The resulting mixture was subjected to sonication for 20 minutes at room temperature. Subsequently, a quantity of 1.5 g of dopamine was introduced and subjected to reflux for 24 hours. The precipitate was separated using filtration, followed by rinsing with a small amount of toluene and subsequently with ethanol. Finally, the precipitate was dried at 100 °C under vacuum conditions.

2.2.3. Synthesis of GO@dopamine/Cu
In a 50 mL round bottom flask equipped with a magnetic stirrer, put 0.5 gr GO@dopamine and the solution of 0.5 g (1 mmol) copper acetate in 10 mL acetonitrile. The reaction mixture was sonicated for 15 minutes and then stirred for 24 hrs at 90 °C. Afterwards, it was filtered off, washed with a few mL of acetone, and dried in an oven for 18 hrs at 50 °C.

2.3. General Procedure for the Synthesis of 4a in the Presence of GO@dopamine/Cu as a Model Reaction
Dimethyl acetylenedicarboxylate (1 mmol), benzaldehyde (1 mmol), and aniline (1 mmol) were introduced into a 25 mL round bottom flask fitted with a magnetic stirrer. Additionally, 0.05 g of nanocatalyst was included in 15 mL of ethanol. The resulting mixture was subjected to stirring and refluxing for 30 minutes. The course of the reaction was seen through thin-layer chromatography (TLC) with a solvent mixture consisting of n-hexane and ethyl acetate at a ratio of 2:10 (v/v). Following the conclusion of the reaction, the resulting mixture was subjected to filtration, followed by a thorough washing with a small volume of ethanol. Subsequently, the obtained solid was subjected to recrystallization in hot ethanol. The spectral data for **4a** is shown here in a representative manner.

*2.3.1. Methyl 5-oxo-2-phenyl-4-(phenylamino)-2,5-dihydrofuran-3-carboxylate (**4a**)*

Light yellow solid (Yield: 85%); M.p. 187-189 °C; FT-IR (KBr): ῡ (cm^{-1}) 3263, 3210, 2958, 1703, 1682, 1499, 1457, 1383, 1234, 1136, 755; ^{1}H NMR (400 MHz, DMSO-d_6, δ, ppm): 3.57 (s, 3H, OCH$_3$), 6.06 (s, 1H, CH), 7.07 (m, 1H, Ar-H), 7.24 (m, 7H, Ar-H), 7.55 (m, 2H, Ar-H), 11.74 (s, 1H, NH); ^{13}C NMR (100 MHz, DMSO-d_6, δ, ppm): 51.1, 60.5, 111.9, 122.5, 127.6, 128.2, 128.6, 136.2, 136.5, 152.5, 162.4, 163.9; MS (m/z): 309.1 (M$^+$, 100%,

base peak), 277, 250, 222, 189, 158, 130, 102, 77, 51.

3. RESULTS AND DISCUSSION

3.1. Synthesis of Nanocatalyst and Dihydrofuran-2(5*H*)-one derivatives

This article first described the synthesis and characterization of a new nanocatalyst of GO@dopamine-Cu (Scheme 1) and followed using this nanocatalyst for the synthesis of dihydrofuran-2(5*H*)-one derivatives **4a-4l** (Table 1).
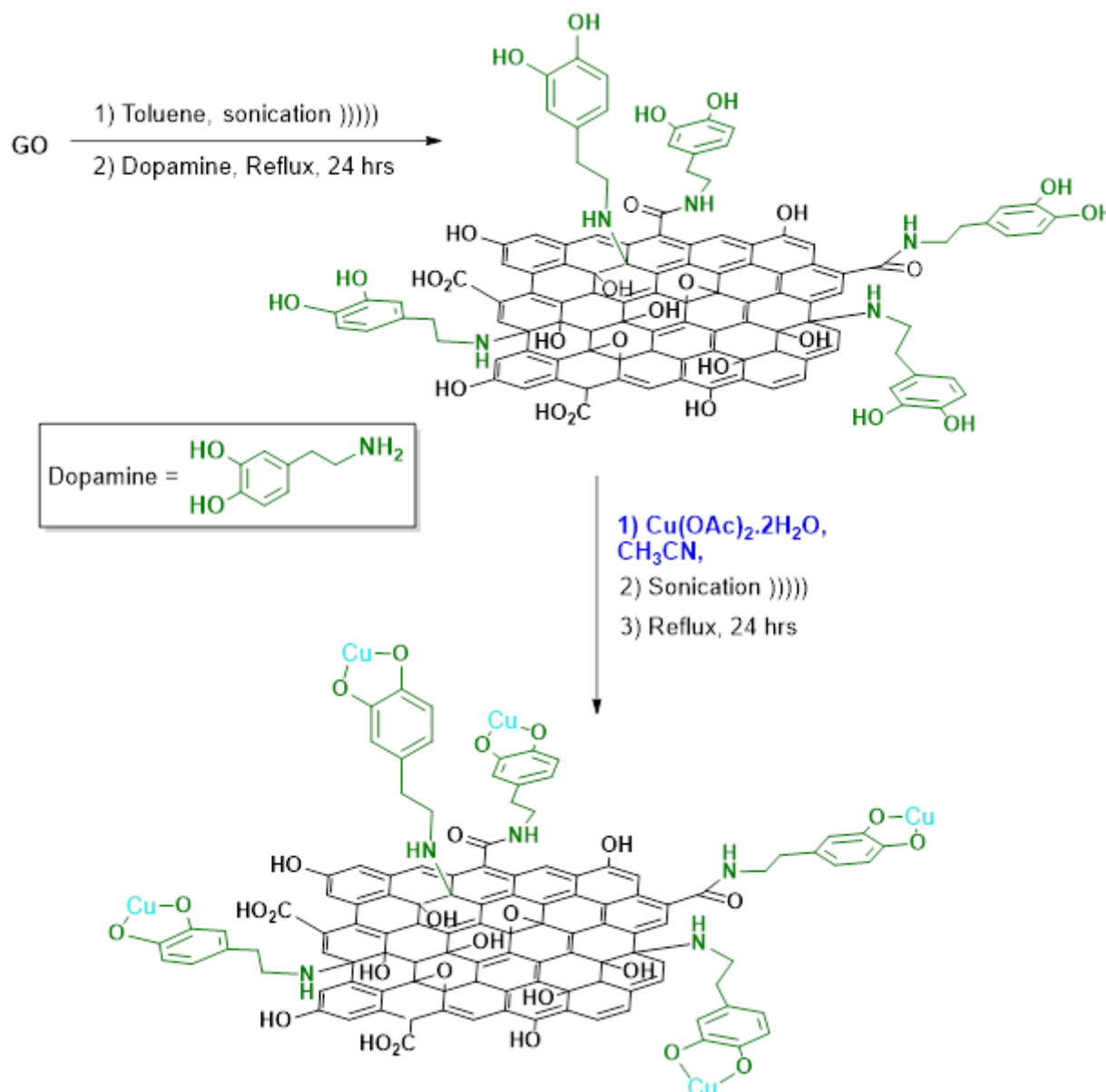
Scheme 1. Synthesis of GO@dopamine-Cu nanocatalyst.

Table 1. Synthesis of dihydrofuran-2(5*H*)-one derivatives in the presence of GO@dopamine-Cu nanocatalyst.
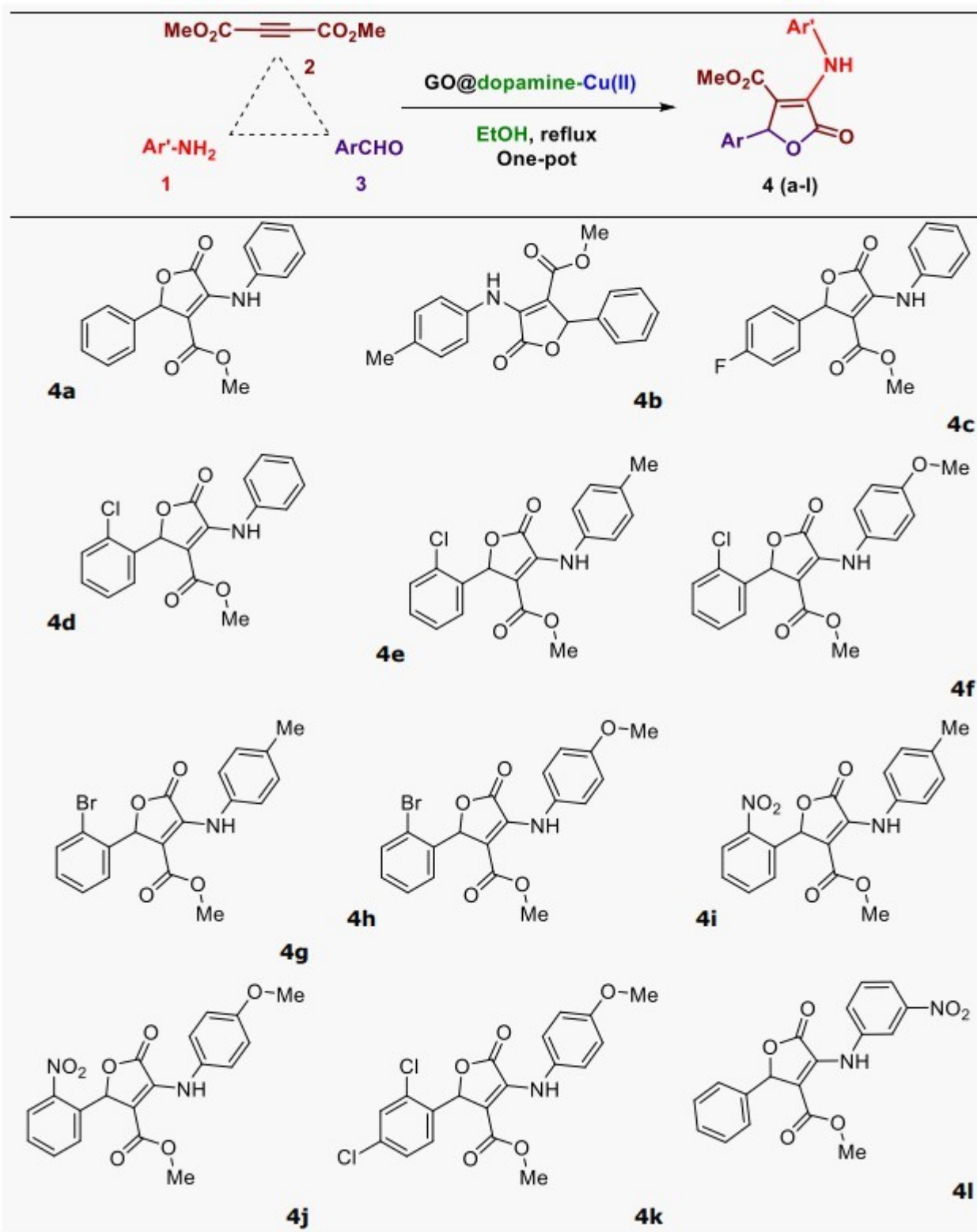
Representatively, the FT-IR spectrum of **4a** showed two bands at 3262 and 3210 cm^{-1} for NH stretching frequencies. Two bands at 1702 and 1681 cm^{-1} correspond to two carbonyl stretching frequencies of dihydrofuran and methyl carboxylate carbonyl groups, respectively. ^{1}H NMR spectrum of this compound showed a broad peak at δ 11.73 ppm for NH proton, at δ 7.10-7.54 ppm for two phenyl protons, a singlet at δ 6.53 ppm for benzylic CH proton, and finally, a singlet at δ 3.57 ppm for OMe

protons. ^{13}C NMR spectrum of this compound showed fourteen distinct peaks and confirmed the assigned structure. Representatively, the spectral data for **4a** is presented in the experimental section. (Other spectral data are available; for more information, see Supplemental materials). The MS spectrum of **4a** showed m/z 309 (100%, base peak, molecular ion mass) as a molecular ion mass and a fragment at m/z 250 (75%) via the loss of methyl carboxylate fragment. The proposed full fragmentation of 4a is shown in Scheme 2, confirming the assigned structure.
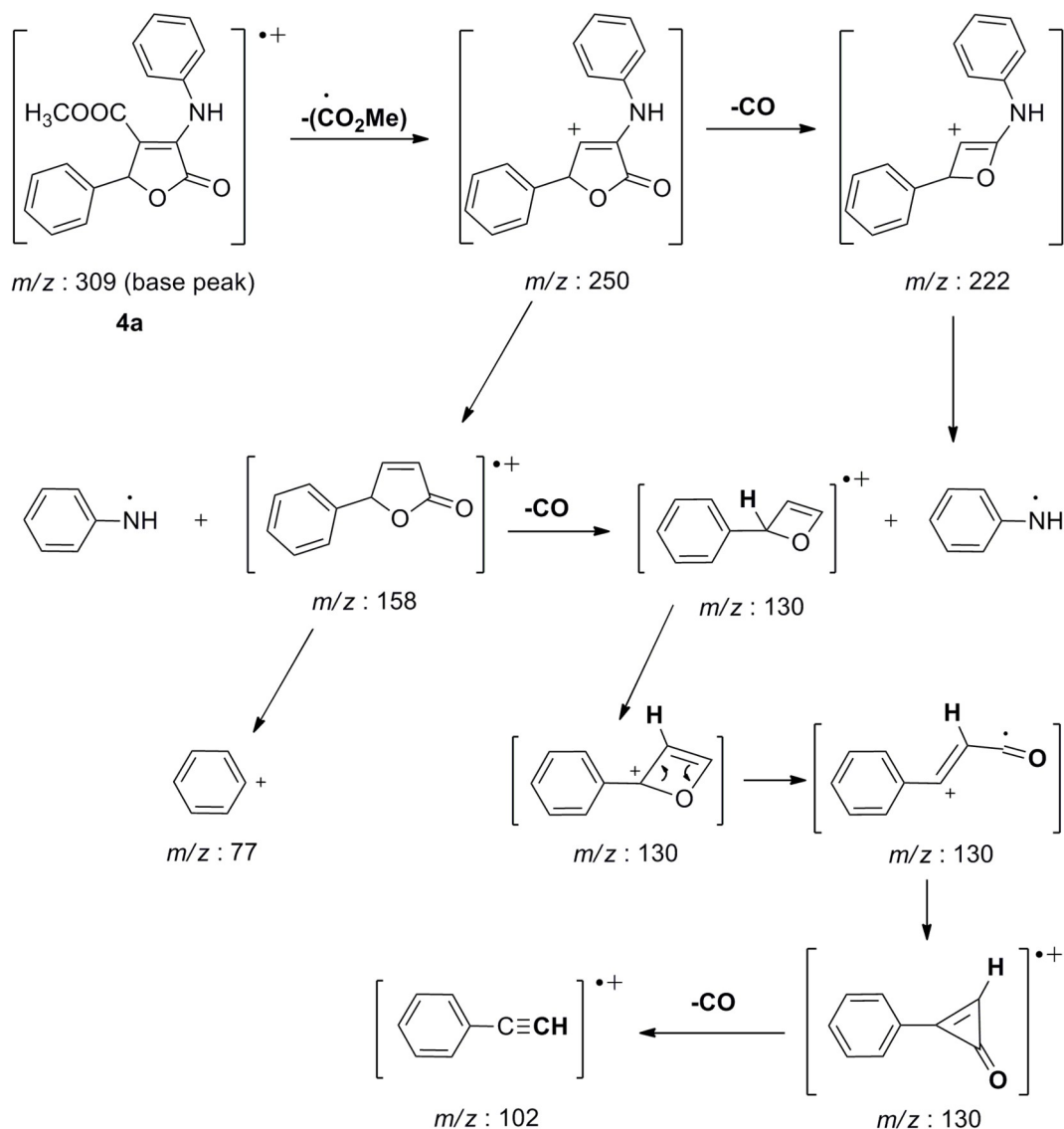
Scheme 2. Representative full mass fragmentations of molecular ion mass of **4a**.

3.2. Nanocatalyst characterization

FT-IR spectra of GO (a), GO@dopamine (b), and GO@dopamine-Cu (c) are shown in Figure 1. As can be seen in Figure 1a, the stretching frequencies at 1725 and 1622 cm^{-1} corresponding to carboxylic acid's carbonyl groups and C=C bond of phenyl rings in GO. The bands at 1050 and 1230 cm^{-1} are of C-O stretching frequencies of hydroxyl and epoxy groups on the GO surface, respectively. In Figure 1b, the bands at 1358 and 1045 cm^{-1} stretching frequencies correspond to the C-O and C-N bonds, respectively, in which dopamine interacted with GO functional groups. Figure 1c shows the spectrum of GO@dopamine-Cu in which nearly all peaks of GO and dopamine are shown. The decrease of the peak at 3350 cm^{-1} is attributed to the immobilization of Cu on dopamine and GO surfaces.
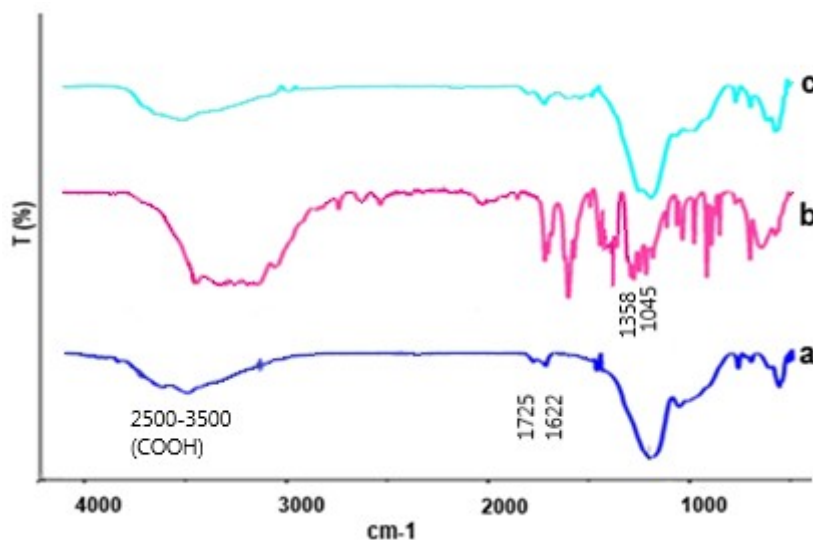
Figure 1. FT-IR spectra of GO (a), GO@dopamine (b), and GO@dopamine-Cu (c).

The XRD patterns of GO and GO@dopamine-Cu are shown in Figure 2. Peaks at 2θ 25° and 43° correspond to GO crystalline sheets. Peaks at 2θ 9.7°, 23,9°, 36.5°, and 42.1° are corresponding to functionalized GO by dopamine and Cu immobilization.
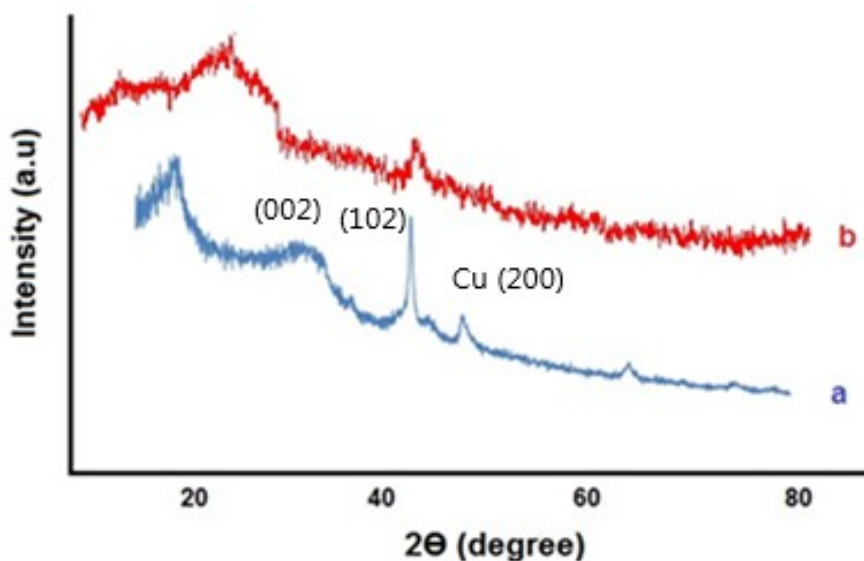
Figure 2. XRD patterns of GO@dopamine-Cu (a) and GO (b).

The morphology of GO@dopamine-Cu according to the scanning electron microscopy (SEM) reveals that the GO parent morphology is retained, as shown in Figure 3a. Transmittance electron microscopy (TEM) image of nanocatalyst obviously showed the graphene oxide nanosheets link to dopamines and also immobilized copper nanoparticles (Cu-NPs) on the GO nanosheets are shown in Figure 3b. These observations confirmed the immobilization of Cu-NPs on the surface of GO@dopamine nanosheets. EDS data demonstrated that the related elements (C, Cu, O, and N) of GO@dopamine-Cu displayed 53.8, 24.6, 11.4, and 10.2 %, respectively (Figure 3c).
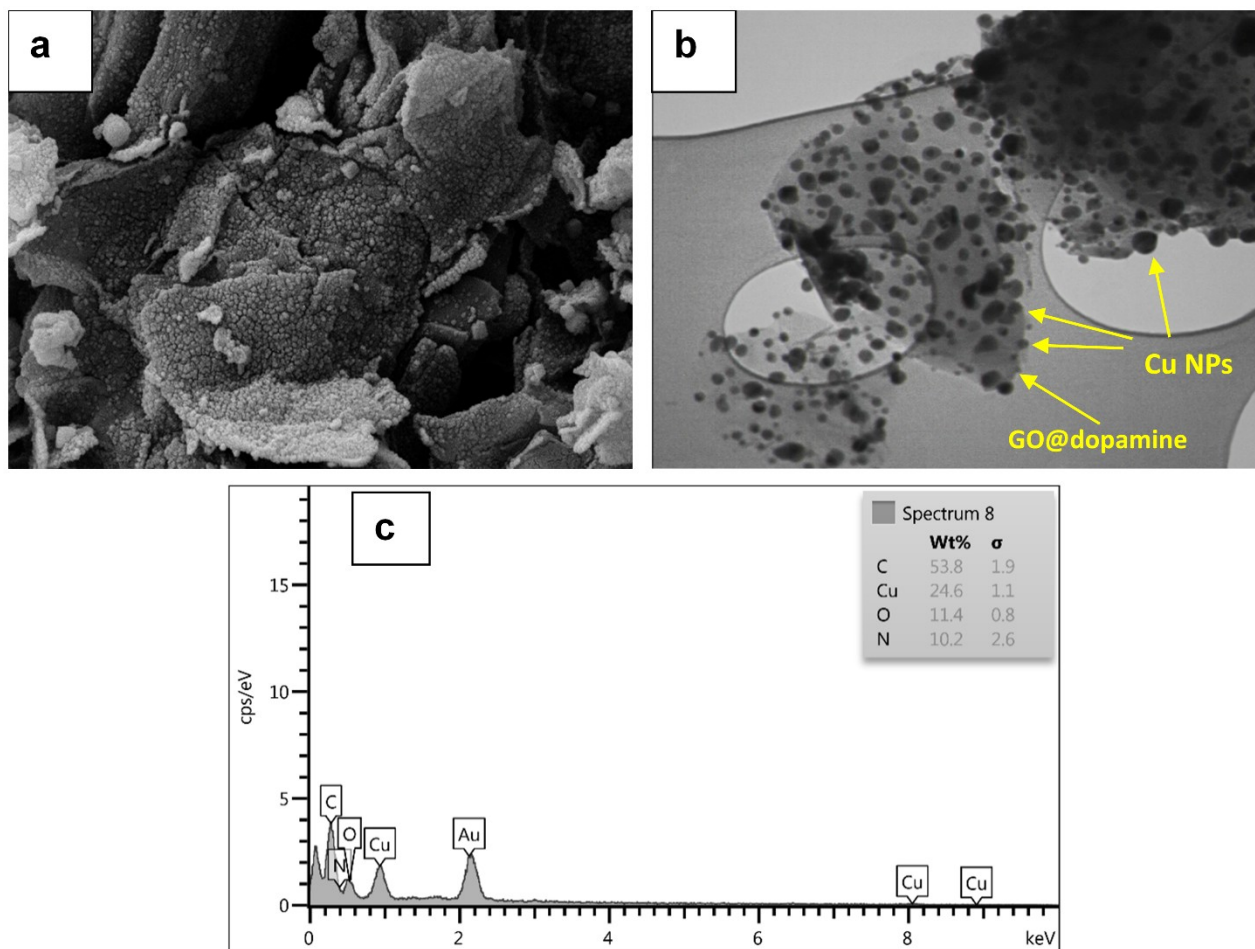
Figure 3. SEM (a) and TEM images (b) and EDS data of GO@dopamine-Cu (c).

TGA and DTA of GO@dopamine-Cu are shown in Figure 4. The weight loss at the range of 0-100 °C corresponds to the loss of solvents and at the range of 135-200 °C related to the loss of copper ions from the nanocatalyst surface. The weight loss at the 200-400 °C range was attributed to the loss of dopamine ligands. Finally, the weight loss at up to 400 °C corresponded to the decomposition of the GO structure.
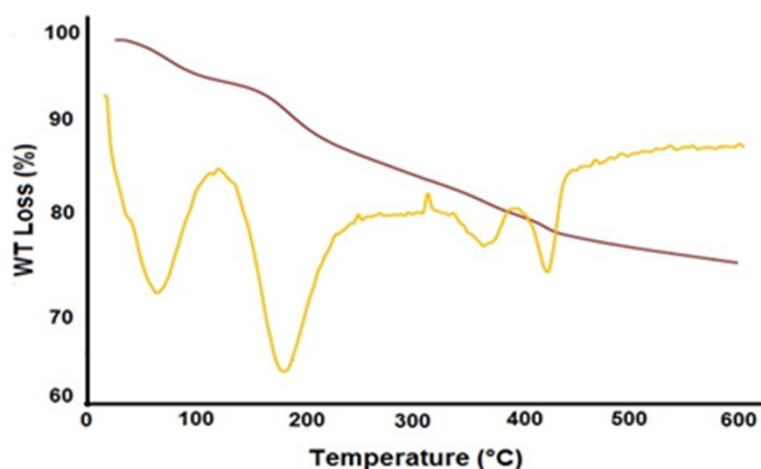
Figure 4. TGA-DTA analysis of GO@dopamine-Cu.

3.3. Catalytic activity

In this step, the activity of the proposed nanostructure was investigated as a beneficial and eco-friendly component in the synthesis of **4a** as a model reaction. To obtain the optimum situation, different amounts of catalyst, various types of solvents, time, and temperatures were appraised. As evident, the reaction yield is 15% in solvent-free conditions in the presence of 0.05 g of nanocatalyst (Table 2, entry 1). With this amount of nanocatalyst in H_2O:EtOH (1:1/ v:v), the reaction yield slightly increased over a long time (Table 2, entry 2). By increasing the amount of nanocatalyst to 0.06 and 0.10 g in EtOH solvent, no significant change in

reaction progress was observed (86 and 85%, respectively) under the same condition (Table 2, entries 5 and 7). By appraising various solvents (H_2O, CH_3CN, and EtOH) within the optimal state, EtOH had the highest efficiency compared to other solvents, and 0.05 g of nanocatalyst was the best amount of catalyst (Table 2, entry 4). The reaction yield was trace when GO was used solely (Table 2, entry 8). Immobilization of dopamine on GO (in the absence of Cu) slightly increased the reaction yield (12%) on GO@dopamine (Table 2, entry 9). All reaction conditions are outlined in Table 2.

Table 2. Optimization of parameters for the synthesis **4a** as a model reaction.

Entry	solvent	Nanocatalyst amount (g)	Temperature (°C)	Time (min)	Yield (%)
1	-	0.05	110	720	15
2	H_2O/EtOH (1:1/ v:v)	0.05	100	1440	20
3	CH_3CN	0.05	Reflux	720	40
4	**EtOH**	**0.05**	**Reflux**	**65**	**82**
5	EtOH	0.06	Reflux	65	86
6	EtOH	0.025	Reflux	65	45
7	EtOH	0.10	Reflux	65	85
8	EtOH	0.06 (GO)	Reflux	720	trace
9	EtOH	0.06 (GO@dopamine)	Reflux	720	12

The plausible mechanism for the synthesis of **4** was presented in Scheme 3. First, the nanocatalyst coordinated to dimethyl acetylenedicarboxylate (**2**), produced intermediate (**A**), then nucleophilic attacking of primary aromatic amine (**1**) to polarized acetylenic carbon atom formed intermediate (**B**) as an enamine. Afterward, the nucleophilic attack of enamine **B** to the polarized carbonyl group of an aldehyde (**3**) formed intermediate (**C**). The cyclization of this intermediate via an intramolecular attack of the hydroxyl group on the activated esteric carbonyl group formed the desired heterocyclic compounds **4** (Scheme 3).

3.4. Recyclability of nanocatalyst

To evaluate the recyclability of the GO@dopamine-Cu nanocatalyst, the reusability of this nanocatalyst was examined in the one-pot reaction of aniline **1a**; dimethyl acetylenedicarboxylate **2** and benzalde-hydes **3a** for the synthesis of **4a** as a model reaction based on optimum conditions (Figure 5). The nanocatalyst was separated at the end of each reaction by centrifugation and then dried by elution with ethanol. Then, the nanocatalyst is used for the next run, indicating that the proposed nanocatalyst is recycled in five runs. After five runs, the recycled nanocatalyst showed no significant decrease in catalytic activity (Figure 5).
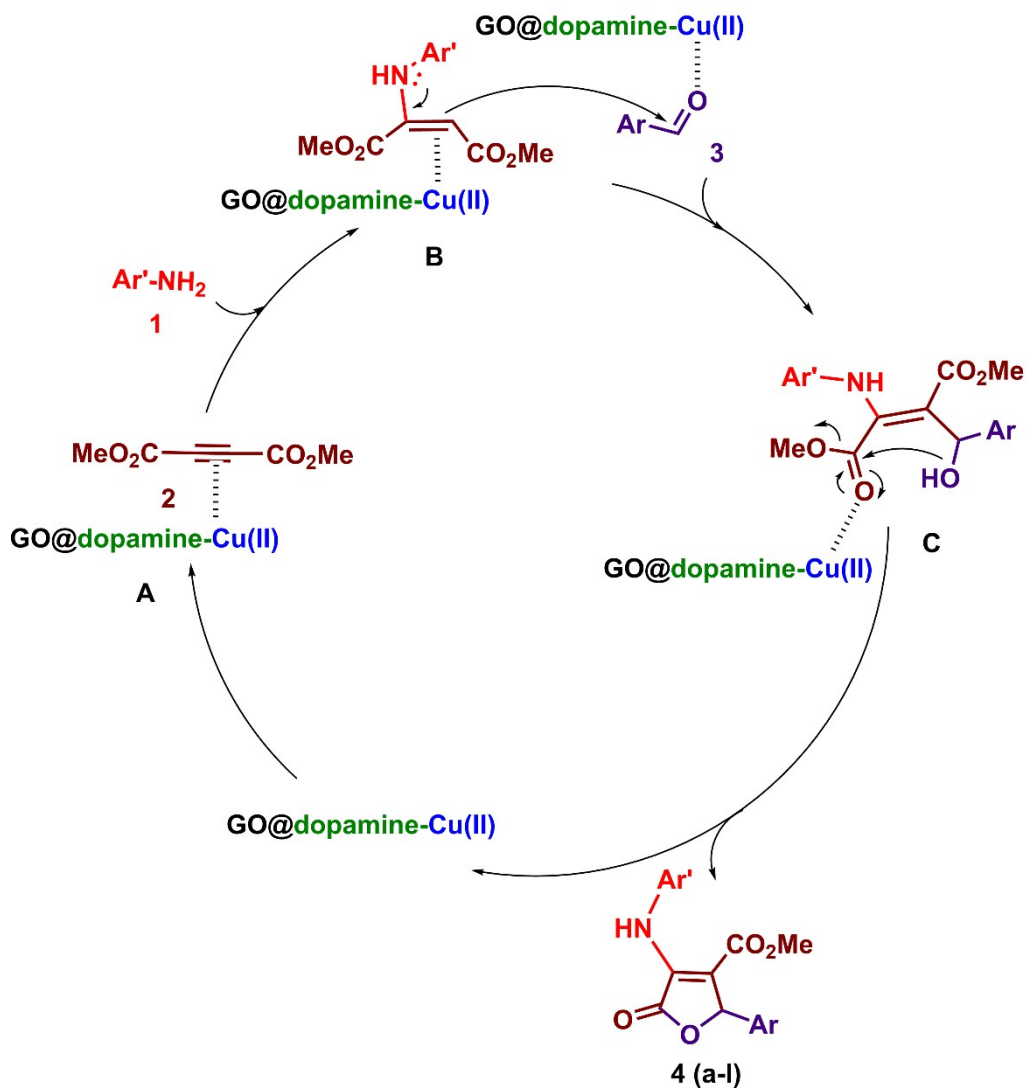
Scheme 3: Plausible reaction mechanism for the synthesis of **4** in the presence of GO@dopamine-Cu nanocatalyst.
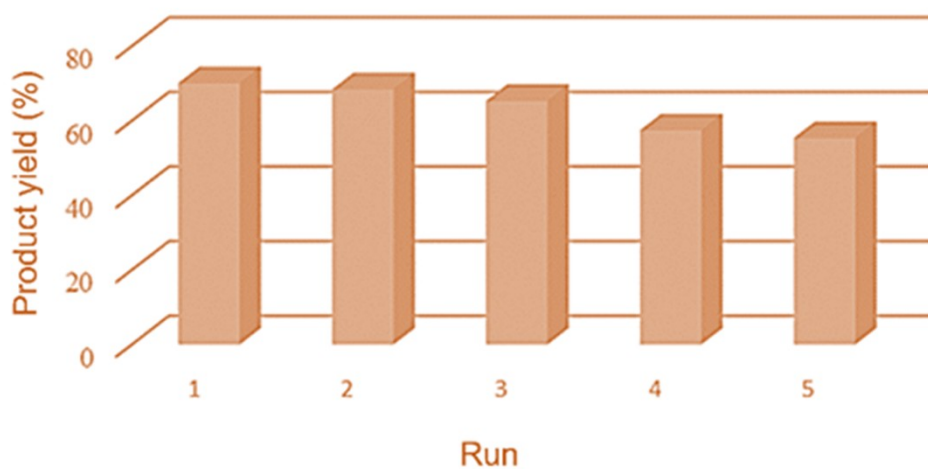
Figure 5: Recyclability of GO@dopamine-Cu in the preparation of **4**.

4. CONCLUSION

In summary, in this work, GO@dopamine-Cu nanocatalyst was synthesized and characterized its structure by FT-IR, XRD, SEM, TEM, EDX, and TGA-DTA techniques. This nanocatalyst was used for a one-pot, three-component reaction of an aromatic aldehyde, arylamine, and acetylenic carboxylate for the synthesis of full substituted furan-2(5*H*)-ones derivatives in high yield. All of the heterocyclic structures were characterized and confirmed their structures by spectroscopic methods. We concluded that GO@dopamine-Cu is an efficient nanocatalyst for the one-pot synthesis of full substituted furan-2(5*H*)-one derivatives. The main advantages of this work were easy reaction, high performance, and easy catalyst recyclability. This nanocatalyst recovered at least five times with negligible decreasing catalytic activity.

5. CONFLICT OF INTEREST

The authors declare no conflict of interest.

6. ACKNOWLEDGMENTS

7. REFERENCES

1. Subodh S, Prakash K, Masram DT. A reversible chromogenic covalent organic polymer for gas sensing applications. Dalton Transactions. 2020;49(4):1007–10. Available from: <URL>.

2. Yadav D, Awasthi SK. An unsymmetrical covalent organic polymer for catalytic amide synthesis. Dalton Transactions. 2020;49(1):179–86. Available from: <URL>.

3. Subodh, Prakash K, Masram DT. Chromogenic covalent organic polymer-based microspheres as solid-state gas sensor. Journal of Material Chemistry C. 2020;8(27):9201–4. Available from: <URL>.

4. Presolski S, Pumera M. Graphene Oxide: Carbocatalyst or Reagent? Angewandte Chemie, International Edition. 2018 Dec 17;57(51):16713–5. Available from: <URL>.

5. Zhang M, Liu YH, Shang ZR, Hu HC, Zhang ZH. Supported molybdenum on graphene oxide/Fe3O4: An efficient, magnetically separable catalyst for one-pot construction of spiro-oxindole dihydropyridines in deep eutectic solvent under microwave irradiation. Catalysis Communications. 2017 Jan;88:39–44. Available from: <URL>.

6. Subodh, Mogha NK, Chaudhary K, Kumar G, Masram DT. Fur-Imine-Functionalized Graphene Oxide-Immobilized Copper Oxide Nanoparticle Catalyst for the Synthesis of Xanthene Derivatives. ACS Omega. 2018 Nov 30;3(11):16377–85. Available from: <URL>.

7. Yadav D, Awasthi SK. A Pd NP-confined novel covalent organic polymer for catalytic applications. New Journal of Chemistry. 2020;44(4):1320–5. Available from: <URL>.

8. Yadav D, Awasthi SK. A Pd confined hierarchically conjugated covalent organic polymer for hydrogenation of nitroaromatics: catalysis, kinetics, thermodynamics and mechanism. Green Chemistry. 2020;22(13):4295–303. Available from: <URL>.

9. Subodh, Prakash K, Masram DT. Silver Nanoparticles Immobilized Covalent Organic Microspheres for Hydrogenation of Nitroaromatics with Intriguing Catalytic Activity. ACS Applied Polymeric Materials. 2021 Jan 8;3(1):310–8. Available from: <URL>.

10. Chaudhary K, Subodh, Prakash K, Mogha NK, Masram DT. Fruit waste (Pulp) decorated CuO NFs as promising platform for enhanced catalytic response and its peroxidase mimics evaluation. Arabian Journal of Chemistry. 2020 Apr;13(4):4869–81. Available from: <URL>.

11. Stankovich S, Dikin DA, Piner RD, Kohlhaas KA, Kleinhammes A, Jia Y, et al. Synthesis of graphene-based nanosheets via chemical reduction of exfoliated graphite oxide. Carbon. 2007 Jun;45(7):1558–65. Available from: <URL>.

12. Dreyer DR, Todd AD, Bielawski CW. Harnessing the chemistry of graphene oxide. Chemical Society Reviews. 2014 Jul 7;43(15):5288-301. Available from: <URL>.

13. Compton OC, Nguyen ST. Graphene Oxide, Highly Reduced Graphene Oxide, and Graphene: Versatile Building Blocks for Carbon-Based Materials. Small. 2010 Mar 22;6(6):711–23. Available from: <URL>.

14. Noori S, Ghorbani-Vaghei R, Azadbakht R, Karamshahi Z, Koolivand M. Graphene-oxide/schiff base N2O4 ligand-palladium: A new catalyst for the synthesis of furan derivatives. Journal of Molecular Structure. 2022 Feb;1250:131849. Available from: <URL>.

15. Dömling A. Recent Developments in Isocyanide Based Multicomponent Reactions in Applied Chemistry. Chemical Reviews. 2006 Jan 1;106(1):17–89. Available from: <URL>.

16. Pour M, Špulák M, Buchta V, Kubanová P, Vopršalová M, Wsól V, et al. 3-Phenyl-5-acyloxymethyl-2 H , 5H -furan-2-ones: Synthesis and Biological Activity of a Novel Group of Potential Antifungal Drugs. Journal of Medicinal Chemistry. 2001 Aug 1;44(17):2701–6. Available from: <URL>.

17. Wu J, Cheng Y, Zhao X, Liu X, Sun W, Ren H, et al. Antibacterial activity and biological performance of a novel antibacterial coating containing a halogenated furanone compound loaded poly(L-lactic acid) nanoparticles on microarc-oxidized titanium. International Journal of Nanomedicine. 2015 Jan;727. Available from: <URL>.

18. Tejedor D, García-Tellado F. Chemo-differentiating ABB ′ multicomponent reactions. Privileged building blocks. Chemical Society Reviews. 2007;36(3):484–91. Available from: <URL>.

19. Shirzaei M, Mollashahi E, Taher Maghsoodlou M, Lashkari M. Novel synthesis of silica-coated magnetic nano-particles based on acidic ionic liquid, as a highly efficient catalyst for three component system leads to

furans derivatives. Journal of the Saudi Chemical Society. 2020 Feb;24(2):216–22. Available from: <URL>.

20. Weber V. Novel 4,5-Diaryl-3-hydroxy-2(5H)-furanones as Anti-Oxidants and Anti-Inflammatory Agents. Bioorganic & Medicinal Chemistry. 2002 Jun;10(6):1647–58. Available from: <URL>.

21. Lattmann E, Ayuko WO, Kinchinaton D, Langley CA, Singh H, Karimi L, et al. Synthesis and evaluation of 5-arylated 2(5 H)-furanones and 2-arylated pyridazin-3(2 H)-ones as anti-cancer agents. Journal of Pharmacy and Pharmacology. 2010 Feb 18;55(9):1259–65. Available from: <URL>.

22. El-Tombary AA, Abdel-Ghany YS, Belal ASF, Shams El-Dine SA, Soliman FSG. Synthesis of some substituted furan-2(5H)-ones and derived quinoxalinones as potential anti-microbial and anti-cancer agents. Medicinal Chemistry Research. 2011 Sep;20(7):865–76. Available from: <URL>.

23. Lipshutz BH. Five-membered heteroaromatic rings as intermediates in organic synthesis. Chemical Reviews. 1986;86(5):795–819.

24. Mortensen DS, Rodriguez AL, Carlson KE, Sun J, Katzenellenbogen BS, Katzenellenbogen JA. Synthesis and Biological Evaluation of a Novel Series of Furans: Ligands Selective for Estrogen Receptor α. Journal of Medicinal Chemistry. 2001 Nov 1;44(23):3838–48. Available from: <URL>.

25. Bassetti M, D'Annibale A, Fanfoni A, Minissi F. Synthesis of α,β-Unsaturated 4,5-Disubstituted γ-Lactones via Ring-Closing Metathesis Catalyzed by the First-Generation Grubbs' Catalyst. Organic Letters. 2005 Apr 1;7(9):1805–8. Available from: <URL>.

26. Bock I, Bornowski H, Ranft A, Theis H. New aspects in the synthesis of mono- and dialkylfurans. Tetrahedron. 1990 Jan;46(4):1199–210. Available from: <URL>.

27. Takahashi S, Kubota A, Nakata T. Total synthesis of muconin. Tetrahedron Letters. 2002 Nov;43(48):8661–4. Available from: <URL>.

28. Bandurraga MM, Fenical W, Donovan SF, Clardy J. Pseudopterolide, an irregular diterpenoid with unusual cytotoxic properties from the Caribbean sea whip Pseudopterogorgia acerosa (Pallas)(Gorgonacea). Journal of the American Chemical Society. 1982;104(23):6463–5.

29. Padakanti S, Pal M, Yeleswarapu KR. An improved and practical synthesis of 5,5-dimethyl-3-(2-propoxy)-4-(4-methanesulfonylphenyl)-2-(5H)-furanone (DFP—a selective inhibitor of cyclooxygenase-2). Tetrahedron. 2003 Sep;59(40):7915–20. Available from: <URL>.

30. Lee ES, Park BC, Paek SH, Lee YS, Basnet A, Jin DQ, et al. Potent Analgesic and Anti-inflammatory Activities of 1-Furan-2-yl-3-pyridin-2-yl-propenone with Gastric Ulcer Sparing Effect. Biological & Pharmaceutical Bulletin. 2006;29(2):361–4. Available from: <URL>.

31. Rossi R, Bellina F, Biagetti M, Mannina L. Stereocontrolled synthesis of lissoclinolide by sequential transition metal-catalyzed lactonization/cross-coupling reactions. Tetrahedron Letters. 1998 Oct;39(42):7799–802. Available from: <URL>.

32. Levy L. 5H-Furan-2-ones from fungal cultures of Aporpium caryae. Phytochemistry. 2003 Jan;62(2):239–43. Available from: <URL>.

33. Hofnung M, Quillardet P, Michel V, Touati E. Genotoxicity of 2-nitro-7-methoxy-naphtho[2,1-b]furan (R7000): A case study with some considerations on nitrofurantoin and nifuroxazide. Research in Microbiology. 2002 Sep;153(7):427–34. Available from: <URL>.

34. Wahab Khan M, Jahangir Alam M, Rashid MA, Chowdhury R. A new structural alternative in benzo[b]furans for antimicrobial activity. Bioorganic & Medicinal Chemistry. 2005 Aug;13(16):4796–805. Available from: <URL>.

35. Pour M, Špulák M, Balšánek V, Kuneš J, Kubanová P, Buchta V. Synthesis and structure–antifungal activity Relationships of 3-Aryl-5-alkyl-2,5-dihydrofuran-2-ones and Their Carbanalogues: further refinement of tentative pharmacophore group. Bioorganic & Medicinal Chemistry. 2003 Jul;11(13):2843–66. Available from: <URL>.

36. Shafiee MRM, Mansoor SS, Ghashang M, Fazlinia A. Preparation of 3,4,5-substituted furan-2(5H)-ones using aluminum hydrogen sulfate as an efficient catalyst. Comptes Rendus Chimie. 2014 Feb;17(2):131–4. Available from: <URL>.

37. Karamshahi Z, Ghorbani-Vaghei R. Efficient synthesis of multiply substituted furans using BF@Propyl/dopamine/Pd as a green catalyst. Applied Organometallic Chemistry. 2020 Apr;34(4):e5530. Available from: <URL>.

38. Wipf P, Rahman LT, Rector SR. A General Strategy for Five-Membered Heterocycle Synthesis by Cycloelimination of Alkynyl Ketones, Amides, and Thioamides. The Journal of Organic Chemistry. 1998;63(21):7132–3.

39. Golonka AN, Schindler CS. Iron(III) chloride-catalyzed synthesis of 3-carboxy-2,5-disubstituted furans from γ-alkynyl aryl- and alkylketones. Tetrahedron. 2017 Jul;73(29):4109–14. Available from: <URL>.

40. Kangani M, Hazeri N, Maghsoodlou MT. Synthesis of pyrrole and furan derivatives in the presence of lactic acid as a catalyst. Journal of the Saudi Chemical Society. 2017 Feb;21(2):160–4. Available from: <URL>.

Synthesis, Spectroscopic Analysis, and Anti-Bacterial Studies of Pd(II) Complexes of Phosphine and Hydrazone Derivatives

Laith H. K. Al-Jibori (iD) **and Ahmed S. M. Al-Janabi*** (iD)

Department of Chemistry, College of Science, Tikrit University, Tikrit, Iraq

Abstract: This study reports the synthesis of seven hydrazone derivative complexes by the treatment equivalent molar of the phosphine ligand $Ph_2P(CH_2)_nPPh_2$ {where n= 1 dppm; n=2 dppe; n=3 dppp; n=4 dppb; $(CH_2)_n = (Cp)_2Fe$} with $[Pd(dbeoz)_2]$ afforded complexes of the type $[Pd(dbeoz)_2(diphos)]$ and $[Pd(dbeoz)_2(dppm)]_2$, whereas the reaction of two moles of Ph_3P with $[Pd(dbeoz)_2]$ gave a complex $[Pd(dbeoz)_2(PPh_3)_2]$ in good yield. CHN analysis, conductivity measurements, Fourier Transform Infrared (FT-IR), ^1H, and ^{31}P-NMR, were used to investigate the structural geometries of the complexes. Further, the biological activity of the synthesized complexes was evaluated against three pathogenic bacteria (*Pseudomonas aeruginosa*, *Bacillus subtilis*, and *Escherichia coli*) using the well diffusion method, the synthesized complexes displayed moderate to good inhibitory activity, and the $[Pd(dbeoz)_2(dppf)]$ complex exhibited the highest inhibitory activity with DIZ is 24, 27, and 28 mm against the three pathogenic bacteria, respectively.

1. INTRODUCTION

Hydrazones are compounds that contain the functional group R-NHN=CR', where R and R' can be a variety of substituents. Hydrazones are usually synthesized by heating hydrazides with different aldehydes using solvents such as acetone and ethanol, which can be easily confirmed from its spectral data. Further, they can be used as an intermediate in Wolff Kishner reductions to reduce the carbonyl functionality of aldehyde and ketones into alkanes. Hydrazones can act as versatile ligands in coordination chemistry, forming complexes with transition metals. These complexes can exhibit a range of interesting properties and potential applications (1-2).

Hydrazone derivative ligands can coordinate to a metal center in different modes, such as monodentate, bidentate (chelating), or bridging to a transition metal center through two of its donor atoms.

The nitrogen atoms in the hydrazine group can form coordination bonds with the metal center. These different coordination modes can lead to the formation of various complex structures and geometries (2-6). The stability of the produced complexes can vary depending on factors such as the nature of the metal, the coordination mode, and the steric and electronic effects of the ligand. Stability can influence the potential applications of these complexes (1). Hydrazones are readily available, hydrolytically stable, and are enolized only under strongly basic conditions, and they would be attractive partners for radical addition (1,7,8). However, the presence of the second nitrogen decreases the electrophilic character of their C=N bond, resulting in decreased efficiency of adding nucleophilic radicals (1,9,10).

Depending on the specific properties of the Hydrazone derivative complexes, they could find applications in catalysis, sensing, medicinal chem-

istry (such as anti-bacterial, anti-fungi, anti-malaria, etc.), and materials science. For instance, catalytic applications could include oxidation, reduction, and cross-coupling reactions (11-21).

In light of the broad range of applications reported for hydrazone compounds and, as well as its complexes with transition metal ions, Here, we report the synthesis and characterization of a series of Pd(II) hydrazone derivative complexes and evaluation of the biological activity against *Pseudomonas aeruginosa*, *Bacillus subtilis*, and *Escherichia coli* bacteria using the diffusion method.

2. EXPERIMENTAL SECTION

2.1 Materials and Apparatus

The chemical compounds and solvent provided were employed without undergoing purification. UV-visible spectra were evaluated within the 900 to 200 nm range utilizing a Cary 100 spectrophotometer in DMSO solutions. FT-IR spectra were recorded 400 to 4000 cm^{-1}, employing KBr discs on a SHIMADZU

FT-IR apparatus. Molar conductance was gauged in a DMSO solution at a 10^{-3} M temperature of 25 °C using an Oakton EC Tester 11 dual-range conductivity tester. The NMR spectra were measured using a Bruker 400 MHz spectrometer, with DMSO-d6 as the solvent.

2.2 General Procedure of the Preparation of Complexes

A solution of Ph$_2$P(CH$_2$)$_n$PPh$_2$ (0.063 mmole) or Ph$_3$P (0.126 mmole) in EtOH (10 mL) was added to a suspension of [Pd(dbeoz)$_2$] (0.05 g; 0.063 mmol) in EtOH (10 mL), a colored solution was formed. The mixture was stirred for four hours, during which a color precipitate formed. The stirring was continued until the designated time elapsed. The solution was filtered and washed with distilled water, followed by ether and ethanol. The precipitate was dried under reduced pressure, and it was crystallized from DMSO (Schemes 1 and 2). The color, yield percentage, m.p. (°C), and other physical properties are listed in Table 1.
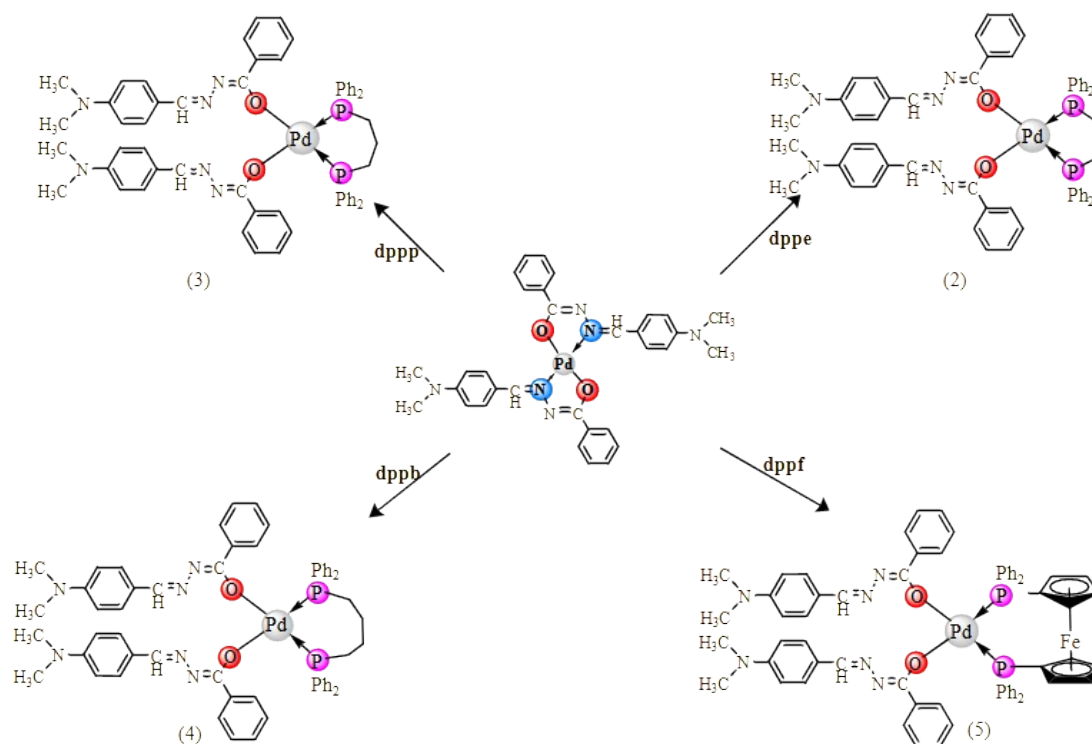
Scheme 1: Preparation of Pd(II) complexes (**2-5**).
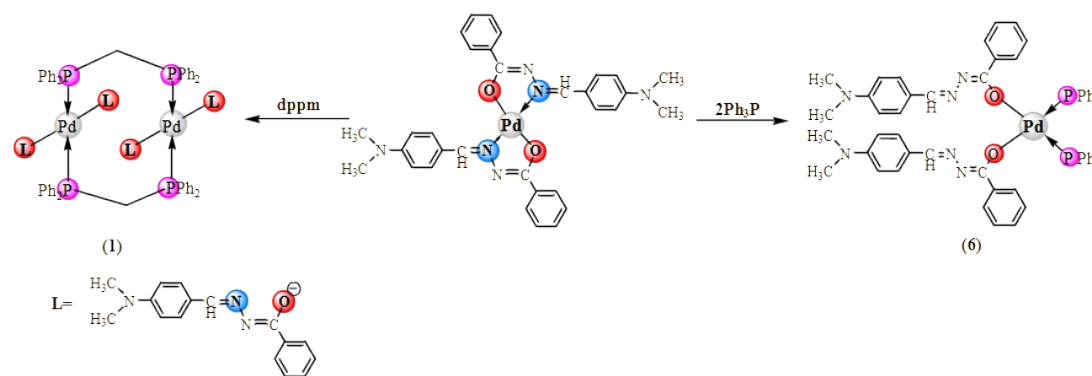
Scheme 2: Preparation of Pd(II) complexes (**1** and **6**).

2.3 Anti-Bacterial Activity

The anti-bacterial activity of the synthesized complexes was assessed against three bacterial strains, namely *Pseudomonas aeruginosa*, *Bacillus subtilis*, and *Escherichia coli*, using the disc diffusion method on the nutrient agar described by Bauer (22). Six synthesized complexes were evaluated at a concentration of 10^{-3} M in DMSO solution, and the results were compared with Tetracycline and dimethyl sulphoxide (DMSO), which were used as positive and negative controls, respectively.

3. RESULTS AND DISCUSSION

3.1 Synthesis

The complexes [Pd(dbeoz)$_2$(diphos)] and [Pd(dbeoz)$_2$(dppm)]$_2$ were prepared by reacting equivalent molar of the diphosphine ligands with [Pd(dbeoz)$_2$] in ethanol as a solvent (Scheme 1) to afford a green complex with the dppm ligand, an orange complex with the dppe ligand, and a red complex with the dppp ligand. Additionally, a brown complex was obtained with the dppf ligand. On the other hand, the complex [Pd(dbeoz)$_2$(PPh$_3$)$_2$] was prepared by treatment of two equivalent moles of the triphenylphosphine ligand (PPh$_3$), with [Pd(dbeoz)$_2$] to afford an olive complex (Scheme 2). The results indicate that the HDmby ligand was coordinated as a monodentate ligand via the oxygen atom of the carbonyl group. The molar conductivity results for the complexes are listed in Table 1, indicating that all complexes were non-conductive, suggesting their non-electrolytic complexes. Furthermore, the elemental analysis results were consistent with the proposed formulas of the prepared complexes.

Table 1: Some of the physical properties and CHN analysis of the synthesized complexes.

No	Complexes	Color	Λ^*	m.p (°C)	Yield %	Elemental analysis (CHN) Calc.(found)		
						C	H	N
1	[Pd(Dmby)$_2$(dppm)]$_2$	Green	10.0	300-303	51	66.89 (67.07)	5.32 (5.43)	8.21 (8.50)
2	[Pd(Dmby)$_2$(dppe)]	Orange	11.0	257-259	91	67.15 (67.08)	5.44 (5.32)	8.10 (8.37)
3	[Pd(Dmby)$_2$(dppp)]	Red	6.8	287-288	80	67.39 (67.56)	5.56 (5.62)	7.99 (8.13)
4	[Pd(Dmby)$_2$(dppb)]	Orange	7.0	297-300	54	67.63 (67.78)	5.68 (5.92)	7.89 (7.94)
5	[Pd(Dmby)$_2$(dppf)]	Brown	8.0	282-283	30	66.42 (66.51)	5.07 (5.28)	7.04 (7.23)
6	[Pd (Dmby)$_2$(PPh$_3$)$_2$]	Olive	2.4	291-293	56	70.19 (70.23)	5.37 (5.43)	7.22 (7.49)

* molar conductivity was measured in DMSO solution at 10^{-3} in (ohm^{-1}. cm^2. mol^{-1})

3.2 Spectral data

3.2.1 IR data

The infrared spectra of [Pd(dbeoz)$_2$(dppm)]$_2$, [Pd(dbeoz)$_2$(diphos)], and [Pd(dbeoz)$_2$(PPh$_3$)$_2$] (Figures SI 1-4) have revealed three characteristic bands that were absent in the spectrum of complex [Pd(dbeoz)$_2$]. These bands confirm complex forma-tion and the incorporation of phosphine ligands within their structures. Specifically, these bands due to ν(P-Ph), ν(P-C), and ρ(P-C) which displayed within (1433-1456) cm^{-1}, (1064-1099) cm^{-1}, and (493-509) cm^{-1}, range, respectively (23-25).

A slight shift in the carbonyl group stretching frequency was noted within the range of (1645-1670) cm^{-1}, suggesting the coordination of the ligand (dbeoz$^-$) via the oxygen atom of the carbonyl group. In contrast, the stretching frequency of the azomethine group has been displaced to a slightly higher wavenumber than in the complex [Pd(dbeoz)$_2$] (1567 cm^{-1}), appearing within the range of (1600-1610) cm^{-1}, approximating or slightly surpassing that of the free ligand. This indicates its lack of involvement in coordination with the Pd(II) ion, thereby supporting the proposed monodentate fashion of the ligand dbeoz$^-$ via the oxygen of the carbonyl group (26-31). New bands have been observed in the prepared complexes due to the ν(Pd-P) and ν(Pd-O), which displayed within the ranges of (455-486) cm^{-1} and (418-443) cm^{-1}, respectively (24-28). Further, the IR spectra displayed the ν(C-H)aromatic and ν(C-H)aliphatic within the range of (3051-3059) cm^{-1} and (2804-2987) cm^{-1}, respectively.

3.2.2 ^{31}P-{^{1}H} and ^{1}H NMR data

The ^{31}P-{^{1}H}NMR spectra of the prepared complexes (Figure 1) displayed a singlet peak for each complex at _P = 23.70 ppm, 09.61 ppm, 11.95 ppm, 30.03ppm, 25.60 ppm, and 25.53 ppm for the [Pd(dbeoz)$_2$ (dppm)]$_2$, [Pd(dbeoz)$_2$ (dppe)], [Pd(dbeoz)$_2$ (dppp)], [Pd(dbeoz)$_2$ (dppb)], [Pd(dbeoz)$_2$ (dppf)] and [Pd(dbeoz)$_2$ (PPh$_3$)$_2$], respectively. The presence of a singlet peak indicates the existence of a single isomer, and the phosphorus atoms are equivalent (23-25).

Table 2. IR selected bands (cm^{-1}) of the prepared complexes.

Band assignment	[Pd(dbeoz)$_2$]	Complexes					
		1	2	3	4	5	6
ν(C-H)$_{Ar}$	3059w	3053w	3055w	3051w	3058w	3053w	3053w
ν(C-H)$_{aliph.}$	2920w 2856w	2963w 2804w	2891w 2852w	2987w 2893w	2893w 2822w	2964w 2804w	2906w 2858w
ν(C=O)	1604m	1606m	1623m	1615m	1608m	1624m	1616m
ν(C=N)	1577s	1592s	1606s	1596s	1594s	1602s	1593s
ν(C=C)	1523s	1540s	1523s	1523s	1523s	1523s	1523s
ν(P-Ph)	-	1434m	1444m	1433m	1434m	1437m	1456m
ν(P-C)	-	1069s	1064s	1097m	1099m	1097m	1097m
ρ(P-C)	-	505s	513m	509m	505m	493m	507m
ν(Pd-O)	462w	472w	486w	455w	476w	464w	481w
ν(Pd-P)	-	442w	443w	420w	433w	418w	441w

s = strong, m = medium, w= weak.

Clearly, the ^{1}H NMR spectra of the [Pd(dbeoz)$_2$(dppm)]$_2$, [Pd(dbeoz)$_2$(diphos)], and [Pd(dbeoz)$_2$(PPh$_3$)$_2$] complexes (Fig. SI 5-10), indicated that the two dbeoz ligands and phosphine ligands include in the structure complexes. The ^{1}H NMR spectra displayed the azomethine proton signals at 8.10-8.38 ppm. Meanwhile, protons of the phenyl groups in the dbeoz ligands and diphosphine ligands are displayed as unresolved multiplet peaks in the aromatic region. The results are listed in Table 3.

Table 3: ^{31}P-{^{1}H}NMR and ^{1}H NMR data (δ, ppm) of the [Pd(dbeoz)$_2$(dppm)]$_2$, [Pd(dbeoz)$_2$(diphos)], and [Pd(dbeoz)$_2$(PPh$_3$)$_2$].

No	Complexes	δP	δH
1	[Pd(Dmby)$_2$(dppm)]$_2$	23.70	8.35(s, 4H, CH=N); 6.74-8.15(m, 76H); 4.05(t, J_{H-P} = 13.6Hz, 4H, CH$_2$-dppm).
2	[Pd(Dmby)$_2$(dppe)]	9.61	8.10(s, 2H, CH=N); 6.35-7.85(m, 38H); 2.75(s, 12H, CH$_3$); 3.06(s, 24H, 2CH$_3$); 2.28(s, 4H, 2CH$_2$-dppe).
3	[Pd(Dmby)$_2$(dppp)]	11.95	8.33(s, 2H, CH=N); 7.07-8.07(m, 34H); 6.79(d, J_{HH} = 8.1Hz, 4H); 2.86-3.10(m, 18H, 2CH$_2$-dppp+ 4CH$_3$); 1.92-2.13(m, 2H, CH$_2$-dppp).
4	[Pd(Dmby)$_2$(dppb)]	30.03	8.33(s, 2H, CH=N); 7.17-8.14(m, 34H); 6.67-6.92(m, 4H); 2.94-3.18(m, 18H, 2CH$_2$-dppb+4CH$_3$); 2.36-2.44(m, 4H, CH$_2$-2dppb).
5	[Pd(Dmby)$_2$(dppf)]	25.60	8.34(s, 2H, CH=N); 6.52-8.21(m, 38H), 4.41, 4.32(s, 8H, 2Cp-dppf); 3.00(s, 12H, 4CH$_3$).
6	[Pd (Dmby)$_2$(PPh$_3$)$_2$]	25.53	8.38(s, 2H, CH=N); 6.60-8.38(m, 48H); 2.89(s, 12H, 4CH$_3$).
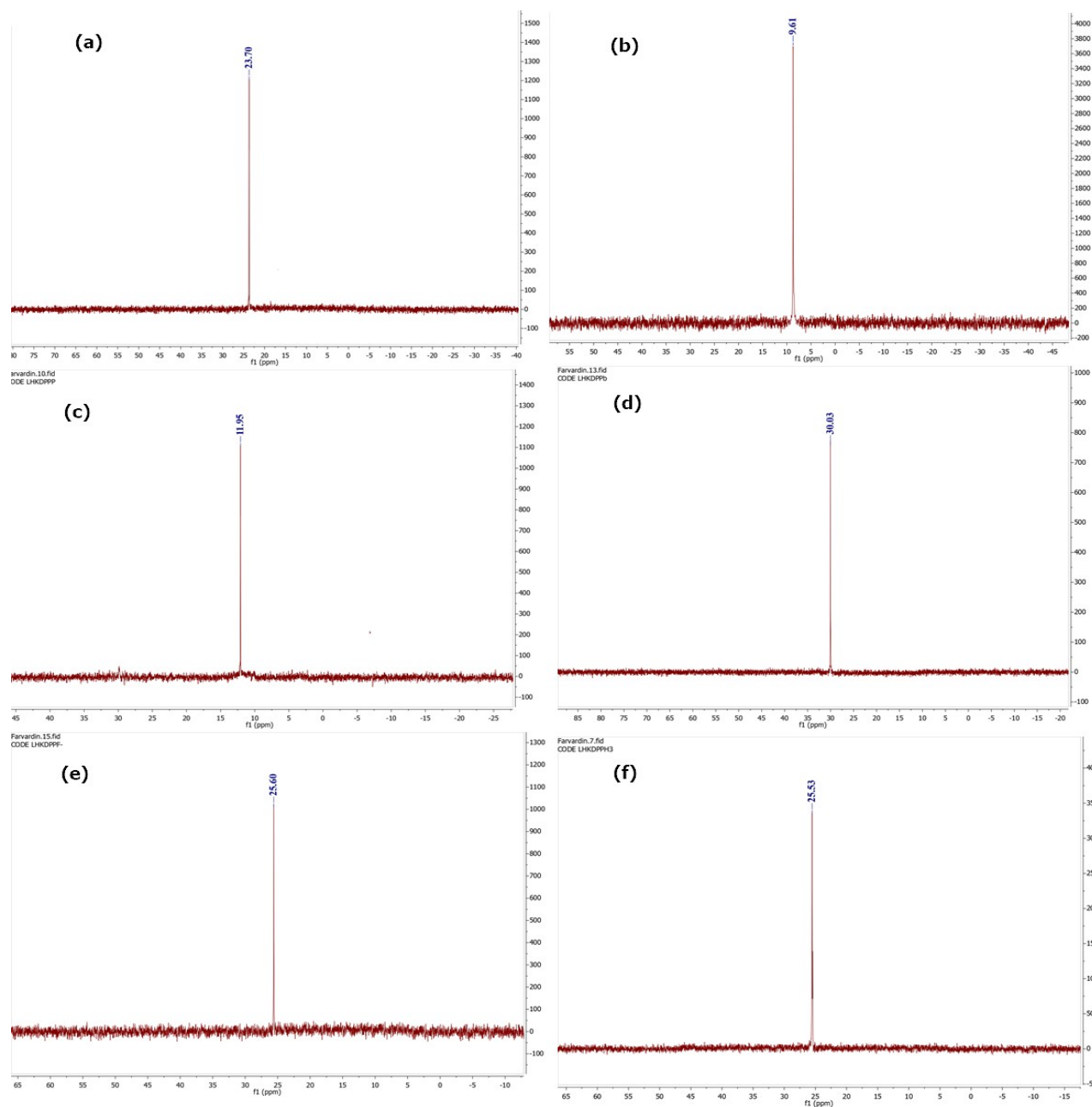
Figure 1: ^{31}P-{^{1}H}NMR spectra of the (a)[Pd(dbeoz)$_2$(dppm)]$_2$, (b) [Pd(dbeoz)$_2$(dppe)], (c) [Pd(dbeoz)$_2$(dppp)], (d)[Pd(dbeoz)$_2$(dppb)], (e)[Pd(dbeoz)$_2$(dppf)] and (f) [Pd(dbeoz)$_2$(PPh$_3$)$_2$].

3.3 Anti-Bacterial Activity Study

The biological activity of the synthesized complexes was evaluated against three pathogenic bacteria *Pseudomonas aeruginosa*, *Bacillus subtilis*, and *Escherichia coli,* using the well diffusion method in the nutrient agar described by Bauer (26).

Six synthesized complexes were evaluated at a concentration of 10^{-3} M in DMSO solution, and the results were compared with Tetracycline and dimethyl sulfoxide (DMSO), which were used as positive and negative controls, respectively. The obtained results were compiled in Table 2, and Figure 4 demonstrates the used compounds as follows:

1. [Pd(dbeoz)$_2$]
2. [Pd(dbeoz)$_2$(dppe)]
3. [Pd(dbeoz)$_2$(dppp)]
4. [Pd(dbeoz)$_2$(dppb)]
5. [Pd(dbeoz)$_2$(dppf)]
6. [Pd (dbeoz)$_2$(PPh$_3$)$_2$]

The results demonstrated that the compounds exhibited inhibitory activity against the studied bacterial strains, as summarized below:

1. The synthesized complexes displayed moderate to good inhibitory activity against the examined bacterial strains compared to the Tetracycline.

2. The complex [Pd(dbeoz)$_2$(dppf)] exhibited the highest inhibitory activity among the studied complexes, followed by [Pd(dbeoz)$_2$(PPh$_3$)$_2$]. This can be attributed to the presence of ferrocenyl and triphenylphosphine ligands.

3. The addition of phosphine ligands to dbeoz complex enhanced inhibitory activity against the tested bacteria.

4. In general, the highest inhibitory activity was observed against *Bacillus subtilis* compared to other bacteria, while the lowest activity was noted against *Pseudomonas aeruginosa*.

5. The inhibitory sequence of the studied complexes in terms of their inhibitory radius was as follows:

[Pd(Dbeoz)$_2$(dppf)] > [Pd(Dbeoz)$_2$(PPh$_3$)$_2$] > [Pd(Dbeoz)$_2$(dppe)] > [Pd(Dbeoz)$_2$(dppb)] > [Pd(Dbeoz)$_2$(dppp)] > [Pd(Dbeoz)$_2$] Decreasing inhibition diameter →
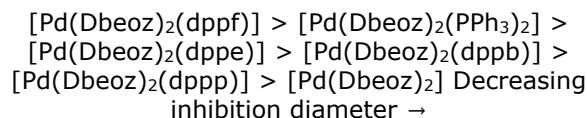
Table 4: Diameter inhibition zone (in mm) of the synthesized complexes at 10^{-3} M in DMSO solution.

Seq.	Complexes	DIZ (mm)		
		P. aeruginosa	*B. subtills*	*E. Coli*
1	[Pd(Dmby)$_2$]	13	12	14
2	[Pd(Dmby)$_2$(dppe)]	17	18	18
3	[Pd(Dmby)$_2$(dppp)]	15	14	17
4	[Pd(Dmby)$_2$(dppb)]	15	16	17
5	[Pd(Dmby)$_2$(dppf)]	24	27	28
6	[Pd (Dmby)$_2$(PPh$_3$)$_2$]	20	21	20
7	Tetracycline	29	30	28
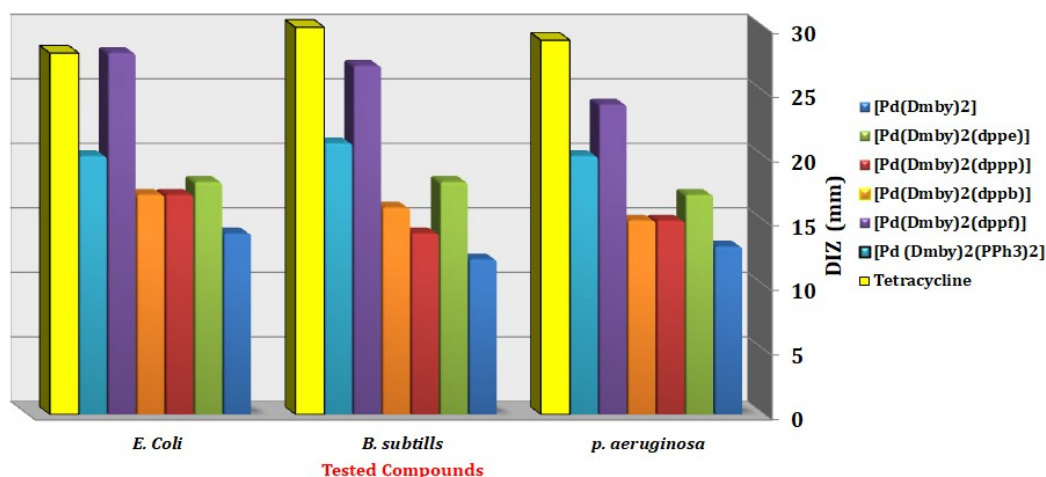
Figure 2. Histogram of the inhibition activity of the synthesized complexes at 10^{-3} M in DMSO solution.

4. CONCLUSION

We demonstrated in this work that [Pd(dbeoz)$_2$] reacts with phosphine ligands to afford [Pd(dbeoz)$_2$(diphos)], [Pd(dbeoz)$_2$(dppm)]$_2$ and [Pd(dbeoz)$_2$(PPh$_3$)$_2$] **(1-6)** in which dbeoz acts as a monodentate through the oxygen atom of the carbonyl group. The prepared complexes were characterized by different spectroscopic and physical methods. Further, the biological activity of the synthesized complexes was screened against *Pseudomonas aeruginosa*, *Bacillus subtilis*, and *Escherichia coli* bacteria species, and the complexes showed moderate to good inhibitory activity, and the [Pd(dbeoz)$_2$(dppf)] complex has a highest inhibitory activity.

5. REFERENCES

1. Shakdofa MME, Shtaiwi MH, Morsy N, Abdel-rassel TMA. Metal complexes of hydrazones and their biological, analytical and catalytic applications: A review. Main Group Chemistry. 2014;13(3):187–218. Available from: <URL>.

2. Kumar M, Roy S, Faizi MdSH, Kumar S, Singh MK, Kishor S, et al. Synthesis, crystal structure and luminescence properties of acenaphthene benzohydrazide based ligand and its zinc(II) complex. Journal of Molecular Structure. 2017 Jan;1128:195–204. Available from: <URL>.

3. Tabernero V, Cuenca T, Herdtweck E. Hydrazonide titanium derivatives. Journal of Organometallic Chemistry. 2002 Dec;663(1–2):173–82. Available from: <URL>.

4. Pelagatti P, Carcelli M, Pelizzi C, Costa M. Polymerisation of phenylacetylene in water catalysed by Pd(NN'O)Cl complexes. Inorganica Chimica Acta. 2003 Jan;342:323–6. Available from: <URL>.

5. Chen L. Ethylene oligomerization by hydrazone Ni(II) complexes/MAO. Applied Catalysis A: General. 2003 Jun 25;246(1):11–6. Available from: <URL>.

6. Zhong X, Wei HL, Liu WS, Wang DQ, Wang X. The crystal structures of copper(II), manganese(II), and nickel(II) complexes of a (Z)-2-hydroxy-N'-(2-oxoindolin-3-ylidene) benzohydrazide—potential antitumor agents. Bioorganic & Medicinal Chemistry Letters. 2007 Jul;17(13):3774–7. Available from: <URL>.

7. Cullen STJ, Friestad GK. Alkyl Radical Addition to Aliphatic and Aromatic N -Acylhydrazones Using an Organic Photoredox Catalyst. Organic Letters. 2019 Oct 18;21(20):8290–4. Available from: <URL>.

8. Kvasovs N, Gevorgyan V. Accessing Illusive E Isomers of α-Ester Hydrazones via Visible-Light-Induced Pd-Catalyzed Heck-Type Alkylation. Organic Letters. 2022 Jun 17;24(23):4176–81. Available from: <URL>.

9. Prieto A, Bouyssi D, Monteiro N. Radical-Mediated Formal C(sp 2)–H Functionalization of Aldehyde-Derived N , N -Dialkylhydrazones. European Journal of Organic Chemistry. 2018 Jun 7;2018(20–21):2378–93. Available from: <URL>.

10. Xu X, Zhang J, Xia H, Wu J. C(sp 2)–H functionalization of aldehyde-derived hydrazones via a radical process. Organic and Biomolecular Chemistry. 2018;16(8):1227–41. Available from: <URL>.

11. El-Tabl AS, Mohamed Abd El-Waheed M, Wahba MA, Abd El-Halim Abou El-Fadl N. Synthesis, Characterization, and Anticancer Activity of New Metal Complexes Derived from 2-Hydroxy-3-(hydroxyimino)-4-oxopentan-2-ylidene)benzohydrazide. Bioinorganic Chemistry and Applications. 2015;2015:1–14. Available from: <URL>.

12. Okagu OD, Ugwu KC, Ibeji CU, Ekennia AC, Okpareke OC, Ezeorah CJ, et al. Synthesis and characterization of Cu(II), Co(II) and Ni(II) complexes of a benzohydrazone derivative: Spectroscopic, DFT, antipathogenic and DNA binding studies. Journal of Molecular Structure. 2019 May;1183:107–17. Available from: <URL>.

13. Katouah HA, Al-Fahemi JH, Elghalban MG, Saad FA, Althagafi IA, El-Metwaly NM, et al. Synthesis of new Cu(II)-benzohydrazide nanometer complexes, spectral, modeling, CT-DNA binding with potential anti-inflammatory and anti-allergic theoretical features. Materials Science and Engineering: C. 2019 Mar;96:740–56. Available from: <URL>.

14. Al-Qadsy I, Al-Odayni AB, Saeed WS, Alrabie A, Al-Adhreai A, Al-Faqeeh LAS, et al. Synthesis, Characterization, Single-Crystal X-ray Structure and Biological Activities of [(Z)-N'-(4-Methoxybenzylidene) benzohydrazide–Nickel(II)] Complex. Crystals. 2021 Jan 26;11(2):110. Available from: <URL>.

15. Korkmaz IN, Türkeş C, Demir Y, Öztekin A, Özdemir H, Beydemir Ş. Biological evaluation and in silico study of benzohydrazide derivatives as paraoxonase 1 inhibitors. J Biochemistry & Molecular Toxicity. 2022 Nov;36(11):e23180. Available from: <URL>.

16. Zuo W, Tourbillon C, Rosa V, Cheaib K, Andrade MM, Dagorne S, et al. Synthesis, crystal structures and use in ethylene oligomerization catalysis of novel mono- and dinuclear nickel complexes supported by (E)-N'-(1-(thiophen-2-yl)ethylidene)benzohydrazide ligand. Inorganica Chimica Acta. 2012 Mar;383:213–9. Available from: <URL>.

17. Burgos-Lopez Y, Del Plá J, Balsa LM, León IE, Echeverría GA, Piro OE, et al. Synthesis, crystal structure and cytotoxicity assays of a copper(II) nitrate complex with a tridentate ONO acylhydrazone ligand. Spectroscopic and theoretical studies of the complex and its ligand. Inorganica Chimica Acta. 2019 Mar;487:31–40. Available from: <URL>.

18. Theppitak C, Kielar F, Dungkaew W, Sukwattanasinitt M, Kangkaew L, Sahasithiwat S, et al. The coordination chemistry of benzhydrazide with lanthanide(iii) ions: hydrothermal in situ ligand formation, structures, magnetic and photoluminescence sensing properties. RSC Advances. 2021;11(40):24709–21. Available from: <URL>.

19. Guan Q, Zhou LL, Dong YB. Metalated covalent organic frameworks: from synthetic strategies to diverse applications. Chemical Society Reviews. 2022; 51(15):6307–416. Available from: <URL>.

20. Zhao J, Yuan J, Fang Z, Huang S, Chen Z, Qiu F, et al. One-dimensional coordination polymers based on metal–nitrogen linkages. Coordination Chemistry Reviews. 2022 Nov;471:214735. Available from: <URL>.

21. Sánchez-Fernández JA. Structural Strategies of Supramolecular Hydrogels and Their Applications [Internet]. Chemistry; 2023 Feb [cited 2023 Dec 1]. Available from: <URL>.

22. Bauer AW. Single-Disk Antibiotic-Sensitivity Testing of Staphylococci: An Analysis of Technique and Results. JAMA Internal Medicine. 1959 Aug 1;104(2):208. Available from: <URL>.

23. Mohamed DS, Al-Jibori SA, Behjatmanesh-Ardakani R, Faihan AS, Yousef TA, Alhamzani AG, et al. Spectroscopic, Anti-Cancer Activity, and DFT Computational Studies of Pt(II) Complexes with 1-Benzyl-3-phenylthiourea and Phosphine/Diamine Ligands. Inorganics. 2023 Mar 16;11(3):125. Available from: <URL>.

24. Al-Janabi ASM, Yousef TA, Al-Doori MEA, Bedier RA, Ahmed BM. Palladium(II)-salicylanilide complexes as antibacterial agents: Synthesis, spectroscopic, structural characterization, DFT calculations, biological and in silico studies. Journal of Molecular Structure. 2021 Dec;1246:131035. Available from:<URL>.

251

25. Al-Jibori SA, Al-Jibori GHH, Saleh SS, Al-Janabi AS, Laguna M, Wagner C. Mercury (II) benzisothiazolinate (bit) complexes with diamine or phosphine co-ligands, and subsequent conversion to 2-mercaptobenzamide complexes. Crystal structures of [Hg(bit)2(L2)], L2 = bipyridine or phenanthroline. Polyhedron. 2021 Sep;206:115353. Available from: <URL>.

26. Salih MM, Saleh AM, Hamad AS, Al-Janabi AS. Synthesis, spectroscopic, anti-bacterial activity, molecular docking, ADMET, toxicity and DNA binding studies of divalent metal complexes of pyrazole-3-one azo ligand. Journal of Molecular Structure. 2022 Sep;1264:133252. Available from: <URL>.

27. Al-Janabi ASM, Oudah KH, Aldossari SA, Khalaf MA, M. Saleh A, Hatshan MR, et al. Spectroscopic, anti-bacterial, anti-cancer and molecular docking of Pd(II) and Pt(II) complexes with (E)-4-((dimethylamino)methyl)-2-((4,5-dimethylthiazol-2-yl)diazenyl)phenol ligand. Journal of Saudi Chemical Society. 2023 May;27(3):101619. Available from: <URL>.

28. Afandi ZS, Al-Jibori SA, Ferjani H, Al-Shammar RH, Aldossari SA, Al-Janabi AS. Ortho-palladated complexes with aromatic N-donor ligands, synthesis, characterization, molecular structures, antibacterial and anticancer activity [Internet]. In Review; 2022 Oct [cited 2023 Dec 1]. Available from: <URL>.

29. Al-Janabi ASM, Elzupir AO, Abou-Krisha MM, Yousef TA. New Dual Inhibitors of SARS-CoV-2 Based on Metal Complexes with Schiff-Base 4-Chloro-3-Methyl Phenyl Hydrazine: Synthesis, DFT, Antibacterial Properties and Molecular Docking Studies. Inorganics. 2023 Jan 29;11(2):63. Available from: <URL>.

30. Al-Janabi AMA, Faihan AS, Al-Mutairi AM, Hatshan MR, Al-Jibori SA, Al-Janabi ASM. Spectroscopic, biological activity studies, and DFT calculations, of Pd(II) and Pt(II) complexes of 4-Methylene-3-phenyl-3,4-dihydroquinazoline-2(1H)-thione. Journal of the Indian Chemical Society. 2022 Nov;99(11):100774. Available from: <URL>.

31. Al-Jibori LH, Al-Janabi AS. Spectroscopic characterization, and anti-bacterial activity studies of the benzohydrazide derivatives complexes. Microbial Science Archives. 2023;3(3):141–6.

DFT and Electrochemical Study of Novel Green Corrosion Inhibitor (Pyrantrin) for 1100-H14 Aluminum Corrosion Remediation in 1 M H₂SO₄ Acidic Environment

Benedict U. Ugi[1]* iD

[1] Department of Pure & Industrial Chemistry, University of Calabar, P. M. B. 1115, Calabar – Nigeria.

Abstract: The study on Corrosion Inhibition of 1100-H14 Aluminum in H₂SO₄ Acidic Deploying pyrantrin as a Green Inhibitor was investigated by adopting different experimental methods, including weight loss, electrochemical impedance spectroscopic, potentiodynamic polarization, and computational methods. It was observed that pyrantrin was a good inhibitor for the 1100–H14–type aluminum. Inhibition efficiency was recorded between 42.5 % and 95.2 % for aluminum at 500 ppm and 1500 ppm concentrations. This high inhibition efficiency was attributed to the strong adsorption of the molecules on both metal surfaces. Electrochemical impedance showed higher and increasing charge transfer resistance values and decreasing values for the double-layer capacitance, indicating better inhibition. From quantum calculations, the EHOMO value was higher than that of the ELUMO, while the energy gap was calculated to be 1.9 with a binding energy of 132.9, indicating stronger adsorption and inhibition.

1. INTRODUCTION

Like death and taxes, corrosion is something we hope to avoid, but ultimately, it is something we must learn to deal with. Metals, especially aluminum, are widely used in today's world, especially in the fields of engineering – shipping, building, construction, machining, automobile, petroleum, mining, etc. (1-2). The beauty and strength experienced by these metals while in use allow for their wider application. However, the wide application of metal is truncated by the damage caused by the effects of corrosion. This aggressiveness from corrosion could tamper with the metal's durability, tensile strength, malleability, ductility, conductivity, lustrousness, etc. Corrosion, the deterioration of metal under unfavorable environmental conditions, has come a long way and seems only to be managed as hopes of complete eradication of the effects are dripping off, considering the different growing environmental conditions experienced today, especially from greenhouse effects (1,3). The cause of corrosion is widely attributed to the chemistry involved – electrochemical or chemical corrosion process and the processes involved in the preparation and treatment of these metals before their application, for instance, during acid pickling, acidization, descaling, fracking processes, etc. (2-4). In the corrosion process, two reactions take place. In one, the anodic reaction, metal atoms are ionized and pass into solution, leaving their electrons within the original metal surface (1-3). In the second, the cathodic reaction, the free electrons within the metal are taken up by chemical species such as O_2 and H_2O in reduction reactions. Corrosion inhibitors have been found to be effective and flexible means of corrosion mitigation. Most organic/inorganic compounds containing elements of groups V B and VI B or functional groups of the amine, carbonyl, and alcoholic groups are more effective corrosion inhibitors (2,3-5). The inhibitor is adsorbed on the entire metal surface, preventing the metal's attack. pyrantrin (Figure 1) is used particularly as the embonate [4,4'-methylenebis(3-hydroxy-2-naphthoate)] salt and as an anthelmintic that is effective against intestinal nematodes, including threadworms, roundworms, and hookworms. This study investigates pyrantrin application as an alternative green corrosion inhibitor of 1100-H14 aluminum alloy in a 1 M H_2SO_4 acid environment.
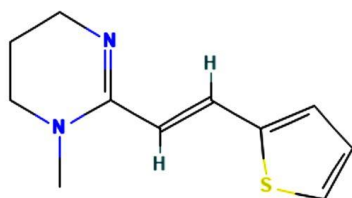
Figure 1: Structure of pyrantrin (4-[(3-carboxy-2-hydroxynaphthalen-1 yl) methyl]-3 hydroxynaphthalene-2-carboxylic acid).

2. EXPERIMENTAL SECTION

2.1. Preparation of Inhibitor Stock Solution and Metal Dressing

5 g of the drug, obtained in a powdered form, was digested in a 1000 ml volumetric flask containing 1.0 M H_2SO_4 and allowed to completely dissolve for 48 hours. It was later filtered, and different inhibitor concentrations (500, 750, 1000, 125, and 1500 ppm) were prepared. The pieces of 1100-H14 aluminum alloy used for this work were obtained from Ibom Metal and Aluminum Company, Akwa Ibom State, Nigeria, with a composition of Cu (0.05 – 0.20 %), Fe (0.95 %), Mn (0.05 %), Si (0.95 %), Zn (0.1 %), Residuals (0.15 %) and Al (98.8 %) for aluminum. The metals were resized into 2.5 cm x 0.08 cm x 2.5 cm dimension for gravimetric analysis and 1 cm x 1 cm for electrochemical impedance analysis. All the resized metals were adequately polished with an electronic UNIPOL- 820 metallographic polishing machine to a mirror surface with different grades of emery papers (300, 1000, and 1200 grades), washed in distilled water, degreased in ethanol, rinsed in Acrastrip 600 Auto reagent, air dried and stored in a moisture free desiccator.

2.2. Mass Loss Experimentation

Polished coupons of dimension 2.5 cm x 0.08 cm x 2.5 cm were initially weighed, and readings were recorded. They were then immersed in the free solution of 1.0 M H2SO4 and other various inhibitor concentrations for 6 hours until the entire experimentation was completed. The coupons were removed from the solutions, washed with distilled water, rinsed in ethanol, degreased with Acrastrip 600 Auto reagent, air dried, and re-weighed every hour. The surface coverage and % inhibition efficiency of the inhibitor was determined from equation 1 and 2

$$Surface coverage (I) = \frac{(C_x - C_y)}{C_x} \qquad (1)$$

$$Inhibition efficiency (\%F) = \frac{(C_x - C_y)}{C_x} x100 \qquad (2)$$

where I is the surface coverage of the inhibitor, C_x and C_y are the corrosion rates of the free and inhibited solutions, and %F is the percentage inhibition efficiency of the inhibitor.

2.3. Electrochemical Method (EIS/PDP)

The EIS was conducted in a Gamry Reference 600 potentiostat. The reference electrode for the system was a saturated calomel (SCE) electrode, a 1 cm²

platinum foil was adopted as a counter electrode, and the working electrode was an aluminum coupon with dimensions 1 cm x 1 cm. Electrochemical tests were conducted within a frequency of 10 Hz - 100,000 Hz with an amplitude of 5 mV. The Potentiodynamic polarization measurement was carried out by altering the electrode potential from – 1.5 to + 1.5 V with respect to the open circuit potential (OCP) at a scan rate of 0.01 mV/s. All experiments were conducted every 60 min with the free and inhibited solutions. From b_{ct} and I_{corr} obtained, the surface coverage and inhibition efficiencies were calculated using Equation 3– 5, respectively.

$$I = \frac{b_{ct}^0 - b_{ct}^i}{b_{ct}^0} \qquad (3)$$

$$\%\wp = \frac{b_{ct}^0 - b_{ct}^i}{b_{ct}^0} x100 \qquad (4)$$

$$\%\wp = 100[1 - \frac{I_{corr}^i}{I_{corr}^0}] \qquad (5)$$

where I is the surface coverage of the inhibitor, b_{ct}^0 and b_{ct}^i represent the charge transfer resistance and I_{corr}^0 and I_{corr}^i is the corrosion density in the free and inhibited solutions of the inhibitor, respectively.

2.4. Computational Method

The studies were conducted with the Material Studio software (version 8.0). The quantum chemistry computations were performed using two computational programs, namely Vamp and Dmol3. Theoretical calculations were conducted at the Restricted Hartree-Fock level (RHF) utilizing the Hamiltonian parametric method 3 (PM3). Information obtained include higher occupied molecular orbital energy (E_{HOMO}), lower unoccupied molecular orbital energy (E_{LUMO}), Fukui positive and negative indices plots, HOMO and LUMO energy plots, energy gap (ΔE), chemical potential (μ), global hardness (η) and global softness (S), electrophilicity index (ω), according to equation 6 – 10 respectively.

$$Energy gap (\Delta E) = E_{HOMO} - E_{LUMO} \qquad (6)$$

$$Chemical potential (\mu) = \frac{-(E_{HOMO} + E_{LUMO})}{2} \qquad (7)$$

$$Global hardness (\eta) = \frac{(E_{HOMO} - E_{LUMO})}{2} \qquad (8)$$

$$Global softness (S) = \frac{1}{2[\frac{(E_{HOMO} - E_{LUMO})}{2}]} \qquad (9)$$

$$Electrophilicity index (\omega) = \frac{\mu^2}{2[\frac{(E_{HOMO} - E_{LUMO})}{2}]} \qquad (10)$$

3. RESULTS AND DISCUSSION

3.1. Weight Loss

From Table 1, it was observed that the loosely bounded particles of the metal were affected by the acid attack, especially where no inhibitor was introduced. This could be due to dissolved non-volatile metal particles accumulating in solution over time (8, 10-13). However, it was not the case when the inhibitor was added, as the weight loss eventually began to decrease with time, implying that the

inhibitor prompted the reduction in the electron flow from the anode. This is again attributed to stronger phyto-atom adsorption on the surface, withholding the dissociation process of loosely held particles (7, 11, 14).

Table 1: Weight loss data showing corrosion rate of 1100 – H14 aluminum, surface coverage, and inhibition efficiency of pyrantrin in 1m H_2SO_4 solutions.

Conc. (ppm)	Cor. Rate (mg/cm²/hr)	Sur. Cov.	Inh. Eff. (%)
Blank	0.0042	-	-
500	0.0025	0.405	40.5
750	0.0019	0.548	54.8
1000	0.0016	0.619	61.9
1250	0.0008	0.810	81.0
1500	0.0002	0.952	95.2

3.2. Electrochemical Impedance Result

Data for the electrical interference of the system with the inhibitor are presented in Table 2, and the corresponding Nyquist plots are shown in Figures 2a-b. It was observed that the inhibitor showed a single capacity loop for 1100 - H14 Aluminum, which is directed toward a single charge transfer (6, 15-17). The sizes of these loops were observed to increase with the rise up to 2500 ppm, which is in line with the increased charge transfer values, indicating adsorption of the inhibitor on both surfaces and a reduction of the exposed area (active sites) of the metal (10,15,16). The data for the double-layer capacitance of the semicircle and inhibition efficiency were determined following Equation 11 - 12 and are presented in Tables 5 and 6.

$$C_{dl} = \frac{1}{\omega Z''} \qquad (11)$$

where Z" is the imaginary component of impedance at any frequency inside the semicircle and ω is the angular frequency (9,11).

$$\%\wp = \frac{b_{ct}^0 - b_{ct}^i}{b_{ct}^0} x100 \qquad (12)$$

where b_{ct}^0 and b_{ct}^i correspond to the charge transfer values in the free and inhibited solutions of expired pyrantrin inhibitors, respectively.

Values from Table 2 showed increased charge transfer resistance as both metals were measured through increased concentration. Considering the increased values of the charge transfer resistance with inhibitor concentration, it is conclusive that a greater difficulty in charge transfer from metal to corrosive media was encountered in the presence of the pyrantrin inhibitor as the electrochemical process was affected; hence strong surface adsorption came to play as well as inhibition of corrosion active sites in metal (18-20).

(a)   (b)
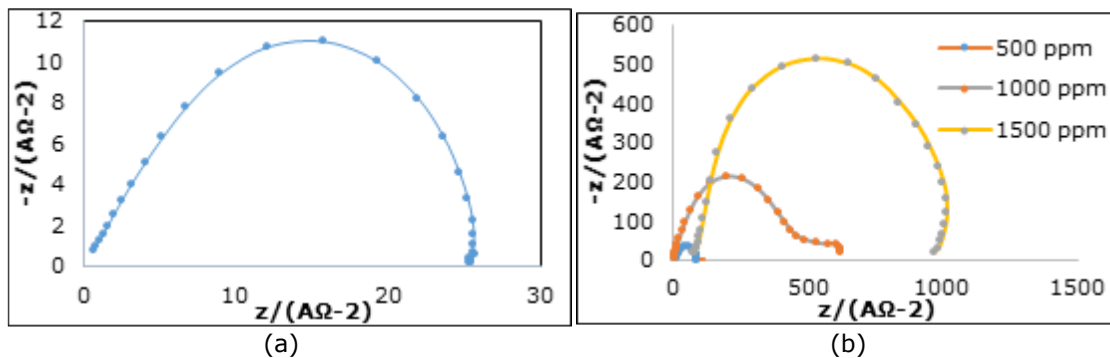
Figure 2: Nyquist plots for the corrosion inhibition of 1100–type aluminum (a) without and (b) with pyrantrin inhibitor in 1 M H_2SO_4 solutions.

Table 2: Nyquist plots values showing charge transfer resistance, double layer capacitance, and inhibition efficiency for the corrosion inhibition of 1100–type aluminum using pyrantrin inhibitor in 1 M H_2SO_4 solutions.

Conc. (ppm)	R_{ct} (A^{-2}Ω)	C_{dl}	IE (%)
Blank	26.4	6.658×10^{-6}	-
500	97.6	4.586×10^{-6}	72.9
1000	658	2.506×10^{-6}	95.9
1500	889	2.267×10^{-6}	97.0

In order to analyze the electrochemical system stability during the corrosion inhibition process with and without the inhibitor, the Phase margins of the Bode plots were derived from the electrochemical

experiment, as shown in Fig. 3. From the plots (Figure 3), it was observed that all the phase lag data fitted well and gave rise to a positive phase margin and higher values (i.e., Blank – 120^0, 500 ppm - 139^0, 1000 ppm - 113^0 and 1500 ppm - 125^0). This implies

that the inhibitor perfectly stabilized the system throughout the electrochemical process, which makes the pyrantel inhibitor a good one for the corrosion inhibition of the metals (21-23).
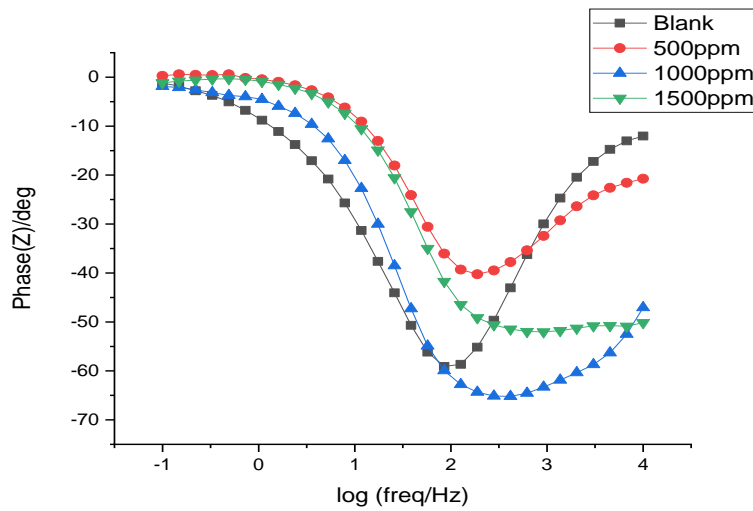
Figure 3: Bode plots for the corrosion inhibition of 1100 – H14 aluminum using pyrantrin inhibitor in 1 M H_2SO_4 solutions.

3.3. Potentiodynamic Polarization Result
Table 3 presents the potentiodynamic polarization values derived from the data depicted in Figure 4. The experimental results indicate that adding inhibitors caused a progressive shift in the corrosion potential values toward a more positive direction. This shift led to alterations in both the cathodic and anodic polarization branches. This observation suggests that the introduced inhibitor molecules mostly functioned as an anodic-type inhibitor (15, 19-21). This can also be confirmed by the anodic and cathodic Tafel slope values presented in Table 3. The

corrosion current density measurements exhibited a downward trend, whereas the comparable inhibition efficiency values derived from corrosion polarization demonstrated an upward trend for both metals when the inhibitor was present. This suggests that the extent of electron loss at the anode was negligible, hence indicating the absence of any oxidation reaction that could have led to the degradation (corrosion) of the anode. Therefore, it can be observed that the cathode remains unaltered (23-25).
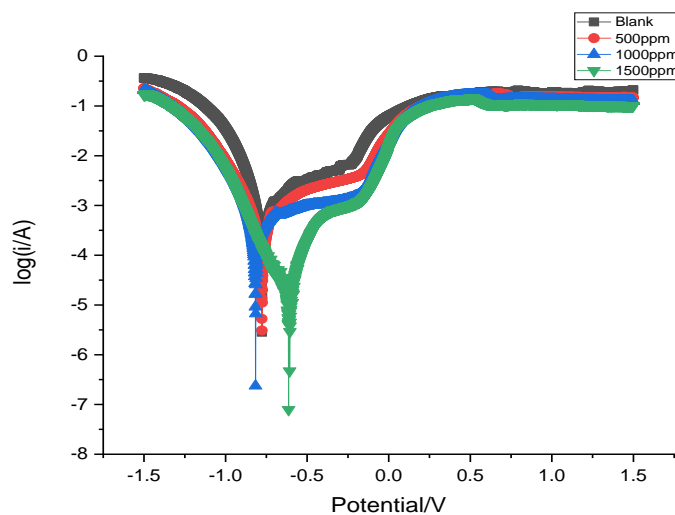
Figure 4: Tafel plots for the corrosion inhibition of 1100–type aluminum using pyrantrin inhibitor in 1 M H_2SO_4 solutions.

Table 3: Tafel plots values for the corrosion inhibition of 1100–type aluminum using pyrantrin inhibitor in 1 M H_2SO_4 solutions.

Conc. (ppm)	I_{corr} (μAcm^{-2})	Slp_c (mV/dec)	Slp_a (mV/dec)	LP (Ω)	IE_{LP} (%)	IE_{Icorr} (%)	E_{corr} (mV)
Blank	9.905	9.706	8.211	1067	-	-	-9.368
500	4.231	7.969 [1.737]	4.179 [4.042]	116	89.1	57.3	-7.256
1000	3.366	7.765 [1.941]	2.661 [5.563]	106	90.1	66.0	-6.758
1500	3.138	4.763 [4.943]	1.412 [6.809]	53	95.0	68.3	-6.405

3.4. Quantum Chemical Calculations

After assessment of both the active component – pyrantel ($C_{11}H_{14}N_2S$) and the inactive components – Butylated hydroxytoluene ($C_{15}H_{24}O$), Citric acid monohydrate ($C_6H_8O_7.H_2O$), Potassium sorbate ($C_6H_7O_2.K$), Sodium benzoate ($C_7H_5O_2.Na$), Sucrose ($C_{12}H_{22}O_{11}$), Water (H_2O) and Xanthan gum of pyrantrin, the researcher concluded on applying the density functional theory (DFT) on the active component which is likely the effective contributor to the corrosion inhibition of 1100-H14 aluminum. This conclusion on the active component contribution to corrosion inhibition was drawn from the fact that the inactive component does not possess characteristics of a typical inhibitor, e.g., the presence of hetero-atoms like N, S, P, etc., no double bond to access pi bonds, not aromatic, etc. Figures 5a -c show the optimized structure and the Frontier molecular orbitals (FMO) distribution density of the energy of the highest occupied molecular orbital (EHOMO) and the energy of the lowest unoccupied molecular orbital (ELUMO) for pyrantel. It is evident from the figures that the electron density distribution at the highest occupied molecular orbital (HOMO) is localized strongly on the heteroatom (Nitrogen), carbon–carbon double bonds on the aromatic benzene ring and in methyl group (CH_3) present in pyrantel (Figures 5 d – e) (17-19). However, the electron density distribution for the lowest unoccupied molecular orbital (LUMO) was distributed on the individual carbon atoms on the aromatic ring and the Sulphur stereogenic centers (Figures 5 d – e). Therefore, the inhibitory power of pyrantrin can be explained mostly by the presence of π electrons and nitrogen heteroatoms favoring the sharing of electrons between the inhibitor and the metal surface (10-12, 23-26).

(a)   (b)   (c)

(d)   (e)
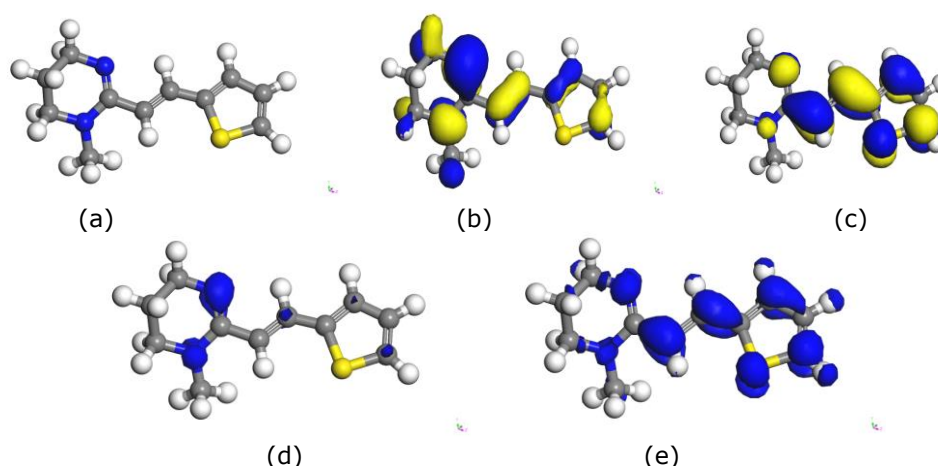
Figure 5: (a) Optimized structure, (b) Highest occupied molecular orbital and (c) Lowest unoccupied molecular orbital (d) Electrophilic (f-) and (e) Nucleophilic (f+) reactive sites of pyrantel molecule.

Table 4: Quantum chemical calculations values for pyrantel molecule.

Parameters	Data (eV)
E_{HOMO}	-4.075
E_{LUMO}	-2.154
ΔE (energy gap)	1.921
χ	3.114
η	0.961
σ	1.848
ω	5.045
δ	0.198
ΔN	2.969
ΔE_{b-d}	0.240
Binding energy	-132.9

Table 4 shows the quantum chemical parameters for pyrantel as an inhibitor of corrosion of 1100 – H14 aluminum. Absolute electronegativity (χ), global hardness (η), global softness (σ), electrophilicity index (ω), and nucleophilicity index (δ) were calculated from equation 13 – 17.

$$\chi = \frac{I.P.+E.A.}{2} \tag{13}$$

$$\eta = \frac{I.P.-E.A.}{2} \tag{14}$$

$$\sigma = \frac{1}{\eta} \tag{15}$$

$$\omega = \frac{\chi 2}{2\eta} \tag{16}$$

$$\delta = \frac{1}{\omega} \tag{17}$$

where φ_m is the work function for the metal surface (work function for Al (111) is 4.02eV), χ_i represents absolute electronegativity of the inhibitor, η_m, and η_i represents global hardness for the metal and inhibitor, respectively. The inhibitor was observed to have a lower energy gap (2.46 eV), suggesting a lower energy requirement for removing an electron from the highest occupied orbital, which entails a better inhibitor (16, 21, 26). From Table 4, the hardness's value was higher than that of softness. This implies a shorter energy gap between the inhibitor/metal interface and a possible lower dissociation energy, giving rise to stronger adsorption and better inhibition (22, 26-28). Also, the global electrophilicity index (ω) has a value of 5.045, implying a higher inhibition efficiency (28).

4. CONCLUSION

Arising from all the experimental techniques under study,
1. It is confirmed that pyrantrin was a reliable alternative inhibitor for inhibiting 1100 – H14 aluminum corrosion in a sulphuric acid environment.
2. Inhibition of corrosion on 1100 – H14 aluminum was observed through strong adsorption of pyrantrin molecules on the surface of the metals.
3. Electrochemical data was in good agreement with those of the chemical and theoretical as charge transfer resistance and inhibition efficiency were increasing while the double layer capacitance was decreasing with concentration, respectively. Features that are attributed to a good inhibitor.
4. Theoretical data shows that the inhibitor was good as the energy gap for pyrantrin was as low as 1.921 ev, and inhibition depends largely on the hetero-atoms of the major constituent of pyrantrin.

5. CONFLICT OF INTEREST

The authors declare no conflict of interest in the research work.

6. REFERENCES

1. Agwamba EC, Udoikono AD, Louis H, Udoh EU, Benjamin I, Igbalagh AT, et al. Synthesis, characterization, DFT studies, and molecular modeling of azo dye derivatives as potential candidate for trypanosomiasis treatment. Chem Phys Impact [Internet]. 2022 Jun 1;4:100076. Available from: <URL>.

2. Ameh PO, Eddy NO. Experimental and Computational Chemistry Studies on the Inhibition Efficiency of Phthalic Acid (PHA) for the Corrosion of Aluminum in Hydrochloric and Tetraoxosulphate (VI) Acids. Prot Met Phys Chem Surfaces [Internet]. 2018 Nov 28;54(6):1169–81. Available from: <URL>.

3. Ammouchi N, Allal H, Belhocine Y, Bettaz S, Zouaoui E. DFT computations and molecular dynamics investigations on conformers of some pyrazinamide derivatives as corrosion inhibitors for aluminum. J Mol Liq [Internet]. 2020 Feb 15;300:112309. Available from: <URL>.

4. Bashir S, Sharma V, Kumar S, Ghelichkhah Z, Obot IB, Kumar A. Inhibition Performances of Nicotinamide Against Aluminum Corrosion in an Acidic Medium. Port Electrochim Acta [Internet]. 2020;38(2):107–23. Available from: <URL>.

5. Ugi BU. Corrosion Inhibition of Cu-Zn-Fe Alloy in Hydrochloric Acid Medium by Crude Ethanol Extracts from Roots-Leaves Synergy of Solanum melongena. Earthline J Chem Sci [Internet]. 2020 Nov 27;5(1):105–18. Available from: <URL>.

6. Buvaneswari M, Santhakumari R, Usha C, Jayasree R, Sagadevan S. Synthesis, growth, structural, spectroscopic, optical, thermal, DFT, HOMO–LUMO, MEP, NBO analysis and thermodynamic properties of vanillin isonicotinic hydrazide single crystal. J Mol Struct [Internet]. 2021 Nov 5;1243:130856. Available from: <URL>.

7. Diki NYS, Coulibaly NH, Kambiré O, Trokourey A. Experimental and Theoretical Investigations on Copper Corrosion Inhibition by Cefixime Drug in 1M HNO3 Solution. J Mater Sci Chem Eng [Internet]. 2021 May 21;9(5):11–28. Available from: <URL>.

8. Ebenso EE, Verma C, Olasunkanmi LO, Akpan ED, Verma DK, Lgaz H, et al. Molecular modelling of compounds used for corrosion inhibition studies: a review. Phys Chem Chem Phys [Internet]. 2021 Sep 22;23(36):19987–20027. Available from: <URL>.

9. Erteeb MA, Ali-Shattle EE, Khalil SM, Berbash HA, Elshawi ZE. Computational Studies (DFT) and PM3 Theories on Thiophene Oligomers as Corrosion Inhibitors for Iron. Am J Chem [Internet]. 2021;11(1):1–7. Available from: <URL>.

10. Ugi BU, Obeten ME, Bassey VM, Boekom EJ, Omaliko EC, Ugi FB, et al. Quantum and Electrochemical Studies of Corrosion Inhibition Impact on Industrial Structural Steel (E410) by Expired Amiloride Drug in 0.5 M Solutions of HCl, H2SO4 and NaHCO3. Moroccan J Chem [Internet]. 2021 Dec 4;9(4):677–96. Available from: <URL>.

11. Fouda AE-AS, El-Askalany AH, Molouk AFS, Elsheikh NS, Abousalem AS. Experimental and computational chemical studies on the corrosion inhibitive properties of carbonitrile compounds for carbon steel in aqueous solutions. Sci Rep [Internet]. 2021 Nov 4;11(1):21672. Available from: <URL>.

12. Joshi BD, Thakur G, Chaudhary MK. Molecular Structure, Homo-Lumo and Vibrational Analysis Of Ergoline By Density Functional Theory. Sci World [Internet]. 2021 Feb 15;14(14):21–30. Available from: <URL>.

13. Liu Q, Song Z, Han H, Donkor S, Jiang L, Wang W, et al. A novel green reinforcement corrosion inhibitor

extracted from waste Platanus acerifolia leaves. Constr Build Mater [Internet]. 2020 Nov 10;260:119695. Available from: <URL>.

14. Majd MT, Ramezanzadeh M, Ramezanzadeh B, Bahlakeh G. Production of an environmentally stable anti-corrosion film based on Esfand seed extract molecules-metal cations: Integrated experimental and computer modeling approaches. J Hazard Mater [Internet]. 2020 Jan 15;382:121029. Available from: <URL>.

15. Onyeachu IB, Abdel-Azeim S, Chauhan DS, Quraishi MA. Electrochemical and Computational Insights on the Application of Expired Metformin Drug as a Novel Inhibitor for the Sweet Corrosion of C1018 Steel. ACS Omega [Internet]. 2021 Jan 12;6(1):65–76. Available from: <URL>.

16. Uwah IE, Ugi BU, Okafor PC, Ikeuba AI. Investigation of the corrosion inhibition effects of Bitters on Mild Steel in acidic medium: A case study of Andrographis paniculata and Vernonia amygdalina. In: Proceedings of the 35th Annual International Conference, Workshop and Exhibition of the Chemical Society of Nigeria (CSN). 2012. p. 304–9.

17. Padash R, Sajadi GS, Jafari AH, Jamalizadeh E, Rad AS. Corrosion control of aluminum in the solutions of NaCl, HCl and NaOH using 2,6-dimethylpyridine inhibitor: Experimental and DFT insights. Mater Chem Phys [Internet]. 2020 Apr 1;244:122681. Available from: <URL>.

18. Rbaa M, Ouakki M, Galai M, Berisha A, Lakhrissi B, Jama C, et al. Simple preparation and characterization of novel 8-Hydroxyquinoline derivatives as effective acid corrosion inhibitor for mild steel: Experimental and theoretical studies. Colloids Surfaces A Physicochem Eng Asp [Internet]. 2020 Oct 5;602:125094. Available from: <URL>.

19. Sharma S, Ganjoo R, Kr. Saha S, Kang N, Thakur A, Assad H, et al. Experimental and theoretical analysis of baclofen as a potential corrosion inhibitor for mild steel surface in HCl medium. J Adhes Sci Technol [Internet]. 2022 Oct 2;36(19):2067–92. Available from: <URL>.

20. Ugi BU, Obeten ME, Bassey VM, Hitler L, Adalikwu SA, Omaliko CE, et al. Adsorption and Inhibition Analysis of Aconitine and Tubocurarine Alkaloids as Eco-friendly Inhibitors of Pitting Corrosion in ASTM – A47 Low Carbon Steel in HCl Acid Environment. Indones J Chem [Internet]. 2022 Jan 25;22(1):1–16. Available from: <URL>.

21. Solomon MM, Umoren SA, Quraishi MA, Tripathy DB, Abai EJ. Effect of akyl chain length, flow, and temperature on the corrosion inhibition of carbon steel in a simulated acidizing environment by an imidazoline-based inhibitor. J Pet Sci Eng [Internet]. 2020 Apr 1;187:106801. Available from: <URL>.

22. Su P, Li L, Li W, Huang C, Wang X, Liu H, et al. Expired Drug Theophylline as Potential Corrosion Inhibitor for 7075 Aluminium Alloy in 1M NaOH Solution. Int J Electrochem Sci [Internet]. 2020 Feb 1;15(2):1412–25. Available from: <URL>.

23. Tan J, Guo L, Wu D, Wang S, Yu R, Zhang F, et al. Electrochemical and Computational Studies on the Corrosion Inhibition of Mild Steel by 1-Hexadecyl-3-methylimidazolium Bromide in HCl Medium. Int J Electrochem Sci [Internet]. 2020 Mar 1;15(3):1893–903. Available from: <URL>.

24. Zaher A, Chaouiki A, Salghi R, Boukhraz A, Bourkhiss B, Ouhssine M. Inhibition of Mild Steel Corrosion in 1M Hydrochloric Medium by the Methanolic Extract of *Ammi visnaga* L. Lam Seeds. Int J Corros [Internet]. 2020 Jan 5;2020:9764206. Available from: <URL>.

Molecular Docking Interaction of Medicines Binding to COVID-19 Proteins

Ammar A. Ibrahim[1]* iD , Entesar A. Sulliman[2], Maher A. Ibrahim[2]

[1] Department of Chemistry, College of Science, University of Mosul, Iraq.
[2] Department of Biochemistry, College of Medicine, University of Mosul, Iraq.

Abstract: In late 2019, in Wuhan, China, a new human coronavirus known as severe acute respiratory syndrome coronavirus 2 (SARS-CoV-2) first appeared. This virus caused the respiratory ailment known as coronavirus disease 2019 (COVID-19), which spread quickly throughout the world. Researchers from all over the world are working feverishly to comprehend SARS-CoV-2 and explore the pathophysiology of this illness to identify viable therapeutic drug candidates and treatments. This research is part of our ongoing search for an effective antiviral medication to combat this devastating illness, which necessitates work in medicinal chemistry. Every day, a sizable number of people die from the terrible disease COVID-19. This research looked at using docking theoretical calculations for dealing with the docking between medicines with proteins. Nine compounds of medicines named Aminoglutethimide, 4-aminosalicylic acid, Felbamate, Hydroflu-methiazide, Methazolamide, Modafinil, Nepafenac, Oxcarbazepine and Trichlormethiazide are used that are commonly active groups like amino group, hydroxyl, and ketone in their conformation structures. Two inhibitions of proteins in the SARS-CoV-2 virus (COVID-19) are applied (6xbg and 6xfn) for docking with nine medicines depending on the software of the Molecular operating environment package (MOE). The docking score was found to be that trichlormethiazide had a more stable value (-6.2955) and (-6.5462) with (6xbg) and (6xfn) proteins respectively.

1. INTRODUCTION

The World Health Organization (WHO) classified a new illness in Wuhan City, China, as a pandemic in March 2020. The coronavirus associated with this pandemic, COVID-19, was proposed as a new variety of SARS-CoV-2 (1). More than one million patients were suffering death and about 40 million have been infected (2-4). Computational features (5) provide new ideas for common medicines used to combat newer coronaviruses. Through molecular docking (6), a virtual screening approach was used to discover the active site of the viral protease for the binding of numerous natural chemicals (7).

To find a new treatment for COVID-19 by putting forth a mechanism for these interactions, a docking study of coumarin derivatives with chloroquine was carried out (8). There is no effective treatment for COVID-19 at this yet (9). The search for novel

medications, particularly those derived from natural plant sources (10), has enormous potential. UV rays, traumas, and bacterial and fungal poisons can all trigger a reaction. Anti-inflammatory, antitumoral, and antiviral agents are various biological functions in human extraction from plants (11-13).

Utilizing molecular docking software, the study of drug interactions with proteins was used to approach drug design and evolution (14,15). SARS-CoV-2-related proteins have been identified as potential therapeutic targets in numerous theoretical investigations, and hundreds of dockings have been conducted with different drugs (16,17).

The best efforts of scientists are being made in this direction. discovery of a chemical to combat this virus, but the outcomes so far are very limited. Since it takes a while, starting from scratch with a new medication in this situation is not a good idea. It

costs a lot of money and time to create a new molecule. COVID-19 is resistant to several known medicines (5, 18). The Food and Drug Administration (FDA) authorized malaria medicine hydroxyl-chloroquine was investigated as a treatment for SARS-CoV-2. Previous research has shown that chloroquine and hydroxychloroquine (19) can suppress the coronavirus (COVID-19) by altering the pH at the cell membrane's surface (20, 21).

Heterocyclic molecules are known as antiviral drugs and are the subject of extensive research for potential medical applications (5, 22). To explore the efficiency of the medicines as COVID-19 inhibitors, comparative research comparing pharmaceuticals with FDA approval and hydroxychloroquine antiviral treatments against a wide range of RNA viruses has been established (15).

Coronaviruses, positive sense-RNA viruses that reproduce in the cytoplasm, are present in infected human cells. A sophisticated replication machinery component that regulates their replication is made up of at least 16 non-structural proteins (23, 24).

COVID-19 was studied in the human body (25), while different types of computations, including pm3, am1, and hf at the basis set (sto-3g), were used to conceptually analyze the medications. Entropy, Gibbs free energy, HOMO, total energy, and LUMO were calculated among other physicochemical data. For the interaction of drugs with various proteins, docking studies were used (26).

Aminoglutethimide is a drug that has been used to treat Cushing's syndrome, breast cancer, prostate cancer, and seizures. While 4-aminosalicylic acid is mainly used as an antibiotic to treat tuberculosis. In particular, it is used in conjunction with other antituberculosis drugs to treat active drug-resistant tuberculosis.

Felbamate is an anticonvulsant that is applied to epilepsy patients. It is used to treat Lennox-Gas taut syndrome-related partial and generalized seizures in children as well as partial seizures in adults, both with and without generalization. Hydroflumethiazide is a thiazide diuretic used to treat liver cirrhosis, congestive heart failure, and hypertension-related edema.

Methazolamide is recommended for the management of elevated intraocular pressure (IOP) in both secondary and chronic open-angle glaucoma. Modafinil is a central nervous system (CNS) stimulant drug used to treat obstructive sleep apnea, narcolepsy, and shift work sleep disorder-related insomnia.

Nepafenac is a nonsteroidal anti-inflammatory drug (NSAID) used to treat cataract surgery-related pain and inflammation. Oxcarbazepine is a drug used for the treatment of epilepsy. It is used to treat both focal and generalized seizures in epilepsy. Trichlormethiazide is typically used to treat hypertension and edema, including those brought on by hepatic cirrhosis, cardiac failure, and cortico-steroid therapy.

2. COMPUTATIONAL METHODS

A docking study was carried out to optimize the medicines with proteins. Structures of the proteins have been chosen from the protein database website (PDB) having the code (6xbg and 6xfn) (27). Water structures, and alternative molecules, were left out of the protein's 3D coordinate information. These proteins were separated from other molecules such as water, alternative compounds, and tiny proteins with a small number of amino acids. These proteins were afterward re-corrected and re-arranged automatically after the hydrogen atoms in the structure were added.

Chem-Bio Office 3D (version 17.1) was used to create the pharmaceutical molecules. The docking software (MOE) (version 2015) was used to characterize all of the ligands and receptors. Simulation of docking was carried out by selecting the active sites of the proteins to arrive at a final optimization to find a configuration that was more stable and had lower steric hindrance.

Using an Intel Core (i7-4810) laptop computer with (8 GB) of RAM and Microsoft Windows 10 Pro as the operating system, docking for ligand and receptor was computed.

3. RESULTS AND DISCUSSION

The docking investigation was used to predict the docking interaction of numerous medications, whose formulas are shown in Figure 1, with various proteins. The activity of these proteins in the SAR-Cov2 virus was taken into consideration when they were chosen.

3.1. Docking of (6xbg)
This protein has (2407) atoms and (300) residues in its structure. Figure 1 shows the complete formula, which comprises 1515 carbon atoms, 405 oxygen atoms, and 27 sulfur atoms (2). There are a lot of active functional groups in these proteins, notably nitrogen, and oxygen.

3.1.1. Docking with Medicines
The binding score energy of (6xbg) protein was calculated. As indicated in Table (1), we selected the optimal location of the protein to interact with different medications to determine the best docking. The (E-9, E-7, E-4, E-6, E-3, E-1, E-5, E-8, and E-2) were discovered to have energy score values of -6.2955, -6.1897, -6.1514, -6.0182, -5.8292, -5.6303, -5.6060, -5.5381, and -4.4638. So, it's clear that every drug is superior to E-9.
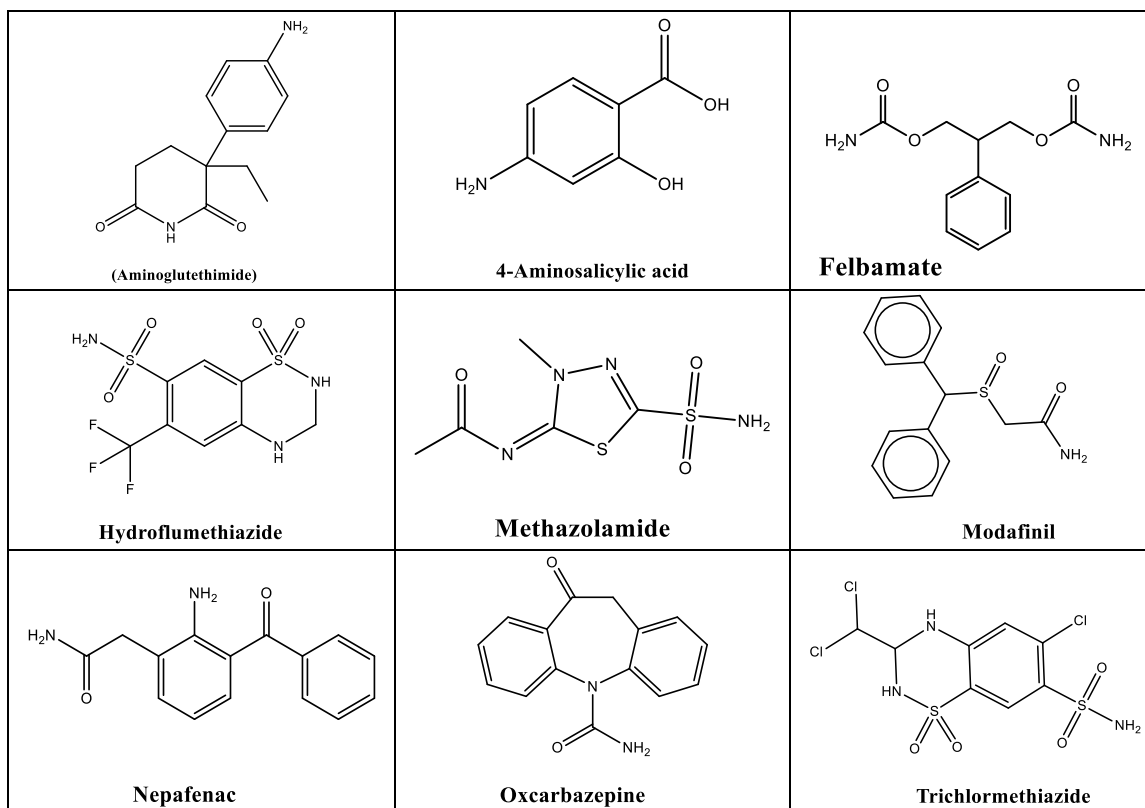
Figure 1: Pharmaceutical substances' molecular structure.
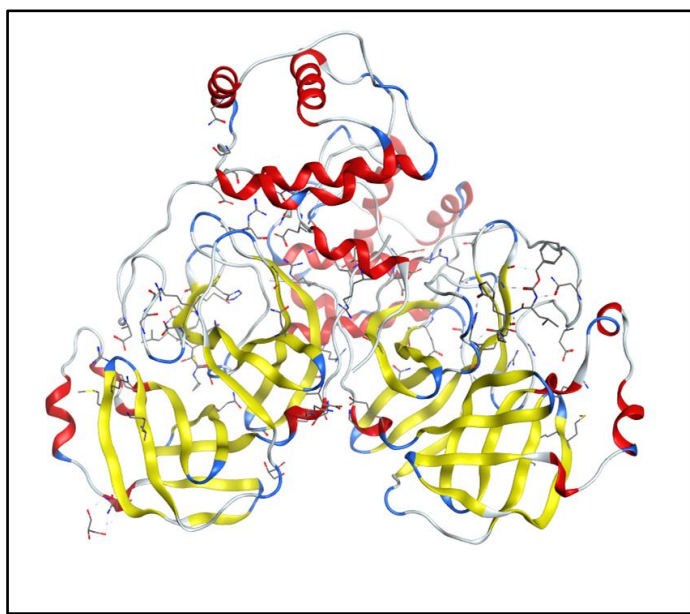
Figure 2: The configuration of (6xbg) protein.

Table 1: Score values for docking of (6xbg) protein with medicines.

Comp. No.	Medicines	Score values
E-1	Aminoglutethimide	-5.6303
E-2	4-Aminosalicylic acid	-4.4638
E-3	Felbamate	-5.8292
E-4	Hydroflumethiazide	-6.1514
E-5	Methazolamide	-5.6060
E-6	Modafinil	-6.0182
E-7	Nepafenac	-6.1897
E-8	Oxcarbazepine	-5.5381
E-9	Trichlormethiazide	-6.2955

When compared to other medicines, trichlormethiazide (-6.2955) had a more stable value, but 4-aminosalicylic acid (-4.4638) did not.

Comp. No.	Docking with Protein	Comp. No.	Docking with Protein
E-1		E-6	
E-2		E-7	
E-3		E-8	
E-4		E-9	
E-5			
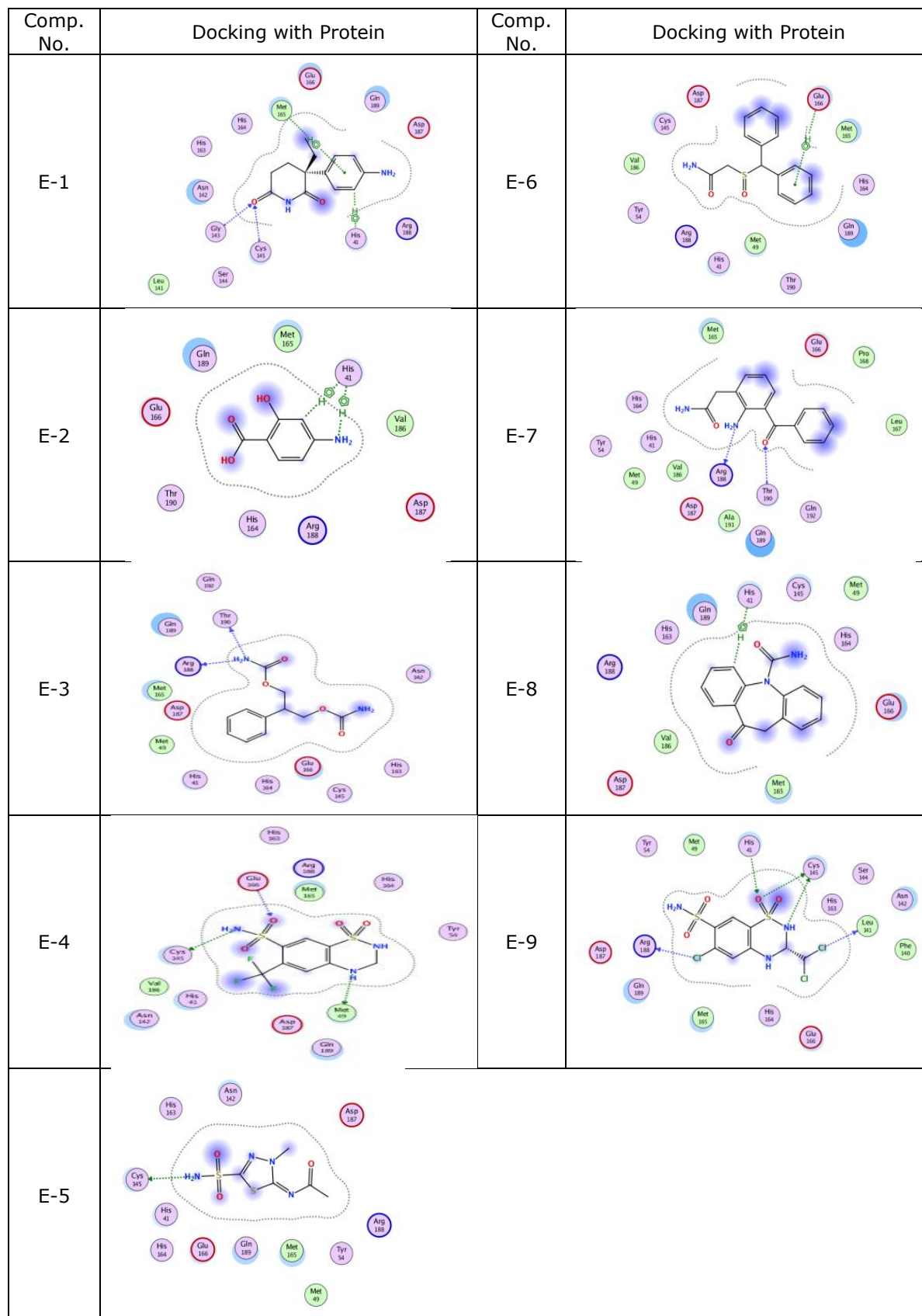
Figure 3: Medicines docking with the (6xbg) protein.
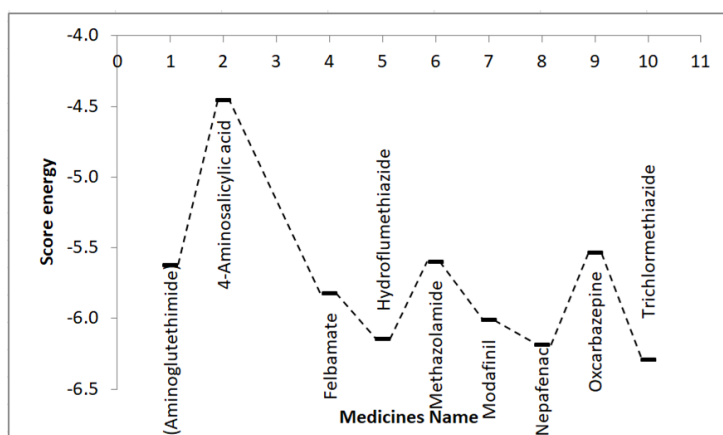
Figure 4: Drug scores at (6xbg) protein.

Various amino acid groups surround the medication (trichlormethiazide). A (His 41) and (Cys 145) intermolecular hydrogen bond linked the active polar site between the medication and the protein, as did (Leu 141) and (Arg188) via free electrons in chlorine as illustrated in Figure (3). By (π) aromatic system, the medication (4-Aminosalicylic acid) came into touch with the amino acid group (His 41).

There are three chlorine atoms in the formula of the medication (Trichlormethiazide), which makes it unique. (NH_2, =O) have active groups, however, this molecule has a higher polarity and is more active. There are a few reasons why Trichlormethiazide was chosen above the others as a medication name.

3.2. Docking of (6xfn)
This protein has around 304 residues and 23488 atoms. As illustrated in Figure 5, the entire formula contained 1486 carbon atoms, 398 nitrogen atoms, 441 oxygen atoms, and 23 sulfur atoms.
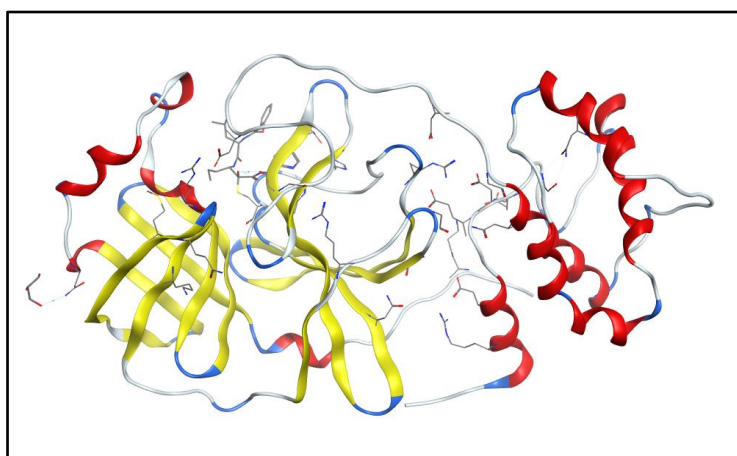
Figure 5: The configuration of (6xfn) protein.

3.2.1. Docking with Medicines
Following that, we chose the optimal location of the protein to interact with various medications to describe the best docking, as indicated in the table below.

Table 2: Score values for docking of (6xfn) protein with medicines.

Comp. No.	Medicines	Score values
E-1	Aminoglutethimide	-5.5095
E-2	4-Aminosalicylic acid	-4.5654
E-3	Felbamate	-5.6109
E-4	Hydroflumethiazide	-5.9720
E-5	Methazolamide	-5.5635
E-6	Modafinil	-5.6988
E-7	Nepafenac	-6.1798
E-8	Oxcarbazepine	-5.5411
E-9	Trichlormethiazide	-6.5462

As indicated in Figure 7, the drug Trichlormethiazide requires a more stable value -6.5462, but the medicine 4-Aminosalicylic acid requires a less stable value -4.5654.

Comp No.	Docking with Protein	Comp No.	Docking with Protein
E-1		E-6	
E-2		E-7	
E-3		E-8	
E-4		E-9	
E-5			
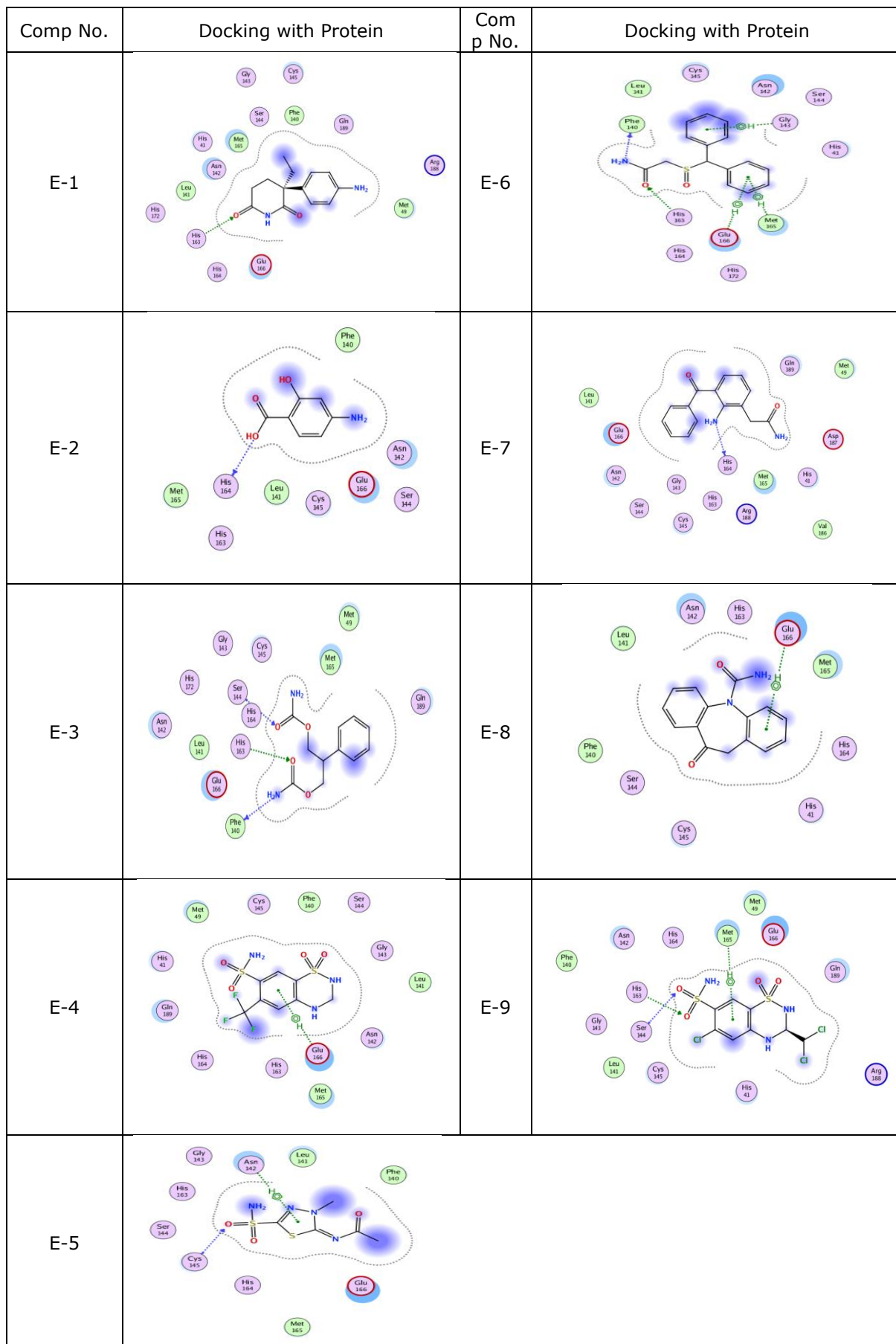
Figure 6: Medicines docking with the (6xfn) protein.
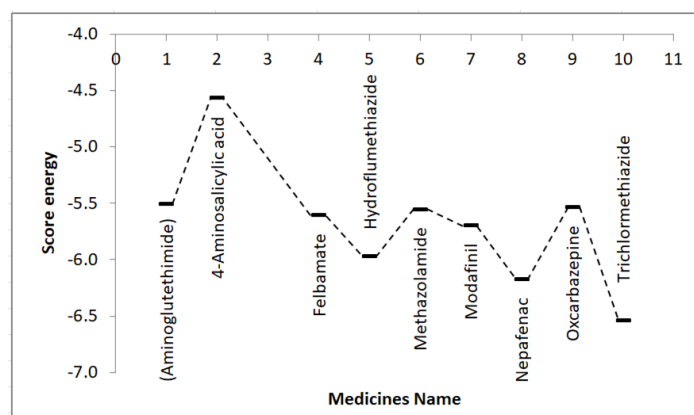
Figure 7: Drug scores at (6xfn) protein.

Many amino acid molecules plagued trichlorme-thiazide therapy. By an intermolecular hydrogen bond, the active site was close to the protein Met 165. In ketone, free electrons were linked to His 163 and Ser 144. Finally, a hydrogen atom joined 4-aminosalicylic acid medication of His 164.

As a result, the medication Trichlormethiazide has three chlorine atoms in its formula, making it more polar and active than other compounds, in addition to having active groups like NH_2, =O in its formula structure. As a result of these factors, the medication name Trichlormethiazide was more stable than the others.

Figure 8 shows the comparison of two medications Trichlormethiazide and 4-aminosalicylic acid and two proteins. In comparison to 6xfn, we may infer that Trichlormethiazide was more active binding docking and more stable compared with 6xbg. In comparison to other medicines, 4-aminosalicylic acid was less stable.
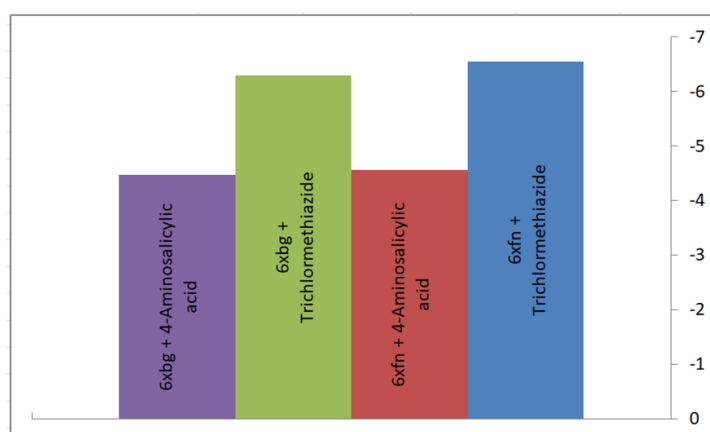
Figure 8: Score comparison of medications containing proteins.

4. CONCLUSION

This study aims to measure the binding affinity of the active compounds within the target protein that are involved in the virus' entry and replication mechanisms, and consequently in the in-silico process of the virus' host cell maturation. The docking results revealed a variety of drug-protein binding interactions, some of which were advantageous. The COVID-19 in complex with the inhibitors exhibited high-affinity interactions with the antiviral medications aminoglutethimide, 4-aminosalicylic acid, Felbamate, hydroflumethiazide, methazolamide, modafinil, nepafenac, oxicarba-zepine, and trichlormethiazide. The docking findings revealed that medication Trichlormethiazide was the most active against the proteins 6xfn and 6xbg with values of -6.5462 and -6.2955, respectively, in comparison to others. With values of -4.5654 and -4.4638, medication 4-Aminosalicylic acid had reduced docking binding with the preceding proteins.

5. ACKNOWLEDGMENTS

6. REFERENCES

1. World Health Organization (WHO). Coronavirus Disease (COVID-19) Situation Reports [Internet]. 2020. Available from: <URL>.

2. Wang C, Horby PW, Hayden FG, Gao GF. A novel coronavirus outbreak of global health concern. Lancet [Internet]. 2020 Feb 15;395(10223):470–3. Available

from: <URL>.

3. Xu X, Chen P, Wang J, Feng J, Zhou H, Li X, et al. Evolution of the novel coronavirus from the ongoing Wuhan outbreak and modeling of its spike protein for risk of human transmission. Sci China Life Sci [Internet]. 2020 Mar 21;63(3):457–60. Available from: <URL>.

4. Mali SN, Pratap AP, Thorat BR. The Rise of New Coronavirus Infection-(COVID-19): A Recent Update. Eurasian J Med Oncol [Internet]. 2020;4(1):35–41. Available from: <URL>.

5. Hagar M, Chaieb K, Parveen S, Ahmed HA, Alnoman RB. N-alkyl 2-pyridone versus O-alkyl 2-pyridol: Ultrasonic synthesis, DFT, docking studies and their antimicrobial evaluation. J Mol Struct [Internet]. 2020 Jan 5;1199:126926. Available from: <URL>.

6. Alnoman RB, Parveen S, Hagar M, Ahmed HA, Knight JG. A new chiral boron-dipyrromethene (BODIPY)-based fluorescent probe: molecular docking, DFT, antibacterial and antioxidant approaches. J Biomol Struct Dyn [Internet]. 2020 Dec 11;38(18):5429–42. Available from: <URL>.

7. Liu C, Ma Y, Zhao J, Nussinov R, Zhang Y-C, Cheng F, et al. Computational network biology: Data, models, and applications. Phys Rep [Internet]. 2020 Mar 3;846:1–66. Available from: <URL>.

8. Ibrahim AA, Yahya OM, Ibrahim MA. Theoretical Prediction of Possible Drug Treatment of COVID-19 using Coumarins Containing Chloroquine Moeity. Asian J Chem [Internet]. 2020 Dec 7;32(12):3120–6. Available from: <URL>.

9. Jiang F, Deng L, Zhang L, Cai Y, Cheung CW, Xia Z. Review of the Clinical Characteristics of Coronavirus Disease 2019 (COVID-19). J Gen Intern Med [Internet]. 2020 May 4;35(5):1545–9. Available from: <URL>.

10. Zhang L, Liu Y. Potential interventions for novel coronavirus in China: A systematic review. J Med Virol [Internet]. 2020 May 3;92(5):479–90. Available from: <URL>.

11. Khaerunnisa S, Kurniawan H, Awaluddin R, Suhartati S, Soetjipto S. Potential Inhibitor of COVID-19 Main Protease (Mpro) From Several Medicinal Plant Compounds by Molecular Docking Study. Preprints [Internet]. 2020 Mar 13;1–14. Available from: <URL>.

12. Khan SA, Zia K, Ashraf S, Uddin R, Ul-Haq Z. Identification of chymotrypsin-like protease inhibitors of SARS-CoV-2 via integrated computational approach. J Biomol Struct Dyn [Internet]. 2021 May 3;39(7):2607–16. Available from: <URL>.

13. Wahedi HM, Ahmad S, Abbasi SW. Stilbene-based natural compounds as promising drug candidates against COVID-19. J Biomol Struct Dyn [Internet]. 2020 May 12;39(9):3225–34. Available from: <URL>.

14. Jorgensen WL. The Many Roles of Computation in Drug Discovery. Science (80-) [Internet]. 2004 Mar 19;303(5665):1813–8. Available from: <URL>.

15. Wang M, Cao R, Zhang L, Yang X, Liu J, Xu M, et al. Remdesivir and chloroquine effectively inhibit the recently emerged novel coronavirus (2019-nCoV) in vitro. Cell Res [Internet]. 2020 Mar 4;30(3):269–71. Available from: <URL>.

16. Wang J. Fast Identification of Possible Drug Treatment of Coronavirus Disease-19 (COVID-19) through Computational Drug Repurposing Study. J Chem Inf Model [Internet]. 2020 Jun 22;60(6):3277–86. Available from: <URL>.

17. Tallei TE, Tumilaar SG, Niode NJ, Fatimawali, Kepel BJ, Idroes R, et al. Potential of Plant Bioactive Compounds as SARS-CoV-2 Main Protease (Mpro) and Spike (S) Glycoprotein Inhibitors: A Molecular Docking Study. Riganti C, editor. Scientifica (Cairo) [Internet]. 2020 Dec 23;2020:6307457. Available from: <URL>.

18. Holshue ML, DeBolt C, Lindquist S, Lofy KH, Wiesman J, Bruce H, et al. First Case of 2019 Novel Coronavirus in the United States. N Engl J Med [Internet]. 2020 Mar 5;382(10):929–36. Available from: <URL>.

19. Hoffmann M, Kleine-Weber H, Schroeder S, Krüger N, Herrler T, Erichsen S, et al. SARS-CoV-2 Cell Entry Depends on ACE2 and TMPRSS2 and Is Blocked by a Clinically Proven Protease Inhibitor. Cell [Internet]. 2020 Apr 16;181(2):271–80. Available from: <URL>.

20. Devaux CA, Rolain J-M, Colson P, Raoult D. New insights on the antiviral effects of chloroquine against coronavirus: what to expect for COVID-19? Int J Antimicrob Agents [Internet]. 2020 May 1;55(5):105938. Available from: <URL>.

21. Yao X, Ye F, Zhang M, Cui C, Huang B, Niu P, et al. In Vitro Antiviral Activity and Projection of Optimized Dosing Design of Hydroxychloroquine for the Treatment of Severe Acute Respiratory Syndrome Coronavirus 2 (SARS-CoV-2). Clin Infect Dis [Internet]. 2020 Jul 28;71(15):732–9. Available from: <URL>.

22. Gong H-H, Addla D, Lv J-S, Zhou C-H. Heterocyclic Naphthalimides as New Skeleton Structure of Compounds with Increasingly Expanding Relational Medicinal Applications. Curr Top Med Chem [Internet]. 2016 Sep 26;16(28):3303–64. Available from: <URL>.

23. den Boon JA, Diaz A, Ahlquist P. Cytoplasmic Viral Replication Complexes. Cell Host Microbe [Internet]. 2010 Jul 22;8(1):77–85. Available from: <URL>.

24. Hackbart M, Deng X, Baker SC. Coronavirus endoribonuclease targets viral polyuridine sequences to evade activating host sensors. Proc Natl Acad Sci [Internet]. 2020 Apr 7;117(14):8094–103. Available from: <URL>.

25. Kareem AM, Al-Azzawi SN. Comparison Between Deterministic and Stochastic Model for Interaction (COVID-19) With Host Cells in Humans. Baghdad Sci J [Internet]. 2022 Oct 23;19(5):1140–7. Available from: <URL>.

26. Ibrahim AA. A Theoretical Study of the Docking of Medicines with some Proteins. Baghdad Sci J [Internet]. 2023 Apr 1;20(2):483–91. Available from: <URL>.

27. https://www.rcsb.org/

Akper Mejidov A et al. JOTCSA. 2024; 11(1): 269-278

RESEARCH ARTICLE

Crystal and Molecular Structure of The Mixed-Metal Manganese(II) and Cobalt(II) Maleate Complex: [Co_xMn_{1-x}(OOCCH=CHCOO).(H$_2$O)$_2$]$_n$

Ajdar Akper Mejidov[1] , **Esmira Arif Aga Guliyeva[1]*** , **Perizad Amrulla Fatullayeva[1]** ,

Bahattin Yalçın[2] , **Mücahit Özdemir[2]** , **Akif Shikhan Aliyev[1]**

[1] Institute of Catalysis and Inorganic Chemistry named after academician M.Nagiev, Ministry of Science and Education of the Republic of Azerbaijan.
[2] Department of Chemistry, Marmara University, Istanbul, Türkiye.

Abstract: For the first time, by the interaction of cobalt maleate tetrahydrate with Mn(II) acetate, a polymeric polynuclear mixed-metal maleate complex of manganese(II) and cobalt(II) was obtained: [Co_xMn_{1-x}(OOCCH=CHCOO).(H$_2$O)$_2$]$_n$. The composition and structure of the resulting complexes were studied by IR spectroscopy, UV-Vis spectroscopy, EPR, and elemental and thermogravimetric analysis. The crystal structure of the complex was established by X-ray diffraction. The results of X-ray diffraction analysis showed that maleic acid dianions coordinate with Mn(II) and Co(II) ions in the bidentate bridging form, forming seven-membered chelate rings with manganese and cobalt ions. Each metal ion achieves octahedral symmetry with coordination from two oxygen atoms of two water molecules and two bridging oxygen atoms of the maleate ligands of neighboring complex molecules. The electronic absorption spectra show the absorption band at 965 nm, which should be attributed to the Mn(II) complex. The band at 516 nm refers to the cobalt complex. In the EPR spectrum, a wide single band with g = 2.031 is observed, indicating an electronic exchange interaction between Mn(II) and Co(II) ions. The presence of two metal ions in the complex was also confirmed by cyclic voltammetry. The voltammograms clearly show two reduction waves related to the two-electron reduction of Co^{2+} (Ec= -0.69 V) and Mn^{2+} (Ec= -0.985 V) ions.

Keywords: Mn(II), Co(II) maleato complex, crystal structure, coordination polymer.

1.INTRODUCTION

Currently, synthetic and theoretical chemists in the field of "molecular magnetism" are drawn to polynuclear complexes featuring metal ions with intramolecular spin bonds (1-3).

The most important problem of molecular design of metal polyhedral complexes is the search for ligands and synthesis conditions for their creation. An effective method for solving this problem is the use of self-association techniques, by selecting appropriate ligands that have the ability to bind metal ions into polynuclear structures due to bridging fragments (atoms or groups). Another way to obtain polynuclear complexes is through the synthesis of mononuclear metal complexes with incomplete coordination saturation of the ligands in the complex.

Maleic acid derivatives are capable of forming bridging carboxylate poly(mono-, bi-, trivial) polymer complexes with metal(Mn) ions (4-8). It is known that only the inclusion of the bidentate chelating ligand phenanthroline, bipyridyl, etc. is favorable for the formation of coordination polymers (9-11).

The synthesis of polynuclear complexes with purely maleate ligand has not been described in the literature (12-15), and there is only one work, in which the polymeric structure of Mn(II) complex with this ligand was shown by X-ray diffraction analysis (16). A polymeric maleate complex of Mn(II) was obtained by the interaction of manganese(II) carbonate with an aqueous solution of maleic acid. Along with this complex, a mononuclear manganese

maleate tetrahydrate complex was obtained in which maleic acid behaved as a monodentate monoanionic ligand. A similar structure was found for the maleates of a number of metals: Co(II) (17), Ni(II) (18), Zn(II) (19), etc.

In order to obtain a polymeric complex containing various metal ions, we reacted mononuclear cobalt maleate with manganese acetate. This very approach to the synthesis of polymeric structures using a complex with coordination-unsaturated ligands has not yet been published. As a result, a polymer polynuclear mixed-metal maleate complex of manganese(II) and cobalt(II) was obtained: $[Co_xMn_{1-x}(OOCCH=CHCOO)\cdot(H_2O)_2]_n$. The polymer-polynuclear structure of the complex was confirmed by X-ray diffraction analysis.

2. EXPERIMENTAL

2.1. General and spectroscopic measurements
All chemicals in the synthesis were used without further purification. IR spectra of samples were recorded in vaseline in the 4000-400 cm^{-1} range using a Nicolet IS10 spectrophotometer. Electronic absorption spectra were taken on a SPECORD 50 spectrophotometer in water solutions. EPR spectra were taken in solid state at room temperature on a Bruker BioSpin GmbH instrument. Thermogravimetric analysis was performed using a NETZSCH STA 449F3 derivatograph in an inert atmosphere; elemental analysis was performed in the analytical laboratory of TUBITAK, Ankara, on a LECO CHNS 932 analyzer. Energy-dispersive X-ray spectroscopy was performed on a SEM JEOL JSM 6610 LV electron microscope.

Polarization curves were taken in an IVIUMSTAT electrochemical interface potentiostat. To prepare the electrolyte, the complex was dissolved in bidistilled water (0.001 M). A glass three-electrode electrochemical cell was used. The working electrode was a Pt electrode with an area of 0.3×10^{-3} cm^2, the reference electrode was a chlorosilver electrode, and the auxiliary electrode was a platinum plate with an area of 4.0 cm^2. The surface of the Pt electrode was cleaned with concentrated nitric acid.

2.1.1. Synthesis of [Co(OOCCH=CHCOO)$_2\cdot$(H$_2$O)$_4$]
Cobalt maleate [Co(OOCCH=CHCOO)$_2\cdot$(H$_2$O)$_4$] was prepared by mixing cobalt chloride hexahydrate and maleic acid in water (at a molar ratio of 1:1). The mixture was brought to a boil and stirred for 30 minutes. Then it was filtered and left to crystallize. After cooling, bright red crystals precipitated out of it. The yield was 1.80 g (82%). FT-IR spectrum:

(v, cm^{-1}): v(OH, coord.H$_2$O) 3382 cm^{-1}, v$_{as}$(COO-) 1549 cm^{-1}, v$_{sym}$(COO-) 1482 cm^{-1}.

2.1.2. Synthesis of [Co$_x$Mn$_{1-x}$(OOCCH=CHCOO)$\cdot$(H$_2$O)$_2$]$_n$
To 0.006 mol (1.00 g) of cobalt maleate tetrahydrate was added 0.005 mol (1.00 g) of manganese acetate. The mixture was brought to a boil and stirred for 1 h. Then the solution was filtered and left to crystallize. Upon cooling, crimson crystals of T$_m$>250 ^{o}C precipitated from the solution. The obtained crystals were filtered and dried in the vacuum at room temperature. The yield was 0.80 g (85%). For C$_8$H$_{16}$O$_{14}$MnCo: Found: C 23.70, H 3.89, Mn 13.52, Co 14.51%. Calculated: C 23.61, H 3.93, Mn 13.56, and Co 14.54%. IR spectrum: (v, cm^{-1}): v(OH, coord.H$_2$O) 3440 cm^{-1}, v$_{as}$(COO$^-$) 1590 cm^{-1}, v$_{sym}$(COO$^-$) 1500 cm^{-1}.

Single crystal X-ray diffraction experiments were performed on a Bruker APEX II CCD diffractometer using monochromatized Mo-Kα X-radiation. Indexing, data collection, data reduction, and absorption correction were carried out using APEX2. The crystal structure was solved using SHELXT and then refined by full-matrix least-squares refinements on F^2 using SHELXL in the Olex2 Software Package. The aromatic and aliphatic C-bound H atoms were positioned geometrically and refined using a riding mode. Crystal structure validations, geometrical calculations, and drawings were performed using Mercury software. The crystallographic data and details of the refinement of the structure of the complex are given in Table 1.

3. RESULTS AND DISCUSSION

Trimers of mixed and homovalent manganese complexes with different nucleation and oxidation degrees are known from the literature (20-22). However, the synthesis of mixed-metallic polymeric polynuclear manganese complexes by the interaction of cobalt maleate with manganese salts has not been described so far. It should be noted that during the interaction of cobalt maleate with sulfate and manganese nitrate the formation of a polymeric complex was not observed, and mononuclear compounds were formed. Polynuclear maleate manganese complexes are usually prepared by the interaction of maleic acid with a metal salt with the addition of a bidentate chelating ligand (23-31). We have found for the first time that the interaction of the mononuclear tetrahydrate complex of cobalt and manganese acetate produces a polymer-polymer mixed-metal maleate complex of manganese(II) and cobalt(II) (Scheme1).
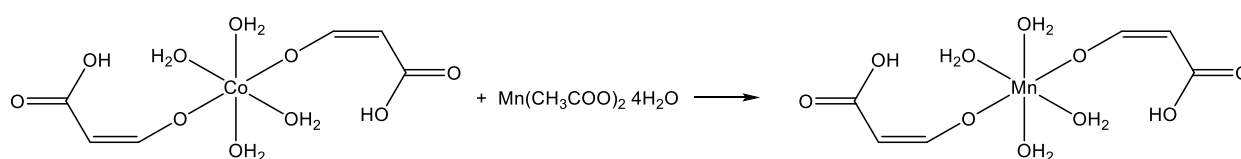
Scheme 1: Polymer-polymer mixed-metal maleate complex of manganese(II) and cobalt(II) structure.

Table 1: Crystal structure data and refinement parameters for [Co$_x$Mn$_{1-x}$(OOCCH=CHCOO)·(H$_2$O)$_2$]$_n$.

Empirical formula	C$_8$H$_{16}$Mn$_2$O$_{14}$
Formula weight	406.52
Temperature/K	299.47
Crystal system	monoclinic
Space group	Cc
a/Å	8.2478(10)
b/Å	13.3183(17)
c/Å	7.7076(15)
α/°	90
β/°	115.3800(10)
γ/°	90
Volume/Å^3	764.9(2)
Z	2
ρ$_{calc}$g/cm^3	1.765
μ/mm^{-1}	1.689
F(000)	397.0
Crystal size/mm^3	0.324 × 0.263 × 0.194
Radiation	MoKα (λ = 0.71073)
2Θ range for data collection/°	6.118 to 54.966
Index ranges	-10 ≤ h ≤ 10, -17 ≤ k ≤ 17, -9 ≤ l ≤ 7
Reflections collected	2799
Independent reflections	1507 [R$_{int}$ = 0.0221, R$_{sigma}$ = 0.0365]
Data/restraints/parameters	1507/2/115
Goodness-of-fit on F^2	0.944
Final R indexes [I>=2σ (I)]	R$_1$ = 0.0171, wR$_2$ = 0.0438
Final R indexes [all data]	R$_1$ = 0.0174, wR$_2$ = 0.0439
Largest diff. peak/hole / e Å^{-3}	0.19/-0.24
Flack parameter	0.027(10)

In the FT-IR spectra of the complex, the absorption bands near 1590 and 1500 cm^{-1} refer to O–C–O asymmetric and symmetric stretching vibrations of maleate groups, respectively. The difference Δv between the wavenumbers of the absorption bands v$_{as}$(COO$^-$) and v$_s$(COO$^-$) is much less than the difference between the wave numbers of the absorption of similar vibrations of the free carboxylate and monodentate coordinated carboxylate groups and is 90 cm^{-1}. It indicates the bidentate or bridging nature of the coordination of the carboxylate group (Scheme 2) (32).
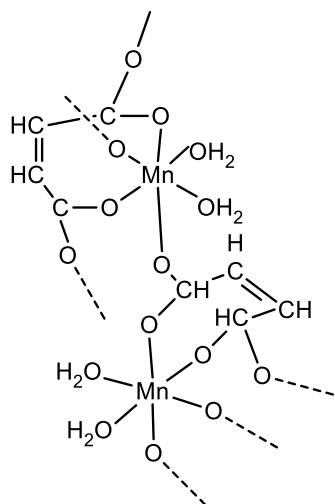
Scheme 2: The fragment of polynuclear complex structure.

X-ray data do not allow us to distinguish between Mn(II) and Co(II) ions and their order in the crystal lattice because of the proximity of their scattering coefficients. According to the data of energy-dispersive X-ray spectroscopy, the content of manganese and cobalt was: Mn-49.49%; Co-28.39%.

The results of X-ray analysis showed that two oxygen atoms, each with a carboxyl group of the maleate dianion, coordinate with Mn(II) and Co(II) ions to form seven-membered chelate cycles, and the remaining two oxygen atoms participate in the formation of bridges between neighboring complexes.

The polynuclear mixed-metal complex is three-dimensional, in which the metal ions have a distorted octahedral structure. The maleate ligand forms a seven-membered cycle with two oxygen atoms. The octahedral coordination in the equatorial plane is achieved by one oxygen atom of the maleate, two oxygen atoms of two water molecules, and one bridging oxygen atom from neighboring complexes. The axial positions are occupied by one oxygen atom of the maleate and one bridging oxygen atom from a neighboring molecule (Figure 1).

The distances between neighboring manganese metals are 5.138 Å. The distances between metal ions and oxygen atoms of water molecules in axial and equatorial positions do not differ significantly

(2.164 Å and 2.166 Å) (Table 2). The metal ion-oxygen distances are in the range of 2.1405-2.221 Å and differ slightly from the distances in the polymeric Mn(II) complex of 2.154-2.23 Å (16).
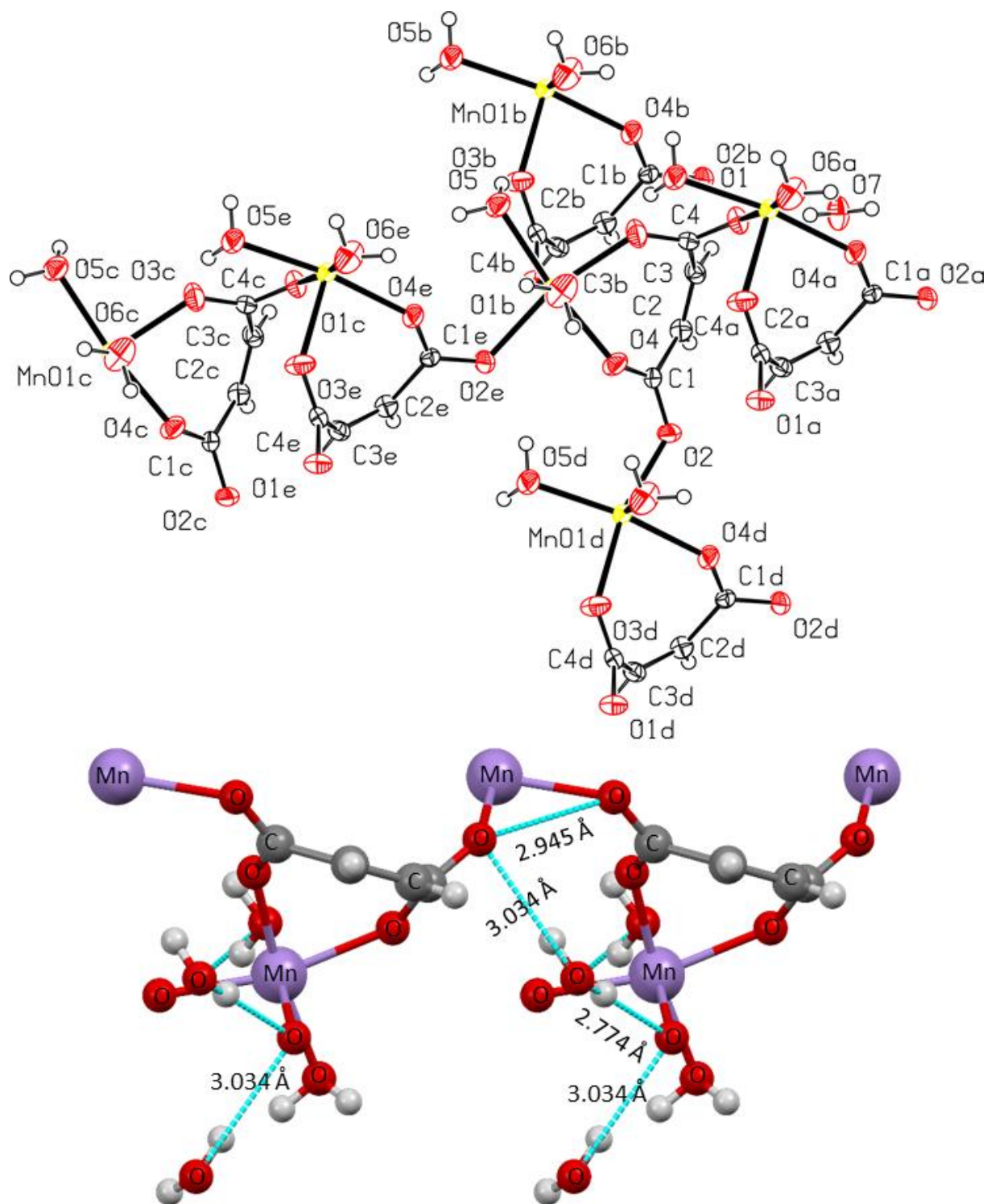
Figure 1: A view of the structure of $[Co_xMn_{1-x}(OOCCH=CHCOO)\cdot(H_2O)_2]_n$, showing the atom-labelling scheme. Displacement ellipsoids are drawn at the 50% probability level. Symmetry codes: (*a*) *x*, $1 - y$, $-1/2 + z$; (*b*) *x*, $1 - y$, $1/2 + z$; (*c*) $1/2 + x$, $-1/2 + y$, $1 + z$; (*d*) $-1/2 + x$, $1/2 - y$, $-1/2 + z$; (*e*) $1/2 + x$, $1/2 - y$, $1/2 + z$.

Table 2: Bond lengths [Å] and angles [°] for $[Co_xMn_{1-x}(OOCCH=CHCOO)\cdot(H_2O)_2]_n$

Atom	Atom	Length/Å
Mn1	O1[1]	2.221(2)
Mn1	O2[2]	2.1573(18)
Mn1	O4	2.1407(18)
Mn1	O5	2.1644(19)
Mn1	O3	2.1717(18)
Mn1	O6	2.166(2)
O1	C4	1.261(3)
O2	C1	1.265(3)
O4	C1	1.236(3)
O3	C4	1.250(3)
C3	C4	1.494(3)
C3	C2	1.324(3)
C2	C1	1.499(3)

[1]+X,1-Y,1/2+Z; [2]1/2+X,1/2-Y,1/2+Z

Atom	Atom	Atom	Angle/°
O2[1]	Mn1	O1[2]	84.53(7)
O2[1]	Mn1	O5	104.09(7)
O2[1]	Mn1	O3	166.08(7)
O2[1]	Mn1	O6	95.64(9)
O4	Mn1	O1[2]	90.68(8)
O4	Mn1	O2[1]	82.25(7)
O4	Mn1	O5	171.94(7)
O4	Mn1	O3	83.86(8)
O4	Mn1	O6	94.25(9)
O5	Mn1	O1[2]	85.04(8)
O5	Mn1	O3	89.83(8)
O5	Mn1	O6	90.12(9)
O3	Mn1	O1[2]	96.61(8)
O6	Mn1	O1[2]	175.04(10)
O6	Mn1	O3	84.41(10)
C4	O1	Mn1[3]	131.57(17)
C1	O2	Mn1[4]	124.42(15)
C1	O4	Mn1	135.02(17)
C4	O3	Mn1	131.66(15)
C2	C3	C4	128.0(2)
O1	C4	C3	115.0(2)
O3	C4	O1	123.3(2)
O3	C4	C3	121.6(2)
C3	C2	C1	126.6(2)
O2	C1	C2	114.8(2)
O4	C1	O2	123.0(2)
O4	C1	C2	122.2(2)

Symmetry codes: (i) x, $-y+1$, $z+1/2$; (ii) $x+1/2$, $-y+1/2$, $z+1/2$; (iii) x, $-y+1$, $z-1/2$; (iv) $x-1/2$, $-y+1/2$, $z-1/2$.

The thermogravimetric analysis of the mixed metal maleate complex $[Co_xMn_{1-x}(OOCCH=CHCOO)\cdot(H_2O)_2]_n$ (Figure 2) revealed that the complex decomposes in four stages within the temperature range of 25-990 °C. Up to 100 °C, hygroscopic water is lost. At 160 °C and 255 °C, both crystallization water and metal-coordinated water molecules are released. The theoretical percentage of water loss is 4.4%, which is in accordance with the experimental results. Subsequently, the weight loss that commences at 395 °C can be attributed to the decarboxylation of the complex. Furthermore, the presence of 24.5% residue at 900 °C indicates that the organic ligand has completely decomposed, while cobalt or manganese metals remain as residues. In light of these results, it has been determined that the manganese maleate complex is resistant up to 400 °C, except for the loss of water molecules.
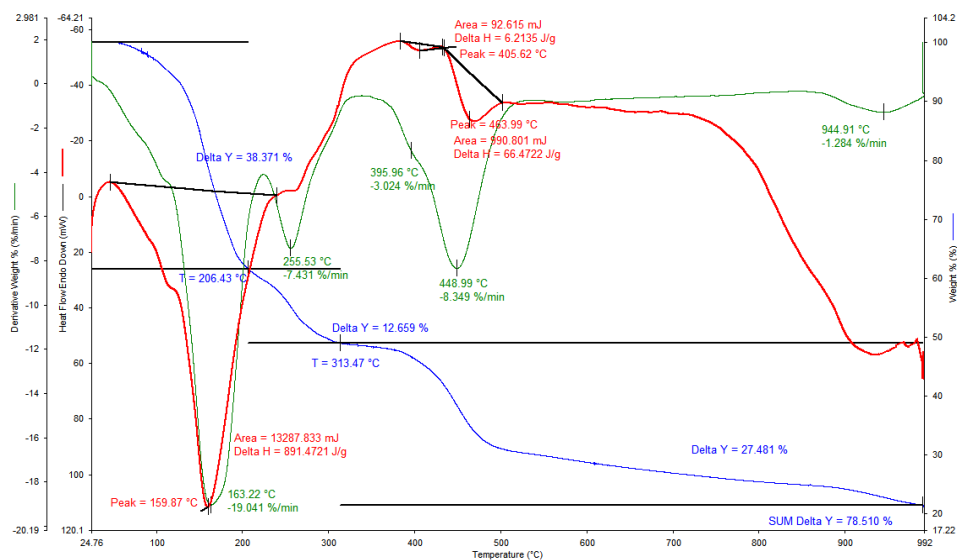
Figure 2: The thermogram of the $[Co_xMn_{1-x}(OOCCH=CHCOO)\cdot(H_2O)_2]_n$ complex.

In the EPR spectrum of the mixed-metal maleate complex, a single wide ($\Delta H=600$ G) somewhat asymmetric signal with $g=2.031$ is observed, which may indicate the electronic exchange interaction between the Mn(II) and Co(II) ions in the octahedral environment (Figure 3). The g-factor is close to that of the Mn(II) compounds, which indicates the main contribution of these ions to the EPR spectrum.
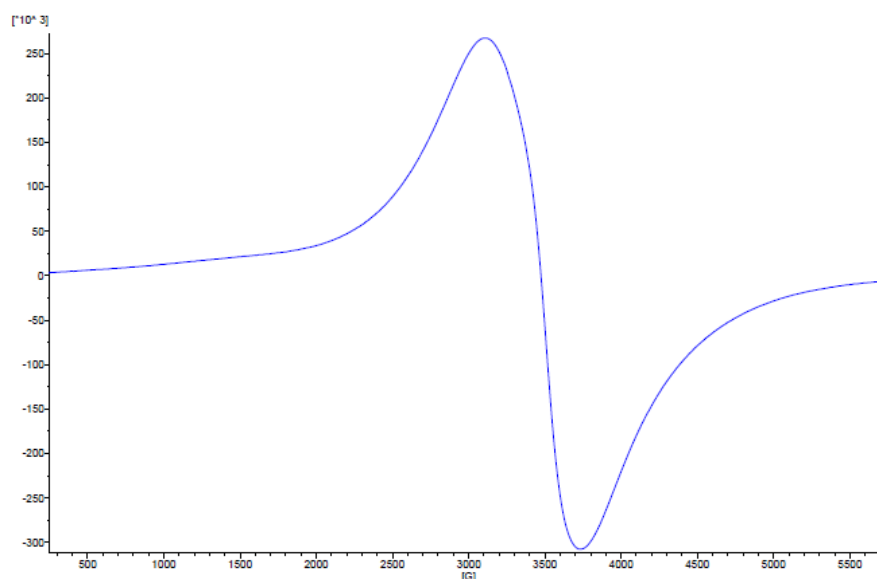
Figure 3: EPR of the $[Co_xMn_{1-x}(OOCCH=CHCOO)\cdot(H_2O)_2]_n$ complex.

In the electronic absorption spectra of the mixed metal maleate complex $[Co_xMn_{1-x}(OOCCH=CHCOO)\cdot(H_2O)_2]_n$ in the visible region, a peak at $\lambda_{max}=516.4$ ($\varepsilon=2$) and very weak in intensity absorption bands at 641.8, 848, 965 nm corresponding to forbidden d-d transitions (with $\varepsilon<0.01$) are observed. There is also absorption above 1100 nm (see Figure 4). These absorption bands belong to cobalt(II) except for the absorption band at 965 nm, which is absent in the electronic absorption spectrum of Co(II) tetrahydrate maleate.

Therefore, the band at 965 nm should be attributed to the Mn(II) complex.

Note that the absorption at 510-520 nm usually refers to the $^4T_{1g} \rightarrow {}^4A_{2g}$ transition in octahedral Co(II) complexes. In our case, it is observed at 516.4 nm. Thus, the electron spectra also indicate the presence of both metal ions Co(II) and Mn(II) in the polymer complex.
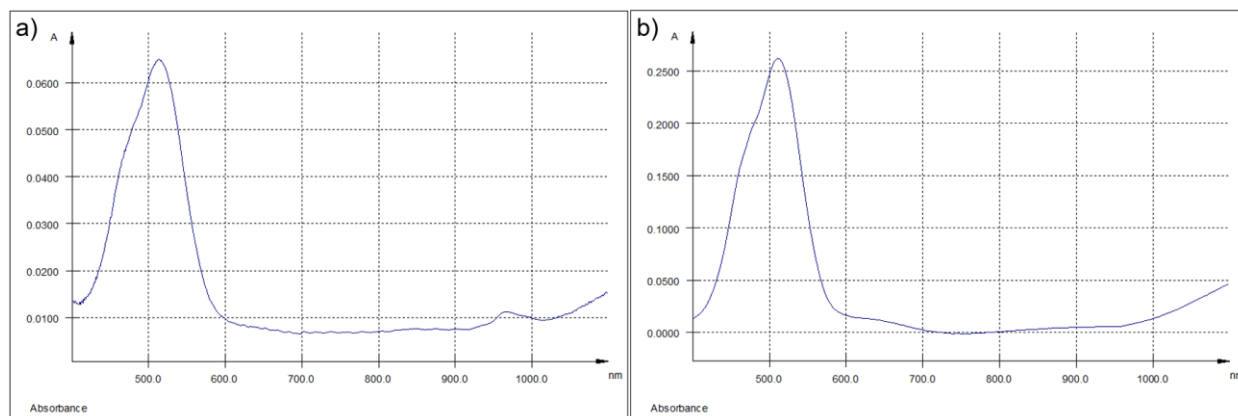
Figure 4: Electronic absorption spectra in water: a) $[Co_xMn_{1-x}(OOCCH=CHCOO)\cdot(H_2O)_2]_n$ complex; b) $[Co(OOCCH=CHCOO)_2\cdot(H_2O)_4]$

Cyclic voltammetry data indicate the presence of both metal ions Mn and Co in the complex (Figure 5). The voltammetry diagrams show two reduction waves, corresponding to the two-electron reduction of Co^{2+} ions (E_c = - 0.69 V) and Mn^{2+} (E_c = -0.985 V) (33).
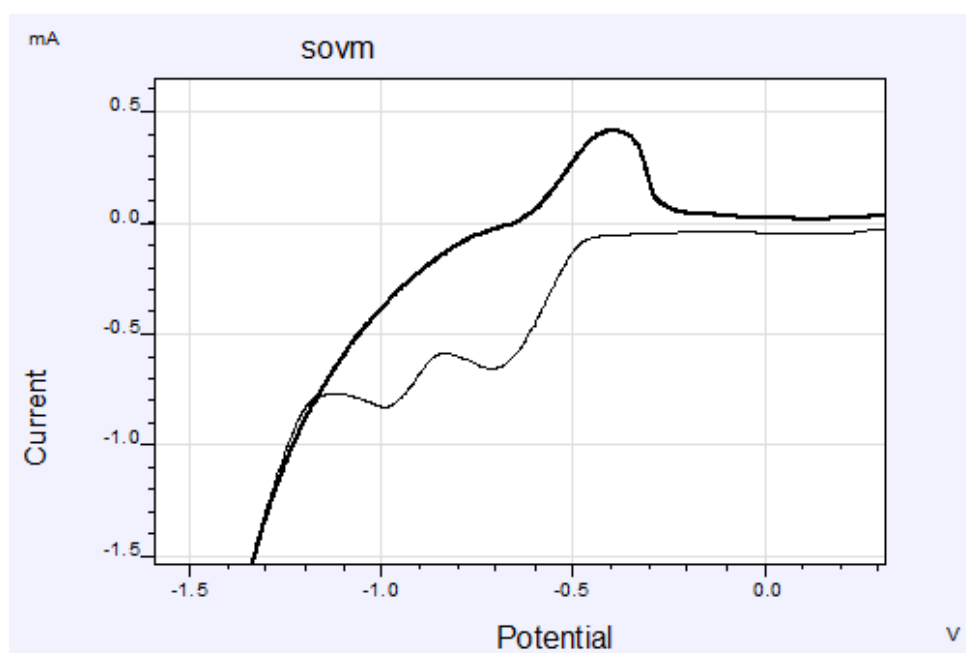
Figure 5: Polarization curve on Pt electrode in electrolyte 0.001 M $[Co_xMn_{1-x}(OOCCH=CHCOO)\cdot(H_2O)_2]_n$, Ev=0.01 V/s, T=298 K.

4. CONCLUSIONS

Thus, it is shown that the interaction of cobalt maleate tetrahydrate with manganese salts results in the formation of a polymer polynuclear mixed-metal manganese(II) and cobalt(II) maleate complex: $[Co_xMn_{1-x}(OOCCH=CHCOO)\cdot(H_2O)_2]_n$. In this complex, Mn(II) and Co(II) ions are interconnected by oxygen bridges of maleate groups. The distances between neighboring manganese ions are 5.138 and 5.414 Å. However, this distance is sufficient for the electronic exchange of interactions between metal ions, as evidenced by the EPR spectrum. In the EPR spectrum, a broad single band g=2.031 is observed, indicating an electronic exchange interaction between Mn(II) and Co(II) ions. The electronic absorption spectra show an absorption band at a wavelength of 965 nm, which should be attributed to the Mn(II) complex. The band at 516 nm refers to the cobalt complex.

Cyclic voltammetry data indicate the presence of both manganese and cobalt metal ions in the complex. Two waves of reduction related to the two-electron reduction of Co^{2+} ions (E_c= - 0.69 V) and Mn^{2+} ions (E_c= -0.985 V) are clearly visible on the voltammetry diagrams.

CCDC- 2210011 contains the supplementary crystallographic data for this paper. These data can be obtained free of charge from The Cambridge Crystallographic Data Centre via deposit@ccdc.cam.ac.uk or http://www.ccdc.cam.ac.uk/data_request/cif).

5. DISCLOSURE STATEMENT

No potential conflict of interest was reported by the authors.

6. ACKNOWLEDGEMENTS

7. REFERENCES

1. Thompson LK, Waldmann O, Xu Z. Polynuclear manganese grids and clusters—A magnetic perspective. Coord Chem Rev [Internet]. 2005 Dec 1;249(23):2677–90. Available from: <URL>.

2. Kiskin MA, Eremenko IL. Chemical design of high spin polynuclear manganese(II) and iron(II) carboxylates. Russ Chem Rev [Internet]. 2006 Jul 31;75(7):559–75. Available from: <URL>.

3. Ribas J, Escuer A, Monfort M, Vicente R, Cortés R, Lezama L, et al. Polynuclear Ni^{II} and Mn^{II} azido bridging complexes. Structural trends and magnetic behavior. Coord Chem Rev [Internet]. 1999 Oct 1;193–195:1027–68. Available from: <URL>.

4. Rardin RL, Poganiuch P, Bino A, Goldberg DP, Tolman WB, Liu S, et al. Synthesis and characterization of novel trinuclear iron(II) and manganese(II) carboxylate complexes: structural trends in low valent iron and manganese carboxylates. J Am Chem Soc [Internet]. 1992 Jun 1;114(13):5240–9. Available from: <URL>.

5. Durot S, Policar C, Pelosi G, Bisceglie F, Mallah T, Mahy J-P. Structural and Magnetic Properties of Carboxylato-Bridged Manganese(II) Complexes Involving Tetradentate Ligands: Discrete Complex and 1D Polymers. Dependence of *J* on the Nature of the Carboxylato Bridge. Inorg Chem [Internet]. 2003 Dec 1;42(24):8072–80. Available from: <URL>.

6. Christian P, Rajaraman G, Harrison A, Helliwell M, McDouall JJW, Raftery J, et al. Synthesis and studies of a trinuclear Mn(II) carboxylate complex. Dalt Trans [Internet]. 2004 Aug 9;2004(16):2550–5. Available from: <URL>.

7. Ma C, Chen C, Liu Q, Chen F, Liao D, Li L, et al. Great Framework Variation of Polymers in the Manganese(II) Maleate/α,α′-Diimine System: Syntheses, Structures, and Magneto-Structural Correlation. Eur J Inorg Chem [Internet]. 2003 Aug 21;2003(15):2872–9. Available from: <URL>.

8. Albela B, Corbella M, Ribas J, Castro I, Sletten J, Stoeckli-Evans H. Synthesis, Structural Characterization (X-ray and EXAFS), and Magnetic Properties of Polynuclear Manganese(II) Complexes with Chlorobenzoato Bridges. Inorg Chem [Internet]. 1998 Feb 23;37(4):788–98. Available from: <URL>.

9. Zheng Y-Q, Kong Z-P. A New Maleato-Bridged Mn(II) Phen Complex: Structure and Magnetic Properties of Mn(phen)(C$_4$H$_2$O$_4$). J Coord Chem [Internet]. 2002 Jan 1;55(11):1241–7. Available from: <URL>.

10. Hua Q, Su Z, Zhao Y, Okamura T, Xu G-C, Sun W-Y, et al. Synthesis, structure and property of manganese(II) complexes with mixed tetradentate imidazole-containing ligand and benzenedicarboxylate. Inorganica Chim Acta [Internet]. 2010 Oct 25;363(13):3550–7. Available from: <URL>.

11. Lazarou KN, Psycharis V, Perlepes SP, Raptopoulou CP.

12. Zhang L, Liu L, Huang C, Han X, Guo L, Xu H, et al. Polynuclear Ni(II)/Co(II)/Mn(II) Complexes Based on Terphenyl–Tetracarboxylic Acid Ligand: Crystal Structures and Research of Magnetic Properties. Cryst Growth Des [Internet]. 2015 Jul 1;15(7):3426–34. Available from: <URL>.

13. Chen M, Chen M-Z, Zhou C-Q, Lin W-E, Chen J-X, Chen W-H, et al. Towards polynuclear metal complexes with enhanced bioactivities: Synthesis, crystal structures and DNA cleaving activities of Cu^{II}, Ni^{II}, Zn^{II}, Co^{II} and Mn^{II} complexes derived from 4-carboxy-1-(4-carboxybenzyl) pyridinium bromide. Inorganica Chim Acta [Internet]. 2013 Aug 24;405:461–9. Available from: <URL>.

14. Huang D, Wang W, Zhang X, Chen C, Chen F, Liu Q, et al. Synthesis, Structural Characterizations and Magnetic Properties of a Series of Mono-, Di- and Polynuclear Manganese Pyridinecarboxylate Compounds. Eur J Inorg Chem [Internet]. 2004 Apr 22;2004(7):1454–64. Available from: <URL>.

15. Andruh M, Roesky HW, Noltemeyer M, Schmidt H-G. Synthesis and x-ray structure of the polynuclear complex bis(μ-trifluoroacetato,O,O′)(1,10-phenanthroline)manganese(II). Polyhedron [Internet]. 1993 Dec 1;12(23):2901–3. Available from: <URL>.

16. Lis T. Structure of manganese(II) maleate trihydrate, [Mn(C$_4$H$_2$O$_4$)].3H$_2$O (I), and reinvestigation of the structure of manganese(II) hydrogen maleate tetrahydrate, [Mn(C$_4$H$_3$O$_4$)$_2$].4H$_2$O (II). Acta Crystallogr Sect C Cryst Struct Commun [Internet]. 1983 Jan 15;39(1):39–41. Available from: <URL>.

17. Ghoshal D, Mostafa G, Kumar Maji T, Zangrando E, Lu T-H, Ribas, J, et al. Synthesis, crystal structure and magnetic behavior of three polynuclear complexes: [Co(pyo)$_2$(dca)$_2$]$_n$, [Co$_3$(ac)$_4$(bpe)$_3$(dca)$_2$]n and [{Co(male)(H$_2$O)$_2$}(H$_2$O)]n [pyo, pyridine-*N*-oxide; dca, dicyanamide; ac, acetate; bpe, 1,2-bis-(4-pyridyl)ethane and male, maleate]. New J Chem [Internet]. 2004 Oct 1;28(10):1204–13. Available from: <URL>.

18. Sergienko VS, Koksharova T V., Surazhskaya MD, Mandzii T V., Churakov A V. Synthesis, Crystal Structure, and Molecular Structure of Maleate Tris(Benzohydrazide) Cobalt(II) Tetrahydrate [Co(L^1)$_3$](Mal) 4H$_2$O and Maleate Tris(Phenylacethydrazide) Nikel(II) Monohydrate [Ni(L^2)$_3$](Mal) H$_2$O. Russ J Inorg Chem [Internet]. 2019 Nov 11;64(11):1396–404. Available from: <URL>.

19. Yang J, Puchberger M, Qian R, Maurer C, Schubert U. Zinc(II) Complexes with Dangling Functional Organic Groups. Eur J Inorg Chem [Internet]. 2012 Sep 16;2012(27):4294–300. Available from: <URL>.

20. Cañada-Vilalta C, Streib WE, Huffman JC, O'Brien TA, Davidson ER, Christou G. Polynuclear Manganese Complexes with the Dicarboxylate Ligand *m* - Phenylenedipropionate: A Hexanuclear Mixed-Valence (3Mn^{III}, 3Mn^{IV}) Complex. Inorg Chem [Internet]. 2004 Jan 1;43(1):101–15. Available from: <URL>.

21. Stamatatos TC, Christou G. Mixed valency in polynuclear Mn^{II}/Mn^{III}, Mn^{III}/Mn^{IV} and Mn^{II}/Mn^{III}/Mn^{IV} clusters: a foundation for high-spin molecules and single-molecule magnets. Philos Trans R Soc A Math Phys Eng Sci [Internet]. 2008 Jan 13;366(1862):113–25. Available

from: <URL>.

22. Tangoulis V, Malamatari DA, Soulti K, Stergiou V, Raptopoulou CP, Terzis A, et al. Manganese(II/II/II) and Manganese(III/II/III) Trinuclear Compounds. Structure and Solid and Solution Behavior. Inorg Chem [Internet]. 1996 Jan 1;35(17):4974–83. Available from: <URL>.

23. Suffren Y, O'Toole N, Hauser A, Jeanneau E, Brioude A, Desroches C. Discrete polynuclear manganese(II) complexes with thiacalixarene ligands: synthesis, structures and photophysical properties. Dalt Trans [Internet]. 2015 Apr 23;44(17):7991–8000. Available from: <URL>.

24. Thompson LK, Matthews CJ, Zhao L, Xu Z, Miller DO, Wilson C, et al. Synthesis, Structure, and Magnetism of a Series of Self-Assembled Polynuclear Mn(II), Co(II), and Cu(II) Cluster Complexes. J Solid State Chem [Internet]. 2001 Jul 1;159(2):308–20. Available from: <URL>.

25. Chen H-B, Zhang H, Yang J-M, Zhou Z-H. Transformation of maleato manganese(II): temperature effect and coordination modes. Polyhedron [Internet]. 2004 Mar 25;23(6):987–91. Available from: <URL>.

26. Gómez V, Corbella M. Versatility in the Coordination Modes of *n* -Chlorobenzoato Ligands: Synthesis, Structure and Magnetic Properties of Three Types of Polynuclear Mn^{II} Compounds. Eur J Inorg Chem [Internet]. 2009 Oct 12;2009(29–30):4471–82. Available from: <URL>.

27. Ming-Xing Li, Gao-Yang Xie, Song-Lin Jin, Yi-Dong Gu, Ming-Qin Chen, Jie Liu, et al. Synthesis and magnetic properties of novel maleato-bridged cyclic tetranuclear manganese(II) complexes: Crystal structure of [Mn$_4$(μ-maleate)$_2$(bipy)$_8$](ClO$_4$)$_4$·(MeOH)$_2$(H$_2$O$_2$)$_2$. Polyhedron [Internet]. 1996 Feb 1;15(3):535–9. Available from: <URL>.

28. Wang H, Qin J. Two Polynuclear Manganese(II) Complexes Based on Multidentate N-Heterocyclic Aromatic Ligand and V-Shaped Polycarboxylate Ligand: Synthesis, Crystal Structure Analysis and Magnetic Properties. Crystals [Internet]. 2022 Feb 17;12(2):278. Available from: <URL>.

29. Cakic S, Nikolic G, Stamenkovic J, Konstantinovic S. Physico-chemical characterization of mixed-ligand complexes of Mn(III) based on the acetylacetonate and maleic acid and its hydroxylamine derivative. Acta Period Technol [Internet]. 2005;(36):91–8. Available from: <URL>.

30. Karmakar A, Baruah JB. Metal carboxylate complexes of L-3-phenyl-2-(3-phenyl-ureido)-propionic acid. Inorg Chem Commun [Internet]. 2009 Feb 1;12(2):140–4. Available from: <URL>.

31. Nockemann P, Thijs B, Hecke K Van, Meervelt L Van, Binnemans K. Polynuclear Metal Complexes Obtained from the Task-Specific Ionic Liquid Betainium Bistriflimide. Cryst Growth Des [Internet]. 2008 Apr 1;8(4):1353–63. Available from: <URL>.

32. Nakamoto K. Infrared and Raman spectra of inorganic and coordination compounds, part B: applications in coordination, organometallic, and bioinorganic chemistry. John Wiley & Sons; 2009.

33. Sukhotin AM. Handbook of chemistry. Leningrad "Chemistry." 1981.

In Silico Exploration of Pharmacological and Molecular Descriptor Properties of Salacinol and Its Related Analogues

Yousif Taha Hussein[1]* , Yousif Hussein Azeez[2] , Idrees Mohammed Ahmed[1]

[1] Sulaimani Polytechnic University, Technical College of Applied Sciences/ Halabja, Medical Laboratory Science, Iraq.
[2] Department of Physics, College of Science, Halabja University, Halabja, Iraq.

Abstract: Salacinol and its related analogues have been known for their potent α-glucosidase inhibitor activity and making them interesting candidates for a new type of anti-diabetic agent. Therefore, it is essential to investigate the physicochemical properties, pharmacological parameters, and toxicity profile of these anti-diabetic agents. In this study, a comprehensive in-silico approach was used to explore the absorption, distribution, metabolism, excretion, and toxicity profiles of salacinol and its related analogues. In addition, to gain a better knowledge of structural and electrical characteristics, global and local reactivity descriptors, and molecular electrostatic potential were calculated and discussed by using DFT at the B3LYP/6−311++G (d, p) level of theory. The results explored that all the studied compounds have low GI absorption and are substrates for P-glycoprotein. None of the compounds can cross the BBB, and none of the compounds are inhibitors of cytochrome P450 isoenzymes. We also found that all compounds have various potential to interact with a wide range of biological targets, including GPCRs, enzymes, ion channels, kinases, and nuclear receptors. Additionally, all compounds have low toxicity and are unlikely to cause any major health hazards in terms of hepatotoxicity, mutagenicity, cardiotoxicity, cytotoxicity, and immunotoxicity. The molecular electrostatic potential map shows that the negative potential sites are in electronegative oxygen atoms, while the positive potential sites are around the hydrogen atoms. The present study concludes that salacinol and its analogues might be a promising safe and effective candidate for the development of therapeutic drugs derived from natural sources. However, some of their properties should be considered in the context of drug development and tissue protection strategies.

1. INTRODUCTION

Plants of the Salacia genus (Hippocrateaceae family) are woody climbers found in India, Sri Lanka, China, and Thailand (1). The stems and roots of Salacia species have been used for the prevention or treatment of diabetes, a common metabolic disorder seen all over the world (2). The bioactive constituent responsible for the postprandial anti-hyperglycaemic activity of these plants is a novel thiosugar sulphonium sulfate inner salt, Salacinol (1) (1). Several analogues have been isolated from Salacia species, that is, Neosalacinol (2), kotalanol (3), neokotalanol (4), Ponkoranol (5), Neoponkoranol (6), Salaprinol (7), and Neosalaprinol (8) (Fig. 1). The mechanism of the anti-diabetogenic action of

these compounds was shown to be mediated by the inhibition of α-glucosidases, and their activities against maltase and sucrose were found to be as potent as the clinical inhibitors such as acarbose or voglibose (1). The results suggest that these compounds are promising leads for a new type of anti-diabetic agent (3). Therefore, the exploration of various physicochemical properties, pharmacokinetic parameters, and toxicity potential of these antidiabetic agents is and will be an important issue for investigation.

The computational methods (In-silico) have been promoted as a valid alternative to experimental procedures for the prediction of pharmacokinetic parameters such as absorption, distribution,

metabolism, excretion ("ADME"), and toxicity, principally at the initial stages when the studied compounds are numerous but the availability of compounds is scarce (4). For instance, at the initial stages of the investigations, the in-silico toxicity assessments are not only faster and inexpensive than the determination of toxic doses in animals, but can also help to decrease the number of animal experiments (5).

It is important to understand the molecular characteristics and bioactivity of the therapeutic effect of the title compound to examine them from a medical aspect. From a molecular point of view, it is believed that the bioactivity of these compounds is strongly linked to their chemical reactivity. As a result, it is essential to use computational chemistry and molecular modeling approaches to explore the chemical reactivity of natural compounds with the potential to become medicines. The Conceptual Density Functional Theory (CDFT), also known as chemical reactivity theory, is perhaps the most powerful tool available for investigating the chemical reactivity of molecular systems from the perspective of molecular modeling and computational chemistry. It uses a global and local reactivity descriptor to predict molecule interactions and understand how chemical reactions work (6). The B3LYP/6−311++G (d, p) basis set was chosen for the geometric and energetic optimization of salacinol and related analogues because it is a well-established and balanced choice for the calculation of both energies and geometries of organic molecules. The B3LYP functional is a hybrid functional that includes both exchange and correlation terms, and it is accurate for a wide range of molecules. The 6−311++G (d, p) basis set represents a triple-zeta foundation augmented with diffuse and polarization functions. This particular basis set proves advantageous in computational endeavors aimed at determining molecular properties, specifically those pertaining to dipole moments and polarizabilities. The employment of such a basis set is particularly pertinent in the context of elucidating the intricate intermolecular interactions involving salacinol and its analogous compounds with other molecular entities. Salacinol and related analogues were selected for these studies because of their potential as drug candidates. Salacinol has already been shown to be safe and effective in clinical trials for the treatment of diabetes. By understanding the reactivity and electrostatic potential of salacinol and its related analogues, we can identify new drug candidates with improved efficacy and fewer side effects.

In this study, we investigated the reactivity of salacinol and related analogues using reactivity descriptors and molecular electrostatic potential (MEP) studies. We found that neokotalanol, one of the salacinol analogues, has a small HOMO-LUMO energy gap and a high MEP, indicating that it is highly reactive. We also found that neokotalanol is more potent than salacinol in inhibiting the growth of cancer cells. These findings suggest that the high reactivity of neokotalanol is important for its bioactivity.

This study aims to explore important information about Salacinol and its related analogues for their possibility as a potential drug originating from natural products and their pharmaceutical research. For this purpose, in silico methods are used to explore the absorption, distribution, metabolism, excretion, and toxicity profile of Salacinol and its related analogues. In addition, to gain a better knowledge of structural and electrical characteristics, molecular descriptors were calculated and discussed by using DFT at the B3LYP/6−311++G (d, p) level of theory.

2. MATERIALS AND METHODS

2.1. Bioactivity Score Prediction
The bioactivity score of the Salacinol and its related analogues was checked by calculating the bioactivity score toward G protein-coupled receptors (GPCR ligand), ion channel modulator, nuclear receptor ligand, a kinase inhibitor, protease inhibitor, and enzyme inhibitor. All of the parameters were explored by feeding the corresponding SMILES (Simplified Molecular Input Line Entry System) notation into the internet-based software Molinspiration (www.molinspiration.com), which predicts the bioactivity score of the synthesized complexes.

2.2. Drug Likeness and Pharmacokinetic Evaluation
The current industrial drug discovery paradigm includes computer-based prediction to explore absorption, distribution, metabolism, excretion, and pharmacokinetics (ADME-PK) properties of bioactive compounds in the initial stages of drug discovery projects. Drug-likeness analyses and ADME predictions were performed via the web-based tool SwissADME (4). In this part of the study, lipophilicity, water solubility, physicochemical properties, and various pharmacokinetics parameters were explored. The drug-likeness analyses were carried out with the use of Lipinski's rule of five (RO5) and Veber rule's (7, 8). Additionally, passive human gastrointestinal absorption, BBB permeation, the potential to become glycoprotein (P-gp) substrate, and inhibition of human cytochrome P450 (CYP) five isozymes—1A2, 2C9, 2C19, 2D6, and 3A4 of all studied molecules were explored.

2.3. Toxicity Potential Evaluation
In this part of the study, the toxicity profile of the studied compounds was predicted using a software-based tool, ProTox-II, a virtual lab for the prediction of toxicities of molecules (5). Also, different levels of toxicity were explored, such as organ toxicity (hepatotoxicity) and toxicological endpoints (such as mutagenicity, cardiotoxicity, cytotoxicity, and immunotoxicity), thereby providing insights into different possible adverse effects of Salacinol and its analogues on the human body.
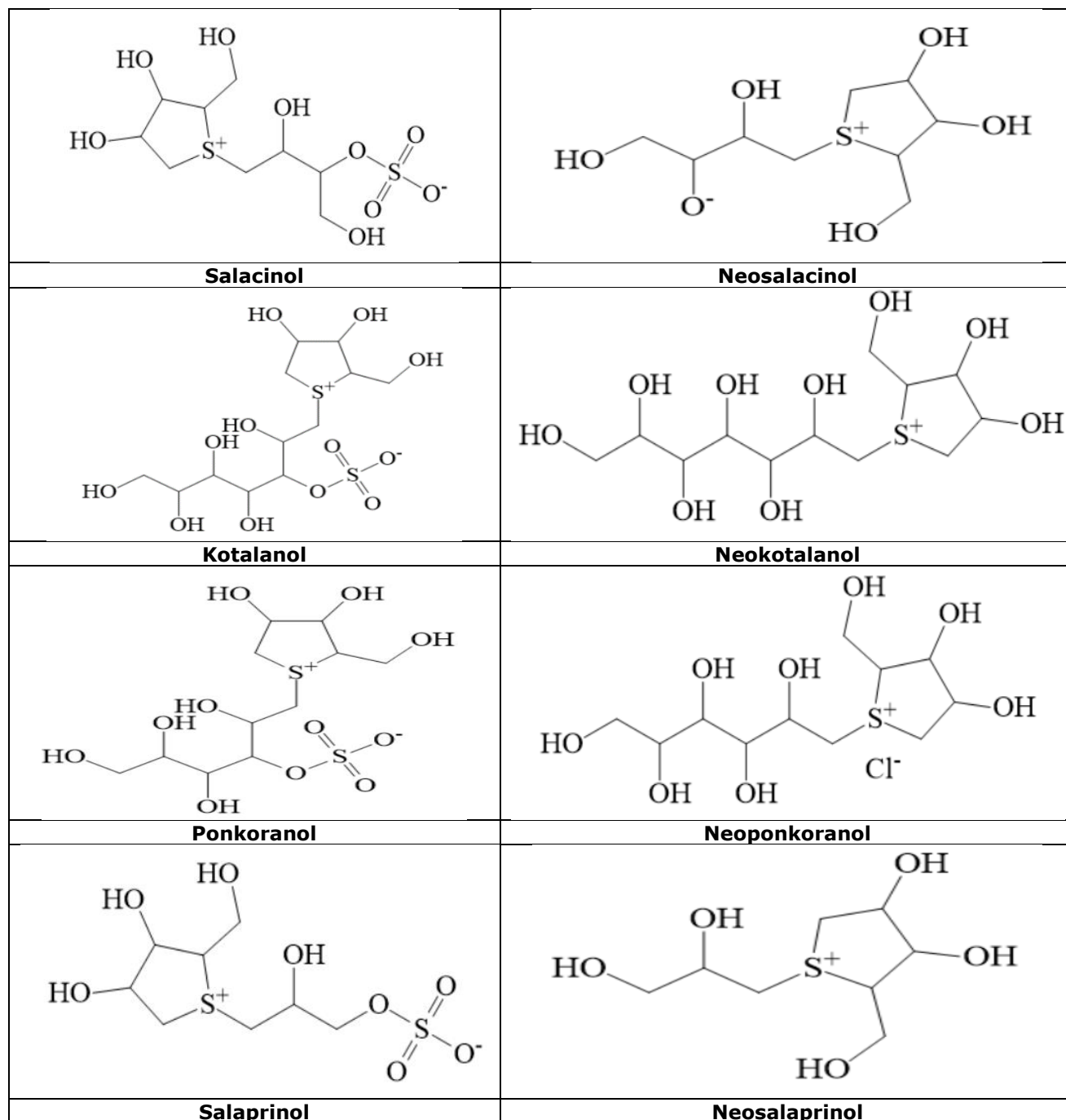
Figure 1: Chemical structure of compounds (1–8) from the plants of the Salacia genus.

2.4. DFT with Global Chemical Reactivity Descriptors

The global reactivity indices provide information on a chemical compound's stability, reactivity, and selectivity. Global reactivity characteristics such as energy gap (E_g), global hardness (η), global softness (S), electronegativity (χ), chemical potential (μ), maximal amount of electronic charge (Q^{max}), electrophilicity (ω), electron-donating power (ω^-), electron-accepting power (ω^+), and net electrophilicity based on DFT with 6311++G (d,p) were calculated by using the energies of the frontier orbitals and Gaussian 09 software (1-11) (6, 9-12).

$$IP = -H_{HOMO} \quad \text{and} \quad EA = -E_{LUMO} \qquad (1)$$

$$E_g = E_{LUMO} - E_{HOMO} \qquad (2)$$

$$\chi = \frac{E_{HOMO} + E_{LUMO}}{2} \qquad (3)$$

$$\mu = -\frac{(E_{HOMO} + E_{LUMO})}{2} \qquad (4)$$

$$\eta = \frac{E_{LUMO} - E_{HOMO}}{2} \qquad (5)$$

$$S = \frac{1}{2\eta} \qquad (6)$$

$$\omega = \frac{\mu^2}{2\eta} \qquad (7)$$

$$(Q^{max}) = \frac{-\mu}{\eta} \qquad (8)$$

$$\omega^+ = \frac{(E_{HOMO} + 3E_{LUMO})^2}{16\,E_g} \qquad (9)$$

$$\omega^- = \frac{(3\,E_{HOMO} + E_{LUMO})^2}{16\,E_g} \qquad (10)$$

$$\Delta\omega^\pm = \omega^+ + \omega^- \qquad (11)$$

2.5. Fukui Function (local reactivity descriptors)

The Fukui Function gives information on the reactivity indices in a given system. For the highest Fukui function values, the atom exhibits a significant degree of reactivity (13, 14). The Fukui functions from (compound 1-8) have been calculated based on the B3LYP/6-311G++(d, p) level of theory, and the results are shown in Table 6. The Fukui Functions $(f_k^-, f_k^+ \; f_k^0)$ are computed using mulliken population analysis charges of neutral, negative, and positive ions and are given in Table 6 using equations (12-14). If (N) represents the number of electrons, then (N + 1) denotes an ion and (N − 1) denotes the system's cation.

$$f_k^+ = q(N+1) - q(N) \qquad (12)$$

$$f_k^- = q(N) - q(N-1) \qquad (13)$$

$$f_k^0 = \frac{q(N+1) - q(N-1)}{2} \qquad (14)$$

3. RESULTS AND DISCUSSION

3.1. Bioactivity Score Prediction

The beneficial or adverse effects of a newly discovered compound on an organism are usually summarized by the term "bioactivity". On the molecular level, biological activity corresponds to the interaction between low-molecular weight compounds and the most common biological targets (receptors), usually proteins such as enzymes, ion channels, and receptors (15). In this study, the results of bioactivity prediction were analyzed as shown in Table 1, and it was explored that:

All the compounds can be considered bioactive as a GPCR ligand, the bioactivity score ranges between (0.00 to 0.30).

All the compounds are moderately active as an ion channel modulator, Kinase inhibitor, and nuclear receptor ligand; the value ranges between -0.05 to -0.27, -0.09 to -0.55, and -0.09 to -0.65, respectively.

All the compounds are active as protease inhibitors and the value ranged between 0.17 to 0.32, except 2 and 8, which has a moderately active value of -0.04 and -0.20, respectively.

All the compounds exhibit active interaction as an enzyme inhibitor, the value ranges between 0.98 to 1.20.

Table 1: Bioactivity scores of the Salacinol and eight Related Analogues based on GPCR ligand, ion channel modulator, nuclear receptor ligand, Kinase inhibitor, protease inhibitor, and Enzyme inhibitor.

Parameters	Salacinol	Neosalacinol	Kotalanol	Neokotalanol
GPCR ligand	0.30	0.07	0.27	0.29
Ion channel modulator	-0.18	-0.14	-0.13	-0.05
Kinase inhibitor	-0.09	-0.38	-0.07	-0.08
Nuclear receptor ligand	-0.13	-0.42	-0.09	-0.12
Protease inhibitor	0.25	-0.04	0.31	0.23
Enzyme inhibitor	1.19	1.04	0.98	1.03

Parameters	Neoponkoranol	Ponkoranol	Salaprinol	Neosalaprinol
GPCR ligand	0.29	0.26	0.14	0.00
Ion channel modulator	-0.14	-0.06	-0.27	-0.20
Kinase inhibitor	-0.08	-0.15	-0.28	-0.55
Nuclear receptor ligand	-0.10	-0.20	-0.30	-0.65
Protease inhibitor	0.32	0.17	0.22	-0.20
Enzyme inhibitor	1.06	1.13	1.20	1.16
>0 - active, -5.0 - 0.0 - moderately active, < -5.0 – inactive.				

3.2. Drug-Likeness Parameters

Various physicochemical features are used to evaluate the potential of a particular molecule to become a drug candidate. The RO5 is commonly used by pharmaceutical chemists in drug design and development to predict the oral bioavailability of potential leads or drug molecules (16). Lipinski's "RO5" states that a candidate molecule will likely be orally active, if: i) the molecular weight is fewer than 500, ii) the calculated partition coefficient is less than 5 (MiLog P<5), iii) there are less than 5 hydrogen bond donors (nONH<5) and, iv) there are less than 10 hydrogen bond acceptors (nON<10). If two parameters are out of range, there is a high probability that absorption or permeability problems will be encountered (7). Additional criteria such as the number of rotatable bonds, which is the measure of molecular flexibility, fewer than 10 (nrotb ≤ 10),

and topological polar surface area equal to or less than 140 Å² (TPSA ≤ 140 Å²) (Veber Rule) were introduced later, (8) which are used to carry out further evaluation of the oral bioavailability of all the compounds. These physicochemical parameters are associated with acceptable aqueous solubility and intestinal permeability and comprise the initial steps in oral bioavailability (17). Good oral bioavailability implies a balance between the potential of a compound to diffuse passively across the various biological barriers and its aqueous solubility (18).

In this study, the drug-likeness properties of Salacinol and the seven related analogues are shown in Table 2. The lipophilicity of all compounds is less than 5 as shown in Table 2. All the values range from -5.64 to -4.92. The molecular weight (MW) of all compounds is less than 500 Da. However, the minimum value is 225.29 and the maximum value is 424.45, this allows them to be easily absorbed, diffused, and transported. The number of hydrogen bond acceptors of the compounds is less than 10, and the values range from 5 to 9, except 3 and 5 which have nON 12 and 11, respectively. The number of

hydrogen bond donors of the 1, 2, 7, and 8 were shown to have four or five. The other compounds, 3, 4, 5, and 6, have more than five nOHNH, ranging from 7-9. Overall, 1, 2, 7, and 8 have no violations of Lipinski's rule. 4 and 6 only have one violation of RO5. The remaining compounds, 5 and 3, have two violations of RO5.

According to veber rules, compounds that meet only two criteria of nrotb ≤ 10 and TPSA ≤ 140 Å² will have a high probability of good oral bioavailability in the rat. In addition, reduced polar surface area correlates better with increased permeation rate than does lipophilicity (C log P), and increased rotatable bond count harms the permeation rate (8). In this study, all compounds are flexible molecules because their number of rotatable bonds ranges between 4-10. The TPSA of compounds is more than acceptable value ((TPSA ≤ 140 Å²), ranging between (147.34 to 228.26), indicating poor bioavailability of the compounds, except for 2 and 8, which have TPSA of 124.20 and 101.14, respectively, which suggests that they have better bioavailability than other studied compounds.

Table 2: Molecular properties of the salacinol and related analogues calculated to verify Lipinski's RO5 and Veber's rule.

Molecules	Lipinski's RO5				Veber's rule
	miLogP	MW	nON	nOHNH	TPSA (Å²)
Rule	≤ 5	< 500	< 10	< 5	≤ 140
Salacinol	-5.30	334.37	9	5	167.57
Neosalacinol	-5.10	254.30	6	5	124.20
Kotalanol	-5.64	424.45	12	8	228.26
Neokotalanol	-5.49	345.39	9	9	182.05
Ponkoranol	-5.55	394.42	11	7	208.03
Neoponkoranol	-5.38	315.36	8	8	161.82
Salaprinol	-5.10	304.34	8	4	147.34
Neosalaprinol	-4.92	225.29	5	5	101.14

Predictions for passive GI absorption and blood-brain barrier permeation are shown in Table 3. It was predicted that gastrointestinal absorption of all studied compounds is low and none of the compounds can cross the BBB. The substrate of P-glycoprotein means that the drug will efflux from the cell by P-glycoprotein and limits the bioavailability by pumping back into the lumen of the digestive tract and may promote the elimination of that drug into the bile and urine (19). Knowledge about compounds being substrate or non-substrate of the P-gp is significant because its major role is to promote drug elimination into bile and urine and protect various tissues (e.g. brain, testis, liver, and fetus) from xenobiotics (20). Additionally, it has been experimentally demonstrated that P-glycoprotein restricts the oral bioavailability and brain penetration of drugs that are its substrates. In P-glycoprotein-deficient mice, oral administration of these drugs increased plasma concentrations by 2 to 5 fold, and intravenous administration increased brain concentrations by 7 to 36 fold (21). In this study, it can be seen that all compounds are substrates for P-glycoprotein, as shown in Table 3. These results suggest that low GI absorption and no BBB

permeability of all the compounds might be partly attributed to the P-glycoprotein efflux.

Knowledge of the interaction of potential therapeutic drugs with cytochromes P450 (CYP) is essential because this group of isoenzymes (CYP1A2, CYP2C19, CYP2C9, CYP2D6, CYP3A4) plays a major role in drug elimination through metabolic biotransformation (4). It is also suggested that inhibition of these isoenzymes leads to toxic or other unwanted adverse effects due to the lower clearance and accumulation of the drug or its metabolites (22). It also suggests that CYP and P-gp can process small molecules synergistically to improve the protection of tissues and organisms (23). A non-inhibitor of cytochrome P450 means that the molecule will not hinder the biotransformation of the compound (drug) metabolized by cytochrome P450 (24). In the present study, the explored results showed that none of the studied compounds act as an inhibiter of the cytochrome P450 isoenzymes, CYP1A2, CYP2C19, CYP2C9, CYP2D6, CYP3A4, and CYP2D6, as shown in Table 3. These results suggest that the studied compounds will not hinder the biotransformation by cytochrome P450 isoenzymes.

Table 3: In silico toxicity prediction of the salacinol and related analogues.

Parameters	Salacinol	Neosalacinol	Kotalanol	Neokotalanol
GI absorption	Low	Low	Low	Low
BBB permeant	No	No	No	No
P-gp substrate	Yes	Yes	Yes	Yes
CYP1A2 inhibitor	No	No	No	No
CYP2C19 inhibitor	No	No	No	No
CYP2C9 inhibitor	No	No	No	No
CYP2D6 inhibitor	No	No	No	No
CYP3A4 inhibitor	No	No	No	No
Parameters	Neoponkoranol	Ponkoranol	Salaprinol	Neosalaprinol
GI absorption	Low	Low	Low	Low
BBB permeant	No	No	No	No
P-gp substrate	Yes	Yes	Yes	Yes
CYP1A2 inhibitor	No	No	No	No
CYP2C19 inhibitor	No	No	No	No
CYP2C9 inhibitor	No	No	No	No
CYP2D6 inhibitor	No	No	No	No
CYP3A4 inhibitor	No	No	No	No

3.3. Toxicity Prediction

The prediction of compound toxicities, along with drug-likeness and other pharmacokinetics evaluations, is an important part of the drug design and development process (5). As shown in Table 4, All the studied compounds belong to toxicity class 5 for acute oral toxicity with a median lethal dose (LD$_{50}$) value of 5000mg/kg, except compounds 3 and 5, which have an LD$_{50}$ value of 2750 mg/kg. None of the molecules studied has a toxicity hazard in terms of hepatotoxicity, mutagenicity, cardiotoxicity, cytotoxicity, and immunotoxicity. Our data is consistent with the experimentally reported results where powder of Salacia plant extract was experimentally tested in various safety studies, including acute toxicity, mutagenicity, reproductive outcome, hepatotoxicity, and other toxicity studies (25-30).

Table 4: Prediction of ADME descriptors of the salacinol and related analogues.

Parameters	Salacinol	Neosalacinol	Kotalanol	Neokotalanol
Hepatotoxicity	Inactive	Inactive	Inactive	Inactive
Carcinogenicity	Inactive	Inactive	Inactive	Inactive
Immunotoxicity	Inactive	Inactive	Inactive	Inactive
Mutagenicity	Inactive	Inactive	Inactive	Inactive
Mutagenicity	Inactive	Inactive	Inactive	Inactive
Cytotoxicity	Inactive	Inactive	Inactive	Inactive
Predicted LD50 (mg/kg)	5000	5000	2750	5000
Toxicity class	5	5	5	5
Parameters	Neoponkoranol	Ponkoranol	Salaprinol	Neosalaprinol
Hepatotoxicity	Inactive	Inactive	Inactive	Inactive
Carcinogenicity	Inactive	Inactive	Inactive	Inactive
Immunotoxicity	Inactive	Inactive	Inactive	Inactive
Mutagenicity	Inactive	Inactive	Inactive	Inactive
Mutagenicity	Inactive	Inactive	Inactive	Inactive
Cytotoxicity	Inactive	Inactive	Inactive	Inactive
Predicted LD50 (mg/kg)	2750	5000	5000	5000
Toxicity class	5	5	5	5

3.4. Frontier Molecular Orbitals (FMOs) and Global Reactivity Descriptors

Understanding the structural behavior of bioactive compounds is crucial to investigating how structural orientation affects biological activity and what factors are responsible for a molecule's biological activity. Thus, the frontier molecular orbitals (FMO) and electronic parameters were estimated and examined. The frontier molecular orbital (FMO) (HOMO-LUMO) can be used to analyze chemical properties including chemical reactivity kinetic stability, and biological properties (31, 32). The FMOs and their energy difference Eg are computed to predict salacinol's energetic properties and reactivity. In addition, the energy gap between HOMO-LUMO explains molecule stability and reactivity. Moreover, the energy gap (HOMO-LUMO) is highly significant for the bio (active/ inactive), and chemical structure. By using the B3LYP/6- 311G ++ (d, p) level of theory, it is possible to determine the HOMO–LUMO values. Table 5 shows the different physical characteristics derived from HOMO–LUMO. The electron affinity (EA) and ionization potential (IP) are linked to LUMO and HOMO energy, according to Koopman's established theorem. Furthermore, the HOMO has an electron-rich capacity that allows it to give electrons. Whereas the LUMO is deficient in electrons, it is always capable of accepting them.

Table 5 shows that neokotalanol has the highest HOMO energy (EHOMO = -0.53 eV). Due to the higher energy, it is the most efficient electron donor. Salaprinol has the lowest LUMO energy (ELUMO = -2.95 eV), indicating that it may be the best electron acceptor.

The lower value of the energy gap indicates that the molecule is more active, polarized, and with small kinetic bioactivity. Neokotalanol and Ponkoranol have smaller energy gaps (Eg = 0.345 eV and 0.64 eV, respectively) than all other compounds as seen in Table 5.

Hardness and softness parameters are important in a chemical system. Molecules with high HOMO-LUMO gaps are referred to as hard molecules, while molecules with small HOMO-LUMO gaps are referred to as soft molecules and are consequently more favorable for reaction. This explanation also supports that Neokotalanol and Ponkoranol are chemically reactive.

The electronegativity refers to the molecule's capacity to attract electrons. According to the values in Table 5, Salacinol has greater electronegativity among all the compounds, making it the best acceptor of electrons.

The term "Chemical Potential" quantifies an electron's propensity to escape and is related to molecule electronegativity. With decreasing chemical potential, it becomes more difficult to lose an electron but easier to get one. As can be seen in Table 5, neokotalanol (-4.381 eV) has a smaller electronic chemical potential than the rest of the molecules. As a consequence of this finding, neokotalanol is more stable and less reactive than the other results.

The maximal charge transfer (Qmax) signifies the system's tendency to acquire more electrical charge from its surroundings. As presented in Table 5, salaprinol is more susceptible to receiving an additional electronic charge than other compounds. The electrophilicity index measures the reduction in energy due to maximum electron flow between donor (HOMO) and acceptor (LUMO). Salaprinol (14.90 eV) has a greater value than the rest of the molecules, making it the strongest electrophile.

Electrodonating power is related to charge donation, while electroaccepting power is connected to charge acceptance. In contrast, having a higher electron-accepting power shows a high capacity to accept an electron, while having a lower electron-donating power suggests a high ability to donate an electron. Based on the data in Table 5, salaprinol has a greater capacity to accept electrons, whereas neokotalanol has a higher ability to donate electrons.

The net electrophilicity index is related to the values of electron-donating and electron-accepting power. As shown in Table 5, salaprinol has a higher net electrophilicity index. As a result, neokotalanol and ponkoranol have the greatest chemical reactivity and bioactivity compared to the other compounds.

3.6. Local Reactivity Descriptors

Depending on the local reactivity descriptors (Fukui Functions), the electron density is utilized to identify the positive reactive locations of the molecule that are essential for the biological substance. The Fukui function (FF) may be used to investigate the reactivity of a molecule. They are among the most helpful reactivity indices derived from the most helpful DFT. Furthermore, it helps in determining the most reactive electrophilic and nucleophilic attack sites on a molecule. when the number of electrons is changed. The study in Fukui shows that the more reactive locations in a molecule contribute to chemical consequences (33). From Table 6, 2S, 9C, and 6C (reactive sites) are locations for a nucleophilic attack for salacinol, neosalacinol, and neokotalanol, respectively. Whereas 44Cl, 46H, and 19O (reactive sites) are locations for an electrophilic attack for neoponkoranol, neokotalanol, and ponkoranol respectively. Moreover, the most reactive sites in radical attacks are 44Cl and 46H (reactive sites), for neoponkoranol, and neokotalanol, respectively.

Table 5: Global chemical reactivity descriptors for all compounds.

Indices	Salacinol	Neosalacinol	Kotalanol	Neokotalanol	Ponkoranol	Neoponkoranol	Salaprinol	Neosalaprinol
E$_{HOMO}$ (eV)	-7.130	-3.65	-5.62	-0.53	-2.16	-6.98	-3.69	-3.36
E$_{LUMO}$ (eV)	-1.633	-2.62	-2.08	-0.185	-1.52	-0.48	-2.95	-1.94
IP (eV)	7.130	3.65	5.62	0.53	2.16	6.98	3.69	3.36
EA (eV)	1.633	2.62	2.08	0.185	1.52	0.48	2.95	1.94
Eg (eV)	5.497	1.03	3.54	0.345	0.64	6.5	0.74	1.42
η(eV)	2.749	0.52	1.77	0.173	0.32	3.25	0.37	0.71
S (eV)$^{-1}$	0.182	0.971	0.283	2.899	1.563	0.154	1.351	0.704
χ(eV)	4.381	3.14	3.85	0.358	1.84	3.73	3.32	2.65
μ (eV)	-4.381	-3.14	-3.85	-0.358	-1.84	-3.73	-3.32	-2.65
ω (eV)	3.493	9.56	7.41	0.371	5.29	2.14	14.90	4.95
Q^{max}	1.568	6.04	2.18	2.05	2.88	1.15	8.97	3.73
ω^+(eV)	1.645	8.04	6.33	0.57	12.5	4.41	16.60	12.72
ω^- (eV)	6.027	11.17	4.10	0.213	8.18	0.68	11.44	7.42
$\omega^\pm$ (eV)	7.672	19.21	10.43	0.78	20.68	5.09	28.04	20.14

Table 6: Order of the reactive sites on all compounds.

	Salacinol		Neosalacinol	
Sites	2 S	7 O	9 C	8 C
F_k^+	0.57	0.40	0.63	0.10
Sites	11 O	2 S	27 H	15 C
F_k^-	0.97	0.02	0.65	0.15
Sites	11 O	2 S	27 H	9 C
F_k^0	0.49	0.29	0.34	0.32
	Kotalanol		**Neokotalanol**	
Sites	15 C	1 S	6 C	5 O
F_k^+	0.53	0.45	0.513	0.449
Sites	13 O	2S	46 H	3 C
F_k^-	0.98	0.02	0.99	0.0007
Sites	13 O	15 C	46 H	6 C
F_k^0	0.49	0.27	0.502	0.256
	Ponkoranol		**Neoponkoranol**	
Sites	1 C	5 S	6 C	5 S
F_k^+	0.520	0.459	0.529	0.445
Sites	19 O	16 S	44 Cl	5 S
F_k^-	0.99	0.008	1.00	0.002
Sites	19 O	5 S	44 Cl	6 C
F_k^0	0.495	0.229	0.500	0.265
	Salaprinol		**Neosalaprinol**	
Sites	16 C	1 S	10 C	1 S
F_k^+	0.490	0.482	0.524	0.455
Sites	31 H	18 C	21 H	27 H
F_k^-	0.659	0.051	0.694	0.209
Sites	31 H	1 S	21 H	10 C
F_k^0	0.329	0.242	0.347	0.262

3.7. Molecular Electrostatic Potential (MEP) Map

Molecular electrostatic potential (MEP) analysis is a valuable method for determining electrophilic and nucleophilic sites of molecular systems, hydrogen bond interactions, and chemical reactivities, such as biomolecules and drugs, in three dimensions. It enables us to compare a molecule's most reactive nucleophilic and electrophilic sites to its reactive biological potentials.

Salacinol

Neosalacinol

Kotalanol

Neokotalanol

Ponkoranol

Neoponkoranol

Salaprinol

Neosalaprinol
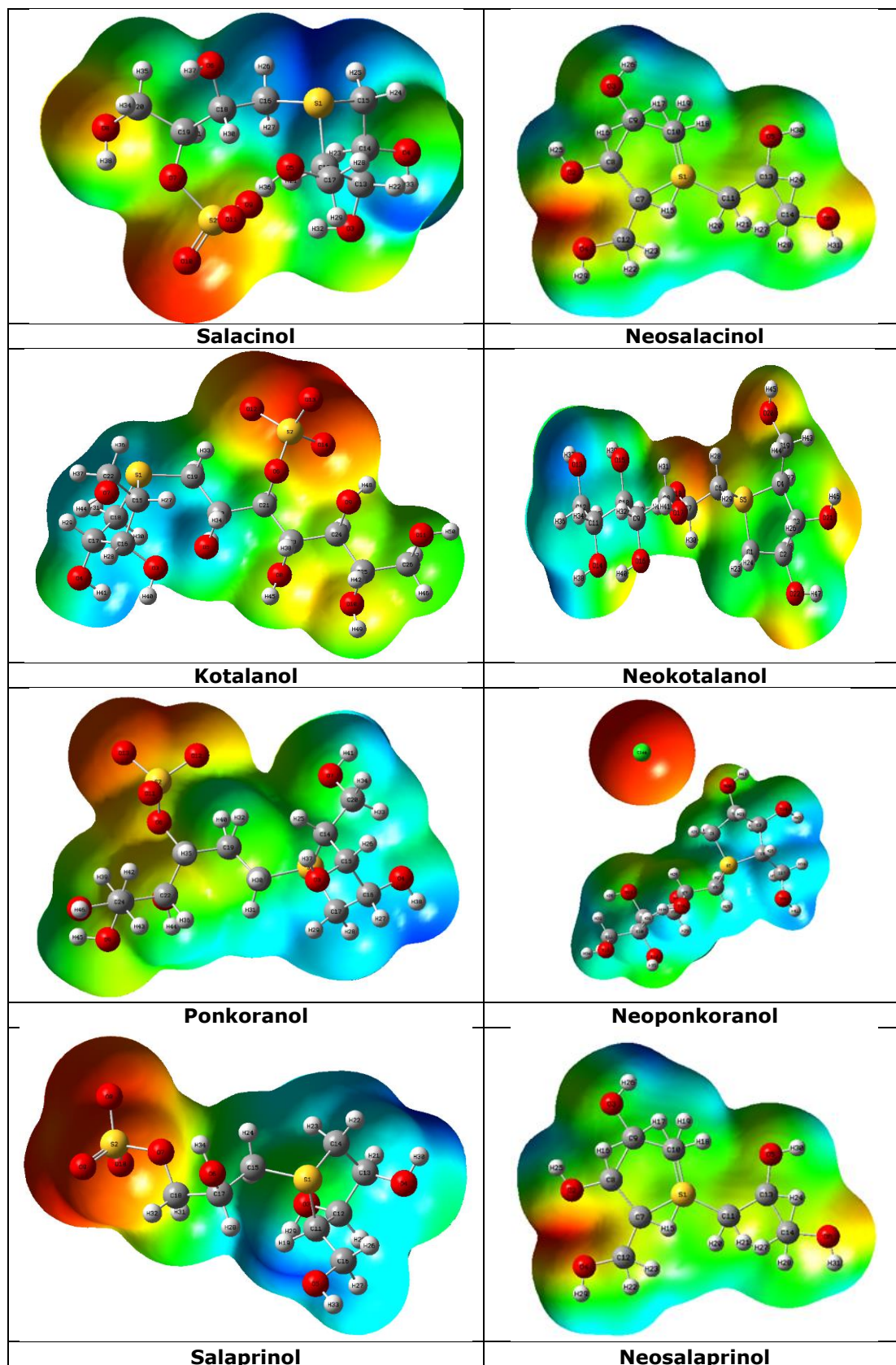
Figure 2: MEP maps for all compounds.

The molecular Electrostatic Potential (MEP) maps for the title compounds were computed by using DFT at the B3LYP/6–311++G (d, p) level. An electrophilic site shows significant attraction, whereas a nucleophilic site shows strong repulsion. The red color is the electrostatic most electronegative possibility (34-37). In this area, atoms prefer to attract electrons (electrophilic). The blue color shows the most electropositive potentials. In this region, atoms prefer to donate electrons (nucleophilic).

In addition, the green color is used to indicate regions where the potentials are equal to zero. As can be seen, the MEP map of all compounds shows that all hydrogen atoms have the greatest positive area, which indicates a potential location for electrophilic attack. As well, the O11, O5, O13, O20, O19, Cl44, O8, and O4 atoms for all compounds respectively have the greatest negative area, which specifies a potential location for nucleophilic attack. Consequently, we can conclude that the positive and area sites provide information about the region where the molecule is capable of forming intermolecular interaction.

4. CONCLUSION

In this study, we conducted a comprehensive in silico evaluation of the potential of salacinol and its related analogues as drug candidates.

Our results predicted that all compounds have various favorable druglike properties.

All the studied compounds exhibit low gastrointestinal absorption, inability to cross the blood-brain barrier and act as substrates for P-glycoprotein. Additionally, none of the compounds function as inhibitors of cytochrome P450 isoenzymes. This suggests that the limited bioavailability and brain penetration of these compounds may be influenced by P-glycoprotein-mediated efflux, limiting the significance of their interaction with this transporter in drug development and tissue protection.

We also found that all compounds have various potential to interact with a wide range of biological targets, including GPCRs, enzymes, ion channels, kinases, and nuclear receptors. This suggests that they could be used to modulate a range of physiological processes.

Additionally, all compounds have low toxicity and are unlikely to cause any major health hazards in terms of hepatotoxicity, mutagenicity, cardiotoxicity, cytotoxicity, and immunotoxicity.

the MEP, FUKUI functions, and HOMO-LUMO energy gap are useful tools for understanding the reactivity of salacinol and its derivatives. This information can be used to design new drugs that target specific biological molecules. This suggests that they are reliable for in vivo applications.

5. CONFLICT OF INTEREST

6. ACKNOWLEDGMENTS

7. FUNDING

8. CODE AVAILABILITY

The calculations have been carried out using Gaussian 09 and GaussView version 6.0.

9. REFERENCES

1. Akaki J, Morikawa T, Miyake S, Ninomiya K, Okada M, Tanabe G, et al. Evaluation of *Salacia* Species as Anti-diabetic Natural Resources Based on Quantitative Analysis of Eight Sulphonium Constituents: A New Class of α-Glucosidase Inhibitors. Phytochem Anal [Internet]. 2014 Nov 1;25(6):544–50. Available from: <URL>.

2. Federation ID. IDF diabetes atlas ninth. Dunia Idf. 2019;9:168.

3. Morikawa T, Akaki J, Ninomiya K, Kinouchi E, Tanabe G, Pongpiriyadacha Y, et al. Salacinol and Related Analogs: New Leads for Type 2 Diabetes Therapeutic Candidates from the Thai Traditional Natural Medicine Salacia chinensis. Nutrients [Internet]. 2015 Feb 27;7(3):1480–93. Available from: <URL>.

4. Daina A, Michielin O, Zoete V. SwissADME: a free web tool to evaluate pharmacokinetics, drug-likeness and medicinal chemistry friendliness of small molecules. Sci Rep [Internet]. 2017 Mar 3;7(1):42717. Available from: <URL>.

5. Banerjee P, Eckert AO, Schrey AK, Preissner R. ProTox-II: a webserver for the prediction of toxicity of chemicals. Nucleic Acids Res [Internet]. 2018 Jul 2;46(W1):W257–63. Available from: <URL>.

6. Hussein YT, Azeez YH. DFT analysis and *in silico* exploration of drug-likeness, toxicity prediction, bioactivity score, and chemical reactivity properties of the urolithins. J Biomol Struct Dyn [Internet]. 2023 Mar 4;41(4):1168–77. Available from: <URL>.

7. Lipinski CA, Lombardo F, Dominy BW, Feeney PJ. Experimental and computational approaches to estimate solubility and permeability in drug discovery and development settings. Adv Drug Deliv Rev [Internet]. 1997 Jan 15;23(1–3):3–25. Available from: <URL>.

8. Veber DF, Johnson SR, Cheng H-Y, Smith BR, Ward KW, Kopple KD. Molecular Properties That Influence the Oral Bioavailability of Drug Candidates.

J Med Chem [Internet]. 2002 Jun 1;45(12):2615–23. Available from: <URL>.

9. Rahuman MH, Muthu S, Raajaraman BR, Raja M, Umamahesvari H. Investigations on 2-(4-Cyanophenylamino) acetic acid by FT-IR,FT-Raman, NMR and UV-Vis spectroscopy, DFT (NBO, HOMO-LUMO, MEP and Fukui function) and molecular docking studies. Heliyon [Internet]. 2020 Sep 1;6(9):e04976. Available from: <URL>.

10. Gaussian 09 RA, Frisch MJ, Trucks GW, Schlegel HB, Scuseria GE, Robb MA, et al. Gaussian 16, Revision A. 02, Gaussian. Inc, Wallingford CT. 2016;2.

11. Gnanamozhi P, Pandiyan V, Srinivasan P, David Stephen A. Exploring the Structure, Electron Density and HOMOLUMO Studies of Tetrathiafulvalene (TTF) as Organic Superconductors: A DFT and AIM Analysis. J At Mol Condens Nano Phys. 2019;10(1):33–43.

12. Choudhary V, Bhatt A, Dash D, Sharma N. DFT calculations on molecular structures, HOMO–LUMO study, reactivity descriptors and spectral analyses of newly synthesized diorganotin(IV) 2-chloridophenylacetohydroxamate complexes. J Comput Chem [Internet]. 2019 Oct 15;40(27):2354–63. Available from: <URL>.

13. R D, Kumar D. Tuning the properties of truxene by successive substitution of nitrogen and sulphur heteroatoms: a DFT insight. J Mol Model [Internet]. 2022 Jan 4;28(1):27. Available from: <URL>.

14. Mu T, Xi Y, Huang M, Chen G. Search for optimal monomers for fabricating active layers in thin-film composite osmosis membranes by conceptual density functional theory. J Mol Model [Internet]. 2020 Dec 6;26(12):334. Available from: <URL>.

15. Gohlke H, Klebe G. Approaches to the Description and Prediction of the Binding Affinity of Small-Molecule Ligands to Macromolecular Receptors. Angew Chemie Int Ed [Internet]. 2002 Aug 2;41(15):2644–76. Available from: <URL>.

16. Husain A, Ahmad A, Khan SA, Asif M, Bhutani R, Al-Abbasi FA. Synthesis, molecular properties, toxicity and biological evaluation of some new substituted imidazolidine derivatives in search of potent anti-inflammatory agents. Saudi Pharm J [Internet]. 2016 Jan 1;24(1):104–14. Available from: <URL>.

17. Lipinski CA. Lead- and drug-like compounds: the rule-of-five revolution. Drug Discov Today Technol [Internet]. 2004 Dec 1;1(4):337–41. Available from: <URL>.

18. Hammoudi N-E-H, Benguerba Y, Attoui A, Hognon C, Lemaoui T, Sobhi W, et al. *In silico* drug discovery of IKK-β inhibitors from 2-amino-3-cyano-4-alkyl-6-(2-hydroxyphenyl) pyridine derivatives based on QSAR, docking, molecular dynamics and drug-likeness evaluation studies. J Biomol Struct Dyn [Internet]. 2022 Jan 22;40(2):886–902. Available from: <URL>.

19. Finch A, Pillans P. P-glycoprotein and its role in drug-drug interactions. Aust Prescr [Internet]. 2014 Aug 1;37(4):137–9. Available from: <URL>.

20. Fromm MF. Importance of P-glycoprotein at blood–tissue barriers. Trends Pharmacol Sci [Internet]. 2004 Aug 1;25(8):423–9. Available from: <URL>.

21. Kim RB, Fromm MF, Wandel C, Leake B, Wood AJ, Roden DM, et al. The drug transporter P-glycoprotein limits oral absorption and brain entry of HIV-1 protease inhibitors. J Clin Invest [Internet]. 1998 Jan 15;101(2):289–94. Available from: <URL>.

22. Kirchmair J, Göller AH, Lang D, Kunze J, Testa B, Wilson ID, et al. Predicting drug metabolism: experiment and/or computation? Nat Rev Drug Discov [Internet]. 2015 Jun 24;14(6):387–404. Available from: <URL>.

23. van Waterschoot RAB, Schinkel AH. A Critical Analysis of the Interplay between Cytochrome P450 3A and P-Glycoprotein: Recent Insights from Knockout and Transgenic Mice. Scott EE, editor. Pharmacol Rev [Internet]. 2011 Jun 1;63(2):390–410. Available from: <URL>.

24. Cheng F, Li W, Zhou Y, Shen J, Wu Z, Liu G, et al. admetSAR: A Comprehensive Source and Free Tool for Assessment of Chemical ADMET Properties. J Chem Inf Model [Internet]. 2012 Nov 26;52(11):3099–105. Available from: <URL>.

25. Kishino E, Ito T, Fujita K, Kiuchi Y. A mixture of Salacia reticulata (Kotala himbutu) aqueous extract and cyclodextrin reduces body weight gain, visceral fat accumulation, and total cholesterol and insulin increases in male Wistar fatty rats. Nutr Res [Internet]. 2009 Jan 1;29(1):55–63. Available from: <URL>.

26. Flammang AM, Cifone MA, Erexson GL, Stankowski LF. Genotoxicity testing of a fenugreek extract. Food Chem Toxicol [Internet]. 2004 Nov 1;42(11):1769–75. Available from: <URL>.

27. Im R, Mano H, Nakatani S, Shimizu J, Wada M. Safety Evaluation of the Aqueous Extract Kothala Himbutu (*Salacia reticulata*) Stem in the Hepatic Gene Expression Profile of Normal Mice Using DNA Microarrays. Biosci Biotechnol Biochem [Internet]. 2008 Dec 23;72(12):3075–83. Available from: <URL>.

28. Jihong Y, Shaozhong L, Jingfeng S, Kobayashi M, Akaki J, Yamashita K, et al. Effects of Salacia chinensis extract on reproductive outcome in rats. Food Chem Toxicol [Internet]. 2011 Jan 1;49(1):57–60. Available from: <URL>.

29. Jayawardena MHS, de Alwis NMW, Hettigoda V, Fernando DJS. A double blind randomised placebo controlled cross over study of a herbal preparation containing Salacia reticulata in the treatment of type 2 diabetes. J Ethnopharmacol [Internet]. 2005 Feb 28;97(2):215–8. Available from: <URL>.

30. Oda Y, Yuasa A, Ueda F, Kakinuma C. A subchronic oral toxicity study of Salacia reticulata extract powder in rats. Toxicol Reports [Internet]. 2015 Jan 1;2:1136–44. Available from: <URL>.

31. Ganesan M, Paranthaman S. Molecular structure, interactions, and antimicrobial properties of curcumin-PLGA Complexes—a DFT study. J Mol Model [Internet]. 2021 Nov 28;27(11):329. Available from: <URL>.

32. Suvitha A, El-Mansy MAM, Kothandan G, Steephen A. Molecular Structure, FT-RAMAN, IR, NLO, NBO, HOMO–LUMO analysis, physicochemical descriptors, adme parameters, and pharmacokinetic bioactivity of 2, 3, 5, 6-tetrachloro-p-benzoquinone. J Struct Chem [Internet]. 2021 Sep 26;62(9):1339–56. Available from: <URL>.

33. Grillo IB, Urquiza-Carvalho GA, Chaves EJF, Rocha GB. Semiempirical methods do Fukui functions: Unlocking a modeling framework for biosystems. J Comput Chem [Internet]. 2020 Apr 5;41(9):862–73. Available from: <URL>.

34. Cardoso FJB, de Figueiredo AF, da Silva Lobato M, de Miranda RM, de Almeida RCO, Pinheiro JC. A study on antimalarial artemisinin derivatives using MEP maps and multivariate QSAR. J Mol Model [Internet]. 2008 Jan 30;14(1):39–48. Available from: <URL>.

35. Obiol-Pardo C, Cordero A, Rubio-Martinez J, Imperial S. Homology modeling of Mycobacterium tuberculosis 2C-methyl-d-erythritol-4-phosphate cytidylyltransferase, the third enzyme in the MEP pathway for isoprenoid biosynthesis. J Mol Model [Internet]. 2010 Jun 15;16(6):1061–73. Available from: <URL>.

36. El-Shamy NT, Alkaoud AM, Hussein RK, Ibrahim MA, Alhamzani AG, Abou-Krisha MM. DFT, ADMET and Molecular Docking Investigations for the Antimicrobial Activity of 6,6'-Diamino-1,1',3,3'-tetramethyl-5,5'-(4-chlorobenzylidene)bis[pyrimidine-2,4(1H,3H)-dione]. Molecules [Internet]. 2022 Jan 18;27(3):620. Available from: <URL>.

37. Haddadi Z, Meghezzi H, Amar A, Boucekkine A, Bennamane N, Nedjar-Kolli B, et al. DFT and QSAR investigations of substituent effects in pyrazolooxazine derivatives: Activity prediction. J Theor Comput Chem [Internet]. 2019 Feb 10;18(01):1950001. Available from: <URL>.

Studying the Effectiveness of an Expired Betamethasone Drug in Sulfuric Acid Solutions to Examine the Corrosive Behavior of Copper Using Weight Loss and Experimental Design

Tarik Attar[1,2]* iD **, Abbes Benchadli[2]** iD

[1]Ecole Supérieure en Sciences Appliquées de Tlemcen, ESSA-Tlemcen, BP 165 RP Bel Horizon, Tlemcen 13000, Algeria
[2]Laboratoire de ToxicoMed, Université Abou Bekr Belkaïd, B.P. 119, Tlemcen 13000, Algeria

Abstract: Utilizing expired pharmaceuticals as corrosion inhibitors for copper in acidic environments offers compelling advantages, including cost-effectiveness, reduced toxicity compared to traditional inhibitors, and contribution to pharmaceutical waste reduction through recycling. This study investigates the corrosion inhibition of copper in a sulfuric acid solution using varying concentrations of Expired Betamethasone Drug, employing weight loss and Experimental Design methods. The influence of temperature on copper's corrosion behavior is examined within the range of 293–333 K. Results show that inhibition efficiency increases with higher inhibitor concentrations but decreases with rising temperature. Thermodynamic analyses elucidate adsorption and activation processes, revealing that the adsorption of Expired Betamethasone Drug on copper surfaces is characterized as endothermic and spontaneous, aligning well with the Langmuir and Frumkin adsorption isotherms. The activation and free energies of inhibition reactions support a mechanism of physical adsorption. To establish the relationship between factors and responses, we employ response surface methodology (RSM) with regression statistical analysis and probabilistic assessment. Statistical analysis demonstrates highly significant quadratic models for inhibition efficiencies (IE) with a coefficient of multiple regressions (R^2) of 0.999. Further model validation confirms a strong fit (adjusted R^2 = 0.997), with experimental observations closely matching predictions and a highly significant model (Q^2 = 0.989). The findings reveal that this expired drug exhibits substantial inhibitory power, exceeding 96%, in both experimental and predictive calculations.

1. INTRODUCTION

Copper stands out among other metals due to its unique combination of corrosion resistance, electrical and thermal conductivity, and mechanical properties (1). It is considered a relatively noble element, contributing to its resistance to rapid corrosion in various atmospheres and chemical environments. Even in corrosive electrolytes such as acids, it effectively shields itself from degradation by developing a protective, non-conductive oxide film (2).

Equipment such as heat exchangers, boilers, pipelines, coils, electrical boards, and circuits constructed from copper and copper alloys often find themselves close to corrosive environments within desalination systems or petroleum pipelines. This has led to numerous studies addressing the degradation of copper and copper alloys under various climatic conditions, including both natural and artificial settings. To protect metal and alloy surfaces from corrosion resulting from atmospheric attack, appropriate inhibitors can be applied (3,4).

Among these inhibitors, both inorganic and organic types are found. Organic compounds and their derivatives, such as azoles, amines, and amino acids, take precedence. Notably, the presence of heteroatoms like oxygen, nitrogen, sulfur, and phosphorus within organic compound molecules enhances their effectiveness as copper corrosion inhibitors (5-7). This phenomenon is attributed to the existence of vacant d orbitals in copper atoms, facilitating the formation of coordinative bonds with atoms capable of donating electrons. Additionally, interactions with rings containing conjugated bonds and pi electrons are also observed (8, 9).

In recent years, the utilization of expired medications as corrosion inhibitors for various metals and alloys has emerged as a novel challenge. These medications, which are increasingly prevalent in households, pharmacies, hospitals, and other sources, present an opportunity for repurposing as corrosion inhibitors. Notably, most of these compounds exhibit high solubility in aqueous solutions and maintain stability in diverse aggressive environments (10). Research has indicated that a significant portion of medications, approximately 90%, retain their active constituents and stability beyond their expiration dates (11,12). These findings suggest that expired medications can be safely repurposed for corrosion inhibition purposes. Their non-toxic attributes and minimal environmental impact position them as potential candidates to replace traditional toxic chemical corrosion inhibitors (13). Expired medications have even been recognized as part of the family of green corrosion inhibitors.

Furthermore, a comprehensive literature survey reveals that a wide range of pharmaceuticals has been successfully employed as sustainable corrosion inhibitors for various metals and alloys. These pharmaceuticals encompass a diverse group, including Phenobarbital (14), Modiaquine (15), Doxycycline (16), Tenormin (17), Ethambutol (18), Salazopyrin (19), Atenolol (20), Ciprofloxacin (21), Moxifloxacin, Betamethasone (22), Tetracycline and Streptomycin (23), Ibuprofen and Diclofenac (24), Telmisartan (25), Cephalothin (26), Tramadol (27), Cephapirin (28), Cefixime and Cefpirome (29), Glimepiride (30), Spironolactone (31), Povidone Iodine (32), Amoxicillin (33, 34), and more.

The statistical design of experiments (DOE) is a technique used to construct an experimental model, aiming to reduce the required number of tests compared to conventional methods. This is achieved by considering selected or all relevant parameters within the experiment. DOE also generates mathematical models for statistical assessment of influencing factors and potential interactions among variables (35, 36). Applying experimental design methods yields more precise results for final responses, such as inhibition efficiency (IE), and interactions among studied parameters. The response surface method (RSM) is an effective tool in this context (37, 38), consistently used for developing, enhancing, and optimizing experimental processes influenced by multiple factors (39). The Central

Composite Design was employed to identify optimal inhibition efficiency. The corrosion inhibition efficiency was evaluated using the weight loss method, and collected data were used to formulate a predictive model for corrosion inhibition performance through ANOVA.

This research investigates the corrosion inhibition potential of betamethasone, an expired pharmaceutical drug, in acidic environments by employing the weight loss method. Additionally, it explores the interactive effects of inhibitor concentration, operating temperature, and immersion duration on inhibition performance using response surface methodology (RSM). The study also estimates and discusses various isotherm models and thermodynamic parameters related to inhibitor adsorption on the copper surface.

2. EXPERIMENTAL

2.1. Materials and methods
A test solution of 0.5 mol/L sulfuric acid was prepared by diluting analytical grade 98% H_2SO_4 with double-distilled water to a final volume of 50 mL. The copper specimen's surface was pre-treated by polishing with various abrasives (ranging from 600 to 1200), followed by washing with double-distilled water and then acetone. After drying, the specimens were weighed before immersion in the freshly prepared test solution. Subsequently, the copper specimens were retrieved, cleaned, and reweighed. Weight measurements were taken using an analytical balance before and after exposure, and recorded to the nearest five decimal places. The expired drug used in this research is Betamethasone 0.5MG/ML (0.05%) SOL.BUV (CELESTENE).

2.2. Weight loss measurements
Weight loss assessments were conducted using copper rectangular specimens. Each specimen was immersed in triplicate within a solution of 0.5 mol/L sulfuric acid, both in the absence and presence of various concentrations of expired Betamethasone drug. This procedure was carried out across different immersion periods and temperatures. The acquired weight loss data was then used to determine corrosion rate (CR), inhibition efficiency (IE), and surface coverage (θ) through the following equations (1,2 and 3) (40):

$$CR = (W - W_{Inh}) / S \times t \qquad (1)$$

$$IE(\%) = 100 \times (CR - CR_{Inh}) / CR \qquad (2)$$

$$\theta = IE / 100 \qquad (3)$$

Where, $W - W_{inh}$ represents the weight loss, which is the difference in mass between the absence and presence of the inhibitor, expressed in milligrams (mg). The sample area S is given in square centimeters (cm²), and the immersion time t is denoted in hours (h). CR represents the corrosion rate observed in the absence of the inhibitor, while CR_{inh} corresponds to the corrosion rate obtained in the presence of the inhibitor.

2.3. Adsorption Isotherm and Thermodynamic Parameter Determination

Adsorption isotherm studies provide a descriptive mechanism for understanding how organic inhibitors adsorb onto metal surfaces. The most suitable adsorption isotherm model that accurately characterizes the adsorption of expired Betamethasone drug on copper in a 0.5 mol/L sulfuric acid medium was determined by fitting various adsorption isotherm models, including Langmuir, Freundlich, Frumkin, Tempkin, Flory-Huggins, and El Awady, expressed in linear form as follows:

Langmuir adsorption isotherm is represented by Equation (4) (41):

$$C / \theta = 1 / K_{ads} + C \qquad (4)$$

By taking the logarithm of both sides of Equation (4), we arrive at Equation (5).

$$\log(C / \theta) = \log C - \log K_{ads} \qquad (5)$$

Freundlich adsorption isotherm (42):

$$\log(\theta) = n \log C + \log K_{ads} \qquad (6)$$

Frumkim adsorption isotherm model (43):

$$\log[C(\theta / 1 - \theta)] = 2\alpha\theta + 2.303 \log K_{ads} \qquad (7)$$

Temkin adsorption isotherm model (44):

$$\theta = \ln C + K_{ads} \qquad (8)$$

Flory-Huggins adsorption isotherm is expressed by Equation (9) (45):

$$\log(\theta / C) = b \log(1 - \theta) + \log K_{ads} \qquad (9)$$

El-Awady adsorption isotherm is formulated as follows (46):

$$\log(\theta / 1 - \theta) = y \log(C) + y \log K_{ads} \qquad (10)$$

where C represents the concentration of the inhibitor, K_{ads} is the adsorption-desorption constant, θ denotes the degree of surface coverage by the inhibitor, n is the positive constant known as the Freundlich exponent, a describes the lateral interaction term characterizing the interaction within the adsorbed layer, b serves as the size parameter, measuring the substitution of adsorbed water molecules with a specific inhibitor molecule, and y indicates the number of inhibitor molecules occupying one active site.

The linear regression coefficient of determination (R^2) was employed to assess the model that best aligns with the experimental values.

The expression for the change in Gibbs free energy of adsorption, as presented in Equation (11) (47), was employed to explore the feasibility and nature of the adsorption process.

$$\Delta G_{ads} = -RT \ \ln(55.5 \ K_{ads}) \qquad (11)$$

Where, K_{ads} represents the adsorption equilibrium constant obtained from the isotherm, and the value 55.5 corresponds to the molar concentration of water in the solution

By utilizing the thermodynamic relation (Eq. 12), it becomes possible to calculate the changes in the enthalpy of the adsorption process at different temperatures (48).

$$\Delta G_{ads} = \Delta H_{ads} - T \Delta S_{ads} \qquad (12)$$

The change of ΔG_{ads} concerning temperature forms a straight line with an intercept ΔH_{ads} and a slope ($-\Delta S_{ads}$).

2.4. Determination of Thermodynamic Activation Parameters

The inhibitory mechanism of the investigated inhibitor can be elucidated by examining the thermodynamic and activation parameters. The impact of temperature on the inhibitory effect can be aptly elucidated through the utilization of the Arrhenius equation. This equation is represented as follows (32):

$$CR = A \times \exp(-\Delta E_a / RT) \qquad (13)$$

where CR denotes the corrosion rate of copper, A represents the Arrhenius pre-exponential factor, ΔE_a (kJ/mol) represents the activation energy, R signifies the gas constant (8.314 J/mol K), and T represents the temperature (K).

The plot of ln of corrosion rate, against 1/T in Eq. (13) gives a slope from which the activation energy, was estimated.

The activation enthalpy (ΔH_a) and activation entropy (ΔS_a) can be determined by analyzing the slope ($-\Delta H_a/R$) and intercept [ln(R/Nh) + ($\Delta S_a/R$)] of the plot ln(CR/T) versus 1/T. This analysis employs the following equation for the transition state (6):

$$ln(CR/T) = [ln(R/Nh) + (\Delta S_a/R)] - \Delta H_a/RT \qquad (14)$$

Where h represents Planck's constant, N stands for Avogadro's number, ΔS_a signifies the activation entropy, and ΔH_a indicates the activation enthalpy.

2.5. Design of experiments study

In this paper, the experimental design and statistical analysis were performed using MODDE Software Version 9.1. The individual and interactive effects of the corrosion process on the independent factors were determined using the standard Response Surface Methodology (RSM) based on the Multiple Linear Regression method. Specifically, the

process variables investigated in sulfuric acid included the concentration of the inhibitor (A), temperature (B), and immersion time (C). These three variables were examined at three different levels. The settings and levels of each parameter are provided in Table 1.

Table 1: Optimization of Betamethasone Drug Inhibition Efficiency on Copper in Acid Medium: Weight Loss and RSM Approach.

Variables	Levels		
	− 1	**0**	**+ 1**
A: Inhibitor concentration (%,v/v)	1	2.5	5
B: Temperature (°C)	20	40	60
C: Immersion time (h)	0.5	1	1.5

3. RESULTS AND DISCUSSION

3.1. Adsorption Isotherm and Determination of Adsorption Thermodynamic Parameters
3.1.1. Adsorption Isotherm
The R^2 values associated with each isotherm model presented in Table 2 were used to identify the most suitable model. While the data in Table 2 exhibited fits with Freundlich, Langmuir, Frumkin, Temkin, Flory-Huggins, and El-Awady's isotherms, the Langmuir and Frumkin isotherms demonstrated the highest R^2 values. This observation suggests that both isotherms provide the most accurate description of the adsorption mechanism of the Betamethasone drug on copper in a sulfuric acid medium. Therefore, the Langmuir and Frumkin isotherms are considered appropriate for evaluating the parameters of adsorption.

Table 2: R^2 values for the various adsorption isotherms considered.

T (K)	Langmuir	Freundlich	Frumkin	Temkin	Flory-Huggins	El-Awady
293	0.989	0.817	0.972	0.791	0.886	0.660
303	0.987	0.932	0.995	0.884	0.879	0.722
313	0.987	0.958	0.998	0.904	0.868	0.765
323	0.993	0.983	0.995	0.942	0.883	0.887
333	0.981	0.971	0.987	0.918	0.850	0.887

3.1.2. Determination of Adsorption Thermodynamic Parameters
By utilizing data obtained from the Langmuir and Frumkin isotherms, it became feasible to determine the equilibrium adsorption constant (K_{ads}) and, subsequently, the free adsorption energy (ΔG_{ads}) of the investigated inhibitor using Equation 11. Table 3 displays positive adsorption equilibrium constants, indicating the feasibility of the inhibitor's adsorption onto the metal surface (49). Furthermore, these equilibrium constants exhibit an increase with rising temperatures.

The presence of negative values for ΔG_{ads} in both Langmuir and Frumkin isotherms indicates the spontaneous nature of the inhibitor adsorption process, with these values falling below -20 kJ/mol. These lower values can be attributed to the electrostatic interaction between the composites and the metal surface (physisorption). The adsorption enthalpy and entropy were calculated using the adsorption equilibrium constant obtained from the Langmuir model and Equation 12. The positive values of ΔH_{ads} (11.13 kJ/mol) validate that the adsorption of inhibitors is an endothermic process (50). Furthermore, the positive sign of ΔS_{ads} (75.81 J/mol K) indicates an increase in the entropy of the process. This process involves both the adsorption of organic compounds (Org) and the desorption of water molecules at the electrode surface. The positive values of ΔS_{ads} suggest an augmented level of disorder among the reactant molecules on the metal electrode surface. This phenomenon serves as a significant driving force for the adsorption of inhibitor molecules onto the metal surface. Collectively, these findings underscore the substantial adsorption of the composites onto the metal surface.

Table 3: Adsorption parameters of copper corrosion in the presence of Betamethasone drug in 0.5 M H_2SO_4 medium.

T (K)	Frumkin		Langmuir	
	K_{ads}	ΔG_{ads} (kJ/mol)	K_{ads}	ΔG_{ads} (kJ/mol)
293	0.022	-0.53	1.557	-10.86
303	0.091	-4.09	2.142	-12.03
313	0.133	-5.19	2.449	-12.78
323	0.177	-6.13	2.566	-13.31
333	0.224	-6.98	2.836	-14.01

3.2. Determination of Thermodynamic Activation Parameters

Data presented in Table 4 indicate that the activation energy (ΔE_a) of the inhibited solution in this study increases with higher inhibitor concentrations, suggesting strong adsorption of inhibitor molecules onto the metal surface (7). The lower or unchanged values of ΔE_a for the inhibited systems compared to the blank test indicate a chemisorption mechanism, whereas the higher values of ΔE_a in the presence of Betamethasone drug suggest a physical adsorption mechanism (51).

Table 4: Values of activation parameters for copper in 0.5 M H_2SO_4 medium in the absence and presence of various concentrations of Betamethasone drug.

C (%,V/V)	$R^2_{(Eq.13)}$	ΔE_a (kJ/mol)	$R^2_{(Eq.14)}$	ΔH_a (kJ/mol)	$\Delta H_a = \Delta E_a - RT$ (kJ/mol)	$-\Delta S_a$ (J/mol K)	$\Delta G_{a(at.313K)}$ (kJ/mol)
Blank	0.999	62.23	0.999	59.63	59.62	89.37	87.60
1	0.994	76.82	0.994	74.23	74.21	48.84	89.51
2	0.999	75.99	0.999	73.40	73.39	53.33	90.09
3	0.997	74.72	0.997	72.13	72.12	59.10	90.63
4	0.995	83.97	0.995	81.38	81.37	32.10	91.42
5	0.997	91.92	0.997	89.32	89.32	12.73	93.30

The positive values of activation enthalpy in both the absence and presence of inhibitors suggest an endothermic nature of the copper dissolution process (52). The obtained ΔH_a values are in good agreement with the calculated ΔH_a from the equation $\Delta H_a = \Delta E_a - RT$ at the average experimental temperature (T = 313K). This result suggests that the corrosion process follows an unimolecular reaction mechanism involving the evolution of hydrogen gas (51). Additionally, an increase in the activation entropy values leads to a decrease in the system's disorder due to the adsorption of Betamethasone drug molecules on the copper surface.

When comparing the ΔG_a (calculated as the average at 313K) values of the process in the presence of the inhibitor to those in its absence, higher values are observed, indicating the dominance of physisorption as the mechanism. Conversely, lower ΔG_a values are indicative of chemisorption (53).

3.3. Design of experiments study
3.3.1. Optimization of inhibition efficiency using RSM

A total of 17 experimental runs were conducted to obtain the responses (inhibition efficiency, IE) of the dependent variables (Inhibitor concentration, A; Temperature, B; and Immersion time, C) as presented in the experimental design (Table 5).

The optimal conditions that yield the highest inhibition efficiency (IE) were determined using Response Surface Methodology (RSM). For the three-factor inputs, the second-order polynomial equation is provided below (Equation 15):

$$IE = 68.49 + 14.57\,A - 9.69\,B - 2.50\,C + 1.72\,A^2 + 0.79\;B^2 - 0.29\,C^2 + 4.18\,AB - 0.62\,AC + 2.89\,BC \qquad (15)$$

Table 5: Responses of experimental design for inhibition process of copper in the presence of Betamethasone drug in 0.5 mol/L H_2SO_4.

Exp No	Run	Factors			Response (%)	
		A (%, v/v)	B (°C)	C (h)	IE_{Obs}	IE_{Pred}
1	15	1	20	0.5	75.14	74.81
2	6	5	20	0.5	96.23	96.84
3	3	1	60	0.5	41.06	41.26
4	5	5	60	0.5	80.15	80.05
5	12	1	20	1.5	65.23	65.26
6	13	5	20	1.5	85.06	84.78
7	10	1	60	1.5	43.98	43.29
8	2	5	60	1.5	79.31	79.57
9	14	1	40	1.0	54.89	55.65
10	11	5	40	1.0	85.31	84.80
11	8	3	20	1.0	79.04	78.98
12	7	3	60	1.0	59.30	59.60
13	17	3	40	0.5	71.12	70.71
14	9	3	40	1.5	65.04	65.70
15	4	3	40	1.0	67.93	68.49
16	16	3	40	1.0	68.37	68.49
17	1	3	40	1.0	69.71	68.49

The histograms depicting the effects of coefficients on the inhibition efficiencies (IE) of the Betamethasone drug are presented in Figure 1. The variables with the most significant impact on IE are inhibitor concentration (A), while the influences of temperature (B) and immersion time (C) are comparatively smaller. Coefficients in the model characterized by positive values denote a synergistic effect, whereas negative values indicate an antagonistic effect (54). Among the model factors, A^2, B^2, AB, and BC positively contribute to the formulation, whereas C^2 and AC exert a negative influence on the developed model.
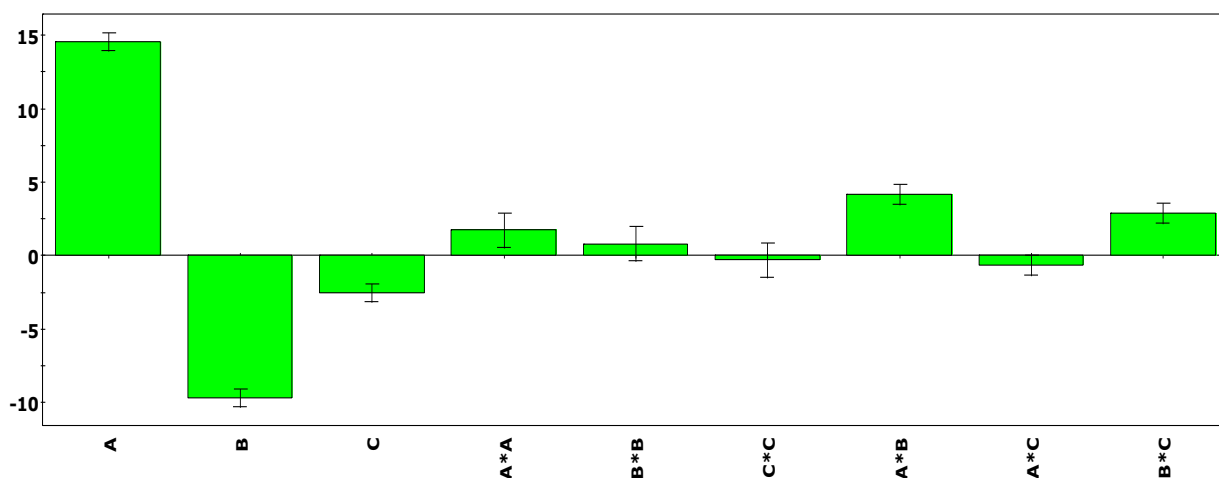
Figure 1: Coefficients plot

In Figure 2, a clear linear trend is evident in the diagnostic plots illustrating the relationship between predicted and experimental inhibition efficiency. These trends affirm the design model's capability to predict not only the inhibition efficiency of the expired drug but also the response variables within the experimental data. The findings from this study on expired medication demonstrate a very

significant inhibitory capability, exceeding 96%, both in experimental and predictive calculations. This inhibition efficiency (IE%) is considered among the best inhibitors in the literature.

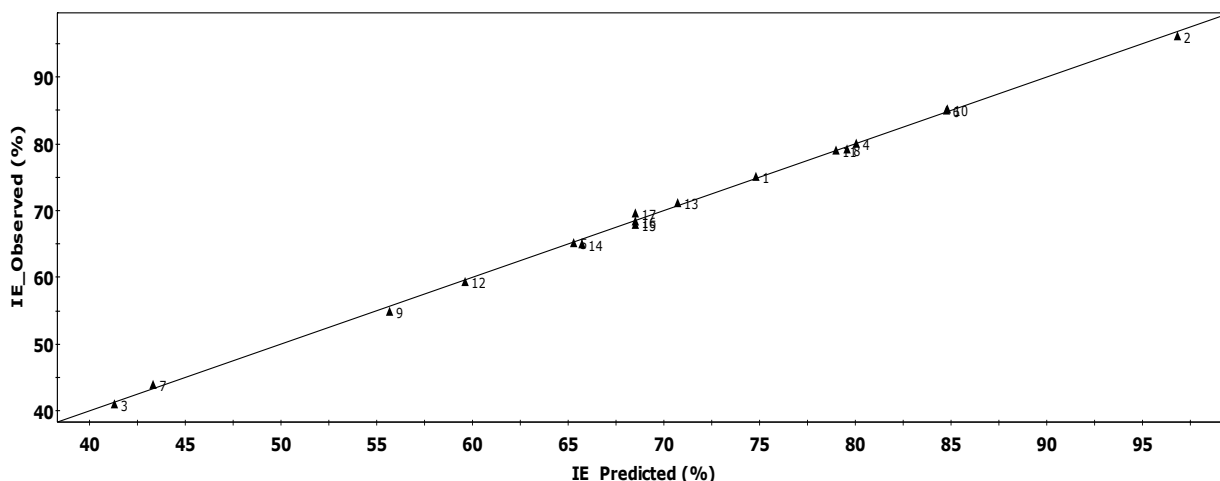**Figure 2:** Diagnostic representation of predicted versus observed inhibition.

3.3.2. Main Effects

The effects of each parameter under consideration are shown in Figure 3. It is important to note that the values represented by each point correspond to the average corrosion inhibition efficiencies obtained at that specific level, regardless of other parameter variations. The overall mean is plotted across each panel. As the concentration of the Betamethasone drug increased, there was a corresponding increase in inhibitor efficiency (IE%). Conversely, the decrease in corrosion inhibition efficiency with the elevation of temperature (55), as observed in this study (Figure 3), suggests a physisorption mechanism.

The decline in inhibition efficiency over time could be attributed to the desorption or dissolution of adsorbed inhibitor molecules. Optimal efficiencies were achieved when copper was immersed in a solution containing 5% (v/v) Betamethasone drug for a duration of half an hour, at a temperature of 20°C. Conversely, the lowest IE was observed when copper was exposed to a solution with 1% (v/v) Betamethasone drug, immersed for 1.5 hours, and maintained at a temperature of 60°C.
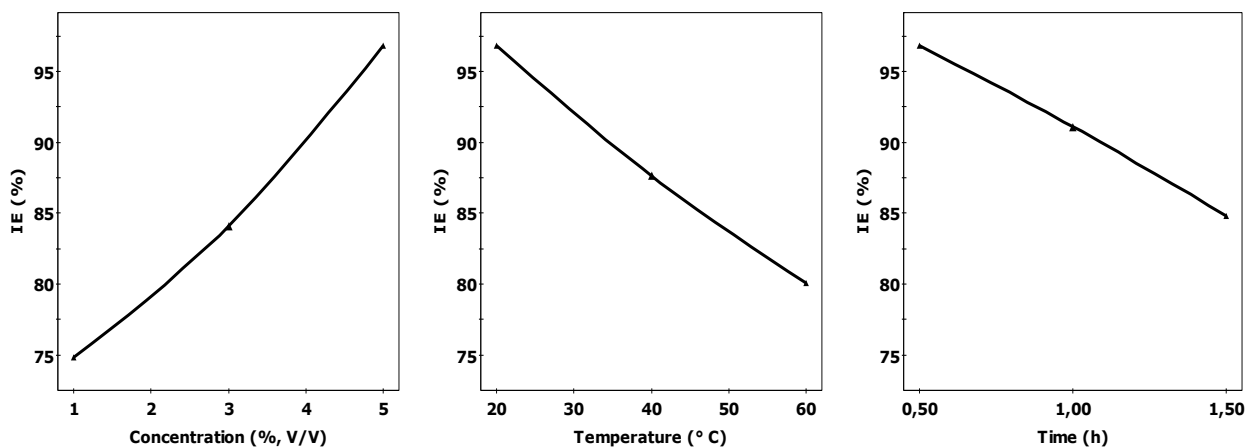
Figure 3: Weight Loss and RSM Optimization of Betamethasone Drug's Inhibition Efficiency on Copper in Sulfuric Acid.

3.3.3 Response Surface and Contour Plots

To identify the optimal zone of inhibition efficiency (IE), surface plots with contour plots have been generated, as depicted in Figures 4 and 5. Given that inhibition efficiency is influenced by various process variables, a thorough investigation becomes essential. This investigation is achieved by constructing contour plots to depict the interplay of two independent variables—working temperature and inhibitor concentration—across different immersion periods (Figure 5).

297
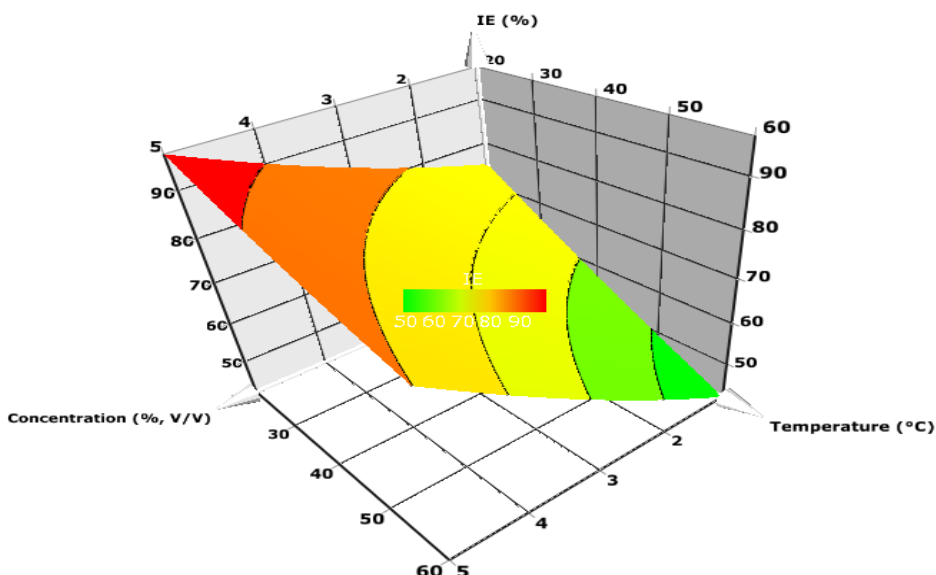
Figure 4: Response Surface Plots of the Effects of Temperature and Inhibitor Concentration on Inhibition Efficiency at Half an Hour.

As evident from both figures, the inhibition efficiency increases with decreasing temperature for a given inhibitor concentration. This decrease in IE (%) can be attributed to the desorption of the inhibitor molecule from the metal surface, leading to the process of physical adsorption.

Figure 5 reveals that as the inhibitor concentration ranges from the minimum to the maximum, IE (%) increases with decreasing temperature and shorter immersion times. For a fixed Betamethasone concentration, the IE decreases with prolonged immersion time but remains higher for higher inhibitor concentrations. The IE attains its peak value at the lowest temperature (20 °C) and shortest immersion time (0.5 h), along with the highest concentration of Betamethasone drug, as illustrated in Figure 5. These results align with findings reported in the literature (56).
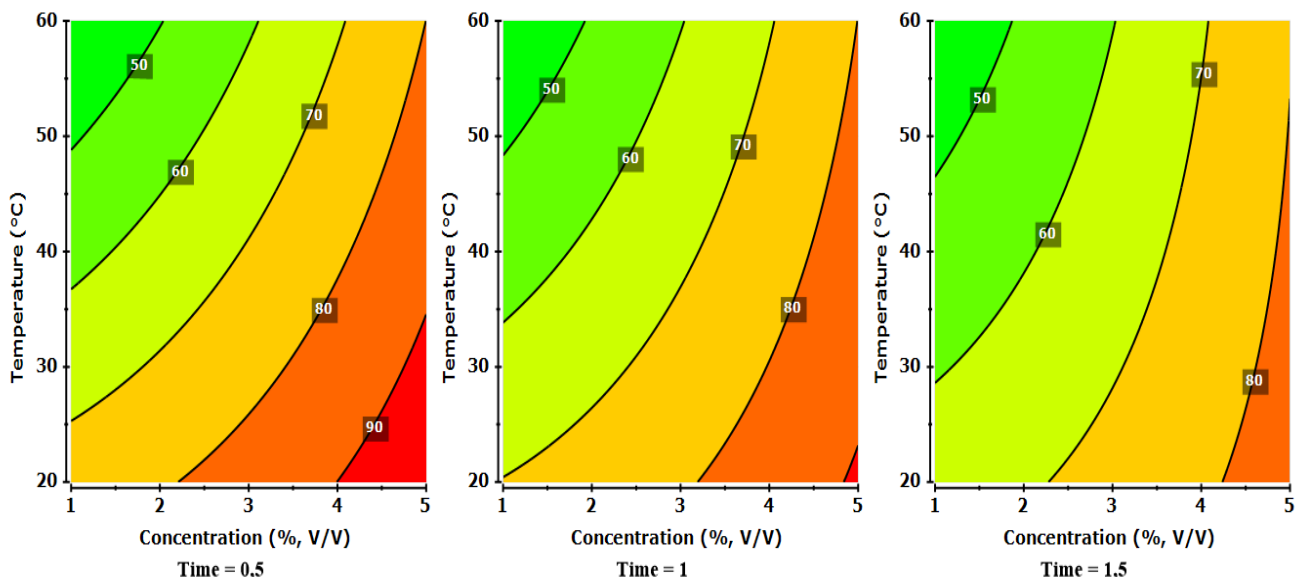
Figure 5: 4D-Contour Plots Showing the Effect of Temperature and Concentration on Inhibition Efficiency at Various Times.

3.1. Statistical test and analysis of models
The quadratic model was developed and applied to the dataset, with the findings presented in the fit plot summary (Figure 6). This comprehensive overview provides valuable insights into the model's robustness and efficacy, encompassing critical parameters such as Model Validity (0.911), Reproducibility (0.996), R^2 (0.999), and Q^2 (0.989).

The current model's prediction of more than 99.9% response variability is shown by the determination coefficient (R^2) value of 0.999. A model is classified as excellent when its Q2 value exceeds 0.9 (56). Furthermore, in this study, a reliable model typically exhibits a difference between R^2 and Q^2 of less than 0.3; here, the difference is merely 0.01. A Model Validity bar exceeding 0.25 indicates the absence of Lack of Fit in the model. In this study, a value of 0.996 is nearly equivalent to unity, signifying a high level of reproducibility.

Analysis variance (ANOVA), which is shown in Table 6, ensured the accuracy of the statistical analysis calculation. P-values and F-values serve as valuable metrics in the context of ANOVA, used to assess the significance of models, specific experimental variables, and their interactions (57). When a model's P-value is below 0.050 and its F-value is significant, it is considered highly significant in statistics. Moreover, with model terms, a P-value less than 0.050 indicates the significance of the corresponding terms, while a value exceeding 0.100 suggests that the terms are not deemed significant (58). A strong significance of the regression model was found utilizing analyses employing an F-value of (581.28) with a low probability "P" value (P= 0.000) at the 95% confidence level. The predicted-R2 value for the model and the corresponding adjusted-R2 value were in good agreement because their difference was less than 0.20 (59). It was determined that the model was highly significant, and values for R^2 and R^2 Adj exceeding 0.99 demonstrated an exceptional agreement between predicted and experimental inhibition efficiency in the drug betamethasone (36). A robust model with a low RSD value closely fits the observed results with the expected values (56).

Figure 6: Summary of fit plot showing model fit (R^2), predictability (Q^2), model validity, and reproducibility.

Table 6: Analysis of Variance for the Quadratic Model of Inhibition Efficiency.

	DF	Sum of Squares	Mean Square	F	p	SD
Total	17	86221.9	5071.87			
Constant	1	82862.4	82862.4			
Total Corrected	16	3359.49	209.968			14.4903
Regression	9	3355	372.778	581.28	0.000	19.3075
Residual	7	4.48914	0.641306			0.800816

Q^2 =0.989	Cond. no.=4.438
R^2 =0.999	RSD=0.8008
R^2 Adj.= 0.997	Conf. lev.=0.95

4. CONCLUSION

In conclusion, Expired Betamethasone drug proved to be a highly effective corrosion inhibitor for copper in an H_2SO_4 solution, ranking among the best inhibitors in the literature. It demonstrated an impressive inhibitory capability, exceeding 96%, in both experimental and predictive calculations.

The adsorption behavior of this inhibitor on copper in a sulfuric acid solution was investigated using Langmuir and Frumkin adsorption isotherms, along with the consideration of Gibbs' free energy. The negative ΔG_{ads} indicates spontaneous adsorption, suggesting a physical adsorption mechanism on the copper surface.

Our corrosion inhibition efficiency (IE) model, developed through response surface methodology (RSM), exhibited an excellent fit, with Q^2 values exceeding 0.989, indicating exceptional model performance. Additionally, the utilization of R^2 statistics, appropriate precision, and diagnostic plots served as pivotal measures to validate the accuracy and comprehensiveness of the IE models.

5. ACKNOWLEDGMENTS

6. REFERENCES

1. Zhao Y, Wu Z, Di Carlo F, Li H, Qian B, Feng Z. Enhancing the Electrical and Mechanical Properties of Copper by Introducing Nanocarbon Derived from Polydopamine Coating. Journal of Alloys and Compounds. 2019; 78:288–293. Available from: <URL>

2. Lee S.K, Hsu H.C, Tuan W.H. Oxidation behavior of copper at a temperature below 300C and the methodology for passivation. Materials Research. 2016;19:51-56. Available from: <URL>

3. Dwivedi A. Bharti P, Shukla S. Surface assimilation and corrosion inhibition characteristic of water-soluble Polyvinyl Alcohol on mild steel surface in 0.5M HCl solution. Journal of the Turkish Chemical Society Section A: Chemistry. 2021; 8(1): 217-228. Available from: <URL>

4. Dwivedi A, Bharti P, Shukla S. K. An Overview of the Polymeric Materials that can be Used to Prevent Metal Corrosion: A Review. Journal of the Turkish Chemical Society Section A: Chemistry. 2021; 8(3): 863-872. Available from: <URL>

5. Hong S, Chen W, Zhang Y, Li M, Li N. Investigation of the inhibition effect of trithiocyanuric acid on corrosion of copper in 3.0 wt. % NaCl. Corrosion Science. 2013;66:308–314. Available from: <URL>

6. Attar T, Benchadli A, Choukchou-Braham E. Inhibition of corrosion of copper by polyvinylpyrrolidone-iodine in sulfuric acid medium. Algerian Journal of Materials Chemistry. 2022;5(1):1–8. Available from: <URL>

7. Belarbi N, Dergal F, El-Haci I, Attar T et al. Gravimetric, Electrochemical, and Surface Morphological Studies of Ammodaucus Lecotrichus Essential Oil as Corrosion Inhibitor for Copper Surface in Hydrochloric Acid Medium. Analytical and Bioanalytical Electrochemistry. 2021;13(3):340-357. Available from: <URL>

8. Attar T, Nouali F, Kibou Z, Choukchou-Braham E. Corrosion inhibition, adsorption and thermodynamic properties of 2-aminopyridine derivatives on the corrosion of carbon steel in sulfuric acid solution. Journal of Chemical Sciences. 2021;133(109):1-10. Available from: <URL>

9. Quraishi M. Electrochemical and theoretical investigation of triazole derivatives on corrosion inhibition behaviour of copper in hydrochloric acid medium. Corrosion Science. 2013;70:161–169. Available from: <URL>

10. Benachour , Abderrahmane S, Athmani S, Gülfeza K. A study on the inhibition effect of expired Amoxicillin on mild steel corrosion in 1N HCl. Materials Research Express. 2019;6:4. Available from: <URL>

11. Yang L, Zhang H, Paul Fawcett J, Mikov M, Tucker I. G. Effect of bile salts on the transport of morphine-6-glucuronide in rat brain endothelial cells. Journal of Pharmaceutical Sciences. 2011;100(4):1516-24. Available from: <URL>

12. Lyon RC, Taylor JS, Porter DA, Prasanna HR and Hussain AS. Stability profiles of drug products extended beyond labeled expiration dates. Journal of Pharmaceutical Sciences. 2006; 95(7):1549-1560. Available from: <URL>

13. Duca D A, Dan M L, Vaszilcsin N. Expired Domestic Drug - Paracetamol - as Corrosion Inhibitor for Carbon Steel in Acid Media. Materials Science and Engineering: A. 2018; 416 : 012043. Available from: <URL>

14. Singh A, Pramanik T, Kumar A, Gupta, Phenobarbital M. A new and effective corrosion inhibitor for mild steel in 1 M HCl solution. Asian Journal of Chemistry. 2013;25:9808–9812. Available from: <URL>

15. Akpan IA, Offiong NO. Amodiaquine drug as a corrosion inhibitor for mild steel in 0.1M HCl solution. Chemistry of Metals Alloys.2014;7:149–153. Available from: <URL>

16. Rotaru I, Varvara S, Gaina L, Muresan L M. Antibacterial drugs as corrosion inhibitors for bronze surfaces in acidic solutions. Applied Surface Science. 2014;321:188–196. Available from: <URL>

17. Fouda AS, Rashwan SM, Kamel MM. Tenormin drug as save corrosion inhibitor for 304 stainless steel in hydrochloric acid solutions. Der Pharma Chemica. 2015;7:22–33. Available from: <URL>

18. Kumar A, Bashir S. Ethambutol: A new and effective corrosion inhibitor of mild steel in acidic medium. Russian Journal of Applied Chemistry. 2016;89:1158–1163. Available from: <URL>

19. Fouda AS, Elewady GY, Abdallah YM, Hussien GM. Anticorrosion potential of salazopyrin drug for copper in nitric acid solution. Research Journal of Pharmaceutical Biological and Chemical Sciences. 2016; 7:267–281. Available from: <URL>

20. Karthik G, Sundaravadivelu M. Studies on the inhibition of mild steel corrosion in hydrochloric acid solution by atenolol drug. Egyptian Journal of Petroleum. 2016;25:183–191. Available from: <URL>

21. Khan M. Z. H, Aziz M. A, Hasan M. R, Al-Mamun M. R. The role of drug as corrosion inhibitor for mild steel surface characterization by SEM, AFM, and FTIR. Anti-Corrosion Methods and Materials. 2016;63:308–315. Available from: <URL>

22. Gece G, Bilgiç S. A quantum chemical insight into corrosion inhibition effects of moxifloxacin and betamethasone drugs. International Journal of Corrosion and Scale Inhibition. 2018;7:25. Available from: <URL>

23. Yavari Z, Darijani M, Dehdab M. Comparative theoretical and experimental studies on corrosion inhibition of aluminum in acidic media by the antibiotics drugs. Iranian Journal of Science and Technology, Transaction A: Science. 2018;42:1957–1967. Available from: <URL>

24. Fajobi MA, Fayomi OSI, Akande IG, Odunlami OA. Inhibitive performance of ibuprofen drug on mild steel in 0.5 M of H2SO4 acid. Journal of Bio- and Tribo-Corrosion. 2019; 5:79. Available from: <URL>

25. Hebbar N, Praveen B. M, Prasanna B. M, Deepa A. Electrochemical and adsorption studies of telmisartan for mild steel in acidic medium. Journal of Bio- and Tribo-Corrosion. 2019; 5:40. Available from: <URL>

26. Aldana-González J, Espinoza-Vázquez A, Romero-Romo M, Uruchurtu-Chavarin J, Palomar-Pardavé M. Electrochemical evaluation of cephalothin as corrosion inhibitor for API 5L X52 steel immersed in an acid medium. Arabian Journal of Chemistry. 2019;12:3244–3253. Available from: <URL>

27. Abdallah M, Gad EAM, Sobhi M, Al-Fahemi JH, Alfakeer MM. Performance of tramadol drug as a safe inhibitor for aluminum corrosion in 1.0 M HCl solution and understanding mechanism of inhibition using DFT. Egyptian Journal of Petroleum. 2019;28:173–181. Available from: <URL>

28. El-Haddad MN, Fouda AS, Hassan AF. Data from chemical, electrochemical and quantum chemical studies for interaction between Cephapirin drug as an eco-friendly corrosion inhibitor and carbon steel surface in acidic medium. Chemical Data Collections. 2019; 22:100251. Available from: <URL>

29. Feng L. Two novel drugs as bio-functional inhibitors for copper performing excellent anticorrosion and antibacterial properties. Colloids and Surfaces B: Biointerfaces. 2020;190:110898. Available from: <URL>

30. Iroha NB, Ukpe RA. Investigation of the inhibition of the corrosion of carbon steel in solution of HCl by glimepiride. Communication in Physical Sciences. 2020;5:246–256. Available from: <URL>

31. Maduelosi NJ, Iroha NB. Insight into the adsorption and inhibitive effect of spironolactone drug on C38 carbon steel corrosion in hydrochloric acid environment. Journal of Bio- and Tribo-Corrosion. 2021;7:6. Available from: <URL>

32. Benchadli A, Attar T, Choukchou-Braham E. Inhibition of Carbon Steel Corrosion in Perchloric Acid Solution by Povidone Iodine. Physical Chemistry Research. 2019;7(4):837-848. Available from: <URL>

33. Emrani V, Zandi M, Asadollahzadeh H. The Inhibitory Effect of Amoxicillin on Aluminum Corrosion in a Gel Electrolyte. International Journal of Electrochemical Science. 2022;17:2. Available from: <URL>

34. Alamry KA, Khan A, Aslam J, Hussein MA, Aslam R. Corrosion inhibition of mild steel in hydrochloric acid solution by the expired Ampicillin drug. Scientific Reports. 2023;13(1):6724. Available from: <URL>

35. Benchadli A, Mellal T, Attar T, Dali Youcef B, Choukchou-Braham E. Optimization of Inhibition Efficiencies Process of Polyvinylpyrrolidone using Response Surface Methodology. Revista Mexicana de Física. 2022;68(4):1-11. Available from: <URL>

36. Attar T, Benchadli A, Mellal T. Application of polyvinylpyrrolidone-iodine complex as a corrosion inhibitor for carbon steel using experimental design method. Algerian Journal of Engineering and Technolog. 2022;6(1):14-18. Available from: <URL>

37. Haladu SA, Mu'azu ND, Ali SA, Elsharif AM, Odewunmi NA, Abd El-Lateef HM. Inhibition of mild steel corrosion in 1 M H2SO4 by a gemini surfactant 1, 6-hexyldiyl-bis-(dimethyldodecylammonium bromide): ANN, RSM predictive modeling, quantum chemical and MD simulation studies. Journal of Molecular Liquids. .2022;350:118533. Available from: <URL>

38. Kumari P, Lavanya M. Optimization of inhibition efficiency of a schiff base on mild steel in acid medium: electrochemical and RSM approach. Journal of Bio- and Tribo-Corrosion. 2021;7(3):110. Available from: <URL>

39. Saikia T, Mahto V. Experimental investigations and optimizations of rheological behavior of drilling fluids using RSM and CCD for gas hydrate-bearing formation. Arabian Journal for Science and Engineering. 2018; 43(11):6541–6554. Available from: <URL>

40. Attar T, Larabi L, Harek Y. The Inhibition effect of potassium iodide on the corrosion of pure iron in sulfuric acid. Advances in Chemistry. 2014; 2014:1-5. Available from: <URL>

41. Benchadli A, Attar T, Messaoudi B, Choukchou-Braham E. Polyvinylpyrrolidone as a Corrosion Inhibitor for Carbon Steel in a Perchloric Acid Solution: Effect of Structural Size. Hungarian Journal of Industry and Chemistry. 2021;49(1):59-69. Available from: <URL>

42. Ogunleye OO, Arinkoola AO, Eletta OA, Agbede OO, Osho YA, Morakinyo AF, Hamed JO. Green corrosion inhibition and adsorption characteristics of Luffa cylindrica leaf extract on mild steel in hydrochloric acid environment. Heliyon. 2020 Jan 17;6(1):e03205. Available from: <URL>

43. Nwabanne J.T, Okafor V.N. Adsorption and thermodynamics study of the inhibition of corrosion of mild steel in H2SO4 medium using Vernonia amygdalina. Journal of Minerals and Materials Characterization and Engineering. 2012;11:885-890. Available from: <URL>

44. Alinnor I.J, Ejikeme P.M. Corrosion inhibition of aluminum in acidic medium by different extracts of Ocimum gratissimum. Journal of the American Chemical Society. 2012; 2:122-135. Available from: <URL>

45. Ebenso E.E, Alamu H, Umoren S.A, Obot I.B. Inhibition of mild steel corrosion in sulphuric acid using alizarin yellow dye and synergistic iodide additive. International Journal of Electrochemical Science. 2008;3(12):1325-1339.

46. Chauhan L.R, Gunasekaran G. Corrosion inhibition of mild steel by plant extract in dilute HCl medium. Corrosion Science.2007;49:1143-1161. Available from: <URL>

47. Attar T, Benkhaled A, Benchadli A, Choukchou-Braham E. Etude de l'inhibition de la corrosion de l'acier au carbone en milieu sulfurique par polyéthylène glycol. Rev mater énerg renouv. 2022;6(1):1-7. Available from: <URL>

48. Akinbulumo OA, Odejobi OJ, Odekanle EL. Thermodynamics and adsorption study of the corrosion inhibition of mild steel by Euphorbia heterophylla L. extract in 1.5 M HCl. Results in Materials. 2020;5: 100074. Available from: <URL>

49. Attar T, Benchadli A, Messaoudi B, Benhadria N. Experimental and Theoretical Studies of Eosin Y Dye as Corrosion Inhibitors for Carbon Steel in Perchloric Acid Solution. Bulletin of Chemical Reaction Engineering & Catalysis. 2020,15(2):454-464. Available from: <URL>

50. Attar T, Messaoudi B, Benchadli A, Choukchou-Braham E. Experimental and theoretical studies of polyvinylpyrrol-idone-iodine on carbon steel corrosion in 1M hydrochloric solution. Revue Roumaine de Chimie. 2021;66(8-9):761–770. Available from: <URL>

51. Attar T, Benchadli A, Messaoudi B, Choukchou-Braham E. Corrosion Inhibition, Adsorption and Thermodynamic Properties of Poly (Sodium 4-Styrenesulfonate) on Carbon Steel in Phosphoric Acid Medium. French-Ukrainian Journal of Chemistry. 2022;10(1):70-83. Available from: <URL>

52. Benchadli A, T. Attar, Choukchou-Braham E. Corrosion inhibition of carbon steel (XC 38) in hydrochloric acid by potassium iodide. The Journal of Applied Research on Science and Technology. 2018;(5):834-844. Available from: <URL>

53. Attar T, Benchadli A, Messaoudi B, Choukchou-Braham E. Corrosion inhibition efficiency, experimental and quantum chemical studies of neutral red dye for carbon steel in perchloric acidic media. Chemistry & Chemical Technology. 2022;(16):440-447. Available from: <URL>

54. Salam KK, Agarry SE, Arinkoola AO, Shoremekun IO. Optimization of operating conditions affecting microbiologically influenced corrosion of mild steel exposed to crude oil environments using response surface methodology. Biotechnology Journal International. 2015;7(2):68–78. Available from: <URL>

55. Dwivedi A, Bharti PK, Shukla SK. Interaction of water soluble polyacrylic acid with mild steel / hydrochloric acid interface. In: International Conference on Contemporary Research in Mechanical Engineering with focus on Materi-als and Manufacturing. Lucknow--India: IOP Conference Series: Materials Science and Engineering; 2018. p. 1–11. Available from: <URL>

56. Attar T, Benchadli A, Mellal T, Dali Youcef B, Choukchou-Braham E. Use of Experimental Designs to Evaluate the Influence of Methyl Green Dye as a Corrosion Inhibitor for Carbon Steel in Perchloric Acid. Malaysian Journal of Chemistry. 2021;(23):60-69. Available from: <URL>

57. Ahmadi S, Khormali A, Meerovich Khoutoriansky F. Optimization of the demulsification of water-in-heavy crude oil emulsions using response surface methodology. Fuel. 2022;323:124270. Available from: <URL>

58. Karimifard S, Alavi Moghaddam MR. Application of response surface methodology in physicochemical removal of dyes from wastewater: a critical review. Science of the Total Environment. 2018;640:772–797. Available from: <URL>

59. Antony J. A systematic methodology for design of experiments. Design of experiments for engineers and scientists, 2nd edn. Elsevier, Netherlands, 2014; 33–50. Available from: <URL>

Sustainable Synthesis of Green Cu₂O Nanoparticles using Avocado Peel Extract as Biowaste Source

Fatih ÖZBAŞ[1] (iD)

[1]Fatih Sultan Mehmet Vakif University, Research Center for the Conservation of Cultural Property of Foundation, 34083, Istanbul, Türkiye

Abstract: In recent years, there has been a significant shift towards the production of advanced nanomaterials using sustainable methods, reflecting a heightened focus on reducing environmental impact and optimizing resource utilization. This growing interest stems from the necessity to address environmental concerns and embrace eco-friendly practices in material synthesis. The primary objective of this study is to explore the eco-friendly synthesis of novel metal oxide nanoparticles (NPs) by utilizing bio-waste as a sustainable precursor. The central theme revolves around employing ultrasound-assisted techniques for Cu₂O NP synthesis, with a specific emphasis on utilizing avocado peel waste as an effective phytochemical compound for capping. Through systematic process optimization, we conducted a comprehensive assessment of the resulting NPs, delving into their chemical, thermal, and surface properties. Advanced characterization techniques, including X-ray Diffraction analysis (XRD), Transmission Electron Microscopy (TEM), Thermogravimetric Analysis (TGA), Differential Scanning Calorimetry (DSC), and Fourier-transform Infrared Spectroscopy (FT-IR), were employed to gain profound insights into the attributes of the synthesized NPs. Our experimental results conclusively demonstrate the successful synthesis of spherical Cu₂O NPs, each with a diameter of 25 ± 2 nm. This was achieved by utilizing avocado peel waste (APW) and ultrasound-assisted cavitation at room temperature. The study significantly contributes to our understanding of the potential applications of green synthesis methods, paving the way for environmentally friendly and cost-effective Cu₂O NPs.

1. INTRODUCTION

Nanotechnology encompasses diverse fields, including health, optics, energy, electronics, mechanics, and the environment, where advanced nanosized materials are meticulously crafted and efficiently utilized. It involves the intricate design, fabrication, and application of nanomaterials, encompassing their physical, chemical, and mechanical properties, as well as the complex relationships between these dimensions (1,2)

When managed with a sustainable approach, nanotechnology holds the potential to introduce unique innovations and solutions across various industrial sectors, such as advanced batteries (3), nanomedicines (4), and nano-adsorbents (5), alongside advancements in

technology. Current studies in nanotechnology have gained significant momentum, especially with the adoption of green approaches in the production of various nanoparticles (NPs) with a diameter of less than 100 nm and a large surface area (6,7). These approaches aim to minimize environmental impacts and promote sustainable manufacturing processes. To achieve this goal, the utilization of materials obtained from natural sources, such as sustainable and environmentally sensitive biopolymers, plant extracts, bio-wastes, and recyclable materials, has taken center stage. Biowastes, being biodegradable and environmentally sustainable residues, are noteworthy for their antimicrobial, antioxidant, and other properties, making them ideal for diverse applications in NP production, providing an environmentally friendly option for industrial use.

The distinctive features of bio-based metal/metal oxide NPs and their potential in various industrial applications have sparked a rapid growth in interest in these materials (8–10). Due to their numerous surface areas and high reactivity, these NPs are well-suited for use in sensor and catalytic applications (11). Additionally, the distinct optical and electrical characteristics of metal NPs promote their utilization in various fields, such as power generation applications. Applications for these NPs are diverse and include energy storage and conversion systems, as well as medicine delivery systems. Furthermore, due to their magnetic characteristics, metal/metal oxide NPs can be applied in medical imaging applications.

Several reports have been published on green nanomaterials composed of various nanostructures, including kiwifruit (12), *Corylus colurna* extract (13), agro-biomass wheatgrass extract (14), and MXene (15) based Cu_2O NPs. In 2021, Al-Hakkani *et al.* developed C@Cu_2O@Cu nanocomposites utilizing *Vicia faba* seeds aqueous extract as a mediator (16). In another study, Ramesh *et al.* investigated the development of novel antibacterial Cu_2O NPs utilizing *Manihot esculenta* leaf extract (17). However, there is a paucity of research focused on developing different strategies to overcome the recognized challenges associated with using avocado waste to synthesize nanostructures at low temperatures. In the pursuit of this study's objectives, our focus was directed towards the environmentally friendly synthesis of innovative metal oxide NPs derived from bio-waste. Our primary objective centered on employing ultrasound-assisted techniques for synthesizing Cu_2O NPs, with a particular emphasis on leveraging avocado peel wastes as phytochemical compounds to serve as effective capping agents. Through rigorous process optimization, we systematically assessed and characterized the chemical,

thermal, and surface properties of the resulting NPs, employing techniques such as X-ray Diffraction analysis (XRD), Transmission Electron Microscopy (TEM), Thermogravimetric Analysis (TGA), Differential Scanning Calorimetry (DSC), and Fourier-transform Infrared Spectroscopy (FT-IR). This comprehensive examination provided a profound understanding of both the surface, thermal, and chemical attributes of the synthesized NPs. Experimental findings conclusively demon-strated the attainability of synthesizing Cu_2O NPs with a spherical morphology and a diameter of less than 50 nm from avocado peel waste, utilizing ultrasound-assisted cavitation at room temperature. The overarching goal of this study was to advance our comprehension of the potential applications of green synthesis methods in the fabrication of green and low-cost Cu_2O NPs.

2. EXPERIMENTAL SECTION

2.1. Materials
Avocados (*Persea americana*) were purchased from a local market in Istanbul, Türkiye. The avocado pulp (APW) exhibited a nutritional composition, with approximately 66% carbohydrates, 5% lipids, 4% proteins, and an estimated 25% of dietary fiber. High-quality copper (II) chloride (anhydrous, purity 99.995%) was purchased from Sigma Aldrich Company in Germany, while ethanol (purity ≥99.5%) and sodium hydroxide (NaOH) were purchased from Merck Company (Germany). To ensure sample purity, all specimens underwent filtration using sterile syringe filters with 0.45 and 0.22-micron retention. It is noteworthy that all chemicals and reagents were employed without the need for additional purification steps.

2.2. Sustainable fabrication of avocado peel extract-based Cu_2O nanoparticles
Utilizing an environmentally friendly and straightforward sonochemical irradiation technique, copper(I) oxide nanoparticles (Cu_2O NPs) derived from avocado peel extract (APE) were intricately synthesized. The initial phase encompassed the meticulous purification of raw avocado peel, ensuring the elimination of impurities through successive washes with distilled water and absolute ethanol, followed by gentle drying at 80 °C. To obtain APE, 40 g of avocado peel in 100 mL ethanol-water (v/v 1/9) underwent sonication at an amplitude frequency of 40% and 37 °C for 30 minutes. Simultaneously, a solution comprising 5 g of $CuCl_2$ in 250 mL distilled water, and another solution containing 0.84 g of NaOH in 50 mL distilled water, were meticulously prepared at 25 °C. The controlled addition of the $CuCl_2$ solution to the APE solution, along with the introduction of 1 mL of NaOH

solution, marked the subsequent stages. The resulting mixture, i.e., the APE/CuCl$_2$ solution, underwent a 20-minute ultrasonication process at an amplitude frequency of 40%. The resultant solution underwent filtration through sterile syringe filters with retention sizes of 0.22 and 0.45 microns. The finalized APE-Cu$_2$O NPs were securely stored in a light-shielded environment at 25 °C for future utilization.

2.3. Characterization Part

The avocado peel extract (APE) and APE-based Cu$_2$O nanoparticles (NPs) underwent comprehensive characterization, employing various techniques to investigate their chemical, thermal, and surface properties. High-Resolution Transmission Electron Microscopy (HRTEM) was performed using a Hitachi HighTech HT7700 model in high vacuum mode at 100 kV. Fourier Transform Infrared (FTIR) Spectroscopy was conducted using a Jasco 6800 model in the frequency range of 4000–400 cm^{-1} wavenumber, with a resolution of 4 cm^{-1} and 64 scans. X-ray diffraction (XRD) analysis utilized Cu Kα radiation at 45 kV and 40 mA, with the Highscore Plus XRD software employed for data interpretation. Additionally, thermogravimetric analysis (TGA) and differential scanning calorimetry (DSC) were carried out using TA Instruments Discovery SDT 650,

featuring a heating rate of 10 °C/min and a flow rate of 100 mL/min, ranging from 20 °C to 900 °C under a nitrogen atmosphere.

The crystalline size of the NPs can be determined using the Debye Scherrer equation (13),

$$D = 0.89\,\lambda / B \cos\theta \qquad \text{(Eq. 1)}$$

where D is the crystalline size, K is the Scherrer constant (0.98), λ is the wavelength (1.54), and β is the full width at half maximum (FWHM).

3. RESULTS AND DISCUSSION

To investigate the chemical, thermal, and surface properties of the APE and APE-based Cu$_2$O NPs, a thorough characterization process utilizing a variety of techniques was conducted. Their structural characteristics were thoroughly revealed by HRTEM. Utilizing FTIR Spectroscopy, their chemical property and functional groups were examined. The APE-based Cu$_2$O NPs were provided information about their crystalline structure and size by XRD technique. Furthermore, their thermal behavior was examined using DSC and TGA techniques.
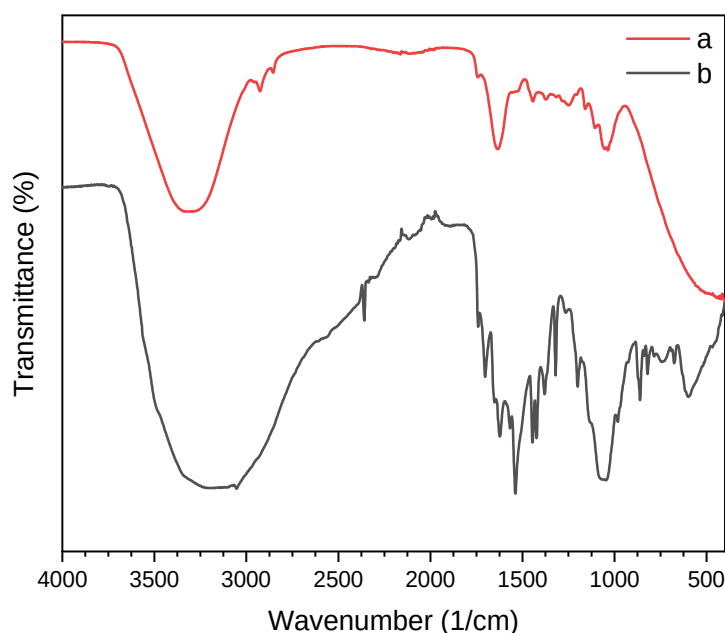
Figure 1: FTIR spectra of (a) APE, and (b) APE-based Cu$_2$O NPs.

The distinctive absorption peaks collectively yielded valuable insights into the molecular composition of both

APE and APE-based Cu$_2$O NPs. The comparative analysis facilitated a comprehensive understanding of the

nanostructure's composition and crystalline nature, enabling the evaluation of changes in functional groups. Figure 1 presents the FTIR spectra, detailing the functional groups and crystalline characteristics of APE (a) and APE-based Cu_2O NPs (b). Upon scrutinizing the FTIR graph of APE (Fig. 1.a), distinct absorption peaks indicative of various functional groups emerged. The region spanning 3345-3268 cm^{-1} featured stretching vibrations of hydroxyl (-OH) and amino (-NH) groups. The peak at 2929 cm^{-1} corresponded to the asymmetric stretching of CH bonds, while the one at 2855 cm^{-1} was attributed to the symmetric stretching of CH bonds. Notably, the absorption band at 1743 cm^{-1} signified the ester C=O group), and at 1635 cm^{-1}, the presence of CN stretching was evident. Additional peaks at 1538 cm^{-1} (-NH), 1443 cm^{-1} (C-H bending), and 1372 cm^{-1} (C-H bending) further characterized the molecular structure. The bands at 1248 cm^{-1}, 1159 cm^{-1}, 1105 cm^{-1}, and 1050 cm^{-1} were attributed to the C–O extension of the ester group within the triglyceride molecule (18,19). The FTIR spectra of the APE-based Cu_2O NPs revealed the O–H stretching mode of alcohols and phenols at 3500–3375 cm^{-1}, along with the C–H stretching of alkyl groups at 1623 cm^{-1}. These observations provide compelling evidence that alcohols, alkyl groups, and phenols remain unbounded during the production of APE-based Cu_2O NPs. Specifically, on Cu_2O NPs, peaks at 1423, 1380, and 1320 cm^{-1} indicated a reduction in the N=O bending vibration of nitro compounds, the C-N stretch of aromatic amines, and the C–C stretch (in-ring) of aromatics. After the sonochemical method, new peaks at 785 and 743 cm^{-1} were observed, indicating the presence of C–Cl alkyl halides. Additionally, a peak at 676 cm^{-1} denoted the C–H bend of alkanes, and a peak at 599 cm^{-1} represented the C–I stretch in aliphatic iodo compounds. These bio-waste not only served as capping agents but also bonded to the Cu_2O NPs. The absence of peaks at 1543 and 2929 cm^{-1}, coupled with the emergence of new peaks at 1066 cm^{-1}, suggested that the formation of Cu_2O NPs had induced structural alterations. The C–H stretching of alkyl groups, the C–N stretch of aliphatic amines, the N–H bending vibration of nitro compounds, and the C–OH of carboxylic acids were identified as the causes of these modifications. The prepared Cu_2O NPs were formed, as indicated by the appearance of new peaks at 820 cm^{-1} and the presence of additional peaks at 468 cm^{-1} (20).
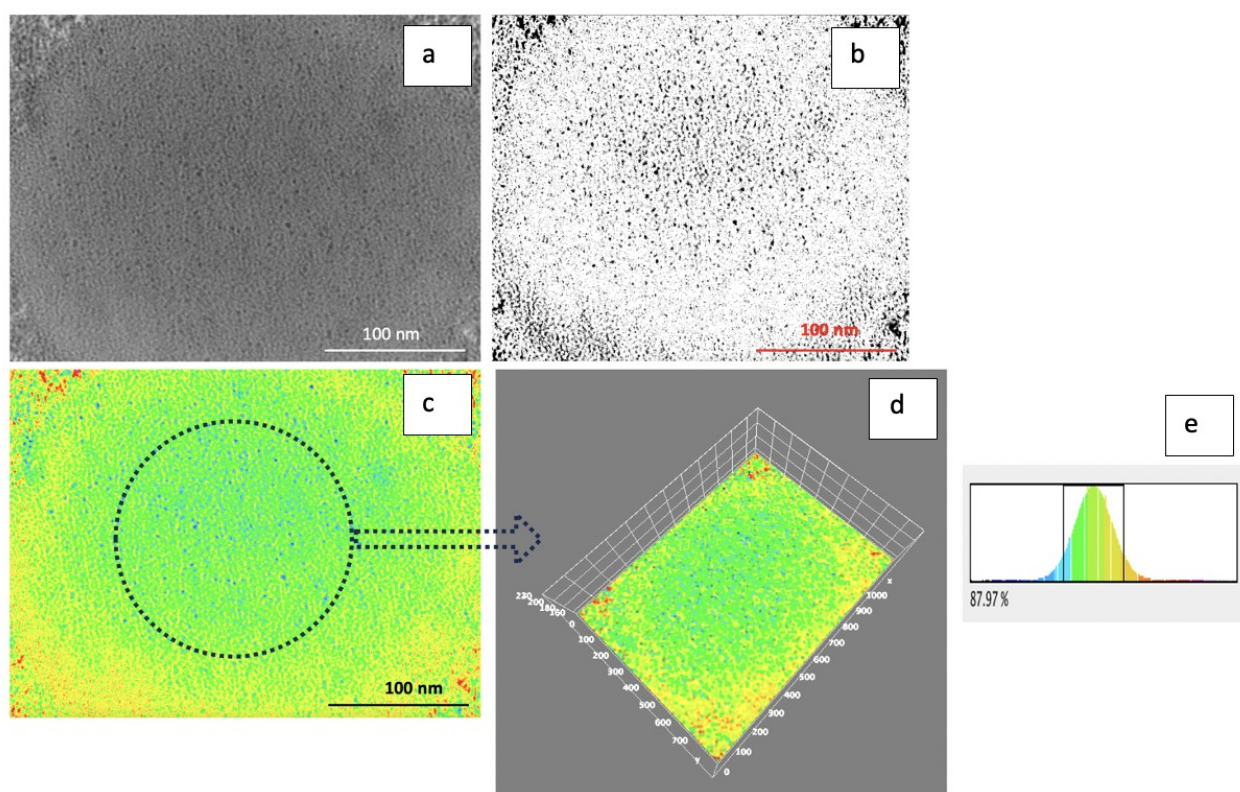

Figure 2: (a) HRTEM, (b) AI-assisted HRTEM image using threshold mode, (c) AI-assisted HRTEM image of the prepared APE-based Cu_2O NPs using RGB color mode, (d) 3D surface plot of AI-assisted HRTEM image of the prepared APE-based Cu_2O NPs, and (e) color distribution graph with the range of white and black.

Figure 2 illustrates various analyses of the prepared APE-based Cu_2O NPs, including (a) HRTEM, (b) AI-assisted HRTEM image using threshold mode, (c) AI-assisted HRTEM image using RGB color mode, (d) 3D surface plot of AI-assisted HRTEM image, and (e) color distribution graph. The TEM image in Figure 2a provided insight into the spherical morphology of APE-based Cu_2O NPs, exhibiting sizes within the range of 25 ± 2 nm. This depiction offered a detailed view of the well-dispersed particles, showcasing their uniform distribution. The integration of artificial intelligence (AI) into image processing has transformed tasks like recognition, localization, segmentation, classification, representation, interpretation, and restoration within the TEM field, as widely acknowledged. In a previous study, detailed in a study by Zheng *et al.* study (21), the synergy of AI and TEM analysis was explored, focusing on color imaging of nanoparticles with nano-sized diameters, particularly employing red-green-blue (RGB) color analysis. This approach has proven to be an efficient and cost-effective means to elucidate the morphological properties of nanostructures and enhance surface analysis.

In the investigation, a comprehensive surface characterization of the APE-based Cu_2O NPs (depicted in black color) below 20 nm was delved into, drawing insights from AI-supported TEM images (Figure 2b). The color analysis, emphasizing tones and intensities, served as a powerful tool for elucidating nanostructure properties by accentuating particle distributions. Our study employed AI-assisted RGB color analysis to unveil the spectrum of color tones (green for matrix-blue for APE-based Cu_2O NPs) within the depicted nanostructure, seamlessly integrating with TEM results (Figure 2c). This was three-dimensionally visualized in Figure 2d-e, where each pixel was represented through the combination of red, green, and blue in the RGB color model. The AI-assisted distribution analysis not only shed light on the image's overall brightness, contrast, and tonal range but also revealed a uniform distribution, particularly emphasizing, blue-based colors. Significantly, the distribution of the APE-based Cu_2O NPs was ascertained by evaluating the combined intensities of the three primary colors, prominently featuring 87.97% blue color. This finding underscored the homogeneous distribution of nanoparticles within the biomatrix, vividly illustrated by the green color representation. The application of a 3D distribution to the APE-based Cu_2O NPs, conducted in 8-bit/RGB mode using the combined intensities of the three primary colors, distinctly highlighted the prevailing blue color.
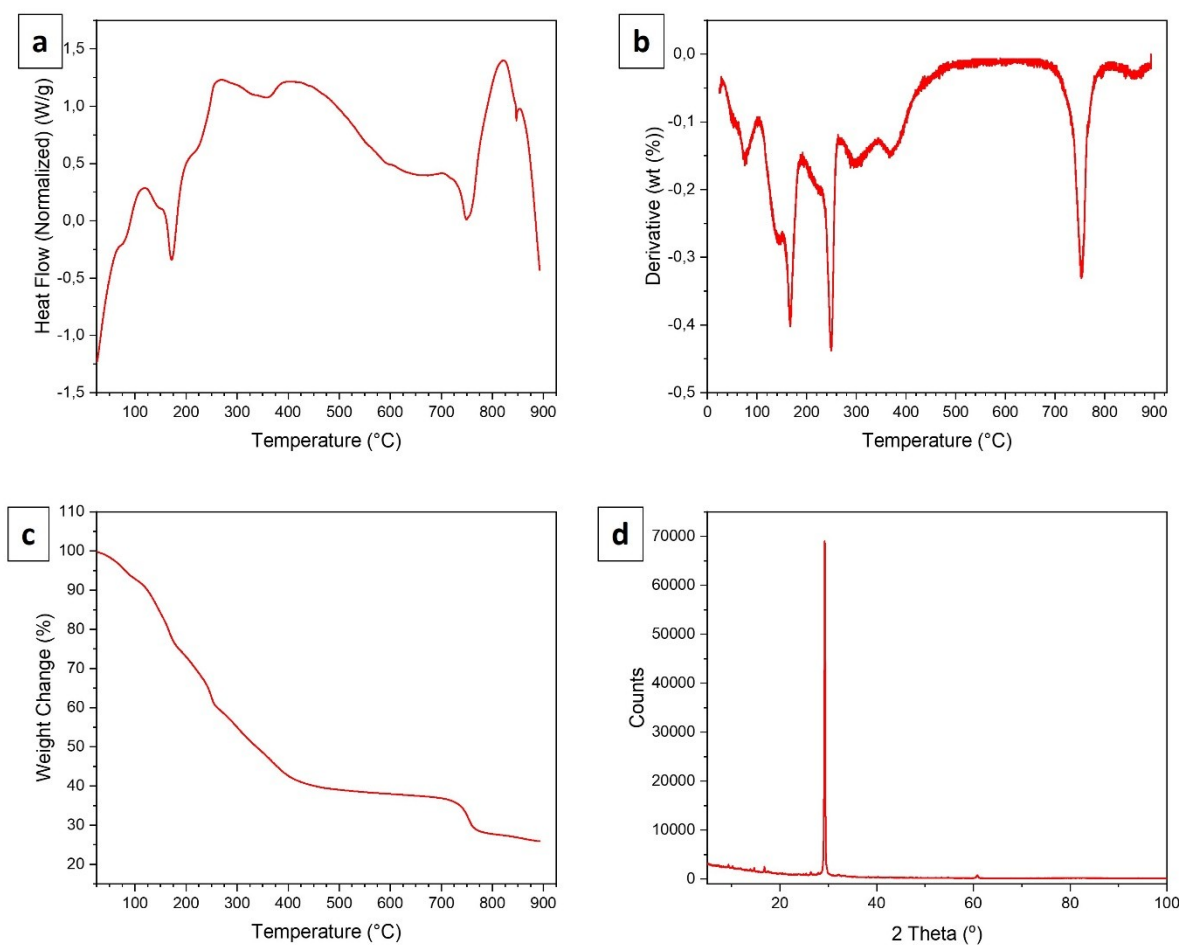
Figure 3: (a) DSC, (b) DTA (c) TGA, and (d) XRD of the prepared APE-based Cu_2O NPs.

Thermal characterization techniques, including DSC, DTA, and TGA, were used to characterize the thermal properties of the APE-based Cu_2O NPs. Figure 3a-c presents all the experimental findings. The exothermic peak of the prepared APE-based Cu_2O NPs was given in Figure 3a at 726.62 °C. A calculation of the heat produced 289.81 J/g. Using the TGA technique, the thermal stability of the prepared APE-based Cu_2O NPs was examined. TGA and DTA curves for the APE-based Cu_2O NPs were shown in Figure 3b-c, and they covered a temperature range of 20 °C to 900 °C. Furthermore, the TGA result indicated three-stage decompositions, which is corroborated by the DTA diagram that was produced, which also has three decomposition phases. With losses of roughly 27.22%, 35.97%, and 10.94%, respectively, the TGA graph of the APE-based Cu_2O NPs showed three distinct stages of decomposition: 20 °C-201 °C (evaporation of water molecules and volatile components), 201 °C-702 °C (breaking down of crosslinking and chains), and 702 °C-897 °C (phase transformation of Cu_2O NPs) (13).

As seen in Figure 3d, the XRD pattern of the prepared APE-based Cu_2O NPs showed discrete diffraction peaks at 29.28°, 35.45°, 40.25°, and 60.82°, which corresponded to the (110), (111), (200), and (220) planes of cuprite, respectively (22). These results, in line with the JCPDS Card number 05-0667, clearly show that the prepared APE-based Cu_2O NPs were successfully formed. Utilizing Debye-Scherrer's formula (Equation 1) to derive the FWHM of the most intense peak at 29.28°, we calculated the average crystalline size of the APE-based Cu_2O NPs. The calculated average crystalline size was determined to be 17 nm. Impressively, the crystal size determined by the XRD models exhibited remarkable consistency and compatibility, aligning well with the data extracted from the TEM images of the prepared APE-based Cu_2O Nps.

In Figure 4 the schematic diagram of the experimental procedure of the prepared APE-based Cu_2O NPs was given. As a result, the synthesis of nanoparticles by the

sonochemical method involves an effective and innovative approach. This method is based on the principle of creating high-intensity ultrasonic vibrations in the solution. The characterization results of the obtained nanoparticles show that the rapid synthesis process facilitates the creation of nanoparticles with nanosize and homogeneous distribution. This study represents an environmentally friendly and sustainable sono-synthesis method in the production of Cu_2O nanostructures, without the need for high temperatures or harmful chemicals. This approach plays an important role in the field of nanotechnology by making nanoparticle synthesis processes more effective, faster, and environmentally friendly.
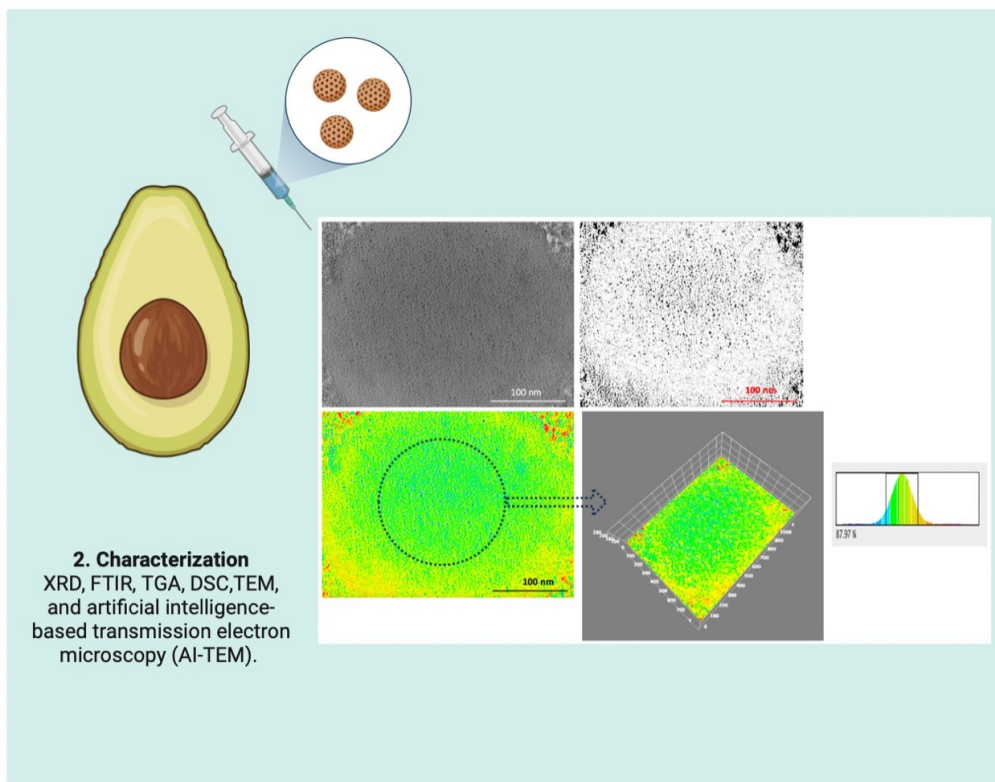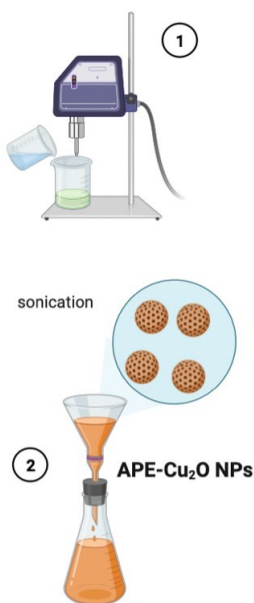
Figure 4: The schematic diagram of the experimental procedure of the prepared APE-based Cu_2O NPs.

Table 1 provides a comprehensive overview of recent progress in a variety of environmentally friendly Cu-based nanostructures, emphasizing advancements in their synthesis and applications. The literature consistently supports the notion that these green nanosystems, comprising green nanostructures, exhibit superior biological and surface efficacies compared to conventional materials, particularly in biomedical applications.

Table 1: Current developments in various green Cu-based nanostructures.

Sample	Characterization	References
Banana pulp extract-based Cu_2O NPs	cubic and octahedral shapes	(23)
Gum-mediated CuO NPs	average crystallite size about 12.91 nm, agglomerated and spherical.	(24)
Poly(butylene adipate-co-terephthalate (PBAT) containing CuO NPs	$30 - 50$ nm and spherical.	(25)
Tree gum extract-CuO NPs	needle-like structures	(26)
Xanthan gum-CuO NPs	100 to 750 nm and spherical.	(27)
Sunflower petal extract-CuO NPs	46 nm.	(28)
APE-based Cu_2O NPs	Particle size: a diameter of 25 ± 2 nm shape: spherical	This study

4. CONCLUSION

In recent years, a notable paradigm shift towards the sustainable production of advanced nanomaterials has emerged, reflecting a heightened emphasis on reducing environmental impact and optimizing resource utilization. This evolving interest is grounded in the imperative to address environmental concerns and adopt eco-friendly practices in material synthesis. The primary aim of this study is to explore the eco-friendly synthesis of novel APE-based Cu_2O NPs by harnessing bio-waste as a sustainable precursor. Our research primarily centers on employing ultrasound-assisted techniques for synthesizing Cu_2O NPs, with a particular emphasis on leveraging APW as a highly effective phytochemical compound for capping. Through systematic process optimization, we conducted a thorough assessment of the resulting NPs, scrutinizing their chemical, thermal, and surface properties. Advanced characterization techniques, including XRD, TEM, AI-supported TEM, TGA, DSC, and FT-IR, were employed to gain profound insights into the attributes of the synthesized NPs. Our experimental results conclusively demonstrate the successful synthesis of spherical APE-based Cu_2O NPs, each with a diameter of 25 ± 2 nm, achieved through the utilization of APW and ultrasound-assisted cavitation at room temperature. This study significantly contributes to our understanding of the potential applications of green synthesis methods, paving the way for environmentally friendly and cost-effective Cu_2O Nps.

5. CONFLICT OF INTEREST

The authors have no conflicts of interest regarding this investigation.

6. ACKNOWLEDGMENTS

7. REFERENCES

1. Kumar V, Kaushik NK, Tiwari SK, Singh D, Singh B. Green synthesis of iron nanoparticles: Sources and multifarious biotechnological applications. International Journal of Biological Macromolecules. 2023 Dec 31;253:127017. Available from: <URL>.

2. Hussain A, Lakhan MN, Hanan A, Soomro IA, Ahmed M, Bibi F, et al. Recent progress on green synthesis of selenium nanoparticles – a review. Materials Today Sustainability. 2023 Sep 1;23:100420. Available from: <URL>.

3. Nshizirungu T, Rana M, Khan MIH, Jo YT, Park JH. Innovative green approach for recovering Co2O3 nanoparticles and Li2CO3 from spent lithium-ion batteries. Journal of Hazardous Materials Advances. 2023 Feb 1;9:100242. Available from: <URL>.

4. Liu S, Xu X, Ye J, Wang J, Wang Q, Liu Z, et al. Metal-coordinated nanodrugs based on natural products for cancer theranostics. Chemical Engineering Journal. 2023 Jan 15;456:140892. Available from: <URL>.

5. Sharma A, Kumar N, Mudhoo A, Garg VK. Phytobiomass-based nanoadsorbents for sequestration of aquatic emerging contaminants: An Overview. Journal of Environmental Chemical Engineering. 2023 Apr 1;11(2):109506. Available from: <URL>.

6. Jena A, Dube D, Mishra S, Kumar Sahoo P, Kumar Sahoo N. Removal of europium by green tea mediated zero valent iron nanoparticles. Materials Today Proceedings [Internet]. 2023 Oct 31 [cited 2023 Nov 12]; Available from: <URL>.

7. Nguyen NTH, Tran GT, Nguyen NTT, Nguyen TTT, Nguyen DTC, Tran T Van. A critical review on the biosynthesis, properties, applications and future outlook of green MnO2 nanoparticles. Environmental Research. 2023 Aug 15;231:116262. Available from: <URL>.

8. Balu S kumar, Andra S, Jeevanandam J, Kulabhusan PK, Khamari A, Vedarathinam V, et al. Exploring the potential of metal oxide nanoparticles as fungicides and plant nutrient boosters. Crop Protection. 2023 Dec 1;174:106398. Available from: <URL>.

9. Kim JW, Aruchamy G, Kim BK. Recent advances in single-entity electrochemistry for metal nanoparticle, nanodroplet, and bio-entity analysis. TrAC Trends in Analytical Chemistry. 2023 Dec 1;169:117358. Available from: <URL>.

10. Hosseinzadeh E, Foroumadi A, Firoozpour L. What is the role of phytochemical compounds as capping agents for the inhibition of aggregation in the green synthesis of metal oxide nanoparticles? A DFT molecular level response. Inorganic Chemistry Communications. 2023 Jan 1;147:110243. Available from: <URL>.

11. Ally N, Gumbi B. A review on metal nanoparticles as nano-sensors for environmental detection of emerging contaminants. Materials Today: Proceedings. 2023 Aug 8; Available from: <URL>.

12. Kodasi B, Kamble RR, Manjanna J, Hoolageri SR, Bheemayya L, Nadoni VB, et al. Adept green synthesis of Cu2O nanoparticles using Kiwi fruit (Actinidia deliciosa) juice and Studies on their cytotoxic activity and antimicrobial evaluation. Journal of Trace Elements and Minerals. 2023 Mar 1;3:100044. Available from: <URL>.

13. Karakuş S, Özbaş F, Baytemir G, Taşaltın N. Cubic-shaped corylus colurna extract coated Cu2O nanoparticles-based smartphone biosensor for the detection of ascorbic acid in real food samples. Food Chemistry. 2023 Aug 15;417:135918. Available from: <URL>.

14. Madhuri Peddada L, Phyu Cho P, Dulgaj S, Annapragada R, Raja Kanuparthy P. Facile synthesis of green engineered CuO/Cu2O-C nano heterostructures with the controlled Cu2O content for the photodegradation of crystal violet. Results in Optics. 2023 Dec 1;13:100537. Available from: <URL>.

15. Qiao Y, Xie W, Yu F, Yu J, Yao P, Fan Z, et al. High-performance flexible energy storage: Decorating wrinkled MXene with in situ grown Cu2O nanoparticles. Journal of Alloys and Compounds. 2023 Dec 15;968:171921. Available from: <URL>.

16. Al-Hakkani MF, Hassan SHA, Saddik MS, El-Mokhtar MA, Al-Shelkamy SA. Bioengineering, characterization, and biological activities of C@Cu2O@Cu nanocomposite based-mediated the Vicia faba seeds aqueous extract. Journal of Materials Research and Technology. 2021 Sep 1;14:1998–2016. Available from: <URL>.

17. Ramesh C, HariPrasad M, Ragunathan V. Antibacterial Behaviour of Cu2O Nanoparticles Against Escherichia coli; Reactivity of Fehling's Solution on Manihot esculenta Leaf Extract. Curr Nanosci. 2011 Oct 1;7(5):770–5. Available from: <URL>.

18. Sotelo-Mazon O, Valdez S, Porcayo-Calderon J, Casales-Diaz M, Henao J, Salinas-Solano G, et al. Corrosion protection of 1018 carbon steel using an avocado oil-based inhibitor. Green Chemistry Letters and Reviews. 2019 Jul 3;12(3):255–70. Available from: <URL>.

19. Putra RS, Amri RY, Ayu M. Turbidity removal of synthetic wastewater using biocoagulants based on protein and tannin. AIP Conference Proceedings. 040028. Available from: <URL>.

20. Chinnaiah K, Maik V, Kannan K, Potemkin V, Grishina M, Gohulkumar M, et al. Experimental and Theoretical Studies of Green Synthesized Cu2O Nanoparticles Using Datura Metel L. Journal of Fluorescence. 2022 Mar 8;32(2):559–68. Available from: <URL>.

21. Zheng H, Lu X, He K. In situ transmission electron microscopy and artificial intelligence enabled data analytics for energy materials. Journal of Energy Chemistry. 2022 May;68:454–93. Available from: <URL>.

22. Du BD, Phu D Van, Quoc LA, Hien NQ. Synthesis and Investigation of Antimicrobial Activity of Cu $_2$ O Nanoparticles/Zeolite. Journal of Nanoparticles. 2017 Jan 9;2017:1–6. Available from: <URL>.

23. Muthukumaran M, Dhinagaran G, Venkatachalam K, Sagadevan S, Gunasekaran S, Podder J, et al. Green synthesis of cuprous oxide nanoparticles for environmental remediation and enhanced visible-light photocatalytic activity. Optik. 2020 Jul;214:164849. Available from: <URL>.

24. Nithiyavathi R, John Sundaram S, Theophil Anand G, Raj Kumar D, Dhayal Raj A, Al Farraj DA, et al. Gum mediated synthesis and characterization of CuO nanoparticles towards infectious disease-causing antimicrobial resistance microbial

pathogens. Journal of Infection and Public Health. 2021 Dec;14(12):1893–902. Available from: <URL>.

25. Hasanin MS, Youssef AM. Ecofriendly bioactive film doped CuO nanoparticles based biopolymers and reinforced by enzymatically modified nanocellulose fibers for active packaging applications. Food Packag Shelf Life. 2022 Dec;34:100979. Available from: <URL>.

26. Ramalechume C, Shamili P, Krishnaveni R, Andrew Swamidoss CM. Synthesis of copper oxide nanoparticles using tree gum extract, its spectral characterization, and a study of its anti- bactericidal properties. Material Today: Proceedings. 2020;33:4151–5. Available from: <URL>.

27. Ponmani S, William JKM, Samuel R, Nagarajan R, Sangwai JS. Formation and characterization of thermal and electrical properties of CuO and ZnO nanofluids in xanthan gum. Colloids and Surfaces A: Physicochemical and Engineering Aspects. 2014 Feb;443:37–43. Available from: <URL>.

28. Khoshsang H, Abbasi K, Ghaffarinejad A. Biosynthesis of ZnO and CuO nanoparticles using sunflower petal extract. Inorg Chem Commun. 2023 Sep;155:111083. Available from: <URL>.

Studies of the Properties of New Electrospun Based on PVA-PEG Polymer Systems Electrolytes for Energy Storage Devices

Rahmat Gul Khattak[1]* iD **, Wan Ahmad Kamil Mahmood[1]**

[1]University Sains Malaysia, School of Chemical Sciences, Pulau Penang, 11800, Malaysia.

Abstract: Solid polymer electrolytes (SPEs) have been considerably investigated due to various electrochemical device applications. Most of the SPEs comprise polymer as a host material to provide strength and good mechanical stability and salt that transfers charge carriers to cause conductivity. Nanocomposite solid polymer electrolyte membranes based on poly(vinyl alcohol) (PVA)-poly(ethylene glycol) (PEG) blend complexed with $LiClO_4$ and nanofillers Al_2O_3 at different weight percent ratios have been obtained by using electrospinning method. The conductivity and structural properties of the different systems have been characterized by using various experimental approaches such as X-ray diffraction (XRD) and Fourier transform infrared FTIR spectroscopy. The ionic conductivity of the systems has been measured by using an LCR meter in a temperature ranging from 298 to 353 K. Maximum ionic conductivity of 1.58×10^{-4} S cm^{-1} at room temperature has been observed for the system of PVA-PEG-$LiClO_4$-Al_2O_3 (50-25-15-10) with 15 wt% weight percent of $LiClO_4$ salt in PVA-PEG blend matrix. The ac conductivity report indicates that the ionic conductivity of the PVA-PEG-$LiClO_4$-Al_2O_3 complex is influenced by the concentration of $LiClO_4$. The effect of temperature on the ionic conductivity of polymer electrolyte complexes has been estimated by changing the temperature ranging from 298 to 353 K. However, the conductivity of the nanofiber polymer electrolyte systems increases with the rise of temperature, and the maximum conductivity of 1.58×10^{-2} S cm^{-1} has been recorded at 353 K. The temperature-dependent conductivity follows the Arrhenius behavior.

1. INTRODUCTION

Solid polymer electrolytes (SPEs) possessing high ionic conductivity have been a subject of considerable attention in recent years because of their wide potential applications in various electrochemical devices such as solid-state rechargeable batteries, chemical sensors, fuel cells, super-capacitors, computers, electrochromic display devices, smart windows and other portable electrochemical devices applications (1-4). These polymer electrolytes have become prominent materials because they can satisfy several requirements due to their special properties including lightweight, high ionic conductivity, good electrode-electrolyte contact, excellent electrochemical stability, flexibility, good mechanical properties, and easy mouldability (5-6). The low cost of SPEs and

their easy processibility make them a promising candidate for a wide variety of applications. However, the low ionic conductivity of the polymer-based materials at room temperature has limited their applications in electrochemical devices. The major efforts in this field have been focused on developing new advanced materials based on polymers having high ionic conductivity values with high mechanical, thermal, and electrochemical stability (7-9). Various experimental techniques, such as copolymerization, plasticization, blending, and addition of ceramic fillers have been used to enhance the ionic conductivity values of the SPEs. It has been shown that the ionic conductivity of the aforementioned polymer-based materials can be increased by the addition of a plasticizer into the polymer matrix due to an increase in the amorphous region (6, 10-15). Though the addition of plasticizers

in the SPEs has caused a significant decrease in crystallinity and thus improved ionic conductivity, the increase of ionic conductivity by the addition of plasticizers has not been acceptable for use in various electrochemical devices. Among the above-mentioned routes, polymer blending is one of the most significant and useful tools for the development of new advanced polymer-based materials with improved high ionic conductivity values and mechanical stability. The significant advantages of the polymer blend systems are ease of preparation and control of physical properties by compositional variations that are superior as compared to the properties of each component polymer (16, 17). Materials with a wide variety of important and useful properties can be designed by using this technique (18). To become mechanically stable thin membranes, complexation formation by dispersion of metal oxides fillers such as Al_2O_3, ZnO, SiO_2, and TiO_2 to the aforesaid materials have become popular recently, as the obtained materials containing metal oxides attain high ionic conductivity value approaching that of liquid electrolytes along with improved stability (19-21). It is noted that the addition of metal oxide fillers not only improves the mechanical stability of the electrolyte membranes but also causes high ionic conductivity. Thus, the incorporation of inorganic metal oxide fillers into the SPEs would be very useful and significant. Various SPEs based on polymer blend matrixes containing inorganic salts and metal oxides have been proposed, but only very little work has been done and a limited number of literature is available on current research interest (22, 23).

An attempt has been made in the present research work to develop, nanofiber composite polymer blend electrolyte thin films based on polyvinyl alcohol and polyethylene glycol complexed with $LiClO_4$ and dispersed with Al_2O_3 nanofillers, which have been prepared by electrospinning technique and the results are discussed. These polymeric systems have been selected and studied because both the above-mentioned polymers are separately reported to complex formations with salts and metal oxides which are highly amorphous. In addition, the above-mentioned polymers possess properties to form good miscible blends (24). The search for Li^+ ion-containing nanofiber SPE membranes can be attractive because of their low cost, ease of fabrication, and application as thin film membranes. Based on properties like high ionic conductivity, and good thermal and electrochemical stabilities, composite polymer electrolytes containing metal oxides have become popular and attained greater importance over conventional polymer electrolytes. Comparative research studies of the structural, and electrical characteristics of the electrolyte systems have been carried out employing conductivity measurement and XRD, FTIR analysis. Thus in the present research, the effect of $LiClO_4$ salt and metal oxide on the ionic conductivity of the system has been investigated through the above-mentioned techniques. The influence of temperature variation on the ionic conductivity of the polymer electrolyte systems has been discussed.

2. EXPERIMENTAL SECTION

2.1. Preparation
Polyvinyl alcohol (PVA) (Mw = 5×10^5, Sigma Aldrich) and polyethylene glycol (PEG) (Mw = 6×10^3, Sigma Aldrich) were vacuum dried at 50°C for 12 hours before use. An equal amount of PVA and PEG (16 wt% weight percent) by weight have been dissolved in doubly distilled water and then stirred for 12 hours at room temperature until the homogeneous solution of polymers is obtained after the complete dissolution of the polymer. 16 wt% weight percent solution of varying content (wt%) of PVA and PEG have been mixed to obtain a uniformly blended solution. The required quantity (5, 10, 15, 20 wt%) of $LiClO_4$ is further added to the polymeric solution with uninterrupted steady stirring for about 12 hours. The concentrations of Al_2O_3 in the solutions are 0, 5, 10, and 15 wt% based on the weight of PVA. The subsequent homogeneous polymeric solutions are degassed for 20 minutes to obtain the bubble-free transparent solution. The nanofibrous membranes are obtained by the ordinary electrospinning technique at room temperature. The electrospinning system practiced in this research study to prepare nanofiber polymer electrolyte membranes consisted of a syringe and needle (ID = 0.35 mm), a syringe pump, a ground electrode, and a huge voltage supply. A stainless steel needle (24 G, outer diameter: 0.50 mm, inner diameter: 0.35 mm) is associated with an electrode of a high voltage power supply (Spellman, model CZE1000R) which could set up voltages up to 30 kV. Appropriate quantity of polymer blend solutions are electrospun at room temperature adapting a syringe withdrawal pump (New Era Pump Systems Inc., Model NE-300) with a stainless steel needle. The electrospun fibers in the form of untwisted membranes have been accumulated on a grounded, polished stainless steel sheet wrapped with a thin aluminum foil, where the ground collector plate and the spinneret needle tip distance have been fixed at 10 cm. Electrospinning of the homogeneous solutions of different samples is accomplished at a flow rate of 3 mL/hour with a huge voltage of 20 kV at room temperature. The polymer blend membrane thickness has been precisely and thoroughly controlled during electrospinning. The electrospun nanofibrous membranes are then accumulated on the collector plate. Electrospun nanofibrous membranes are collected and desiccated at room temperature for 12 hours to inhibit the contraction of fibers and then finally dried under vacuum at 50 °C for 24 hours before further use. After complete drying, the films were peeled off from the aluminum and kept in vacuum desiccators before use.

3. RESULTS AND DISCUSSION

3.1. Conductivity Analysis
The ionic conductivity of the electrospun nanofiber polymer blend electrolyte systems has been studied by a. c. conductivity analysis from 298 to 353 K. Fig. 1 shows the variation of ionic conductivity as a function of inverse temperature for the electrospun nanofiber composite polymer blend electrolyte systems prepared by electrospinning technique and

containing various concentrations of LiClO$_4$ salt and aluminum oxide filler. Similar linear relationships can be seen in all complex polymer electrolyte system curves at all temperatures and this means that there is no phase transition occurs in the polymer blend matrix by the incorporation of lithium salt in the temperature range studied. The variation of ionic conductivity with temperature has been examined to follow Arrhenius-type behavior described by the relation

$$\sigma = \sigma_\circ \exp(-E_a/KT)$$

where $\sigma_\circ$ is the pre-exponential factor while E_a, K, and T are the activation energy, Boltzmann constant, and absolute temperature, respectively.

The ionic conductivity results indicate that the conductivity of all the systems increases with a step

up in temperature. The reason may be because, with the rise in the temperature of the samples, the motion of the polymer chain improved, thereby increasing in fraction of free volume in the polymer systems due to the expansion of the polymer. The increase in free volume results in improved translational motion of ions and segmental mobility of polymers. Thus starts easy movement of charge carriers into the available free volume that will cause enhanced conductivity. The polymer segmental motion contributes a pathway for ion transportation. Hence, the ionic mobility in the polymer electrolytes may be due to the mobility of ions between different sites and polymeric segmental motion, which causes improved ionic conductivity of the systems. Therefore the resulting ionic conductivity can be expressed by the around mobility of ion and polymer segmental motion.
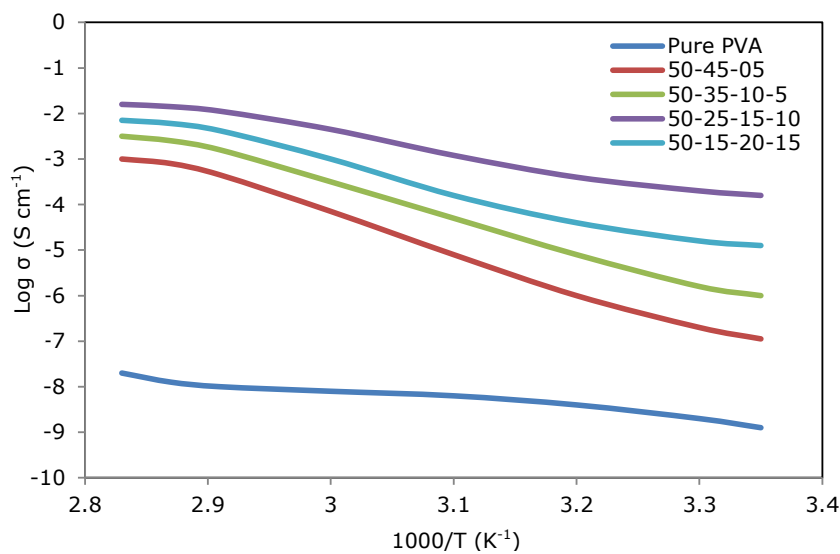
Figure 1: Arrhenius plot of log conductivity versus reciprocal temperature for PVA-PEG-LiClO$_4$-Al$_2$O$_3$ Polymer electrolyte complexes.

The activation energy (E_a) values of electrospun nanofiber-based polymer electrolytes systems containing various concentrations of LiClO$_4$ salt and Al$_2$O$_3$ filler have been obtained from the slopes of log σ versus 1/T plots at common temperature by using the Arrhenius relation and are presented in Table 1. From the table, it can be noted that E_a values markdown with the increase in the concentration of

LiClO$_4$ salt up to 15 wt% beyond which it exhibits an increase, whereas ionic conductivity values increase up to 15 wt% beyond which these values decrease due to high activation energy. The variation in the ionic conductivity and E_a values of polymer electrolyte films can be elucidated on the basis that the nano-fibrous membranes may be a hybrid association of amorphous and crystalline zones.

Table 1: Activation energies (E_a) of pure PVA and PVA-based nanofiber composite polymer electrolyte films.

Polymer electrolyte	Activation energy (eV)
Pure PVA	0.60
PVA-PEG-LiClO$_4$-Al$_2$O$_3$ (50-45-05-0)	0.49
PVA-PEG-LiClO$_4$-Al$_2$O$_3$ (50-35-10-05)	0.42
PVA-PEG-LiClO$_4$-Al$_2$O$_3$ (50-25-15-10)	0.39
PVA-PEG-LiClO$_4$-Al$_2$O$_3$ (50-15-20-15)	0.43

Fig. 2 shows the ionic conductivity values of electrospun nanofiber polymer-based electrolyte systems (PVA-PEG-LiClO$_4$-Al$_2$O$_3$) as a function of LiClO$_4$ salt concentration 0, 5, 10, and 20 wt% in the temperature range 298-353 K. Ionic conductivity of electrospun nanofiber polymer-based electrolyte

systems increases with increasing salt concentration up to 15 wt%, but any further incorporation of the salt beyond 15 wt% causes decrease in ionic conductivity. It can be noted that at lower concentrations of LiClO$_4$ salt, the ionic conductivity steps up initially with an increase in salt

concentration while at higher salt concentrations, the conductivity declines. The high value of ionic conductivity at low salt concentrations may be due to the buildup of charge carriers while at higher salt concentrations, the lower value of ionic conductivity may be due to the reason of ion pairs effect and ion aggregations which may influence the overall mobility of ions by the retarding effect and the

number of effective charge carriers (25). The maximum ionic conductivity of 1.58×10^{-4} S cm^{-1} has been obtained for the nanofiber polymer blend electrolyte system PVA-PEG-LiClO$_4$-Al$_2$O$_3$ (50-25-15-10) containing 15 wt% LiClO$_4$ salt at 298 K. The eminent value of ionic conductivity in an electrolyte may be due to improved ionic mobility and high concentration of ionic charge carrier.
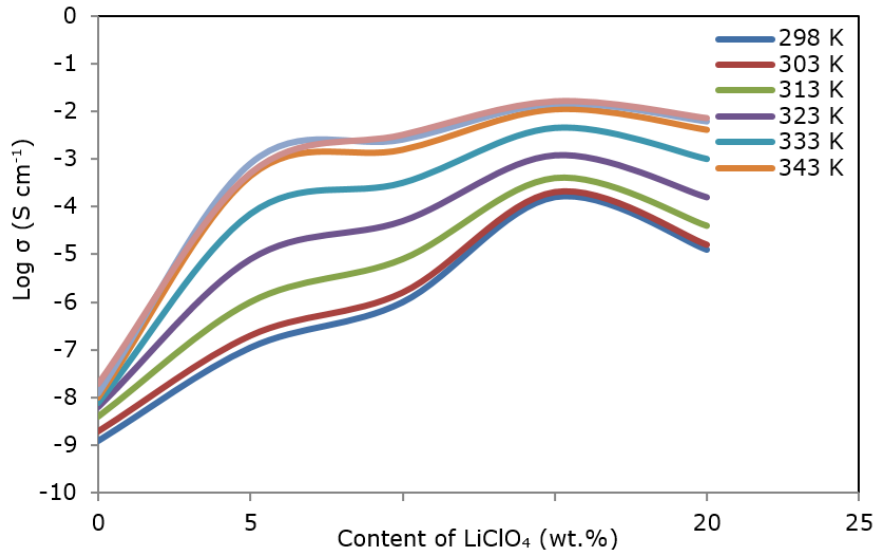
Figure 2: Plot of log conductivity vs. composition of PVA-PEG-LiClO$_4$-Al$_2$O$_3$ at various temperatures.

3.2. XRD Analysis
Fig. 3 illustrates the XRD patterns of pristine materials PVA, LiClO$_4$ salt together with that of pure PVA-PEG polymer blend (50-50) weight percent ratio. The figure also displays the XRD pattern of electrospun composite polymer electrolyte systems (PVA-PEG-LiClO$_4$-Al$_2$O$_3$) containing various concentrations of LiClO$_4$ salt and nanoparticles of aluminum oxide (Al$_2$O$_3$) in the complex polymer matrix. XRD pattern of pure PVA film shows a characteristic peak at $2\theta = 19.6°$ (curve a) which indicates its semicrystalline nature (12, 26, 27). When the two-component polymers are added to form a blend (50-50 ratio), a relatively less intense broad amorphous peak at $2\theta = 17.6°$ and $33.8°$ (curve b) is observed indicating interaction amongst component polymers of blend leading to the occurrence of the observed peak which different from its any component polymers. Therefore, the appearance of broad amorphous peaks around 17.6° and 33.8° can be attributed to the development of polymer blend. The occurrence of the less intense peak at a lower 2θ value can also indicate the compatibility of PEG with PVA which makes it an acceptable plasticizer for PVA (28, 29). A broad amorphous peak centered at $2\theta = 18.5°$ can be observed in the PVA-PEG film containing 5 wt% LiClO$_4$ salt (curve c).

However, no such peak appears in the PVA-PEG-LiClO$_4$-Al$_2$O$_3$ films containing a higher concentration of LiClO$_4$ salt (curve d-f) which indicates an increase in the complexation between polymer matrix and salt (30, 31). The absence of a peak corresponding to LiClO$_4$ salt shows the thorough dissolution of salt in the polymer complexes. When LiClO$_4$ is added to the PVA-PEG-Al$_2$O$_3$ blend electrolyte to form a complex system, the observed peaks corresponding to the salt appear to decrease, signifying an increase in the amorphous nature of membranes due to complexation between polymer blend matrix and salt (curve d-f). The decrease in the peaks and shift in 2θ values indicates interaction among various components leading to the development of the PVA-LiClO$_4$ complex. A new peak has appeared at $2\theta = 45°$, $50.4°$ and $75.1°$ for polymer electrolyte films (PVA-PEG-LiClO$_4$-Al$_2$O$_3$) containing 10, 15, and 20 wt% of LiClO$_4$ salt (curve d-f), which may be due to the interaction of LiClO$_4$ salt and aluminum oxide fillers with the polymer matrix. This indicates the structural changes of the polymer electrolyte systems by the addition of aluminum oxide fillers and LiClO$_4$ salt. It is obvious from Fig. 3 that the amorphicity is retained at lower concentrations of LiClO$_4$ salt while at higher concentrations of salt, the amorphicity of the complex is found to decrease, which may be the basis for the decreased conductivity of the films containing higher than 15 wt% concentration of LiClO$_4$ salt.
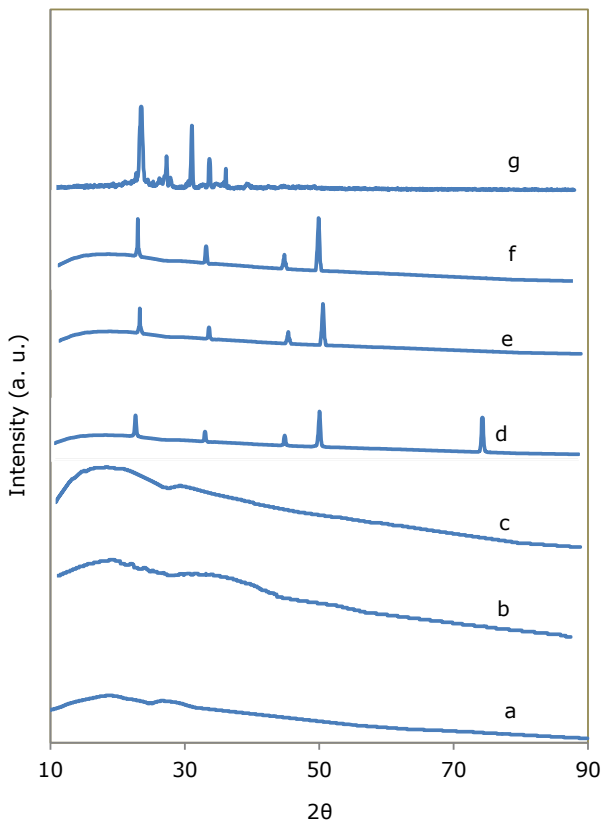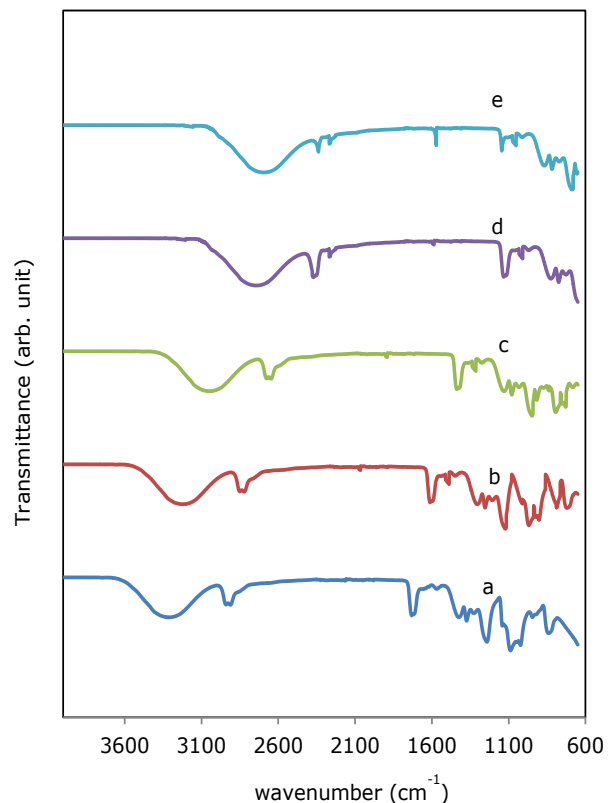
Figure 3: X-ray diffraction spectrum of (a) Pure PVA (b) PVA-PEG (50-50) (c) PVA-PEG-LiClO$_4$-Al$_2$O$_3$ (50-45-05-0) (d) PVA-PEG-LiClO$_4$-Al$_2$O$_3$ (50-35-10-05) (e) PVA-PEG-LiClO$_4$-Al$_2$O$_3$ (50-25-15-10) (f) PVA-PEG-LiClO$_4$-Al$_2$O$_3$ (50-15-20-15) (g) pure LiClO$_4$

3.3. FTIR Analysis

The addition of salts and inorganic metal oxide fillers to the host polymer matrix causes interactions and complexation of the host polymer matrix. Such interactions and complexation may affect significantly the sections of polymer backbones and their flexibility. FTIR analysis studies will provide the confirmation of complexation and interactions that occur in polymer matrix after the addition of salt and metal oxide. Fig. 4(a-e) shows the FTIR spectra of pure PVA, PVA-PEG, and PVA-PEG-LiClO$_4$-Al$_2$O$_3$ complex polymer electrolyte films containing 5-20 wt% of LiClO$_4$ salt. The most significant structural changes have been noticed after incorporation of LiClO$_4$ salt and aluminum oxide nanoparticles which causes shifts in the vibrational approaches of PVA. These changes have been observed through FTIR spectra recorded in the range 650-4000 cm^{-1}. Figure 4 shows that the enlarged band in the range of 3000-3624 cm^{-1} associated with the Intermolecular hydrogen-bonded O-H stretching vibration frequency of PVA has been shifted to 2942-3517, 2778-3374, 2455-3125, and 2416-3000 cm^{-1} in the PVA-PEG-LiClO$_4$-Al$_2$O$_3$ films containing 5, 10, 15 and 20 wt% of LiClO$_4$ salt respectively. This changeover in vibration frequency may be due to the complexation of dopants with the host polymer. The peak found at 2881-2982 cm^{-1} associated with C-H stretching frequency of PVA has been displaced to 2794-2889, 2622-2733, 2317-2924, and 2320-2412 cm^{-1} in PVA-PEG-LiClO$_4$-Al$_2$O$_3$ electrolyte systems containing 5, 10, 15 and 20 wt% of LiClO$_4$ salt, respectively.

Furthermore, the peak occurred at 1758-1818 cm^{-1} associated with carbonyl stretching vibration frequency of pure PVA film and shifted to 1573-1687, 1461-1532, 1088-1117 and 1188-1235 cm^{-1} for PVA-PEG-LiClO$_4$-Al$_2$O$_3$ polymer electrolyte films containing 5, 10, 15 and 20 wt% of LiClO$_4$ salt, respectively. Similarly, frequency corresponding to C-H bending mode is found at 1568 cm^{-1} in pure PVA film and displaced to 1449, 1235, 914, and 962 cm^{-1} for PVA-PEG-LiClO$_4$-Al$_2$O$_3$ polymer electrolyte films containing 5, 10, 15 and 20 wt% of LiClO$_4$ salt, respectively. The C-O stretching and O-H bending vibrations frequency are found to be observed at 1180-1310 cm^{-1} for pure PVA film and has been displaced to 1080-1176, 930-998, 701, and 669 cm^{-1} for PVA-PEG-LiClO$_4$-Al$_2$O$_3$ films containing 5, 10, 15 and 20 wt% of LiClO$_4$ salt, respectively. It can be confirmed that there is no characteristic frequency peak corresponding to LiClO$_4$ salt found in the FTIR spectra of the polymer electrolyte systems. However, it has been noticed that vibration frequency bands either displaced or disappeared with the addition of LiClO$_4$ salt in the pure PVA film. The shifting of frequency peaks and the appearance of new peaks in the polymer electrolyte systems indicates the occurrence of interaction and complexation of LiClO$_4$ salt with the host polymer matrix in the PVA-based blend polymer electrolyte system. The characteristic vibration frequency bands of aluminum oxide nanoparticles are not observed in the spectra which may be due to the reason that the size of the particles is very small and therefore only the local structural changes may occur (32).


Figure 4: FTIR spectrum of pure PVA and PVA-PEG-LiClO$_4$-Al$_2$O$_3$ complex solid polymer electrolytes (a) Pure PVA (b) PVA-PEG-LiClO$_4$-Al$_2$O$_3$ (50-45-05-0) (c) PVA-PEG-LiClO$_4$-Al$_2$O$_3$ (50-35-10-05) (d) PVA-PEG-LiClO$_4$-Al$_2$O$_3$ (50-25-15-10)(e) PVA-PEG-LiClO$_4$-Al$_2$O$_3$ (50-15-20-15)

3.4. Scanning Electron Microscopy

The morphology of the electrospun nanofibers-based PVA-PEG blend polymer electrolyte membranes containing $LiClO_4$ salt and inorganic metal oxide (Al_2O_3) prepared with various compositional ratios wt% by weight percent have been examined by using scanning electron microscopy (SEM) and are presented in Fig. 5. SEM images reveal the influence of composition on morphology of the fibers of the membranes. It can be observed that the membranes on aluminum foil are composed of well interconnected network of interlaid, random, and ultrafine straight fibers which arises due to the operating processing parameters. SEM images also show that the electrospun membranes consist of multi-fibrous layers and fully interconnected porous fibrous structures. The exceptionally porous structure of the electrospun membranes may be due to the interlaying of the fibers. SEM micrographs indicate that the fiber morphology of the electrospun PVA-PEG blend polymer electrolyte membranes mainly depends on the number of component ratios (33). When the amount of $LiClO_4$ salt is increased,

the average spacing between the fibers is observed to decrease. It can also be noted that the cross-linking of the fibers depends on the content of lithium perchlorate. In the PVA-$LiClO_4$ sample, the highest cross-linking of the fibers has been achieved in the presence of a high concentration of salt in the polymer matrix. No phase separation can be observed in electrospun fiber polymer electrolyte membranes which indicates compatibility of PVA and PEG blend polymer. It can be observed that the surface of the fibrous membranes is partially amorphous which may be due to the amount of water that remains on the surface of membranes after electrospinning which possibly dissolves the fibers. The residual water molecules may also cause the development of a considerable number of cross-links resulting in smaller pore size (34). SEM micrographs also reveal that the diameters of the fibers are not homogeneous and uniformly distributed throughout. It can be observed that all the polymer blend electrolyte membranes show long and straight fibrous morphology.
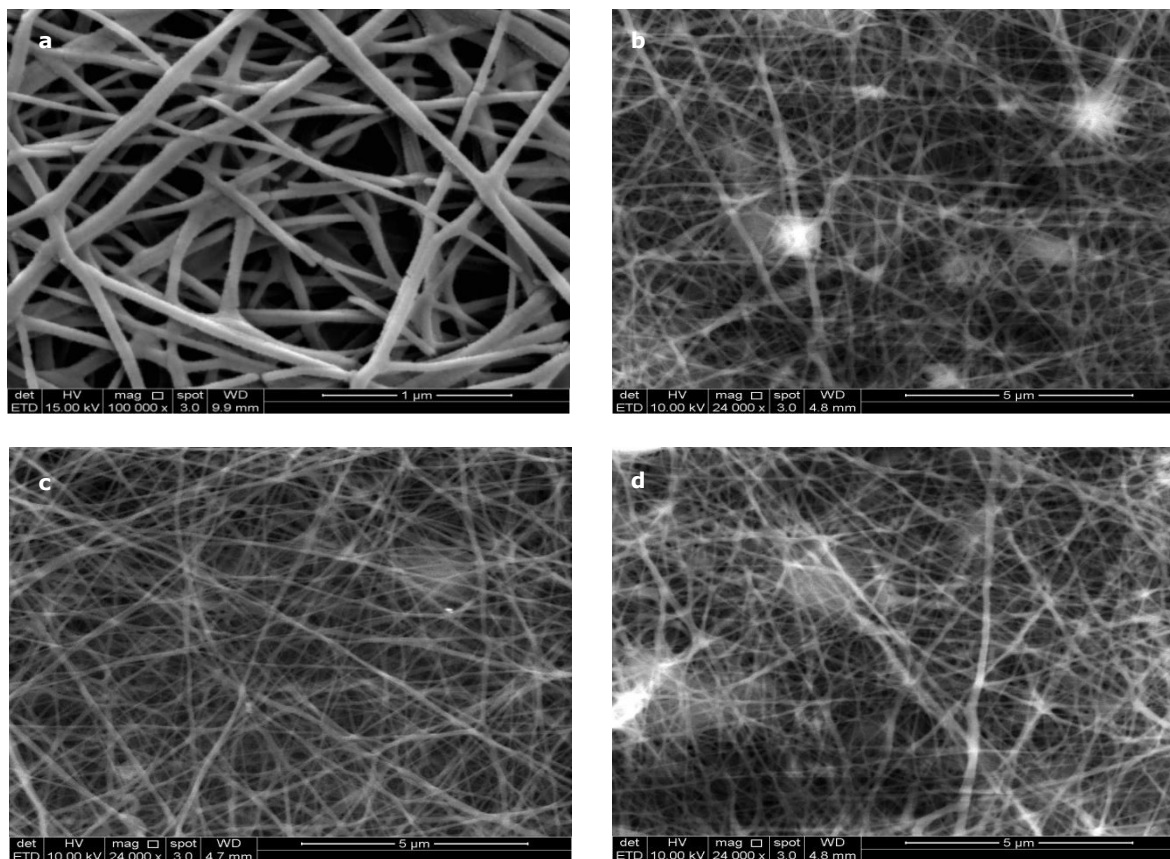
Figure 5: SEM images of (a) Pure PVA (b) PVA-PEG-$LiClO_4$-Al_2O_3 (50-35-10-05) (c) PVA-PEG-$LiClO_4$-Al_2O_3 (50-25-15-10) (d) PVA-PEG-$LiClO_4$-Al_2O_3 (50-15-20-15)

4. CONCLUSIONS

The new type of fibrous electrospun polymer blend (PVA-PEG) electrolyte systems are prepared successfully by the electrospinning technique and reported in the present research work. The highest ionic conductivity has been obtained to be $1·58 \times 10^{-4}$ S cm^{-1} at 298 K when the polymer blend is complexed with 15 wt% of lithium perchlorate. The temperature-dependent ionic conductivity of

polymer-based electrolyte systems shows the Arrhenius behavior with two distinct regions. The dependence of the ionic conductivity on temperature is found to be linear on a logarithmic scale. It follows the Arrhenius behavior of ionic conductivity. The XRD and FTIR research studies indicate the complex formation of salt with the polymer with a decrease in crystallinity upon the addition of salt and the results also indicate that the polymers are completely miscible with each other. The results based on high

ionic conductivity and low crystallinity show that electrospun PVA-PEG blend polymer electrolyte membranes (PVA-PEG-LiClO$_4$-Al$_2$O$_3$) are a possible candidate for solid-state batteries and can be used in the forthcoming imminent lithium-ion batteries.

5. CONFLICT OF INTEREST

All authors have shared in (a) planning, designing, and explanation of the data; (b) drafting of the manuscript; and (c) recommendation of the final interpretation. This article has not been submitted to, nor is it under consideration at any other journal or publishing venue.

6. ACKNOWLEDGEMENT

7. REFERENCES

1. Armand MB. Polymer Electrolytes. Annu Rev Mater Res [Internet]. 1986;16:245–61. Available from: <URL>.

2. MacCallum JR, Vincent CA. Polymer electrolytes reviews Elsevier. London; 1987.

3. Ratner MA, Shriver DF. Ion Transport in Solvent-Free Polymers. Chem Rev [Internet]. 1988;88:109–24. Available from: <URL>.

4. Bhide A, Hariharan K. Ionic transport studies on (PEO)6:NaPO3 polymer electrolyte plasticized with PEG400. Eur Polym J [Internet]. 2007 Oct 1;43(10):4253–70. Available from: <URL>.

5. Gray FM. Solid polymer electrolytes: fundamentals and technological applications [Internet]. New York, NY; 1991. Available from: <URL>.

6. Wieczorek W, Such K, Chung SH, Stevens JR. Comparison of Properties of Composite Polymeric Electrolytes Based on the Oxymethylene-Linked Poly (ethylene oxide) NaClO4 Electrolyte with Polyacrylamide or. alpha.-Al2O3 Additives. J Phys Chem [Internet]. 1994;98(36):9047–55. Available from: <URL>.

7. Linford RG. Electrochemical Science and Technology of Polymer-I. London: Elsevier; 1987.

8. Patel SK, Patel RB, Awadhia A, Chand N, Agrawal SL. Role of polyvinyl alcohol in the conductivity behaviour of polyethylene glycol-based composite gel electrolytes. Pramana [Internet]. 2007 Sep 26;69(3):467–75. Available from: <URL>.

9. Scrosati B. Applications of Electroactive Polymers. London: Chapman and Hall; 1993.

10. Gray FM. Fundamentals and technological applications. New York: VCH; 1991.

11. Sekhon SS. Conductivity behaviour of polymer gel electrolytes: Role of polymer. Bull Mater Sci [Internet]. 2003 Apr;26(3):321–8. Available from: <URL>.

12. Joykumar Singh T, Bhat SV. Morphology and conductivity studies of a new solid polymer electrolyte: (PEG)xLiClO4. Bull Mater Sci [Internet]. 2003 Dec;26(7):707–14. Available from: <URL>.

13. Wieczorek W, Such K, Florjanczyk Z, Stevens JR. Polyacrylamide based composite polymeric electrolytes. Electrochim Acta [Internet]. 1995 Oct 1;40(13–14):2417–20. Available from: <URL>.

14. Wieczorek W, Such / K, Florjanczyk Z, Stevens JR. Polyether, Polyacrylamide, L1CIO4 Composite Electrolytes with Enhanced Conductivity. J Phys Chem [Internet]. 1994;98:6840–50. Available from: <URL>.

15. Shukla PK, Agrawal SL. Effect of PVAc dispersal into PVA-NH4SCN polymer electrolyte. Ionics (Kiel) [Internet]. 2000 May;6(3–4):312–20. Available from: <URL>.

16. Rand DAJ. Battery systems for electric vehicles — a state-of-the-art review. J Power Sources [Internet]. 1979 Jan 1;4(2):101–43. Available from: <URL>.

17. Rocco AM, Pereira RP, Felisberti MI. Miscibility, crystallinity and morphological behavior of binary blends of poly(ethylene oxide) and poly(methyl vinyl ether–maleic acid). Polymer (Guildf) [Internet]. 2001 Jun 1;42(12):5199–205. Available from: <URL>.

18. Choi N-S, Lee Y-G, Park J-K, Ko J-M. Preparation and electrochemcial characteristics of plasticized polymer electrolytes based upon a P(VdF-co-HFP)/PVAc blend. Electrochim Acta [Internet]. 2001 Mar 15;46(10–11):1581–6. Available from: <URL>.

19. Hashmi SA, Thakur AK, Upadhyaya HM. Experimental studies on polyethylene oxide–NaClO4 based composite polymer electrolytes dispersed with Na2SiO3. Eur Polym J [Internet]. 1998 Sep 1;34(9):1277–82. Available from: <URL>.

20. Jaipal Reddy M, Sreekanth T, Subba Rao UV. Study of the plasticizer effect on a (PEO+NaYF4) polymer electrolyte and its use in an electrochemical cell. Solid State Ionics [Internet]. 1999 Nov 1;126(1–2):55–63. Available from: <URL>.

21. Zhang Z, Fang S. Novel network polymer electrolytes based on polysiloxane with internal plasticizer. Electrochim Acta [Internet]. 2000 Mar 1;45(13):2131–8. Available from: <URL>.

22. Pradhan DK, Samantaray BK, Choudhary RNP, Thakur AK. Effect of plasticizer on structure—property relationship in composite polymer electrolytes. J Power Sources [Internet]. 2005 Jan 4;139(1–2):384–93. Available from: <URL>.

23. Pitawala HMJC, Dissanayake MAKL, Seneviratne VA, Mellander B-E, Albinson I. Effect of plasticizers (EC or PC) on the ionic conductivity and thermal properties of the (PEO)9LiTf: Al2O3 nanocomposite polymer electrolyte system. J Solid State Electrochem [Internet]. 2008 Aug 29;12(7–8):783–9. Available from: <URL>.

24. Paul DR, Newman S. Polymer Blends [Internet]. Elsevier; 1978. Available from: <URL>.

25. MacCallum JR, Tomlin AS, Vincent CA. An investigation of the conducting species in polymer electrolytes. Eur Polym J [Internet]. 1986 Jan 1;22(10):787–91. Available from: <URL>.

26. Prajapati GK, Gupta PN. Comparative study of the electrical and dielectric properties of PVA–PEG–Al2O3–MI (M=Na, K, Ag) complex polymer electrolytes. Phys B Condens Matter [Internet]. 2011 Aug 1;406(15–16):3108–13. Available from: <URL>.

27. Agrawal SL, Awadhia A. DSC and conductivity studies on PVA based proton conducting gel electrolytes. Bull Mater Sci [Internet]. 2004 Dec;27(6):523–7. Available from: <URL>.

28. Finch CA. Polyvinyl alcohol, properties and applications. New York: Wiley & Sons; 1973.

29. Gong K-C, Shou-Cai H. Electrical Properties of Poly(Vinyl Alcohol) Complexed with Phosphoric Acid.

MRS Proc. 1988 Feb 21;135:377.

30. Bhargav PB, Mohan VM, Sharma AK, Rao VVRN. Structural and electrical studies of sodium iodide doped poly(vinyl alcohol) polymer electrolyte films for their application in electrochemical cells. Ionics (Kiel) [Internet]. 2007 Aug 2;13(3):173–8. Available from: <URL>.

31. Bhargav PB, Mohan VM, Sharma AK, Rao VVRN. Investigations on electrical properties of (PVA:NaF) polymer electrolytes for electrochemical cell applications. Curr Appl Phys [Internet]. 2009 Jan 1;9(1):165–71. Available from: <URL>.

32. Ahmad S, Bohidar HB, Ahmad S, Agnihotry SA. Role of fumed silica on ion conduction and rheology in nanocomposite polymeric electrolytes. Polymer (Guildf) [Internet]. 2006 May 3;47(10):3583–90. Available from: <URL>.

33. Min H-S, Ko J-M, Kim D-W. Preparation and characterization of porous polyacrylonitrile membranes for lithium-ion polymer batteries. J Power Sources [Internet]. 2003 Jun 1;119–121:469–72. Available from: <URL>.

34. Wu G, Yang H-Y, Chen H-Z, Yuan F, Yang L-G, Wang M, et al. Novel porous polymer electrolyte based on polyacrylonitrile. Mater Chem Phys [Internet]. 2007 Aug 15;104(2–3):284–7. Available from: <URL>.

Photo-Induced Tautomerism of Isocytosine in Aqueous Solution when Irradiated with UVC Light

Tsvetina D. Cherneva iD , **Mina M. Todorova** iD, **Rumyana I. Bakalska** iD, **Vassil B. Delchev**[*] iD

University of Plovdiv, Faculty of Chemistry, Department of Chemistry, Plovdiv, 4000, Bulgaria

Abstract: It was found that the irradiation of aqueous solution of isocytosine with UVC light provokes an oxo-hydroxy phototautomerism of the compound with a rate constant of 5.29×10^{-3} min^{-1}. It was observed a backward reaction, after removing the UV light source, with a rate constant of 0.12×10^{-3} min^{-1}. Two mechanisms of the phototautomerism were investigated at the B3LYP/aug-cc-pVDZ theoretical level in water surroundings (PCM). The first one showed a consecutive dissociation and association of a proton through conical intersections S_0/S_1 whose structures were located at the same theoretical level in the gas phase. It occurs along the $^1\pi\sigma^*$ excited-state reaction pathway. The more probable mechanism includes an excited-state H-transfer supported by a water molecule as a catalyst. It occurs along the $^1\pi\pi^*$ excited-state reaction pathway which we found over the IRC ground-state energy curve. The water molecule drastically reduces the energy barrier in the ground state as well in the excited state.

1. INTRODUCTION

Nucleobases are major chromophores in macromolecules of DNA and RNA (1-4). It is known they are photostable compounds (5-8) since they absorb and utilize the UV light as in this way they prevent the normal functioning of the nucleic acids. The high photostabiliy of pyrimidine bases leads to another question namely why their close analogues do not exhibit such features!

One analogue of nucleobase cytosine is isocytosine. The two compounds differ only by the positions of the functional groups NH$_2$ and C=O – they have exchanged positions in the two analogues. However, cytosine is known to be photostable whereas isocytosine is not (9-11).

Isocytosine is known as a "rare" nucleobase because of its very low frequency of distribution in the macromolecules of nucleic acids. Despite that there is an experimental evidence for investigations of isocytosine pairing with isoguanine in the helix of DNA (12,13). Moreover isocytosine has been tested for an application for the treatment of Alzheimer's disease (14,15).

Jeffrey has studied the crystal structure of isocytosine and has proposed the next unit cell parameters: a=8.745 Å, b=11.412 Å, c=10.414 Å, β=94.79°, with a space group P2$_1$/n and unit cell volume V=1038 A^3 for multiplicity Z=8 (16,17).

Isocytosine exists in two oxo tautomers which are available in aqueous solution (18-21). However, Vranken (22) has reported for some other tautomers which are formed when matrix isolated isocytosine is irradiated with UV light (λ_{max}=308 nm) about 45 min. The analysis of the IR spectra of the photoproducts has shown OH stretching vibrations which come from the hydroxy tautomers of isocytosine. The ratio of the concentrations of the oxo and hydroxy tautomers is [oxo]/[hydroxy] = 0.11 (23). Recently we reported on the irradiation of

acetonitrile solution of isocytosine (λ_{max}= 330 nm, for 60 min). It was established an oxo → hydroxy tautomerism (10). Unfortunately, the mechanism of this tautomeric conversion is not well documented especially when a water molecule is engaged in the excited-state proton transfer process. The role of the water molecule from the solution can be regarded as a catalyst of the photoreaction.

The tautomerism in pyrimidines has been explained by the PIDA (photo-induced dissociation association) mechanism (24,25) and it has been shown that the driven state is the repulsive $^1\pi\sigma^*$ excited state (26-28). However, when a water molecule is attached to the H-atoms which should be detached the dissociation of the proper N-H/O-H bond should occur by another mechanism, different from PIDA.

The aim of the current research is to through light upon the mechanism of the excited state proton transfer process oxo → hydroxy in isocytosine. Two mechanisms are tested – PIDA and IRC with a water molecule. The importance of the research comes from the experimental fact that pyrimidine nucleobases are photostable compounds whereas their analogues usually are not. Such research would answer partially to the question why the nature "has chosen" cytosine to be a chromophore present in nucleic acid macromolecules and not isocytsine.

2. THEORETICAL METHODS

The ground-state equilibrium geometries of several tautomers of isocytosine were optimized at the B3LYP/aug-cc-pVDZ and CC2/aug-cc-pVDZ levels in the gas phase and in water medium (only for the DFT calculations). The calculation at the DFT level involves the Becke (29) 3-parameter and Lee–Yang–Parr (30) exchange-correlation functional. The CC2 calculations are based on coupled cluster methods (31).

Subsequent frequency calculations were performed to prove that the found structures are located in minima on the corresponding PESs. No imaginary frequencies were calculated for all geometries. The equilibrium geometries were used to compute the vertical excitation energies at the TD DFT (32,33) and CC2 (31) theoretical levels.

In order to study the water assisted H-transfer we optimized, at the B3LYP/aug-cc-pVDZ and water surroundings (PCM, polarized continuum model (34)), the structures of selected H-bonded complexes of tautomers of isocytosine with one water molecule. The transition state of the intermolecular proton transfer was found with one imaginary frequency whose form describes the H-motion between the proper centres in order to form a stable H-bonded complex. Using the IRC structures standing between the initial complex and the

complex-product we followed the excited-state reaction paths of the tautomeric process.

The conical intersections S_0/S_1 connected with the elongation of the corresponding N-H and O-H bonds in the tautomers were optimized at the B3LYP/aug-cc-pVDZ level of theory in the gas phase. The structures were used for linear interpolation in internal coordinates (LIIC) with the geometries minima. The linear interpolation was performed by the equation:

$$Q_i = Q_i(I) + \varepsilon.[Q_i(F) - Q_i(I)] \qquad (1)$$

where $Q_i(I)$ is the i-th coordinate of the initial structure (tautomer – minimum); $Q_i(F)$ is the same coordinate of the final structure (conical intersection S_0/S_1 in this case); ε is the interpolation parameter, which changes in the interval 0 (initial structure) ÷ 1 (final structure). It means that the interpolation parameter ε can be treated as a reaction coordinate of the—mechanism under study. The vertical excitation energies of the structures along the reaction coordinate were computed at the TD B3LYP/aug-cc-pVDZ level in order to get the excited-state reaction paths of the H-detachment processes.

All calculations–were performed with the GAUSSIAN 16 software (35). The conical intersections S_0/S_1 were found with the GAMESS-US program (36).

3. EXPERIMENTAL METHODS

The experiment includes a preparation of aqueous solution of isocytosine (Sigma-Aldrich) with concentration 1.3×10^{-4} mol.L^{-1}. The solution was deaerated with nitrogen for 15 min to turn out of the air. After that the solution was irradiated in a standard photochemical reactor (220 cm^3) with a low pressure mercury lamp TNN 15/32 (Hanau Original) emitting light at λ_{max} = 254 nm. Samples with volume of 3 cm^3 were taken in 10 min intervals for registering of the UV absorption spectra and following the changes in the mixture in the course of the irradiation. After removing the UV light source, the changes of the reaction mixture in dark were checked out in 60 min intervals. The UV spectra were recorded on an Agilent Cary 60 UV/Vis spectrophotometer, double beam, and spectral range of 190 – 1100 nm.

4. RESULTS AND DISCUSSIONS

4.1. Ground-state equilibrium geometries and conical intersections S_0/S_1

The ground-state equilibrium geometries of isocytosine tautomers optimized in water surroundings (PCM) are illustrated in Figure 1. Two oxo-amino tautomers are included in the research – iC$_A$ and iC$_D$. The pyramidal character of the amino group of these tautomers could be estimated by the sum of the bond angles (Σ) around N$_7$ and its deviation (δ) from 360°. For oxo-amino forms iC$_A$ and

iC$_D$ the Σ values are 355.5° and 358.1°, whereas the δ quantities are 4.5° and 1.9° correspondingly. It means that the pyramidal character is more pronounced in tautomers iC$_A$. The amino group in the oxo-amino form iC$_D$ is in a greater degree conjugated with the aromatic ring. In tautomer iC$_E$ the pyramidal character of the amino group is the most pronounced: Σ = 355.1° and δ = 4.9°.
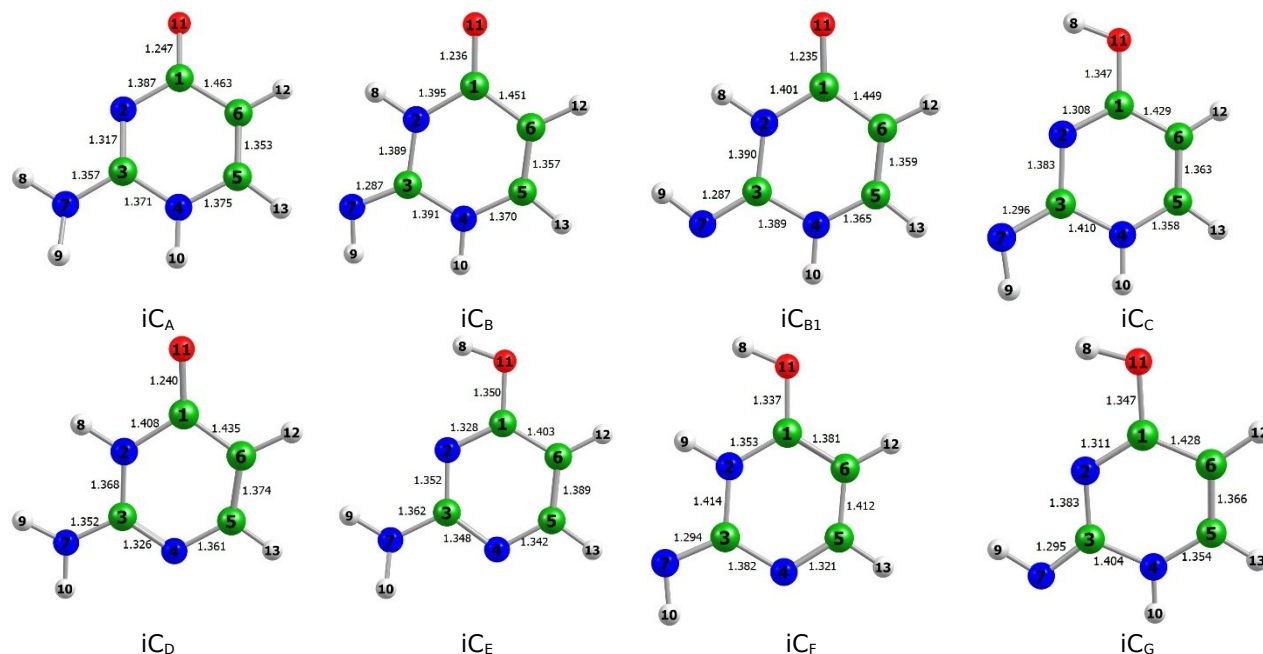
Figure 1: Ground-state equilibrium geometries of isocytosine tautomers in water environment (B3LYP/aug-cc-pVDZ and PCM).
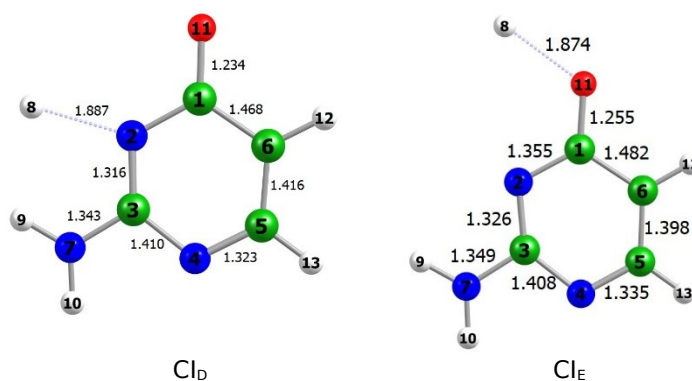
Figure 2: Optimized conical intersections S$_0$/S$_1$ of tautomers iC$_D$ and iC$_E$ at the B3LYP/aug-cc-pVDZ in the gas phase.

The structure of two conical intersections S$_0$/S$_1$ of tautomers iC$_D$ and iC$_E$ connected with elongation of the N$_2$-H and O$_{11}$-H bonds are illustrated in Figure 2. As seen the dissociations of the corresponding bonds occur in the molecular plane. The amino groups in the two structures are completely conjugated with the aromatic rings which can be deduced by the Σ values: both are equal to 360° (δ = 0°). These structures are used further for linear interpolation in internal coordinates.

4.2. Vertical excitation energies and experimental UV absorption spectra

The calculated vertical excitation energies of all tautomers of isocytosine are listed in Table 1. The first excited state of all tautomers, except iC$_A$ is the spectroscopically bright $^1\pi\pi^*$ electronic state. Only for the oxo-amino tautomer iC$_A$ the first excited state calculated at the B3LYP/aug-cc-pVDZ theoretical level is the dark $^1n\pi^*$ one. According to the TD B3LYP computations the $^1\pi\sigma^*$ excited states of the two oxo-amino tautomers iC$_A$ and iC$_D$ in the gas phase have lower energies (~4.9 eV) than in aqueous medium (more than 5.3 eV). With regards to the PIDA mechanism (24,25) in water medium this driven state should be populated with a lower probability than in the gas phase.

In order to assign the available tautomers in the non-irradiated and irradiated aqueous solution of

isocytosine we simulated the theoretical spectra of all tautomers. We found that only the simulated spectra of tautomers iC$_D$ and iC$_E$ in a largest degree fit to the experimental UV curves. They are illustrated in Figure 3. The experimental spectrum of the non-irradiated solution shows an insignificant shoulder at about 227 nm which corresponds to the π→π* electron transition of tautomer iC$_D$. Furthermore, a π→π* electron transition of the same tautomer is the origin of the maximum at 285 nm. In the course of the irradiation is decreases the absorption and transforms into a shoulder whose origin is the π→π* electron transition in tautomer iC$_E$. The shoulder at 227 nm gets more structured and starts to shape a peak which could be assigned to the π→π* electron transition of tautomer iC$_E$. The experimental spectrum of the non-irradiated solution in Figure 3 shows also a presence of oxo-amino tautomer iC$_A$. The two most intensive absorption maxima were assigned to be for the ¹ππ* excited states.

Table 1: Vertical excitation energies – B3LYP/aug-cc-pVDZ and CC2/aug-cc-pVDZ. Oscillator strength f.10^2 (in Italic).

iC$_A$						iC$_B$					
1				**2**		**1**				**2**	
water		gas		gas		water		gas		gas	
	eV		eV		eV		eV		eV		eV
¹nπ*	4.671 *0.02*	¹nπ*	4.215 *0.01*	¹ππ*	4.260 *0.01*	¹ππ*	4.456 *7.44*	¹ππ*	4.508 *4.14*	¹ππ*	4.722 *0.0*
¹ππ*	5.192 *6.27*	¹ππ*	4.808 *0.08*	¹ππ*	4.797 *0.13*	¹nπ*	4.926 *0.00*	¹nπ*	4.621 *0.00*	¹ππ*	4.852 *8.23*
¹ππ*	5.409 *0.15*	¹πσ*	4.912 *0.04*	¹πσ*	4.927 *0.32*	¹πσ*	5.389 *1.16*	¹πσ*	4.883 *0.28*	¹πσ*	5.070 *0.35*
¹ππ*	5.519 *3.41*	¹nσ*	4.922 *0.13*	¹ππ*	5.231 *3.37*	¹ππ*	5.673 *19.21*	¹ππ*	5.560 *9.82*	¹ππ*	5.760 *12.73*
¹πσ*	5.699 *0.97*	¹ππ*	5.141 *3.30*	¹πσ*	5.258 *3.81*	¹ππ*	5.926 *30.08*	¹πσ*	5.772 *0.01*	¹πσ*	5.979 *0.01*
iC$_{B1}$						iC$_C$					
1				**2**		**1**				**2**	
water		gas		gas		water		gas		gas	
	eV		eV		eV		eV		eV		eV
¹ππ*	4.434 *8.48*	¹ππ*	4.474 *5.76*	¹ππ*	4.748 *11.73*	¹ππ*	4.017 *3.82*	¹ππ*	3.891 *2.38*	¹ππ*	4.043 *3.38*
¹nπ*	4.888 *0.00*	¹nπ*	4.636 *0.00*	¹nπ*	4.758 *0.02*	¹πσ*	5.094 *1.19*	¹πσ*	4.531 *0.32*	¹πσ*	4.667 *0.36*
¹πσ*	5.395 *1.27*	¹πσ*	5.126 *0.51*	¹πσ*	5.297 *0.67*	¹nπ*	5.289 *0.19*	¹nπ*	4.887 *0.06*	¹nπ*	5.213 *0.17*
¹ππ*	5.688 *22.01*	¹πσ*	5.581 *0.17*	¹πσ*	5.792 *0.17*	¹πσ*	5.591 *0.01*	¹nπ*	5.264 *0.08*	¹πσ*	5.590 *0.24*
¹πσ*	5.889 *0.01*	¹ππ*	5.612 *10.82*	¹ππ*	5.846 *11.21*	¹ππ*	5.599 *34.78*	¹πσ*	5.370 *0.24*	¹nπ*	5.609 *0.04*
iC$_D$						iC$_E$					
1				**2**		**1**				**2**	
water		gas		gas		water		gas		gas	
	eV		eV		eV		eV		eV		eV
¹ππ*	4.607 *21.41*	¹ππ*	4.629 *14.69*	¹ππ*	4.614 *18.50*	¹ππ*	4.750 *8.77*	¹ππ*	4.814 *6.84*	¹ππ*	4.768 *8.08*
¹nπ*	5.072 *0.01*	¹nπ*	4.814 *0.00*	¹nπ*	4.820 *0.08*	¹nπ*	5.008 *0.38*	¹nπ*	4.942 *0.30*	¹nπ*	5.081 *0.40*
¹πσ*	5.339 *0.78*	¹πσ*	4.897 *1.15*	¹πσ*	5.300 *0.89*	¹πσ*	5.485 *1.18*	¹πσ*	5.312 *1.07*	¹πσ*	5.567 *2.14*
¹nπ*	5.476 *0.02*	¹nπ*	5.381 *0.01*	¹nπ*	5.658 *0.05*	¹ππ*	5.713 *27.00*	¹nπ*	5.654 *0.18*	¹nπ*	5.829 *1.26*
¹ππ*	5.756 *17.57*	¹πσ*	5.756 *0.87*	¹nσ*	5.925 *9.42*	¹nπ*	5.721 *3.49*	¹πσ*	5.701 *1.66*	¹ππ*	5.849 *26.57*
iC$_F$						iC$_G$					
1				**2**		**1**				**2**	
water		gas		gas		water		gas		Gas	

	eV		eV		eV		eV		eV		eV
$^1\pi\pi^*$	3.861 *8.50*	$^1\pi\pi^*$	3.784 *5.61*	$^1\pi\pi^*$	3.750 *8.71*	$^1\pi\pi^*$	3.970 *3.79*	$^1\pi\pi^*$	3.820 *2.48*	$^1\pi\pi^*$	3.926 *3.66*
$^1\pi\sigma^*$	4.890 *0.42*	$^1\pi\sigma^*$	4.139 *0.00*	$^1\pi\sigma^*$	4.520 *0.03*	$^1\pi\sigma^*$	5.120 *1.26*	$^1\pi\sigma^*$	4.770 *0.45*	$^1\pi\sigma^*$	4.927 *0.57*
$^1n\pi^*$	4.924 *0.22*	$^1n\pi^*$	4.690 *0.14*	$^1n\pi^*$	4.870 *0.20*	$^1n\pi^*$	5.400 *0.15*	$^1n\pi^*$	5.105 *0.00*	$^1n\pi^*$	5.458 *0.07*
$^1\pi\sigma^*$	5.402 *0.78*	$^1n\pi^*$	5.113 *0.22*	$^1\pi\sigma^*$	5.371 *1.11*	$^1\pi\sigma^*$	5.574 *0.02*	$^1\pi\sigma^*$	5.252 *0.04*	$^1\pi\sigma^*$	5.591 *0.11*
$^1n\pi^*$	5.450 *0.17*	$^1\pi\sigma^*$	5.197 *0.82*	$^1n\pi^*$	5.447 *0.28*	$^1\pi\pi^*$	5.589 *35.95*	$^1n\pi^*$	5.315 *0.30*	$^1n\pi^*$	5.609 *0.54*

1: B3LYP/aug-cc-pVDZ; **2**: CC2/aug-cc-pVDZ.
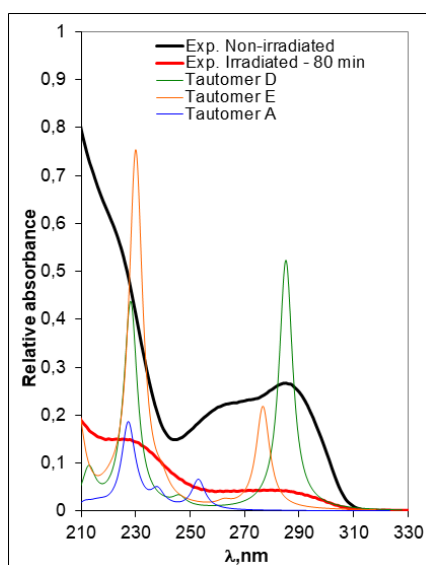
Figure 3: Experimental and theoretical spectra of isocytosine. The experimental spectra are for not-irradiated and irradiated (80 min) aqueous solutions of the compound. The theoretical spectra were simulated with a Lorentzian broadening of the bands. The theoretical spectra (B3LYP/aug-cc-pVDZ) are scaled with a scale factor of 1.06.
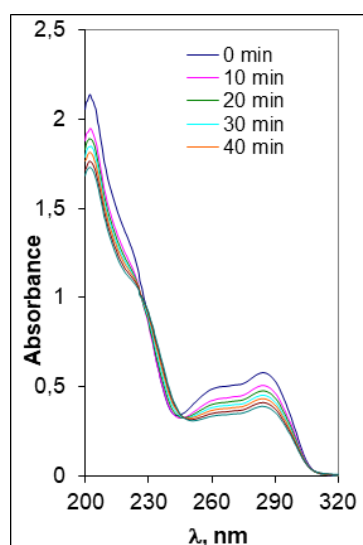
Figure 4: UV spectra of irradiated aqueous solution of isocytosine at different irradiation times.
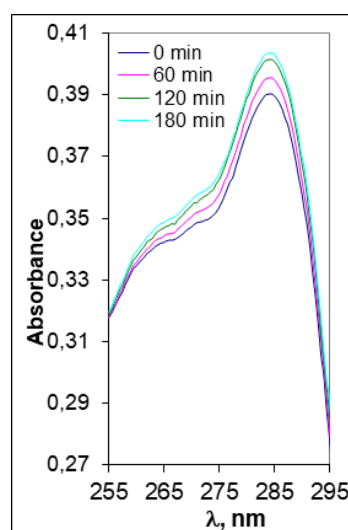
Figure 5: UV spectra of the aqueous solution of isocytosine after removing the UV light source (reaction in dark).

In Figure 4 are presented the UV spectra of the irradiated aqueous solution of isocytosine at different irradiation times. The spectra show regular decrease of the maxima at 285 nm and 202-203 nm. Using the first maximum we calculated the rate constant of the photoreaction which is 5.29×10^{-3} min^{-1}. The order of the reaction (first) implies a tautomeric process. The analysis of the UV spectra reveals that it should be a transformation of tautomer iC_D into hydroxy form iC_E.

We also followed the kinetics of the dark (thermal) reaction after removing the UV light source. It is observed in Figure 5 a slight restoration of the initial positions of the peaks as before the irradiation. It means that the tautomerization goes back thermally (in the ground state) and leads to the formation of the stable iC_D oxo-amino form. The calculated rate constant of the "dark" reaction of is 0.12×10^{-3} min^{-1} and it indicates that the thermal reaction is 44 times slower than the photochemical one.

4.3. Excited-state reaction pathways

LIIC pathways
We performed linear interpolation in internal coordinates in three stages: i) interpolation between tautomers iC_D and the conical intersection CI_D; ii) interpolation between the two conical intersections CI_D and CI_E; iii) interpolation between the conical intersection CI_E and tautomers iC_E. The results are summarized in Figure 6. As seen the ground-state energy barrier of the transformation $iC_D \rightarrow iC_E$ is very high - 5.732 eV. Along the $^1\pi\sigma^*$ excited-state reaction path the tautomerization can occur through a much lower energy barrier of 0.535 eV. Moreover, the $^1\pi\sigma^*$ excited-state reaction curve shows two clear minima where the excited system can be trapped. In the reaction interval $iC_D \rightarrow CI_D$ the photoreaction could prolong towards the stabilization of the ground state of the initial tautomer (iC_D) through internal conversion. In other words, two competitive reactions are expected: the phototautomerism of iC_D into iC_E and stabilization of tautomer iC_D through internal conversion. This fact agrees well with the low value of the rate constant of the photoreaction given above.
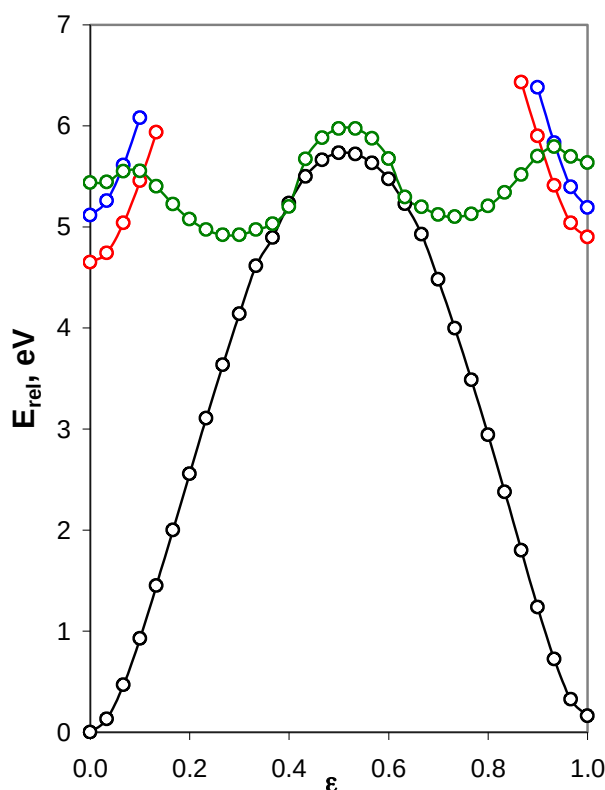
Figure 6: Linearly-interpolated excited-state reaction paths of the transformation $iC_D \rightarrow CI_D \rightarrow CI_E \rightarrow iC_E$, found at the B3LYP/aug-cc-pVDZ theoretical level in water surroundings (PCM). The relative energy was calculated according to the energy of tautomer iC_D (-395.012484 a.u.)

Excited-state water-assisted proton transfer
In order to apply the IRC approach for the study of the tautomerism $iC_D \rightarrow iC_E$ we oprimized the H-

bonded-complexes of tautomers iC_D and iC_E and the ground state transition state located between them. Their structures are given in Figure 7.
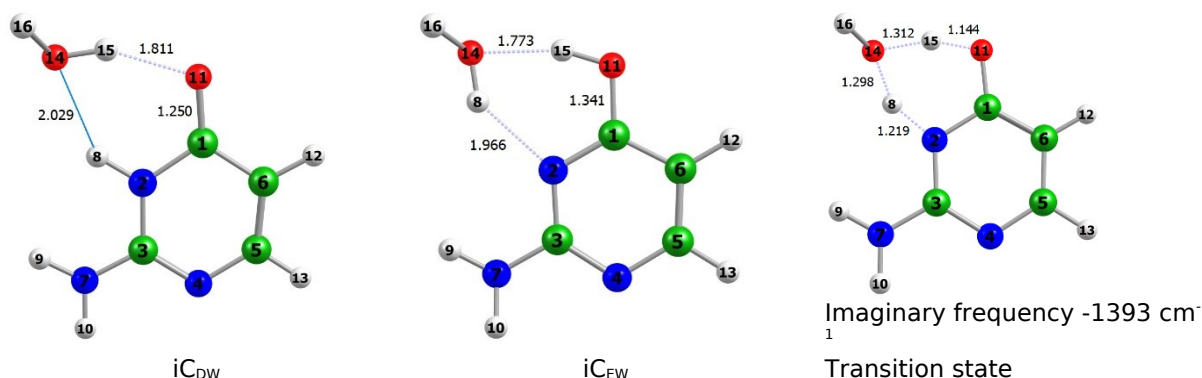
Figure 7: H-bonded complexes of iC$_D$ and iC$_E$ and the transition state of their mutual interconversion, all found at the B3LYP/aug-cc-pVDZ level in water surroundings (PCM).

The transition state has one imaginary vibration (Figure 7) whose form describes the motion of atoms H$_8$ and H$_{15}$ in order to form tautomers iC$_{DW}$ and iC$_{EW}$. With the structure of the transition state we performed IRC calculations to get the ground-state energy curve of the thermal reaction – Figure 8. We found a drastic reduction of the energy barrier which is 0.662 eV (about 9 times) as compared to the mechanism discussed in Figure 6. Furthermore, we studied the excited-state paths over the thermal energy curve. It is clear that the water assisted proton transfer occurs photochemically along the $^1\pi\pi^*$ excited-state reaction path with a low energy barrier of 0.462 eV.
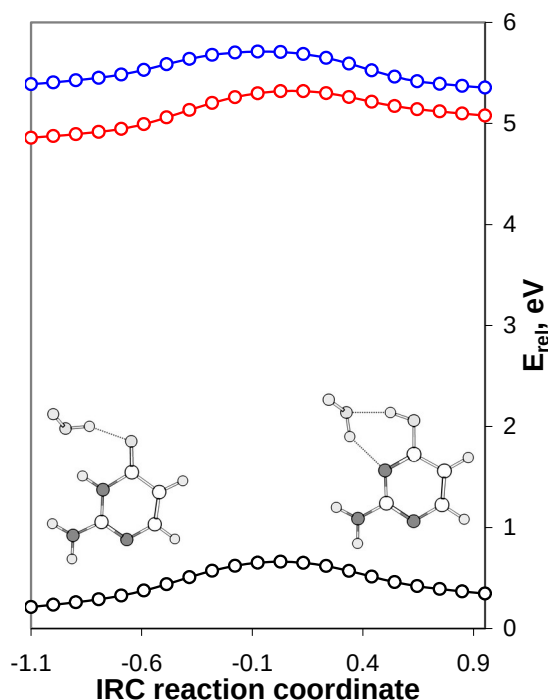
Figure 8: Excited-state reaction paths of the water assisted proton transfer iC$_{DW}$→iC$_{EW}$ in water medium (PCM). The relative energy was calculated by the energy of the ground-state equilibrium geometry of the system iC$_{DW}$ (-471.473381 a.u.).

No conical intersections between the energy curves are observed. We believe that this mechanism can explain the tautomeric conversion of isocytosine when irradiated with UV light.

5. CONCLUSION

The irradiation of aqueous solution of isocytosine with UVC light showed that a tautomeric photoconversion is a first order reaction with a rate constant of 5.29×10^{-3} min^{-1}. After removing the UV light source, we observed a dark reaction and a restoration of initial tautomer with a rate constant of

0.12×10^{-3} min^{-1}. The careful analysis of the UV absorption spectra of the irradiated and non-irradiated solution and the theoretically simulated UV spectra of several tautomers of isocytosine led to the conclusion that the photoreaction is between the amino-oxo and amino-hydroxy tautomers of the compound. The mechanism of this oxo-hydroxy phototautomeris was studied at the B3LYP/aug-cc-pVDZ theoretical level in water surroundings according to PCM. We tested two principally different mechanisms – PIDA (24-28) and a water-assisted excited-state proton transfer. The first mechanism proposed a consecutive dissociation and association of N-H and O-H bonds through conical intersections S$_0$/S$_1$ which occur along the $^1\pi\sigma^*$ excited-state reaction pathway. The second mechanism, which we believe is the much more probable one, is supported by a water molecule and occurs along the $^1\pi\pi^*$ excited-state reaction pathway. This energy curve was found over the ground state IRC reaction pathway. The water molecule drastically reduces the energy barrier in the ground state as well in the excited state.

The findings here are important since they give an answer of the question why the nature "has chosen" cytosine for a pyrimidine base to be included in nucleic acid macromolecules instead of isocytosine.

6. CONFLICT OF INTEREST

We declare no conflict of interest.

7. ACKNOWLEDGMENTS

7. REFERENCES

1. Callis PR. Electronic States and Luminescence of Nucleic Acid Systems. Annual Review of Physical Chemistry. 1983 Oct;34:329-28. Available from: <URL>..

2. Daniels MH, Hauswirth WW. Fluorescence of the purine and pyrimidine bases of the nucleic acids in neutral aqueous solution at 300 degrees K. Science 1971 Feb;171:675-2. Available from: <URL>.

3. Crespo-Hernandez CE, Cohen B, Hare PM, Kohler B. Ultrafast Excited-State Dynamics in Nucleic Acids. Chemical Reviews. 2004 Apr;104:1977-42. Available from: <URL>..

4. Cohen B., Crespo-Hernandez CE, Kohler B. Strickler–Berg analysis of excited singlet state dynamics in DNA and RNA

nucleosides. Faraday Discussions. 2004 May;127:137-10. Available from: <URL>. .

5. Shukla M., Leszczynski J. (Eds.). Radiation Induced Molecular Phenomena in Nucleic Acids, Springer,2008. ISBN: 978-1-4020-8183-5.

6. Rios AC, Tor Y. On the Origin of the Canonical Nucleobases: An Assessment of Selection Pressures across Chemical and Early Biological Evolution. Israel Journal of Chemistry. 2013 May;53:469-14. Available from: <URL>. .

7. Hünig I, Plützer C, Seefeld KA, Löwenich D, Nispel M, Kleinermanns K. Photostability of Isolated and Paired Nucleobases: N-H Dissociation of Adenine and Hydrogen Transfer in its Base Pairs Examined by Laser Spectroscopy. ChemPhysChem 2004 Sep;5:1427-4. Available from: <URL>.

8. Egel R, Lankenau A, Mulkidjanian AY (Eds.). Origins of Life: The Primal Self-Organization, Berlin, Springer-Verlag, 2011. ISBN: 978-3-642-21624-4.

9. Dimitrov BH, Bakalska RI, Delchev VB. Phototautomerism of isocytosine in water medium: theoretical and experimental study. Journal of Structural Chemistry (Zhurnal Strukturnoi Khimii). 2019 Jan;60: 937-10. Available from: <URL>.

10. Bakalska RI, Delchev VB. Comparative study of the relaxation mechanisms of the excited states of cytosine and isocytosine. Journal of Molecular Modeling. 2012 Jul;18:5133-13. Available from: <URL>.

11. Merchan M, Gonzalez-Luque R, Climent T, Serrano-Andres L, Rodriguez E, Reguero M, Pelaez D. Unified Model for the Ultrafast Decay of Pyrimidine Nucleobases. The Journal of Physical Chemistry B 2006 Dec; 110:26471-5. Available from: <URL>..

12. Switzer C, Moroney SE, Benner SA. Enzymatic incorporation of a new base pair into DNA and RNA. Journal of the American Chemical Society. 1989 Oct;111:8322-1. Available from: <URL>.

13. Roberts C, Bandaru R, Switzer C. Theoretical and Experimental Study of Isoguanine and Isocytosine: Base Pairing in an Expanded Genetic System. Journal of the American Chemical Society. 1997 May; 119:4640-9. Available from: <URL>..

14. Edwards PD, Albert JS, Sylvester M, Aharony D, Andisik D, Callaghan O, Campbell JB, Carr RA, Chessari G, Congreve M, Frederickson M, Folmer RHA, Geschwindner S, Koether G, Kolmodin K, Krumrine J, Mauger RC, Murray CW, Olsson LL, Patel S, Spear N, Tian G. Application of Fragment-Based Lead Generation to the Discovery of Novel, Cyclic Amidine β-Secretase Inhibitors with Nanomolar Potency, Cellular Activity, and High Ligand Efficiency. Journal of Medicinal Chemistry. 2007 Nov;50:5912-13. Available from: <URL>.

15. Congreve M, Chessari G, Tisi D, Woodhead AJ. Recent developments in fragment-based drug discovery. Journal of Medicinal Chemistry. 2008 May;51:3661-19. Available from: <URL>.

16. Jeffrey GA, Kinoshita Y. The crystal structure of cytosine monohydrate. Acta Crystallografica. 1963; 16:20-8. Available from: https://doi.org/10.1107/S0365110X63000049.

17. McConnell JF, Sharma BD, Marsh RE. Co-crystallization of Two Tautomers: Crystal Structure of Isocytosine. Nature 1964 Jul;203:399-1. Available from: <URL>.

18. Morita H, Nagakura S. The electronic absorption spectra and the electronic structures of cytosine, isocytosine, and their anions and cations. Theoretica Chimica Acta 1968 Jan;11:279-16. Available from: <URL>. .

19. Dračínský M, Jansa P, Ahonen K, Buděšínský M. Tautomerism and the Protonation/Deprotonation of Isocytosine in Liquid- and Solid-States Studied by NMR Spectroscopy and Theoretical Calculations. European Journal of Organic Chemistry. 2011 Jan; 2011:1544-7. Available from: <URL>.

20. Raczyńska ED. On Analogies in Proton-Transfers for Pyrimidine Bases in the Gas Phase (Apolar Environment)—Cytosine Versus Isocytosine. Symmetry 2023 Jan;15:342. Available from: <URL>.

21. Brown DJ, Lyall JM. The Fine Structure of Cytosine. Australian Journal of Chemistry. 1962;15:851-6. Available from: <URL>.

22. Vranken H, Smets J, Maes G. Infrared spectra and tautomerism of isocytosine; an ab initio and matrix isolation study. Spectrochimica Acta A 1994 May;50:875-14. Available from: <URL>.

23. Nowak MJ, Lapinski L, Fulara J. Matrix isolation studies of cytosine: The separation of the infrared spectra of cytosine tautomers. Spectrochim Acta A 1989;45:229-13. Available from: <URL>.

24. Chmura B, Rode M, Sobolewski AL, Lapinski L, Nowak M. A Computational Study on the Mechanism of Intramolecular Oxo−Hydroxy Phototautomerism Driven by Repulsive πσ* State. The Journal of Physical Chemistry A 2008 Dec;112:13655-6. Available from: <URL>.

25. Sobolewski AL, Domcke W. The chemical physics of the photostability of life. Europhysics News 2006 Oct;37:20-3. Available from: <URL>.

26. Perun S, Sobolewski A, Domcke W. Conical intersections in thymine. The Journal of Physical Chemistry A 2006 Nov;110:13238-6. Available from: <URL>.

27. Delchev VB, Sobolewski AL, Domcke W. Comparison of the non-radiative decay mechanisms of 4-pyrimidinone and uracil: an ab initio study. Physical Chemistry Chemical Physics. 2010 Apr;12:5007–8. Available from: <URL>.

28. Delchev VB, Ivanova IP. Theoretical study of the excited-state reaction paths of the OH- and NH-dissociation processes in barbituric acid. Monatsh Chem. 2012 May;143:1141-9. Available from: <URL>.

29. Becke AD. Density-functional thermochemistry. III. The role of exact exchange. Journal of Chemical Physics. 1993 April; 98:5648-4. Available from: <URL>.

30. Lee C, Yang W, Parr RG. Development of the Colle-Salvetti correlation-energy formula into a functional of the electron density. Physical Review B. 1988 Jan ;37:785-4. Available from: <URL>.

31. Hättig C, Weigend F. CC2 excitation energy calculations on large molecules using the resolution of the identity approximation. The Journal of Chemical Physics. 2000 Oct;113:5154-7. Available from: <URL>.

32. Bauernschmitt R, Ahlrichs R. Treatment of electronic excitations within the adiabatic approximation of time dependent density functional theory. Chem Phys Lett. 1996 July; 256:454-10. Available from: <URL>.

33. Stratmann RE, Scuseria GE, Frisch MJ. An efficient implementation of time-dependent density-functional theory for the calculation of excitation energies of large molecules. J Chem Phys. 1998 Nov; 109:8218-6. Available from: <URL>.

34. Miertuš S, Scrocco E, Tomasi J. Electrostatic Interaction of a Solute with a Continuum. A Direct Utilization of ab initio Molecular Potentials for the Prevision of Solvent Effects. Chem Phys. 1981 Feb; 55:117-12. Available from: <URL>.

35. Frisch MJ, Trucks GW, Schlegel HB, Scuseria GE, Robb MA, Cheeseman JR, et al. Gaussian˜16 Revision C.01. Wallingford, CT: Gaussian, Inc.; 2016.

36. Barca GMJ, Bertoni C, Carrington L, Datta D, De Silva N, Deustua JE, Fedorov DG et al. Recent developments in the general atomic and molecular electronic structure system. The Journal of Chemical Physics. Sep 2020; 152: 154102. Available from: <URL>.

Cherneva TD, Todorova MM, Bakalska RI, Delchev VB. JOTCSA. 2024; 11(1): 321-330. **RESEARCH ARTICLE**

330

A Densitometric Method for Determination of Mangiferin, an Antioxidant Compound, with Thin Layer Chromatography in the Leaf Extracts of Coffee (*Coffea Arabica* L.)

Yuni Retnaningtyas[1*] (iD), Nora Putri Narindra[1] (iD), Nia Kristiningrum[1] (iD)

[1]Department of Pharmaceutical Chemistry Faculty of Pharmacy, University of Jember, Jember 68121, Indonesia

Abstract: Mangiferin is one of the antioxidants in Coffea arabica L. leaves that has many pharmacological effects. The content of secondary metabolites in the leaves including mangiferin can be affected by age. A Thin Layer Chromatography (TLC) method for the quantitative analysis of mangiferin in Coffea arabica L. leaves extract was developed and validated. The method was developed using a mobile phase prepared with analytical grade solvents: ethyl acetate, methanol, formic acid, and deionized water (8:2:1:1 v/v/v/v). Regression functions were established over the 199.98-600.00 ng/spot range with r=0.999. The limit of detection (LOD) and limit of quantification (LOQ) were 13.87 and 41.61 ng, respectively. The method was selective with a resolution value of more than 1.5 and specific with the spectra correlation value for purity and identity check of more than 0.99. The percentage RSD was found to be 2.43% for repeatability precision and 2.05% for intermediate precision. The method's accuracy was determined through the standard addition method by adding known quantities of standard mangiferin to the pre-analyzed test solution and the mean recovery was 101.69± 1,21%. This TLC Densitometry method was linear, sensitive, selective and specific, precise, accurate, and can be used for routine analysis of mangiferin. On the young Coffea arabica L. leaves, the concentration of mangiferin ± RSD was 0.830 ± 1.71% w/w, and on the old Coffea arabica L. leaves was 1.128± 1.59% w/w.

1.   INTRODUCTION

Coffea arabica L. is the most developed Coffee in the world (1). *Coffea arabica L.* leaves contain highly antioxidant compounds. One of the antioxidants in *Coffea arabica L.* leaves is mangiferin (MGF). MGF is a natural xanthonoid with various biological activities they are antioxidant (2,3), anti-inflammatory (4,5), radioprotective, immunomodulatory (4), hypouricaemic (6), antimicrobial (7), anticancer (8), and antidiabetic (9,10,11). MGF has been isolated from various parts of *Mangifera indica*, but in 2008, a report that mangiferin was isolated from leaves of a wild *Coffea arabica L.*, *Coffea pseudozanguebariae* (11,12).

MGF is a C glucopyranoside of 1, 3, 6, and 7-tetrahydroxyxanthone. MGF features a highly condensed aromatic ring system coupled to a glucose moiety via an unusual C-C bond. The structure of MGF satisfies Lipinski's rules for druglike properties: molecular weight less than 500, cLogP = 2.73, fewer than 5 donor functions for hydrogen bonds; and fewer than 10 acceptor functions for hydrogen bonds (13). Some research results show that their age can affect the phenolic compound content in plant parts. MGF is also a phenolic compound whose content in *Coffea arabica L.* leaves is suspected to be affected by its age.

Literature review revealed that MGF can be determined by High-Performance Thin Layer

Retnaningtyas Y et al. JOTCSA. 2024;11(1):331-340.

RESEARCH ARTICLE

Chromatography (HPTLC) (14), High-Performance Liquid Chromatography- Ultra Violet (HPLC-UV) (15), High-Performance Liquid Chromatography (HPLC) and Mass spectrometry with Nuclear Magnetic Resonance (NMR) methods (12). The existing method for determining mangiferin levels has several drawbacks, including requiring expensive equipment, long analysis time, and requiring special skills. Thin-layer chromatography (TLC) is a chromatographic technique widely used for qualitative and quantitative analysis of organic compounds, isolation of the individual compound from multicomponent mixtures, and preparative-scale isolation (16). Conventional TLC is a quick, inexpensive, flexible, and portable method of surveying the composition of mixtures (16). With the development of modern precoated layers and the introduction of partially or completely automated equipment for the various stages of operation of TLC, not only are highly accurate quantitative determinations now possible but also the requirement that the work should comply with the Good Manufacturing Practice (GMP) and (Good Laboratory Practice (GLP) guidelines can be fulfilled (17). This study aimed to develop and validate the TLC-densitometry method to determine MGF levels in *Coffea arabica L.* leaves extracts of different ages, as an initial effort to utilize *Coffea arabica L.* leaves as a potential source of MGF.

2. MATERIAL AND METHOD

2.1. Sourcing and preparation of MGF extract from *Coffea arabica L.* leaves

Coffea arabica L. leaves as raw materials (Research Center for *Coffea arabica L.* and Cocoa, Jember, East Java). *Coffea arabica L.* leaves were separated from the peels, washed, and the washed leaves were then air-dried. The dried leaves were then blended and sieved with a B40 sieve to obtain *Coffea arabica L.* leaves powder with a uniform size. For sample extraction, 225 mg *Coffea arabica L.* leaves powder was extracted with petroleum ether (2 x 2 L, 6 h each time) to remove fatty matter, with cold acetone (4 x 2 L, 24 h each time) to remove tannins and finally with 70% ethanolic solvent (4 x 1 L, 6 h each time) (18). For sample preparation, 72 mg extract was diluted with 10 mL methanol and filtered with Whatman filter paper no.40.

2.2 Chromatographic condition

Planar chromatography was performed by spotting the sample on TLC plates Silica Gel 60 F254 (10 cm x 10 cm with 250 µm thickness, E. Merck, Germany). Linear ascending development was carried out in a Camag Twin Through Chamber containing eluent ethyl acetate: formic acid: methanol: DI water (8:1:2:1 v/v/v/v) was saturated. The spot moves to a distance of 9 cm. Densitometric scanning in the absorbance 325 nm for all measurements. Quantitative evaluation was performed via peak areas by WinCats software (version 1.4.1.8154).2.3

2.3. Standard solution preparation

A Standard stock solution was prepared by dissolving 5.0 mg of MGF in methanol and transferred to a 10.0 mL calibration volumetric flask and 10.0 mL until a mangiferin stock solution was obtained with a concentration of 500.0 ug/mL. The standard stock solution of MGF was then diluted with methanol to obtain a standard solution with a concentration range of 30-100 ug/mL.

2.4. Construction of calibration curves

Calibration solutions were prepared by diluting the stock solution, so that the application of 6 µL volume gave a series of spots, covering the calibration range 199.98-600.00 ng of mangiferin. Sample application on 10 cm x 20 cm aluminum-backed silica gel 60 F254 TLC plates (E. Merck, Darmstadt, Germany) stored in a desiccator was used for the stationary phase. The sample application was in the form of bands with a band length of 5 mm and the distance between the bands was 5.0mm. Bands were applied 10 mm apart and 10 mm from the bottom edge. The linear ascending development of plates was performed to a distance of 8 cm in a twin-trough chamber (20 · 10 cm) previously saturated for 30 min with the mobile phase ethyl acetate: formic acid: methanol: deionized water (8:1:2:1 v/v/v/v). Following the TLC running, the plates were dried with an air dryer. After elution, the plate densitometry scanning was performed at 25 nm on a Camag TLC scanner 3 operated by winCATS software version 1. .4.1.8154. The area under the peak was recorded and calibration curves relating the integrated area under the peak versus the corresponding concentrations as ng/band were then constructed, from which the polynomial regression equations were computed.

2.5. Validation method
The validation parameters tested in this study include linearity, sensitivity (LOD&LOQ), selectivity and specificity, precision, and accuracy. The determination of all the validation parameters is carried out under the conditions of the analysis of the optimization results.

2.6. Determination of mangiferin
Young and old *Coffea arabica L.* leaf extracts were prepared as a sample preparation method. Determination of MGF levels in young and old Coffea arabica L. leaves extracts was carried out by spotting 6 µL of the sample on a silica gel 60 F254 TLC plates and analyzing it under optimum conditions and scanning with densitometry at a wavelength of 325. Assays were replicated (n=3) and spotted on plates.

2.7 Data analysis
The data were analyzed using a One-Way ANOVA test with a 99% confidence level to determine whether there were significant differences among the three levels of data average MGF in an extract of *Coffea arabica L.* young and old leaves obtained. The analysis was conducted to test the normality and homogeneity. The normality test used the Shapiro-Wilk and the homogeneity test was performed using the Levene test.

2.   RESULTS AND DISCUSSION

3.1 Optimation of the eluent and wavelength
Good separation in the TLC system can be produced at optimum separation conditions. The analytical conditions that greatly affect the separation process in TLC are the mobile phase selection (19). In addition to selecting the mobile phase, other analytical conditions optimized for determining MGF include solvent, test concentration, measurement wavelength, and development mode. The optimum separation conditions for MGF separation in *Coffea arabica L.* leaves extract are shown in (Table 1)

Table 1: Optimum condition for analysis of mangiferin.

Condition	optimum
Solvent	Methanol
Stationary phase	Silica Gel 60 F$_{254}$
Eluent	Ethyl acetate: methanol: formic acid: deionized water (v/v/v/v) = 8:2:1:1
Wavelength	325 nm
Method development	Ascending

(Table 1) showed the optimum conditions for the analysis of MGF using TLC densitometry. The selected mobile phase was a mixture of Ethyl acetate: methanol: formic acid: deionized water = 8:2:1:1(v/v/v/v) with the value of Rf is 0.8 (included in the range of 0.1-0.9), the value of N = 1024 and H = 0.0009. Selection of the maximum wavelength for MGF was done using the light of UV and UV Vis with a range between 200-700 nm, and the selected wavelength is 325 nm. Selected wavelength is the wavelength of the spectrum in high intensity. The results of standard MGF scanning spectra can be seen in (Figure 2).
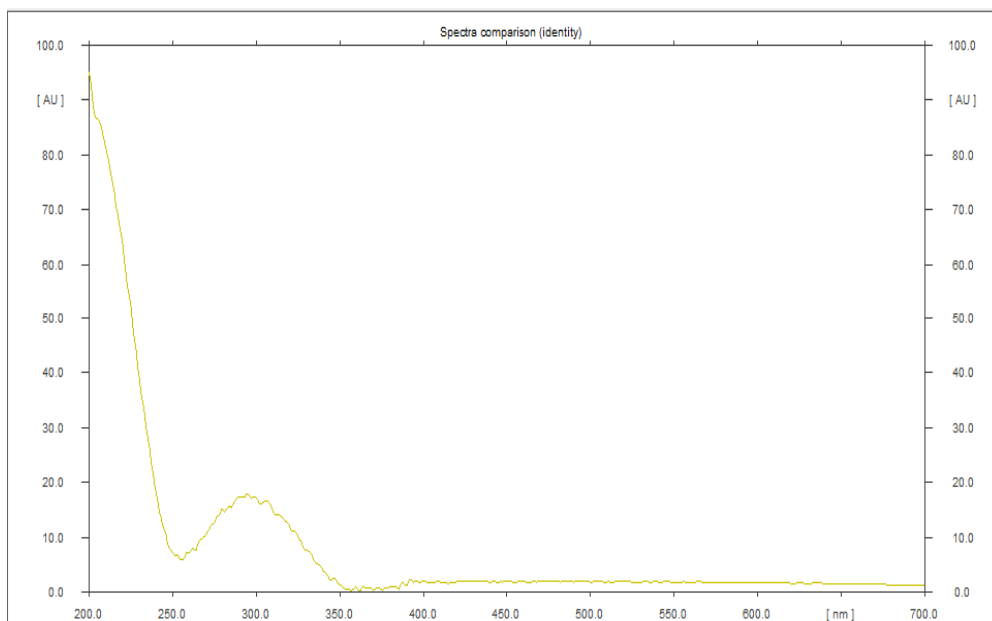
Figure 1: Spectrum of MGF standard at a wavelength of 200-700 nm.

Based on the spectra, it can be seen that the highest spectra intensity is reached when the wavelength at 325 nm with an absorbance signal of MGF is 49.9 AU. The chromatogram of the results of the MGF analysis at optimum conditions is shown in (Figure 3)
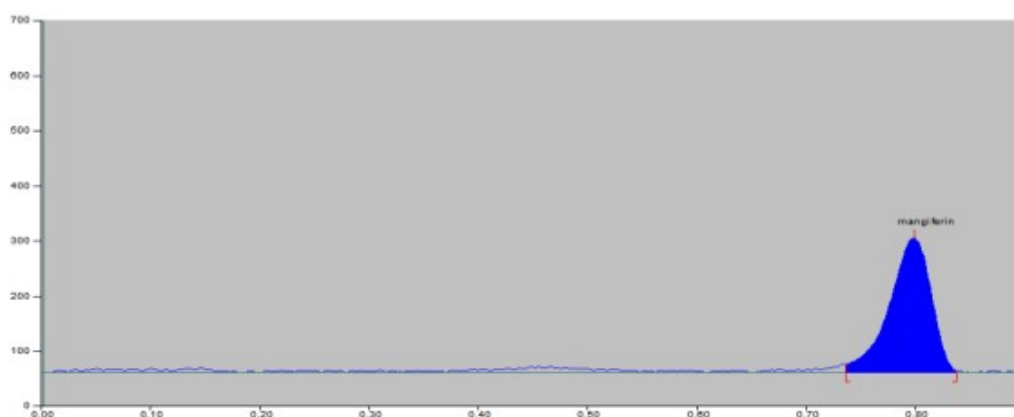
Figure 2: Chromatogram of mangiferin standard.

The chromatogram shown in (Figure 3) proves that under optimum conditions the developed TLC-Densitometri method is capable of separating and detecting MGF properly.

3.2. Validation of analysis method

3.2.1. Linearity
Linearity is the capacity of an analytical technique to produce an outcome that is directly related to the concentration of an analyte in the sample (20). The standard linearity curve for MGF at a series of concentrations in this study is shown in Figure (Figure 4) below.
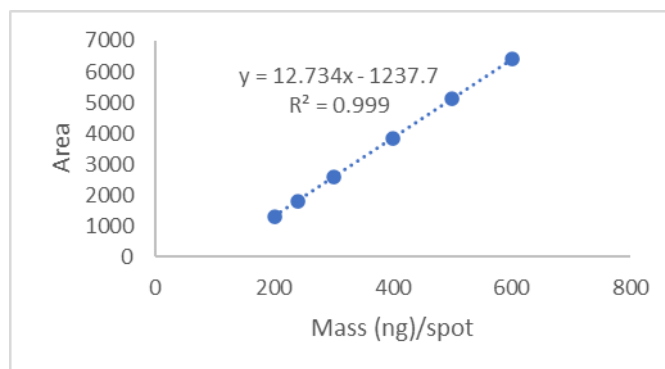
Figure 4: Graph of equation curve the correlation between area and mass (ng)/spot of MGF.

The linearity curve shown in (Figure 4) is a linearity curve of 6 standard concentrations of MGF with concentration ranges of 200-600 ng/spot. The equation obtained from 6 standard concentration measurements is y=12.73x–1237.66 with correlation coefficient (r) 0.999, Vx0=0.15%, and Xp=3.72 ng. The result showed that the MGF compound has a proportional correlation between mass and area indicated with an r value more than 0.99 (21), which is known to have met the requirements of the r value > 0.99, Vxo <5% (21), (22) then the curve said to be linear.

3.2.2. Limit of Detection (LOD) and Limit of Quantification (LOQ)

The determination of the Limit of Detection (LOD) and Limit of Quantification (LOQ) in this study was to determine the sensitivity of the TLC-Densitometry method for determining the levels of MGF in *Coffea arabica L.* leaves extract.

The LOD value is the minimum concentration of an analyte that can be detected and LOQ is the minimum amount of an analyte that can be quantified (23). Determination of LOD and LOQ values in this study was carried out by making a standard calibration curve for MGF in the concentration range of 36-132ng/spot. then the LOD and LOQ values are determined using software of validation method version 1.03. The LOD and LOQ were found to be 13.87 ng and 41.61 ng with correlation coefficients 0.998, Vx0= 2.5%, and Xp=13.87 ng. This result indicates that the resulting method is sensitive because the LOQ value was ≤ 400 ng/spot (22)

3.2.3. Selectivity/Specificity

The selectivity/ specificity of an analytical method is its ability to measure accurately an analyte in the presence of interferences that may be expected to be present in the sample matrix (24). Selectivity was determined by analyzing the sample. Selectivity was shown by the resolution that was calculated from the MGF peak to the unknown peak in the sample chromatogram. The results of separation with TLC show that no interferences were observed, meaning that it can separate MGF from other components in the sample, this is evidenced by the resulting resolution value (Rs) > 2, as shown in (Figure 5.)
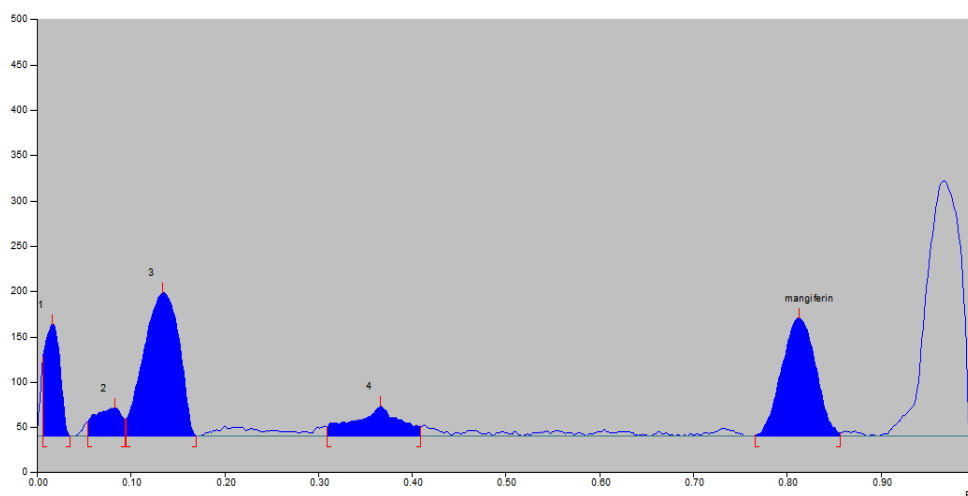
Figure 4: TLC-chromatogram of MGF in ethanol extract of *Coffea arabica L.* leaves using a selected solvent.

Specificity was determined by analyzing standards and samples. The purity and identity test showed specificity, which was determined by scanning at 200 nm–700 nm. Calculations for identity checks were from r(S.S) and r(S.A) where S is spectrum standard and A is spectrum sample and purity checks were from r(S.M) and r(M.E) where S = start, M = center; and E = end of the spectrum. The result of the specificity test is shown in (Figure 6); (Tables 2 and 3).

(a)

Wavelength (nm)

☐　MGF standard=

☐　Sample =

(b)

Wavelength (nm)

☐　MGF standard=
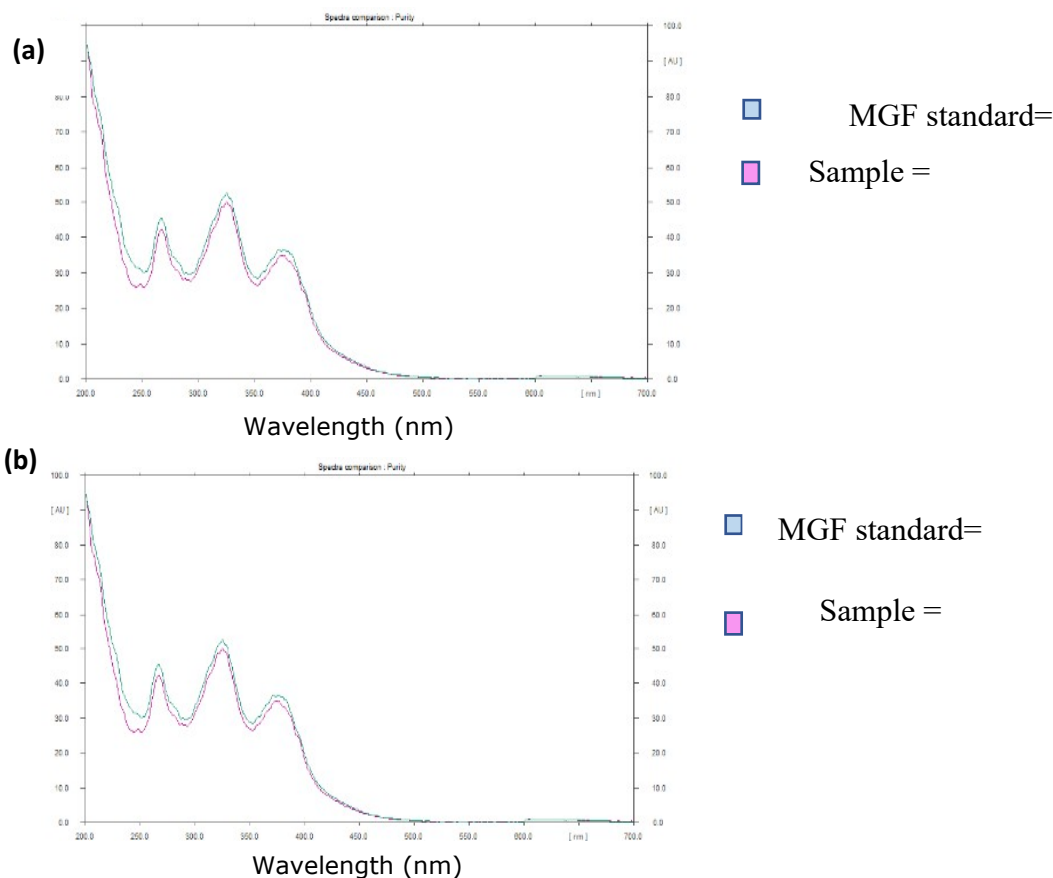
☐　Sample =

Figure 6: Spectra of standard and MGF samples in the **(a)** identity test; and **(b)** purity test.

Table 2: Purity Test of the Proposed Method.

Test	Track	Rf	r(s,m)[a]	r(m,e)[b]	Conclusion
Purity	Standard	0.81	0.998642	0.991039	*Pure*
	Sample	0.82	0.997896	0.993178	*Pure*

[a]: the correlation coefficient between the start position (s) and the top position (m) of the peak
[b]: the correlation coefficient between the top position (m) and the end position of the peak (e)

Table 3. Identity test of the proposed method.

Test	Track	Rf	r(s,s)[a]	r(s,a)[b]	Conclusion
Identity	Standard	0.81	0.998947	0.99778	MGF
	Sample	0.82	0.998947	0.99275	MGF

[a]: the correlation coefficient between the two tracks' standard spectra(s,s) in the same concentration
[b]: the correlation coefficient between the spectra of the standard track (s) and the track of the analyte (a) in the sample

Based on (Figure 5) ;(Tables 2 and 3) it can be seen that the spectra of standard and inulin samples have identical spectra. It can be concluded that the sample was containing MGF. The purity check of the analyte spots using winCATS software showed that the analyte spots were pure. The values of r (s, m) and r (m, e) were >0.99 in the identity check showing that analyte spots in samples were identical with standard mangiferin. This purity and identity assay demonstrates that the proposed TLC Densitometry method is highly specific (Figure 5).

3.2.4. Precision
The precision was performed by repeatability and intermediate precision studies. Repeatability studies were performed by analyzing the 100% concentration of the sample six times on the same day. The intermediate precision was checked by repeating repeatability studies on three different days (25) In this research, the precision that was used is repeatability and intermediate precision. Repeatability test, measured test analyte concentration in the sample with 6 replications. To determine the intermediate precision, performed the

same experiment as the repeatability test, but performed on three different days. Precision is measured by the value of RSD / CV (relative standard deviation / relative standard deviation). The result of repeatability and intermediate precision can be seen in (Table 4).

Table 4: The precision of MGF in ethanol extract of Coffea arabica L. leaves

Weight of samples (mg) (Mean ±SD)	Intra-day		Inter-day		
	Conc. % (Mean±SD)	RSD (%)	Day	Conc.% (Mean ± SD)	RSD (%)
73.517 ± 1.141	1.028 ± 0,025	2.43	1	1.028 ± 0.025	2.43
			2	0.993 ± 0.016	1.57
			3	1.051 ± 0.023	2.16

Based on the results shown in (Table 4), the RSD values for repeatability and inter-day precision of the analysis method are respectively 2.43% and 1.57-2.43%. Based on the RSD value obtained, it can be concluded that the method is precise and meets the precision requirements of AOAC, which is 2.7% (22)

3.2.5. Accuracy
The accuracy of the analysis method is expressed as the nearness of agreement

between the values found and values that are already available. It can also be defined as the closeness between the true value and observed value, which is determined based on the value of % recovery (20). The accuracy test is done by calculating the % recovery resulting from the addition of standard as much as 30%, 45%, and 60% of the analyte concentration in a sample obtained from the precision test with 3 replications at each level (26). The accuracy test results of the analytical method expressed as % recovery are shown in (Table 5).

Table 5: Accuracy of the proposed method.

Inulin added to the analyte (%)	Weight of samples addition (mg)	Theoretical content (mg)	Concentration found (mg)	*Recovery* (%)	RSD (%)
30	72.25	961.8 10^{-3}	983.0 10^{-3}	101.3	0.6
45	72.25	1072.8 10^{-3}	1067.0 10^{-3}	102.23	1.13
60	72.25	1184.0 10^{-3}	1213.0 10^{-3}	101.47	1.91

Test requirements for accuracy concentration of 1% MGF are 97-103% with RSD ≤ 2.7% (26), (22). The mean recoveries obtained should be included in that range. From (Table 5), it can be seen that the analytical method produced % recovery ± RSD = 101,3-102.23% ± 0.6-1.91%, so it can be concluded that this analytical method generated accurate data.

3.3. MGF assay in ethanol extract of coffee arabica leaves in different age
The result of the determination of MGF concentration in the extract coffee arabica leaves with three replications at each age is shown in (Table 6).

Based on the results in (Table 6), show that there are differences in the MGF content in *Arabica coffee* leaves of different maturities. Old leaves have a mangiferin content of 1.128±1.59 % while young leaves have an MGF content of 0.830 ±1.71 These results are also by previous research conducted by Campa et al where the highest MGF content was found in leaves with the highest maturity (27).

A homogeneity test was performed using the Levene test which obtained a significance value is 0.56 > 0.01 which indicates that the data variance is homogeneous. Because the data is the same variant, the ANOVA test is valid. In the ANOVA test, the obtained significance value is 0.001<0.05, meaning there are at least MGF levels that were significantly different in the two groups.

Table 6: Result of MGF assay in ethanol extract of coffee arabica leaves

Sample	Level of MGF (%)	RSD (%)
Young leaves	0.830	1.71
Old Leaves	1.128	1.59

4. CONCLUSION

Determination of MGF in the ethanol extract of coffee arabica leaves can be achieved by TLC densitometry and the result analysis was Linear, sensitive, persistent, and accurate. Based on the results of the assay, it can be concluded that the MGF content in Arabica coffee leaves is affected by age, where the older the age, the higher the MGF content.

5. CONFLICT OF INTEREST

The authors declare that there are no conflicts of interest.

6. REFERENCES

1. van der Vossen H, Bertrand B, Charrier A. Next generation variety development for sustainable production of arabica coffee (Coffea arabica L.): a review. Euphytica. 2015;204(2):243–56. Available from: <DOI>

2. Jain PK, Kharya M, Gajbhiye A. Pharmacological evaluation of mangiferin herbosomes for antioxidant and hepatoprotection potential against ethanol induced hepatic damage. Drug Development and Industrial Pharmacy. 2013;39(11):1840–50. Available from:<DOI>

3. He L, Peng X, Zhu J, Chen X, Liu H, Tang C, et al. Mangiferin attenuate sepsis-induced acute kidney injury via antioxidant and anti-inammatory effects. American Journal of Nephrology. 2014;40(5):441–50. Available from:<DOI>

4. Wauthoz N, Balde A, Saïdou E, Marc B. Ethnopharmacology of Mangifera indica L . Bark and Pharmacological Studies of its Main C-Glucosylxanthone, Mangiferin. Journal of Pharmaceutical Sciences [Internet]. 2007;1(2):112–9. Available from:<URL>

5. Márquez L, García-Bueno B, Madrigal JLM, Leza JC. Mangiferin decreases inflammation and oxidative damage in rat brain after stress. European Journal of Nutrition. 2012;51(6):729–39. Available from: <DOI>

6. Niu Y, Liu J, Liu HY, Gao LH, Feng GH, Liu X, et al. Hypouricaemic action of mangiferin results from metabolite norathyriol via inhibiting xanthine oxidase activity. Pharmaceutical Biology. 2016;54(9):1680–6. Available from:<DOI>

7. Singh SK, Tiwari RM, Sinha SK, Danta CC, Prasad SK. Antimicrobial evaluation of mangiferin and its synthesized analogues. Asian Pacific Journal of Tropical Biomedicine [Internet]. 2012;2(2 SUPPL.):S884–7. Available from:<DOI>

8. Rajendran P, Rengarajan T, Nandakumar N, Divya H, Nishigaki I. Mangiferin in cancer chemoprevention and treatment: Pharmacokinetics and molecular targets. Journal of Receptors and Signal Transduction. 2015;35(1):76–84. Available from: <DOI>

9. Luo F, Lv Q, Zhao Y, Hu G, Huang G, Zhang J, et al. Quantification and purification of mangiferin from Chinese mango (Mangifera indica L.) cultivars and its protective effect on human umbilical vein endothelial cells under H₂O₂-induced stress. International Journal of Molecular Sciences. 2012;13(9):11260–74. Available from:<DOI>

10. Liu YW, Zhu X, Yang QQ, Lu Q, Wang JY, Li HP, et al. Suppression of methylglyoxal hyperactivity by mangiferin can prevent diabetes-associated cognitive decline in rats. Psychopharmacology (Berl). 2013;228(4):585–94. Available from: <DOI>

11. Shinde K, Shinde V, Sharma K, Mahadik K. Phytochemical and Pharmacological Investigation on Vitex negundo Linn. Planta Medica. 2010;76(05). Available from:<DOI>

12. Talamond P, Mondolot L, Gargadennec A, de Kochko A, Hamon S, Fruchier A, et al. First report on mangiferin (C-glucosyl-xanthone) isolated from leaves of a wild coffee plant, Coffea pseudozanguebariae (Rubiaceae). Acta Botanica Gallica. 2008;155(4):513–9. Available from:<DOI>

13. Chi. Therapeutic Potential of the Natural Product Mangiferin in Metabolic Syndrome. The Journal of Nutrition. 2013;74–9. Available from: <DOI>

14. Jyotshna, Srivastava P, Killadi B, Shanker K. Uni-dimensional double development HPTLC-densitometry method for simultaneous analysis of mangiferin and lupeol content in mango (Mangifera indica) pulp and peel during storage. Food Chemistry [Internet]. 2015;176:91–8. Available from: <DOI>

15. Trevisan MTS, Farias de Almeida R, Soto G, De Melo Virginio Filho E, Ulrich CM, Owen RW. Quantitation by HPLC-UV of Mangiferin and Isomangiferin in Coffee (Coffea arabica) Leaves from Brazil and Costa Rica After Solvent Extraction and Infusion. Food Analytical Methods [Internet]. 2016;9(9):2649–55. Available from:<DOI>

16. Marston A. Thin-layer chromatography with biological detection in phytochemistry. Journal of Chromatography A [Internet]. 2011;1218(19):2676–83. Available from:<DOI>

17. Hahn-Deinstrop E. Applied Thin-Layer Chromatography : Best Practice and Avoidance of Mistakes Second, Revised and Enlarged Edition. WILEY-VCH Verlag GmbH dan Co. KGaA, Weinheim.; 2007. Available from:<URL>

18. Dineshkumar B, Mitra A, Manjunatha M. Studies on the anti-diabetic and hypolipidemic potentials of mangiferin (xanthone glucoside) in streptozotocin-induced type 1 and type 2 diabetic model rats. The International Journal of Advanced Pharmaceutical Sciences and Research. 2010;1(1):75–85. Available from:<DOI>

19. Retnaningtyas Y, Wulandari L, Wimala M. Inulin determination of yam bean tuber (Pacyrrhizus erosus l.)

water extract from different altitude areas using TLC-Densitometry. Pharmaciana. 2022;12(1):21. Available from:<DOI>

20. Sharma S, Goyal S, Chauhan K. A review on analytical method development and validation. International Journal of Applied Pharmaceutics. 2018;10(6):8–15 Available from:<DOI>

21. Campanelli M. Chapter-2 Analytical Method Development and Validation Overview : 2020;2(May):123–40. Available from:<URL>

22. Michael E.Swartz ISK. analitycal method development and validation. 2017. Available from:<DOI>

23. AOAC International. Guidelines for Standard Method Performance Requirements. AOAC Official Methods of Analysis. 2016;9.

24. Bhardwaj, P., Banarjee, A., Jindal, D., Kaur, C., Singh, G., Kumar, P., Sharma, A., & Kumar, R. . Validation of TLC-Densitometry Method for Estimation of Catechin in Acacia catechu Heartwood. Pharmaceutical Chemistry. 2020; *54*(2): 184–189. Available from:<DOI>

25. Abdelaleem EA, Abdelwahab NS. Stability-indicating TLC-densitometric method for simultaneous determination of paracetamol and chlorzoxazone and their toxic impurities. Journal of Chromatographic Science. 2013;51(2):187–91. Available from: <DOI>

26. Sonia K, Shree BB, Lakshmi KS. HPTLC method development and validation: An overview. Journal of Pharmaceutical Sciences and Research. 2017;9(5):652–7. Available from : <URL>

27. Campa C, Mondolot L, Rakotondravao A, Bidel LPR, Gargadennec A, Couturon E, et al. A survey of mangiferin and hydroxycinnamic acid ester accumulation in coffee (Coffea) leaves: biological implications and uses. Annals of Botany. 2012;110(3):595–613. Available from : <DOI>.

Chitosan, Its Derivatives, Sources, Preparation Methods, and Applications: A Review

Hadia Hemmami[1,2], Ilham Ben Amor[1,2]* , Asma Ben Amor[1,2], Soumeia Zeghoud[1,2], Shakeel Ahmed[3,4], Ali Alnazza Alhamad[5]

[1]Department of Process Engineering and Petrochemical, Faculty of Technology, University of El Oued, El Oued 39000, Algeria.
[2]Renewable Energy Development unit in Arid Zones (UDERZA), University of El Oued, El Oued 39000, Algeria.
[3]Department of Chemistry, Government Degree College Mendhar, Jammu and Kashmir 185211, India.
[4]Higher Education Department, Government of Jammu and Kashmir, India.
[5]Department of Chemistry, Faculty of Science, University of Aleppo, Syria.

Abstract: Chitosan is a type of biopolymer that can be derived from various natural sources, including animals and marine organisms. When determining its quality, molecular weight, crystallinity, and degree of deacetylation of chitosan are considered. Biocompatibility, bioadhesive, solubility, and polycationic character are all based on these traits. Chitosan's characteristics make it a good and appealing material for a variety of physical and chemical alterations. This review talks about the structure of chitosan and its properties. It also covers how chitosan is extracted from different sources. Special emphasis is placed on its utilization in the formation of metallic nanoparticles, drug delivery, and wastewater treatment.

1. INTRODUCTION

Chitin is a polysaccharide composed of β-(1-4) N-acetyl-D-glucosamine units. Cellulose, being the most prevalent biopolymer globally, is followed by this particular biopolymer as the second most abundant (1). Chitin serves as the primary constituent of the exoskeleton in crustaceans like crabs and shrimp, as well as the skeletal framework of insects. Additionally, it is present in the cellular walls of fungus (2). Because of its non-toxicity, antioxidative nature, biocompatibility, biodegradability, and renewability, this substance finds use in several domains, including food science, agriculture, cosmetics, biotechnology, and pharmaceuticals. Chitosan (CS), a polysaccharide derived from the deacetylation of chitin, has a wide range of applications across several industries (3).

Chitin and its derivatives are commercially obtained from the exoskeletons of various crustaceans like crab, shrimp, crayfish, and krill (4). Following the 1970s, chitin, chitosan, and its derivatives gained prominence in Various applications, such as water treatment for the removal of dyes, proteins, and metal ions (5). Additionally, these compounds are used in the food business for purposes such as weight management, nutritional supplementation, and as antioxidant coatings. They are also often used in industrial sectors such as the paper and textile industries (6). Crustaceans, including crab, lobster, and shrimp, possess a composition characterized by around 30-50% calcium carbonate, 30-40% protein, and 20-30% chitin inside their exoskeleton. In the process of chitin manufacturing from shell wastes, the wastes undergo treatment with alkali and acid solutions to eliminate protein and mineral components. As a result, it is possible to get chitin of superior quality from shells, as well as chitosan derived from this chitin, using appropriate treatment techniques (4). The chitin concentration of blue crab is around 14% (7).

It is economically feasible to turn food waste from crab shells into chitosan. Crabs, shrimp, desert locusts, honey bees, beetles (8), crayfish, corals,

fungi (9, 10), and cockroaches (11) could be exploited for the commercial production of CS (12, 13).

This review aims to provide a comprehensive exploration of chitosan and its derivatives, delving into the origins of this biopolymer and the different methods used to extract and modify it. The variety of sources from which chitosan can be extracted will be examined, ranging from crustaceans such as shrimp and crab to other marine organisms and even fungi. Furthermore, we will delve into preparation methods, including traditional chemical processes and contemporary enzymatic methods, highlighting the most important developments in recent applications of chitosan.

2. STRUCTURE, PRIMARY SOURCES, AND CHARACTERISTICS OF CHITOSAN

2.1. Chemical Structure
Chitin, which serves as the precursor of chitosan, is the most prevalent biopolymer in nature, second only to cellulose. It is abundantly present in several including insects, crustaceans, and fungi (14). Chitin is a biopolymer composed of N-acetyl-D-glucosamine units. When subjected to deacetylation, the acetyl functional groups are removed, resulting in a polymer largely consisting of β-1,4-D-glucosamine units. This polymer is called chitosan (Figure 1) (15). The degree of acetylation (DA) is defined as the mole fraction of the N-acetylated repeating units, while the degree of deacetylation (DD) is defined as the percentage of the repeating units of β-1,4-D-glucosamine in the polysaccharides (15).
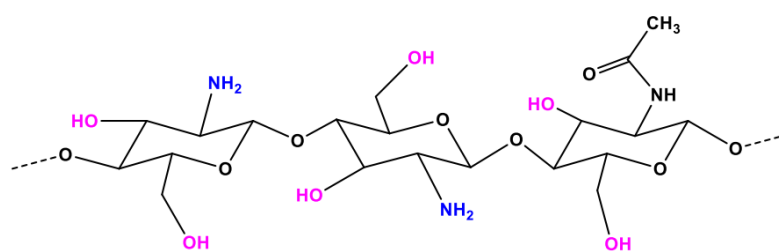
Figure 1: Structure of chitosan.

2.2. Sources
Among the various sources available for chitosan production, *shrimp* is one of the most promising and much discussed, and many other species, such as beetles and insects, have also been used, according to Figure 2 (4).
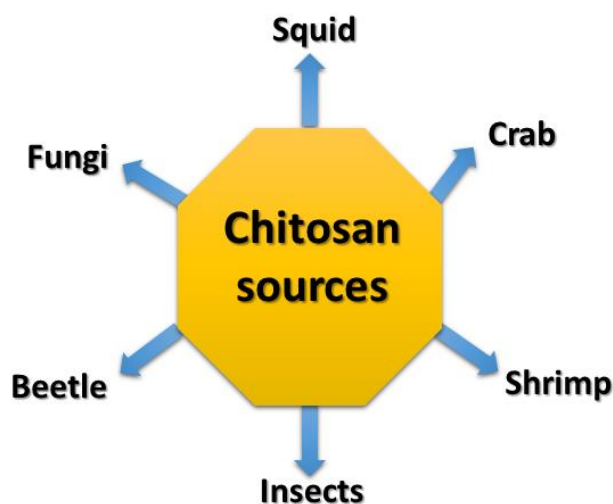
Figure 2: The most significant chitosan sources.

2.2.1. Crustaceans
Crab and shrimp waste are the main sources of chitosan for industrial production (16). Chitin, a substance found in the exoskeleton of these crustaceans, is used to make chitosan. Exoskeletons are waste from the fishing industry. Depending on the crustacean species, the chitin concentration in dried exoskeletons is between 5% and 42% (17, 18). In summary, chitosan derived from crab and shrimp waste is particularly attractive as these sources are readily available, renewable, and less expensive. In addition, it is an alternative method for the proper disposal of solid waste in the fishing industry.

2.2.2. Insects
Insects have emerged as a viable alternative supply of chitosan; nevertheless, this development has only occurred in recent times, and studies have only been conducted on a laboratory scale. Kaya et al. (19) reported that chitosan was obtained from the Colorado potato beetle (larvae and adults). The chitin concentration in larvae and adult beetles was determined on a dry weight basis to be 7% and 20%, respectively. Furthermore, it was shown that adult beetles yielded a chitosan production rate of 72%, while larvae exhibited a slightly lower rate of 67%. The use of insects to produce chitosan is based on

biodiversity, with insects representing 95% of all animal species. In addition, insect cuticles contain less inorganic material compared to crustacean shells, which facilitates demineralization treatment (5). Another advantage is the control of insects in agricultural land (20).

2.2.3. Mollusks
Mollusks provide an additional source of chitosan. The use of species such as *Sepia kobiensis*, *Sepia spp*, *Loligo lessoniana*, and *Loligo formosana* has been seen in this regard (20, 21). *S. kobiensis* cuttlebone was used to make chitosan, which had an 85.55 % deacetylation rate, a molecular weight of 322.04 kDa, and good antioxidant qualities (22). Chitosan and chitin were also extracted from the Chiton, and the antioxidant activity of the extracted chitosan was higher than that estimated for commercial chitosan (23).

2.2.4. Fungi
Compared to crustaceans, fungi are a source of chitosan and chitin that is not seasonal and not influenced by geographical factors. Chitin extraction from this source requires less use of chemicals, as there is usually no need for mineral removal and decoloration. In fungal chitin and chitosan, there are generally no heavy metal contaminants or allergenic proteins that can be found in marine sources (24). Furthermore, fungal chitin and chitosan have more consistent characteristics and properties due to their production by controlled fermentation, and they seem to be more suitable for agricultural applications in enhancing plant immune response. Despite these advantages, the availability and quantity of fungal biomass for the production of chitin and chitosan are much lower than marine sources. Furthermore, the extraction process has not yet been optimized for fungi, and lower yields are obtained (24).

The major components of the fungal cell wall are chitin and chitosan, glucans, glycoproteins, and mannans. Although not ubiquitous in the fungi kingdom, chitin is widely distributed in many fungal classes, including *Basidiomycetes*, *Ascomycetes*, *Zygomycetes*, and *Chytridiomycetes*, comprising 1-15% of the cell wall mass (25). The components of the fungal cell wall are all covalently cross-linked to each other. Chitin forms interchain hydrogen bonds with glucans, creating a glucan/chitin matrix that can assemble into microfibrils that form a scaffold around the cell (25). Different from crustaceans, chitosan can also be directly extracted from the cell walls of some species of fungi. For this purpose, the most investigated species include Mucor rouxii, Absidia spp., and *Rhizophus oryzae*, all belonging to Zygomycetes, *Aspergillus niger* (Ascomycetes) and *Lentinus edodes* (Basidiomycetes).

Three categories of potential fungal sources for the commercial production of chitosan and chitin have been described: waste biomass from biotech industries, fungus fermentation, and exploitation of existing mycothec products. Biotech industries annually generate thousands of tons of waste fungal biomass residue from various processes, including the production of bread, beer, antibiotics, and other drugs, enzymes, and the cultivation of edible mushrooms. From the latter activity, for instance, around 50,000 tons of waste mushroom stalks and irregular fruit bodies are produced every year (26). Additional 80,000 tons of waste biomass are derived annually from the cultivation of A. niger to produce organic acids, and more than one billion tons of fungal waste is generated annually from the penicillin production process. These huge amounts of biomass usually are disposed of in landfills or incinerated. By exploiting them for chitin and chitosan production, waste from biotech industries could be turned into a profitable solution to waste management (4).

For the commercial production of chitosan and chitin by fermentation, several fungal species have been evaluated. Different results in terms of yields and polymer characteristics are obtained using different fungal growth mediums. Moreover, different forms of mycelia (e.g., aerial mycelia for sporulation and submerged mycelia for absorption of nutrients) with different chitosan and chitin content are produced by single filamentous fungi. Experimentation focuses mainly on zygomycetes because of the potential to extract chitin and chitosan directly. Analysis of the cell wall of several Zygomycetes conducted by Campos-Takaki and co-workers to evaluate the most promising species for industrial production of these polymers showed an average chitin content of 10-16% of the cell wall and 26-28% chitosan. The species analyzed were Gongronella butleri, Absidia blakesleeana, Mucor javanicus, Rhizopus arrhizus, Syncephalastrum racemosum, and Cunninghamella elegans. A. blakesleeana and R. arrhizus had the highest content of chitin plus chitosan (43% of the cell wall) (27). Chitosan content in Zygomycetes generally ranges from 1 to 10% of the cells' dry weight. However, fungal chitin and chitosan yields vary depending on fungus strain, type of cultivation (solid or submerged fermentation), growth rate and nutritional requirements of fungi, and extraction process.

In another study, chitosan and chitin were extracted from the biomass of the fungal Termitomyces titanicus, and the chitin extraction rate reached 38.04% (28).

Finally, it is worth mentioning that the production of fungal chitosan and chitin is not completely free of risk. Some genera of Zygomycetes used to extract these polymers (Absidia and Rhizopus) include pathogenic species to humans or animals. For example, Rhizopus oryzae can cause pulmonary mucormycosis in humans, and some species of Absidia cause abortion in domestic animals. Therefore, specific safety measures should be adopted when handling these potentially pathogenic fungi to prevent their dispersal (29).

2.3. Properties of Chitosan
2.3.1. Molecular weight (Mw)
One of the most fundamental properties of a macromolecule is its Mw (21). Understanding the Mw of polysaccharides is crucial to understanding their functions and roles in biological systems. The molecular weight of CS can be measured using gel

permeation chromatography, light scattering (30), and viscometry, which is highly dependent on the deacetylation conditions. The simplest and most widely used technique for estimating Mw of CS is viscometry. However, because it is based on a correlation between intrinsic viscosity and molecular weight data, the problem with this technique is that it needs to be more absolute.

2.3.2. Determining molar mass
Estimating molar mass is one of the most significant analyses in the evaluation of CS since it defines the polymer's biological activity. According to a significant study, chitosan activity rises when molar mass and degree of deacetylation(DD) (31, 32). In medical CS, where the link between biological function and molecular structure appears to be crucial, determining molar mass is critical. It enables researchers to explore the biochemical processes generated by chitosan in cells (33).

2.3.3. Viscosity
From a technological point of view, the viscosity of polymers is a parameter of great interest because high-viscosity solutions are difficult to control. Although not an exact method and therefore requires the identification of solvent-specific constants, viscometry is an effective tool for determining the molecular weight of chitosan. The Mark-Houwink-Sakurada equation connects average molecular weight to intrinsic viscosity:

$$\eta = KM_v^{\alpha} \qquad (1)$$

where K and α are parameters to be determined experimentally, different K values have been reported depending on ionic strength, pH, and solvent composition (15). The viscosity of chitosan is affected by the Mw of the polymer, DD, and the viscosity of chitosan increases with increasing concentration and molecular weight. Viscosity increases with the extent of deacetylation. Due to charge repulsion within the molecule, high and low deacetylation chitosan exhibits various conformations in aqueous solution. When chitosan is significantly deacetylated, the chain is more flexible, and the conformation stretches. At low levels of deacetylation, the CS molecule adopts a spiral or rod shape due to the low charge density in the polymer chain. Temperature and concentration factors can affect the viscosity of CS solutions. The viscosity increases with decreasing temperature and increasing CS content. Due to depolymerization, the CS viscosity decreases with increasing demineralization time. The intrinsic viscosity of chitosan can be affected by physical factors (ultrasonic, milling, autoclaving, heating) and chemical (ozone) processes. Chitosan concentrated solutions with various levels of deacetylation differ in their viscosity and flow characteristics. As the DD of chitosan increases, there is a corresponding increase in the viscosities of the solutions and the manifestation of non-Newtonian flow characteristics. Conversely, the addition of salt decreases the viscosity and alters the non-Newtonian flow properties of the chitosan solution (34).

2.3.4. Deacetylation degree (DD)
The ratio of glucosamine groups to the total number of glucosamine and acetylglucosamine groups gives DD. The DD value of a polymer identifies if it is chitosan or chitin. If a polymer has a DD value of more than 60%, it is considered to be chitosan (35). Infrared spectroscopy (36), UV spectroscopy, near-infrared spectroscopy, potentiometric titration (37), and magnetic resonance (38) are a few of the analytical methods used to determine DD.

In Catharsius molossus, the chitosan DD was 94.9 %; in locusts, honeybees, and beetles, 80.96% (39); in Zophobas morio, the chitin DD was 86%, 133%,121%, 120%, 117%, and 86% in Anaz imperator, Ranatra linearis, Notoneeta glauca, Hydrophilus piceus, Agabus bipustulatus, and Asellus aquaticus, respectively (40). Several techniques have been developed to measure the amount of DD found in insect chitosan and chitin. Among them, the FT-IR, the conductometric, the acid-base, and the potentiometric titration methods are useful for completely soluble compounds. Fish, shrimp, and crab shells yielded chitosan with DDs of 75%, 78%, and 70%, respectively. According to earlier research, a greater DD represents a noteworthy advancement in chitin that may be applied to scaffolds and implantations in the biomedical industry (41).

2.3.5. Crystallinity
One of the most important physical properties that determine the functionality of chitosan is its crystallinity. In the solid state, CS molecules often self-assemble into highly ordered crystallites within large amorphous domains. There are two primary crystal polymorphs of CS (42). The most common polymorph is the "tendon chitosan" polymorph, which is a hydrated form. The anhydrous crystal form is referred to as the "tempered polymorph". Two antiparallel chitosan molecules with a double helix shape supported by hydrogen bonds form the crystal cell in both polymorphs. The presence of water molecules between the crystal cells stabilizes the structure through multiple hydrogen bonds, resulting in differences between the polymorphs (43). X-ray diffraction (XRD) is used to measure the crystallinity of chitosan, which detects and analyzes the pattern created by X-ray diffraction through a dense atomic lattice in a crystal.

2.3.6. Complex formation with metals
Under near-neutral conditions, metal cations can be absorbed by chelating the amino groups of CS. The sorption of metal anions in acidic solutions is caused by the electrostatic attraction of the protonated amino groups. On the other hand, the effectiveness of the sorption (sorption isotherm) and the absorption process (the chelation mechanism could become an electrostatic attraction mechanism if the metal speciation is disturbed) is significantly influenced by the presence of ligands and the pH value (44). In addition, CS can bind metal ions more effectively than chitin. It chelates various transition metal ions and has a reactive amino and hydroxyl group. Chelation is influenced by the distribution of the amino groups and their content. The nature of the cation is crucial in the interaction mechanism.

Various processes have been proposed as mechanisms for the formation of complexes between CS and metal ions, including adsorption, chelation, and ion exchange. Both metal and pH influence the type of interaction that takes place (45).

3. EXTRACTION OF CHITOSAN

Chitosan is obtained from the shells, fungi, and exoskeletons of insects. Shrimp shell wastes and crabs are currently the most common industrial biomass source for large-scale chitosan manufacturing. To extract pure chitosan, a variety of techniques have been proposed and tested. In general, chemical procedures could be used to conduct both demineralization and deproteinization. For the extraction of CS, these traditional chemical procedures (Figure 3) are used because they are both simple and economical. In this article, the chemical extraction of CS from a variety of sources is detailed in Table 1.
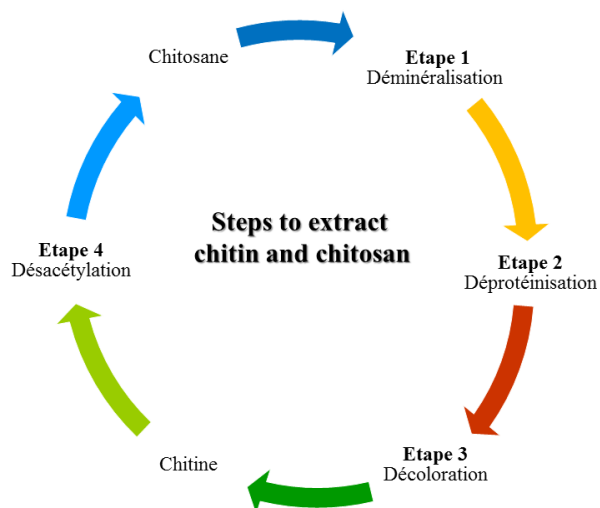
Figure 3: Chitin and chitosan extraction technique.

Table 1: Extraction techniques and characterization of CS from many sources.

Source	Demineralization	Deproteinization	Decoloration	Deacetylation	Yield Chitosan (%)	Characterization	Ref.
Shrimp	1M HCl	24 hours of 1 M NaOH	KMnO$_4$ and Oxalic acid	50% NaOH	-	FT-IR, TGA, SEM	(43)
	4% HCl for12 h	24 hours with 4% NaOH at ambient temperature	1% KMnO$_4$ and 1% oxalic acid for 30 mins to 2 hours	65% NaOH for three days	46	FT-IR, XRD, SEM	(44)
Crab	1 N HCl for 6 hours	3 hours of NaOH at 100°C	1% KMnO$_4$ for 1h, 1% oxalic acid for 1h	40% NaOH for two h at 105°C	32.2	XRD, SEM, TGA,	(45)
Tenebrio molitor	3 hours for 2 N HCl at 20°C	3 hours for 5 % NaOH at 95°C	-	50% NaOH for 3 h at 105°C	10.20		(46)
Catharsius molossus	30 minutes at 80°C and 1.30 M HCl	4 M NaOH for 6 hours at 90°C	3% KMnO$_4$ for 30 min and 2% oxalic acid for 30 min at 70 °C	24 hours of 8 M NaOH at ambient temperature	24	XRD, FT-IR, TGA, SEM	(47)
Leptinotarsa decemlineata	2 M HCl at 65–75 °C for 2 h	80-90°C for 2 M NaOH	methanol, water, and chloroform in a 1:2:4 ratio for one hour	3 hours at 100 °C with 50% NaOH	-	SEM, XRD, FT-IR, TGA,	(19)
Goliathus orientalis Moser,	1M HCl for two h at 95°C	36 hours for 2 M NaOH at 95°C	H$_2$O$_2$ (50%) for 4 hours at 25°C	50% (w/w) NaOH at 95°C	80	FT-IR, TGA, SEM	(48)
Mealworm Beetle	7% HCl at 25 °C for 24 h	10% NaOH at 80 °C for 24 h	-	9 hours for 55% NaOH at 90°C	83.37	FT-IR, XRD	(49)
Clanis bilineata	7% HCl at 25 ◦C for 24 h	10% NaOH at 60◦C for 24 h	-	4 hours for 55% at 120°C	95.9	HPLC	(50)
Bombyx mori	HCl for 20min at 100°C	24 hours for NaOH at 80°C	0.4% Na$_2$CO$_3$	NaOH (40 %), with NaBH	88.40	C NMR, SEM	(51)
Ganoderma Lucidum Mushroom	1M HCl	4 M NaOH at 50 °C		2 hours for 60% NaOH at 50°C	-	H-NMR	(52)
Grasshopper	1 M HCl in 30◦C for 2 h	1 M NaOH in 90 °C for 2 h	2 hours for 2 % KMnO$_4$	8 hours for 60% NaOH at 100°C	5.7	SEM, FT-IR, TGA, XRD	(53)
Hermetia illucens	2 hours for 2% HCl at 20°C	NaOH for 2h at 50 °C	-	NaOH at 100◦C for 2	32	NMR, FT-IR	(54)

3.1. Demineralization

Not all species of crustaceans have the same mineral composition in their exoskeleton. To dissolve calcium carbonate as $CaCl_2$, demineralization is typically performed using acids like hydrochloric acid (HCl), nitric acid, and acetic acid in concentrations up to 10 % at 25°C with continuous stirring. Although it is employed at a concentration of 0.2-2 M for 1 to 48h at temperatures ranging from 0 to 100°C, HCl is the preferred acid. Calcium chloride is produced in significant volumes when minerals are demineralized for 1–3 hours at room temperature using diluted (1–8%) HCl (1). The typical solid-to-solvent ratio is 1:15; an indication of how well the demineralization process worked is the amount of ash in the demineralized shell (15).

3.2. Deproteinization

Chitin naturally exists in conjunction with protein. Stable complexes are created when the protein forms covalent connections with chitin via aspartyl, histidyl, or both residues (57). Alkaline treatment is typically used to deproteinize chitin. The shells are subjected to potassium or sodium hydroxide treatments at temperatures between 65 and 100°C with a minimum shell-to-alkali ratio of 1:4 for between 1 and 12 hours. When these circumstances exist, the protein separates from the solid portion of the shrimp waste. To improve the deproteinization efficiency, solid-to-alkali solution ratios of 1/20 or 1/10 are utilized in conjunction with appropriate agitation. The process is typically carried out in a nitrogen environment and with sodium borohydride present to avoid oxidation of the products ($NaBH_4$). The protein hydrolysate is simply removed when the deproteinization step is finished by separating the particles from the protein slurry by filtration. Depolymerization and deacetylation are the results of protracted alkaline treatment under difficult circumstances. Table 2 summarizes the results of chemical deproteinization.

Table 2: Deproteinization processes involving chemicals.

Technique	Source types	Concentration	Temperature /Duration	Residual Protein /Chitin Yield	Ref.
NaOH	Lagoon crab (Callinectes amnicola)	2.39 M	70 ° C for 2 h	19.36 % / -	(47)
NaOH	Rock lobster (Jasis lalandii)	5%	80–85 °C for 2 × 30 min	24.0% /-	(48)
NaOH	White shrimp (Litopenaeus vannamei)	0.68 M	Ambient for 24 h	-/0.92 – 0.96%	(49)
Boiling water under pressure	Gray shrimp (Crangon crangon)	-	180 °C for1 h	-/4.7%	(50)

3.3. Decoloration

Chitin is a colored substance that is produced during the demineralization and deproteinization of shell debris. The chitin must be bleached or decolored to produce cream-colored chitin powder for commercial use (62). Chitin and the pigment found in crab shells combine to produce complexes. (63)discovered three 4, 4'-dike to-ß-carotene derivatives and one 4-keto-ß-carotene derivative securely attached to the red kelp crab's exoskeletal chitin. The degree of chitin and pigment connection varies among crab species. The leftovers are dyed using oxidants or solvents. The chemical that is employed during the decolorization process shouldn't have an impact on the physicochemical or functional characteristics of CS and chitin. Based on a dry shell, (64)were able to create a near-white crawfish chitin by extracting it with acetone, drying it for two hours at 25°C, and then bleaching it for five minutes with a 0.315% NaClO solution (carrying 5.25 %available chlorine).

3.4. Deacetylation

The process of deacetylation involves the removal of the acetyl group from chitin, resulting in the conversion of chitin into chitosan. The alkali concentration and duration of deacetylation, temperature, previous chitin isolation techniques, atmosphere, density, the ratio of chitin to alkali solution, and the size of the particle are just a few of the significant factors that significantly affect DD. The ideal deacetylation process condition should produce CS that is not damaged and is soluble in diluted acetic acid in the shortest amount of time (2), taking into account all of these prerequisites. Alkaline techniques must be used for N-deacetylation because the polysaccharide cannot be hydrolyzed without the N-acetyl groups being removed (65). The trans arrangement of the C2-C3 substituents in the sugar ring imposes a resistance of groups that necessitates severe alkaline hydrolysis processes. With a solid-to-solvent ratio of 1:10 (w/v), it is typically accomplished by treating the polymer with concentrated Na or KOH solution (40-60%), typically for 30 min at 80-140 °C or more (57). As an alkali, sodium hydroxide is chosen. After deacetylation, CS is thoroughly washed to remove any alkali that may have remained, and it is then dried to produce flakes. Ash and protein levels should be low in the substance. Chitosan is produced chemically, which has many drawbacks, including environmental contamination, variable degrees of acetylation, and molecular weights.

4.CHITOSAN DERIVATIVES

Despite being widely and effectively employed in several industrial applications and biomedical, CS has several disadvantages, including the fact that it

is insoluble at physiological pH. When protonated, CS is soluble and works as a permeation enhancer in an acidic environment. As a result, several alkylated derivatives of CS have been created. These partly quaternized chitosan derivatives have been employed in place of chitosan because they exhibit strong water solubility across a wide pH range.

The chemical alteration may readily improve the structural features of chitosan for a specific application. Fortunately, CS is open to chemical modification. Due to the presence of acetamido, amine, and hydroxyl functional groups, changes result. Because of this, chemical modifications would preserve the original biochemical and physicochemical properties of CS and would not alter its basic structural components.

4.1. Enzymatic and Chemically Modified Functional Chitosan Derivatives
By directly altering the reactive amino and OH groups with a limited number of chemical processes, a wide variety of CS derivatives with various functional substituents have been produced. Using chemocatalytic or moderate and selective enzymatic conversion, it is possible to make chitosan derivatives that are highly cationic and quaternized, anionic with arylated or carboxyl, sulfate groups, hydrophobic, or nonpolar.

4.2. Derivatives of Anionic Chitosan
Cationic and polyelectrolytes are anionic CS derivatives with acidic groups on the polymer backbone. The charge density and level of substitution may have an impact on the pH-dependent behavior of these derivatives. Typically, carboxymethylation with monohalocarboxylic acids is utilized to produce carboxyalkyl CS derivatives that have both O and N substituted to achieve N/O selectivity (66, 67).

Carboxypropyl chitosan, N/O and O-carboxymethyl CS, and carboxybutyl CS derivatives [16], with antimicrobial characteristics, have been produced using this technique. Using reduced-oxidant amination with glyoxylic acid and 2carboxybenzaldehyde (68), respectively, glycine and carboxybenzyl pending group-containing derivatives of carboxyalkyl CS have been created. N-carboxymethyl CS is appropriate for food and cosmetics because it can form films and gels, has a high viscosity, has a large hydrodynamic volume, and is soluble in water (66). Using cross-linking glutaraldehyde, a pH-responsive hydrogel for colon-specific drug delivery, n -n-carboxybenzyl CS is created (69).

Using N / O acylation with glutaric, and succinic anhydrides, CS compounds with anticoagulant and antiplatelet action have been produced (69, 70). A recently developed sophisticated and gentle chemoenzymatic method for the selective oxidation of the C6-hydroxyl group, which is used to create carboxyl chitosan derivatives (71), and controlling the reaction conditions led to the production of a variety of oxidized CS derivatives with various levels of oxidation and characteristics. These compounds displayed reduced viscosity and higher solubility in solution. A cross-linked CS derivative that may create a self-assembling pH-responsive hydrogel was created when CS was disintegrated in weak hydrochloric acid before TEMPO (2,2,6,6-tetramethylpiperidine-1-oxyl) laccase oxidation (71). The developed pH-responsive CS derivative had a sol-gel transition that was roughly at physiological pH (7.4) and had the potential to be used as a platform for the transport of medicines to the stomach.

4.3. Hydroxyalkylchitosans
In a popular process for modifying polysaccharides, such as cellulose and starch, hydroxyalkyl CS, also known as hydroxypropyl CS, glycol CS, and hydroxyethyl CS, are created using reacting alkyl epoxides (such as propylene oxide, butylene oxide, and ethylene oxide) with glycidol. The reaction conditions can be exploited to regulate the selective synthesis of different process temperatures and catalysts employed for O- or N- hydroxyalkyl derivatives. Water-soluble hydroxyalkyl chitosans have the potential to be used as temperature-sensitive injectable carriers for cells (72) and, additionally, as self-assembled nanoparticles for use in drug delivery (73). They also exhibit antibacterial capabilities.

4.4. Chitosan Derivatives That are Quaternarized and Water Soluble
For chitosan, solubilities at pH levels lower than six are not preferred. Its derivatives are used in food, medicine, and cosmetic products (74). To increase its solubility at a neutral pH, it is first derivatized with quaternary amino group substituents, then carboxymethylated, and then sulfonated by adding a highly hydrophilic substituent. Trimethyl ammonium salt is chitosan's most basic by-product. Chitosan was treated with NaOH, chloride ion, and methyl iodide in N-methyl-2 pyrrolidone to produce the trimethyl ammonium salt of CS, which has a high degree of substitution. Iodide must undergo anionic modifications with chloride ions to stabilize, producing a product that is water soluble at a pH of 7 (75).

4.5. Some Chitosan Derivatives
4.5.1. Chitosan-grafted copolymers
In recent years, there have been notable advancements in the field of chitosan-grafted copolymers, marking a significant stride in the realm of biomaterials and polymer science (76). Chitosan, a biodegradable and biocompatible biopolymer, has been ingeniously modified through grafting with various copolymers to enhance its properties and widen its scope of applications. For instance, chitosan-grafted polyethylene glycol (PEG) copolymers have shown great promise in drug delivery systems, improving drug solubility and bioavailability. Additionally, chitosan can be reductively aminated using PEG-aldehyde to add PEG(54). Polypeptides have been bonded by reacting with N-carboxy anhydrides of amino acids to produce new biomaterials (55). These copolymers can be tailored to achieve controlled release of pharmaceuticals, making them pivotal in precision

medicine and cancer therapy (77). This is just one example among many, demonstrating the versatility and potential of chitosan-grafted copolymers, which hold the key to numerous innovations in areas such as tissue engineering, biomedicine, and environmental remediation (78).

4.5.2. Alkylated chitosans
As polysaccharide-based amphiphilic polymers, alkylated chitosans play a crucial role. Highly substituted derivatives with poor regularity were produced on CM-chitosan using carboxylic anhydrides with various chain lengths. They had a reduced capacity for biodegradation and were insoluble in water (79).

The properties of alkylated chitosans with high solubility under acidic situations are particularly fascinating. They are initially evaluated against equivalent low molecular weight surfactants based on surface activity (80). They then greatly enhance the stability of the interfacial coating while having a negligible effect on the lowering of surface tension (81). A basic surfactant and modified chitosan display radically distinct behaviors, as has been demonstrated (82). Second, due to interactions between hydrophobic chains, a physical gel is produced; the creation of this gel depends on the pH and salt concentration. These gels result from a delicate balance between hydrophobic attraction caused by alkyl chains, particularly about their length, and electrostatic attraction between positively charged CS chains (6).

Because it has been shown, it is important to remember that alkyl chitosan works with both neutral and cationic surfactants and that cationic surfactant adsorbed on the alkyl chain grafted on chitosan increases its solubilization (83).

4.5.3. Chitosan 6-O sulfate
In recent years, there have been notable developments in the field of biopolymers, especially in the case of chitosan 6-O sulfate. This modified form of chitosan has received significant attention due to its unique properties and diverse applications. For example, chitosan 6-O sulfate has shown great potential in the development of wound healing materials, as it can promote tissue regeneration and reduce inflammation. In addition, it has shown promising results in the field of drug delivery, where it can serve as a carrier for controlled and targeted release of pharmaceutical compounds. The latest developments in 6-O chitosan sulfate highlight the ongoing innovation in biopolymers, with the potential to impact various industries such as medicine, biotechnology, and pharmaceuticals.

A recent study published by Bolshakov et al. (84)explored the optimization of chitosan 6-O sulfate synthesis. The researchers used a method of quaternizing chitosan with sulfate-containing ingredients to produce a product with a high percentage of sulfate groups.

In a study conducted by Samet et al. (85), it was found that sulfated chitosan oligomer (ShCsO) is a heparin mimetic. The researchers modified chitosan oligomers into ShCsO and studied its chemical composition and biological properties. Chitosan 6-O sulfate was used in developing composite scaffolds for cartilage tissue engineering. A study reported that the coupling of dermatan sulfate (DS) and chondroitin-6 sulfate (CSC) with chitosan scaffolds could improve chondrocyte culture, extracellular matrix (ECM) production, and chondrogenesis. It was reported that the high molecular weight of 6-O chitosan sulfate can effectively reduce the infectivity of porcine virus type 2 (PCV2) in PK15 cells (86). These recent developments demonstrate the potential of 6-O chitosan sulfate in various applications, including biomedical applications, tissue engineering, and inhibition of viral infection.

4.5.4. O-and N-Carboxymethyl chitosan
Carboxymethyl chitosan, a soluble polymer that is amphoteric and varies on pH, and which can be converted to O- and N-carboxymethylation in a well-regulated process (with sodium monochlorocetate when NaOH is present), is the chitosan derivative that has been the subject of the most research. Phase separation was observed because of the balance between the negative and positive charges on the polymer at pH values of 2.5 to 6.5, which extends the pH range in which CS is water soluble. NMR was used to calculate the yield of the three locations' substituted compounds (35).

The process of making N-carboxymethyl chitosan from glyoxylic acid in the presence of a reducing agent is the most intriguing. By using ^{1}H and ^{13}C NMR, it was possible to determine the disubstituted (-N(-CH$_2$COOH)$_2$) and distribution of monosubstituted (-NH-CH$_2$COOH) groups.

O-carboxymethyl chitosan has demonstrated its potential as a drug delivery system, effectively delivering therapeutic agents to target sites, while N-Carboxymethyl chitosan has proven its worth as a wound healing material, facilitating tissue regeneration. These latest developments underscore the ongoing evolution of chitosan-based materials, offering innovative solutions with the potential to improve drug delivery and medical treatments, as well as enhance food safety and quality in various applications (87).

4.5.5. N-methylene phosphonic chitosan
These intriguing anionic derivatives, which exhibit certain amphoteric properties, were created under diverse circumstances and shown effective complexation with cations, for example, Ca^{2+} and transition metals (Cd, Zn, Cu, etc.) (88, 89). Metal surfaces are protected from corrosion by the complexation (90). Additionally, these compounds were altered and grafted with alkyl chains to provide amphiphilic qualities that may be used in cosmetic applications (91).

4.5.6. Trimethyl chitosan ammonium
This cationic derivative was thoroughly described by NMR (92)and is generated by quaternizing chitosan with CH$_3$I in NaOH under experimental conditions. It is soluble in water over the entire process pH range.

Under all of the investigated circumstances, a significant reduction in molecular weight is seen during this process. With kaolin dispersions, these polymers exhibit effective flocculating properties, indicating potential applications in paper manufacturing. It has been claimed that additional quaternized derivatives have antistatic properties (93).

4.5.7. Chitosan chains with nanosheets of graphene oxide (GO)

The latest developments in materials science have seen a fascinating collaboration between chitosan chains and graphene oxide (GO) nanosheets, offering a range of interesting applications. GO has high mechanical strength, and when combined with chitosan, it can enhance the overall mechanical properties of the material. Adding GO to chitosan can reduce electrical impedance, making it suitable for applications that require conductivity, such as tissue engineering scaffolds (94). For example, Researchers have successfully designed chitosan-GO nanocomposites for drug delivery systems, taking advantage of chitosan's biocompatibility and GO's excellent drug-loading capabilities. These nanocomposites can efficiently deliver therapeutic agents to targeted sites in the body, potentially revolutionizing the field of pharmaceuticals. Moreover, this innovative combination has also proven beneficial in water purification processes, as GO nanosheets enhance the adsorption capacity of chitosan to remove heavy metals and organic pollutants from contaminated water sources due to its high adsorption capacity and biodegradability. These pioneering developments promise to address critical challenges in healthcare and environmental sustainability and demonstrate the exciting potential of chitosan-GO composites (95, 96).

5. STRUCTURAL CHARACTERIZATION

Scanning electron microscopy, x-ray diffraction, thermogravimetric analysis, nuclear magnetic resonance spectroscopy, and Fourier transform infrared spectroscopy were used to characterize the structure of chitosan and chitin.

5.1.Scanning Electron Microscopy (SEM)

One useful technique for visually verifying the shape and physical condition of the chitin surface is scanning electron microscopy. The surface shape of chitin and chitosan varies depending on the source species. Table 3 lists the surface morphologies of insect chitin and chitosan as nanofibre, nanofibre, nanopores without nanofibres, nanopore, nanofibres without nanopores, smooth surface, and (VI) rough surface. Both nanofibre and nanopore structures are seen in the chitin of house crickets, grasshoppers, orthopteran species, and crickets (11) (Figure. 4). The chitosan of aquatic insects, water-scavenger beetles, desert locusts, and Colorado potato beetles is nanofibrous. According to a few studies, the chitin of black army flies, and cockroaches exhibited both nanopores without nanofibres and nanofibres without nanopore structures (97). Furthermore, the surface morphologies of the chitosan from *Catharsis molossus* and the chitin from *Zophobas morio* and *Holotrichia parallela* were both smooth and rough (98). In this regard, Anand et al. (98) stated that chitin from crabs and squillas was shown to have a morphology similar to that of sponges and cauliflower leaves. Conus chitin's microfibrillar crystalline structure and porosity were revealed via SEM investigation. The chitin derived from krill, shrimp, and lobster shells likewise showed closely spaced fibers. Additionally, microfibril and porous structures were revealed by SEM study of P. monodon's chitin and chitosan surface morphologies (67). One of the key characteristics that influence how well chitin and chitosan are used is their surface shape. Chitin and chitosan in their nanofibre and nanopore forms have potential uses in food, medicine, and textiles.

Table 3: Surface morphology of chitin and chitosan (SEM analysis).

Species	Surface morphology				References
	Chitin	**Pore diameter**	**Chitosan**	**Pore diameter**	
Ranatra linearis	Nanofiber	NA	Nanofibre	NA	(20)
Chrysomya megacephala	NA	NA	Fine regular fibril structure	NA	(88)
Brachytrupes portentosus	Nanopores, thread-like fibrous	0.30–0.89 μm	Big pores and fibres	72.1 nm to 0.12 μm	(89)
Calliptamus barbarus and Oedaleus decorus	Smooth surface	NA	porous and nanofibrillar structure	100–200	(11)
Ephestia kuehniella	Pores and parallel nanofibers	5.2 μm NA	NA	NA	(90)
Hermetia illucens	Honeycomb structure and no porosity	NA	NA	NA	(86)
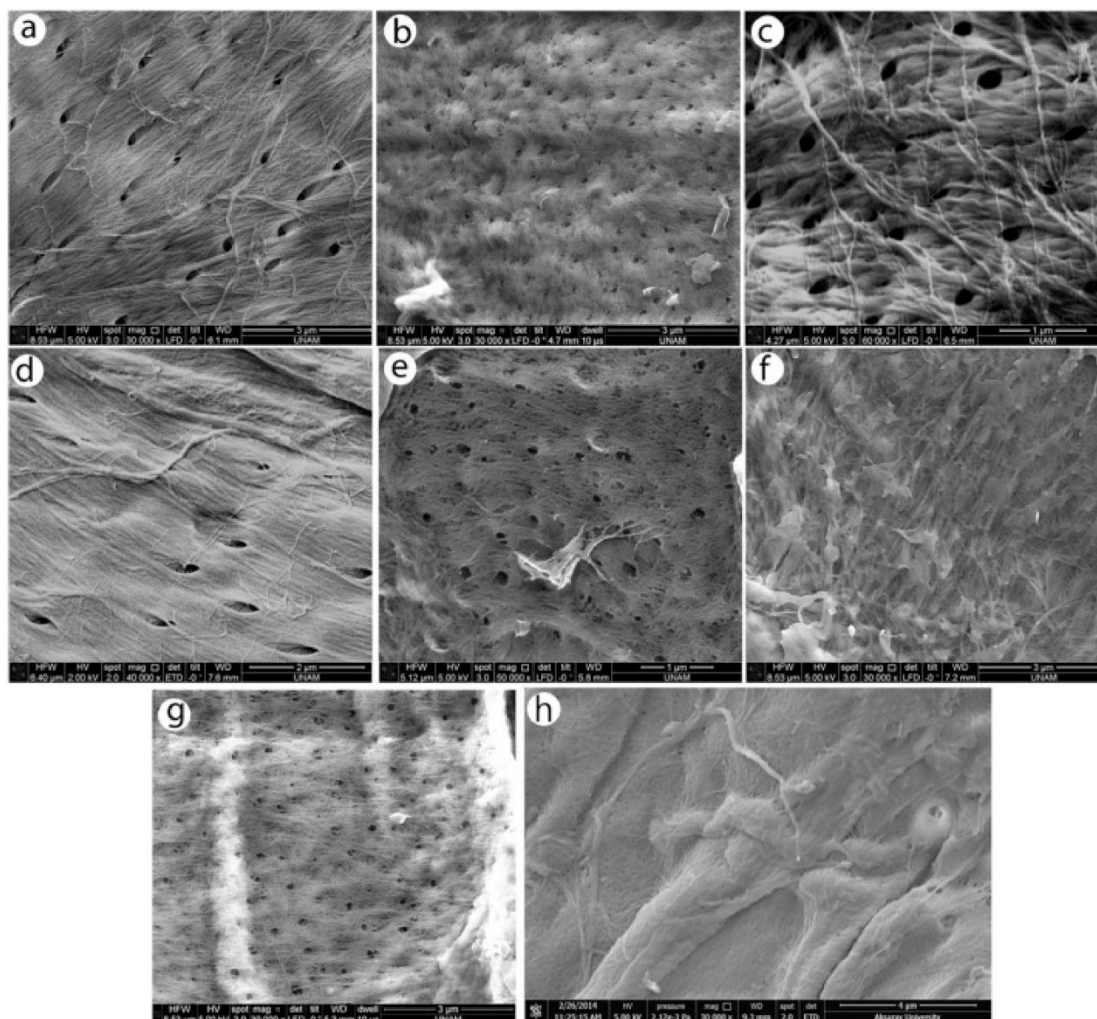
Figure 4: Electron microscopy images of seven different species of grasshoppers (a. Ailopus simulatrix chitin, b. Ailopus strepens chitin, c. Duroniella fracta chitin, d. Duroniella laticornis chitin, e. Oedipoda miniata chitin, f. O. caerulescens chitin, g. Pyrgomorpha cognata chitin and h. Commercial chitin). Reprinted with permission from Kaya et al. (20).

5.2. Fourier Transform Infrared Spectroscopy (FT-IR)

Generally speaking, organic sample identification is done using FT-IR spectroscopy. Chitin comes in three crystalline forms: beta, alpha, and gamma. However, not much is known about the gamma form. The amide I band's existence or absence may be used to distinguish between the α- and β-forms utilizing FT-IR spectra. The amide I band in the α-form splits into two bands at around 1650 and 1620 cm^{-1}, but in the β-form, the 1656 cm^{-1} area has just one amide I band. α- chitin is found in the order Arthropoda, whereas beta chitins are found in squid pens. The amide I band in the FT-IR spectra of the chitin and chitosan extracted from different insects (Figure. 5) is split at 1654 cm^{-1}, 1663 and 1618 cm^{-1}, 1647 and 1654 cm^{-1}, 1654 and 1621 cm^{-1}, 1654, 1617 and 1550 cm^{-1}, and 1656 $cm-1$, respectively. These insects include *Zophobas morio* (51),*Hermetia illucens* (97),*Periplaneta americana* (12), and *Apis mellifera* (102). Chitosan isolated from crab, conus shell, squilla, krill, lobster, and shrimp has an amide I band whose FT-IR spectra are separated at 1643 cm^{-1}, 1634 cm^{-1}, 1625 cm^{-1}, 1628 cm^{-1}, and 1667 cm^{-1}, respectively (103-105). These findings demonstrate that the α-form of chitin and chitosan is extracted from insects and crustacean shell debris.
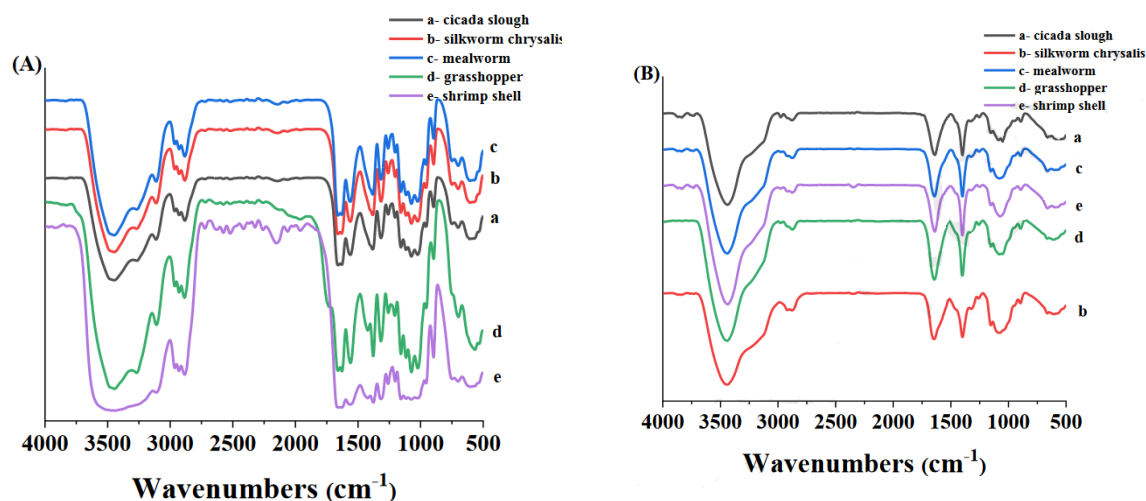
Figure 5: FTIR spectrograms of chitosan and chitin, respectively, taken from five different sources. .Reprinted with permission Luo et al., (96).

5.3. Crystalline Properties

Because they rely on whether chitin and chitosan are crystalline or amorphous, the CrI values of these substances are important in identifying possible application regions. One may use X-ray diffraction to identify this. However, the crystalline structure also symbolizes the size and purity of the biopolymer's crystals. As observed in earlier research, chitin from Hermetia illucens in the larval (33.05%) and prepupal (35.14%) stages has a low crystalline index (CrI%) (106). Nonetheless, significant CrI values have also been reported for the same species' puparium (68.4%) and adult (87.92%) stages. It has been discovered that high molarity (2 M) NaOH increases the amorphous character and decreases the crystallites of insect chitin during the deproteinization process (106). Additionally, compared to the higher CrI that had a rough and uneven surface, the resulting chitin's surface morphology had a lower CrI with an amorphous area and a porous surface. Park et al. (107) state that the ratio of the crystalline contributing area to the overall area was used to calculate the CrI. Likewise, Agabus bipustulatus and Brachytrupes portentosus yielded seven and ten different peaks at 2θ, respectively, with the highest CrI values of 90.6% and 88.02% among the total XRD peaks. This result also shows the impurity of the chitin that was extracted with N-6.02% from B. portentosus. The crystallinity indices of the chitosan from mealworms, shrimp shells, and grasshoppers were comparable, and the CrI values of the chitosan from *silkworm chrysalises*, *cicada slough*, *grasshoppers*, and mealworms were found to be 32.9%, 64.8%,51.9%, 49.1%, and 50.1%, respectively (Figure 6). Anand et al. (98) reported that the chitosan derived from crab and squilla had two distinct crystalline peaks at 2θ = 10.3° and 19.2° and 2θ = 10.2° and 19.5°. These peaks were slightly moved to a higher diffraction angle and demonstrated semi-crystalline chitosan. Six crystalline peaks with a CrI between 69 and 76% were shown by *Vespa orientalis*, *Vespa crabro*, V*espula Argynnis Pandora,germanica*, and Ailopus simulatrix (12).
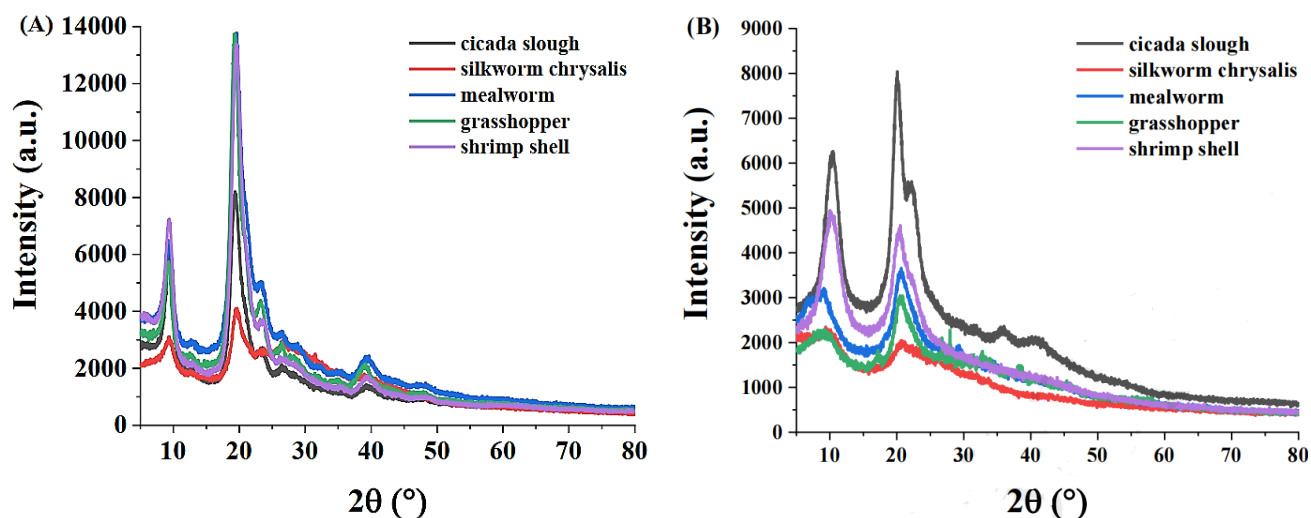
Figure 6: XRD of (A) chitin and (B) chitosan extracted from five sources: shrimp shells , mealworm, grasshopper, silkworm chrysalis, and cicada slough. Reprinted with permission Luo et al., (96).

6. APPLICATIONS OF CHITOSAN

Chitosan has garnered considerable scientific and commercial attention due to its macromolecular structure, biodegradability, biocompatibility, bioactivity, and other intrinsic functional features. CS has practical applications in the cosmetology industry, food, paper industries, textile, agriculture, sludge dewatering, and wastewater treatment (108). Figure 7 lists the main uses of chitosan. The most significant and recent uses of chitosan are highlighted in this section.
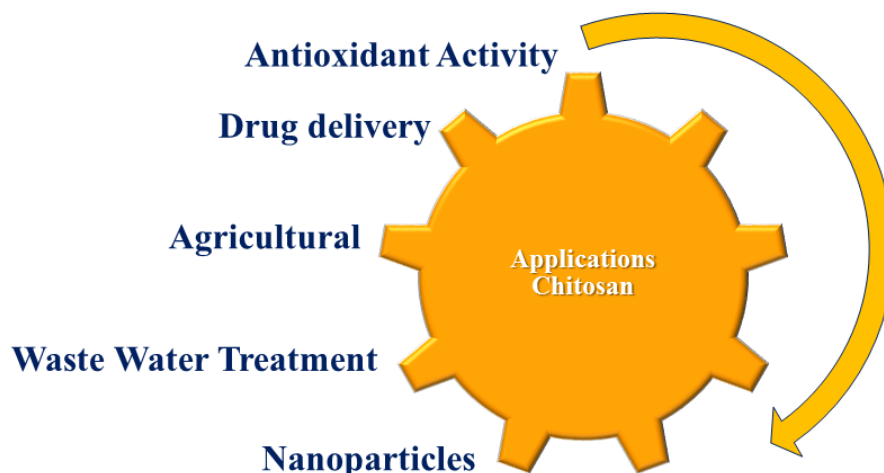
Figure 7: Different applications of chitosan.

6.1. Chitosan's Influence on How Metal Nanoparticles are Formed

CS can be utilized as a multipurpose agent in the environmentally friendly manufacturing of metal nanoparticles. CS can have an impact on metal nanoparticles both during the production and functionalization processes. Chitosan, which has a positive charge, interacts electrostatically with nanoparticles, which have a negative charge (which have the negative capping agent) occurs when the cationic polymer CS is introduced to the reaction solution (109, 110), or CS is absorbed on the surface of the metal nanoparticles, as shown in Figure 8 (111), resulting in a CS shell surrounding the nanoparticles. The CS can be added either before or after the nanoparticles are created, depending on the production procedure. As a result, CS directly affects how nanoparticles are made. Therefore, CS has a direct impact on how nanoparticles are produced. CS can function as a reducing, stabilizing, and size-controlling agent for the synthesis of metal nanoparticles. CS is used to modify the surface of nanoparticles during the functionalization process to enhance their biocompatibility and drug-carrying capabilities. The harmful effects on the environment and human health can be mitigated by using CS in the production of metal nanoparticles (112, 113).
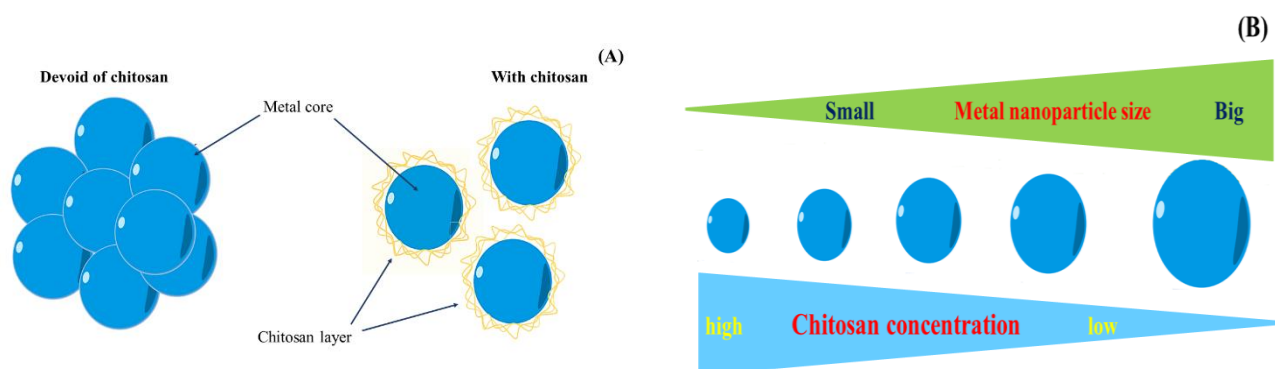
Figure 8: Influence of CS capping on the dispersion of NPs (A) and The relationship between chitosan concentration and the size of NPs (B).

6.2. Application of Chitosan in Agriculture

Plant diseases can be prevented and treated in agriculture with chitosan. They are effective against bacteria, viruses, fungi, and other pests in the soil. Adding chitosan changes the rhizosphere and phyllosphere's environmental conditions, tipping the microbial balance in favor of beneficial organisms and against plant pathogens. It is known that chitosan fragments in host plants cause the accumulation of phytoalexins, lignin synthesis, callose formation, and proteinase inhibitors, among other defense responses. Chitosan and its derivatives also exhibit antiviral and antibacterial properties. In soil, parasitic nematodes have been successfully

eliminated by using these polysaccharides. Chitosan film provides antibacterial protection and increases the fruits' and vegetables' storage life (114). Chitosan and its derivatives positively impact the metabolism of fruits and plants. This leads to increased crop yields and germination.

6.3. Food Industry
Enclosing beef in electrospun chitosan fibers while it is being dry-aged for up to three weeks produced superior outcomes than conventional dry-aging in terms of lower counts of bacteria, lighter look, molds, yield, yeasts, and less muscle denaturation. While lactic acid bacteria formation was seen, wet-aging of beef had low weight and trimming losses (115).

6.4. Waste Water Treatment
Water pollution is caused by a variety of harmful elements, for example, heavy metals, dyes, aromatic chemicals, etc (116). There is a significant environmental problem that could have serious health implications (117). As a result, chitin and chitosan, which are both inexpensive, are now extensively suggested for wastewater treatment. Giabl et al. (118)investigated the effects of chitosan characteristics on heavy metal, dye, and organic chemical adsorption. Chitosan-based materials can be used to remove anionic dyes, as Crinni and Badot have discovered. Chitosan has been applied to the treatment of aquaculture effluent as a coagulant, adsorbent, and bactericide. Low molecular weight and high DD chitosan samples increase the effectiveness of chitosan in coagulating and flocculating organic solutions at pH levels close to neutral and with little ionic strength (119).

Chitosan has emerged as a prominent solution for the mitigation of heavy metal contamination. Numerous studies have shown that chitosan can effectively remove Cr (VI), As (III), As (V), heavy metal oxyanions (Cu (II), Pb (II), Cd (II), Hg (II), Pd (II) and Pt (IV) (120). According to Ghinia et al. (121), chitosan has demonstrated significant efficacy as an adsorbent for zinc and many other metal ions present in wastewater, with the added advantage of being recyclable. For use in composites, the mechanical properties of chitosan are stabilized and improved by grafting, cross-linking, and functionalization. In contrast to poly (4-vinyl pyridine) modified activated carbon (53.7 mg/g) and ethylenediamine-functionalized Fe_3O_4 (61.35 mg/g). Effective elimination of Cr(VI) (67.66 mg/g) was demonstrated in another investigation by Li et al. (45).

The occurrence of water pollution due to metal ions is widespread and commonly attributed to industrial activities. Toxicity is a characteristic shown by certain substances, which can have detrimental impacts on organisms. Water and wastewater can undergo the process of biosorption utilizing chitosan to facilitate their removal. Heavy metal (including Pb, Cu, Ag, Ni, Cr, As, and others)adsorption has been demonstrated for chitosan and its derivatives, precious metals (such as Pd, Au, and Pt), as well as radionuclides.

In their study, Li et al. (45) synthesized a magnetic-cyclodextrin-chitosan (CC) material that exhibits enhanced separation properties and increased adsorption capacity. Furthermore, the incorporation of graphene oxide (GO) into the carbon composite (CC) was utilized to enhance the adsorption competence for metal elimination by chemical bonding. The findings of the study revealed that the adsorption capacity of magnetic-cyclodextrin-chitosan/graphene oxide (CCGO) for Cr(VI) exhibited a higher removal efficiency (67.66 mg/g) compared to other sorbents like poly(4-vinyl pyridine) modified activated carbon (53.7 mg/g)and ethylenediamine-functionalized Fe_3O (61.35 mg/g). The observed phenomenon can be attributed to the augmentation in the surface area resulting from the greater abundance of hydroxyl and amino groups, in addition to the magnetic characteristics shown. The findings of the study indicate that the efficacy of removal was greater under conditions of low. Additionally, it was observed that the adsorption equilibrium of CCGO followed the Langmuir isotherm model.

6.5. Antioxidant Activity
CS and its derivatives have been shown to have powerful antioxidant effects. By scavenging free radicals, they can lessen lipid oxidation thanks to their ability to bind metals. Molecular weight, viscosity, and DD all have an impact on the antioxidant properties of CS and chitin (122).

6.6. Chitosan as Lipid-Lowering Agent
Because of its capacity to lower serum cholesterol, chitosan is utilized as a dietary additive. It decreases lipid absorption by forming hydrophobic interactions with neutral lipids like cholesterol and other sterols. Chitosan works in the digestive system as a fat scavenger, excreting fat and cholesterol as a result of its inhibitory effect on fat absorption. Chitosan satisfies dietary fiber requirements such as high viscosity, non-digestibility, and lower GI tract water-binding ability. From a physiological standpoint, the primary role of dietary fiber is to reduce cholesterol levels and promote weight loss by reducing intestinal lipid absorption. Its positive ionic charge distinguishes it from other dietary fibers, allowing it to chemically bind with fats, bile acids, and negatively charged lipids.CS has an LD_{50} (median lethal dosage) of roughly 16 $g.kg^{-1}$, which is equivalent to salt and glucose values, indicating that it is safe to use for lengthy periods (123).

6.7. Delivery of Drugs
The goal of drug delivery systems is to enable controlled drug release, increase delivery time, increase target specificity, and reduce drug dose and time. These systems are considered a breakthrough in the pharmaceutical industry and are designed for the delivery of active ingredients, peptides, vaccines, proteins, and genes (124). Due to their degradability, natural polymers, in particular chitosan, offer a wide range of vehicles for drugs. Other advantages of CS as a drug carrier are its good biocompatibility and low toxicity. CS can be formulated in various ways depending on the management and the goals of the function. In addition, the protonated amino groups of D-

glucosamine in the chitosan structure allow it to adhere to negatively charged mucus layers and penetrate deep layers of the epithelium through electrostatic contact. CS has been used as a vehicle for drug delivery via the nasal, buccal, pulmonary, and ocular routes because of its mucoadhesive effect (125, 126). Chemical modifications such as carboxymethylation, acetylation, thiolation, quaternization, and others affect the problem of the insolubility of chitosan under physiological conditions, which is disadvantageous for successful drug delivery (127). N, N, N-Trimethyl-CS (TMC), thiolated CS obtained by exchanging amino groups with thioglycolic acid, N-acylated CS products, and carboxymethylated CS are examples of quaternary ammonium chitosan derivatives with permanent positive charges. They are known for their high solubility over a wide pH range, thereby increasing the mucosa (128). Growth factors, anti-inflammatories, antibiotics, vaccines, and chemotherapeutic agents have been delivered to target cells using CS-based drug carriers in micro/nanoparticles, gels, films, sponges, and fibers. In dentistry, CS-based drug delivery systems are used to treat periodontitis, root canal treatments (endodontics), and dental caries and to administer long-acting local anesthesia (129).

Chitosan derivatives have been used in targeted drug delivery systems to improve treatment outcomes and reduce side effects. Colon-specific delivery systems have been developed for diseases like Crohn's disease, ulcerative colitis, and irritable bowel syndrome. These systems use water-soluble amphoteric chitosan derivatives and o-carboxymethyl chitosan to prevent drug degradation in the stomach and small intestine. Spherical microcapsules have been used for intestine-targeted drug delivery, improving bioavailability and stability. Liver-targeted delivery systems use reticulated endothelial passive capture microparticles or active targeting based on liver receptor recognition. Insulin administration using fatty-acid-modified quaternary ammonium chitosan derivative nanoparticles has shown improved anti-diabetic effectiveness and increased hepatocyte absorption. Ferulic acid has been delivered to the liver using modified chitosan nanoparticles and glycyrrhizic acid. Acetylated low molecular weight chitosan is used in kidney and lung-targeted administration to facilitate renal medication delivery. The potential of a newly synthesized folic acid-grafted polyethylene glycol chitosan copolymer to lessen the adverse effects of very hazardous medications has been shown.

Chitosan derivative nanoparticles have the potential to improve drug delivery and transport by improving bioadhesion and permeability. These nanoparticles are used in targeted drug preparation, sustained release, and increasing drug absorption. Delivery carriers of chitosan include microspheres, nanoparticles, micelles, and gels, with particle sizes ranging from 1–500 µm. These nanoparticles can pass through biological barriers and provide better stability, tissue permeability, and sustained drug-release properties (83).

Chitosan derivative nanoparticles are also being researched for controlled drug delivery, as some drugs have short release times and require more doses to maintain plasma balance. The continuous delayed release of chitosan derivative nanoparticles may increase bioavailability and therapeutic effectiveness while lowering negative effects. Protein drugs are preferred due to their targeting and biocompatibility, but they have drawbacks such as enzyme degradation, low permeability in the intestinal epithelium, and poor oral absorption (130).

Peptide-loaded nanoparticles with improved thermal stability and controlled in vitro release are produced when chitosan derivative nanoparticles interact with peptides via hydrogen bonds and static electricity. Insulin-loaded quaternary ammonium chitosan nanoparticles modified by fatty acid have shown excellent loading capacity and efficiency (131, 132).

Gene therapy is a promising strategy for challenging diseases, and a safe and effective gene delivery system is critical for successful application. Non-viral vectors offer advantages such as ease of production, high yield, and low cost, making them suitable for gene delivery (133).

The mucosal immune system, which includes lymphoid tissues in the respiratory, gastrointestinal tract, genitourinary mucosa, and some exocrine glands, plays a crucial role in preventing infectious diseases. Mucosal vaccines have shown potential in enhancing mucosal immunity, as local antibodies work faster than serum antibodies and have a longer maintenance time. The process of immunity is shown in Figure 9 (134).
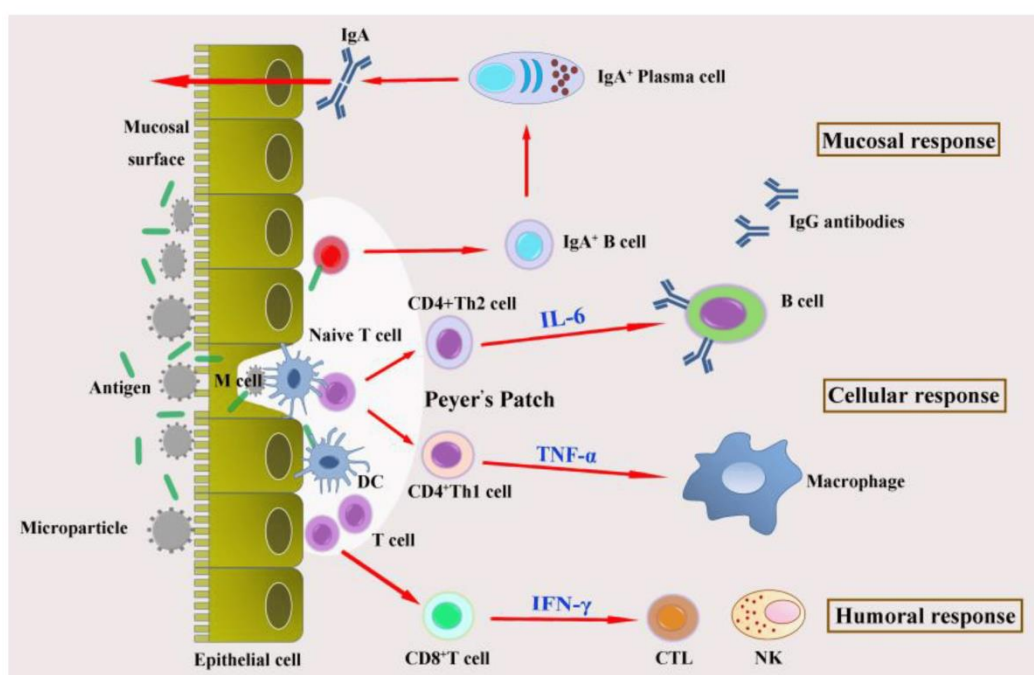
Figure 9: The generation of antibodies is immune-related. Reproduced with permission from Wang et al. (72).

Chitosan derivative nanoparticles can facilitate transmembranal drug delivery and have better water solubility, mucoadhesivity, and antigen absorption. They can serve as vaccine adjuvants or delivery carriers for mucosal immunity. Composite biological nanomaterials have been synthesized to achieve a higher mucosal immune effect. Intranasal immunization with chitosan nanoparticles induced stronger cellular, humoral, and mucosal immune responses than commercially available vaccines. Chitosan-coated PLGA nanoparticles have also been shown to induce humoral, stronger cellular, and mucosal immune responses than plasmid DNA alone. These results imply that, in the case of DNA vaccines, chitosan-coated nanoparticles may serve as an effective mucosal immunization delivery mechanism (135, 136).

6.8. Antimicrobial Activity
In recent years, there have been exciting developments in the understanding and application of the antimicrobial activity of chitosan (137). The ability of chitosan to inhibit the growth of various microorganisms, including bacteria and fungi, has drawn great attention in the fields of medicine, food preservation, and agriculture. For example, chitosan has been used as a natural, environmentally friendly antimicrobial agent in food packaging materials, extending the shelf life of perishable goods and reducing the need for chemical preservatives. In healthcare, chitosan-based wound dressings have been developed to prevent infection and speed up the healing process. As antibiotic resistance becomes a growing concern, exploring and utilizing chitosan's antimicrobial properties represents a promising avenue for infection control health promotion and sustainability in diverse industries (138).

6.9. Other Applications
6.9.1. Cosmetics
Chitosan has excellent film-forming abilities and a bioadhesive nature. Thus, it can function either as a delivery system or as an active component, prolonging the contact time of an active substance with the dermis and enhancing the penetration of active compounds in a regulated and long-term manner. These are the two main uses in cosmetic and cosmetic products. Essential oils and, for example, active ingredients, antioxidants, enzymes, and vitamins are partly contained in cosmeceuticals, with chitosan as the main component. Due to its antibacterial properties, CS is often used in dental care. In toothpaste, it can slow down the growth of oral germs and stop tooth erosion (139). Additionally, it can be used as a healthy substitute for traditional preservatives. CS is also an effective ingredient for hair care. Increases hair softness and flexibility, reduces static electricity, removes oils and sebum, retains moisture in the hair, fights dandruff fungus, and stimulates hair growth.

6.9.2. Tissue engineering
It is the process of improving or replacing biological functions by combining cells, artificial materials, and appropriate biochemical variables. It can be applied to several things, including partial or complete tissue replacement or repair (for instance, muscle, bone, blood vessels, skin, the bladder, and cartilage) (140). With recent significant advancements, chitosan-based biomaterials have emerged as a key area of study in tissue engineering. It gives the restored tissues certain mechanical and structural qualities that allow them to function properly (140).

Chitosan-based biomaterials have shown promising potential in skin tissue engineering due to their biodegradable, non-toxic, and biocompatible properties. These materials can be modified to

develop multifunctional structures with a morphology similar to the natural matrix (141).

Several studies have explored the potential of chitosan-based membrane formulations in skin tissue engineering. For example, one study designed a chitosan coating using titanium dioxide nanoparticles, which demonstrated potential structural and functional regenerative properties. The membranes also exhibited antibacterial activities against Staphylococcus aureus and showed rapid growth and reduced oxidative stress and apoptosis when applied to L929 mouse fibroblast cells (142).

Another study prepared chitosan membranes loaded with glycerol and antibacterial agents, which provided long-term stability and antibacterial activity against the growth of *S. aureus* and *E. coli*. An in vitro culture test of dermal fibroblasts showed enhanced proliferation of fibroblast cells on membranes, suggesting that these membranes could be used as an antimicrobial dressing system to treat skin burns (143).

In a different study, the combined use of ibuprofen and chitosan-polyvinyl alcohol membrane was examined for its capacity to cure wounds. The drug release was shown to be maintained, and normal human dermal fibroblasts were not adversely affected. Additionally, biocompatible microfibre membranes made of silk and chitosan demonstrated improved mechanical qualities and increased cell proliferation (144).

Another study examined the anti-inflammatory performance of the chitosan-hyaluronan-edaravone membrane during wound healing, which resulted in a lower inflammatory response and supported the migration of fibroblasts, keratinocytes, and endothelial cells, effectively promoting wound healing (144).

Another study prepared iodine-sodium alginate complex systems based on hydroxylated lecithin and chitosan and tested them on burn wound rat models. The fabricated membranes showed superior repair properties in deep, partial-thickness rat burn models, with high vascular endothelial growth factor expression observed (144).

Chitosan-based hydrogels have gained great interest in skin tissue engineering due to their high porosity, water absorption, swelling ability, satisfactory mechanical properties, biocompatibility, and biodegradability. These hydrogels have been widely reported for their skin rejuvenation potential. However, since chitosan hydrogels have poor mechanical strength, mixes of chitosan with other natural or synthetic polymers work better. Hydrogels based on chitosan may also have their mechanical strength increased by cross-linkers (144).

Several studies have investigated the use of chitosan-lignin hydrogels, which have shown improved cell growth capabilities and increased fibroblast penetration. Chitosan gelatin loaded with human dermal fibroblasts has also been investigated

for its wound-healing potential in mice. The scaffold was highly porous and cross-linked, with human dermal fibroblasts showing attachment and migration onto the scaffold. In vivo experiments in mice demonstrated enhanced re-epithelialization of a skin wound treated with a transdermal fibroblast-loaded hydrogel (145).

When the regeneration capacity of chitosan hydrogel made with oxygenated fluorinated methacrylamide was evaluated, it revealed higher collagen fiber contents, better re-epithelialization, and enhanced vascularization. Another study examined alginate-chitosan hydrogel synthesized with hesperidin on injured mouse models, which demonstrated biodegradability and bactericidal properties. It has been discovered that the hydrogel reduces inflammation and encourages fibroblast growth, which speeds up the creation of epidermal layers, tissue granulation, and remodeling (145).

A chitosan-polyethylene glycol hydrogel impregnated with silver nanoparticles has been tested for the treatment of chronic diabetic wounds. The hydrogel showed high porosity and swelling properties, increased antimicrobial activity against *E. coli*, Pseudomonas aeruginosa, *Bacillus subtilis*, and *S. aureus*, and strong antioxidant activity. In investigations on wound healing, the hydrogel outperformed the control group in terms of keratinocyte migration, re-epithelialization, and wound contraction (146).

7. CONCLUSIONS

In this comprehensive review of chitosan, its sources, properties, extraction methods, derivatives, structural characterization, and wide-ranging applications are explored. From the depths of crustaceans to the intricacies of fungi, we have navigated through various sources, revealing the unique qualities of chitosan, including its molecular weight, viscosity, degree of deacetylation, crystallinity, and its interesting ability to form complexes with metals. The extraction process, which includes demineralization, deproteinization, decolorization, and deacetylation, is dissected to highlight methods that unleash chitosan's potential.

Furthermore, the article highlighted the diversity of chitosan derivatives and provided insight into their structural characterization. By exploring the applications of chitosan in diverse fields, from pharmaceuticals to agriculture, the study underscores the importance of this biopolymer in addressing contemporary challenges.

In concluding this review, it is clear that chitosan, with its countless properties and applications, represents a promising and sustainable material for future progress. The journey through its complexities invites researchers and practitioners alike to further explore and harness the potential of chitosan for innovative solutions in many industries.

8. CONFLICT OF INTEREST

The authors possessed no relevant financial or non-financial interests.

9. REFERENCES

1. Elamri A, Zdiri K, Hamdaoui M, Harzallah O. Chitosan: A biopolymer for textile processes and products. Text Res J [Internet]. 2023 Mar 3;93(5–6):1456–84. Available from: <URL>.

2. Pellis A, Guebitz GM, Nyanhongo GS. Chitosan: Sources, Processing and Modification Techniques. Gels [Internet]. 2022 Jun 21;8(7):393. Available from: <URL>.

3. Erdogan S, Kaya M. High similarity in physicochemical properties of chitin and chitosan from nymphs and adults of a grasshopper. Int J Biol Macromol [Internet]. 2016 Aug 1;89:118–26. Available from: <URL>.

4. Terkula Iber B, Azman Kasan N, Torsabo D, Wese Omuwa J. A Review of Various Sources of Chitin and Chitosan in Nature. J Renew Mater [Internet]. 2022;10(4):1097–123. Available from: <URL>.

5. Amor I Ben, Hemmami H, Laouini SE, Abdelaziz AG, Barhoum A. Influence of chitosan source and degree of deacetylation on antibacterial activity and adsorption of AZO dye from water. Biomass Convers Biorefinery [Internet]. 2023 Jan 11;1–11. Available from: <URL>.

6. Broek L, Boeriu CG, Stevens C. Chitin and Chitosan: Properties and Applications. 2019;

7. Allman AL, Williams EP, Place AR. Growth and Enzyme Production in Blue Crabs (*Callinectes sapidus*) Fed Cellulose and Chitin Supplemented Diets. J Shellfish Res [Internet]. 2017 Apr 1;36(1):283–91. Available from: <URL>.

8. Liu S, Sun J, Yu L, Zhang C, Bi J, Zhu F, et al. Extraction and Characterization of Chitin from the Beetle Holotrichia parallela Motschulsky. Molecules [Internet]. 2012 Apr 17;17(4):4604–11. Available from: <URL>.

9. Vetter J. Chitin content of cultivated mushrooms Agaricus bisporus, Pleurotus ostreatus and Lentinula edodes. Food Chem [Internet]. 2007 Jan 1;102(1):6–9. Available from: <URL>.

10. Di Mario F, Rapanà P, Tomati U, Galli E. Chitin and chitosan from Basidiomycetes. Int J Biol Macromol [Internet]. 2008 Jul 1;43(1):8–12. Available from: <URL>.

11. Kaya M, Baran T. Description of a new surface morphology for chitin extracted from wings of cockroach (Periplaneta americana). Int J Biol Macromol [Internet]. 2015 Apr 1;75:7–12. Available from: <URL>.

12. Kaya M, Baran T, Karaarslan M. A new method for fast chitin extraction from shells of crab, crayfish and shrimp. Nat Prod Res [Internet]. 2015 Aug 3;29(15):1477–80. Available from: <URL>.

13. Marei NH, El-Samie EA, Salah T, Saad GR, Elwahy AHM. Isolation and characterization of chitosan from different local insects in Egypt. Int J Biol Macromol [Internet]. 2016 Jan 1;82:871–7. Available from: <URL>.

14. Kou S (Gabriel), Peters LM, Mucalo MR. Chitosan: A review of sources and preparation methods. Int J Biol Macromol [Internet]. 2021 Feb 1;169:85–94. Available from: <URL>.

15. Aranaz I, Alcántara AR, Civera MC, Arias C, Elorza B, Heras Caballero A, et al. Chitosan: An Overview of Its Properties and Applications. Polymers (Basel) [Internet]. 2021 Sep 24;13(19):3256. Available from: <URL>.

16. Campana-Filho SP, Britto D de, Curti E, Abreu FR, Cardoso MB, Battisti M V., et al. Extraction, structures and properties of alpha-and beta-chitin. Quim Nova [Internet]. 2007 Jun;30(3):644–50. Available from: <URL>.

17. Bastiaens L, Soetemans L, D'Hondt E, Elst K. Sources of Chitin and Chitosan and their Isolation. In: Chitin and Chitosan: Properties and Applications [Internet]. Wiley; 2019. p. 1–34. Available from: <URL>.

18. Sanuja RG, Kalutharage NK, Cumaranatunga PRT. Selection of the most suitable crustacean exoskeleton waste from fish processing industry to isolate chitosan. Sri Lanka J Aquat Sci [Internet]. 2017;22(1):45–53. Available from: <URL>.

19. Casadidio C, Peregrina DV, Gigliobianco MR, Deng S, Censi R, Di Martino P. Chitin and Chitosans: Characteristics, Eco-Friendly Processes, and Applications in Cosmetic Science. Mar Drugs [Internet]. 2019 Jun 21;17(6):369. Available from: <URL>.

20. Kaya M, Baran T, Erdoğan S, Menteş A, Aşan Özüsağlam M, Çakmak YS. Physicochemical comparison of chitin and chitosan obtained from larvae and adult Colorado potato beetle (Leptinotarsa decemlineata). Mater Sci Eng C [Internet]. 2014 Dec 1;45:72–81. Available from: <URL>.

21. Trabelsi I, Ayadi D, Bejar W, Bejar S, Chouayekh H, Ben Salah R. Effects of Lactobacillus plantarum immobilization in alginate coated with chitosan and gelatin on antibacterial activity. Int J Biol Macromol [Internet]. 2014 Mar 1;64:84–9. Available from: <URL>.

22. Al Sagheer FA, Al-Sughayer MA, Muslim S, Elsabee MZ. Extraction and characterization of chitin and chitosan from marine sources in Arabian Gulf. Carbohydr Polym [Internet]. 2009 Jun 10;77(2):410–9. Available from: <URL>.

23. Rasti H, Parivar K, Baharara J, Iranshahi M, Namvar F. Chitin from the Mollusc Chiton: Extraction, Characterization and Chitosan Preparation. Iran J Pharm Res IJPR [Internet]. 2017 Dec 1;16(1):366. Available from: <URL>.

24. Hahn T, Roth A, Ji R, Schmitt E, Zibek S. Chitosan production with larval exoskeletons derived from the insect protein production. J Biotechnol [Internet]. 2020 Feb 20;310:62–7. Available from: <URL>.

25. Hamed I, Özogul F, Regenstein JM. Industrial applications of crustacean by-products (chitin, chitosan, and chitooligosaccharides): A review. Trends Food Sci Technol [Internet]. 2016 Feb 1;48:40–50. Available from: <URL>.

26. Huet G, Hadad C, Husson E, Laclef S, Lambertyn V, Araya Farias M, et al. Straightforward extraction and selective bioconversion of high purity chitin from Bombyx eri larva: Toward an integrated insect biorefinery. Carbohydr Polym [Internet]. 2020 Jan 15;228:115382. Available from: <URL>.

27. Jucker C, Lupi D, Moore CD, Leonardi MG, Savoldelli S. Nutrient Recapture from Insect Farm Waste: Bioconversion with Hermetia illucens (L.) (Diptera: Stratiomyidae). Sustainability [Internet]. 2020 Jan 2;12(1):362. Available from: <URL>.

28. John Kasongo K, Tubadi DJ, Bampole LD, Kaniki TA, Kanda NJM, Lukumu ME. Extraction and characterization of chitin and chitosan from Termitomyces titanicus. SN Appl Sci [Internet]. 2020 Mar 14;2(3):406. Available from: <URL>.

29. Kaczmarek MB, Struszczyk-Swita K, Li X, Szczęsna-Antczak M, Daroch M. Enzymatic Modifications of Chitin, Chitosan, and Chitooligosaccharides. Front Bioeng Biotechnol [Internet]. 2019 Sep 27;7:243. Available from: <URL>.

30. Zielinska K, Shostenko AG, Truszkowski S. Analysis of chitosan by gel permeation chromatography. High Energy Chem [Internet]. 2014 Mar 5;48(2):72–5. Available from: <URL>.

31. Aranaz I, Mengibar M, Harris R, Panos I, Miralles B, Acosta N, et al. Functional Characterization of Chitin and Chitosan. Curr Chem Biol [Internet]. 2009 May 1;3(2):203–30. Available from: <URL>.

32. Lavertu M, Méthot S, Tran-Khanh N, Buschmann MD. High efficiency gene transfer using chitosan/DNA nanoparticles with specific combinations of molecular weight and degree of deacetylation. Biomaterials [Internet]. 2006 Sep 1;27(27):4815–24. Available from: <URL>.

33. Dutta PK, Ravikumar MN V., Dutta J. Chitin and Chitosan for Versatile Applications. J Macromol Sci Part C Polym Rev [Internet]. 2002 Aug 19;42(3):307–54. Available from: <URL>.

34. Franco TT, Peter MG. Advances in chitin science [Internet]. 2010. Available from: <URL>.

35. Rinaudo M. Chitin and chitosan: Properties and applications. Prog Polym Sci [Internet]. 2006 Jul 1;31(7):603–32. Available from: <URL>.

36. Fatima B. Quantitative analysis by IR: determination of chitin/chitosan DD. In: Khan M, do Nascimento GM, El-Azazy M, editors. Modern Spectroscopic Techniques and Applications [Internet]. London: IntechOpen; 2020. Available from: <URL>.

37. Rusu-Balaita L, Desbrieres J, Rinaudo M. Formation of a biocompatible polyelectrolyte complex: chitosan-hyaluronan complex stability. Polym Bull [Internet]. 2003 Apr 1;50(1–2):91–8. Available from: <URL>.

38. Heux L, Brugnerotto J, Desbrières J, Versali M-F, Rinaudo M. Solid State NMR for Determination of Degree of Acetylation of Chitin and Chitosan. Biomacromolecules [Internet]. 2000 Dec 1;1(4):746–51. Available from: <URL>.

39. Ma J, Xin C, Tan C. Preparation, physicochemical and pharmaceutical characterization of chitosan from Catharsius molossus residue. Int J Biol Macromol [Internet]. 2015 Sep 1;80:547–56. Available from: <URL>.

40. Kaya M, Baran T, Mentes A, Asaroglu M, Sezen G, Tozak KO. Extraction and Characterization of α-Chitin and Chitosan from Six Different Aquatic Invertebrates. Food Biophys [Internet]. 2014 Jun 8;9(2):145–57. Available from: <URL>.

41. Akpan EI, Gbenebor OP, Adeosun SO. Synthesis and characterisation of chitin from periwinkle (Tympanotonus fusatus (L.)) and snail (Lissachatina fulica (Bowdich)) shells. Int J Biol Macromol [Internet]. 2018 Jan 1;106:1080–8. Available from: <URL>.

42. Ogawa K, Yui T, Okuyama K. Three D structures of chitosan. Int J Biol Macromol [Internet]. 2004 Apr 1;34(1–2):1–8. Available from: <URL>.

43. Kawada J, Yui T, Okuyama K, Ogawa K. Crystalline Behavior of Chitosan Organic Acid Salts. Biosci Biotechnol Biochem [Internet]. 2001 Jan 22;65(11):2542–7. Available from: <URL>.

44. Kalita N, Baruah PP. Cyanobacteria as a potent platform for heavy metals biosorption: Uptake, responses and removal mechanisms. J Hazard Mater Adv [Internet]. 2023 Aug 1;11:100349. Available from: <URL>.

45. Guibal E. Interactions of metal ions with chitosan-based sorbents: a review. Sep Purif Technol [Internet]. 2004 Jul 15;38(1):43–74. Available from: <URL>.

46. Teli MD, Sheikh J. Extraction of chitosan from shrimp shells waste and application in antibacterial finishing of bamboo rayon. Int J Biol Macromol [Internet]. 2012 Jun 1;50(5):1195–200. Available from: <URL>.

47. Bello VE, Olafadehan OA. Comparative investigation of RSM and ANN for multi-response modeling and optimization studies of derived chitosan from Archachatina marginata shell. Alexandria Eng J [Internet]. 2021 Aug 1;60(4):3869–99. Available from: <URL>.

48. Yen M-T, Yang J-H, Mau J-L. Physicochemical

characterization of chitin and chitosan from crab shells. Carbohydr Polym [Internet]. 2009 Jan 5;75(1):15–21. Available from: <URL>.

49. Song Y, Kim M, Moon C, Seo D, Han YS, Jo YH, et al. Extraction of chitin and chitosan from larval exuvium and whole body of edible mealworm, *Tenebrio molitor*. Entomol Res [Internet]. 2018 May 23;48(3):227–33. Available from: <URL>.

50. Fournier P, Szczepanski CR, Godeau R-P, Godeau G. Chitosan Extraction from Goliathus orientalis Moser, 1909: Characterization and Comparison with Commercially Available Chitosan. Biomimetics [Internet]. 2020 Apr 26;5(2):15. Available from: <URL>.

51. Shin C-S, Kim D-Y, Shin W-S. Characterization of chitosan extracted from Mealworm Beetle (Tenebrio molitor, Zophobas morio) and Rhinoceros Beetle (Allomyrina dichotoma) and their antibacterial activities. Int J Biol Macromol [Internet]. 2019 Mar 15;125:72–7. Available from: <URL>.

52. Xia Z, Chen J, Wu S. Hypolipidemic activity of the chitooligosaccharides from Clanis bilineata (Lepidoptera), an edible insect. Int J Biol Macromol [Internet]. 2013 Aug 1;59:96–8. Available from: <URL>.

53. Simionato JI, Paulino AT, Garcia JC, Nozaki J. Adsorption of aluminium from wastewater by chitin and chitosan produced from silkworm chrysalides. Polym Int [Internet]. 2006 Nov 22;55(11):1243–8. Available from: <URL>.

54. Savin S, Craciunescu O, Oancea A, Ilie D, Ciucan T, Antohi LS, et al. Antioxidant, Cytotoxic and Antimicrobial Activity of Chitosan Preparations Extracted from *Ganoderma Lucidum* Mushroom. Chem Biodivers [Internet]. 2020 Jul 5;17(7):e2000175. Available from: <URL>.

55. Luo Q, Wang Y, Han Q, Ji L, Zhang H, Fei Z, et al. Comparison of the physicochemical, rheological, and morphologic properties of chitosan from four insects. Carbohydr Polym [Internet]. 2019 Apr 1;209:266–75. Available from: <URL>.

56. Khayrova A, Lopatin S, Varlamov V. Black Soldier Fly Hermetia illucens as a Novel Source of Chitin and Chitosan. Int J Sci [Internet]. 2019;8(4):81–6. Available from: <URL>.

57. Chawla S, Kanatt S, Sharma A. Chitosan, Polysaccharides. Switzerland: Springer International Publishing: Cham; 2015.

58. Olafadehan OA, Ajayi TO, Amoo KO. Optimum Conditions for Extraction of Chitin and Chitosan from Callinectes amnicola Shell Waste. Theor Found Chem Eng [Internet]. 2020 Nov 15;54(6):1173–94. Available from: <URL>.

59. Blumberg R, Southall CL, Van Rensburg NJ, Volckman OB. South african fish products. XXXII.—The rock lobster: A study of chitin production from processing wastes. J Sci Food Agric [Internet]. 1951 Dec 1;2(12):571–6. Available from: <URL>.

60. Trung TS, Tram LH, Van Tan N, Van Hoa N, Minh NC, Loc PT, et al. Improved method for production of chitin and chitosan from shrimp shells. Carbohydr Res [Internet]. 2020 Mar 1;489:107913. Available from: <URL>.

61. Yang H, Gözaydın G, Nasaruddin RR, Har JRG, Chen X, Wang X, et al. Toward the Shell Biorefinery: Processing Crustacean Shell Waste Using Hot Water and Carbonic Acid. ACS Sustain Chem Eng [Internet]. 2019 Mar 4;7(5):5532–42. Available from: <URL>.

62. Kalut SA. Enhancement of degree of deacetylation of chitin in chitosan production. UMP; 2008.

63. Schloemer GC, Schloemer DA. Preparation of 4,4'-diketo-β-carotene derivatives. Google Patents [Internet]. 2002 Sep 13; Available from: <URL>.

64. Szymańska E, Winnicka K. Stability of Chitosan—A Challenge for Pharmaceutical and Biomedical Applications. Mar Drugs [Internet]. 2015 Apr 1;13(4):1819–46. Available from: <URL>.

65. Little DJ, Bamford NC, Pokrovskaya V, Robinson H, Nitz M, Howell PL. Structural Basis for the De-N-acetylation of Poly-β-1,6-N-acetyl-d-glucosamine in Gram-positive Bacteria. J Biol Chem [Internet]. 2014 Dec 26;289(52):35907–17. Available from: <URL>.

66. Mourya VK, Inamdar NN. Chitosan-modifications and applications: Opportunities galore. React Funct Polym [Internet]. 2008 Jun 1;68(6):1013–51. Available from: <URL>.

67. Shariatinia Z. Carboxymethyl chitosan: Properties and biomedical applications. Int J Biol Macromol [Internet]. 2018 Dec 1;120:1406–19. Available from: <URL>.

68. Lin Y, Chen Q, Luo H. Preparation and characterization of N-(2-carboxybenzyl)chitosan as a potential pH-sensitive hydrogel for drug delivery. Carbohydr Res [Internet]. 2007 Jan 15;342(1):87–95. Available from: <URL>.

69. Skorik YA, Kritchenkov AS, Moskalenko YE, Golyshev AA, Raik S V., Whaley AK, et al. Synthesis of N-succinyl- and N-glutaryl-chitosan derivatives and their antioxidant, antiplatelet, and anticoagulant activity. Carbohydr Polym [Internet]. 2017 Jun 15;166:166–72. Available from: <URL>.

70. Petrova VA, Panevin AA, Zhuravskii SG, Gasilova ER, Vlasova EN, Romanov DP, et al. Preparation of N-succinyl-chitin nanoparticles and their applications in otoneurological pathology. Int J Biol Macromol [Internet]. 2018 Dec 1;120:1023–9. Available from: <URL>.

71. da Silva SB, Krolicka M, van den Broek LAM, Frissen AE, Boeriu CG. Water-soluble chitosan derivatives and pH-responsive hydrogels by selective C-6 oxidation mediated by TEMPO-laccase redox system. Carbohydr Polym [Internet]. 2018 Apr 15;186:299–309. Available from: <URL>.

72. Peng Y, Han B, Liu W, Xu X. Preparation and antimicrobial activity of hydroxypropyl chitosan. Carbohydr Res [Internet]. 2005 Aug 15;340(11):1846–51. Available from: <URL>.

73. Park EK, Kim SY, Lee SB, Lee YM. Folate-conjugated methoxy poly(ethylene glycol)/poly(ε-caprolactone) amphiphilic block copolymeric micelles for tumor-targeted drug delivery. J Control Release [Internet]. 2005 Dec 5;109(1–3):158–68. Available from: <URL>.

74. Ahmed S, Ikram S. Chitosan & its derivatives: a review in recent innovations. Int J Pharm Sci Res [Internet]. 2015 [cited 2023 Dec 20];6(1):14–30. Available from: <URL>.

75. Thanou M, Florea BI, Geldof M, Junginger HE, Borchard G. Quaternized chitosan oligomers as novel gene delivery vectors in epithelial cell lines. Biomaterials [Internet]. 2002 Jan 1;23(1):153–9. Available from: <URL>.

76. Morimoto M, Saimoto H, Shigemasa Y. Control of Functions of Chitin and Chitosan by Chemical Modification. Trends Glycosci Glycotechnol [Internet]. 2002;14(78):205–22. Available from: <URL>.

77. Thang NH, Chien TB, Cuong DX. Polymer-Based Hydrogels Applied in Drug Delivery: An Overview. Gels [Internet]. 2023 Jun 27;9(7):523. Available from: <URL>.

78. Feldman D. Polymers and Polymer Nanocomposites for Cancer Therapy. Appl Sci [Internet]. 2019 Sep 17;9(18):3899. Available from: <URL>.

79. Argüelles-Monal W, Lizardi-Mendoza J, Fernández-Quiroz D, Recillas-Mota M, Montiel-Herrera M. Chitosan Derivatives: Introducing New Functionalities with a Controlled Molecular Architecture for Innovative Materials. Polymers (Basel) [Internet]. 2018 Mar 20;10(3):342. Available from: <URL>.

80. Zargar V, Asghari M, Dashti A. A Review on Chitin and Chitosan Polymers: Structure, Chemistry, Solubility, Derivatives, and Applications. ChemBioEng Rev [Internet]. 2015 Jun 30;2(3):204–26. Available from: <URL>.

81. Schulze-Zachau F, Braunschweig B. C $_n$ TAB/polystyrene sulfonate mixtures at air–water interfaces: effects of alkyl chain length on surface activity and charging state. Phys Chem Chem Phys [Internet]. 2019 Apr 10;21(15):7847–56. Available from: <URL>.

82. Chiappisi L, Gradzielski M. Co-assembly in chitosan–surfactant mixtures: thermodynamics, structures, interfacial properties and applications. Adv Colloid Interface Sci [Internet]. 2015 Jun 1;220:92–107. Available from: <URL>.

83. Wang W, Meng Q, Li Q, Liu J, Zhou M, Jin Z, et al. Chitosan Derivatives and Their Application in Biomedicine. Int J Mol Sci [Internet]. 2020 Jan 12;21(2):487. Available from: <URL>.

84. Bolshakov IN, Gornostaev LM, Fominykh OI, Svetlakov A V. Synthesis, Chemical and Biomedical Aspects of the Use of Sulfated Chitosan. Polymers (Basel) [Internet]. 2022 Aug 22;14(16):3431. Available from: <URL>.

85. Kocabay S, Bahar MR, Tekin S, Akkaya R, Akkaya B. Chemical and biological characterization of sulfated chitosan oligomer as heparin mimics. Polym Polym Compos [Internet]. 2021 Nov 11;29(9_suppl):S1023–32. Available from: <URL>.

86. Ding K, Wang Y, Wang H, Yuan L, Tan M, Shi X, et al. 6- O -Sulfated Chitosan Promoting the Neural Differentiation of Mouse Embryonic Stem Cells. ACS Appl Mater Interfaces [Internet]. 2014 Nov 26;6(22):20043–50. Available from: <URL>.

87. Liu Q, Chen J, Yang X, Qiao C, Li Z, Xu C, et al. Synthesis, structure, and properties of N-2-hydroxylpropyl-3-trimethylammonium-O-carboxymethyl chitosan derivatives. Int J Biol Macromol [Internet]. 2020 Feb 1;144:568–77. Available from: <URL>.

88. Heras A, Rodríguez NM, Ramos VM, Agullo E. N-methylene phosphonic chitosan: a novel soluble derivative. Carbohydr Polym [Internet]. 2001 Jan 1;44(1):1–8. Available from: <URL>.

89. Ramos V., Rodríguez N., Díaz M., Rodríguez M., Heras A, Agulló E. N-methylene phosphonic chitosan. Effect of preparation methods on its properties. Carbohydr Polym [Internet]. 2003 Apr 1;52(1):39–46. Available from: <URL>.

90. Wojcik G. Metal corrosion inhibiting compositions containing chitosan derivatives. US Pat. 2003;6:958.

91. Ramos V, Rodrıguez N, Rodrıguez M, Heras A, Agullo E. Modified chitosan carrying phosphonic and alkyl groups. Carbohydr Polym [Internet]. 2003 Mar 1;51(4):425–9. Available from: <URL>.

92. Sahariah P, Gaware V, Lieder R, Jónsdóttir S, Hjálmarsdóttir M, Sigurjonsson O, et al. The Effect of Substituent, Degree of Acetylation and Positioning of the Cationic Charge on the Antibacterial Activity of Quaternary Chitosan Derivatives. Mar Drugs [Internet]. 2014 Aug 21;12(8):4635–58. Available from: <URL>.

93. Suzuki K, Oda D, Shinobu T, Saimoto H, Shigemasa Y. New Selectively N-Substituted Quaternary Ammonium Chitosan Derivatives. Polym J [Internet]. 2000 Apr;32(4):334–8. Available from: <URL>.

94. Saravanan S, Sareen N, Abu-El-Rub E, Ashour H, Sequiera GL, Ammar HI, et al. Graphene Oxide-Gold Nanosheets Containing Chitosan Scaffold Improves Ventricular Contractility and Function After Implantation into Infarcted Heart. Sci Rep [Internet]. 2018 Oct 10;8(1):15069. Available from: <URL>.

95. Feng W, Wang Z. Biomedical applications of chitosan-graphene oxide nanocomposites. iScience

[Internet]. 2022 Jan 21;25(1):103629. Available from: <URL>.

96. Bao H, Pan Y, Ping Y, Sahoo NG, Wu T, Li L, et al. Chitosan-Functionalized Graphene Oxide as a Nanocarrier for Drug and Gene Delivery. Small [Internet]. 2011 Jun 6;7(11):1569–78. Available from: <URL>.

97. Waśko A, Bulak P, Polak-Berecka M, Nowak K, Polakowski C, Bieganowski A. The first report of the physicochemical structure of chitin isolated from Hermetia illucens. Int J Biol Macromol [Internet]. 2016 Nov 1;92:316–20. Available from: <URL>.

98. Anand M, Kalaivani R, Maruthupandy M, Kumaraguru AK, Suresh S. Extraction and Characterization of Chitosan from Marine Crab and Squilla Collected from the Gulf of Mannar Region, South India. J Chitin Chitosan Sci [Internet]. 2014 Dec 1;2(4):280–7. Available from: <URL>.

99. Song C, Yu H, Zhang M, Yang Y, Zhang G. Physicochemical properties and antioxidant activity of chitosan from the blowfly Chrysomya megacephala larvae. Int J Biol Macromol [Internet]. 2013 Sep 1;60:347–54. Available from: <URL>.

100. Ibitoye EB, Lokman IH, Hezmee MNM, Goh YM, Zuki ABZ, Jimoh AA. Extraction and physicochemical characterization of chitin and chitosan isolated from house cricket. Biomed Mater [Internet]. 2018 Jan 30;13(2):025009. Available from: <URL>.

101. Mehranian M, Pourabad RF, Bashir NS, Taieban S. Physicochemical characterization of chitin from the Mediterranean flour moth, *Ephestia kuehniella* Zeller (Lepidoptera: Pyralidae). J Macromol Sci Part A [Internet]. 2017 Oct 3;54(10):720–6. Available from: <URL>.

102. Kaya M, Bağrıaçık N, Seyyar O, Baran T. Comparison of chitin structures derived from three common wasp species (Vespa crabro Linnaeus, 1758, Vespa orientalis Linnaeus, 1771 and Vespula germanica (Fabricius, 1793)). Arch Insect Biochem Physiol [Internet]. 2015 Aug 7;89(4):204–17. Available from: <URL>.

103. Srinivasan H, Kanayairam V, Ravichandran R. Chitin and chitosan preparation from shrimp shells Penaeus monodon and its human ovarian cancer cell line, PA-1. Int J Biol Macromol [Internet]. 2018 Feb 1;107(PartA):662–7. Available from: <URL>.

104. Sayari N, Sila A, Abdelmalek BE, Abdallah R Ben, Ellouz-Chaabouni S, Bougatef A, et al. Chitin and chitosan from the Norway lobster by-products: Antimicrobial and anti-proliferative activities. Int J Biol Macromol [Internet]. 2016 Jun 1;87:163–71. Available from: <URL>.

105. Mohan K, Ravichandran S, Muralisankar T, Uthayakumar V, Chandirasekar R, Rajeevgandhi C, et al. Extraction and characterization of chitin from sea snail Conus inscriptus (Reeve, 1843). Int J Biol Macromol [Internet]. 2019 Apr 1;126:555–60. Available from: <URL>.

106. Caligiani A, Marseglia A, Leni G, Baldassarre S, Maistrello L, Dossena A, et al. Composition of black soldier fly prepupae and systematic approaches for extraction and fractionation of proteins, lipids and chitin. Food Res Int [Internet]. 2018 Mar 1;105:812–20. Available from: <URL>.

107. Park JH, Saravanakumar G, Kim K, Kwon IC. Targeted delivery of low molecular drugs using chitosan and its derivatives. Adv Drug Deliv Rev [Internet]. 2010 Jan 31;62(1):28–41. Available from: <URL>.

108. Crini G, Lichtfouse E. Sustainable agriculture reviews 36: chitin and chitosan: applications in food, agriculture, pharmacy, medicine and wastewater treatment. Crini G, Lichtfouse E, editors. Vol. 36. Cham: Springer International Publishing; 2019.

109. Collado-González M, Montalbán MG, Peña-García J, Pérez-Sánchez H, Víllora G, Díaz Baños FG. Chitosan as stabilizing agent for negatively charged nanoparticles. Carbohydr Polym [Internet]. 2017 Apr 1;161:63–70. Available from: <URL>.

110. Amor I Ben, Hemmami H, Laouini SE, Temam H Ben, Zaoui H, Barhoum A. Biosynthesis MgO and ZnO nanoparticles using chitosan extracted from Pimelia Payraudi Latreille for antibacterial applications. World J Microbiol Biotechnol [Internet]. 2023 Jan 21;39(1):19. Available from: <URL>.

111. Frank LA, Onzi GR, Morawski AS, Pohlmann AR, Guterres SS, Contri RV. Chitosan as a coating material for nanoparticles intended for biomedical applications. React Funct Polym [Internet]. 2020 Feb 1;147:104459. Available from: <URL>.

112. Phan TTV, Phan DT, Cao XT, Huynh T-C, Oh J. Roles of Chitosan in Green Synthesis of Metal Nanoparticles for Biomedical Applications. Nanomaterials [Internet]. 2021 Jan 21;11(2):273. Available from: <URL>.

113. Ben Amor I, Hemmami H, Laouini SE, Mahboub MS, Barhoum A. Sol-Gel Synthesis of ZnO Nanoparticles Using Different Chitosan Sources: Effects on Antibacterial Activity and Photocatalytic Degradation of AZO Dye. Catalysts [Internet]. 2022 Dec 8;12(12):1611. Available from: <URL>.

114. Galed G, Fernández-Valle M., Martínez A, Heras A. Application of MRI to monitor the process of ripening and decay in citrus treated with chitosan solutions. Magn Reson Imaging [Internet]. 2004 Jan 1;22(1):127–37. Available from: <URL>.

115. Gudjónsdóttir M, Gacutan MD, Mendes AC, Chronakis IS, Jespersen L, Karlsson AH. Effects of electrospun chitosan wrapping for dry-ageing of beef, as studied by microbiological, physicochemical and low-field nuclear magnetic resonance analysis. Food Chem [Internet]. 2015 Oct 1;184:167–75. Available from: <URL>.

116. Ben Amor I, Hemmami H, Laouini SE, Zeghoud S, Benzina M, Achour S, et al. Use of Insect-Derived Chitosan for the Removal of Methylene Blue Dye from Wastewater: Process Optimization Using a Central

Composite Design. Materials [Internet]. 2023 Jul 17;16(14):5049. Available from: <URL>.

117. Masindi V, Muedi KL. Environmental Contamination by Heavy Metals. In: El-Din M. Saleh H, Aglan R, editors. Heavy Metals [Internet]. London: InTech; 2018. p. 115–32. Available from: <URL>.

118. Nechita P. Applications of Chitosan in Wastewater Treatment. In: Shalaby E, editor. Biological Activities and Application of Marine Polysaccharides [Internet]. London: InTech; 2017. p. 209–28. Available from: <URL>.

119. Hesami F, Bina B, Ebrahimi A. The effectiveness of chitosan as coagulant aid in turbidity removal from water. Int J Environ Health Eng [Internet]. 2014 Apr 1;2(6):46–51. Available from: <URL>.

120. Akhouairi S, Ouachtak H, Addi AA, Jada A, Douch J. Natural Sawdust as Adsorbent for the Eriochrome Black T Dye Removal from Aqueous Solution. Water, Air, Soil Pollut [Internet]. 2019 Aug 25;230(8):181. Available from: <URL>.

121. Hegab HM, Wimalasiri Y, Ginic-Markovic M, Zou L. Improving the fouling resistance of brackish water membranes via surface modification with graphene oxide functionalized chitosan. Desalination [Internet]. 2015 Jun 1;365:99–107. Available from: <URL>.

122. Ivanova DG, Yaneva ZL. Antioxidant Properties and Redox-Modulating Activity of Chitosan and Its Derivatives: Biomaterials with Application in Cancer Therapy. Biores Open Access [Internet]. 2020 Mar 1;9(1):64–72. Available from: <URL>.

123. Tan C, Wei H, Zhao X, Xu C, Peng J. Effects of dietary fibers with high water-binding capacity and swelling capacity on gastrointestinal functions, food intake and body weight in male rats. Food Nutr Res [Internet]. 2017 Jan 3;61(1):1308118. Available from: <URL>.

124. Liu D, Yang F, Xiong F, Gu N. The Smart Drug Delivery System and Its Clinical Potential. Theranostics [Internet]. 2016;6(9):1306–23. Available from: <URL>.

125. Mansuri S, Kesharwani P, Jain K, Tekade RK, Jain NK. Mucoadhesion: A promising approach in drug delivery system. React Funct Polym [Internet]. 2016 Mar 1;100:151–72. Available from: <URL>.

126. Khutoryanskiy V V. Advances in Mucoadhesion and Mucoadhesive Polymers. Macromol Biosci [Internet]. 2011 Jun 14;11(6):748–64. Available from: <URL>.

127. Chen K, Guo B, Luo J. Quaternized carboxymethyl chitosan/organic montmorillonite nanocomposite as a novel cosmetic ingredient against skin aging. Carbohydr Polym [Internet]. 2017 Oct 1;173:100–6. Available from: <URL>.

128. Zhang J, Tan W, Wang G, Yin X, Li Q, Dong F, et al. Synthesis, characterization, and the antioxidant activity of N,N,N-trimethyl chitosan salts.

Int J Biol Macromol [Internet]. 2018 Oct 15;118:9–14. Available from: <URL>.

129. Zhang L, Wang J, Chi H, Wang S. Local anesthetic lidocaine delivery system: chitosan and hyaluronic acid-modified layer-by-layer lipid nanoparticles. Drug Deliv [Internet]. 2016 Nov 21;23(9):3529–37. Available from: <URL>.

130. Wang J, Xu M, Cheng X, Kong M, Liu Y, Feng C, et al. Positive/negative surface charge of chitosan based nanogels and its potential influence on oral insulin delivery. Carbohydr Polym [Internet]. 2016 Jan 20;136:867–74. Available from: <URL>.

131. Lee SH, Song JG, Han H-K. Development of pH-responsive organic-inorganic hybrid nanocomposites as an effective oral delivery system of protein drugs. J Control Release [Internet]. 2019 Oct 1;311–312:74–84. Available from: <URL>.

132. Bajracharya R, Song JG, Back SY, Han H-K. Recent Advancements in Non-Invasive Formulations for Protein Drug Delivery. Comput Struct Biotechnol J [Internet]. 2019 Jan 1;17:1290–308. Available from: <URL>.

133. Trivedi A, Hoffman J, Arora R. Gene therapy for atrial fibrillation - How close to clinical implementation? Int J Cardiol [Internet]. 2019 Dec 1;296:177–83. Available from: <URL>.

134. Singh B, Maharjan S, Cho K-H, Cui L, Park I-K, Choi Y-J, et al. Chitosan-based particulate systems for the delivery of mucosal vaccines against infectious diseases. Int J Biol Macromol [Internet]. 2018 Apr 15;110:54–64. Available from: <URL>.

135. Sousa Â, Almeida AM, Faria R, Konate K, Boisguerin P, Queiroz JA, et al. Optimization of peptide-plasmid DNA vectors formulation for gene delivery in cancer therapy exploring design of experiments. Colloids Surfaces B Biointerfaces [Internet]. 2019 Nov 1;183:110417. Available from: <URL>.

136. Chuan D, Jin T, Fan R, Zhou L, Guo G. Chitosan for gene delivery: Methods for improvement and applications. Adv Colloid Interface Sci [Internet]. 2019 Jun 1;268:25–38. Available from: <URL>.

137. Confederat LG, Tuchilus CG, Dragan M, Sha'at M, Dragostin OM. Preparation and Antimicrobial Activity of Chitosan and Its Derivatives: A Concise Review. Molecules [Internet]. 2021 Jun 17;26(12):3694. Available from: <URL>.

138. Sahariah P, Másson M. Antimicrobial Chitosan and Chitosan Derivatives: A Review of the Structure–Activity Relationship. Biomacromolecules [Internet]. 2017 Nov 13;18(11):3846–68. Available from: <URL>.

139. Tanikonda R, Ravi RK, Kantheti S, Divella S. Chitosan: Applications in dentistry. Trends Biomater Artif Organs [Internet]. 2014;28(2):74–8. Available from: <URL>.

140. Ahsan SM, Thomas M, Reddy KK, Sooraparaju

SG, Asthana A, Bhatnagar I. Chitosan as biomaterial in drug delivery and tissue engineering. Int J Biol Macromol [Internet]. 2018 Apr 15;110:97–109. Available from: <URL>.

141. Kabashima K, Honda T, Ginhoux F, Egawa G. The immunological anatomy of the skin. Nat Rev Immunol [Internet]. 2019 Jan 14;19(1):19–30. Available from: <URL>.

142. Behera SS, Das U, Kumar A, Bissoyi A, Singh AK. Chitosan/TiO 2 composite membrane improves proliferation and survival of L929 fibroblast cells: Application in wound dressing and skin regeneration. Int J Biol Macromol [Internet]. 2017 May 1;98:329–40. Available from: <URL>.

143. Chen Y, Qiu H, Dong M, Cheng B, Jin Y, Tong Z, et al. Preparation of hydroxylated lecithin complexed iodine/carboxymethyl chitosan/sodium alginate composite membrane by microwave drying and its applications in infected burn wound treatment. Carbohydr Polym [Internet]. 2019 Feb 15;206:435–

45. Available from: <URL>.

144. Madni A, Kousar R, Naeem N, Wahid F. Recent advancements in applications of chitosan-based biomaterials for skin tissue engineering. J Bioresour Bioprod [Internet]. 2021 Feb 1;6(1):11–25. Available from: <URL>.

145. Xie Y, Yi Z, Wang J, Hou T, Jiang Q. Carboxymethyl konjac glucomannan - crosslinked chitosan sponges for wound dressing. Int J Biol Macromol [Internet]. 2018 Jun 1;112:1225–33. Available from: <URL>.

146. Adeli H, Khorasani MT, Parvazinia M. Wound dressing based on electrospun PVA/chitosan/starch nanofibrous mats: Fabrication, antibacterial and cytocompatibility evaluation and in vitro healing assay. Int J Biol Macromol [Internet]. 2019 Feb 1;122:238–54. Available from: <URL>.

Hemmami H et al. JOTCSA. 2024; 11(1): 341-364

REVIEW ARTICLE

Comparative Analysis of Glycoform Profiles Between Biosimilar and Originator Monoclonal Antibodies by Liquid Chromatography–Mass Spectrometry

A. Emin Atik[1,2*] iD

[1]Turgut Pharmaceuticals, Kocaeli, 41400, Turkey.
[2]Acibadem Mehmet Ali Aydınlar University, Faculty of Engineering and Natural Sciences, Department of Natural Sciences, Istanbul, 34752, Turkey.

Abstract: Glycosylation is considered as a critical quality attribute for monoclonal antibodies (mAbs) and needs routine monitoring during production. This study aims to compare the glycoform profiles of biosimilar and four originator mAbs using ultra-performance liquid chromatography (UPLC) coupled to electrospray ionization-quadrupole time of flight-mass spectrometry (ESI/Q-TOF MS). The resultant mass spectrum showed that seven different glycoform pairs, including G0F–GN/G0, G0F–GN/G0F, G0F/G0F, G0F/G1F, G1F/G1F, G1F/G2F, and G2F/G2F were identified via intact mass analysis for all tested mAb samples. The correct identification of each glycoform pair was achieved by comparing the observed mass with its theoretical mass using high-resolution mass spectrometry data (with mass accuracies of less than 100 ppm). The most abundant paired glycoforms detected at the intact protein level are G0F/G0F and G0F/G1F, with relative abundance ranges of 38.45 – 43.43% and 19.32 – 22.20%, respectively. The obtained data demonstrated that biosimilar and originators have the same types of glycoform pairs, and the relative abundances of each pair were comparable among biosimilar and four originator mAb samples. Additionally, the reduced mass analysis revealed that five different glycans (G0F–GN, G0, G0F, G1F, and G2F) were attached to the heavy chain of the mAb, and the relative abundance of G0F ranged from 75.21 to 77.90%. The detected mass accuracies for reduced mass analysis were below 25 ppm. The results of the intact and reduced mass analyses showed that the biosimilar is similar to its originator in terms of glycoform percentages and molecular masses.

1. INTRODUCTION

Immunoglobulin G (IgG)-based monoclonal antibodies (mAbs) are one of the most critical therapeutic biological products and have rapidly expanded in the biopharmaceutical field since the approval of the first mAb by the Food and Drug Administration (FDA) in 1986 (1). mAbs have been utilized for numerous therapeutic applications, such as treating inflammatory, autoimmune disorders, cardiovascular, and oncologic diseases due to their targeted selectivity, high functionality, and low adverse effects (2-3). Biosimilars are supposed to provide patients with more economical

treatment alternatives by lowering overall healthcare costs. The patent protection for most of the top-selling therapeutic mAbs has expired or will soon expire; therefore, biosimilar versions have been developed by several biopharmaceutical companies. A biosimilar drug can be defined as a therapeutic protein that is highly similar to its originator product by showing no clinically meaningful differences in terms of quality, safety, and efficacy. To demonstrate the similarity, a biosimilar candidate has to be analyzed side-by-side with the originator regarding physicochemical and functional properties to confirm the quality of the product.

mAbs are recombinant glycoproteins with a total molecular mass of around 150 kDa. They have a Y-shaped homodimeric structure consisting of two identical light chains (LC, ~25 kDa each) and two heavy chains (HC, ~50 kDa each) linked together via disulfide bonds. The structure is inherently heterogeneous due to having various chemical and enzymatic post-translational modifications (PTMs) such as N-linked glycosylation, N-terminal pyroglutamic acid formation, C-terminal lysine truncation, deamidation of asparagine, and oxidation of methionine (4-5). Among them, N-linked glycosylation, a covalent attachment of carbohydrates (oligosaccharides) to the protein, is one of the most prominent PTM in mAbs, which adds heterogeneity to the structure. Most of the mAbs are glycosylated at the asparagine (Asn, N) residue in the fragment crystallizable (Fc) region of the constant heavy chain domain 2 (CH2). This attribute should be monitored throughout mAb development and production stages due to its potential impact on safety, stability, and efficacy profiles (6-8). Therefore, state-of-the-art analytical methodologies should be employed to characterize biosimilars comprehensively.

Today, mass spectrometry (MS)-based analytical methods have become a gold standard for characterizing mAbs at intact, reduced, subunit, and peptide levels (9-15). The preliminary assay in biosimilar characterization is intact and reduced mass analyses via high-resolution mass spectrometry, *e.g.*, ESI-Q-IM-TOF-MS and ESI-TOF-MS systems (16-18). Intact mass analysis is used to determine the molecular weight of therapeutic proteins and the relative quantification of major glycoform pairs with a minimum or no sample preparation step (19-20). Additionally, a reduced mass analysis provides a more accurate mass measurement for subunits (LC and HC) and allows for quantifying the attached glycans on the chains (21-22). Recent studies demonstrated that intact and reduced mass workflows had been preferred over released *N*-glycan and glycopeptide analysis for monitoring mAb glycosylation profiles (23-25). Schilling et al. (23) introduced a novel reduced mass analysis platform method as an in-process control test for monitoring mAb glycosylation. The authors reported that the proposed method could provide early-stage glycosylation characteristics from cell culture harvest upon process development (23). Similarly, a study by Lanter et al. (24) showed that the intact mass-based multi-attribute method (MAM) could be used to determine the *N*-linked glycosylation profile during upstream process development. The authors highlighted that the glycoform profile revealed by intact mass MAM is highly comparable with released *N*-glycan and glycopeptide mapping analyses. Moreover, Martelet and co-workers utilized MS-based MAM workflows at the intact and subunit levels to comprehensively characterize antibody-drug conjugates (ADCs) (25). These reports have shown that intact and reduced mass workflows are today preferred for glycoform characterization over released *N*-glycan and

glycopeptide analysis due to the assays' rapid, simple, and robust features. In recent publications, hyphenated mass spectrometric techniques, namely capillary electrophoresis-mass spectrometry (CE-MS) and supercritical fluid chromatography-tandem mass spectrometry (SFC-MS/MS), were demonstrated for high-throughput screening of mAb glycosylation (26-27) with high sensitivity.

In the current study, the glycoform profiles of the biosimilar and the four originator mAb batches were analyzed and compared side-by-side via intact and reduced protein levels by using an ultra-performance liquid chromatography (UPLC) coupled to electrospray ionization-quadrupole time of flight mass spectrometry (ESI/Q-TOF MS). This hybrid system offers a high mass accuracy and mass resolution for the intact and reduced mass analyses of mAbs.

2. EXPERIMENTAL SECTION

2.1. Chemicals and Reagents
All chemicals and reagents were of analytical grade. HPLC-grade acetonitrile, methanol, isopropanol, and formic acid (>99%) were purchased from Merck (Darmstadt, Germany). Ammonium bicarbonate (≥99.0%), sodium iodide (NaI, ≥99.5%), and dithiothreitol (DTT, >99%) were obtained from Sigma-Aldrich (St.Louis, MO, USA). Leucine enkephaline (YGGFL–OH) was purchased from Waters Corporation (Milford, MA, USA). Ultra-pure water (18.2 MΩ.cm) was prepared in-house using a Milli-Q water purification system (Merck-Millipore, Darmstadt, Germany).

The biosimilar candidate was developed and produced by Turgut Pharmaceuticals (Istanbul, Turkey). Four originator batches (2 batches from the European Union-EU and 2 from the United States-US) were procured and stored per the manufacturer's recommendations until further use. The biosimilar and originators are recombinant humanized immunoglobulin G (IgG1) monoclonal antibodies expressed by Chinese hamster ovary (CHO) cells. Both products have only one N-glycosylation site in the Fc region. The biosimilar is purified using standard chromatographic steps (capture step with Protein A chromatography, purification with cation exchange and hydrophobic interaction chromatography, followed by buffer exchange and concentration) in Turgut Pharmaceuticals. The composition of the formulation buffer of biosimilar and originator products is identical.

2.2. Sample Preparation
Sample preparations were performed as previously described (20, 24) with slight modifications. Briefly, for intact mass analysis, antibody samples were diluted to a concentration of 1 mg/mL with 50 mM ammonium bicarbonate solution, and 100 μL sample solution was transferred into UPLC vials for LC-MS analysis. For reduced mass analysis, antibody samples were diluted

to a concentration of 1 mg/mL with 50 mM ammonium bicarbonate solution, and then 1 μL of 500 mM DTT solution (prepared in ultrapure water) was added for reduction. The mixture was then incubated on a thermomixer at 80 °C for 60 minutes for a complete reduction. After incubation, the samples were allowed to cool for 5 minutes on the bench, and then 100 μL of sample solution was transferred into UPLC vials for LC–MS analysis.

2.3. Liquid Chromatography – Mass Spectrometry (LC–MS)

All LC–MS experiments were conducted on ultra-performance liquid chromatography (ACQUITY H-Class Bio UPLC) coupled online to a Xevo G2–XS QTOF hybrid mass spectrometer (Waters Corporation, Milford, MA, USA). The MS instrument was equipped with an electrospray ionization (ESI) source operating in positive ion mode with full MS scan functionality over a mass range of 400 – 4000 *m/z*. LC–MS settings were set to the same parameters for intact and reduced mass analysis. The capillary and cone voltages were set at 3000 V and 30 V, respectively. The source temperature was kept at 150°C, and the desolvation temperature was set at 500°C. The sampling cone and desolvation gas flows were 50 L/h and 1000 L/h, respectively. The autosampler temperature was maintained at 10 °C during the analyses. Before analysis, the instrument was calibrated externally with a sodium iodide solution (2 μg/μL) in a mass range of 400 – 4000 *m/z*. Leucine enkephaline, a pentapeptide (YGGFL–OH, [M+H]$^+$ *m/z* 556.2766) was continuously applied during data acquisition as a reference standard to correct mass accuracy drift.

For each analysis, 3 μg of antibody samples (biosimilar or originator) were injected onto the column separately (Waters Acquity UPLC Protein BEH C4, 2.1 x 50 mm, 1.7 μm particle size, 300 Å pore size) for chromatographic separation. At least three blank injections were performed between sample runs to eliminate any carryover problems. Mobile phase A was ultrapure water, mobile phase B was acetonitrile, and mobile phase C was 1% formic acid in ultrapure water. The mAb sample was eluted off from the column with increasing acetonitrile with a constant level of mobile phase C. Total gradient time 5 minutes with mobile phase B from 5% to 90% in 2.7 min at a flow rate of 0.2 – 0.5 mL/min. Mobile phase C was used as a weaker ion-pairing modifier in the column, and the column temperature was maintained at 80 °C during the analysis. The eluted antibody samples were detected by UV absorbance at 280 nm before entering the MS. Triplicate injections were performed for each sample, and the average abundance for each glycoform pair was reported.

The instrument control and data processing were achieved using UNIFI (v1.9.4) Scientific Information System software. The deconvolutions of the ESI mass spectra of intact and reduced antibody samples were done by applying the maximum entropy deconvolution (MaxEnt1™) algorithm with a maximum of 20 iterations. The start and end peak widths were set to 2.4 and 3.5, respectively, and the charge carrier was selected as hydrogen. The minimum intensity ratio was selected as 80%. The output mass ranges of deconvolutions were set to 140,00 – 150,000 Da and 20,000 – 60,000 Da for intact and reduced protein analyses, respectively. The raw data were extracted and further analyzed with the Igor Pro software package (WaveMetrics, Lake Oswego, OR).

3. RESULTS AND DISCUSSION

3.1. Intact Mass Analysis

The molecular masses and glycoform profiles of the biosimilar and four originator batches were determined at the intact protein level by LC–MS analysis. Throughout the study, the glycoform pair term was used to represent different combinations of two glycan residues attached to the HC of the antibody. Briefly, monosaccharides (galactose (G), fucose (F), and mannose (M)) and amino sugar (N-acetylglucosamine (GN)) are linked together via glycosidic bonds to form a glycan structure. For instance, G0F, G1F, and G2F represent core-fucosylated and 0, 1, and 2 terminal galactose-containing glycan types, respectively. Similary, G0 displays afucosylated and agalactosylayed glycan, and G0F-GN glycan shows a core-fucosylated agalactosylated structure without one terminal GN. Figure 1 shows the overlaid full mass spectra of the biosimilar and originator batches over the m/z 2000 – 4000 mass range. The envelopes of charge distribution were symmetrical and centered on 51+ and 50+ charge states, ranging from 38+ to 70+ in all mass spectra (see Figure 1). As a rule of thumb, ESI generates a series of multiply charged states for all tested samples.

Each full mass spectrum was automatically deconvoluted (zero charged) using the MaxEnt1 deconvolution algorithm (processed by UNIFI) to yield its intact mass spectrum. The deconvoluted intact mass spectra for biosimilar and originator mAbs are compared in Figure 2. The assignments of each paired glycoform peak were established by comparing the observed molecular mass against its theoretical molecular mass via high-resolution mass spectrometry. It is apparent that the intact mass spectra of the biosimilar and originator batches possess a high degree of similarities in terms of having the same glycoform pairs together with comparable relative peak abundances (see Figure 2).
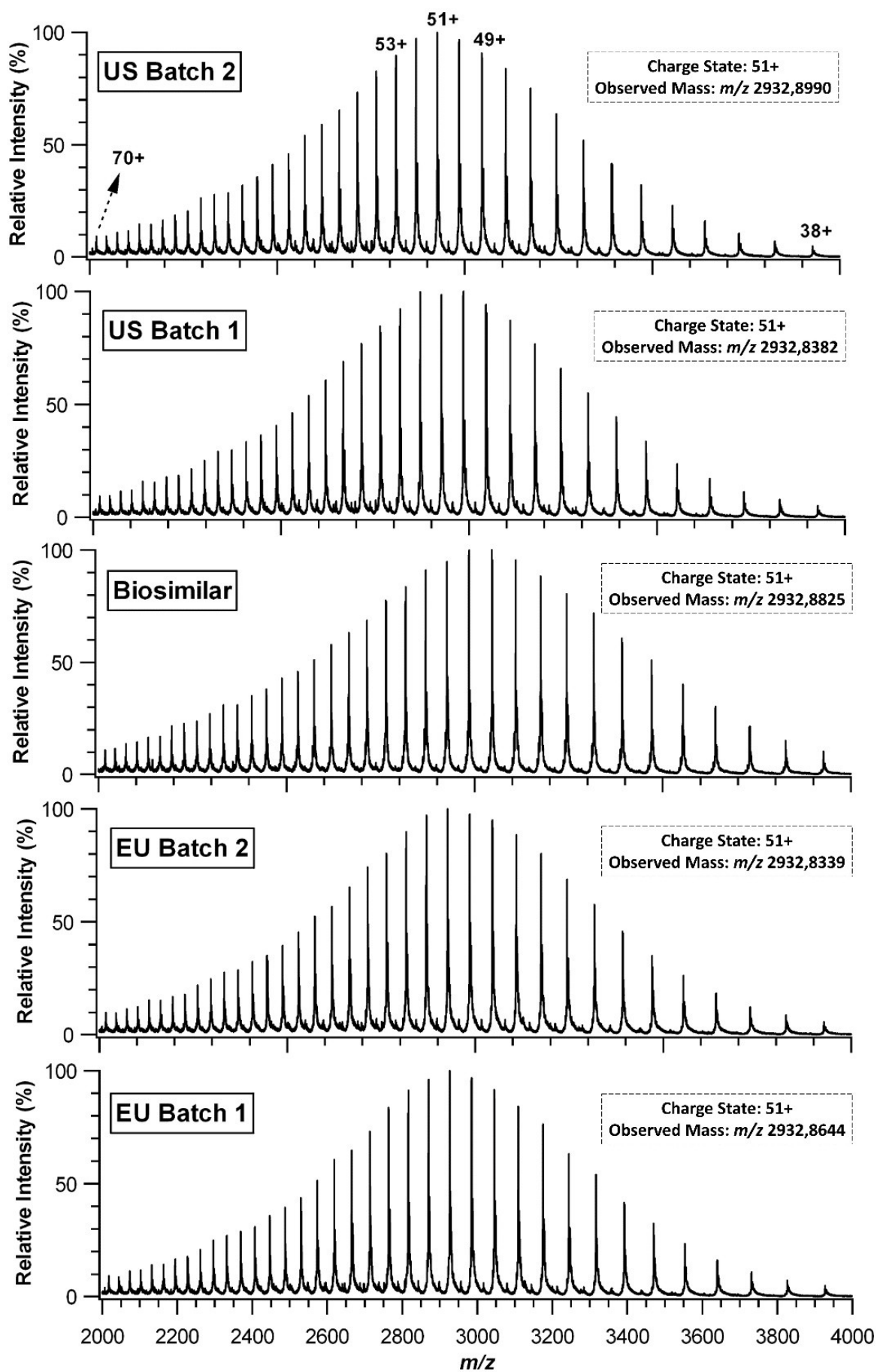
Figure 1: Comparison of overlaid full mass spectra for biosimilar and four originator batches.
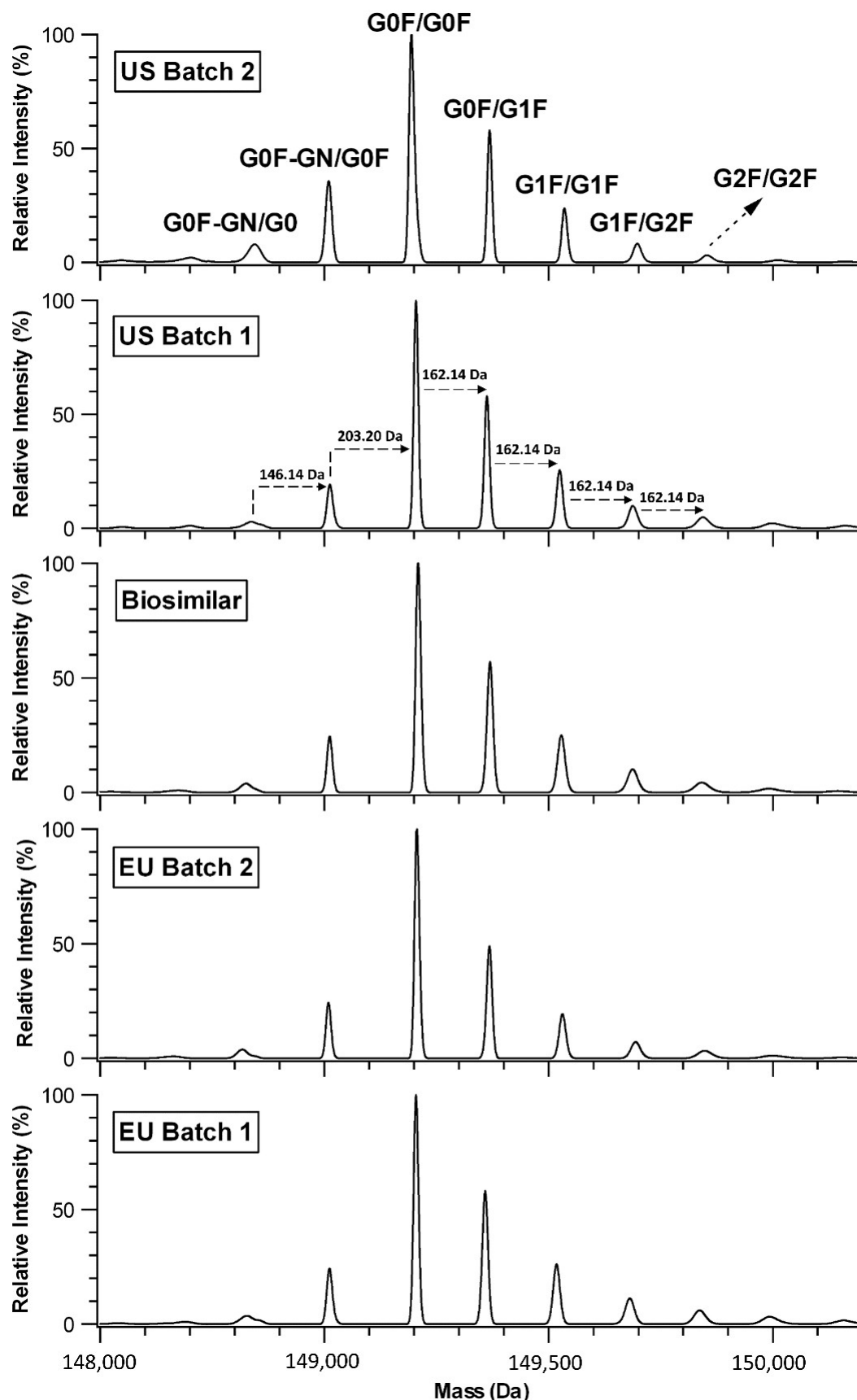
Figure 2: Comparison of deconvoluted intact molecular mass spectra for biosimilar and four originator batches.

Seven different glycoform pairs were detected for biosimilar and originator batches. Briefly, the major glycoforms (>50% of maximum MS peak height) were identified as G0F/G0F and G0F/G1F pairs, together with moderate contributions (20% to 40% of maximum MS peak height) from G0F–GN/G0F and G1F/G1F paired glycoforms. Moreover, G0F–GN/G0, G1F/G2F, and G2F/G2F glycoform pairs were detected at low levels (<10%) in the deconvoluted mass spectra.

The theoretical molecular mass of an aglycosylated antibody (an antibody that lacks glycans on its heavy chain) is calculated as 146,306.15 Da based on its theoretical amino acid sequence. As expected, the addition of glycans to the structure inherently increases the total molecular mass of the antibody (18, 20). The theoretical masses of the antibody that contain different combinations of glycoform pairs are 148,847.48 Da (G0F–GN/G0), 148,993.62 Da (G0F–GN/G0F), 149,196.82 Da (G0F/G0F), 149,358.96 Da (G0F/G1F), 149,521.10 Da (G1F/G1F), 149,683.24 Da (G1F/G2F), and 149,845.38 Da (G2F/G2F). Theoretical masses were calculated assuming all cystines are paired and C-terminal lysine on both heavy chains is truncated. Table 1 compares the observed and theoretical masses for each glycoform pair from biosimilar and originator batches.

Briefly, the observed intact molecular mass of the biosimilar containing two G0F residues (G0F/G0F pair) is 149,202.13 Da, where it ranges from 149,194.29 to 149,204.32 Da for four originator batches. Similarly, the observed intact molecular masses for the other paired glycoforms of biosimilar were within the range of four originator batches, as tabulated in Table 1. It is apparent that the observed intact molecular masses of each glycoform pair were matched entirely with their theoretical molecular masses (see Table 1). Furthermore, the observed molecular mass of the biosimilar with G0F/G0F glycoform (149,202.13 Da) agrees well with its theoretical molecular mass (149,196.82 Da), with a 36 ppm mass error. All glycoform pair identifications were achieved with a mass error of 100 ppm or less for all tested samples (the mass errors were listed in parenthesis in Table 1). Nevertheless, due to the limitations of the QTOF system, the isotopic peaks at each charge state cannot be resolved. The only instruments are orbitrap or FTMS systems that are capable of resolving isotopic spaces for multiply-charged states.

Table 1: Comparison of theoretical masses of each glycoform pair with observed masses for biosimilar and originator batches.

Glycoform Pair Type	Theoretical Mass (Da)	Observed Mass (Da) (Mass Error)				
		EU Batch 1	EU Batch 2	Biosimilar	US Batch 1	US Batch 2
G0F–GN/G0	148,847.48	148,834.08 (-90 ppm)	148,854.65 (48 ppm)	148,851.71 (28 ppm)	148,840.48 (-47 ppm)	148,843.59 (-26 ppm)
G0F–GN/G0F	148,993.62	149,003.45 (66 ppm)	149,008.20 (98 ppm)	149,004.93 (76 ppm)	149,006.75 (88 ppm)	149,007.13 (91 ppm)
G0F/G0F	149,196.82	149,203.63 (46 ppm)	149,194.29 (-17 ppm)	149,202.13 (36 ppm)	149,204.32 (50 ppm)	149,194.65 (-15 ppm)
G0F/G1F	149,358.96	149,357.13 (-12 ppm)	149,365.85 (46 ppm)	149,362.65 (25 ppm)	149,361.51 (17 ppm)	149,368.07 (61 ppm)
G1F/G1F	149,521.10	149,515.25 (-39 ppm)	149,528.19 (47 ppm)	149,524.79 (25 ppm)	149,523.25 (14 ppm)	149,535.04 (93 ppm)
G1F/G2F	149,683.24	149,677.62 (-38 ppm)	149,687.54 (29 ppm)	149,689.23 (40 ppm)	149,686.75 (23 ppm)	149,697.32 (94 ppm)
G2F/G2F	149,845.38	149,833.26 (-81 ppm)	149,840.94 (-30 ppm)	149,841.48 (-26 ppm)	149,842.72 (-18 ppm)	149,853.64 (55 ppm)

The relative abundances of each glycoform pair were calculated based on the peak area of individual glycoform pairs relative to the total peak areas of all identified glycoform pairs. Table 2 summarizes the average relative abundances of each glycoform pair detected in biosimilar and originator batches (averages of three runs were reported for each glycoform pair, and data were shown as mean ± standard deviation (SD, n = 3)). The obtained data demonstrated that the relative abundances of all paired glycoforms of biosimilar fall within the originator's paired glycoform range (see Table 2). For instance, the G0F/G0F type has an abundance of 39.79% for the biosimilar, where EU-batches and US-batches have ranged from 38.45 to 43.43% and 39.64 to 40.16%, respectively. The calculated relative standard deviation (RSD) of G0F/G0F pair was 0.35% for biosimilar and varied from 0.22% to 0.47% for originators, showing a high repeatability among injections. The overall data revealed that the intact molecular masses and relative abundances of each glycoform pair of the biosimilar were within the range of four originator batches. It can be concluded that the biosimilar candidate is highly similar to the originator in terms of glycoform pair content as well as their intact molecular masses.

Manufacturing of a biosimilar candidate comprises a multistep process and unique production parameters, starting from the cell line to the final drug product. Therefore, each biosimilar has its own product quality

characteristics. An intact mass analysis has recently been preferred as the first assay to demonstrate the similarity between biosimilar and originator products (28-30). Montacir et al. (28) demonstrated a comparability study of the original rituximab and its biosimilar through intact mass analysis. Four abundant glycoforms (G0F/G0F, G1F/G0F, G1F/G1F, and G2F/G1F) were found on the heavy chains of both the biosimilar and the original with almost the same relative abundances (28). In another study by Hutterer and co-workers, similarities in the glycoform profile of trastuzumab biosimilar have been reported compared to several US- and EU-source originators (29). The

authors emphasized that intact mass analysis revealed the same type of glycoforms in both biosimilar and originators. Seo et al. (30) studied the analytical and functional similarity of bevacizumab biosimilar to several originators' batches. It was shown that the predominant glycoforms for biosimilars were totally in agreement with the originators via high-resolution MS analysis. These literature studies have revealed that the most common glycoform species observed in mAbs are G0F/G0F, G0F/G1F, and G1F/G1F, and the data collected in our study were consistent with those findings in the literature.

Table 2: Comparison of relative glycoform pair abundances for biosimilar and originator batches. Data are shown as mean ± SD (n = 3).

Glycoform Pair Type	%Glycoform (n=3)				
	EU Batch 1	EU Batch 2	Biosimilar	US Batch 1	US Batch 2
G0F–GN/G0	4.28 ± 0.04	4.15 ± 0.05	4.40 ± 0.10	4.96 ± 0.12	7.34 ± 0.10
G0F–GN/G0F	10.81 ± 0.08	11.16 ± 0.05	11.61 ± 0.10	9.85 ± 0.11	14.50 ± 0.10
G0F/G0F	38.45 ± 0.11	43.43 ± 0.20	39.79 ± 0.14	39.64 ± 0.13	40.16 ± 0.09
G0F/G1F	22.11 ± 0.13	21.12 ± 0.10	22.20 ± 0.14	21.78 ± 0.17	19.32 ± 0.05
G1F/G1F	11.44 ± 0.22	10.54 ± 0.11	11.32 ± 0.11	11.45 ± 0.06	10.91 ± 0.12
G1F/G2F	7.62 ± 0.10	5.82 ± 0.12	6.43 ± 0.26	7.40 ± 0.09	5.56 ± 0.22
G2F/G2F	5.29 ± 0.10	3.78 ± 0.10	4.25 ± 0.08	4.92 ±0.06	2.21 ± 0.17

3.2. Reduced Mass Analysis

In reduced mass analysis, the biosimilar and four originator batches were chemically reduced using DTT to their light chain (LC, ~ 25 kDa) and heavy chain (HC, ~ 50 kDa) subunits. In comparison to intact mass analysis, a more accurate mass measurement was achieved (mass error of ± 25 ppm) with reduced mass analysis. Figure 3 shows a comparison of the deconvoluted mass spectra of LCs originating from biosimilar and originator batches.

The deconvoluted mass spectra of LCs comprise a single major peak at 23,451.02 Da for biosimilars, where the originator batches have a mass range of 23,450.98 – 23,451.05 Da, as listed in Table 3. Peaks labeled with asterisks were presumably loss of water (-18 Da) from LC and sodium adduct (+22 Da) of LC. The observed masses of each LC were comparable across all tested materials, with no meaningful differences among samples (see Table 3). The calculated mass error was below 15 ppm, which shows that all LCs have the same amino acid sequence order. The single peak was assigned to the mass of LC based on the known amino acid sequence of the target mAb. Additionally, the observed masses of LCs were in full agreement with their theoretical masses (23,450.74 Da), with a mass error of below 13 ppm (see Table 3). The observation of

a single peak in the deconvoluted mass spectra indicates no glycan attachment site on the LC.

Figure 4 demonstrates the comparison of deconvoluted mass spectra of the HCs obtained from biosimilar and originator batches. It is obvious that the deconvoluted mass spectra of HC is more complicated than LC's mass spectra. This complexity is explained by having a N-glycosylation site in the Fc region of the HC.

As Figure 4 illustrates, biosimilar and originator batches have the same types of glycans (*e.g.,* G0F–GN, G0, G0F, G1F, and G2F) along with similar relative abundances. Peaks labeled with asterisks were loss of water (-18 Da) from HC and sodium adduct (+22 Da) of HC. For biosimilar products, the observed molecular masses of 50,960.15 Da, 51,017.11 Da, 51,163.70 Da, 51,325.84 Da, and 51,487.60 Da represent G0F–GN, G0, G0F, G1F, and G2F glycan containing HC, respectively. The most abundant peak is HC+G0F, with an observed mass of 51,163.70 Da for the biosimilar, closely matched with its calculated theoretical mass (51,163.79 Da) with a mass error of -2 ppm. The originator batches have a mass range of 51,163.60 – 51,163.76 Da for G0F comprising HC. In addition, G0F–GN, G0, G1F, and G2F glycans were also identified with minor intensities (<15% of maximum MS peak height) in the deconvoluted mass spectra. The calculated theoretical masses of HC containing G0F–GN,

G0, G1F, and G2F glycans were 50,960.60 Da, 51,017.65 Da, 51,325.93 Da, and 51,488.07 Da, respectively. Table 3 demonstrates that the observed masses of HC with different glycans for biosimilar and originator batches were totally in agreement with their theoretical molecular masses. The calculated mass errors for all samples were below 25 ppm.
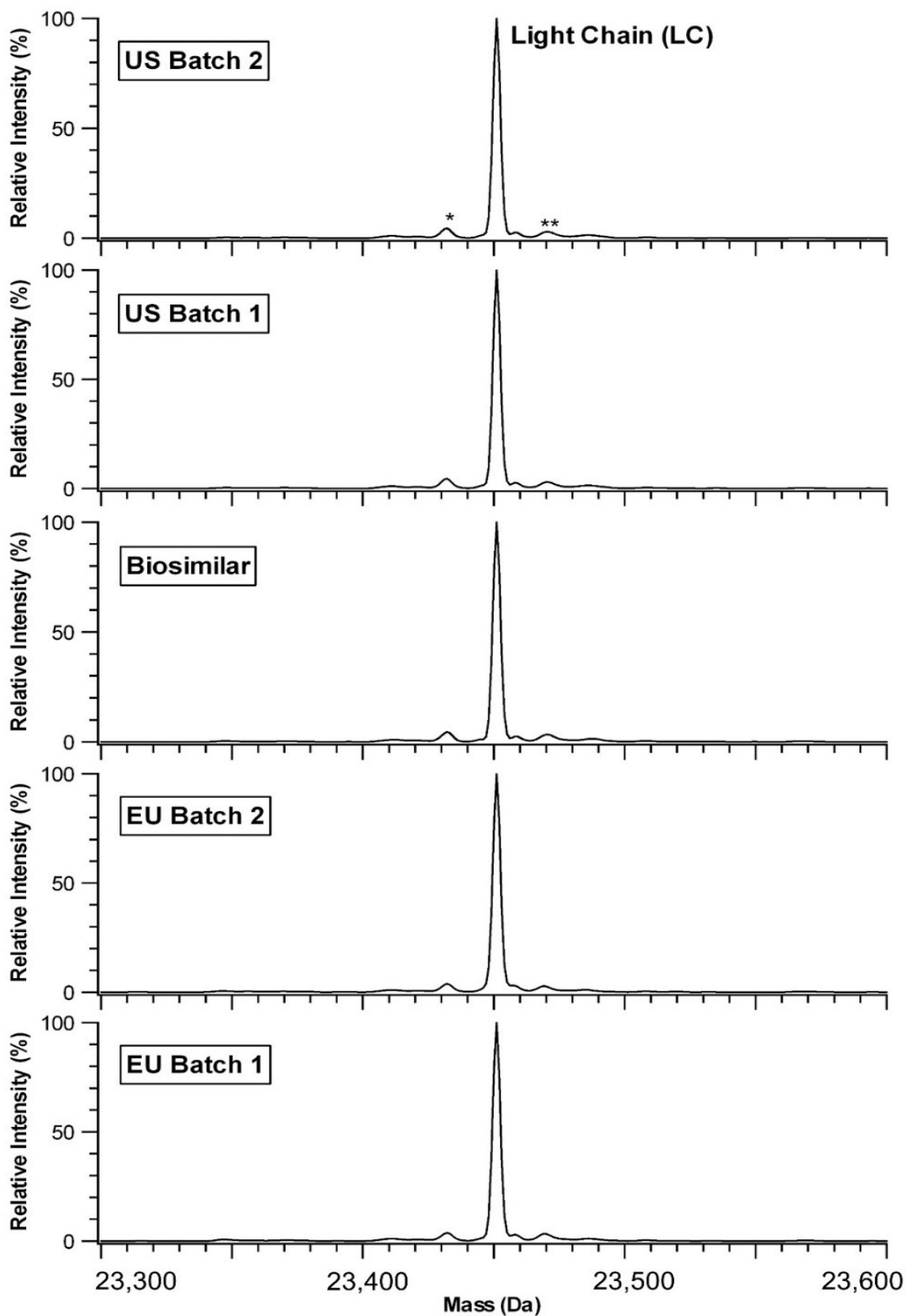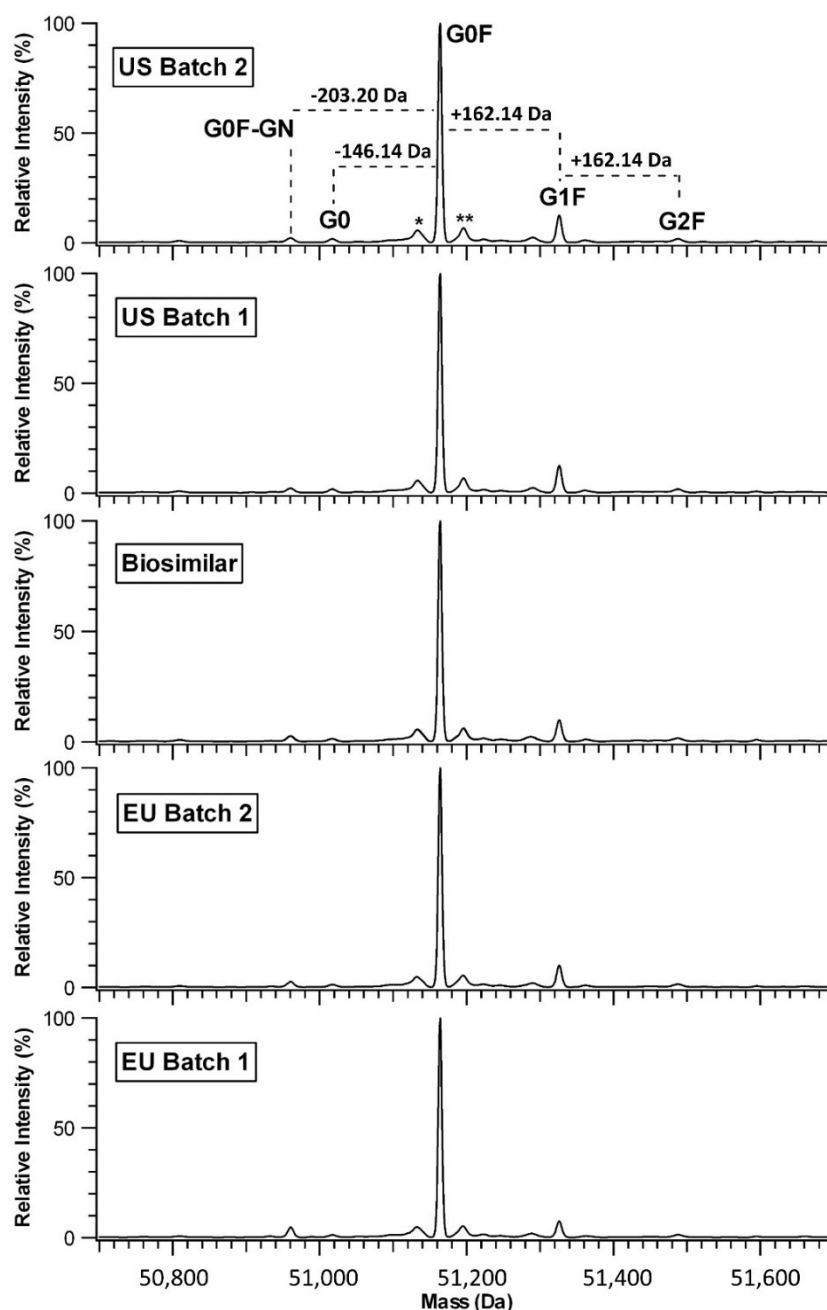

Figure 3: Comparison of deconvoluted mass spectra of light chains of the biosimilar and the four originator batches.

Table 3: Comparison of theoretical mass of light chain (LC) and heavy chain (HC) with observed masses for biosimilar and originator batches.

Chain Name + Glycan Type	Theoretical Mass (Da)	Observed Mass, Da (Mass Error)				
		EU Batch 1	EU Batch 2	Biosimilar	US Batch 1	US Batch 2
LC	23,450.74	23,450.98 (10 ppm)	23,451.04 (13 ppm)	23,451.02 (12 ppm)	23,451.04 (13 ppm)	23,451.05 (13 ppm)
HC + G0F–GN	50,960.60	50,960.27 (-6 ppm)	50,960.07 (-10 ppm)	50,960.15 (-9 ppm)	50,959.83 (-15 ppm)	50,959.92 (-13 ppm)
HC + G0	51,017.65	51,017.17 (-9 ppm)	51,017.19 (-9 ppm)	51,017.11 (-11 ppm)	51,017.06 (-12 ppm)	51,016.52 (-22 ppm)
HC + G0F	51,163.79	51,163.72 (-1 ppm)	51,163.76 (-1 ppm)	51,163.70 (-2 ppm)	51,163.60 (-4 ppm)	51,163.62 (-3 ppm)
HC + G1F	51,325.93	51,325.81 (-2 ppm)	51,325.91 (-0 ppm)	51,325.84 (-2 ppm)	51,325.85 (-2 ppm)	51,325.87 (-1 ppm)
HC + G2F	51,488.07	51,487.80 (-5 ppm)	51,487.24 (-16 ppm)	51,487.60 (-9 ppm)	51,487.41 (-13 ppm)	51,486.88 (-23 ppm)

The calculated relative abundances of glycan-containing peaks are summarized in Table 4 for all tested samples (averages of three runs were reported for each glycoform pair, and data were shown as mean ± SD (n = 3)). The relative abundances were calculated by considering the peak intensities of each identified peak in the deconvoluted mass spectra of the heavy chain. For instance, G0F comprising HC has an abundance of 76.73% for the biosimilar, whereas EU-batches and US-batches have ranged from 77.44 to 77.90% and 75.21 to 76.92%, respectively. The data showed that the abundances of each biosimilar glycan were within the range of four originator batches (see Table 4). The predominant *N*-linked glycan identified in all samples was core-fucosylated biantennary complex type without galactose (G0F), along with a minor contribution of core-fucosylated biantennary type with one galactose residue (G1F). In addition to these forms, minor contributions of core-fucosylated biantennary type glycan with two galactose residues (G2F), afucosylated biantennary type (G0), and lacking the terminal N-acetylglucosamine (G0F–GN) glycans were also detected in the deconvoluted mass spectra. As represented in Figure 4, the mass difference between HC+G0F and HC+G1F peaks was 162.14 Da, indicating that they differ from each other by one galactose residue. Similarly, HC+G1F and HC+G2F peaks differ by only 162.14 Da, the mass of one galactose residue. On the other hand, HC+G0 and HC+G0F peaks have a mass difference of 146.14 Da, showing the mass of one fucose (F) residue, and the mass difference between HC+G0F and HC+(G0F–GN) was 203.20 Da, representing the mass of one terminal N-acetylglucosamine residue.

Figure 4: Comparison of deconvoluted mass spectra of heavy chains of the biosimilar and the four originator batches.

Table 4: Relative glycan abundances of biosimilar and originator batches. Data are shown as mean ± SD (n = 3).

Glycan Type	% Glycan (n=3)				
	EU Batch 1	EU Batch 2	Biosimilar	US Batch 1	US Batch 2
G0F–GN	6.51 ± 0.09	4.48 ± 0.06	5.64 ± 0.08	4.17 ± 0.07	4.65 ± 0.16
G0	2.81 ± 0.08	2.93 ± 0.04	2.97 ± 0.06	3.30 ± 0.08	3.03 ± 0.09
G0F	77.90 ± 0.17	77.44 ± 0.10	76.73 ± 0.16	75.21 ± 0.09	76.92 ± 0.12
G1F	9.26 ± 0.15	11.25 ± 0.23	10.58 ± 0.12	13.18 ± 0.08	11.19 ± 0.08
G2F	3.52 ± 0.05	3.90 ± 0.06	4.08 ± 0.12	4.14 ± 0.04	4.21 ± 0.08

Together with intact mass analysis, a reduced mass assay has also provided comprehensive data for comparability assessment studies. Ayoub et al. (31) have conducted a combination of intact and reduced mass analyses for the routine structural assessment of marketed cetuximab products. They monitored and compared biosimilar and originator glycoforms and glycosylation profiles using ESI and matrix-assisted laser desorption ionization (MALDI) mass spectrometry techniques. Xie et al. (32) demonstrated that intact and reduced mass analyses combined with peptide mapping and released glycan assays are accepted as routine techniques for detailed comparability studies. Liu and colleagues (33) have reported reduced and deglycosylated mass data for the adalimumab biosimilar and originators via electrospray ionization time-of-flight mass spectrometer. With the help of a reverse-phase column, buffer components were removed from the samples prior to the introduction to the interface of the mass spectrometer. The authors have shown that both products have the same polypeptide compositions with the help of reduced mass analysis (33). These literature studies have highlighted that accurate mass measurement via reduced mass analysis provides fast and reliable mass data for biosimilarity demonstration. In this study, we implemented both intact and reduced mass analyses for the comparison of glycoform entities of biosimilar and originator through high-resolution MS. Therefore, these assays can be used as appropriate tests for comparability studies in quality control laboratories.

4. CONCLUSION

This manuscript compares biosimilar and four originator batches' molecular masses and glycoform profiles via intact and reduced mass analyses. The deconvoluted intact mass spectra revealed that the relative abundances of the detected glycoform entities were comparable for all tested samples. G0F/G0F and G0F/G1F pairs comprise the highest abundance compared to the other glycoform pairs. Additionally, reduced mass analysis demonstrates that the same types of glycans (namely G0F, G1F, G2F, G0, and G0F-NG) are localized on the HC of biosimilar and four originator batches. No differences between the biosimilar and originators were observed regarding LC and HC masses, while the mass errors were below 15 ppm and 25 ppm, respectively. Overall data have revealed that the results are consistent with the expected amino acid sequence of the antibody. Additionally, the results showed that intact and reduced mass analyses can be implemented to monitor the glycosylation heterogeneity of mAbs during the manufacturing process. These assays require no or minimum sample preparation step and also the analysis time is short compared to the other assays. The data also provided that EU-sourced and US-approved originator batches have a batch-to-batch variability in terms of glycoform contents as well as their molecular masses.

5. CONFLICT OF INTEREST

There are no conflicts of interest declared by the author.

6. ACKNOWLEDGMENTS

7. REFERENCES

1. Liu JKH. The history of monoclonal antibody development - Progress, remaining challenges and future innovations. Ann Med Surg [Internet]. 2014 Dec 1;3(4):113–6. Available from: <URL>.

2. Brekke OH, Sandlie I. Therapeutic antibodies for human diseases at the dawn of the twenty-first century. Nat Rev Drug Discov [Internet]. 2003 Jan 1;2(1):52–62. Available from: <URL>.

3. Scott AM, Wolchok JD, Old LJ. Antibody therapy of cancer. Nat Rev Cancer [Internet]. 2012 Apr 22;12(4):278–87. Available from: <URL>.

4. Liu H, Ponniah G, Zhang H-M, Nowak C, Neill A, Gonzalez-Lopez N, et al. In vitro and in vivo modifications of recombinant and human IgG antibodies. MAbs [Internet]. 2014 Sep 3;6(5):1145–54. Available from: <URL>.

5. Liu H, Gaza-Bulseco G, Faldu D, Chumsae C, Sun J. Heterogeneity of Monoclonal Antibodies. J Pharm Sci [Internet]. 2008 Jul 1;97(7):2426–47. Available from: <URL>.

6. Costa AR, Rodrigues ME, Henriques M, Oliveira R, Azeredo J. Glycosylation: impact, control and improvement during therapeutic protein production. Crit Rev Biotechnol [Internet]. 2014 Dec 6;34(4):281–99. Available from: <URL>.

7. Jefferis R. Recombinant antibody therapeutics: the impact of glycosylation on mechanisms of action. Trends Pharmacol Sci [Internet]. 2009 Jul 1;30(7):356–62. Available from: <URL>.

8. Sinclair AM, Elliott S. Glycoengineering: The effect of glycosylation on the properties of therapeutic proteins. J Pharm Sci [Internet]. 2005 Aug 1;94(8):1626–35. Available from: <URL>.

9. Zhang Z, Pan H, Chen X. Mass spectrometry for structural characterization of therapeutic antibodies. Mass Spectrom Rev [Internet]. 2009 Jan 20;28(1):147–76. Available from: <URL>.

10. Chen G, Warrack BM, Goodenough AK, Wei H, Wang-Iverson DB, Tymiak AA. Characterization of protein therapeutics by mass spectrometry: recent developments and future directions. Drug Discov Today [Internet]. 2011 Jan 1;16(1–2):58–64. Available from: <URL>.

11. Lyubarskaya Y, Houde D, Woodard J, Murphy D, Mhatre R. Analysis of recombinant monoclonal antibody isoforms by electrospray ionization mass spectrometry as a strategy for streamlining characterization of recombinant monoclonal antibody charge heterogeneity. Anal Biochem [Internet]. 2006 Jan 1;348(1):24–39. Available from: <URL>.

12. Beck A, Sanglier-Cianférani S, Van Dorsselaer A. Biosimilar, Biobetter, and Next Generation Antibody Characterization by Mass Spectrometry. Anal Chem [Internet]. 2012 Jun 5;84(11):4637–46. Available from: <URL>.

13. Sandra K, Vandenheede I, Sandra P. Modern chromatographic and mass spectrometric techniques for protein biopharmaceutical characterization. J Chromatogr A [Internet]. 2014 Mar 28;1335:81–103. Available from: <URL>.

14. Rathore D, Faustino A, Schiel J, Pang E, Boyne M, Rogstad S. The role of mass spectrometry in the characterization of biologic protein products. Expert Rev Proteomics [Internet]. 2018 May 4;15(5):431–49. Available from: <URL>.

15. Sokolowska I, Mo J, Rahimi Pirkolachahi F, McVean C, Meijer LAT, Switzar L, et al. Implementation of a High-Resolution Liquid Chromatography–Mass Spectrometry Method in Quality Control Laboratories for Release and Stability Testing of a Commercial Antibody Product. Anal Chem [Internet]. 2020 Feb 4;92(3):2369–73. Available from: <URL>.

16. Olivova P, Chen W, Chakraborty AB, Gebler JC. Determination of N-glycosylation sites and site heterogeneity in a monoclonal antibody by electrospray quadrupole ion-mobility time-of-flight mass spectrometry. Rapid Commun Mass Spectrom [Internet]. 2008 Jan 15;22(1):29–40. Available from: <URL>.

17. Sinha S, Pipes G, Topp EM, Bondarenko P V., Treuheit MJ, Gadgil HS. Comparison of LC and LC/MS methods for quantifying *N* -glycosylation in recombinant IgGs. J Am Soc Mass Spectrom [Internet]. 2008 Nov 1;19(11):1643–54. Available from: <URL>.

18. Damen CWN, Chen W, Chakraborty AB, van Oosterhout M, Mazzeo JR, Gebler JC, et al. Electrospray ionization quadrupole ion-mobility time-of-flight mass spectrometry as a tool to distinguish the lot-to-lot heterogeneity in N-glycosylation profile of the therapeutic monoclonal antibody trastuzumab. J Am Soc Mass Spectrom [Internet]. 2009 Nov 1;20(11):2021–33. Available from: <URL>.

19. Thompson NJ, Rosati S, Rose RJ, Heck AJR. The impact of mass spectrometry on the study of intact antibodies: from post-translational modifications to structural analysis. Chem Commun [Internet]. 2013 Dec 12;49(6):538–48. Available from: <URL>.

20. Gomes RA, Almeida C, Correia C, Guerreiro A, Simplício AL, Abreu IA, et al. Exploring the analytical power of the QTOF MS platform to assess monoclonal antibodies quality attributes. Banoub J, editor. PLoS One [Internet]. 2019 Jul 10;14(7):e0219156. Available from: <URL>.

21. Yu L, Remmele RL, He B. Identification of N-terminal modification for recombinant monoclonal antibody light chain using partial reduction and quadrupole time-of-flight mass spectrometry. Rapid Commun Mass Spectrom [Internet]. 2006 Dec 30;20(24):3674–80. Available from: <URL>.

22. Liu P, Zhu X, Wu W, Ludwig R, Song H, Li R, et al. Subunit mass analysis for monitoring multiple attributes of monoclonal antibodies. Rapid Commun Mass Spectrom [Internet]. 2019 Jan 15;33(1):31–40. Available from: <URL>.

23. Schilling M, Feng P, Sosic Z, Traviglia SL. Development and validation of a platform reduced intact mass method for process monitoring of monoclonal antibody glycosylation during routine manufacturing. Bioengineered [Internet]. 2020 Jan 1;11(1):1301–12. Available from: <URL>.

24. Lanter C, Lev M, Cao L, Loladze V. Rapid Intact mass based multi-attribute method in support of mAb upstream process development. J Biotechnol [Internet]. 2020 May 20;314–315:63–70. Available from: <URL>.

25. Martelet A, Garrigue V, Zhang Z, Genet B, Guttman A. Multi-attribute method based characterization of antibody drug conjugates (ADC) at the intact and subunit levels. J Pharm Biomed Anal [Internet]. 2021 Jul 15;201:114094. Available from: <URL>.

26. Naumann L, Schlossbauer P, Klingler F, Hesse F, Otte K, Neusüß C. High-throughput glycosylation analysis of intact monoclonal antibodies by mass spectrometry coupled with capillary electrophoresis and liquid chromatography. J Sep Sci [Internet]. 2022 Jun 27;45(12):2034–44. Available from: <URL>.

27. Haga Y, Yamada M, Fujii R, Saichi N, Yokokawa T, Hama T, et al. Fast and Ultrasensitive Glycoform Analysis by Supercritical Fluid Chromatography–Tandem Mass Spectrometry. Anal Chem [Internet]. 2022 Nov 22;94(46):15948–55. Available from: <URL>.

28. Montacir O, Montacir H, Eravci M, Springer A, Hinderlich S, Saadati A, et al. Comparability study of Rituximab originator and follow-on biopharmaceutical. J Pharm Biomed Anal [Internet]. 2017 Jun 5;140:239–51. Available from: <URL>.

29. Hutterer KM, Polozova A, Kuhns S, McBride HJ, Cao X, Liu J. Assessing Analytical and Functional Similarity of Proposed Amgen Biosimilar ABP 980 to Trastuzumab. BioDrugs [Internet]. 2019 Jun 10;33(3):321–33. Available from: <URL>.

30. Seo N, Polozova A, Zhang M, Yates Z, Cao S, Li H, et al. Analytical and functional similarity of Amgen biosimilar ABP 215 to bevacizumab. MAbs [Internet]. 2018 May 19;10(4):678–91. Available from: <URL>.

31. Ayoub D, Jabs W, Resemann A, Evers W, Evans C, Main L, et al. Correct primary structure assessment and extensive glyco-profiling of cetuximab by a combination of intact, middle-up, middle-down and bottom-up ESI and MALDI mass spectrometry techniques. MAbs [Internet]. 2013 Sep 27;5(5):699–710. Available from: <URL>.

32. Xie H, Chakraborty A, Ahn J, Yu YQ, Dakshinamoorthy DP, Gilar M, et al. Rapid comparison of a candidate biosimilar to an innovator monoclonal antibody with advanced liquid chromatography and mass spectrometry technologies. MAbs [Internet]. 2010 Jul 27;2(4):379–94. Available from: <URL>.

33. Liu J, Eris T, Li C, Cao S, Kuhns S. Assessing Analytical Similarity of Proposed Amgen Biosimilar ABP 501 to Adalimumab. BioDrugs [Internet]. 2016 Aug 26 [cited 2023 Dec 21];30(4):321–38. Available from: <URL>.

Fluorescent Polymeric Sensor for Selective and Sensitive Detection of Cu(II) Ions in Aqueous Medium

Soner Çubuk[*,1] (iD)**, Nur Koçoğlu**[1] (iD)**, Gülay Bayramoğlu**[2] (iD)**, Hatice Birtane**[1] (iD)**,
M. Vezir Kahraman**[1] (iD)

[1]Chemistry Department, Faculty of Science, Marmara University, 34722 Istanbul, Türkiye.
[2]Yalova Vocational School, Department of Textile - Clothing, Shoes and Leather, Yalova University, 77200 Yalova, Türkiye.

Abstract: In our study, a selective and sensitive determination method was developed for Cu(II) ions by spectrofluorimetry. For this purpose, a polymeric membrane was prepared to determine Cu(II) ions by curing crosslinkers, functional monomers, and photoinitiators under UV light. The membrane was characterized, and the optimum conditions for determining Cu(II) ions were systematically investigated. The detection was performed at pH 5.0 in as little as 20 seconds at excitation and emission wavelengths of 376 nm and 455 nm, respectively. The linear range was $7.86 \cdot 10^{-9}$-$1.57 \cdot 10^{-7}$ mol/L, and the method's detection limit was $2.24 \cdot 10^{-9}$ mol/L. In addition, the sensor's repeatability, stability, and life were examined, and recovery studies were conducted. As a result, the developed method has been successfully applied to wastewater samples as a real sample. In addition, determining Cu(II) ions at low concentrations can be done quickly, reliably, and with high selectivity and sensitivity.

1. INTRODUCTION

With the development of industry and the increase in population, environmental pollution has become an enormous problem. Although some metal ions are essential nutrients required for various biological and physiological functions, they become toxic even at very low concentrations (1-3). Even metals such as iron, zinc, copper, and manganese may have adverse health effects when they exceed threshold concentrations (4,5). Heavy metals are considered significant environmental pollutants that enter the surroundings naturally and through human activities (6). Mainly, water and soil pollution by heavy metals is seen because of human activities such as mining, agriculture, transportation, and industrial production (7-9). When heavy metals are released into the air, water, and food, they are taken into the body directly or indirectly through inhalation, ingestion, or skin absorption (10,11).

Copper, a bio-element, is one of the most abundant heavy metals. It plays a vital role in iron absorption from the intestine, tissue maturation, formation of red blood cells, cellular respiration, electron transfer, and biological systems. It is also a cofactor in at least 30 essential enzymes (12-16). Copper is found in the oxidized Cu(II) and reduced Cu(I) states in biological systems, and their fundamental functions are dictated by their redox chemistry (17). The human body's primary sources of copper intake are seeds, grains, nuts, beans, salmon, spinach, shellfish, and beef liver (18). The Recommended Dietary Allowance (RDA) for adults over 19 years of age is 900 µg per day, while the Tolerable Upper Intake Level (UL) is 10 mg per day (19). The average copper intake from dietary sources is about 1.0 to 1.6 mg daily for adults.

The copper level in the body is maintained through the absorption of copper from the intestine and the release of copper from the liver. Therefore, as its critical side effect is cytotoxic, high copper ion levels in the body can cause liver damage (18-20). High levels of copper in the body can result in gastrointestinal symptoms such as abdominal pain, cramps, vomiting, dizziness, and diarrhea. In addition, they can lead to genetic disorders such as Menkes and Wilson's diseases (21-24). Even though the copper intake mostly depends on food, drinking water also becomes a potential source of excess exposure. The widespread use of copper, especially in agriculture, industry, and chemistry, causes contamination of the community water sources. Besides, old, corroded household pipes, plumbing fixtures, and faucets cause copper leaks and increase copper levels in tap water. The maximum copper contaminant level in drinking water has been recommended by the World Health Organization (WHO) as 20 μM (25). Even though the risk of excess intake of copper from food, water, and supplements seems to be low for adults, it is possible for children, especially those aged 1 through 8 years. Considerably high intakes, the long-term effect of excess copper intake, and the toxicity of copper are not well studied in humans.

For these reasons, it is essential to determine the copper content in environmental systems such as soil, air, water, and humans. Up to now, many methods have been established for determining Cu(II) ions. These include ion chromatography (26), surface plasmon resonance spectroscopy (SPR) (27), voltammetry (28), atomic absorption spectrophotometry (AAS) (29), inductively coupled plasma-mass spectrometry (ICP-MS) (30), UV-vis spectrophotometry (31), laser-induced fragmentation spectroscopy (LIBS) (32) and inductively coupled plasma-optical emission spectroscopy (ICP-OES) (33). Although most of the abovementioned methods provide precision, high accuracy, sensitivity, and low detection limits, they require sophisticated and expensive equipment, highly qualified personnel, and rigorous sample preparation.

Studies and significant efforts have been made to determine Cu(II) ions with short analysis time, accuracy, reliability, and low instrument costs in recent years. Many fluorescent sensors such as coumarin and derivatives (34), rhodamine (35), fluorescein (36), truxene (37), and quinoline (38) were reported and have been reported in some applications. Whether their properties (selectivity, sensitivity, response time) were improved, they all interacted with copper and formed Cu(II) complexes that resulted in distinct fluorescence responses.

In this study, we aimed to develop a new UV-curable polymeric fluorescent sensor to detect Cu(II) ions in aqueous medium. UV curing is a fast, easy, and environmentally friendly method for synthesizing polymeric membranes. These types of one-step synthesized membranes that can detect Cu(II) ions can attract attention due to their stable structure,

high efficiency and accuracy, low cost, low time consumption, and operational simplicity.

2. EXPERIMENTAL SECTION

2.1. Materials
Poly(ethylene glycol) diacrylate (PEGDA) (M_n=575) that contains 400-600 ppm MEHQ as an inhibitor, technical grade trimethylolpropane triacrylate (TMPTA) that contains monomethyl ether hydroquinone as an inhibitor, triphenylphosphine (TPP) (>99.0% (GC)), technical grade glycidyl trimethylammonium chloride (GTAC) that contains 2-4% chlorohydrin (>90.0% (GC)), 2-hydroxyethyl methacrylate (HEMA) (>99.0%) that contains <50 ppm monomethyl ether hydroquinone as inhibitor, N-Isopropylacrylamide (NIPAM) (>99.0%,), and all other chemicals were purchased from Sigma-Aldrich and used without purification. The photoinitiator 1-hydroxy cyclohexyl-phenyl-ketone (Irgacure 184) (>99.0%) was obtained from Ciba Specialty Chemicals. In preparing the aqueous solutions, ultrapure water with a specific resistance of 18.2MΩ obtained from the Merck-Millipore Direct-Q® 3UV water purification system was used.

2.2. Instrumentations
Perkin Elmer Spectrum 100 spectrometer and Philips XL30 Environmental Scanning Electron Microscope with Field Emission Gun (Equipped with EDAX-Energy Dispersive X-ray Analysis Unit) scanning electron microscope were used to obtaining Fourier Transform Infrared (FT-IR) spectrum and scanning electron microscope (SEM) images of the prepared polymeric membranes, respectively. The FTIR spectrum of the solid polymeric membrane was recorded on Perkin Elmer Spectrum 100 ATR-FTIR spectrometer in the range of 4000–400 cm^{-1} at room temperature with 4 cm^{-1} resolution mode. Before SEM imaging, the membrane surfaces were coated with an approximately 300 Å thick platinum layer with Edwards S 150 B sputter coater. The Varian Cary Eclipse Fluorescence Spectrophotometer containing a 1 cm path-length quartz cuvette was used for fluorescence measurements. All pH measurements were performed using the Hanna pH-213 model pH meter.

2.3. Preparation of Polymeric Sensor
Several compositions were studied to find optimum membrane composition without fractures, cracks, and non-dispersion in the aqueous environment. First, a polymeric sensor containing aGTAC was prepared by mixing aGTAC (30% wt.), HEMA (15% wt.), TMPTA (15% wt.), PEGDA (30% wt.), NIPAM (10% wt.) and photoinitiator Irgacure184 (3% of total weight) in a beaker. PEGDA was used as a binder, which provides physical and mechanical properties, and TMPTA was used as a reactive diluent, which controls the cross-linking density during polymerization. NIPAM and HEMA were used to render the membrane with environmental-sensitive properties such as swelling.

As in our previous study, the aGTAC was synthesized by reacting its oxirane groups with acrylic acid in the presence of TPP (39). The UV curing process was conducted and covered under ambient conditions. The mixture, homogenized by mixing, was poured into a Teflon® mold (12x40x 3; WxLxD, mm), covered with transparent Teflon® film to prevent the inhibiting effect of oxygen and cured under a high-pressure UV lamp (OSRAM 300 W, λ_{max}: 365 nm) for 3 minutes. Then, the polymeric membrane was removed from the mold. To remove unreacted monomers, obtained membranes were soaked overnight in distilled water, frozen in a freezer, and dried with a lyophilizer. The preparation of the membrane is shown in Scheme 1.
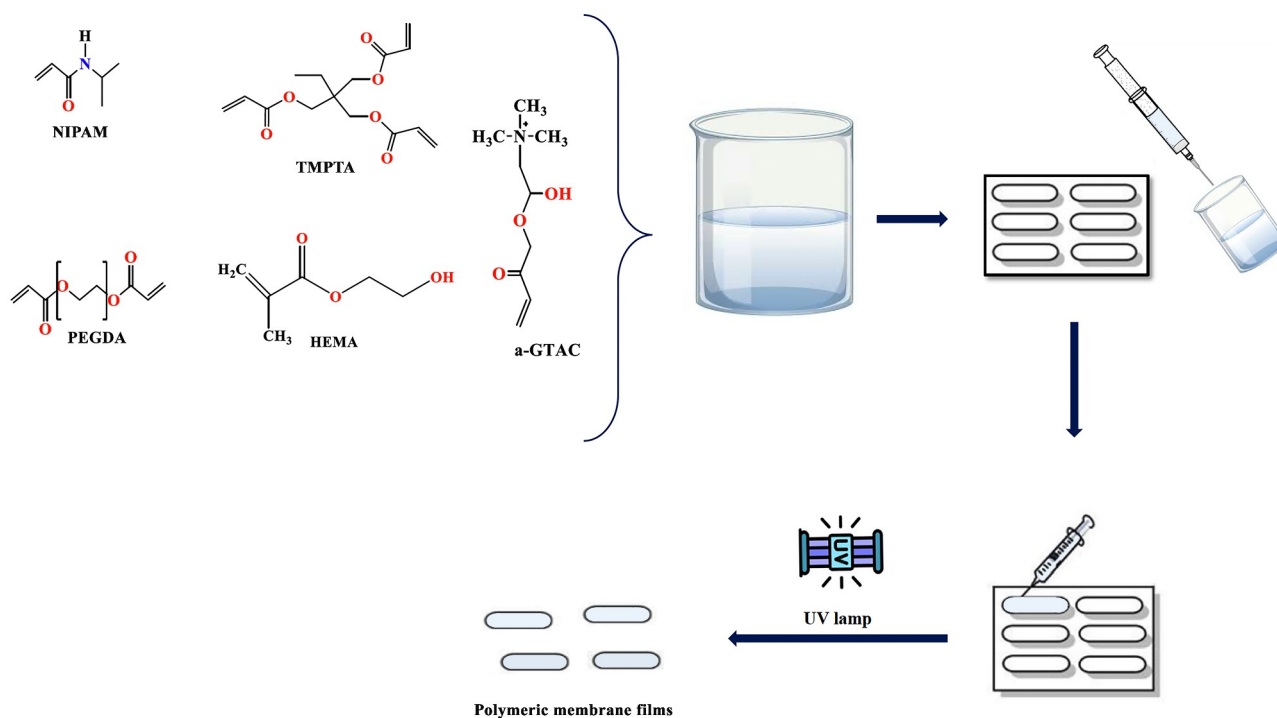

Scheme 1. The preparation of the membrane.

3. RESULTS AND DISCUSSION

3.1. Characterization

3.1.1. FTIR Analysis
The ATR-FTIR spectrum of the solid membrane is demonstrated in Figure 1. The spectrum shows a broad peak at 3352 cm^{-1}, indicating the presence of –OH groups in aGTAC and HEMA. Another peak observed at 1707 cm^{-1} is associated with the vibration band of the –C=O group. Additionally, the spectrum shows a stretching vibration band of the C–N bond at 1449 cm^{-1} in NIPAM. Finally, the absence of a vibrational band at approximately 1634 cm^{-1} showing acrylates in the FT-IR spectrum of the membrane indicates that the cross-linked membrane was prepared successfully (39,40).
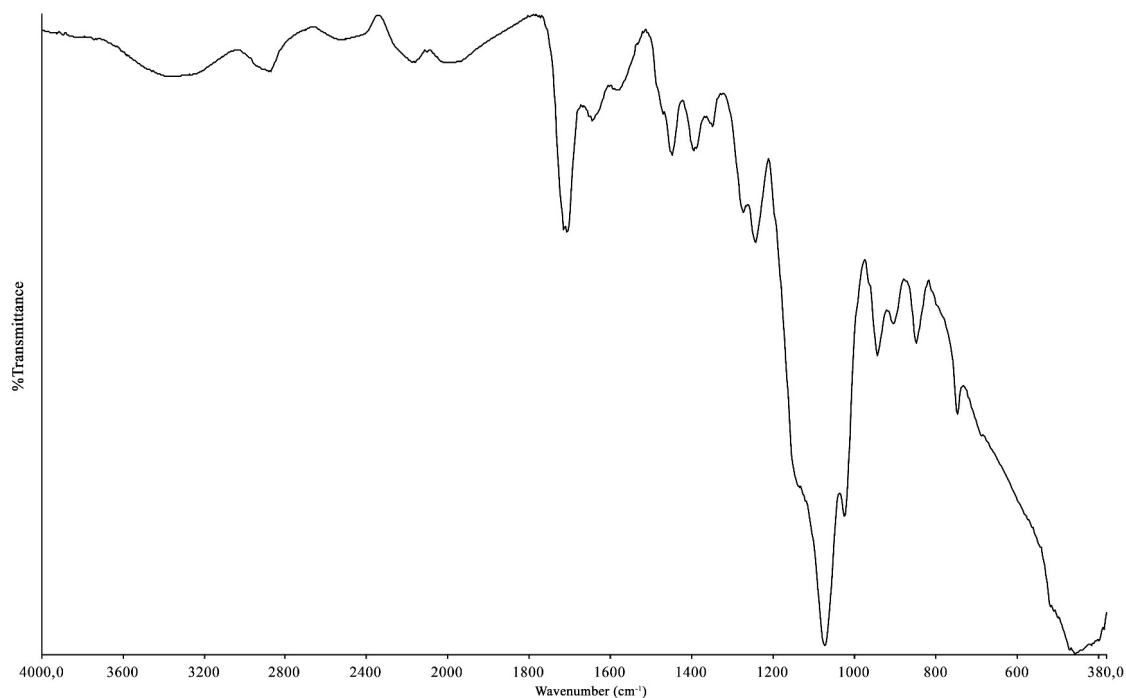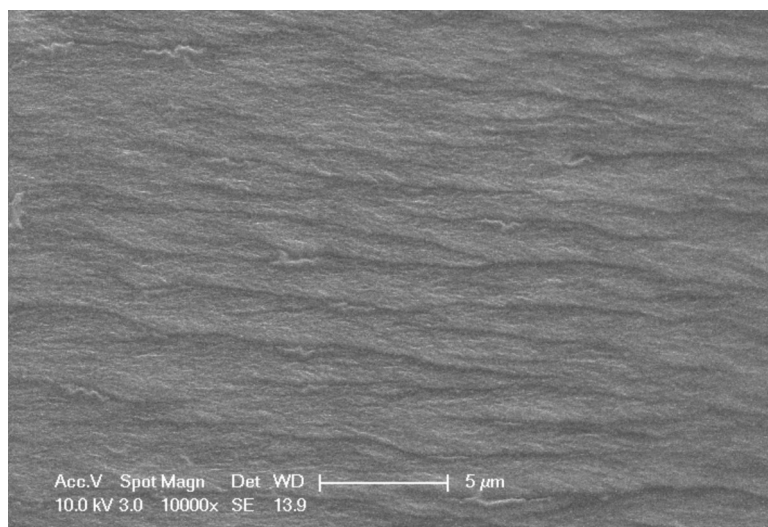
Figure 1: FTIR spectra of the membrane.

3.1.2. Surface Morphology Analysis Results
Functional groups that react with ions must be distributed uniformly throughout the polymer sensor membrane. In addition, surface homogeneity is critical for improving the polymeric membranes' sensing properties as fluorescence sensors. The 10000x magnified image of the SEM analysis performed for this purpose of the polymeric membrane is given in Figure 2. The texture shown in the SEM image in Figure 2 reveals a uniform, crack-free, and nonporous structure as desired.


Figure 2: SEM image of the polymeric membrane at 10000X magnification.

3.1.3. Spectral characterization studies
Using fluorescent spectroscopy, the excitation and emission spectra of the polymeric membrane were recorded in the presence and absence of Cu(II) solution at a concentration of 1.57×10^{-8} mol/L. The excitation wavelength, emission wavelength, photomultiplier tube (PMT) voltage, and slit widths were 376 nm, 455 nm, 600 V, and 10 nm, respectively. The obtained spectrum is given in Figure 3. The fluorescence intensity decreased in the presence of Cu(II) ion. It was thought to be a concurrency of static quenching in the presence of Cu(II) ions as Cu(II)– aGTAC interaction was started.

380
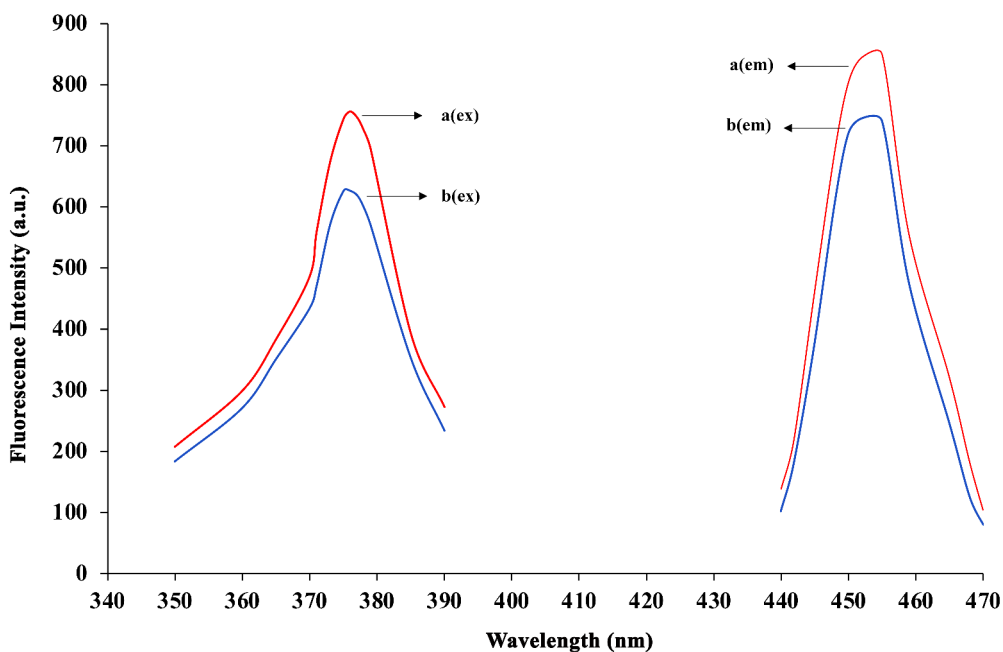
Figure 3: Excitation and fluorescence spectra of the polymeric membrane in the (a) absence (line) and the (b) presence of 1.57×10^{-8} mol/L Cu(II) (dot line); (λ_{ex}=376 nm, λ_{em}=455 nm, slit widths=10 nm, photomultiplier tube voltage= 600 V).

3.1.4. Optimization of the experimental conditions
In this study, the key factor in the design of fluorescent polymeric sensors is Cu(II) recognition.

Since Cu(II)–aGTAC interaction depended on pH, fluorescence intensity could be altered between different pH ranges. Because of that, pH should be controlled to be the optimum value. To determine the pH effect on the polymeric sensor, fluorescence intensity measurements were made in the presence of 1.57×10^{-8} mol/L Cu(II) ions using buffer solutions between pH 1.0-8.0 values. The pH change trends of the fluorescence intensity of the polymeric sensor are shown in Figure 4. The fluorescence intensity slightly decreases in the range of pH 1.0-3.0, sharply increases in the range of pH 3.0-5.0, and sharply decreases after reaching the maximum level at pH 5.0. The decrease at a lower pH range can be attributed to two different mechanisms. First, the protonation of hydroxonium ions of the nitrogen atom penetrates the polymeric membrane because of its greater affinity for protons and reduced mobility of electrons of the conjugated bonds. At a higher pH range, copper hydroxide precipitation competed with Cu(II)-aGTAC interaction, and the polymeric membrane was slightly swelled to decrease the fluorescence intensity. The second one is Cu(II)-NIPAM complex formation. All the acrylic/methacrylic groups of the components react with each other under UV light with the presence of a photoinitiator, thereby resulting in an efficiently aGTAC grafted cationized membrane along with amine and hydroxyl groups. Especially with the reaction of NIPAM and aGTMAC, the polymeric membrane results in an anionic exchanger forming both amine and quaternary amine groups. It is known that Cu(II) ions can interact with -OH groups of both aGTAC and HEMA and the amine group of NIPAM. The cross-linked structure of the polymeric membrane inhibits the interaction of the quaternary ammonium groups from aGTMAC with the amine groups of NIPAM. Since NIPAM molecules have a hydrophobic group on the backbone, they tend to swell when the NIPAM-attached membrane is treated with water. This increases chain mobility and surface area, allowing functional groups and Cu(II) attachment to interact easily.

Nevertheless, amine groups of NIPAM lead to a cationic moiety at low pH degrees. Tertiary amine groups of NIPAM protonated at a pH below 2 and positively charged NIPAM would repel Cu(II) ions like aGTMAC. Cu(II) ions induce deprotonation of -NH groups in amide bonds and lead to the formation of Cu(II) complexes (41). Considering the obtained results, pH 5.0 was chosen to conduct further experiments.
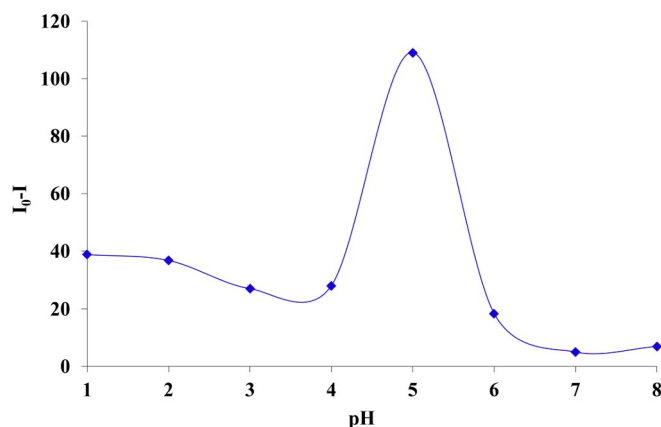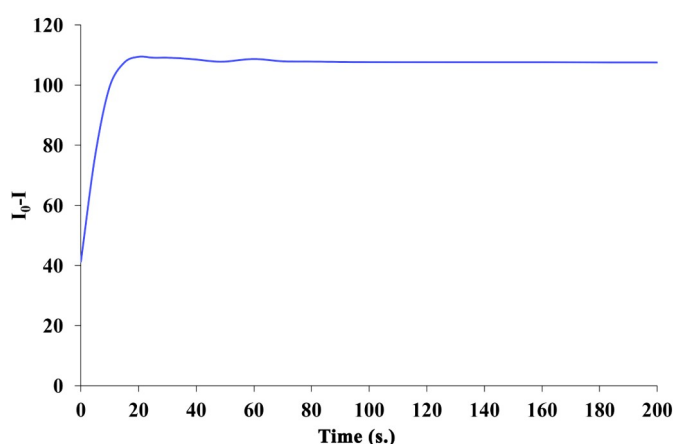
Figure 4: pH effect on fluorescence intensity (C=1.57×10^{-8} mol/L Cu(II).

3.1.5. Determination of the Response Time
To determine the change in fluorescence intensity of the sensor with time, measurements were made in the presence of 1.57×10^{-8} mol/L Cu(II) ions at 5-second intervals for 200 seconds. As shown in Figure 5, the fluorescence intensity of the polymeric sensor increased with the increase of time, reached equilibrium within 20 seconds, and did not change until 200 seconds. Since the fluorescence intensity remained constant within 20-200 seconds, the polymeric sensor could serve as a rapid and reliable probe for Cu(II) ions with the minimum 20-second waiting requirement.

**Figure 5:** Effect of time on fluorescence intensity (C=1.57×10^{-8} mol/L Cu(II), pH=5).

3.1.6. Linear Range and Limit of Detection (LOD)
A calibration curve was established with the fluorescence intensities against the concentration of 6 samples containing Cu(II) ions within the 7.86×10^{-9} - 1.57×10^{-7} mol/L (0.5 - 10 ppb) to determine the calibration range. All samples were prepared in optimum conditions according to the experimental procedure, and fluorescence intensities were measured at 455 nm emission and 376 nm excitation wavelengths. The results indicated that increased Cu(II) ion concentration in the given range decreases the fluorescence intensity significantly. As a result, a linear plot with good linearity (R^2=0.9954)

was obtained to determine the slope, as shown in Figure 6.

Solutions (n=7) containing 7.86×10^{-9} mol/L Cu(II) were used to calculate the proposed method's detection limit. The detection limit (LOD:3xSD / m) was calculated according to the IUPAC recommendations (42). It was found to be 2.24×10^{-9} mol/L. In this equation, SD indicates the standard deviation of 7 replicate measurements of 7.86×10^{-9} mol/L Cu(II) solution, and m shows the slope of the calibration line.
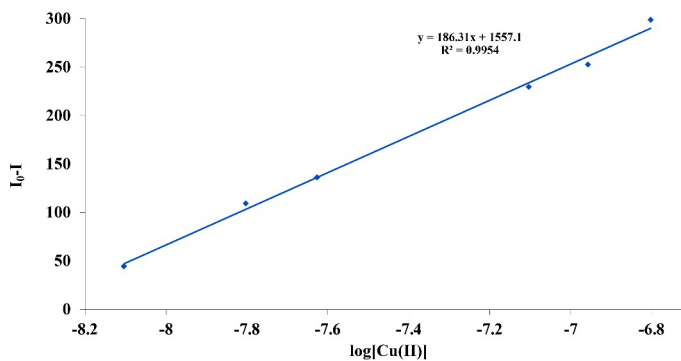
Figure 6: The calibration curve of the polymeric membrane ($\lambda_{ex}\lambda_{em}$: 376 nm/455 nm; pH:5.0; t= 20 s); (Io-I) where I_0 and I are the fluorescence intensities in 7.86×10^{-9} and 1.57×10^{-7} mol L^{-1} Cu(II), respectively.

3.1.7. Sensor Regeneration and Reusability Studies

The regeneration of the polymeric membrane was performed by a 1-minute distilled water washing followed by 30 seconds of pH 5.0 buffer solution washing. It was observed that the fluorescence intensity was found to almost fully recover after the washing process, even after 250 washing cycles. This can be attributed to the non-affinity of the buffer solution with the polymeric membrane. One can see 30 regeneration results obtained from the regeneration process in Figure 7. The standard deviation (SD) of fluorescence intensities was calculated as ±3.7.
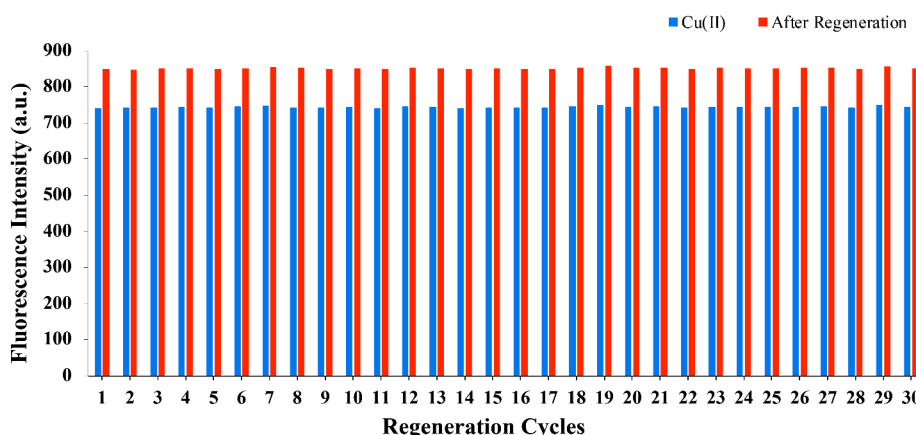

Figure 7: The effect of regeneration on fluorescence intensity of the sensor with distilled water and pH:5.0 buffer after 1.57×10^{-7} mol/L Cu(II) ion contact.

3.1.8. Reliability, Stability, and Repeatability

Reliability, stability, and repeatability are essential factors in evaluating the sensors' performance, and they play a crucial role in sensor applications. To investigate the reliability and stability of the prepared polymeric membrane sensor, it was stored in a desiccator, which was kept in the dark. The fluorescence intensity was recorded at regular intervals over six months; the results are shown in Figure 8. In line with the results in Figure 8, the change between the initial and final fluorescence intensities was only within a range of ±5% at the end of 6 months, which means the lifetime of the polymeric membrane is acceptable for analytical applications. To determine the short-term stability of the polymeric membrane, it was exposed to a 1.57×10^{-8} mol/L Cu(II) solution for ten hours, and fluorescence intensity measurements were recorded at intervals of 10 min. The standard deviation of ±3.4% was achieved, and based on this result, it can be said that the short-term stability of the polymeric membrane is reasonable. The stability results can be ascribed to effective Cu(II)-aGTAC interaction. The repeatability of the results was also determined by using five polymeric membranes with the same formulation, and the fluorescence intensity measurements were carried out under optimum conditions according to the above-mentioned experimental procedure. A standard deviation of ±2.3% was achieved.
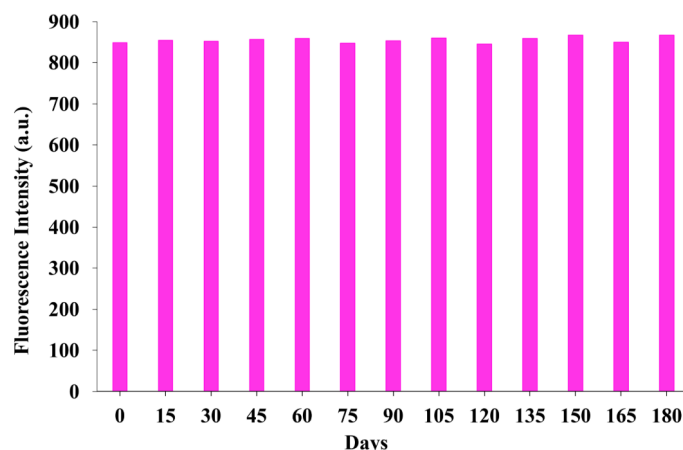
Figure 8: The fluorescence intensity changes at regular intervals during six months membrane These results indicate satisfactory repeatability of the polymeric membrane. ($\lambda_{ex}/\lambda_{em}$: 376 nm/455 nm; pH 5.0; t= 20 s).

3.1.9. Selectivity of Cu(II) ions toward metal ions
Selectivity is a crucial factor for a new sensor in real analytical applications. Since the interference of different ions can have a negative or positive effect on Cu(II) detection, the selectivity of the polymeric membrane to Cu(II) against other ions, including using Zn^{2+}, Fe^{3+}, Ni^{2+}, Cd^{2+}, Au^{3+}, Ag^+, Mn^{2+}, and Hg^{2+} were investigated. To investigate the selectivity of the prepared polymeric sensor membrane against Cu(II) ions, the fluorescence intensities of 1.57×10^{-8} mol/L Cu(II) solution were measured in the presence of 10 equivalents of each of the eight metal ion solutions. Measurements were completed by increasing the amount of coexisting ions up to the concentration where the change in fluorescence intensity was a maximum of ±5%. The upper limit concentration values of coexisting species results are given in Table 1. As a result, it was found that the detection of Cu(II) ions could be made selectively in the presence of ions above with mole amounts that vary from 950 to 1172.

Table 1: The effect of common metal ions on determining Cu(II) under optimum conditions.

Species	x-fold higher than Cu(II) mol number	Concentration of the foreign ions (mol/L) (mol L^{-1})
Fe(III)	1133	1.78×10^{-5}
Hg(II)	950	1.49×10^{-5}
Zn(II)	968	1.52×10^{-5}
Cd(II)	1127	1.77×10^{-5}
Mn(II)	1153	1.81×10^{-5}
Ag(I)	1172	1.84×10^{-5}
Au(III)	962	1.51×10^{-5}
Ni(II)	1083	1.70×10^{-5}

3.1.10. Analytical applications of the sensor
SPS-WW1 and SPS-WW2 certified wastewater reference (CRM) solutions diluted with pH:5 buffer solution were used to evaluate the analytical application of the polymeric membrane. The Cu(II) ion concentrations were 6.49×10^{-6} and 3.25×10^{-5} mol/L for SPS-WW-1 and SPS-WW-2, respectively. The relative error values were calculated as 2.78% and 3.07%. The obtained results were by the certificate value (Table 2).

Table 2: Real sample analysis results with our method (n = 6).

Sample	Our Method (mol/L)	Certificate Value (mol/L)	Relative Error (%)
SPSWW-1	$(6.49\pm0.08) \times10^{-6}$	$(6.30\pm0.01) \times10^{-6}$	2.78
SPSWW-2	$(3.25\pm0.11) \times10^{-5}$	$(3.15\pm0.04) \times10^{-5}$	3.07

To evaluate the recovery performance of the polymeric membrane, tap water samples were spiked with three different concentrations of Cu(II) (1.57×10^{-8}, 4.71×10^{-8}, and 7.85×10^{-8} mol/L, respectively) were tested. No treatment was applied to it before the tap water analysis. As shown in Table 3, the recovery values of tap water samples spiked with Cu(II) were 102.5%, 103.3%, and 104.1%, respectively.

Considering all the results obtained, one can see that the proposed method has the potential for Cu(II) determination in water samples with high accuracy.

Table 3: The application of polymeric membrane for Cu(II) detection in tap water samples (n=6).

Sample	Spiked Cu(II) (mol/L)	Our study (mol/L)	Recovery (%)
Tap water	1.57×10^{-8}	$(1.61\pm0.10) \times10^{-8}$	102.5
	4.71×10^{-8}	$(4.87\pm0.06) \times10^{-8}$	103.3
	7.85×10^{-8}	$(8.17\pm0.08) \times10^{-8}$	104.1

3.1.11. Comparison of the proposed method with other techniques for Cu(II) determination
In Table 4, the selected methods used to determine Cu(II) and our proposed method were compared briefly, and some performance characteristics were given (43-51). As we mentioned before, atomic absorption spectroscopy (AAS), atomic emission spectrometry (AES), and inductively coupled plasma mass spectrometry (ICP-MS) are mainly used for the determination of Cu(II) (52-54). Although the detection limits of these methods are sufficient, there are disadvantages, such as expensive and large instrumentation and extended analysis time. Nevertheless, its 20-second response time, relatively low LOD value, and high recovery rate are superior to those reported for copper ion detection.

Table 4: Comparison of selected Cu(II) detection methods.

Reference	Method	pH	LOD	Linear range	Time	Medium	Recovery
43	Voltammetric	pH:4.6	2.10^{-8} mol/L (1.29 ppb)	$5.10^{-8} – 3.54.10^{-6}$ mol/L (3 - 225 ppb)	15 min.	River water, human hair	%95.97-98.22
44	Colorimetric	pH:7	$3.4.10^{-6}$ mol/L (0.22 ppm)	$3.93.10^{-6} – 9.4.10^{-5}$ mol/L (0.25 - 6 ppm)	5 min.	Wastewater	%93.48- 114.04
45	Spectrophotometric	pH:6	$2.5.10^{-7}$ mol/L (0.015 ppm)	$7.0.10^{-7} – 1.0.10^{-4}$ mol/L (0.04 – 6.35 ppm)	2 min.	Tap water, river water, lake water	%98.5-102.1
46	Spectrofluorimetric	pH:7	$3.7.10^{-8}$ mol/L (2.35 ppb)	$0.5.10^{-8} - 8.10^{-8}$ mol/L (0.31 - 5 ppb)	20 min.	Tap water, pool water,	%95-106
47	Flame Atomic Absorption Spectrophotometric (FAAS)	-	1.10^{-5} mol/L (635 ppb)	$7.9.10^{-7} – 7.9.10^{-5}$ mol/L (0.05 - 5 ppm)	10 min.	Oil seed samples	%95.5-102.7
48	Modified Screen Printed (MSPE; electrode VI) Potentiometric	pH:3-7	$8.8.10^{-8}$ mol/L (55.9 ppb)	$8.8.10^{-8} – 1.0.10^{-2}$ mol/L (5.59 -6.35.10^{6} ppb)	3 s.	Tap water, river water, well water	%98.67-100.61
48	Modified Gold nanoparticle Screen Printed (GNP's,SPE; electrode X) Potentiometric	pH:2-8.5	$5.3.10^{-10}$ mol/L (0.03 ppb)	$5.3.10^{-10} – 1.0.10^{-2}$ mol/L (0.03 -6.35.10^{5} ppb)	7 h.	Tap water, river water, well water	%99.78-100.2
49	Cloud Point Extraction / Spectrophotometric	pH:7	$2.2.10^{-9}$ mol/L (0.140 ppb)	$3.10^{-8} – 7.9.10^{-7}$ mol/L (2 - 50 ppb)	10 min.	Lake water, fish muscle	%97-98.2
50	Cloud Point Extraction / Spectrophotometric	pH:6	$8.9.10^{-9}$ mol/L (0.57 ppb)	$2.10^{-8} – 5.5.10^{-7}$ mol/L (1 - 35 ppb)	15 min.	Mineral water, sea water, lettuce, cabbage, spinach, nuts, white bread, tomatoes	%95.6-104.3
51	Inductively coupled plasma– atomic emission (ICP-AES)	pH:5-7	2.10^{-8} mol/L (1 ppb)	$3.93.10^{-9} - 3.10^{-8}$ mol/L (0.25 - 2 ppb)	300 min.	Wastewater	%98
This study	**Spectrofluorimetric**	**pH:5**	**$2.24.10^{-9}$ mol/L (0.142 ppb)**	**$7.86.10^{-9} – 1.57.10^{-7}$ mol/L (0.5-10 ppb)**	**20 s.**	**Wastewater**	**%102.4-104.1**

4. CONCLUSION

Even though aGTAC and Cu(II) were used to prepare antimicrobial systems, aGTAC for Cu(II) detection is a new approach. A new fluorescent polymeric sensor for selective and sensitive detection of Cu(II) ions in aqueous media was successfully prepared by UV curing by introducing aGTAC and NIPAM into the commercially available acrylic oligomers. UV light induces the polymerization and leads its preparation with high yields, stable structures, low energy consumption, low reaction times, lower volume of unreacted components, no need for further purification methods, and zero volatile organic components. This method allows the production of an easy and efficient polymeric sensor. Our new UV-curable polymeric fluorescent sensor with hydrophilic positively charged glycidyl trimethylammonium functionalities showed selective fluorescent quenching against Cu(II) ions with a detection limit of $2.24.10^{-9}$ mol/L and a response time of 20 seconds.

Furthermore, the method was applied with excellent recovery results for Cu(II) ions added to real water samples. Again, selective detection of Cu(II) ions in the presence of coexisting ions with mole amounts ranging from 950 to 1172 was achieved. As a result, our method can be an alternative to existing methods as an eco-friendly approach in terms of large-scale production, practical use as a sensor, not containing organic solvents for the extraction step and analysis, and minimizing waste generation.

5. CONFLICT OF INTEREST

There are no conflicts to declare.

6. REFERENCES

1. Kiran RB, Renu S. Effect of heavy metals: An overview, Materials Today: Proceedings. 2022; 51(1): 880-5. Available from: <URL>..

2. Marchetti C. Role of calcium channels in heavy metal toxicity.International Scholarly Research Notices. 2013; 2013:184360. Available from: <URL>.

3. Potocki S, Rowinska-Zyrek M, Witkowska D, Pyrkosz M, Szebesczyk A, Krzywoszynska K, Kozlowski H. Metal transport and homeostasis within the human body: Toxicity associated with transport abnormalities. Curr. Med. Chem. 2012; 19:2738–59. Available from: <URL>.

4. Cannas D, Loi E, Serra M, Firinu D, Valera P, Zavattari P. Relevance of Essential Trace Elements in Nutrition and Drinking Water for Human Health and Autoimmune Disease Risk. Nutrients. 2020; 12(7):2074. Available from: <URL>.

5. Brindha K, Paul R, Walter J, Tan ML, Singh MK. Trace metals contamination in groundwater and implications on human health: comprehensive assessment using hydrogeochemical and geostatistical methods.

Environmental Geochemistry and Health. 2020; 42, 3819–39. Available from: <URL>.

6. Jaishankar M, Tseten T, Anbalagan N, Mathew BB, Beeregowda KN. Toxicity, mechanism and health effects of some heavy metals. Interdisciplinary Toxicology. 2014; 7(2):60-72. Available from: <URL>.

7. Briffa J, Sinagra E, Blundell R. Heavy metal pollution in the environment and their toxicological effects on humans. Heliyon 2020; 6(9): e0469. Available from: <URL>.

8. He ZL, Yang XE, Stoffella PJ. Trace elements in agroecosystems and impacts on the environment. Journal of Trace Elements in Medicine and Biology. 2005; 19(2–3):125–40. Available from: <URL>.

9. Gautam PK, Gautam RK, Banerjee S et al. Heavy metals in the environment: fate, transport, toxicity and remediation technologies. Editor(s): Pathania D, Heavy Metals: Sources, Toxicity and Remediation Techniques, Nova Sci Publishers. 2016; 60, 101-30.

10. Jaishankar M, Tseten T, Anbalagan N, Mathew BB, Beeregowda KN. Toxicity, mechanism and health effects of some heavy metals. Interdisciplinary Toxicology. 2014; 7(2):60-72. Available from: <URL>.

11. Tchounwou PB, Yedjou CG, Patlola AK, Sutton DJ. Heavy metal toxicity and the environment. Molecular, Clinical and Environmental Toxicology. 2012; 101:133-64. Available from: <URL>.

12. Bost M, Houdart S, Oberli M, Kalonji E, Huneau JH, Margaritis I. Dietary copper and human health: Current evidence and unresolved issues. Journal of Trace Elements in Medicine and Biology. 2016; 35:107- 15. Available from: <URL>.

13. Feng S, Gao Q, Gao X, Jiao Y. Fluorescent sensor for copper(II) ion based on coumarin derivative and its application in cell imaging. Elsevier Inorganic Chemistry Communications. 2019; 102:51–6. Available from: <URL>.

14. Schultze MO, Elvehjem CA, Hart EB. Studies on the copper content of the blood in nutritional anemia. Journal of Biological Chemistry. 1936; 116, 107- 18. Available from: <URL>.

15. Ramdass A, Sathish V, Babu E, Velayudham M, Thanasekaran P, Rajagopal S. Recent developments on optical and electrochemical sensing of copper (II) ion based on transition metal complexes. Coordination Chemistry Reviews. 2017; 343:278–307. Available from: <URL>.

16. Gholivand MB; Nasrabadi MR, Ganjali MR, Salavati-Niasari M. Highly selective and sensitive copper membrane electrode based on a new synthesized Schiff base. Talanta. 2007; 73(3):553–60. Available from: <URL>.

17. Zhu Z, McKendry R, Chavez CL Signaling in Copper Ion Homeostasis. Editor(s): Storey KB, Storey JM. Volume 1, 2000, Pages 293-300. Available from: <URL>:

18. Tapiero H, Townsend DM, Tew KD. Trace elements in human physiology and pathology. Copper. Biomedicine & Pharmacotherapy. 2003; 57(9):386-98. Available from: <URL>.

19. Institute of Medicine. Dietary Reference Intakes for Vitamin A, Vitamin K, Arsenic, Boron, Chromium, Copper, Iodine, Iron, Manganese, Molybdenum, Nickel, Silicon,

Vanadium, and Zinc. Washington, DC: The National Academies Press. 2001. Available from: <URL>.

20. Gray JP, Suhali-Amacher N, Ray SD. Metals and Metal Antagonists. Editor(s): Sidhartha D. Ray, Side Effects of Drugs Annual. 2017; 39:197-208. Available from: <URL>.

21. Pizarro F, Olivares M, Uauy R, Contreras P, Rebelo A, Gidi V. Acute gastrointestinal effects of graded levels of copper in drinking water. Environmental Health Perspectives. 1999; 107(2):117–21. Available from: <URL>.

22. Taylor AA, Tsuji JS, Garry MR, McArdle ME, Goodfellow Jr WL, Adams WJ, Menzie CA. Critical Review of Exposure and Effects: Implications for Setting Regulatory Health Criteria for Ingested Copper. Environmental Management. 2020; 65(1):131-59. Available from: <URL>.

23. Shi F, Cui S, Liu H, Pu S. A high selective fluorescent sensor for Cu2+ in solution and test paper strips. Dyes and Pigments. 2020; 173:107914. Available from: <URL>.

24. Zhang X, Guo X, Yuan H, Jia X, Dai B. One-pot synthesis of a natural phenol derived fluorescence sensor for Cu(II) and Hg(II) detection. Dyes and Pigments. 2018; 155:100-6. Available from: <URL>.

25. WHO (World Health Organization). Guidelines for drinking-water quality: fourth edition incorporating the first and second addenda. Geneva: World Health Organization; 2022. Licence: CC BY-NC-SA 3.0 IGO.

26. Ali A, Shen H, Yin X. Simultaneous determination of trace amounts of nickel, copper and mercury by liquid chromatography coupled with flow-injection on-line derivatization and preconcentration. Anal Chim Acta. 1998; 369(3):215–23. Available from: <URL>.

27. Chen H, Jia S, Zhang J, Jang M, Chen X, Koh H, Wang Z. Sensitive detection of copper (II) ion based on conformational change of peptide by surface plasmon resonance spectroscopy. Analytical Methods. 2015; 20(7): 8942-6. Available from: <URL>.

28. Mefteh W, Chevalier Y, Bala C, Jaffrezic-Renault N. Voltammetric Detection of Copper Ions on a Gold Electrode Modified with a N-methyl-2-naphthyl-cyclam film. Analytical Letters. 2018; 51(7): 971-82. Available from: <URL>.

29. Şahan S, Şahin U. Determination of Copper(II) Using Atomic Absorption Spectrometry and Eriochrome Blue Black R Loaded Amberlite XAD-1180 Resin. Clean- Soil Air Water. 2010; 38:485-91. Available from: <URL>.

30. Cao Y, Feng J, Tang L, Yu C, Mo G, Deng B. A highly efficient introduction system for single cell- ICP-MS and its application to detection of copper in single human red blood cells. Talanta. 2020; 206:120174. Available from: <URL>.

31. Zhou F, Li C, Zhu H, Li Y. A novel method for simultaneous determination of zinc, nickel, cobalt and copper based on UV–vis spectrometry. Optik. 2019; 182:58-64. Available from: <URL>.

32. Cao F, Jiao F, Ma S, Dong D. Laser-induced breakdown spectroscopy mediated amplification sensor for copper (II) ions detection using click chemistry. Sensors and Actuators B: Chemical. 2020; 371:132594. Available from: <URL>.

33. Karadjov M, Velitchkova N, Veleva O, Vekichkov S, Markov P, Daskalova N. Spectral interferences in the determination of rhenium in molybdenum and copper concentrates by inductively coupled plasma optical emission spectrometry (ICP-OES). Spectrochimica Acta Part B: Atomic Spectroscopy. 2016; 119:76-82. Available from: <URL>.

34. Feng S, Gao Q, Gao X, Yin J, Jiao Y. Fluorescent sensor for copper(II) ions based on coumarin derivative and its application in cell imaging. Inorganic Chemistry Communications. 2019; 102:51-6. Available from: <URL>.

35. Fan J, Zhan P, Hu M, Sun W, Tang J, Wang J, Sun S, Song F, Peng X. A fluorescent ratiometric chemodosimeter for Cu2+ based on TBET and its application in living cells. Organic Letters. 2013; 15(3):492-5. Available from: <URL>.

36. Jiang Y, Huang Z, Dai H, Wang L, Ying L, Kou X. A highly selective and sensitive fluorescent sensor for copper(II) ion characterized by one dichlorofluorescein moiety and two azathia-crown ether. Asian Journal of Chemistry. 2013; 25:8292- 6. Available from: <URL>.

37. Sam-ang P, Silpcharu K, Sukwattanasinitt M, Rashatasakhon P. Hydrophilic Truxene Derivative as a Fluorescent off-on Sensor for Copper (II) Ion and Phosphate Species. Journal of Fluorescence. 2019; 29:417-24. Available from: <URL>.

38. Farhi A, Firdaus F, Saeed H, Mujeeb A, Shakir M, Owais M. A quinoline-based fluorescent probe for selective detection and real-time monitoring of copper ions- A differential colorimetric approach. Photochemical and Photobiological Sciences. 2019; 18:3008-15. Available from: <URL>.

39. Birtane H, Şen F, Bozdağ B, Kahraman MV. Antibacterial UV-photocured acrylic coatings containing quaternary ammonium salt. Polymer Bulletin. 2021; 78, 3577–88. Available from: <URL>.

40. Cubuk S, Taşci N, Kahraman MV, Bayramoğlu G, Kök Yetimoglu E. Reusable fluorescent photocrosslinked polymeric sensor for determining lead ions in aqueous media. Spectrochimica Acta Part A: Molecular and Biomolecular Spectroscopy. 2016; 159:106-12. Available from: <URL>.

41. Liu SR, Wu SP. An NBD-based Sensitive and Selective Fluorescent Sensor for Copper (II) Ion. Journal of Fluorescence. 2010; 21:1599–1605. Available from: <URL>.

42. MacDougall D, Crummett WB et al. Guidelines for data acquisition and data quality evaluation in environmental chemistry. Analytical Chemistry. 1980; 52(14):2242-9. Available from: <URL>.

43. Mohadesi A, Taher MA. Voltammetric determination of Cu (II) in natural waters and human hair at a meso-2, 3-dimercaptosuccinic acid self-assembled gold electrode. Talanta. 2007; 72(1):95-100. Available from: <URL>.

44. Poosinuntakul N, Parnklang T, Sitiwed T, Chaiyo S, Kladsomboon S, Chailapakul O, Apilux A. Colorimetric assay for determination of Cu (II) ions using L-cysteine functionalized silver nanoplates. Microchemical Journal. 2020; 158:105101. Available from: <URL>.

45. Pourbasheer E, Morsali, S, Banaei A, Aghabakazadeh S, Ganjali MR, Norouzi P. Design of a novel optical sensor for determination of trace amounts of copper by UV–visible spectrophotometry in real samples. Journal of Indus-

trial and Engineering Chemistry. 2018; 32(3):e4110. Available from: <URL>.

46. Mei L, Xiang, Y, Li N, Tong A. A new fluorescent probe of rhodamine B derivative for the detection of copper ion. Talanta. 2007; 72(5):1717-22. Available from: <URL>.

47. Peronico VCD, Raposo JL Jr. Ultrasound-assisted extraction for the determination of Cu, Mn, Ca, and Mg in alternative oilseed crops using flame atomic absorption spectrometry. Food Chemistry. 2016; 196:1287-92. Available from: <URL>.

48. Ali TA, Abd-Elaal AA, Mohamed GG. Screen printed ion selective electrodes based on self-assembled thiol surfactant-gold-nanoparticles for determination of Cu (II) in different water samples. Microchemical Journal. 2021; 160:105693. Available from: <URL>.

49. Bilal M, Kazi TG, Afridi HI, Arain MB, Baig JA, Khan M, Khan N. Application of conventional and modified cloud point extraction for simultaneous enrichment of cadmium, lead and copper in lake water and fish muscles. Journal of Industrial and Engineering Chemistry. 2016; 40:137-44. Available from: <URL>.

50. Durukan İ, Arpa Şahin A, Şatıroğlu N, Bektaş S. Determination of iron and copper in food samples by flow injection cloud point extraction flame atomic absorption spectrometry. Microchemical Journal. 2011; 99(1):159-63. Available from: <URL>.

51. Atanassova D, Stefanova V, Russeva E. Co-precipitative pre-concentration with sodium diethyldithiocarbamate and ICP-AES determination of Se, Cu, Pb, Zn, Fe, Co, Ni, Mn, Cr and Cd in water. Talanta. 1998; 47(5):1237-43. Available from: <URL>.

52. Almeida JS, Souza OCCO, Teixeira LSG. Determination of Pb, Cu and Fe in ethanol fuel samples by high-resolution continuum source electrothermal atomic absorption spectrometry by exploring a combination of sequential and simultaneous strategies. Microchemical Journal. 2017; 137:22–6. Available from: <URL>.

53. Hachmöller O, Aichler M, Schwamborn K, Lutz L, Werner M, Sperling M, Walch A, Karst U. Investigating the influence of standard staining procedures on the copper distribution and concentration in Wilson's disease liver samples by laser ablation-inductively coupled plasma-mass spectrometry. Journal of Trace Elements in Medicine and Biology. 2017; 44:71-5. Available from: <URL>.

54. Yu J, Yang S, Lu Q, Sun D, Zheng J, Zhang X, Wang X, Yang W. Evaluation of liquid cathode glow discharge-atomic emission spectrometry for determination of copper and lead in ores samples. Talanta. 2017; 164(1):216-21. Available from: <URL>.

RESEARCH ARTICLE

The Effect Study of Various Parameters on the Synthesis of Benzoxazole Derivatives Utilizing Cadmium Oxide Nanoparticles

Asmaa M Abdullah[1] iD **, Abdull jabar Kh. Attia[1]** iD **, and Sergei N. Shtykov[2]** iD

[1]Department of Chemistry, College of Science, Al-Mustansiriyah University, Baghdad, Iraq
[2]College of Analytical and Environmental Chemistry, Institute of Chemistry, Saratov State University, Russian Federation

Abstract: Due to its straightforward approach, the co-precipitation technique for producing nanomaterials has gained popularity over time. In this study, we employed cadmium nitrate to synthesize cadmium oxide nanomaterials (CdO NPs). The morphology and size of the synthesized CdO NPs were determined using Scanning Electron Microscopy (SEM) and Atomic Force Microscopy (AFM) respectively. To find the functional groups that are present in the nanoparticles and are involved in their decrease and stabilization, a Fourier Transform Infrared Spectroscopy (FTIR) study was carried out. Additionally, X-ray diffraction analysis (XRD) was employed to confirm the crystalline nature of the NPs. By utilizing the synthesized catalyst CdO NPs, we successfully synthesized benzoxazole derivatives with improved yields by reacting o-amino phenol with various aldehydes, achieving yields of 90-93%. The structures of the synthesized molecules were characterized using NMR and FTIR spectroscopy. Noteworthy advantages of this method include its short reaction time, high product yields, and the catalyst's recyclability.

1. INTRODUCTION

Nanomaterials have become very promising compounds in the field of nanochemistry in recent years. They are more catalytically active than bulk materials because of their smaller size and higher surface area (1). Due to its outstanding catalytic activity and several biological uses, such as antioxidant, anticancer, and antibacterial capacity, cadmium oxide nanoparticles (CdO-NPs) in particular have attracted substantial attention in the field of nanotechnology (2-6). In the synthesis of new organic compounds and biologically active molecules, heteroaromatic compounds have received a lot of attention (7-10). Due to their importance in biology and pharmacology, heterocyclic molecules containing oxygen and nitrogen have attracted the most attention. We have chosen to focus on benzoxazoles in our ongoing search for effective strategies to synthesize physiologically relevant heterocyclic chemicals. The "isosteres of natural nucleotides" known as oxazole derivatives have drawn the attention of various researchers who want to develop synthetic analogs with effective chemotherapeutic properties (11-16). Many naturally occurring and synthesized bioactive chemicals, which show a variety of biological functions, have the benzoxazole scaffold. Inhibition of the eukaryotic topoisomerase II enzyme (17-19), effectiveness against multidrug-resistant cancer cells (20-25), antimalarial and antileishmanial effects (26), antiviral properties (27,28), antibacterial activity (29), are a few of these activities. The literature contains numerous attempts to synthesize the benzoxazole scaffold. Ortho-aminophenol is often condensed with a carboxylic acid (COOH) or

acyl chloride (COCl) in the presence of a strong acid at a high temperature in order to produce the O1-C2 and N3-C2 linkages (30). The oxidative cyclization of phenolic Schiff bases derived from aldehydes is another frequently used approach. This method makes use of a various of oxidizing agents, including $Mn(OAc)_3$ (31), DDQ (32), $ThClO_4$ (33), NiO_2 (34), $ZrOCl_2 \cdot 8H_2O$ (35), PCC-supported silica gel (36), DessMartin reagent (37), $BaMnO_4$ (38), and $Pb(OAc)_4$ (39). The development of heterogeneous catalysts has received significant attention in modern synthetic chemistry. With homogeneous catalysts, it has proven to be extremely difficult to separate the catalysts from the reaction mixture while under catalytic conditions. Researchers have looked into using suitable supports, in particular nanoscale materials, as homogeneous catalysts to solve this problem. High atomic efficiency, simplified product purification, and the possibility of reusing the catalysts are only a few benefits of this method (40). The fabrication of cadmium oxide nanoparticles and their use in the synthesis of benzoxazole derivatives are the goals of this study. The study also intends to evaluate the effects of several conditions on the reaction process, such as reaction time, catalyst type and quantity, and solvent type.

2. Experimental

2.1. Materials and methods
The necessary materials utilized in the experiment were obtained from Sigma-Aldrich or BDH and were not purified. To track the progress of the reaction, Thin Layer Chromatography (TLC) was employed, utilizing Silica Gel 60 TLC plates and UV light at 254 nm. The melting points of the synthesized compounds were evaluated using a Stuart melting point apparatus, SMP30. The products obtained were analyzed using FTIR spectra, obtained from a Bruker alpha 2 instrument (Germany), and H-NMR spectra, obtained from a Bruker Bio Spin GmbH Spectrometer (400 MHz), with DMSO as the solvent.

2.2. Co-precipitation procedure for the fabrication of CdO NPs-Ther
To form CdO NPs-Ther, a method known as co-precipitation was utilized (40). In a round bottom flask equipped with a magnetic stirrer, a solution of 15 mmoles of Cd $(NO_3)_2 \cdot 4H_2O$ was prepared in a mixture of (60 mL) of water and ethanol (1:1). While continuously stirring, a solution containing 4 mmoles of threonine in 1 mL of deionized (DI) water was added. The pH value of the mixture was adjusted to 10 using a 2 M aqueous solution of NaOH. The finding combination was stirred for 12 hours at room temperature. Subsequently, the solution was centrifuged at (5000 rpm) for 25 minutes. The producing precipitate pellet was then subjected to another round of centrifugation and washed with a solution of DI water and ethanol (ratio: 1:1). As well as, the precipitate was dried in an oven at 80 °C for 20 hours to obtain the desired product, CdO NPs-Ther. Additionally, CdO NPs and $CdNiO_2$ NPs without threonine surface modification were synthesized utilizing the same procedure, but threonine was not added.

2.3. Characterization of nano cadmium oxide NPs
The morphology and surface of the fabricated nano cadmium oxide NPs were analyzed for characterization purposes. The NPs compounds were characterized using X-ray diffraction (XRD) with a Rigaku model. XRD measurements of the samples were conducted at ambient temperature in the 2θ range of 0^0-80^0, utilizing Copper (Cu) with a wavelength (λ) of 1.54056 Å. Scanning Electron Microscope (SEM) images of the samples were captured utilizing a Zeiss SEM analyzer, operating at a voltage of (20 KV). Additionally, Atomic Force Microscopy (AFM) images were obtained using a DME dualscope c21 instrument from Denmark.

2.4. Synthesis of 2-aryl benzoxazole derivatives using CdO NPs
A solution containing 0.001 mol of various aldehydes and 0.001 mol of o-amino phenol in 3 mL of ethanol was prepared, to which 10 mg of cadmium oxide NPs were added. The reaction solution was stirred at laboratory temperature for 3 hours. The progress of the reaction was monitored utilizing Thin Layer Chromatography with ethyl acetate-n-hexane (2:1) as the eluent. Once the reaction was complete, the solution was filtered to remove the catalyst. The solvent was then evaporated, and the residue was purified through recrystallization using ethanol. The structures of the synthesized compounds were characterized utilizing FTIR and HNMR spectra, with most of the compounds being well-known.

$R= Br, N(CH3)2, NO_2$
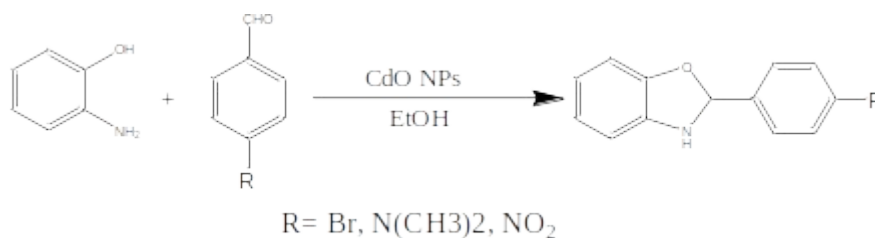
Scheme 1: CdO NPs- catalyzed synthesis of benzoxazole derivatives.

2-(4-nitrophenyl)benzoxazole. Solid compound; m.p:272-275 ^{0}C (lit.(41) 275-277 ^{0}C); FTIR: 3358 cm^{-1}(NH), 1624 cm^{-1} (C=N), 3082 cm^{-1} (C-H or.), 1586 cm^{-1} (C=C), 1479 cm^{-1} (NO$_2$); H-NMR (DMSO-d6, 400 MHz): δ9.240 (s,1H, NH), 8.900 (s,1H, H-oxazole), 6.844-8.368(m,8H, aromatic proton).

2-(4-N, N-dimethyl phenyl)benzoxazole. Solid compound; m.p:286-288 ^{0}C (lit.(42) 285-288); FTIR: 3323 cm^{-1} (NH), 1611 cm^{-1} (C=N), 3068 cm^{-1} (C-H or.), 1583 cm^{-1} (C=C), 2903 cm^{-1} (CH$_{al}$.); H-NMR (DMSO-d6, 400 MHz): δ8.682 (s,1H, NH), 8.511(s,1H, H-oxazole), 6.794-7.856(m,8H, aromatic proton), 3.011(s,6H,N(CH$_3$)$_2$).

2-(4-bromophenyl)benzoxazole. Solid compound; m.p:163-165-275 °C (lit.(43) 166-169 °C); FTIR: 332 cm^{-1} (NH), 1624 cm^{-1} (C=N), 3066 cm^{-1}(C-H or.), 1586 cm^{-1} (C=C), 757 cm^{-1} (C-Br); H-NMR (DMSO-d6, 400 MHz): δ9.049 (s,1H, NH), 8.710 (s,1H, H-oxazole), 6.814-8.002 (m,8H, aromatic proton).

3. RESULTS AND DISCUSSION

The fabrication of cadmium oxide nanoparticles (NPs), cadmium oxide NPS-Threonine, and NiCdO$_2$ NPs was achieved using a co-precipitation method. Cd(NO$_3$)$_2$.4H$_2$O and Ni(NO$_3$)$_2$.6H$_2$O were utilized as the sources of cadmium and nickel, respectively, while sodium hydroxide served as the precipitation agent. To form the solution, Cd(NO$_3$)$_2$ was mixed with an amino acid solution (threonine) in a dropwise manner. The pH was adjusted to 10 by adding sodium hydroxide solution. The suggested reaction mechanism is illustrated in Scheme 2.
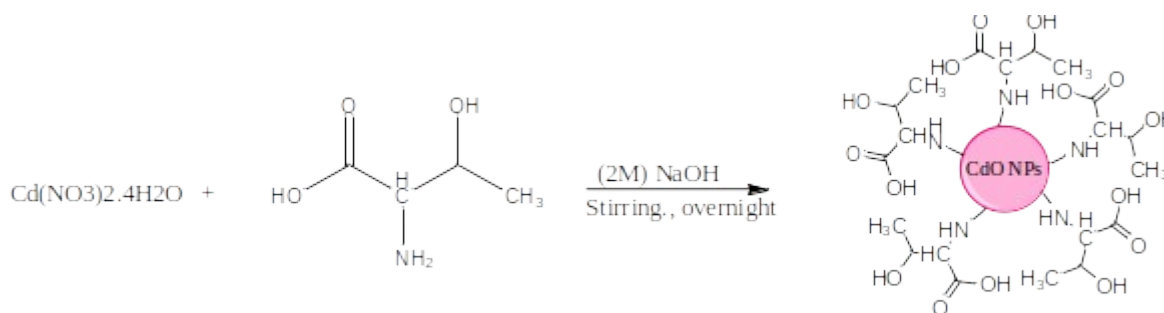

Scheme. 2. Synthesis of CdO NPs derivatives.

3.1. Surface Functional Group Analysis.
FTIR spectroscopy was utilized to evaluate the groups present on the surface of CdO nanoparticles. In Figure 1, the FTIR spectrum of the synthesized CdO nanoparticles clearly appears at a peak at 3555 cm^{-1}, which corresponds to the stretching vibration of (OH groups) on the CdO surface (2). Additionally, the band at 1390 cm^{-1} is characteristic of CdO (44). The FTIR spectrum of CdO nanoparticles with Threonine exhibits prominent peaks at 3451 and 3619 cm^{-1}, indicating (N-H) symmetric stretching and the presence of (OH groups) (45). The peaks at 1630 cm^{-1} can be attributed to the C=O vibration modes of the carbonyl group in threonine (45). The presence of the Cd-O bond is indicated by the peak at 633 cm^{-1} (47). Furthermore, the spectra of CdNiO$_2$ nanoparticles reveal that the peaks between 690 cm^{-1} and 1451 cm^{-1} are assigned to CdO (3). The peak at 1362 cm^{-1} corresponds to the stretching of the Cd-O-Ni bond, which is formed by tetrahedral building units in the structure (48).
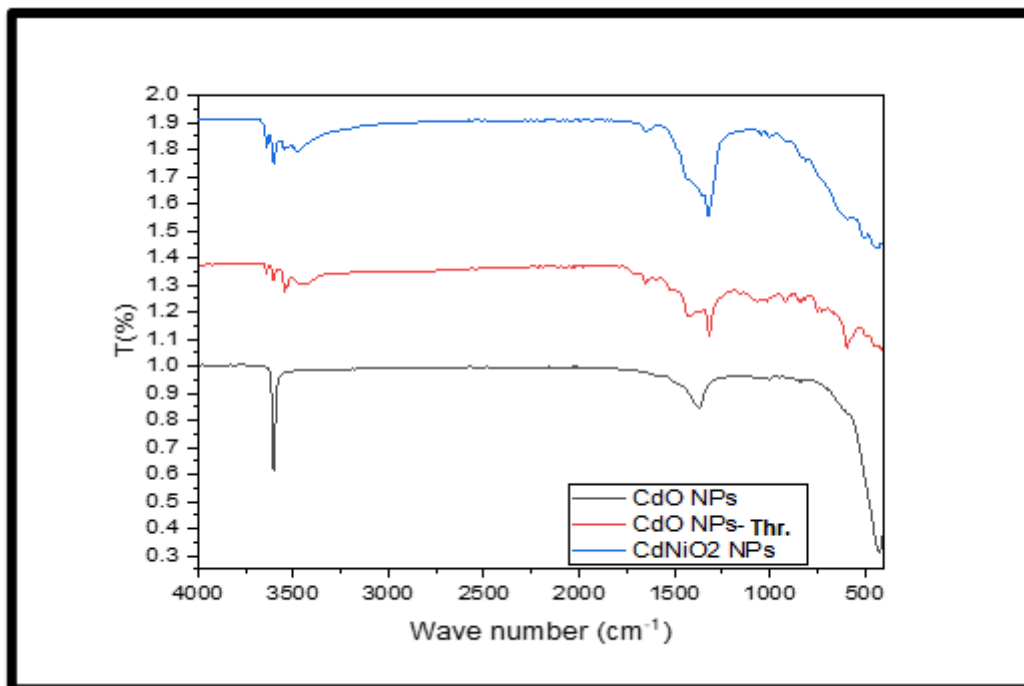
Figure 1: FTIR spectra of synthesized CdO Nanoparticles.

3.2. Xray diffraction analysis (XRD)

In order to evaluate the size of the CdO nano-particles (NPs) formed through the co-precipitation procedure with the inclusion of an amino acid like threonine or NiO, we can employ the Scherrer equation. This equation establishes a relationship between the broadening of peaks observed in X-ray diffraction (XRD) patterns and the size of the crystallites.

$$D = K\lambda/\beta cos\theta$$　　　　(Eq. 1)

The Scherrer equation defines the variables as follows: D represents the crystallite size, K is the Scherrer constant (approximately 0.9), λ denotes the wavelength of the X-ray source (typically Cu Kα, 1.5406 Å), β represents the full width at half maximum (FWHM) of the XRD peak, and θ corresponds to the Bragg angle. Depending on the Scherrer equation, the crystallite size of the samples is presented in the following table.

3.3. Morphological study

An SEM analysis was conducted on CdO nanoparticles (NPs) synthesized utilizing the co-precipitation procedure. The SEM image revealed a mixture of spherical and needle-shaped CdO NPs, with agglomerated clusters. Furthermore, the SEM image indicated the absence of impurities in the sample, suggesting that all reactants were thoroughly eliminated during the synthesis process. The J image software was employed to evaluate the size distribution of the CdO NPs, with the average size of the spherical particles measuring 258 nm.

Similarly, when CdO NPs were synthesized via the co-precipitation method with the addition of an amino acid like threonine, an SEM image provided valuable insights into the morphology, size, and distribution of the particles. The SEM image demonstrated the presence of spherical CdO + amino acid (threonine) NPs, which were uniformly dispersed. Additionally, no impurities were observed in the sample, indicating the complete removal of all reactants during synthesis. The average size of these particles was measured to be 108.07 nm.

In the case of CdNiO2 NPs, the SEM image revealed irregularly shaped particles. The image also exhibited that the CdNiO2 NPs were agglomerated in clusters, appearing as white foreign particles, suggesting the presence of residual precursors or reactants that were not entirely eliminated during synthesis. The average size of these particles was determined to be 367.4 nm.

**Table.1:** Crystalline size of synthesized nanoparticles.

Sample	crystallite size (nm)
CdO NPs	33.9 nm
CdO + amino acid(threonine)	28.3 nm
CdNiO$_2$ NPS	27.9 nm
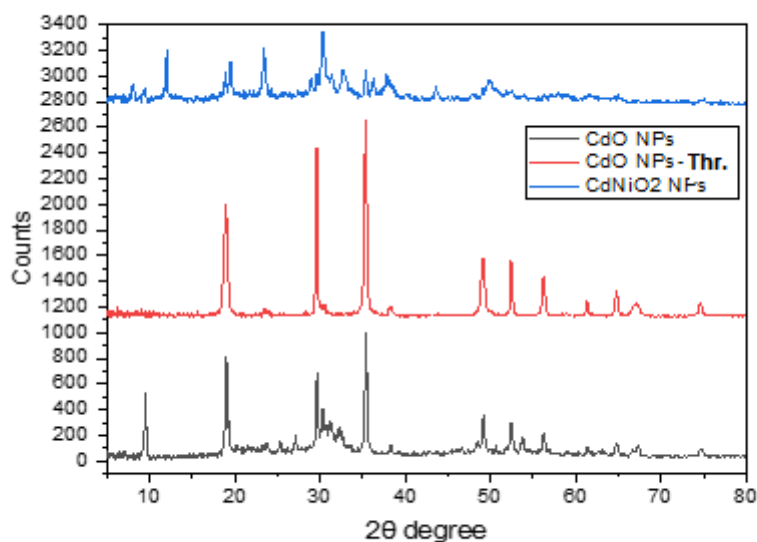
Figure 2: XRD diagram of synthesized CdO Nps.

3.4. Optimization for benzoxazole derivatives synthesis method

We conducted a study on synthesizing benzoxazole derivatives through the cyclocondensation of o-amino phenol and various substituted aromatic aldehydes. In this study, we utilized cadmium oxide nanoparticles as catalysts and investigated the influence of different factors such as catalyst type and amount, solvent type, and reaction time. Among the catalysts tested, namely Cd(NO$_3$)$_2$, CdO NPs, CdO NPs-Thr, and CdNiO$_2$ NPs, CdO NPs demonstrated favorable yields of 88%, 80%, and 87% for 2(4-NO$_2$PY)OX, 2(4-N(Me)$_2$PY)OX, and 2(4-BrPY)OX, respectively. However, despite having a smaller particle size compared to CdO NPs and CdNiO$_2$ NPs, CdO NPs-Ther. yielded lower amounts of synthesized benzimidazole derivatives. This can be attributed to the coating of CdO NPs with the amino acid (threonine), resulting in high roughness and heterogeneity, as depicted in Figure 5.
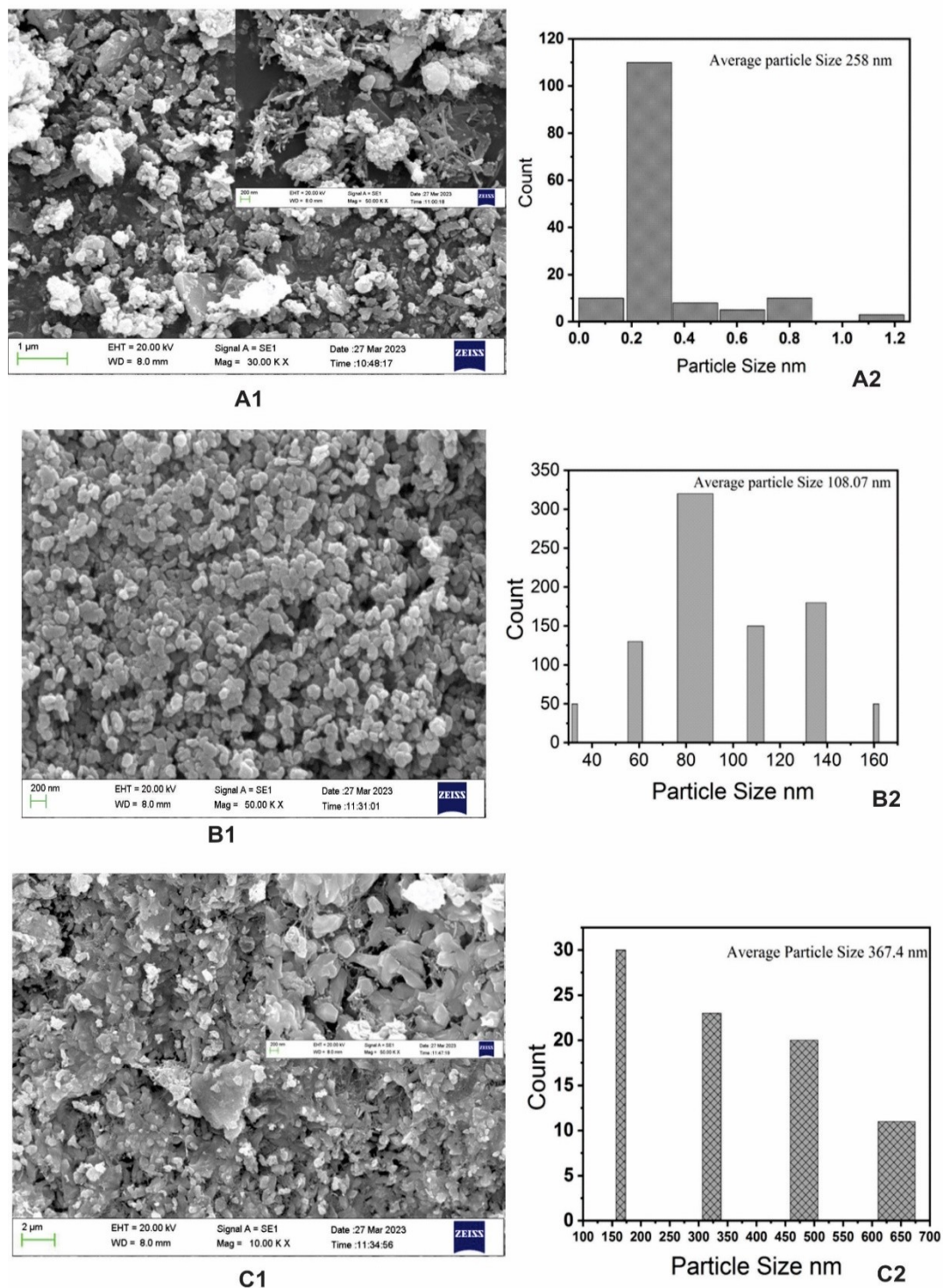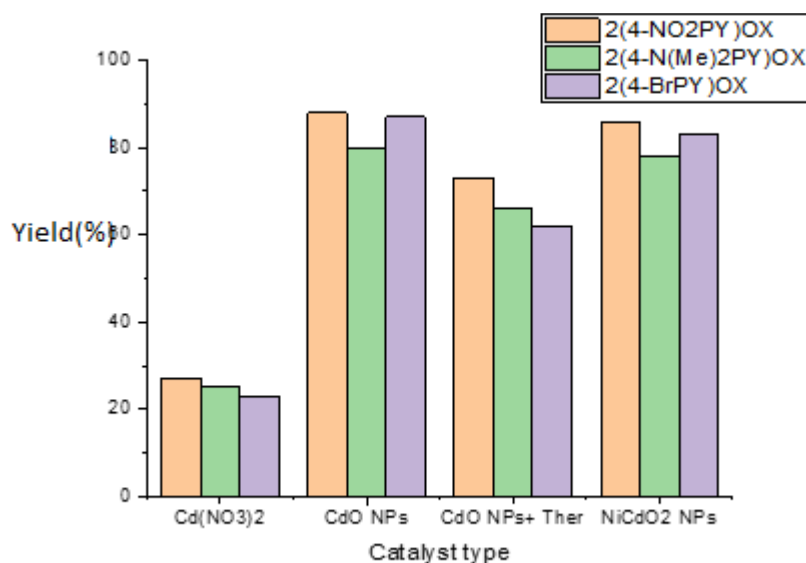
Figure 3: SEM and histogram of CdO NPs (A1&A2), CdO NPs-Thr (B1&B2) and CdNiO$_2$ NPs(C1&C2).

Figure 4 illustrates the surface characteristics of compound CdO NPs-Thr, demonstrating its high roughness and heterogeneity compared to CdO NPs and CdNiO$_2$ NPs.
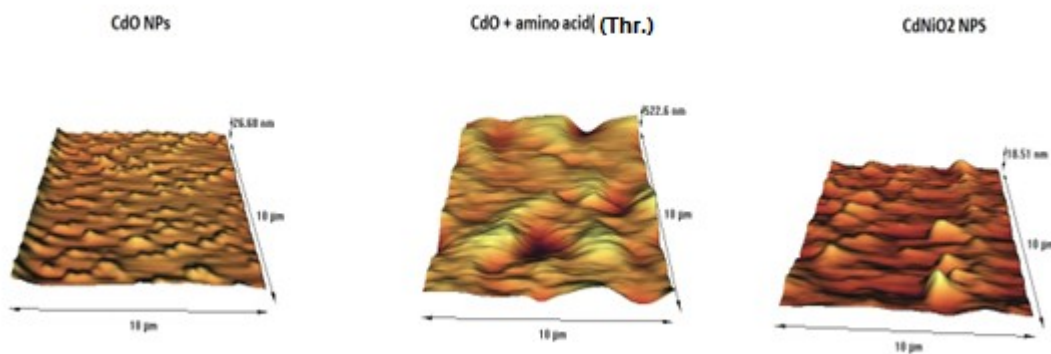
Figure 4: 3D AFM picture and distribution map of granularity accumulation of CdO nanostructure.

Figure 5: Effect of catalyst type on the yield of product.
*2-(4-nitrophenyl)benzoxazole [2(NO$_2$PY)OX]; 2(4-(N(Me)$_2$phenyl)benzoxazole [2(4-(Me)$_2$PY)OX];
2(4-bromophenyl)benzoxazole [2(4-BrPY)OX]

Certainly, the catalyst amounts play a crucial role in determining the yields of the different compounds in the chemical reaction. A catalyst is a substance that facilitates a chemical reaction without being consumed in the process. It speeds up the reaction rate by providing an alternative reaction pathway with lower activation energy. Various quantities of catalyst (Cdo NPs) ranging from 0.005 to 0.02 g were investigated. According to Figure .6, the perfect yields for 2(4-NO$_2$PY) OX, 2(4-N(Me)$_2$PY) OX, and 2(4-BrPY)OX were obtained with catalyst amounts of 0.005 g, 0.02 g, and 0.015 g, respectively. For 2(4-NO$_2$PY)OX, the highest yield was obtained with a catalyst amount of 0.005 g. This suggests that a smaller quantity of catalyst was sufficient to promote the reaction and achieve a desirable yield for this particular compound. On the other hand, 2(4-N(Me)2PY)OX demonstrated the highest yield when the catalyst amount was 0.02 g. This indicates that a larger quantity of catalyst was required to optimize the reaction and maximize the yield of this compound. Similarly, 2(4-BrPY)OX

exhibited the highest yield with a catalyst amount of 0.015 g. This suggests that an intermediate catalyst quantity was most effective in promoting the reaction and obtaining a favorable yield for this compound. Overall, the findings highlight the importance of carefully selecting the appropriate catalyst amount to achieve optimal yields for different compounds. The specific amounts can vary depending on the nature of the compounds, the reaction conditions, and the catalytic properties of the catalyst itself.

The polarity of solvents plays a significant role in chemical reactions, particularly in terms of solubility and reaction rates. The polarity of a solvent refers to the separation of electric charge within the molecule, resulting in regions of partial positive and partial negative charges. Various solvents including ethanol, acetonitrile, dichloromethane, THF, and toluene were utilized, and their outcomes are illustrated in figure.7. As a result of ethanol's higher polarity in comparison to the other solvents, it

yielded favorable results of 88%, 85%, and 89% for 2(4-NO$_2$PY)OX, 2(4-(Me)$_2$PY)OX, and 2(4-BrPY)OX, respectively. In the case of the mentioned compounds, their favorable yields with ethanol can be attributed to the high polarity of ethanol. The polar nature of ethanol facilitates the dissolution of the reactants and products involved in the reaction, resulting in efficient molecular interactions and a higher likelihood of successful reactions. In contrast, solvents with lower polarity, such as acetonitrile, dichloromethane, THF, and toluene, may have exhibited lower yields due to reduced solubility or less favorable molecular interactions with the reactants. Overall, the choice of solvent with the appropriate polarity is crucial in optimizing reaction conditions and achieving desired yields. The polarity of solvents influences the solubility of reactants, the stability of reaction intermediates, and the overall reaction kinetics.
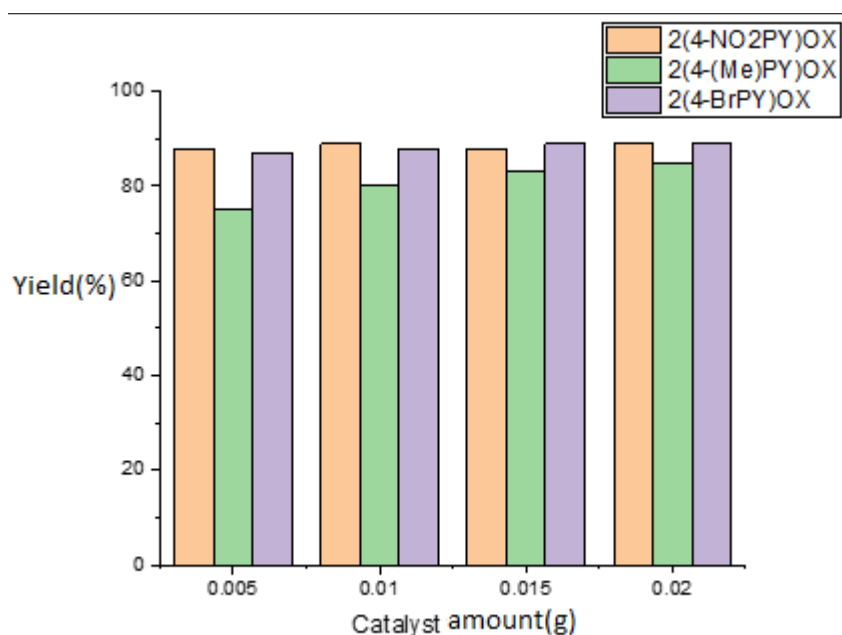
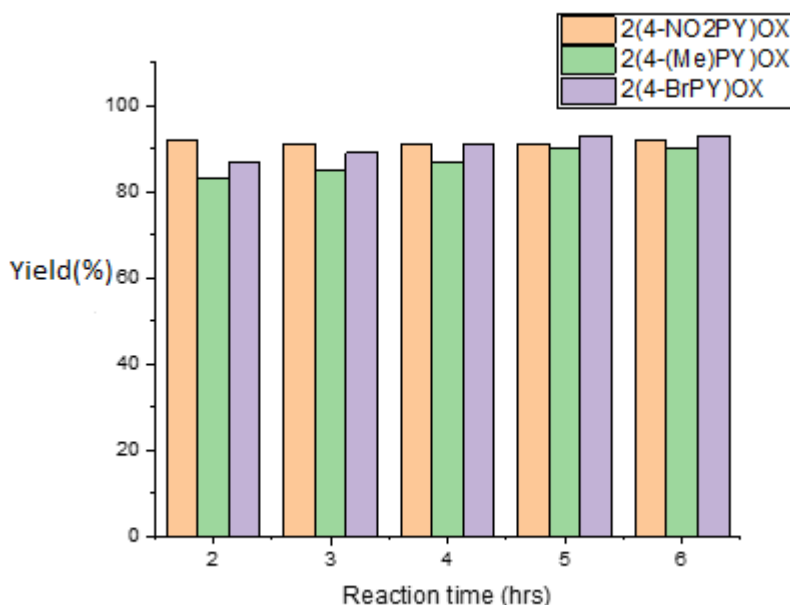**Figure 6:** Effect of catalyst amount on the yield of product.
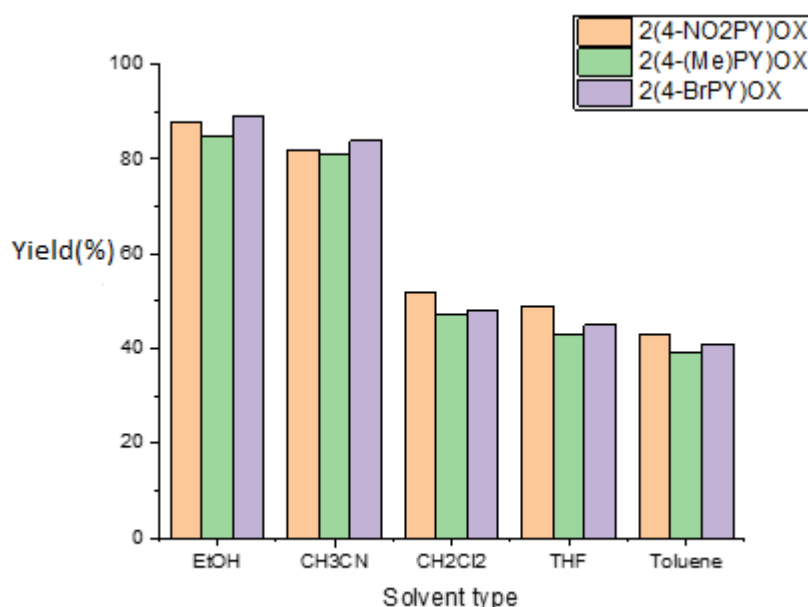
Figure 7: Effect of solvent type on the yield of product.

Figure 8 presents the investigation of different time intervals ranging from 2.0 to 6.0 hours. The results indicate that time intervals of 2.0 and 5.0 hours yielded high percentage yields for 2(4-NO$_2$PY)OX, 2(4-N(Me)$_2$PY)OX, and 2(4-BrPY)OX, respectively.

Figure 8: Effect of reaction time on the yield of product.

Table 2 presents the optimal conditions for benzoxazole synthesis and explores the impact of substituted groups on the benzene ring. Interestingly, it was observed that the addition of the catalyst nullified the influence of the substituted group on the percentage of the product.

Table 2: Optimum conditions and effect of substituted group.

Substituted group(R)	Type of catalyst	Solvent type	Amount of catalyst (g)	Time (hrs)	m.p ^{0}C	Yield (%)
NO$_2$			0.005	2	272-274	92
N(Me)$_2$	CdO NP$_S$	EtOH	0.02	5	286-288	90
Br			0.015	5	165-167	93

4. CONCLUSION

Cadmium oxide nanoparticles were successfully synthesized using the co-precipitation method, and various characterization techniques were employed to determine the size, crystallinity, and stability of the nanoparticles. The size of the CdO NPs, CdO NPs-Thr, and CdNiO$_2$ NPs crystallites was calculated to be approximately 33.9 nm, 28.3 nm, and 27.9 nm, respectively, using the Scherrer equation based on XRD data. The SEM images confirmed that the particles exhibited spherical and needle, spherical, and irregular shapes for CdO NPs, CdO NPs-Thr, and CdNiO$_2$ NPs, respectively. This method is the sole approach known for producing benzoxazole derivatives with high yields using CdO NPs. The current methodology offers a simple workup process, shorter reaction time, and reduced costs.

5. ACKNOWLEDGMENTS

6. REFERENCES

1. Mahesh S, Narasaiah BP, Balaji G. Fabrication of titanium dioxide nanoparticles using sunflower leaf extract and their applications towards the synthesis and biological evaluation of some novel phenanthro imidazole derivatives. Biointerface Research in Applied Chemistry. 2022;12:3372–89. Available from: <URL>.

2. Skheel AZ, Hlail Jaduaa M, Abd AN. Green synthesis of cadmium oxide nanoparticles for biomedical applications (antibacterial, and anticancer activities). Materials Today: Proceedings. 2021;45:5793–9. Available from: <URL>.

3. Ranjithkumar R, Albert Irudayaraj A, Jayakumar G, Dhayal Raj A, Karthick S, Vinayagamoorthy R. Synthesis and Properties of CdO and Fe doped CdO Nanoparticles. Materials Today: Proceedings. 2016;3(6):1378–82. Available from: <URL>.

4. Mostafa AM, Yousef SA, Eisa WH, Ewaida MA, Al-Ashkar EA. Synthesis of cadmium oxide nanoparticles by pulsed laser ablation in liquid environment. Optik. 2017 Sep;144:679–84. Available from: <URL>.

5. Giribabu K, Suresh R, Vijayalakshmi L, Stephen A, Narayanan V. Synthesis of Cadmium Oxide and its Electrochemical Detection of Pollutants. Advanced Materials Research. 2013 Mar;678:369–72. Available from: <URL>.

6. Reza Khayati G, Dalvand H, Darezereshki E, Irannejad A. A facile method to synthesis of CdO nanoparticles from spent Ni–Cd batteries. Materials Letters. 2014 Jan;115:272–4. Available from: <URL>.

7. Gorepatil PB, Mane YD, Ingle VS. Zirconyl (IV) Nitrate as Efficient and Reusable Solid Lewis Acid Catalyst for the Synthesis of Benzimidazole Derivatives. Journal of Chemistry. 2013;2013:1–7. Available from: <URL>.

8. Mohamed Ahmed MS, Kobayashi K, Mori A. One-Pot Construction of Pyrazoles and Isoxazoles with Palladium-Catalyzed Four-Component Coupling. Org Lett. 2005 Sep 1;7(20):4487–9. Available from: <URL>.

9. Kidwai M, Poddar R, Diwaniyan S, Kuhad RC. Laccase from Basidiomycetous Fungus Catalyzes the Synthesis of Substituted 5-Deaza-10-oxaflavins via a Domino Reaction. Adv Synth Catal. 2009 Mar;351(4):589–95. Available from: <URL>.

10. Ahmed A, Majeed I, Asaad N, Ahmed R, Kamil G, Abdul Rahman S. Some 3,4,5-Trisubstituted-1,2,4-triazole Synthesis, Antimicrobial Activity, and Molecular Docking Studies. Egypt J Chem. 2021 Sep 23;65(3):395–401. Available from: <URL>.

11. Yalçin İ, Ören İ, Şener E, Akin A, Uçartürk N. The synthesis and the structure-activity relationships of some substituted benzoxazoles, oxazolo(4,5-b)pyridines, benzothiazoles and benzimidazoles as antimicrobial agents. European Journal of Medicinal Chemistry. 1992 Jun;27(4):401–6. Available from: <URL>.

12. Díez-Martin D, Kotecha NR, Ley SV, Mantegani S, Menéndez JC, Organ HM, et al. Total synthesis of the ionophore antibiotic CP-61,405 (routiennocin). Tetrahedron. 1992 Jan;48(37):7899–938. Available from: <URL>.

13. Abdelgawad MA, Al-Sanea MM, Zaki MA, Mohamed EIA, Khan SI, Tekwani BL, et al. New Benzoxazole Derivatives as Antiprotozoal Agents: In Silico Studies, Synthesis, and Biological Evaluation. Ramalho TC, editor. Journal of Chemistry. 2021 Mar 3;2021:1–11. Available from: <URL>.

14. Oren I, Temiz O, Yalçin I, Sener E, Akin A, Uçartürk N. Synthesis and microbiological activity of 5(or 6)-methyl-2-substituted benzoxazole and benzimidazole derivatives. Arzneimittel-forschung. 1997 Dec;47(12):1393–7. Available from: <URL>.

15. Al-Sanea M, Abdelazem A, Park B, Yoo K, Sim T, Kwon Y, et al. ROS1 kinase inhibitors for molecular-targeted therapies. Current medicinal chemistry. 2016;23(2):142–60.

16. Alsayed SSR, Elshemy HAH, Abdelgawad MA, Abdel-Latif MS, Abdellatif KRA. Design, synthesis and biological screening of some novel celecoxib and etoricoxib analogs with promising COX-2 selectivity, anti-inflammatory activity and gastric safety profile. Bioorganic Chemistry. 2017 Feb;70:173–83. Available from: <URL>.

17. Pinar A, Yurdakul P, Yildiz I, Temiz-Arpaci O, Acan NL, Aki-Sener E, et al. Some fused heterocyclic compounds as eukaryotic topoisomerase II inhibitors. Biochemical and Biophysical Research Communications. 2004 Apr;317(2):670–4. Available from: <URL>.

18. Temiz-Arpaci O, Tekiner-Gulbas B, Yildiz I, Aki-Sener E, Yalcin I. 3D-QSAR analysis on benzazole derivatives as eukaryotic topoisomerase II inhibitors by using comparative molecular field analysis method. Bioorganic & Medicinal Chemistry. 2005 Dec;13(23):6354–9. Available from: <URL>.

19. Tekiner-Gulbas B, Temiz-Arpaci O, Yildiz I, Aki-Sener E, Yalcin I. 3D-QSAR study on heterocyclic topoisomerase II inhibitors using CoMSIA. SAR and QSAR in Environmental Research. 2006 Apr;17(2):121–32. Available from: <URL>.

20. Lage H, Aki-Sener E, Yalcin I. High antineoplastic activity of new heterocyclic compounds in cancer cells with resistance against classical DNA topoisomerase II-targeting drugs. Intl Journal of Cancer. 2006 Jul;119(1):213–20. Available from: <URL>.

21. Abdelgawad MA, Belal A, Ahmed OM. Synthesis, molecular docking studies and cytotoxic screening of certain novel thiazolidinone derivatives substituted with benzothiazole or benzoxazole. Journal of Chemical and Pharmaceutical Research. 2013;5(2):318–27.

22. Abdellatif KRA, Abdelall EKA, Abdelgawad MA, Amin DME, Omar HA. Design, synthesis and biological evaluation of new 4-(4-substituted-anilino)quinoline derivatives as anticancer agents. Med Chem Res. 2017 May;26(5):929–39. Available from: <URL>.

23. Kandeel MM, Ali SM, ElALL E, Abdelgawad MA, Lamie PF. Synthesis and antitumor activity of novel pyrazolo [3,4-d] pyrimidines and related heterocycles. Der Pharma Chemica. 2012;4:1704–15.

24. Abdellatif KRA, Abdelgawad MA, Labib MB, Zidan TH. Synthesis and Biological Evaluation of New Diarylpyrazole and Triarylimidazoline Derivatives as Selective COX-2 Inhibitors. Archiv der Pharmazie. 2017 Aug;350(8):1600386. Available from: <URL>.

25. Abdellatif KRA, Abdelgawad MA, Elshemy HAH, Alsayed SSR, Kamel G. Synthesis and anti-inflammatory evaluation of new 1,3,5-triaryl-4,5-dihydro-1H-pyrazole derivatives possessing an aminosulphonyl pharmacophore. Arch Pharm Res. 2015 Nov;38(11):1932–42. Available from: <URL>.

26. Tipparaju SK, Joyasawal S, Pieroni M, Kaiser M, Brun R, Kozikowski AP. In Pursuit of Natural Product Leads: Synthesis and Biological Evaluation of 2-[3-hydroxy-2-[(3-

hydroxypyridine-2-carbonyl)amino]phenyl]benzoxazole-4-carboxylic acid (A-33853) and Its Analogues: Discovery of N -(2-Benzoxazol-2-ylphenyl)benzamides as Novel Antileishmanial Chemotypes. J Med Chem. 2008 Dec 11;51(23):7344–7. Available from: <URL>.

27. Akbay A, Ören İi, Temiz-Arpacı Ö, Akı-Sener E, Yalcçın I. Synthesis and HIV-1 Reverse Transcriptase Inhibitor Activity of Some 2,5,6-Substituted Benzoxazole, Benzimidazole, Benzothiazole and Oxazolo(4,5-b)pyridine Derivatives. Arzneimittel-forschung. 2011 Dec 25;53(04):266–71. Available from: <URL>.

28. Plemper RK, Erlandson KJ, Lakdawala AS, Sun A, Prussia A, Boonsombat J, et al. A target site for template-based design of measles virus entry inhibitors. Proceedings of the National Academy of Sciences of the Unitedt States of America. 2004 Apr 13;101(15):5628–33. Available from: <URL>.

29. Yildiz-Oren I, Tekiner-Gulbas B, Yalcin I, Temiz-Arpaci O, Akı-Sener E, Altanlar N. Synthesis and Antimicrobial Activity of New 2-[p-Substituted-benzyl]-5-[substituted-carbonylamino] benzoxazoles. Archiv der Pharmazie. 2004 Jul;337(7):402–10. Available from: <URL>.

30. Yoshida S, Shiokawa S, Kawano K ichi, Ito T, Murakami H, Suzuki H, et al. Orally Active Benzoxazole Derivative as 5-HT 3 Receptor Partial Agonist for Treatment of Diarrhea-Predominant Irritable Bowel Syndrome. J Med Chem. 2005 Nov 1;48(22):7075–9. Available from: <URL>.

31. Chen TR. Synthesis and characterization of cyclometalated iridium(III) complexes containing benzoxazole derivatives and different ancillary ligands. Journal of Organometallic Chemistry. 2008 Sep;693(19):3117–30. Available from: <URL>.

32. Varma RS, Kumar D. Manganese triacetate oxidation of phenolic schiffs bases: Synthesis of 2-arylbenzoxazoles. Journal of Heterocyclic Chem. 1998 Nov;35(6):1539–40. Available from: <URL>.

33. Chang J, Zhao K, Pan S. Synthesis of 2-arylbenzoxazoles via DDQ promoted oxidative cyclization of phenolic Schiff bases—a solution-phase strategy for library synthesis. Tetrahedron Letters. 2002 Feb;43(6):951–4. Available from: <URL>.

34. Nakagawa K, Onoue H, Sugita J. Oxidation with Nickel Peroxide. IV. The Preparation of Benzoxazoles from Schiff's Bases. Chem Pharm Bull. 1964;12(10):1135–8. Available from: <URL>.

35. Iranpoor N, Baltork IM. Mild, Efficient and Selective Opening of Epoxides with Alcohols Catalyzed by Ceric(IV) Ammonium Nitrate. Synthetic Communications. 1990 Sep;20(18):2789–97. Available from: <URL>.

36. Praveen C, Kumar KH, Muralidharan D, Perumal PT. Oxidative cyclization of thiophenolic and phenolic Schiff's bases promoted by PCC: a new oxidant for 2-substituted benzothiazoles and benzoxazoles. Tetrahedron. 2008 Mar;64(10):2369–74. Available from: <URL>.

37. Bose D, Idrees Mohd. Dess-Martin Periodinane Mediated Intramolecular Cyclization of Phenolic Azomethines: A Solution-Phase Strategy toward Benzoxazoles and Benzothiazoles. Synthesis. 2010 Feb;2010(03):398–402. Available from: <URL>.

38. Srivastava RG, Venkataramani PS. Barium Manganate Oxidation in Organic Synthesis: Part III: Oxidation of Schiff'S Bases to Benzimidazoles Benzoxazoles and Benzthiazoles. Synthetic Communications. 1988 Sep;18(13):1537–44. Available from: <URL>.

39. Patil MR, Bhanushali JT, Nagaraja BM, Keri RS. TiO 2 ZrO 2 composite: Synthesis, characterization and application as a facile, expeditious and recyclable catalyst for the synthesis of 2-aryl substituted benzoxazole derivatives. Comptes Rendus Chimie. 2018 Mar;21(3–4):399–407. Available from: <URL>.

40. Talodthaisong C, Plaeyao K, Mongseetong C, Boonta W, Srichaiyapol O, Patramanon R, et al. The Decoration of ZnO Nanoparticles by Gamma Aminobutyric Acid, Curcumin Derivative and Silver Nanoparticles: Synthesis, Characterization and Antibacterial Evaluation. Nanomaterials. 2021 Feb 9;11(2):442. Available from: <URL>.

41. Nguyen LHT, Nguyen TT, Nguyen HL, Doan TLH, Tran PH. A new superacid hafnium-based metal–organic framework as a highly active heterogeneous catalyst for the synthesis of benzoxazoles under solvent-free conditions. Catalysis Science & Technology. 2017;7(19):4346–50. Available from: <URL>.

42. Bhat R, Karhale S, Arde S, Helavi V. Acacia concinna pod catalyzed synthesis of 2-arylbenzothia/(oxa) zole derivatives. Iranian Journal of Catalysis. 2019;9(2):173–9.

43. Chikhale RV, Pant AM, Menghani SS, Wadibhasme PG, Khedekar PB. Facile and efficient synthesis of benzoxazole derivatives using novel catalytic activity of PEG-SO 3 H. Arabian Journal of Chemistry. 2017 Jul;10(5):715–25. Available from: <URL>.

44. Mazaheritehrani M, Asghari J, Orimi RL, Pahlavan S. Microwave-assisted synthesis of nano-sized cadmium oxide as a new and highly efficient catalyst for solvent free acylation of amines and alcohols. Asian Journal of Chemistry. 2010;22(4):2554.

45. Majdalawieh A, Kanan MC, El-Kadri O, Kanan SM. Recent Advances in Gold and Silver Nanoparticles: Synthesis and Applications. Journal of Nanoscience and Nanotechnology. 2014 Jul 1;14(7):4757–80. Available from: <URL>.

46. Aldeen TS, Mohamed HEA, Maaza M. Bio-inspired Single Phase Monteponite CdO Nanoparticles via Natural Extract of Phoenix roebelenii Palm Leaves. Journal of Inorganic and Organometallic Polymers and Materials. 2020 Nov;30(11):4691–701. Available from: <URL>.

47. Kumar S, Ahmed B, Ojha AK, Das J, Kumar A. Facile synthesis of CdO nanorods and exploiting its properties towards supercapacitor electrode materials and low power UV irradiation driven photocatalysis against methylene blue dye. Materials Research Bulletin. 2017 Jun;90:224–31. Available from: <URL>.

48. Taiwade MA. Synthesis, Characterization of Nanocrystalline CdFe2O4, its Antibacterial Activity against Escherichia Coli. Der Pharma Chemica. 2013;5:301–6.